

## IFAC SYMPOSIA SERIES

Janos Gertler, *Editor-in-Chief*, George Mason University, School of Information Technology and Engineering,  
Fairfax, VA 22030-4444, USA

- 
- DHURJATI & STEPHANOPOULOS: On-line Fault Detection and Supervision in the Chemical Process Industries (1993, No.1)  
BALCHEN *et al*: Dynamics and Control of Chemical Reactors, Distillation Columns and Batch Processes (1993, No.2)  
OLLERO & CAMACHO: Intelligent Components and Instruments for Control Applications (1993, No.3)  
ZAREMBA: Information Control Problems in Manufacturing Technology (1993, No.4)  
STASSEN: Analysis, Design and Evaluation of Man-Machine Systems (1993, No.5)  
VERBRUGGEN & RODD: Artificial Intelligence in Real-Time Control (1993, No.6)  
FLIESS: Nonlinear Control Systems Design (1993, No.7)  
DUGARD, M'SAAD & LANDAU: Adaptive Systems in Control and Signal Processing (1993, No.8)  
TU XUYAN: Modelling and Control of National Economies (1993, No.9)  
LIU, CHEN & ZHENG: Large Scale Systems: Theory and Applications (1993, No.10)  
GU YAN & CHEN ZHEN-YU: Automation in Mining, Mineral and Metal Processing (1993, No.11)  
DEBRA & GOTTCZEIN: Automatic Control in Aerospace (1993, No.12)  
KOPACEK & ALBERTOS: Low Cost Automation (1993, No.13)  
HARVEY & EMSPAK: Automated Systems Based on Human Skill (and Intelligence) (1993, No.14)
- 

- BARKER: Computer Aided Design in Control Systems (1992, No.1)  
KHEIR *et al*: Advances in Control Education (1992, No.2)  
BANYASZ & KEVICZKY: Identification and System Parameter Estimation (1992, No.3)  
LEVIS & STEPHANOUD: Distributed Intelligence Systems (1992, No.4)  
FRANKE & KRAUS: Design Methods of Control Systems (1992, No.5)  
ISERMANN & FREYERMUTH: Fault Detection, Supervision and Safety for Technical Processes (1992, No.6)  
TROCH *et al*: Robot Control (1992, No.7)  
NAJIM & DUFOUR: Advanced Control of Chemical Processes (1992, No.8)  
WELFONDER, LAUSTERER & WEBER: Control of Power Plants and Power Systems (1992, No.9)  
KARIM & STEPHANOPOULOS: Modeling and Control of Biotechnical Processes (1992, No.10)  
FREY: Safety of Computer Control Systems 1992

### NOTICE TO READERS

If your library is not already a standing/continuation order customer or subscriber to this series, may we recommend that you place a standing/continuation or subscription order to receive immediately upon publication all new volumes. Should you find that these volumes no longer serve your needs your order can be cancelled at any time without notice.

Copies of all previously published volumes are available. A fully descriptive catalogue will be gladly sent on request.

---

### AUTOMATICA and CONTROL ENGINEERING PRACTICE

The editors of the IFAC journals *Automatica* and *Control Engineering Practice* always welcome papers for publication. Manuscript requirements will be found in the journals. Manuscripts should be sent to:

#### *Automatica*

Professor H A Kwakernaak  
Deputy Editor-in-Chief  
AUTOMATIC  
Department of Applied  
Mathematics  
University of Twente  
P O Box 217, 7500 AE Enschede  
The Netherlands

#### *Control Engineering Practice*

Professor M G Rodd  
Editor-in-Chief, CEP  
Institute for Industrial  
Information Technology Ltd  
Innovation Centre  
Singleton Park  
Swansea SA2 8PP  
UK

*For a free sample copy of either journal please write to:*

Pergamon Press Ltd  
Headington Hill Hall  
Oxford OX3 0BW, UK

Pergamon Press Inc  
660 White Plains Road  
Tarrytown, NY 10591-5153, USA

*Full list of IFAC publications appears at the end of this volume*

# AUTOMATIC CONTROL IN AEROSPACE 1992

*Selected Papers from the 12th IFAC Symposium,  
Ottobrunn, Germany, 7 - 11 September 1992*

Edited by

**D.B. DeBRA**

*Department of Aeronautics and Astronautics,  
Stanford University, Stanford, USA*

and

**E. GOTTCZEIN**

*Deutsche Aerospace, Munich, Germany*

Published for the

INTERNATIONAL FEDERATION OF AUTOMATIC CONTROL

by

**PERGAMON PRESS**

OXFORD • NEW YORK • SEOUL • TOKYO

---

UK	Pergamon Press Ltd, Headington Hill Hall, Oxford OX3 0BW, England
USA	Pergamon Press, Inc., 660 White Plains Road, Tarrytown, New York 10591-5153, USA
KOREA	Pergamon Press Korea, KPO Box 315, Seoul 110-603, Korea
JAPAN	Pergamon Press Japan, Tsunashima Building Annex, 3-20-12 Yushima, Bunkyo-ku, Tokyo 113, Japan

---

This compilation copyright © 1993 IFAC

*All Rights Reserved. No part of this publication may be reproduced, stored in a retrieval system or transmitted in any form or by any means: electronic, electrostatic, magnetic tape, mechanical, photocopying, recording or otherwise, without permission in writing from the copyright holders.*

First edition 1993

**Library of Congress Cataloging in Publication Data**

A catalogue record for this book is available from the Library of Congress

**British Library Cataloguing in Publication Data**

A catalogue record for this book is available from the British Library

ISBN 0-08-041715-9

*These proceedings were reproduced by means of the photo-offset process using the manuscripts supplied by the authors of the different papers. The manuscripts have been typed using different typewriters and typefaces. The lay-out, figures and tables of some papers did not agree completely with the standard requirements: consequently the reproduction does not display complete uniformity. To ensure rapid publication this discrepancy could not be changed: nor could the English be checked completely. Therefore, the readers are asked to excuse any deficiencies of this publication which may be due to the above mentioned reasons.*

*The Editors*

# IFAC SYMPOSIUM ON AUTOMATIC CONTROL IN AEROSPACE 1992

*Sponsored by*

International Federation of Automatic Control (IFAC)  
Technical Committees on  
- Aerospace  
- Manufacturing Technology  
- Joint Working Group on Intelligent Autonomous Vehicles

*Co-sponsored by*

Deutsche Gesellschaft für Luft- und Raumfahrt (DGLR)  
Fachgruppe 4: Flugmechanik und Flugführung  
American Institute of Aeronautics and Astronautics (AIAA)

*Supported by*

Messerschmitt-Bölkow/Deutsche Aerospace

*Organized by*

VDI/VDE-Gesellschaft Mess- und Automatisierungstechnik (GMA)

*International Programme Committee*

D.B. DeBra (USA)	(Chairperson)	K. Reinel (D)
E. Gottzein (D)	(Co-chairperson)	U. Renner (D)
M. Amaud (F)		H. Reynaud (CDN)
L.V. Basanez (E)		A.J. Samecki (UK)
G. Bertoni (I)		J.Z. Sasiadek (CDN)
U. Butter (D)		S.M. Seltzer (USA)
S.C. Gupta (IND)		N.N. Sheremetjevsky (RUS)
W. Haeussermann (USA)		D. Soo (NL)
C.J. Harris (UK)		T. Tanabe (J)
J.W. Hursh (USA)		H. Tolle (D)
R.A. Jarvis (AUS)		P. Willmens (B)
G.I. Kharitonov (RUS)		W. Wimmer (D)
K. Lorell (USA)		J.C. Yang (PRC)
S. Manabe (J)		M.B. Zaremba (CDN)
S.C. Mohleji (USA)		G.R. Zou (PRC)
J.L. Nevins (USA)		
M.J. Pelegrin (F)		
J.J.M. Prins (NL)		

*National Organizing Committee*

E. Gottzein	(Chairperson)
H. Wiefels	(Co-chairperson)
H.J. Daume	
A. Keller	
R. Onken	
K. Reinel	
H. Rosenzweig	
G. Sachs	
H. Schreiber	
H. Siemann	
D. von Pelchrzim	

## **FOREWORD**

The 12th IFAC Symposium on Automatic Control in Aerospace is the latest of a series which was started in Stavanger, Norway, in 1965. For the first time the symposium is jointly sponsored by the Technical Committees on Aerospace and Manufacturing Technology, Joint Working Group on Intelligent Autonomous Vehicles and co-sponsored by the American Institute of Aeronautics and Astronautics (AIAA) and the Deutsche Gesellschaft für Luft-und Raumfahrt (DGLR).

The symposium location, the Wolf Ferrari Haus in Ottobrunn near München, Germany, was selected because it is very close to one of the centers of German aerospace activities.

Space systems technology has matured in some areas to the extent of becoming an essential part of our daily life and struggle for survival. Here before all others communication and earth observation by satellites are to be mentioned. Space vehicles have become increasingly complex and the number of missions has multiplied as a result of extending frontiers in the exploration of our planetary system and the universe beyond. The advancement of automatic control in aerospace reflects this development.

Some key areas are:

- The size and complexity of the spacecraft and the increasingly stringent performance requirements to be fulfilled in a harsh and even unpredictable environment. This requires extensive interaction between control system designers and system engineers to produce an overall sensible and optimal configuration.
- The merger of space vehicles and airplanes into space planes to launch and to retrieve payloads by reusable winged vehicles. Various two stage and single stage to orbit vehicles are under investigation. Space control engineering has to grow into aerospace control engineering to successfully design and evaluate the guidance, navigation and control systems for such vehicles.
- The demand to increase space automation and autonomy to reduce human involvement as much as possible in manned, man-tended and unmanned missions. This leads to decentralized hierarchical concepts for command, control and monitoring with man in supervising function only.

To cover the classical issues of guidance, navigation and control as well as the newly evolving key technologies adequately in a well rounded symposium program, a new approach was chosen to prepare and organise the Aerospace Control Symposium: Distinguished experts have been asked to prepare plenary presentations on principal topics and encourage other authors to submit complementary abstracts.

To cope with the large number of high quality papers and to continue with the philosophy of single sessions another important innovation was introduced: The organization of two story boards on two evenings during the symposium week each of these with around 32 poster presentations which were carefully selected to support the principal topic areas by posters, pictures, videos, and models. A generous time frame of three hours was reserved for each of these events to give authors and experts plenty of time for an in depth exchange of ideas and fruitful discussions.

You will find the list of the principal topics of the Aerospace Control '92 Symposium and their patrons on the following page. We owe it to their efforts and great dedication that we can offer you such an exciting and well rounded overview on the present state of the art and evolving new developments in aerospace control.

The Aerospace Control '92 international program committee recognises the high quality of the technical papers submitted and extends its thanks and appreciation to the authors for their effort and kind collaboration.

The organizers and the international program committee are greatly indebted to Messerschmitt-Bölkow-Blohm/Deutsche Aerospace for its generous support of this Aerospace Control '92 symposium.

**The Editors**

**Daniel B. DeBra**  
Stanford

**Eveline Gottzein**  
Ottobrunn

## **PRINCIPAL TOPICS**

Guidance, navigation and control of aerospace vehicles with emphasis on the atmospheric flight regime including air traffic management

**M. Pelegrin (F)**

Parallel processing architectures for aerospace applications

**H.A. Thompson (UK)**

GNC development life cycle experience with emphasis on validation and verification on ground and including flight experiments

**J. Broquet (F)**

New development in aerospace guidance and control

**R. Onken (D)**

Space robotics and manipulators

**J.Z. Sasiadek (CDN)**

Intelligent autonomous vehicles

**C.J. Harris (UK)**

Dynamics and control of flexible aerospace structures: Modelling, control and experimental verification

**S. Seltzer (USA)**

Control challenges from space and ground based astronomical telescopes

**D. Redding (USA)**

Trajectories optimization and guidance for ascent and descent

**K. Well (D)**

Emerging new technologies in sensors, actuators and on-board processing

**G. Monier (F)**

**TOWARDS A FULLY AUTOMATIC FLIGHT FOR  
PASSENGER AIRCRAFT  
AND  
SPACE AND EARTH REFERENCE SYSTEMS**

**M.J. Pélegrin**

*clo CERT, B.P. 4025, 31055 Toulouse Cédex, France*

*(This plenary paper arrived late and is placed at the end of this volume starting on page 531)*

## PARALLEL PROCESSING ARCHITECTURES FOR AEROSPACE APPLICATIONS

H.A. Thompson

*Marconi Radar and Control Systems, GEC Marconi, Chelmsford, CM1 3BN, UK*

**Abstract.** The advent of cheap processing has resulted in the use of parallel processing in a variety of fields. Image processing, signal processing, modelling and forming of radar images, interactive simulation and training, fluid dynamics, shock wave dynamics studies and spacecraft structures have all benefited from this new technology. However, the ability to make light-weight low-cost processors will result in dramatic changes in the application of digital processing to on-board aircraft systems. Traditionally computing has been performed in a centralised manner, however, it is now possible to think of a truly distributed avionics architecture with intelligence being assigned locally to actuators and sensors. In this paper the application of modern parallel processors and "smart" technology is explored highlighting the advantages of these technologies and also areas which need to be addressed when using parallel processing in distributed aircraft systems.

**Keywords** Parallel Processing, Distributed Architectures, Fault Tolerance, Smart Technology.

### PROCESSING DEMANDS IN AIRCRAFT

The improvement in processing power of microprocessors over the past two decades has been rapid. For instance, in 1969 the total computing power of a Jaguar Light attack aircraft was 10 MIPS. A present day aircraft such as the European Fighter Aircraft (Corney, 1986) uses 50 processors which are each capable of 10 MIPS in an equivalent processing card size about 1 hundredth the size of the Jaguar system (Endres, 1991).

The use of digital processing in aircraft has mainly been driven by the needs of the military market. Growing combat requirements have resulted in a highly complex and interactive array of avionics systems (Fig.1). Early requirements were for enhancements to improve mission effectiveness resulting in the development of systems such as fire control radar, electronic warfare and forward looking infra red sensors. More recently full Fly-By-Wire systems have been accepted as being essential for combat aircraft where a large degree of stability augmentation is needed to achieve high agility and manoeuvrability. Current aircraft, among them the F16, F18, Experimental Aircraft Project and European Fighter Aircraft (EFA) are totally reliant on the correct operation of the Flight Control System (FCS) to make the aircraft flyable. The increasing trend for the integration of weapon systems with the FCS now means that mission survivability of an

aircraft is directly related to the availability of a whole host of onboard systems. To maintain the high integrity levels demanded for military aircraft (typically one failure in  $10^6$  flying hours) high levels of fault tolerance are required. This is achieved through redundancy in the form of replicated computer lanes using dissimilar hardware and software to avoid common mode failures. The shear complexity of these new digital systems makes fault diagnosis and maintenance difficult requiring extensive built-in test and pre-flight test.

For commercial aircraft processing requirements are less severe being restricted mainly to flight management and navigation systems. Although Fly-By-Wire is now the logical choice for large airliners due to the reductions in expense, weight and hence fuel operating costs which are achievable, a cautious approach has been taken to its use due to safety concerns and the potential for disastrous loss of life in the case of a failure. Notable commercial applications of FBW to date are Concorde which used an early FBW analogue control and the Airbus which incorporated FBW in gradual stages going from fly-by-wire spoiler control in 1978 on the A310, to FBW slats, flaps and spoilers in 1983, to full fly-through-computer technology in 1984 on the A320 and A300-600 (Puyplat, 1991). Full FBW is now being embraced by Boeing for commercial aircraft following their experience on military aircraft.

Increased safety can also be achieved through flight envelope protection by feeding the pilot input through a computer which compares altitude, speed and configuration with the limits of the flight envelope to prevent the pilot from flying too fast, stalling or performing violent manoeuvres. It also allows safe input of full deflections in an emergency. Other benefits from using a flight management system (FMS) are that an "autothrust" facility can be provided which allows the pilot to select engine settings such as idle, climb, max-continuous, take-off/go-around or reverse to give optimum performance, extending engine life and minimising maintenance.

### CONTROL LAW COMPLEXITY

Traditionally a cautious approach has been taken to digital system integration. The F16 for instance originally flew using analogue electronics which restricted the type and complexity of the control laws used (Wills, 1988). Nowadays a fully digital solution is adopted from inception allowing far greater flexibility for control law design and implementation.

New airframe designs and extended aircraft performance envelopes (e.g. post stall manoeuvres) require complex control laws to be computed at high sampling rates. Although some very specialised integrated circuits have been designed, particularly where signal processing demands and computational loads are high, such as in Kalman Filtering for navigation systems and Fast Fourier Transforms for radar processing, in the case of flight controllers a more general purpose architecture is needed. The demands of new complex control laws in many cases outstrip the capabilities of a general purpose processor requiring a number of processors to be used in a parallel system to meet the required performance. A commercial example of this is the ASRAAM Missile developed by BAe which uses an array of 5 transputers to meet processing demands.

### CURRENT CONCERNS OF AVIONICS SYSTEMS DEVELOPERS

Before embarking upon a discussion of the use of parallel processing it is important to highlight some of the practicalities which effect how this technology can be used. The move towards increasingly complex avionics is not without reservations from procurers and for military avionics in particular reliability and availability are causing escalating costs. This presents a dilemma since to meet mission requirements functional capability, and hence the complexity, of weapons systems is increasing inexorably. The electronics systems alone have been estimated to account for 40% of the acquisition cost of a modern combat aircraft (Little, 1991). More importantly life-cycle costs and logistics support costs are also increased. Similar problems exist in the commercial

sector, to a lesser extent at present, but it is foreseen that this situation will worsen in the future.

As electronic systems have been added in a gradual manner or retrofitted to existing aircraft the general approach is to use subsystems with poor integration. This leads to high maintenance costs and a reduction in availability due to the many diverse types of boards, and at a lower level processors, being employed. It is these problems that aircraft manufacturers are now trying to address. In the following sections parallel implementations of controllers will be discussed. Later the key technologies which are required in order for truly distributed systems to become a reality are explored and the need for modular avionics and cohesive system integration will be highlighted.

### PARALLEL PROCESSING

There are two ways in which parallel processing can be exploited for aerospace applications. The first is to use parallel processing to speed up the execution time of a task. This is achieved through task subdivision to make several subtasks which are then executed simultaneously on a number of processing elements. The second is to exploit the inherent redundancy in a parallel processing system to introduce fault tolerance for safety-critical control tasks. Examples of such applications will be introduced in the next section but here the key attributes of a parallel processing system will first be described.

The two most common forms of parallel processing system are Single Instruction, Multiple Data stream (SIMD) and Multiple Instruction, Multiple Data stream (MIMD). The former tend to be restricted to specialist applications such as "front-end" radar processing where large numbers of similar operations are performed in very short sample times with a wide bandwidth for local communication. The latter are used for more general purpose applications since they can be programmed to perform a variety of tasks (such as control functions) and tend to have a narrower intercommunication bandwidth. The two most important attributes of a parallel system are *scalability* which affects the number of processors which can be connected and *granularity* which describes the amount of work allocated to individual processors.

For scalability one must take care when choosing a communication strategy between processors. If a bus structure is chosen then its throughput can constrain system expansion and introduce variable time delays dependent upon its loading. If dual-ported memory is used then the number of processors that can be attached is limited. An effective solution to this is to use a network approach of point-to-point links, such as that used by transputers (Inmos, 1989), so that as new processing elements are included the communication bandwidth increases.

The effects of granularity are equally important since it effects:

- 1) Size or power of individual microprocessors
- 2) Number of processors
- 3) Architecture of the system

Systems are categorised into fine, medium or coarse grain parallelism. SIMD systems are fine grain with large numbers of relatively small and simple processors that each execute a single statement. MIMD systems tend to be classed as medium or coarse grain depending on how the application software is divided. The key to obtaining the best performance from a parallel implementation is the partitioning of the application task into a granularity which exploits the architecture of the processing element efficiently while at the same time minimising communication between elements. This has been described by Stone (1987) as the R/C ratio where R represents compute time and C represents communication time.

#### **SOFTWARE PARTITIONING AND TASK ALLOCATION STRATEGIES**

Partitioning of signal processing functions, such as FFT's for radar processing for instance, is readily achieved through data parallelism and large arrays (5000+) of transputers giving GFLOP's of performance are already being exploited for signal processing by GEC Marconi (Thompson, 1992a). However, the concurrent realisation of a control law is more problematical particularly if many sequential paths exist through the code. To illustrate this the realisation of a typical avionics control system, a gas turbine engine controller, using parallel processing is presented to highlight how improved throughput and fault tolerance can be achieved. For a more detailed description of this work which was performed for Rolls-Royce Military Aero-Engines readers are referred to Thompson and Fleming (1991a) and Thompson (1992b).

#### **EXECUTION TIME REDUCTION**

Control of a gas turbine engine provides a suitably complex problem for demonstrating the power of parallel processing. A typical structure for a gas turbine engine controller is shown in Fig. 2. For dry engine control (i.e. an engine without reheat) partitioning can be performed using a heuristic approach. This is relatively straight forward taking advantage of the parallel limiter branches in the controller. The dynamic compensation, however, which is effectively an inverse model of the gas turbine is inherently sequential and presents a bottleneck in computation. This originally accounted for 61% of the overall controller execution time but was reduced to 35% by extracting further parallelism

from this section. The controller was mapped onto different arrays of transputers. Closed-loop results were acquired by also modelling the engine and partitioning this onto transputers so that real-time performance could be simulated. To further complicate the controller reheat control was added (see Fig. 3). This is more difficult to partition since several sequential paths exist which make several "optimum" solutions possible.

Timings on arrays of T800-20 transputers are shown in Table 1 for closed loop engine, controller and reheat simulations demonstrating the speed up in execution time relative to an implementation on a single processor. The reduction in speed-up as processors are added demonstrates clearly how the coarse grain parallelism used for partitioning within the controller is exhausted after relatively few processors are employed. This is a trade-off as if finer granularity is used communication overheads become more significant swamping any speed up obtained from parallel processing.

**TABLE 1 Transputer Mapping Results (ms)**

No. of Processors	1	2	3	4
Engine Timings	0.93	0.63	0.53	0.42
Controller Timings	0.52	0.36	0.31	0.30
Reheat Timings	0.95	0.61	0.56	0.47

Similar studies for autopilot control laws have also been performed and successfully test flown on a BAC 1-11 at RAE Bedford (Garcia-Nocetti, Thompson and De Oliveira, 1990). This work demonstrated control of an aircraft using an array of 5 transputers performing the controller. The difficulties encountered in the parallelisation of the control laws for this particular application highlighted the need for automatic parallelisation tools and lead to the development of a CAD tool. This allows the development of control laws in MATLAB which can then be directly downloaded into an occam program and run on transputer arrays as shown in Fig. 4.

#### **FAULT TOLERANCE**

In addition to improved computational performance the inherent redundancy in a parallel system can be exploited to give fault tolerance. This has been explored for gas turbine engine control and safety-critical flight control applications (Thompson and Fleming, 1991b; Thompson, 1992c). Here, gas turbine engine control is taken as an example although the ideas are applicable to other systems.

In the case of gas turbine engine control, sensors are extremely expensive so only two lanes of inputs and

outputs are available. Since failures in the input and output lanes are more likely, any fault tolerant architecture must allow direct connection to both lanes in the event of a computer failure. Traditionally these systems use two computer lanes each containing self-checking pairs of processors as shown in Fig. 5. If a disagreement occurs between the two lanes the system is switched to the secondary lane.

If parallel processing is used one can try to introduce the benefits of a triplex system into this inherently dual-lane system and replace the two controller boxes which are usually used with a single high integrity computer module. To achieve this two triad pairs as shown in Fig.6 were used to form an "overlapping triad" configuration to meet integrity requirements and prevent Byzantine disagreement (Lamport, 1978) by using a mixture of duplex and triplex topologies.

To exploit the parallel processing power the controller tasks were organised into three major tasks and two were performed on each of the member processors of a triad. This allowed a dual-lane comparison to be performed to identify a fault occurrence. The fault was then located by accessing the results of the opposing triad to allow a three-way vote to be performed. Once a permanent fault was located the system was switched to the appropriate lane. This system was successfully tested with various induced faults to exercise the fault detection and integration routines. The response of the system to a communication link failure is shown in Fig. 7. As two triads of processors are being used the reconfiguration time is minimal as the results from the other lane are used immediately.

A five processor system using "Hot Splicing" was also implemented (See Fig. 8) which used four processors to emulate the hardware redundancy of a quadruplex system but partitioned the software to remove some of the software overhead and exploit the parallel processing power. In this novel architecture an outer quadrant of four transputers performed the controller while a spare was available to take over the tasks of any one of the four outer processors. A programmable link switch was used to provide dynamic reconfiguration of transputer links and multiplexing in the event of a failure. An extension of the task overlapping scheme was employed where the controller was partitioned into four tasks with three tasks being performed per processor to exploit parallel processing. The spare transputer runs a core of the essential controller tasks. Exchange of results is performed at each iteration and voting takes place to identify a failed processor.

These ideas have been subsequently modified and developed further at Dowty Controls for a commercial Pratt and Whitney engine and to produce a general purpose processor for other safety-critical applications (Thompson, 1991c).

## DISTRIBUTED ARCHITECTURES AND NETWORK TOPOLOGIES

So far parallel processing at the avionics subsystem level has been described i.e. a current subsystem module is replaced by an array of parallel processors. If viewed in a wider context a natural extension of this in future systems is to truly distribute the control tasks around the system. There are many advantages to this from the point of view of resilience to failures and battle damage due to physical separation of control tasks. However, there are disadvantages. In this section the three main types of architecture used in avionics systems today, *Centralised*, *Federated* and *Distributed* are introduced and a brief description of each type of system is given to highlight their relative merits and pitfalls.

### Centralised Architectures

In centralised architectures the signal conditioning and computations take place in one or more computers located in the avionics bay with signals transmitted over one-way data buses. This has been the traditional approach as digital avionics evolved from analogue systems. The advantage of this technique is that the computers are located in the readily accessible avionics bay in a relatively benign environment simplifying equipment qualification. Software is also easier to write and validate since there are only a few processor types and a few large programs to be integrated. However, there are disadvantages. Long buses are needed to collect and distribute data and commands and there is increased vulnerability to damage from a single hazardous event in the avionics bay area. Software changes are also difficult due to the possible impact of changes on a large number of subroutines.

### Federated Architectures

In a federated architecture each major system such as thrust management or flight management share input and sensor data from a common set of hardware and share computer results over data buses. The advantage of this is that the design configuration and optimization of major systems can be performed independently (with perhaps some sharing of a common data base). Partitioning is thus easier since changes to system hardware or software are relatively simple to make. Federated architectures are frequently found in aircraft designed and built in the early 80's.

### Distributed Architecture

In a distributed architecture multiple processors throughout the aircraft are assigned computing tasks on a real-time basis as a function of mission phase and/or system status. Processing is performed in the sensors or actuators. There are many advantages to

this, fewer shorter buses are needed, program execution is faster, the system is intrinsically partitioned and vulnerability to a hazardous event is reduced since only a fraction of the entire capability will be destroyed. However, there are disadvantages since there is potentially a great diversity in processor types (aggravating software generation, validation and spares stocking). Processors may also be placed in more severe, less accessible environments such as the wings and empennage.

## COMMUNICATION TECHNIQUES

The architecture used centralised, federated or distributed, is highly dependent upon the bus standard which is adopted. Here the most common bus standards are highlighted with respect to suitability for distributed architectures to demonstrate their advantages and disadvantages.

ARINC 429 is a one-way bus with a single transmitter and one or more receivers on a single bus. In a typical installation with one transmitter per wire the weight of wire often exceeds the weight of the electronics because of the number of interconnections and communication interfaces required. Thus two-way buses which allow three types of topology, linear, mesh and star Fig. 9 are becoming more popular.

Linear systems tend to use MIL-STD-1553 which through time division multiplexing allows up to 32 units (monitors or remote terminals) to be attached to a data bus. There is a substantial reduction in cost and weight of wire and connectors using this approach. However, a central bus controller is required which is a potential single point of failure unless precautions are taken. The 1553 standard is limited to systems which do not require continuous high bandwidth transmission, e.g. video and fileservers, but in a multiple transmitter configuration is very good for distributed intelligence and sensors. This has not gone unnoticed and has lead to the development of the similar ARINC 629 high speed bi-directional bus.

Mesh topologies are an emerging concept which are being proposed for advanced fault tolerant systems. In a mesh topology failed or damaged mesh segments can be switched out by node controllers and re-routing can be used to re-establish capability allowing very high levels of fault tolerance. Mesh topologies are currently being exploited in space applications (Armstrong and Mercer, 1987; Castro and Gough, 1992) where long-life operational reliability is required.

Star topologies which use a point-to-point communication strategy are receiving more attention as interest in fibre optics increases. Fibre optics offer immunity to electromagnetic interference, lightning strike and inherent fault containment in the event of a

failure. The advantage of a star topology is that if the links between processors only carry data, rather than information required for the FCS operation, then software/hardware faults within a module can be effectively localised allowing fault recovery action to be taken. Also if sensors can made to be totally optical they do not require power supplies resulting in major weight savings. Star topologies tend to be adopted for optical avionics systems because linear and mesh designs are limited by the intrinsic losses in optical components. A star configuration reduces coupling losses but constrains flexibility. A standard, MIL-STD-1773, (the fibre optic version of 1553) exists but as yet lacks maturity since there are still practical problems in alignment and securing of fibres and keeping optical interfaces clean within connectors which need to be solved.

It is envisaged by the author that future aircraft will use parallel processing arrays connected via point-to-point communication links in a mesh topology for local computing, interconnected to other meshes via a star topology of replicated fibre optic buses and sensors.

## SMART ACTUATION

For distributed systems to become a reality smart actuation systems must be developed. Traditionally control has been centralised with dumb peripheral actuators being driven in feedback loops (See Fig. 10a). This leads to complex wiring which affects aircraft weight significantly. It has been estimated that the use of "smart" technology could produce a 25% reduction in wiring weight and simplify routing problems giving lower actuator installation and life cycle costs (Belmont, 1985). In addition the tight coupling found in present systems with numerous dumb peripherals can be reduced making alterations and maintenance easier.

The intelligence imparted to actuators can be used for local control and a number of other functions such as self-calibration, error detection and health monitoring if two-way communication with the main computer is employed (Fig. 10b). This will allow more accurate monitoring of performance and failures through improved BITE, increase the probability of correct failure diagnosis and allow reconfiguration on failure and automatic compensation for degradation by local feedback. By making the actuators "smart" they can be altered with little impact on the system. The flight control laws will not be related to the actuator so that, for instance, an output need only specify output for an elevator in degrees and the local controller will automatically compensate for mechanical nonlinearities, dead zones and offsets. This requires standardisation of data and scaling on the bus from the main computer, but this will also reduce interfacing problems with the actuator. Maintenance and support can be reduced by incorporating autorigging and self-

calibration functions and self-test features can be used to reduce test equipment. Flexibility may be incorporated so that a given actuator can be reprogrammed and used for a variety of functions.

Before smart actuation gains acceptance work needs to be performed in a number of areas. Distributed controller algorithms to decouple control loops must be developed. The level of error detection and redundancy required for actuators performing flight-critical control functions needs also to be specified. The architecture adopted may be dual or triple-lane, with analogue/digital mixtures and perhaps manual reversion. The method of actuator control particularly in digital case may also cause undue wear and fatigue on servo-valves and hydraulic lines due to the effect of quantisation. It may also create higher hydraulic fluid heating and leakage rates so there is a need to model and assess these effects. The availability of suitable electronic components is also a problem and although current packaging technology can meet vibration, shock, altitude and contaminant resistance (sand/dust/oil) levels, there is a need for high temperature electronics which can operate reliably at the temperatures experienced by actuators on the flying surfaces, typically around 200 degrees celsius (Przybylko, 1990). Other considerations which need addressing are cost and weight requirements for distribution of power to the actuator processor/s and the impact that requirements for two-way communication on the data bus will have.

### SMART STRUCTURES

A further future step which is possible is to integrate the intelligence into the fabric of the aircraft itself (Fig. 10c). Any material which reacts to other than a mechanical stimulus e.g. thermal, electrical, magnetic or light (via the photoelectric effect) input can be considered for "smart" applications. By embedding these materials in composites a highly distributed control system can be realised with rapid failure detection and control system reconfiguration. Perhaps even neural networks may be embedded into the composite to allow on-line system identification. For sensing, work has centred on the use of fibre optics through their response to thermal or mechanical stress. For both sensing and actuation piezoceramic materials and shape memory alloys (SMA) are being investigated.

PVDF actuators have been around for some time (Bailey and Hubbard, 1985) giving high damping at low vibrational levels, but poor authority make them impractical for a wide range of control problems. Emerging piezoceramic materials such as PZT (Lead zirconate-lead titanate blend) have fast response times, high efficiency, low temperature and radiation sensitivity and a potential for large force authority. The potential of this material to damp vibration modes

in a composite beam has been demonstrated by Griffen, Bronowicki and Betros (1991).

Embeddability in graphite epoxy composites is possible (to circumvent their brittle nature) but a major drawback is that piezoelectric actuators require high voltage electronics which generally increases the control system weight. There is now much interest in "Smart Patches" which contain surface mounted or embedded piezoceramic sensors and actuators along with miniaturised control and power electronics. A key problem will be deciding on the size and location of these patches which will require extensive system modelling.

Applications so far have been aimed at space systems such as space-based telescopes and optical interferometers where precise pointing, shape control, vibration control and low control system weight are required over a 10-20 year lifespan (Wada and Fanson, 1991). A positional accuracy of a few microns during an observation period for a structure which can be tens of metres in size is not uncommon. Health monitoring allows the structure to react to gradual ageing and failures. Once mature this technology will find increasing applications in aircraft particularly in active damping control. One possible future application could be in dynamically changing the aerofoil shape to give "wing warping" and active control. An added advantage is that smart control surfaces can be made inherently highly fault tolerant as control capability reduction is a function of the area damaged.

### THE FUTURE-NEURAL NETWORKS

Neural networks which rely on large scale SIMD parallelism are currently an active area for research. Application of neural networks in avionics has been limited to non-safety critical tasks such as mission management, image processing, identification and health monitoring. However, work is being performed on using neural networks for controllers (Hopfield, 1982; Narendra, 1990) and flight control applications for primary control of aircraft and maintenance of control for severely damaged aircraft are now beginning to be reported (Josin, 1990).

Pattern recognition applications for image processing, target and feature recognition are well documented. However, an interesting development is in pilot interfacing where systems are being developed to allow the pilot to talk to the aircraft (FBS, Fly-by-Speech) to change course and arm missiles while keeping "hands on controls and eyes out". The advantage of using a neural network for speech recognition is that there are several external factors, "garbling" from noise cancelling microphones, pilot stress effects of g force vibration (helicopters) and the oxygen mask which all effect the larynx and cause voice distortion. Currently Logica (U.K.) are

developing the Direct Voice Input (DVI) system for EFA which allows the pilot to issue instructions to key instruments using a 600 word vocabulary. In France the Sextant Avionique Dialogue Vocale is being developed for the Dassault Rafale and has already been flight tested on the Mirage 111, Rafale A and Aerospatiale Puma and Gazelle Helicopters. Although FBS will soon become a reality in combat aircraft, its use in commercial applications is not foreseen as pilots do not fly "hands on throttle and stick".

Neural networks are also being applied to Health Usage and Monitoring Systems (HUMS) for aircraft and rocket engines (Dietz, Kiech and Ali, 1989). Systems are being developed for the Apache AH64 helicopter and commercially Smiths Industries and Bristow Helicopters are jointly investigating HUMS for oil rig operation with a system which performs health trend analysis, recording temperature, speed, engine starts and running hours.

#### MODULAR AVIONICS AND INTEGRATION

Of course a move to a distributed avionics architecture introduces its own problems, a key problem being that of integration of the diverse avionics systems which are supplied by a number of manufacturers. In this final section the need for modular avionics and software in integrated systems is highlighted and a review of programmes that are investigating these areas is given. Motivating factors for modular avionics are affordability, reducing the cost of acquisition and ownership, size reductions, lower weight, more efficient power consumption and greater reliability and safety. Aircraft operators are particularly interested in modular avionics because they would like interchangeable general purpose LRU's and I/O boards to reduce maintenance costs. The Airbus for example currently uses 70-80 different types of processing cards. A more convenient architecture would have perhaps 10 general purpose processing units in a single easily accessible cabinet and a number of general purpose intelligent actuators to make support easier.

Several programmes have investigated these concepts and in the U.K. the Advanced Avionics Architectures and Packaging (A<sup>3</sup>P) feasibility study performed by RAE demonstrated the need for operating systems to allow portability of software, dynamic reconfiguration, task migration, and downloading of software from CD ROM. These ideas resulted in the APEX Core Executive Interface and Health Executive Interface (Little, 1991).

Currently the Control Technology Plan (CTP) a collaboration between British Aerospace and a number of British Companies and Universities is investigating fault tolerance via software means providing valuable input for ARINC 651. European

effort is not directed at the immediate future although EFA and Rafale will feature some modular avionics integration. The Experimental Aircraft Programme (EAP) a tri-National (UK, Germany, Italy) demonstrator programme intends to integrate a large variety of advanced technology features into one airframe. This includes composite structures, advanced avionics and displays, canard delta configuration and a high degree of negative static instability (Comey, 1986).

In America the USAF has also been a prime mover in this area with the Digital Avionics Information System (DAIS) programme (Endres, 1991) in the 1970's. This used a standard computer set for multiple applications with a common high order language and data multiplexing, sending different sets of data in packets through one network to reduce the complexity of integrated systems. Later in the 1980's the Pave Pillar program (Rowe, 1990) investigated integration for the next generation of combat aircraft. This program was significant in producing high speed integrated circuits and very large scale integration technology. The latest Pave Pace program aims to develop technologies for the next generation equipment using microwave millimetre wave integrated circuit technology based on one chip, incorporating the latest advances in parallel processing. New packaging and cooling techniques are also being investigated to improve equipment reliability.

Modular avionics is central to the electronics system design of the F-22 Advanced Tactical Fighter. The Common Integrated Processor (CIP) designed by Hughes for the F-22 is a powerful application of this concept. The total available signal and data processing performance is over 450 MIPS for general purpose processing and 9 billion operations per second of parallel programmable signal processing. The CIP performs all signal and data processing, digital input and output and data storage functions using a single integrated hardware and software design incorporating Pave Pillar concepts. The avionics configuration processes data from the integrated communications and navigation system, the identification and electronic combat systems, fire control radar, infra-red search and track sensors and mission avionics functions including display processing.

In the commercial sector the Boeing 777 has taken a major step towards cockpit systems integration with the Honeywell Airplane Information Management System (AIMS) avionics architecture and a new fault tolerant integrated Air Data/Inertial Reference System (Endres, 1991). In the system dual integrated cabinets contain central processing and input/output hardware to perform flight management, displays (flat panel liquid crystal), central maintenance, aircraft condition monitoring, digital communications management and engine data interface. Significant cost, weight,

reliability and maintenance benefits are obtained by using high speed processing, strict separation of software functions on common systems and application specific integrated circuits.

## CONCLUSION

This paper has presented the key ideas behind the use of parallel processing in avionics systems and demonstrated how it can be applied to speed-up an application and improve fault tolerance. Examples of systems which have been physically realised are given highlighting the benefits and problems in using this technology. The need for the development of CAD tools for parallelisation and load balancing of control laws for efficient mapping on to the architecture being used is demonstrated. A future look is then made to the development of distributed control architectures, highlighting the enabling technologies which are required (or which are already available) to make this possible. Bus architectures, smart actuation, smart structures and neural networks are explored. Finally modular avionics is vital for the application of this technology and an overview of development programmes in this area has been given.

## ACKNOWLEDGEMENTS

Thanks to Chris Stubbs of GEC Avionics Combat Aircraft Controls Division and Peter Jones, GEC Avionics Civil Controls Division, Rochester, U.K.

## REFERENCES

- Armstrong, R.H. and Mercer, I.C (1987). Final report on a programme to evaluate occam and the transputer for use in orbit. Smiths Associates Ltd.
- Bailey, T. and Hubbard, J.E. (1985). Piezoelectric-polymer active vibration control of a cantilever beam. Journal of Guidance, Control and Dynamics, Vol. 8, No. 5, Sept-Oct.
- Belmont, H.H. (1985). Digital Fault-Tolerant Flight Actuation Systems. AGARD-LS-143.
- Castro, H. and Gough, M.P. (1992). A reconfigurable transputer architecture for critical applications. In Joosen, W. and Milgrom, E. (Eds.), Parallel Computing from Theory to Sound Practice, EWPC Worshop, IOS Press, pp. 476-483.
- Corney, JM. (1986). The evolution of the EAP flight control system. Proc. International Symposium on Aeronautical Science and Technology of Indonesia, June.
- Dietz, W.E., Kiech, E.L. and Ali, M. (1989). Jet and rocket engine fault diagnosis in real-time. Journal of Neural Network Computing, Summer, pp. 5-18.
- Endres, G. (1991). Towards the intelligent aircraft. Interavia Aerospace Review, April pp. 57-61.
- Garcia-Nocetti, F., Thompson, H.A., De Oliveira, M.C.F. and Fleming, P.J. (1990). Implementation of a transputer-based flight controller. Proc. IEE, Part D, Vol. 137 No.3, May.
- Griffen, S.F., Bronowicki, A.J. and Betros, R.S. (1991). Piezoceramic sensors and actuators for smart composite structures. Proc. 30th IEEE Conference on Decision and Control, Brighton, Dec., pp. 2543-2545.
- Hopfield, J.J. (1982). Neural networks and physical systems with emergent collective computational abilities. Proc. National Academy of Science, USA 79, pp. 2254-2558.
- Inmos Ltd. The transputer reference manual. Prentice Hall, 1989.
- Josin, G.M. (1990). Development of a neural network autopilot model for a high performance aircraft. IJCNN, Vol. 2, pp. 547-554.
- Lamport, L. (1978). Time, clocks and the ordering of events in a distributed system. Communications of the ACM, Vol. 21, No. 7, pp. 558-565.
- Little, R. (1991). Advanced avionics for military needs. Computing and Control Engineering Journal Jan. pp. 29-34.
- Nahrendra, K.S. and Parthasarathy, K. (1990). Identification and control of dynamical systems using neural networks. IEEE Transactions on Neural Networks, Vol. 1, No. 1, March.
- Przybylko, S. (1990). High-temperature electronics for aircraft engines. Proc. AIAA/SAE/ASME/ASEE 26th Joint Propulsion Conference, Orlando.
- Rowe, J. (1990). Airborne computers take off. Defense Electronics, August.
- Stone, H.F. (1987). High-performance computer architectures. Addison Wesley.
- Thompson, H.A. and Fleming, P.J. (1991a). Parallel implementations of gas turbine simulations using transputers. IMechE Journal of Systems and Control Engineering, December.
- Thompson, H.A. and Fleming, P.J. (1991b). Fault-tolerant transputer arrays for gas turbine engine control. IEE Computing and Control Engineering Journal, Vol. 2, No.5 Sept.
- Thompson, H.A. (1991c). Transputer-based fault tolerance in safety-critical systems. Microprocessors and Microsystems, Vol. 15, No. 5, June, pp. 243-248.
- Thompson, H.A. (1992a). Applications of parallel processing in real-time radar signal processing. European Workshop on Parallel Computing, Barcelona, March.
- Thompson H.A. (1992b). Parallel processing for jet engine control. Springer-Verlag.
- Wada, B.K. and Fanson, J.L. (1991). Adaptive structures to enable future missions by relaxing ground test requirements. Proc. of 60th Shock and Vibration Symposium, Virginia Beach, VA, Nov., Vol.1, pp. 67-85.
- Wills, D.P.M. (1988). The evolution of a parallel processing computer for flight control. In Fleming, P.J. (Ed.), Parallel Processing in Control-The Transputer and Other Architectures, Peter Peregrinus Ltd., IEE.

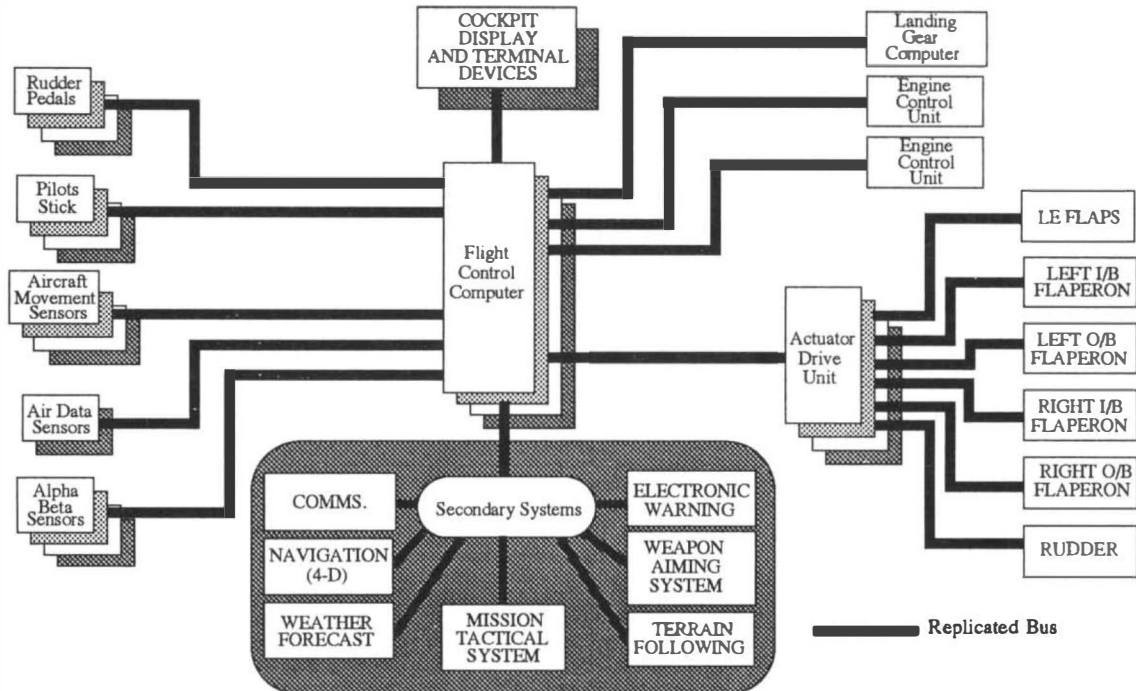


**Fig. 1 Typical Avionics System for a Combat Aircraft**

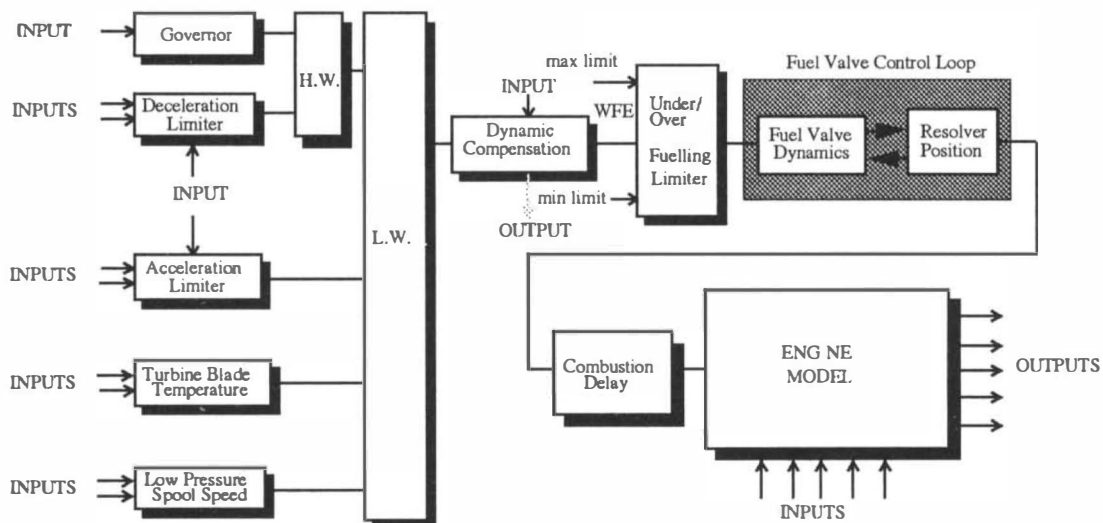


**Fig. 2 Dry Engine Control**

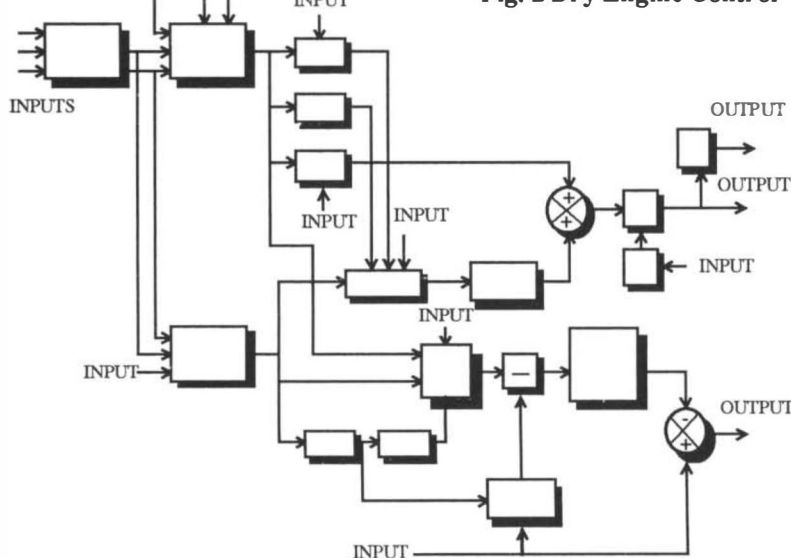


**Fig. 3 Reheat Control**

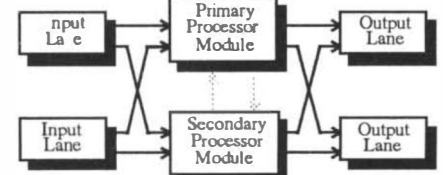


**Fig. 5 Dual Lane System**

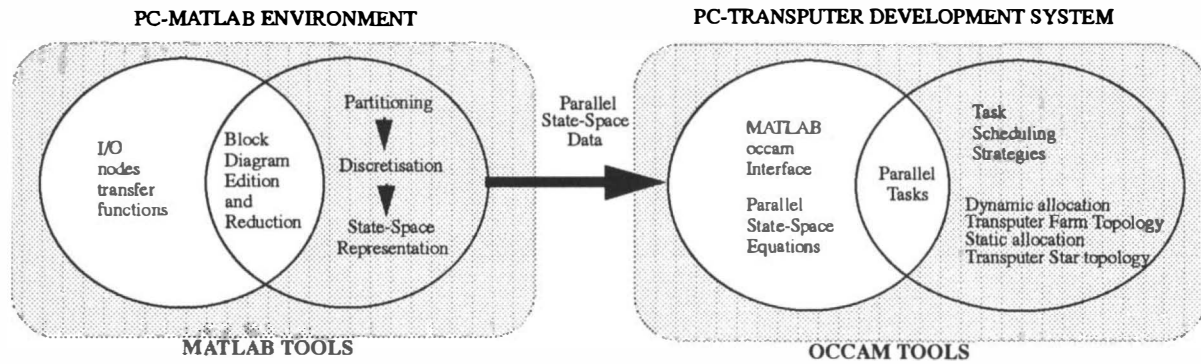


**Fig. 4 Software Tools for mapping controllers on a transputer-based system**

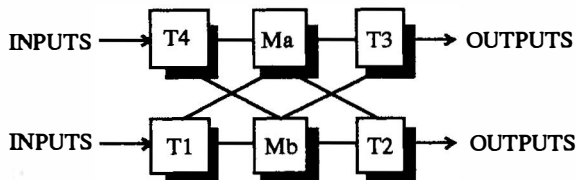


**Fig. 6 Overlapping Triads Topology**

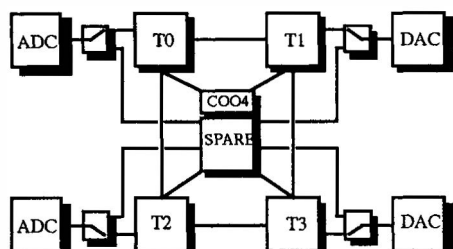


**Fig. 8 Hot Splicing Topology**

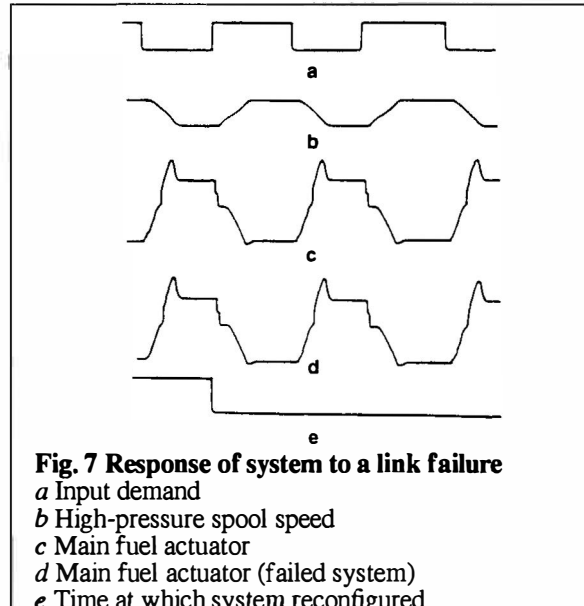


**Fig. 7 Response of system to a link failure**

**a** Input demand  
**b** High-pressure spool speed  
**c** Main fuel actuator  
**d** Main fuel actuator (failed system)  
**e** Time at which system reconfigured

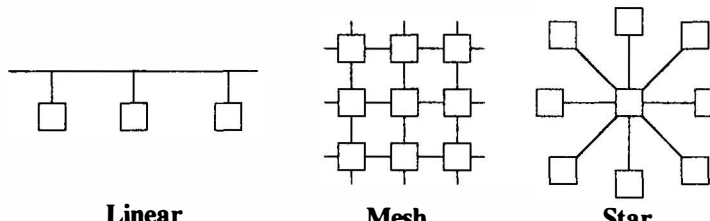


**Fig. 9 Communication Topologies**

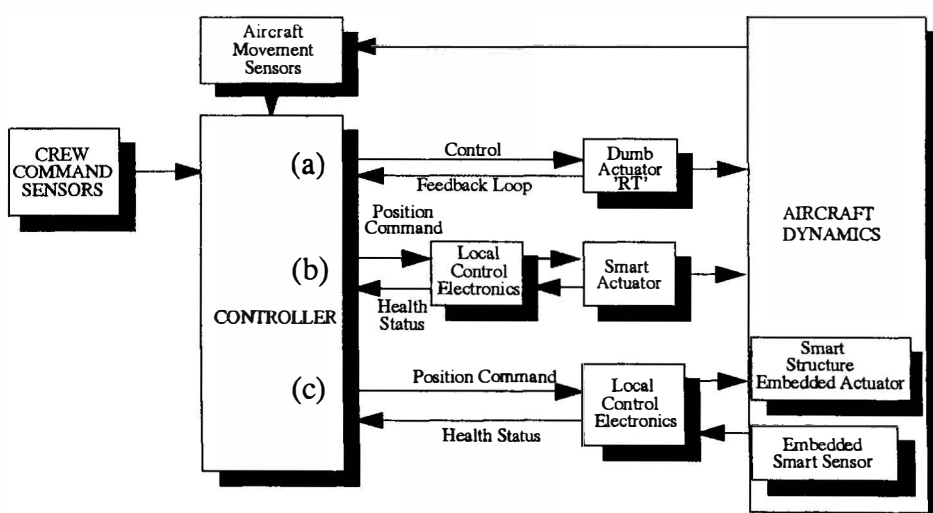


**Fig. 10 The move from Conventional Actuation Systems to Smart Actuators, to Smart Structures**

# GNC AND AUTOMATIC CONTROL SYSTEMS DEVELOPMENT, VALIDATION AND VERIFICATION

J. Broquet, B. Claudinon, E. d'Andrimont and A. Benoit

MATRA MARCONI Space, 31 rue des Cosmonautes, Z.I. du Palais, 31077 Toulouse Cedex, France

**Abstract :** During the last twenty years, Attitude and Orbit Control Subsystems of increasing performance and complexity have been developed in Europe. The test requirements have followed the same way. A large experience has been gained in the area of AOCS development and validation.

In this paper, a description of AOCS test set-ups is given from early experiences in the seventies to modern developments like TELECOM 2 and HELIOS. The key elements of those test set-ups are described. The overall development and validation logics for AOCS follows with a specific discussion of in-orbit experience. Future trends, as seen by the authors, are then identified.

**Keywords :** AOCS, test, validation, simulation, life cycle, in-orbit experience.

## 1 - INTRODUCTION

For more than twenty years, European satellite developments have been subdivided into subsystems. The Attitude and Orbit Control Subsystem (AOCS) is likely the most complex one in terms of functional requirements and interfaces with the satellite system engineering. The validation and verification of its integrity and performance has involved complex closed loop test benches where all equipments of the loop (sensors, computers, electronics, actuators) are physically implemented with a representative simulation of the satellite attitude motion.

AOCS subsystem tests are the final step of the AOCS validation process, before delivery and integration onto the platform. They make safer performance prediction made with theoretical simulations through a cross-correlation of the AOCS behaviour in few typical cases. They are also a powerful way to check the electrical and software integrity of the subsystem, since all interfaces are then performing under real situation. Finally, during AOCS subsystem tests, the first verification of AOCS operability is performed, thus allowing to anticipate problems which could appear later in the development or even in orbit.

The considerable experience accumulated in-orbit has increased our confidence in models used especially for environment and spacecraft dynamics. A continuous feedback is done to the AOCS design, architecture, technology and to the validation approach.

For commercial programs, when most of the satellite technology is recurring, a two steps satellite development is implemented, leading to avoid subsystem specifications and

then to cancel the need for AOCS subsystem tests. The AOCS function is then verified with uncomplete and simple environment during system test.

The paper is presenting AOCS subsystem tests as key steps in a satellite AOCS validation process. Its future, as seen by the authors, is also addressed.

## 2 - AOCS TEST SET-UPS

### 2.1 - Foreword

In the seventies, the prime concern when devising AOCS test benches was to get a good physical representativity of the satellite dynamics by putting the combined AOCS sensors and actuators in real motion. For instance, the MATRA OTS AOCS test set-up, shown in Figure 1, used an hybrid approach :

- an air bearing table to have free dynamics around the pitch axis (control through the infra-red earth sensor and the momentum wheel),
- simulated motions on the roll and yaw axis.

A more complex approach was followed by MBB on the SYMPHONIE satellite with the design of a three axis servo controlled platform supporting the sensors.

This class of test bench is still in use today, either for small satellites equipped with simple and relatively low performance AOCS, or for sounding rockets GNC subsystems, where the movement can be generated by the real cold gas thrusters.

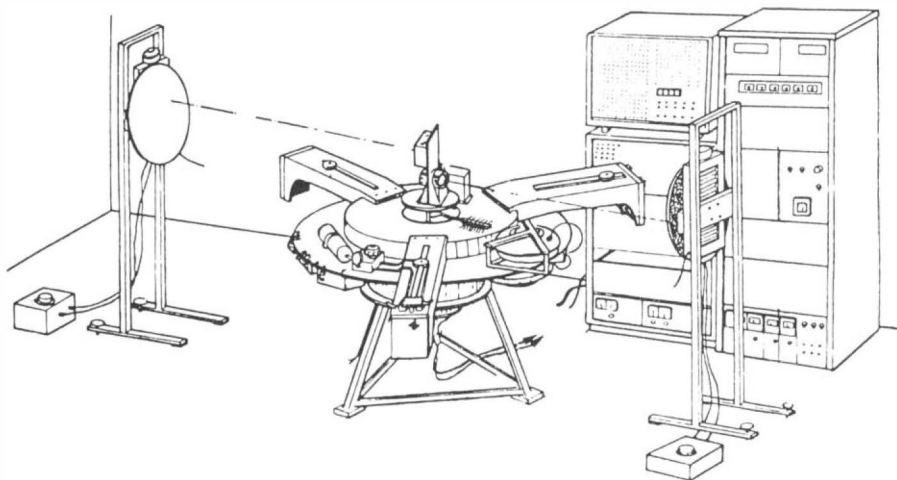


Figure 1 : OTS AOCS test set-up overview

However, since the accuracy and complexity of AOCS have increased, the modern AOCS subsystem test benches design follows a modular approach in which only the critical sensors are physically stimulated, independently of the actuators. The following paragraphs present the AOCS subsystem test set-ups used by MMS for the EURECA family of Telecommunication satellites, the first generation of SPOT/ERS observation satellites, and finally the HELIOS military observation satellite, to be launched in 1994.

They illustrate the modular approach followed which can be adapted to the specific test requirements of each AOCS. The availability of standard computers having an ever greater computing capacity makes possible the simulation in real time of the satellite dynamics and orbital kinematics "in-the-loop", with the level of modelling accuracy necessary with respect to the AOCS performances. Thus real and accurate motion can be limited to individual sensors.

## 2.2 - EURECA telecommunication satellites

An overview photograph of the AOCS subsystem test facility is shown in Figure 2. One can notice that most AOCS Flight Model sub-assemblies are present, namely :

- the Control Law Electronics (CLE) Computer on which the AOCS real-time control software runs,
- one Infra Red Earth Sensor (out of two),
- the two gyropackages,
- the two fixed momentum wheels.

This facility has been used successfully to test the AOCS of the INMARSAT II and TELECOM 2 satellites, which are the first of the EURECA family. It has also been used in a slightly modified version to test the ITALSAT F1 AOCS.

A functional synopsis of the test set-up is shown in Figure 3. The AOCS sensors are either physically installed or

simulated :

- one Infra Red Earth Sensor is optically simulated by an Earth Simulator. The other one being simulated,
- the two Gyro Packages are simulated by high accuracy current generators,
- the simpler sensors of which the models are straightforward, namely the Solar Array Sun Sensors (SASS), the Sun Acquisition Sensors (SAS) and the Earth and Sun elevation Sensor (ESS), are simulated and their output signals are generated by electrical stimuli generators.

On the output side of the Actuator Drive Electronics, only the two fixed momentum wheels are physically installed. Both the thrusters and the solar array drive motors are simulated by electric loads incorporating the detection of the actuator commands.

The loop between the actuator outputs and the sensor inputs is closed within the test bench by a simulation software running in real time ; its algorithms model with high fidelity the dynamics and kinematics of the satellite on its orbit. It is completed for missing sensors and actuators by corresponding models : i.e. for actuators the electrical commands are converted into torques applied around the satellite three axis, through the "actuator transforms" block.

For EURECA satellites having identical AOCS architectures and closely related characteristics, the AOCS subsystem test set-up can be simplified to a simpler scheme, shown in Figure 4. Only a functional breadboard of the Control Law Electronics computer loaded with the flight control software is put inside the real time control loop. All sensors and actuators are simulated. This approach, which is more economical than a "full fledged" AOCS test campaign, still permits a thorough validation of the flight software "in the loop", in real time, with an accuracy as high as the one obtained with complete control simulations, which are not run in real time.

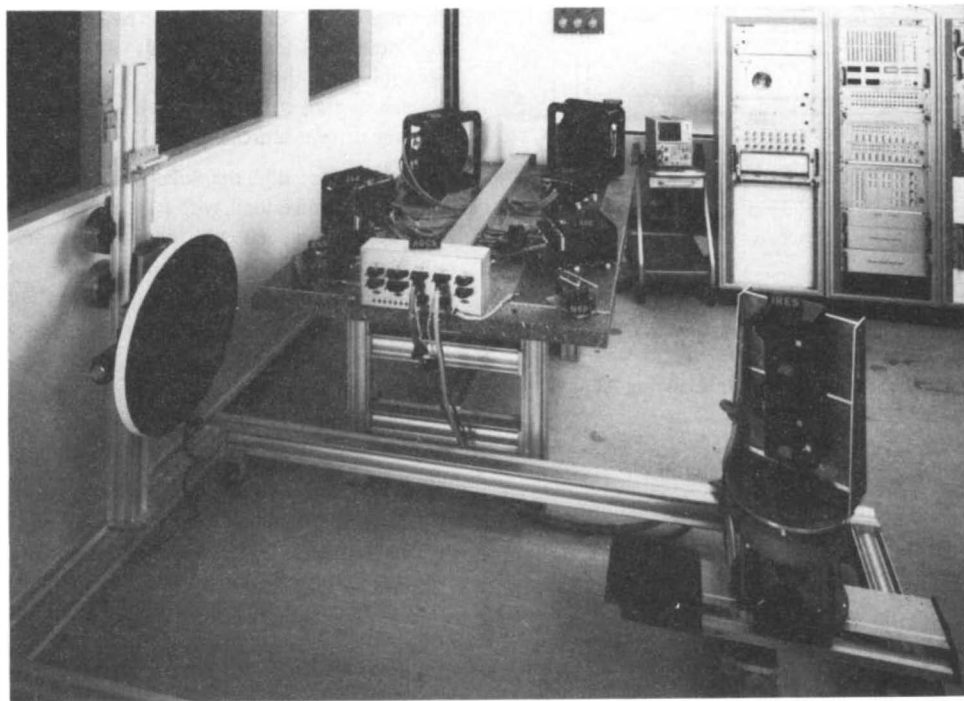


Figure 2 : EUROSTAR AOCS test set-up overview

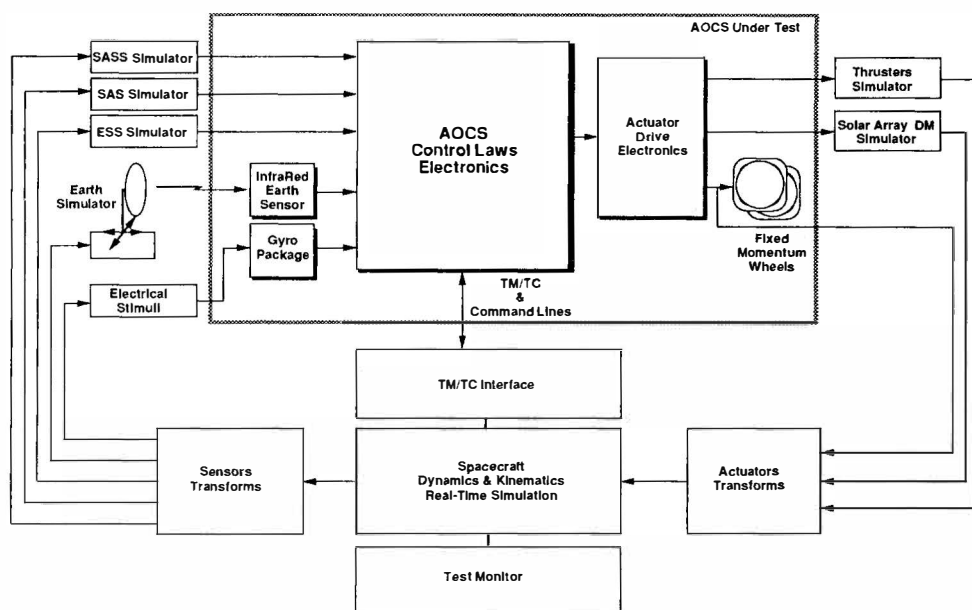


Figure 3 : Functional synopsis of EUROSTAR AOCS test set-up

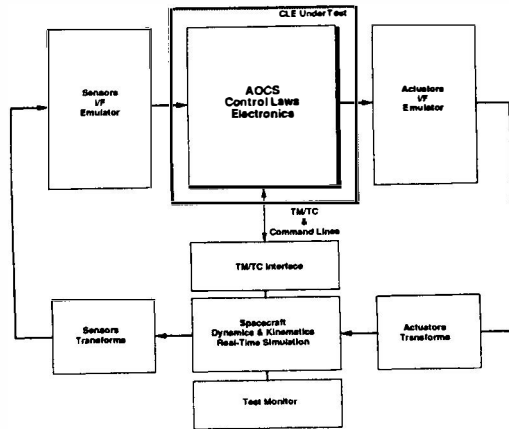


Figure 4 : Simplified test set-up for recurring AOCS

### 2.3 - SPOT 1 and ERS 1 Observation Satellites

These two satellites share the same SPOT platform, and their AOCS architectures are very similar, even if their flight characteristics are different : SPOT 1 is equipped with two HRV (High Resolution Visible) cameras, whilst ERS is equipped with a Synthetic Aperture Radar.

Basically, the same test facility was used for the integration and validation tests of both satellites ; its functional synopsis in ERS configuration is shown in Figure 5.

On the sensor side, all sensors are physically present. However, only one earth sensor and one sun sensor out of two are stimulated optically, respectively by an earth simulator and a sun simulator. The redundant sensors are stimulated by electrical signals injected in the sensor electronics at the output of the optical to electrical conversion stage. The gyros are stimulated by very high accuracy current sources.

On the actuator side, the Solar Array Drive Mechanism is linked to an active load, with a gyroscope and a motor. The three reaction wheels and the two magneto-couplers are also physically installed. Only the thrusters are simulated by electrical loads incorporating detection circuits to measure the thrusters firing durations.

As for the EUROSTAR AOCS test set-up, the dynamics and kinematics of the satellite on its orbit are simulated "in the loop" in real time, using a simulation software similar to the one used for functional studies, with some simplifications.

The actuators command signals or measured parameters are converted by the "Actuators Transforms" block to forces and torques which are input to the dynamics and kinematics model. This one computes the new state vector of the satellite (position, attitude and rotation rates) which are then converted into command signals fed to the earth and sun simulator motorized tables and the signal generators emulating the missing sensors outputs.

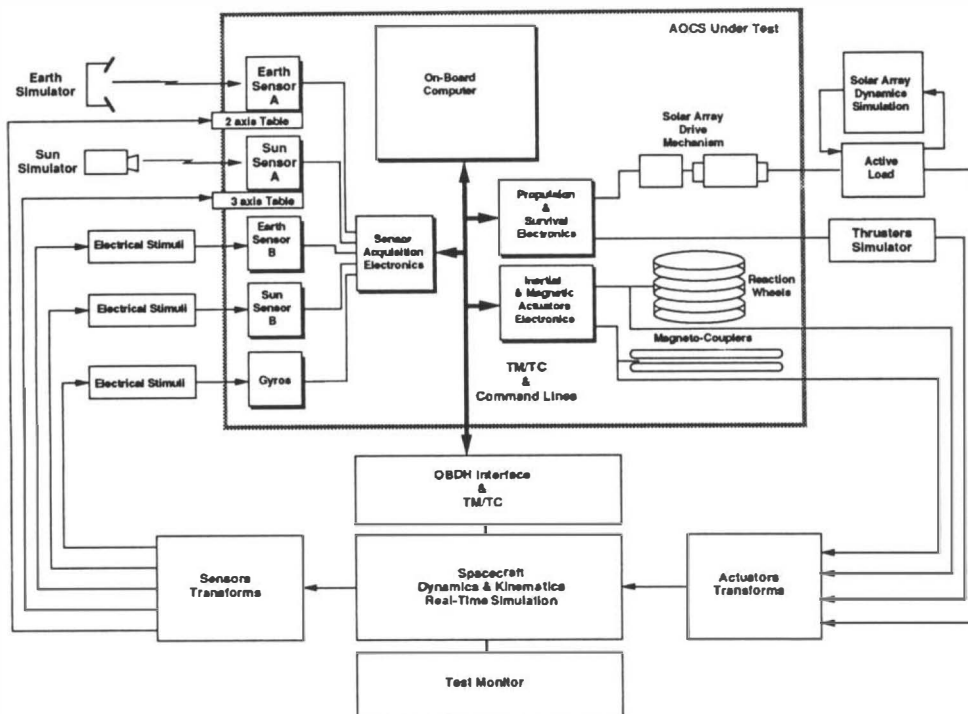


Figure 5 : Functional synopsis of ERS AOCS test set-up

## 2.4 - HELIOS observation satellite

This "second generation" military satellite is under development. Its AOCS has an architecture similar to the one used for SPOT and ERS first generation satellite, but is upgraded itself by very high accuracy gyroscopes and the addition of star sensors.

The AOCS test bench designed by MMS is drawn along the same lines as the previous SPOT and ERS test benches, but represents a further step in performance and complexity, given the very stringent test specifications.

A general view of the test facility is shown in Figure 6, and the functional synopsis of the test set-up is shown in Figure 7.

The outstanding differences with respect to the SPOT/ERS facility are a three-axis table capability to stimulate "physically" the gyros in some phases of the test and a star simulator to stimulate optically the star sensor. Another

visible difference is the simplification of the solar array drive motor set-up which is no longer loaded. This is justified by the in-orbit experience of SPOT 1 and SPOT 2, which validated this element characteristics.

A less visible difference is the modularity of the test bench hardware and software, which allows to test separately each major sub-assembly (i.e. the sensors acquisition and survival sub-assembly, the solar array and propulsion electronics, and the inertial and magnetic actuators electronics) in open or closed loop, before running complete subsystem tests.

In the full HELIOS test configuration, all elements of the test set-up are active and work together in real time. The dynamics and kinematics simulation software is identical to the one used for functional studies, thanks to the very powerful real time computing capability of the test bench.

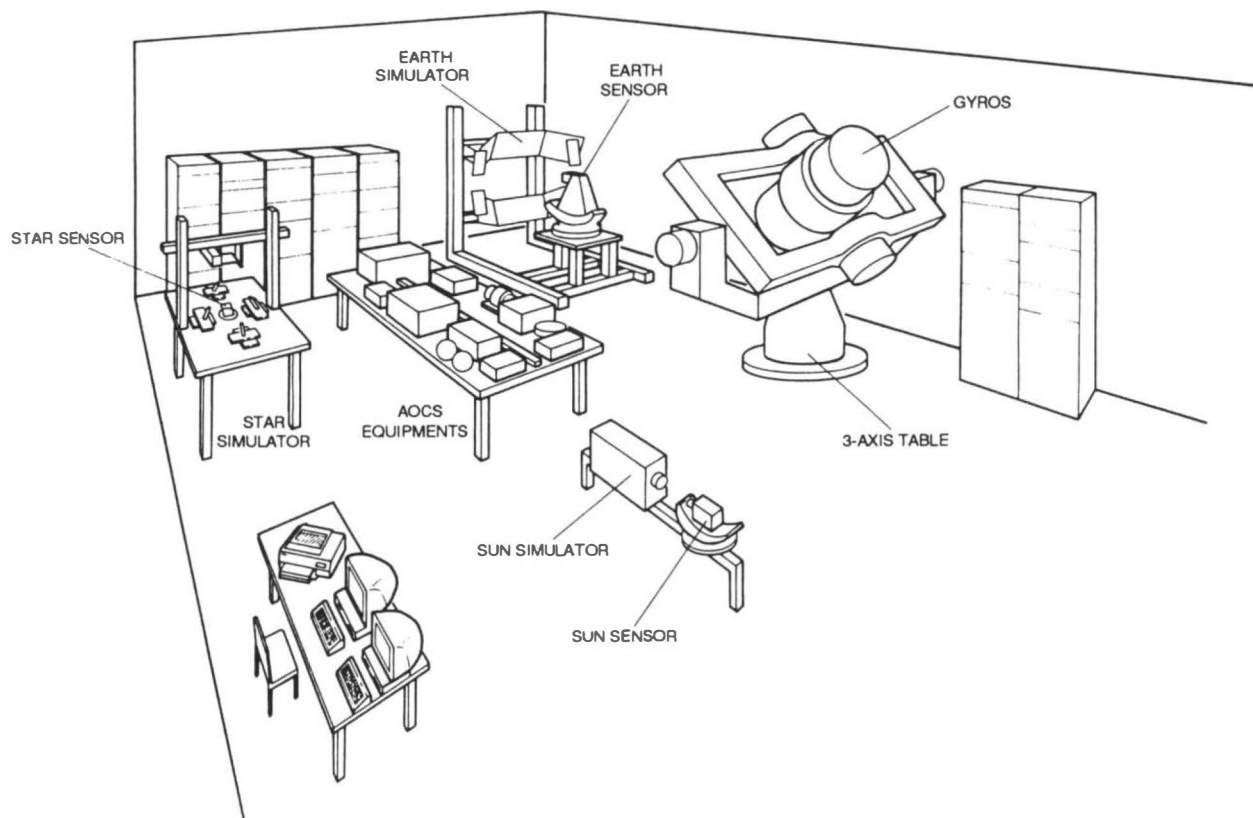


Figure 6 : HELIOS AOCS test set-up overview

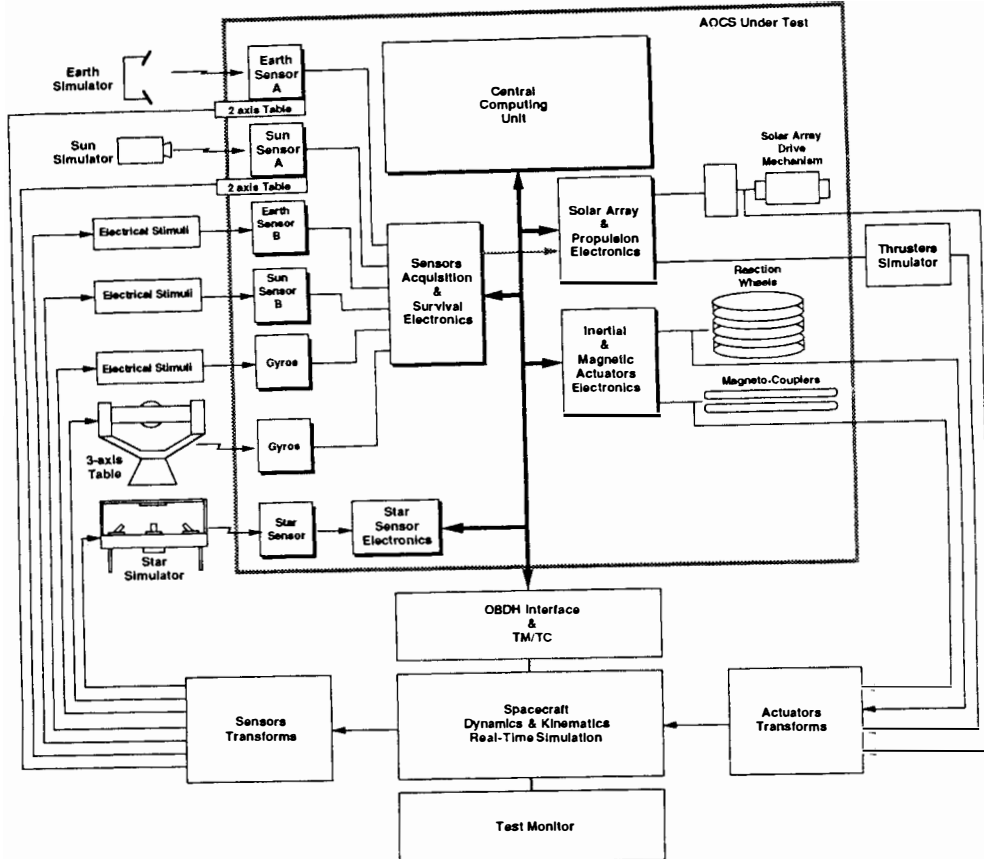


Figure 7 : Functional synopsis of HELIOS AOCS test set-up

### 3 - KEY ELEMENTS OF AOCS TESTS

#### 3.1 - Dynamics simulator

Both one axis and three axis air bearing tables were developed in the mid-sixties, offering a direct representation of the system behaviour through a free dynamics simulator.

A structure, representative of the satellite inertiae, supports sensors and actuators such as reaction wheels or cold gas thrusters. This method is mostly adapted to rigid body dynamics simulation and can still be used for testing small satellite simple AOCS or sounding rockets control systems.

A physical approach can also be used to verify a motor in its mechanical environment. The solar array drive mechanism (SADM) of SPOT 1, for instance, generates torque harmonic components which can interact with the array flexible modes and affect the rate stability of the platform. A specific set-up has been incorporated in SPOT 1 subsystem test. The SADM is passively loaded by a beam supporting a gyroscope and actively loaded by an external

torque computed by the test processor. Flexible modes, torque harmonic components and irregularities are measured by the gyroscope and fed back.

The increasing complexity and accuracy of modern spacecraft and AOCS are no longer compatible with a real physical set-up which is limited by gravity and friction, limited rates and angles, and built-in parameters. On the other hand, digital computers are today fast and accurate enough to run mathematical models of the satellite dynamics and environment, which provide an extremely good prediction for exoatmospheric vehicles.

This approach permits a detailed modelling of the disturbing forces and torques acting on the satellite. A complete versatility is provided for the mass properties, initial conditions and range of variation of the dynamic parameters. The kinematics is generally worked out using a quaternion representation and it feeds either sensor models or the commands of physical stimulators.

### 3.2 - Sensors and Actuators

This paragraph is a fast walk-through of the ways sensors and actuators are handled in the subsystem test set-up described in the previous chapter.

#### **Infra-red Earth Sensors**

Those sensors are used on geostationary (GEO) communication satellites as well as low earth orbit (LEO) observation satellites. Their design is complex and therefore their modelling is not always accurate. This is why they are physically installed in the test set-ups, and are stimulated by earth simulators of different types, depending on the apparent earth diameter.

The type used for LEO satellites is shown in Figure 8. The rotations around the roll and pitch axis are simulated by a motorized two axis table. The earth to space transitions are simulated by heated and cold panels.

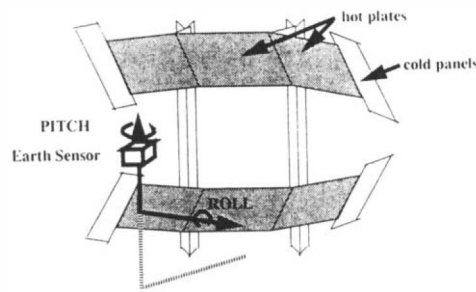


Figure 8 : Earth simulator

#### **Sun Sensors**

Coarse analog sun sensors are most often simulated. However, for high accuracy digital sensors (LEO satellites, GEO 3-axis transfer), a sun simulator of the type shown in Figure 9 is used. A motorized two axis table simulates the rotation of the satellite with respect to the sun direction.

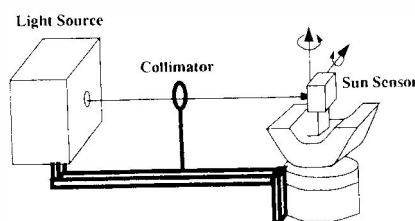


Figure 9 : Sun simulator

#### **Stellar Sensors**

MMS has designed under CNES contract a star simulator of which an outline is shown in Figure 10. It has the capability to simulate simultaneously the movements of four stars of programmable magnitude. Another and more complex approach consists in simulating the celestial sphere, as seen by the sensor. Both approaches have their merits and drawbacks ; the first one allows for more accurate positioning of the stars with respect to the sensor line of sight.

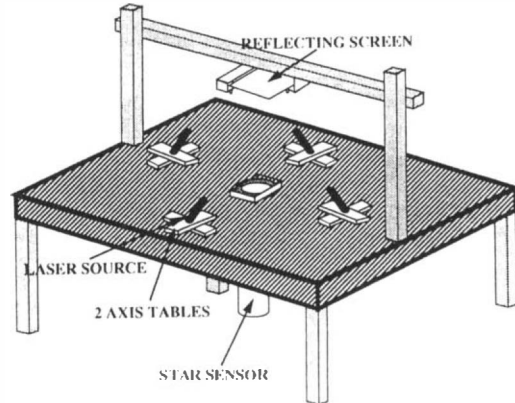


Figure 10 : Stellar simulator

#### **Propulsion**

Apart from cold gas thrusters, it is not advisable to release hot gases in clean room environments. However, since the environment is not representative, the measurements of the forces and torques would not be significant. This is why the straightforward method of measuring only the firing times at the inputs of electrical loads simulating the thruster command electronics is used. However, it implies that an accurate model of each thruster in its spacecraft environment is available.

#### **Fixed momentum and reaction wheels**

If the wheels are available, the easiest way consists in installing them in the AOCS test set-up, and deriving the torque from measurements of the speed and/or current. For wheels which are not contained in vacuum enclosures, it is necessary to install them in a vacuum container.

#### **Mechanisms**

The mechanisms which are directly controlled by the AOCS are the solar array drive mechanisms. The previous paragraphs have shown that three methods are used : either to simulate the mechanism or to install it physically, with or without a mechanical load. In the latter case, if the combined effects of the motor commands and the solar panels flexible modes have to be simulated, an active load is necessary.

#### **Gyroscopes**

Because of the difficulty of modelling gyroscopes, it is preferable to have the real gyroscopes in the loop. The most basic technique to stimulate them consists in generating a highly accurate current which is input in the control loop of the gyroscope. A more representative method is to use a three axis table. However, the response time of the table is not always fast enough to simulate the dynamics of the satellite during manoeuvres.

#### 4 - DEVELOPMENT AND VALIDATION LOGICS FOR AOCS

The subsystem test facilities above mentioned are major contributors to AOCS development and validation. They are part of a wider logic which is shown on Figure 11. An important coordination is led by the AOCS functional studies. They have strong interactions with equipments and software developments, and with the characterisation of the satellite dynamics and environment. Having successfully passed the subsystem tests, the AOCS still requires some verifications at system and satellite level.

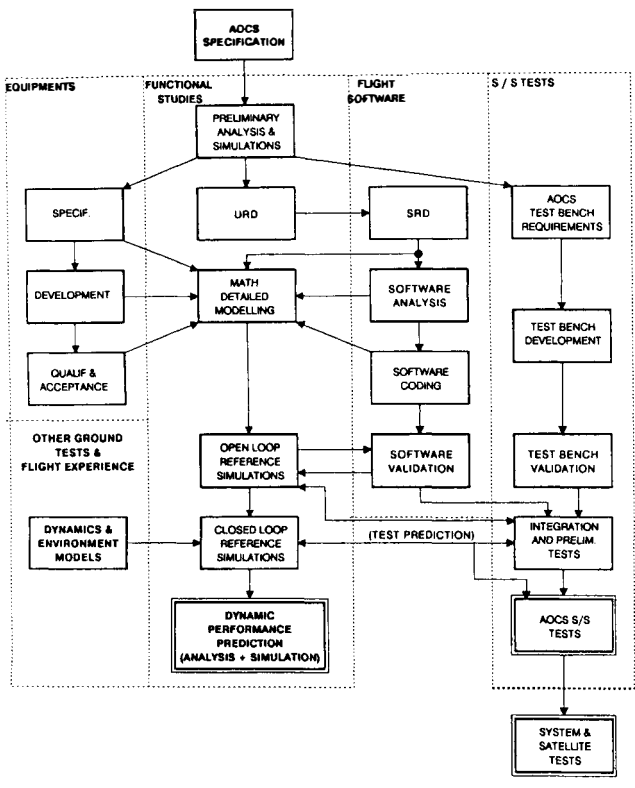


Figure 11 : AOCS development and verification logics

##### 4.1 - Equipment activities

The major milestone of the development of AOCS equipments (sensors, actuators, electronics) is the qualification and acceptance. Equipment specifications, General Design and Interface Requirements are the main references against which major items are verified : technological aspects such as reliability and life duration, power budget, interfaces, and performances aspects such as noise, biases.

Equipment manufacturers use a dedicated test set-up, providing high accuracy but limited environment compared with the subsystem test facility. One output of the equipment activities is also the mathematical model of the equipment which will be used for AOCS analysis and simulations. Characterisation and validation of the equipment model can be necessary and are sometimes conducted on dedicated rigs (possibly parts of the subsystem test facility).

##### 4.2 - Dynamics and environment

The modelling of the satellite dynamics and environment used for the AOCS simulations is validated through ground tests and in-orbit experience.

Ground tests can include for example flexible modes characterisation, sloshing time constant determination with a drop-free tower, microvibration level measurements. In-orbit analysis appear however to be very useful to confirm or complete ground analysis and tests.

##### 4.3 - Functional studies

AOCS development is characterised by a very tough functional studies activity taking place all along the project. It consists in AOCS functional design and modelling parameters tuning and optimisation, and performance prediction through detailed sensitivity analysis and closed-loop simulations.

Preliminary analysis and simulations contribute to the delivery of specifications towards equipment manufacturers, User Requirement Document (URD) towards the Software Engineer and general subsystem test bench requirements.

All the mathematical models are coded (usually FORTRAN or C) and are the building blocks of the detailed closed-loop simulation software. This computer program, running faster than real time, sweeping easily sensitive input parameters (such as satellite mass properties, sensor and actuator characteristics, initial conditions) appears to be the major tool for the AOCS functional prediction (pointing, accuracy and stability, acquisition capability, fuel budget, etc). Numerous simulations are run to predict typical, 3 sigma and worst case performances. Dedicated open-loop simulations are also produced and delivered to software, equipment and subsystem test engineers. They constitute reference simulations which are compared to the results obtained with the flight software and real hardware submitted to the same inputs. Any difference must be corrected or judged acceptable, leading to a cross validation of the detailed simulation software and associated mathematical models with the flight software and real equipments.

##### 4.4 - Flight software

The development of the flight software is initiated by Software Requirement Document (SRD) based on the User Requirement Document (URD) issued by the AOCS designers. An iterative early activity permits to simplify and optimise the functional architecture before entering detailed analysis and coding. A close cooperation is again profitable to develop both the flight software algorithms and its modelling in the closed-loop simulation program of the study team (high level language prototypes can be exchanged).

The software validation is achieved against its specification. Additional verification can be done, using the open-loop reference simulations generated by the study team.

#### 4.5 - Subsystem tests

This activity starts with the design and the development of the subsystem test facilities. The AOCS equipments, the flight software, the complementary simulated models will be integrated as soon as possible, first in a preliminary version, to permit an early debug of the AOCS elements in a representative configuration. The relationships between AOCS units and between AOCS and the external environment is displayed in Figure 12. Four main items must be verified at subsystem level :

- Verification of interfaces between equipments (including both Hardware and Software interfaces),
- Verification of ground command and monitoring capability,
- Verification of AOCS automatic reconfiguration,
- Contribution to AOCS dynamic performance verification.

The three first items are widely validated during the subsystem tests. Some complementary tests are achieved later. A final end-to-end test on the satellite itself is, for instance, mandatory to check the polarity of the control loops. Some aspects of the flight procedures can also be verified later at system level. The fourth item, concerning the dynamic performance verification, was already described in the functional studies section. The subsystem test bench contributes to the mathematical models verification, and to a global typical performance check-out, ensuring that no functional aspect has been ignored by the study team's modelling activity. All the verification items, with the associated tests are summarised in Figure 13.

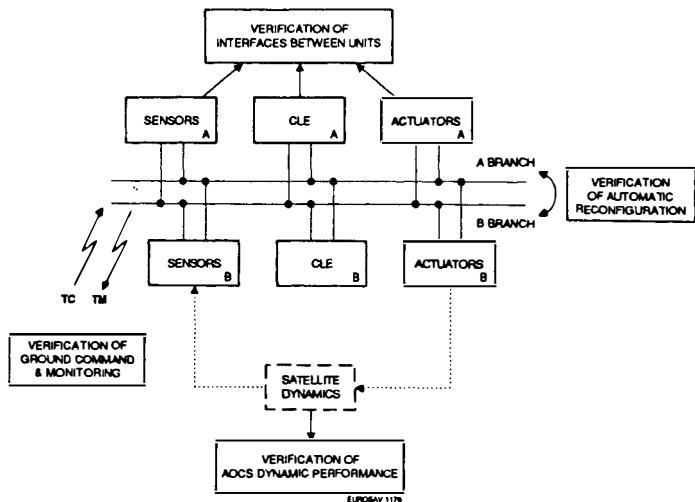


Figure 12 : AOCS verification items

	Major verification layer	Secondary layer
Unit performance	Unit test & analysis	Subsystem test
S/W performance	S/W test	Subsystem test
Interfaces between units (+ polarity check)	Subsystem test	Satellite test
Ground command & monitoring capability	Subsystem test	System test
Automatic reconfiguration	Subsystem test	System test. Satellite test
Dynamic performance . unit models . S/W model . dynamics & environment	Studies & detailed simulations . unit test & analysis . S/W test . ground tests	Subsystem test . subsystem test . subsystem test . flight experience

Figure 13 : AOCS verification layers

## 5 - IN-ORBIT EXPERIENCE RETURN

### 5.1 - Failures or anomalies

An unpleasant but highly valuable experience gain is unwillingly earned through in-orbit failures and severe anomalies. The thermal failure propagation within the Bus Regulator Electronics of TELECOM 1-B has for instance led to the physical segregation of nominal and redundant functions into separate boxes. Early gyro failures on-board a number of satellites have emphasized the interest of in-orbit reconfiguration capability with minimum hardware, even through survival modes and degraded performances.

According to a compilation of 355 all origin malfunctions publicly reported in 1965-1990 by Ray Sperber on geostationary communications satellites, the AOCS is the second misbehaving subsystem, causing 20 % of the failures (the payload being the first cause with 40 % of the failures).

More fortunately the very good behaviour of HIPPARCOS under an unforeseen severe environment on its elliptical orbit also brings new lessons.

### 5.2 - Technological return

A very profitable return is gained through detailed analysis on satellites which behave globally correctly or reveal only minor disfunctioning. Sensors and actuators in one hand, satellite dynamics and environment (e.g. disturbing torques) in the other hand are mainly concerned. A clarification of these activities, with their usual feedback is proposed in Figure 14 and a series of examples from MMS experience follows.

Some phenomena which are neglected or unmodelled for a satellite can sometimes suggest innovative concepts for a new generation. For example, the observation of a dynamic coupling between solar array slewing and satellite nutation on TELECOM 1 (which used a normal mode with thruster control) permitted to design the EUSTAR nutation control associated with the Solar Sailing (it uses solar array products of inertia created by a deliberated 2 deg. tilt with respect to the nominal axis.

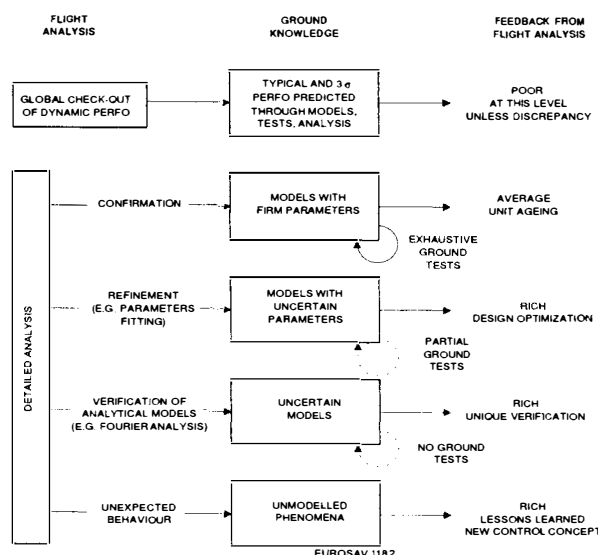


Figure 14 : Flight experience contribution

Disturbing torques verification on ground is very limited. The prediction mainly relies on analytical models, which can be highly complex or necessitate input parameters difficult to verify. An accurate in-orbit analysis was conducted recently on SPOT 1 through an inhibition of the magnetorquers over several orbits (reaction wheels evolution directly revealing the external torques). A residual internal magnetic momentum could then be found with the right orientation compatible with an Invar element of the payload which had not been demagnetised. On INMARSAT II, the analysis of the solar torques enlightened an unmodelled wind-mill torque of about  $2.10^{-6}$  Nm which indeed enlarge the solar sailing torque capability. Repeatable on each satellite, and since on TELECOM 2, it was found to be caused by a thermal retrodiffusion of the array back side towards the lateral flaps. Another learning was gained on TELECOM 2 during East-West station keeping maneuvers. The analysis of the torque produced by the plume interaction on the lateral antenna dishes permitted to adjust an accommodation coefficient in the prediction software (parameter related to the ratio of specular reflection on the dishes).

Some elements contributing to the modelling of the satellite dynamics are also difficult to analyse and test on ground.

For a spinning satellite with a large amount of liquids, stability margins or dedamping time constants are a critical area and can have an impact on the satellite mass budget. SKYNET 4 confirmed a good accuracy of the sloshing tests which had been achieved at INTESPACE Toulouse. TELECOM 2 transfer phases analysis confirmed the "equivalent solid" approach developed by MMS to predict free and perturbed motion (during apogee boost) of a spinner with an inertia ratio close to unity. This flight experience could permit to save several kilograms of equilibrium masses on future spinning spacecraft.

Analyses recently conducted on HIPPARCOS attitude estimation have permitted to determine thermo-elastic distortion (between star mapper and gyros) and confirm at least for one axis the ground analysis and tests which had been quite complex.

Three-axis stabilization raises also some concerns in the dynamic modelling area. One is the damping ratio of the solar array (or other appendage) flexible modes. Analyses on SPOT 1 in 1987 confirmed about  $5.10^{-3}$  as it was considered for analysis. But recent in-orbit tests on TELECOM 2 proved a higher figure than assumed, i.e. about  $10^{-2}$  instead of  $3.10^{-3}$ . With resonance peaks twice smaller than foreseen, the design of the station keeping control laws would become less difficult and less expensive. Many other lessons were learned from flight experience in the area of earth luminance variations, solar array drive mechanism perturbations, chemical thrusters ageing... It is never easy to process rough telemetry and fight against everlasting problems of labels, formats and scaling... but this is a unique way to improve the quality and effectiveness of future systems while optimizing their design and cost.

## **6 - FUTURE TRENDS**

The presented AOCS validation approach which involves a multi steps verification ending with a complete closed loop hardware/software test has been proven to be a safe and efficient way to secure our satellite operation and performance.

The very good performance and behaviour of all AOCS developed by european companies are certainly due to this widely used approach.

Subsystem tests are now structured with a flexible architecture that allows to accomodate easily new control systems such as guidance, navigation and control (GNC) systems which are to be developed in the very near future. A full computer simulated motion dynamics gives now a much better performance and representativity, together with a large flexibility for adaptation to new and complex dynamical motion. Real motion simulation is to be considered with new sensors and actuators, when dynamic conditions are to be tested or when it is the cheapest way to stimulate their inputs.

Most of the electronics and software involved in the control systems will be progressively introduced in the test, replacing the related simulated model and thus validating both the model quality and hardware/software interfaces.

When considering emerging needs for Europe space activities, it will be necessary on the one hand to develop large motion simulator to validate orbital manoeuvring systems such as those required for autonomous rendezvous, capture and robotics. On the other hand, the emerging very high pointing accuracy systems require complex end to end performance test which largely include the pointing subsystem.

A photograph of a large robotic arm and associated test set-up is shown in Figure 15. They are developed under CNES contract and offer a representative 2-axis zero-g environment to test large external manipulator control.

Another large set-up, the six degrees of freedom Docking Dynamics Test Facility developed under CNES contract is shown in Figure 16.

It permits to test new hardware under realistic conditions. A full scale docking mechanism front end has been developed for ESA and is shown implemented for validation.

Rendezvous sensor, targets and hand controllers for spationautes training are also in the loop.

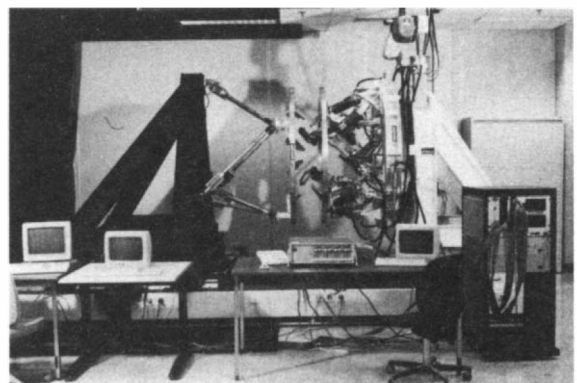


Figure 16 : Dynamic Docking Test Facility

As a conclusion, we can expect in the coming years an increasing interest for end to end testing of dynamics control systems more particularly focused on the new technologies validation :

- test benches more integrated with system elements for very high accuracy pointing,
- more complex and larger control system test facilities for orbital operation.

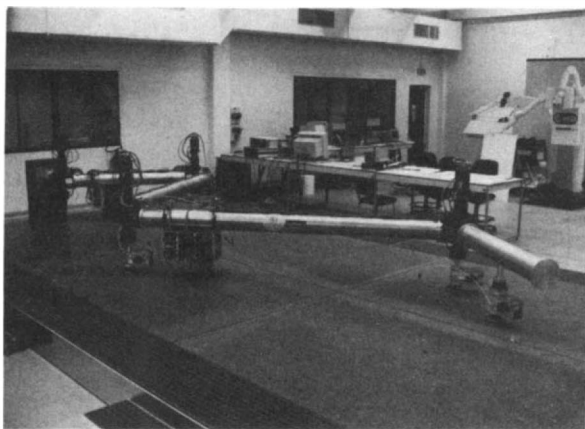


Figure 15 : MFB Robotics Arm test set-up

# NEW DEVELOPMENTS IN AEROSPACE GUIDANCE AND CONTROL: KNOWLEDGE-BASED PILOT ASSISTANCE

R. Onken

*Universität der Bundeswehr München, Institut für Systemdynamik und Flugmechanik, Werner-Heisenberg-Weg 39,  
D-8014 Neubiberg, Germany*

**Summary.** New developments in aerospace guidance and control are focussed to a great extent on the functional system enhancement through knowledge processing. In particular, the main traits of knowledge-based pilot assistance and the state of the art in this field will be addressed with this paper. Knowledge-based pilot assistance provides the capacity of autonomous support functions for situation assessment, including pilot action and intent monitoring, planning and lower level service functions. The assistance becomes effective only, if a comprehensive dynamic model of the human cockpit crew is incorporated in the system design. For illustration purposes, the German development of a cockpit assistant system for instrument flight operation is presented as a representative example.

## 1. INTRODUCTION

Developments in new techniques for knowledge processing have elicited powerful capabilities and functionalities which can be exploited for process control in two ways:

- Autonomous process control
- Autonomous or knowledge-based assistance of the human operator in process control

The latter application seems to be less demanding. In truth, for the ideal case of assistance for the human operator not only knowledge about the process, the process goals, the way how to achieve the goals under various constraints, has to be taken into account, but also as much knowledge as possible of human factors and the human operator's normative and individual behavior while controlling the process.

In the meantime, knowledge-based pilot assistant systems are being proposed by several research and development teams worldwide for civil and military application. In the following, partly as an introduction for session 7 on "New Developments in Aerospace Guidance and Control" with presentations of main developments of knowledge-based pilot assistant systems [1,2,3,4,5,6,7] among other new developments, the basic functional structure of these systems and the underlying techniques will be described, forming a kind of umbrella under which all known system developments can be placed, whether being consciously used or not. The basic structure shows, where to aim at for the functional development of a knowledge-based pilot assistant system. It does not necessarily confine itself to only reflect the actually presented functions of the different developments underway.

Since German work on this field will not be presented in more detail in session 7, this will be incorporated in the

following as an representative example for civil aviation, known as ASPIO (Assistant for Single-Pilot IFR Operation) as first generation and CASSY (Cockpit Assistant SYstem) as second generation development. CASSY is being developed in cooperation with Dornier Luftfahrt GmbH.

## 2. FUNCTIONAL MODULES OF BASELINE STRUCTURE

The main functional structure, as depicted in figure 1, shows the interfacing between the crew assistant system, generally labelled as **Electronic Crew Member (ECM)**, and its functional environment as well as the main internal functions.

Basically, three interfaces between the ECM and its external world have to be considered, the interface to the

- Ground segment (e.g. air traffic control)
- Aircraft systems (avionic systems, sensors, etc.) and
- Human cockpit crew (HCC).

All possible environmental impacts like weather, other air vehicles and threats, which can be detected by sensors onboard the aircraft, on the ground or through communication, can be considered as covered by the above-mentioned interfaces.

The interface with the HCC is likely the most demanding one. The information media have to be chosen very carefully in order to ensure easy handling and command delivery as well as easily perceivable information to be provided by the ECM. Speech input and output are crucial ingredients. The information flow is to be controlled by the knowledgeable '**Dialogue Manager**'(DM), a very important internal functional module of the ECM, in order to present comprehensive and timely messages in the con-

text of the current situation and the pertinent HCC needs and priorities.

The elements and pieces of information to be worked on by the Dialogue Manager are the HCC inputs and suggestions from the Adviser (AD) module of the ECM for messages to the HCC. The AD module, in turn, is drawing on information from the **ECM submodules for situation assessment, planning and plan execution**.

The AD module in connection with the DM module is serving the key purpose of the ECM, i.e. forming supportive advising messages for the HCC. The remaining submodules of the ECM can be considered as service modules for the AD and the DM, in the first place. They autonomously keep track with all occurrences and aspects relevant for mission accomplishment through situation assessment, they prepare plans for evaluation purposes based on the situation assessment and they provide a reference for plan execution performance. As such, they are principally representing a machine capability of carrying out all of the functions the HCC is trained to perform. There might be differences in performance quality compared to the HCC, though.

The design criterion for these AD service modules might be either to copy the HCC performance as closely as possible or to look for the globally optimal function accomplishment, possibly beyond the HCC capabilities. It has to be carefully sorted out when the latter criterion can be adopted.

For instance, for certain AD functions like generation of plan advices, it can be desirable to look for the absolutely best solution, subject to certain information and criteria, which could not be generated by the HCC because of mental restrictions like working memory limitations. Machine performance close to that of the HCC might be important, for instance, for HCC monitoring purposes.

As mentioned earlier, the service modules intrinsically represent the capability of flying the airplane autonomously. There are applications, where this not only might be used to provide advices to the HCC but also to let the system take over aircraft control at the HCC's request. Even active intervention of the ECM might be appropriate for certain cases on the basis of these capable service modules, performing

- Situation assessment
- Flight planning and decision support, possibly decision making
- Action taking for plan and decision execution.

All of these three HCC-like service functions of the ECM are, of course, subject to the global mission goal which is usually determined outside of the system, for instance at the ground segment.

At this point, some more decomposition of the function of situation assessment seems appropriate. On the basis of a representation of elements of the current situation, in parallel and orthogonal to the time axis, including monitoring results for HCC condition, intention and performance as well as entire system condition, the function of situation assessment consists of:

- Instantiation of actual values for elements of current situation
- Extrapolation of current situation
- Evaluation of the situation subject to the mission goal and the constraints (tactical reasoning), taking also into account the results of monitoring of HCC actions and HCC intents.

The planning function might support longterm as well as shortterm decisions, which are to resolve the problems as being elicited by the situation assessment function.

Once the decision(s) are made, the plan execution function comprises all services which can be made available for carrying out the decision, i.e. the agreed plan.

In order to work in this way, obviously, the ECM has to understand and evaluate the HCC actions. Therefore, most of the ECM functions are based on continuous information about the expected HCC performance for both the normative HCC behaviour and behavioural instantiations for the actually flying HCC. Also actual information about values of the HCC human factors and condition parameters have to be incorporated as well as the HCC's intentions and error contingencies. Since the actually flying HCC is not able or chargeable to provide this information permanently, The ECM has to generate it on its own.

This very crucial subfunction is readily available by means of a dynamic model of the HCC (fig. 2), covering all of the abovementioned aspects and being incorporated within the ECM functions, in particular the AD service modules. The incorporation can be carried out separately for each of the ECM submodules. Another approach can be that all modules are drawing the information necessary for their particular function from a single HCC model representation accessible for all of them. The kinds of functions to be considered in that model are again, by virtue, those already discussed for the AD service modules, i.e.

- Situation assessment
- Planning and
- Plan execution

as they are performed by the HCC, with outcomes not necessarily equal to those of the AD service modules.

This model will primarily yield the HCC outcomes to be expected at every instant, possibly in the form of ranges for the output values. For the determination of these ranges objective safety limits or thresholds of comfort are taken into account.

It has to be made use of both kinds of HCC modelling, that of normative crew member performance and that of the actually flying crew member. Several dynamic HCC models might work in parallel, possibly as a generic HCC model with the following instantiations:

- Normative behavioural characteristics  
(with and without HCC mismatching contingencies)
- Individual HCC characteristics, condition and behaviour (with and without HCC mismatching contingencies)

Once more, by inferring on the outcomes of these models, prediction of crew member actions as well as recognition of their intents is being achieved. This, in turn, can be used

to detect discrepancies with respect to the mission goal and subgoals and to evaluate these discrepancies with respect to their causes. These discrepancies are not always caused by HCC errors. Here it is of great importance that the discrepancies due to HCC errors can be discriminated from those caused by sensible changes of HCC intents. HCC errors might be caused by mismatches due to certain cognitive deficiencies or because of violations of limits of the principal human capabilities. This complex task of discrimination is facilitated through modelling of the individual HCC condition and behaviour as well as mismatching contingencies.

It might be worthwhile to note that all ECM modules are heavily drawing on the outcomes of the dynamic HCC model. Therefore, the better this HCC model, the more assistance can be accomplished by the ECM.

The baseline structure of knowledge-based pilot assistant systems, as outlined, is a functionally maximised one. Of course, in particular with regard to the dynamic model of the HCC, only parts of it have been realised in the existing system developments. This model, though, is the key component in order to ensure a crew centered design solution and overall functional success.

### 3. KNOWLEDGE REPRESENTATION METHODS AND TECHNIQUES

A number of methods and techniques have been developed during the last 20 years or even earlier, in particular by people working in the field of computer science or cognitive science. These methods are powerful instruments for knowledge processing and well suited for the development of the ECM functions. The probably most important ones are those for the knowledge representation.

Which kind of knowledge is needed? In the first place, knowledge is needed about how to react in the face of a given situation. The possible situations can be classified globally as those which can be considered as regular and those which are characterized by irregularities. For regular situations, there exists a pertinent, well-defined and unambiguous reaction to be carried out. These are the situations which are dealt with by the human operator through skilled or rule-based behavior [8]. For situations with irregularities, there are several alternatives to be considered for an appropriate reaction, i.e. a more or less complex selection process has to be carried out among these alternatives, what can be called a decision-making or planning process. These are the situations which could be dealt with by the human operator through knowledge-based behavior [8].

Therefore, declarative and procedural knowledge representations have to be established for

- classes and subclasses of possible situations and possible transitions from one class to another
- (Re-)actions associated with regular situations
- Action alternatives associated with situations due to irregularities or derivation procedures for the relevant alternatives
- Guidelines for the selection process among relevant alternatives

Another complementary basic idea of knowledge representation is the object oriented one. Physical objects as well as semantic objects like flight task related aspects are instantiated through actual information represented by the situation state vector and its actual values. A distinction can also be made between objects affected or not affected by crew actions or resulting ownship operations.

In order not to have to consider the full set of objects everytime, problem reduction can be employed, for instance by breaking down the entire flight into flight phases, well-defined by transition conditions.

Frequently used methods for knowledge representation of rule-based transitions or /and conditioned tasks, i.e. pilot behavior, are

- decision trees, And/Or graphs
- automata
- petri nets

and recently artificial neural nets (ANN), too.

Probably the most favored tool of representation is the petri net as a place-transition net, which is very powerful for the modelling of event-driven concurrent systems [9]. Higher level nets can activate lower level nets according to the abstraction level of pilot tasks. Place-transition nets are characterized by places containing more than one token and integer valued arcs, describing the number of tokens passing the arc when the transition is fired. By associating token quantities with limited resources and place capacities with resource consumption, these nets allow explicit modelling of resource availability and load. In many petri net applications, net theory is used for system analysis, design and simulation, but after verification petri net mechanisms are mostly transformed to real time software by code generation or complete reimplementation. On the other hand one can make use of a real-time petri net interpreter processing a special net description language.

Other forms of transition net representations like decision trees or finite automata are used successfully in a similar way.

Recent work [10] has shown that individual situation-dependent human operator nonlinear behavior can be modelled with surprising consistency by multi layer perceptron ANNs. Figure 3 gives an example for the performance of an ANN which was trained to model an individual pilot's elevator control behaviour during final approach. The ANN performance is shown in comparison with the pilot's control performance for a test flight. The test flight data were not seen by the ANN in the context of its training process. These data were gained from flight simulator runs with little familiarization of the test pilot to the somewhat special handling characteristics of the simulator. The results show that HCC identification is also possible and individual error contingencies can be modelled in this way as well as a global picture of the HCC's condition, which is extremely important for ECM subfunctions such as advice adaptation to the HCC and HCC intent recognition.

Artificial neural nets seem to be a suitable means, too, to represent the HCC's operational expert knowledge, also under uncertainties. Another approach to deal with uncertainties is the application of fuzzy logic [11] or the use of

the Bayes-theorem [12]. Fuzzy logic is already successfully applied in the ECM development CASSY for the selection of plan alternatives through the evaluation of GOOD/BAD membership functions for weighted criteria as part of the ECM planning function. One contribution in session 7 of this conference will be devoted to similar applications of fuzzy logic [13].

#### 4. STRUCTURE OF CASSY

##### 4.1 Main structure

Following the basic structure of knowledge-based assistant systems, CASSY comprises the following task specific modules as shown in figure 4:

- Situation Assessment with Monitoring of Flight Status
- (MFS), Systems (MS) and Environment (ME)
- Automatic Flight Planner (AFP)
- Piloting Expert (PE)
- Pilot Intent and Error Recognition (PIER)
- Dialogue Manager (DM)
- Execution Aid (EA)

As long as there is no data link capability available, the Air Traffic Control (ATC) Interface is not explicitly realised within the cockpit assistant. The important ATC Instructions and Information have to be transferred to CASSY by the pilot crew through speech input. This can be operationalised rather easily because the ATC instructions are to be acknowledged verbally by the pilot anyway. In the following, the modules are described in more detail.

##### 4.2 Situation Assessment with Monitoring Modules

Situation assessment is achieved by a situation representation on the basis of the flight chronology and potential tasks and events pertinent to the flight segments. A data base contains the actual values of state variables to be instantiated in that representation. Situation evaluation as part of the situation assessment is accomplished by means of a number of monitoring modules along with the Pilot Intent and Error Recognition module (PIER).

The Monitor of Flight Status (MFS) has got the task to monitor the flight progress in order to be aware of the arrival at any subgoals of interest of the flight. Thereby, the actual state with respect to the flight plan can be determined and the expected pilot actions can be generated in the PE module. There are also standard callouts, which might be of relevance at these points in flight and which would have to be delivered to the pilot crew by speech output.

The health status of the aircraft systems is monitored by the Monitor of Systems (MS). This module works on the information about defects in aircraft systems in order to generate messages to the pilot crew. This information is also rendered to the AFP and the PE, since replanning could be necessary and the expected pilot actions could be different subsequent to system defects or failures.

Sensor information for the assessment and evaluation of weather conditions and surrounding traffic are gathered in the Monitor of Environment (ME). This monitoring module

also identifies deviations from normal with respect to the immediate aircraft environment and reports to the pilot crew and the CASSY modules concerned.

##### 4.3 Automatic Flight Planner (AFP)

For every flight, a flight plan is to be issued before takeoff. This flight plan can be generated by the AFP or is being provided by means of other facilities and then fed into the system as part of the initial conditions.

During flight, the AFP autonomously is started, when significant deviations from the current flight plan have occurred because of events such as new ATC instructions not in accordance with the flight plan, adverse weather conditions or system failures. This module can also be activated by the pilot crew who might feed in their intent of changes. Also the PIER module might initiate flight plan changes when recognizing changes of pilot intentions. An evaluation of the current situation and its future projection might pinpoint where conflicts with the original flight plan will arise. As part of this replanning, algorithms for the selection of alternate destinations and flight route alternatives have been developed by use of fuzzy logic. Since for instance aircraft system failures as well as resulting sudden performance breakdown are included as events for current flight plan abortion, the AFP function not only covers strategic but also tactical planning. The AFP results are presented to the crew as recommendations. If not corrected by the crew, agreement for the new flight plan is achieved.

##### 4.4 Piloting Expert (PE)

On the basis of the flight plan as generated by the AFP and acknowledged by the crew, the PE is capable of performing automatically the management of the flight plan execution. This is carried out by following the instructions of ATC essentially rule-based through known regulations for piloting procedures, which are extensively elaborated and published for civil aviation. Hereby, the PE is construed as a model of the pilot crew covering both the standard pilot procedural activities and the behaviour of the crew actually flying the aircraft. In this way, the pilot crew model determines the expected actions the pilot crew is supposed to carry out during the various flight phases.

##### 4.5 Pilot Intent and Error Recognition (PIER)

The PIER function bears upon the information of situation assessment and monitoring but also on information about normative pilot behaviour and tolerances for the pilot behaviour as well as tolerances with regard to safety margins. The information about pilot behaviour and tolerances is being provided by the PE. Expert knowledge about possible situation dependent pilot intentions will be used in order to examine deviations from the flight plan, whether these deviations are caused by a change of the pilot crew's intention or by a pilot error. If no intent hypothesis can be verified directly by this procedure, *a priori* and *aposteriori* probabilities for the hypotheses will be evaluated in order to discriminate between pilot error and sensible change of pilot intent not in accordance with the flight plan, though. This is the main task of this situation assessment component. Recognition of the pilot intent or error follows

directly from this. The recognition results are reported to the other relevant modules and to the pilot crew. The resulting messages to the pilot crew might be warnings in case of pilot error or indications about the systems view of what the pilot crew's intentions are.

#### 4.6 Dialogue Manager (DM)

The Dialogue Manager (DM) comprises all components for the information transfer between CASSY and the pilot crew, including the management of information flow to the pilot crew.

Extensive use is made of speech communication in either direction. Speech input is used for acknowledgement and rejection of assistant system recommendations and as a medium for instructions to the EA. For this purpose, a speaker dependent speech recognition system is used, based on the standard phraseology of civil aviation. Synthetic speech is used for speech output, with different voices for different categories of assistant messages. More complex information like comprehensive flight plan recommendations for a revised flight plan is presented through one of the visual displays.

Hereby, the DM controls the syntax of the speech recognition system, the priority and category of the speech messages and visual information presentation.

#### 4.7 Execution Aid (EA)

In order to support the pilot crew in the course of executing the actual flight plan, the EA offers a variety of optional service functions, conventionally performed by the co-pilot without automatic aiding. Among these functions are automatic instrument setting, flap and gear setting and navigational calculations. All of these functions can be commanded by the pilot crew through speech inputs.

### 5. EXPERIMENTAL TEST RESULTS

#### 5.1 General remarks

The cockpit assistant system implementation in a flight simulator facility at the University of German Armed Forces in Munich is continuously extended. A one-seat fixed base cockpit with computer generated outside vision and head down display, artificial stick force as well as speech input and output is employed. The simulation comprises aircraft dynamics (6-degree of freedom model), autopilot system, radio navigation systems and a wind model.

A first prototype implementation of the cockpit assistant system was tested late 1989. This implementation, named ASPIO, differed from CASSY in a number of ways.

ASPIO was

- Intentionally limited to support a single pilot
- Not able to consider and recognise considerably deviating pilot intentions
- Characterized by the use of an isolated-word speech recognizer
- Realised only for the flight phases from arrival through final approach.

This prototype comprised the main functions, though, of a knowledge-based cockpit assistant system, which are necessary for a representative flight simulator evaluation.

The experiments were aimed at proving hypothesised enhancements in overall performance and safety without increase of pilot workload. For this purpose, the following criteria were investigated:

- Flight accuracy
- Pilot errors in situation assessment and system operation
- Duration and quality of planning
- Pilot workload
- Pilot acceptance

The pertinent parameters were evaluated for a number of test runs of IFR approaches. Three different IFR scenarios were developed which consisted of standard situations as well as of unusual events and emergencies. A total of nine professional pilots, everyone with a great amount of IFR flight experience, have performed these test runs. Some of the evaluation results are presented in the following.

#### 5.2 Evaluation of flight accuracy

As an indication for flight accuracy, the airspeed deviation was considered to be most appropriate for evaluation. It was supposed to be controlled manually by the pilots.

The evaluation results for the standard deviation of airspeed for all pilots are depicted in figure 5. It could be shown that the improvement in flight accuracy by use of the assistant functions was highly significant.

#### 5.3 Evaluation of pilot errors

Pilot errors could be detected directly and unambiguously. One can say that, by definition, no major deviations from normal flight could be observed for the flights with activated monitoring function of the cockpit assistant, although pilot errors occurred as usual. However, without cockpit assistant, deviations from normal flight were detected due to pilot errors, also more serious ones.

#### 5.4 Evaluation of planning and decision processes

The time needed for planning and decision making was determined for this evaluation. The planning activity was triggered by an ATC instruction, where also an immediate reply about the pilot's further intentions was demanded. The time between the ATC instruction and the pilot's reply was measured.

In figure 6, the pilot's decision time without support by the cockpit assistant is shown in comparison to that with assistant aid. For this particular example, the planning and decision task was to check for an alternative approach procedure under consideration of weather and airport data, after the information was given about the breakdown of the instrument landing system at the destination airport. The differences are obvious. Moreover, the pilots stated that all decisions recommended by the cockpit assistant, made sense.

## 5.5 Evaluation of pilot workload

The pilot workload was assessed by means of subjective rating and the introduction of a secondary task. For subjective rating the SWAT method (Subjective Workload Assessment Technique) was used. As a secondary task, periodical tapping was specified. The experimental data showed slight reduction in pilot workload, but statistical significance could not be determined.

## 5.6 Evaluation of pilot acceptance

Pilot acceptance was evaluated from subjective pilot statements in a questionnaire which they furnished after their testruns in the simulator. As part of the questionnaire, the technique of semantic differential was used, as shown in figure 7. The median values show positive mean scores, that is good acceptance by the pilots. The neutral overall assessment for the component 'not distracting/ distracting' was explained by the pilots by the insufficient familiarization in system handling they experienced, in particular with respect to the specific speech recognition system used for these experiments.

## 6. CONCLUDING REMARKS

Knowledge-based process control has been considered in this talk as a representative field of new developments in Aerospace guidance and control. This field is making use of a number of new technologies and is driving the applicability of these technologies.

The baseline structure of knowledge-based cockpit assistant systems is outlined along with methods and techniques to be applied for the development of these systems. It has become evident that the HCC model is the key component in order to ensure a crew centered design solution and overall functional success.

For illustration purposes, the German approach is presented as an example for such a support system in IFR flight operation.

## 7. REFERENCES

- [1] Lizza, C.S.; Rouse D.M. et al. Pilot's Associate: An Evolving Philosophy, 2nd Joint Workshop GAF/RAF/USAF on Human-Electronic Crew Teamwork, 1990
- [2] Amalberti, R.; Champigneux G. Man Machine Coupling: A Key for Electronic Copilot Architecture, 2nd Joint Workshop GAF/RAF/USAF on Human-Electronic Crew Teamwork, 1990
- [3] Pipe H. The UK Mission Management Aid Project, 12th IFAC Symposium on Automatic Control in Aerospace, 1992
- [4] Geddes N.D.; Hosmer D.M. Knowledge Integration in the Pilot's Associate, 12th IFAC Symposium on Automatic Control in Aerospace, 1992
- [5] Hoshstrasser B. Inferring Operator Intent as a Basis for Aiding in Man Machine Systems, 12th IFAC Symposium on Automatic Control in Aerospace, 1992

- [6] Onken R. Knowledge-based Cockpit Assistant for IFR Operation, AGARD GCP Symposium, Madrid, 1990
- [7] Prevot T.; Onken R.; Dudek H.-L. Knowledge-based Planning for Controlled Airspace Operation as Part of a Cockpit Assistant, 53rd AGARD Symposium of GCP, 1991
- [8] Rasmussen, J. Skills, Rules and Knowledge; Signals, Signs and Symbols, and other Distinctions in Human Performance Models, IEEE-SMC-13, No. 3, 1983
- [9] Ruckdeschel W.; Dudek H.-L. Modellbasierte Fehlererkennung In der Flugzeugführung, VDI-Tagung "Menschliche Zuverlässigkeit", 1992
- [10] Zadeh L.A. Fuzzy Sets and Applications: Selected Papers, J. Wiley and Sons, 1987
- [11] Wittig, T.; Onken R. Knowledge-based Cockpit Assistant for Controlled Airspace Flight Operation, IFAC, 1992
- [12] Ihara H. Fuzzy Logic for Control Systems, 12th IFAC Symposium on Automatic Control in Aerospace, 1992

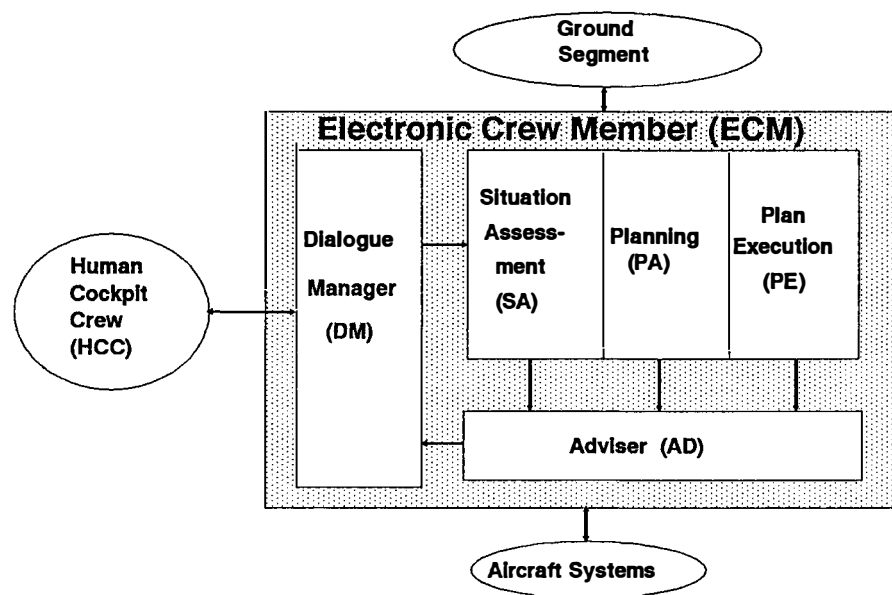


Figure 1. Knowledge-based Pilot Assistant System (baseline structure)

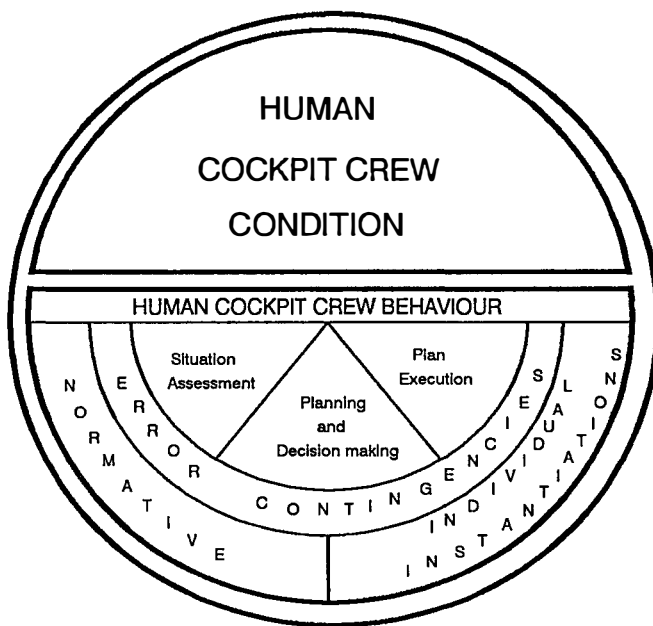


Figure 2. Dynamic Model of Human Cockpit Crew (HCC)

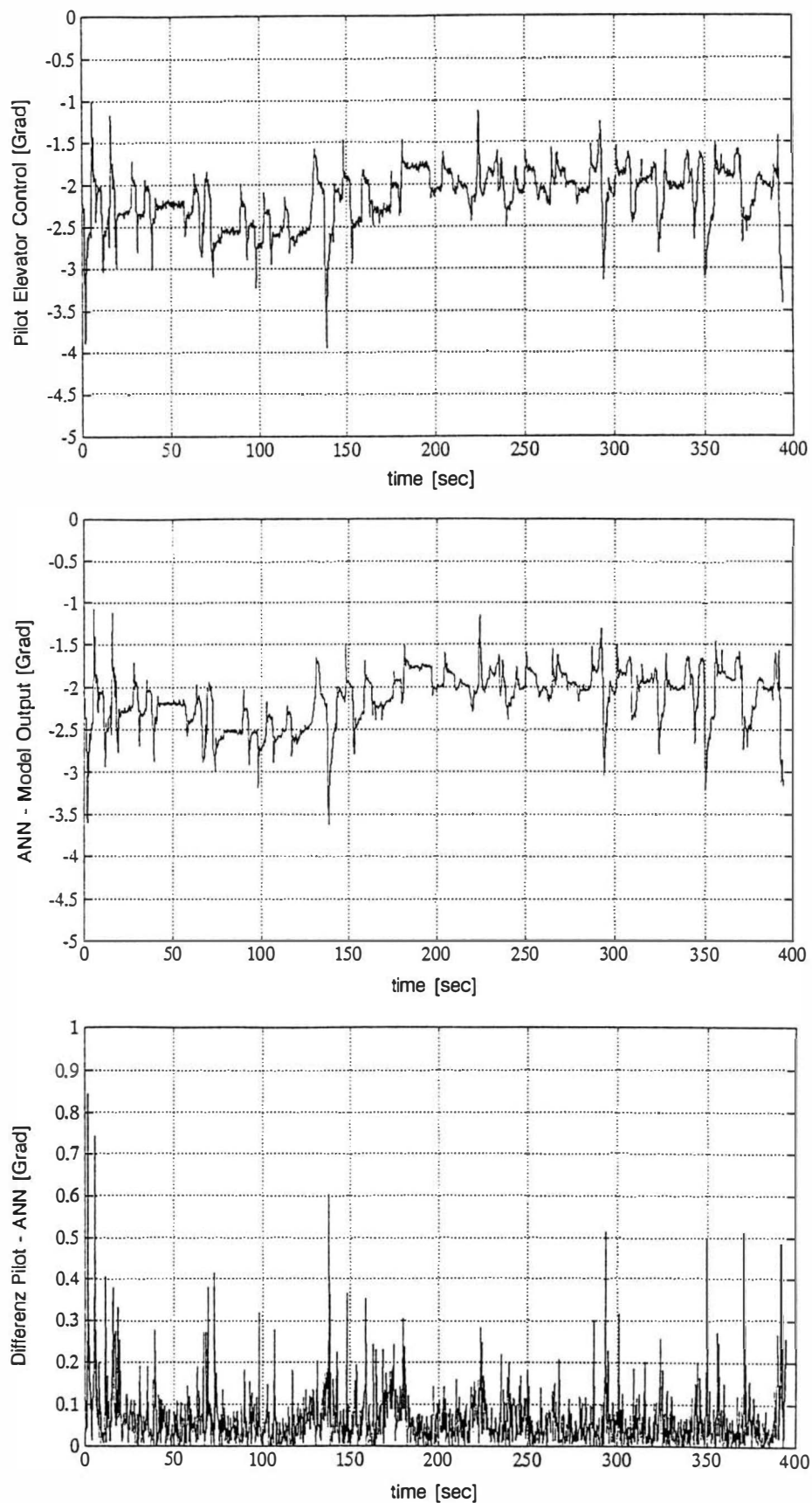


Figure 3. Comparison of Individual Pilot Elevator Control and Output of Trained ANN for a Final Approach Test Flight

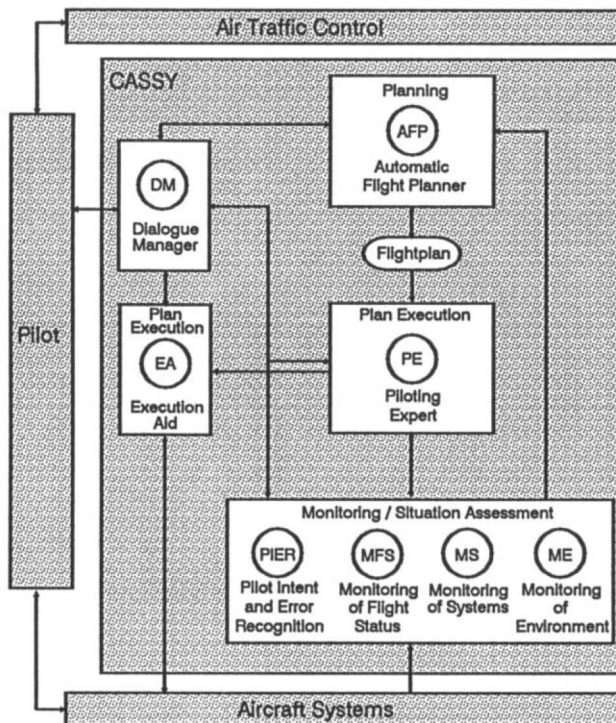


Figure 4. Structure of CASSY

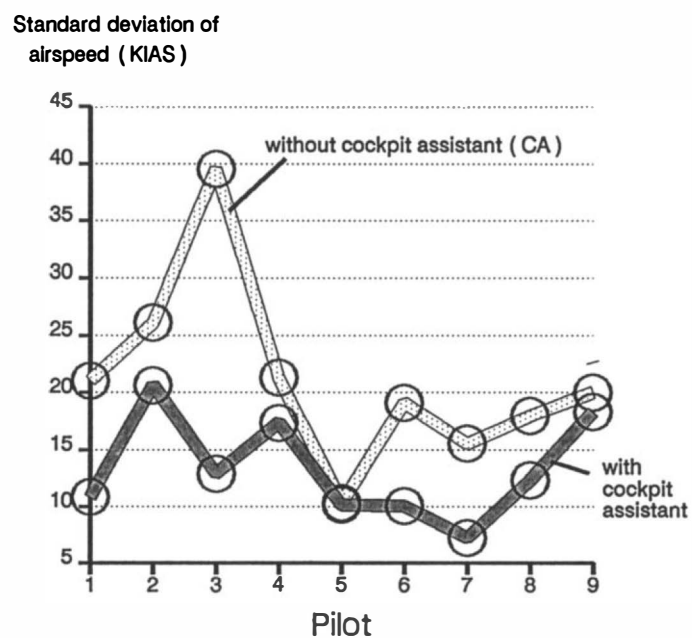


Figure 5. Enhancement of Flight Accuracy with CA

Time to decision [ sec ]

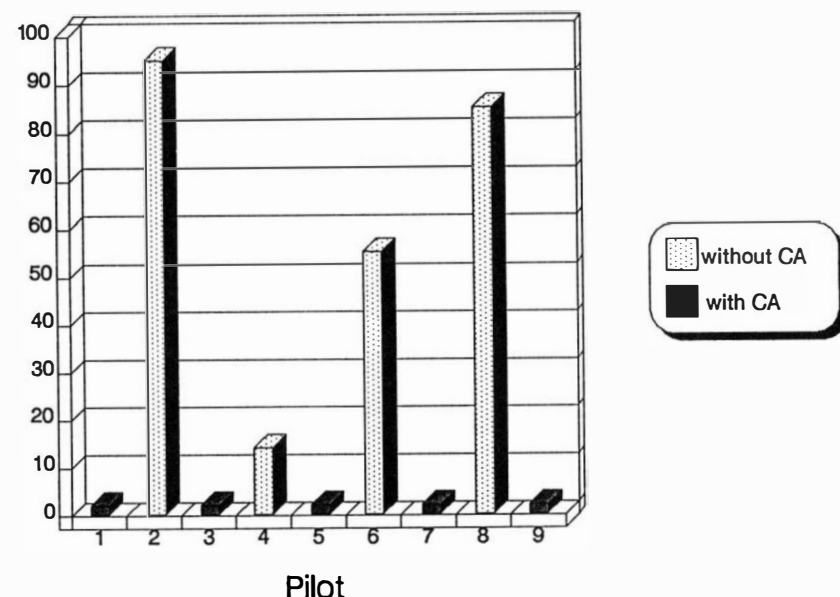


Figure 6. Reduction of Time to Decision with CA

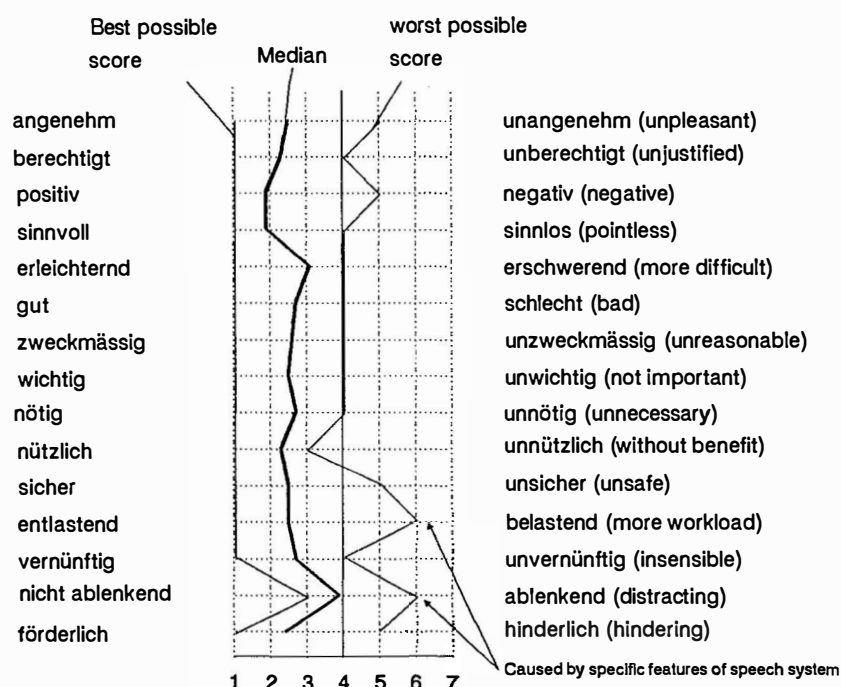


Figure 7. Results for Pilot acceptance related Semantic Differentials

# SPACE ROBOTICS AND MANIPULATORS: LESSONS LEARNED FROM THE PAST AND FUTURE MISSIONS AND SYSTEMS

J.Z. Sasiadek

*Department of Mechanical and Aerospace Engineering, Carleton University,  
Ottawa, Ontario, Canada*

**Abstract.** This paper presents the current state of the technology in space robotics. Some historical developments and the experience gained during those projects have been discussed. The challenge of space exploration and related danger requires even larger use of robotics devices. Many tasks and jobs are being automated. The exploration of the Moon and Mars requires the autonomous, mobile robots to gather various information, measurements and data. An introduction of Space Shuttle and related activities required an efficient robotic manipulator for in orbit operations. The Space Station Mir (in orbit) and especially Space Station Freedom (planned for nearest future) require advanced robots and manipulators. The Space Station Remote Manipulator System (SSRMS) and Special Purpose Dextrous Manipulator (SPDM) have been shown and briefly reviewed. Those and other robots for future missions are discussed in this paper.

**Keywords.** Robotics; manipulators; space robots; aerospace control; automation; automatic control.

## INTRODUCTION

Space exploration requires extensive use of robotics. This has been done in the past and will be done in the future on much and ever larger scale. Robotic devices in Space could be divided into three groups:

- mobile robots;
- flying robots;
- robots and manipulators.

The second group may be considered as a subset of the first group but because of its distinctive features flying robots have been grouped as a separate entity. Robots in Space can operate in three different modes:

- manual;
- automatic;
- teleoperation.

Mobile robots operating in an automatic mode can be further divided into autonomous and nonautonomous. From locomotion point of view robots may be divided into rovers (wheeled), walking and other. In the past mobile robots have been used in several unmanned missions. The best known are Lunokhod 1 and Lunokhod 2 used in Luna 17 and 21 missions respectively. Both used wheels as locomotion (8 wheels). Their respective weights were 456 and 539 kilograms. "Lunokhods" were designed to perform technical and scientific research on the Moon's surface.

Flying robots can be divided into two groups: first - flying orbital probes like Mariners and Vikings (USA) or Lunas and Mars (Russia), second - flying teleoperator like Flight Telerobotic Servicer (FTS). Robots and manipulators are used on board of spacecraft (Space Shuttle) or space stations (Mir and Freedom -planned).

## ROBOTS AND MANIPULATORS

Robots and manipulators in Space are designed to perform the following operations: capture, maneuvering, berthing/deberthing, support of Extra-Vehicular Activities (EVA), positioning and release. One of the most important features of all robots deployed in Space is their flexibility. Robots and manipulators used in Space are built out of light materials, and very often their links deflect. Those robots are considered to be flexible. The first robot used in Space was the Remote Manipulator System (RMS) mounted on Space Shuttle. This robot was used for the first time on 12 November 1981 in Columbia Shuttle. It is 15 meters long has three hinged joints for pitch and three other for yaw and roll which makes in total six degree of freedom (DOF). The remote Manipulator System has been shown in Fig. 1

and its kinematics in Figure 2 (Scott and Dameo, 1991).

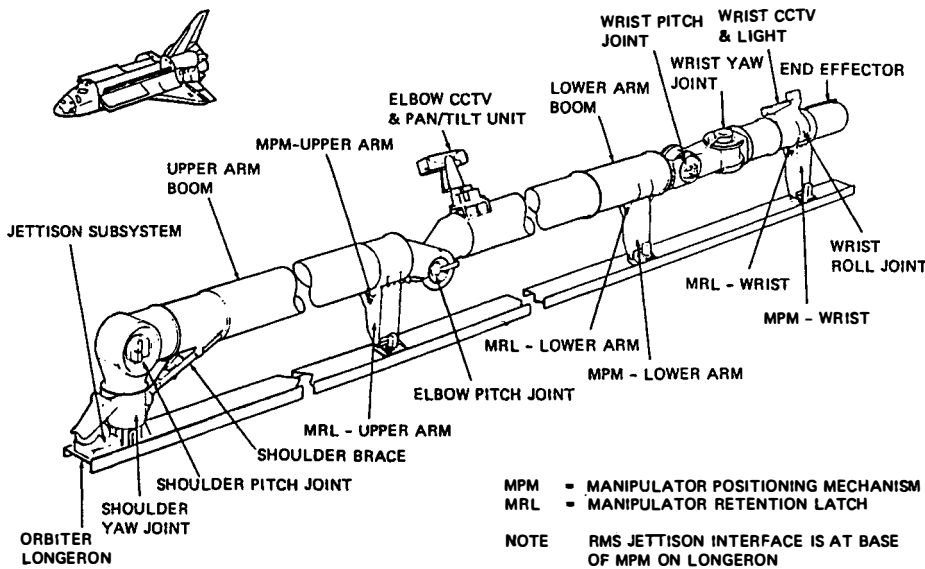


Fig. 1 Space Shuttle Remote Manipulator System (RMS).

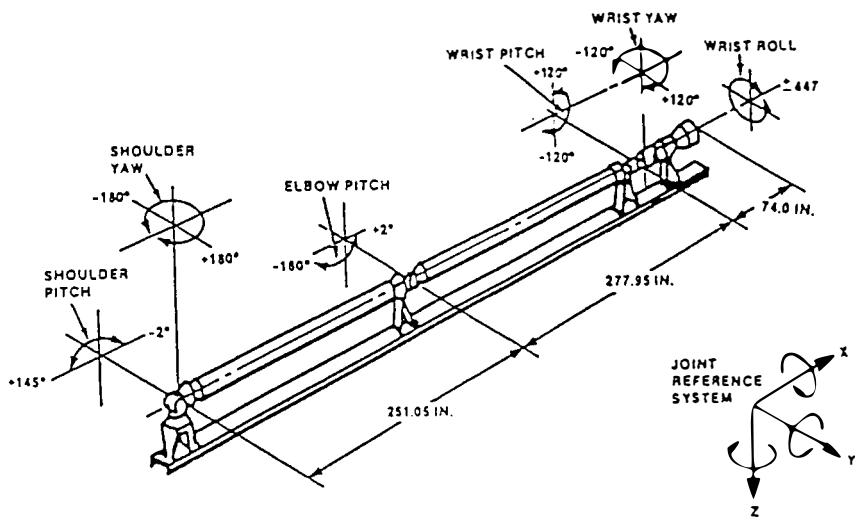


Fig. 2 RMS kinematics, dimensions, joint limits and coordinate system.

The Space Station Remote Manipulator System (SSRMS) which has been design for use in the Space Station "Freedom" is shown in Fig.3 . It is more than 17 meters long, has seven degree of freedom and is a redundant DOF manipulator. The seventh degree of

freedom has been introduced to avoid singularities in some important positions.  
The SSRMS is a part of a larger system called the Mobile Servicing Centre (MSC), shown in Fig.4 ( Stieber, M.E. and Fung, P.T.K. (1991) )

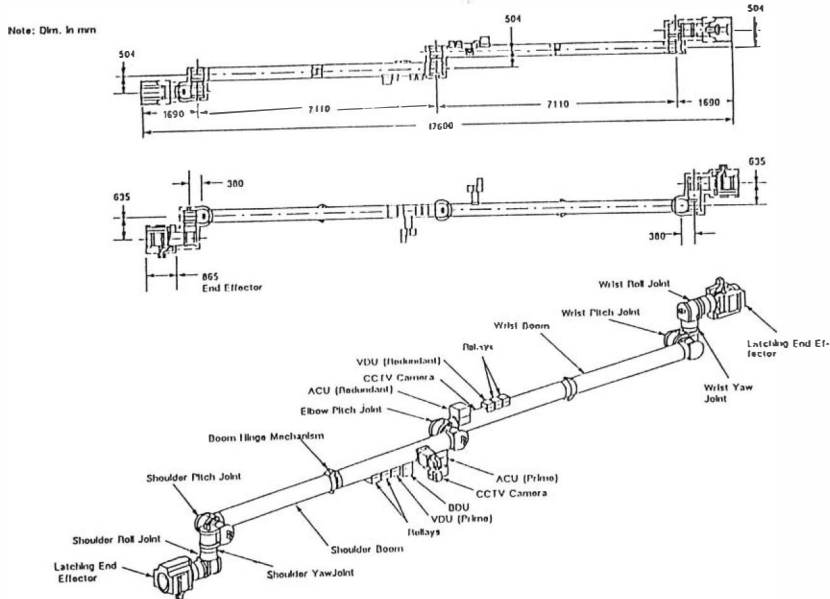


Fig. 3 The Space Station Remote Manipulator System (SSRMS).

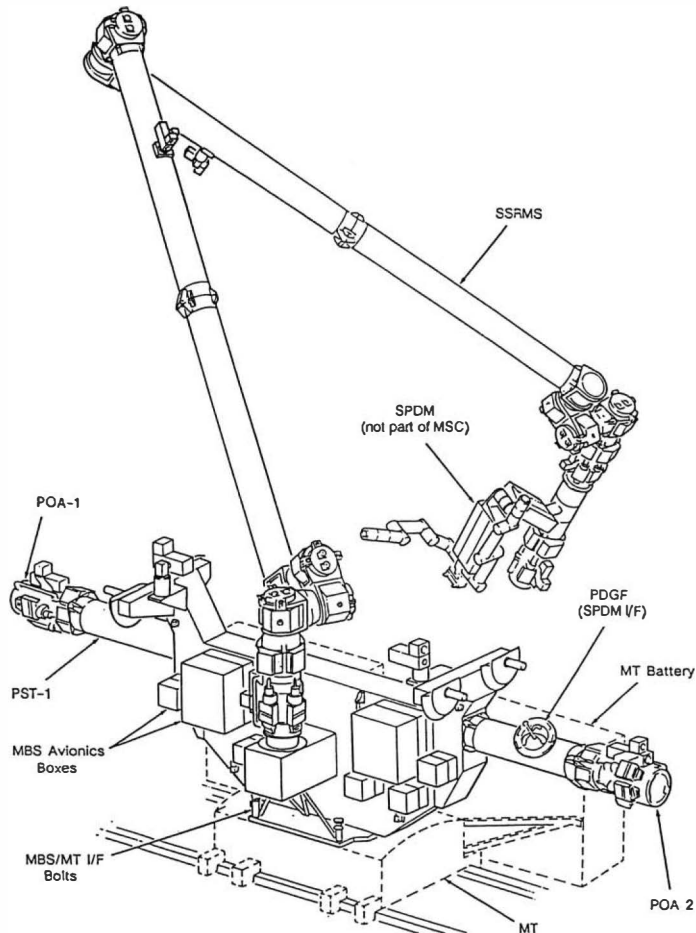


Fig. 4 The Mobile Servicing Centre (MSC).

The Special Purpose Dextrous Manipulator (SPDM) shown in Fig.5 and 6 (Ravindram, 1990) is a two-arm manipulator designed for the Space Station "Freedom" application. The SPDM has two 7 DOF arms (Fig.6) and will be placed at the end tip of SSRMS. The length of each arm is 1.99m .

### Special Purpose Dextrous Manipulator (SPDM)

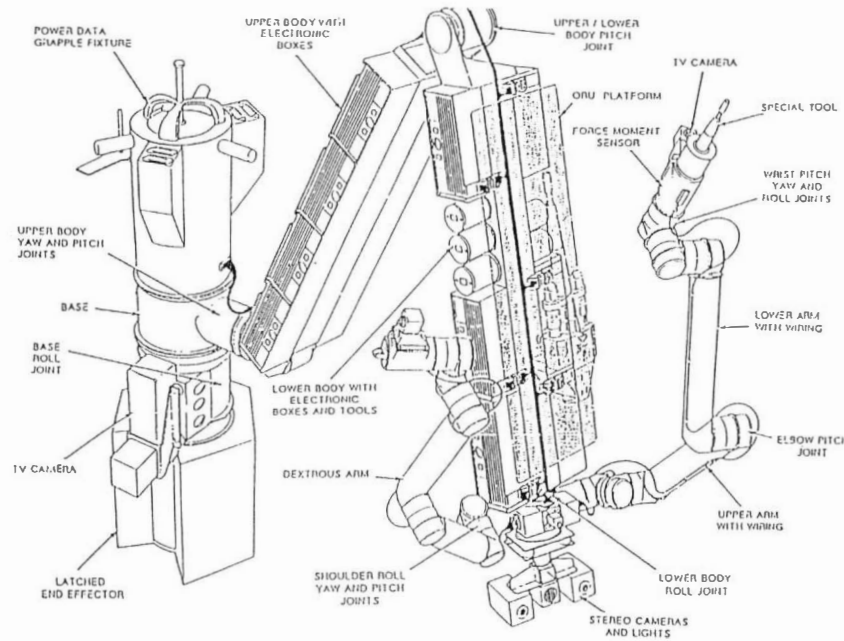


Fig. 5 The Special Purpose Dextrous Manipulator (SPDM).

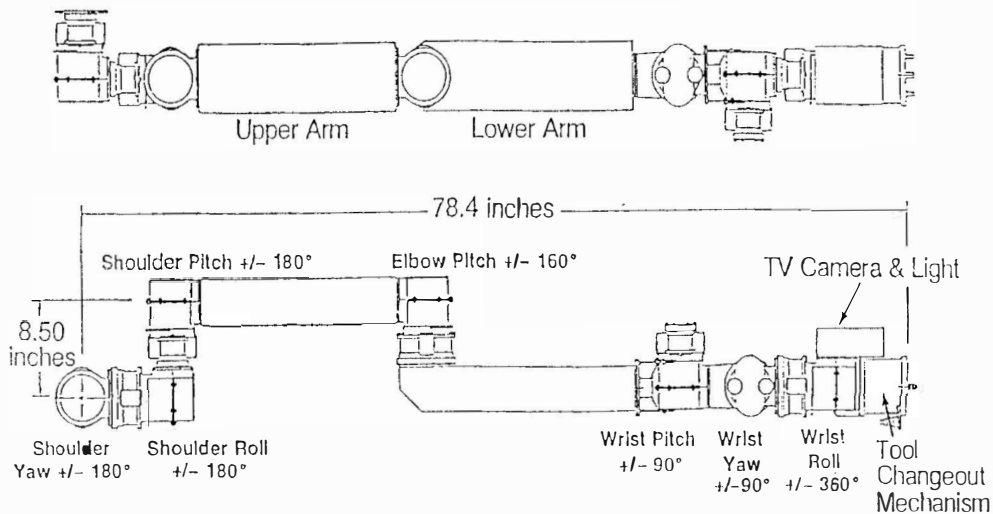


Fig. 6 SPDM Arm Configuration.

## LESSON LEARN FROM THE PAST

The Space Shuttle Remote Manipulator System was originally planned to be used in two modes: manual and automatic (computer controlled). In practice RMS is being used only in manual mode. There are numerous problems related to the use of the RMS in Space. One of the most important problem is related to its positioning. As it was already mentioned this manipulator is built out of light materials to minimize the launch cost which is ~\$118K per kilogram for geostationary orbit (Wertz and Larson, 1991). The RMS may be considered as a very flexible manipulator, which means that its links deflect substantially. When the arm is accelerated and stopped; large vibrations occur which makes the positioning of the tip very difficult. The astronauts experience while handling Space Shuttle cargo or satellites indicates that one has to wait more than 20 minutes for manipulator's tip to stabilized. If more complex assembly tasks or operations are being performed on the orbit, the cumulative settling time before the arm's tip vibrations damp down to within 1 inch amplitude's margin could be 10-20 hours or more for 15 Space Station Freedom (SSF) related flights. That has a major impact on efficiency of any operation in the orbit. There are two main methods of improving positioning accuracy of the RMS: passive and active.

The passive method is focused on redesigning the manipulator and application of different materials. This alone could bring a substantial improvement in robot's dynamics performance. The drawback of this method is that it would increase the manufacturing cost of the arm. The performance of the manipulator would be improve but that could limited only to certain type of operations.

The second, an active method has more potential for improving posititing of arm's tip in various situations. There are two different methods to reduce the tip oscillations caused by commanded motions: first; the command input is preshaped and second; using position, velocity or force feedback to derive joint commands which are designed to damp oscillations. The "preshaped input" method is simpler, because it does not require identification of parameters like frequency, damping and friction. The drawback of this method is that it cannot take into account disturbances coming from the shuttle attitude changes. The "feedback" method may allow better damping but it requires the knowledge of the system in form of mathematical model and its parameters. There were several studies done on active vibration damping control (Dameo, 1990; Scott and Dameo, 1991) for the RMS. They all bring substantial improvement of positioning accuracy and they reduce the settling time. Scott and Dameo, 1991 show some identification results (Fig. 7) and the typical free responses (Fig. 8) which follows 10 seconds rotation command to the shoulder-yaw joint. The other joints are held fixed. Results obtained by Scott and Dameo, 1991 and shown in Figures 9 and 10 (Scott and Dameo, 1991) indicate that the

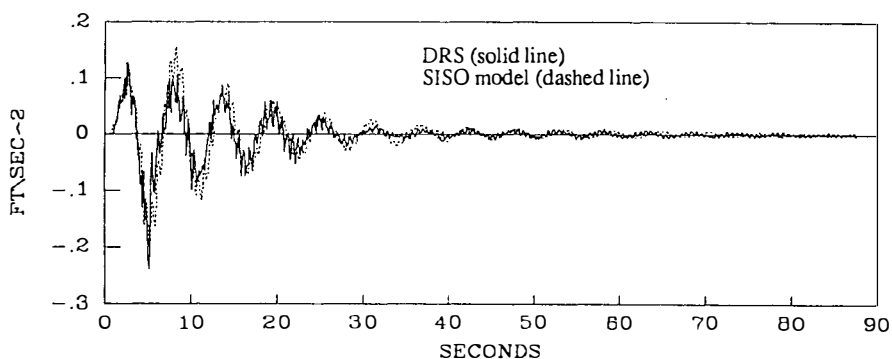


Fig. 7 RMS Identification Results for the Tip Accelerometer (from Scott and Dameo, 1991). (with the AIAA permission)

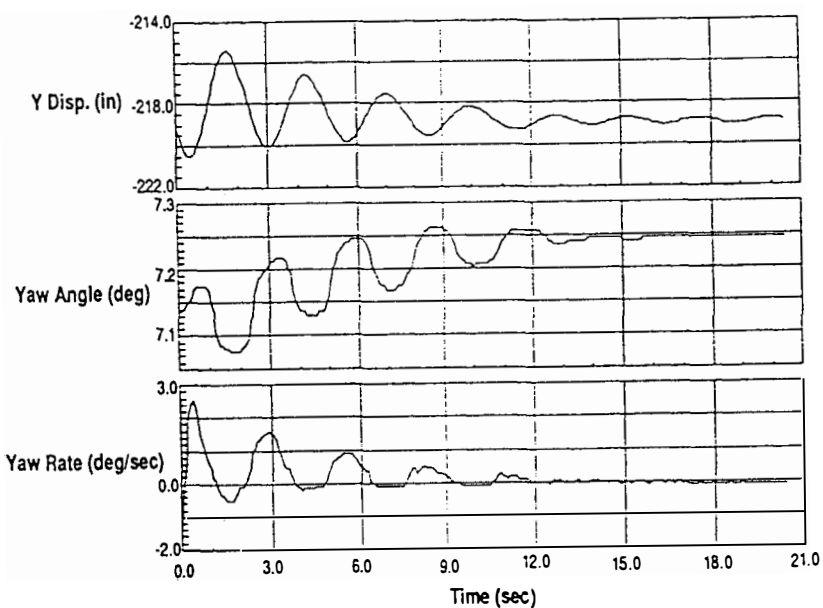


Fig. 8 Free Response of RMS (from Scott and Dameo, 1991).  
(with the AIAA permission)

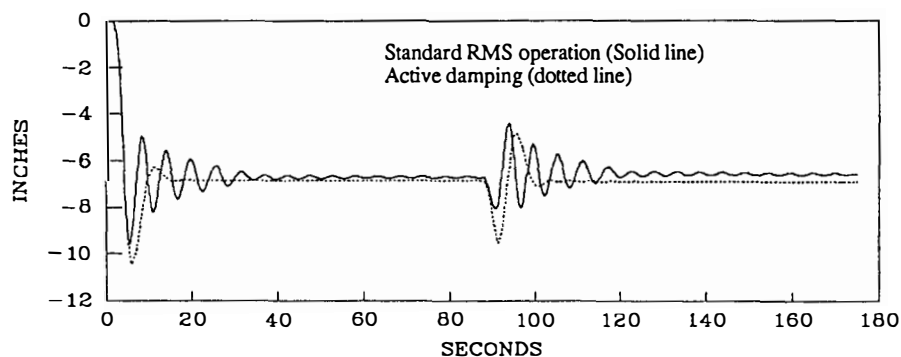


Fig. 9 RMS Tip Position during standard operation (from Scott and Dameo, 1991). (with the AIAA permission)

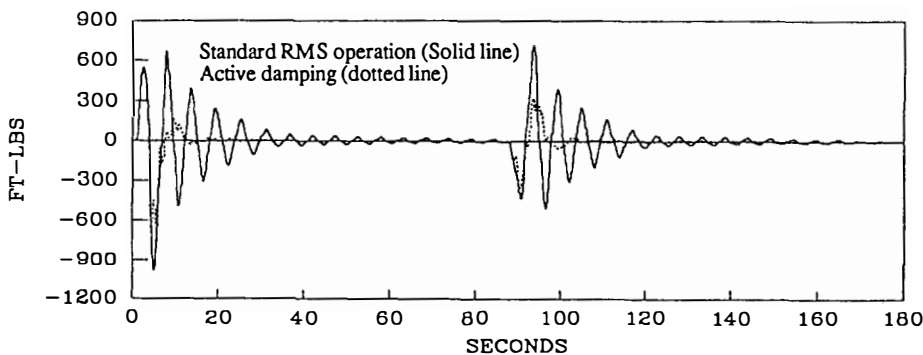


Fig. 10 RMS Shoulder Yaw Servo Torque during standard operation  
(from Scott and Dameo, 1991).  
(with the AIAA permission)

active control improves significantly damping (by factor of 3) and reduces the demand for peak joint torque (by factor of 2).

The numerous experiments indicate that the velocity feedback (from tachometers) and the acceleration feedback (from accelerometers) are needed for accurate and fast position control of the RMS. A simple PID control or optimal control might be satisfactory but more research is being done on adaptive control (Sasiadek and Srinivasan, 1989).

The Shuttle Remote Manipulator System handles often fragile payloads and a force control loop would greatly enhance its capabilities. Nguyen et al., 1991 described his concept of force accommodation control.

Another viable option for the RMS control is to couple both methods: passive and active. It calls for better structural design but also it requires an implementation of one or more feedback control loops.

The following lessons have been learned from 11 years long use of the Remote Manipulator System:

- speed of manipulation should be drastically improved;
- the positioning accuracy is one of the most important issues in day to day operations;
- the new manipulators should be designed to include a passive vibration control capabilities;
- new, active vibration control should be added in order to improve the positioning accuracy and shorten the settling time.
- the new force loop could add significantly to the capabilities of the manipulator.

#### FUTURE MISSIONS AND SYSTEMS

The planned assembly of Space Station "Freedom" creates new challenges for Space applications of robotics. Large payloads and main assembly operations will be performed with the help of newly designed SSRMS. The SSRMS is designed for payload capability up to 116,000 kg. The maximum tip velocity is 0.37 m/s. Its kinematics have been shown in Fig.2. This figure also shows range limits for manipulator's joints. The tip positioning accuracy is 4.5 cm with respect to the shoulder. The control system for the SSRMS has been shown in Fig.11. As it was already mentioned, the SSRMS is part of Mobile Servicing Centre (MSC). The MSC together with SPDM and the Mobile Maintenance Depot (MMD) form the Mobile Servicing System (MSS) responsible for majority of assembly and maintenance operations. The flow of information and data management architecture in the MSS has been discussed by Dignard, 1991. The MSS is controlled and operated from the pressurized environment and its human/machine interface is provided by the MSS Control Equipment (MCE).

The MCE is composed of the Hand Controller Assembly (HCA), Human-Computer Interface Software (IHS), the MSS Computing and Control Facility (MCCF), the Artificial Vision Unit (AVU) the Backup Drive Control Software (BDCS) and the Backup

Drive Human-Computer Interface Software (BDIHS).

The SPDM is a two arm robot which will be placed at the end of the SSRMS. Its payload capacity is 600kg. Unloaded manipulators could be positioned with the accuracy of 0.6cm. The SPDM is planned to be used for operations where higher accuracy is needed. It handles also much lower payload than the SSRMS. The SPDM control system has been presented in Fig. 12. Some aspects of SPDM and SSRMS control systems have been discussed by Stiber and Fung, 1991. The control system for SPDM is quite sophisticated. It involves simultaneous position/force control of dual-arm manipulator in complex tasks and hostile environment. The basic concept of dual-arm adaptive control has been discussed by Sasiadek and Srinivasan, 1987. One of the most important issues are the position/force control and grasping control.

The original plans for the Space Station Freedom (SSF) called for the Flight Telerobotic Servicer (FTS) which could fly in space in close proximity of the SSF and service the area difficult to reach for the SSRMS and SPDM. The FTS has two arms built on flying base. That introduces at least three additional degrees of freedom and makes the design of control system even more challenging.

The following problems are considered the most important and challenging in future development of Space robots:

- increasing autonomy of Space Robots;
- broad application of telerobotics;
- improved and more efficient position and force control systems;
- development of new free flying robots;
- design of a new, autonomous mobile robots for exploration of planets.

#### CONCLUSIONS

The exploration of the Space poses new problems and requirements for development of robotic devices. The Space voyages will take more time and astronauts will spend longer time in Space. However, before man is sent to other planets or systems, the thorough exploration has to be done using various kind of robots. The characteristic feature of development of Space Robots is that two main streams are being pursued simultaneously; one related to autonomous robots and second involving telerobotics with force feedback. This may help astronauts to perform various tasks and operation without leaving the pressurized environment.

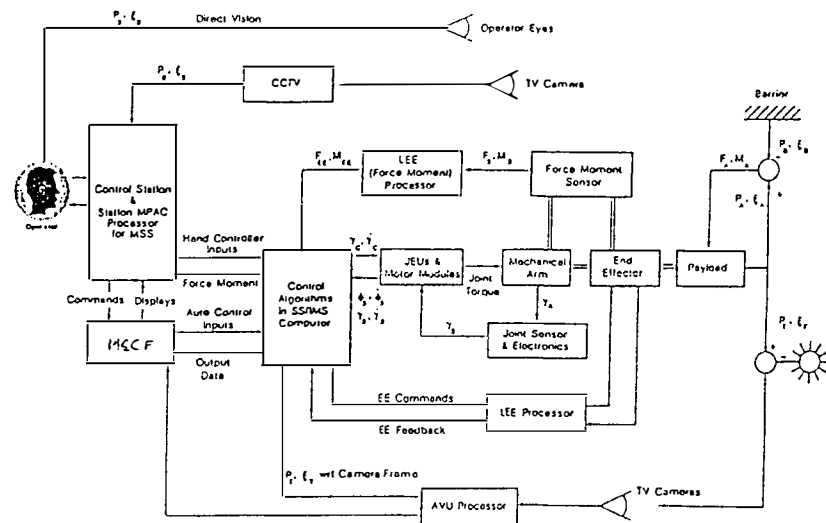


Fig. 11 SSRMS Control System. (from Stieber, M.E. and Fung, P.T.K. (1991))

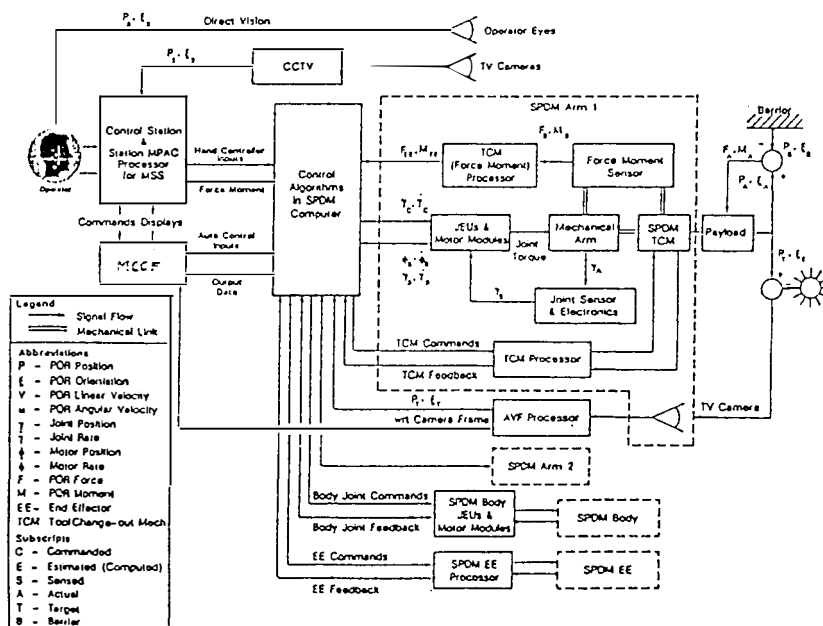


Fig. 12 SPDM Control System. (from Stieber, M.E. and Fung, P.T.K. (1991))

## REFERENCES

- Dameo, M.E. (1990). Remote Manipulator System (RMS)-Based Controls-Structures Interaction-Flight Experiment Feasibility Study. *NASA Report 181952*, January 1990.
- Scott, M.A. and Dameo, M.E. (1991). Active Vibration Damping of the Shuttle remote manipulator system. *Proceedings of the AIAA Guidance, Navigation and Control Conference*, New Orleans, Louisiana, USA, August 12-14, 1991.
- Dignard, N. (1991). Mobile Servicing System (MSS); System Configuration Document. *Spar Aerospace Limited Report (Spar-SS-R-0100)*, Toronto, Ontario, Canada, November 1991.
- Nguyen, T. (1991). Force Accommodation Control of Space Shuttle Remote Manipulator System: a Unique Problem. *Proceedings of the IEEE International Conference on Robotics and Automation*, Sacramento, California, USA, April 1991.
- Ravindram, R. (1990). The SPDM Design Status and Design Reference Missions. *The STEAR Technology Forum*, Ottawa, Ontario, Canada, May 24, 1990.
- Sasiadek, J.Z. and Srinivasan R. (1989). Dynamic Modelling and Adaptive Control of a Single-Link Manipulator. *AIAA Journal of Guidance, Control and Dynamics*, Volume 12, No. 6, November-December 1989.
- Sasiadek, J.Z. and Srinivasan, R. (1987). Adaptive Control of Dual Arm. *Proceedings of the IEEE International Conference on Systems, Man and Cybernetics*, Alexandria, Virginia, USA, 1987.
- Stieber, M.E. and Fung, P.T.K. (1991). Control System Challenges Associated with the Mobile Servicing System for Space Station Freedom. *Proceedings of the 14-th Annual AAS Guidance and Control Conference*, Keystone, Colorado, USA, February 2-6, 1991.
- Wertz, J.R and Larson W.J. (1991). *Space Mission Analysis and Design*, Kluwer Academic Publishers, Dordrecht, The Netherlands, 1991.

## COMMAND AND CONTROL FOR INTELLIGENT AUTONOMOUS VEHICLES: AN APPROACH EMPHASISING INTEROPERABILITY

C.J. Harris and R.J.C. Fraser

Advanced Systems Research Group, University of Southampton, Southampton, SO9 5NH, UK

**Abstract** The Command and Control ( $C^2$ ) system for intelligent autonomous, supervised or teleoperated vehicles comprises three infrastructural elements; the system architecture, the system processes and the management processes. This paper addresses each of these  $C^2$  issues through a unified framework for the achievement of "quality" in system design and performance, with greater compatibility, extensibility and reusability of subsystems between different Intelligent Autonomous Vehicles (IAV's). The paper objectives are to support increased interoperability of subsystems and components within developing standards for open systems architectures for real-time intelligent autonomous vehicles, and highlights an emergent approach to this problem based on the application of the techniques of object orientation.

**Keywords** Autonomous Systems Architectures, Command and Control, C++, Extensibility, Interoperability, Object Oriented Systems, Reusability, Robot Command Languages, Temporal Knowledge Based Systems, Temporal Planning.

### INTRODUCTION.

There are increasing applications in Aerospace for which a robotic or unmanned vehicle has to operate in large, unstructured and uncertain domains (for example, assembling space structures, deep space vehicles, intelligent remote sensing and surveillance, inspecting and repairing subsea structures, and planetary mobile vehicles such as the MARS AMBLER). Autonomous systems should have the capability to perform specified tasks, without external intervention, over extended periods of time. In order to deal with unanticipated situations, abstract high level reasoning about decisioning is frequently required. This involves learning which is called *intelligent*. Intelligent autonomous systems are therefore those systems which are self-organising, self-managing and have the capability to learn. Human intelligence is frequently associated with abstract conceptual *symbolic* reasoning and associated learning, so it is interesting to conjecture that if learning is numeric algorithmic based (for example by a stochastic approximation algorithm), it is no longer intelligent<sup>1</sup>. Uncertainty

dominates the problem domain for intelligent autonomous vehicles (IAV's), through *sensing* the vehicles location, *interpreting* the sensory data (the *perception* process), adapting to changes in the environment through *adaptive reasoning*, and with *replanning* (both in the spatial and temporal domains) that selects options and actions necessary to achieve the optimal subset of the prime mission goals.

However overall progress within the field of IAV's continues to fall short of expectations, principally due to the disparate nature of the many technologies and disciplines utilised (such as Artificial Intelligence, Operational Research, Software Engineering, and Control Theory, see Harris(1991)). IAV's require the integration and effective interface of these disciplines and technologies, yet there is an absence of an accepted theory and associated standards to define strong interfaces and achieve the commonality and modularity of components that support integration and validation requirements.

What is essentially required is a change to what Meyer(1989) describes as a *Product Culture*, where progress is measured, not in terms of the completion of individual projects, but in

<sup>1</sup>See Harris, Brown and Moore(1992) for a discussion of the nature of intelligent control.

terms of the number and quality of reusable components, libraries, tools and subsystems developed. The highly desirable result of the product (rather than *project*) centred approach is the associated development of portable generic subsystems technologies that may be transferred from system to system. However, to achieve these objectives and resolve the integration problems it is necessary to construct a framework for representing IAV systems. It is conventional in complex system design to decompose the overall problem into a series of subproblems and associated solutions, then perform integration, test and performance validation. This traditional top-down (Waterfall Model) approach does not, in general, support the construction of systems from reusable components (Meyer, 1987). What is required is a methodology for system analysis and design that is structured to support an eventual systems design that conforms to a required architecture model. This process must also support an "inverse engineering" approach, in that the design process should be directed towards the inclusion of those subsystem modules already available. *Reference Architectures* are designed to provide a universal schema for defining structural composition, connectivity and interrelationships to allow portability and provide a mechanism for system analysis and design with reuse as a principal goal. Associated with such architectures are the establishment of viable robust standards for IAV's (akin to the Integrated Modular Avionics Architecture ARINIC 651) that are precursors to the development of multi-vendor markets for IAV's and IAV equipments.

When considering the requirements of candidate architectures, the need to support *interoperability* of components and subsystems is fundamental. Interoperability is the ability to interchange elements of different systems through the use of a standard that ensures compatibility of such subsystems between the different target systems. Interoperability has its foundations in *strong modularity*, that is, modular design and implementation coupled with well defined, generic, module interfaces. This modularity must extend through all infrastructural elements and be applied in a coherent, rigorous manner. Modularity is supported by an extensible, open systems architecture that facilitates pluggable system processes in both hardware and software. Any viable architecture must be survivable, robust, and must provide for extensibility and reuse of those systems elements conforming to it.

## COMMAND AND CONTROL FOR AUTONOMOUS SYSTEMS.

In order to cope with unpredictable, dynamic environments, the Command and Control(C<sup>2</sup>) sys-

tem for an IAV must be defined in such a manner that it is possible to establish a methodology for the analysis, representation, design and construction of IAV infrastructures that support interoperability through the minimal conformance of quality in the systems infrastructure. *Quality factors* that define the central characteristics of interoperable systems are; correctness, robustness, extensibility, compositability and reusability. Meyer (1988) defines these factors as essential external properties of software architectures that support quality and the "Product Culture". Meyer argues that Object Orientation of software provides a substrate for such systems quality. Object Orientation<sup>2</sup> uses strong interfaces and the encapsulation of functionality to model the problem domain in software "objects". Inheritance and polymorphism are used to provide extensibility and support reuse. The *principles* on which Object Orientation is based (Parnas(1972) for example) apply equally to systems other than just software. The application of object orientation to robotics is an emergent theme in research, and will be discussed later.

In generating a Command and Control (C<sup>2</sup>) methodology that supports interoperability for IAV's it is suggested that there are three principle infrastructural elements to be defined (see fig. 1):

1. **Systems Architectures** that specify the functional and behavioural interfaces between component subsystems and the way in which different elements interact<sup>3</sup>.
2. **System Processes** are those units within the systems architecture that represent, manipulate and transform command and sensor data at various levels of abstraction. The subgroups of processes include:
  - Sensory Processing (sensors ⇒ sensor data fusion ⇒ situation assessment and perception),
  - World Modelling, and
  - Task Planning (planning ⇒ navigation ⇒ piloting (or guidance) ⇒ servo control),
 which are all hierarchically structured at varying levels of abstraction and intelligence.
3. **Systems Management Infrastructure** is the formalised methodology that provides

---

<sup>2</sup>see for example, Rentsch(1982);Stroustrup(1988)

<sup>3</sup>Reviews of Intelligent Autonomous Vehicles architectures are presented in Corfield, Fraser and Harris(1991) and Antsaklis and Passino(1992)

for the management, co-ordination and direction of the system tasks and processes. It is instantiated by a *Robot Command Language*(RCL) which specifies the hierachial management structure *within* the systems architecture into which the command and reporting vocabulary can be integrated for interprocess communications. The RCL formalises the system functionality and that of each system element, so as to specify interfaces at an abstract level during the analysis and design stage, as well as instantiating message flows through interfaces at the implementation stage.

## INTELLIGENT CONTROL ARCHITECTURES.

Increasing system complexity with concomittant stringent demands upon closed loop systems performance, necessitate the utilisation of increasingly complex and sophisticated controllers, that can match process nonlinearities, changes in operating points and environment, variations in process parameters and unpredictable disturbances. Intelligent Controllers (Harris, Brown and Moore, 1992) have been proposed to deal with such situations. The purpose of intelligent control is to incorporate the positive intelligent, creative attributes of human controllers, who cope well with complex control tasks with variable environments and goals, whilst avoiding the human characterisitcs of inconsistency, unreliability, temporal instability and fatigue. Intelligent controllers must perform under significant system uncertainties, cope with complexity, be able to cope with system failures (within limits) without external intervention and be sufficiently adaptable to deal with the unexpected and new control goals. A natural approach is to utilise a hierachial or nested control architecture in which there is a successive delegation of functions or tasks from the higher to lower levels, with sensory based information flows from the lower to higher levels. Figure 2 illustrates such an hierachial architecture with three levels of control (sometimes referred to as Planner, Navigator and Pilot levels). Higher levels involve imprecise conceptual reasoning operating in non-real time at low bandwidth, whereas at lower levels more precise and quantitative algorithmic methods dominate in near or real time at high bandwidth. Increasing (decreasing) precision is accompanied by decreasing (increasing) intelligence (Saradis, 1985).

In considering any candidate intelligent control architecture it is desirable to identify those minimal features or requirements that the open system architecture should support:

- **Correctness** - the ability to perform to a specified set of operational requirements, for which the minimal set of safety critical criteria can be validated. The incorporation of safety and dynamic constraints (say limits on accelerations) in the higher levels of the architecture, should ensure correctness and conformance through constraint satisfying controller designs at the lowest level.
- **Robustness** - the ability of the system to retain functionality under abnormal or unanticipated (a posteriori) internal and external conditions. Level 3 of the architecture of fig. 2 must make provision for *temporal reasoning* to cope with unknown situations and associated replanning and reconfiguration. At each level within the architecture there must be sufficient bandwidth to cope with the temporal reasoning/processing requirements, for all potential situations. At level 1, the intelligent servo-controller must deal with process nonlinearities, variable operating points, noise and parametric variations through their inherent self-organising and learning capabilities, offer a degree of reconfiguration through system faults, and ultimately for large parametric changes due to failures, provide graceful operational degradation.
- **Extensibility** - is included in intelligent control architectures for both planned and unplanned growth in subsystems hardware and software, *without* overall system redesign. The important design metaphor to achieve extensibility is *modularity*. Functional extensibility through the addition of new control systems should minimise as well as localise the controller design (incorporated into levels 2 and 3 of fig. 2). A modular architecture for extensibility requires well defined interfaces and command information flows. A modular extensible architecture will permit varying degrees of autonomy from level 1 (teleoperational control) through to level 3 (fully autonomous).
- **Reusability and Compatability (or Interoperability)** is the ability of the subsystems or components to be used in different applications. To achieve these attributes the architecture must be generic, i.e. have open transparent applications independent subsystems that permit modification and substitution (without additional interface and integration overheads), support modularity and provide unambiguous specification of module interfaces and communications.

There are few current intelligent control architectures that feature all of the above *minimal* characteristics, although there are emerging standards such as the distributed Integrated Modular Avionics Architecture (IMA, ARINIC 651) for future civil aircraft, and for IAV's, the NIST Reference Model Architecture for Real Time Intelligent Control - ARTICS(Albus,1990), which defines these features as minimum requirements for implementation<sup>4</sup>. ARTICS is foreseen as an evolving set of standards and guidelines for Intelligent Control Systems, and follows on from the definition of the NASREM hierachial robot architecture for the Space Station Telerobotic Servicer (Albus,1989). The NASREM architecture is shown in fig. 3 - it attempts to satisfy the minimum architectural requirements through a task decomposition architecture with heterarchial sensory processing, world modelling and planning structure, implemented at varying levels of abstraction in the system hierarchy. This architecture incorporates many AI concepts such as goal decomposition, hierachial real time planning and modelling, model driven sensory processing, blackboards and expert systems. Unfortunately there are few practical validated implementations of NASREM derived architectures, though partial implementations do exist (Albus, 1988).

The architecture of fig. 4. is derived from the NASREM architecture, and represents the C<sup>2</sup> architecture used for the European mobile robotics project PANORAMA (Esprit II Project No. 2483). It has a hierachial and heterarchial structure, the task decomposition processes containing planning (P), control execution (C) and feedback and reporting (R) modules. The first 4 hierachial levels correspond to an individual robot or IAV. Planning and Systems Management occur at the *Task* level, with localised navigation and perception being controlled by the *Local* level. Piloting and low level control occur in the *Guidance* and *Servo* levels. An important distinction between the Guidance and Servo levels is that the Guidance level represents vehicle(system) *independant* control, whereas the Servo level executes vehicle *dependant* control.

It has an orthogonal *task decomposition architecture* representing the system hierachial structure. This results in the three dimensional structure of the reference model shown in fig. 5. It retains the extensive system interfaces of NASREM, but does not support a global memory. Instead, hierachially restricted access to system databases is provided.

<sup>4</sup>Corfield, Fraser and Harris(1991) discusses the equivalence of the ARTICS requirements with the quality factors already described.

This architecture, together with a complementary management infrastructure called RCL, is used as the reference model for the synthesis of IAV command and control systems.

## INTELLIGENT CONTROL PROCESSES.

Within the reference model architecture, intelligent control processes are integrated at each level of the hierarchy, higher levels corresponding to increasingly intelligent, autonomous capabilities, using symbolic rather than geometric representations in the control processes. For the PANORAMA robot, intelligent control processes exist at each of the four levels of fig. 4 associated with an individual. At the task level, mission goals set by the operator are used to synthesise a mission plan. This is achieved through a dialogue between the operator and the mission management process, the global route planner and the perception planning system, all of which are contained within an Intelligent Systems Controller (ISYC). Once an acceptable plan has been assembled, subgoals are passed to the local level for further decomposition by the Localisation and Navigation System (LNS) to subgoals for the Piloting System (PISY), which exists at the Guidance and Servo Levels.

Temporal reasoning is a key feature of any IAV infrastructure, and is required to log events, predicted future events, reason about time dependent functions such as task and resource scheduling, sensor and perception management and piloting (Albus, 1990). At the Task Level, a Temporal Knowledge Based System (TKBS) has been implemented within the PANORAMA ISYC module, being integrated within a rule language system implemented in C++ (Fraser and others, 1991). The TKBS uses a logic of temporal intervals, developed by Allen(1983), extended to include time point objects and implemented in C++ classes. Relationships between two temporal objects are expressed as a vector, or set of primitive simple relations such as *before*, *after* and *started\_by*. There are seven simple relations, which together with their inverses make a total of 13 primitive temporal relations. These vectors represent knowledge about the temporal world, either in the form of facts ("A is before B") or in the form of constraints on the world ("A cannot overlap B"). For a group of statements about time intervals and points, the set of describing vectors are formed into a network in which the nodes represent temporal objects, and the arcs represent the temporal relationship between them. Rules exist for the transitive propagation of relations amongst this set of temporal objects. Some relationships will be indefinite, in the sense that they specify more than one possi-

ble temporal relationship between the two temporal objects. However these indefinite relationships can still be propagated through the network of vectors using the same rule-based reasoning process. The reasoning process can work on a *least commitment* strategy, where uncertainty is only resolved within the TKBS when required.

Hierarchical task decomposition architectures, such as NASREM and PANORAMA, generate hierarchies of tasks and subtasks during mission plan synthesis at all levels in the C<sup>2</sup> system architecture. These hierarchies can be represented very efficiently through the use of reference intervals or scopes (Allen, 1983) and hierarchies of reference intervals. Each node within a network of temporal objects and vectors can represent another network (or Temporal Knowledge Base) at a lower architecture level. Figure 6 illustrates the formation of such a hierarchy. At each level in the TKBS hierarchy, the temporal information can be mapped to a timeline for use in subtask generation and subtask execution monitoring. Heuristics are used to remove uncertainty from the TKBS before this timeline mapping takes place, such that the mapping is consistent with all the facts and constraints in the input field. The TKBS can be used to construct a command sequence at any hierarchical level, to allow plan or control synthesis to be completed within the temporal constraints specified.

Intelligent control processes are implemented within the Piloting Module (PISY) at the Guidance and Servo levels of the architecture. The Guidance level represents the vehicle *independant* part of the pilot, the Servo level the vehicle *dependant* part of low level control. Within the PANORAMA project, this dichotomy has been emphasised, such that the only the Servo level of the C<sup>2</sup> architecture changes between various testbed implementations (testbeds include a four-wheel Honda vehicle and a tracked rock drilling machine). Intelligent control processes such as neurocontrollers and fuzzy logic controllers are being implemented at this level (Harris, Brown and Moore, 1992).

The command and control of subordinate levels within the system architecture is facilitated by an interprocess communication scheme, which forms an integral part of the C<sup>2</sup> system infrastructure. The *systems management infrastructure* supports message passing between processes, based around a command vocabulary. The Robot Command Language RCL(Fraser and Harris, 1990) instantiates the command vocabulary for the IAV C<sup>2</sup> system. Figure 7 shows two examples of the RCL command vocabulary, used for commanding vehicle motions to the Servo level controllers. These commands form

part of the interface between the vehicle dependant and independant levels of the Piloting System.

## IAV's MANAGEMENT INFRASTRUCTURES.

The purpose of a command language within an IAV architecture is to specify the management structure through a systematic well formed framework into which the system and application specific command and reporting vocabulary can be placed. The prime features of a robot command language (RCL) are:

- generic in nature
- provide universal interprocess communications within the architecture
- provide unambiguous inter-layer command flow
- be survivable and robust
- support both inter- and intra-layer command flow.

Additionally the RCL must define the structures, syntax and semantics for providing IAV C<sup>2</sup>. This requires

- definition of a common "skeleton" into which the system vocabulary can be placed
- a minimum set of generic commands
- protocols for implementation

### RCL Structure.

A generic RCL will have a set of substructures which in combination with the language syntax, semantics and underlying logic, forms a means of performing command and control within the architecture. The main substructures are:

- Logic, Primitives and Rules
- Descriptors
- Commands.

Logic, Primitives and Rules specify the syntax, semantics and primitives of the language and the manner in which knowledge is represented. The Descriptors are sets of labels, which describe the system and its environment at varying levels of abstraction. Command structures are used for specifying system actions in the broadest sense.

### Logic, Rule Sets and Primitives.

Logic represents the fundamental, underlying representation of knowledge within the language.

The logic may be conventional crisp logic, fuzzy logic, or with temporal extensions. The language must provide command information to hierarchical planning processes, and therefore must express tasks and goals in terms of the constraints and reasoning processes supported by the underlying logic.

The *Rule Sets* are of two forms: (i) *Syntax Rule Sets*, which define the syntax of the command language. They define how the elements of the language, the descriptors, environmental predicates and abstract structures are constructed and expressed. (ii) *Semantic Rule Sets*, define the generic meaning of RCL structures, providing unambiguous reference to language usage and interpretation. The command semantics of RCL are *task oriented*, in that language commands focus on describing IAV actions relative to its environment, and not simply on specifying vehicle motions explicitly.

*Primitives* are fundamental tokens, the fixed alphabet used in the RCL. This group includes integers, logical symbols, and other labels used in the underlying logic. This can include fuzzy labels such as likely, almost etc, or constraint and priority labels such as critical, hard, soft, minimum etc. An example could be:

```
holds (10:00 , temp_hard,
       10:15 , temp_soft,
       location(IAV1, L2)
     );
```

where this temporal logic expression uses the labels *holds*, *temp\_hard*, *temp\_soft*, and *location* which have logical meaning. Note that *IAV1* and *L2* are the names of agents or objects, rather than being primitive tokens, and 10:00 and 10:15 are time point values.

#### Descriptor Sets.

Descriptor Sets are those language structures that are used to label entities (things) within the IAV world, and the relationships between them. There are four groups of descriptors in the RCL (see fig. 8):

- Entities
- Entity States
- Relationships between Entities
- Relationships between Entity States.

An *entity* is anything that exists in the IAV world. There are two distinct classes of entity: (i) **Objects**, which are any structures within the IAV world. The object list could include airfield,

landmarks or waypoints, beacons, roads, crossings, trees, woods etc. Object descriptions are hierachial, in that the list includes objects and *subobjects*. (ii) **Agents** are that subset of objects with one or more states under command. As with the object list, the agent list forms a hierachial description of commanded objects. For example, in the C<sup>2</sup> reference model architecture, they might be for a multirobot system: Group (level 5), Robot (level 4), Manipulator Arm (level 3), Joint (level 2) and Motor (level 1).

Each of these objects is commanded directly or through the task decomposition process. It is possible to command the system at each of these levels, i.e. commands can be issued to groups, robots, joints or motors. Hence each agent can be regarded as multilevel, defined by one or more levels in the C<sup>2</sup> architecture.

Every entity, object or agent, has an associated state space. This is divided into two subgroups: (i) *Internal* (local) states which describe "inherent" properties of the entity such as mass, dimension, surface etc and (ii) *External* (global) states which describe entity properties which exist by virtue of its presence in the world. These "relative" properties include states such as position, orientation, velocity, acceleration etc.

Given definitions of entities and their states, the RCL essentially operates on *relationships* between the entities and/or between their states. *Relationships between Entities*(RE) include relationship descriptors such as *has\_part*, *is\_member\_of*, *has\_elements*, *belongs\_to* etc. They may be used to define the hierarchy of entities that exists in the object or agent lists. Similarly, *Relationships between Entity States* (RES) specify the ways in which different entity states compare with each other. There are two subgroups of RES descriptors:

(i) *Internal* RES descriptors which compare internal or local states. These include greater\_than, less\_than, equal etc. A typical syntax rule might be:

<E:ES> RES <E:ES>

or

<IAV1:mass> less\_than <IAV2:mass>

(ii) *External* RES descriptors, which describe the relative states of entities through descriptors such as faster\_than, left\_of, near, far, on\_top\_of, below etc.

Note that descriptors are given meaning by the semantic rule base, their use and format are defined by the syntax rules, and their interpretation and processing are defined by the reasoning processes.

### Environment Predicates

Environment Predicates provide extended and abstract descriptions of the system in its environment, by utilising the descriptors and logic structures. They are grouped into Situations, Events and Actions.

A *Situation* is a recognised condition, or set of conditions in the world. One situation might include another from the list, e.g.

```
UNSAFE( holds(<IAV:x_velocity>
               greater_than
               <IAV:x_velocity_limit>)
        );
```

Note here that the use of the UNSAFE predicate is a recognised situation. In perception, a VIEW or expected sensory pattern can be recognised as a situation definition. A GOAL is defined as a desired situation in the IAV world e.g.

```
GOAL( holds(10:00, temp_hard,
             10:15, temp_soft,
             location(IAV1, L2))
      );
```

An *Event* is a recognised set of *changes* in the IAV world, represented by changes in entity states, the relationships between entity states, or the relationships between entities.

An *Action* defines an event that is directly attributable to the execution of a command by an agent in the environment.

Situations, Events and Actions are hierachial in the same sense as Agents and Objects. For example, an action can be defined as a set of lower level actions, structured to correspond to the agent list hierarchy. Note that in turn, the agent list hierarchy corresponds to the architecture task decomposition hierarchy.

### Abstract Structures and Qualifiers.

Abstract Structures and Qualifiers are the most abstract descriptors of the IAV in its environment. They express *concepts* that are used in processes at the highest levels of the architecture. For example, the command *Do\_Mission* is an executable series of actions which is separate from the concept of a *mission* which is used during the planning of those executable actions. The mission is not simply a set of events or situation descriptions, but an ordered list of goals with constraints on how they are to be achieved. MISSION\_DISTANCE is a structure defining the distance travelled between mission start and end events. MISSION\_TIME is the time between the two. RISK, PAYOFF, UTILITY, THREAT and

PRIORITY are other examples. These concepts are very important in intelligent planning and replanning, where they can be used to *qualify* action commands and predicates, eg;

```
Do_Mission( Minimum( MISSION-TIME));
Commands.
```

Commands that are issued to Agents have a hierachial structure which corresponds to the agent list hierarchy and the task decomposition architecture of the reference model. This hierachial structure is an essential characteristic of RCL. The command vocabulary is itself hierarchially structured, to represent the generic *types* of IAV commands. The command structure for IAV architectures, such as that defined by the C<sup>2</sup> reference model, may be defined as shown in fig. 9.

Within a generic command language such as RCL there is a requirement for a *minimum* specified set of unambiguous generic commands, defined by the semantic rule sets and containing no conditional elements (such as *If-Then-Else* or *Do-While*). Note that all branching of the process flow in the C<sup>2</sup> reference model is either specified in a high level control program or handled within the logic (program) of the planning modules. The semantics of the command set are task orientated, describing IAV motions only implicitly at the higher levels of command. For example, PICK\_UP<Object> or GRASP<Object> are used rather than CLOSE\_GRIPPER for a manipulator arm. The reason for this is that the former commands necessarily require compliance monitoring in terms of the commands effect on the world (has an object been grasped?). At lower levels, the command CLOSE\_GRIPPER will be used to effect the action, but it should be avoided in the semantics of the higher level command and control so that the causality of a command, and any side effects, can be monitored.

The definition of generic commands is hierachial, as indicated by fig. 9. Within the reference model architecture, the *horizontal* command flow specifies requests for information and replies. This is used for co-ordination of processes at the same hierachial level, and for database update and query. The reference model supports the use of proprietary database systems, with the command language structured such that it is possible to integrate corresponding query language facilities into the RCL framework.

Also within the minimum generic command set, it is necessary to be able to support system interface facilities, such as extensive operator monitoring, opportunity for operation intervention by the operator and performance assessment.

## POLYMORPHIC ROBOT COMMAND LANGUAGE.

The RCL described above has been introduced as an instantiation of the systems management infrastructure for an IAV command and control system. It establishes a common framework for the integration of intelligent control processes into a reference model architecture for such systems. It is, however, only one instantiation of this "management infrastructure" for IAV's. Three separate, but inherently linked instantiations have been defined as part of the C<sup>2</sup> Reference Model:

- **RCL:** This is the lexicographical, parsed language definition described above.
- **RPL:** Robot Programming Language (RPL) is a set of class library extensions to the C++ language. Using a common core of the command and descriptor definitions from RCL, RPL defines an *application oriented* programming language for IAV's. It is defined hierarchically, RPL programs running on a *Virtual Machine* consisting of the IAV intelligent control processes integrated within an operating system implementing the C<sup>2</sup> Reference Model Architecture.
- **pRCL:** Polymorphic Robot Command Language (pRCL) is an implementation of the RCL definition in persistent C++ software objects<sup>5</sup>. Whereas RCL requires software tools (such as the UNIX Lex and Yacc utilities) to provide parsing structures, this object form relies on inheritance and type conformance to implement language features.

The pRCL objects are used within an object oriented operating system for IAV's, which conforms to the C<sup>2</sup> Reference Model Architecture. Control processes that integrate into this operating system architecture are implemented as objects, with visible (or public) interfaces that conform to the various pRCL *types*. Each command type is open for extension by subtyping, using the inheritance mechanism of C++. In this way, the extensibility of the RCL syntax is mirrored in the object form by use of inheritance which maintains subtype conformance.

The Operating System for the C<sup>2</sup> Reference Model is being implemented using a *coroutine* style of programming, allowing pseudo-parallel system execution. The C++ library task.h is being used to implement the coroutine software (Sun Microsystems, 1991).

<sup>5</sup>In the NASREM architecture, commands are implemented using a hierachial frame representation, rather than as objects.

## OBJECT ORIENTATION IN ROBOTICS.

In this paper, interoperability has been introduced as an essential intelligent control system quality. Quality is defined in terms of a set of factors, originally defined for open software architectures, but which can be applied to architectures for IAV's, and other robot systems.

The Command and Control approach to the specification of IAV systems infrastructures emphasises the systems management infrastructure within a reference model architecture as an approach contributing towards the achievement of interoperability. The multilevel, hierachial concepts of this approach support extensibility through evolution in system functionality at higher architecture levels. The defintion of an extensible framework for interprocess command and control, in terms of the RCL definition of a command and reporting vocabulary framework, is an instantiation of this management infrastructure. An object oriented operating system for IAV's is under development, which uses an object based form of RCL for interprocess communication. Further, the types of the RCL objects used specify the interfaces to the integrated control processes. These object types, and hence the interface definitions, are extensible, whilst retaining "backwards" compatibility, by using inheritance to create subtypes that remain conformant to their supertypes.

This approach represents an attempt to apply the principles of object orientation to IAV systems infrastructures. Indeed, it is suggested here that *IAV (robot) infrastructures can be viewed as object oriented systems*. Object Orientation is intended to produce software systems architectures which prove to be extensible and support reusability - the quality attributes sought in a viable IAV systems architecture. Object orientation emphasises the importance of interface specification to software objects, and all inter-process communications is by means of message passing through these interfaces, which results in the isolation of changes to process specifications within individual modules. These principles apply equally to hardware and software systems. In our approach, the IAV system consists of a hierarchy of objects, with functionality encapsulated and hidden behind a "visible" interface. The interface specifications are provided by the RCL structures, which also instantiate the messages passed between objects (processes). As such, these messages correspond to elements of the visible object interface.

This approach is one amongst a number of recent examples to apply object orientation

to robot systems infrastructures. Volz and Mudge(1984) proposed that robot workcell programming could be structured around the use of abstract data types (implemented as classes) representing individual system elements. Miller and Lennox(1991) describe an Object Oriented Environment for Robot Systems Architectures called RIPE, in which inheritance from generic system classes is used to create a uniform interface protocol to different robot system elements. The generic class interfaces then form the definition of a Robot Independant Programming Language. Rodseth(1991) describes an Object Oriented Software System for Autonomous Underwater Vehicle Control, where inheritance and polymorphism are used for the uniform handling of events, in a similar way to the operation of pRCL objects. Zheng(1990) implements a mission configurable robot systems architecture, based on hierachial and layered control, using object orientation and event-based programming.

The need for analysis and design methodologies for Robotics and Automation has been recognised, and is being addressed. For example, Elfving and Kirchhoff(1991) provide a Control Definition Methodology for space-based robotics and automation, based on structured design principles. Menga(1989) applies object orientation to the synthesis of factory automation reference models.

Taking the view of complex robot systems, such as IAV's, as object oriented systems, is an approach that can allow the application of the principles and methods of object oriented analysis and design to the definition of a development life-cycle for robot systems infrastructures. In combination with reference models and the essential element of an integrated systems management infrastructure, this defines a development methodology for IAV's that emphasises the achievement of interoperability.

#### **ACKNOWLEDGEMENT.**

This work has been funded by the ESPRIT II Project 2483 PANORAMA. Professor Harris is supported by Lucas Aerospace.

#### **REFERENCES.**

- Albus, J.S. (1988). System Description and Design Architectures for Multiple Autonomous Underwater Vehicles. NIST-TN-1251. USA.
- Albus, J.S., McCain, H.G. and Lumia, R. (1989). NASA/NBS Standard Reference Model for Telerobot Control System Architecture (NASREM). NIST Tech. Note 1235, 1989.
- Albus, J.S. (1990). Concept for a reference model architecture for realtime intelligent control - ARTICS. NIST/NBS. Tech. Note. TN-1227. USA.
- Allen, J.F. (1983). Maintaining Knowledge about Temporal Intervals. Commun. ACM. Vol 26 (11), 1983, pp832-843.
- Antsaklis, P.J., Passino, K.M. (1992) Introduction to Intelligent Control Systems with High Degrees of Autonomy. In Antsaklis & Passino(Eds.), An Introduction to Intelligent and Autonomous Control, Kluwer, May 1992 Chapter 1.
- Corfield, S.J., Fraser, R.J.C., Harris, C.J.(1991). Architectures for Real-Time Control of Autonomous Vehicles. IEE Computing and Control Engineering Journal Vol. 2, Number 6 November 1991 p254-262.
- Elfving, A., Kirchhoff, U. (1991). Design Methodology for Space Automation and Robotics Systems. ESA Journal Vol 15 Number 2 1991 p149-164.
- Fraser, R.J.C., and Harris, C.J. (1990). Draft Robot Command Language Specification. Esprit II - Panorama Project No. 2483. Technical Report SOU TN5, 1990.
- Fraser, R.J.C., Harris, C.J., Mathias, L.W., and Rayner, N.J.W. (1991). Implementing Task level Mission Management for Intelligent Autonomous Vehicles. Engineering Applications of Artificial Intelligence Journal, Vol. 4 (4). pp257-268.
- Harris, C.J. (1991) Editorial on Special Issue in Intelligent Autonomous Vehicles. Engineering Applications of Artificial Intelligence Journal, Vol. 4 (4). pp.251-255.
- Harris, C.J., Brown, M. and Moore, C.G. (1992). Intelligent Control: aspects of Fuzzy Logic and Neural Nets. World Scientific, Singapore, 1992.
- Menga, G., Morisio, M., La Russo, G. (1989) A Framework for Object Oriented Design and Prototyping of Manufacturing Systems. In Technology of Object Oriented Languages and Systems, TOOLS-89, p59-73.
- Meyer, B. (1987). Reusability: The Case for Object Oriented Design. IEEE Software March 1987 p50-64.
- Meyer, B. (1988). Object Oriented Software Construction. Prentice Hall.
- Meyer, B. (1989). The New Culture of Software Development: Reflections on the Practise of Object Oriented Design. In Technology of Object Oriented Languages and Systems, TOOLS-89, p13-23.
- Miller, D.J., Lennox, R.C. (1991). An Object

Oriented Environment for Robot Systems Architectures. IEEE Control Systems Magazine, February 1991 Vol. 11 No. 2, p14-23.

Parnas, D.L. (1972) On the criteria to be used in decomposing systems into modules. Communications of the ACM, Vol. 15, No. 12, December 1972 p1053-1058.

Rentsch, T. (1982). Object Oriented Programming. SIGPLAN Notices Vol. 17, No. 9, September 1982 p51-57.

Rodseth, O.J. (1991). Object Oriented Software Systems for AUV control. Engineering Applications of Artificial Intelligence Journal Vol. 4 (4), pp269-278.

Saradis, G.N. (1985). Intelligent Control for Robotics and Advanced Automation. In G.N.Saradis(ed), Advances in Automation and Robotics. Vol. 1, 1985 JAI Press Inc, London, England. ISBN 0-89232-399-X, Chapter 1.

Stroustrup, B. (1988). What is Object Oriented Programming? IEEE Software 5(3) p10-20 May 1988.

Sun Microsystems (1991). AT&T C++ Language System Library Manual. In Sun C++ v2.1 Documentation.

Volz, R.A., Mudge, T.N. (1984). Robots are (Nothing More Than) Abstract Data Types. Proceedings of the SME Conference on Robotics Research, Society of Manufacturing Engineers, Dearborn, Michigan, August 1984.

Zheng, X. (1990). Object Oriented Software Architecture for Mission Configurable Robots. Proceedings of the 1<sup>st</sup> Workshop on Mobile Robots for Subseas Environments (IARP), Monterey, Calif. USA. Oct. 23-26. pp.63-73.

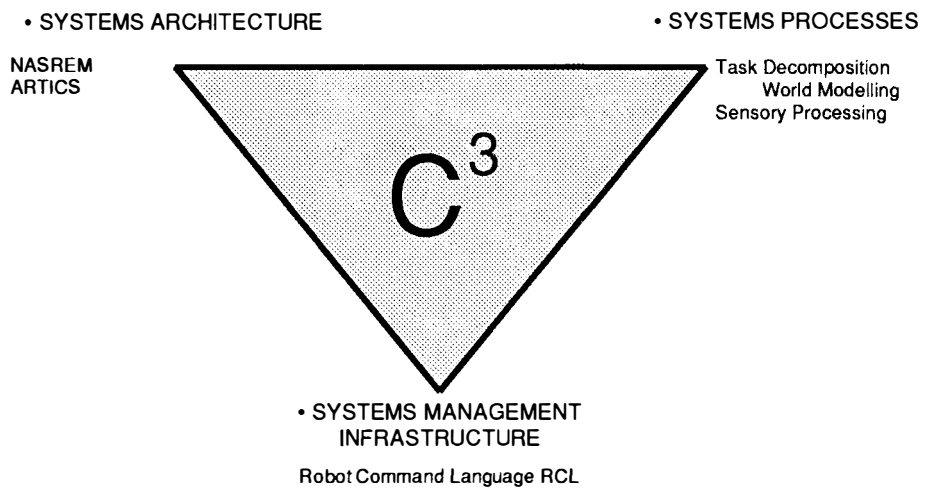


Fig. 1. Command, Control and Communications Infrastructure for Teleoperated, Supervised and Autonomous Systems.

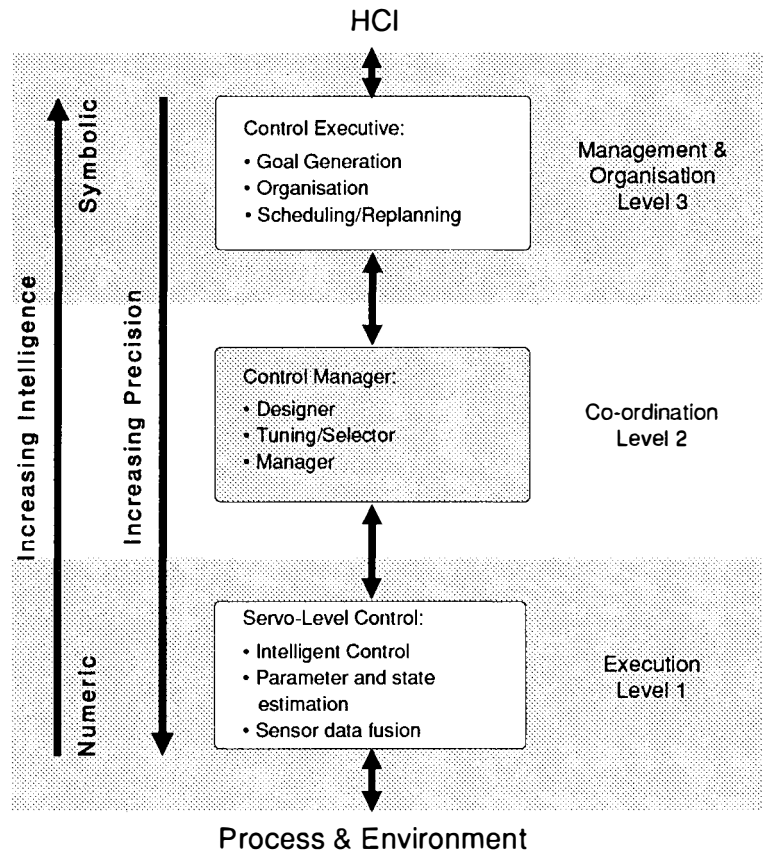


Fig. 2. Classical three level Intelligent Control Architecture.

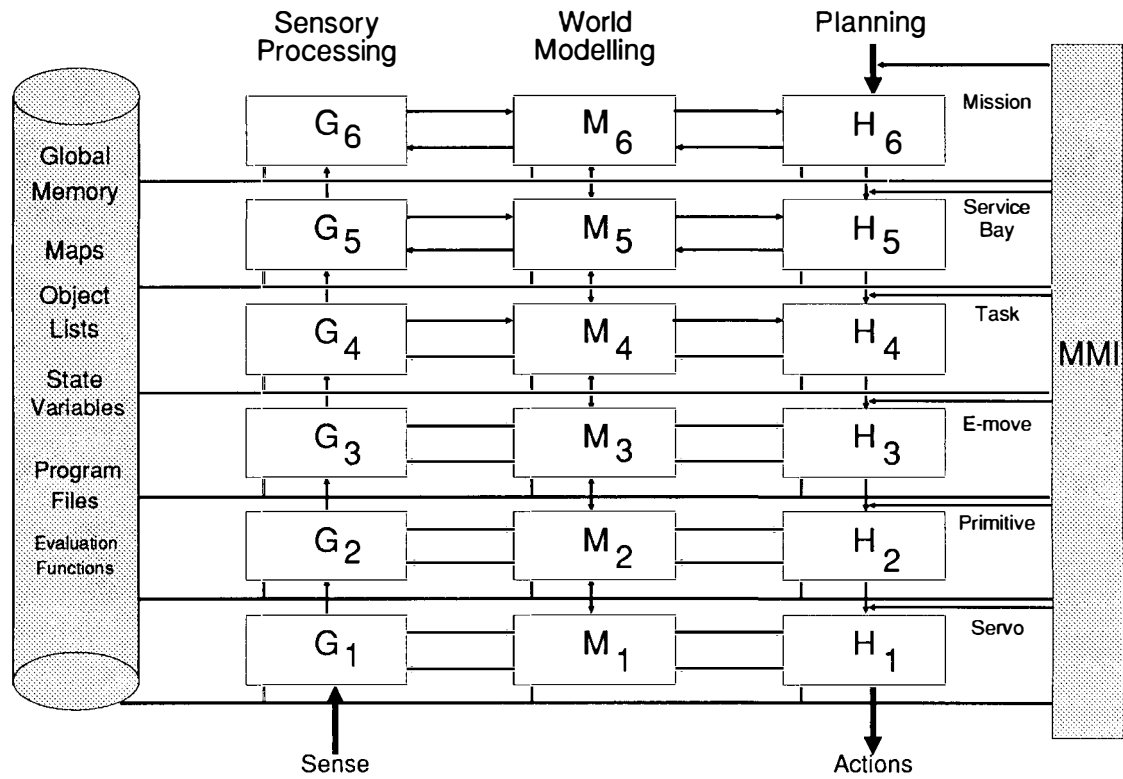
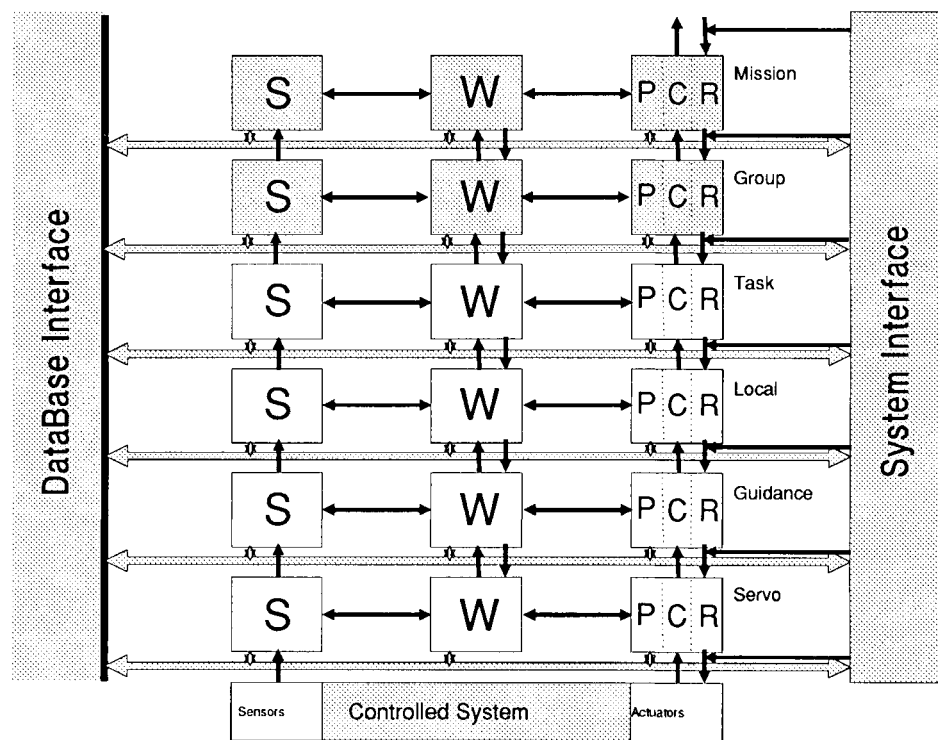


Fig. 3. N.I.S.T. National Standard Reference Model Architecture for Telerobot Control Systems (NASREM).



S • Sensory Process W • World Modelling Process  
 P • Planning C • Control Process R • Reporting

Fig. 4. Reference Model Architecture.

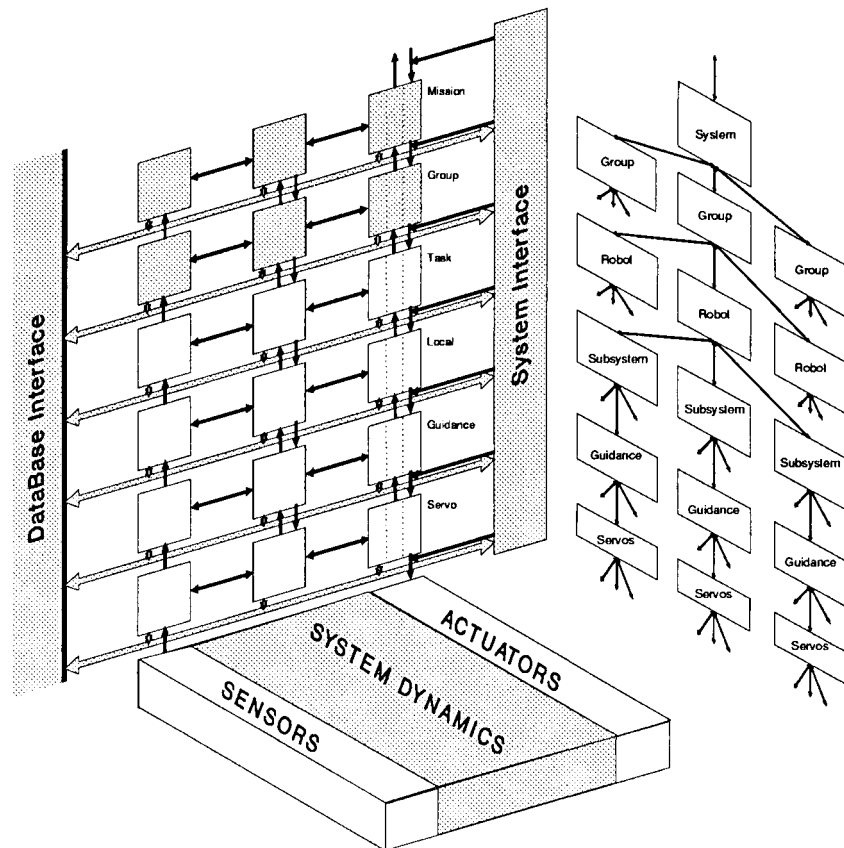


Fig. 5. 3D Reference Architecture Model Structure.

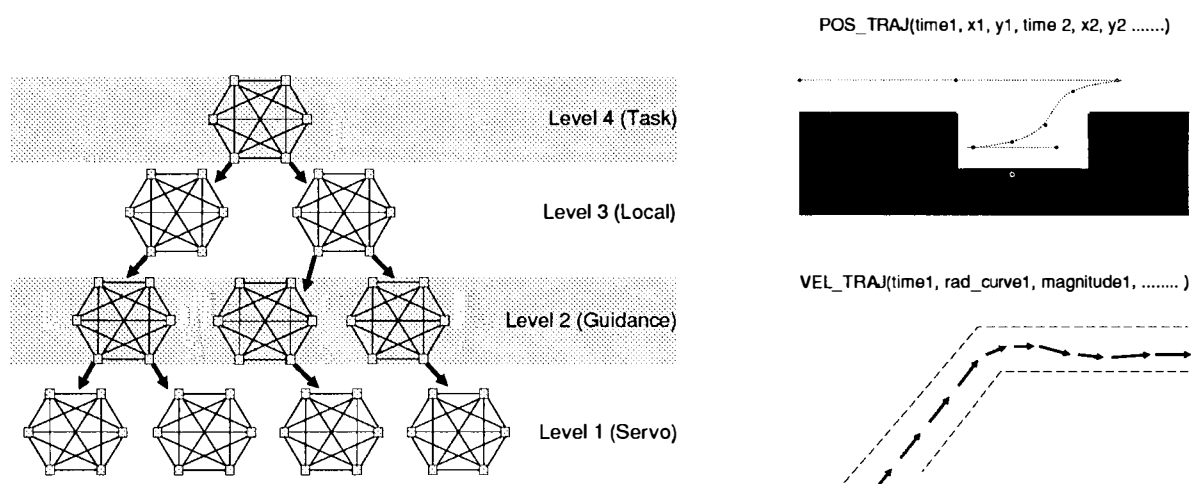


Fig. 6. Hierarchy of Temporal Knowledge Bases within the Task Decomposition Architecture.

Fig. 7. RCL Servo Level Commands.

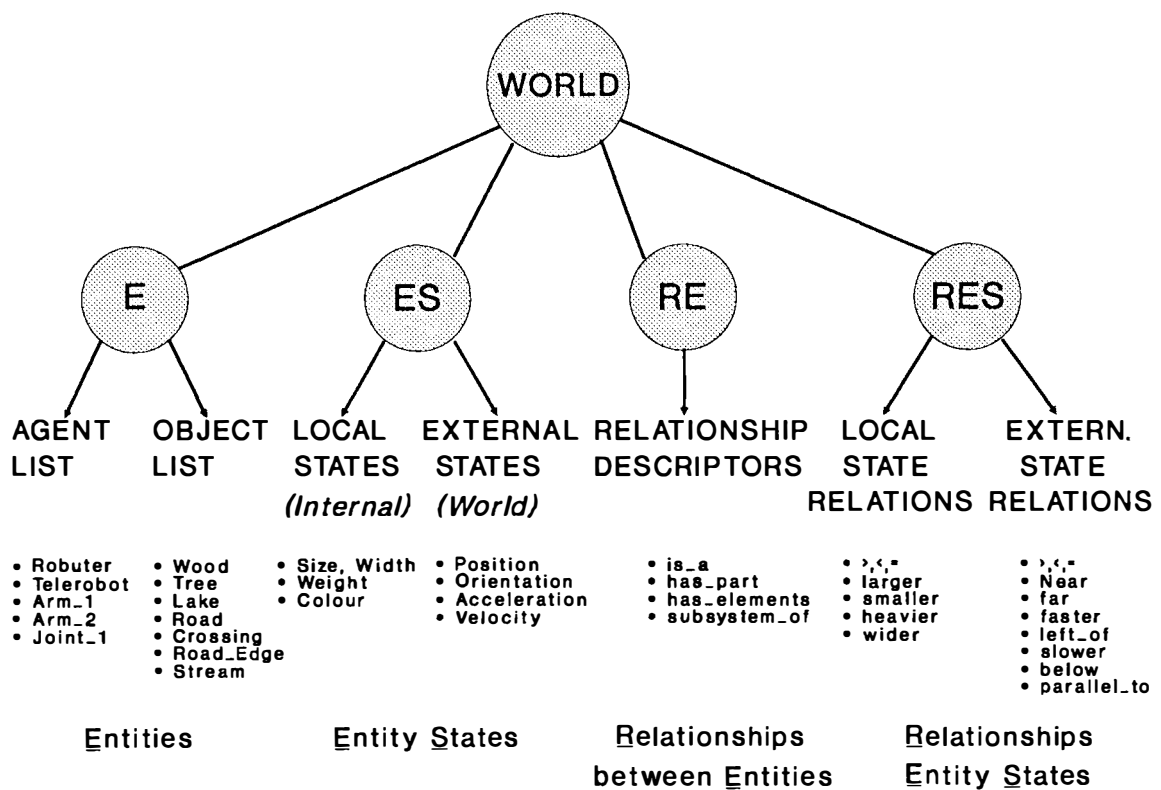


Fig. 8. RCL Descriptor Sets.

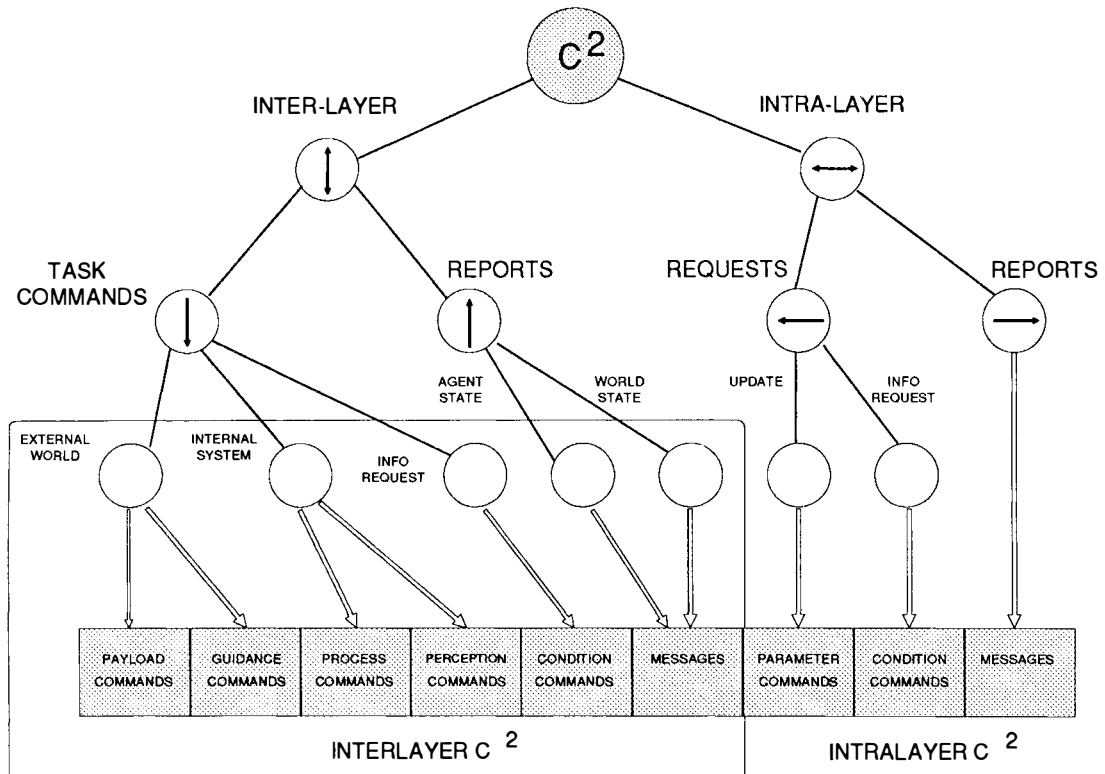


Fig. 9. RCL Command Group Structure.

## DYNAMICS AND CONTROL OF FLEXIBLE AEROSPACE STRUCTURES

S.M. Seltzer\* and J.R. Mitchell\*\*

\*2786 Hurricane Road, New Market, Alabama, USA

\*\*Department of Electrical and Computer Engineering, Ohio University, Athens, Ohio, USA

**Abstract** The dynamics and control of flexible aerospace structures exercises many of the engineering disciplines. This plenary paper sets forth the importance of clearly establishing the mission and performance requirements of the flexible aerospace structure. Means of developing a system model are described, along with model reduction techniques. Several control system design methods are then discussed. Techniques for estimating and verifying system performance are described. Examples of existing techniques and facilities are set forth.

**Keywords** Control systems design, Dynamic response, Flexible aerospace structures, Modeling, Model reduction, Multivariable systems, Performance verification, Simulation, System Identification, Vibration control.

### INTRODUCTION

SKYLAB -- the world's first manned orbiting space station -- introduced the myriad of problems associated with the dynamics and control of flexible aerospace structures (FAS's) that must be pointed and controlled with great accuracy. (Seltzer, 1975). The problems included the development of accurate dynamic models of the system and its subsystems, the development of hierarchical control systems that could perform under demanding environmental and on-board disturbances, the ability to predict the system performance before launch, the capability to redesign the control system on orbit, and the ability to replace or accommodate failed components. The structural flexibility of the system became a major consideration that arose early in the design and continued to be a problem throughout the mission. In the ensuing years since SKYLAB, these problems have become more severe, primarily because the performance requirements have become more demanding and because the ability to place heavy structures into orbit has decreased.

Beginning in 1979-80 the US Department of Defense initiated a program, entitled "Active Control of Space Structures" (ACOSS), to develop techniques that would enable the dynamic modeling, control system design, and experimental verification of flexible aerospace structures with stringent

performance requirements (Control Dynamics, 1984). The pointing and vibration suppression controls techniques that resulted are Filter-Accommodated Model Error Sensitivity Suppression (General Dynamics, 1980), High Authority/Low Authority Control (HAC/LAC) (Lockheed, 1982), and Positivity (TRW, 1983). Several severe problems surfaced. First, the difficulty in obtaining sufficiently accurate dynamic models of the aerospace system and the disturbances acting upon it once again became evident. Second, the need to verify system performance before flight was found to be costly, time-consuming, and the subject of considerable unpleasant debate.

Shortly after the ACOSS Program was completed, NASA's George C. Marshall Space Flight Center (MSFC) embarked on a program to develop a ground test facility to emulate technical pathologies associated with FAS's (Waites, 1987). Because of the associated cost and effort, it has only been recently that other comparable facilities have been developed.

The progress in the area of dynamics and control of FAS's can be measured partially by the related meetings and symposia in the area. In the past seventeen months these have included the IFAC Workshop in "Dynamics and Control of Flexible Aerospace Structures: Modeling and Experimental Verification" in Huntsville, Alabama, on 2-4 April

1991; a number of dedicated sessions conducted by the American Institute of Aeronautics and Astronautics (AIAA), the American Astronautical Society (AAS), NASA/DoD (Department of Defense) and, of course, the 12th IFAC Symposium on Automatics Control in Aerospace held at Ottobrunn, Germany in September 1992.

## REQUIREMENTS AND PERFORMANCE

Although not much fun and not of obvious engineering delight, it is extremely important to clearly set forth the system and performance requirements at the beginning of a program. In the end, the manner in which these requirements are met will be judged by the on-orbit performance of the system. However, the engineers must have a means of predicting how well the system will perform. These predictions are made by the use of several (or all) of the following means:

1. Analysis - Engineering and mathematical analyses must be made to estimate system performance such as stability, vibration suppression, disturbance rejection, target acquisition, pointing accuracy, reacquisition and re-pointing, etc.

2. Computer and hardware-in-the-loop simulations - A computer simulation can incorporate higher fidelity equations of motion. If the results do not compare closely to those of Step #1 (above), the reasons for the discrepancies must be ferreted out and clearly understood. Selected pieces of hardware can be incorporated into the simulation, gaining even greater confidence in the predictions.

3. Ground hardware facilities - Hardware testing facilities are now used to investigate the dynamic performance associated with flexible aerospace structures. These results are also used to update computer simulations, resulting in cost-effective investigations. Such facilities often contain actual space structure hardware, emulated software, and extensive instrumentation.

4. Sub-orbital test facilities - Another way of determining performance is with the use of sub-orbital test facilities, such as a high tower from which the test article is dropped in "free fall". A more accurate, longer-duration test may be performed on board an aircraft flying a parabolic trajectory or high altitude balloons.

5. Orbital test facilities - All of the above simulations possess significant shortcomings when used alone to emulate the dynamics of FAS. Space

experiments are the ultimate but are costly and should be used in conjunction with other less costly simulations and/or ground test facilities. One such orbital test facility is the Shuttle Orbiter. Dedicated free-flying research satellites pose another class of orbital test facilities.

6. Design on Orbit - If, after all the precautions, the FAS does not perform adequately in space, the control system can be fine-tune and/or redesigned on-orbit. However, this requires planning. Simple dynamic tests can be conducted so that the dynamic characteristics of the system can be identified from on-orbit data. Then the control system can be modified to improve the performance to an acceptable level.

Several performance problems that have occurred in the past and have a habit of recurring are as follows:

1. Inaccurate modeling - Historically, the most oft-recurring problem has been inaccurate modeling of the structure, the sensors, and the actuators.

2. Sensor & actuator failures - The sensors and actuators that are used to implement control laws for flexible aerospace structures often fail on-orbit.

3. Accidents - Accidents sometimes occur during launch or on-orbit which alter the dynamic behavior of the system. (Seltzer 1975).

4. Mission changes - Sometimes unexpected and unplanned changes in the mission are deemed necessary. (Seltzer 1975).

## MODEL DEVELOPMENT

Before the design of a FAS and its control system can progress very far, a model of the structure, its environment in space, and the disturbances expected to act upon it must be developed. There are basically three approaches to developing models for flexible space structures: (1) a mathematically developed model using the laws of physics, (2) a numerically developed model using finite element techniques, and (3) data and/or mathematical models extracted from test results via system identification (ID).

Models developed from the first two approaches are useful in preliminary analyses and designs. The mathematical model forms the basis for engineering judgement and a computer simulation. It must be simplified, e.g., linearized and/or frozen at several time points, so that it is analytically tractable. This simplified form is used to design controllers and

predict results, which are eventually compared to a complex computer simulation, using the higher fidelity, more complex form of the mathematical model. An alternate approach is to use a numerically developed (e.g., finite element) model.

Controllers designed using mathematically or numerically derived models will seldom satisfy on-orbit performance requirements. A satisfactory control system design will typically not be achieved until the control system has been fine-tuned and/or redesigned using models extracted and/or updated from test results. A question that naturally arises is "What is gained from the preliminary design and analysis process?". The answer is that prudent engineering decisions and estimates of the performance of the system are achieved. For example, information on the correct location of sensors and actuators can be ascertained, the needed bandwidths of sensors and actuators can be determined, the resolution of sensing devices can be evaluated, various control laws can be compared, etc.

In order to develop a model for finalizing the control system design for a FAS, a model must be extracted and/or fine-tuned from test results. Of course testing must be done with care to ensure that the model developed accurately represents the system. Most control systems will be implemented with a digital computer; thus, in collecting data to perform system ID the system should be excited with the control system actuators and data should be measured with the control system sensors at the same rate at which the control system will operate. Then, the data from which a model is extracted will have included the effects due to sampling, the effects of actuator and sensor dynamics, and, with a simple extra step, the effects of an expected controller computational delay.

Exciting a system for performing system ID is an art within itself (Stroud, 1989). The excitation should be chosen to excite the modes from 0 hz up to the half sample rate. If little knowledge is known about the frequencies of the modes, the excitation should normally have a flat spectrum (Mitchell, et al, 1988). Also, the amplitudes of the inputs should be limited to minimize nonlinear effects, such as saturations.

Several system ID approaches that have been used with reasonable success for flexible structures are briefly discussed in the following:

1. Transfer Function Determination Code (TFDC) - A weighted least squares problem is solved to determine coefficients of single-input, single-output

(SISO) transfer function coefficients so that frequency response data are fitted. It is applicable to either s-plane (Mitchell, et al, 1982) or z-plane transfer function ID (Medina, 1991).

2. Transfer Functions Using Chebyshev Polynomials - This is similar to TFDC except an ordinary least-squares problem is solved to determine the coefficients of Chebyshev polynomials for fitting frequency response data. The Chebyshev polynomials are then used to compute coefficients of s-plane transfer functions (Dayley et al, 1986; Balas & Doyle, 1989).

3. Eigen Realization Algorithm (ERA) - Digital unit pulse responses between all input/output (I/O) pairs are used to form a Hankel matrix that is decomposed using a singular value decomposition (SVD). Using the constituents of the SVD and derivations by Ho and Kalman (1965), estimates of discrete A, B, and C matrices are made, along with the order of the system (Juang & Pappa, 1985; Theter, 1970). ERA produces models for multi-input, multi-output (MIMO) discrete systems. The unit pulse responses are found using signal processing techniques to estimate the frequency response of each element of the transfer function matrix and, then, taking inverse fast Fourier transforms (FFT's). (Medina, 1991; Collins, 1991).

4. Residue Identification (RID) - Using frequency response data estimates of "modal type" models, i.e., a sum of the product of residue matrices and modal transfer functions, are identified. Apriori estimates of modal frequencies and damping ratios are required to use RID. Estimates of the residue matrices are determined so that the frequency response of each transfer function between each I/O pair is a best weighted least squares fit to the respective frequency response data. The needed estimates of the modal frequencies and damping ratios are determined experimentally, numerically from eigenvalues of the A-matrix from an ERA modeling process, or numerically from SISO modeling of the determinant of the frequency response of the transfer function matrix. The weighted least squares problem in RID is solved by a SVD. Since frequency response data are used, signal processing averaging techniques can be used to significantly reduce the effects of measurement noise. (Medina, 1991; Irwin, 1992)

Models developed from finite element data or system identification are typically very high order, e.g., 100 or more. High order models can not be numerically handled by many control system design approaches and can produce unnecessary complexity in a simulation, while adding little to the

fidelity of the results. As a consequence, models are often reduced to a more amenable order. Model reduction has been a research topic for many years. Probably the first model reduction procedure used for FAS's was modal truncation, i.e., simply discard all modes above a certain frequency. If the modal truncation frequency is set too low, important modes can be discarded. Nevertheless, modal truncation is justified for eliminating modes well above the control system bandwidth, since a good design will gain stabilize these modes, and, consequently, accurate models are not needed in this regime.

A simple model reduction for SISO systems that has been used by engineers at MSFC for many years (sometimes called "Olde Tried and True" or OT<sup>2</sup>) is as follows. A modal type model of a transfer function between an I/O pair is

$$G(s) = \sum_{n=0}^N \frac{K}{s^2 + 2\zeta_n \omega_n s + \omega_n^2}$$

where K is the modal gain product or residue, N is the number of modes,  $\zeta_n$  is the damping ratio of the n-th mode and  $\omega_n$  is the natural frequency of the n-th mode. The frequency response of the transfer function is affected the most by individual modes at the natural frequencies of the modes. (Of course this assumes small damping which is certainly the case for FAS's.) The peak magnitude frequency response of each mode is  $K/(2\zeta_n \omega_n^2)$ . The peak magnitudes are computed and tabulated; then, the values are compared, and using a heuristic rule modes are eliminated, e.g., modes having peak values less than one tenth of the maximum value are discarded. OT<sup>2</sup> is a practical and effective approach and has been recently extended and given more analytical basis (Mitchell, 1990).

OT<sup>2</sup> is a sound approach to model reduction for SISO systems. However, FAS's are inherently MIMO in nature. As pointed out by Mitchell, et. al., (1990), if SISO techniques are used to reduce the models for each I/O pair in a MIMO system, and the resulting sets of modes are unioned to form a MIMO reduced model, few modes may be eliminated. In fact, if this problem is given additional thought, it is quickly realized that the overall order of a "so-called reduced order" model for a MIMO system can increase, since the elimination of modes in individual I/O pairs can mathematically cause multiple modes at the same frequency. As a consequence, a more "global" approach must be taken for MIMO system model reduction. Recently, the OT<sup>2</sup> approach has been extended to MIMO systems by using residue

matrices in place of residues and by using singular value frequency responses (Mitchell, et. al., 1990). This technique takes full advantage of the modal type model and can be used on models developed from finite element data or from system ID techniques that produce modal type models, such as RID.

Other model reduction techniques that have been used for FAS's are balanced model reduction (Moore, 1981), real Schur model reduction (Safonov, 1988), Hankel model reduction (Glover, 1986), q-Markov Cover (Skelton, 1987), and Component Cost Analysis (Skelton, 1983). These techniques guarantee bounds on the norm of defined error between the full and reduced order model. All of these techniques start with state-variable descriptions and produce reduced order state-variable descriptions. If the full order model has a modal form, the reduced order model will not, in general. The modal frequencies and mode shapes of the reduced order model will differ from the full order model. As with the OT<sup>2</sup> approach, a heuristic rule must be used to decide "where to draw the line" in the practical application of these techniques. Also, these techniques are numerically intensive and may fail before a reduced model is produced.

## CONTROL SYSTEM DESIGN AND DEVELOPMENT

In recent years there has been considerable research in the developing and tailoring of control system design techniques for flexible space structures. This problem involves designing a control system for a MIMO system that satisfies various performance criteria, such as vibration suppression, disturbance/noise rejection, attitude control and slewing control. Considerable progress has been made and demonstrated in control system design techniques for FAS's. Some of the techniques and/or philosophies are listed and briefly described below:

1. Classical Based Approaches - These techniques are basically SISO in nature; however, they are applied to the FAS problem by sequentially designing and closing loops one at a time. One of these approaches is call the One Controller at the Time Technique (1-CAT), which includes a design philosophy tailored for FAS's and analytical results for numerically including the effects of loop closures on the transfer function matrix of the system as individual loops are closed (Mitchell & Lucas, 1986).

In using loop at the time approaches phase and gain stabilization are used to satisfy stability and vibration suppression requirements. Disturbance rejection using cascade compensation is achieved by making the compensator gain very high over the frequency range of the disturbance (Chu et al, 1990). The minimization of the excitation of lightly damped modes by slewing control is accomplished by shaping the slewing command signal so as not to excite the lightly damped modes (Byers, et al 1990). The advantages of the classical approach to flexible space structure control system design include simplicity of the controller, i.e., low order, clear objectives the designer attempts to achieve, and the insight that a designer has in what is being achieved. In addition using frequency response techniques, the design can be accomplished using frequency response data, which can be derived from experimental testing. The disadvantages include designing to simultaneously achieve several performance objectives and fine-tuning complex controllers, especially underdamped second order terms. Root locus and parameter space (Siljak, 1969) type techniques require an analytical model of the system, i.e., transfer functions or state space, and can be cumbersome to carry out for high order systems.

**2. Linear Quadratic Gaussian (LQG)** - This is a two phase design procedure. In the first phase an optimal, full state, constant feedback controller is designed. The optimal controls to the plant are determined so as to minimize an integral performance index, whose integrand is a sum of quadratic terms of the states and control inputs. The optimal controls are realized as a linear combination of the states. In the second phase a state estimator is designed using a Kalman filter. The controller is implemented by feeding the system inputs and the measured outputs to the Kalman filter and then feeding those states directly measured and estimated states (from the Kalman filter) of those not measured to the controller, hence, forming a plant/controller feedback arrangement. The design of the controller and the state estimator both require state-variable models of the plant. The controller design requires the solution of a steady-state Riccati equation. A mismatch between the actual plant and the model can result in a significant degradation in closed-loop performance and even system instability.

**3. Pole Placement** - This is very similar to LQG in that the design process is two phase. In fact the second phase and implementation of the controller are identical with the exception that an observer may replace the Kalman filter. In the first phase the design is accomplished so as to place the

closed-loop poles of the system at specified locations (Kailath 1980). As with LQG the system performance can be highly sensitive to mismatches between the model and the actual plant. In the design of the observer numerical problems may be encountered for medium and high order systems.

**4. High Authority Control/Low Authority Control (HAC/LAC)** - This is a two phase iterative procedure (Lockheed, 1982). In the first phase an LQG controller is designed using a reduced order model, called a design model. The modes included in the design model are those perceived to need significant damping in order to meet performance specifications. Then, the performance of the system is evaluated using the full order model. If modes left out of the design model cause spillover problems that degrade the performance, e.g., causes stability problems, then a constant feedback controller is designed, assuming collocated, complementary actuators and sensors. The strategy is to add a small but sufficient amount of damping to the spillover modes so that lost performance is recovered. Since there is no assurance that the spillover problem will be solved by the second phase, more and/or different modes may have to be included in the design model and the process repeated. (Lockheed 1982).

**5. Maximum Entropy and Optimal Projection (MEOP)** - This is a single phase procedure that produces reduced order controllers and takes into account uncertainty in the plant. The process trades off performance for robustness. The solution process involves solving four coupled matrix equations, two Riccati and two Lyapunov (Hyland, et al 1984; Bernstein, et al 1986).

**6. H-infinity ( $H^\infty$ )** - The goal is to design a controller to shape singular value frequency responses of various matrices associated with the closed loop performance. As examples, assuming  $G$  as the plant and  $K$  as the controller, then maximizing the smallest singular value of  $[I + GK]$  or alternately  $[I + KG]$  over all frequencies maximizes robustness to unstructured perturbations or maximizing the smallest singular value of  $[I + (KG)^{-1}]$  or alternately  $[I + (KG)^{-1}]$  over all frequencies maximizes performance.  $H^\infty$  designs attempt to achieve multiple objectives by combining them into a single functional and optimizing it. An  $H^\infty$  solution requires the solution to two Riccati equations (Masciejowski 1989; King 1990).

**7. Design with Data Models** - The basic philosophy of this approach is to start with a stabilizing controller and frequency response data that describes the plant; then, iteratively vary the free

parameters of the controller so that performance metrics come closer to satisfying design specifications. The frequency response data can be either experimentally derived or analytically derived. One "design with data" algorithm is called the Compensator Improvement Program (CIP) (Mitchell, 1977). It designs controllers for MIMO systems so that classical gain, phase, and attenuation margins are achieved. In CIP a MIMO system is viewed as a coupled multiple loop system. The mathematical problem that CIP solves is the determination of a solution to multiple inequalities. The center-piece of the CIP algorithm is the constraint improvement techniques which is used to calculate a parameter change vector that guarantees a feasible improvement in all unsatisfied performance metrics from one iteration to another. Recently a CIP type algorithm has been demonstrated for achieving  $H^\infty$  type design specifications, using experimentally derived data from the ACES facility at Marshall Space Flight Center (Frazier & Irwin, 1992).

The above list of control techniques is not all inclusive. Others that have been given attention are  $\mu$ -synthesis (Doyle, 1982; Fan et al, 1986) and more recently a combined system identification controller design approach (Juang, 1990).

The key to designing control systems for FAS's that meet stringent performance requirements is an accurate model. It has become apparent that theoretically and/or finite-element generated models do not provide the needed accuracy. Almost all successful demonstrations of control designs techniques have involved using test results for fine-tuning a model or for extracting a model using system ID techniques. This provides clear evidence that on-orbit testing and control system fine-tuning and/or redesign should be an integral part of a flexible space structure plan.

Even if system ID is used to extract a model, control system design techniques requiring analytical models will probably have to utilize a reduced order versions of these models, because of numerical problems in determining the controller. Hence, more errors between the model and actual plant will be introduced. On the other hand, in a data model, such as used by CIP, order is immaterial. Another important feature of iterative techniques that use data models is the capability to fine-tune designs, whereas the analytical techniques must design from "scratch".

## SIMULATIONS AND THEIR USE

Beginning in the days of the SATURN-APOLLO space rockets (1960's), simulations of space vehicle dynamics have been attempted (with varying levels of success) by massive, often full-scale hardware emulations. A number of hardware facilities have been developed in the U.S. They are described briefly: detailed descriptions are available in the references.

1. NASA/MSFC Large Space Structure Ground Test Facility - From its modest beginnings, the NASA/MSFC has expanded into a large sophisticated facility consisting of several laboratories (Waites, 1987 & Buckley, 1992). This national testbed facility is used to investigate the controls and dynamics issues associated with large complex FAS's. It is comprised of a Single Structure Control (SSC) Laboratory and a Controls and Structures Experiment in Space (CASES) Laboratory (Jones et al. 1991). The SSC Laboratory was used to assess and compare the pointing and vibration suppression techniques developed under the ACROSS Program. The CASES Laboratory is the baseline for the MSFC Controls-Structures Interaction (CSI) advanced development. A third laboratory under development is the Unobtrusive Sensor Experiment (USE) Laboratory. This laboratory will be used to investigate sensors and actuators that do not significantly modify the structure dynamics, called "unobtrusive" sensors and actuators.
2. NASA Langley Research Center (LaRC) Controls-Structures Interaction (CSI Evolutionary Model (CEM) Phase-0 Testbed - The CEM Phase-0 Testbed (Belvin et al. 1990) is a laboratory testbed designed and constructed at NASA LaRC for experimental validation of control design methods and integrated design methodologies. The Phase-Zero Evolutionary Model basically consists of a 62-bay central truss, two vertical towers, and two horizontal booms. The structure is vertically suspended by two cables. Several CSI experiments have been performed on the facility (Maghami et al, 1992; Neat et al, 1992).
3. US Air Force Phillips Laboratory SPICE - The "Space Integrated Controls Experiment" (SPICE) testbed is designed to integrate various mature technologies in a representative large FAS (Blankinship et al, 1992). The SPICE facility is located at the Phillips Laboratory on Kirtland Air Force Base, Albuquerque, NM. The testbed is, in essence, a large precision optical structure consisting of a large segmented primary mirror, a bulkhead truss structure supporting the primary

mirror, and a tripod secondary mirror support system. One of the objectives of the SPICE Precision Pointing Experiment is to demonstrate a factor of 100:1 reduction to mechanical induced disturbances. This challenging task is being pursued by applying active control to obtain the principal improvement and passive damping to provide a robustly stable system.

4. US Air Force Phillips Laboratory ASTREX - The "Advanced Space Structures Technology Research Experiments" (ASTREX) testbed was developed to ground test a cost effective way of testing new technologies associated with precision control of FAS's (Das et al, 1990). The testbed is located at the Phillips Laboratory's facility on Edwards Air Force Base in California. The structure represents a dynamically scaled modal of a Space Based Laser's three-mirror beam expander. The facility consists of a structure mounted on an air bearing system having a load capacity of approximately 6,600 Kg. It can slew about three axes: +/- 180 deg in yaw and +/-20 deg in pitch and/or roll. Slew is achieved through the firing of eight lb force vernier thrusters. The control/data acquisition computer can handle 32 inputs and 32 outputs in real time control at 11.5 MFlops. Modular structure permits modifications as desired.

5. US Army Space Defense Command R2P2 - The Rapid Retargeting and Precision Pointing (R2P2) facility (Skidmore, 1992) is anchored on a gigantic natural rock (granite) formation in the Rocky Mountains southwest of Denver. The simulator can perform extremely precise pointing measurements without local seismic interference. Essentially, the R2P2 simulator is an adaptable testbed for various space based optical systems, requiring pointing agility and extreme pointing precision. The R2P2 is capable of performing pointing, tracking, and repointing scenarios of precision optical systems with full-scale angular dynamics. Spacecraft dynamics are represented in one (horizontal) plane. Typically, spacecraft structural dynamics adversely affect the line-of-sight (LOS) of precision optical systems. Rather than employing actual or subscale structures, the R2P2 is designed to simulate the effects of structural dynamics on the spacecraft and the LOS pointing. The ability to readily reconfigure the simulated structural dynamics permits easy alteration of the structural dynamics. The nominal control system uses a reaction control subsystem to move the spacecraft through large angle maneuvers. It uses relative (between the two bodies) torques to point the articulated forward body (with respect to the aft body) through a smaller range of angles. Beam steering mirrors are used to perform precision pointing of the spacecraft

LOS with a limited range of motion relative to the forward body.

6. US Navy Research Laboratory Test Facility - This rather new facility attempts to overcome problems induced by gravity by mounting a test article on an air bearing sphere approximately 41 cm. in diameter. This sphere is capable of supporting a flexible test article of approximately 1000 kg. in weight. In essence, it isolates the test article from external disturbances.

A number of lessons have been learned in the development and use of ground test facilities (Waites & Worley, 1987). Many of these lessons deal with the problems of testing a space (zero-g) structure in an Earth (1-g) environment. One obvious problem is the need to suspend the structure, either from overhead or from the floor. A number of approaches that attempt to ameliorate this problem have been tried: suspension with cables, resting on an air bearing sphere or pad, etc. Another associated problem is "pendulum" modes of vibration which are not a space structural modes at all. Still, they usually have the lowest frequencies of oscillation and must be dealt with -- on Earth -- by the control system. The effects of the Earth's rotation on sensed accelerations and angular rates must be accounted for with strapdown algorithms. When sensing or actuating instruments are added to the structure, counterweights must be added to balance their gravity-induced effects. Of course the dynamics caused by laboratory cables and wiring must be accounted for. Beams that would be undeformed in space are bent (under the influence of gravity) on Earth. None of these problems is insurmountable, but they must be carefully considered. An additional problem encountered in large scale testing is the mundane but important problem of scheduling and ensuring that skilled test technicians and engineers are available.

## ORBITAL OPERATIONS AND USE OF DATA

A plenary paper on the topic of dynamics and control of flexible aerospace structures would not be complete without addressing the support of orbital operations. When everything is going well, the ground support of flight operations is reduced to monitoring the performance and state-of-health of the aerospace structure. If the system is manned, of course, a whole set of requirements arise (which will not be addressed here). However, history provides every reason to suspect that all will not go well. As indicated above, launch and orbital

accidents can occur which may significantly affect the dynamics of the structure. Program Managers can exert an equally significant change in system dynamics by changing or altering the mission of the system. Sufficient instrumentation must be placed carefully on the structure so that bending characteristics can be deduced from on-orbit measurements. These characteristics may be required to alter the description of the plant in case the control system must be modified. Again, the Program Manager must be convinced of the importance of this instrumentation, for he/she will resist the cost. Finally, sufficient orbital data must be collected to permit assessment of mission success and compliance.

## CONCLUSIONS

The authors of this plenary paper have attempted to overview the status of engineering capabilities, techniques, and simulation hardware for the design and verification of the dynamics and control of flexible aerospace structures. An extensive list of references have been provided to enable the reader to delve into selected topics in more depth. In the opinion of the authors, the development of the state-of-the-art of control system development has significantly exceeded the ability to accurately model the dynamics of flexible aerospace structures and the disturbances acting upon them. Over the past several years, it is truly amazing how many large hardware simulation facilities have been developed. Even more amazing is the different simulation philosophies and techniques used in them!

## REFERENCES

- Balas, G. J.; Doyle, J. C. (1989). "Identification for robust control of flexible structures", 1989 American Control Conference, 8th, Pittsburgh, PA, June 21-23, 1989.
- Belvin, W.K. et al (1990). "The LaRC CSI Phase-0 Evolutionary Model Testbed: Design and Experimental Results," Proceedings of Fourth Annual NASA/DoD Conference on Controls-Structures Interaction Technology, Orlando, Florida.
- Bernstein, D. S.; Greely, S. W. (1986). "Robust Controller Synthesis Using Maximum Entropy Design Equations", IEEE Transactions on Automatic Control, Vol. AC-31, 1986.
- Blankinship, R. M. et al (1990). "The Spice Program", Proceedings of the 15th Annual AAS Guidance and Control Conference, Keystone, Co.
- Bukley, A.P. et al (1992). "Dynamic Test Results for the Cases Ground Experiment," Proceedings of NASA-DoD Controls-Structures Interaction Conference, Lake Tahoe, Nevada.
- Byers, R. M.; Vadali, S. R.; Junkins, J. L. (1990). "Near Minimum Time Closed-Loop Slewing of Flexible Structures", Journal of Guidance, Control, and Dynamics, Vol. 13, No. 1, 1990.
- Chu, P. Y. et al (1990). "Approach to Large Space Structure Control System Design Using Traditional Tools", AIAA Journal of Guidance, Control, and Dynamics, Vol. 13, No. 5, p. 881.
- Collins, E. G., JR., et al (1991). "Robust decentralized control laws for the ACES structure," IEEE Control Systems Magazine, (ISSN 0272-1708), vol. 11, April 1991, pp. 62-70.
- Control Dynamics Co. (Seltzer, S.M. et al; 1984), "ACOSS SEVENTEEN (Active Control of Space Structures)," Department of Defense Advanced Research Projects Agency Report RADC-TR-84-186.
- Dayley, R. L.; Lukich, M. S., (1986), MIMO Transfer Function Curve Fitting Using Chebyshev Polynomials", TRW Space & Technology Group, Electronic & Defense Sector.
- Das, A. et al (1990). "ASTREX - A Unique Test Bed for CSI Research", Proceedings of the 29th IEEE Conference on Decision and Control.
- Doyle, J. C. (1982). "Analysis of Feedback Systems with Structured Uncertainties", IEE Proceedings, Vol. 129, No. 6, pp. 242-250, 1982.
- Fan, M. K. H.; Tits, A. L.; Doyle, J. C. (1988). "Robustness in the Presence of Joint Parametric Uncertainty and Unmodeled Dynamics", Proceedings of the 1988 American Control Conference, Atlanta, GA, pp. 1195-1200, 1988.
- Frazier, W. G.; Irqin, R. D. (1992). "A Numerical Approach to Controller Design for the ACES Facility", Proceedings of the 1992 NASA/DoD Controls and Structures Interaction Conference, Lake Tahoe, CA, March 1992.
- General Dynamics (Sesak, J. et al; 1980), "ACOSS ONE (Active Control of Space Structures) Phase I"

Department of Defense Advanced Research Projects Agency Report RADC-TR-80-79.

Glover, K. (1986). "Multiplicative Approximation of Linear Systems with L-Infinity Error Bounds", Proceedings of the American Control Conference.

Hyland, D. C.; Bernstein, D. S. (1984). "The Optimal Projection Equations for Fixed Order Dynamic Compensation, IEEE Transactions on Automatic Control, Vol. AC-29, 1984.

Ho, B. L.; Kalman, R. E. (1965). "Effective Construction of Linear State-Variable Models from Input/Output Data", 3rd Allerton Conference on Circuit and System Theory, University of Illinois, Department of Electrical Engineering, 1965.

Jones, V. L. et al (1991. "NASA/MSFC Large Space Structures Ground Test Facility ", AIAA Guidance, Navigation and Control Conference, New Orleans, LA, Aug. 1991.

Juang, J-N., Pappa, R. S. (1985). "An Eigensystem Realization Algorithm for Modal Parameter Identification and Model Reduction", AIAA Journal of Guidance and Control, Vol. 8, No. 5, pp 620-627, 1985.

Juang, J-N.; Lew, J-S. (1990). "Integration of system identification and robust controller designs for flexible structures in space", AIAA Guidance, Navigation and Control Conference, Portland, OR, Aug. 1990.

Kailath, T., (1980). Linear Systems, Prentice-Hall, Englewood Cliffs, NJ, 1980.

King, J. A. (1990). "Application of H-infinity Optimal Control to Large Space Structures", Masters Thesis, Ohio University, Department of Electrical and Computer Engineering, Athens, OH.

Lockheed Missiles & Space Co. (Aubrun, J.N. et al; 1982), "ACOSS Five (Active Control of Space Structures) Phase IA," Department of Defense Advanced Research Projects Agency Report RADC-TR-82-21.

Macciejowski, J. M., (1989). Multivariable Feedback Design, Addison-Wesley Publishing Company, New York, NY, 1989.

Maghmami, P.G. et al (1992), "Integrated Controls-Structures Design Methodology for a Flexible Spacecraft," AAS Paper 92-060, Proceedings of 15th Annual AAS Guidance & Control Conference, Keystone, Colorado.

Medina, E. A. (1991). "Multi-Input, Multi-Output System Identification from Frequency Response Samples with Applications to the Modeling of Large Space Structures", Masters Thesis, Ohio University, Department of Electrical and Computer Engineering, Athens, OH, November 1991.

Mitchell, J. R. et al (1977). "Compensator Improvement for Multivariable Control Systems", Final Report (Contract No. NAS8-31568), NASA, MSFC, August 1977.

Mitchell, J.R. et al (1982). "Development of a Modeling Technique: The Transfer Function Determination Code", Final Report, Air Force Weapons Laboratory (Contract No. F29601-80-C-0045), Albuquerque, NM, February 1982.

Mitchell, J. R.; Lucas, J. C. (1986). "1-CAT: A MIMO Design Methodology", Structural Dynamics and Control Interaction of Flexible Structures, Huntsville, AL, USA, April 1986.

Mitchell, J. R., et al (1988). "Formulation and verification of frequency response system identification techniques for large space structures", Guidance and Control 1988; Proceedings of the Annual Rocky Mountain Guidance and Control Conference, Keystone, CO, Jan. 30-Feb. 3, 1988.

Mitchell, J. R., et al (1990), Practical Model Reduction for Flexible Structures", Guidance and Control 1990; Proceedings of the Annual AAS Guidance and Control Conference, Keystone, CO, Feb. 1990.

Moore, B. C. (1981). "Principal Component Analysis in Linear Systems: Controllability, Observability, and Model Reduction", IEEE Transactions on Automatic Control, Vol. AC-26, pp. 17-32, 1981.

Neat, G.W. et al (1992). "Joint Langley Research Center/Jet Propulsion Laboratory CSI Experiment," AAS Paper 92-061, Proceedings of 15th Annual AAS Guidance & Control Conference, Keystone, Colorado.

Safonov, M. G.; Chiang, R. Y. (1988). "Model Reduction for Robust Control: A Schur Relative-Error Method", Proceedings of the 1988 American Control Conference, Atlanta, GA, pp. 1685-1690, 1988.

Seltzer, S.M. et al (1975), "Flight Performance of Skylab Attitude and Pointing Control System," AIAA Paper 75-301, Proceedings of AIAA 11th Annual Meeting in Baltimore, Maryland.

Siljak, D. D. (1969). Nonlinear Systems, John Wiley & Sons, New York, NY, 1969.

Skelton, R. E.; Yousuff, A. (1983). "Component Cost Analysis for Large Scale Systems", International Journal of Control, Vol. 37, No. 2, pp. 285-304, 1983.

Skelton R. E.; Collins, E. G. (1987). "Set of q-Markov Equivalent Models of Discrete Systems", International Journal of Control, Vol. 46, No. 1, pp 1-12, 1987.

Skidmore, G.R. (1992). "Dynamic Simulation of Precision Optical Systems Using R2P2,"

Stroud, R. C. (1989). "Excitation, Measurement, and Analysis Methods for Modal Testing", Synergistic Technology Inc., Journal, Santa Clara, CA, 1989.

Theter, A. J. (1970). "Construction of Minimal Linear State-Variable Models from Finite-Output Data", IEEE Transactions on Automatic Control, vol. AC-15, No. 4, pp 427-436, 1970.

TRW (Iwens, R. et al; 1983), "ACOSS FOURTEEN (Active Control of Space Structures)," Department of Defense Advanced Research Projects Agency Report RADC-TR-83-51.

Waites, H.B., et al (1987). "Cost Effective Development of a National Test Bed," Proceedings of NASA-DoD Controls- Structures Interaction Conference, Colorado Springs, Colorado.

Waites, H.B. & Worley, E. (1987). "Large Space Structures Testing" AAS Paper 87-036, Proceedings of AAS Annual Guidance & Control Conference, Keystone, Colorado.

# CONTROL CHALLENGES FROM SPACE AND GROUND BASED ASTRONOMICAL TELESCOPES

D.C. Redding

*Charles Stark Draper Laboratory, Inc., Jet Propulsion Laboratory 185, California Institute of Technology,  
4800 Oak Grove Drive, Pasadena, CA 91109, USA*

**Abstract.** Actively controlled optics are revolutionizing the telescope builders art, by enabling the use of active atmospheric compensation, large segmented mirrors, multiple-aperture telescopes, space telescopes and other innovations. Designing high-performance controllers for these instruments requires an accurate means of calculating optical performance: a particular method is presented. A survey of the field and a detailed example illustrate some of the challenges that arise.

**Keywords.** Control system synthesis, modeling, sensors, actuators, optical variables control.

## 1.0 HIGH-PERFORMANCE ASTRONOMICAL INSTRUMENTS

The performance of astronomical telescopes depends on a number of factors. Prime among these are:

- Light-gathering power
- Angular resolution or spatial sampling characteristics
- Optical quality
- Atmospheric distortion effects

Recent designs have used innovative and ambitious techniques to go beyond old limits and improve performance with respect to these fundamental factors. Many of these techniques depend on active controls.

A telescope's light gathering power - the number of photons it can collect from an astronomical source - is a key factor in its ability to detect dim objects. One approach to increase light collecting ability is to increase telescope size: to make the primary optics very large. Another approach is to remove the intervening atmosphere by flying the telescope in space. Atmospheric absorption and scattering reduces light by different amounts depending on wavelength. For some wavelengths, space telescopes provide the only alternative.

Whether ground- or space-based, large telescopes also have more favorable spatial sampling or angular resolution characteristics. Diffraction – the bending of light beams by wave effects – determines one limit on the ability of a telescope to resolve small objects<sup>1</sup>. For a circular aperture telescope, the resolution limit is set by the “ringing” of the edges of the aperture. The diffraction limit set by the closest resolvable spacing of 2 objects is:

$$\text{Angular resolution} = 1.22(\lambda/D) \quad (1)$$

Here  $\lambda$  is the wavelength of the light and D is the telescope aperture diameter. Clearly, better resolution is obtained by telescopes with larger apertures. Science goals that are being considered for larger instruments include direct and indirect extra-solar planet detection for nearby stars, study of star formation complexes including resolution of protostellar disks of 5-50 AU, and resolution of larger structures in galactic nuclei or quasars.

Very large telescopes are difficult and expensive to build using conventional monolithic glass optics. The chief difficulty is achieving and maintaining the required high levels of optical quality.

Distortions in mirror surfaces must be kept below a small fraction of a wavelength, typically  $\lambda/20 - \lambda/40$  rms. For telescopes operating in the ultraviolet, surface figure quality is thus required to be in the 1–10 nanometer rms range. At the other end of the spectrum, far-infrared telescopes require surface quality in the range of 0.3–3 micron rms.

Alignments between the various optical elements of a telescope have similarly stringent requirements. The figure and alignment quality must be maintained through the full operating environment of the instrument.

Conventional telescopes rely on passive structural stability to meet these requirements, forcing the use of very large and massive optics and support structures. The drive to ever larger conventional telescopes has limits: as they get larger and heavier, they become increasingly difficult and expensive to fabricate.

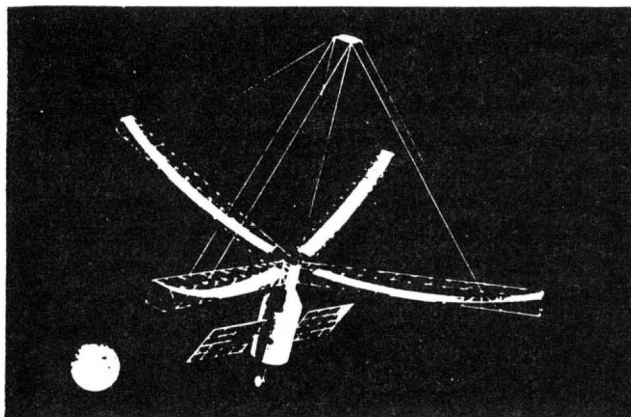
As a result, astronomers are turning to new, unconventional approaches to increase the size of their instruments. For instance, large telescopes can be assembled using less massive segmented mirrors, as

witness the Keck telescope and other infra-red to millimeter-wave telescopes<sup>2</sup>. Mirror segments are smaller than conventional monolithic mirrors, hence easier and less expensive to manufacture. Another approach, exemplified by the European Southern Observatory<sup>3</sup>, uses large thin mirrors that can be slightly deformed to preserve proper figure. Advances such as spin casting make it possible to fabricate large lightweight optics of good quality at relatively low cost.

These lighter-weight mirrors do not have the passive stability required to preserve adequate optical quality at visible wavelengths. "Active optics," or low-bandwidth control of mirror or segment position is used to counter structural deformations due to thermal or gravity sag effects. We examine the problem of segmented-mirror active figure control later in this paper.

Very large apertures can also be synthesized from a number of smaller apertures<sup>4</sup>. "Sparse aperture" telescopes (Fig. 1) offer greater resolution at sometimes significantly lower mass and expense<sup>5</sup>. They of course do not have the same light gathering power as equivalent filled aperture telescopes. They combine light coherently at the image plane, and therefore have relative phase requirements that are just as stringent as filled aperture telescopes. Their resolving power is indicated by their point-spread functions, which have a sharp central peak, indicating good resolution, but also have larger side-lobes, indicating reduced sensitivity at some spatial frequencies. Sparse aperture telescopes are particularly suited to the task of resolving near-neighbor objects, such as binary stars.

**FIGURE 1. A Sparse Aperture Telescope**



"Pupil-plane" optical interferometers carry the sparse aperture approach to its extreme. Multiple independent small telescopes, separated by known baseline lengths, measure interferograms that contain particular spatial frequency components of the light from a source (Fig. 2). Images can be synthesized by observing in different geometries, that is, at different baseline lengths and at different aspect angles. The interferograms are combined to estimate the total spatial frequency response of the source. This is then inverse-transformed to obtain an image. This technique is already familiar

from Very Long Baseline Interferometry (VLBI) using radio telescopes.<sup>6,7</sup>

Pupil-plane interferometers are the most efficient sort of instrument from a resolution point of view. They provide maximum resolution with minimum glass area and structure mass. This makes them ideal instruments for stellar astrometry, or star-angle measurement.

Astrometry at the 10 micro-arcsecond level is sufficient to determine the dynamics of many astronomical objects, such as the motions imparted to a star by orbiting planets or close binaries, or the motions of individual stars within clusters<sup>7,8</sup>. It will also enable accurate parallax distance measurements of very distant objects.

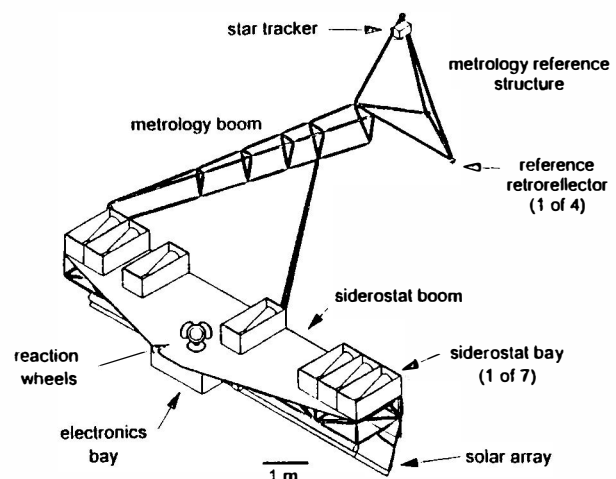
The resolution limit for a pupil-plane interferometer is set by the baseline length, rather than by the telescope aperture diameters. The baseline length  $B$  is the distance between the two apertures projected into the plane perpendicular to the line-of-sight to the object. For a single baseline pair, the resolution limit is:

$$\text{Angular resolution} = \lambda/B \quad (2)$$

To achieve diffraction limited performance requires extremely precise knowledge of the baseline geometry, using laser metrology to achieve measurement accuracies of below 1 nanometer. Very accurate telescope pointing and pathlength delay-line control are also required. For space-based interferometers in particular, active disturbance isolation and rejection is essential. These challenges are reviewed in 2 companion papers<sup>9,10</sup> and in other references<sup>7,8</sup>.

The most significant factor limiting the resolution of ground-based telescopes is distortion due to atmospheric turbulence. Turbulence within the path of the light captured by the telescope causes local variations in the index of refraction, changing the transmission characteristics spatially across the beam. These characteristics also vary in time, as a function of wind speeds. The net effect is that the image of the star jitters, spreads out, or even breaks up.

**FIGURE 2. A Pupil-Plane Interferometer**



The amount of distortion depends on many factors, but according to the theory developed by Fried, Noll, Greenwood and others<sup>11</sup>, it can be simply expressed for a particular viewing condition in terms of an atmospheric coherence length,  $r_0$ , and a coherence time,  $\tau_0$ . The coherence length  $r_0$  is roughly the size of the largest aperture that will be capable of nearly diffraction-limited resolution. Typical values for  $r_0$  at good observing locations are 5-20 cm. Without correction, larger telescopes apertures do not improve resolution performance! Similarly, telescopes that require longer than  $\tau_0$  (typically a few milliseconds) to collect photons will be subject to jittering of the source, causing smearing of the image.

There are several techniques being used to get around these atmospheric effects. One is “adaptive optics,” which uses active sensing and control of a deformable or segmented mirror within the telescope to cancel out the atmospheric distortions at high bandwidth<sup>11</sup>. Other methods use post-processing techniques. One such is “speckle interferometry,” which takes many fast pictures of a source, each capturing multiple small diffraction-limited images (which look like spots or speckles) from different cells of the turbulent atmosphere<sup>25</sup>. The pictures are taken fast enough to avoid turbulence jitter effects. The images are combined in post-processing to remove the atmospheric effects. These techniques require relatively bright sources, and are limited in their ability to reconstruct structurally complex objects, as detailed phase information is not available from intensity data alone.

Hybrid approaches using a combination of adaptive optics and post-processing have been developed. These achieve partial resolution improvement from the adaptive optics. In addition, the residual atmospheric effects can be estimated using data from the adaptive optics system wavefront sensor, which provides information directly related to wavefront phase. The post-processing uses this information to deconvolve the atmospheric distortion from the images.

Adaptive optics brings very significant challenges to the controls engineer, especially when applied to large telescopes. Large adaptive optics systems operating at short wavelengths must apply coordinated control to many subapertures (10,000 to over 150,000 in some designs) consisting of actuator zones on a deformable mirror or separate segments on a segmented mirror. This must be done at high bandwidth, typically 100-1,000 Hz. The “phase reconstruction” processing step required to determine the commands for the deforming optic is a classical estimation step, but one involving up to 1,000,000 degrees of freedom! Implementing a 1 kHz, mega-state estimator is indeed a challenge, one that we believe can be met with massively parallel computing and hierarchical estimator architectures.

The technologies of mechanisms and sensors must be pushed hard as well, so as to bring mass-production

cost advantages to the manufacture of extremely precise and stable components. It may be that the most difficult obstacle to adoption of adaptive optics – or any other controls-based technologies for improving telescope performance – is the cost of the required high-precision componentry.

By removing the intervening atmosphere, space telescopes remove the need for adaptive optics for atmospheric correction. Active optics may still be required, however, to compensate for structural deformations due to thermal disturbances, outgassing, misalignment due to launch shock loading, gravity release, or other effects. These effects are likely to occur on time scales of minutes or days, and can be controlled at low bandwidths.

As mentioned earlier, space telescopes are also freed from signal attenuation due to atmospheric scattering and absorption. Other advantages of space telescopes include the potential for a benign thermal and dynamical environment.

Space telescopes offer compelling performance advantages. At the same time, they are subject to some very challenging problems, as was illustrated recently by the ROSAT and Hubble missions.

The remote location of space telescopes makes servicing and upgrading them difficult or impossible. Failures of critical components can require heroic measures to reconfigure the spacecraft to preserve operational capabilities or even to save the spacecraft. ROSAT, the German X-ray observatory, is an outstanding example<sup>16</sup>. Loss of nearly all its gyros and other critical attitude control hardware was compensated by innovative reprogramming of its on-board controllers to use magnetic torquer coils as attitude measurement devices. Used in conjunction with its startracker, this fix restored operational capability from what could have been a fatal condition.

Hubble has also had problems with failures and out-of-specification components. Unanticipated thermoelastic response of the solar arrays to crossing the terminator led to large pointing errors. This behavior has been substantially reduced through reprogramming of the pointing controller, based in part on dynamic models that incorporate parameters identified from telemetry<sup>17</sup>.

More controversial was the misfigured Hubble primary mirror. Errors made in optical testing left the Hubble primary with a large degree of spherical aberration. Unlike ROSAT, Hubble can be serviced by the Shuttle. Replacement optics designed to correct for this problem will be flown in 1993. Before designing these new optics, however, it was necessary to determine the exact figure of the primary mirror. To this end, several studies were performed<sup>19</sup>. Some of these examined primary mirror test and fabrication hardware and procedures<sup>20</sup>; others used phase retrieval

approaches based on image data<sup>21</sup>. We performed a “prescription retrieval,” or optical parameter identification study that determined the figure of the primary mirror and other parameters from a sequence of images<sup>22</sup>. Our results agreed with the hardware studies.

This experience highlights an interesting challenge for optical control: using image intensity data to determine misalignments or element deformations. With sufficient diversity of images, model-matching techniques can be used to determine nearly any effect that influences imaging performance. This technique is truly end-to-end, using the science detector to determine system errors. It has potential for alignment in space, where alignment aids such as optical test interferometers are not commonly available. It can even be used for active optics control, such as for initializing segmented mirrors, as we discuss below.

## 2.0 MODELING CONTROLLED OPTICAL SYSTEMS

Designing controllers for high-performance telescopes requires the ability to precisely quantify the effect of control system parameters on system-level optical performance objectives, such as image quality (to be maximized), or image jitter (to be minimized). Often the sensors used for feedback control are optical as well. Incorporating detailed optical models into the standard dynamics and controls analysis and simulation framework is a prerequisite to achieving the highest levels of overall system performance.

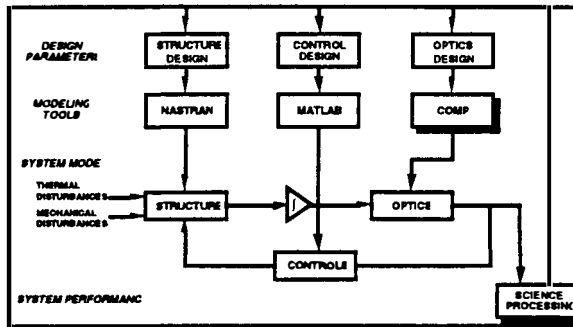
Figure 3 sketches the instrument design process in block-diagram form. The creation of a system-level instrument model is familiar to most controls engineers. Computer codes such as NASTRAN or DISCOS are used to create structure models. Thermal models are generated using codes such as SINDA and TRASYS. We have written a code called the Controlled Optics Modelling Package (COMP)<sup>12</sup> to generate linear and nonlinear optical models that can be driven directly by the outputs of standard dynamics, controls and thermal models. Controls design and system performance calculations are commonly done in a MATLAB-type analysis environment. We are also writing a self-contained integrated modeling environment that realizes these capabilities in a single package<sup>13</sup>.

Complete integrated models are assembled by connecting subsystem models to realize the dynamical, optical, thermal and control signal flow. The connections are established by multiplying subsystem matrices if using linear models, or by stringing together subroutine calls or special-purpose code if using nonlinear models.

These integrated models can be used in several ways. During the design phase, linear models are used in

classical or modern control design using time or frequency domain techniques, in controllability/observability analysis, or in static error analysis<sup>15</sup>. Nonlinear models are used in detailed simulations or in nonlinear parameter optimization or optical system identification programs.

**FIGURE 3. Optical Instrument Design Process**

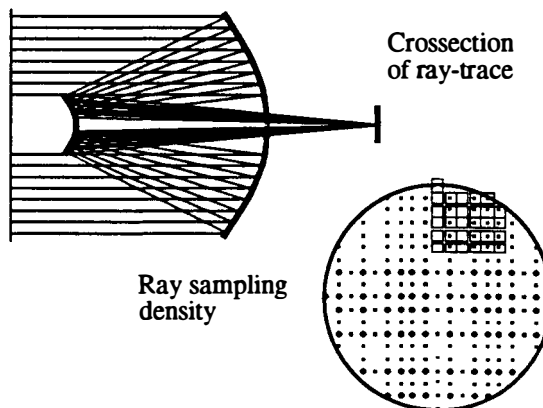


Integrated system models are also useful after the instrument is built, during its operational phase. Detailed modeling enables precise systematic calibration of an instrument, allowing adjustments to be made to improve performance. Where adjustments cannot be made, a calibrated instrument model can be used in post-processing, to subtract systematic instrument errors from the science data.

The key to this process, and the aspect least familiar to most controls engineers, is the optical modeling. The remainder of this section provides a brief introduction to optical modeling as we practise it<sup>14</sup>.

There are two main approaches to modeling optics. Geometric optics, or “ray-tracing,” treats light beams as bundles of rays, which are the trajectories of individual “light particles.” Rays are generally composed of numerous straight-line segments, which start at the light source, propagate through the optical train with direction changes at the reflective or refractive surfaces of optical elements (curved segments occur in regions of continuously changing refractive index), and terminate at a detector such as a CCD array. Ray-tracing is the process of propagating a bundle of rays through the entire optical system (Fig. 4).

**FIGURE 4. Ray trace of a Cassegrain telescope**

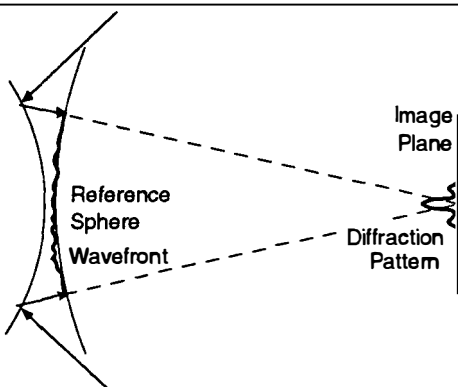


Ray-tracing can be used to determine the effects of aberrations, such as optical element motions or deformations, on the output of a sensor, such as the location of a star image on a detector. It can also be used to compute the effects of aberrations on optical performance metrics, such as RMS wavefront error or blur spot size<sup>15</sup>. Ray-tracing is the standard technique for optical design optimization.

The other main approach to optical modeling is physical optics, which captures the wave nature of light. Physical optics derives from Huygen's Principle, which states that each point within a beam of light radiates a spherical wave of light. A wavefront is the envelope of all the waves emitted at a particular instant of time. Waves of light propagate through an optical train by bouncing off of mirrors or bending through lenses, much as predicted by geometric optics. Unlike geometric optics, however, physical optics predicts that light can leak back into areas of shadow, or areas outside of the edge of the geometric beam. This process is diffraction, and it is of importance when modeling detailed images produced by a telescope, or computing the intensity distribution of a laser beam at long distances, or many other effects.

Aberrations influence the diffracted wavefront by introducing phase disturbances into the path of the beam, causing different parts of the beam to wander or to interfere, reducing the overall image intensity and causing blurring and spreading of a star image. As indicated in Fig. 5, the ideal condition for imaging is for the telescope to perfectly focus all of the light from a source to a single point on the detector, with the converging wavefronts aligned with perfect spheres centered at that point. Aberration-induced phase errors cause deviation from the ideal wavefront, leading to degraded image quality.

**FIGURE 5.** Imaging geometry



The physics underlying diffraction and the free-space propagation of light are captured in simplified theories based on Maxwell's equations. Scalar diffraction theory assumes time invariance and ignores polarization effects. Fresnel propagation theory makes a further assumption about the geometry of the light beam: that the beam is paraxial, or does not diverge very much. This allows the expression of the propagation of light

from one planar or spherical surface to another using the paraxial wave equation, whose solution can be computed using 2-dimensional Fourier transforms<sup>18</sup>. In COMP, these diffraction computations are driven by the geometric phases determined using ray-tracing.

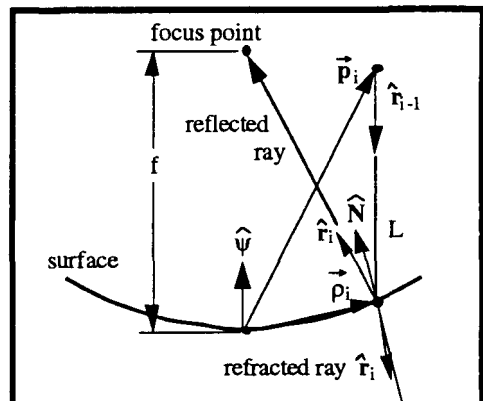
Geometric optics is also a simplified theory based on approximate forms of Maxwell's equations. In geometric optics, the wavelength of light is assumed to be infinitely small. For imaging systems, this is a good approximation until the width of the light beam approaches its wavelength, such as near focus. Even in systems with long wavelengths and large diffraction effects, however, ray-trace provides a precise method for quantifying phases for diffraction calculations or for optical performance metrics.

To facilitate the optical modeling process, we found it useful to derive a coordinate-free set of geometric optics equations similar in some ways to kinematic equations<sup>14,24</sup>. This form was chosen for generality. It also offers an easily differentiable set of equations for deriving linear models, and translates to computationally efficient code for computation.

To illustrate this approach, consider the intersection of a ray with an optical conic-of-revolution surface as illustrated in Fig. 6 (other surface types are handled in similar fashion<sup>24</sup>). The ray originates at a point  $\hat{p}_i$  (with respect to the surface vertex) with direction  $\hat{r}_{i-1}$ . The conicoid surface can be represented in vector three-space in terms of a "surface dyadic"  $M$  and a vector  $\hat{N}_0$ . Denoting the surface principal axis direction as  $\hat{\psi}$ , the surface eccentricity as  $e$ , and its focal length as  $f$ ,  $M$  is

$$M \equiv (I - e^2 \hat{\psi} \hat{\psi}) \quad (3)$$

**FIGURE 6.** Ray trace geometry



The principal axis is defined as pointing from the surface vertex towards its focus. For flat surfaces we say that  $e = 0$  and  $f = \infty$ . Writing  $\hat{p}$  for a vector from the mirror vertex to an arbitrary point on the surface, the surface is defined by

$$\hat{p} \cdot M \cdot \hat{p} + 2\hat{N}_0 \cdot \hat{p} = 0 \quad (4)$$

$\vec{N}_0$  is a vector parallel to the surface normal at the vertex of the surface with magnitude equal to the radius of curvature evaluated at the mirror vertex:

$$\vec{N}_0 = -f(1+e)\hat{\psi} \quad (5)$$

The vector  $\vec{N}$  with respect to the vertex is:

$$\vec{N} = \vec{N}_0 + M\vec{p} \quad (6)$$

$\vec{N}$  is parallel to the surface normal at  $\vec{p}$ . By convention:

$$\hat{N} = -\text{sign}(\hat{i} \cdot \vec{N}) \frac{\vec{N}}{N} \quad (7)$$

The point of incidence is determined as:

$$\vec{p} = \vec{p} + L\hat{i} \quad (8)$$

where  $L$  is the geometrical length of the incident ray. Substituting for  $\vec{p}$  in Eq. 4,  $L$  is a solution of the scalar quadratic equation:

$$(\hat{r}_{i-1} \cdot M \cdot \hat{r}_{i-1})L_g^2 + 2\hat{r}_{i-1} \cdot (M \cdot \hat{p} + \vec{N}_0)L_g + \hat{p} \cdot (M \cdot \hat{p} + 2\vec{N}_0) = 0 \quad (9)$$

The optical pathlength of the ray is  $L_g$  scaled by the index of refraction  $n$  of the medium that contains it:

$$L = nL_g \quad (10)$$

The reflected ray is written in terms of the “reflection dyadic”  $R$  as

$$\hat{r}_i = R \cdot \hat{r}_{i-1} \quad (11)$$

where  $R$  is defined as

$$R = I - 2\hat{N}\hat{N} \quad (12)$$

This dyadic form of the law of reflection is derived in Ref. 14; it apparently first appeared in Ref. 23. The refracted ray is:

$$\hat{r}_i = \mu\hat{r}_{i-1} - \frac{1 - \mu^2}{\sqrt{1 - \mu^2 + \mu^2(\hat{N} \cdot \hat{r}_{i-1})^2}} \hat{N} \quad (13)$$

where  $\mu$  is the ratio of the incident-ray and refracted-ray refraction indices  $n_a$  and  $n_b$ :

$$\mu = n_a/n_b \quad (14)$$

These equations provide a complete description of a single ray segment. A complete ray is traced by repeating this procedure in sequence for each optical element until the terminal surface is reached. To describe a complete beam, multiple rays distributed across the aperture are traced (Fig. 4).

If an optical system is perturbed “slightly,” the changes in optical signals will behave linearly. For instance, if a mirror is tilted through a small angle, the reflected light will change direction by about twice that angle, and the beam will walk over the next optic by an amount proportional to that angle. This linearity usually holds over the ranges of motion typical of astronomical telescopes.

Linear optical models that can be directly integrated with dynamical structures and controls models can be

assembled using analytic differential ray-trace equations obtained by directly differentiating Eqs. 10-13. The derivations are presented in some detail in Ref. 14. A brief summary of the form of the resulting linear models is presented here.

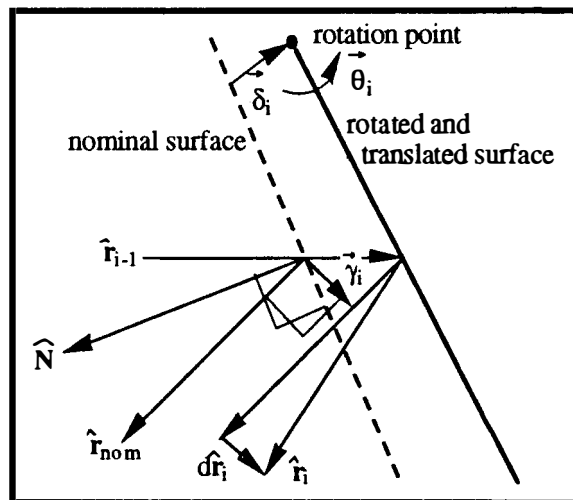
The perturbed ray state vector at the  $i^{\text{th}}$  element can be written as a 7 by 1 column matrix

$$\vec{x}_i = \begin{bmatrix} \hat{d}\vec{r}_i \\ \vec{\gamma}_i \\ dL_i \end{bmatrix} \quad (15)$$

Here (Fig. 7)  $d\vec{r}_i$  is the perturbation to the ray direction at element  $i$ ,  $\vec{\gamma}_i$  is the transverse aberration of the ray at surface  $i$ , and  $dL_i$  is the OPD associated with surface  $i$ . Similarly,  $\vec{u}_i$  is a 6 by 1 column matrix consisting of the small translation  $\vec{\theta}_i$  and rotation  $\vec{\delta}_i$  of the  $i^{\text{th}}$  element:

$$\vec{u}_i = \begin{bmatrix} \vec{\theta}_i \\ \vec{\delta}_i \end{bmatrix} \quad (16)$$

FIGURE 7. Perturbation geometry



The ray state at any element is a function of the ray state at the previous element and the perturbations of that element, as expressed in the difference equation

$$\vec{x}_i = \frac{\partial \vec{x}_i}{\partial \vec{x}_{i-1}} \vec{x}_{i-1} + \frac{\partial \vec{x}_i}{\partial \vec{u}_i} \vec{u}_i \quad (17)$$

where  $\partial \vec{x}_i / \partial \vec{x}_{i-1}$  is the transition matrix from the  $i^{\text{th}}$  to the  $i^{\text{th}}$  element, and  $\partial \vec{x}_i / \partial \vec{u}_i$  is the influence matrix at the  $i^{\text{th}}$  element. Sensitivities of the ray perturbation state at one element to ray or element perturbations at another element are easily calculated as products of these matrices. The sensitivity of the ray at the  $n^{\text{th}}$  element to the ray at the  $i^{\text{th}}$  element is:

$$\frac{\partial \vec{x}_n}{\partial \vec{x}_i} = \frac{\partial \vec{x}_n}{\partial \vec{x}_{n-1}} \dots \frac{\partial \vec{x}_{i+1}}{\partial \vec{x}_i} \quad (18)$$

The sensitivity of the ray at the  $n^{\text{th}}$  element to perturbations of the  $i^{\text{th}}$  element is:

$$\frac{\partial \vec{x}_j}{\partial \vec{u}_i} = \frac{\partial \vec{x}_j}{\partial \vec{x}_{j-1}} \dots \frac{\partial \vec{x}_{i+1}}{\partial \vec{x}_i} \frac{\partial \vec{x}_i}{\partial \vec{u}_i} \quad (19)$$

A complete linear model of a beam train combines the effects of perturbations of the rays and elements as seen at a reference surface. Tracing m rays through a system of n elements:

$$\begin{bmatrix} \vec{x}_{n_{ray} 1} \\ \vdots \\ \vec{x}_{n_{ray} m} \end{bmatrix} = C \begin{bmatrix} \vec{x}_0 \\ \vec{u}_1 \\ \vdots \\ \vec{u}_n \end{bmatrix} = \begin{bmatrix} \left[ \frac{\partial \vec{x}_n}{\partial \vec{x}_0} \frac{\partial \vec{x}_n}{\partial \vec{u}_1} \dots \frac{\partial \vec{x}_n}{\partial \vec{u}_n} \right]_{ray 1} \\ \vdots \\ \left[ \frac{\partial \vec{x}_n}{\partial \vec{x}_0} \frac{\partial \vec{x}_n}{\partial \vec{u}_1} \dots \frac{\partial \vec{x}_n}{\partial \vec{u}_n} \right]_{ray m} \end{bmatrix} \begin{bmatrix} \vec{x}_0 \\ \vec{u}_1 \\ \vdots \\ \vec{u}_n \end{bmatrix} \quad (20)$$

This “C matrix” is the linear model, giving the perturbed states of all of the rays in a beam as a matrix function of element motions. The COMP software automates the assembly of these models, including transformations between actuator and sensor coordinates. Once assembled, they are exported to a MATLAB environment for analysis.

### 3.0 SEGMENTED MIRROR FIGURE CONTROL EXAMPLE

The control of the segments of a space-based far-IR telescope provides an example of “active optics:” low-bandwidth closed-loop figure control. It also provides a dramatic demonstration of the advantages of designing optical controllers using integrated modeling techniques.

The subject telescope, the Sub-Millimeter Moderate Mission (SMMM)<sup>30</sup>, has a 3.65 m aperture primary with 7 segments as shown on Fig. 8. Each segment is equipped with 3 linear actuators, positioned to provide 3 degrees of freedom of control per segment: tip, tilt and piston.

Segmented mirror figure control for space telescopes such as SMMM can be performed in different ways, using different sensing techniques. The performance objective for any figure controller is to maximize image quality. Appropriate performance metrics are: wavefront error; Strehl ratio, or peak intensity; encircled energy; blur spot radius. These are all extremized at the perfect image quality condition, though they behave differently away from optimum<sup>15</sup>.

The ideal sensor system for control would directly measure the quantity of interest using the existing science sensor directly. For SMMM, such a system is used for “Figure Initialization” control.

To develop and test various figure initialization algorithms, we developed a software testbed, called FCSim, which incorporates a detailed linear structure model, a nonlinear actuator model and a full COMP

diffraction optics model, including color and noise effects. We tested several algorithms, including:

- Co-alignment/Co-phasing<sup>26</sup>. This approach operates on pairs of segments, sequentially aligning them by overlaying their spots, and then phasing them by finding the sharpest intensity peak. Repeating for each segment leaves the full telescope aligned, usually in several hundred iterations. The performance metric used is encircled energy, measured directly as peak intensity in the central pixel of the 11x11 bolometer imaging sensor array.
- Simulated Annealing<sup>27</sup>. A simple, robust approach that generates random changes of segment position, and then accepts them if they improve the metric. Steps that decrease the metric may also be accepted, a feature that allows the algorithm to escape local minima. Usually converges in 2,000-3,000 iterations. This approach uses the same peak-intensity-in-the-central-pixel metric
- Model-based Nonlinear Least Squares. The same approach we used to find the Hubble prescription<sup>22</sup>, this approach drives a model of the optical system to generate simulated images that match the real images. Solutions require 2-3 images but no iterations of the real actuators - just a single correction step. The performance metric used here is the chi-squared of the intensity in each of the 121 pixels. This turned out to be a much more sensitive function.

**FIGURE 8. SMMM Layout**

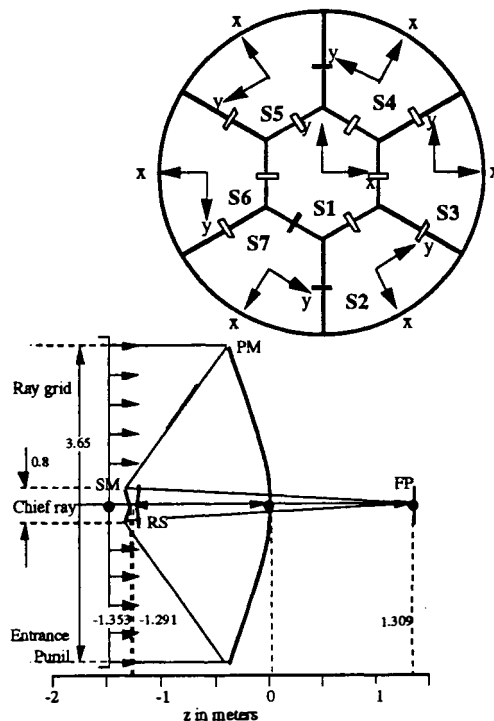


Figure initialization control works well provided the star being observed is bright and of limited angular extent. Most science targets are too dim, and some are extended objects, so that this control mode is not usu-

ally available. When observing, either passive structural stability or some other sensing method must be relied on.

For SMMM, we investigated a “Figure Maintenance” controller that relies on structural measurements to maintain figure quality. We examined the use of several sensor configurations before selecting an “optical truss” of laser gauges to measure segment position states<sup>29,28</sup>. This approach was chosen because it provides full observability of all the segment states (6DOF), and so of all the segment contributors to image quality.

We choose wavefront-squared error as the metric for figure maintenance control. Wavefront error is computed as the optical path difference (OPD) for a large number of rays at the exit pupil, represented by a spherical reference surface as indicated in Fig. 8. We generated a linear model of the wavefront OPD which takes the form

$$\vec{w} = C\vec{x} \quad (21)$$

Here  $\vec{w}$  is a vector of n ray OPDs, and  $\vec{x}$  is the state vector, composed of six segment state vectors  $\vec{x}_i$ , each of which is in the form

$$\vec{x}_i = [\theta_x, \theta_y, \theta_z, \delta_x, \delta_y, \delta_z]^T \quad (22)$$

$C$  is the linear model of ray OPDs as a function of segment states as computed and exported by COMP. Of the segment states only tip, tilt and piston ( $\theta_x, \theta_y, \theta_z$ ) are controllable. The effect of the actuators is thus:

$$\dot{\vec{x}}_{act} = A\vec{u} \quad (23)$$

where the  $\vec{u}$  are the (3DOF per segment) commands and the action matrix  $A$  is

$$A = \begin{bmatrix} A_{seg1} & 0 & 0 \\ 0 & \dots & 0 \\ 0 & 0 & A_{segN} \end{bmatrix}, A_{seg_i} = \begin{bmatrix} \hat{x}_{seg_i} & \hat{y}_{seg_i} & 0 \\ 0 & 0 & 0 \\ 0 & 0 & \hat{z}_{seg_i} \\ 0 & 0 & 0 \end{bmatrix} \quad (24)$$

The unit vectors  $\hat{x}_{seg_i}$  etc. are the lines of action of the segment actuators.

A single step of the system produces a new state vector

$$\dot{\vec{x}}_1 = \vec{x} + A\vec{u} \quad (25)$$

which yields a wavefront

$$\vec{w}_1 = C\vec{x} + CA\vec{u} \quad (26)$$

The wavefront-squared metric is

$$J = \frac{1}{2} (\vec{w}_1 \cdot \vec{w}_1) \quad (27)$$

This is minimized when  $dJ = 0$ , which is satisfied by the optimal “wavefront compensation” control law:

$$\dot{\vec{u}}_{opt} = -(A^T C^T C A)^{-1} A^T C^T C \dot{\vec{x}}_{est} + \dot{\vec{q}} \quad (28)$$

Here  $\dot{\vec{x}}_{est}$  is the estimated state derived through a Kalman filter from the optical truss measurements. This control law determines actuator commands that minimizes residual wavefront error based not on wavefront measurements, but on structural measurements weighted to “simulate” wavefront measurements.

As a point of comparison, consider a different controller which ignores the optics and seeks to minimize the state error squared. Cost function for this “segment error compensator” is

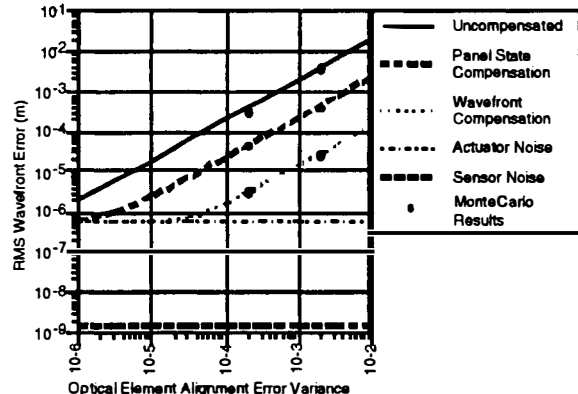
$$J = \frac{1}{2} (\dot{\vec{x}}_1 \cdot \dot{\vec{x}}_1) \quad (29)$$

and the control law is

$$\dot{\vec{u}}_x = -(A^T A)^{-1} A^T \dot{\vec{x}}_{est} + \dot{\vec{q}} \quad (30)$$

Comparative performance of these controllers computed using linear covariance and nonlinear Monte Carlo analyses, is shown in Fig. 9. The wavefront compensation controller reduces the uncorrected wavefront error by a factor of about 120. The segment state compensator does not perform as well, reducing the initial errors by about 8 times, 15 times worse than the wavefront compensator.

**FIGURE 9. Figure Maintenance Control Performance**



The wavefront compensation approach performs better because it is able to counter the wavefront effects of errors in the uncontrollable segment degrees of freedom (decenter or twist) by biasing its response in the controllable degrees of freedom. More generally, the wavefront compensator works better because it is explicitly designed to minimize the appropriate optical performance metric.

## 4.0 CONCLUSION

There are many intriguing control and estimation challenges emerging from the field of astronomy. Most of these involve controlled optical elements, optical sensors or measurements. Certainly the performance bottom line is optical: best image quality. The example presented here is meant to illustrate a perhaps obvious

point: that to obtain the best system performance, the controllers should be designed explicitly to optimize the optical performance objective. Means to do this are now available.

## 5.0 ACKNOWLEDGEMENT

Thanks to Mark Colavita, Brad Hines, Marty Levine, George Seaston and Sam Sirlin for their contributions to this paper. The research described was performed at the Jet Propulsion Laboratory, California Institute of Technology, under contract with the National Aeronautics and Space Administration.

## 6.0 REFERENCES

1. J. W. Goodman, *Introduction to Fourier Optics*, McGraw-Hill, New York, Chapters 3 and 4, 1968.
2. T.S. Mast and J.E. Nelson, "The Figure Control of Segmented Telescope Mirrors," Ten Meter Telescope Report No. 80, March, 1983.
3. G. Enard, "ESO VLT Project I: A Status Report," in *Advanced Technology Optical Telescopes IV*, L. Barr, editor, SPIE Proc 1236, 1990.
4. A. Meinel and M. Meinel, "Multiple Aperture Diffraction Images," *Applied Optics and Optical Engineering*, Vol. IX, Ch. 5, R. Shannon and J. Wyant, editors, Academic Press 1983.
5. **Astrotech 21 Workshop Proceedings: Technologies for Optical Interferometry in Space**, G. Illingworth and D. Jones, editors, JPL Internal Document D-8541, Vol. 1, Jet Propulsion Laboratory, 1991.
6. A. Thompson, J. Moran and G. Swenson, Jr., *Interferometry and Synthesis in Radio Astronomy*, Wiley, 1986.
7. M. Shao and M. Colavita, "Long-Baseline Optical and Infrared Stellar Interferometry," in press, *Annual Review of Astronomy and Astrophysics*, 1992.
8. R. Reasenberg et al, "Microarcsecond Optical Astrometry: An Instrument and its Astrophysical Applications," *Astronomical Journal*, Vol 32, 1988.
9. M. Colavita and M. Shao, "Control and Metrology Issues in Long-Baseline Stellar Interferometers," IFAC Aerospace '92 Symposium, Ottobrun, Germany, September 1992.
10. J. Spanos, "Control/Structure Interaction in Long Baseline Space Interferometers," IFAC Aerospace '92 Symposium, Ottobrun, Germany, September 1992.
11. R.K. Tyson, *Principles of Adaptive Optics*, Academic Press, 1991.
12. L. Kaffer, A. Böinghoff, E. Brüderle, W. Shrempp, P. Wullstein, "ROSAT In-Orbit Attitude Measurement Recovery," Paper AAS 92-075, 15th Annual AAS Guidance and Control Conference, Keystone, Colorado, February 1992.
13. **Astrotech 21 Workshop Proceedings: Technologies for Large Filled-Aperture Telescopes in Space**, G. Illingworth and D. Jones, editors, JPL Internal Document D-8541, Vol. 4, Jet Propulsion Laboratory, 1991.
14. E.A. Sziklas and A.E. Siegman, "Mode calculations in unstable resonators with flowing saturable gain. 2: Fast Fourier transform method", *Applied Optics*, v14, 1874-1889, 1975.
15. D. Moore, "Findings of Hubble Independent Optical Review Panel," in *Space Optics*, Vol. 19 of OSA 1991 Technical Digest Series (Optical Society of America, Washington DC, 1991)
16. L. Furey, T. Dubos, D. Hansen and J. Samuels-Schwartz, "Hubble Space Telescope Primary Mirror Characterization," in *Space Optics*, Vol. 19 of OSA 1991 Technical Digest Series (Optical Society of America, Washington DC, 1991)
17. J. Fienup, "Hubble Space Telescope Aberrations and Alignment Determined by Phase Retrieval Algorithm," in *Space Optics*, Vol. 19 of OSA 1991 Technical Digest Series (Optical Society of America, Washington DC, 1991)
18. Redding, D., Dumont, P. and Yu, J., "Hubble Space Telescope Prescription Retrieval," in *Space Optics*, Vol. 19 of OSA 1991 Technical Digest Series (Optical Society of America, Washington DC, 1991)
19. D. Redding, L. Needels, K. Wallace, J. Yu and M. Levine, *Controlled Optics Modelling Package User Manual, Version 1.0*, JPL Internal Document D-9816, Jet Propulsion Laboratory, 1992.
20. H.C. Briggs, *Integrated Modelling of Optical Systems User Guide, Version 1.0*, JPL Internal Document D-9836, Jet Propulsion Laboratory, 1992.
21. Redding, D., Milman, M. and Loboda, G., "Linear Analysis of Opto-Mechanical Systems," *Controls for Optical Systems*, J.A. Breakwell, editor, Proc.-SPIE 1696 (1992).
22. D. Redding and W. Breckenridge, "Optical Modeling for Dynamics and Control Analysis," *Journal of Guidance, Control and Dynamics*, Vol. 14, No. 5 (1991), pp. 1021-1032.
23. Silberstein, *Simplified Method of Tracing Rays Through Any Optical System*, Longmans Green Co., London, 1918.
24. Redding, D. and Breckenridge, W., "Coordinate-Free Raytrace Equations for Aspheric and Deformed Optical Surfaces," Draper Laboratory Internal Memo DCR-91-38, July 13, 1991.
25. J.C. Dainty, "Stellar Speckle Interferometry", *Laser Speckle and Related Phenomena*, Chapter 7, J.C. Dainty, ed., second edition, Springer-Verlag, New York, 1984.

- 26.** M.J. Mahoney, "Four NASA submillimeter-wave-length space-astrophysics missions", Paper IAF-91-422 presented at the 42nd Congress of the International Astronautical Federation, Montreal, Quebec Canada, 5-9 October 1991.
- 27.** Sirlin, S. and Redding, D., "Modeling and Initialization Control of a Segmented Telescope," **Controls for Optical Systems**, J.A. Breakwell, editor, Proc.SPIE 1696 (1992).
- 28.** B.M. Levine, S. Shaklan, T. Buxman and P. Dumont, "Phasing of a Space-Based Segmented Submillimeter Wavelength Telescope Using Focal Plane Measurements," **Controls for Optical Systems**, J.A. Breakwell, editor, Proc.SPIE 1696 (1992).
- 29.** Lau, K., Breckenridge, W., Nerheim, N. and Redding, D., "Active Figure Maintenance Control Using an Optical Truss Laser Metrology System for a Space-Based Far-IR Segmented Telescope," **Controls for Optical Systems**, J.A. Breakwell, editor, Proc.SPIE 1696 (1992).
- 30.** Redding, D., Breckenridge, W., Lau, K., Sevaston, G., Levine, B.M. and Shaklan, S., "Segmented Mirror Figure Control for a Space-Based Far-IR Astronomical Telescope," in **Structures, Sensing and Control**, J. Breakwell, V. Varadan, editors, Proc. SPIE 1489, April 1991.

## TRAJECTORY OPTIMIZATION TECHNIQUES AND SOFTWARE IMPLEMENTATION

K.H. Well\* and K. Ebert\*\*

\*Universität Stuttgart<sup>1</sup>, Institut für Flugmechanik und Flugregelung, Stuttgart, Germany

\*\*Messerschmitt-Bölkow-Blohm, Antriebs- und Kommunikationssysteme, Ottobrunn, Germany

**Abstract:** In the past years many in-depth studies on new launch vehicles with airbreathing engines have been conducted worldwide. The extreme performance requirements and the small design margins for such vehicles have in particular renewed the interest in trajectory optimization. The paper reports on recent progress in the state of the art of numerical techniques and their implementation. Questions of robustness, ease of use, efficiency are addressed; user- and software requirements as well as a particular architecture are described. The prototype of an advanced user-interface is presented. The optimal ascent of an advanced launch vehicle is discussed as an example.

**Keywords:** Optimal Control, Optimization, Nonlinear Programming, Numerical Methods, Aerospace Trajectories, Software

### INTRODUCTION

Software for solving nonlinear programming problems (NLP's) is commercially available in libraries such as the IMSL, SOL, NAG since about 1975 and is widely in use at universities, research institutions and in industry. Software for trajectory optimization (TO) has until today not yet been made available on a commercial basis. There are mainly two reasons for this non-availability:

- in comparison to NLP-solvers there is less demand for trajectory optimizations software.
- the optimal control problems (OCP's) are more complex in nature since the solutions consist of functions and parameters and the constraints are differential and algebraic. In addition, the optimal solutions can be unconstrained, constrained or singular, any combinations of these types are in principle possible, each type corresponding to a different set of necessary optimality conditions. The sequence and type of subarcs for the optimal solution can depend very strongly on the boundary conditions and on parameters of the OCP.

Table 1 shows some TO- codes. The sequential gradient restoration algorithm (SGRA) is described in Miele (1975) and has been used extensively, for instance in Miele et al. (1986). BNDSCO in its first version was published by Bulirsch(1971) and has also found widespread use, for instance recently in Bulirsch et al. (1991), Oberle (1990), Chudej (1991), Sachs et al. (1991), Bocvarov et al. (1992). Both SGRA and BNDSCO are developed at universities and have been distributed to expert users in industry and at research centers throughout the world. POST and OTIS are documented programs that have been developed by US industries, Brauer et al. (1977) and Hargraves et al. (1987). They are in widespread use at NASA and at various US government laboratories as well as US universities - but are not available commercially. MUSCOD (Bock et al. 1984) is a university code that is used in Germany, no documentation is available yet. TOMP, TROPIC and PROMIS are codes developed by DLR ( Deutsche Forschungsanstalt fur Luft und Raumfahrt), Kraft (1980), Jänsch (1990), Schnepper (1992). These three codes have found use within Germany, in industry as well as at universities and in laboratories of ESA (European Space Agency). All three codes have documentation.

<sup>1</sup>This work was performed while the co-author was with the Deutsche Forschungsanstalt für Luft- und Raumfahrt

**TABLE 1.** Optimization Codes

	year	type of method
SGRA	1972	gradient, adjoints
BNDSCO	1972	multiple shooting, indirect method, adjoints
POST	1977	parameterized OCP, direct shooting
TOMP	1980	parameterized OCP, direct shooting
MUSCOD	1984	parameterized OCP, direct multiple shooting
OTIS	1987	direct collocation
TROPIC	1990	direct collocation
PROMIS	1992	parameterized OCP, direct multiple shooting

Besides these codes many other computer programs have been developed, in Germany for instance by Horn(1989), Dickmanns et al.(1975), Bock et al. (1978), in the UK by Biggs et al.(1987) and probably many other authors who never published their work.

The selection of the “best” code for a particular problem depends on the complexity of the problem, on the level of user expert knowledge in optimization theory, on user experience and intend, and on features of the candidate code such as efficiency, achievable accuracy, robustness, ease of use, and convergence behaviour. For problems of moderate size and complexity indirect methods such as multiple shooting with its implementation BNDSCO have been applied successfully, especially since recently a direct collocation method has been introduced as a “preprocessor” which has made the cumbersome task of estimating the values for the Lagrange multipliers much easier, see for instance v.Stryck et al.(1991). The level of expert knowledge in using this technique is nevertheless very high, since one needs to implement the necessary optimality conditions for each individual problem and thus needs a priori knowledge of the sequence of subarcs of the optimal solution. In addition, the right hand sides of the system differential equations must be sufficiently differentiable which requires some effort in interpolation and approximation. Once these initial difficulties(usually 95 % of total time spent in solving a particular problem) are overcome, indirect methods such as BNDSCO are extremely accurate and efficient - better than any other technique. Thus this approach is to be favored if user intend is to generate a large number of solutions for varying system parameters.

On the other side of the spectrum is the class of methods that are based on parameterization of the control functions or on direct collocation, that is parameterization of both the controls and the states. These techniques require less knowledge of optimization theory, no a priori knowledge of the type and

sequence of subarcs of the optimal solution, they are robust, that is relatively insensitive to non-smoothness of the mathematical models(right hand sides of the differential equations). In addition, they converge to an approximation of the solution from rather bad initial estimates. They are much less efficient and accurate than the indirect approaches, and they have a tendency to produce local minima and a “Zig-Zagging” behaviour of the control time histories. Despite these deficiencies these techniques are usually preferred by non-expert users(for instance engineers) for solving complex and even large sized problems. The limit on problem size is determined by the maximum number of parameters that the available NLP-codes can handle. Here, numerical experiments with MUSCOD, PROMIS have shown that multiple shooting enlarges the convergence region in comparison to single shooting(TOMP) considerably. Also, direct collocation (TROPIC) has a larger convergence region than TOMP but lacks accuracy compared to the other methods.

The code SGRA has found widespread use, too. It uses a fixed stepsize integrator and a Valentine’s-device -like procedure to handle path constraints. The adjoint differential equations are generated numerically. We do not consider this code in more detail because the gradient method is known to be very slow in converging and we conjecture - based on some numerical experiments - the method not to be competitive with the other candidate codes.

## USER and SOFTWARE REQUIREMENTS

User requirements on the one hand are the requirements *on* the user, that is requirements on the level of user knowledge. For the codes TOMP, MUSCOD, TROPIC, PROMIS - and for those in POST and OTIS - the minimal required user knowledge consists of the ability to formulate a well posed optimal control problem, a basic knowledge of nonlinear programming, in particular a conceptual understanding of sequential quadratic programming, and a profound knowledge of the system dynamics of his problem.

A typical TO problem consists of ordinary differential equations(dynamics), a set of constraints on the current, intermediate and final states and controls (pointwise satisfaction of path constraints and intermediate boundary conditions), a performance criterion(cost function). The objective is to determine the state- and control time histories subject to the dynamics and constraints of the problem such that the cost is maximized or minimized. For TO of conventional and advanced launch vehicles as well as reentry problems an in depth knowledge of flight and orbital mechanics is needed. Typical control functions are pitch and yaw angle time histories - or angle of attack- and bank angle time histories - and “throttle setting”, typical parameters of the problem are the

duration of coasting arcs. Performance criteria are payload mass, final orbital energy or specific final orbital parameters, typical constraints are initial fuel loadings, perigee height of ballistic arcs, dynamic pressure and heat-flux as well as lower and upper limits on the values of the controls and states and state rates.

In the mathematical formulation of a trajectory optimization problem, one expresses the equation of motion of a launch vehicle as a multi-phased system of the form,

$$\dot{x} = f^j(x, u, \rho^j, t)$$

where  $t \in [t_j, t_{j+1}]$  for  $j = 1, \dots, m$

( $m$  = the number of phases). The objective is to determine the control functions  $u(t)$ , the initial, final and phase separation times  $E = [t_1, \dots, t_{m+1}]^T$  and the design parameters  $\rho = [\rho^1, \dots, \rho^{m+1}]^T$  such that the scalar functional,

$$I = \phi(x(t_o), x(t_f), E, \rho)$$

is minimized. At the initial, final and each phase separation time, equality and inequality boundary constraints of the form

$$\psi_{eq}^i(x(t_i), \rho, t_i) = 0$$

$$\psi_{iq}^i(x(t_i), \rho, t_i) \leq 0$$

must be satisfied. Within each phase, equality and inequality path constraints of the form

$$p_{eq}^j(x(t), u(t), \rho^j, t) = 0$$

$$p_{iq}^j(x(t), u(t), \rho^j, t) \leq 0$$

have to be satisfied, and at the phase separation times, jump conditions of the form

$$x(t_j^+) = h^j(x(t_j^-), t_j)$$

might be imposed. Jump conditions are necessary to model, for instance, the discontinuous change of mass (and possible other states) at booster jettisoning, at stage separation and at payload fairing jettisoning.

User requirements, on the other hand, are those features or capabilities that the user desires from a particular software, that is requirements of the user, see for instance Mehlem (1988). For ascent TO, for instance, one needs the earth model (shape, atmosphere, windfields), the vehicle model (limits on stages, propulsion systems, aerodynamics, dynamic pressure, heat flux, bending moments), the trajectory

model (equations of motion, controls, walking impact point, tracking station coverage), a description of input data (sequence of events, initial estimates of the controls and states and their upper and lower bounds, initial, intermediate, and final constraints for the trajectory, changes in controls - if any), and the output data (relevant state-, control-, and derived information)

The software requirements specify how the above summarized user requirements are implemented. Usually a TO package is supposed to optimize as well as to simulate a trajectory (for given control function time histories). A switch-over from one mode to the other should easily be possible. The SR's define, in addition, programming language, file input and output specifications, error handling procedures, subroutine and function naming conventions, and the software structure and the various interfaces between the models, the simulation- and optimization environment. A file-management system is proposed in Paus (1989).

Fig. 1 shows a sample structure of an optimization/model interface. The models consist of code (upper block inside dashed rectangle) and descriptor files (lower block inside dashed rectangle). For a particular class of problems the user does not change the source code, he specifies a particular problem within its class by editing the system descriptor file which consists of components associated with each routine. The system descriptor completely defines the particular problem by specifying the number of phases, within each phase number of states and controls and "design" parameters (which can vary from phase to phase), number and type (equality or inequality) of boundary conditions at the end of the phase (initial conditions of the TO problem are given as phase 0 boundary conditions), number and type of path constraints within the phase. Fig. 3 shows as an example a descriptor file content for a two phase aerospace vehicle. The system descriptor language is "natural", that is it can easily be edited - without having to refer to a user manual. In this way constraints can easily be "switched on" or "switched off", or can be converted from equality to inequality as is convenient during the solution process. Fig. 2 shows the mathematical formulation of the routine interfaces.

## SPECIAL SOFTWARE FEATURES AND DATA STRUCTURE

Fundamental to all optimization techniques is the method of parameter- and function scaling, handling of box constraints, phase connect conditions, and the definition of an appropriate data structure. A basic rule for scaling is to scale all quantities to the same order of magnitude and of order unity, because convergence criteria within the optimization technique are usually based on some notion of "small" or

“large”. Jänsch (1990) gives scaling rules for the optimizable parameters and the functions as follows: Given the original parameter vector  $P$  apply the transformation

$$\bar{P} = DP + E, \quad D = \text{diag}\{d_1, \dots, d_n\},$$

$$E = [e_1, \dots, e_n]^T$$

with

$$e_i = 0, \quad d_i = (1/|p_i|), \quad \text{if } |p_i| \geq 1 \quad \text{for all}$$

$$i \in \{1, 2, \dots, n\}, \quad \rightarrow O(\bar{p}) = 1 \text{ or}$$

$$d_i = 2/(b_i - a_i), \quad e_i = (a_i + b_i)/(b_i - a_i)$$

for every  $i \in \{1, 2, \dots, n\}$ , where  $a_i \leq p_i \leq b_i$ ,  $n$  being the dimension of the parameter vector  $\rightarrow \bar{p}_i \in [-1, 1]$ .

The values of  $a_i$  and  $b_i$  are taken from the lower and upper bounds of the parameters.

Given the original function value  $F$  apply the transformation

$$\bar{F} = DF, \quad \text{with } D \text{ being a scaling factor computed individually from}$$

$$D = 1/(|F|)^{1/2} \text{ or } D = 1/(|c_i|)^{1/2}$$

for function - or constraint values respectively.

These scaling rules have been shown to work well for a variety of test problems, see for instance Jänsch et al. (1990).

Upper and lower bounds of the parameters are called “box”-constraints. In many TO problems one sometimes wants to hold a particular parameter at a fixed value while optimizing all the rest. This can easily be accomplished by setting upper and lower box constraint at the same constant value. However, the Sequential Quadratic Programming Solver expects full rank constraint Jacobian, and using this box constraint setting would result in a rank deficiency. Therefore, it is advisable to remove all “tagged” parameters from the NLP problem. This has been realized in both the codes TROPIC and PROMIS. Multi-phase OCP’s as stated above may exhibit jumps in the controls and/or states across a phase boundary. In order to avoid a duplication of unknown parameters at the phase boundaries in a direct collocation method, states and controls are only discretized at the final time of a phase - not at the initial time of phases greater than one. The state- and control connect conditions are used to determine the appropriate values at the beginning of a phase. This feature is not as problematic with PROMIS, since state values at the end of a phase are obtained by

numerical integration , anyhow. Global design parameters are treated as local parameters in each phase, they are connected by way of a real design parameter connect condition. This increases the dimension of the overall parameter vector by a factor of number of phases\* number of design parameters, but it preserves the band structure of the Hessian of the Lagrangian in the NLP code. Although this band structure is not yet exploited in the used NLP-solver (SLLSQP, Kraft (1988)), it leaves room for attaching an advanced NLP-solver.

Fig. 1 shows two particularly important files: The input timegrid and the output time grid. These files contain all the information needed by the optimization codes. In order to allow maximum flexibility as far as phase selection, grid selection, choice of control approximations, values of box constraints is concerned, an appropriate data structure must be defined. This data should be hierarchically structured with the aid of a data description format that contains all relevant data types, see for instance Schnepper, Jänsch (1989). Fig. 4 shows a general data structure for parameterized optimal control problems. The *phase timegrid* has a *phase gridpoint record* attached to it at every phase time. Each *phase gridpoint record* contains besides lower and upper bounds for the phase time, data of the real design parameters for that phase, of the integer design parameters associated with the phase, and additional *collocation- or multiple shooting (MS) gridpoint records*. These records contain lower and upper bounds for the MS gridpoint times, state vector values with their lower and upper bounds, *control approximation records*, and values of those gridpoints at which the path constraints need to be evaluated. The *control approximation record* is further refined into *control no. records*, one for each control function of the OCP. Each of the *control no. record* contains information about the type of control approximation, continuity conditions, and *control gridpoint records* that have lower and upper bounds for each of the control time gridpoints as well as all values of the control with its bounds.

This data structure enables a user to choose a discretization of the original OCP that most closely approximates the type of optimal solution to be expected and the associated time histories of the state and the control.

## ADVANCED USER INTERFACE (UI)

For a moderately sized parameterized OCP one may have, as an example, 3 to 5 phases, 10 state variables, 4 control variables, 3 path constraints. Using a multiple shooting refinement of 3 gridpoints per phase, of 5 control gridpoints per multiple shooting mesh, 5 path constraint evaluation points per multiple shooting mesh, one obtains between 480 to 800 parameters, each of them with a lower and upper bound. In

order to be able to manage the input for these parameters in a reasonable way a graphical editor assisting the user is absolutely necessary. In addition, a user interface should assist the user in problem solving, since the key to a successful software implementation of as complex a software system as is needed for general TO problems is the ability of a user to interact effectively with the system. The main functionality of a UI consists of i) input file definitions (alphanumeric and graphic) and conversion of these files into a form needed by the optimization and simulation programs, templates of all files need to be available, ii) file management and process control, iii) graphical simulation and optimization result analysis. Fig. 5 shows a possible architecture. Optimization- and simulation programs are compiled separately, they communicate with the model through internal binary data transfer. The UI is a separate program that communicates with both optimization and simulation and the dynamic model data files via external data transfer. Fig. 6 shows 11 activities which are supported by the UI. One of the 11 - in this case *model* - is showing two more cascade menus with which the model can be specified via appropriate data files. Fig. 7 shows another cascade menu: With the click of a mouse button the user can initialize the UTG2PTG(a separate main program that generates from an input file called UTG a program time grid (PTG) consistent with the data structure discussed above) or open the graphical input facility to generate a PTG or open the UTG file to be edited with the editor phase by phase. A detailed description of the capabilities of a sample UI is given in Crues (1991). Once the initialization is completed the user can switch over to simulation or optimization. Each of these main buttons have further cascade menus attached to it. At any stage of the optimization process the user can activate a *help* facility that contains an on-line documentation. Fig. 8 shows a sample menu for graphically inputting a control time grid, control estimates with lower and upper bounds. Each gridpoint can be moved, removed, inserted; each estimate can be adjusted with the help of a mouse button, various interpolation schemes can be selected (linear, constant), and box constraints can be set individually or globally (as a "hose" around the initial estimates, for instance). The results of this editing process is automatically stored in the appropriate position of the PTG. With the help of such a facility even complex problems can be solved within a few days - in comparison to weeks and months that had to be spent in the past for the same task.

#### EXAMPLE: ASCENT of a SSTO

As an example for a multi-phase TO problem the maximum payload ascent of a single-stage-to-orbit launcher with a hybrid propulsion system consisting of rocket- and ramjet engines is considered. In phase 1 the vehicle is accelerated to speeds at which the

ramjet can operate, in phase 2 both rocket and ramjet engines are operated simultaneously, phase 3 sees ramjet power only, and in phase 4 rocket engines are used to accelerate to orbital speed. The objective is to take-off in ISTRES and reach a transfer orbit with perigee/apogee altitudes of 80/350km at an inclination of 28.5°. During the ascent dynamic pressure is limited to 68kPa, axial acceleration to 3.5g's.

**TABLE 2.** Selected controls for various phases

controls\phases	1	2	3	4
power setting	x	x	x	x
horizontal load	x	x	x	
vertical load	x	x	x	
vertical load	x	x	x	
angle of attack				x

Table 2 shows that in different phases of the problem different controls are used. The TO problem is solved using PROMIS with no intermediate multiple shooting (MS) point in phase 1 (single shooting), 1 intermediate MS grid in phase 2, 4 intermediate MS-gridpoints in phase 3, and 1 intermediate in phase 4. Figs. 9 and 10 show selected state- and control time histories of the optimal ascent trajectory. Flight is mostly along the dynamic pressure constraint, the times of switching from rocket- to ramjet, to rocket/ramjet, and to rocket power are selected by the optimizer. The size of the nonlinear program is about 250 parameters. Trial and error simulations were performed in order to get an initial guess from which the optimizer would converge. It took about one week to solve this problem.

#### CONCLUSIONS

General software for solving TO problems needs to be designed in such a way that a user can easily specify or modify his model, generate initial estimates, check the physical significance of the intermediate and final results, monitor the performance of the optimizer, modify initial or intermediate values of the controls and parameters if necessary, switch to a simulation mode or continue the optimization process, and analyze all results graphically. To this end robust optimization methods are to be integrated into a user interface that supports all tasks a user might want to execute. A sample TO-system has been described using as optimizers either a direct collocation or a direct multiple shooting method and in which a UI has been realized for any UNIX operated machine that has X-WINDOWS/MOTIF. This system has been implemented under contract of the European Space Agency under the name ALTOS (Advanced Trajectory Optimization Software) as a joint MBB/DLR Softwareproject.. The system is presently being used by ESA personnel at ESTEC, by MBB personnel in Ottobrunn at DLR in Oberpfaffenhofen, and part

of the system is being used at the University of Stuttgart. In a next version of the system it is planned to attach the indirect multiple shooting code BNDSCO thus combining the advantages of parameterized optimal control codes (robustness, problem -“set-up”- effort, convergence behaviour) with those of an indirect code (efficiency, accuracy).

#### ACKNOWLEDGEMENT

In this paper the authors have summarized ideas and work of the following persons: E. Berger, W. Buhl, E. Crues, H. Herbst, C. Jänsch, M. Paus, E. Röllecke, K. Schnepper, H. Wolff. The authors gratefully acknowledge their contributions. Part of this work was supported by the European Space Agency through Contract No. 8046/88/NL/MAC, part of the work was supported by the Deutsche Forschungsgemeinschaft (DFG).

#### REFERENCES

- Bartholomew-Biggs, M. C., Dixon, L. C., Hersom, S. E., Maany, Z. A., Hechler, M. (1987). *From High Thrust to Low Thrust: Application of Advanced Optimization Methods to Mission Analysis*. Journal 11, ESA.
- Bock, H. G. (1978). *Numerical solution of nonlinear multipoint boundary value problems with applications to optimal control*. Zeitschrift für Angewandte Mathematik und Mechanik, 58:407-409.
- Bock, H. G. , Plitt, K. J. (1984). *A multiple shooting algorithm for direct solution of optimal control problems*. In Preprints of IFAC International Federation of Automatic Control, pages 243-247, Budapest, Hungary, 9th World Congress.
- Bocvarov, S., Lutze, F. H., Cliff, E. M., Well, K. H. (1992). *Time-Optimal Reorientation Maneuvers for an Aircraft With Thrust-Vector Control*, Aerospace and Ocean Engineering Department and Interdisciplinary Center for Applied Mathematics, Virginia Polytechnic Institute and State University, Proceedings, AIAA Guidance, Navigation, and Control Conference, Hilton Head, USA.
- Brauer, G. L., Cornick, D. E., Stevenson, R. (1977). *Capabilities and Applications of the Program to Optimize Simulated Trajectories (POST)*, Program Summary Document , NASA Contractor Report, NASA CR-2770, National Aeronautics and Space Administration, Washington, D. C.
- Bulirsch, R.; Montrone, F.; Pesch, H. J. (1991). *Abort Landing in the Presence of a Windshear as a Minimax Optimal Control Problem*, Part 2: Multiple Shooting and Homotopy. J. of Optim. Theory and Appl. 70 No. 2, s. 221-252.
- Bulirsch, R. (1985). *Die Mehrzielmethode zur numerischen Lösung von nichtlinearen Randwertproblemen und Aufgaben der optimalen Steuerung*. Lehrgang über Flugbahnoptimierung, Carl-Cranz-Gesellschaft, Heidelberg, (1971), Nachdruck: TU München, Math. Institut.
- Chudej, K. (1991). *Optimale Steuerung und Stufung eines zweistufigen Raumtransporters*. Z. angew. Math. Mech. 71, T 700-T 703.
- Crues, E. Z. (1991). XALTOS: X-Windows User Interface, Software User Manual, Contractor Report, ALTOS (ESA Contract No. 8046/88/NL/MAC).
- Dickmanns, E. D., Well, K. H. (1975). *Approximate solution of optimal control problems using third order hermite polynomial functions*. Springer Lecture Notes, Com. Sci. 27:158-166.
- Hargraves, C. R., Paris, S. W. (1987). *Direct trajectory optimization using nonlinear programming and collocation*. Journal of Guidance, Control and Dynamics, 10(4):338-342.
- Herbst, H., Ebert, K., Buhl, W. (1992). *ALTOS, Advanced Launcher Trajectory Optimization* (ESA Contract No. 8046/88/NL/MAC) Software Test Results, Part 2: Advanced Launchers.
- Horn, M. K. (1989). *Solution of the Optimal Control Problem Using Software Package STOMP*. Proceedings of the 8th IFAC Workshop on Control Applications of Optimization, Pergamon Press, London.
- Jänsch, C. (1990). *ALTOS Advanced Launcher Trajectory Optimization Software* (ESA Contract No. 8046/88/NL/MAC) Software User Manual, Part 4: TROPIC Optimization Program
- Jänsch, C., Kraft, D., Schnepper, K., Well, K. H. (1990). *Comparative Study of Nonlinear Programming Codes for Trajectory Optimization*, Technical Note TN1, ALTOS, ESA Contract No. 8046/88/NL/MAC.
- Kraft, D. (1988). *A Software Package for Sequential Quadratic Programming*. Scientific Report 88-28, Deutsche Forschungs- und Versuchsanstalt für Luft- und Raumfahrt (DFVLR), Oberpfaffenhofen, FRG.
- Kraft, D. (1980). *FORTRAN-Programme zur numerischen Lösung optimaler Steuerungsprobleme*. Technical Report IB 515-80/3, Deutsche Forschungs- und Versuchsanstalt für Luft- und Raumfahrt (DFVLR), Oberpfaffenhofen, FRG.
- Mehlem, K. (1988). *Specification for the Development of an Advanced Launcher Trajectory Optimization Software (ALTOS) Appendix 1 to AO/I-2161/88/NL/MAC*. Report of Mathematical Studies Section, ESTEC, Noordwijk, the Netherlands.
- Miele, A. (1975). *Recent advances in gradient algorithms for optimal control problems*. Journal of Optimization Theory and Applications, 17 (5,6) Survey Paper, dedicated to Prof. A. Busemann.

- Miele, A., Wang, T., Melvin, W. W., (1986). *Optimal Take-Off Trajectories in the Presence of Wind-shear*, *Journal of Optimization Theory and Applications*, Vol. 49, No. 1, pp. 1-45.
- Oberle, H. J., (1990). *Numerical Computation of Singular Control Functions in Trajectory Optimization Problems*, (Vol. 13, No. 1, Jan.-Febr.).
- Paus, Michael (1989). *FORTRAN, IO-Interfaceroutinen*, DLR-Internal Report, Institut für Dynamik der Flugsysteme.
- Sachs, G., Lesch, K., Steinbach, M.; Bock, H. G.(1991). *Optimal Periodic Trajectories with Singular Control for Aircraft with High Aerodynamic Efficiency*, Proc. of the 1991 Oberwolfach Meeting on Optimal Control, to appear.
- Schnepper, K. (1992). *ALTOS Advanced Launcher Trajectory Optimization Software* (ESA Contract No. 8046/88/NL/MAC) Software User Manual, PROMIS Optimization Program
- Schnepper, K., Jänsch, C. (1988). *The Data Description Language BMATH*, Software Reference Manual, DLR-Internal Report, Institut für Dynamik der Flugsysteme
- Stryk, O. von, Bulirsch, R., (1991). *Direct and Indirect Methods for Trajectory Optimization*, Schwerpunktprogramm der Deutschen Forschungs-gemeinschaft Anwendungsbezogene Optimierung und Steuerung, Report Nr. 271, Technische Universität München.

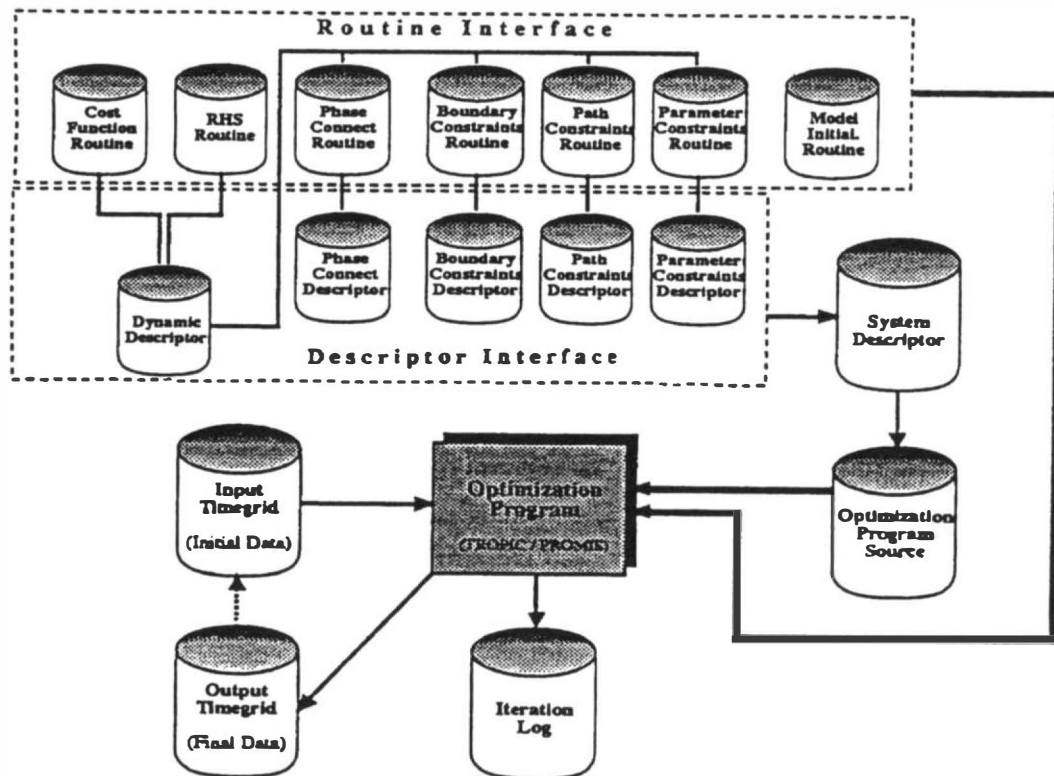


Fig. 1: Software Interface for Optimization

Function	Mathematical Model	Subroutine Name
Right Hand Side of the System	$\dot{x}^i = f^i(t, x^i, u^i, \rho^i)$	RHS
Phase Connect Conditions	$x(t_p^i) = h^i(t_p, x(t_p), u(t_p), \rho^i)$ $u(t_p^i) = g^i(t_p, x(t_p), u(t_p), \rho^i)$ $\rho^{i+1} = k^i(t_p, x(t_p), u(t_p), \rho^i)$	PHASEC
Cost Functional	TROPIC: $\min \sum_i F^i(t_e, x^i(t_e), \rho^i)$ PROMIS: $\min \sum_i \int_0^{t_e} L^i(\tau, x^i, u^i, \rho^i) d\tau$	TCOST PCOST <sup>2</sup>
Boundary Constraints	$\psi^i(t_e, x^i(t_e), u^i(t_e), \rho^i) = 0 \geq 0$	BCONST
Path Constraints	$p^i(t, x^i(t), u^i(t), \dot{u}^i(t), \rho^i) = 0 \geq 0$	PCONST
Nonlinear Parameter Constraints	$w^i(\rho^i) = 0 \geq 0$	PARCON

Fig. 2: Mathematical Description of Routine Interface

```

#      >>> Optimization Descriptor File <<<
#-----
# Version 2.0
#-----
# In this example, the description of a two stage advanced
# launcher ascent problem is given. The description is not
# intended to be a complete specification of such a problem.
# Instead it's purpose is to illustrate the format of the
# optimization system descriptor.
#-----
No_of_phases : 2
#
# First the initial boundary constraints description is
# specified. This information belongs to the imaginary
#
# zero's phase.
#
Phase: O
#
No of boundc : 3
Boundc: 1 , Type: EQ , Enforce: YES , NAME: initial_h ,
Description: Constraint on the initial altitude ;
Boundc: 2 , Type: Iq , Enforce: Yes , Name: initial_v ,
Description: Constraint on the initial velocity :
Boundc: 3 , Type: eq , Enforce: no , name: initial_gamma ,
Description: Initial flight path angle constraint;

# Now follows the description of the Phase 1 information
#
Phase: 1
#
# In the following the states, controls, integer and real
# design parameters are described. The various forms which
# are used for the description, indicate the benefit of the
# free format arrangement and the option to leave out items
# in the description.
#
No_of_states : 7
State: 6 , NAME: r , Description: Re + altitude in [km] ;
State: 4 , name: lamda ,
Description: geographical latitude in [rad] ;
State: 5 , Name: delta,
Description: geographical longitude in [rad] ;
State: 1 , Name: v , Description: velocity in [1km/s] ;
State: 2 , Description: azimuth in [rad] , Name: chi ;
State: 3 , Name: gamma ;
State: 7 , Description: mass of total vehicle in [kg],
Name : m ;
#
No_of_controls: 3
Control: 1 , Name: xi, Description: Engine throttle factor;
Control: 2 , Name: alpha ;
Control: 3 , Name: mu ;
#
No_of_rpars : 2
Rpar: 1 , NAME: TO_heading,
Description: Take off heading angle ;
Rpar: 2 , Name: Payload_mass ;
#
No_of_ipars : 1
IPAR: 1 , Name: Engine_type,
Description: Determines 1st stage engine type;
#
# The following is the constraint description. There the
# final boundary constraints, path constraints and parameter
# constraints of the 1st phase are specified..
#
No_of_boundc : 2
Boundc: 1, Name: trans_altitude , Type: IQ ,
Description: Upper bound on transition altitude;
Boundc: 2, Name: trans-gamma , Type: IQ , Enforce: no ,
Description: Lower bound on transition gamma ;
#
No_of_pathc : 4
Pathc: 1, Name: Dyn_pressure , Type: IQ , Enforce: yes ,
Description: Dynamic pressure upper limit ;
Pathc: 2, Name: Thermal_flow , Type: IQ ;
Pathc: 3, Name: nv , Type: IQ , Enforce: no ,
Description: Vertical load factor constraint ;
Pathc: 4, Name: nh , Type: IQ , Enforce: no ,
Description: Horizontal load factor constraint :
#
No _of_parc : 0
# -
# Now follows the description of the Phase 2 information
#
Phase: 2
#
# In the following the states, controls, integer and real
# design parameters are described. Note that the Connected
# and Link_from specifications are needed to describe the
# phase transition.
#
No_of_states: 7
State: 1 , Name: v , Description: velocity in [km/s] ,
... Connected: yes , Link_from: 1 ;
State: 2 , Name: gamma , Connected: yes , Link_from: 3 ;
State: 3 , Name: chi , Connected: yes , Link_from: 2 ;
State: 4 , Name: lamda , Connected: yes , Link_from: 4 ;
State: 5 , Name: delta, Connected: yes , Link_from: 5 ,
Description: geographical longitude in [rad] ;

State: 6 , NAME: r , Description: Re + altitude in [km] ,
Connected: yes , Link_from: 6 ;
#
# Note the last state (mass of upper stage) is taken to
# be independent of the total vehicle mass and thus not
# connected and linked to a state in the previous phase.
#
State: 7 , Name: m, Description: mass of upper stage [kg] ;
#
No_of_controls: 2
Control: 1 , Name: alpha , Connected: yes, Link_from: 2 :
Control: 2 , Name: mu , Connected: yes, Link_from: 3 ;
#
No_of_rpars: 2
Rpar: 1 , Name: Payload_mass , Connected: yes ,
Link from: 2 ;
#
No_of_ipars : 0
#
# The following is the constraint description. There the
# final boundary constraints, path constraints and parameter
# constraints of the 2nd phase are specified.
#
No_of_boundc: 3
Boundc: 1, Name: perigee , Type: IQ ,
Description: Lowerbound on final perigee ;
Boundc: 2, Name: apogee , Type: EQ ,
Description: Final apogee constraint ;
Boundc: 3, Name: i , Type: EQ , Enforce: no ,
Description: Final inclination constraint ;
#
No_of_pathc : 2
Pathc: 1, Name: nv , Type: IQ , Enforce: yes ,
Description: Vertical load factor constraint ;
Pathc: 2, Name: nh , Type: IQ , Enforce: no ,
Description: Horizontal load factor constraint ;
#
No of parc: 0

```

Fig. 3: A Sample System Descriptor File

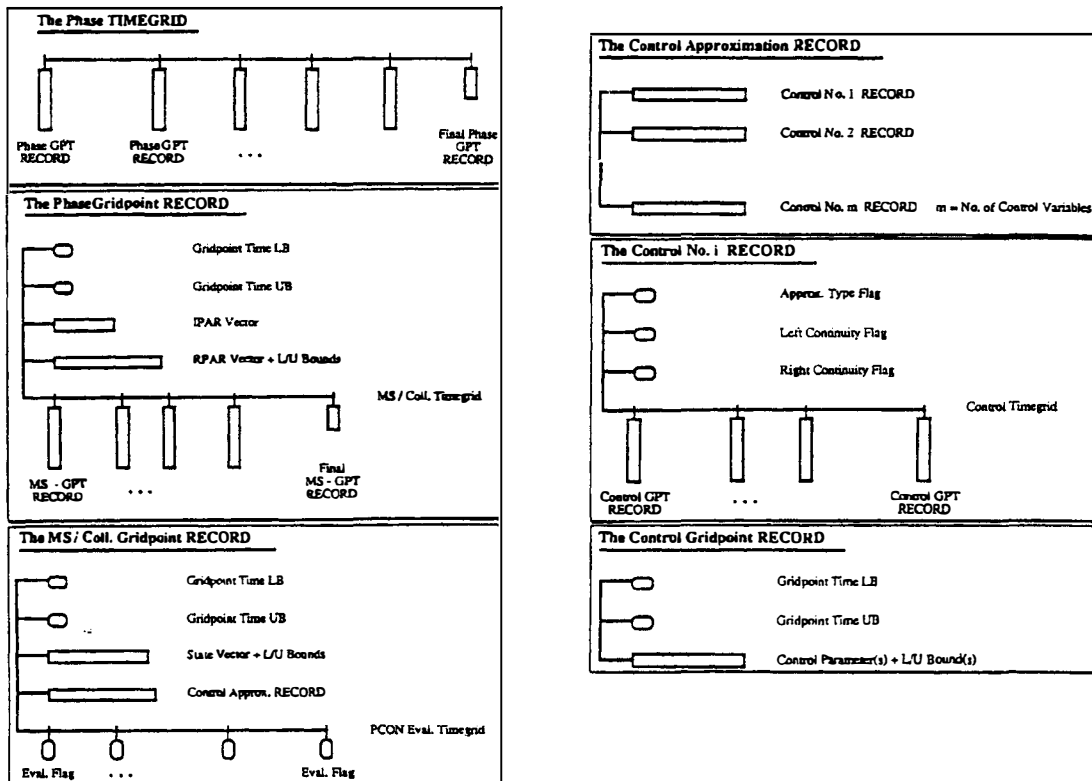


Fig. 4: Data Structure for Parameterized Optimal Control Problems

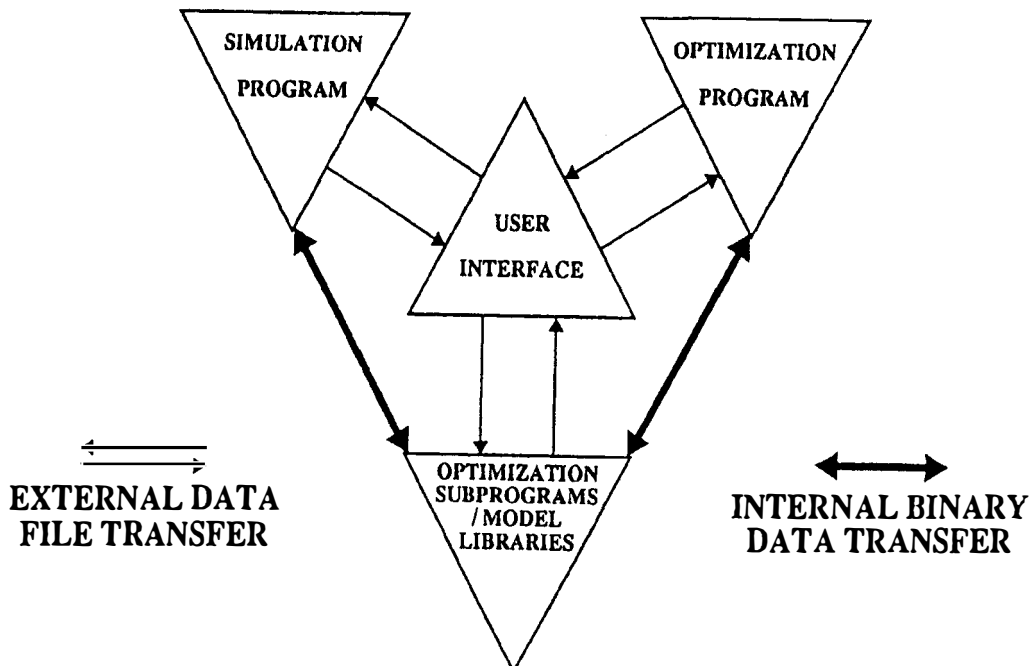


Fig. 5: User Interface

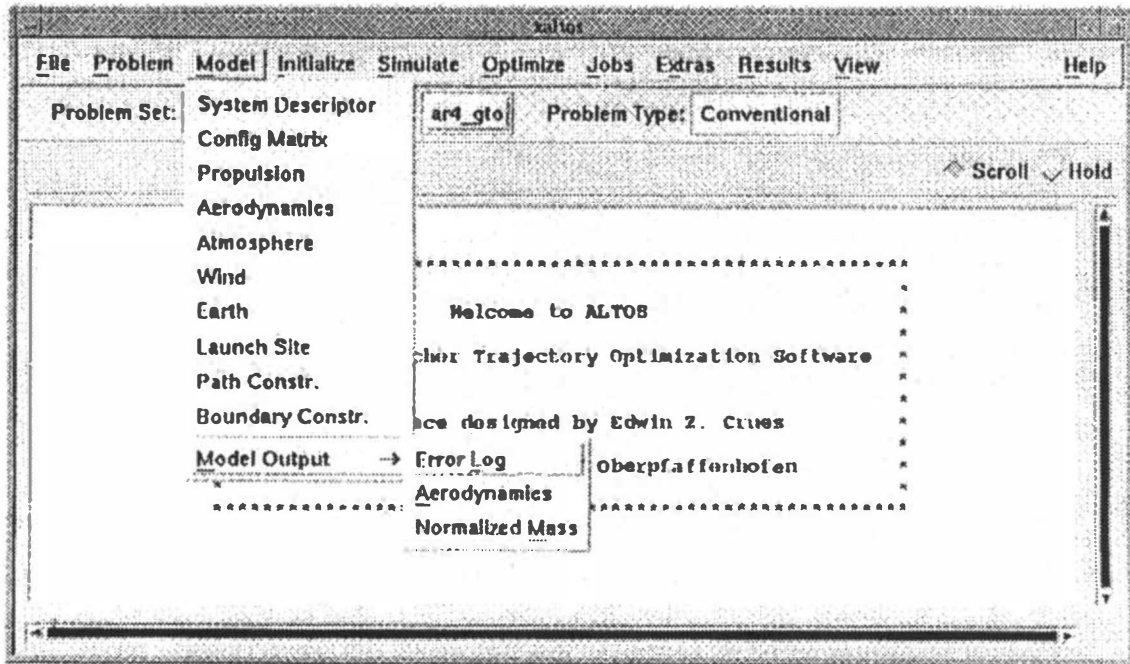


Fig. 6: Services of a User Interface

Fig. 7: Sample Menue from a User Interface

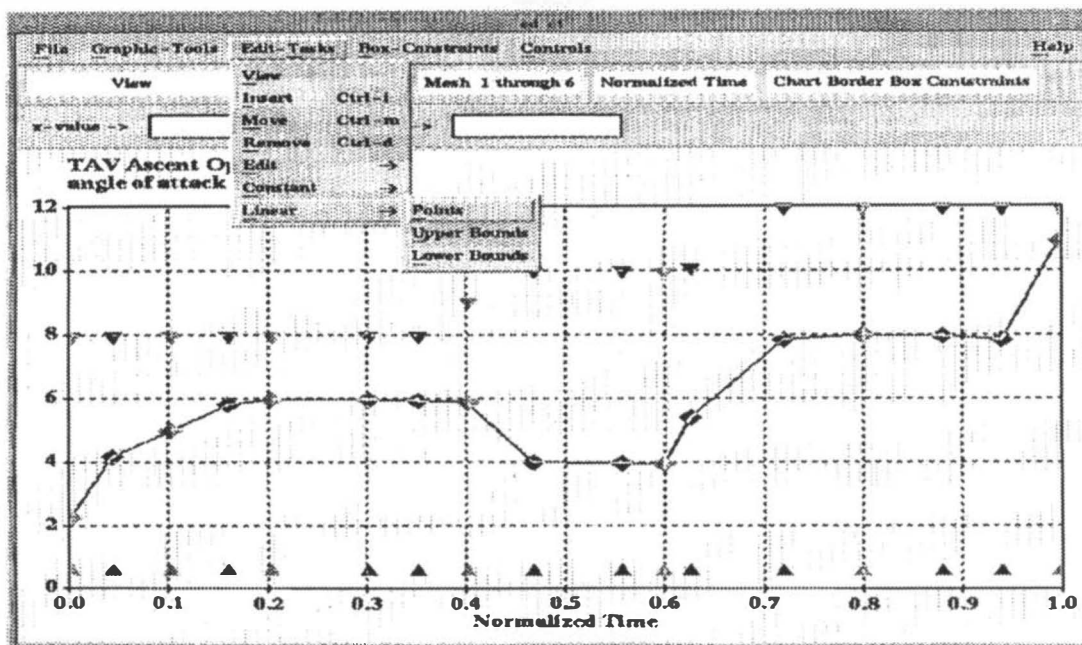
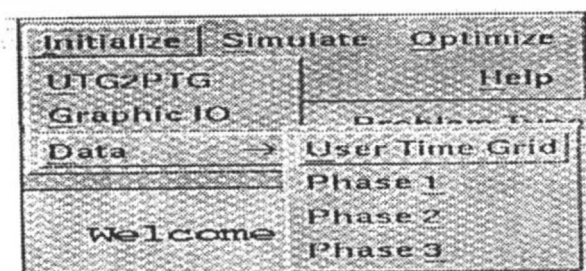


Fig. 8: Sample Menue of a Graphical Input Facility

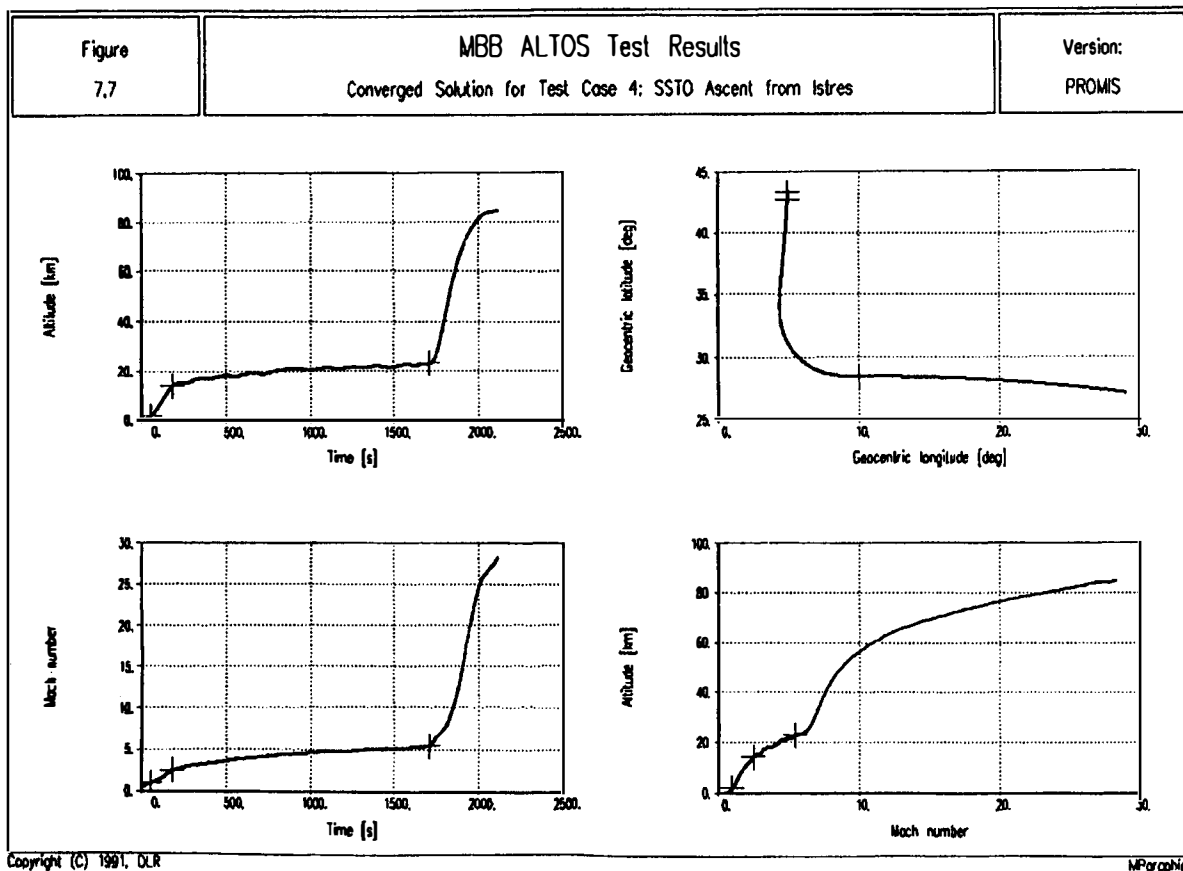


Fig. 9: State time histories of optimal SSTO ascent

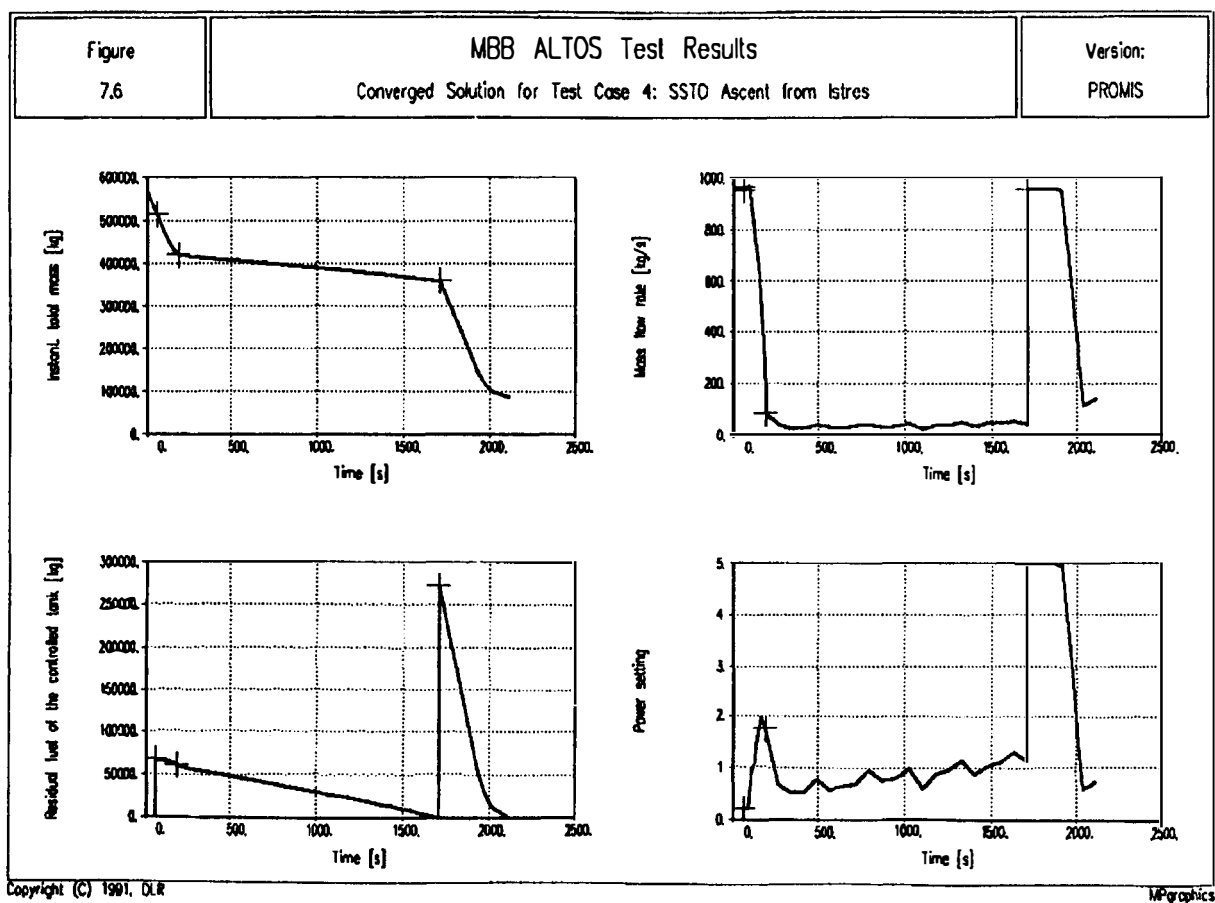


Fig. 10: Mass- and power setting time histories for optimal SSTO ascent

# PROBLEMS IN CONTROL SYSTEM DESIGN FOR HYPERSONIC VEHICLES

D.K. Schmidt

*Aerospace Research Center, Arizona State University, Tempe, AZ 85287-8006, USA*

## Abstract

The unique problems to be encountered in the design of systems for the precise control of hypersonic vehicles are to be presented and discussed. These problems pose significant research challenges if successful guidance and control systems are to be developed for this new class of vehicle. These challenges will be shown to arise due to the stringent mission requirements on the vehicle, and the highly integrated configuration designs being considered. In this paper, the mission requirements and operational goals of these vehicles will be first reviewed, and in particular, the heating problems and trajectory performance issues highlighted. Then the presence of critical coupling between several vehicular subsystems will be clearly exposed, and the dynamic interactions between these subsystems will be presented while considering a selected generic hypersonic configuration. This vehicle configuration, similar to the X-30 vehicle, is shown to be an unstable, highly-coupled, aeropropulsive/aeroelastic system, with large variations in its attitude-dynamic characteristics over its extensive flight envelope. The genesis of these interactions is explored, the magnitudes quantified, and their significance in the context of control-system design presented. Since these issues may ultimately limit the feasibility of some configurations, the flight-dynamic modeling and analysis must be performed early in the design cycle such that critical dynamics and control issues associated with a candidate configuration may be exposed. Therefore, such dynamics and controls analysis cannot be postponed until detailed numerical models are available, because configuration changes may then be too expensive.

## Introduction

Hypersonic vehicles such as the National Aerospace Plane (NASP) promise to be among the greatest technological challenges ever taken on by the American aerospace community. If successful, the NASP, also known as the X-30, would be the first fully reusable, single-stage-to-orbit, manned aerospacecraft. It will most likely use liquid hydrogen ( $LH_2$ ) fuel, be 100 to 150 feet in length, and weigh approximately 250,000 lbs.<sup>1</sup> The NASP

is to be capable of horizontal take-off and landing, accelerating to Mach 25 on orbit, as well as cruising at Mach 5 to 15 in the upper atmosphere. It is expected to have great potential as a low-cost launch vehicle, a high-speed yet economical civilian transport, and a highly responsive military aircraft.

In order to meet the above stated mission requirements, the vehicle will utilize an air-breathing propulsion system for as much of its trajectory as possible. Perhaps the most technically challenging aspect of this class of vehicle is the entry into the hypersonic speed regime. In this speed regime, the untested air-breathing SCRAMjet engine will be the primary propulsive mode. In order to obtain high propulsive efficiency, the SCRAMjet engine must be operated at a high-dynamic-pressure. However, since aerodynamic heating and drag also increase with dynamic pressure, the benefits of high propulsive efficiency must be balanced against temperature and structural constraints. It is estimated that the highest practical dynamic pressure will be approximately 2000 psf. This is about eight times that encountered by a commercial airliner<sup>2</sup>. Figure 1 below indicates typical trajectories. Finally, real gas and viscous effects become important at hypersonic speeds.

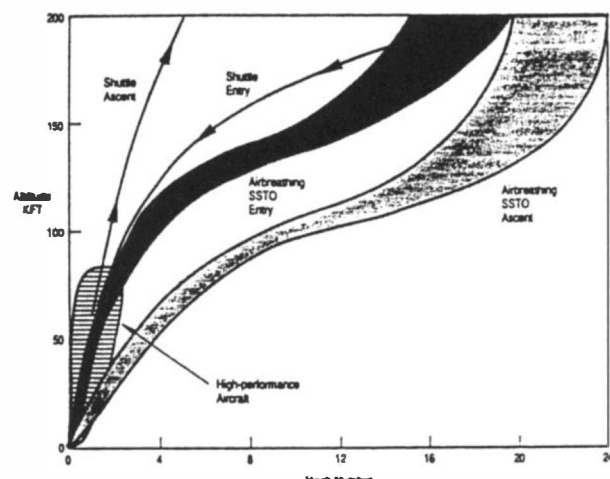


Figure 1. Probable NASP Trajectory

Wind-tunnel testing of the SCRAMjet engines and the aerodynamic characterization will be very limited, due to the lack of facilities with the required

capabilities. The inadequacy of the ground test facilities means that many aerodynamic and propulsion uncertainties must be resolved in flight. Thus, in contrast to the shuttle, the first NASP will not go into orbit on the first flight. Instead, following the precedent of classic NASA research airplane programs like the X-15, its flight envelope will carefully and gradually expanded<sup>2</sup>.

Due to its extremely wide range of operating conditions and mass distributions, the hypersonic vehicle's dynamic characteristics will vary much more over the flight envelope than do those of conventional vehicles. Furthermore, as noted in [12], the ability to predict the critical aerodynamic characteristics for these vehicles is marginal at best, and the opportunities for extensive experimental determination of these characteristics are limited. As a result, the guidance and control laws and the system architecture must deliver an extremely robust control system. In addition, a significant amount of guidance and control system integration will be necessary in order to achieve the requisite system performance and stability robustness. This is due to the fact that dynamic coupling between the flight-path and attitude dynamics is more prevalent at hypersonic flight, and as noted copiously throughout this paper, the airframe, propulsion system, and structural dynamics are highly interactive. Consequently, the classical techniques of inner- and outer-loop closures for control and guidance need to be re-examined in this light, functional integration of guidance and control addressed, and techniques developed for integrated flight and propulsion system control synthesis and implementation.

In this paper, we will address some of these issues further, first in general, and then in more specific terms based on our investigation into the dynamics and control of this class of vehicle.<sup>16-18</sup> The vehicle geometry considered in this study is generic, but was selected to reflect key characteristics similar to the X-30 vehicle described in [1]. The study configuration is 150 ft. in length, with a gross weight of 250,000 lbs and a first-body-bending mode of 3 hz. [13] The results being reported here are based on Newtonian theory utilized for characterizing the quasi-steady aerodynamic characteristics, and a one-dimensional aero-thermodynamic model of the engine. Finally, in all numerical results to be presented, forces are in pounds, pressures are in psf, and angles are in radians.

### Aerodynamics

The primary lifting surface for the NASP, shown in Figure 2, taken from [1], will be the body itself, because a thin wing is an inefficient structure compared to a lifting body. The static stability of this configuration will be quite variable. In a study of several hypersonic research aircraft similar to the NASP, the effect of Mach number on stability margins was assessed. The results showed that the static stability margins generally decrease as Mach number increases<sup>3</sup>. Figure 3 below shows the

variation of longitudinal stability with Mach number. Although not shown, the variation in directional stability and dihedral effect with Mach number is also significant.

From the above, one can see that in order to obtain reasonable static margins at hypersonic speeds, high static margins will be required at lower speeds. The associated large control deflections and decreased maneuverability at lower speeds must be balanced against using an unstable configuration at hypersonic speeds.

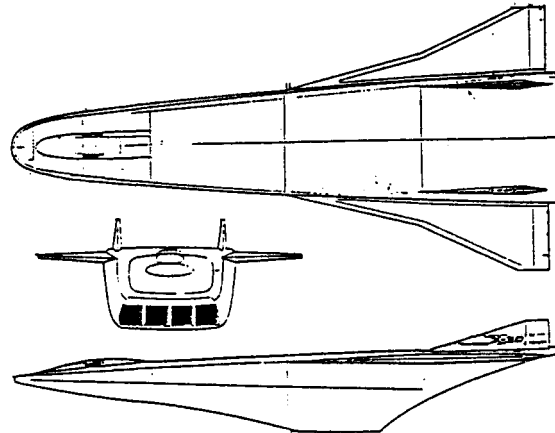


Figure 2, X-30 Configuration [1]

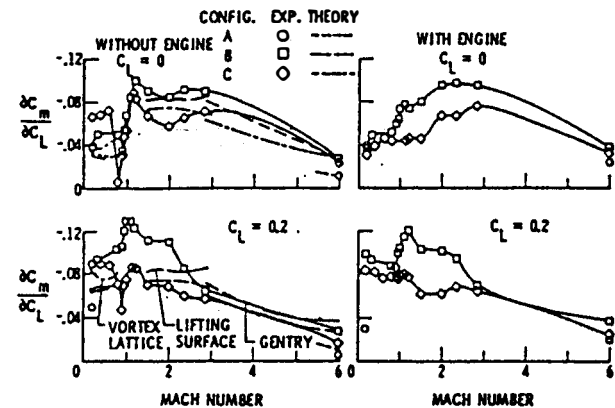


Figure 3, Aerodynamic Stability Variations

The NASP will re-enter the atmosphere at high angles of attack similar to the shuttle. This creates strong shock waves to dissipate heat and increase drag. Unlike the shuttle, however, the NASP has a high slenderness ratio and thus will more than likely have highly nonlinear stability characteristics. Furthermore, the center of pressure will move radically aft as the angle of attack increases and the rudder will be shielded and ineffective<sup>2</sup>. This combination will make the NASP extremely difficult to trim in the pitch plane, while the directional stability is lost in the yaw and roll planes. In order to keep control forces in the pitch plane within bounds, the center of mass may have to be located between the extreme positions of the center of pressure. As noted previously, then, this will result in positive stability during descent and negative stability during ascent<sup>2</sup>. Finally, in order to

improve directional stability during descent non-conventional roll and yaw control surfaces may be required on the windward side.

Due to the complexity of hypersonic flow fields, modern Computational Fluid Dynamic (CFD) techniques are ultimately required to predict the aerodynamic forces. However, Newtonian impact theory is still the basis for most "rapid prediction" techniques. It helps develop insight, and may be used in conjunction with experimental and numerical results to improve accuracy. While impact theory does not take into account real gas, viscous, or boundary-layer interaction effects, estimates based on this approach can be further refined with CFD techniques and experimental results. Such semiempirical techniques based on impact theory have shown surprisingly good agreement with experimental data over a wide range of conditions<sup>5,12</sup>. The numerical results presented in the later sections of this paper are based on Newtonian aerodynamic predictions.<sup>17</sup>

### SCRAMjet Propulsion

A SCRAMjet's operating principles are the same as those for a ramjet engine except combustion takes place at supersonic speeds. An obvious disadvantage of supersonic combustion is that the fuel and air have less time to mix and react before exiting the combustor. In order to compensate for this, the length and therefore the weight of the combustor must be increased. Nonetheless, supersonic combustion is necessary at hypersonic speeds because dissociation losses that result from slowing the high-velocity airstream to subsonic speeds greatly reduce performance. The end result is that the SCRAMjet engine has the highest performance (as measured by specific impulse) in the hypersonic speed regime<sup>6</sup>.

In order to obtain the required thrust at higher Mach numbers, the SCRAMjet engine inlet area must be large enough to capture nearly all the airflow captured by the vehicle's undersurface bow shock. This suggests an annular inlet area contiguous with the vehicle undersurface<sup>7</sup>. By splitting the annular area into smaller rectangular modules, the primary engine becomes a system of identical units of a size and shape which would be appropriate for testing in ground facilities<sup>6</sup>. The three primary engine components, (forebody inlet, internal module, and exhaust nozzle) are shown in the figure below and will be described in more detail in the subsequent sections.

Treating the engine in this way yields two important advantages: the vehicle's forebody performs a significant part of the inlet compression process, and its afterbody constitutes a large part of the nozzle. The engine design thus encompasses the entire undersurface of the vehicle. This approach has other drag-reducing advantages. The engine's external surfaces can easily be shaped to minimize

installation losses by making them parallel to the local flow<sup>7</sup>. The large exit area provided by the afterbody allows it to generate 50% or more of the total thrust without incurring an excessive drag penalty<sup>8</sup>.

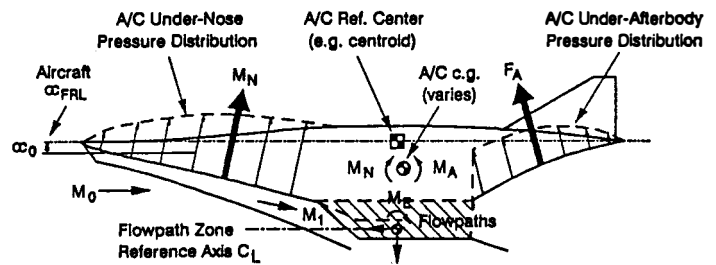


Figure 4, Effect of SCRAMjet Concept on External Forces

A disadvantage of this concept is that the propulsive system will interact significantly with the aerodynamic control of the vehicle. With reference to Figure 4, from [14], the increased pressure acting on the forebody generates lift and creates a nose-up pitching moment. A counter-acting nose down pitching moment is generated by the external nozzle. Non-uniform output of the engine modules can also generate non-zero roll and yaw moments. Such interactions of the propulsion system with the aerodynamic controls is a major issue<sup>4</sup>, and this will be addressed in more detail later in this paper.

It is also interesting to note that the net thrust of the SCRAMjet engine is a small difference between two extremely large gross-thrust and ram-drag forces. In fact, the gross thrust can be an order of magnitude larger than the net thrust. At Mach 12, for example, the vehicle is predicted to have a ram drag of 1,950,000 lbs and a gross thrust of 2,100,000 lbs leaving a net thrust of only 150,000 lbs<sup>2</sup>. One can see that this does not leave much margin for airframe drag or trim drag forces. Also, the effects of an engine shutdown are significant.

### Inlet System

The primary function of the inlet system is to capture the approach mass flow and process it for combustion in the internal engine modules. The approach mass flow to be captured is a stream tube of air which extends vertically from the nose of the vehicle to a horizontal line parallel to the cowl leading edge of the internal engine<sup>9</sup>. The forebody increases the static pressure of the flow by compressing it in the vertical direction. The spanwise characteristics of the flow at the internal engine inlet must be quite uniform to minimize distortion and enhance inlet efficiency<sup>4</sup>. How effectively the approach mass flow is captured and compressed by the internal engine is determined by the characteristics of the bow shock wave.

The free stream properties and vehicle angle of attack determine the characteristics of the bow shock wave. The bow shock pressure ratio determines the compression of the approach mass flow and the bow shock angle determines the spillage mass flow. Spillage mass flow is that which, due to the bow shock wave, is turned sufficiently so as not to be captured by the engine at the cowl leading edge<sup>9</sup>.

#### *Internal Engine Module*

The internal engine design is based on a NASA-Langley Research Center SCRAMjet concept. The complete engine will consist of several of these modules located symmetrically with respect to the vehicle plane of symmetry<sup>2</sup>.

The approach-mass-flow-compression process is continued in the internal engine module. The module sidewalls are wedges to compress the flow horizontally and compression is completed by three wedge-shaped fuel injection struts located at the minimum-area section of the module. These struts also provide multiple planes for fuel injection. This allows the fuel to be mixed over a wide range of flight conditions and therefore shortens the required length of the combustor. After the fuel is injected it must mix with the captured approach mass flow and auto-ignite in the fraction of a millisecond residence times of a supersonic combustor<sup>6</sup>.

It is desirable to burn at as low a Mach number as possible to increase the heat added to the mass flow. Engine performance generally improves when more heat is added, so performance depends primarily on the temperature limit imposed by the material constraints of the combustor wall<sup>10</sup>. The combustor wall will be actively cooled to increase performance but caution must be exercised because too much cooling can have an adverse effect on auto-ignition temperature. For example, tests performed at NASA Langley showed a 200° R difference in combustor wall temperature caused up to a 700° R difference in auto-ignition temperature<sup>6</sup>. Increased auto-ignition temperature delays reaction thereby decreasing combustion efficiency.

#### *External Nozzle*

The purpose of the external nozzle is to trade the pressure developed in combustion for flow momentum, or to transfer flow potential energy to kinetic energy. The flow kinetic energy will be at a maximum when the exhaust static pressure reaches free stream pressure. The lower edge of the expansion surface is formed by the shear layer between the exhaust flow and the free stream. This lower shear layer expansion surface provides an increased expansion area for the transfer of potential energy to kinetic energy and eliminates the additional weight and drag of a lower expansion surface<sup>9</sup>. The nozzle efficiency is a function of both expansion angle<sup>3</sup> and nozzle length<sup>7</sup>. An expansion angle of 20° is typical. The nozzle should be long

enough so that the pressure at the aft end of the nozzle is near the free stream pressure. However, because of weight considerations the nozzle length should be minimized. The optimum nozzle length is around seven module throat heights<sup>8</sup>.

Because only the top portion of the external nozzle is a solid (unchanging) surface, the nozzle plume has a highly three-dimensional structure. This structure changes with engine operating conditions, altitude, flight speed, angle of attack, etc. Interactions between adjacent module wakes, spillage from the inlet, and non-uniform inlet conditions also contribute to the three-dimensional structure<sup>7</sup>.

In addition to increasing thrust and reducing overall weight, the external nozzle configuration also generates propulsive lift, as shown in Fig. 4. The additional lift increases the lift-to-drag ratio and, consequently, can improve cruise performance. Since the lift-to-drag ratio of these vehicles is inherently low, due to the large fuselage volume needed to contain the low density LH<sub>2</sub> fuel, propulsive lift can make a large contribution to vehicle performance<sup>2</sup>. The external nozzle also creates a nose-down pitching moment. This counteracts the nose-up pitching moment created by the vehicle's forebody, and the nozzle moment varies with flight condition (altitude and velocity). Previous studies of this problem, dating back to 1970, have shown that the vehicle's aerodynamic control surfaces can handle these variations, albeit with an additional aerodynamic penalty due to increased trim drag<sup>2</sup>.

#### *Engine Control Mechanisms*

The block diagram in Figure 5 conceptually shows how the fuel flow rate, angle of attack, and dynamic pressure affect the net forward thrust, vehicle lift, and pitching moment. Since maneuvering flight may affect each module differently, as discussed above, propulsive yaw and roll moments can also result.

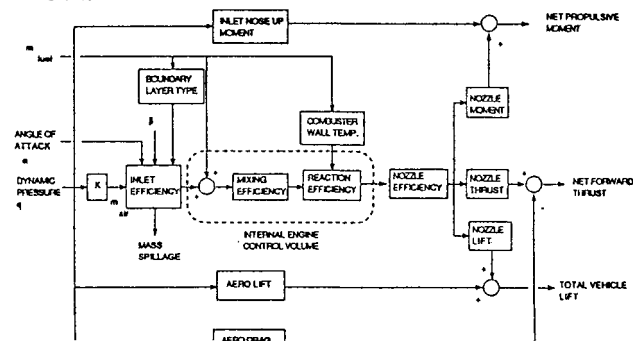


Figure 5, Conceptual Airframe - Engine System

In addition to fuel flow rate, the engine control effectors will probably include some form of active inlet device, or some other mechanism for controlling the effective inlet/diffuser area ratio A<sub>D</sub>. In addition, active control of the exit area of the internal nozzle may be desired if not required.

Considering now our generic study configuration as an example, initial estimates<sup>17,18</sup> of the thrust response of just the engine module (i.e., no external nozzle thrust included) are presented in Figs. 6 and 7. In these results, the engine is modeled quasi-statically, with no internal dynamics. The dynamic response characteristics indicated are due exclusively to the engine-airframe coupling, discussed further below. These two engine control inputs are clearly effective in affecting thrust, but can also excite the elastic structural mode as discussed further below.

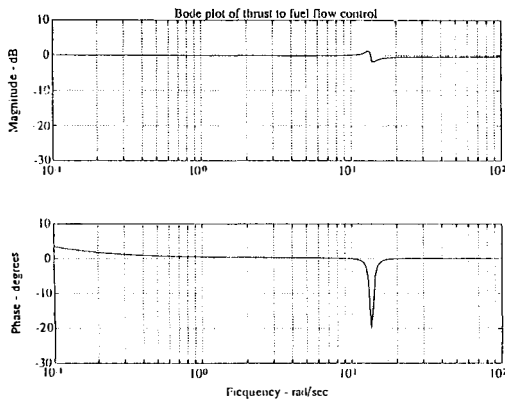


Figure 6 Engine Thrust-to-Fuel-Air-Ratio Frequency Response ( $T \sim \text{lb}/500$ ;  $f \sim 1/0.1$ )

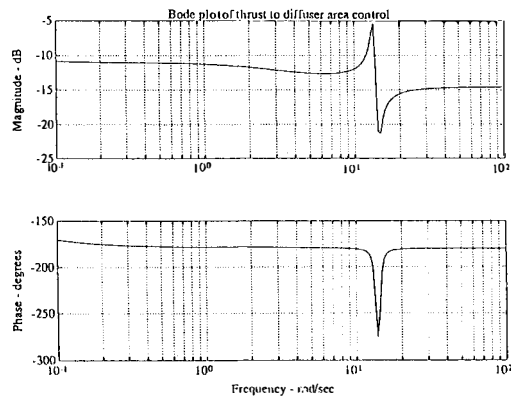


Figure 7, Engine Thrust-to-Diffuser-Area-Ratio Frequency Response ( $T \sim \text{lb}/500$ ;  $A_D \sim 1/0.05$ )

### Propulsion-Aerodynamic Coupling

An earlier study<sup>9</sup> considered the thrust performance sensitivity of a generic SCRAMjet powered vehicle to variations in flight dynamic pressure and angle of attack. In general, performance parameters showed sensitivity to changes in bow shock pressure ratio, mass flow spillage, forebody total pressure losses, inlet inviscid total pressure losses, combustion kinetics, and exhaust flow/freestream shear layer position. All of these vary with dynamic pressure and angle of attack.

This study also showed that at low Mach number acceptable performance can only be achieved by extreme flight conditions, such as an angle of attack of 9° and a dynamic pressure greater than 2000 psf. However, as Mach number increases performance is

less sensitive to variations in dynamic pressure and the angle of attack required for acceptable performance decreased. Additionally, as approach mass flow spillage reaches a minimum, thrust specific impulse reaches a maximum; at low angles of attack, a decrease in performance with decreasing angle of attack results from poor combustion; as combustion efficiency decreases, the nozzle plume expansion area decreases; and as angle of attack reaches large values, spillage may increase to have a detrimental impact on performance.

In addition to these "static" effects on engine performance, an even more challenging issue is the dynamic coupling between the vehicle attitude and propulsion system. Our analysis<sup>16-18</sup> indicates a strong dynamic relationship, over a wide frequency range. Specifically, Figure 8 reveals the estimated dynamic thrust response to aerodynamic pitch control surface deflection for our study configuration. Also, the response of the pressure at the engine inlet to this same pitch control surface deflection is indicated in Figure 9. This result would

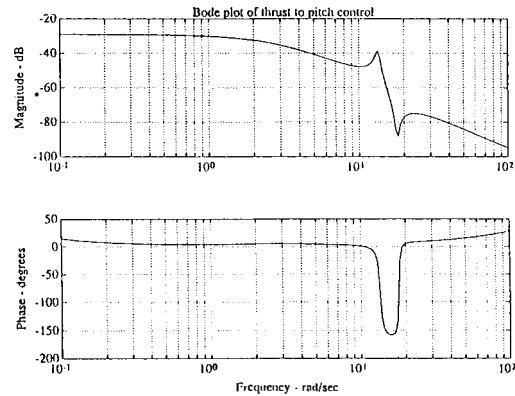


Figure 8 Engine Thrust-to-Pitch-Control Frequency Response ( $T \sim \text{lb}/500$ ;  $\delta \sim \text{deg}/5\text{deg}$ )

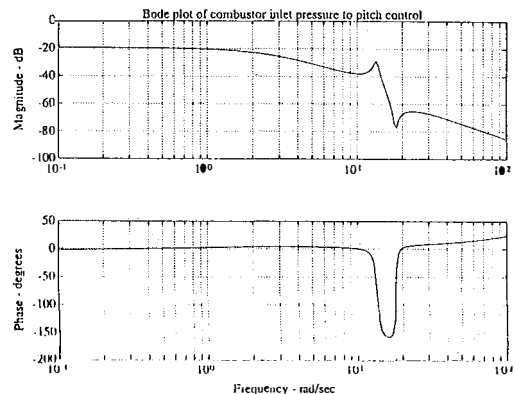


Figure 9 Combustor Inlet-Pressure-to Pitch-Control Frequency Response ( $p \sim \text{psf}/2.7 \times 10^5$ ;  $\delta \sim \text{deg}/5\text{deg}$ )

indicate the clear necessity for some form of high-bandwidth, active control of the inlet/diffuser. The

airframe-to engine response coupling exhibited here is dramatic.

The engine-to-airframe coupling for these vehicles is also dramatic. Shown, for example, in Figures 10 and 11 are the airframe pitch-rate responses to the two engine control inputs, fuel flow rate and diffuser area ratio. Consequently, strong two-directional coupling between airframe and engine is present, and the implications of such coupling on integrated flight and propulsion control is addressed, for example, in [15].

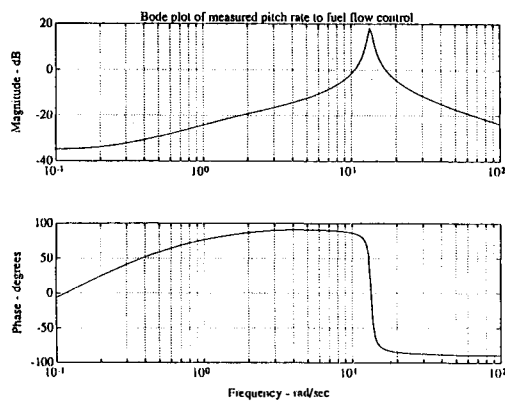


Figure 10, Pitch Rate Response to Fuel-Air Ratio  
( $q \sim r/s/2r/s$ ;  $f \sim 1/0.1$ )

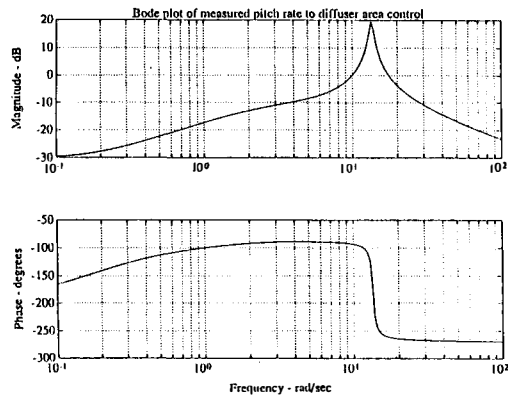


Figure 11, Pitch Rate Response to Diffuser Area Ratio  
( $q \sim r/s/2r/s$ ;  $AD \sim 1/0.05$ )

### Structural Dynamic and Aeroelastic Effects

Elastic mode and propulsion system coupling on these vehicles has already been clearly evident in the previous results. Bending of the forebody influences the inlet conditions, the effects of which propagate through the engine and on to the external nozzle. Additionally, bending of the afterbody changes the effective angle of the exhaust nozzle, and affects the nozzle efficiency and the direction of the thrust vector.

Furthermore, due to the requirement for very low structural weight mass fraction, the structural

vibration frequencies will be close to those of the rigid-body (e.g., short-period) natural frequency. For the generic study vehicle considered, this separation is about one decade in frequency at the Mach 8, 85,000 ft. flight condition. (This is consistent with the structural dynamic characteristics described in [13].) This in turn gives rise to significant elastic-rigid body mode interactions.

Shown in Figure 12 and 13 are the sensed angle-of attack and pitch-rate responses of the vehicle to inputs from the pitch-control aerodynamic surface. Evidence of the effect of the aeroelastic mode near 13 rad/sec is clear, especially in the pitch rate. To carefully control aerodynamic heating and drag, for mission performance, precise control of the angle of attack will be required. The limitations on the achievable performance in this regard is currently under study.

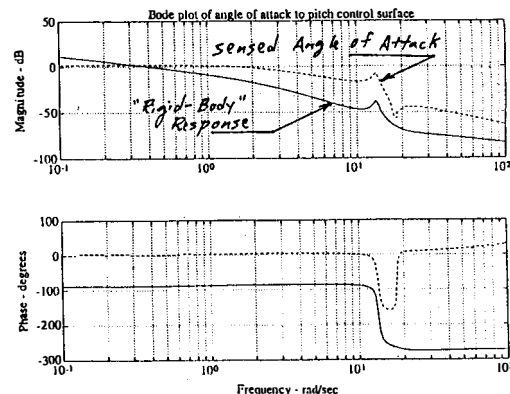


Figure 12,  
Sensed Angle-of-Attack-to-Pitch-Control-Surface Frequency Response( $\alpha \sim \text{rad}/5/57.3\text{rad}$ ;  $AD \sim 1/0.05$ )

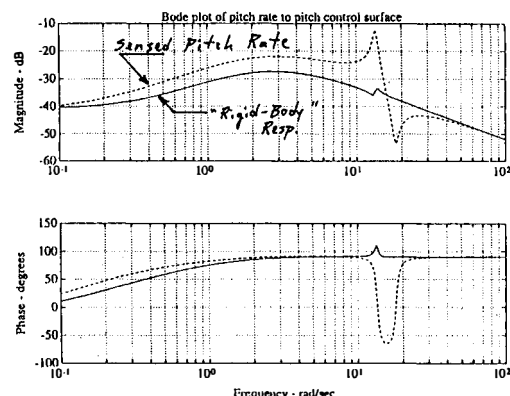


Figure 13 Pitch-Rate-to-Pitch-Control-Surface Frequency Responses( $q \sim r/s/2r/s$ ;  $\delta \sim \text{deg}/5\text{deg}$ )

Thus, accurate determination of elastic mode shapes and natural frequencies will be a critical requirement for control system design. But structural analysis will be exacerbated by the use of exotic composite materials, severe nonuniform aerodynamic heating, and the shell type structure of the vehicle. The severe nonuniform aerodynamic heating caused by hypersonic flight in the earth's atmosphere will result in thermally-induced stresses and elastic moduli reduction. This produces reduced structural

stiffness which will cause additional mode shape and natural frequency variability and uncertainty.<sup>13</sup> An experiment on a simple stainless steel cantilevered lifting surface demonstrated the effect of a nonuniform temperature distribution on mode shapes. A 20% variation in mode shape was seen with a modest cordwise temperature variation of a few hundred degrees. With the 2000°F and higher temperatures and exotic composite materials on these hypersonic vehicles, much more than 20% variation in mode shapes can be expected<sup>11</sup>. With such changes in structural dynamic characteristics, robust control laws with adaptive gain scheduling appears essential.

### **Further Dynamics and Control Issues**

In summary, considering all the interactions discussed above, one might depict the system as shown in Figure 14. To appreciate the issues in the synthesis of the flight and engine control systems, consider the fact that control problems are difficult if

1. Significant cross-coupling exists between the inputs and outputs being controlled
2. The open-loop system is highly unstable, has right-half-plane transmission zeros in the frequency range around crossover, or both
3. The system model possess significant modeling uncertainty in the frequency range around crossover

As we shall see, all these situations are the case with hypersonic vehicles like NASP.

Next, consider the fact that with a pole near 2.5 r/s, gain crossover in the pitch loop will be at least that high in frequency. By observing the pitch transfer function in Figure 13, one can see that the aeroelastic-mode dipole near 13 r/s must be dealt with carefully in light of this high gain crossover frequency.

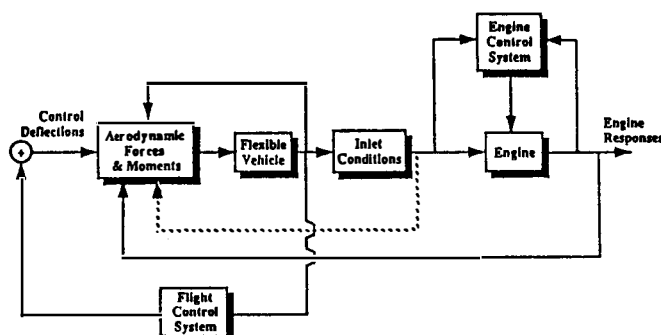


**Figure 14, Hypersonic Vehicular Dynamic System**

First consider the system modes shown in Figure 15. The vehicle modes includes a conventional lightly damped phugoid mode, a lightly damped aeroelastic mode, and a coupled pitch and elastic mode

characterized by two real eigenvalues with one quite unstable (~2.5 r/s).

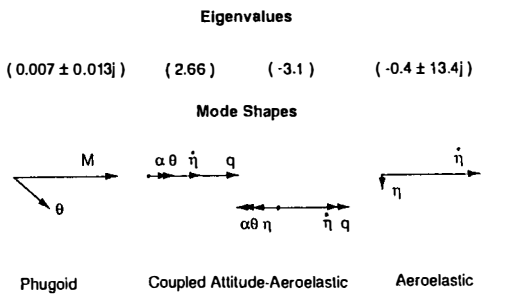


**Figure 15, System Modes**

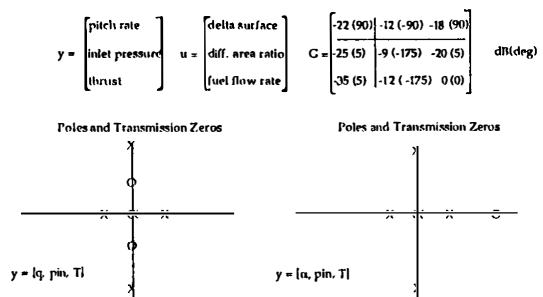


**Figure 16 System Transfer Matrix and Transmission Zeros**

Now consider the data shown in Figure 16. Let the three control inputs be the aerodynamic pitch control surface  $\delta$ , the diffuser area ratio  $A_D$ , and fuel flow  $f$ . Now consider the three critical controlled responses to be pitch attitude, engine inlet pressure, and engine thrust. This gives rise to a three-by-three matrix of transfer functions. If these transfer functions are all evaluated at 3 r/s, the approximate frequency of crossover in the pitch loop, the result is the matrix given in this figure. (The two entries in each element of this matrix are gain in dB and phase in degrees.) It is clear from observing this matrix, for example, that the engine control inputs  $A_D$  and  $f$  are very effective in producing pitch responses. In fact, these two inputs are more effective in this regard than the aerodynamic pitch control surface. This is a clear indication of significant cross coupling.

Regarding the systems transmission zeros, they are depicted for this input-output set in Figure 16 as well. Since they are all on the imaginary axis, high gain loops can lead to close-loop pole locations near the imaginary axis, which is probably unacceptable. If the three controlled responses include vehicle angle of attack rather than pitch attitude, the resulting transmission zeros are in even worse locations. As also shown in Figure 16, this input-output set leads to transmission zeros in the right-half-plane to the right of the unstable pitch pole. Consequently, this system will be very difficult to stabilize, and stability robustness can be most difficult to obtain.

## Conclusions

The dynamics of hypersonic vehicles, with geometry and propulsion system similar to the X-30, exhibit significant interactions between the elastic airframe and engine. The pitch control surface inputs will give rise to large disturbances in the engine inlet conditions as well as thrust response. Furthermore, the engine control inputs considered, fuel flow rate and effective diffuser area ratio, give rise to significant attitude disturbances. This coupling will necessitate a highly integrated airframe-engine control system. The statically unstable vehicle, furthermore, will dictate an attitude-control bandwidth sufficient to cause significant aeroservoelasticity interactions. And the effects of non-uniform structural heating will require a robust, adaptive gain-scheduling attitude control law. With all these interactions and uncertainties, adequate stability margins will be difficult to obtain. Consequently, the achievable performance and stability robustness of the highly-integrated and complex guidance and control systems for these vehicles may be a fundamental factor determining their ultimate viability.

## Acknowledgments

This research is being conducted under grant NAG-1-1341, supported by NASA's Langley Research Center Ms. Irene Gregory is the technical monitor.

## References

1. Aviation Week and Space Technology, Oct. 29, 1990, p. 46.
2. Johnson, P.J., Whitehead, A. H., Jr., and Chapman, G. T., "Fitting Aerodynamics & Propulsion into the Puzzle", Aerospace America, Sept. 1987, pp. 32-34.
3. Penland, J. A., Dillon, J. L., and Pittman, J. L., "An Aerodynamic Analysis of Several Hypersonic Research Airplane Concepts from  $M = 0.2$  to 6.0", Journal of Aircraft, Vol. 15, No. 11, November 1978, pp 716-723.
4. Whitehead, A. H. Jr., "NASP Aerodynamics", AIAA Paper 89-5013, 1989.
5. East, R. A., and Hutt, G. R., "Comparison of Predictions and Experimental Data for Hypersonic Pitching Motion Stability", Journal of Spacecraft and Rockets, Vol. 25, No. 3, May-June 1988, pp 225-233.
6. Beach, H. L., Jr., "Hypersonic Propulsion", NASA Conference Publication 2092, Proceedings of a Conference on Aeropropulsion, Lewis Research Center, Cleveland, Ohio, May 15-16, 1979, pp. 387-407.
7. Jones, R. A., and Huber, P. W., "Airframe Integrated Propulsion System for Hypersonic Cruise Vehicles", 11th Congress of the International Council of the Aeronautical Sciences, Lisbon, Portugal, Sept. 10-16, 1978.
8. Weidner, J. P., Small W. J., and Penland, J. A., "Scramjet Integration on Hypersonic Airplane Concepts", Journal of Aircraft, Vol. 14, No. 5, May 1977, pp 460-466.
9. Walton, J. T., "Performance Sensitivity of Hypersonic Vehicles to Change Angle of Attack and Dynamic Pressure", AIAA Paper 89-2463, 1989.
10. Schindel, L., "Design of High Performance Ramjet or Scramjet Powered Vehicles", AIAA Paper 89-0379, 1989.
11. Swaim, R. L., "Aeroelastic Interactions with Flight Control of Transatmospheric Vehicles", Proceedings of the National Aerospace & Electronics Conference, May 23-27, 1988, pp 574-581.
12. Maughmer, et al, "Prediction of Forces and Moments for Flight Vehicle Control Effectors," Final Report for NASA Grant 1-849, for the NASA Langley Research Center, May, 1990.
13. Gilbert, M.G., et al, "The Application of Active Controls Technology to a Generic Hypersonic Aircraft Configuration," NASA TM 1097, May, 1990.
14. McRuer, D., "Design and Modeling Issues for Integrated Airframe/Propulsion Control of Hypersonic Flight Vehicles," Proceedings of the American Control Conference, Boston, Mass., June, 1991, 729-735.
15. Schmidt, D.K., Schierman, J., and Garg, S., "Analysis of Airframe/Engine Interactions - An Integrated Control Perspective," Proceedings of the Joint Propulsion Conf., Paper no. 90-1918, (Also to appear in the *Journal of Guidance, Control, and Dynamics*)
16. Schmidt, D. K., Mamich, H., and Chavez, F., "Dynamics and Control of Hypersonic Vehicles - The Integration Challenge for the 1990's," AIAA Paper 91-5057, Dec., 1991.
17. Schmidt, D. K. and Chavez, F., "An Integrated Analytical Aeropropulsive/Aeroelastic Model for the Dynamic Analysis of Hypersonic Vehicles," AIAA Paper 92-4567, Atm. Flight Mech. Conf., August, 1992.
18. Schmidt, D. K., "Dynamics and Control of Hypersonic Aeroelastic/Aeropropulsive Vehicles," AIAA Paper 92-4326, GN&C Conf., August, 1992.

# DEVELOPMENT OF A ROBUST FLIGHT CONTROL LAW FOR A VSTOL AIRCRAFT

R.A. Hyde and K. Glover

*Department of Engineering, Cambridge University, Trumpington Street, Cambridge CB2 1PZ, UK*

**Abstract.** A flight control law is being developed for a VSTOL aircraft. Extensive design studies have already been carried out on a Generic VSTOL Aircraft Model (GVAM) developed by the Defence Research Agency (D.R.A.), and subsequently tested on the D.R.A. motion simulator at Bedford. This paper describes further development of these designs with a view to future implementation on the D.R.A. research Harrier. The transition between powered lift and wingborne flight considerably complicates both closed-loop control design and flight mode-design, and as such provides a very interesting design example. For linear design, the longitudinal motion of the aircraft is treated as a multivariable system, and linear controllers are designed for different operating points using the loop-shaping plus  $\mathcal{H}_\infty$  robust stabilisation procedure of Glover and McFarlane. The controllers are then scheduled using the unique observer structure associated with this design formulation. Results are presented of non-linear simulation of the controller on the GVAM model.

**Keywords :** flight control, H-infinity, robust control, loop-shaping, scheduling, VSTOL.

## 1 INTRODUCTION

Automatic control offers great potential for reducing pilot workload, increasing operational flexibility and improving aircraft safety. Benefits for Vertical Short Take-Off and Landing (VSTOL) aircraft are potentially very large due to the wide operating envelope of the aircraft resulting from the powered lift capability. The Defence Research Agency (DRA) (formally the Royal Aerospace Establishment) at Bedford has a Vectored thrust Aircraft Advanced flight Control (VAAC) programme [1, Nicholas and Stephens], [2, Smith] to evaluate the benefits of modern control techniques. The DRA have developed detailed non-linear model of a Generic VSTOL Aircraft Model (GVAM) [3, Muir and Kellet] which can be used for design studies. The model is based both on direct physical modelling and wind tunnel aerodynamic data, and as such the model is assumed to exhibit many of the non-linear effects which occur on the real aircraft. Controllers developed for the GVAM can then be tested in piloted simulation using the DRA motion simulator at Bedford. When fully tested in simulation, control laws can then be implemented and flown on the DRA research Harrier for in-flight testing.

The design presented in this paper is a development of previous design studies carried out on the GVAM [4, Hyde], [5, Hyde and Glover], [6, Hyde and Glover]. In these previous studies extensive piloted simulations were carried out, and current efforts are now directed at producing a design suitable for implementation on the aircraft itself. The linear part of the design approach centres around treating the aircraft as a multivariable system and using loop-shaping to specify performance. Robustness to plant uncertainty is then achieved using the  $\mathcal{H}_\infty$  ("H-infinity") robust stabilisation approach of [7, Glover and McFarlane], [8, McFarlane and Glover] which makes use of normalised coprime factor plant descriptions. The relative advantages of using this approach for the GVAM design study and a discussion of the relation of this study to other GVAM studies can be found in [4, Hyde].

Control law design for a VSTOL aircraft presents additional problems to those encountered when designing for a conventional aircraft. The large change in dynamics between hover and fully wingborne flight means that it is impossible to meet performance requirements across the whole flight envelope with a single linear controller, and so some form of gain scheduling is required. The VSTOL capability gives an extra degree of freedom in that there are three fast actuation systems for longitudinal control of the aircraft, namely thrust magnitude, thrust direction and tailplane/reaction-jet setting. Three independent quantities can therefore be controlled, and the system is inherently multivariable. Figure 1 illustrates the actuators and some of the key quantities of interest for control purposes. The choice of which variables to control is discussed later in the paper. The system is highly coupled - for example, a change in nozzle angle disturbs pitch attitude, vertical speed and horizontal speed. For the manually flown aircraft this results in a very high workload on the pilot - for example, the approach

to an aircraft carrier requires the pilot to make successive adjustments to the nozzle and throttle levers with the left hand whilst simultaneously holding the pitch attitude of the aircraft at 8 degrees by making continuous corrective demands on the stick with the right hand. A multivariable controller has great potential to give good decoupling of the pilot demands, and thus reduce pilot workload.

The paper is organised as follows. In §2 the idea of flight control modes is introduced, and some of the issues affecting the specification of these modes are discussed. In terms of the pilot's reaction to the overall control law, careful design of control modes is crucial. In §3 a summary of the modes chosen for the design are given with reference to the ideas in §2. Then in §4 the structure of the overall controller is presented which has a high-integrity inner-loop multivariable controller to obtain good stability and decoupling. On top of this are single-input single-output outer loops to achieve the inceptor functionality specified in §3. The multivariable loop-shaping and robust stabilisation approach is then summarised in §5 and applied to a linear design example in §6. Non-linear time responses of the scheduled inner-loop control law applied to the GVAM are then given in §7. Finally conclusions and a discussion of current work is given in §8.

## 2 FLIGHT CONTROL MODES

In its simplest form, Fly-by-Wire (FBW) is just used to remove heavy mechanical and hydraulic control runs and thus reduce aircraft weight. However, the full advantages of FBW are only realised when the direct links from the conventional cockpit controls to the aerodynamic surfaces are broken and routed via a flight computer. With this system, the flight computer reads in the pilot's demands and then makes appropriate changes to the control surfaces. This gives rise to a whole host of possibilities, including the use of feedback to change the flying qualities of the aircraft. An example might be to change the short period and phugoid modes of the controlled aircraft so that they give better flying qualities or even emulate those of another aircraft. With such systems the pilot is still using the same cockpit controls which still have the same functionality as those of the uncontrolled aircraft. It is, however, possible to take it one step further, and to change the functionality of the cockpit levers or even give the pilot a completely new set of control levers. Such an example would be to give the pilot a flight path angle demand on a side stick instead of the conventional aileron demand from centre stick. The advantages of giving the pilot unconventional demands are numerous. For example, commanding flight path angle leads to easy landing approaches which are typically carried out at constant flight path angle; with a conventional aircraft the pilot is putting in continual stick corrections in order to hold the desired flight path.

A potential problem arising from changing the inceptor functionality is that a particular set of cockpit demands tailored for one flight

regime may be totally inadequate for another. An example might be that flight path angle is appropriate for the landing approach, whereas commanding pitch rate is preferred during the landing flare as this gives a conventional aircraft response. This necessitates different "control modes" across the flight envelope, and this has two important consequences. Firstly, the question of how and when to initiate modes must be tackled - and in particular how to indicate clearly to the pilot which modes he is in. Secondly, the demands for the mode which is about to come on line must be correctly initialised either directly by the pilot, or by the flight computer.

Another potential danger with changed inceptor functionality is so-called "reversion to type", which essentially means that the pilot reverts to using the cockpit inceptors as if he were flying the conventionally controlled aircraft. This typically happens when there is a sudden increase in pilot workload, and can potentially be dangerous. An example on a Harrier would be giving the pilot a horizontal acceleration demand on the left-hand inceptor and vertical acceleration demand on the right-hand inceptor across the flight envelope; if when performing a vertical landing the pilot suddenly had to abort, he might be tempted to push fully forward on the left-hand inceptor corresponding to a thrust demand on a conventionally flown Harrier instead of pulling back in the right-hand inceptor.

The following broad philosophy was used for the development of the flight control law. It is in no way claimed that this is a "best" philosophy, but it is used to justify the decisions made when specifying control modes for the design.

- **P1** Keep the pilot in touch with the aircraft - don't remove him unnecessarily far from the machine e.g. if the aircraft has a force motivator, give him an acceleration demand rather than a position or velocity demand. This way the aircraft "state" changes only when the pilot makes a change in the controls. An aircraft height demand system, for example, would not operate like this; the pilot would set a height, and then a while later when the height is achieved the pilot would perceive sudden changes in attitude and thrust.
- **P2** Avoid reducing the operating envelope of the aircraft; for example, if the pilot knows he can satisfactorily fly the aircraft manually up to 20 degrees angle of incidence at a given speed, he is not going to be impressed with a control system which only lets him fly up to 15 degrees incidence. If possible, extend the operating envelope of the aircraft if this gives rise to any mission benefits e.g. greater manoeuvrability.
- **P3** Don't restrict the pilot's authority to handle redundancy, and ensure that it is handled in a natural way. For example, with a conventionally flown Harrier it is possible to achieve a given airspeed and descent rate with a variety of thrust, nozzle angle, tailplane and flap settings. The actual combination selected by the pilot might depend on factors such as how much surplus fuel he has - if it's low, then he'll aim to get as much aerodynamic lift as possible necessitating a high alpha. If fuel isn't a problem he may wish to have a low alpha giving him a lower pitch attitude and hence better view out of the cockpit. A control law which restricts this freedom is likely to attract criticism.
- **P4** In as far as is possible, attempt to get the directional functionality of the inceptors as close their functionality on a manually flown aircraft. This should minimise the risks if the pilot reverts to type demanding (see discussion above).
- **P5** Keep the number of command modes needed to cover the whole operating envelope to a minimum, and ensure that it is clear which mode the flight controller is in at any time. The higher the number of modes, the higher the chances become of incorrect mode selection and initialisation. A high number of modes also increases the overall complexity of the flight controller, and hence the amount of pilot training required is increased.
- **P6** Capitalise as much as possible on the benefits of multivariable feedback i.e. decoupled demands and disturbance rejection. Ensure that if the pilot lets go of all the controls that the aircraft is stable in the sense that airspeed, flight path and pitch attitude tend to constant mean values.

As will become clear in the following discussion of the inceptor functionality specification, the above desirable characteristics often have to be traded off against each other. This trade-off is particularly difficult for VSTOL aircraft since the vectored thrust gives rise to many more control possibilities than for conventional aircraft (see for example [9, Gainza]). By its nature the vectored thrust makes the manually flown aircraft very difficult to fly to its full potential, and hence the benefits of multivariable control can be high.

### 3 INCEPTOR SPECIFICATION

In this section a design specification is drawn up which covers the whole flight envelope. The present control study is restricted to longitudinal control of the aircraft as at present lateral sensors and actuation systems are not available to the flight controller on the VAAC research Harrier. However, longitudinal control of the Harrier presents both the greater control challenge and also the greatest potential for reduction in pilot workload. An attempt is made to justify the choices made in the specification alongside its exposition. The specification has been arrived at using a variety of sources including the above considerations. Discussions D.R.A. pilots and flight control engineers were highly influential, as was the design study and flight simulations carried out in [4, Hyde].

#### Inceptor 1 (throttle lever of the conventional Harrier cockpit)

Inceptor 1 commands a combination of forward acceleration and forward speed. If  $\ddot{x}$  represents forward acceleration,  $\dot{x}$  forward velocity, and  $d$  the inceptor demand, then

$$\ddot{x} + \alpha\dot{x} = d$$

At high frequencies (short term time response) it looks like an acceleration command, and at low frequencies (long term time response) it looks like a speed demand. In other words,  $\ddot{x}$  initially follows a change in  $d$ , and then  $\ddot{x}$  tends to zero as  $\alpha\dot{x} \rightarrow d$ . This behaves in a similar fashion to the throttle control when in conventional wingborne flight on the manually flown aircraft; a step change causes an initial acceleration which blends into a constant speed as the aerodynamic drag increases to counter the increased engine thrust. The term  $\alpha\dot{x}$  in the demand equation above is thus equivalent to the drag term in the equations of motion for the aircraft. This is consistent with point P1 of the design philosophy of §2 in that it gives a conventional response and reflects the aircraft's natural performance capability.

The possibility of commanding pure acceleration was also considered on the grounds that gradual accelerations and decelerations could be effected without requiring continuous adjustments to the inceptor to maintain the trajectory. This was rejected on the grounds that the resulting aircraft state with hands off the inceptor doesn't tend to a stable equilibrium; even if a speed hold were implemented for centred inceptor (zero acceleration demand), there is still the danger that the pilot misses the detent and the aircraft speed drops off unbeknown to the pilot whose concentration is directed elsewhere.

In the interests of minimising the number of control modes (see P5) this functionality specification is used for the entire flight envelope. Note that the speed-hold for constant control demand makes vertical landing on a carrier easy in that the demand can be set so that the relative speed is zero.

There is one serious compromise which has been made with the above choice; in the hover a change in the left-hand inceptor demand gives an unconventional response in that the manually flown aircraft would respond by accelerating vertically. This goes against P4, but the advantage of having a single control mode across the whole flight envelope has been judged to be the higher priority.

#### Inceptor 2 (Stick in conventional cockpit)

Inceptor 2 is operated with the right hand, and for the purposes of piloted simulation the conventional cockpit stick is used. It has been chosen to command vertical acceleration during hover and transition to wingborne flight; this satisfies P1 in that the nozzle/throttle combination gives rise to an acceleration over short time periods. This is blended to a more conventional pitch rate demand in conventional flight. This mode change is unavoidable given the very different operational requirements and performance possibilities for the hover and conventional flight; in the hover the pilot wants the pitch attitude held constant and to directly command vertical motion, whereas in conventional flight tight control of pitch rate is needed for rapid manoeuvres and pitch pointing. However, the directional functionality (see P4) of the controls is always the same in that pulling back on the stick effects a climb in both modes. During an acceleration, the initiation of the blend is clearly indicated to the pilot by changing the Head-Up Display (HUD) from VSTOL to Navigational mode.

For centered inceptor a flight-path hold is implemented, blending into a vertical speed hold below 50 knots. This satisfies P6, and gives rise to landing approaches with very low pilot workload in that the pilot just has to set the HUD flight path symbol on the end of the runway of the aircraft carrier, and then centre the stick. For speeds below 50 knots the hold facility relies on having speed measurements (possibly from ground radar) - in the absence of a speed measurement the hold is not activated.

### Inceptor 3 (stick trim switch)

The third inceptor is used to command pitch attitude. As has already been discussed, for hover and transition the pilot would normally like to keep the pitch attitude fixed at 8 degrees i.e. the landing attitude. However, so as not to reduce the operational envelope (**P2**) and to allow the pilot flexibility in achieving a given speed and descent rate (**P3**), the pilot is given the possibility of altering this nominal 8 degrees attitude using a trim switch located on the stick. Pushing the trim switch forward effects nose down at 2 degrees per second, and pulling back effects nose up at 2 degrees per second. As the nozzles go aft obviously one of the inceptors must lose authority as only two actuators remain. The trim switch authority is therefore washed out, and pitch rate demand blended across to inceptor 2 (the stick) as discussed above. When the pilot returns to the transition and hover regime, the pitch demand is always reset to 8 degrees.

## 4 FEEDBACK VARIABLES

The two issues of what controls to give the pilot and which measurements or derived measurements to feedback are clearly related, but there is also a lot of freedom to choose the measurements and feedback strategy given a particular choice of pilot controls. The approach taken has been to design an inner-loop multivariable feedback controller using very different variables for feedback to those directly commanded by the pilot. This is a different approach to that taken in earlier design studies (see [4, Hyde]) where, for example, if the pilot wished to control ground speed, then ground speed was used for feedback. The three variables selected for the inner-loop feedback are

- Body axis forward acceleration, UBF DOT (feet/s<sup>2</sup>).
- Body axis vertical acceleration, WBF DOT (feet/s<sup>2</sup>).
- Pitch rate, QD (degrees/sec).

This choice was arrived at from the following considerations:

- These measurements are generated from accelerometers and gyros in the aircraft itself and have good signal to noise characteristics around the desired bandwidth. Measurements which rely on ground radar (e.g. ground speed) could drop out at any stage, and hence cannot be relied on. Aerodynamic measurements are very unreliable at low speeds, and do not measure what is required during turbulence.
- These three measurements can be used across the whole flight envelope, and hence there is no need for any mode changes within the inner loop. In previous design studies it was found that transients could sometimes occur when switching between control modes; with the approach here mode changing involves working only with the outer single-input single-output control loops which lend themselves much more easily to blending.
- The design of a desaturation controller for actuator authority and rate limits is much easier. For example, thrust and thrust direction are essentially force motivators and hence result in accelerations. Hence if the engine saturates, then the appropriate action is to back off an acceleration demand. If accelerations are being fed back, then this is easy. Furthermore it is possible to prioritize which acceleration demand to back off first e.g. forward acceleration before vertical if in the hover regime.
- All three measurements are body axis ones, and hence no orientation problems occur if the aircraft is rolled upside down.

This inner loop robustly stabilises the aircraft and also achieves a reasonable degree of decoupling. The design of the three outer single-input single-output loops is then relatively straightforward, and can be done using classical loop-shaping. In the rest of this paper we concentrate on the inner-loop design.

## 5 MULTIVARIABLE LOOP-SHAPING

Linear design has been carried out using the loop-shaping plus robust stabilisation approach of [7, Glover and McFarlane], [8, McFarlane and Glover]. The robust stabilisation makes use of a normalised left coprime factorisation (LCF) of the plant  $G$  which is given by  $G = \tilde{M}^{-1}\tilde{N}$  where  $\tilde{N}$  and  $\tilde{M}$  are coprime matrices in  $R\mathcal{H}_\infty$  and

$$\tilde{N}\tilde{N}^* + \tilde{M}\tilde{M}^* = I.$$

Consider the class of perturbed system models given by the family

$$\mathcal{G}_\epsilon = \left\{ (\tilde{M} + \Delta_M)^{-1}(\tilde{N} + \Delta_N) : [\Delta_M, \Delta_N] \in R\mathcal{H}_\infty^{p \times (p+m)}, \|\Delta_M, \Delta_N\|_\infty < \epsilon \right\}$$

Robustness is achieved by finding the single fixed controller,  $K$ , which stabilises the largest class of such systems, i.e. the maximum of  $\epsilon$ ,  $\epsilon_{\max}$ , such that  $\mathcal{G}_{\epsilon_{\max}}$  can be stabilised by the single fixed controller,  $K$ . The

solution is given by solving the  $\mathcal{H}_\infty$  problem

$$\epsilon_{\max}^{-1} = \gamma_{\min} = \inf_K \left\| \begin{bmatrix} K \\ I \end{bmatrix} (I - GK)^{-1} \tilde{M}^{-1} \right\|_\infty.$$

In [7, Glover and McFarlane] it is shown that the solution to this problem has a special structure, and does not need the iteration usually required in  $\mathcal{H}_\infty$  problems to find  $\gamma_{\min}$ . Note that the perturbation,  $\Delta_M$ , in the denominator can cause the system's poles to move from being stable to unstable or vice-versa.

To achieve the desired closed-loop performance the plant singular values are shaped using open-loop pre- and/or post- weighting functions  $W_1$  and  $W_2$ . The shaped plant is given by  $G_s = W_2 G W_1$ . A controller  $K_\infty$  is then found which robustly stabilises  $G_s$ . The final controller for  $G$  is therefore given by

$$K = W_1 K_\infty W_2.$$

As discussed in [8, McFarlane and Glover], the  $\epsilon_{\max} = \frac{1}{\gamma_{\min}}$  can be used as a design indicator. Very small  $\epsilon_{\max}$  indicates that the loop shape is incompatible with robust stability, whereas a reasonable value of  $\epsilon_{\max}$  (e.g.  $> 0.25$ ) indicates that the loop shapes specified by the designer are compatible with robust stability, and that the loop shapes will not be significantly altered by  $K_\infty$ . Bounds on the achieved loop shapes are given in [8, McFarlane and Glover] in terms of  $W_1$ ,  $W_2$  and the normalised left coprime factors.

A procedure for selecting the weighting matrices  $W_1$  and  $W_2$  has been developed, and can be found in [4, Hyde], [6, Hyde and Glover]. Basically it consists of careful input and output scaling, followed by an inspection of the transfer functions of all the input-output pairs.  $W_1$  and  $W_2$  are then usually chosen to be diagonal and their elements chosen so as to achieve the desired bandwidths and roll-off rates for the various loops. Low and high frequency gains of the loops are chosen to reflect performance and roll-off requirements in much the same way as is done using classical loop-shaping design. Space precludes a more detailed description here, but the design example in the next section illustrates the key features of the approach.

Some of the advantages of using this loop-shaping approach are listed briefly below.

- The solution to the  $\mathcal{H}_\infty$  robust stabilisation step does not require an iteration to find  $\epsilon_{\max}$  as is required for the general  $\mathcal{H}_\infty$  problem solution. This enables the designer to see the results of a change in weighting functions very quickly in terms of closed-loop frequency responses and time responses.
- The procedure has been applied to a variety of design examples, and the selection of weights has been found to be highly intuitive. For example, if following time-domain analysis it is found that a particular actuator saturates too much, then it is clear which element of  $W_1$  to alter and how to alter it. One key advantage is that there aren't too many knobs to twiddle when changing the weights, and this results in trade-offs between robustness and performance being made in a very intuitive way.
- As noted in [10, Sefton and Glover], the controller from the normalised coprime factor robust stabilisation problem can be written as a plant observer. This in turn means that controllers designed at different operating points on the flight envelope can be scheduled by linearly interpolating the coefficients of the observer [11, Hyde and Glover].
- Redesign (or retuning)-at a later date could be automated. During the service life of an aircraft components will age - for example the dynamic response of the engine may deteriorate. Measurable changes like these could be used to update the model, and then a new set of linear controllers automatically generated.
- Unlike some other  $\mathcal{H}_\infty$  formulations, this approach does not cancel stable plant poles - see [10, Sefton and Glover], [12, Postlethwaite *et al.*].
- The uncertainty description allows unstable plant perturbations. This is particularly appropriate here as the GVAM longitudinal motion has three unstable poles when in the hover which all move to the left-half plane as the aircraft transitions to wingborne flight.
- It is observed that good time responses are very easily achieved by placing  $K_\infty$  in the feedback loop and correcting the references with an appropriate constant gain matrix.

## 6 EXAMPLE LINEAR DESIGN

In this section the design for one fixed operating point is given, namely for an airspeed of 105 feet/sec (32 m/s) and incidence of 8 degrees. The linear designs carried out at other airspeeds on the operating envelope use exactly the same procedure.

To reduce the dependency of linearisations for a given airspeed on nozzle angle, instead of working with inputs of thrust magnitude and thrust direction, resolved thrust demands are used i.e. if  $PA$  and  $NOZZA$  represent thrust demand and nozzle angle demand, then the resolved thrusts are

$$XA = PA \times \cos(NOZZA)$$

$$ZA = PA \times \sin(NOZZA)$$

We now follow the procedure of [4, Hyde] for the design.

1. Scale the inputs. The throttle demand limits are

$$0.26 \leq PA \leq 1.0$$

Hence both  $XA$  and  $ZA$  vary roughly in the range 0 to 1. The tailplane demand ( $ETADA$ ) can vary in the range

$$-11.75 \leq ETADA \leq 12.75$$

and is scaled  $\times 10$  so that the demand is now expected to vary roughly in the range -1 to 1. Note that this scaling is only necessary when interpreting closed-loop transfer functions at the plant input - the scaling is lost in the weight  $W_1$  in stage 6.

2. Scale the outputs. The outputs are scaled so that 1 unit of coupling into any of the scaled outputs is as equally undesirable. The horizontal and vertical acceleration outputs are scaled in units of ' $g$ ', the acceleration due to gravity. The pitch rate,  $QD$ , is scaled  $\times 0.1$ . The interpretation of this is that a coupling of  $0.1g$  (10 % of the maximum achievable in any direction due to powered lift) is as equally undesirable as the pitch attitude wandering off at one degree per second.
3. Bandwidth requirements and restrictions. The maximum frequency upto which each actuator can be used may be determined by a number of factors including the speed of the dynamics, rate limits and modelling uncertainty. From such considerations the following limitations were arrived at:

- Throttle/engine : upto 4 rad/s in the hover, and upto 2 rad/s in conventional flight.
- Nozzle : upto 10 rad/s.
- Tail/reaction jets : upto 6 rad/s in the hover, and upto 10 rad/s in conventional flight.

The second figure of 2 rad/s for the engine is to avoid unnecessary cycling of the engine which would reduce its life - precision thrust control is only necessary during the hover regime. The lower figure of 6 rad/s for the reaction-jet system in the hover is due to a lightly damped mechanical control run which back-drives the front reaction jet from the tailplane setting.

Note that if different bandwidths are used for the throttle and nozzle, then the bandwidths at which the resolved thrust demands are used will be dependent on nozzle angle. This would thus necessitate making the controller a function of nozzle angle as well as airspeed. As a consequence, a bandwidth of 4 rad/s is specified for both the throttle and nozzle use during hover and transition.

The maximum bandwidth at which the tailplane/reaction-jet is to be used is chosen to be 6 rad/s for the hover and transition.

4. Sensor models and second order Padé approximations to represent computational delays and anti-aliasing filters are added to the linear model. A notch filter is used to avoid exciting the front reaction-jet control run. For the purposes of design, the sensors, Padé approximations and actuators are cascaded together and approximated with equivalent low order actuator models which have the same gain and phase characteristics at the corresponding bandwidths specified in step 3. The sensor dynamics can be pulled through to the plant input as all three sensors are modelled with the same dynamics. This keeps the order of the controller down without unduly compromising the robustness of the final closed-loop system. More conventional model reduction approaches such as balanced truncation cannot be used as the structure of the design plant must be preserved so that the  $\mathcal{H}_\infty$  controllers can be scheduled.
5. Plot the plant singular values and all plant input-output pairs to determine which inputs affect which outputs and whether there are any output directions which are hard to control. Fig 2 shows the plant singular values, and it can be seen that the plant is well conditioned in the 4 to 6 rad/s region. Examining the input-output pairs (not given here for lack of space) indicated a predominantly diagonal plant.
6. Selection of loop-shaping weights. First a  $2 \times 2$  constant align matrix is found to align the first two singular values at 4 rad/s.

Note that for a design in the hover this matrix is just the  $2 \times 2$  identity matrix multiplied by a scalar. As airspeed increases, a step change in horizontal thrust results in an ever increasing vertical acceleration as well as a forward acceleration due to increased lift at increased speed. The align matrix counters this, and hence improves decoupling of the final closed-loop. The align matrix is filled out with a 1-entry in the (3,3) element to give a 3 by 3 compensator  $W_A$ . Next each of the loops is shaped in turn to have the required low frequency gain, high frequency roll-off, and a roll-off rate in the region of 20 to 30 dB/decade at cross over.

The simple weight

$$W_P = \begin{bmatrix} \frac{3(s+2)}{(s+0.1)^2} & 0 & 0 \\ 0 & \frac{3(s+2)}{(s+0.1)^2} & 0 \\ 0 & 0 & \frac{250(s+5)^2}{(s+0.1)(s+50)^2} \end{bmatrix}$$

is used to achieve this. The overall precompensator is thus given by  $W_1 = W_A W_P$ . Figure 3 shows the singular values of the shaped plant with the full order actuator, sensor and computational delay models.

7. Calculate the optimal controller. The optimal  $\gamma_{\min} = 1/\epsilon_{\max}$  is 2.72 indicating that the specified loop shapes are consistent with robust stability ( $\gamma < 4$  is usually taken to indicate an acceptable design.)  $\gamma$  was set to 10 % suboptimal giving  $\gamma = 2.99$ . Figure 4 shows the final loop shapes when  $K_\infty$  is cascaded with the full-order shaped plant.
8. Time response analysis. Figures 5,6 and 7 show responses to step demands on the references. Clearly a good degree of decoupling has been achieved, and the time-domain properties look good.

## 7 NON-LINEAR SIMULATION

Linear designs were carried out at airspeeds of 105, 175, 235 and 340 feet/sec to cover the hover and transition part of the flight envelope. Here results are given for the 0 to 175 feet/sec controller schedule. Below 105 feet/sec the controller gains are kept fixed because there is very little change in the dynamics in this region other than the rear reaction-jet is augmented with the front reaction jet below about 100 feet/sec. The observer for designs below 100 feet/sec thus have extra states corresponding to the front reaction jet actuation system, and this added complication was judged best avoided. Between 105 and 175 feet/sec the observer gains for the two controller designs are linearly interpolated.

Before implementing on the non-linear model, the achieved loop-shaping/ $\mathcal{H}_\infty$  cost function,  $\gamma$ , was checked at the mid-point of the schedule and was found to be 3.16. This compares well with those achieved at the design points, namely 2.99 and 3.04.

Figure 8 shows the results of a non-linear time response on the GVAM model. Note that an outer-loop pitch hold controller has been implemented so that time-responses of accelerations and decelerations can be carried out over long time periods without the pitch attitude wandering. The responses look much as one would expect from the linear analysis, and in particular the decoupling looks good. With such performance, the design of the outer-loop holds will be very straightforward. Note the small drift on UBFDDOT (forward acceleration in  $\text{feet}/\text{s}^2$ ). This is to be expected as the plant has low gain at low frequency (see Fig 2). The outer-loop acceleration/speed loop will counter this when implemented.

## 8 CONCLUSIONS

Preliminary results have been presented of a flight control law intended for future implementation on the D.R.A. research Harrier. The importance of careful design of control modes has been discussed, as this is the main factor which affects the pilot's perception of the control law behaviour. The control law presented here has been developed with a slightly different philosophy to that used for previous designs in the design study, both in terms of control modes and the overall structure of the feedback controller. It is hoped that piloted simulation in July 1992 will quantify the benefits from this different approach.

An example linear design has been given in some detail, and illustrates the relatively systematic nature of the loop-shaping design procedure. This design procedure has been applied to many other design examples by the authors, and has been found to generally produce sensible controllers with a modest amount of effort. Some justification for using this loop-shaping/ $\mathcal{H}_\infty$  design approach has been given.

Currently the controller envelope is being extended to the fully wingborne flight regime. The control law to be tested in piloted simulation in July 1992 will cover the full flight envelope, have the prioritized anti-windup procedure used in [4, Hyde] implemented, and also have all the outer-loop controllers implemented. It is hoped that the control law will be ready for possible flight trials in early 1993.

## Acknowledgements

The authors would like to thank the D.R.A. at Bedford for providing the GVAM model, and for their involvement in the project, particularly with respect to piloted simulation of our designs. Also, we would like to thank Dr.S.J. Williams of Cambridge Control Ltd. for providing useful practical advice, and drawing many of the implementation problems of multivariable controllers to our attention. The work is being funded by the U.K. Science and Engineering Research Council under grant RG13793.

## References

- [1] O.P. Nicholas and C.M. Stephens. The VAAC/VSTOL flight control research project. *Aerospace*, July 1989. Published by The Royal Aeronautical Society.
- [2] P.R. Smith. Aircraft flight control system design concepts. *Proceedings of the Institute of Measurement and Control*, 24:73-77, April 1991.
- [3] E.A.M. Muir and M.G. Kellett. The RAE generic VSTOL aircraft model — GVAM87. Technical report, Royal Aerospace Establishment, Bedford, 1987.
- [4] R.A. Hyde. *The Application of Robust Control to VSTOL Aircraft*. PhD thesis, University of Cambridge, August 1991.
- [5] R.A. Hyde and K. Glover. VSTOL aircraft flight control system design using  $\mathcal{H}_\infty$  controllers and a switching strategy. In *Proceedings of Conference on Decision and Control*, Honolulu, Dec 1990.
- [6] R.A. Hyde and K. Glover. The application of scheduled  $\mathcal{H}_\infty$  controllers to VSTOL aircraft. Submitted to IEEE/Automatica Special Issue on Control Applications.
- [7] K. Glover and D.C. McFarlane. Robust stabilization of normalized coprime factor plant descriptions with  $\mathcal{H}_\infty$ -bounded uncertainty. *IEEE Transactions on Automatic Control*, 34(8):821-830, August 1989.
- [8] D.C. McFarlane and K. Glover. *Robust Controller Design Using Normalized Coprime Factor Plant Descriptions*. Lecture Notes in Control and Information Sciences. Springer-Verlag, 1990.
- [9] M. Gainza. Flying the Sea Harrier. *Pilot*, pages 29-34, February 1990. Pilot Publishing Company.
- [10] J.A. Sefton and K. Glover. Pole/zero cancellations in the general  $\mathcal{H}_\infty$  problem with reference to a two block design. *Systems and Control Letters*, 14:295-306, 1990.
- [11] R.A. Hyde and K. Glover. Meeting VSTOL performance specifications using scheduled  $\mathcal{H}_\infty$  controllers. In *Proceedings of American Control Conference*, Boston, June 1991.
- [12] I. Postlethwaite, M.-C. Tsai, and D.-W. Gu. Weighting function selection in  $\mathcal{H}_\infty$  design. In *Proceedings of IFAC Congress on Automatic Control*, 1990.

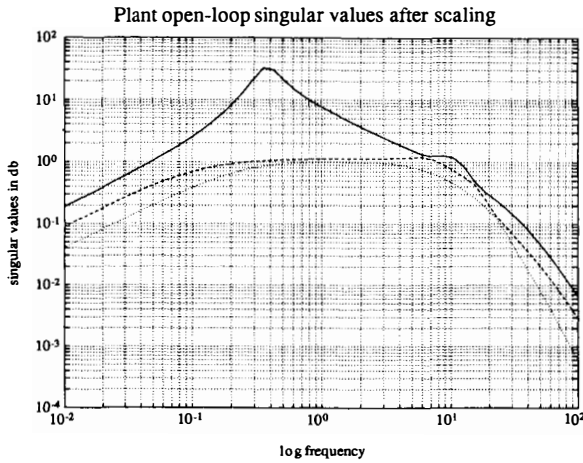
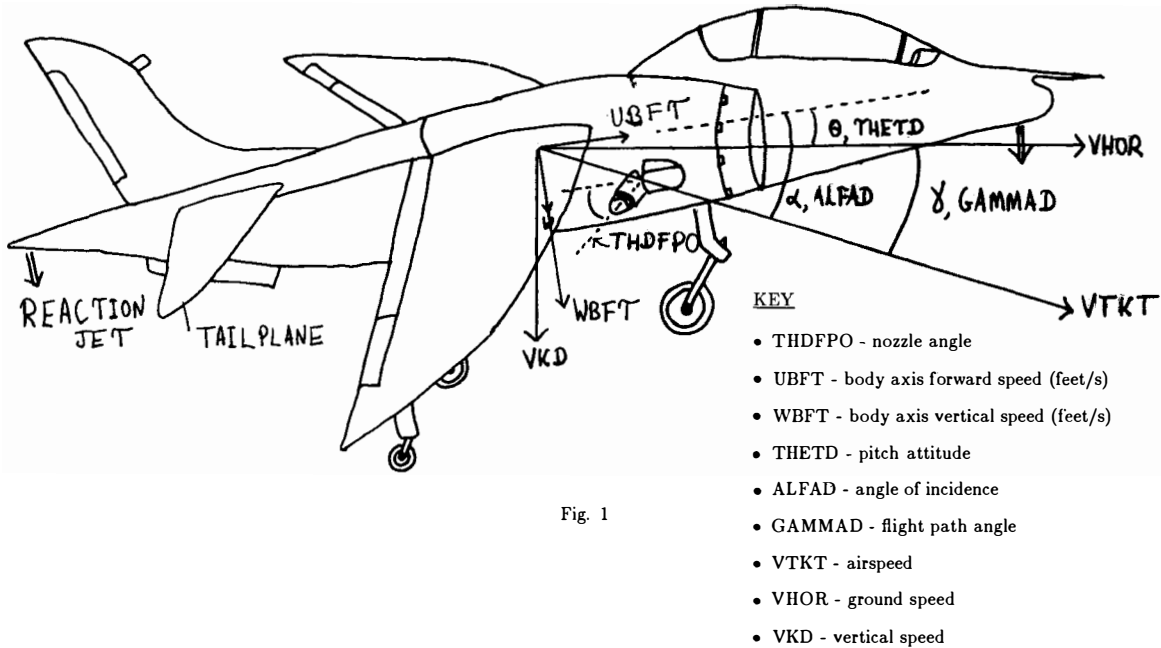


Fig. 2

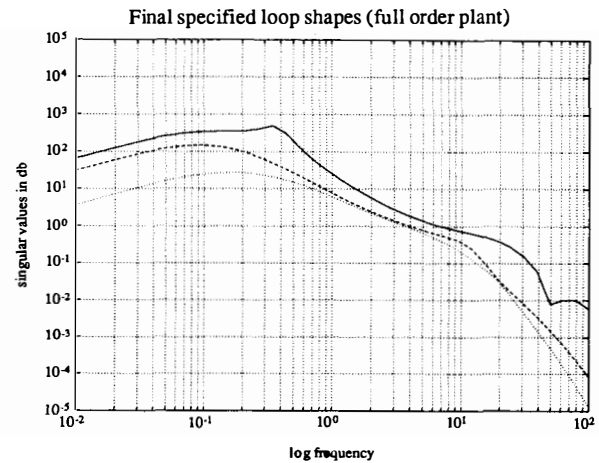


Fig. 3

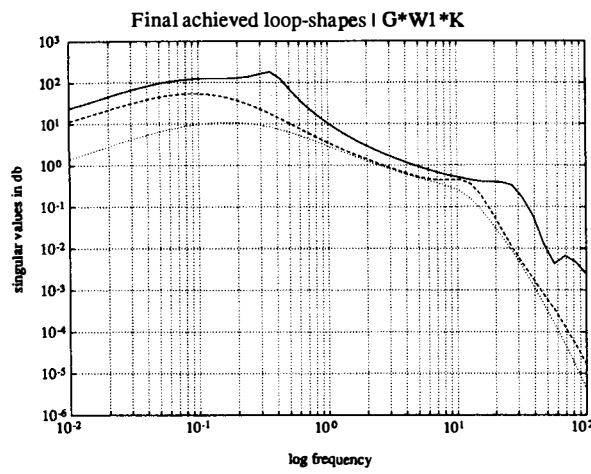


Fig. 4

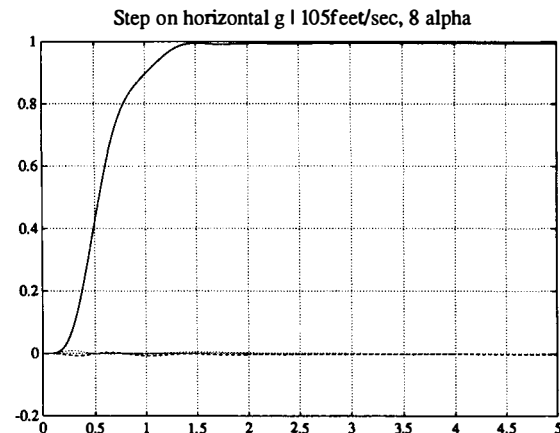


Fig. 5

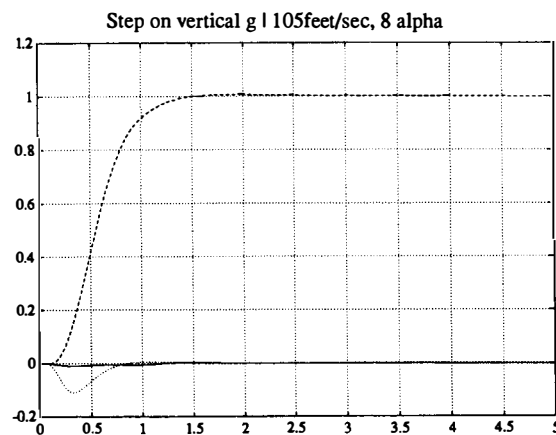


Fig. 6

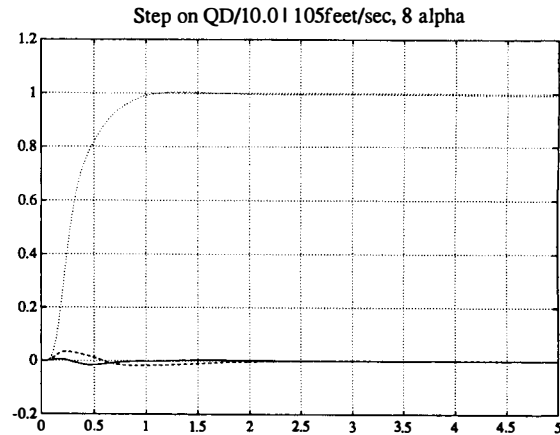


Fig. 7

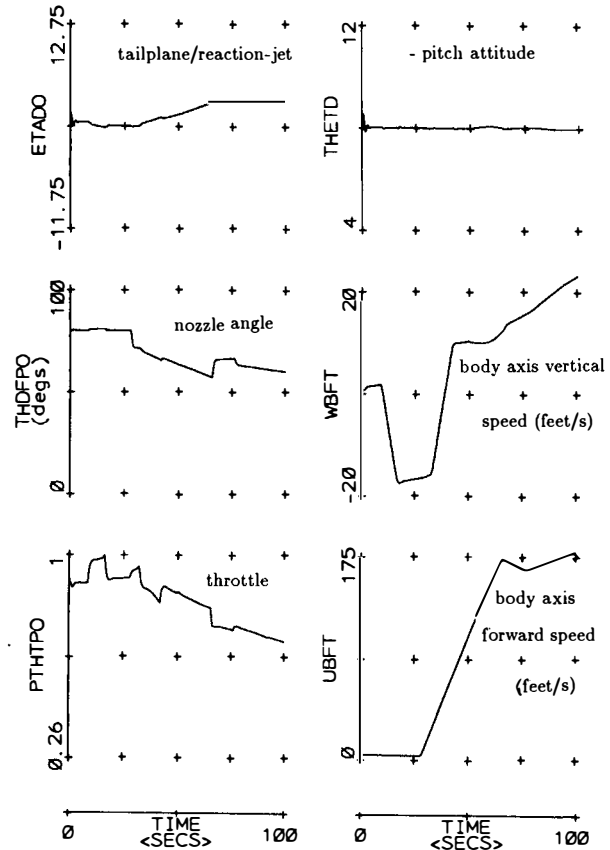
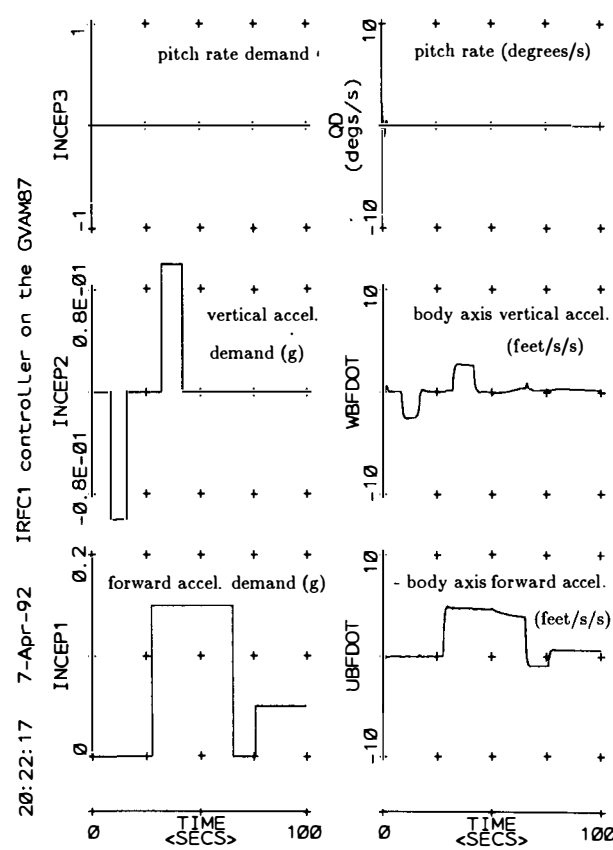


Fig. 8

## APPLICATION OF RESTRUCTURABLE FLIGHT CONTROL SYSTEM TO AN AIRLINER

Y. Ochi and K. Kanai

*Department of Aerospace Engineering, National Defense Academy, 1-10-20 Hashirimizu, Yokosuka, 239 Japan*

**Abstract.** The authors have proposed a flight control system which is able to accommodate failures occurring in the airframe as well as at the control effectors. It is based on the feedback linearization method and online parameter identification. This paper presents such a system designed considering application to large scale airliners. Its major new point is that the stabilators or the engines are used as feedforward control inputs to counteract the disturbances caused by stuck control surfaces. Those effectors are too slow to be used along with other fast control surfaces. However, they can produce large forces or moments. So, taking advantage of them would help the aircraft recover from failures. The performance of the control system is demonstrated through computer simulation using a six-degree-of-freedom nonlinear aircraft model of Boeing 747.

**Keywords** flight control, system failure and recovery, adaptive control, nonlinear control systems, recursive least squares, feedback linearization, digital control

### INTRODUCTION

Importance of failure accommodation for aircraft came to be emphasized and studies started in large with the concept of restructurable or reconfigurable flight control systems(RFCS), which was proposed in NASA workshop in 1982. Many papers have been reported since then. Among them, Self-Repairing FCS(Huber and McCulloch, 1984), which is a simple and practicable approach, is evaluated not only by numerical simulation but also by motion-based simulation(Anderson and Clark, 1988). Furthermore, flight tests on the F-15 were carried out(Stewart and Shuck, 1990). However, from the point of view of controller design, most of the studies are based on linearized mathematical models and linear control theories. Although linear controllers are known to be useful in practice even in some nonlinear environments, failures often cause severe nonlinearity, such as highly coupled motions or large motions apart from the nominal trim point. In that situation, the linearized models can no longer describe the impaired aircraft dynamics well. It may make the RFCS fail to accommodate failures.

The authors proposed a digital RFCS using the feedback linearization method(Ochi and Kanai, 1991;Ochi, 1991). The first feature of the RFCS is that failures are identified as parameter changes in the six-degree-of-freedom(6-DOF)nonlinear equations of motion by the recursive least square algorithm. And the control parameters are updated using the latest estimated parameters. Therefore, the RFCS has the potential to accommodate failures which considerably change the characteristics of the aircraft dynamics. The second feature is that the parameters are identified using generic inputs which are introduced to

decrease the number of parameters to be identified. The control law is also determined for generic inputs. The underlying idea of the RFCS is taking full advantage of remaining normal components to compensate for the functions which are lost due to failures. It is called functional redundancy(Weiss, and others, 1986). The performance of the RFCS was demonstrated through computer simulation using the nonlinear model of an F-14 class fighter aircraft which has half of the right wing broken off(Ochi, 1991).

In this paper, the RFCS is applied to an airliner(Boeing 747) to recover from control failures such as partial loss of control surfaces, actuator jam, etc. Large scale airliners are different from fighter aircraft in the following points.

- 1) Control surfaces of airliners are able to produce less forces and moments relative to the scale of the airframe than those of fighter aircraft.
- 2) Control effectors such as stabilators, flaps, engines etc., have much larger time constants than other surfaces such as elevators, ailerons or rudders.

The first feature makes the ability of airliners to recover from failures less than that of fighters. The second feature makes it difficult to use the slow control effectors along with the fast ones in transient attitude control. In fact, using the slow ones that may makes them liable to cause disturbances because of their rate or traveling limits. However, since some slow effectors can produce large forces or moments, it is important to take advantage of them from the first stage of recovery before the aircraft motions become too large. The above observation leads to the idea of using the slow effectors to counteract the disturbances caused by

stuck control surfaces. And their inputs, which are applied in the step way, are determined using the nominal parameters of the aircraft model. To illustrate the performance of the RFCS, computer simulation was conducted using a 6-DOF nonlinear aircraft model of Boeing 747. Failure cases considered include elevator or rudder jam which causes significant disturbances.

In this work, sensors and computers are assumed to be normal, and sensor noises are not taken into account.

### DIGITAL RFCS

This section gives a brief outline of the digital RFCS design. The state equation is assumed to be given by

$$\dot{X} = A(X) + B(X)U \quad (1)$$

where  $X \in R^n$  is a state vector and  $U \in R^m$  a control vector. Elements of  $A(X) \in R^{n \times n}$  and  $B(X) \in R^{n \times m}$  are assumed to have the form of linear combination of constant parameters and known functions of  $X$ . Let the outputs to be controlled be  $Y \in R^l$ . The control objective is to make  $Y$  track some desired reference outputs,  $Y^*$ . The control law by which the objective can be reached is derived by the feedback linearization method.

Now, let us introduce a generic input vector,  $U_G \in R^{m'}$ , which is defined by

$$U = PU_G \quad (2)$$

where  $P \in R^{m \times m'}$  is a constant matrix.  $P$  is called control distributor matrix. The control law is determined for the generic inputs, and then actual ones,  $U$ , by Eq. (2).

The effects of failures on aircraft dynamics are identified by estimating the parameters of the state equation, Eq. (1). The identification algorithm used is the recursive least square method. The generic inputs are used also in identification instead of the actual inputs. The control parameters are modified using the estimated ones.

The control law is a continuous-time one. Since using digital computers is inevitable in implementation, the control law must be digitalized. In addition, the actuator and the engine dynamics must be considered. For these reasons, discrete-time servo controllers are designed for the actuators and the engines. The reference inputs,  $U_G^*$  and  $T_h^*$ , are given by the continuous-time control law.

### FEEDFORWARD CONTROL USING SLOW EFFECTORS

Let us consider a large scale transport, Boeing 747. In Eq. (1), state variables and control variables are defined as follows.

$X = [u, w, q, \theta, v, r, p, \phi]^T$ , where  $u$ :forward speed(m/sec),  $w$ :downward speed(m/sec),  $q$ :pitch rate(rad/sec),  $\theta$ :pitch angle(rad),  $v$ :sideward speed(m/sec),  $r$ :yaw rate(rad/sec),  $p$ :roll rate(rad/sec),  $\phi$ :roll angle(rad).

$U = [\delta_{f\text{st}}^T, \delta_{s\text{lw}}^T, T_h^T]^T$ , where  $\delta_{f\text{st}} = [\delta_{e\text{iL}}, \delta_{e\text{iR}}, \delta_{e\text{oL}}, \delta_{e\text{oR}}, \delta_{a\text{iL}}, \delta_{a\text{iR}}, \delta_{a\text{oL}}, \delta_{a\text{oR}}, \delta_{r\text{up}}, \delta_{r\text{lw}}]^T$ ,  $\delta_{s\text{lw}} = [\delta_{s\text{tL}}, \delta_{s\text{tR}}]^T$ ,  $T_h = [T_{h1}, T_{h2}, T_{h3}, T_{h4}]^T$ , and the subscripts denote  $e$ :elevator,  $a$ :aileron,  $r$ :rudder,  $s$ :stabilator,  $i$ :inboard,  $o$ :outboard,  $L$ :left side,  $R$ :right side,  $u$ :upper side,  $l$ :lower side. For example,  $\delta_{e\text{iL}}$  is the left side inboard elevator.  $\delta_{f\text{st}}$  and  $\delta_{s\text{lw}}$  include the fast and the slow control surfaces respectively.  $T_h$  ( $i=1, \dots, 4$ ) indicates the  $i$ -th engine output.

The actuator and the engine dynamics are assumed to be described by the first order system,

$$\dot{U} = \Lambda (-U + U_c) \quad (3)$$

where  $\Lambda = \text{diag}\{1/T_i\}$  and  $T_i$  is the time constant of the actuators and the engines.  $U_c$  indicates the command input vector.

The second term of the right-hand side in Eq. (1) can be rewritten as

$$B(X)U = B_{f\text{st}}(X)\delta_{f\text{st}} + B_{s\text{lw}}(X)\delta_{s\text{lw}} + B_{th}T_h \quad (4)$$

where  $B_{f\text{st}}(X) \in R^{8 \times 10}$ ,  $B_{s\text{lw}}(X) \in R^{8 \times 2}$ , and  $B_{th} \in R^{8 \times 4}$  (a constant matrix).

Let deflection angles of the stuck surfaces be  $\delta_f$ , the nominal coefficient matrix  $B_f$ , and deviation of the stuck surfaces from the nominal trim position  $\Delta\delta_f$ .  $\Delta\delta_f$  is assumed to be known. Then in order to counteract the disturbances caused by the stuck surfaces using the stabilators or the engines, the following equations must be satisfied.

$$B_f \Delta\delta_f + [B_{s\text{lw}}(X), B_{th}][\Delta\delta_{s\text{lw}}^T, \Delta T_h^T]^T = 0 \quad (5)$$

where  $\Delta\delta_{s\text{lw}}$  and  $\Delta T_h$  are the stabilator angles and the engine outputs to be corrected respectively. Solving Eq. (5) for  $[\Delta\delta_{s\text{lw}}^T, \Delta T_h^T]^T$  yields

$$[\Delta\delta_{s\text{lw}}^T, \Delta T_h^T]^T = -[B_{s\text{lw}}(X), B_{th}]^+ B_f \Delta\delta_f \quad (6)$$

where '+' denotes pseudo-inverse.

Thus, disturbances caused by the surfaces can be rejected by the modification of the stabilator angles and the engine outputs. However, the use of engines is to be limited to yawing control in the case of rudder jam. And the differential thrust should be kept less than a certain percentage of the maximum thrust. The reasons for the restrictions are:

- 1) The engines have little effect on the aircraft motions except for the linear one along  $X$ -axis and the angular one about  $Z$ -axis.
- 2) When airspeed is high or stuck rudder angles are large, counteracting the yawing moment caused can require too much differential thrust. Since thrusts are also used for airspeed control, producing large yawing moment by the thrusts can affect airspeed control.

Eq. (5) can be rewritten as

$$B_f(X) \Delta\delta_f + B_{s\text{lw}}(X) \Delta\delta_{s\text{lw}} = 0 \quad (7)$$

$$B_{fr}(X) \Delta\delta_{fr} + B_{thr} \Delta T_h = 0 \quad (8)$$

where  $B_{fr}(X) \in R^{1 \times 2}$  and  $B_{thr} \in R^{1 \times 4}$  are the control derivatives for the yawing motion, and  $\Delta\delta_{fr}$  is the displacement of the stuck rudder.  $\Delta\delta_{s\text{lw}}$  can be determined from Eq. (7).

$$\Delta\delta_{s\text{lw}} = -B_{s\text{lw}}(X)^+ B_f(X) \Delta\delta_f \quad (9)$$

Assuming that  $\Delta T_{h1} = \Delta T_{h2} = -\Delta T_{h3} = -\Delta T_{h4}$ , Eq. (8) can be solved uniquely for  $\Delta T_h$ , i.e.,

$$\Delta T_h = -(1/2)B_{tr}(X) \Delta \delta_{tr}/(B_{thr}(1,1)+B_{thr}(1,2)) \quad (10)$$

$\Delta T_h$  is added to  $T_h^*$ , and  $\Delta \delta_{silw}$  to  $\delta_{silw,tr}$ , which are the trim angles of the slow surfaces, to give  $\delta_{silw}$ .

There are two points to be noted in the control laws. One is that the nominal parameters are used in Eqs.(9) and (10). Since those effectors are slow and not used for transient motion control, they should be applied in the step way on detecting failures. It requires to use the nominal parameters to determine the inputs. In addition, estimated parameters are not true values in general. And a trim point computed using the state equations is sensitive to the parameters. So, there is a possibility that an inadequate or unacceptable trim point may come out, if the estimated parameters of the state equations are used.

The other point is that in the case of rudder jam the ↑ ↓

$$\begin{bmatrix} \dot{u} \\ \dot{v} \\ \dot{w} \end{bmatrix} = \begin{bmatrix} -g\sin\theta \\ g\cos\theta\sin\phi \\ g\cos\theta\cos\phi \end{bmatrix} + \begin{bmatrix} vr-wq \\ wp-ur \\ uq-vp \end{bmatrix} + \frac{P_{dy1}}{m} \begin{bmatrix} C_{x1} \\ C_{y1} \\ C_{z1} \end{bmatrix} + \frac{P_{dy2}}{m} \begin{bmatrix} C_{x\delta}^T \\ C_{y\delta}^T \\ C_{z\delta}^T \end{bmatrix} \delta + \frac{1}{m} \begin{bmatrix} C_{xTh} \\ 0 \\ 0 \end{bmatrix} T_h + \frac{P_{dy2}}{m} \begin{bmatrix} C_{x0} \\ C_{y0} \\ C_{z0} \end{bmatrix} \quad (11)$$

$$E_1 \begin{bmatrix} \dot{p} \\ \dot{q} \\ \dot{r} \end{bmatrix} = E_2 \begin{bmatrix} pq \\ qr \\ rp \end{bmatrix} + E_3 \begin{bmatrix} p^2 \\ q^2 \\ r^2 \end{bmatrix} + P_{dy1} \begin{bmatrix} bC_{11} \\ cC_{m1} \\ bC_{n1} \end{bmatrix} + P_{dy2} \begin{bmatrix} bC_{1\delta}^T \\ cC_{m\delta}^T \\ bC_{n\delta}^T \end{bmatrix} \delta + \begin{bmatrix} 0 \\ C_{mTh}^T \\ C_{nTh}^T \end{bmatrix} \Delta T_h \quad (14)$$

$$(15) \quad (16)$$

With the above equations of motion and the following kinematic relations,

$$\dot{\theta} = q\cos\phi - r\sin\phi \quad (17)$$

$$\dot{\phi} = p + (q\sin\phi + r\cos\phi)\tan\theta \quad (18)$$

the aircraft rigid body motions are described, where  $P_{dy1} = \rho VS/2$ ,  $P_{dy2} = \rho V^2 S/2$ ,  $V = (u^2 + v^2 + w^2)^{1/2}$

$$C_{x1} = C_{xu} \Delta u + C_{xw} \Delta w, \quad C_{y1} = C_{yw} \Delta v,$$

$$C_{z1} = C_{zu} \Delta u + C_{zw} \Delta w + (c/2)C_{zq}q,$$

$$C_{11} = C_{1u} \Delta v + (b/2)(C_{1r}r + C_{1p}p),$$

$$C_{m1} = C_{mu} \Delta u + C_{mw} \Delta w + (c/2u)C_{mw}w + (c/2)C_{wq}q,$$

$$C_{n1} = C_{nv} \Delta v + (b/2)(C_{nr}r + C_{np}p),$$

$\Delta u = u - u_{tr}$ ,  $\Delta v = v - v_{tr}$ ,  $\Delta w = w - w_{tr}$ ,  $\Delta \delta = \delta - \delta_{tr}$ ,  $\Delta T_h = T_h - T_{htr}$ ,  $\delta = [\delta_{fst}, \delta_{silw}, T_h]^T$  and the subscript, 'tr', denotes the trim value.  $C_{xu}$ ,  $C_{yu}$ , etc. are non-dimensional derivatives(constant),  $C_{x0}$ ,  $C_{y0}$ ,  $C_{z0}$ , and  $C_{m0}$  are non-dimensional aerodynamic forces and moment at the trim point, respectively. The numerical data are from the report(Heffley and Jewell, 1972).  $E_1$ ,  $E_2$ , and  $E_3$  are matrices whose elements are determined from the moments of inertia and the products of inertia. Other symbols mean  $m$ :mass,  $S$ :wing area,  $b$ :wing span,  $c$ :wing mean aerodynamic chord lenght,  $\rho$ : density of atmosphere, and  $g$ :acceleration of gravity. The identification model is similar to that used in the paper(Ochi, 1991).

The control objective is to trim the aircraft at a desired attitude. So, the outputs to be controlled are selected as  $Y = [u, \alpha, \theta, v, \phi]^T$  ( $\alpha$ :angle of attack). Corresponding to  $Y$ , the reference outputs  $Y^* = [u^*, \alpha^*, \theta^*, v^*, \phi^*]^T$  are given by the time functions,  $Y^*(t) = Y^*(\infty) + \text{diag}(\exp(-.5t), \exp(-t), \exp(-.5t), \exp(-.5t))x$

↑ stabilator angles and the thrusts are determined independently. There may be a concern that the stabilators and the thrusts might cause disturbances in the yawing motion to each other, if they are used at the same time. However, since the stabilators can produce little yawing moment, they cannot affect the yawing control by the thrusts. On the other hand, the thrusts have little effect on the pitching or rolling control by the stabilators. Therefore, there is no problem in giving the inputs by Eqs.(9) and (10). Figure 1 shows a block diagram of the RFCS.

## SIMULATION

The performance of the RFCS is evaluated through computer simulation. The mathematical model used is the 6-DOF nonlinear equations of motion of an airliner, Boeing 747. They are as follows. ↓

$(Y(0)-Y^*(\infty))$ , where  $Y^*(\infty)$  is a reference output vector at the desired trim point.

Generic inputs are chosen as

$$\delta_G = [\delta_{Gfst}^T, \delta_{Gsilw}^T, T_{hg}^T]^T \quad (19)$$

where  $\delta_{Gfst} = [\delta_{h1}, \delta_{h2}, \delta_a, \delta_r]^T$ ,  $\delta_{Gsilw} = [\delta_{stcl}, \delta_{stdf}]^T$ ,  $T_{hg} = [T_{hcl}, T_{hdf}]^T$ .  $\delta_{Gfst}$ ,  $\delta_{Gsilw}$ , and  $T_{hg}$  are generic inputs for  $\delta_{fst}$ ,  $\delta_{silw}$ , and  $T_h$  respectively. That is,

$$\delta_{fst} = P_{fst} \delta_{Gfst} \quad (20)$$

$$\delta_{silw} = P_{silw} \delta_{Gsilw} \quad (21)$$

$$T_h = P_{th} T_{hg} \quad (22)$$

The control distributor matrices are given as follows.

$$P_{fst} = \begin{bmatrix} .5236 & .2618 & .2618 & .0 \\ .5236 & .2618 & -.2618 & .0 \\ .5236 & .5236 & .5236 & .0 \\ .5236 & .5236 & -.5236 & .0 \\ .2618 & .5236 & .5236 & .0 \\ .2618 & .5236 & -.5236 & .0 \\ .2618 & .2618 & .2618 & .0 \\ .2618 & .2618 & -.2618 & .0 \\ .0 & .0 & .0 & .5236 \\ .0 & .0 & .0 & .5236 \end{bmatrix} \quad P_{silw} = \begin{bmatrix} 1 & 1 \\ 1 & -1 \end{bmatrix}$$

$$P_{th} = \begin{bmatrix} 1 & 1 \\ 1 & 1 \\ 1 & -1 \\ 1 & -1 \end{bmatrix}$$

$\delta_{Gfst}$  and  $T_{hg}$  are given by the feedback linearization control law.  $T_{hdf}$  ( $= \Delta T_h$ ) is determined from Eq.(10).

The flight condition chosen is that altitude is 6080(m) and airspeed 205(m/sec). At the nominal trim point,  $\alpha = 2.5(\text{deg})$ ,  $\theta = 2.5(\text{deg})$ ,  $T_h(x4) = 1.56 \times 10^5(\text{N})$ ,  $\delta_{stL} = \delta_{stR} = .5(\text{deg})$ , and other control surface angles:0(deg).

Besides, the following conditions are assumed. Time constants: 2(sec) for the stabilators, .1(sec) for the other surfaces, and 5(sec) for the engines. The deflection limits:  $\pm 20(\text{deg})$  for the stabilators and  $\pm 30(\text{deg})$  for the other surfaces. The available thrust of each engine:  $0 \leq T_h \leq 7.1 \times 10^4(\text{N})$ , and  $-2 \times 10^4 \leq \Delta T_h \leq 2 \times 10^4(\text{N})$ . Updating intervals: .02(sec) for the inputs to the actuators, 1(sec) for those to the engines, .05(sec) for the estimated parameters, .05(sec) for the control parameters. The initial condition:  $X(0) = [210, 21, 0, 1, 1, 0, 0, 0, 1]^T$ .

The following four failure cases are considered here. Failure A : the inboard right elevator and the outboard right and left elevators are stuck at .3(rad).

Failure A': in addition to Failure A, the effectiveness of the left stabilator reduces by 40%.

Failure B: the upper rudder is stuck at -.2(rad) and the effectiveness of the lower rudder reduces by 50%.

Failure B': in Failure B, the effectiveness of the lower rudder becomes 0.

The investigated cases are summarized in TABLE 1.

TABLE 1 Simulation Cases

Case	Failure	$\Delta \delta_{s,L}, \Delta \delta_{s,R}(\text{deg})$	$\Delta T_h(\text{N})$
1	A	.0, .0	0
2	A	-4.24, -4.35	0
3	A'	-4.24, -4.35	0
4	B	.858, -.858	0
5	B	.858, -.858	$-2 \times 10^4$
6	B'	.858, -.858	$-2 \times 10^4$
7	B'	-11.46, 11.46	$-2 \times 10^4$

Case 1: In this case, the flight control system is restructured using the fast control surfaces only. The slow effectors, i.e., the stabilators, are not used. Figure 2 shows the results. The aircraft dives, rolling as much as 180(deg). It falls into out of control, and eventually crashes to the ground around 40(sec) after the failure. In the piece of Fig.2 depicting the roll angle response, the reference output changes abruptly at 23(sec). It is because the reference trim value,  $\phi^*(\infty)$ , is changed so that  $|\phi(t) - \phi^*(\infty)|$  can be less than 180(deg).

Case 2: By contrast, as Fig.3 shows, the aircraft recovers a level flight. It means that the stabilators counteract the disturbance caused by the stuck elevators.

Case 3: This case is taken to see the performance when the nominal parameters in Eq.(9) or (10) have changed. The results shown in Fig.4 indicate that the effects of the parameter change can be accommodated by adjusting the control parameters for the fast effectors. Though it takes more time to trim the aircraft than in Case 2, a level flight is attained in spite of using the wrong parameters.

Case 4 and Case 5: While in Case 4 only the stabilators are used to counteract the rudder jam, in Case 5 both

stabilators and differential thrusts are used. In either case, as Fig.5 and Fig.6 show, the aircraft recovers a level flight. However, convergence of the outputs in Case 4 is slower than that in Case 5. Besides, while the sideslip angle does not converge to 0(deg) in Case 4, it does in Case 5. And the deflection angles of the control surfaces in Case 5 are smaller than those in Case 4. It means that in Case 5 the more control power is left after the failure accommodation. In Failure B, displacement of the stuck rudder is so large that the required differential thrust exceeds the limit,  $-2 \times 10^4(\text{N})$ . However, the differential thrust, which is not enough, improves the performance of the RFCS.

Case 6 and Case 7: In the above two cases, it is because the lower rudder, whose effectiveness reduces by half, is available that the level flight can be recovered. In Failure B', however, the effectiveness becomes 0. So, the yawing moment caused by the stuck rudder cannot be canceled by any means. In fact, Fig.7 shows that the aircraft loses control and crashes to the ground at about 47(sec) after the failure. Thus, the control law given by Eqs.(9) and (10) cannot save the aircraft. Considering aircraft dynamics, first the stuck rudder produces the positive yawing moment and the negative rolling one directly. But next the yawing motion generates the large positive rolling moment resulting from the lift difference between the left and the right wings. As Fig.7 shows, while the sideslip angle is not so large, the roll angle increases up to about 150(deg). Note that Eq.(8) gives the stabilator angle to counteract the negative rolling moment caused by the rudder jam, but unfortunately it results in accelerating the positive rolling. As seen from the results, the effect of the rudder jam is more serious in the rolling stability. Therefore, when failures produce large yawing moment and it cannot be canceled, some way to counteract the rolling moment must be taken. In Case 7, the stabilators are driven to produce the negative rolling moment. The angles are given appropriately. As seen from Fig.8, the aircraft motions do not diverge, though they are not settled perfectly. The responses can be improved by changing the desired trim point. It is expected that a trim point with a negative sideslip angle and a negative roll angle will be good. In fact, given, for example,  $\beta^*(\infty) = -.06(\text{rad})$  and  $\phi^*(\infty) = -.2(\text{rad})$ , the better time responses, which are shown in Fig.9, are obtained.

## CONCLUSION

This paper presents a way to accommodate failures affecting aircraft dynamical characteristics, especially control surface jam. The point of the way is to use the slow effectors, such as the stabilators or the engines, in the feedforward manner. It is desirable to apply the way particularly to large scale airliners. The simulation results indicate the performance of the RFCS. In some cases of control surface jam, the aircraft cannot recover without using the stabilators. Although the inputs to the slow effectors are determined using the nominal parameters, the effects of parameter change can be accommodated by adjusting the control parameters for

the fast surfaces. In the case of rudder jam, if the remaining control surfaces and the differential thrusts are to cancel the moments produced by the stuck rudder, using the engine control as well improves the time responses and reduces the deflection angles of the control surfaces. If not, however, the aircraft starts the large rolling motion following the yawing one. In that case, the stabilators should be used to damp the induced rolling motion instead of trying to directly cancel the moments caused by the stuck rudder. Unfortunately, the proposed control law for the stabilators does not give such inputs, because it does not take into account the dynamical effects which failures have on the aircraft motions. However, the results of Case 7 mean that there is a way to save the aircraft, though it is not given yet in the form of a control law. Finally let us mention the selection of the desired trim point. Can the aircraft be trimmed at the point? And if possible, can it reach the point using the remaining control effectors? These problems are also pointed out by Wagner(1991). The results shown in Case 7 illustrate the importance of selecting the trim point adequately. How to find the best trim point for impaired aircraft will be one of the most difficult questions in RFCS design.

#### REFERENCES

Anderson, J. and Clark, C. (1988). Reconfigurable flight

- control system simulation. *Aerospace Simulation, the Society for Computer Simulation*, pp.89-101.
- Heffley, R.K. and Jewell, W.F. (1972). Aircraft handling qualities data, section IX. *NASA CR-2144*, pp. 212-234.
- Huber, R.R. and McCulloch, B. (1984). Self-repairing flight control system. *SAE Technical Paper Series*, 841552, 1-20.
- Ochi, Y. and Kanai, K. (1991). Design of restructurable flight control systems using feedback linearization. *AIAA, J. of Guidance, Control and Dynamics*, Vol. 14, 903-911.
- Ochi, Y. (1991). Application of feedback linearization method in a digital restructurable flight control system. *Proc. of AIAA Guidance, Navigation and Control Conf.*, pp. 984-992(also to appear in *AIAA J. of Guidance, Control and Dynamics*).
- Stewart, J.F. and Shuck, T.L. (1990). Flight-testing of the self-repairing flight control system using the F-15 highly integrated digital electronic control flight research facility. *AIAA-90-1321, Proc. of 5th Bi-annual Flight Test Conf.*, pp.1-13.
- Wagner, E.A. (1991). Onboard automatic aid and advisory for pilots of control-impaired aircraft. *AIAA, J. of Guidance, Control and Dynamics*, Vol.14, 823-833.
- Weiss, J.L., Looze, D.P., Eterno, J.S., and Ostroff, A.J. (1986). Simulation results of automatic restructurable flight control system concept. *Proc. of AIAA Guidance, Navigation, and Control Conf.*, pp.190-197.

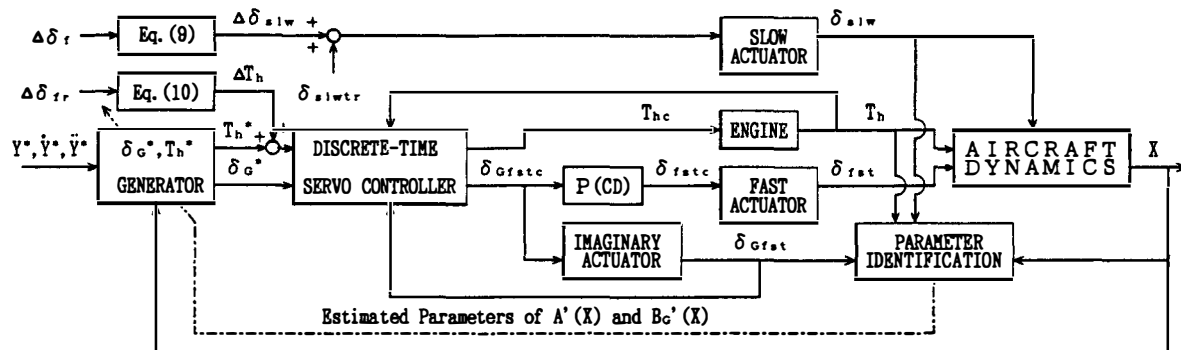


Fig. 1 Block diagram of the RFCS

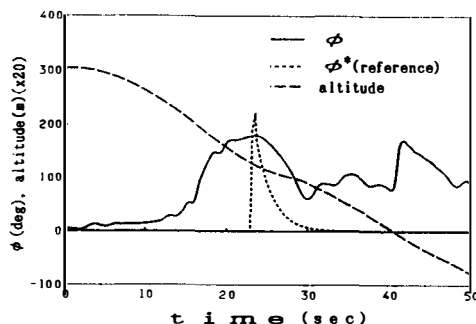
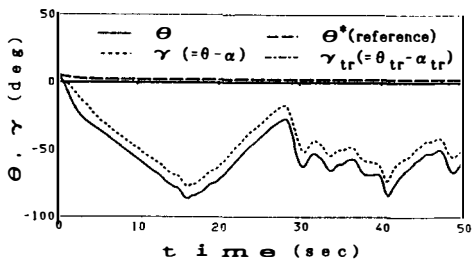


Fig. 2 Time responses without using the stabilizers(Case 1:Failure A)

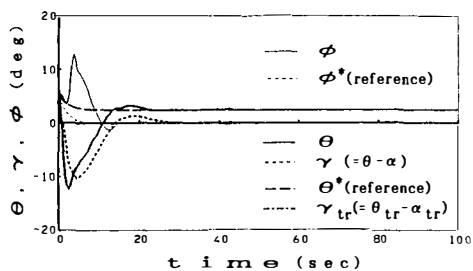


Fig. 3 Time responses using the stabilators(Case 2:Failure A)

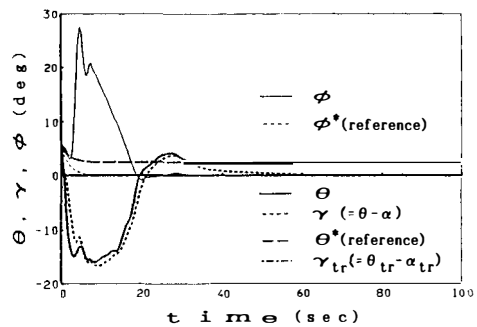


Fig. 4 Time responses using the stabilators(Case 3:Failure A')

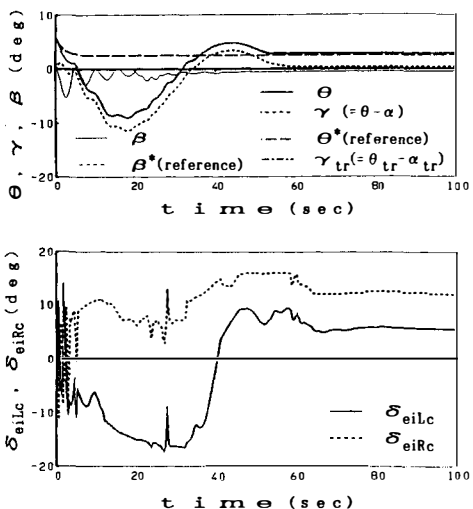


Fig. 5 Time responses using the stabilators(Case 4:Failure B)

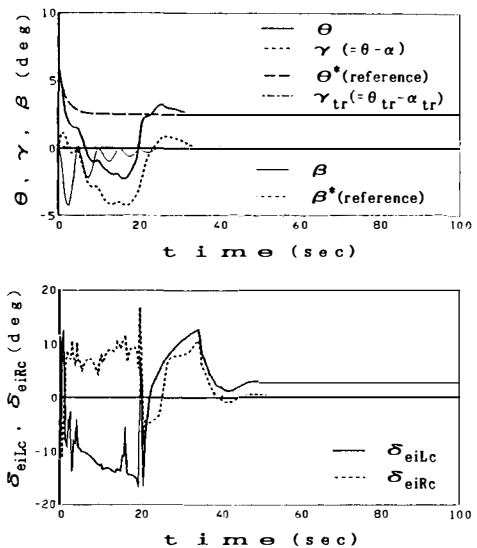


Fig. 6 Time responses using the stabilators and the dif.thrust (Case 5:Failure B)

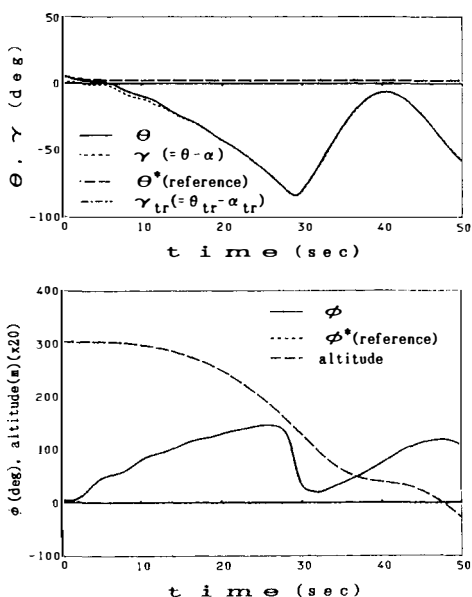


Fig. 7 Time responses using the stabilators and the dif.thrust (Case 6:Failure B')

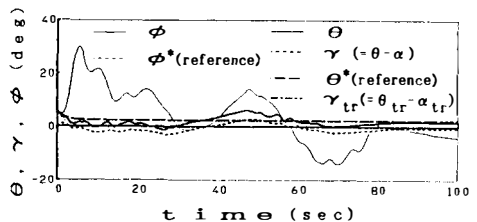


Fig. 8 Time responses using the stabilators and the dif.thrust (Case 6:Failure B',nominal trim point)

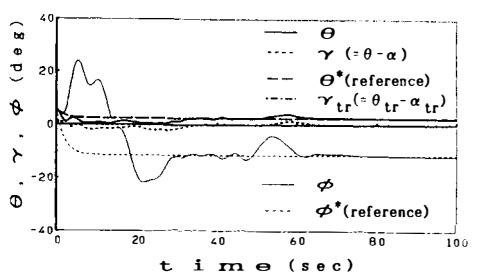


Fig. 9 Time responses using the stabilators and the dif.thrust (Case 6:Failure B',new trim point)

## USE OF OPTIMAL INTEGRAL CONTROL TO RESTORE TRIM IN A RECONFIGURABLE FLIGHT CONTROL SYSTEM

D. McLean and S. Aslam-Mir

*Department of Aeronautics and Astronautics, University of Southampton, Southampton, UK*

### ABSTRACT

**Description of State-of-the-Art Features.** In a reconfigurable flight control system actuator or control surface failures are detected from output signals obtained from the system's motion sensors. When such a failure occurs the control law of the flight control system is reconfigured in a manner that results in the aircraft retaining an acceptable degree of control and handling. The reconfiguration is achieved by arranging for the new control law to use, sometimes in a manner different from custom, all the other appropriate serviceable actuators and control surfaces. In practice, such reconfiguration schemes have greater effectiveness when used in aircraft which possess much greater control freedom than is usually found in conventional aircraft. On fighter aircraft there are generally more control surfaces with a capacity to act independently, differentially, or collectively. The motion of such types of aircraft may be coupled quite strongly so that the loss of a single control can have significant effects on the resulting closed-loop motion. In this paper the proposed reconfiguration system is developed for a generic fighter aircraft with eight control surfaces and whose lateral and longitudinal motion is to be controlled simultaneously.

First, a baseline AFCS is studied and some typical responses from such a system for combinations of control surface failure, and for different actuator failures, are presented to provide some results against which to compare the performance of the reconfigurable flight control system in response to the same failures. The reconfiguration scheme does not employ the control distribution technique proposed in some early papers (1, 2 & 3) because, in certain failure conditions, its use can lead to an

unstable AFCS. Instead a scheme involving a weighted control distribution was used (4, 5) to achieve superior reconfiguration performance, even when the failures occurred in conditions of moderate atmospheric turbulence.

**Description of the New Contributions.** From the results obtained with the reconfiguration system it became evident that in using different control surface deflections to recover aircraft control, the aircraft did not recover to the original trim condition. Work was carried out to improve the baseline AFCS by modifying its control law to use optimal integral control which was beneficial in removing the steady-state errors whenever control surface or actuator failures occurred. Naturally, the effects of such failures on the performance of the new baseline AFCS were greater. The control distribution matrix was then re-designed and the resulting reconfiguration scheme was studied. Acceptable flying qualities were achieved with this system even in the presence of several simultaneous failures and atmospheric gusts, without loss of the trimmed state for most failure cases. An extensive investigation of the fullest extent of the system's capacity for reconfiguration was also undertaken. A summary is given of the results obtained which showed that when as many as five of the eight control surfaces had failed simultaneously, reconfiguration could still be achieved. A greater number of simultaneous surface failures resulted, in almost every case, in loss of control of the aircraft.

### KEYWORDS

Optimal control, aerospace control, control systems design.

## INTRODUCTION

So necessary to the achievement of acceptable flying qualities in modern combat aircraft are automatic flight control systems (AFCS) that it is necessary to arrange that any failure of such AFCS does not impair, to any significant degree, the aircraft's ability to be flown safely. To date such arrangements have involved the use of hardware redundancy in which three, or even four, functionally-identical channels of flight control have been used. Although it has been usual to employ dissimilar methods of generating the flight control law, to avoid any common-mode failures, the required degree of reliability for actuators and sensors has been achieved by simple replication of identical types. Such an approach to achieving the required reliability is expensive in weight and cost, and recourse to analytical redundancy techniques is now being considered to avoid that expense. However, the problem of assuring acceptable flying qualities in the event of a failed control surface, or defective or inoperative actuator, has to be approached by providing some form of reconfigured control.

By detecting from the output signals of the motion sensors, which are used as the feedback signals in the AFCS, that an actuator, or control surface, or combinations of these, has failed, the established control law is reconfigured to make use of the remaining serviceable actuators and control surfaces to retain acceptable control of the aircraft. In practice, such reconfiguration can only be achieved in aircraft which have already been designed to have much greater control freedom than is usual on conventional aircraft. On combat aircraft with a reconfigurable AFCS there is a greater number of control surfaces which can be made to act independently, differentially or collectively. Since the longitudinal and lateral motion of such combat aircraft can be strongly coupled, the loss of one control can have a significant effect on the aircraft's motion, although not every loss of control has an important impact on the flying qualities. When reconfiguration is achieved, the resulting control action must achieve at least level 3 flying qualities to ensure the safety of the aircraft. However, the types of reconfiguration so far proposed<sup>1,2,3</sup> in the literature even when successful, usually result after a failure has been detected in the reconfigured aircraft failing to return to the trimmed state which existed prior to the failure. Such a change of trim can add

significantly to a pilot's difficulties in flying a damaged aircraft with a reduced level of flying quality.

This paper will deal with a proposed reconfiguration control scheme, with optimal integral control, which will result in the damaged aircraft being successfully reconfigured at its former trim state.

## AIRCRAFT DYNAMICS

A sketch of the combat aircraft dealt with is shown in Figure 1. It has five control surfaces; the control inputs available are listed below.

### Longitudinal control

- |                    |                                   |
|--------------------|-----------------------------------|
| $\delta_{S_{SYM}}$ | symmetrical stabilator deflection |
| $\delta_{LEF}$     | leading edge flap deflection      |
| $\delta_{TEF}$     | trailing edge flap deflection     |

### Lateral control

- |                     |  |
|---------------------|--|
| $\delta_{S_{DIFF}}$ | differential stabilator deflection         |
| $\delta_{LEF_D}$    | differential leading edge flap deflection  |
| $\delta_{TEF_D}$    | differential trailing edge flap deflection |
| $\delta_A$          | aileron                                    |
| $\delta_R$          | rudder                                     |

The small perturbation, linear equations of motion, for a stability axis system, can be expressed in the form (McLean, 1990)

$$\dot{x} = Ax + Bu \quad (1)$$

where

$$u' = \begin{bmatrix} \delta_{S_L} \delta_{S_R} \delta_{LEF_L} \delta_{LEF_R} \delta_{TEF_L} \\ \dots \\ \dots \delta_{TEF_R} \delta_{A_L} \delta_{A_R} \delta_{R_L} \delta_{R_R} \end{bmatrix} \quad (2)$$

and

$$x' = \begin{bmatrix} u & w & q & \theta & v & r & p & \phi \end{bmatrix} \quad (3)$$

The state variables represent changes in the following motion variables: forward velocity, vertical velocity, pitch rate, pitch attitude, sideslip velocity, roll rate, yaw rate and roll attitude. These are denoted by  $u$ ,  $w$ ,  $q$ ,  $\theta$ ,  $v$ ,  $r$ ,  $p$  and  $\phi$  respectively. A number of motion

variables were of particular interest and were chosen as output variables,  $y_i$ .

The output equation was given by

$$y = Cx + Du \quad (4)$$

in which

$$y' = \begin{vmatrix} q & n_{y_{cg}} & \alpha & r & p & n_{y_{cg}} & \phi \end{vmatrix} \quad (5)$$

$n_{z_{cg}}$  and  $n_{y_{cg}}$  denote the normal and lateral load factors at the aircraft's c.g.  $\alpha$  denotes the angle of attack.

The corresponding matrices  $A$ ,  $B$ ,  $C$  and  $D$  are shown in Figure 2.

The basic aircraft is stable and has good basic longitudinal flying qualities although the damping ratio of the short period mode (0.35) needs augmenting if pitch attitude control is to be used. The flying qualities related to the lateral motion are excellent: the Dutch roll mode is acceptably damped, (Chalk et al, 1969), the rolling subsidence mode is very rapid, and the spiral mode is very slow and stable.

#### RECONFIGURABLE FLIGHT CONTROL SYSTEMS

A full state feedback control system, designed on the basis of obtaining a solution to a linear quadratic output regulator problem, for which the state and control weighting matrices  $Q$  and  $G$  were selected as indicated in eq.(6) and (7), was used as the baseline FCS.

$$Q = \text{diag}(200, 7.0, 7.0, 10.0, 1.0, 6.0, 1.0) \quad (6)$$

and

$$G = \text{diag}(1, 1, 100, 100, 50, 50, 5, 5, 10, 10) \quad (7)$$

The dynamic response of the optimal baseline FCS was entirely acceptable, but in the event of a failure of the right stabilator, which integrated up to a level of 0.5 radians in about 2.5 seconds and then stuck at the limit of deflection, the dynamic responses for forward velocity, pitch attitude, yaw rate and bank angle are shown in Figure 3. Note how there are steady state values of change in forward velocity,  $u$ , bank angle,  $\phi$ , pitch

attitude  $\delta$  and yaw rate,  $r$ . The optimal baseline FCS is unable to maintain the aircraft's flight path in the event of such a stabilator failure. Using a reconfiguration scheme based upon weighted control distribution (Huang, 1988 and McLean & Aslam-Mir, 1991) in which the control law is expressed as:

$$u = K_{D_o} K_{FB} x \quad (8)$$

where  $K_{D_o}$  is the control distribution matrix, and  $K_{FB}$  is the feedback control matrix obtained as a result of solving the optimal control problem for the undamaged aircraft. For perfect reconfiguration it is necessary that

$$B_1 u_1 = B_o u \quad (9)$$

where  $B_1$  is the driving matrix of the aircraft corresponding to the operative controls,  $B_o$  is the driving matrix of the undamaged aircraft,  $u_1$  is the control vector corresponding to the remaining serviceable control inputs, and  $u$  is the complete control vector. With the use of a weighting matrix,  $Z$  to penalize large or persistent errors between the undamaged and reconfigured responses, and another,  $M$ , to constrain the amplitude of the elements of the control distribution matrix,  $K_1$ , minimization of the performance index,  $J$ , viz:

$$J = \left( B_1 K_{D_1} - B_o K_{D_o} \right)^T Z \left( B_1 K_{D_1} - B_o K_{D_o} \right) \dots \dots + K_{D_1}^T M K_{D_1} \quad (10)$$

results in the optimal control distribution matrix:

$$K_{D_1} = \left( B_1^T Z B_1 + M \right)^{\dagger} B_1^T Z B_o K_{D_o} \quad (11)$$

The results of using such a reconfiguration distribution matrix with the optimal baseline FCS can be seen from the dashed curves in Figure 3. Note how much reduced are the excursions of the motion variables  $u$ ,  $\theta$ ,  $r$  and  $\phi$ . Note too how much the control action of the left stabilator has had to be increased. However, although the reconfiguration scheme has provided good control of the aircraft in the presence of the failed right stabilator, there still remain finite steady state errors (see the bank angle and yaw rate

responses, for example) which correspond to a failure of the reconfiguration system to restore the aircraft to its original trim state. Such a failure can add significantly to a pilot's workload in the flight condition where a control surface has failed. It is necessary to remove it; the proposed method is to use integral control.

Suppose a new vector,  $z$ , is defined as:

$$z = \begin{bmatrix} \dot{x} \\ y \end{bmatrix} \quad (12)$$

then

$$\dot{z} = \begin{bmatrix} \ddot{x} \\ \dot{y} \end{bmatrix} = \begin{bmatrix} A & O \\ C & O \end{bmatrix} \begin{bmatrix} \dot{x} \\ y \end{bmatrix} + \begin{bmatrix} B \\ D \end{bmatrix} u \quad (13)$$

Let

$$v = \begin{bmatrix} \cdot \\ u \end{bmatrix} \quad (14)$$

then

$$\dot{z} = \tilde{\mathbf{A}} z + \tilde{\mathbf{B}} v \quad (15)$$

If the performance index to be minimized is chosen to be

$$J = \frac{1}{2} \int_0^{\infty} (z^T Q z + v^T G v) dt \quad (16)$$

it can be shown<sup>(1b)</sup> that

$$u^0 = K_A x + K_B c + K_c \int_0^t y(\lambda) d\lambda \quad (17)$$

where  $c$  represents the initial conditions of the integrators (taken as zero in this work).

Use of such an optimal integral control produces a basic closed loop FCS which operates satisfactorily, but which, in the presence of the 'ramp up' failure of the right stabilizer, produces the dynamic response  $S$  shown in Figure 4. Notice how reduced, but finite, the steady state errors are in the presence of the failure. Use of a new control distribution matrix, based on the existence of the integral terms, resulted in the responses shown by the dashed line curves of Figure 4. Note how the new reconfiguration scheme

has removed the steady state errors and has restored the aircraft to its trimmed state, even in the presence of the serious control surface failure, and has achieved this response in a very stable manner. The cost of achieving this performance is the increased control activity - see left stabilator deflection in Figure 4

## CONCLUSIONS

The weighted distribution matrix technique is effective in restoring safe flight to a control damaged aircraft. However, such a technique cannot restore the reconfigured aircraft to its original trimmed state which can add to a pilot's difficulties in a damaged aircraft. The use of optimal integral feedback control, allied to control distribution, can achieve satisfactory dynamic response with complete restoration of the aircraft to its original trimmed state.

## ACKNOWLEDGEMENTS

This research was carried out with the generous assistance of a grant, reference GR/E/4449.9, from the Science and Engineering Research Council of the United Kingdom.

## REFERENCES

- (1) Raza, S.J. (1984). "Use of the Pseudo-inverse for the Design of a Reconfigurable Flight Control System." M.S.Thesis, NASA Star Theses, Issue 16, AFIT/GAE/AA/81D-23
- (2) Raza, S.J. and J.T. Silverthorne. (1985). "Use of the Pseudo-Inverse for the Design of a Reconfigurable Flight Control System." Proc. 1985 AIAA Guid. & Contr. Conf., 349-356.
- (3) Rattan, K.S. (1985). "Evaluation of the Control Mixer Concept for Reconfiguration of Flight Control Systems." Proc. NAECON, Dayton, OH, May 1985, 560-569.
- (4) Huang, C.Y. (1988). "Analysis and Simulation of a Control Distributor Concept for a Control Reconfigurable Aircraft." Proc. J.A.C.C. 1988, Paper 88-4139-99.
- (5) McLean, D. and S. Aslam-Mir. (1991). "Reconfigurable Flight Control Systems." In IEE Conf. Proc. CP 332, "Control 91", 234-242.
- (6) McLean, D. (1990). Automatic Flight Control Systems. Prentice Hall, London, 41-50(a), 248-249(b)
- (7) Chalk, C.R. et al. (1969). "Background Information and User Guide for MIL-F-8785B(ASG)." AFFDL-TR-69-72, USAF WPAFB, Dayton, OH. U.S.A.

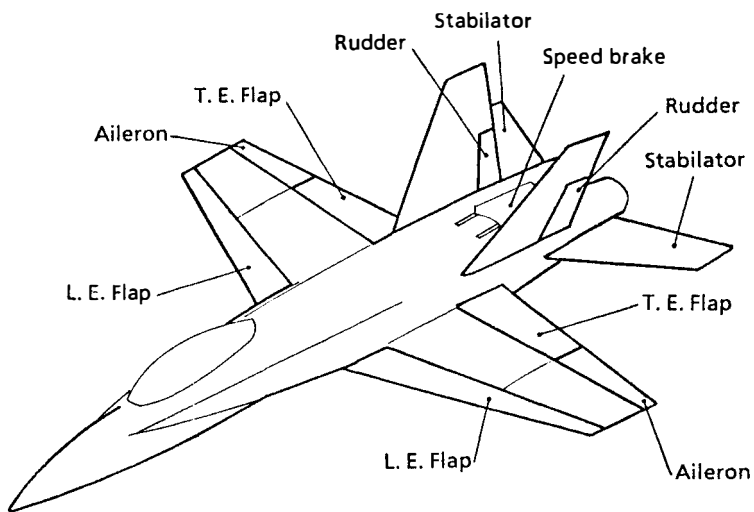


Figure 1: Combat Aircraft Control Surfaces.

$$\begin{aligned}
 \mathbf{A} &= \begin{bmatrix} -0.0133 & -0.0173 & -29.2 & -32.2 & 0 & 0 & 0 & 0 \\ -0.0728 & -1.14 & 636 & -1.46 & 0 & 0 & 0 & 0 \\ 0 & -0.0109 & -0.81 & 0.5 & 0 & 0 & 0 & 0 \\ 0 & 0 & 1 & 0 & 0 & 0 & 0 & 0 \\ 0 & 0 & 0 & 0 & -0.2440 & -645 & 29.5 & 32.2 \\ 0 & 0 & 0 & 0 & 0.70 & -0.2170 & -0.0153 & 0 \\ 0 & 0 & 0 & 0 & -0.0291 & 0.7010 & -3.12 & 0 \\ 0 & 0 & 0 & 0 & 0 & 0 & 1 & 0 \end{bmatrix} \\
 \mathbf{B} &= \begin{bmatrix} 0 & 0 & 0 & 0 & 0 & 0 & 0 & 0 & 0 & 0 \\ -5.7128 & -5.7128 & 18.4793 & 18.4793 & -13.0673 & -13.0673 & 0 & 0 & 0 & 0 \\ -6.9075 & -6.9075 & -14.9897 & -14.9897 & 9.4029 & 9.4029 & 0 & 0 & 0 & 0 \\ 0 & 0 & 0 & 0 & 0 & 0 & 0 & 0 & 0 & 0 \\ 0.2100 & -0.2100 & 0 & 0 & 0 & 0 & 0 & 0 & 15.1850 & 15.1850 \\ -0.5736 & 0.5736 & 0 & 0 & 0.3270 & -0.3270 & -0.0044 & 0.0044 & -0.2325 & -0.2325 \\ -0.3950 & 0.3950 & 0 & 0 & -2.4900 & 2.4900 & -25.2000 & 25.2000 & 20.6500 & 20.6500 \\ 0 & 0 & 0 & 0 & 0 & 0 & 0 & 0 & 0 & 0 \end{bmatrix} \\
 \mathbf{C} &= \begin{bmatrix} 0 & 0 & 1 & 0 & 0 & 0 & 0 & 0 \\ -0.0023 & -0.0354 & -0.3236 & -0.0453 & 0 & 0 & 0 & 0 \\ 0 & 0.0015 & 0 & 0 & 0 & 0 & 0 & 0 \\ 0 & 0 & 0 & 0 & 0 & 1 & 0 & 0 \\ 0 & 0 & 0 & 0 & 0 & 0 & 1 & 0 \\ 0 & 0 & 0 & 0 & -0.0076 & 0.0440 & 0.9162 & 0 \\ 0 & 0 & 0 & 0 & 0 & 0 & 0 & 1 \end{bmatrix} \\
 \mathbf{D} &= \begin{bmatrix} 0 & 0 & 0 & 0 & 0 & 0 & 0 & 0 & 0 & 0 \\ 0.1774 & 0.1774 & 0.6017 & 0.6017 & -0.4068 & -0.4068 & 0 & 0 & 0 & 0 \\ 0 & 0 & 0 & 0 & 0 & 0 & 0 & 0 & 0 & 0 \\ 0 & 0 & 0 & 0 & 0 & 0 & 0 & 0 & 0 & 0 \\ 0 & 0 & 0 & 0 & 0 & 0 & 0 & 0 & 0 & 0 \\ 0.0065 & -0.00650 & 0 & 0 & 0 & 0 & 0 & 0 & 0.4716 & 0.4716 \\ 0 & 0 & 0 & 0 & 0 & 0 & 0 & 0 & 0 & 0 \end{bmatrix}
 \end{aligned}$$

Figure 2: **A**, **B**, **C**, and **D** Matrices.

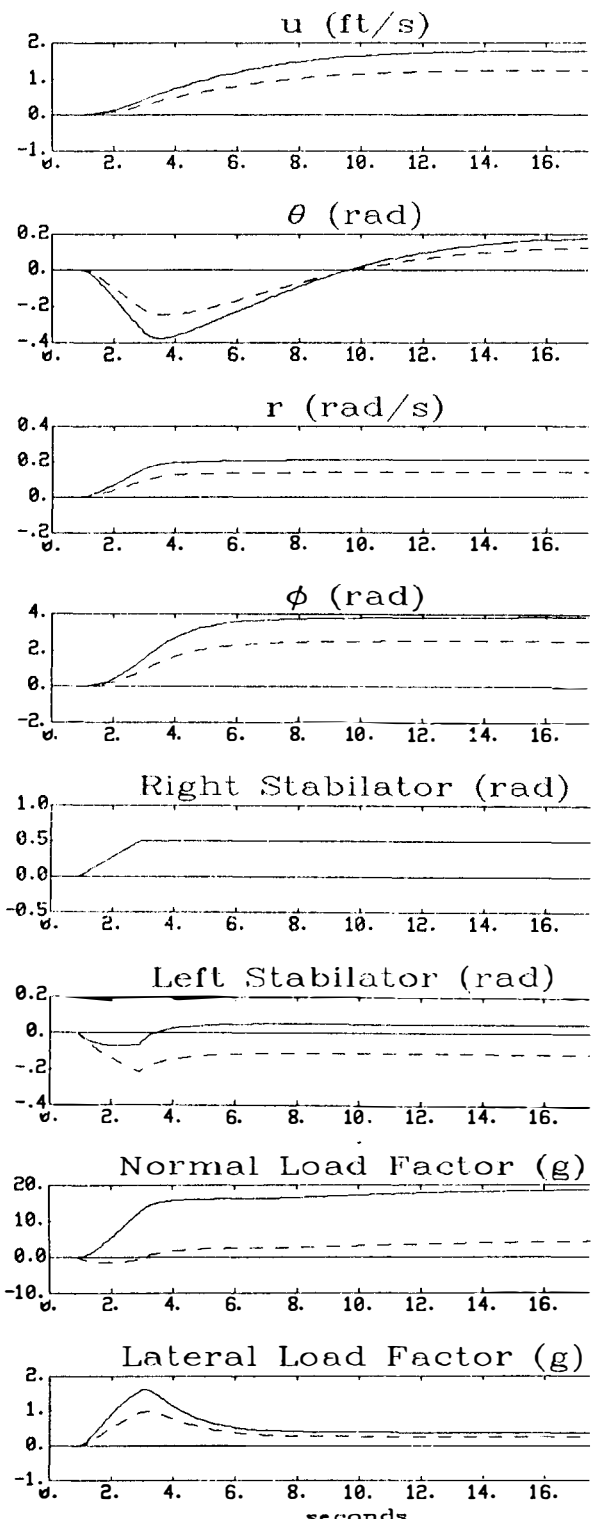


Figure 3: Non-Integral Controller Results.

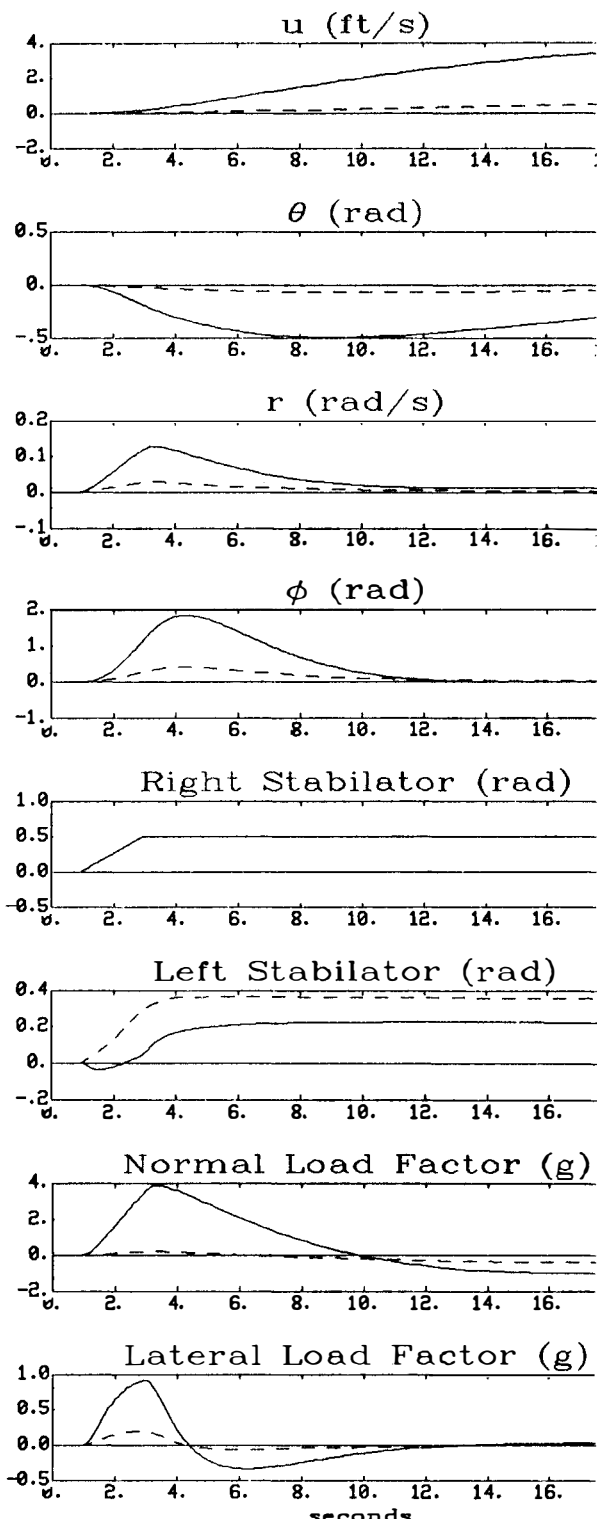


Figure 4: Integral Controller Results.

# ADAPTIVE ON-LINE SYSTEM IDENTIFICATION OF AEROSPACE STRUCTURES USING MX FILTERS

J. Melcher

Deutsche Forschungsanstalt für Luft- und Raumfahrt (DLR), Institut für Aeroelastik, Bunsenstr. 10,  
3400 Göttingen, Germany

**Abstract.** This paper describes a new method of system identification of dynamic structures, which is based on an adaptive signal processing that considers structural dynamic aspects and can thus be realized as an on-line procedure. The principle, performance, and realization of the new technique are shown. System identification experiments on a "smart" structure, a carbon fiber reinforced epoxy beam with embedded NiTi wires, demonstrates that the structural parameters to be identified are known each time, even in cases where they are time-varying. Further applications of the new tool are given in the areas of structural health monitoring and controller observations.

**Keywords.** System identification, digital signal processing, adaptive systems, MX filter, shape memory alloys, experiments.

## INTRODUCTION

With the advent of the capability to place sophisticated large flexible structures into orbit, new challenges are evolving. The performance of space structures in future missions can be improved decisively by using active control technologies to design them as so-called "smart" or "adaptive" structures. A survey of European activities and programs in adaptive structures was given by Breitbach (1991) with a special focus on the DLR program ARES (Actively Reacting Elastic Structures). It is well-known that actively controlled systems actually have new eigenproperties that are functions of the actuator control forces and, in cases of adaptive controllers, depend on the external disturbances. These system changes are the consequences following the strategies of shape control, vibration suppression, or positioning control. The fundamental objectives to decrease mass and energy needs also require for efforts to be focused on the development of new tools for the design and development of adaptive structures. One essential and well-tried discipline using this new design strategy is system identification.

In the past, researchers have investigated system identification of aerospace structures with embedded actuators and sensors, e.g. Chen and Garba (1986). Unfortunately, all of the previously developed methods were off-line definitions. An overview of these is given by Füllkrug (1988). For adaptive structures, however, on-line methods must be used that are defined by properties where the structural parameters are calculated during the measurements and where the real-time condition is fulfilled, i.e. all computational instructions to calculate the neces-

sary mathematical operations are done within the sampling rate.

The most promising way to develop an on-line system identification tool seems to be the use of adaptive filter theory, which is discussed by Widrow and Stearns (1985) and by Haykin (1991), among others. The basic class of adaptive filtering applications dealing with identification is the adaptive modeling as shown in Fig. 1. An adaptive filter system is used as a model that represents the best estimation for a structure to be identified in correspondence with the responses.

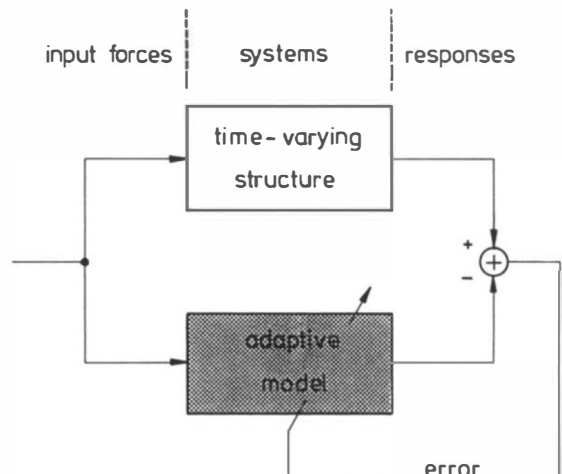


**Fig. 1.** Adaptive modeling for the on-line system identification applications.

Both the structure and the filter are fed identically by external forces. An adaptation algorithm calculates the best model parameters (in this case, filter coefficients) to minimize the error signal, which is the difference between the measured and adapted response signals. Now, new problems arise: which digital filter forms, types, and adaptive algorithms are sufficient to allow the on-line calculation of structural parameters by transformations from the filter coefficients?

Thus, the intention of this paper is to propose an adaptive filtering technique that overcomes the above-mentioned requirements and is able to identify the eigenfrequencies and damping values of each structural mode in an on-line procedure. The first step to solve these problems for single-degree-of-freedom (SDOF) applications was proposed by Melcher (1991) using MX filters. The extension of this technique to multi-degrees-of-freedom (MDOF) applications are contents of a German patent of the DLR (1992).

In the subsequent chapters, the basic idea of the filtering technique - the MX filter system - is illustrated, and its performance is experimentally demonstrated. Further applications of this brand-new technique are also presented.

### THE NEW METHOD: ON-LINE SYSTEM IDENTIFICATION USING MX FILTERS

The adaptive model shown in Fig. 1 consists of two components: the so-called MX and the MX-LMS filter systems (see Fig. 2 for the latter). These parts are the main ideas of the new system identification method. The MX filter system is based on digital lattice-typed filterings and represents a linear dynamic system with any modal density. The other part of the model, the MX-LMS filter system, includes the adaptation algorithm which influences the MX filter system by copying new or better coefficients to it. For this update, the following must be known: the input force, the MX filter system state, the actual coefficients, and, finally, the error signal containing information as to whether or not the model is already operating perfectly.

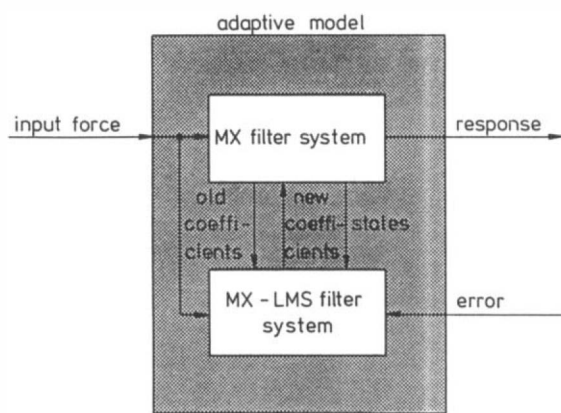


**Fig. 2.** Components of the adaptive model.

The aim of the next two sections is the comprehensive presentation of the model filter systems. It will be shown that it is possible to identify the eigenfrequencies and damping values, but it is obviously not possible to calculate the eigenvectors with the single channel version discussed here.

### The MX Filter System

The signal flow and form of the MX filter system are shown in Fig. 3. Calling it after its property (modally formulated due to the parallel form) and its appearance (cross-coupled structure), it was named MX by Melcher (1991). In the discrete form presented here, the filter is non-canonical (the number of delays  $z^{-1}$  is higher than the order of the represented transfer function) and has  $(1 + 4m)$  real coefficients, where  $m$  is the number of modes:

- the transversal coefficients  $c$ ,  $a'_i$ ,  $a''_i$  and
- the recursive coefficients  $b'_i$  with  $i \in [1, m]$ .

The functional relationship between the input samples  $f(n)$ , ( $n$  is the discrete integer time step) and the resulting output samples  $y(n)$  can be described in different ways:

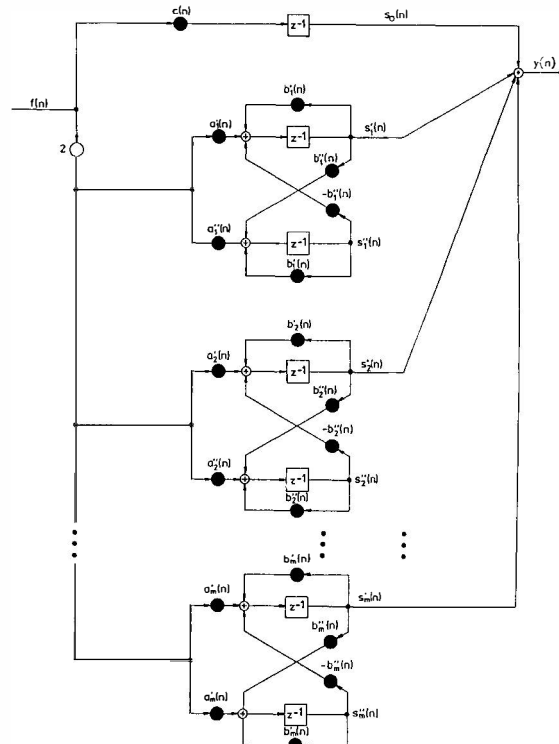


**Fig. 3.** Signal flow of the MX filter system representing  $m$  modes.  $f(n)$  is the input force signal and  $y(n)$  is the output signal.  $c(n)$ ,  $a'_i(n)$ ,  $a''_i(n)$ ,  $b'_i(n)$  and  $b''_i(n)$  are the coefficients at the time step  $n$ , and  $s'_i(n)$  and  $s''_i(n)$  are the elements of the filter state vector.

a) Description in the time domain using the MX filter difference equations:

$$s_0(n) = c(n)f(n-1)$$

$$s_i'(n) = 2a_i'f(n-1) + b_i'(n)s_i'(n-1) - b_i''(n)s_i''(n-1)$$

$$s_i''(n) = 2a_i''f(n-1) + b_i'(n)s_i''(n-1) + b_i''(n)s_i'(n-1)$$

$$y(n) = s_0(n) + \sum_{i=1}^m s_i'(n) \quad (1)$$

for all  $i \in [1, m]$ .

b) Description in the time domain using the state space formulation:

$$\mathbf{s}(n+1) = \mathbf{A}(n)\mathbf{s}(n) + \mathbf{B}(n)\mathbf{f}(n) \quad (2)$$

$$y(n) = \mathbf{C} \cdot \mathbf{s}(n)$$

with the input vector

$$\mathbf{f}(n) = f(n) \cdot [1 \ 2 \ 2 \dots 2 \ 2]^T, \quad (3)$$

the state vector

$$\mathbf{s}(n) = [s_0(n) \ s_1'(n) \ s_1''(n) \ \dots \ s_m'(n) \ s_m''(n)]^T, \quad (4)$$

the system matrix

$$\mathbf{A}(n) = \begin{bmatrix} b_1'(n) - b_1''(n) & 0 \\ b_1''(n) & b_1'(n) \\ & \ddots & \ddots & b_m'(n) - b_m''(n) \\ 0 & & & b_m''(n) & b_m'(n) \end{bmatrix}, \quad (5)$$

the input matrix

$$\mathbf{B}(n) = \begin{bmatrix} c(n) & 0 \\ a_i'(n) & a_i''(n) \\ & \ddots & \ddots & a_m'(n) & a_m''(n) \\ 0 & & & & \end{bmatrix}, \quad (6)$$

and the output vector

$$\mathbf{C}(n) = [1 \ 1 \ 0 \ 1 \ 0 \ \dots \ 1 \ 0]. \quad (7)$$

c) Description in the discrete frequency domain ( $z$ -plane):

Let  $H(z)$  be the transfer function of the MX filter system

$$H(z) := \frac{Y(z)}{F(z)}, \quad (8)$$

where  $Y(z)$  and  $F(z)$  are the  $z$ -transforms of the input and output signal

$$Y(z) = \sum_{i=-\infty}^{\infty} y(i) z^{-i} \quad (9)$$

$$\text{and } F(z) = \sum_{i=-\infty}^{\infty} f(i) z^{-i}.$$

The scalar transfer function can be calculated from

$$H(z) = \mathbf{C} [z \cdot \mathbf{I} - \mathbf{A}]^{-1} \mathbf{B} \quad (10)$$

( $\mathbf{I}$  is the identity matrix). The result is

$$H(z) = \left[ c(n) + \sum_{i=1}^m \left( \frac{a_i'(n) + ja_i''(n)}{1 - (b_i'(n) + b_i''(n))z^{-1}} + \frac{a_i'(n) - ja_i''(n)}{1 - (b_i'(n) - b_i''(n))z^{-1}} \right) \right] z^{-1} \quad (11)$$

or in a shorter form

$$H(z) = \left[ c(n) + \sum_{i=1}^m \left( \frac{a_i(n)}{1 - b_i(n)z^{-1}} + \frac{a_i^*(n)}{1 - b_i^*(n)z^{-1}} \right) \right] z^{-1} \quad (12)$$

with the substitutions

$$\begin{aligned} a_i(n) &:= a_i'(n) + ja_i''(n) \\ b_i(n) &:= b_i'(n) + jb_i''(n) \end{aligned} \quad (13)$$

for all  $i \in [1, m]$ , where the sign \* denotes complex conjugation. Eq. 12 clearly demonstrates three essential properties: the MX filter system represents only systems that can be formulated mathematically with conjugate complex pairs of residues  $a_i$  and poles  $b_i$ . Furthermore, in practice the stability of this filter system can be proved easily by taking the conditions

$$|b_i'(n)|^2 + |b_i''(n)|^2 < 1 \quad \forall i \in [1, m] \quad (14)$$

at each time step  $n$ .

Finally,  $H(z)$  is modeling a dynamic system transfer function which is multiplied with  $z^{-1}$ . This means that the structural response must be time-delayed with  $z^{-1}$  for the calculation of the error signal. The coefficient  $c(n)$  only plays an important role if accelerations are measured to yield the structural responses, see Melcher (1991).

A comparison between the modal description of the dynamic system to be identified and the model description leads to the relation between the system parameters as eigenfrequencies  $f_i$  in Hz and damping factors  $\delta_i$ , respectively, and the recursive filter coefficients

$$f_i(b'_i, b''_i) = \frac{1}{2\pi\tau} \sqrt{\frac{1}{4} \ln^2(b'^2_i + b''^2_i) + \arctan^2\left(\frac{b''_i}{b'_i}\right)} \quad (15)$$

$$\delta_i(b'_i, b''_i) = -\frac{\ln(b'^2_i + b''^2_i)}{2 \sqrt{\frac{1}{4} \ln^2(b'^2_i + b''^2_i) + \arctan^2\left(\frac{b''_i}{b'_i}\right)}}$$

for all  $i \in [1, m]$ .  $\tau$  is the sampling rate in seconds.

### The MX-LMS Filter System

When choosing the MX filter system as the model component which should include the essential properties of the unknown structure or system, the question arises: which is the algorithm of the other model component that optimizes the MX filter system respective to its response by varying the filter coefficients? Thus, the derivation and analysis of such an adaptation algorithm, the above-mentioned MX-LMS algorithm in filter realization, are the aims of this section.

The most often used cost function in adaptive signal processing, and the one to be minimized here, is the mean square error function

$$\psi(n) = E[e^2(n)] \quad (16)$$

with  $E[\cdot]$  as the statistical expectation operator and  $e(n)$  as the discrete error signal. This performance function defines a transformation from a vector space spanned by the MX filter coefficients into the space of a real scalar. The MX filter system is optimized by finding the coefficient vector

$$\mathbf{w}(n) = [c(n) \ a'_1(n) \ a''_1(n) \ b'_1(n) \ b''_1(n) \dots \ a'_m(n) \ a''_m(n) \ b'_m(n) \ b''_m(n)]^t \quad (17)$$

that minimizes the mean square error criterion.

The search for optimal values that is proposed here is the iterative method of the negative gradients

$$\mathbf{w}(n+1) = \mathbf{w}(n) - \boldsymbol{\mu} \cdot \nabla \psi(n). \quad (18)$$

In this adaptation formula, the variables are

$$\boldsymbol{\mu} = \text{diag} [\mu_c \ \mu_{a'_1} \ \mu_{a''_1} \ \mu_{b'_1} \ \mu_{b''_1} \dots \ \mu_{a'_m} \ \mu_{a''_m} \ \mu_{b'_m} \ \mu_{b''_m}] \quad (19)$$

as the diagonal matrix of convergence parameters which define the compromise between convergence accuracy and convergence rate, and

$$\nabla \psi(n) \approx \nabla e^2(n) = -2e(n) \nabla y(n) \quad (20)$$

as the estimated spatial gradient of the coefficient-dependent performance function.

Now, the MX-LMS algorithm is completely derived, calculating the derivatives of the MX filter system output  $y(n)$ . With

$$\begin{aligned} \nabla y(n) &= \left[ \frac{\partial y(n)}{\partial c} \ \frac{\partial y(n)}{\partial a'_1} \ \frac{\partial y(n)}{\partial a''_1} \ \frac{\partial y(n)}{\partial b'_1} \ \frac{\partial y(n)}{\partial b''_1} \dots \ \frac{\partial y(n)}{\partial a'_m} \ \frac{\partial y(n)}{\partial a''_m} \ \frac{\partial y(n)}{\partial b'_m} \ \frac{\partial y(n)}{\partial b''_m} \right]^t \\ &=: [\gamma(n) \ \alpha'_1(n) \ \alpha''_1(n) \ \beta'_1(n) \ \beta''_1(n) \dots \ \alpha'_m(n) \ \alpha''_m(n) \ \beta'_m(n) \ \beta''_m(n)]^t \end{aligned} \quad (21)$$

and the further substitutions

$$\begin{aligned} \alpha'_{0,i}(n) &:= \frac{\partial s_i''(n)}{\partial a'_i} \\ \alpha''_{0,i}(n) &:= \frac{\partial s_i''(n)}{\partial a''_i} \\ \beta'_{0,i}(n) &:= \frac{\partial s_i''(n)}{\partial b'_i} \\ \beta''_{0,i}(n) &:= \frac{\partial s_i''(n)}{\partial b''_i} \end{aligned} \quad (22)$$

for all  $i \in [1, m]$ , the MX-LMS algorithm becomes

$$\begin{aligned} 1) \gamma(n) &= f(n-1) \\ 2) \alpha'_i(n) &= 2f(n-1) + b'_i \alpha'_i(n-1) - b''_i \alpha''_i(n-1) \\ \alpha'_{0,i}(n) &= b'_i \alpha'_{0,i}(n-1) + b''_i \alpha''_{0,i}(n-1) \\ 3) \alpha''_i(n) &= b'_i \alpha''_i(n-1) - b''_i \alpha'_{0,i}(n-1) \\ \alpha''_{0,i}(n) &= 2f(n-1) + b'_i \alpha''_{0,i}(n-1) + b''_i \alpha''_i(n-1) \quad (23) \\ 4) \beta'_i(n) &= s'_i(n-1) + b'_i \beta'_i(n-1) - b''_i \beta''_i(n-1) \\ \beta'_{0,i}(n) &= s''_i(n-1) + b'_i \beta'_{0,i}(n-1) + b''_i \beta''_i(n-1) \\ 5) \beta''_i(n) &= -s''_i(n-1) + b'_i \beta''_i(n-1) - b''_i \beta'_{0,i}(n-1) \\ \beta''_{0,i}(n) &= s'_i(n-1) + b'_i \beta''_{0,i}(n-1) + b''_i \beta''_i(n-1), \end{aligned}$$

in Eqs. 2-5 for all  $i \in [1, m]$ . The filter realization of this algorithm, as shown in Figs. 4a and 4b, clearly illustrates that the derivation of gradient components also lead to MX filters. It should be mentioned that although the MX filter system is linear, activation of the MX-LMS filter system leads to a nonlinear adaptive model.

## EXPERIMENTS: ON-LINE IDENTIFICATION OF A TIME-VARYING STRUCTURE

The previous chapter explained the principle and analysis of the adaptive model components. Many questions concerning their performance arise. For instance, is the adaptive MX-LMS algorithm fast enough to have a change of the structure be slower than a change of the model? If so, what is the behavior of the MX-LMS filter system in the presence of more than one mode? Is the algorithm still stable, even if the cost function  $\psi$  has more than one minimum? What is a good choice of the step size parameter matrix  $\boldsymbol{\mu}$  to allow fast but sure performance? Furthermore, what happens if the number of modes to be identified is unknown?

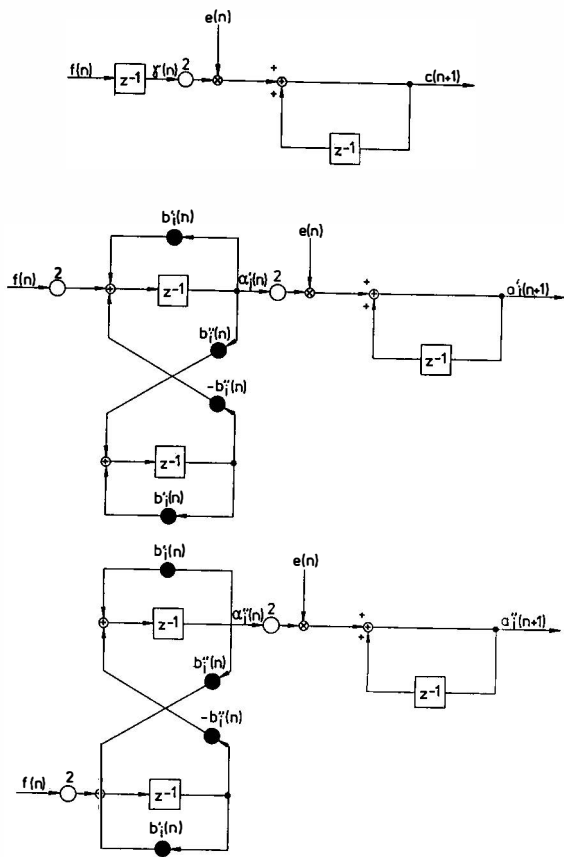


**Fig. 4a.** Components of the MX-LMS filter system calculating the MX filter system coefficients  $c(n+1)$ ,  $a'_i(n+1)$  and  $a''_i(n+1)$  for all  $i \in [1, m]$ ;  $m$  is the number of modes.

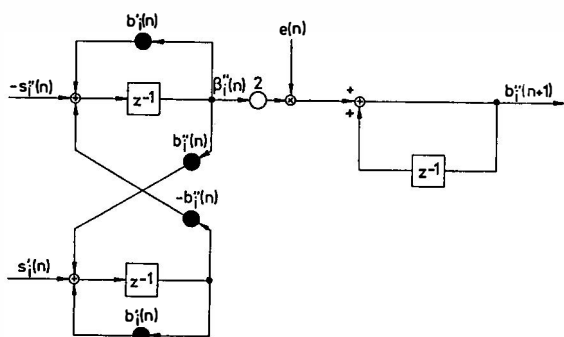
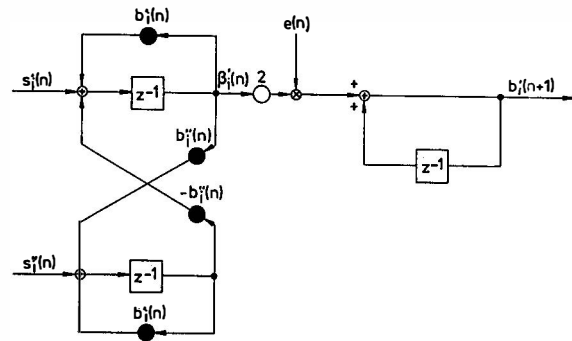


**Fig. 4b.** Further components of the MX-LMS filter system calculating the MX filter system coefficients  $b'_i(n+1)$  and  $b''_i(n+1)$  for all  $i \in [1, m]$ .

To cope with these practical aspects, special consideration is devoted to experimental investigations of the application of the proposed tool to a dynamic structure with time-varying parameters, see Fig. 5. The structural system, whose eigenfrequencies and damping factors should be identified, consists of a simple carbon-fiber-composite beam with 8 NiTi wires embedded in the neutral plane. The length of the beam in the clamped-clamped configuration is 53 cm, its thickness is 0.782 mm, and its width is 2.1 cm. The diameter of the shape memory wires is 0.385 mm. Activation of the wires by an electrical current  $I$  leads to a recovery stress that increases the bending eigenfrequencies. The performance of these active control mechanisms was studied exactly by Mooi (1992).

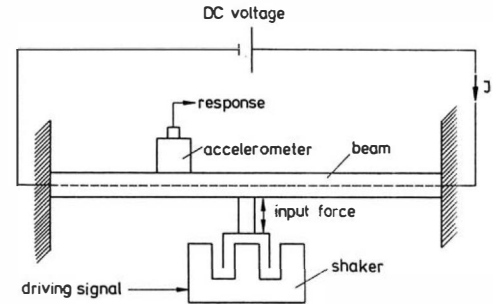


**Fig. 5.** Experimental set-up for an on-line system identification of a "smart" beam.

For transfer function measurements, a usual shaker is attached near the middle of the beam. An accelerometer is located on the left half of the beam, observing bending eigenfrequencies. Figure 6 clearly illustrates the change of the first and second bending eigenfrequencies after the current through the NiTi wires has increased from zero to 5 A. As soon as the MX-LMS algorithm was started with  $m = 2$ , both the structural and adaptive model transfer functions were approximately equal, which is an absolute precondition of an on-line system identification. This precondition was fulfilled for each time step, even in cases where the NiTi wires were heated or cooled.

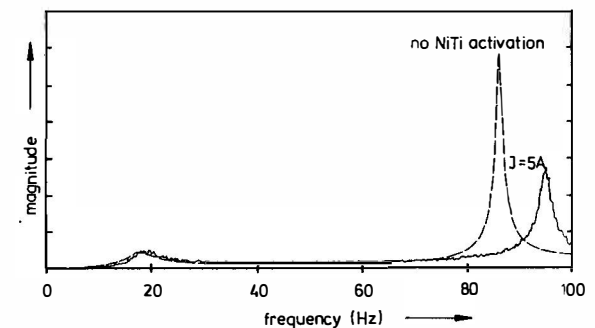


**Fig. 6.** Active control of eigenfrequencies by electrically activating the NiTi wires. The first eigenfrequency is changed by nearly 2 Hz, the second by nearly 10 Hz.

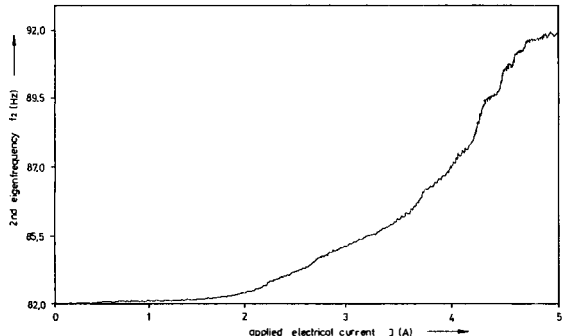


Fig. 7. On-line identified eigenfrequencies depending on electrical current through the NiTi wires.

Direct measurements of the functions  $f_1(I)$  or  $\delta_1(I)$  are available, such as  $f_2(I)$  as shown in Fig. 7, which is the result of a heating process that occurs by changing the electrical current from zero to 5 A. The MX-LMS algorithm was stable in many variations of the convergence parameter matrix  $\mu$ . Furthermore, some tests were carried out in order to understand the behavior of the model in the presence of unknown numbers of modes. The choice  $m = 1$  (the model has less modes than the structure) led to the identification of only one mode, either the first or the second bending mode, depending on the coefficient start values and therewith on the location on the six-dimensional performance surface. The choice  $m \geq 3$  has a remarkable result: two modes were identified that were distributed at all available MX filter sections. The residues of two identical model modes are half the size of the one which represented the mode in the case  $m = 2$  mentioned above.

#### CONCLUDING REMARKS AND FURTHER APPLICATIONS

The intention of this investigation was to propose an adaptive filtering technique that allows an on-line system identification of any dynamic system, especially aerospace systems in flight. The components of the new method are

- the MX filter system,
- the MX-LMS filter system, and
- a performance calculation realizing the transformations from the adapted filter coefficients to the structural parameters.

Experiments on a "smart" structure, a graphite epoxy composite beam with embedded shape memory alloy wires, clearly demonstrates the performance and facilities of this new tool: structural parameters can be identified although they are varying due to internally induced stresses. To cope with practical aspects, i.e. to have an adaptation algorithm which functions independently from the amplitude of the system's input signal, a normalized version of the MX-LMS filter system is helpful.

The use of an on-line system identification in connection with an adaptive model based on MX filters demonstrates features that imply the need for some further applications (Melcher, 1992): it justifiably gives the hope to be a powerful device for health monitoring of aerospace systems. Whenever damages change measurable structural dynamic properties, the damages can be detected by an in-flight identification. Furthermore, the proposed technique can be applied to aerospace structure optimization or to dynamic system optimization in general, e.g. the optimal design of tuned mass dampers or the optimal tuning of active or passive dynamic vibration absorbing systems. Even controllers can be optimized by using this new tool.

#### ACKNOWLEDGEMENTS

The author would like to thank Dr. E. Breitbach, Head of the DLR program ARES, for his encouragement and support of this work. A special thanks also goes to Prof. C.A. Rogers of VPI&SU, Blacksburg, VA, USA, who put the test specimen to the disposal of DLR'S ARES group.

#### REFERENCES

- Breitbach, E.J. (1991). Research Status on Adaptive Structures in Europe. *Proc. of the 2nd Joint Japan/U.S. Conference on Adaptive Structures*, Nagoya, Japan, Nov. 1991.
- Chen, J.C. and Garba J.A. (1986). System Identification for Large Space Structures Damage Assessment. *Workshop on Structural Dynamics and Control Interaction of Flexible Structures*, April 23-24, 1986, Marshall Space Flight Center, Alabama, USA.
- Füllekrug, U. (1988). Survey of Parameter Estimation Methods in Experimental Modal Analysis. *Journal of the Society of Environmental Engineers*, Vol. 27-1, March 1988.
- Haykin, S. (1991). *Adaptive Filter Theory*. Prentice Hall, Inc., Englewood Cliffs, New Jersey, USA, 2nd ed.
- Melcher, J. (1991). Synthesis of Optimized Adaptive Digital Filters for System Identification and Vibration Control. *Int'l Forum on Aeroelasticity and Structural Dynamics Combined with a One-Day Workshop on Smart Material Systems and Structures*, Eurogress Center, Aachen, Germany, June 1991.
- Melcher, J. (1992). Verfahren und Vorrichtung zur Identifikation von dynamischen Kenngrößen. German Patent of the DLR, AZ P4202578.8.
- Mooi, H. (1992). Active Control of Structural Parameters of a Composite Strip Using Embedded Shape Memory Alloy Wires. DLR Report IB 232 - 92 J 02.
- Widrow, B. and Stearns, S.D. (1985). *Adaptive Signal Processing*. Prentice Hall, Inc., Englewood Cliffs, New Jersey, USA.

## ONLINE GUIDANCE AND CONTROL OF A SPACECRAFT FOR AN AEROASSISTED ORBIT TRANSFER

J.C. Albert\*, A. Glumineau\*\*, M. Guglielmi\*\*, E. Le Carpentier\*\* and C.H. Moog\*\*

\*ACRI S.A., Villantipolis No. 10, 473 Route des Dolines, Sophia-Antipolis, 06560 Valbonne, France

\*\*Laboratoire d'Automatique de Nantes, Unité Associée au C.N.R.S., Ecole Centrale de Nantes, 1 rue de la Noë, 44072 Nantes Cedex 03, France

**Abstract** The atmospheric flight of a spacecraft is considered when a aeroassisted orbit change maneuver is performed. Both guidance and control problems are solved and make respectively use of nonlinear control theory and classical adaptive control schemes. The originality of the work lies in the consideration of the overall guidance and control problem. A second point which is worth to be noticed is that focus is set on computational time. Whereas gain scheduling is known to be compatible with limited computing power, the main stream in literature consists in implementing some optimizing routines when the guidance problem is tackled. This scheme is dramatically time consuming and is deliberately skipped in the paper ; it is replaced by a trajectory tracking guidance policy issued from modern nonlinear control theory. The guidance and control solution is shown to be quite unsensitive to atmospheric density deviations which constitute major unknown parameters in the higher layers of the atmosphere.

**Keywords** spacecraft, guidance, control, nonlinear control systems, adaptive control, robustness.

### INTRODUCTION

The paper relates a global study on the so-called aeroassisted orbit transfer mission. In order to bring a spacecraft from a high orbit to low orbit, it is necessary to decrease its velocity. Instead of using only the thrusters, one uses the atmosphere which provides a natural braking. For this issue, a de-orbit impulse occurs so that the vehicle follows a trajectory crossing the atmosphere. The atmospheric flight is the center of the problem which is solved in this paper. Some exit conditions have to be fulfilled so that the vehicle reaches the low orbit with a suitable velocity. A re-orbit impulse is then given. The three phases of the mission are illustrated on Figure 1.

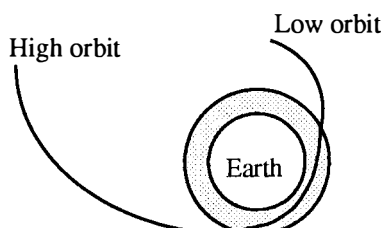


Figure 1

### MODEL EQUATIONS

The spacecraft is supposed to be axisymmetric and the data for its model are taken from an AFE type vehicle (Miele *et al.*, 1989 a, b), (Gamble *et al.*, 1988). Thus, the aerodynamic forces on the vehicle are limited to the drag and lift.

#### MOTION OF THE CENTER OF MASS

$$\dot{r} = V \sin \gamma$$

$$\dot{\delta} = V \cos \gamma \sin \chi / r$$

$$\dot{\tau} = V \cos \gamma \cos \chi / (r \cos \delta)$$

$$\dot{V} = \frac{\text{Drag}}{m} - \frac{\mu}{r^2} \sin \gamma + \omega^2 r \cos \delta (\sin \gamma \cos \delta - \cos \gamma \sin \delta \sin \chi)$$

$$\dot{\gamma} = -\frac{\text{Lift cos } \sigma}{mV} + \left[ \frac{V}{r} - \frac{\mu}{r^2 V} \right] \cos \gamma + 2\omega \cos \delta \cos \chi + \frac{\omega^2 r}{V} \cos \delta (\cos \gamma \cos \delta + \sin \gamma \sin \delta \sin \chi)$$

$$\dot{\chi} = -\frac{\text{Lift sin } \sigma}{mV \cos \gamma} - \frac{V}{r} \cos \gamma \cos \chi \tan \delta - 2\omega (\sin \delta - \tan \gamma \cos \delta \sin \chi) - \frac{\omega^2 r}{V \cos \gamma} \sin \delta \cos \delta \cos \chi$$

$$\text{Drag} = -P_{\text{dyn}} S_{\text{ref}} C_D$$

$$\text{Lift} = -P_{\text{dyn}} S_{\text{ref}} C_L$$

Nomenclature :

- $r$  = distance from the center of the earth
- $\delta$  = latitude
- $\tau$  = longitude
- $V$  = velocity of the vehicle
- $\gamma$  = flight path angle
- $\chi$  = heading angle

$\sigma$  = bank angle = guidance input

$\rho$  = atmospheric density (US 76 Standard)

$P_{\text{dyn}} = \rho V^2 / 2$  = aerodynamic pressure

$\omega$  = angular velocity of earth =  $0.729 \cdot 10^{-4}$  rad/s.

$\mu$  = gravitational constant =  $0.3986 \cdot 10^{15} \text{ m}^3/\text{s}^2$

$S_{\text{ref}}$  = reference area =  $12 \text{ m}^2$

$C_D, C_L$  = Drag & Lift coefficients

$m$  = mass of the AFE = 1408.6 kg

#### ATTITUDE EQUATIONS

$$I_{xx} \dot{\omega}_p = (I_{yy} - I_{zz}) \omega_q \omega_r + L + T_x$$

$$I_{yy} \dot{\omega}_q = (I_{zz} - I_{xx}) \omega_p \omega_r + M + T_y$$

$$I_{zz} \dot{\omega}_r = (I_{xx} - I_{yy}) \omega_p \omega_q + N + T_z$$

$$\dot{\alpha} = \omega_q - (\omega_p \cos \alpha + \omega_r \sin \alpha) \tan \beta$$

$$- [\delta \cos \chi \sin \gamma + \dot{\chi} \cos \gamma \\ + (\omega + \dot{\tau}) (\sin \delta \cos \gamma - \cos \delta \sin \chi \sin \gamma)] \frac{\sin \sigma}{\cos \beta} \\ + [(\omega + \dot{\tau}) \cos \delta \cos \chi + \delta \sin \chi - \dot{\gamma}] \frac{\cos \sigma}{\cos \beta}$$

$$\dot{\beta} = \omega_p \sin \alpha - \omega_r \cos \alpha$$

$$+ [\delta \cos \chi \sin \gamma + \dot{\chi} \cos \gamma \\ + (\omega + \dot{\tau}) (\sin \delta \cos \gamma - \cos \delta \sin \chi \sin \gamma)] \cos \sigma \\ - [(\omega + \dot{\tau}) \cos \delta \cos \chi + \delta \sin \chi - \dot{\gamma}] \sin \sigma$$

$$\dot{\sigma} = (\omega_p \cos \alpha + \omega_r \sin \alpha) \cos \beta + (\dot{\alpha} - \omega_q) \sin \beta$$

$$- \delta \cos \chi \cos \gamma + \dot{\chi} \sin \gamma \\ + (\omega + \dot{\tau}) (\cos \delta \sin \chi \cos \gamma + \sin \delta \sin \gamma)$$

Nomenclature

$[\omega_p, \omega_q, \omega_r]$  = rotation of the body with respect to inertial frame expressed in body frame,

$[L, M, N]$  = aerodynamic torque (in the center of mass) expressed in body frame,

$[T_x, T_y, T_z]$  = torque of the thrusters forces expressed in body frame, control inputs.

$I_{xx}, I_{yy}, I_{zz}$  = inertial moments in body frame,

$\alpha$  = attack angle,

$\beta$  = sideslip angle,

$\sigma$  = bank angle.

We suppose that for attitude time-scale, the motion of the center of mass is almost galilean, so that  $\omega=0, \dot{\delta}=0, \dot{\tau}=0, \dot{\chi}=0, \dot{\gamma}=0$ . Then:

$$\dot{\alpha} = \omega_q - (\omega_p \cos \alpha + \omega_r \sin \alpha) \tan \beta$$

$$\dot{\beta} = \omega_p \sin \alpha - \omega_r \cos \alpha$$

$$\dot{\sigma} = (\omega_p \cos \alpha + \omega_r \sin \alpha) \frac{1}{\cos \beta}$$

With the axisymmetry hypothesis,  $L, M$  and  $N$  depend on four coefficients  $C_{mq}^a, C_{ms}^a, C_D^a$  and  $C_L^a$  (tabulated with respect to  $V$  and the total attack angle  $\alpha_T = \arccos(\cos \alpha \cos \beta)$ , but which depend only on  $\alpha_T$  for  $V > 10 \text{ mach}$ ), in the following way: with  $[x_{cm}, 0, z_{cm}]$  the coordinates of the center of mass in body frame, we have:

$$L = -P_{\text{dyn}} S_{\text{ref}} \mathcal{L}_2(\alpha_T) \frac{\sin \beta}{\sin \alpha_T}$$

$$M = P_{\text{dyn}} S_{\text{ref}} \left[ \mathcal{L}_1(\alpha_T) + \frac{L_{\text{ref}} C_{mq}^a}{V} \dot{\alpha}_T \right] \frac{\sin \alpha \cos \beta}{\sin \alpha_T} + \mathcal{L}_3(\alpha_T)$$

$$N = -P_{\text{dyn}} S_{\text{ref}} \left[ \mathcal{L}_1(\alpha_T) + \frac{L_{\text{ref}} C_{mq}^a}{V} \dot{\alpha}_T \right] \frac{\sin \beta}{\sin \alpha_T}$$

where:

$$\mathcal{L}_1(\alpha_T) = L_{\text{ref}} C_{ms}^a(\alpha_T) \\ - x_{cm} (\sin \alpha_T C_D^a(\alpha_T) + \cos \alpha_T C_L^a(\alpha_T))$$

$$\mathcal{L}_2(\alpha_T) = z_{cm} (\sin \alpha_T C_D^a(\alpha_T) + \cos \alpha_T C_L^a(\alpha_T))$$

$$\mathcal{L}_3(\alpha_T) = z_{cm} (\cos \alpha_T C_D^a(\alpha_T) - \sin \alpha_T C_L^a(\alpha_T))$$

#### PROBLEM STATEMENT

To control the motion of the center of mass, one uses here a single input, the bank angle  $\sigma$  and the angle of attack  $\alpha$  is supposed to be constant, equal to a nominal value. The desired function  $\sigma(t)$  solution to the guidance problem is a command for the attitude control problem as well as the constant value of  $\alpha$ . Figure 2 displays the standard cascade decomposition for this global problem

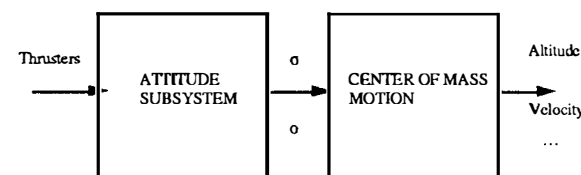


Figure 2

#### GUIDANCE

To solve the guidance problem, it is first necessary to give a minimal analysis of the system and the crucial point concerning the controllability of the system. It is well known in nonlinear system theory that when the so-called strong accessibility condition is fulfilled, one can not necessarily reach any final point. This is just the case for the problem under interest. It is important to realize what reachable trajectories look like, independently from any guidance law. This is done next, with a short discussion on one single initial state, the flight path angle  $\gamma_0$ . The reachable area is shown as the area with lies between the two limiting trajectories, one (A) corresponding to full lift up ( $\sigma = 0^\circ$ ) and the second limit (B) corresponding to full lift down ( $\sigma = 180^\circ$ ).

Reachable trajectories : Altitude (m) vs time (s)

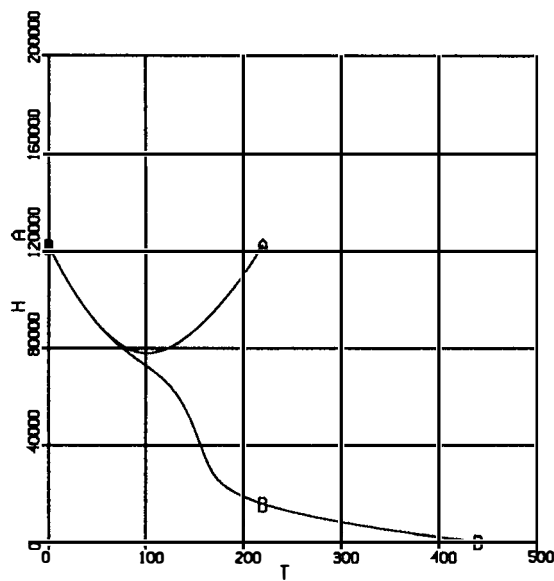


Figure 3 - Reachable trajectories for  $\gamma_0 = -4.67^\circ$   
(nominal value)

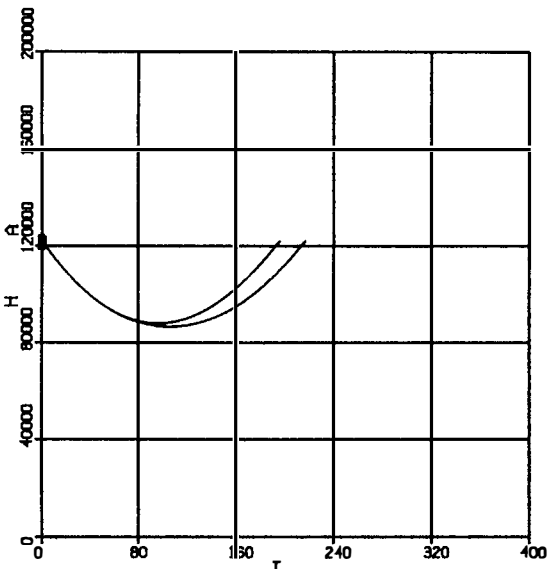


Figure 4 - Reachable trajectories for  $\gamma_0 = -4^\circ$

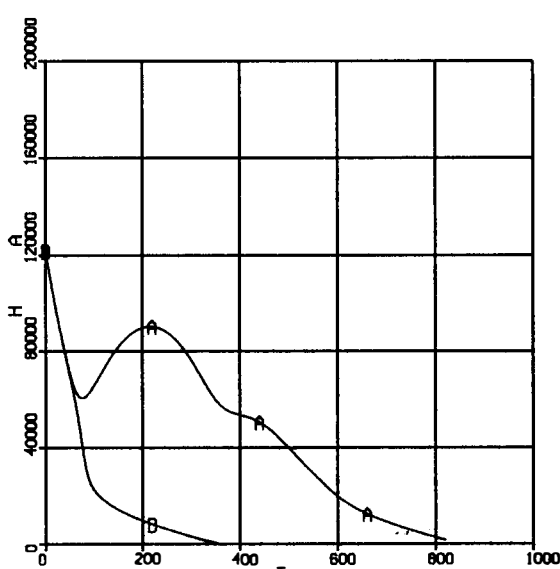


Figure 5 - Reachable trajectories for  $\gamma_0 = -7^\circ$

An easy conclusion is that any "robust" guidance scheme won't be able to cope with initial state deviations as considered above, just for some reachability conditions.

It is easy to check that the system is mainly controllable in the lower layers of the atmosphere while in the higher layers the vehicle is almost unsensitive to the aerodynamic forces. So in this ill conditioned situation, the guidance scheme which follows will just saturate the bank angle in the two limits which correspond to either full lift up (entry phase) or full lift down (exit phase).

### TRAJECTORY TRACKING

When the altitude is constrained to follow a given reference altitude, the system output is defined as  $y = r - r_{\text{ref}}(t)$ .

Compute the consecutive time derivatives as

$$\dot{y} = \dot{r} - \dot{r}_{\text{ref}}(t) = V \sin \gamma - \dot{r}_{\text{ref}}(t)$$

$$\begin{aligned} \ddot{y} &= \dot{V} \sin \gamma + V \dot{\gamma} \cos \gamma - \ddot{r}_{\text{ref}}(t) \\ &= \sin \gamma \left\{ -\frac{P_{\text{dyn}} S_{\text{ref}} C_D}{m} - \frac{\mu}{r^2} \sin \gamma \right. \\ &\quad \left. + \omega^2 r \cos \delta (\sin \gamma \cos \delta - \cos \gamma \sin \delta \sin \chi) \right\} \\ &\quad + V \cos \gamma \left\{ \frac{P_{\text{dyn}} S_{\text{ref}} C_L \cos \sigma}{mV} \right. \\ &\quad \left. + \left[ \frac{V}{r} - \frac{\mu}{r^2 V} \right] \cos \gamma + 2 \omega \cos \delta \cos \chi \right. \\ &\quad \left. + \frac{\omega^2 r}{V} \cos \delta (\cos \gamma \cos \delta + \sin \gamma \sin \delta \sin \chi) \right\} \\ &\quad - \ddot{r}_{\text{ref}}(t). \end{aligned}$$

Solve the following equation in  $\cos \sigma$ :

$$\ddot{y} = -\omega_n^2 y - 2\xi \omega_n \dot{y}$$

Consequently, if the absolute value of the RHS of next equation is less than 1, the trajectory tracking problem is solvable and the error is the response of a linear second order system with damping  $\xi$  and natural pulsation  $\omega_n$ . The command bank angle  $\sigma_c$  is such that:

$$\begin{aligned} \cos \sigma_c &= -\left[ \frac{V}{r} - \frac{m}{r^2 V} \right] \cos \gamma + 2 \omega \cos \delta \cos \chi \\ &\quad + \frac{\omega^2 r}{V} \cos \delta (\cos \gamma \cos \delta + \sin \gamma \sin \delta \sin \chi) \\ &\quad + \frac{1}{V \cos \gamma} \left( -\omega_n^2 y - 2\xi \omega_n \dot{y} + \ddot{r}_{\text{ref}}(t) \right. \\ &\quad \left. - \sin \gamma \left[ -\frac{P_{\text{dyn}} S_{\text{ref}} C_D}{m} - \frac{\mu}{r^2} \sin \gamma \right. \right. \\ &\quad \left. \left. + \omega^2 r \cos \delta (\sin \gamma \cos \delta - \cos \gamma \sin \delta \sin \chi) \right] \right) \end{aligned}$$

In the higher layers of the atmosphere, the RHS of the above is outside the bounds -1 and +1, so the command bank angle will just be saturated by  $\cos \sigma_c = \pm 1$  and won't solve the tracking equation.

The guidance law has to satisfy dramatic robustness conditions which are very crucial, specially since the atmospheric density is poorly modeled for the high

altitudes under interest. A nice solution has been implemented which consists in modifying slightly the above guidance law. Instead of tracking a reference altitude w.r.t. time, one tracks a reference altitude given as a function of the vehicle's energy  $E = (V^2/2) - (\mu/r)$ .

Note that it is possible to implement a tracking guidance law w.r.t. a reference energy or a reference drag. Such solutions seem to have the advantage to reflect the physical response of the vehicle to the real aerodynamic forces, the tracking of a reference altitude being essentially a geometric concept. In fact, some new problems arise which render such schemes difficult to implement. Whenever the tracking equation has no exact solution, i.e.  $\cos \sigma_c$  is saturated, then it is necessary to switch to a decision to an elementary question: apply full lift up or full lift down? This question is easy to answer in the case of an error in altitude. Considering an error in drag e.g., it is much more involved since one has to consider a function of two variables, the altitude and the velocity, which yield two antinomic decisions depending on which variable is considered.

#### Lateral guidance:

The sign of the commanded bank angle is determined by the lateral guidance. It follows the lines in (Gamble *et al.*, 1988).

The philosophy of this lateral guidance is to bank in the direction of the desired orbital plane, in order to minimize the wedge angle. If the wedge angle is nulled, then both the velocity and position vector errors are nulled, and the actual and desired orbital planes are aligned.

Finally, the commanded bank angle is given by :  
 $\sigma_c = \text{sign}(\sigma_c) \arccos(\cos(\sigma_c))$

#### ATTITUDE CONTROL : GAIN SCHEDULING

##### Linearized model:

The previous attitude model is linearized for  $(\alpha, \beta, \omega_p, \omega_q, \omega_r)$  around  $(\alpha_n, 0, 0, 0, 0)$ , where  $\alpha_n$  is the nominal value of  $\alpha$ . We obtain:

$$\dot{\alpha} = \omega_q$$

$$\dot{\beta} = \omega_p \sin \alpha_n - \omega_r \cos \alpha_n$$

$$\dot{\sigma} = -(\omega_p \cos \alpha_n + \omega_r \sin \alpha_n)$$

$$\dot{\omega}_p = \frac{T_x}{I_{xx}} + \frac{L}{I_{xx}}$$

$$\dot{\omega}_q = \frac{T_y}{I_{yy}} + \frac{M}{I_{yy}}$$

$$\dot{\omega}_r = \frac{T_z}{I_{zz}} + \frac{N}{I_{zz}}$$

$$L = -P_{dyn} S_{ref} \frac{\mathcal{L}_2(\alpha_n)}{\sin \alpha_n} \beta$$

$$M = P_{dyn} S_{ref} [\mathcal{L}_1(\alpha_n) + \mathcal{L}_3(\alpha_n) + \frac{L_{ref}^2 C_{mq}^a}{V} \omega_q + (\alpha - \alpha_n) (\mathcal{L}_1(\alpha_n) + \mathcal{L}_3(\alpha_n))]$$

$$N = -P_{dyn} S_{ref} \frac{\mathcal{L}_1(\alpha_n)}{\sin \alpha_n} \beta$$

$$\begin{aligned} \mathcal{L}_1(\alpha_n) &= L_{ref} C_{ms}^a(\alpha_n) \\ &\quad - x_{cm} (\sin \alpha_n C_D^a(\alpha_n) + \cos \alpha_n C_L^a(\alpha_n)) \\ \mathcal{L}_2(\alpha_n) &= z_{cm} (\sin \alpha_n C_D^a(\alpha_n) + \cos \alpha_n C_L^a(\alpha_n)) \\ \mathcal{L}_3(\alpha_n) &= z_{cm} (\cos \alpha_n C_D^a(\alpha_n) - \sin \alpha_n C_L^a(\alpha_n)) \\ \dot{\mathcal{L}}_i(\alpha_n) &= \frac{d\mathcal{L}_i}{d\alpha}(x_{cm}) \end{aligned}$$

Then, the equations of  $\alpha, \beta, \sigma$  are 2<sup>nd</sup> order ones, whose damping coefficient can be shown to be nearly zero. Furthermore, if the spacecraft is well-balanced, i.e.  $\mathcal{L}_1(\alpha_n) + \mathcal{L}_3(\alpha_n) = 0$ , then the equations reduce to:

$$\ddot{\alpha} + \omega_{0\alpha}^2 (\alpha - \alpha_n) = T_\alpha$$

$$\ddot{\beta} + \omega_{0\beta}^2 \beta = T_\beta$$

$$\ddot{\sigma} = T_\sigma$$

$$\text{with } \begin{cases} \omega_{0\alpha}^2 = -P_{dyn} S_{ref} \frac{\mathcal{L}_1(\alpha_n) + \mathcal{L}_3(\alpha_n)}{I_{yy}} \\ \omega_{0\beta}^2 = P_{dyn} S_{ref} \left( \frac{\mathcal{L}_2(\alpha_n)}{I_{xx}} - \frac{\mathcal{L}_1(\alpha_n)}{I_{zz} \tan \alpha_n} \right) \end{cases}$$

$$\text{and } \begin{cases} T_\alpha = \frac{T_y}{I_{yy}} \\ T_\beta = \frac{\sin \alpha_n}{I_{xx}} T_x - \frac{\cos \alpha_n}{I_{zz}} T_z \\ T_\sigma = -\frac{\cos \alpha_n}{I_{xx}} T_x - \frac{\sin \alpha_n}{I_{zz}} T_z \end{cases}$$

##### PID regulator:

To regulate  $\alpha$ , we propose the following PID regulator, which depends on 3 parameters  $\omega_{1\alpha}, K_\alpha$ , and  $\zeta_\alpha$ :

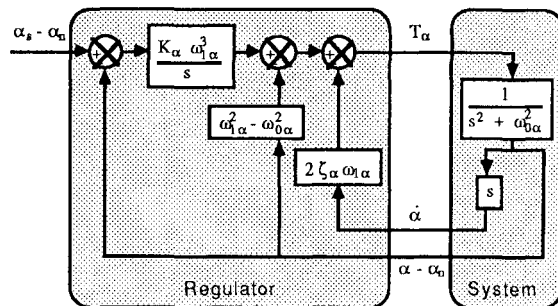


Figure 6

The control  $T_\alpha$  is:

$$\begin{aligned} T_\alpha(t) &= K_\alpha \omega_{1\alpha}^3 \int_0^t (\alpha_s(\tau) - \alpha(\tau)) d\tau \\ &\quad + (\omega_{1\alpha}^2 - \omega_{0\alpha}^2) (\alpha_n - \alpha(t)) - 2\zeta_\alpha \omega_{1\alpha} \dot{\alpha}(t) \end{aligned}$$

If the control is sampled with period  $\Delta$ , the control law becomes:

$$T_\alpha(k\Delta) = K_\alpha \omega_{1\alpha}^3 \Delta \sum_{i=0}^k (\alpha_s(i\Delta) - \alpha(i\Delta)) + (\omega_{1\alpha}^2 - \omega_{0\alpha}^2) (\alpha_n - \alpha(k\Delta)) - 2\zeta_\alpha \omega_{1\alpha} \dot{\alpha}(k\Delta)$$

Then, the transfert function between the setpoint  $\alpha_s$  and  $\alpha$  is:

$$K_\alpha = \frac{(\frac{s}{\omega_{1\alpha}})^3 + 2\zeta_\alpha (\frac{s}{\omega_{1\alpha}})^2 + (\frac{s}{\omega_{1\alpha}}) + K_\alpha}{(\frac{s}{\omega_{1\alpha}})^3 + 2\zeta_\alpha (\frac{s}{\omega_{1\alpha}})^2 + (\frac{s}{\omega_{1\alpha}})}$$

which is independant of the physical system. For the output,  $\omega_1$  is nothing but a time scale factor, which has to be set so that the physical constraints are respected.

In our case,  $\alpha$  and  $\beta$  are regulated (so the setpoints are the nominal values:  $\alpha_s = \alpha_n$ ,  $\beta_s = 0$ ), and the setpoint  $\sigma_s$  is the command bank angle  $\sigma_c$  given by the guidance law. Then, at time  $k\Delta$ , the three regulators are:

$$T_\alpha = K_\alpha \omega_{1\alpha}^3 \Delta \sum_{i=0}^k (\alpha_n - \alpha(i\Delta)) + (\omega_{1\alpha}^2 - \omega_{0\alpha}^2) (\alpha_n - \alpha) - 2\zeta_\alpha \omega_{1\alpha} \dot{\alpha}$$

$$T_\beta = -K_\beta \omega_{1\beta}^3 \Delta \sum_{i=0}^k \beta(i\Delta) - (\omega_{1\beta}^2 - \omega_{0\beta}^2) \beta - 2\zeta_\beta \omega_{1\beta} \dot{\beta}$$

$$T_\sigma = K_\sigma \omega_{1\sigma}^3 \Delta \sum_{i=0}^k (\sigma_c(i\Delta) - \sigma(i\Delta)) - \omega_{1\sigma}^2 \sigma - 2\zeta_\sigma \omega_{1\sigma} \dot{\sigma}$$

We obtain an adaptive regulator for  $\alpha$  and  $\beta$ , since the proportional coefficient depends on  $\omega_{0\alpha}$  (or  $\omega_{0\beta}$ ) which depends on the aerodynamic pressure  $P_{dyn}$ . Then, the moments  $T_x$ ,  $T_y$ ,  $T_z$  can be computed:

$$T_x = I_{xx} (\sin \alpha_n T_\beta - \cos \alpha_n T_\sigma)$$

$$T_y = I_{yy} T_\alpha$$

$$T_z = -I_{zz} (\cos \alpha_n T_\beta + \sin \alpha_n T_\sigma)$$

The algorithm of the gain-scheduling regulation becomes :

Control at time  $k\Delta$ :

measure of  $\alpha$ ,  $\beta$ ,  $\sigma$ ,  $\omega_p$ ,  $\omega_q$ ,  $\omega_r$ ,  $P_{dyn}$

$$\dot{\alpha} = \omega_q - (\omega_p \cos \alpha + \omega_r \sin \alpha) \tan \beta$$

$$\dot{\beta} = \omega_p \sin \alpha - \omega_r \cos \alpha$$

$$\dot{\sigma} = -(\omega_p \cos \alpha + \omega_r \sin \alpha) \frac{1}{\cos \beta}$$

Calculus of  $\omega_{0\alpha}^2$ ,  $\omega_{0\beta}^2$

Calculus of  $T_\alpha$ ,  $T_\beta$ ,  $T_\sigma$ .

Calculus of  $T_x$ ,  $T_y$ ,  $T_z$ .

## SIMULATION RESULTS

Figure 7 displays the altitude trajectory (A), the command bank angle (B) and the real bank angle (C), when the cascaded system (control + guidance,

see Fig. 2) is considered. The trajectory guidance scheme was tuned so that the feedback linearized second order system has damping  $\xi = 1.5$  and a natural pulsation  $\omega_n = 0.1$  rad/s. The gain scheduling control is tuned to respect the physical constraints ( $\dot{\sigma} < 20$  deg/s,  $\dot{\sigma} < 5$  deg/s<sup>2</sup>); we choose  $K_\alpha = K_\beta = K_\sigma = 0.28$ ,  $\zeta_\alpha = \zeta_\beta = \zeta_\sigma = 0.7$ ,  $\omega_{1\alpha} = \omega_{1\beta} = 3$ ,  $\omega_{1\sigma} = 1$ . Figure 8 displays the angle of attack (A) and the sideslip angle (B).

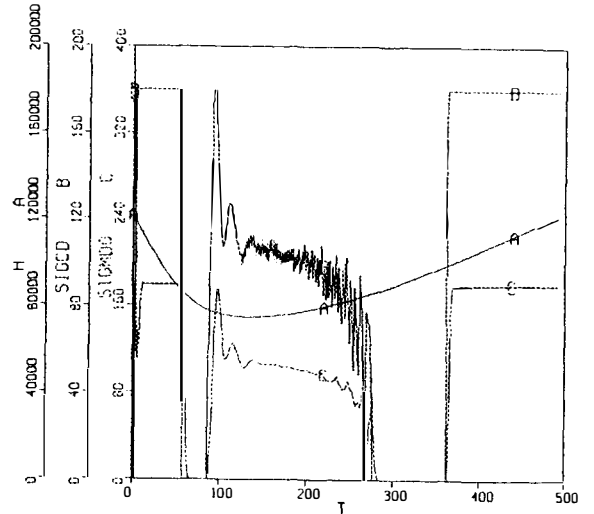


Figure 7 - Overall system : (A) altitude (m), (B) command bank angle (deg), (C) real bank angle (deg)

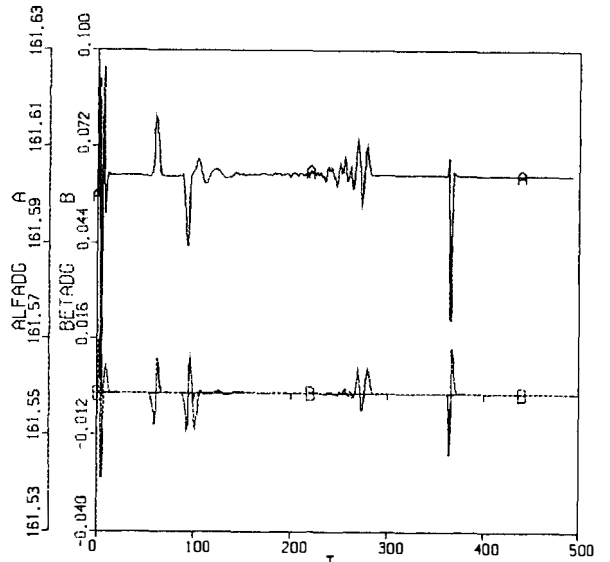


Figure 8 - Overall system : (A) angle of attack (deg), (B) sideslip angle (deg)

To examine the robustness of the guidance scheme, one measures its quality by Delta V, the difference between the atmospheric exit velocity value and the desired exit condition. The value of Delta V is displayed next when some deviations on  $\gamma_0$  or on  $\rho$  are considered.

## SENSITIVITY TO THE INITIAL PATH ANGLE

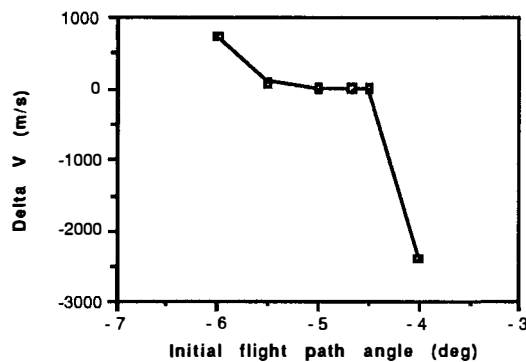


Figure 9

It is worth to remind the controllability analysis of the system which shows, e.g., that the initial condition -4. deg for the flight path angle will yield an uncontrollable system. This phenomenon should be distinguished from a notion of robustness.

## ROBUSTNESS W.R.T. DENSITY DEVIATIONS

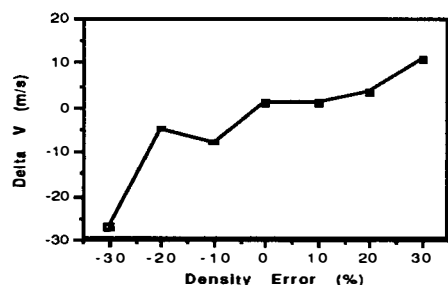


Figure 10

The total orbit transfer "cost" several thousands m/s de-orbit and re-orbit impulses, so the above small values for Delta V are totally negligible.

## CONCLUSION

In this paper, only one single guidance and control policy was explained. The motivation was to highlighten the issues provided by some very simple (in the computational sense) schemes. Although there is no online re-actualization of the various

tuning parameters, particularly for the guidance problem, one has the benefit of some good robustness properties which are shown to be quite the best one can expect, considering the severe controllability conditions of the system.

Alternative methods for both problems will be developed in a forthcoming work.

ACKNOWLEDGMENT : This work was performed under ESA Contract N° 9359/91/NL/JG (SC).

## REFERENCES

Miele, A., T. Wang, W.Y. Lee and Z.G. Zhao (1989 a). Optimal trajectories for the aeroassisted flight experiment, Part 3, Formulation, results and analysis, *Aero-Astronautics Report N° 242*, Rice University.

Miele, A., T. Wang, W.Y. Lee, H. Wang and G.D. Wu (1989 b). Optimal trajectories for the aeroassisted flight experiment, Part 4, Data, tables and graphs, *Aero-Astronautics Report N° 243*, Rice University.

Gamble, J.D., C.J. Cerimele, T.E. Moore and J. Higgins (1988). Atmospheric guidance concepts for an aeroassist flight experiment, *Journal of the Astronautical Sciences*, vol. 36, pp. 45-71.

Mishne, D. and L. Speyer (1986). Optimal control of aeroassisted plane change maneuver using feedback expansions, *Proc. AIAA Conf.*, AIAA Paper 86-2136, pp. 259-271.

Calise, A.J. and G.H. Bae (1987). Optimal heading change with minimum energy loss for a hypersonic gliding vehicle, *Proc. AIAA Conf.*, AIAA Paper 87-2568, pp. 417-421.

Van Buren, M.A. and K.D. Mease. Aerospace plane guidance using geometric control theory, *Proc. AIAA Conf.*, pp. 1829-1838.

Van Buren, M.A. and K.D. Mease (1991). A geometric approach to regulator and tracker design for an aerospace plane, *Proc. AIAA Conf.*, Orlando, 1991.

## SMART STRUCTURES AND MATERIALS SYSTEMS

P.T. Gardiner

*Smart Structures Research Institute, University of Strathclyde, 204 George Street, Glasgow G1 1XW, UK*

**Abstract:** Smart Structures technology has been the subject of attention for several years for structural monitoring and control in aerospace vehicles. The technology focuses broadly on the integration of functions including sensing, actuation, processing and controls with materials enhancing functionality forming Smart Structures.

Smart Structures are capable of monitoring and responding to changes in the surrounding environment. Responding implies the ability to recognise, discriminate, notify and adapt; *an intelligent response*. The monitoring function is targeted mainly towards structural integrity where the benefits are safety and maintenance scheduling improvements and parameters include strain and temperature. The response function entails the ability of a structure to control its elasto-mechanical properties (shape/profile, vibration, stiffness) and produces a number of benefits including higher performance and reduction in weight.

This paper will provide a brief overview of smart structures activity in space and aircraft related applications in North America, Europe and Japan. This emergent technology will undoubtedly yield a range of new materials, new sensing and actuation approaches and also signal processing and controls technology. Developments in this latter area of particular importance will be highlighted.

**Keywords:** Adaptive control; Structural controllability; Sensors

### 1. INTRODUCTION

The terms *Smart Structures* and *Smart Materials* have only recently penetrated the lexicon of accepted technical terminology. However, the concepts that it entails, that of enhancing the functionality of materials and structures, is not new and has been a desirable for many years. Now with recent developments in technology, including materials along with mechanical and electronic engineering, the concept can be brought much closer to reality.

The functionality that is integrated with basic materials to generate *smartness* is most easily understood by considering the three primitive functions:

- sensing
- adaption
- information processing

The sensing function can be used in isolation, and in this limited approach can provide considerable benefit. For example, a bridge or an aircraft wing

with embedded sensors will provide knowledge of the behaviour of the structure under various loading and environmental conditions. The availability of the on-line information can improve safety and allow more efficient inspection and maintenance procedures to be undertaken, and hence yield cost savings.

Along with the sensing function, the actuation and processor function can also be integrated to enable the structure to respond to changes in the environment. Responding implies the ability to recognise, discriminate, notify and adapt; *an intelligent response*. A response can manifest as something as dramatic as an adaptation of structural characteristics, for example, stiffness, vibration behaviour, or shape/profile or something simple such as a colour change.

Considerable investment and effort has been expended world-wide however, before wholesale commitment to projects can proceed, the range of

multidisciplinary technologies must be established and the design process must evolve to enable the smart system contributors to be integrated at the conception of the design.

The following text focuses on the potential offered by this rapidly developing design methodology and provides a review of some activities undertaken to date.

## 2. THE CONCEPT

There is currently considerable world-wide debate as to the exact definition of Smart Structures and Materials, however, a convenient way of understanding the concept is by considering the functional schematic (Figure 1). This shows a number of functional elements:

- material
- sensors
- actuators
- communications
- controls/signal processing

These areas exist in their own right and each encompasses their own scientific and engineering field. All these disciplines have witnessed significant development, but most notably has been the phenomenal growth in capability and availability of digital computing. This particularly applies to the controls field, where ever more detailed and complex modelling of mechanical systems can be achieved leading to the generation of new sophisticated control laws.

The key to the Smart Structures concept is the integration of the functional elements to enable the overall system to fulfil its purpose, by adapting to changes in its environment. This integration issue forms the crux of the challenge that now faces the technical community and exemplifies a truly interdisciplinary problem.

It is worthwhile pointing out meanwhile, that subsets of the all encompassing, closed loop Smart Structure can be applied to generate benefit in use. Systems that employ solely a sensory function can be very effective, such as in structural monitoring where a structure such as a bridge, aircraft or pipeline can be strewn with sensors to provide information on structural integrity and performance. However, the fact that these sensors are generating information means that to be effective there must at least be some communication function to take the information to where it is wanted and then something useful done. In many structural monitoring systems, a human operator acts on this information to decide for example a maintenance operation; an open loop type system.

Thus far, the description has strongly hinted that individual, elemental components such as sensors, and actuators are physically placed and incorporated with some base material. However, there

are developments to implement these functions inherently at a material level, without the need for man-made instrumentation, communication and controls. There is a close analogy here to biological systems which, when you consider nature has evolved over billions of years, may not be a bad model to try and emulate.

This approach has been termed *Intelligent Materials* and the concept is undeniably elegant and attractive. Although on first pass it may appear rather far fetched, there are a number of interesting, albeit simple, examples that are close to commercial exploitation. For example;

- Polymer gel materials that can adapt their properties under specific chemical stimuli to release drugs or water in a controlled manner.
- Organic dyes can turn excess mechanical stress into a colour change and/or a change in the transmission properties for polarised light. The latter has been used for many years for stress analysis and the former is a well known effect in plastic bags. The overall idea can be developed into a more refined form, for example, the "smart" climbing rope currently under development (*Shennan, 1992*) incorporates stress dependent colour into the rope structure.
- Liquid crystals can be arranged to change apparent colour with temperature.
- Materials which change optical signals, thermal signals and/or stress signals and intermodulations in overall volume are available.

There is also an intermediate stage which the Japanese have christened "mesoscopic" materials (*Japanese Science & Technology Agency, 1989*). In these materials, the structure of clusters of molecules rather than individual molecules is manipulated in order to change their mechanical, electromagnetic or other properties. The mesoscopic order could also be changed as a consequence of applied mechanical and/or thermal fields so that significant changes in structural effects could be anticipated. At present this type of study is restricted to substances such as colloids whose optical properties can be modulated by mechanical and thermal effects.

These aside, the remainder of this paper will concentrate on the more familiar, engineering approach of integrating sensor and actuator components with host materials.

## 3. THE ENABLING, CONTRIBUTORY FUNCTIONAL ELEMENTS

In each of the following areas, a wealth of technology has been developed and available to the design of smart structure systems.

### 3.1 Materials

With the tremendous development of electronic computer hardware and software technology, it is easy to forget the perhaps equally important advancement in materials technology.

Materials such as polymer based materials, reinforced with various species such as glass, carbon, ceramic; metal matrix ceramics; light weight metallic alloys and bio-composites have all reached a certain level of maturity and the options available are broad.

It is interesting to note that new materials development is probably the highest on the list of research priorities in US and Japanese funding agencies.

### 3.2 Sensors

There are countless sensing technologies and the key mechanical parameters of strain and temperature can be readily accessed using conventional techniques such as thermocouples, semiconductor strain gauges and ultrasonics. However, the key in the realisation of the smart structure, because the number of sensory elements can be very large, is the availability of a simplified wiring harness to enable the interconnect of the sensory elements. This could be done by using, for example, smart semiconductor sensors multiplexed onto a simple transmission line system and addressed using one of the standard protocols (Figure 2). This approach has been utilised in a number of trial adaptive structures but there are a number of implicit disadvantages (*Wada, 1990*). The principal ones are that the network must of course be connected using metallic conductors with their attendant radiation and pick up problems and that this metallic network often will have lower yield strain than the material from which the structure is fabricated (especially if the latter is a carbon or glass fibre composite). Consequently, there is also significant interest in the use of fibre optic sensing techniques since this offers a non-metallic transmission medium with mechanical properties comparable to those of the reinforcing fibres in the composite materials. At present many fibre optic sensor networks have been proved in the laboratory (*Culshaw & Michie, 1992; Murphy and others, 1991; Thursby and others, 1991*), and a few have been demonstrated in the field. In particular, strain and temperature may be monitored reasonably accurately. Key features of fibre optic instrumentation is that spatially distributed sensors are possible with effectively inherent multiplex capability.

### 3.3 Actuators

Actuators remains the least mature of the enabling functional elements and much uncertainty surrounds their development. Current technology is effectively limited to point acting devices with either small stroke/high force or low force/high stroke performance. As a result, applications are

constrained to small actuator movements but where a large resonant type effects can be generated.

Many of the demonstration systems have relied upon piezoelectric stacks as the basis for the actuation technology. This gives a very stiff short throw actuator. Piezos can also be configured into longer throw "inchworm" actuators. A few other demonstrators have involved the use of conventional electromechanical actuators such as worm drives and stepper motors. Yet others have adapted conventional hydraulic and/or pneumatic systems. Of the "new" technologies shape memory alloys, magnetostrictive actuators and electro-rheological fluids are interesting contenders whilst electrostrictive materials have the potential for somewhat different performance characteristics to piezoelectrics. Some actuator concepts also rely upon relatively stiff drives to fluidic amplifiers which permit long throw actuation further downstream but with attendant uncertainties in the gain of the amplifier chain.

The available actuator technology has a profound influence on the design of the structure. Basically it is a question of matching the impedance available from the actuator, that is "stiff" or "compliant", into the appropriate point in the structure to ensure optimum power transfer from the actuator into the structure (or vice-versa in the case of vibration damping). There are also occasions when the actuator and/or its driving circuit must dissipate considerable quantities of power when the system is used in the vibration damping mode for large structures.

One fundamental feature of actuator devices is that to get the effect you want, you need to input the equivalent energy. This can be significant and all the technologies cited above utilise transfer of input energy over a transmission line which can be very lossy. A radical new concept is effectively to mimic biology (and the automobile!) by transmitting fuel instead of energy, and then very locally converting for use. This could be extremely efficient.

The final important feature of actuators for smart structures, is that their role must be accurately predictable within the structural assembly. Ideally this implies that they function without backlash - another area in which the piezoelectric stack shows excellent properties. If there is backlash in the system then the uncertainty in the transfer function between the actuator and the structure must be incorporated into the control system.

### 3.4 Communications

This is largely associated with transfer of sensor information out of, and control data into, the structure. A range of mature technology is now available including conventional copper based transmission systems and more recently fibre optic systems. Important issues in overall design include systems access protocols and reduction of interconnects through multiplexing.

### **3.5 Controls/Signal Processing**

In many of the envisaged smart structure systems, sensing and actuation devices may be large in number and may be distributed over large areas (*Wada, 1990*). The signal processing task associated with this is computationally very intensive and input signals may be diverse in nature. This is further complicated as the input signals will be contaminated by noise and uncertainties. Such a requirement lends itself to a parallel processing architecture and the use of state-of-the-art techniques such as artificial neural networks is growing. The control system must accurately model the response of the structure, which may be very complex and by nature implies that the response of the mechanical structure must be repeatable. This is an onerous task and may not be totally reliable and as a result adaptive control systems are essential.

From this review, it becomes clear that the biggest technical hurdle is not only the selection of the most appropriate option, but how the various functional elements are integrated to generate efficient design.

## **4. USES & BENEFITS OF SMART STRUCTURES AND MATERIALS**

Two important uses for smart structures and materials technology have thus far been identified:

- Structural Monitoring
- Structural Control

### **4.1 Structural Monitoring**

The availability of on-line information from sensors, detailing inherent structural condition of a structure offers some important benefits:

- improved manufacturing through monitoring key process parameters enabling increased quality, less wastage and hence reduced production costs.
- the higher confidence in structural integrity hence safety improvements.
- improved maintenance procedures, as on condition maintenance can replace routine, repeated maintenance, hence cost savings.
- access to records of structural loading and environmental exposure and the effects of these on the structure, helps next generation design.
- by monitoring performance of new light weight materials such as composites, greater confidence of use can be provided, hence reduces over engineering.

### **4.2 Structural Control**

Such systems consist of some sensory function(s) complemented by a control system to effectively permit, via a dynamic control loop, the use of actuators to control structural properties. This can involve the control or tuning of elasto-mechanical properties such as shape/profile, stiffness or natural frequency and also position or displacement of components. This capability presents a number of benefits:

- improvements in structural life times arising from the inherent ability to adapt structural condition including vibration control (reduces fatigue), positional control in bearings and joints (reduces wear).
- improvements in structural performance by maintaining positional accuracy (stability), controlling surface features (hydro-dynamic and aerodynamic flow).

The above points to a very promising potential future for this technology and this has stimulated a significant research and development activity world-wide, as summarised later.

## **5. OVERVIEW OF WORLD-WIDE ACTIVITY**

To date, the bulk of effort has been in the US and Japan, but interest in Europe is now developing apace.

In Japan, their approach has been well coordinated with significant up front planning on their overall philosophy (*Japanese Science & Technology Agency, 1989*). In response to this, the Japanese Intelligent Materials Forum has been established with representation from Government, Industry and academia.

US efforts have been initiated in the Defence Sector with nearly every funding agency having programmes of one form or another. With the shift in the world-wide military scene, much effort is now being re-directed to non-military areas, very noticeably to transport infrastructure (*Sabadel, 1992*).

More recently awareness has grown in Europe, but effort is still fragmented and lacks coordinated direction. Even though considerable research activity has been performed in various focussed areas of materials development, to date, the key issue of integration of the various disciplines to generate multi-functionality has not been properly addressed. Nevertheless, increased interest worldwide has provided stimulus for the publication of dedicated technical journals (*IOPP, Technomic*).

The potential application base for smart structures and materials is sectorially broad, and activity has been cited in a number of industries.

- civil engineering (bridges & tunnels)

- marine/offshore
- aerospace/defence
- manufacturing
- transport
- environmental
- leisure

Of growing importance is the application in civil engineering.

A number of concrete bridge structures have been instrumented to monitor the effect of integrated vibrational strain or, in more advanced systems, distributed strain as a function of position with a resolution of a few metres along the sensor length (*Wolf & Miesseler, 1992, Griffiths, 1991*). The sensing system is a simple single fibre optic cable which functions as a reliable integrated strain measurement system in contrast to localised strain gauges which are only indicative of the strain on a particular point on the bridge.

Given the uncertainty surrounding the state of decay of many concrete bridge structures both in the US and Europe, which is becoming a very big problem, the availability of a simple, reliable distributed monitoring system can substantially improve maintenance and replacement procedures (*Caussignac, 1991*).

Earthquake proof buildings have been designed and built in Japan (*Blakeslef, 1991*) using a large mobile weight on the top of the building to compensate for seismically induced perturbations at the bottom. There is a school of thought which subscribes to an improvement in this system with actuators at the base of the building to absorb the incoming strain distribution and compensate for its presence at the bottom rather than at the top. This is effectively all a question of impedance matching between the available actuator system and the requirement in the building. A very stiff actuator at the base would have to absorb considerable quantities of energy and dissipate this presumably as heat. The compliant actuator at the top of the building transforms the energy from the seismic wave into the motion of the proof mass.

However, the prime driver for the growth in this technology has been in the aerospace industry, particularly in the more advanced sectors such as space platforms and high performance platforms.

## 6. AEROSPACE APPLICATIONS FOR SMART STRUCTURES

Much of the work in has taken place in N. America, particularly in the US. A main thrust has been in the embedment of fibre optic systems into fibre reinforced composite structures to provide a structural monitoring function. This is being done to indicate deterioration of structural integrity either through fatigue degradation or damage. A great deal of synergy exists between fibre optics and fibre reinforced composites, and

the monitoring function could well provide the user with greater confidence in using such materials (*Measures, 1990*). This is illustrated in Figure 3.

Another area of key interest is that of adaptive structures which infers the use of embedded actuator systems. The applications include changing the aerodynamic profile of aerodynamics cross-sections, e.g. helicopter blades (*Nitsche & Brierbach, 1992*), and also adapting surface profile to change flow characteristics; this approach is being seriously looked at for submarine applications (*Miller, 1991*).

Other applications for adaptive structures include active vibration damping of structures, of particular importance in space systems, and to actively control communications antenna structures to maintain pointing accuracy. This area has received much attention, not only in the US but Japan and Europe.

The aerospace industry in the US is also heavily interested in the integration of avionics systems hardware within the basic air frame structure to form a truly multifunctional structure. This includes the concept of a conformal radar and communications antenna, and is termed the smart skins concept. Variations on this theme have obvious implementations for "stealth" operations.

A history of US Government-funded smart structures programmes is presented below in Table 1.

Early 1980s -	Classified contracts on structurally integrated conformal aircraft radar antennas
1985 -	Project Forecast II Recommendations
1987 -	Phase I Wright Patterson AFB Smart Skins contract awarded to Simmonds Precision
1988 -	Phase I AFAL Adaptive Structure contract awarded to TRW and Boeing
1989 -	Phase II Wright Patterson AFB Smart Skins contract awarded to Northrop
1990 -	Phase II AFAL Adaptive Structure contract awarded to TRW

Table 1 : US Government-Funded Smart Structures Programmes

Of key importance in Table 1 are the recommendations of Project Forecast II, which defined a plan of development for the US Air Force for the time period 1985-2005. The programme identified extensive R&D funding to be made by the Air Force to a range of US contractors, leading to a flight demonstration of an embedded structural monitoring system in 1993.

This initiative greatly expanded the concept of smart structures beyond just structural monitoring, to include propulsion system monitoring, weapons status monitoring, threat sensors, etc. The philosophy of this concept is that integration of this data and subsequent processing, will enable far greater knowledge on behaviour of the overall systems. As a result, the flight control system can be reconfigured to give maximum safe performance and the availability of such information should greatly reduce down time because of improved diagnostics.

Nearly all the US aerospace companies have some activity in the development of this technology, and very importantly, are working closely with various academic research teams. Work has been undertaken in Europe, mainly in the structural monitoring in composites and structural control, for example *Culshaw & Michie (1992)* and *Sansonetti and others (1989)*, but generally developments are far less than in the US. European efforts are more fragmented and there is little networking between active bodies.

The overall prospects for the sphere of smart structures are considerable and indications are that the technology will mature in the next 8-12 years (for aerospace) and will stimulate a range of new opportunities.

## 7. IMPLICATIONS OF SMART STRUCTURES TECHNOLOGY

The potential for smart structures is enormous but there are a number of key problems that must be thoroughly assessed and action taken. An assessment of this technology at the Smart Structures Research Institute at the University of Strathclyde, Glasgow, has revealed a number of issues concerning the nature of the technology and the implications upon design.

Smart structures and materials is truly multidisciplinary, and even fundamental research must be undertaken with this in mind and be efficiently co-ordinated across disciplines. One key conclusion that has arisen from the attempts to co-ordinate the work between Japan and the US is:

"To make meaningful progress in the field of smart/intelligent materials systems an interdisciplinary approach and international collaboration is needed."

Figure 1, exemplifies illustrates the various disciplines that contribute to a smart structure; sensing, host material and structural design, actuation, communications, signal processing and controls. All these elements constitute the "material systems" building block and all must be considered at the structural/system design conception.

Before the benefits offered by smart structures and materials technology can be realised, the barriers to the use of these concepts must be thoroughly understood and addressed. Two key issues have been identified.

### ■ technical barriers

*How is the design process influenced to ensure the smart structure concept is designed in at birth and not added on later.*

*How is the design process handled due to the diverse range of disciplines involved.*

This has considerable implications on the current approaches to aero-vehicle structural design. The partition between *material* and *structure* and *electronics* will disappear and co-exist in the context of design, and cannot be considered in isolation. Traditional *stress office* and structural design approaches will have to take into account the essential electronic functions that now form part of the material system. Another influence will be the fact that knowledge will be available, throughout the life of the vehicle, concerning its structural condition. The design process will become more and more integrated and will require a "systems approach"; requirements and all interfaces must be clearly and precisely defined. This implies a major culture change in the design process.

### ■ commercial barrier

*How can the responsibility chain of specifier, designer, manufacturer, user/maintainer and the range of suppliers be influenced to ensure optimum implementation.*

It is vital that the beneficiary of using the technology has a major input. All links in the chain should be involved in all parts of the product design and development cycle, therefore minimising any link inertia and maximising performance.

## 7. CONCLUDING REMARKS

The *smart structures and materials system* concept is rapidly emerging as a critical contributor to 21st century aerospace technology and offers considerable benefits.

Smart structures and materials technology will undoubtedly yield a wide range of new materials, plus new material sensing and actuation technologies, and this will have a radical effect on current approaches to structural design. To date, a considerable amount of resources have been applied, but the technology is not mature enough for wholesale application and there is a necessity to develop the underpinning interdisciplinary science base.

The integration of materials and electronics/sensors/actuators, to form *functional material systems* which can then be used to formulate *smart structures*, will have a profound effect upon approaches taken to the design process for aerospace vehicles. This will require vehicle and systems designers to work together in a far more integrated way than ever before. If this can be achieved, the great potential of smart structures technology will be realised.

## 8. BIBLIOGRAPHY

Blakeslef, S. (1991), Engineers Teach "Smart" Buildings to Foil Quakes, New York Times, July 2nd.

Caussignac, J-M. (1991), Civil Engineering Applications for Smart Structures, Inaugural European Seminar, Paris, Smart Structures Research Institute, University of Strathclyde

Culshaw, B. and Michie, W.C., (1992), Fibre Optic Strain and Temperature Measurement in Composite Materials - A review of the OSTIC Programme, Conference on Recent Advances in Adaptive and Sensory Materials and their Applications, Virginia Polytechnic Institute, Blacksburg VA.

Griffiths, R.W. (1991), Fibre Optic Monitoring in the Electric Utility Power Plant Environment, EPRI Conference on Optical Sensing in Utility Applications

IOPP, Smart Materials & Structures, ISSN. 0964-1726

Japanese Science & Technology Agency (1989), The Concept of Intelligent Materials and the Guidelines on R&D Promotion.

Measures, R. (1990), Progress Towards Fiber Optic Smart Structures at UTIAS, Proc. F.O. Smart Structures & Skins III, SPIE Vol. 1370, Paper 33.

Miller, W.C. (1991) Navy Science & Technology Perspective on Active Materials and Adaptive Structures, Proc. AMAS, American Defence Preparedness Association.

Murphy, K.A., Gunter M.F., Vengsarkar, A.M. and Claus, R.O. (1991), Fabry Perot Fibre Optic Sensors in Full Scale Fatigue Testing on and F-10 Aircraft, Proc. F.O. Smart Structures & Skins IV, SPIE Vol. 1588, Paper 14

Nitzsche, F. and Brietbach, E. (1992), The Smart Structure Technology in the Vibration Control of Helicopter Blades in Forward Flight, Proc. First European Conference on Smart Structures & Materials, IOPP/SPIE Vol. 1777, pp.321-325

Sabadell, E.J. (1992), Structural Control Research at the National Science Foundation, Proc. First European Conference on Smart Structures & Materials, IOPP/SPIE Vol. 1777, pp.227-231

Sansonetti, P. and others (1992), Unidirectional Glass Reinforced Plastic Composite Monitoring with White Light Quasi Distributed Polarimetric Sensing Networks, Proc. First European Conference on Smart Structures & Materials, IOPP/SPIE Vol. 1777, pp.77-81

Shennan, F. (1992), Smart Rope Trick Points Towards New Pinnacles of Stress-Relief, Scotland on Sunday, August 9th, p.16.

Technomic Publishing, J. Intelligent Material Systems & Structures, ISSN. 1045 389X.

Thursby, M.H., Koo, Y. and Grossman, B. (1991), Neural Network Controlled Smart Antenna, Proc. F.O. Smart Structures & Skins IV, SPIE Vol. 1588, paper 25.

Wada, B.K. (1990), Adaptive Structures - An Overview, J. Spacecraft & Rockets, 27 330-337.

Wolff, R. and Miesseler, H-J. (1992), Proc. First European Conference on Smart Structures & Materials, IOPP/SPIE Vol. 1777, pp.23-29

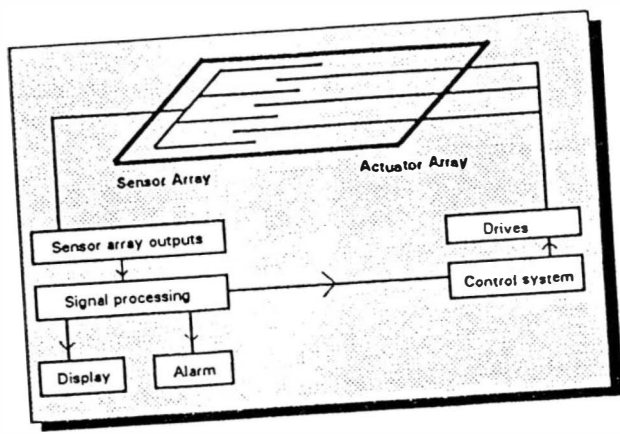


**Figure 1 : Schematic of Typical Smart Structure System**

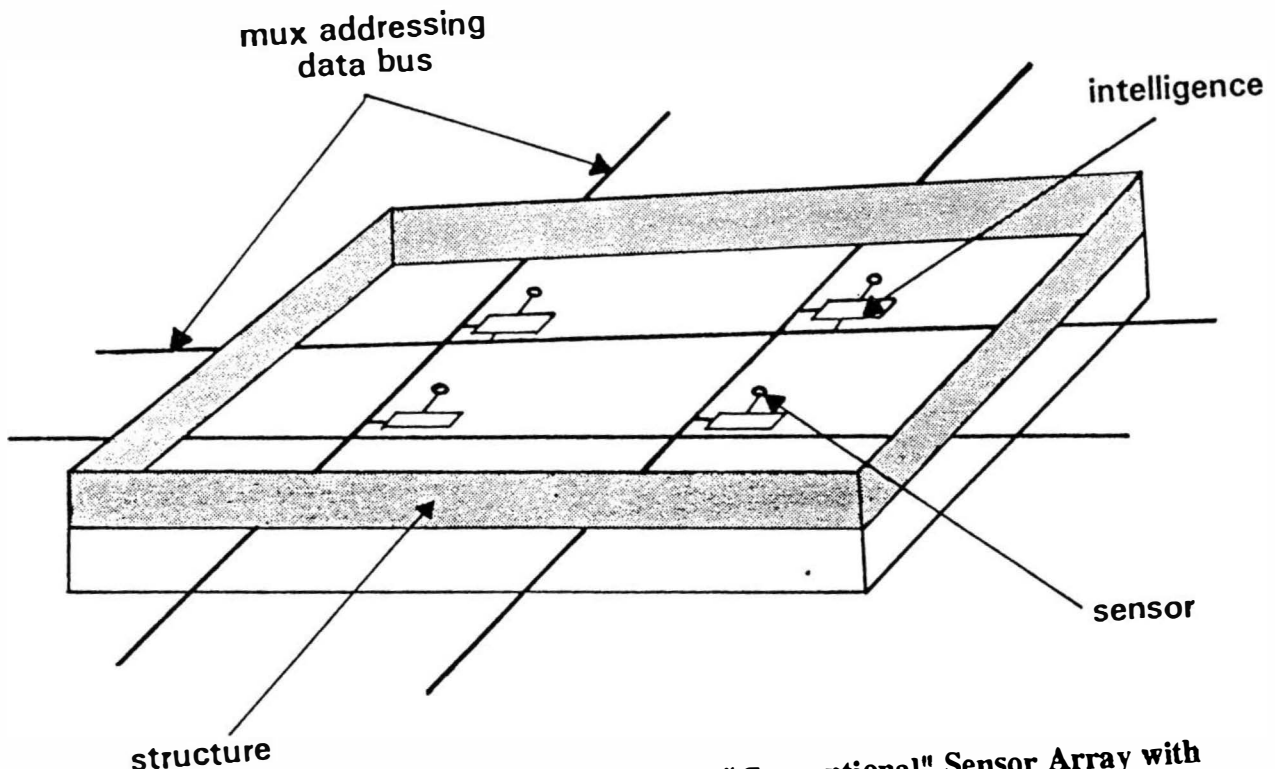


**Figure 2 : Conceptual Diagram of Embedded, "Conventional" Sensor Array with Local Intelligence**

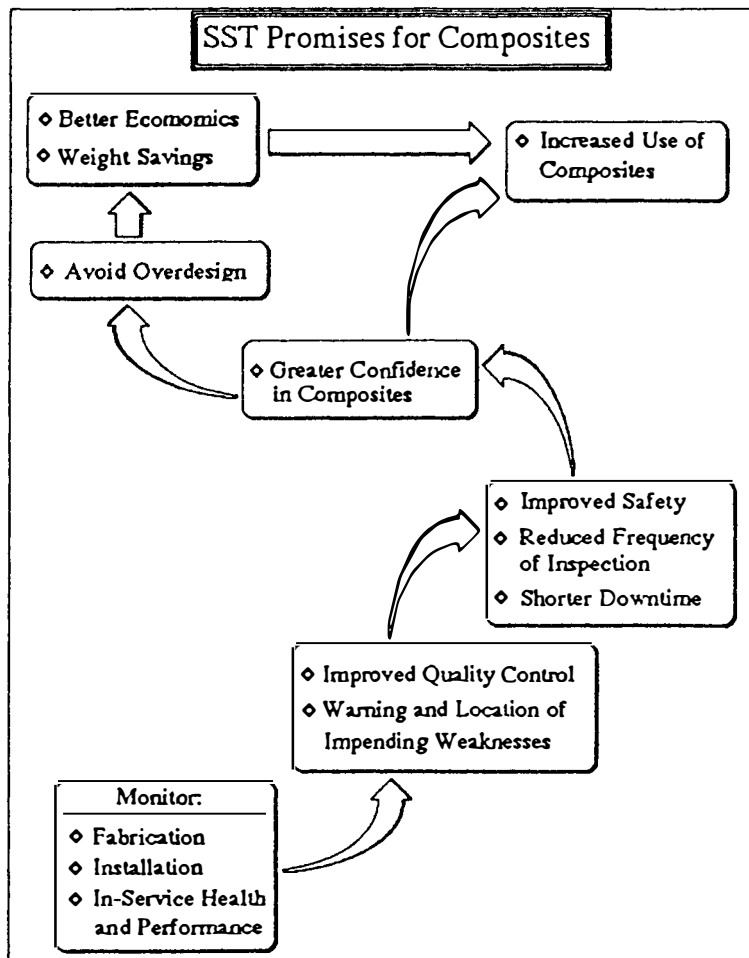


**Figure 3 : The Impact of Smart Structures Monitoring Technology on Composite Materials (Source: Measures, 1990)**

# ATTITUDE CONTROL SYSTEM OF THE AUTONOMOUS SPACECRAFT "MARS", DEVELOPMENT, GROUND VALIDATION AND VERIFICATION, FLIGHT CONTROL OPERATION

A. Vinokurov, Yu. Glinkin and A. Uliashin

Lavotchkine Science and Production Association, Babakin Engineering and Research Center, 24 Leningradskoe sh.,  
Khimki, Moscow reg., Russia 141400

**Abstract.** The conception of the Attitude Control System (ACS) is described for the spacecraft (SC) designed for exploration of the planets of the Solar System. Particularities of Mars mission are noted.

The multi-functionality of the ACS is a particularity of the ACS for the future mission, i.e. control of the SC injection into the trajectory of flight to Mars, the SC attitude control during transit, control of the probes release for their landing onto the Mars surface, as well as control of the on-board automated equipment, high gain antenna actuator etc.

The problems are discussed reflecting the phases of the System development and procedure of the ground testing providing the cycles of the hardware and software tests in all possible extreme modes taking into account the real program of flight to Mars.

The procedure of the ACS interaction with the ground control station is described. The procedure of development and ground testing of the ACS is as a result of experience accumulated during many years in such the programs as missions to Venus, Mars, Phobos.

**Key words.** Attitude control system; optical sensor; inertial measurement unit; acceptance tests; on-board computer complex; ground tests; flight control.

## INTRODUCTION

The Lavotchkine Association began the development of the spacecraft since end of 1960-s, including the craft designed for the exploration of the planets of the Solar System: Mars and Venus. As a result of this activity were 16 launches to Venus and 8 to Mars.

Main purpose of any mission - to deliver to the region of planet of the maximum possible payload: exploration equipment, with provision of its operation and transmission of acquired data to the Earth - defines the requirements to the parameters of the attitude control system (ACS), to its functional capabilities and impose the severe requirements for minimization of its mass and power consumption.

The conditions of operation of the autonomous Spacecraft (SC) with the distance of flight from the Earth up to 400 millions of kilometers

require to point the high gain antenna (HGA) permanently to the Earth, and absence of the constant RF visibility of the SC from the ground tracking stations (at sufficiently long time of the signal propagation through the link "Earth-SC-Earth") requires from the control system of the maximum independence, especially in the possible emergency situation.

Use of the solar energy for powering of the on-board subsystems and for the necessary thermal control is the most optimum, but it requires from the ACS to keep the SC attitude pointed to the Sun at any emergency situations in the control units.

Not the least of the problems during the control system designing are choice of the conception of the actuators, definition of necessary fuel mass and optimization of the dynamic algorithms of control. The following requirements can be briefly formulated which

the control subsystem must meet:

- . accuracy of the attitude and minimum angular rate of stabilization;
- . capability to perform the manoeuvres at the SC re-pointing;
- . endurance and independence;
- . minimum of equipment mass and power consumption.

### OPTIONS OF THE CONTROL SYSTEM CONCEPTION

The following two options of the ACS conception were developed and realized during Lavotchkkin Association activity in the field of the interplanetary SC designing.

First option includes two separate subsystems:

- . subsystem of the autonomous control during SC powered flight which function was to solve the problems during the SC injection into the mission trajectory, mid-course corrections, SC de-acceleration for its transfer in the planet's orbit;
- . subsystem of the SC attitude control providing the SC orientation and stabilization based on the reference points: Sun and star during interplanetary transit and operations in the near-planetary space (unpowered flight). In this case the dedicated subsystem provides the control of the on-board housekeeping units (pyrotechnics, power supply, thermal control, etc).

In this conception the HGA is rigidly attached to the SC body. Optics/electronics for the pointing to the Sun and star were equipped by the boresight devices steering by a special mechanism providing both the change of the SC attitude relative to these sources and keeping the designed Sun-SC-star angle during mission.

Canopus as a primary star and Sirius and Vega as a secondary stars (in case of necessity) were used as the reference points.

Fig. 1 Shows the cinematic of this option. This option of the control system conception was used for all SC designed for the exploration of Venus and Mars up to 1988. Search of ways to

increase the SC payload mass provided the decisive modifications of the ACS that required unifying of functions both of the subsystem of the SC control during powered flight and subsystem of attitude control during unpowered flight as well as the on-board automatic units providing operation of the housekeeping subsystems.

Due to the broadening of capabilities of such equipment as the on-board computing complex, inertial measurement units, commutation and amplification/conversion instrumentation it became possible to use these equipment both during the powered and unpowered flights as well as to provide centralized control of the housekeeping subsystems during whole mission. According to evaluation of experts, this allowed to increase the payload mass more than 100 kg.

In this option of the ACS conception the HGA is hinge mounted with the degrees of freedom providing the steering angle of +/-90 degrees. In this case the star sensor boresight axis has single degree of freedom which allows to keep the designed angle Sun-SC-star during whole mission. Despite of the more complicated SC design as a whole, such the configuration is more preferable from the point of view of the energetic and thermal stability of the SC.

Such an option of the ACS was for the first time used for the PHOBOS spacecraft and it was adopted for the mission to Mars scheduled for 1994.

The cinematic of this option is shown in Fig. 2. Fig. 3 shows the block-diagram of the ACS of the MARS spacecraft.

### ACS PHASES OF OPERATION

#### *Launch and Injection*

The ACS is switched ON during the phase of the SC/LV complex pre-launch preparation on the launch pad. The on-board equipment testing and calibration, the on-board digital computer complex loading by flight program, the inertial units launch targeting are carried out during this time.

Since the moment of take off the inertial units of the ACS perform the measurement of

motion of the SC center of mass and the on-board computer complex executes the calculations according to its deviations from the programmed position during operations of all the launcher stages.

The ACS begins to control of flight from the moment of the SC/upper stage composite separation from the launcher in the circular parking orbit where the counteraction of injection errors, induced by the launcher, is carried out.

Beginning from this moment the ACS provides the attitude and stabilization control, firing of the thrust engine of the launcher upper stage and than thrust engine of the SC in the desired point of the parking orbit.

### ***Flight.***

When the SC thrust engine shut down, the ACS generates the signals for deployment of the folded elements of the SC structure (solar panels, beams of the antennas and scientific instruments etc...) from the transport position to the operational one, it performs damping of the SC body rates and provides the SC necessary attitude relative to Sun.

In 1 to 2 days search and acquisition of the reference star are carried out and the SC is transferred in the mode of three-axis orientation which is kept practically during whole mission time.

The star search and acquisition are carried out in one of two options:

- . either the ACS performs automatic acquisition of the most bright star in the belt of the celestial sphere which is observed by the sensor field of view,
- . or the command for the star "acquisition" is generated on the Earth and it is transmitted to the SC after evaluation of the TM data acquired during the searching revolution.

The HGA pointing is maintained by the periodical switching ON of the actuators according to data calculated by the on-board computer.

This phase lasts 315 days. Three mid-course

corrections of the trajectory are provided for this phase.

### ***Near-Planet Flight***

This phase of flight is comparatively short but is characterized by very tense program of operation and it requires the essential energetic expenses. It begins from the moment of the probes release on the Mars surface with the following last correction of the trajectory. Then the SC is de-accelerated and transferred in the orbit of the Mars artificial satellite. Few orbit corrections are carried out to adjust orbit with designed parameters. Long-term solar eclipses (more than 3 hours of duration) is a particularity of this phase. To minimum energy expenses during eclipses it is planned to provide the SC gyro stabilization by its spin up about axis with maximum moment of inertia.

### ***Operations in Mars Orbit.***

This is main phase of mission and main attitude control mode is the Sun/star one. The ACS operation in the Mars orbit is characterized by often occultation of reference points - Sun and star by Mars. In order to keep the desired three-axis attitude, the ACS uses the inertial units / rate gyros assambly and gyroscopic platform/. These units are used at the pointing of the different instruments to the parts of the Mars surface as well, in this case the ACS provides the mode of the SC programmed turning with given rate.

### ***Modes of Equipment Operation***

Conditionally, the ACS equipment can be divided in two parts:

- . units which are in operation during "powered" modes such as mid-course corrections, search of the reference points, SC turns out to perform the scientific observations, probes release and compensation of the emergency situations in the ACS;

- equipment providing the SC attitude and stabilization in stationary modes i.e. during unpowered flight. The first part of equipment is characterized by high power consumptions and by the comparatively short periods of operation. These are: the on-board digital computer complex, gyro-stabilized platform, amplification and converting electronics.

The second part of equipment has low power consumption and it is used during whole mission. These are: the optical/electronic sensors and microprocessor of stabilization which forms the stabilization algorithm in the hibernation mode of operation and others. The Rate Gyros Assambly (RGA) is included in this equipment composition to provide the ACS functioning during the sun-star occultation by the planet while on the Mars orbit.

At the ACS designing for the MARS project the most of the technical approaches concerning the equipment, programs and algorithms were based on those of the PHOBOS

#### *Project.*

Achieved parameters of the ACS for the mission of 1988 such as accuracies of the SC attitude and stabilization, correction manoeuvres execution, HGA pointing, as well as the fuel-flow rate and the power consumption in the hibernation mode, are essentially higher than the specification requirements, so for the MARS mission it is sufficiently simply to repeat them.

Main attention was paied on increasing of the SC "survivability" and for this aim the number of equipment and modes was incorporated in the ACS composition, and the composition of algorithms, destined to overcome the unplanned situations, was enlarged as well.

At the same time a number of measures to increase the MARS SC reliability as a whole are fulfilled, namely:

- special tests and choice of the electric/radio components,
- modification of the communication and power subsystems,
- increase of amount of the ground tests of all the SC subsystems.

#### GROUND TESTS

The ACS ground testing is carried out in two ways:

- tests of the equipment composing this system.
- work out of the programs and algorithms.

The control system, as a complex of equipment, is tested in its manufacturing factory in the following sequence:

- Autonomous laboratory tests of the first testing models of the ACS units designed to verify that their parameters correspond to the validity requirements
- These tests are carried out at the extreme operational conditions. The elements which are the most susceptible to the effect of the environmental factors are revealed during these tests; the structural margins of the components are checked out as well.
- Integrated laboratory tests of the control system designed to work out the interaction of the system units both between them and with adjacent systems or their simulators.
- The programs and algorithms are tested out in the dedicated analogue/digital set up. This facility provides work out of the on-board algorithms including the algorithms of stabilization and control.
- The last phase of the ACS tests at the factory are the acceptance tests using the integrated facility. The Electric Ground Support Equipment (EGSE) include special computer through the interfaces of which the total simulation of the adjacent systems (such as the communication subsystem, automated units, power subsystem etc ...) is provided. This facility allows to work out the on-board algorithms taking into account the real dynamics of data exchange with the units flight models, to monitor whole equipment state, including checking of their margins.

The amount of tests in this set up is based on the checking of the sequence of all modes which are maximum close to the real program of flight. Emergency situations are worked out as well. Essentially, this set up is a last phase of work out of the ACS philosophy, programs and algorithms, meanwhile the full cycle of the ACS testing is not completed in this stage.

The next stage of the ACS tests is its testing together with the SC engineering model which is completely identical to the SC flight model.

These tests begin from the autonomous testing repeating the tests on the integrated set up but at the somewhat decreased amount. When the autonomous tests are completed, the ACS is mated with the flight equipment of the on-board subsystems: communication, power supply, commutator, switch, etc. Only the single-use devices as well as pyrotechnics and thrust engine are replaced by their simulators.

This phase of testing provides the check out and work out of interaction of all the on-board sub-systems according to program which is as close as possible to the flight one. Using its digital computers the control system EGSE provides the computers loading with the software and check out of operations to be executed during the communication contacts.

The ground-based temporary memory allowing quickly correct the programming/algorithmic software is used during all above testing stages. When the tests of the ACS together with the SC engineering model are completed, this temporary memory is replaced by the permanent one with the final version of the on-board program.

The ACS flight model is tested in identical way, but after transport to the Space Launch Site it is supplementary tested together with the SC.

The equipment margins check ups are provided for all phases of tests.

## FLIGHT CONTROL

Control of flight of the SC, designed for exploration of the planets of the Solar System, is carried out at the stations of the Center of Far Space Communication (CFSC). Main station of the SC flight control with the operational personnel is that of Evpatoria in Crimea. The duplicated station is at Ussuryisk. The data link between the stations is provided by the ground and space-based relaying facilities. The CFSC is equipped with the computing complexes controlling the ground-based communication complexes designed for reception and transmitting of the data, processing of the TM and trajectory data, preparation and realization of the control

programs.

Personnel of the Lavotchkine association elaborated a certain approach to development of the programs of control during years of work bounded up with control of the interplanetary spacecraft.

The integrated program of the craft control is created during the phase of the mission designing. The chronographic of the communication contacts for the SC control are developed during this phase taking into account the program of flight and restrictions conditioned by the limits of radio visibility, energetics and requirements of the communication link data rate.

To the moment of launch the team of experts of planning prepares the program of control for the first month.

The operational planning of next communication contacts is performed by dedicated group and it is terminated one day before the contact execution. This group consists of the sub-group of the SC flight control and that of analysis of the on-board sub-systems health; experts of control are also included in this second sub-group.

The TM data reception begins from the moment of the launcher take off and continues practically interoptionally during whole phase of injection. The ground and sea-based tracking stations are in use for reception of the TM data; the received data are relayed to the Space Flight Control Center. The SC injection and all "powered" mid-course SC trajectory corrections as well these of the Mars orbit are executed completely autonomy.

The SC active flight control begins after its injection into the trajectory of interplanetary flight. The control commands for the MARS ACS can be divided in the following groups:

- . commands of choice of the attitude modes,
- . digital control data of the modes ,
- . commands and programmed/digital data used in the emergency situations.

During designed mission program execution while on the unpowered path the ACS uses

minimum number of commands destined only for choice of the attitude modes (for instance Sun pointing or Sun/star attitude). The attitude control is performed using the programs of the permanent memory and it is autonomous.

The communication contacts for the mid-course corrections as well as the operations for the science equipment pointing to the different Mars regions, provision of the communications with the probes, the SC re-pointing to the different reference stars (Sirius, Vega) require the on-board computer complex loading by the programmed/digital data.

If necessary during flight (or in the case of emergency situation) the on-board computer software correction is executed. The program of the algorithms correction is firstly worked out in the simulating set-up of the manufacturing factory, then in the engineering model and only after that it is transmitted to the SC. The data communication channel between the set up, engineering model and SACS is provided to generate such a program.

The most qualified experts directly participating in the ground and space-borne equipment development work in the group of operational control.

Experts of the ACS sub-group provide operational monitoring of the ACS functioning, post-communication contact analysis and preparation of the programmed/digital data for the next communication session.

The control sub-group prepares the next communication contact for the SC control on the basis of the data streams formed by experts of each of the sub-groups. The elaborated data stream is checked using the mathematical model and it is transmitted to the SC during next communication session.

The condition of the obligatory check out of given program execution by the SC using the TM data is a basis of either program execution.

## CONCLUSION

The described approach to designing and tests of the ACS as well as the conception of the space flight control were used for many spacecraft including the GRANAT SC which now successfully performs its tasks. The ACS equipment and program/algorithm software are ameliorated with each mission. At the same time the EGSE, the computing means and programming/algorithmic software designed for the SC flight control are ameliorated. We would like to hope that all our efforts will allow successfully fulfil the planned program.

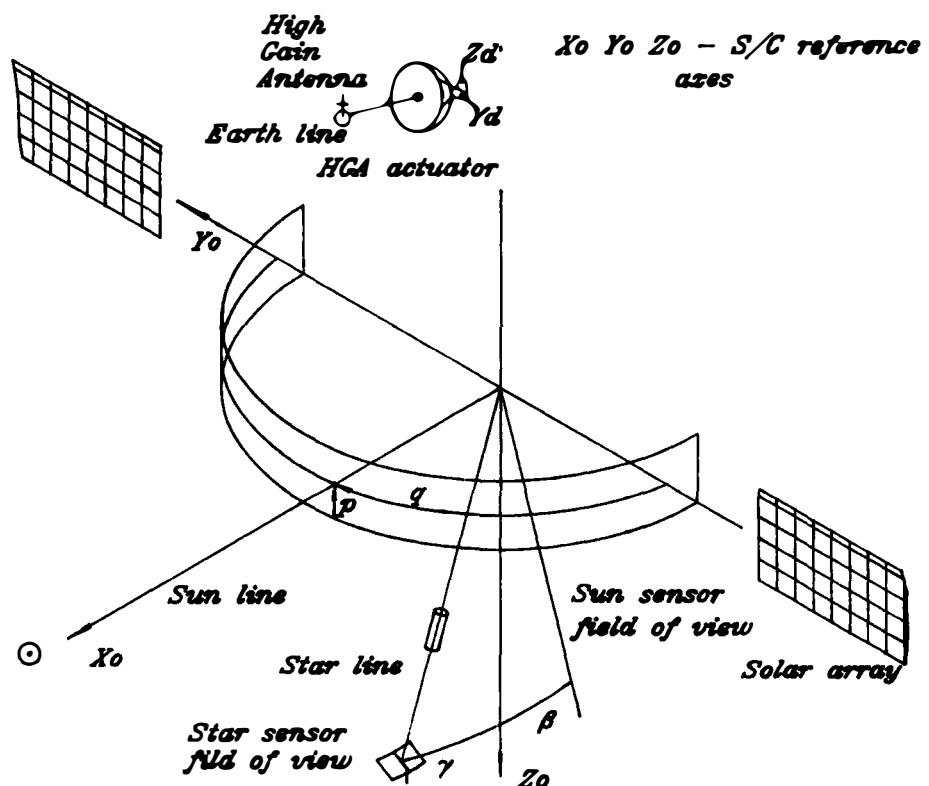


Fig.2

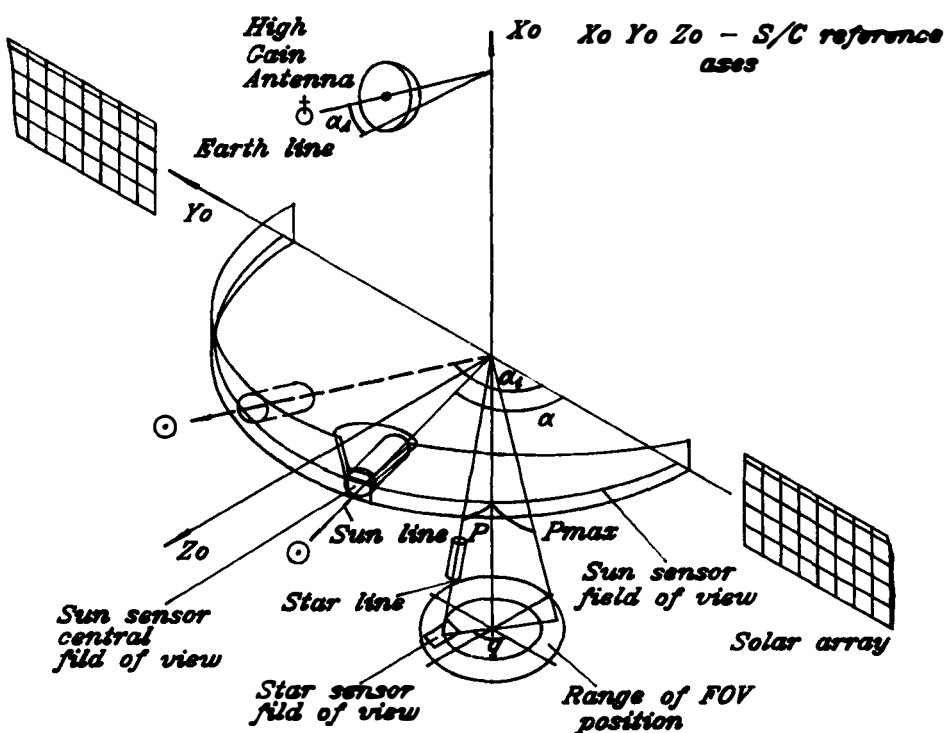


Fig.1

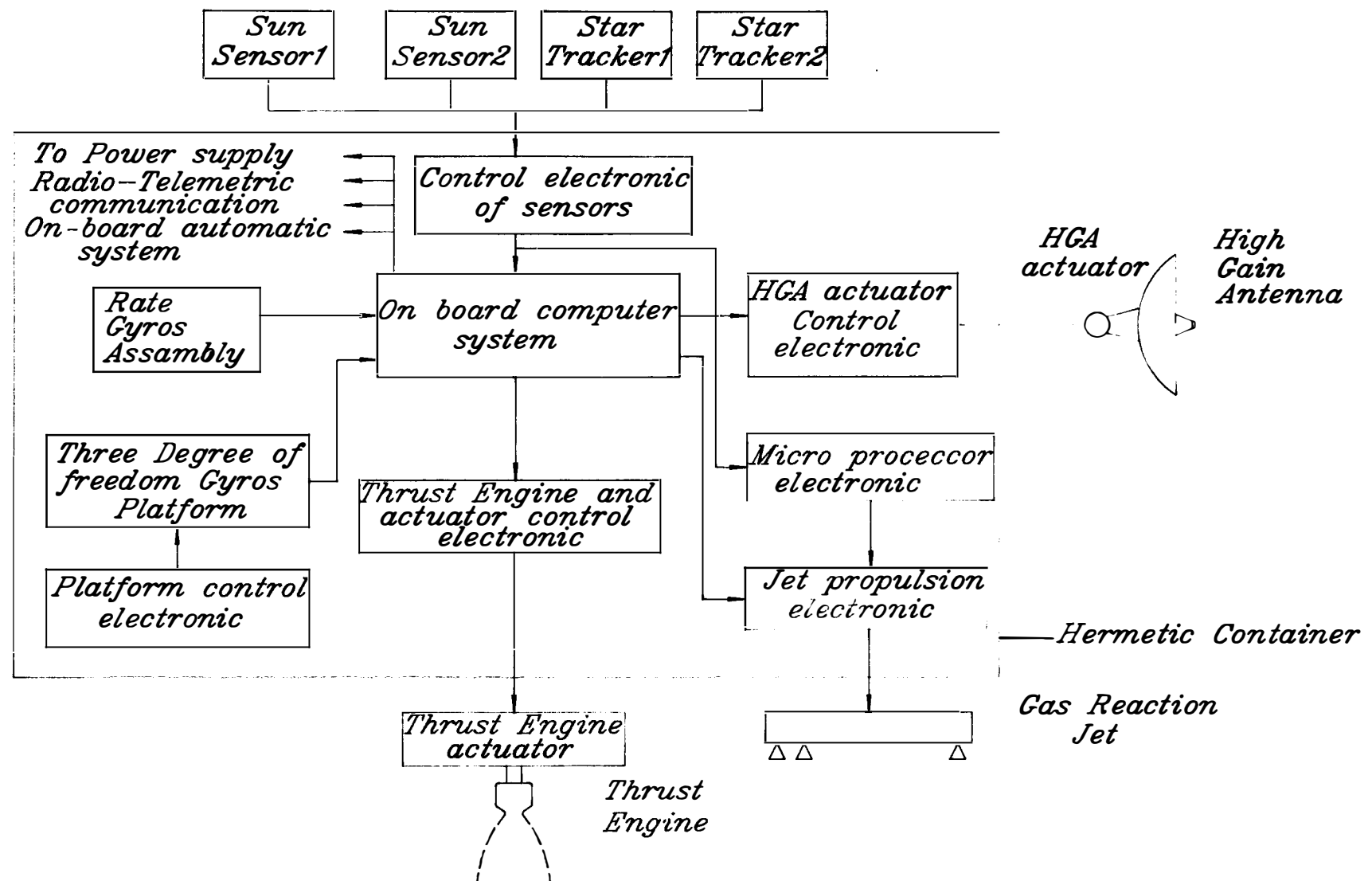


Fig.3 Attitude Control System

## ROSAT FLIGHT EXPERIENCE WITH H/W-DEGRADATIONS AND S/W-RECOVERY MEASURES

W. Schrempp, A. Böinghoff, E. Brüderie, L. Kaffer and P. Wullstein

Messerschmitt-Bölkow-Blohm GMBH, Space Communications and Propulsion Systems Division, P.O. Box 80 11 69,  
8000 München 80, Germany

ROSAT, launched on the 1st of June 1990, has opened a new era of X-ray astronomy. After about one year of operation, the attitude measurement system became faced with severe degradations of components. The paper describes how the fully autonomous mission could be reestablished by an onboard evaluation of magnetometer and coarse sun sensor measurements.

### INTRODUCTION

ROSAT is a large astronomical satellite designed to observe X-Ray sources. It was built as part of a cooperative US-German-UK programme with primary responsibility for manufacture of the spacecraft falling to German industry contracting to the German Research and Testing Institute for Aeronautics and Astronautics (DLR). Responsibility for the Attitude Measurement and Control Subsystem (AMCS) was with Messerschmitt-Bölkow-Blohm (MBB), who carried out design, development and test of the subsystem as a whole, and also manufactured or procured the measurement and control hardware.

The scientific mission consists of 2 different operational modes which also define the essential tasks of the attitude measurement and control system.

- scanmode (sky survey)

In this mode one axis of the S/C is oriented to the sun and the S/C rotates around the sun line with a scan rate equal to the orbital rate. The telescopes mounted perpendicular to the rotation axis scan the sky along a great circle. Due to the apparent motion of the sun of 1°/day with respect to the stars, a complete survey of the celestial sphere is performed within half a year (180 days).

- pointingmode

After the sky survey long term observation of selected targets are performed with high pointing accuracy and at the end of each observation period wide angle slew manoeuvres are performed to the next target at a frequency of about 20 - 30 slews per day. The attitude measurement accuracy is better than 2 arcsec during the pointing phases.

Basis of the attitude measurement and control system are the following equipments with the manufacturers mentioned in brackets:

- two high precision star sensors (MBB/SIRA)
- a gyro package consisting of 4 single axis high precision rate integrating gyros (Ferranti)
- one three axis magnetometer (Institut Dr. Förster)
- 3 coarse sun sensors (TPD/TNO)
- 4 reaction wheels (Teldix)
- 3 magnetic coils (Fokker)

An attitude measurement and control data system (AMCD) based on a microprocessor onboard computer with an INTEL 8086 central processing unit and 24 k \* 16 bit ROM and 12 k \* 16 bit RAM, makes the connection between the different equipment together with an attitude measurement and control electronics (AMCE) [1].

### EVENTS IN THE ROSAT LIFETIME

One can say that the ROSAT AMCS worked nearly per-

fectly during the first 7 months of lifetime [2]. Determination and compensation of gyro biases and scale factors was performed only once just after the launch and allowed large angle slew manoeuvres with an accuracy better than a few arcminutes.

After 7 months the mission became influenced by AMCS H/W-degradations with the following situation after about 1.5 year:

- loss of one star sensor
- loss of one gyro (y-gyro)
- severe degradation of the x-gyro with non-predictable drift after a significant rate change
- significant degradation of the z-gyro drift and scale factor
- moderate degradation of the s-gyro (aligned in diagonal).

The loss of the star tracker redundancy did not lead to an interruption of the nominal operation since a redundant star tracker is available. In December '90 drift and scale factors for several gyros were out of specification and moreover time varying. Especially the x-gyro drift was out of specification by an order of magnitude. It was no longer predictable and jumped drastically with slew rate direction changes. The normal operation was therefore performed with the remaining three gyros and could only be maintained with a very busy groundstation for determination and compensation of gyro errors as often as possible.

As a consequence of the gyro failures, an automatic star acquisition after a slew manoeuvre was no longer possible which led to an interruption of the normal operation. Only a much reduced pointing program of one target per day could be performed by manual control from the ground station.

Therefore an entire reprogramming of the measurement system was performed which derived the attitude information from the magnetometer and coarse sun sensor and used a new star acquisition procedure. After the loss of the y-gyro in May 91 the bad x-gyro had to be used again and the normal operation could no longer be maintained. The attitude errors after a slew manoeuvre became too large to allow automatically a successful star acquisition. Due to the few groundstation contacts per day it was only possible to continue the pointing mode mission with one target each day. With high priority a survival mode was worked out and loaded in order to avoid the risk of S/C loss in case of a further gyro failure.

In addition a new attitude measurement strategy was developed to enable a normal continuation of the mission with the evaluation of both sun sensor and magnetometer information together with a new star acquisition procedure, fully operational in the middle of October 1991.

The development, test and in-orbit experience with this new S/W are described in this paper.

## IN-ORBIT REPROGRAMMING OF THE AMCS-S/W

### Provisions in the onboard computer

For a reprogramming of AMCS-S/W almost optimum conditions were given, partly planned from the very beginning partly due to luck. A so-called "degraded mode" had been installed for in-orbit reprogramming [1]. Due to the modular structure of the S/W, the degraded mode can use all suitable routines of any other mode. 12 k \* 16 bits RAM are available for variables of the ROM routines and for reprogramming. New telecommands can be sent by the available "memory load" and some flexibility in the telemetry is given by 4 TM words whose addresses can be selected by telecommand.

In addition an accuracy much better than specified of both the coarse sun sensor and the magnetometer together with an excellent alignment were basic contributions for a successful redefinition of the new AMCS-S/W.

### First modifications of onboard S/W and groundstation measures

For the compensation of gyro drift and scale factor errors it has been assumed at beginning of the project that it would be sufficient to determine these errors on the ground and to send from time to time respective compensation commands. For the first 7 months they had to be commanded only once: drift values in the order of 0.1°/h and scale factor errors in the order of 0.001. In January 1991 the drift values increased by one order of magnitude and the scale factor errors went up to 0.03 which could no longer be commanded due to range limitations. These difficulties were overcome with a first modification of the onboard-S/W and new groundstation routines. In the onboard-S/W the following features were introduced:

- a command capability for a scale factor error compensation of up to  $\pm 0.125$
- a command for a correction quaternion vector to be multiplied from the left hand side to the actual onboard quaternion to support attitude corrections
- a command for a bias angular momentum component in the sun direction for increase of survival chances in case of AMCS failures.

### Redesign of AMCS after gyro failure

#### Survival mode

After the loss of redundancy in the gyro information it was decided that the most urgent activity was the installation of a survival mode to orient the -x-axis towards the sun from any initial orientation using only the coarse sun sensor information. For the realization two cases have been distinguished:

**Sun conditions:** From the sun sensor measurements the sun unit vector  $s_B$  in body coordinates is constructed and from this  $s_B$  is obtained by numerical differentiation. The best possible estimate for the angular rates is then derived from

$$\omega_{est} = \dot{s}_B \times s_B .$$

The control torques are then obtained by application of rate and attitude feedback with appropriate limiters and omission of roll attitude feedback.

**eclipse conditions:** In eclipse conditions no attitude control is performed but only a wheel speed

control maintaining the speeds measured at eclipse entrance. Due to the stored angular momentum in the wheels, the sun orientation is also maintained in eclipse.

The unloading of the accumulated angular momentum is performed as follows:

No unloading is performed under eclipse conditions. For the unloading in the sun phase the S/C angular momentum vector is needed. While the wheel angular momentum can be measured easily, a problem arises for the determination of the S/C angular rates. Under steady state sun pointing conditions it can be assumed that  $\omega_y$  and  $\omega_z$  are about zero. But no rate information about the x-axis can be derived from the sun sensor. It was decided not to consider additional magnetometer measurements for roll rate derivation but to take directly gyro information and to use

$$\omega_x = \frac{1}{2} (\omega_{xG} + \omega_{sG})$$

where

$\omega_{xG}$ : roll gyro measurement

$\omega_{sG}$ : measurement of gyro in diagonal

and where under steady state conditions the relation

$$\omega_{xG} = \omega_{sG}$$

holds. This means that the unloading still works properly even if one of the used gyros would fail.

### New attitude reference generation and star acquisition procedure in normal mode

In the normal operational pointing mode the AMCS has to perform automatically slew manoeuvres and to acquire and to identify catalogue stars, once the target direction is reached. The two main difficulties due to gyro degradations are

- inaccurate performance of slew manoeuvres with the consequence of unsuccessful star acquisition
- violation of a required safety cone angle of 20° for the -x-axis and subsequent transition to survival mode in case of long periods without star reference.

They have been overcome with the following, basically new features of the ROSAT attitude measurement system:

- establishment of three axis inertial attitude information from coarse sun sensor and magnetometer with an accuracy better than 1° in each axis
- star acquisition and identification with 6 catalogue stars for any target and attitude errors up to 1° in each axis.

The two new measurement sources for inertial reference of sun and earth magnetic field are used in periods where no star sensor measurements are available. Two surveillance functions are introduced:

- If an attitude error is detected which is larger than a commandable lower limit, either by the sun sensor or the magnetometer in eclipse an attitude correction is performed.
- If the star acquisition is not successful during sun phases, a three axis attitude correction is performed using the sun sensor and magnetometer measurements.

Due to the variation of the magnetic field direction over the flight path the above means provide a three axis attitude information of the required quality both in sun and eclipse phases and guarantee always prevention of survival mode triggering. Moreover, the attitude information has been improved by an automatic onboard x-gyro drift estimation and compensation when star reference is available. In periods without star reference the latest estimate is then used for compensation.

For the star acquisition and identification a new routine was available from the ASTRO-SPAS project currently in development at MBB. Fig. 1 gives an overview about the new design of the normal mode attitude measurement system. More details about the inertial reference derivation and the acquisition procedure are given in the following sections.

### Two axis attitude reference from sun sensor

The coarse sun sensor is aligned along the negative x-axis and measures directly the y- and z-components of the sun vector in body coordinates.

Denoting:

$s_B$ : measured sun unit vector in body coordinates

$s_i$ : sun unit vector in inertial frame obtained by computation

$q$ : quaternion vector describing the onboard knowledge of the S/C attitude w.r.t. the inertial frame

$Q$ : direction cosine matrix computed from  $q$

a correction quaternion vector  $q_c$  is derived from the available  $s_B$  and  $s_i$  according to

$$\Delta s = (s_B - Q \cdot s_i)/2$$

$$\Delta q = \Delta s \times s_B^T$$

$$q_c = (\Delta q, 1)^T$$

By evaluation of the sun sensor measurement the best estimate for  $q$  is then obtained by the quaternion multiplication

$$q_{\text{new}} = q \cdot q_c$$

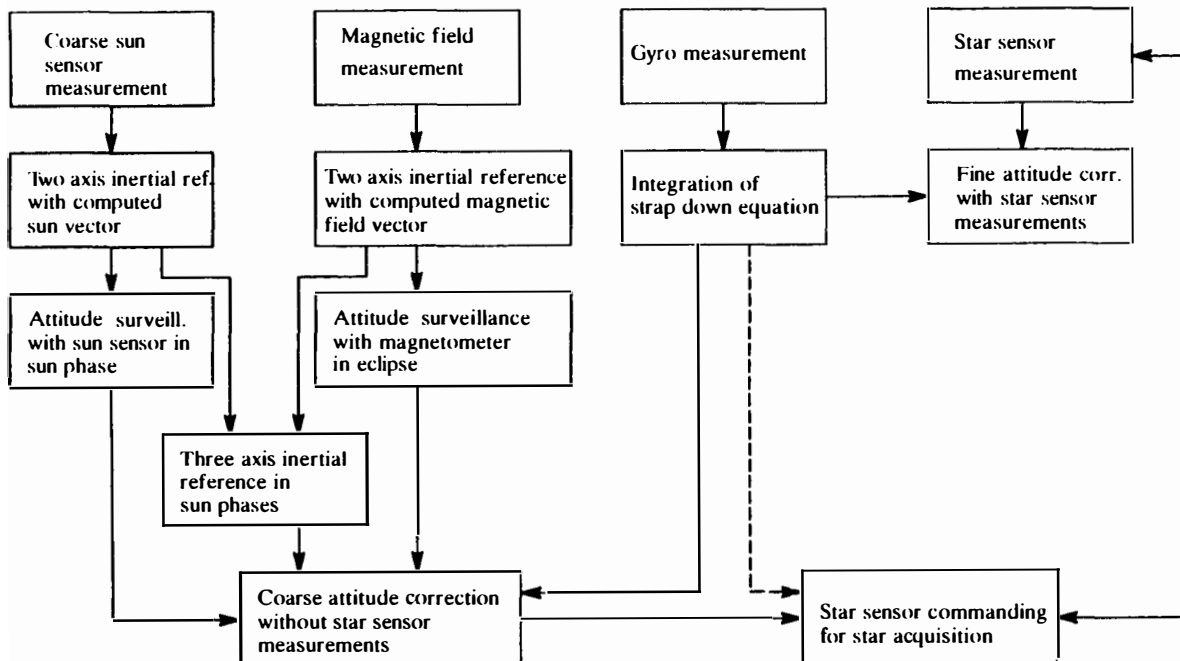


Fig. 1: Functional Blockdiagram of Attitude Measurement System

### Two axis attitude reference from magnetometer

The attitude reference derivation from the magnetometer is in analogy to that one from the sun sensor. Denoting

$B_B$ : measured magnetic field vector of the earth in body frame

$B_i$ : magnetic field vector in inertial frame obtained by computation

the correction quaternion  $q_c$  is derived as follows:

$$B_c = Q \cdot B_i$$

$$BB = B_B \cdot B_i$$

$$\Delta B = (B_B - B_c)/2$$

$$\Delta q = \Delta B \times B_B/BB$$

$$q_c = (\Delta q, 1 - 1/2 (\Delta q_1^2 + \Delta q_2^2 + \Delta q_3^2))^T$$

where it is assumed that the angle between  $B_B$  and  $B_c$  is small and therefore

$$BB \approx |B_B| \cdot |B_c|$$

The computation of the magnetic field vector is of course of considerable complexity. An 8th order model is used with coefficients of the 1990 International Geomagnetic Reference Field model which have been extrapolated to 1991 [3].

A correction quaternion is obtained only every two minutes since the magnetic unloading of the angular momentum has a 2 minute period. 110 sec the coils are on and 10 seconds they are off. In this 10 second interval the update quaternion is derived with a filtering over the last 7 seconds thus avoiding disturbances of the magnetometer by the coils.

### Three axis attitude reference from sun sensor and magnetometer

A full three axis attitude information is derived by combination of sun sensor and magnetometer measurements as long as the angle between  $B_i$  and  $s_i$  is larger than 30°. Pitch and yaw attitude is derived from the sun sensor and roll attitude with the magnetometer information according to

$$\begin{aligned}\Delta q_1 &= (B_{c2} \cdot \Delta B_2 - B_{c2} \cdot \Delta B_3 + B_{c1} \cdot (B_{c2} \cdot \Delta s_3 - B_{c3} \cdot \Delta s_2)) / (B_{c2}^2 + B_{c3}^2) \\ \Delta q_2 &= -\Delta s_3 \\ \Delta q_3 &= \Delta s_2 \\ q_c &= (\Delta q_1, 1 - 1/2(\Delta q_1^2 + \Delta q_2^2 + \Delta q_3^2))^T\end{aligned}$$

where every two minutes an update is derived as described in the previous section and where  $\Delta q_i$  is filtered.

### Star acquisition and identification strategy

In Fig. 2 the star acquisition and identification strategy is illustrated. The procedure depends strongly on the  $4.4^\circ \times 5.9^\circ$  sensor FOV and the property of finding the three brightest stars in windows with commandable centre and size. In a first step a search operation for the first catalogue star (guide star) is performed. The found stars are one after the other interpreted as the catalogue star looked for. The deviation from the nominal position in the FOV is assumed as attitude error where a rotation around the optical axis is neglected. With this assumption further catalogue stars are searched with dedicated small windows. If in this second step stars are found, a distance and magnitude criterion is applied for identification.

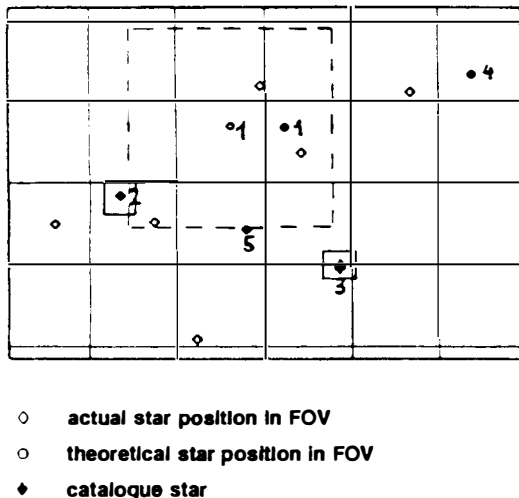


Fig. 2: Star Finding Strategy

When the first catalogue star does not lead to a successful result, the procedure is repeated with the next catalogue star as guide star and so on. In principle, the strategy will be successful if at least two catalogue stars are in the sensor FOV and if the catalogue stars are selected in an appropriate manner. This means that the procedure works for attitude errors up to about  $2^\circ$ .

### S/W-IMPLEMENTATION ASPECTS, GROUND TEST AND IN-ORBIT EXPERIENCE

Due to the limitations of the CPU used, the coding of the new S/W had to be performed in assembler language and suffered from the fact that no floating point arithmetic could be applied and each algorithm had to be scaled, always necessitating a compromise between maximum value limitation and accuracy.

The only library functions being available in the ROM-S/W were the sine/cosine functions. For the new S/W, however, the sqrt-function and the arctg-/arcsin-function became necessary. While the sqrt-operation could easily be circumvented by linearization, the transformation from orbit angles to spherical coordinates for the computation of the earth magnetic field vector such as

$$\begin{aligned}\gamma &= \text{arctg } [\tan \alpha \cdot \cos \beta] \quad \alpha: \text{true anomaly}, \\ \gamma &= \text{arcsin } [\sin \alpha \cdot \cos \beta] \quad \beta: \text{inclination}\end{aligned}$$

caused many more difficulties because the full  $[0, 2\pi]$  range is required for  $\alpha$ . The solution was seen not in the establishment of respective new library routines but in the integration of the time derivatives of the above expressions where an accumulation of the integration error was prevented by setting proper initial values every  $45^\circ$  for  $\alpha$ . With this mean all trigonometric transformations could be performed with an accuracy better than  $0.1^\circ$ . For the ground tests of the new S/W a very lucky circumstance helped us. For training and mission preparation purposes an AMCS-simulator with an engineering model of the AMCD was available and still operable at the German spaceflight operation centre (GSOC). With this adequate facility all ground tests were exceedingly efficient and only two minor problems were encountered:

- although the drift estimation consisted only in a few statements, the estimated drifts were always wrong by about  $0.5^\circ/\text{h}$ . The reason was finally found in inaccuracies of simulator-H/W, the S/W working properly later in the orbit.
- the synchronization between the simulated magnetic field and the onboard model was not accurate enough in the beginning. With easy means it was, however, possible to reduce the error to about  $1^\circ$  which just allowed representative tests.

The loading of the new mode was performed in three steps according to the completion schedule:

- survival mode and sun sensor attitude surveillance
- star acquisition and gyro drift estimation
- attitude derivation from magnetometer completing the new mode

After several weeks of successful running of the S/W of the first step the sun sensor attitude surveillance caused several times a transition to the survival mode rather than preventing it. The reason was found in an erroneous attitude update due to penumbra effects just before entering eclipse which faced the AMCS with survival mode conditions after eclipse. With the second S/W loading this problem could be solved by a 10 % increase of the sun presence threshold. The second part of the S/W ran successfully from the very beginning and provided the first significant relaxation of the groundstation activities.

From an evaluation of telemetry data for a period of four days the following typical results have been obtained:

- 118 automatic slew manoeuvres were performed, only in one case the subsequent star acquisition was not successful within a 43 minute steady state pointing interval. The reason for this failure was found in a long period of star occultation by the earth and an unfavourable angle between  $s_i$  and  $B_i$  for another period which did not allow a three axis attitude update.
- During the 117 successful manoeuvres in total 336 attitude updates occurred, comprising 46 magnetometer updates during the slewing and 290 updates in steady state. The 290 updates consist of
  - 157 star sensor updates (3 axes)
  - 27 magnetometer updates (2 axes)
  - 8 sun sensor updates (2 axes)
  - 98 sun sensor & magnetometer updates (3 axes)
- In all of the 117 manoeuvres the last update

leading to steady state star sensor measurements was obtained from the star sensor. The following figures for acquisition support have been obtained:

- 33 cases with only star sensor update
- 15 cases with star sensor and magnetometer update
- 69 cases with star sensor, sun sensor and magnetometer update

This shows that all implemented attitude measurement function contribute to the acquisition

- The average acquisition time from completion of the slew manoeuvre until steady state star sensor measurements of identified stars amounts to about 9 minutes.
- In 5 cases a wrong star identification was performed leading to wrong attitude updates of up to  $10^\circ$  about the star sensor optical axis. The erroneous updates were, however, immediately corrected by the surveillance functions.
- From periods with star reference the following measurement accuracies could be derived:  
sun sensor: about  $0.5^\circ$  near the optical axis and up to  $1^\circ$  for directions  $15^\circ$  apart  
magnetometer: an RMS value of about 0.01 for  $|\Delta B|/|B|$ , with occasional maximum values, however, of up to 0.1. The reason for these excursions is seen in magnetic disturbances by payload operations not yet identified. The distribution function for the errors of the magnetometer derived attitude is shown in Fig. 3.
- Occasional large update errors from sun sensor/magnetometer were always corrected a few minutes later proving again the robustness of the design.

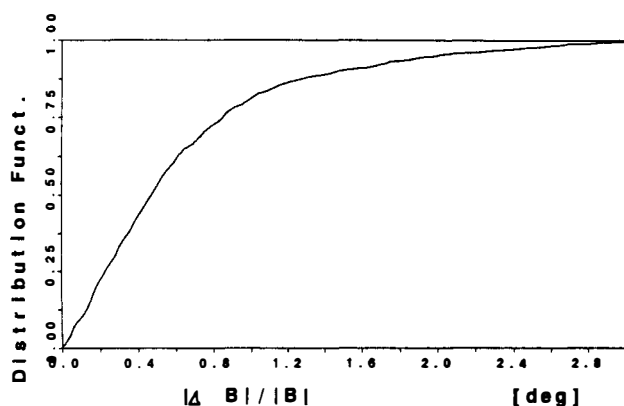


Fig. 3: Accuracy of magnetometer derived attitude

- The star acquisition procedure was as efficient as expected. In some cases star acquisition and identification was successful even for more than  $2^\circ$  initial attitude error.

#### ROSAT POINTING MODE OPERATION WITH LESS THAN 3 GYROS

With the loss of the y-gyro considerations have been started how to continue the mission if another gyro failure would occur. Although the z-gyro failure on 5th February 92 could be overcome with a S/W patch consisting in a change of the scalefactor from about 1.0 to 2.7, this event initiated a S/W development for a mission continuation with less than 3 gyros.

The new S/W gets the best rate estimation from the following sources:

- integration of the EULER equations
- derivation of the coarse sun sensor measurements
- derivation of the star sensor measurements
- use of remaining gyros.

Rate derivation by integration of EULER equations: With the assumption of the conservation of the angular momentum, with the measurement of the wheel rates and an initial value of the S/C rates, the nonlinear EULER equations are integrated and deliver a first estimate for the angular rates.

Rate derivation from sun sensor measurements:

In sun phases two axis rate information is obtained by evaluation of the equation

$$S_B + \omega \times S_B = 0$$

Additional  $\omega_x$  information is, however necessary for derivation of the entire  $\omega$  vector.

Rate derivation from star sensor measurements:

Three axis rate information is derived from two successive star sensor measurements providing three axis attitude information.

Use of remaining gyro information:

Evaluation of the afore mentioned sources results in a best rate estimate without use of gyro measurements, where the sources are listed with increasing accuracy. Available gyro measurements are now introduced that the resulting  $\omega$  vector meets the gyro measurement equations.

From the considerations above it can be concluded that for the continuation of the mission either the x-gyro or the s-gyro must be available because

- the EULER equation integration requires an initialization
- the sun sensor measurements needs  $\omega_x$  information as supplement for a complete  $\omega$  derivation
- prior to a star acquisition the rates have to be derived from other sources.

Rate derivation from the magnetometer measurements could be an additional possibility. The required rate accuracy of about 20 arcsec/sec for a star acquisition is, however, considered to be not directly achievable.

#### CONCLUSION

After about 7 months of nearly perfect AMCS function the gyro degradations complicated the operation and after one year the nominal mission could no longer be maintained.

The paper describes how the redesign of the attitude measurement using inertial reference generation from coarse sun sensor and magnetometer together with a new star acquisition procedure led to the reestablishment of the nominal mission. This success was only possible because sufficient reprogramming provisions in the onboard computer were available. The new S/W now occupies nearly the complete RAM area and increases the computation time from about 50 msec to 300 msec per 1 sec cycle. This proves that deficiencies of the H/W can be overcome by a more intelligent S/W. The redesign and implementation of the new AMCS S/W was performed in the short time of less than 5 months. This was only possible because the key engineers who developed the original ROSAT AMCS could be made available for the recovery activities.

Presently means of continuing the mission in the event of loss of further gyros by use of additional S/W in the remaining 0.7 K RAM is being studied. It has turned out too, that even after the loss of the remaining star sensor a recovery will be possible by a utilization of experiment data within the AMCS, although the level of pointing performance will be lower than that which is currently achieved.

## **ACKNOWLEDGEMENT**

The authors greatly acknowledge the encouragement for utilization of the magnetometer for attitude reference purposes by Mr. Hasinger, Max-Planck Institute, and the provision of the International Geomagnetic Reference Field. The test activities were intensively supported by the German Space Operation Centre engineers Messrs. Böllner and Feucht.

## **REFERENCES**

- [1] Design and Test of the ROSAT AMCS  
Schrempp, Alexander, Böinghoff, Brüderle,  
Herbst, Kaffer, Möckl, Oesterlin, Stins-  
hoff  
10th IFAC World Congress, Munich, FRG,  
1987
- [2] Evaluation of Flight Results of the ROSAT  
AMCS  
Schrempp, Böinghoff, Brüderle, Gradmann,  
Herbst, Kaffer, Oesterlin  
14th annual AAS Guidance and Control Con-  
ference, Feb. 1991, Keystone, Colorado
- [3] A set of FORTRAN subroutines for computa-  
tions of the geomagnetic field (GEOPACK)  
N.A. Tsyganenko, Institute of physics,  
Leningrad University, Stary Peterhof  
198904, Leningrad, USSR

# VALIDATION APPROACH FOR THE MODULAR ATTITUDE DETERMINATION CONTROL SUBSYSTEM IMPLEMENTED ON TOPEX/POSEIDON (T/P)

R.V. Welch and C. Gay

*Fairchild Space and Defense Corporation, Fairchild Space Company, 20301 Century Blvd.,  
Germantown, Maryland, USA*

**Abstract.** The Modular Attitude Control Subsystem (MACS) was developed as part of the Multi-mission Modular Spacecraft for NASA Goddard Space Flight Center in the late 1970s. This subsystem has demonstrated performance on multiple low earth orbit scientific missions. Application on T/P is derived from the flight proven LANDSAT-5 design and represents the first Fairchild development of the MACS. Design and development are complete with final ground verification underway to support a July 1992 T/P launch. The philosophy of the ground verification process is described in detail. The discussion will provide the approach of subsystem verification from component level testing through ever increasing levels of subsystem and satellite integration. The role of analyses will be described and some on-orbit subsystem performance issues are presented. This work was performed for the Jet Propulsion Laboratory, California Institute of Technology, sponsored by the National Aeronautics and Space Administration.

**Keywords.** Attitude Control; Ground Support Systems; Space Vehicles; Spacecraft Testing; Satellites; System Integrity.

## INTRODUCTION

In the first part of this paper, the Fairchild Modular Attitude Control Subsystem (MACS) developed for the T/P Mission will be presented and the heritage use of MACS modules on other spacecraft missions will be given. Description of the functional and performance requirements for the T/P MACS will be described.

The second part of this paper will present the ground validation approach used on T/P which relies on previous qualification tests for heritage design implementation. A discussion of the test/validation philosophy will be given showing the validation process from the component through full-up spacecraft testing. The last section will present some of the on-orbit performance verification issues.

## MACS MODULE DESCRIPTION

The MACS was developed for NASA Goddard Space Flight Center as an element of the Multi-mission Module Spacecraft (MMS) in the late 1970s. To date, variations of the MACS have been flown as part of the MMS on Solar Max Mission (SMM-1980), LANDSAT 4 (1982) and 5 (1984), and Upper Atmosphere Research Spacecraft (UARS-1991). In addition, the MACS was changed out on-orbit as part of the Solar Max Repair Mission (1984). During 1992, two missions (Explorer Platform and T/P) will be launched using MACS. These MMS missions are all low earth satellites which include earth pointers with pure pitch rotation (LANDSAT 4

and 5), earth pointers with pitch and yaw rotations (UARS, T/P), sun pointer (SMM) and anti-sun pointer with controlled roll about the sun line (Explorer Platform). Except for changes in actuator sizing, the MACS described in this paper, along with mission unique flight software, is capable of supporting all these missions.

The MACS module was originally specified to support sun pointers, synchronous earth pointers, and inertial pointers with inertia requirements between 1000 to 2000 slug-ft<sup>2</sup>. However, initial applications on the SMM and the LANDSAT-4/5 missions were for satellite inertias of 3000-4000 slug-ft<sup>2</sup>. In addition, UARS has inertia in excess of 43,000 slug-ft<sup>2</sup>. The continual growth in satellite requirements to support larger payloads and a variety of mission scenarios, has resulted in the necessity of augmenting the MACS Module to support these new requirements.

These augmentations have taken the form of larger Reaction Wheel Assemblies (RWA) (UARS, Explorer Platform, T/P), Magnetic Torquer Bars with increased dipole and/or mounted external to the MACS (UARS, Explorer Platform, T/P), Modified Attitude Control Electronics (ACE) (Explorer Platform, T/P). These changes were incorporated in an evolving design, whereby, overall design heritage and test qualification status was not greatly effected for each change. The MACS modules for all MMS missions prior to T/P were developed by General Electric. T/P MACS was developed by Fairchild Space using the LANDSAT implementation as a baseline from which to make only those design changes required for mission success.

The Fairchild MACS is derived from the flight-proven LAND-SAT-4<sup>1</sup> design and meets all the baseline LAND-SAT attitude control requirements. The functional block diagram and hardware layout of the Fairchild MACS are shown in Figures 1 and 2, respectively. The digital On-Board Computer (OBC), the Earth Sensor Assembly Module (ESAM) (mounted externally on the Earth-viewing face of the satellite) and externally mounted Coarse Sun Sensors (CSS) provide support to the MACS hardware complement. The specific Fairchild MACS hardware suite consists of a Teledyne Dry Rotor Inertial

Reference Unit (DRIRU-II) with redundant axis outputs, four Honeywell RWAs, three of which are orthogonal and the fourth is equiangular from the other three, redundant Fairchild ACEs, redundant Ithaco MTBs and Magnetic Torquer Bar Drive Assemblies (MTBDA), redundant Fairchild Remote Interface Units (RIU) and Expander Units (EU), one non-redundant Adcole Digital Fine Sun Sensor (DFSS), redundant Hughes Advanced Star Trackers (ASTRA), redundant Schonstedt Three-Axis Magnetometer (TAM) and a Fairchild Power Switching Unit (PSU).

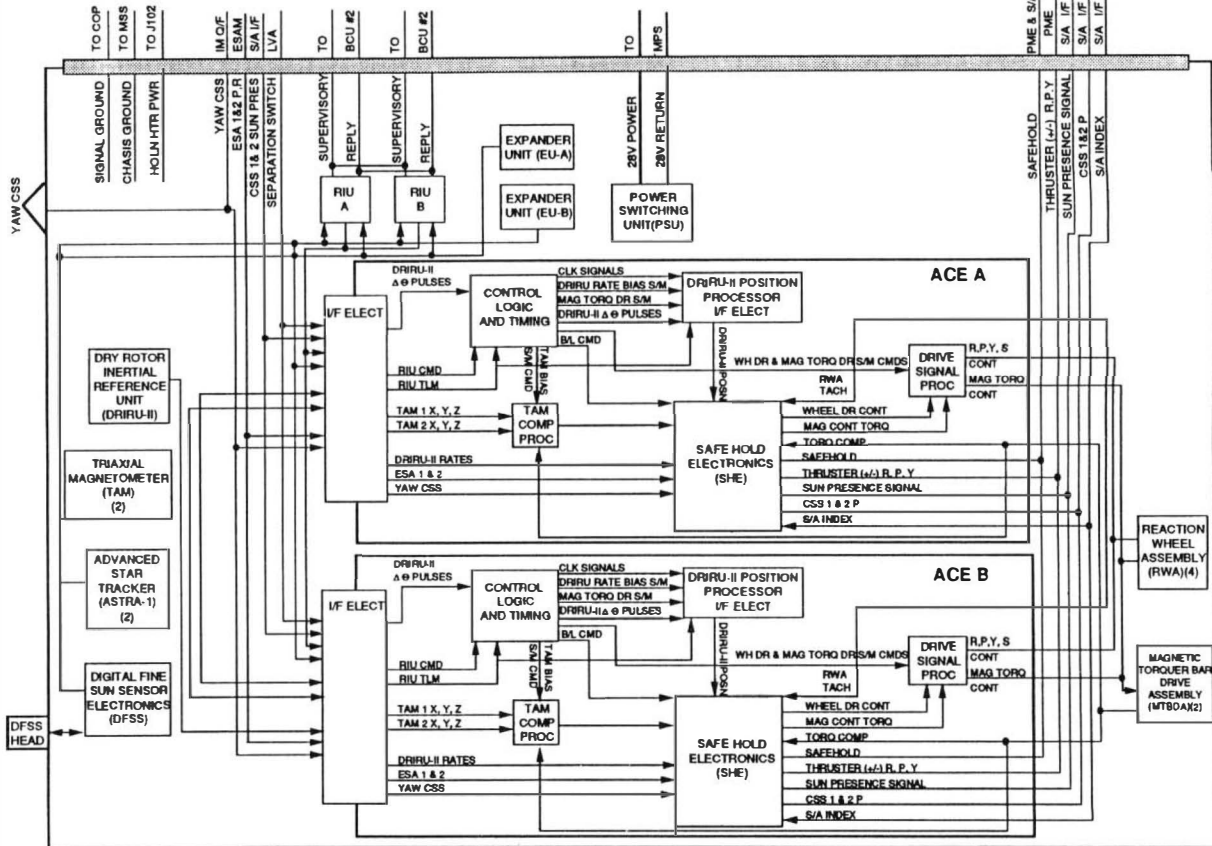


Figure 1: T/P MACS Functional Block Diagram

#### APPLICATION OF THE MACS TO T/P

The Fairchild MACS Module was developed to satisfy the T/P mission requirements. The T/P remote sensing mission is a joint scientific program sponsored by NASA and the Centre National d'Etudes Spatiales (CNES)<sup>2</sup>. The T/P satellite is being designed to make highly accurate measurements of the sea surface elevations over entire ocean basins for several years. The joint U.S./French T/P mission will provide the international oceanographic research community with a space-based capability to determine global ocean circulation patterns via high-resolution radar altimeter measurements of sea-surface topography. The primary T/P mission science requirement is to make geocentric measurements of the global ocean sea level with an accuracy of +/-14.0 cm and a precision of +/-2.4 cm along a fixed ground track that is repeated every 10 days for a period of three years, with a possible mission extension to five years (see Table 1). Fairchild serves as a prime T/P contractor responsible for the design, development, integration, test and launch of the T/P satellite under contract to the Jet

Propulsion Laboratory (JPL). Mission plans call for the T/P to be launched using an ARJANE-42P Expendable Launch Vehicle in July of 1992.

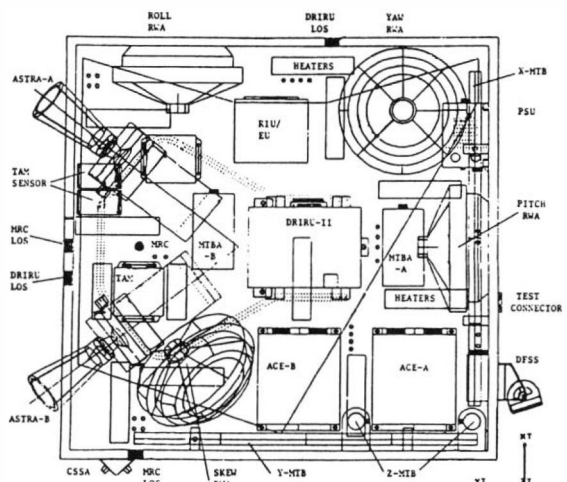


Figure 2: T/P MACS Module Hardware Layout

<sup>1</sup>The French National Space Studies Center

**Table 1: T/P Operational Orbit Characteristics**

Orbit Parameter	Value
Altitude	1335.5 Km
Inclination	65.1°
Eccentricity	<0.001
Phasing	Ground track over the Calibration Sites
Nodal Period	112.4 min
Ascending Node Crossings	12.7 per day
Ascending Node Longitude Increments	28.35°
Repeat Cycle (for ground track coverage)	9.91 days (127 revs)
Ground Cross Track Repeatability at Equator	±1.0 Km

### T/P SATELLITE DESCRIPTION

The on-orbit fully-deployed configuration of the T/P satellite is illustrated in Figure 3. When operating in the Normal Mission Mode (MMS), T/P is a local vertical oriented spacecraft (S/C) with the +Z (Yaw) axis pointed in the nadir direction. The nadir direction is specified to be along the local normal of the reference Earth geoid which is defined as an ellipsoid. At zero yaw angle, the longitudinal +X (Roll) axis points in the direction of the vehicle's orbital velocity vector. The lateral +Y (Pitch) axis is orthogonal to both the X and Z axes completing the spacecraft's right-handed coordinate frame.

As shown in Figure 3, the T/P satellite consists of two basic elements:

- the Instrument Module (IM) which houses the six mission sensors and associated electronics and provides the mounting provisions for both the deployable solar array and the deployable High Gain Antenna (HGA) used for communications with the Tracking and Data Relay Satellite (TDRS)
- the T/P MMS bus which accommodates the essential subsystems required to support mission payload operations.

### T/P MACS REQUIREMENTS

The T/P spacecraft is a three axis stabilized, zero momentum, Earth pointing satellite. The following sections describe the functional and performance requirements which the augmented MACS Module must satisfy in order to be used on the T/P satellite. Table 2 summarizes the Attitude Determination Control System operational control modes.

### FUNCTIONAL REQUIREMENTS

- Provide attitude pointing and stabilization immediately following separation from the third stage of the Ariane-42P booster to acquire the Earth.
- Accommodate OBC based Normal Mission Mode (NMM) attitude pointing and stabilization capability during all science taking periods without the use of the propulsion system.

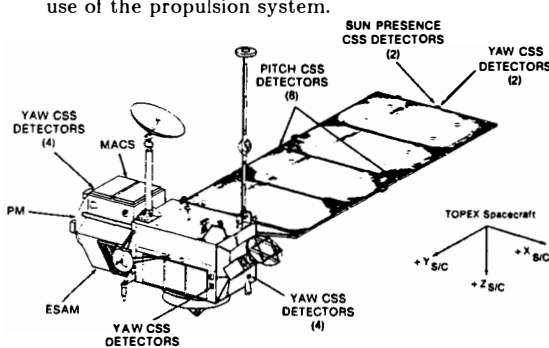


Figure 3: On-Orbit Fully Deployed T/P Satellite

**Table 2. T/P Required Operational Modes**

Operational Mode	Primary Sensors	Primary Actuators	Description
Computer Controlled Modes			
Earth Acquisition	DRIRU-II ESA	RWA	Use ESA pitch and roll outputs to acquire the Earth and DRIRU-II rate outputs to rate damp the roll, pitch and yaw axes.
Stellar Acquisition	DRIRU-II TAM DFSS ASTRA	RWA	Follows Earth or Fine Sun Acquisition. Use DFSS and TAM data to refine the initial attitude information.
Orbit Adjust	DRIRU-II	Thrusters	Use DRIRU-II data and thrusters to hold inertial attitude during orbit adjust burns. Low level thrusters used for roll control, high level thrusters modulated on/off for pitch/yaw control.
Calibration	DRIRU-II ASTRA	RWA	Use DRIRU-II to calibrate the ASTRA and the DFSS alignment errors.
Normal Mission	DRIRU-II, DFSS, ASTRA	RWA	Use ASTRA and DRIRU-II data for precision Earth Pointing. Requires high accuracy ephemeris data to achieve desired pointing accuracy.
Safe Hold Modes			
Earth Pointing (Gyrocompass)	ESA, DRIRU-II	RWA	Use pitch and roll data from ESA for position control and the angular roll rates from DRIRU-II for yaw control. Rate information is obtained from the DRIRU-II.
Earth Pointing (Yaw-Slew)	DRIRU-II, YCSSA, ESA	RWA	Use pitch and roll data from the MSS mounted ESA for position control and the YCSSA for yaw position control. Rate information is obtained from the DRIRU-II.
Sun Pointing	DRIRU-II, YCSSA, PCSSA	RWA	Use the PCSSA and YCSSA for pitch and yaw position inputs. Rate information is obtained from the DRIRU-II.

- Provide an analog backup Safe Hold Mode (SIIM) attitude pointing capability without the use of the OBC. Both an Earth pointing and Sun pointing mode of operation is required.
- Provide attitude pointing and stabilization during all thruster actuated orbit adjust mode maneuvers.
- Provide spacecraft yaw slewing control capability for proper solar array orientation in both the NMM and SHM modes of operation.

### PERFORMANCE REQUIREMENTS

The T/P MACS is designed to operate in two modes, Computer Controlled Mode (CCM) and SHM, each of these operating modes contains various sub-modes as listed in Table 5. In the CCM, the OBC contains the attitude control and stabilization algorithms to maintain the pointing and control requirements of the T/P satellite. The primary on-orbit sub-mode of operation is the NMM.

During NMM operations, the T/P MACS must provide precise pointing knowledge and control of the NASA radar altimeter radio frequency boresight axis relative to the nadir direction. The 1- $\sigma$  altimeter boresight nadir pointing knowledge and pointing control requirements are 180 arc-seconds (0.05°) and 288 arc-seconds (0.08°), respectively. Out of these system requirements, the resulting MACS NMM 1- $\sigma$  requirements for attitude determination accuracy and control were derived. These requirements are 54 arc-seconds (0.015°) and 144 arc-seconds (0.04°), respectively, per axis.

The capability for an autonomously initiated, powersafe and thermal-safe Earth Pointing mode of operation without the use of the OBC is required to provide a viable backup control capability in the event of OBC anomalies. The Earth Pointing Safe Hold Mode (EPSHM) controls the pitch and roll axes so that the spacecraft yaw axis is oriented towards the Earth while simultaneously controlling the yaw axis so that solar array is oriented approximately normal to the Sunline.

During on-orbit EPHM operation, the spacecraft pitch and roll axes must be controlled such that the spacecraft Z-axis is maintained towards nadir to within +/-3°. The spacecraft yaw axis must be controlled during EPHM such that the solar array normal is, on average during a given orbit, pointed along the Sunline to within +/- 15°<sup>3,4</sup>.

The Sun Pointing SHM locks the cell side of the Solar Array (S/A) along the -X axis of the spacecraft (index position). The spacecraft pointing requirements for this operational mode is to maintain the -X axis (array cell side) to the Sun within +/-10°.

## GROUND VERIFICATION PROCESS

The T/P Attitude Determination and Control Subsystem (ADCS) verification process encompasses the test and analysis efforts necessary to demonstrate the sufficiency of the ADCS design with respect to T/P requirements. This section reviews the structure and content of the T/P ADCS verification process. The ADCS consists of the MACS, ESAM, CSS, PM and flight software.

An outline of the ADCS verification process is presented below.

- Hardware Verification
  - Component Level Test
  - Modular Attitude Control Subsystem (MACS) Level Test
  - Multimission Modular Spacecraft (MMS) Level Test
  - Satellite Level Test
- Software Verification
  - Level 1 Engineering Development Test
  - Level 2 Flight Code Development Test
  - Level 4 Software Development and Verification Test
  - Level 5 Satellite Level Test
- Analysis and Simulation
  - Control Loop Stability
  - Attitude Knowledge and Control Error Budget

## REQUIREMENTS OVERVIEW

The primary objective of the ADCS verification process is to demonstrate compliance with established requirements via test and/or analysis. ADCS requirements are traceable to the T/P Satellite System Design Specification and the T/P Attitude Determination and Control Subsystem Specification. These documents provide a detailed breakdown of ADCS functional and performance requirements.

The T/P System Design Verification and Test Requirements Document collects the design requirements for all of the T/P subsystems and establishes the methods of validation (i.e. test or analysis). For validation by test, the document also specifies test configuration requirements.

The T/P Satellite System Integration and Test Plan along with the T/P MMS Test Specification Plan identify specific test procedures in accordance with the established test requirements. These formal test procedures constitute the basis of ADCS requirements validation at the module and satellite level. The Integration and Test Plan document also provides a cross reference of satellite design specifications test requirements and associated test procedures.

## VERIFICATION APPROACH

In addition to the objective task of demonstrating requirements compliance, the verification process must incorporate a structured program of test and analysis in order to promote a strong sense of confidence in the subsystem as a whole. The ADCS verification process provides a phased, or multi-level approach for both hardware and software validation. This approach promotes a testing sequence that allows the knowledge and experience gained from lower level tests to be applied to tests of increasing complexity. For hardware, this philosophy means testing initially at the component level, followed by a series of higher level tests as the integration process proceeds. Similarly, software verification is phased from the algorithm level through flight vehicle demonstration.

Analysis and simulation is an integral part of the verification process. While analysis is employed for evaluation of all ADCS performance requirements, it is used as the primary verification means only when flight system testing is insufficient to demonstrate requirements compliance. Closed-loop controller performance and pointing error budget assessment are prime examples of areas requiring verification by analysis and simulation.

In addition, the verification approach relies heavily on the heritage experience of previously flown MACS for the LANDSAT 4, 5 missions. Based on the LANDSAT design/test data, some intermediate level tests were omitted for T/P. Thermal Vacuum, EMI and vibration were performed at component level either for the T/P components or as a part of the component design heritage. Components were then integrated into the MMS and performance tests run. MACS integration to MMS and to the T/P spacecraft followed without environmental tests at either MACS or MMS. Subsequent environments at satellite level were run to finalize subsystem ground verification. This approach fully tests the subsystem for flight without excessive redundant tests which would drive up costs unnecessarily and may jeopardize hardware reliability by over testing; e.g., performing excessive vibration by testing at all levels of integration.

## HARDWARE VERIFICATION

Verification of hardware functionality and performance is accomplished with four distinct levels of test. Specifically, testing is performed at the component, MACS, MMS and satellite levels or configurations.

**Component Level Verification:** The initial phase of hardware verification begins with component level tests performed by the respective manufacturers prior to Fairchild Space acceptance of the hardware. Specifications developed by Fairchild Space (refer to Table 3) identify environmental design and component-specific performance requirements that must be met and demonstrated as part of acceptance test. Acceptance test plans, procedures, and end item data packages are provided by each vendor to document the performance of each component. The ACE, PSU, RIU, and EU, while developed in-house, are required to adhere to the same formal acceptance structure as subcontracted hardware.

Table 4 summarizes the methods of qualification for all ADCS components. Although inspection of this table reveals that many of the T/P components are heritage designs, thermal cycle (or in some cases thermal vacuum) and random vibration tests are performed as a

**Table 3. Component Specification Definitions**

Component Specification Definition	
Procedure	Component
968-PF1003	DRIRU Specification
968-PF1007	Reaction Wheel Assembly Specification
968-PF1008	ASTRA Star Tracker Specification
968-PF1010	Earth Sensor Specification
968-PF1012	Attitude Control Electronics Specification
968-PF1014	Coarse Sun Sensor Specification
968-PF1015	Digital Fine Sun Sensor Specification
968-PF1019	Magnetic Torquer Bar Specification
968-PF1021	Tri-axial Magnetometer Specification
968-PF1036	Remote Interface Unit Specification
968-PF1037	Expander Unit Specification
968-PF1047	Magnetic Torquer Bar Drive Assembly Specification
968-PF1049	Power Switching Unit Specification

**Table 4. MACS Module and ADCS Components**

MACS MODULE AND ADCS COMPONENTS	TRANSPORTATION & HANDLING																
	TEMP/GROUND HANDLING	HUMIDITY	STATIC ACCELERATION	ACOUSTICS	RANDOM VIBRATION	SINE VIBRATION	PYRO SHOCK	LAUNCH PRESSURE PROFILE	HERMAL CYCLE	HERMAL VACUUM	EMC CONDUCTED SUSCEPTIBILITY	EMC CONDUCTED EMISSION	EMC RADIATED EMISSION	MAGNETIC	METEOROID/DEBRIS	SEU & LATCH-UP EFFECTS	TOTAL RADIATION DOSE
MACS MODULE	1	1	1	A	2	2	2	2	A/N/A	2	N/A	3	2	3	A	3	3
ATTITUDE CONTROL ELECTR.	1	1	1	A	2	X	2	2	A/N/A	X	N/A/N/A	2	A	N/A	A	A	
POWER SWITCHING UNIT	1	1	1	A	2	X	2	2	A/N/A	X	N/A/N/A	2	A	N/A	N/A	A	
REACTION WHEELS (H)	1	1	1	A	2	X	2	2	A/X	X/H21	X/H	H2	H4/H	N/A	A	A	
TAM ELECTRONICS (H)	1	1	1	A	2	X	H2	2	A/X	X/H21	X/H	H2	H	N/A	A	A	
TAM SENSOR (H)	1	1	1	A	2	X	H2	2	A/X	X/H21	X/H	H2	H	N/A	A	A	
DFSS ELECTRONICS (H)	1	1	1	A	2	X	2	2	A/N/A	X/H	N/A/H	H2	H	N/A	A	A	
DFSS HEAD (H)	1	1	1	A	2	X	2	2	A/X	X/H	N/A/H	H2	H	A	A	A	
MAG TORQUER BAR (H)	1	1	1	A	2	X	H2	2	A/X	X/H21NA	X/N/A	H2	H	N/A	N/A	N/A	
MTB DRIVER	1	1	1	A	2	X	2	2	A/X	X/X	X/X	X	A	N/A	A	A	
ASTRA	1	1	1	A	2	X	2	2	A/N/A	X/X	N/A/X	X	A	A	A	A	
OPT BENCH HEAT PIPE	1	1	1	A	2	X	H2	2	A/X	X/X	N/A/X	N/A/N/A	N/A/N/A	N/A	N/A	N/A	
DRIRU (H)	1	1	1	A	2	X	H2	2	A/X	X/X	N/A/X	N/A/H	H2	H	N/A	A	
COARSE SUN SENSOR (H)	1	1	1	A	2	X	H2	2	A/N/A	X/X	N/A/H	H2	H	A	A	A	
EARTH SENSOR ASSEMBLY	1	1	1	A	2	X	H2	2	A/X	X/H	H2	H	H	A	A	A	
ESAM (BRACKET)	1	1	1	A	2	X	2	2	A/N/A	N/A/N/A	N/A/N/A	N/A/N/A	N/A	N/A	N/A	N/A	

(1) APPROVED PROCEDURES FOLLOWED AND ACCEPTED ENVIRONMENTAL CONDITIONS MAINTAINED.  
(2) QUALIFIED AT A HIGHER LEVEL OF ASSEMBLY OR IN CONJUNCTION WITH OTHER ASSEMBLIES.  
(3) SUBSYSTEM QUALIFICATION ACHIEVED THROUGH ITS COMPOSITE ASSEMBLY TEST/ANALYSIS.  
(4) QUALIFIED DURING DEVELOPMENTAL TESTING ON A UNIT IDENTICAL TO THE QUALE UNIT.

(H) HERITAGE  
(X) PROTOTIPLIGHT TEST  
(A) ANALYSIS  
(N/A) NOT APPLICABLE

minimum at the component level to verify workmanship. "Heritage design" means that the unit has flown on similar missions previously. Also evident from the table is the fact that acoustics, sine vibration, and pyro shock tests are performed exclusively at the satellite level.

**MACS Level Verification:** The second level of hardware verification is performed at the MACS subsystem level and includes integration, performance and phasing tests. Integration tests include safe-to-mate verification, interface verification for command and telemetry, and some limited functional verification. Table 5 identifies the integration procedure associated with each MACS component. The mechanical integration processes for MACS component installation include component alignment within the MACS.

**Table 5. Integration Procedure Definition**

Integration Procedure Definition	
Procedure	Components
968-ITP4001 GSE	Ground Support Equipment Set-up
968-ITP4002 MACS Vol I	MACS harness, thermistors & heaters (thermostats/ heaters verified using Quick-Freeze)
968-ITP4003 MACS Vol II	MTBDA harness, MTB, and MTB component level phasing using compass
968-ITP4004 MACS Vol III	DRIRU and ASTRA harness
968-ITP4005 PSU	
968-ITP4006 RIU	
968-ITP4007 EU	
968-ITP4008 ACE	
968-ITP4009 RWA	RWA component level phasing using 'Lazy Susan' table
968-ITP4010 TAM	
968-ITP4011 CSS/DFSS	
968-ITP4012 MTBDA	
968-ITP4013 ASTRA	
968-ITP4014 DRIRU	
968-SM56010 ESAM	Includes performance test using ESA Electronics Test Set

The integration procedures for the MTBs and RWAs are somewhat unique in that they include component level phasing checks that are fundamental in establishing the basis for spacecraft phasing validation. The MTB integration procedure employs a magnetic compass to verify MTB magnetic moment polarity, while the RWA procedure verifies reaction wheel rotation direction via a 'Lazy Susan' fixture.

Once components are integrated in the MACS module, performance testing is initiated to exercise the hardware and their interfaces at the subsystem level. The MACS performance test (MACSPERF), summarized in Table 6, is an automated test that is defined in Standard Test Operations Language (STOL). The contents of MACSPERF is derived from the test requirements outlined in the T/P Satellite System Integration and Test Plan. MACSPERF relies on the use of the MACS Stimulator, an electronics test set, for the simulation of CSS, Earth Sensor (ES), and Dry Rotor Inertial Reference Unit (DRIRU) inputs to the ACE. An external TAM stimulator consisting of wire-wound coils is employed to vary the ambient magnetic field for the purpose of demonstrating TAM functionality.

In addition to the MACS performance test, a series of MACS phasing tests (MACSPHAS and CSSPIII STOL procedures - Tables 7 and 8) are performed using direct sensor stimulation wherever permitted by the hardware configuration. Specifically, DRIRU earth rate input and optical illumination of the MACS yaw CSS are incorporated to demonstrate end-to-end phasing of the gyro rate damp/inertial position and CSS position control loops, respectively.

In order to verify end-to-end phasing of the yaw CSS position control loop, individual cells of the A550 CSS assembly (mounted on the -x face of the MACS module) were individually illuminated to provide error signal inputs to the ACE.

**MMS Level Verification:** MMS Level testing was performed with the MACS module integrated with the Modular Power Subsystem (MPS), Communication and Data Handling module (C&DH), Propulsion Module (PM), and Earth Sensor Assembly Module (ESAM) on the Module Support Structure (MSS). This configuration introduced the earth sensors and propulsion subsystem thrusters, providing the opportunity for further end-to-end testing.

**Table 6. MACSPERF Performance Test Definition**

Test Number	Test Description	Comments
1	Power Profile	Record bus voltages and current after powering on each component
2	Launch Mode	Verify LM inhibited
3	Separation Logic	Verify Sep enabled
4	Wheel Breakaway	Trend RWA breakaway torque
5	CSM	Verify Computer Status Monitor operation
6	TAM Aliveness	Verify TAM earth field measurements and external stimulation
7	ACE/RIU X-Strap	Verify MACS Cross-strap configurations
8	Wheel Cmds	Verify phasing and proportionality of RWA commands
9	Torquer Cmds	Verify phasing and proportionality of MTB commands
10	Wheel run-up/down	Trend RWA run-up and run-down times (+/- 2500 rpm)
11	DFSS Aliveness	Verify sun presence and changing vehicle data
12	Heater Test	Verify MACS heater enable/disable operation
13	SPISIM	Exercise sun point safehold using MACS Stimulator for CSS and gyro
14	EPSIM	Exercise earth point safehold using MACS Stimulator for ESA, CSS and gyro
15	TAM Compensation	Verify magnitude and polarity of TAM Compensation for MTB
16	Torquer Bias	Verify phasing and proportionality of MTB bias commands
17	CSS 1 Loop	Verify primary CSS position control loop using MACS Stimulator
18	CSS 2 Loop	Verify redundant CSS position control loop using MACS Stimulator
19	IHU 1 Loop	Verify primary gyro rate control loop using earth rate
20	IHU 2 Loop	Verify redundant gyro rate control loop using earth rate
21	Wheel Unload	Verify magnetic and thruster unloading control
22	Thruster Control	Verify operation of safehold thruster commands with strip chart recorder
23	TAM Bias	Verify phasing and proportionality of TAM bias commands
24	ASTRA Aliveness	Verify response to test fixture (not performed)

**Table 7. MACSPHA Phasing Test Definition**

MACSPHAS Phasing Test Definition				
Control Loop	Sensor Input	Sensor Stimulus	Actuator Configuration	End/End*
Rate Loop	DRIRU	Earth Rate	Primary RWAs	x
			Skew RWA substituted for roll	x
			Skew RWA substituted for pitch	x
			Skew RWA substituted for yaw	x
			Thrusters (strip chart verification)	
CSS Position Loop	CSS	MACS Stim	Primary RWAs	
			Skew RWA substituted for roll	
			Skew RWA substituted for pitch	
			Skew RWA substituted for yaw	
			Thrusters (strip chart verification)	
ESA Position Loop	ESA	MACS Stim	Primary RWAs	
			Skew RWA substituted for roll	
			Skew RWA substituted for pitch	
			Skew RWA substituted for yaw	
			Thrusters (strip chart verification)	
Inertial Position Loop	DRIRU	Earth rate	Primary RWAs	x
			Skew RWA substituted for roll	x
			Skew RWA substituted for pitch	x
			Skew RWA substituted for yaw	x
			Thrusters (strip chart verification)	
Magnetic Unloading Loop	TAM/RWA Tach	Earth field/RWA drive	Primary RWAs	x
			Skew RWA substituted for roll	x
			Skew RWA substituted for pitch	x
			Skew RWA substituted for yaw	x
			Thrusters (strip chart verification)	
Thruster Unloading Loop	RWA Tach	RWA drive	Primary RWAs	
			Skew RWA substituted for roll	
			Skew RWA substituted for pitch	
			Skew RWA substituted for yaw	
			Thrusters (strip chart verification)	
N/A	DFSS	Sun lamp	(Verified alpha/beta in each quadrant)	

\*Note: x indicates end-to-end test using direct sensor input and actuator output

**Table 8. CSSPH Phasing Test Definition**

CSSPH Phasing Test Definition				
Control Loop	Sensor Input	Sensor Stimulus	Actuator Configuration	End/End*
Yaw CSS Position Loop	CSS A550	Optical	Primary RWAs	x
			Skew RWA substituted for roll	x
			Skew RWA substituted for pitch	x
			Skew RWA substituted for yaw	x
			Thrusters (strip chart verification)	

Both performance and phasing tests are executed at the MMS level. Table 9 summarizes the MACS related performance test aspects of the ORBITS STOL procedure. As in the case of MACS level performance testing, the contents of the ORBITS procedure was derived from test requirements outlined in the T/P Satellite System Integration and Test Plan.

Additional phasing verification is performed at the MMS level as part of the MACSPHAS, EARTH and PMTHR STOL procedures. While some of the tests are carried over from MACS level verification, end-to-end verification of the earth sensors and thruster actuators is accomplished for the first time at this level. Table 10 summarizes the phasing tests performed at the MMS level.

**Satellite Level Verification:** Satellite level testing is performed with the MMS integrated with the IM. The same ORBITS STOL procedure used at the MMS level is executed at satellite level to serve as a comprehensive performance test (refer to Table 7).

Introduction of the IM provides access to IM mounted yaw CSS assemblies A625 and A627. End-to-end phasing verification for the yaw channel of the CSS position safehold control loop was performed by individually illuminating each cell of the CSS assemblies. End-to-end verification of the solar array mounted pitch, yaw and sun presence CSS assemblies are performed after integration of the solar array to the Instrument Module.

Satellite environmental tests have been defined for EMI/EMC, pyroshock, sine vibration, acoustics and thermal vacuum. During these tests, the spacecraft is operated in applicable mission modes and monitored for any indication of off-nominal performance. A performance test is run following each environmental test to assure that

no failure or degradation has been sustained by any subsystem. Alignment measurements are made prior to, and following, the major environmental tests in accordance with T/P Satellite Alignment Procedure to assess alignment stability.

## SOFTWARE VERIFICATION

The T/P flight software verification process consists of four specific levels of testing. Level 1 testing is the engineering development phase whereby executable FORTRAN is derived from the flight software Program Development Language (PDL). The FORTRAN engineering code is executed in a stand-alone fashion to evaluate flight algorithm sufficiency and to generate a set of benchmark test cases for comparison with Level 2 test.

Level 2 testing involves the use of flight assembly code in a NASA Standard Spacecraft Computer (NSSC) emulator environment. Proper flag manipulation, conditional processing, and computation results are verified during this test phase. An evaluation of numeric precision and range is also performed using the results of the Level 1 benchmark tests.

T/P Attitude Determination and Control flight software used the LANDSAT 5 flight software as a baseline. Significant portions of this baseline code were not modified for T/P. Level 1 and 2 testing is only performed for T/P flight software routines which are new or heavily modified from the Landsat baseline.

**Table 9. ORBITS Performance Test Definition (MACS Related)**

ORBITS Performance Test Definition (MACS Related)		Comments
Test Number	Test Description	
1	LM test	Verify Launch Mode inhibit
2	Gyro rate switching	Verify gyro lo/hi rate switching
3	CSM test	Simulates OBC failure and safehold entry; command safehold off
4	RWA breakaway	Test RWA breakaway torque
5	ACE/RIU X-strap	Verify ACE/RIU cross-strap; power MACS components off/on
6	Serial Commands	Modem select, TAM select, gyro rate, MTB drive, RWA drive
7	TAM Aliveness	Verify earth field and external stimulus
8	TAM Bias	Verify phasing and proportionality of TAM bias commands
9	MTB Bias	Verify phasing and proportionality of MTB bias commands
10	TAM Compensation	Verify magnitude and polarity of TAM Compensation for MTB
11	EPSIM	Exercise sun point safehold using MACS stimulator for CSS and gyro
12	EPSIM	Exercise earth point safehold using MACS stimulator for ESA, CSS and gyro
13	MTB Unloading	Verify magnetic unloading control loop
14	Thruster Unloading	Verify thruster unloading control loop using PM
15	Gyro Compass	Verify EPSIM gyro compass control (forward and backward)
16	Eclipse Bias	Verify EPSIM for yaw eclipse bias (+ and -)
17	Rate Damp	Verify rate damp RWA control loop using earth rate input
18	Thruster Cmds	Verify direct thruster commands using PM
19	ITSIIM	Verify inertial pointing safehold control with REMs A/C and B/D
20	Gyro Bias	Verify magnitude and polarity of gyro bias commands (must repeat at satellite level)
21	RWA run-up/down	Test RWA run-up and run-down times (+/- 2500 rpm)
22	EPS Aliveness	Verify sun presence and changing vehicle data
23	ESA Functional	Verify ESA functional performance using Electronics Test Set

**Table 10. MACSPHAS Phasing Test Definition**

MACSPHAS Phasing Test Definition				
Control Loop	Sensor Input	Sensor Stimulus	Actuator Configuration	End/End*
Rate Loop	DRIRU	Earth Rate	Primary RWAs	x
			Skew RWA substituted for roll	x
			Skew RWA substituted for pitch	x
			Skew RWA substituted for yaw	x
			Thrusters (strip chart verification)	
CSS Position Loop	CSS	MACS Stim	Primary RWAs	
			Skew RWA substituted for roll	
			Skew RWA substituted for pitch	
			Skew RWA substituted for yaw	
			Thrusters (strip chart verification)	
Inertial Position Loop	DRIRU	Earth rate	Primary RWAs	x
			Skew RWA substituted for roll	x
			Skew RWA substituted for pitch	x
			Skew RWA substituted for yaw	x
			Thrusters (strip chart verification)	
EARTH Phasing Test Definition				
ESA Position Loop	ESA	ESA Test Set	Primary RWAs	
			Skew RWA substituted for roll	
			Skew RWA substituted for pitch	
			Skew RWA substituted for yaw	
			Optical	x
PMTHR Phasing Test Definition				
Thruster Unloading Loop	N/A	Command	PME-A A/C, B/D REMs	x
			PME-B A/C, B/C REMs	x
			PME-A A/C REMs	
			PME-B B/C REMs	
			Primary RWAs/REM A/C B/D	x

\*Note: x indicates end-to-end test using direct sensor input and actuator output

Level 3 testing is restricted to flight software executive tasks and does not involve any applications processors.

The most rigorous flight software testing is performed at Level 4 using the Software Development and Verification Facility (SDVF). A complete software build consisting of a flight executive with applications processors is executed real-time on a non-flight NSSC that is interfaced with a test simulator (TSIM). TSIM provides a closed-loop test capability with simulated sensor inputs, rigid body spacecraft dynamics, and actuator models.

During Level 4 testing, the flight software Computer Software Configuration Item (CSCI) is treated much like any other ADCS component in the sense that compliance to a design specification must be demonstrated. The T/P Flight Software Requirements document serves as the flight software design specification. The T/P Flight Software Test Plan defines the method of verification for each requirement, provided in the form of a requirements compliance matrix. Flight software test description documents and the T/P Flight Software Acceptance Test Description contain the detailed definition of the formal test procedures, while the T/P MACS Flight Software Test Report summarizes the integration and acceptance test results for the T/P Flight Software CSCI. The latter document also identifies the Software Trouble Reports (STRs) generated during formal test case execution and addresses their resolution.

Level 5 testing is designed to be performed on the flight vehicle to verify proper interaction between flight software and flight hardware. The T/P Flight Software Spacecraft Level OBC Environment and Interface Test Description and T/P Flight Software Spacecraft Level ACS Mission Mode Test Description define the software-specific tests necessary to verify commanding, sensor data acquisition and processing, sensor and actuator phasing, and open-loop controller processing. The T/P Flight Software Spacecraft Level TMON Group Test Description defines the tests required for validating the telemetry monitoring process.

## ANALYSIS AND SIMULATION

As stated earlier, analysis and simulation are an integral part of ADCS verification. Numerous analyses have been performed to support the evolution of the T/P ADCS design. While most design aspects can be verified by test, there remains a subset that can only be substantiated through analysis alone.

Verification by analysis and simulation is mandated for closed-loop controller performance and pointing error budget assessment. Stability margins for computer mode and safehold mode controllers have been determined using single axis frequency domain linear analysis (References [5] through [7]). A three-axis non-linear time domain computer simulation was subsequently used to evaluate controller performance in conjunction with sensor and actuator dynamics and flexible body effects. Analysis to date has demonstrated acceptable performance and margin (References [7] through [11]).

Compliance with pointing requirements is based on a statistical analysis of derived knowledge and control er-

rors. Knowledge errors are derived from star position uncertainty, star tracker resolution and alignment uncertainty, as well as characteristics of the on-board update filter processor as determined by analysis and Level 4 test performance assessment. Control errors are a function of internal and external disturbance torques and control law characteristics. Analysis results presented in reference [12] demonstrate positive error budget margin for both knowledge and control.

## FLIGHT PERFORMANCE ISSUES

As part of the early mission checkout phase, certain tests of MACS components and software will be performed which either cannot be easily performed on the Earth or are inappropriate to be performed on ground. No performance assessment tests are planned for the early mission phases of rate damping and earth acquisition immediately after separation. During the orbit raising phase, thruster calibrator burns are performed to evaluate thruster performance for accurate determination of future burn times. After the control system is in the NMM of operation, the system will be configured to allow data to be telemetered to the ground for ground estimation of the co-alignment errors between the two Star Trackers and the Fine Sun Sensor. In addition, gyro drift parameters including scale factor assymetry may be required. At present, all pointing errors detected by the Kalman Filter process are attributed to gyro bias drift stability errors. This approach worked well for the baseline since that vehicle was only moving at a constant rate in one direction. During most of the mission, T/P performs sinusoidal yaw maneuvers of orbit period for sun tracking. These maneuvers will introduce DRIRU-II scale factor stability and assymetry errors which may require estimation and correction. Early on-orbit pointing data will be assessed to verify the system performs within specification without such estimation/correction. At this time, it is assumed that all errors are (at worst) static; i.e., calibration will result in corrections which will not require further changes. However, if this assumption proves incorrect, the flight software easily accommodates periodic calibration updates.

## CONCLUSION

The T/P ADCS consists of flight software, the MACS, and other internal hardware (ESAM, CSS, and PM). The heart of the ADCS is the MACS which has flown successfully on several other scientific low earth orbit missions. The similarity of these previous missions is used as a basis for developing the ADCS test program. The ADCS verification process is structured as a sequence of incremental level tests for both hardware and software, culminating in satellite level testing that demonstrates software compatibility with the flight vehicle. Analysis and simulation is used extensively throughout the process for the development of ADCS design parameters as well as for the verification of performance aspects that are not observable in test. On-orbit calibration and data evaluation will be performed to determine the need for additional flight operation to improve performance.

## REFERENCES

1. Das, A., "The On-Orbit Attitude Determination and Control System for the LANDSAT-D Spacecraft," AIAA Paper 82-310.
2. Stewart, R.A., and M. Lefebvre, "T/P: A Contribution to the World Climate Research Program," AAS Paper 86-306, February 1986.
3. TOPEX Satellite System Design Specification, Fairchild Space Company Document 968-PF1000C, September 1988.
4. TOPEX Satellite System Performance Requirements, NASA/JPL Document D-2226, June 1987.
5. TOPEX/POSEIDON NMM Linear Frequency Domain Analysis with New Flexible Modes, GNC: TOPEX:91-022, D. Zimbelman, 8 April 1991.
6. Updated TOPEX/POSEIDON Safe Hold Mode Frequency Domain Analysis Including Flexibility, GNC: TOPEX:90-130, D. Zimbelman, 8 October 1990.
7. CDy Task 6 Final Report: TOPEX OAM Final Design, Analysis and Simulation, GNC:TOPEX:90-013, N. Dennehy, 29 January 1990.
8. TOPEX/POSEIDON Orbit Adjust Mode (OAM) Performance with Small Delta- V Jet Mismatches, GNC: TOPEX:90-104, P. Sanneman, 16 July 1990.
9. TOPEX/POSEIDON Thermal Elastic Shock Analysis Revisited, GNC:TOPEX:90-108, D. Zimbelman, 25 July 1990.
10. TOPEX/POSEIDON Attitude Errors During Altimeter Calibration Maneuver, GNC:TOPEX:91-047, B. Lee and P. Sanneman, 16 July 1991.
11. TOPEX/POSEIDON Earth Pointing Safe Hold Mode - Updated Simulation Results, B. Lee and P. Sanneman, to be released early 1992.
12. Revised Normal Mission Mode ADCS Error Budgets for the TOPEX/POSEIDON Spacecraft, GNC: TOPEX:91-025, B. Lee, 6 May 1991.

# ADVANCED ATTITUDE- AND ORBIT CONTROL CONCEPTS FOR 3-AXIS-STABILIZED COMMUNICATION AND APPLICATION SATELLITES

M. Surauer, H. Bittner, W. Fichter and H.D. Fischer

*Space Communication and Propulsion System Division, MBB/Deutsche Aerospace, Germany*

## Abstract:

The rapidly increasing demands and the large variety of technical and economic requirements for future communication- and application satellites necessitate an advance of the efficiency in all areas of system development.

In addition to technical performance improvements, optimal use of equipment, and ease of operability especially stringent economic boundary conditions are to be met.

Such ambitious goals cannot be achieved on the basis of efforts made on the level of an individual subsystem and its equipment only but requires a well balanced overall system approach.

Presently, based on a cooperation agreement between DASA/MBB and Aerospatiale companies, joint efforts are being undertaken towards an optimized approach of this kind, within the so-called "Spacebus Improvement Program" (SIP). The key issue of the approach adopted is an Integrated Control and Data System (ICDS), which combines the versatility and flexibility inherent to the Attitude- and Orbit Control Subsystem (AOCS) with the Data Management and Control (DMC) tasks, making best possible use of modern equipment technology and onboard processing capabilities.

**Keywords:** SIP, ICDS, AOCS, DMC

## 1. INTRODUCTION

Advanced attitude- and orbit control concepts for future 3-axis stabilized communication and application satellites are requested to provide technical improvements like increased pointing accuracy, reliability, onboard autonomy, S/C collocation strategies and autonomous station-keeping, inclined orbit operation, optimal use of equipment (sensor and actuator fusion) and ease of operability, as well as stringent economic boundary conditions, e.g. extended mission duration, short development time, and reduction of development and manufacturing cost.

In the past S/C design has often been performed with the emphasis primarily placed on the mechanical and structural configuration aspects, without taking into account the impact on other subsystems to the necessary extent. In particular, the Attitude- and Orbit Control Subsystem (AOCS), the one with the largest number of interfaces within a S/C then had to cope with any associated dynamic- and perturbation environment, which often necessitated major AOCS design adaptations or even redesigns very late in the development programs under then already largely "frozen" boundary conditions, which in turn caused schedule problems and additional costs.

It is, of course, understood that S/C overall design optimization has to be performed on the basis of a proper priority ranking to ensure compliance with mission objectives, operational- and payload requirements. It is furthermore understood that especially the AOCS - because of its internal and external communication- and access capabilities - can provide the necessary flexibility for late adaptations and correction of unforeseen inconsistencies showing up during the development. For this very reason it is regarded necessary to enhance the inherent flexibility features of the AOCS to the maximum possible extent for the benefit of the S/C overall system. However this also imposes certain demands on the S/C bus and equipment configuration.

### 1.1 The Spacebus Improvement Program

Presently, based on a cooperation agreement between DASA/MBB and Aerospatiale companies, joint efforts are being undertaken towards an optimized approach of this kind, within the so-called "Spacebus Improvement Program" (SIP). Possible solutions for communication and application satellite AOCS of the next generation are discussed subsequently and the results of analyses, simulation studies and currently running predevelopment work as well as assessments of the innovation potential are given.

For typical 3-axis stabilized transfer orbit and injection sequences and on-station S/C operational procedures new acquisition- and control concepts are presented, covering amongst others the aspects of:

- Equipment type and arrangement (sensors, actuators) for maximum operational flexibility
- Functional redundancy and back-up solutions with minimum number of components
- Characteristics of new components presently under development, like:
  - High precision, wide-angle digital sun sensor
  - High performance, low thrust level liquid bipropellant thrusters
  - A powerful Integrated Control and Data management Electronics (ICDE)
- Characteristics of control strategies and control laws
- Momentum management (with and without solar sailing)
- Implementation and functional testing of the control algorithms
- Failure Detection, Isolation and Recovery (FDIR) criteria and strategy

## 1.2 Heritage

About 20 years of experience in the development of Attitude- and Orbit Control Subsystems for SYMPHONIE, the spacecraft families INTELSAT V, MOS-1, TV-SAT/TDF, DFS-KOPERNIKUS, EUTELSAT 2 form a solid background of expertise for the current activities. The most essential AOCS-characteristics of these S/C, 26, of which are presently operational in orbit will be shortly outlined to demonstrate the improvements incorporated in the past and to consolidate the confidence in the new approach.

- The 3-axis stabilization technology for commercial geosynchronous communication satellites using the bias momentum principle was first established with the French-German experimental technology satellites SYMPHONIE, developed from 1967, launched in Dec. 1974 and Aug. 1975 respectively, both flight models successfully operated for more than 5 years. The S/C was spin stabilized in transfer orbit and during (liquid bipropellant) apogee boost and despun by yo-yo. Normal Mode (NM) attitude stabilization in GSO was performed with onboard closed loop pitch control using IRES and fixed momentum wheel (FMW), roll/yaw corrections by cold gas thruster pulses commanded from ground. Closed loop attitude control during orbit corrections (SKM) was based on sun and (IR-) earth reference and modulation of 10 N liquid bipropellant thrusters.
  - The series of 15 INTELSAT V S/C, developed, manufactured and launched in the period from 1976 to Jan. 89 was also spin stabilized in transfer orbit and during (solid propellant) apogee boost. Roll/yaw NM control is based on IRES (roll-) reference and the WHECON principle, using monopropellant hydrazine thrusters. Attitude control during SKM was performed as established in SYMPHONIE with sun- and earth reference and thruster modulation (ref 1, 2). Two S/C were lost due to launch vehicle failures, all others are still operational, partly already exceeding their design life (7 years) by a factor of 2. Dedicated, automatic sun acquisition and safety modes and concepts for stabilizing solar panel structural flexibility effects have been developed.
  - A significant progress in AOCS technology has been made during development of the direct television and broadcasting satellites TV-SAT/TDF and TELE-X (ref. 3). Apart from new designs of attitude measurement equipment (sun-, earth sensors, gyros) incorporated in the AOCS, the 3-axis stabilization technology for transfer orbit operations and during (repeated) apogee boost maneuvers has been established, using for the first time a unified liquid bipropellant propulsion system for attitude control, orbit control and Apogee Boost Maneuver (ABM). Furthermore these S/C are equipped with a coarse body control and an additional antenna fine pointing system based on RF-sensing and control of the TX-antenna beam orientation w.r.t. a ground beacon to an accuracy better than  $\pm 0.025$  deg. Special reacquisition concepts in case of attitude loss or battery failure (recovery after eclipse) have been incorporated. All attitude measurement, data updating, formatting, monitoring, mode sequencing and control functions except antenna (structural flexibility) stabilization have been implemented in a central, digital,
- internally redundant onboard computer. Two flight models each of TV-SAT and TDF have been launched in Nov. 87, Aug. 89 or respectively Oct. 88, June 90 and one TELE-X in March 89. The S/C are presently operational except for TV-SAT/FM1, which had to be deorbited because one solar array wing failed to deploy in GSO and simultaneously blocked an antenna reflector deployment. The robustness of the AOCS design operating then under most abnormal conditions, was, however, unintentionally demonstrated, as well as its flexibility offered by in-orbit reprogramming of the onboard computer when different attempts of rescue maneuvers, additional control modes and sequences have been implemented.
- Development of DFS-KOPERNIKUS (ref. 4), a smaller class S/C of different geometrical configuration ("rabbit-ear" antenna arrangement, liquid bipropellant tanks in ABM direction) was started end of 1984. Flight models 1 and 2 have been launched in June 1989 and July 90 respectively, their AOCS performance being better than expected (except some spurious anomalies in one of the sun sensor output signals). FM3 is scheduled for launch in Sept. 92. The S/C are 3-axis stabilized in TO and GSO, the solar arrays being fully deployed already in transfer orbit and during (repeated) liquid bipropellant ABM phase. For this operational mode the AOCS design had to cope with panel oscillations and propellant sloshing phenomena in overlapping frequency bands, the sloshing dynamics experiencing pole-zero inversion during the maneuver. Concepts and provisions for in orbit gyro calibration have been incorporated to also ensure compatibility with midnight launch conditions. A hybrid AOCS electronics composed of a 1802  $\mu$ -processor (mode logic, sensor data processing) with analog filters and pseudo-rate modulators is used for control law implementation.
- The innovations incorporated in the EUTELSAT 2 AOCS (ref. 5) comprise:
- the capability to acquire the earth any time of the day
  - a S/W safe mode for minimization of outage duration in GSO
  - an optimum Nutation and Angular Momentum Control (NAMC-) concept to ensure higher yaw accuracy (as compared to WHECON) in presence of high disturbance torques (NM roll/yaw control)
  - the capability to perform orbit corrections with yaw reference from gyro, i.e. any time per day (also in colinearity regions)
  - high pointing accuracy during station keeping maneuver (SKM) transients
  - in-flight recording of the thruster firing history for propellant budget monitoring
- Development started in 1988. Flight models 1 to 3, presently operational, have been launched in Aug. 90, Jan. 91 and Dec. 91 respectively. FM4 launch is scheduled for the 10 of July 1992.

## 2. ADVANCED AOCS REQUIREMENTS

As already addressed in the introduction an advanced AOCS has to meet economical, mission related, technical performance and operational requirements.

### 2.1 General and Economical Requirements

For the field of activity in question here, market conditions and competition situation impose general demands, which may be summarized as follows:

- Cost saving in the area of
  - non-recurring costs, which necessitates transparency and modularity of the concept to facilitate design and analysis work and incorporation of additional or replacement of functional modules, to restrict modifications, adaptations and parameter updates to limited areas and keep delta-qualification efforts low.
  - recurring costs which imply minimum number/best possible use of equipment, easy integration, and testing
  - management and documentation efforts, e.g. by applying standard procedures
- Time saving in
  - the development period e.g. by applying efficient development tools, involving experienced teams, etc.
  - the manufacturing, qualification and testing on equipment, subsystem and system level
  - parts procurement by stock-holding of essential parts and/or head start activities
- Technical performance improvements in
  - pointing accuracy and/or line of sight stability
  - orbit correction and station position accuracy
  - operational life time (equivalent e.g. to propellant mass saving, increase of reliability etc.)
  - outage minimization (transients, short recovery periods, automatic FDIR and so on)

### 2.2 Mission and Payload Requirements

The objective of the SIP is to establish the baseline and perform the necessary predevelopments for

Table 2.3-1: Typical AOCS Performance Requirements

an ICDS, which satisfies the general conditions of section 2.1. for communication and application satellites, i.e. for different types of missions and payloads. In the first step the emphasis of the activities is concentrated on S/C operating in GSO or similar orbits (e.g. LOOPUS) and payloads for establishing services in the area of:

- classical communication links "earth-satellite-earth"
- intersatellite communication
- multi-antenna and tracking systems
- optical data- and communication
- earth observation capabilities
- multi-mission applications

The ICDS design concept, i.e. the AOCS and DMC baseline is requested to be compatible with the requirements for low earth orbit observation and scientific missions of earth orbiting S/C. The extension to such applications, which will require the incorporation of additional and/or different equipment (like star sensors, telescopes, SAR, magnetic torquers etc.), control functions (repointing, slewing, scanning, tracking) and data management functions (data collection, compression, formatting) is the objective of the next step. The priority for the design, development, and incorporation of additional I/F-H/W and S/W modules will of course depend on the needs for upcoming projects.

### 2.3 Technical Requirements

From the mission and payload requirements the detailed functional and performance requirements are derived.

Typical attitude control accuracy and line-of-sight stability requirements are summarized in table 2.3-1.

The Data Management and Control (DMC) requirements comprise for communication satellites the standard OBDH-functions, i.e. surveillance and control of subsystems like thermal- and power monitoring and control, payload management and - within the ICDS concept - will also cover additional data processing for mission control, fault detection, -isolation and -recovery, and tasks associated with packet TM/TC, reprogramming etc.

Orbit	Mission	Pointing accuracy [deg]		Required Rate Accuracy [deg/sec]		
		half cone Roll/pitch	Yaw	x-axis	y-axis	z-axis
GEO	COMMUNICATION	SEH	0.05	0.15	---	---
		NM	0.03	0.12	---	---
		ION Prop	0.03	0.12	---	---
	inclined orbit operat.		0.05	0.20	---	---
	Optical Data Links		0.01	0.02 (over 150 to 6000 sec period)	---	---
						--
	WEATHER	scan phase (fine pointing and low rate phase)	0.03	0.10	0.002	0.002
		Normal and SK-Mode	0.10	0.30	---	---
LEO	ENVIRONMENTAL MONITORING	Normal Mode	0.03	0.05	0.002	0.002
		Re-Positioning	0.05	0.15	---	---
	HIGH RESOLUTION	Normal Mode	0.007	0.02	0.0005	0.0005
		Re-Positioning	0.05	0.15	---	---
Highly in- clined (e.g. LOOPUS)	COMMUNICATION	Operational Phase	0.03	0.10	---	---
		Orbit Correction Phase	0.15	0.35	---	---

## 2.4 Operational Requirements

The most essential AOCS requirements to be met from the S/C operation point of view are:

- The station position accuracy for communication satellites in GSO is typically requested to be within 0.05 deg N/S and E/W.
- N/S station keeping with Ion Propulsion (IP) thrusters shall be possible, without degradation of Normal Mode attitude accuracy limits.
- Complete onboard autonomy for 48 hrs in case of TT&C failure shall be guaranteed.
- Inclined orbit operation for inclination angles up to 3 deg (no N/S-station keeping for a period of about 3 years) shall be possible with attitude control accuracy equivalent to SKM requirements.
- Autonomous station keeping over limited periods (3 to 4 weeks) in the first ICDS design step shall be envisaged and extended later on (goal: 2 to 3 months).
- Incorporation of collocation strategies is furthermore envisaged.

## 3. DESIGN APPROACH

### 3.1 ICDS Baseline Concept

The baseline approach adopted for the SIP presently in progress shall not only take advantage of the background experience outlined in section 1.2 but of course also make use of up-to-date technologies and provide the flexibility and growth capabilities to satisfy future challenges. To achieve this goal a prerequisite is to ensure access to all information available onboard of the S/C to make optimum use of the equipment and to combine the versatility and flexibility inherent to the AOCS with the Data Management and Control (DMC) tasks in an Integrated Control and Data System (ICDS), the heart of which is a powerful modern onboard processor, data transmission system and associated flexible operations S/W.

#### Hardware

Figure 3.1-1 shows the ICDS hardware configuration (without redundancies) i.e. not only the AOCS-, but also the DMC hardware units are represented.

The functional sharing of these units and comments on the notation within figure 3.1-1 are listed in table 3.1-1.

The serial OBDH Data Bus is the foundation of a modular extandable AOCS.

As far as newly developed equipment and signal conditioning electronics are concerned (e.g. sun sensor electronics, UPSE), the interfaces are designed such as to directly match the data bus I/F requirements. The signal conditioning for classical, off-the-shelf equipment (earth sensors, gyros, wheels) to the OBDH data bus format is performed in the Platform Interface Unit (PFIU).

The central component of the ICDS hardware is the On Board Computer Unit (OBCU). It has functional interfaces with the ground segment and all onboard S/C subsystems for the distribution of commands and the acquisition of data. Figure 3.1-2 shows the blockdiagram of the OBCU. The functional units are:

- Processor Module (PM)
  - 16 bit processor, MIL-STD 1750 A instruction set architecture
  - processing power at least 1000 kips for DAIS MIX (Digital Aeronautics Instr. Set - 20MHz)
  - RAM 128 kwords of 16 bits
  - ROM 96 kwords of 16 bits
- Telecommand Decoder Module (TC)
- Telemetry Module (TM)
- Reconfiguration Module (RM)
  - supports autonomous satellite failure detection, isolation and recovery (FDI)
  - functional elements: Alarm Level Management, OBCU Reconfiguration Commands, OBDH-bus Reconfiguration Commands, Thruster On-Time Control
- Safeguard Memory (SGM)
  - contains the H/W system configuration data and dynamic S/W parameters
- Precision Clock Module (PCLK)
- Power Converter Modules (PCV)
  - provides necessary voltages for the OBCU modules
  - provides central on board reference time counter

#### Software

The complete on board software (S/W) will be executed in one central redundant on board computer and runs fully automatic and autonomously under normal circumstances. Figure 3.1-3 gives an overview of the static decomposition of the ICDS S/W. Before the mission, the S/W will be (pre-) stored in the PROM and copied into the RAM after its first activation in the orbit. This allows modifications - as far as the application S/W is concerned - at any time via telecommands ("memory load"). It is also possible to adapt important system tables and the S/W configuration from ground.

Telemetry and telecommand S/W parts are implemented according to the ESA "standard packet TM/TC". A central role within the on board S/W plays the MOSES II operating system, an updated version of the MOSES operating system used in the shuttle pallet satellite (SPAS)-program. It is especially designed for the

- management of parallel processes and asynchronous events under real-time conditions

but can also meet the requirements of

- strictly synchronous operation modes, e.g. sensor data acquisition, activation of the UPS.

The maintainability and adaption capability of the S/W-system necessitate a transparent modular functional structure, hierarchically organized and properly defined interfaces not only within the operation system, but also to the application S/W modules. The shell model in figure 3.1-3 gives an overview of this system organization.

The application S/W-parts (jobs) are divided into one or several tasks. Additionally, there are specific error tasks, which can be attached to a job/task. They will be activated automatically by the operating system in case of a failure (exception handling).

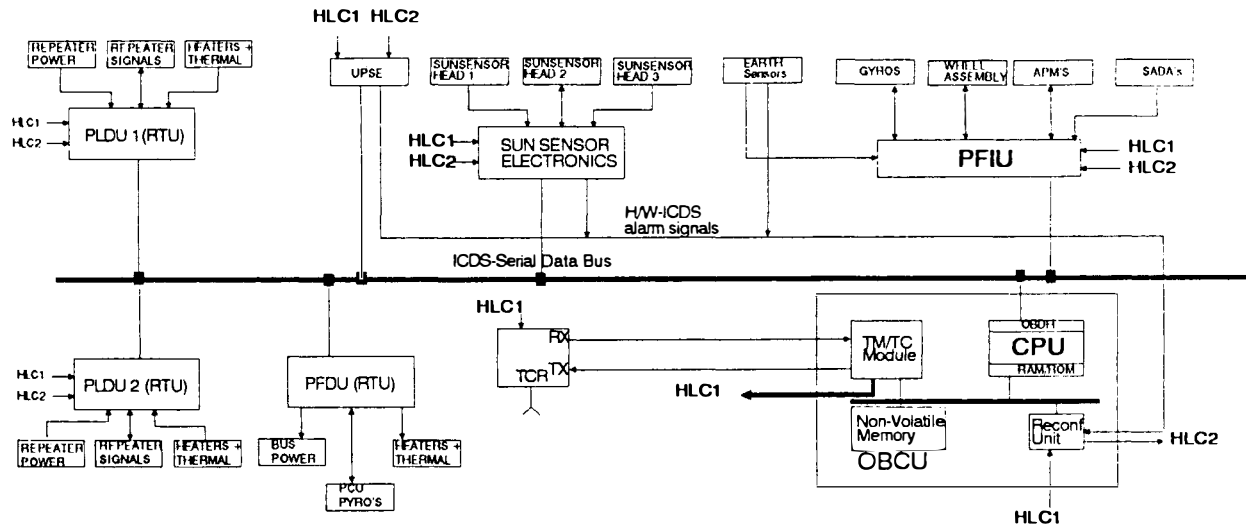


Fig. 3.1-1: ICDS Hardware Architecture

OBCU	Kernel of the ICDS (On Board Computer Unit)	Ground Station I/F High priority telecommand decoding $\mu$ -Processor + memory Reconfiguration and safeguard memory	UPSE	Thruster Valve Drivers
Data Bus	Data Transmission Link	OBDH protocol for ML16/DS16 exchange On/Off command execution Analogic Thermistor	PSSE	Precision Sun Sensor Electronics
PFIU	Platform Interface Unit	Interface adaptation to AOCS sensors On/Off distribution for PF units Acquisition of PF units temperatures	HLC1	High Level Priority TC-commands
PF DU	Platform Distribution Unit	Power distribution and protection of PF Unit Pyro. of the whole S/C I/F with PCU (Power Conditioning Unit) Battery protection HW PF heater (relays)	HLC2	High Level Priority Reconfiguration Commands
PLDU	Payload Distribution Unit	Power distribution and protection of P/L unit P/L unit temperature acquisition P/L heater relay On/Off distribution to P/L unit TM/TC of payload	SADA	Solar Array Drive Assembly

Table 3.1-1: Functional Sharing of ICDS Hardware Units

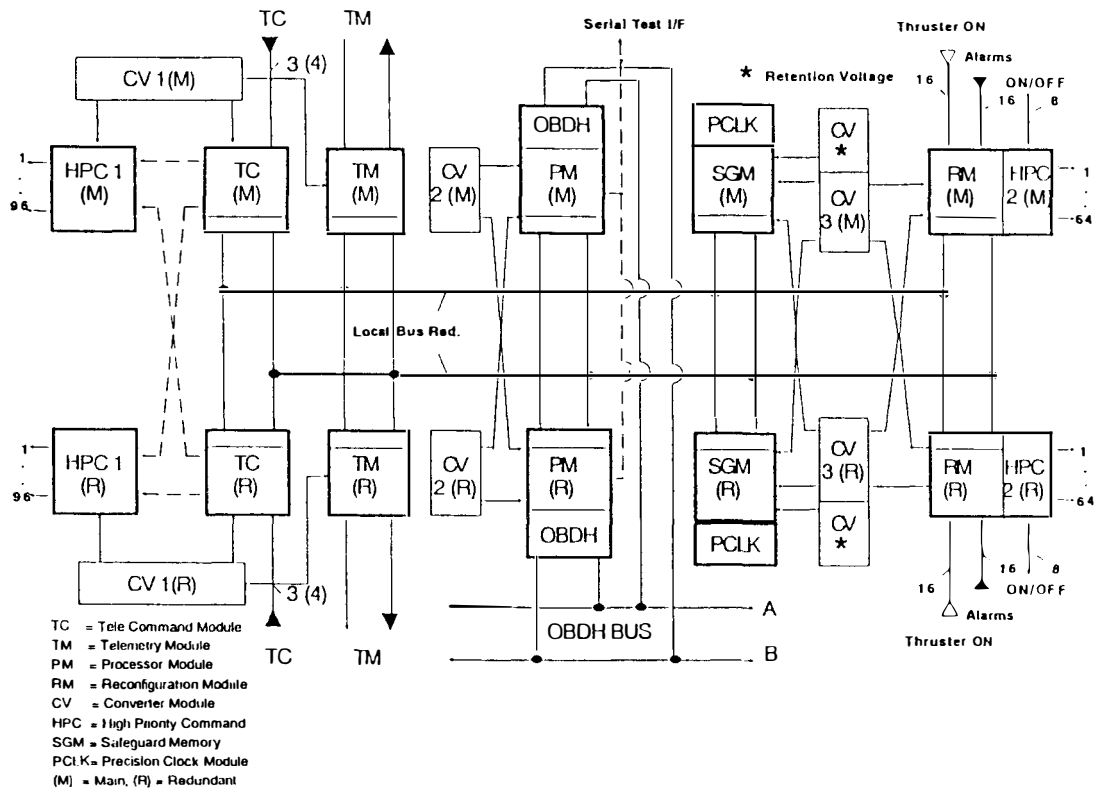


Fig. 3.1-2: Blockdiagram On-Board Computer Unit (OBCU)

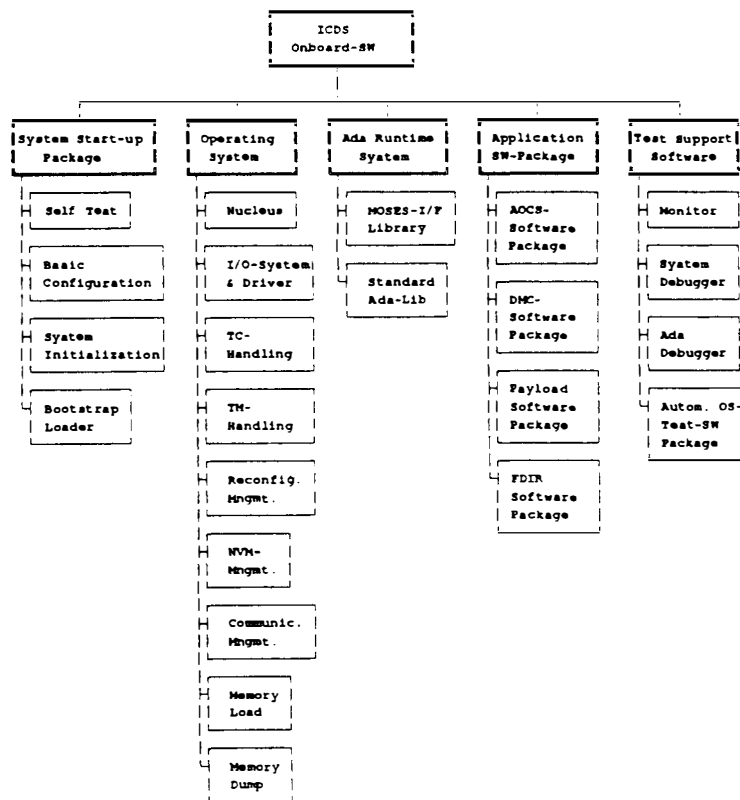


Fig. 3.1-3: Static Decomposition of ICDS-Software

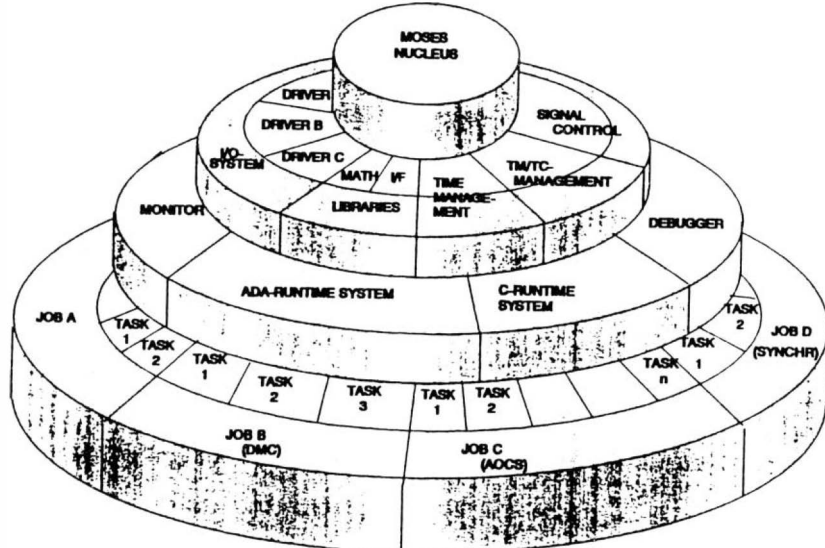


Fig. 3.1-4: ICDS Onboard-S/W Shell Model

### 3.2 Development and Functional Test Concept

For AOCS H/W and S/W functional-, performance and subsystem acceptance testing a test concept has been established at DASA-MBB and applied in all satellite programs reviewed under section 1.2 (see e.g. ref. 1), which is based on closed loop dynamic testing of all real components (optical and inertial sensors, control electronics, (wheel-) actuators, interfaces) under most realistic real time conditions using 3-axis motion simulators (Dynamic Bench Test Facilities - DBTF) and simulated S/C dynamics. This test strategy proved to be very effective and was therefore also adopted in other countries (USA, France, Japan, China) by most of the companies engaged in the field of activity under discussion here. A different approach, primarily for S/C verification/validation and flight S/W acceptance testing in closed loop simulation environment using dedicated "S/W Ground Support Equipment - SGSE" has also been established at DASA-MBB and used e.g. for EURECA (ESA project - "European Retrievable Carrier"). Static signal - and I/F tests for AOCS H/W equipment can also be performed, but dynamic testing is principally restricted to the OBCU functions. The advantage of this approach is, however, that the test environment (SGSE, test procedures, etc.) can accompany the equipment from the development - to the integration - and launch area, enabling repetition of tests and comparison with previous results when and where ever necessary and to the extent required.

For the ICDS both methods in integrated form will be applied:

- Functional modules of AOCS and DMC algorithms will be established directly in the OBCU target language and continuously used on development level within the subsystem closed loop analysis and performance simulation
- The AOCS (and DMC) S/W modules, already extensively dynamically tested will be integrated into the MOSES II operation system and data handling environment in the SGSE

- In the final development step dynamic bench tests for all functions and sequences including all sensor and I/F-hardware will be performed in an integrated DBTF SGSE simulation computer set-up.

### 4. S/C CONFIGURATION AND MISSION CONDITIONS

For the ICDS baseline design the following general assumptions on S/C configuration, mission conditions and axes conventions in TO and GSO are being made:

#### 4.1 Mission Baseline Assumptions

- launch into GS-T0 (ARLANE-APEX)
- launch window 2h/day within 11h period
- typical T/O sequence/parameters (ARLANE)
- 3-axis stabilization throughout TO, ABM, GSO
- repeated ABM burns (liquid bipropellant apogee engine)

#### 4.2 S/C Configuration and Axes Convention

- in TO partially or fully deployed S.A,
- ABM in S/C z-direction
- tank arrangement in z-direction (possibly propellant sloshing stab. inversion)
- "rabbit-ear" configuration in GSO
- satellite axes convention in TO and GSO as shown in figure 4.2-1

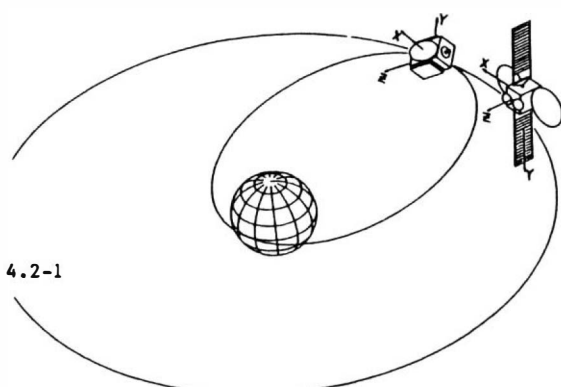


Fig. 4.2-1

## 5. AOCS EQUIPMENT CHARACTERISTICS

The requirements listed in section 2 lead to the following criteria for the selection and configuration of the AOCS equipments:

- Increase of
  - 3-axis attitude determination capability during GSO,
  - number and flexibility of back-up solutions for attitude determination as well as for actuation purposes.
- Decrease of
  - absolute number of sensors and actuators
  - numbers of sensors utilized only in transfer orbit,
  - fuel consumption.

The sensor- and actuator configuration which was chosen to fulfill these criteria to a best possible extent is described subsequently. It shall be regarded as a basis and has to be checked on compatibility with system aspects and to be harmonized occasionally by a modular extension, which is possible by the overall design approach (see section 3).

### 5.1 Sensor Configuration

The following sensors will be used:

- 3 two axis sun sensor heads with electronics (PSS 1,2,3),
- 1 two-axis infrared earth sensor (IRES),
- 1 single axis gyro.

All sensors are fully redundant.  
Their arrangements are defined subsequently.

#### Sun Sensor

A sun sensor assembly of three two axis sun sensor heads of  $\pm 64^\circ$  field of view ( $\pm \alpha_{FOV}$ ) provides full coverage around the satellite y-axis as shown in fig. 5.1-1. The sun sensor electronics output consists of two angles, which are used to derive the sun vector  $\underline{S}_B$  (unit vector) in the S/C body frame.

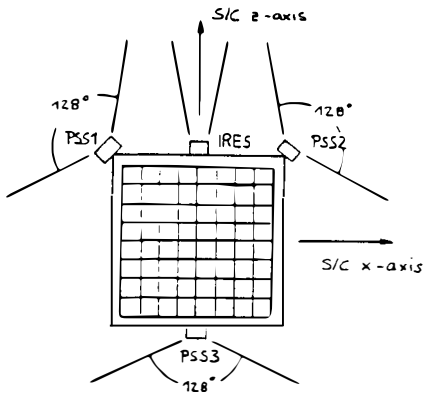


Fig. 5.1-1: Sun sensor arrangement

#### Earth Sensor

A two axis infrared earth sensor aligned along the S/C +z-axis provides roll and pitch attitude information.

#### Gyro

A single axis gyro in skewed arrangement will be used. The gyro orientation in the S/C body frame is shown in fig. 5.1-2 and depends on mission constraints and operational modes:

- The angle  $\beta$  (see fig. 5.1-2) must be such that sun presence is guaranteed in the sun search phase of the Sun Acquisition Mode. It must be

$$\beta \geq \pi - \alpha_{FOV},$$

- The angle  $\alpha$  must be such that the reorientation to the apogee boost attitude is feasible with 3-axis reference, i.e. that gyro and sun sensor provide attitude information about three axes. This is the case for

$$\underline{g}^T \underline{S}_B = 0$$

where  $\underline{g}$  is a unit vector in gyro input axis direction, expressed in the S/C body frame.

- The angle  $\alpha$  must be such that the sun vector  $\underline{S}_B$  in the S/C body frame is always within the FOV of the sun sensor, i.e.

$$|\underline{S}_{By}| \leq \sin(\alpha_{FOV})$$

This seems rather trivial, but is a very hard constraint especially for large angle rotations (ABM Reorientation).

The dependency of the above requirement on the sun vector  $\underline{S}_B$  causes a consideration of the

- launch site, i.e. transfer orbit inclination and the
- launch window

for the choice of the design parameter  $\alpha$ .

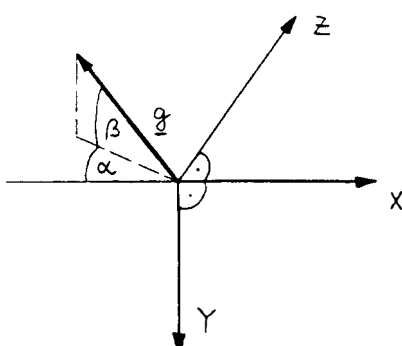


Fig. 5.1-2: Gyro orientation w.r.t. spacecraft axes

## 5.2 Actuator Configuration

Following actuators will be used

- 4N/10N reaction jets for attitude control during transfer orbit operation, reacquisition and orbit correction maneuver back-up,
- Momentum wheels and reaction wheels for on-orbit operation,
- 410 N engine for apogee boost.

The arrangement and the torque/force generation concept of the different actuators is described subsequently.

### 5.2.1 AOCS Reaction Jets

The attitude control and station keeping maneuvers are performed by 14 double valve thrusters, see figure 5.2-1. The following notation for the different thruster sets is used for the subsequent discussion, where each individual thruster is denoted by a number and a character:

```

Set A   := (1A, 2A, 3A, 4A)
Set B   := (1B, 2B, 3B, 4B)
Set C   := (1C, 2C, 3C, 4C)
Set A/B := (1A, 2B, 3B, 4A)
Set B/A := (1B, 2A, 3A, 4B)

```

Table 5.2-1 gives an overview of the thrust levels and the principal orientations of the different thruster sets.

The positioning of the thrusters and the apogee boost engine is sketched in figure 5.2-1. Note that the 4 thrusters of each set are placed and oriented symmetrically w.r.t. the COG and the principal axis, respectively. This arrangement implies, that the relation between the 4x1 thruster activation vector  $\underline{a}$  and the 3x1 torque vector  $\underline{\tau}$  applied on the S/C

$$\underline{\tau} = T_c \underline{a}$$

is qualitatively the same for each thruster set, or with other words, the 3x4 torque matrix  $T_c$  has always the form

$$T_c = \begin{bmatrix} t_{cx} & t_{cx} & -t_{cx} & -t_{cx} \\ t_{cy} & -t_{cy} & t_{cy} & -t_{cy} \\ t_{cz} & -t_{cz} & -t_{cz} & t_{cz} \end{bmatrix}$$

where  $t_{cx}$ ,  $t_{cy}$ ,  $t_{cz}$  are the nonzero absolute values of the torque levels around the S/C x-, y-, z-axis. They will be optimized according to system requirements (e.g. disturbance torque due to thrust misalignment during boost phases), by an appropriate choice of the placement, i.e. the lever arm w.r.t. COG and orientation of the thrusters.

For set A, set B, set A/B and set B/A even the numerical values of  $t_{cx}$ ,  $t_{cy}$ ,  $t_{cz}$  are ideally identical, due to the symmetry property. This fact has consequences on the redundancy concept, which will be discussed further below.

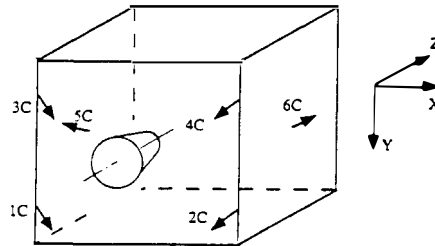


Figure 5.2-1a: Thruster positioning and orientation

Thrusters	Thrust Level	Orientation	Placement
Set A	4 N	tilted in the S/C (x,y)-plane --> zero z-component	on the corners of the central cube
Set B	4 N	tilted in the S/C (x,y)-plane --> zero z-component	on the corners of the central cube
Set C	10 N	tilted in the S/C (x,z)-plane --> zero y-component	on the edges of the S/C -z-side; the y-component will be chosen according to disturbance torque compensation requirements of the apogee boost phase
5C/6C	4 N	tilted into +z-direction for minimization of plume effects on antennas and disturbance torques	S/C east and west side
Apogee Boost Motor	410 N	points into -z-direction	S/C -z-side

Table 5.2-1: Thrust levels, orientations and placements

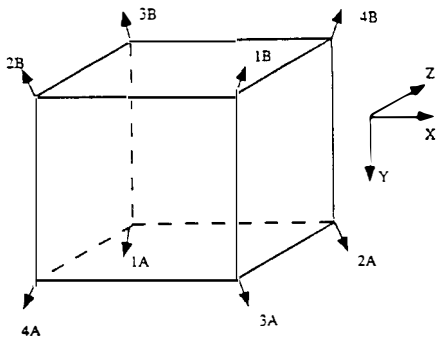


Figure 5.2-1b: Thruster positioning and orientation

#### Torque Generation Logic

The relation between the torque vector  $\underline{\tau}$  and the thruster activation vector  $\underline{a}$  is requested to be

$$\text{diag}(\tau_{cx}, \tau_{cy}, \tau_{cz}) \underline{m} = T_c \underline{a}$$

where  $\underline{m}$  is the modulator output vector with its elements consisting of -1, 0, +1, i.e. there are 27 values of  $\underline{m}$ .

Using the singular value decomposition of the torque matrix

$$T_c = V \Sigma \begin{bmatrix} U_1^T \\ U_2^T \end{bmatrix}$$

it follows

$$\underline{a} = T_c^{-1} \text{diag}(\tau_{cx}, \tau_{cy}, \tau_{cz}) \underline{m} + U_2 c$$

with the pseudoinverse  $T_c^{-1}$ . The constant  $c$  will be chosen such that all elements of  $\underline{a}$  are  $\geq 0$ . The solution of this equation for all 27 combinations of the modulator output signal results in the values of 0, 0.5, 1 for the elements of  $\underline{a}$ . The value 0.5 will be realized "on the average" by operating the corresponding thruster over half the modulator output time increment.

Of course, the above equation will not be solved on board, but the solutions, i.e. the correspondances between the modulator output  $\underline{m}$  and the thruster activation  $\underline{a}$  are stored in the on board computer memory according to table 5.2-2.

#### Torque Generation Redundancy

From the preceding explanations it is obvious that in case of failure of any individual thruster there are 2 independent back-up combinations of thruster sets for generating control torques about all S/C axes. For instance, in case of failure of one thruster of set A (resp. set B), the double valve thruster configuration permits to choose the thruster of set B (resp. set A) with the same number to assure the redundancy. As a second backup, thruster set C will be used. Table 5.2-3 summarizes the nominal and backup thruster sets for attitude control purposes.

thruster activation thruster no. 1 - 4		
torque requirement	1 <sup>st</sup> half modulator time increment	2 <sup>nd</sup> half modulator time increment
(-1, -1, -1) (-1, -1, 0) (-1, -1, 1)	(0, 1, 1, 1) (0, 0, 0, 1) (0, 0, 0, 1)	(0, 1, 1, 1) (0, 1, 1, 1) (0, 0, 0, 1)
(-1, 0, -1) (-1, 0, 0) (-1, 0, 1)	(0, 0, 1, 0) (0, 0, 1, 1) (0, 0, 0, 1)	(0, 1, 1, 1) (0, 0, 1, 1) (1, 0, 1, 1)
(-1, 1, -1) (-1, 1, 0) (-1, 1, 1)	(0, 0, 1, 0) (0, 0, 1, 0) (1, 0, 1, 1)	(0, 0, 1, 0) (1, 0, 1, 1) (1, 0, 1, 1)
(0, -1, -1) (0, -1, 0) (0, -1, 1)	(0, 1, 0, 0) (0, 1, 0, 1) (0, 0, 0, 1)	(0, 1, 1, 1) (0, 1, 0, 1) (1, 1, 0, 1)
(0, 0, -1) (0, 0, 0) (0, 0, 1)	(0, 1, 1, 0) (0, 0, 0, 0) (1, 0, 0, 1)	(0, 1, 1, 0) (0, 0, 0, 0) (1, 0, 0, 1)
(0, 1, -1) (0, 1, 0) (0, 1, 1)	(0, 0, 1, 0) (1, 0, 1, 0) (1, 0, 0, 0)	(1, 1, 1, 0) (1, 0, 1, 0) (1, 0, 1, 1)
(1, -1, -1) (1, -1, 0) (1, -1, 1)	(0, 1, 0, 0) (0, 1, 0, 0) (1, 1, 0, 1)	(0, 1, 0, 0) (1, 1, 0, 1) (1, 1, 0, 1)
(1, 0, -1) (1, 0, 0) (1, 0, 1)	(0, 1, 0, 0) (1, 1, 0, 0) (1, 0, 0, 0)	(1, 1, 1, 0) (1, 1, 0, 0) (1, 1, 0, 1)
(1, 1, -1) (1, 1, 0) (1, 1, 1)	(1, 1, 1, 0) (1, 0, 0, 0) (1, 0, 0, 0)	(1, 1, 1, 0) (1, 1, 1, 0) (1, 0, 0, 0)

Table 5.2-2: Correspondance between torque requirements  $\underline{m}$  and thruster activation  $\underline{m}$

#### Force Generation Logic

Nominally, the maneuvers are performed by the following thrusters:

- Apogee Boost Maneuver: The main force is provided by the Apogee Boost Motor and the thruster set C is used for the attitude control.
- North Maneuver: The four thrusters of set A give the force and are OFF modulated to realize the attitude control torques.
- South Maneuver: The four thrusters of set B give the force and are OFF modulated to realize the attitude control torques.
- East Maneuver: The thruster 5C gives the force and the thruster set A/B realizes the attitude control torques.
- West Maneuver: The thruster 6C gives the force and the thruster set B/A realizes the attitude control torque.

	Acquisition T0	ABM	GEO
nominal	Set C	Set C	Set A or Set B
backup	Set A Set B	Set A and Set C (remaining thrusters)	Set A, Set B Set C

Table 5.2-3: Thruster activation for attitude control

	North	South	East	West	ABM
nominal	Set A	Set B	5 C	6 C	Apogee Boost Motor
backup 1	Set B	Set A	Set A/B	Set B/A	Set C
backup 2	1A+3A or <sup>2</sup> 2A+4A	1B+3B or <sup>2</sup> 2B+4B	1A+2B or <sup>1</sup> 3B+4A	1B+2A or <sup>1</sup> 3A+4B	Set C (remaining thrusters) <sup>3</sup>

<sup>1</sup> Remaining roll disturbance torque compensation and attitude control by set C

<sup>2</sup> Remaining pitch disturbance torque compensation and attitude control by set C

<sup>3</sup> Remaining disturbance torque compensation and attitude control by set A and/or set B

Table 5.2-4: Thruster activation for orbit correction

In any case, the thrusters used for attitude control contribute to the velocity increment of the maneuver. So the extra fuel consumption due to attitude control will be very small.

#### Force Generation Redundancy

Each of the orbit correction maneuvers has a first and a second backup strategy in case of thruster failures. These are summarized in table 5.2-4.

**ABM backup:** In case of failure of the apogee boost motor, the maneuver can be performed without any modification of the logic of the mode (but the boost duration) using the thruster set C with OFF modulation for the attitude control.

As a second backup in case of an additional failure of one thruster of the set C, the residual thrusters of this set can be used for generating the velocity increment and the thruster sets A and/or B for attitude control and the compensation of the disturbance torque originating from the unsymmetrical force generation.

#### 5.2.2 Momentum and -reaction wheels

The wheel arrangement as shown in fig. 5.2-2 consists of

- Two flywheels in a V-configuration in a plane rotated about the y-axis by an angle  $\eta$
- Two reaction wheels along the x- and z-axes

In the nominal configuration only one flywheel (either FMW 1 or FMW 2) and both reaction wheels are in operation, all running at bias speeds such

that a residual bias angular momentum vector is generated parallel to the S/C negative y-axis. In case of a failure of one reaction wheel the residual reaction wheel and both flywheels will be used.

If on the other hand the "nominal" flywheel fails, the cold redundant fixed momentum wheel is activated and the bias speed of both reaction wheels is reversed to re-establish the bias momentum vector along the S/C -y-axis.

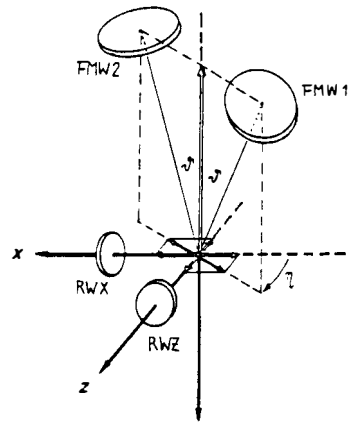


Fig. 5.2-2: Momentum and reaction wheel arrangement

### 5.3 Equipment Performance Parameters and Utilization Matrix

Table 5.3-1 gives a summary of typical performance data of the equipments.

The table 5.3-2 shows the correspondances between the utilization of the equipments and the operational modes, detailed in section 6., 7. and 8..

Component	Output	Range	Accuracy	Manufacturer
Sun Sensor	Sun vector in sun sensor head coordinates	$\pm 64^\circ$ off the S/C (x,y)-plane, full coverage around S/C y-axis	constant 0.01 deg daily 0.005 deg noise $3\sigma < 0.015$ deg resolution $< 10^{-3}$ deg	MBB
Earth Sensor	roll- and pitch-angle $(\phi, \theta)$ in the linear range sign( $\phi$ ) sign( $\theta$ ) in the saturation range	linear: $ \phi  < 2.5$ deg $ \theta  < 8.0$ deg saturation: $2.5\text{deg} <  \phi  < 14.5\text{deg}$ $8.0\text{deg} <  \theta  < 8.5\text{deg}$	constant 0.015 deg daily 0.01 deg noise $3\sigma < 0.09$ deg	Galileo
Gyro	rate $\omega_m$ around the gyro input axis	linear: $ \omega_m  < 2.1$ deg/sec saturation: $2.1$ deg/sec $<  \omega_m  < 50$ deg/sec	drift rate $< 0.15^\circ/\text{h}$ after calibration	Northrop
Control Thrusters		4N/10N	liquid propellant double valve	MBB
Apogee Boost Motor		410 N	liquid propellant	MBB
Momentum Wheels		speed range 1500 - 6000 rpm	satur. torque 0.1Nm friction torque uncertainty 0.002 Nm	TELDIX
Reaction Wheels		speed range $\pm 3000$ rpm	wheel speed measurement 24 pulses/revolution	TELDIX

Table 5.3-1: Typical performance data of equipments

operational mode	Sun sensor	Earth sensor	Gyro	Thrusters	Wheels
Stand-by Mode	y	0	y	0	n
Sun Acquisition Mode (TO)	y	0	y	y	n
Sun Acquisition Mode (GEO)	y	y	y	y	n
Gyro Calibration Mode (TO)	y	y	y	y	n
Gyro Calibration Mode (GEO)	y	y	y	y	y
Earth Acquisition Mode (TO)	y	y	y	y	n
Earth Acquisition Mode (GEO)	y	y	y	y	n
Apogee Boost Mode	y	0	y	y	y
Earth Acquisition Mode (GEO) On Orbit Mode	y	y	y	y	y
Antenna Mapping Mode	y	y	y	y	y
Pitch Reacquisition Mode (GEO)	y	y	y	0	y

Table 5.3-2: Utilization matrix of equipments

## 6. ATTITUDE CONTROL IN TRANSFER ORBIT

### 6.1 Transfer Orbit Sequence of Events

A schematic graphical representation of the sequence of events in transfer orbit up to apogee boost is shown in fig. 6.1-1.

The transfer orbit sequence starts with the separation from the launcher. The AOCS will be in stand-by-mode (SBM). Gyros and sun sensor electronics are activated but all actuators are disabled. An onboard timer is started to initialize a safety sequence after a preset time interval in case no ground command should be received. Nominally all transfer orbit sequences will be initiated by ground command if full TM/TC coverage is ensured otherwise automatically by time tagged commands. As soon as initial check routines (power availability, UPS-venting, AOCS check, etc.) have been completed, the AOCS will be activated and first sun acquisition will be commanded.

Starting from the initial conditions at S/C separation from the launcher and the attitude at the moment of SAM command, the AOCS will automatically search the sun, orient a desired S/C principal axis towards the sun and initiate a slow rotation of 0.5 deg/sec around the sunline. After disabling the thrusters in this orientation partial or full panel deployment will be commanded, and the propulsion system will be reactivated by ground command.

The sun pointing mode simultaneously represents the transfer orbit safe mode which is automatically reestablished in case of failures.

Upon entry into eclipse all thrusters will be inhibited (SBM) and after termination of the eclipse period and reenabling the thrusters the S/C will enter again into transfer orbit sun acquisition mode.

Earth Acquisition Mode (EAM) is required at least before approaching the apogee region if a subsequent apogee boost maneuver (ABM) will be performed, in order to establish 3 axis attitude reference. EAM is nominally entered from the SAM sun pointing submode. Parameters related to the sun-S/C-earth constellation are transmitted from ground and the S/C is reoriented such that the earth is brought into the earth sensor linear field of view, still maintaining a controlled attitude w.r.t. the sun.

Prior to the ABM, gyro drift estimation and compensation is required. Although gyro calibration can also be performed with sun reference only, it is preferred, for reasons of simplicity and reduction of ground station efforts to calibrate the gyros under 3-axis attitude reference conditions in earth pointing mode.

From earth pointing orientation slewing of the S/C z-axis into the apogee motor firing direction is performed by commanding appropriate bias values to the sun sensors and the gyro to establish the correct inertial attitude. After termination of each of the last apogee boost maneuver the S/C is commanded SAM.

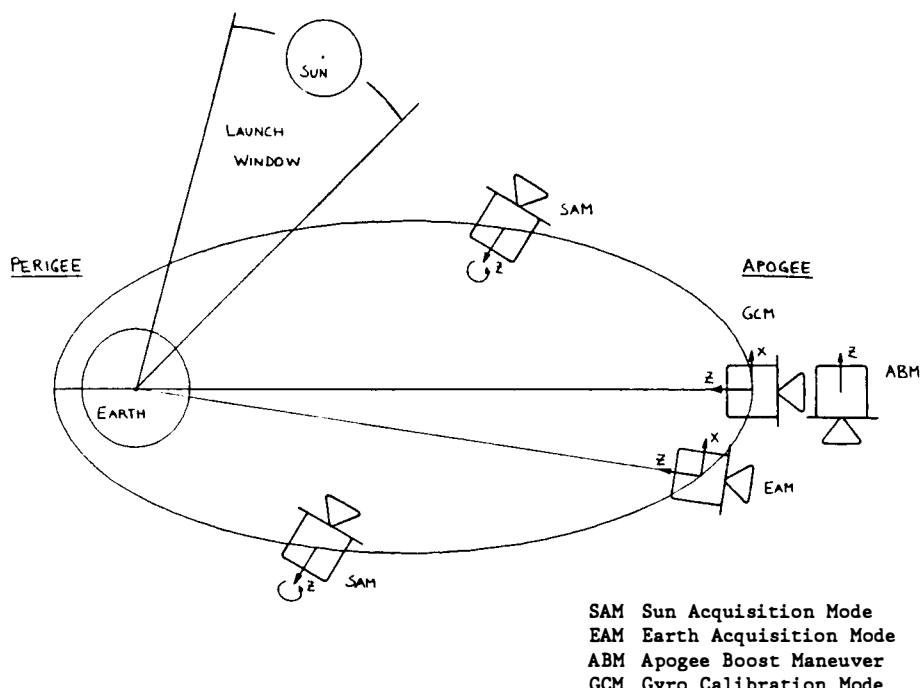


Fig. 6.1-1: Sequence of events in transfer orbit

## 6.2 Transfer Orbit Control Loops and Mode Logic

### 6.2.1 General

The general structure of the controller used in transfer orbit is shown in fig. 6.2-1. It consists of 4 modules:

- Sensor Data Processing and Estimation Module  
This module delivers the data which is necessary for the subsequent controller module. The angular rates are estimated from the sun vector components and its first derivatives (2 DOF) and from the gyro output (1 DOF).

Note that there are attitudes, where the gyro and the sun sensor (PSS) deliver dependent signals, so-called singular attitudes. In this case a stable control law requiring only sun sensor data is applied, in order to leave the singular attitude.

Inertial 3-axis attitude measurement data for large angle reorientations will be derived from the sun sensor- and integrated gyro output. As already described in chapter 5.1, the orientation of the gyro ensures that the attitude will never be singular for these maneuvers.

#### - Controller Module

The controller module consists of

- nonlinear control laws, that consider the non-linear coupling between the S/C axes and
- three axes related standard controllers (linear filters).

#### - Reference Data Module

This module supplies the reference data for the control laws, e.g. rate reference for sunline rotation, sun vector reference values for 3-axis stabilization etc.

#### - Actuator Command Module

The actuator command consists of

- a vectorial torque limiter, in order to consider the physically limited torque capability,
- three axis related fully digital pseudorotate modulators (PSRM), which convert the time discrete output signal of the controller into a pulse train,
- a thruster selection logic in order to distribute these axis related pulse trains onto 4 thrusters, see also section 5.2.

Figure 6.2-2 shows a simplified state graph of the transfer orbit phase logic.

Each bubble represents a discrete state, i.e. an operational mode or submode. The edges represent state transitions which will be activated if the corresponding boolean expression is true. For example starting with the stand-by mode (SDM), the control process will remain in this mode (else) until a boolean expression of a state transition (SAM•ECL) is true. Then the control process will change its discrete state, i.e. its operational mode to sun acquisition (SAM).

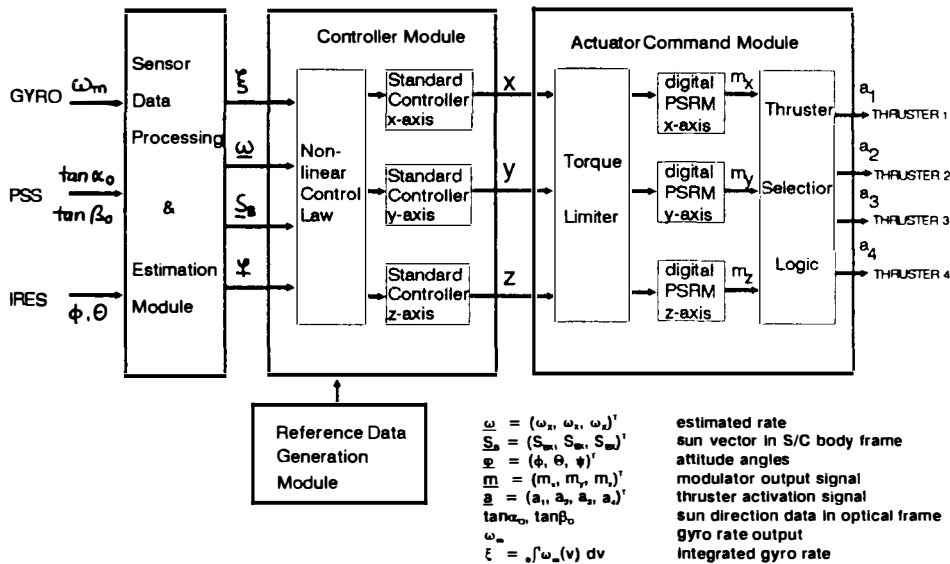
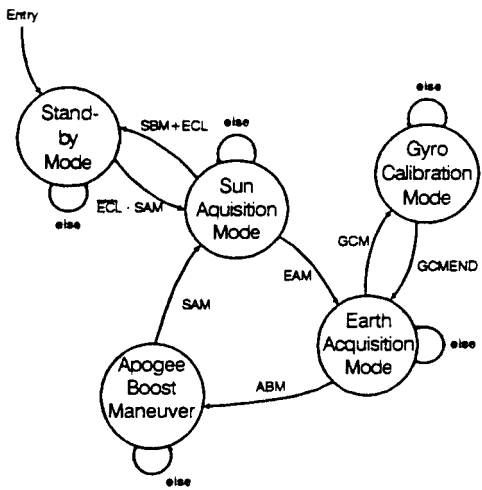


Fig. 6.2-1: General structure of the transfer orbit controller



SBM  
 SAM  
 EAM  
 ABM  
 GCM  
 ECL  
 GCMEND  
 +  
 \*  
 -  
 else

Telecommands  
 Eclipse  
 End of Gyro Calibration  
 logical 'or'  
 logical 'and'  
 logical 'not'  
 no state exit condition satisfied

Fig. 6.2-2: Simplified state graph of the transfer orbit logic

Concerning the overall strategy, there are some important facts that shall be pointed out here:

- Generally, the transfer orbit modes with a single, skewed gyro do not differ very much from a strategy using 3 axis-related gyros, because the angular rates can always be estimated except for non-singular attitudes and the sun search phase.
- The transfer orbit control law structures are designed in such a way that they can deal with both, singular and non singular attitudes, i.e. there is almost no additional software effort due to the single gyro arrangement.
- Maneuvers with inertial 3-axis reference (ABM) have the largest impact on the transfer orbit control strategy, because they require non-singular attitudes during the whole maneuver duration, see also section 5.1.

The different operational modes are outlined in the subsequent chapters.

### 6.2.2 Stand-by Mode

The objective of this mode is to let the S/C uncontrolled either

- in order to wait for the automatic sun acquisition mode invocation after separation or
- in order to wait for ground intervention or
- in order to pass through the eclipse.

The uncontrolled state of the S/C is obtained by setting all actuator inputs explicitly to zero.

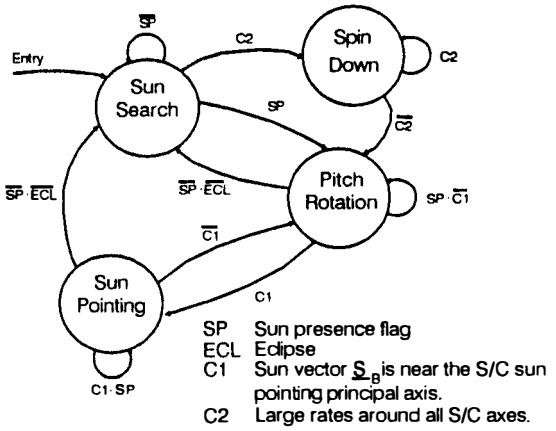


Fig. 6.2-3: State graph of the sun acquisition mode logic

### 6.2.3 Sun Acquisition Mode

This mode shall bring the S/C from an arbitrary initial condition to a sun pointing attitude, i.e. the desired principal axis is pointed to the sun and the S/C is to rotate around the sunline with a constant rate.

Figure 6.2-3 shows a state graph of the sun acquisition mode logic.

Sun presence is guaranteed during the sun search submode, due to the gyro orientation, see section 5.1.

The spin down submode is optional in case of a spinning S/C after separation.

### 6.2.4 Earth Acquisition Mode

This mode aims at acquiring the earth from an initial sun pointing state, in order to get the S/C three axes stabilized.

A pitch rotation is performed in order to approach the sun vector reference of the earth search submode. Then a rotation around the sunline and an appropriate choice of the sun vector reference guarantees earth presence.

Figure 6.2-4 shows a state graph of the earth acquisition mode logic.

### 6.2.5 Gyro Calibration Mode

The objective of this mode is to evaluate the gyro drift rate, in order to get accurate rate and integrated rate information from the single gyro during the subsequent apogee boost maneuver(s).

The gyro calibration can be done alternatively in two different ways:

- In earth pointing, i.e. 3 axis stabilized mode. This will be done in the apogee region of the orbit, in order to minimize the effects of the elliptical transfer orbit.
- With 2 axis inertial reference, choosing the sun vector reference  $S_B$  such that it is perpendicular to the gyro direction  $g$ , i.e.

$$g^T S_B = 0$$

In this case the gyro will only sense the drift rate, which is evaluated as the integrated rate output signal divided by the integration time.

#### 6.2.6 Apogee Boost Maneuver

By this mode the S/C will be reoriented from earth pointing attitude to an inertial reference attitude, in order to align the ABM thrust vector along the desired inertial thrust direction (given by orbit parameters). Then the apogee boost motor will be fired to obtain orbit changes. The ABM reorientation is done around an axis that is perpendicular to the S/C z-axis and the gyro direction  $\mathbf{g}$ , in order to apply simple control laws.

Figure 6.2-5 shows a state graph of the apogee boost maneuver logic.

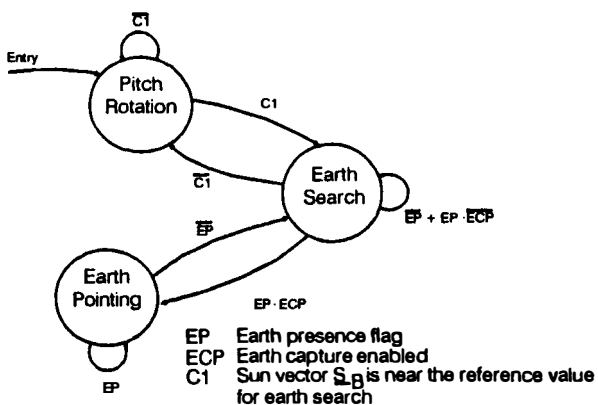


Fig. 6.2-4: State graph of the earth acquisition mode logic

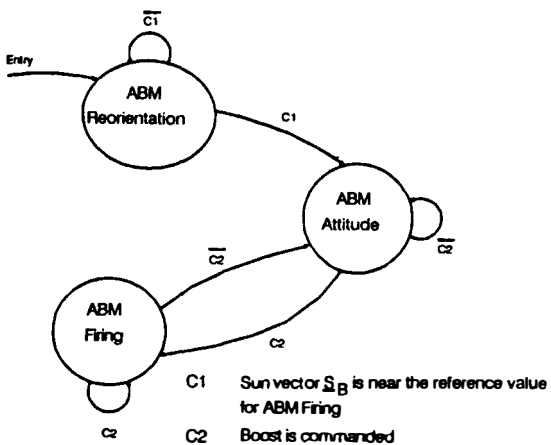


Fig. 6.2-5: State graph of the apogee boost maneuver logic

#### 6.2.7 Simulation Results

Typical preliminary simulation results of acquisition modes are based on

- a rigid body S/C-model with a moments of inertia tensor  
 $I = \text{diag} (1690, 1570, 1535) \text{ kgm}^2$
- absolute values of the torque level  
 $T_f^\top = (8.5, 15.1, 3.1) \text{ Nm}$
- quantized sun sensor output with a resolution of  $5 \cdot 10^{-3} \text{ deg}$
- a time-discrete controller, 0.1 sec sampling time
- simplified models for the IRES and the gyro (saturation functions).

The time histories of the S/C-rate  $\omega$ , the sun vector  $S_B$  and earth vector  $E_B$  are expressed in the S/C body coordinate system.

Figure 6.2-6 shows a typical plot of the sun acquisition mode, where the S/C y-axis is initially pointing towards the sun, i.e. the sun is not within the FOV of the sun sensor.

Figure 6.2-7 shows an earth acquisition from an initial sun pointing state.

Figure 6.2-8 shows a 70 deg reorientation in order to point the S/C +z-axis to an inertially fixed thrust direction for the apogee boost. The angle  $\gamma$  denotes the deviation angle w.r.t. the reference direction. It can be seen that its final value is within the modulator deadband.

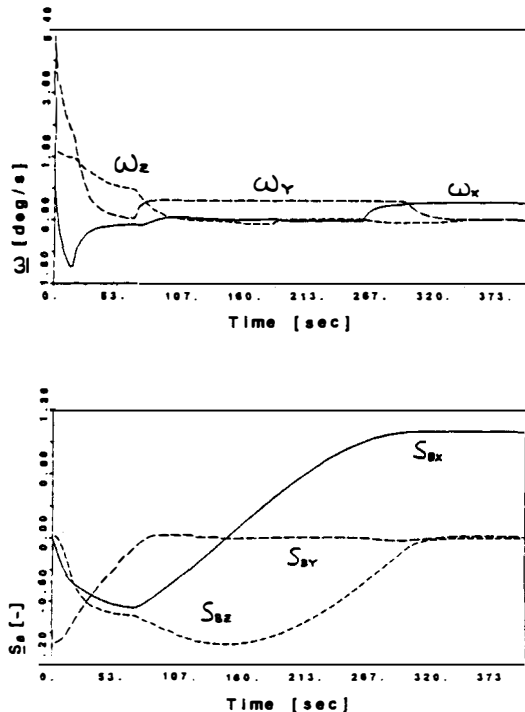


Fig. 6.2-6: Sun acquisition mode time history

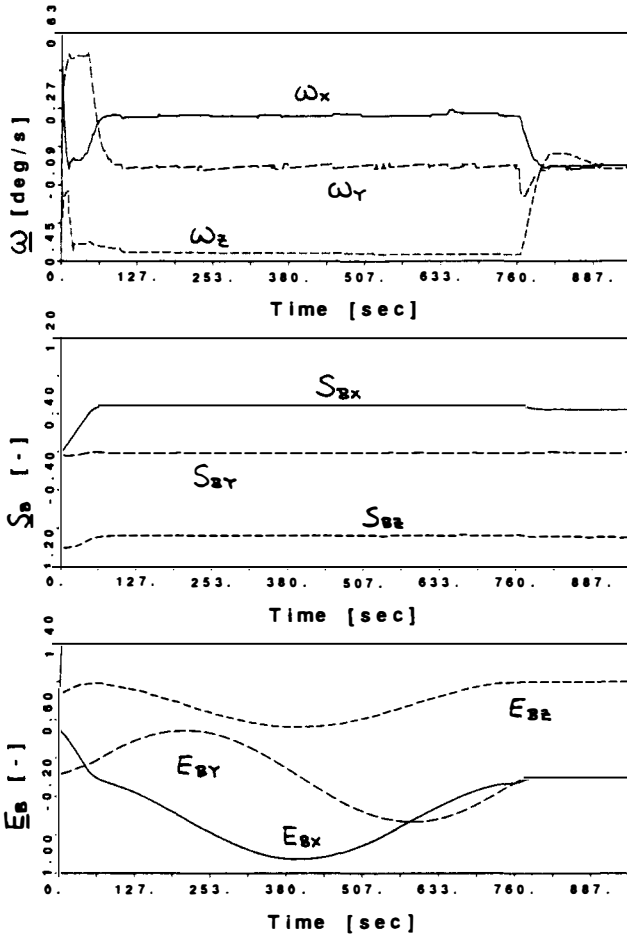


Fig. 6.2-7: Earth acquisition mode time history

## 7. ATTITUDE AND ORBIT CONTROL IN GEOSTATIONARY ORBIT

### 7.1 On-Orbit Sequence and Operational Modes

#### Acquisition

After full deployment of the solar arrays performed in sun pointing mode after the last apogee maneuver, EAM in GSO is commanded, which follows the same principles as in transfer orbit concerning the regulator structure and mode logic (see section 6.2). However, due to the different S/C configuration, in particular panel structural flexibility effects, the regulator parameters will be set to appropriately adjusted, different values. Furthermore the sun reference direction must be autonomously calculated onboard on the basis of the onboard local time and not from ground data.

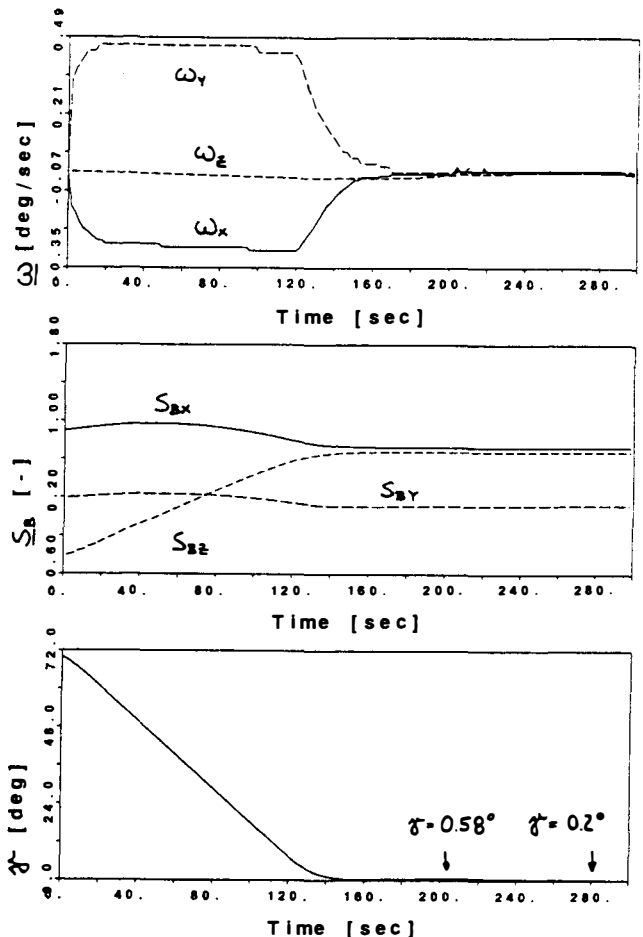


Fig. 6.2-9: Apogee boost maneuver, reorientation

#### Normal Mode

The subsequent mission sequences incorporate wheel run-up and switching to normal mode operation. Normal mode attitude control is based on 3-axis attitude reference established by the optical (sun and earth) sensors supported by yaw estimation and disturbance torque prediction algorithms.

#### Station Keeping

Nominally no North/South trim maneuver is necessary since the last apogee correction is accurate enough. The necessary East/West trim maneuvers will be performed in the station keeping mode. Station keeping maneuvers nominally use 4N liquid bipropellant thrusters. Sufficiently small and timely spaced impulse bits are issued to ensure that the NM wheel control system can cope with the attitude disturbances generated simultaneously. For backup strategies with different sets of thrusters in case of failures reference is made again to section 5.2.1.

### Antenna mapping

The AOCS will provide the possibility for on-orbit measurement of antenna patterns for all coverages from a single test earth station. For these measurements a bias capability of  $\pm 15$  deg in pitch and in roll will be provided, where three axis reference is derived from the two-axis sun sensors and the rate integrating gyro, which must be calibrated previously. The antenna mapping procedures are performed in the on-orbit control mode using fly-wheels and reaction wheels for control torque generation.

### 7.2 On-orbit Control Loops

In classical satellite attitude and orbit control concepts clear distinction is made between attitude control during station keeping maneuvers and in normal mode, these modes of operation employing essentially different control principles (e.g. SKM reaction jet control and NM pitch wheel control and WHECON principle for roll/yaw). For the ICDS concept under discussion here a common control approach is regarded superior. The most obvious advantages are:

- Inherent back-up capabilities using different types of actuators if required.
- Common 3-axis attitude measurement estimation and reference generation principle throughout.
- Smooth transitions between different operational conditions due to continuous state propagation of estimation and control variables.
- Control w.r.t. arbitrary bias functions, in order to compensate thermal distortions.

A schematic blockdiagram of the on-station attitude control mode is shown in fig. 7.2-1.

The raw sensor data from the 2-axis sun sensors, the two output channels of the earth sensor (and gyro in back-up cases) are processed to generate 3-axis attitude information ( $\phi^*$ ,  $\psi^*$ ,  $\theta^*$ ). Based on system models orbit parameter updates from ground and additional measurements (wheel speed) optimal estimates of system state variables  $\hat{H}_x$  (prop.  $\psi$ ),  $\hat{H}_z$  (prop.  $\phi$ ),  $\hat{\omega}_x$ ,  $\hat{\omega}_y$ ,  $\hat{\omega}_z$ , ( $\omega_y$  prop.  $\omega_0$ ),  $\hat{H}_x$ ,  $\hat{H}_z$  and  $\hat{\theta}$  are generated. In colinearity regions yaw attitude is propagated by means of the observer equations of the angular momentum in orbit coordinates suppressing the nutation by adequate filtering. Under normal mode conditions attitude stabilization is performed by controlling the fly-wheel and reaction wheels in torque mode. In order to compensate for the impact of limited resolution in the torque commands as well as unknown internal wheel friction torque, contribution of cross-axis angular momentum components and external disturbance torques under colinearity conditions, a model following loop is incorporated to match the wheel control torques to the correct values. This technique as used for closed loop AOCS dynamic bench testing with real hardware at MBB is well proven. In view of the fact that in the wheel control concept in question here the wheel speed variation exceeds the usual range considerably, a nonlinear friction torque compensation loop is additionally superimposed. In order to improve the pointing accuracy and stability to the level required from future payloads (e.g. SILEX), disturbance torque estimation and compensation is applied. These estimates furthermore ensure, that the necessary yaw attitude prediction accuracy during colinearity passage is achieved.

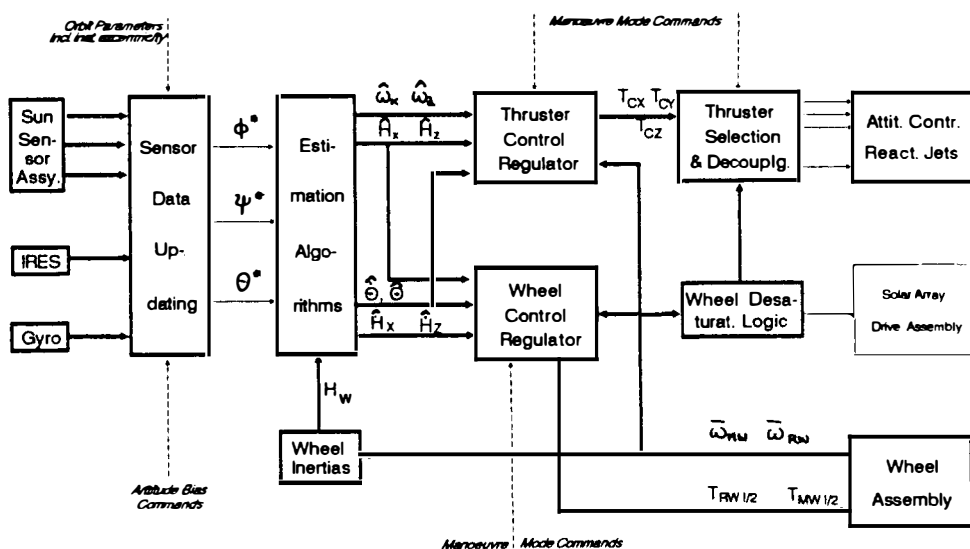


Fig. 7.2-1: Schematic block diagram of on-orbit NM/SKM control loops

The angular momentum storage capacity of the baseline wheel arrangement has been designed such as to also cope with the accumulated disturbance torque levels during N/S orbit correction with ion thrusters. Wheel desaturation is required only once per day using chemical thrusters of 4N thrust level. To minimize transient overshoots due to the unloading pulses a torque precompensation strategy is adopted, i.e. compensation torques of lower magnitude but extended duration equivalent to the angular momentum increment of the unloading pulse are applied to the wheels and symmetrically distributed about the unloading instant. The precompensation technique also allows to perform E/W orbit correction maneuvers (minipulse strategy) without violating the performance requirements. The same approach is used to minimize transients originating from slewing torques encountered in fast target acquisition of low earth orbiting satellites with the onboard tracking antenna. In fig. 7.2-1 a back-up control concept of classical type for orbit correction in both N/S and E/W directions using chemical thrusters is indicated.

However, the present design is different in the following respects:

- Nutation control by means of the wheels is continuously performed also during and after SKM.
- Incorporation of an adaptive filter in the SKM control loops provides active damping of solar generator oscillations for amplitudes exceeding a predefined limit.
- A nonlinear disturbance torque observer is applied to prevent body limit cycle motion in absence of disturbance torques or at low disturbance torque levels during the maneuver.

Additionally in fig. 7.2-1 the possibility of angular momentum dumping by solar torque compensation is schematically shown. Within the ICDS program a design concept is available, which ensures wheel desaturation by only modulating the solar array rotation angle. This capability can be activated on request.

### 7.3 Simulation and Analysis Results

One of the features of the AOCS Concept is that all GSO-Modes (NM, SKM, EAM, SAM) are nominally operating without use of gyros. Especially the

SKM-thruster regulator takes care about robustness to panel parameters and active or passive panel flexibility damping. The principle how this adaptive controller works is shown in the simulation results in Fig. 7.3-1 and the gain phase plots in Figs. 7.3-2 and 7.3-3, respectively.

The simulation run in Fig. 7.3-1 starts with a large initial condition in the 1th normal bending mode of the solar array. At the beginning the oscillations with large amplitudes will be actively damped which corresponds to a classical phase advance control of the panel motion shown in Fig. 7.3-2. If the panel motion amplitudes are reaching a required range, than passive damping of the panel oscillations will continue which corresponds to a classical phase lag stabilization shown in Fig. 7.3-3.

The outstanding pointing performance during SKM is supported by the new MBB 4N-bi-propellant thrusters. A typical simulation result is given in Fig. 7.3-4 and Fig. 7.3-5 for S/C x- and z-axis, respectively.

The results of these typical N/S-SK-maneuver demonstrates the outstanding good pointing accuracy in SKM (roll, yaw overshoot <  $3 \cdot 10^{-2}$  deg).

The meaning of different curves in the gain-phase plots, which is representative for all theoretical stability analysis results, is as follows:

$L(j\omega)$	linear transfer function in the frequency domain including sensor dynamics, controller frequency response and S/C dynamic motion
$-N^{-1}(\omega, A_{MIN})$	boundary curve of the negative inverse describing functions given in the investigated frequency range for input amplitude levels $A_{MIN}$ to reach exactly the actual modulator deadband (worst phase condition with respect to nonlinear stability margin)
$-N^{-1}(\omega_0, A)$	negative inverse describing function at frequency $\omega_0$ depending on input amplitude $A$ .

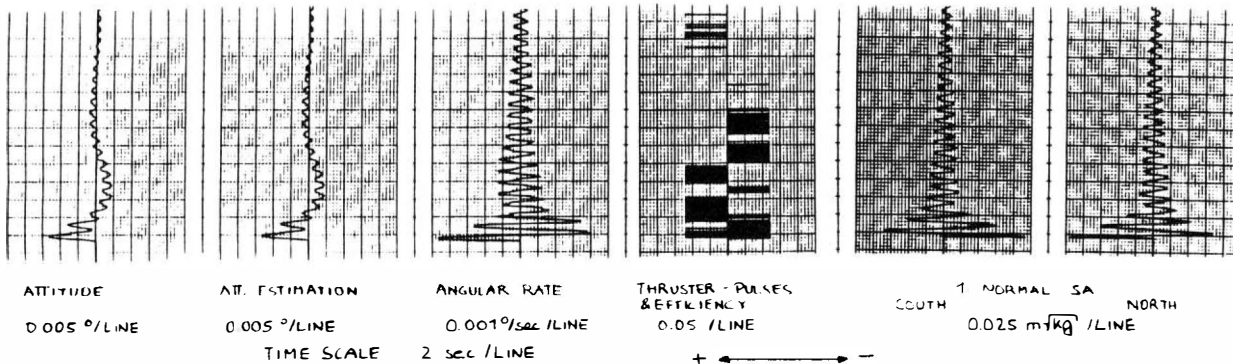


Fig. 7.3-1: Station Keeping mode, time history for large initial conditions

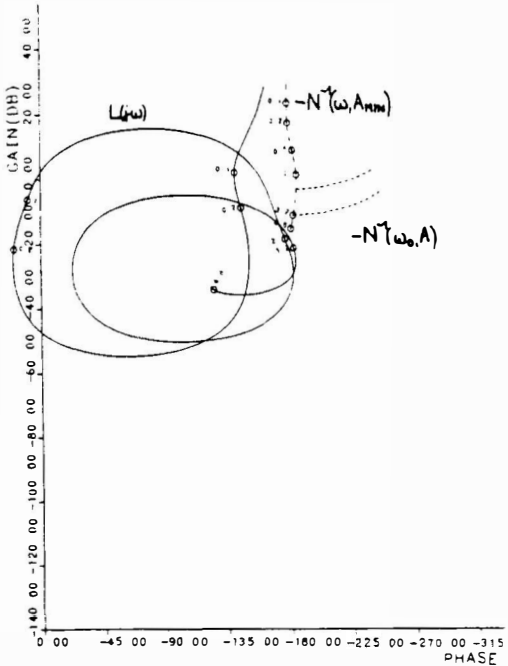


Fig. 7.3-2: Gain phase plot, active damping

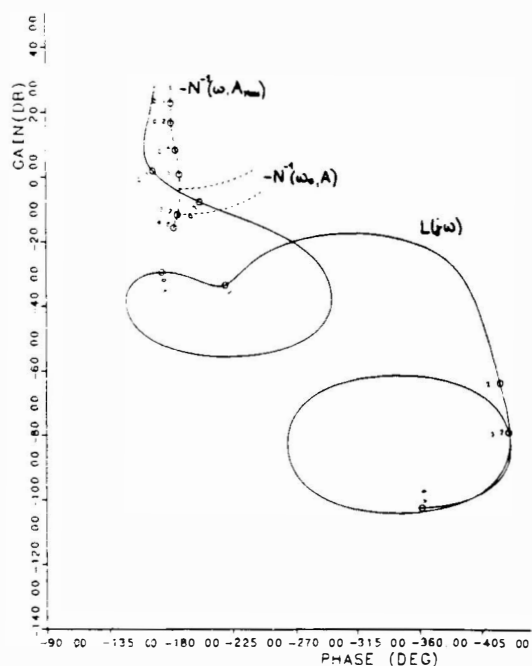


Fig. 7.3-3: Gain phase plot, passive damping

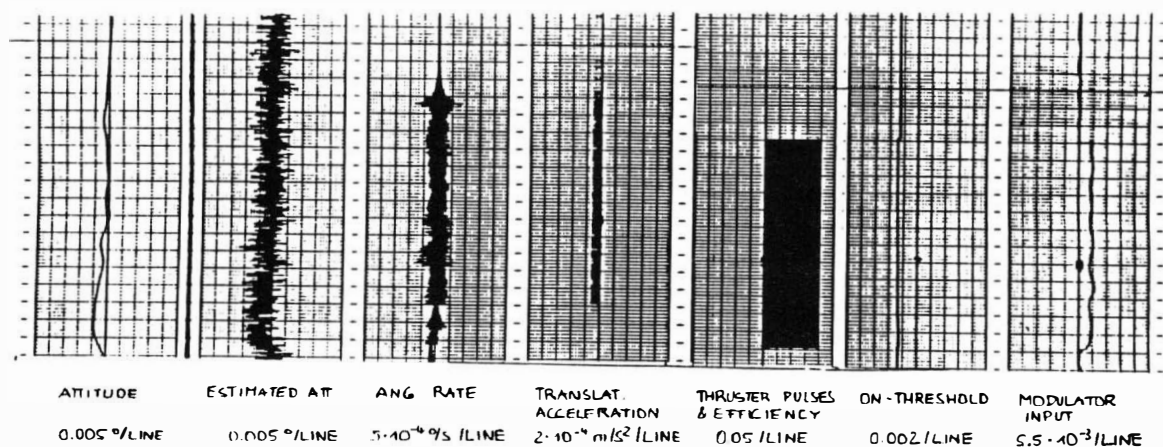


Fig. 7.3-4: Station keeping mode, time history  
x-axis

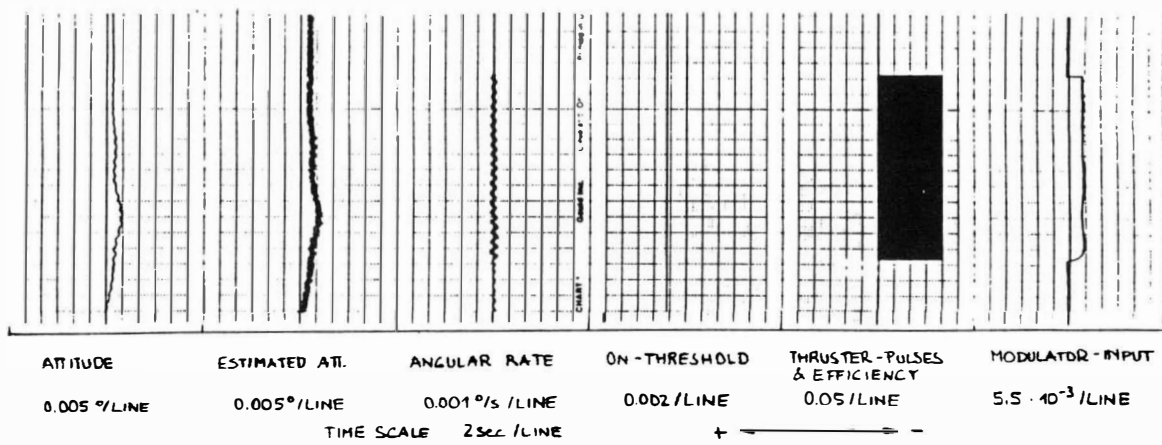


Fig. 7.3-5: Station keeping mode, time history  
z-axis

## 8. SAFE MODES

The primary objectives of safe mode concepts are to retain or to reestablish the S/C operational states and conditions in which an anomaly occurred. If this cannot be achieved within a predefined period, the S/C shall be transferred into mode conditions as close as possible to the previous state and from there - if also not successful - in consecutive steps into a secure, ultimate survival mode.

### 8.1 Transfer Orbit Safe Mode

During S/C manoeuvring in TO operational mode there is reasonably only one safety condition available, the sun pointing mode, which ensures proper thermal and power conditioning. Furthermore TM/TC contact must be provided.

### 8.2 On-Orbit Safe Modes

For the geostationary orbit operation the safe mode comprises the following steps:

- 1) Try an earth reacquisition with conservation of the angular momentum, using the flywheels and reaction wheels as actuators (ERAW)
- 2) Try an earth acquisition manoeuvre (EAM) if measures under 1) are not possible respectively successful. If EAM is found successful, control will be automatically transferred to NM.
- 3) Go to the ultimate step of the safe mode of SAM if measures under 2) are not successful.

Step 1 of the safe mode is characterized as follows:

- Earth reacquisition with wheels and flywheels (ERAW)  
For the ERAW the attempt to reacquire the earth will be performed by rotation of the S/C around the S/C y-axis. This requires the computation of the instantaneous angular momentum direction in S/C axes from the wheel speed measurements. For the earth search rotation torques have to be applied to the wheels such that the y-component of the instantaneous angular momentum is not changed. Still only flywheels and reaction wheels are used as actuators for the ERAW.  
When the earth presence is available the earth will be first acquired in pitch and then in roll and yaw. If the ERAW is found successful according to preselected criteria within a predefined time interval control will be switched automatically to normal mode.

The procedures associated with steps 2 and 3 are identical to the mode description of section 6.2. Provisions are made that transition to steps 2 and 3 can be inhibited by ground command or respectively initiated automatically only after preset time intervals (e.g. time necessary to remove the stored onboard angular momentum).

- Earth acquisition (EAM)  
In case of reacquisition the procedure for calculating the sun reference in the S/C is different from the transfer orbit case. The sun vector reference is calculated autonomously on board as in the normal mode. Therefore provisions are made that in any case the absolute

time is saved in case of complete reconfiguration of the OBCU.

Prior to earth acquisition, wheel run-down will be performed.

- Sun acquisition (SAM)

Eclipse periods will also be identified autonomously, due to the availability of the absolute time.

## 9. FAILURE DETECTION, ISOLATION & RECOVERY

In order to meet the requirements of section 2, in particular the (48 h) onboard autonomy and request for outage minimization a specific FDIR strategy is being implemented in the ICDS. Depending on the criticality of the failure appropriate reactions of the ICDS will be initiated. Four main failure classes, the method of failure detection and the associated actions for recovery have been identified and will be outlined subsequently.

### Class 1: Unit internally recoverable Errors

#### Assumption:

A unit has detected an internal failure, which is present either temporarily or permanently. In any case, the unit is capable to recover from the failure by internal measures.

#### Failure Detection:

These failures are detected by unit internal self check features. The features are realized in hardware and/or software. The OBCU for instance applies software and hardware functions to detect and recover from OBCU related class 1 failures like

- single bit failure (single event upset)
- operation time-out conditions
- illegal addresses and so on

#### Reaction:

The unit carries out the failure assigned recovery procedure. No other external device will be involved. An error message is sent to ground for status information and failure analysis.

### Class 2: S/W detected ICDS Equipment Anomalies

### Class 2a: Failures within ICDS "Front End" Equipment

#### Assumption:

The OBCU i.e. S/W and H/W of the Processor Module (PM) is considered to be healthy. Software functions are provided, which can detect failures within ICDS equipments like sensors or actuators connected to the OBDH bus directly or by means of bus couplers. The OBCU will be capable to isolate faulty equipment.

#### Failure Detection:

Failure detection of equipment is performed e.g. by

- limit sensing of data
- filtering of health states,
- surveillance of earth and sun presence etc.

#### Reaction:

The reaction of the software to class 2a errors results in a change of the suspected equipment, according to the health status stored in the Non-Volatile Memory (NVM). If the failure cannot be isolated by switching to a redundant device, in worst case the software provokes switch-over of the PM (see class 2). The AOCS sub-system will disable all actuator outputs.

### Class 2b: Failures within ICDS "interfacing" Equipment

#### **Assumption:**

If a failure is encountered on the OBDH bus and bus coupler level, it has an impact on all ICDS sub-systems. Hence the failure detection and recovery will be performed by an overall ICDS FDIR module.

#### **Failure Detection:**

The failure detection for the OBDH bus and the couplers takes into account e.g.

- the internal H/W signal status,
- the burst transfer status of the data related to the coupler itself and the
- "front end" units

#### **Reaction:**

At first the FDIR module requests the ICDS sub-systems to stop any interfacing with the defective units. Afterwards the overall FDIR module switches over to the redundant unit (bus or coupler) and after a predefined time allows the sub-systems to communicate again with their "front end" equipments.

### Class 3: Processor Module (PM) Hardware and/or Software Failures

This class comprises all severe H/W and S/W failures of the PM. Such failures have an impact on the outer world e.g. on the system. Class 3 is subdivided into 3 sublevels as stated below.

#### Class 3a: Failures leading to a S/W initiated PM Restart (Warm Start)

##### **Assumption:**

PM failures, which occur only once and can be handled by the S/W itself may be invoked by hardware or software malfunctions. Multiple occurrences are related to class 3c.

##### **Failure Detection:**

The failures are detected by software modules, which make also use of supporting hardware features. The surveillance functions are

- RAM double bit errors
- illegal instructions
- task run-time
- error counter and
- non-consistency of data

##### **Reaction:**

A partial or complete restart of the ICDS S/W is initiated. An error indication is stored in the non-volatile memory (see also class 3c).

#### Class 3b: Failures leading to a H/W initiated PM Restart (Cold Start)

##### **Assumption:**

The OBCU is considered to have a spurious failure, which is assumed to be corrected by a restart of the actually powered PM. The failure is detected by H/W features of the RM. The failure may be caused by software or hardware malfunctions.

##### **Failure Detection:**

The detection mechanism for the PM failures reacts only on one fatal error condition. A restart is provoked on the first detection of the missing S/W "alive" signal over a defined time period (watch-dog logic).

##### **Reaction:**

The reaction to class 3b error results in a complete reset of the ICDS software (cold start). The main steps of the cold start are stated subsequently which necessitates a complete initialization sequence from OBCU hardware initialization (controller), actuator disabling, load of NVM data up to restart of previous jobs and tasks

The cold start does not include the switch-over of external devices like sensors or actuators.

### Class 3c: Failures leading to PM switch-over

#### **Assumption:**

A permanent failure is detected in the PM of the OBCU.

#### **Failure Detection:**

The class detection mechanisms takes into account

- multiple occurrence of watch-dog time-out and
- PM power loss

#### **Reaction:**

The ICDS reacts with a switch-over to the redundant PM and the surveillance circuits of the Re-configuration Module (RM). ICDS software is requested to carry out a cold start including the initialization sequence indicated under 3b.

### Class 4: H/W Surveillance detected Failures

#### **Assumption:**

It is assumed that one or more errors of class 1 to 3 have not been detected by any surveillance function resp. that the recovery from these malfunctions was not successful in time. This leads to a violation of the Reconfiguration Module (RM), hard wired health criteria.

#### **Failure Detection:**

The failure detection functions are performed by the hardware surveillance logic of the RM. It reacts in case of

- loss of earth presence,
- loss of sun presence,
- violation of thruster on-time and
- temporary power loss

#### **Reaction:**

The reaction to class 4 errors results in a switch-over of the Processor Module (PM) too. The surveillance functions of the redundant RM are autonomously disabled and can only be enabled by ground command.

The ICDS software reacts to class 4 failures with a cold start and a complete switch-over of all required AOCS equipments.

## 10. SUMMARY

Presently predevelopment work on design and implementation of advanced attitude and orbit control concepts for 3-axis stabilized communication- and application satellites is being performed at DASA-MBB, which is part of the "Spacebus Improvement Program - SIP", a company funded joint cooperation program carried out at Aerospatiale and DASA-MBB. An "Integrated Control and Data System - ICDS" which combines Attitude- and Orbit Control (AOC) and Data Management- and Control (DMC) functions in a flexible, versatile onboard computer, serial data bus system and associated interface units is being designed, developed, integrated and tested. The ICDS baseline incorporates all necessary hardware and software for short term application in communication- and application satellite projects. Based on typical performance requirements for present and future applications, the characteristic features of the AOCS baseline design and associated equipment are discussed in detail.

## 11. ACKNOWLEDGMENT

The authors are most indebted to E. Gröger (DASA-MBB Dept. RTT 122, H. Widmann (DASA-MBB Dept.

RTT142) who have provided the inputs for section 3.1 and to Fr.P. Lein for typing the manuscript.

## 12. REFERENCES

- 1) Bittner,H., Brüderle,E., Roche,Ch.,  
Schmidts, W.  
The Attitude and Orbit Determination and Con-  
trol Subsystem of the INTELSAT V Spacecraft  
ESA AOCS-Conference, Noordwijk, 1977-ESA  
SP - 128
- 2) Göschen,W., Bittner,H., Brauch,A., Brüderle E.  
Three-axis Stabilization of Communication Sa-  
tellites, Past Experience with SYMPHONIE and  
Application in Follow-on Projects  
Proceedings of the 8th IFAC SYMPOSIUM on Auto-  
matic Control in Space, July 2-4, Oxford, Eng-  
land 1979
- 3) Bittner,H., Brauch,A., Brüderle,E., Roche,Ch.,  
Scheit,A.  
The Attitude and Orbit Control Subsystem of the  
TV-SAT/TDF1 Spacecraft  
Proceedings of the 9th IFAC SYMPOSIUM on Auto-  
matic Control in Space, July 5-7, Noordwijker-  
hout, 1982
- 4) Bittner,H., Fischer,H.D., Roche,Ch.,  
Surauer,M., Vieler,H.  
The Attitude and Orbit Control Subsystem of the  
DFS KOPERNIKUS  
10 IFAC World Congress, Munich, 1987
- 5) Bittner,H., Fischer,H.D., Froeliger,J.L., Mil-  
tenberger, K., Popp,H., Porte,F., Surauer,M.  
The Attitude and Orbit Control Subsystem of  
the EUTELSAT 2 Spacecraft  
11th IFAC Symposium on Automatic Control in  
Space, Tsukuba, Japan, July 1989

## DISCRETE FREQUENCY DISTURBANCE REJECTION IN MULTIVARIABLE DIGITAL CONTROLLERS

N.J. Kasdin

*W.W. Hansen Experimental Physics Laboratory, Stanford University, Stanford, CA 94305, USA*

**Abstract.** The rejection of sinusoidal plant disturbances is a primary objective of closed loop control systems, particularly on spacecraft. In addition, all modern spacecraft use digital, or sampled data, controllers. This paper describes methods for analyzing the frequency response of sampled data controllers to plant disturbances at discrete frequencies. It then describes the proper method for performing direct digital LQR/LQG design with plant augmentation to exactly reject these disturbances. It is shown that the traditional method of mapping to the discrete domain the augmented continuous system does not result in a digital controller that cancels the disturbances. In fact, the disturbance model must be mapped to digital separately with augmentation taking place in the discrete time problem. An example is presented to verify the technique.

**Keywords.** Digital control, Direct digital control, Disturbance rejection, Multivariable control systems, Optimal control, Sampled data systems.

### **1. Introduction**

The primary objective of a large number of automatic control systems, including most spacecraft, is the rejection of plant disturbances, particularly sinusoidal disturbances at discrete frequencies. In spacecraft these disturbances can occur from aerodynamic drag, solar wind, gravity gradient, or magnetic forces and torques. The objective, therefore, of the attitude or translation control system designer is to place a notch in the closed loop frequency response (complex zeros at the disturbance frequencies).

In most modern spacecraft the control system is implemented in a digital computer. Unfortunately, the methods for designing digital controllers for disturbance rejection are less completely explored than that for continuous ones (*Franklin, Powell, and Workman, 1990; Stengel, 1986; Hirate, 1989*). This paper specifically addresses the problem of sinusoidal disturbance rejection in sampled data control systems. First, a new method is presented for analyzing the discrete frequency response to disturbances that does not ignore the action of the disturbance on the plant between sampling instants. The paper then shows how the standard extension of continuous LQR/LQG methods to the digital control problem does not result in the desired zero placement. Therefore, a modification of this technique is developed for digital LQR/LQG controller design that guarantees perfect rejection at a finite number of frequencies. Simulation is used to verify the controller performance.

When implementing a digital controller, it is common to design based on discrete LQR/LQG methodology by mapping the continuous models and cost functions to the digital domain and then solving the appropriate discrete algebraic Riccati equation. It is intuitively natural to expect that an exact discrete mapping of the augmented system would produce the best controller design, as it exactly accounts for the disturbance action during the sample interval. In fact, this is what is normally recommended in design textbooks (*Franklin, Powell, and Enami-Naeini, 1986*). However, it is shown below that this is not the case. Rather, the plant must be mapped independently and separately augmented with a zero-order hold model of the disturbance in order to guarantee perfect rejection.

A simple example, consisting of an SISO,  $1/s^2$  plant being regulated in the presence of a sinusoidal disturbance, is presented. This work was also used in the design of the Gravity Probe B spacecraft pointing control system (*Kasdin, 1991*). Details of that mission and design are discussed in the oral presentation.

### **2. Frequency Response in Sampled Data Controllers**

The frequency response of linear feedback control systems, such as that in Fig. 1, is a well defined and frequently used measure. As is well established, the

output of a linear system excited by a sinusoidal input is a sinusoid of the same frequency but (possibly) different magnitude and phase. The frequency response is then a measure of the amplitude and phase of the output signal divided by that of the input signal. In this paper I am concerned in particular with the disturbance rejection properties of the feedback control system. In particular, the goal is to design strong attenuation, in amplitude, of sinusoidal plant disturbances by the closed loop control system. This is in contrast to *white noise* disturbances used in the selection of weighting matrices for the LQR/LQG design process. Normally, this task involves designing transmission zeros into the controller to result in exactly zero response at the disturbance frequencies.

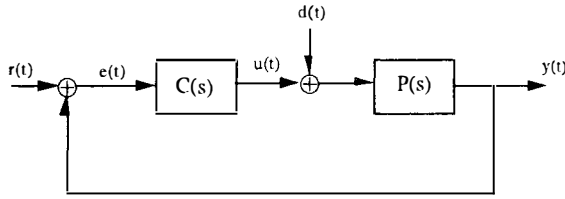


**Fig. 1: Basic Feedback System**

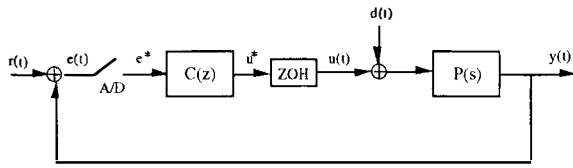


**Fig. 2: Sampled Data Feedback System**

A discussion of the frequency response of the sampled data controller (SDC) in Fig. 2 is more problematic. I will review in this section the fact that the SDC system is non-linear. As a result, sinusoidal input disturbances produce output signals not only at the input frequency, but numerous harmonics shifted by multiples of the sampling frequency, commonly referred to as intersample ripple. This raises the question, what does the expression "frequency response" mean in a sampled data control system? Not only does the control system produce output harmonics, but superposition no longer holds. In the strictest sense, the effects of plant disturbances and reference inputs cannot be considered separately with the output summed at the end. Rather, when considered together, intermodulation frequencies may appear in the output, further complicating the task of characterizing response.

These observations complicate the issue of evaluating, in analysis, the efficacy of any controller design for disturbance rejection. In most applications, the system is considered in the discrete domain and the frequency response is examined, up to the Nyquist frequency, for discrete inputs. That is, the system is modeled as linear via approximations of the input. This approach, however, ignores the effects of the disturbance during the sampling interval and any intersample ripple in the output. Though normally quite small, with the need for ultra-precise con-

trollers their consideration can become more important.

In the remainder of this section, I will present the necessary equations for describing the output of the SDC when excited by sinusoidal plant disturbances. These expressions will prove useful when designing digital control systems for disturbance rejection in section 3.

## 2.1 Continuous Input/Output Property

The Laplace transform equation for the response of the feedback system in Fig. 2 can be found using simple block diagram algebra and the modeling of the sampler by impulse modulation [Franklin and Powell, 1990]. The Fourier Transform of  $y(t)$  is:

$$Y(j\omega) + [I + L(j\omega)]^{-1} L(j\omega) \sum_{n=0} Y(j\omega - jn\omega_s) \\ = [I + L(j\omega)]^{-1} P(j\omega) D(j\omega) \quad (1)$$

where  $\omega_s = 2\pi/T$  is the sampling frequency in rad/sec,

$$L(j\omega) = e^{-j\omega T/2} \text{sinc}(\omega T/2) P(j\omega) C(e^{j\omega T}), \quad (2)$$

and  $P(j\omega)$  and  $D(j\omega)$  are the Fourier transforms of the plant and disturbance respectively.

Using equation (1) it is possible to examine the meaning of frequency response for sampled data controllers. For a cosine wave disturbance of frequency  $\omega_i$ ,  $D(j\omega)$  in equation (1) is replaced by  $0.5\delta(\omega - \omega_i) + 0.5\delta(\omega + \omega_i)$ . The Fourier transform of  $y(t)$  is then examined at the frequencies  $\omega = k\omega_s \pm \omega_i$  for all integer  $k$  ( $Y(j\omega)$  is zero at all other frequencies). Equation (1) thus becomes:

$$Y(kj\omega_s \pm j\omega_i) + [I + L]^{-1} L \sum_{n=0} Y((k-n)j\omega_s \pm j\omega_i) = \\ [I + L]^{-1} P(kj\omega_s \pm j\omega_i) \delta(jk\omega_s), \quad (3)$$

where  $L$  refers to the quantity:

$$L = L(kj\omega_s \pm j\omega_i)$$

It is very difficult to find a closed form solution to equation (3) for all  $k$ , even numerically. However, it is possible, qualitatively, to determine the character of the solution. The output signal,  $y(t)$ , contains most of its information in the fundamental frequency,  $\omega_i$ , but it also has frequency content at all harmonics shifted by the sampling frequency. The Fourier transform, therefore, is a string of delta functions of decreasing magnitude (see Fig. 3). This is not surprising, as the non-linear element of the sampled data control system of Fig. 2 is the zero-order hold, which produces a periodic output at the fundamental frequency in addition to harmonics at multiples of the sampling frequency.

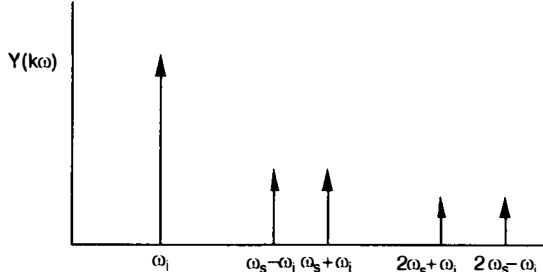


**Fig. 3: Response of  $Y(j\omega)$  to Sinusoidal Disturbance at  $\omega_i$**

## 2.2 Discrete Frequency Response

Despite the caveats above, it is convenient, and quite common to design digital control systems using frequency response techniques. These methods simply apply a new definition of the frequency response. That is, the discrete frequency response is the amplitude (and phase) of the *component* in the output at the same frequency as the input divided by the amplitude of the input.<sup>1</sup> Because the magnitudes of the higher order harmonics are so much smaller than that of the fundamental, the response of sampled data controllers can be evaluated using this definition by examining frequencies only up to the Nyquist frequency with very little error.

A very common design technique, particularly for LQR/LQG state space design, is to map the plant and zero order hold to the digital domain and perform a direct discrete design. The resulting digital system is an exact description of the continuous one *at the sample instants* (or, equivalently, up to the Nyquist frequency).

In this section, a state space formalism is used to derive an exact formula for computing frequency response of the sampled data feedback system in Fig. 2 to sinusoidal disturbances,  $d(t) = d_0 e^{j\omega t}$ . Using the state space form of  $P(s)$ ,  $\{F, G, H, D\}$ , the digital state equations are:

$$\begin{aligned} x(t_k) &= \Phi x(t_{k-1}) \\ &+ \Phi \int_0^T e^{-F\tau} G [u(\tau + t_{k-1}) + d_0 e^{j\omega(\tau+t_{k-1})}] d\tau \end{aligned} \quad (4)$$

where  $\Phi = e^{FT}$ . Since the control  $u$  is a zero-order hold over the sampling interval, this equation becomes:

$$x_k = \Phi x_{k-1} + \Gamma u_{k-1} + \Lambda d_{k-1} \quad (5)$$

where,

$$\Gamma = [\Phi - I] F^{-1} G \quad (6)$$

(Stengel, 1986)

and,

---

<sup>1</sup>This is equivalent to Describing Function analysis in non-linear systems.

$$\Lambda(\omega) = \Phi \int_0^T e^{-F\tau} G e^{j\omega\tau} d\tau \quad (7)$$

The conventional method of computing the frequency response for a digital feedback system up to the Nyquist frequency is to use  $\Gamma$  from equation (6), which is independent of frequency, as the input matrix (that is, approximate the disturbances with a zero-order hold).

However, equations (4) to (7) show that the correct frequency response of the sampled data feedback system uses  $\Lambda(\omega)$  as the input matrix. Note the significant difference –  $\Lambda(\omega)$  is a function of frequency and thus the integral in (7) must be solved separately for each frequency point. The frequency response is given by:

$$P(j\omega) = H [e^{j\omega T} I - \Phi]^{-1} \Lambda(\omega) \quad (8)$$

and is not periodic.

The integral in equation (7) can be solved exactly to yield the formula for  $\Lambda(\omega)$ :

$$\Lambda(\omega) = \Phi [e^{j\omega T - FT} - I] (j\omega I - F)^{-1} G \quad (9)$$

The formula for  $\Lambda(\omega)$  in equation (9) can be computed very easily with any of the common control software packages, as there are many convenient algorithms for computing the matrix exponential. Thus, the exact discrete frequency response from disturbances can be computed up to the Nyquist frequency.

Fig. 4 presents a standard block diagram for this digital control system. The plant,  $P(z)$ , has the usual discrete frequency response from control but uses equation (8) for that from disturbances.

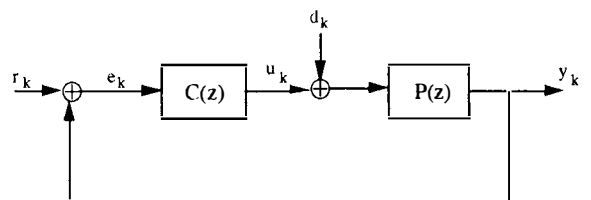


**Fig. 4: Discrete Feedback System**

## 3. Continuous LQR/LQG Controller with Disturbance Rejection

I now turn to the main task, designing a feedback controller using LQR/LQG methods that results in a closed loop response from disturbances with zeros at discrete disturbance frequencies. Before embarking on the sampled data design, it is helpful to review the standard method for continuous, multivariable systems (Franklin, Powell, and Emami-Naeini, 1986; Stengel, 1986; Kasdin, 1991).

Because the feedback system in Fig. 1 is well-posed and minimal, the plant can be represented by a mini-

mal order linear system,  $\{F, G, H, D\}$ . The full state feedback LQR controller is then found by minimizing the usual cost function with weights A and B to find the feedback gain matrix K by solving an algebraic Riccati equation.

The closed loop notches at the disturbance frequencies are produced via the method of bias estimation (*Franklin and Powell, 1990*). That is, the estimator model is augmented with a model of the disturbances. These disturbance estimates are then feed-forward in the control. Let the disturbances be modeled by:

$$\begin{aligned}\dot{\xi} &= F_\xi \xi + G_\xi w_\xi \\ d &= H_\xi \xi\end{aligned}\quad (10)$$

where  $\xi \in \mathbf{R}^{2m}$ ,  $w_\xi \in \mathbf{R}^{2m}$ , and  $d \in \mathbf{R}^m$ . If all the disturbances are pure sinusoids, then the eigenvalues of  $F\xi$  are:

$$\text{eig}\{F_\xi\} = \{\pm j\omega_1, \pm j\omega_2, \dots, \pm j\omega_m\}$$

These are the frequencies of the m sinusoidal disturbances. The estimator is augmented with this model for the full estimator equation:

$$\begin{bmatrix} \dot{\hat{x}} \\ \dot{\xi} \end{bmatrix} = \begin{bmatrix} F & GH_\xi \\ 0 & F_\xi \end{bmatrix} \begin{bmatrix} \hat{x} \\ \xi \end{bmatrix} + \begin{bmatrix} G \\ 0 \end{bmatrix} u + L(y - H\hat{x}) \quad (11)$$

where the steady state Kalman filter estimator gains, L, are partitioned:

$$L = \begin{bmatrix} L_x \\ L_\xi \end{bmatrix}$$

Note that for a steady state solution to exist, some finite process noise on the disturbance model ( $w_\xi$ ) must be used. Varying this parameter results in variations in the width (Q factor) of the eventual notch in the closed loop response.

With this estimator scheme the separation principle is used to compute the control as a full state feedback of the state estimates with feedforward of the disturbance estimates:

$$u = -K\hat{x} - H_\xi \hat{\xi} \quad (12)$$

The final compensator is then found by combining the full state feedback and estimator:

$$C(s) = [K \quad H_\xi] \begin{bmatrix} sI - F + GK + L_x H & 0 \\ -L_\xi H & sI - F_\xi \end{bmatrix}^{-1} \begin{bmatrix} L_x \\ L_\xi \end{bmatrix} \quad (13)$$

This compensator, C(s), is used in the feedback system. It can easily be shown that this feedback system exactly cancels the disturbance frequencies. That is, there are transmission zeroes in the closed

loop transfer matrix at the discrete disturbance frequencies. For brevity, the proof of this fact is omitted (see *Kasdin, 1991*).

The key to the success of this design procedure was the matching of the input matrix G from disturbances in the plant estimator model and the control to cancel the disturbance input. This left the zero in the upper right block of the compensator matrix in equation (13). This zero block guarantees that the compensator has poles at the disturbance frequencies and thus zeros in the closed loop response.

#### 4. Discrete LQR/LQG Design for Disturbance Rejection

The previous section described a method for designing a continuous controller with disturbance estimation to exactly cancel the poles of the disturbances in the closed loop. In this part I present how to achieve equivalent response in the sampled data feedback system. One approach would be to simply map the continuous compensator C(s) using one of the standard methods, such as bilinear transform or pole-zero mapping (*Franklin and Powell, 1990*). However, here I am examining only the direct design method using discrete LQR/LQG theory.

The first step is to find the discrete equivalent of the plant to a zero-order hold control input as in section 2.2. As before, the result is the discrete feedback system in Fig. 4, where P(z) is given by the discrete state space system  $\{\Phi, \Gamma, H, D\}$ .

Note that the response of the feedback system in Fig. 4 to reference input  $r_k$  is exactly that of the sampled data system in Fig. 2 at the sample instants. As discussed earlier, the response to disturbances is more problematic, as  $d(t)$  is not a zero-order hold but acts continuously on P during the sample interval. Its response is given by equation (3) or, evaluated only at the sampling instants and ignoring intersample ripple, by equation (8).

The LQR/LQG design process then follows as usual. First, the discrete full state feedback gains (LQR) are found by minimization of a discrete cost function for control  $u_k = -K_d x_k$ . The weighting matrices can be picked *a priori* or as a mapping of the continuous ones (*Stengel, 1986; Van Loen, 1978*).

Selection of the estimator system is more subtle. The traditional method is to map the continuous augmented system to digital (*Franklin and Powell, 1990*). This accounts exactly for the action of each sinusoidal disturbance during the sample interval. At first glance this would appear to be the superior approach since it best models the dynamics of the problem. However, as will be shown, this does not produce the desired notch compensation.

##### **4.1 Traditional Method**

Mapping the continuous, augmented estimator model to the discrete domain results in the partitioned estimator model:

$$\begin{bmatrix} \hat{x} \\ \hat{\xi} \end{bmatrix}_{k+1} = \begin{bmatrix} \Phi & \Gamma_\xi \\ 0 & \Phi_\xi \end{bmatrix} \begin{bmatrix} \hat{x} \\ \hat{\xi} \end{bmatrix}_k + \begin{bmatrix} \Gamma \\ 0 \end{bmatrix} u_k + L(y_k - H\hat{x}_k) \quad (14)$$

where  $L$  is found from the usual steady state predicting estimator (Kalman filter) equations and is partitioned as before (*Bryson and Ho, 1975; Stengel, 1986; Franklin and Powell, 1990*).

The control is again given by:

$$u_k = -K\hat{x}_k - H_\xi \hat{\xi}_k \quad (15)$$

The final compensator then becomes:

$$C(z) = \begin{bmatrix} K_\alpha & H_\xi \end{bmatrix} \begin{bmatrix} zI - \Phi + \Gamma K_\alpha + L_\alpha H & -\Gamma_\xi + \Gamma H_\xi \\ -L_\xi H & zI - \Phi_\xi \end{bmatrix}^{-1} \begin{bmatrix} L_\alpha \\ L_\xi \end{bmatrix} \quad (16)$$

Observe that the upper right block is not zero here. This results in a compensator without poles at the discrete disturbance frequencies  $\{e^{\pm j\omega_1}, e^{\pm j\omega_2}, \dots, e^{\pm j\omega_m}\}$ . As a result, the closed loop system does not have transmission zeros at these frequencies and thus does not guarantee rejection (*Kasdin, 1991*).

## 4.2 More Accurate Technique

The alternative design is to map the plant and disturbance models to digital separately. This results in the same plant model as in equation (14) but a digital disturbance model:

$$\begin{aligned} \xi_{k+1} &= \Phi_\xi \xi_k + \Gamma_\xi w_k \\ d_k &= H_\xi \xi_k \end{aligned} \quad (17)$$

where  $\Phi_\xi = e^{F_\xi T}$ ,  $\Gamma_\xi = [\Phi_\xi - I] F_\xi^{-1} G_\xi$ , and  $T$  is the sample frequency.

In other words, the disturbances are modeled with a zero-order hold fit rather than considering the integrated effect on the plant. Thus, the predicting estimator model is:

$$\begin{bmatrix} \hat{x} \\ \hat{\xi} \end{bmatrix}_{k+1} = \begin{bmatrix} \Phi & \Gamma H_\xi \\ 0 & \Phi_\xi \end{bmatrix} \begin{bmatrix} \hat{x} \\ \hat{\xi} \end{bmatrix}_k + \begin{bmatrix} \Gamma \\ 0 \end{bmatrix} u_k + L(y_k - H\hat{x}_k) \quad (18)$$

with the same control as before.

The compensator now becomes:

$$C(z) = \begin{bmatrix} K_\alpha & H_\xi \end{bmatrix} \begin{bmatrix} zI - \Phi + \Gamma K_\alpha + L_\alpha H & 0 \\ -L_\xi H & zI - \Phi_\xi \end{bmatrix}^{-1} \begin{bmatrix} L_\alpha \\ L_\xi \end{bmatrix} \quad (19)$$

In this method, the zero in the upper right block has been retrieved, thus guaranteeing eigenvalues at the disturbance frequencies and thereby perfect rejection.

It seems somewhat counter-intuitive that the disturbance model in the alternative design, a zero-order

hold fit, produces better rejection than that in the traditional method. Mapping the entire augmented estimator would seem to produce a better model of the process. The explanation, however, is not hard to understand. In the digital feedback system the control is a zero-order hold. It is therefore impossible, in the discrete formulation, for this control to cancel exactly anything but a zero-order hold disturbance. When the disturbance is modeled as a step input like the control, it is a simple matter to design a compensator that exactly cancels it.

This raises the obvious question: Does this compensation also result in exact cancellation of the disturbances in the sampled data feedback system, where their true form is considered rather than the zero-order hold approximation? The answer is yes and is stated formally in Theorem 1, the main result of this work:

### Theorem 1:

Let  $P(s)$  be the strictly proper, minimal plant with state space system  $\{F, G, H, D\}$ . Let  $d(t)$  be the sum of  $m$  sinusoidal plant disturbances at discrete frequencies  $\{\omega_1, \omega_2, \dots, \omega_m\}$ . Let  $C(z)$  be the stabilizing compensator in equation (19) including disturbance estimation. Then the sampled data closed loop feedback system from disturbances with the transcendental frequency response given by equation (1) has zero transmission at the discrete disturbance frequencies  $\{\pm j\omega_1, \pm j\omega_2, \dots, \pm j\omega_m\}$ .

### Proof

The compensator in equation (1),  $C(e^{j\omega T})$ , can be factored:

$$C(e^{j\omega T}) = \frac{N(e^{j\omega T})}{d(e^{j\omega T})} \quad (20)$$

where the denominator,  $d(e^{j\omega T})$ , has roots at the controller poles and at the disturbance frequencies  $\{\pm j\omega_1, \pm j\omega_2, \dots, \pm j\omega_m\}$  (eigenvalues of the inner matrix in equation (19)). Thus, the quantity  $[I + L(j\omega)]^{-1} P(j\omega)$  in equation (1) can be rewritten:

$$d(e^{j\omega T}) \left[ \frac{d(e^{j\omega T})I +}{e^{-j\omega T/2} \operatorname{sinc}(\frac{\omega T}{2})P(j\omega)N(e^{j\omega T})} \right]^{-1} P(j\omega) \quad (21)$$

Since  $d(e^{j\omega_i T}) = 0$ , substitution of equation (21) into equation (3) at the disturbance frequencies results in:

$$Y(kj\omega_s \pm j\omega_i) = 0 \quad \forall k \quad (22)$$

done

Not only has the alternative design resulted in complete rejection of the disturbances, it also guarantees zero response at all harmonics of the disturbances shifted by multiples of the sampling frequency. Again, the key point is the zero block in the upper right hand corner of the transfer matrix in equation (19). This ensures that the eigenvalues (poles) are equal to the poles of the two diagonal block sub-

matrices. This is in contrast to the traditional design method, where the compensator in equation (16) has a full inner matrix and thus all poles have been moved.

## **5. Example**

Consider the attitude control of a 3-axis stabilized spacecraft. In any one axis, the control system is a simple SISO feedback loop with a  $1/s^2$  plant. The spacecraft is torqued due to aerodynamic drag, producing a fixed sinusoidal disturbance at the orbit frequency,  $n$ . The state space models for the spacecraft and disturbance are:

Plant:

$$\begin{bmatrix} \dot{x}_1 \\ \dot{x}_2 \end{bmatrix} = \begin{bmatrix} 0 & 1 \\ 0 & 0 \end{bmatrix} \begin{bmatrix} x_1 \\ x_2 \end{bmatrix} + \begin{bmatrix} 0 \\ 1 \end{bmatrix} (u + d) \quad (23)$$

$$y = [1 \ 0] \begin{bmatrix} x_1 \\ x_2 \end{bmatrix}$$

Disturbance:

$$\begin{bmatrix} \dot{\xi}_1 \\ \dot{\xi}_2 \end{bmatrix} = \begin{bmatrix} 0 & 1 \\ -n^2 & 0 \end{bmatrix} \begin{bmatrix} \xi_1 \\ \xi_2 \end{bmatrix} + \begin{bmatrix} 0 \\ 1 \end{bmatrix} w_d \quad (24)$$

$$d = [1 \ 0] \begin{bmatrix} \xi_1 \\ \xi_2 \end{bmatrix}$$

For clarity in the result, the disturbance frequency,  $n$ , was chosen at the somewhat high frequency, 0.05 Hz. The continuous LQR weighting matrices were  $A=\text{diag}(1 \ 0)$ ,  $B=1/4$ . These were mapped to digital using the Van Loen algorithm for discrete full state feedback gain selection. A sample rate of 10 Hz was used. The discrete sensor noise covariance,  $R_d$ , was 5 and the continuous process noise was 1. The process noise covariance for the digital model of the disturbance was 10 in each channel (again, this adjusts the width of the notch).

A compensator was designed for this system using each of the design methods with disturbance modeling described above. A Runge-Kutta simulation was performed of the closed loop sampled data system for each design. The result is shown in Fig. 5. Note that while the traditional design has a residual oscillation in the steady state due to the disturbance, the more accurate method has completely rejected it.

## **6. Conclusions**

This paper studied the closed loop control of a sampled data feedback system subject to sinusoidal disturbances at a discrete set of frequencies. The meaning of the frequency response in such a nonlinear system was discussed and a new method was presented for computing the digital frequency response from disturbances to output of a continuous plant in a sampled data feedback system.

With these results, the traditional method of performing direct digital LQR/LQG design for distur-

bance rejection was analyzed. It was shown that mapping the augmented continuous system and performing a full state feedback/estimator design did not result in the desired system, i.e., one with zeros at the disturbance frequencies. It was then proven that an alternative approach that maps the disturbances to the discrete domain separately followed by the LQR/LQG design does result in perfect rejection.

A simple SISO example was used to verify this effect. The method was also used in the design of a pointing controller for the Gravity Probe B spacecraft. This is discussed in the oral presentation.

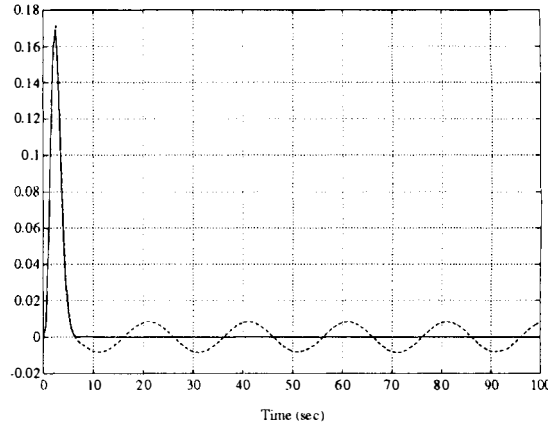


**Fig. 5: Closed Loop Simulation of Sampled Data Control System with Unit Sinusoidal Disturbance  
solid = Accurate Design, dashed = Traditional**

## **7. Acknowledgments**

This work was performed under NASA Grant NAS8-36125.

## **8. References**

- Bryson, A.E. and Y.C. Ho (1975), *Applied Optimal Control*. Hemisphere Publishing Corp., New York.
- Franklin, G.F., J.D. Powell, and A. Emami-Naeini (1986), *Feedback Control of Dynamic Systems*. Addison-Wesley Publishing Co., Reading, MA.
- Franklin, G.F., J.D. Powell, and M.L. Workman (1990), *Digital Control of Dynamic Systems*. Addison-Wesley Publishing Co., Reading, MA.
- Hirate, Hidetoshi (1989), Sample Rate Effects on Disturbance Rejection for Digital Control Systems. Ph.D. Dissertation, Stanford University, SUDAAR No. 587.
- Kasdin, N. Jeremy (1991), Precision Pointing Control of the Spinning Gravity Probe B Spacecraft. Ph.D. Dissertation, Stanford University, SUDAAR No. 606.
- Stengel, R.F. (1986), *Stochastic Optimal Control*. John Wiley & Sons, New York.
- Van Loen, C.F. (1978). Computing Integrals Involving the Matrix Exponential, *IEEE Transactions on Automatic Control*, Vol. AC-23, No. 3.

## A REVIEW OF CHINESE SPACECRAFT CONTROL

Yang Jiachi\*, Zhou Guangrui\*\* and Lu Zhendou\*\*

\*Chinese Academy of Space Technology (CAST), P.O. Box 2714, 100081 Beijing, PRC

\*\*Beijing Institute of Control Engineering (BICE), P.O. Box 2729, 100080 Beijing, PRC

**ABSTRACT:** This paper outlines the development of Chinese spacecraft control system. In order to meet the need of national economy construction, four series of spacecraft, such as scientific test satellite, recoverable earth observation satellite, meteorological satellite and geostationary communication satellite, have been developed in CAST. Correspondingly various spacecraft control system have been developed in BICE, and some of them have been applied successfully to the launched spacecrafsts, others are at developing stage. This paper also introduces the characteristic and development direction of Chinese spacecraft control system.

**KEYWORDS:** Recoverable satellite control; Sun-synchronous satellite control; Characteristic of Chinese spacecraft control system

### PREFACE

Since the first artificial satellite was launched in the world, China launched successfully her first satellite "DFH-1" 13 years later. After developing and launching test satellite for several years, China began to develop application satellite around about 1970. Four series of spacecraft, such as scientific test satellite, recoverable earth observation satellite, meteorological satellite and synchronous communication satellite, have been developed. The satellite application technology has become one component of China national economy construction [1].

Although the variety and quantity of satellite launched in China are limited, we have made progress for the development of space technology. To meet the need of the development we have done advance research and study in many subject, such as spacecraft with flexible structure, on-board fault-tolerance control computer, real-time

spacecraft attitude determination system [2], on-line fault diagnosis expert system of attitude control system [3] and space robotics. Some techniques above-mentioned have been applied in spacecraft development. During the past decades, we have developed control system of medium and low altitude orbits and geostationary orbit. According to control modes, control system is classified to spin and dual-spin stabilized satellite control system, three-axes stabilized satellite control system and gravity gradient stabilized satellite control system. Except for the gravity gradient control satellite, the other kinds of control systems have been brought into actual space mission.

The control system of satellites, which had been launched or to be launched, are presented respectively as following.

### SPACECRAFT CONTROL IN MEDIUM AND LOW ALTITUDE ORBIT

### (1) Recoverable Satellite Control

The three-axes stabilized attitude control system is applied in China recoverable earth observation satellite. And the analog controller was adopted in the first generation recoverable satellite, its accuracy was as follows:

Pitch and roll error	< 1 deg.
Yaw error	< 2 deg.
Rate error	< 0.02 deg/s

To meet the user's higher demands, the control accuracy has been greatly raised by using digital controller (on-board computer) instead of analog controller, and particularly using digital fine sun sensor for yaw axis.

The attitude sensors used in the system are as follows:

1. Two scanning infrared horizon sensors, one for roll and other for pitch. The scanning frequency is 1 Hz. The measuring error is about 1 deg.

2. Two digital fine Sun sensors. Each of them has field of view  $120^\circ \times 128^\circ$ . The measuring error is about 0.05 deg. The usage of Sun sensors is mainly to improve yaw attitude determination accuracy. The installation geometry schematic is shown in Fig. 1 where  $ox, oy$  and  $oz$  are the axes of body coordinate frame,  $\ell$  is the entrance slit.

3. Three single degree-of-freedom rate integrating gyros. Their input axes are parallel to body axes, respectively. The magnitude of constant drift is about one degree per hour. The random drift is less than 0.3 deg/hour.

The actuator of the control system is a cold gas jet system. The control angular acceleration produced by a single thruster is 0.1 deg/s<sup>2</sup> for roll and yaw axes. However, for pitch axis, it is 0.6 deg/s<sup>2</sup> which is required for attitude maneuvering.

The on-board digital microcomputer employed greatly enhances the ability and the flexibility of processing information. The length of word is 16 bits and the storage includes ROM 6k words and RAM 2k words. The sampling period (computation

period) is 1.04 second. In this time period the computer collects the data obtained from attitude sensors, processes them and generates command of jet pulse if it is necessary. Since the computation of orbit and Sun direction which is required for measurement updating filter using Sun sensor signals is rather complicated, the computation period of measurement updating using Sun sensor signals is longer. It is about 5 seconds. Through telecommand channel the computer receives the orbital elements transmitted by ground station once a day in order to renew the orbital dynamical model used on-board.

The mathematical simulation of the system demonstrates that it has excellent performance to meet the design specification. The accuracy of attitude determination is within 0.1 deg and that of control is within 0.2 deg. The digital control system performed successfully in flights. In the light of telemetry data the requirements for control system were met. In general, the angular rate is below 0.003 deg/s. The amount of gas consumption in all orbit operation periods of eight days is about 2.5 kg which is a value approximate to that given by mathematical simulation. The attitude determination filter worked stably. The attitude determination accuracy was verified by a star mapper on board the satellite (Fig. 2).

In order to enhance reliability and adaptability, all-attitude recapture capability was implemented in new developed satellite. In some fault case the attitude datum of control system had been lost, it can be re-set up by ground command so as to recover the satellite to normal operation.

Up to 1990, China had launched 11 recoverable satellites, and each satellite capsule was exactly returned to a predetermined land area.

### (2) Sun-synchronous Satellite Control

China had launched successfully two three-axis stabilized Sun-synchronous meteorology satellites in 1988 and 1990. These satellite's pointing accuracy is within 1 deg., attitude rate accuracy

within 0.06 deg/s. Two scanning infrared earth sensors are used for getting pitch and roll information, two single degree-of-freedom banked gyros (installed at 30 deg. apart from roll-pitch plane) are used for getting yaw information with redundancy. In addition, gyros at roll axis are used for earth capture. The central controller is on-board computer, the actuator is three reaction-wheels. Six cold gas jets are used to provide control torques for acquisition and to desaturate the flywheel[6](Fig.3). The first satellite lost its efficacy after 39 days of normal operation. In order to enhance reliability, biased momentum wheel, on-board control computer and magnetic moment unit are adopted as spare parts, meanwhile static infrared earth sensors are used as spare of scanning infrared earth sensor.

The three-axis stabilized Sun-synchronous Earth Resources Satellite developed in cooperation with Brazil is to be developed. In this satellite, on-board computer, reaction wheels and magnetic controller are installed, so that control accuracy, especially transient attitude stabilized accuracy have been greatly improved.

Flight test results are as follows:

A. Attitude Determination Accuracy

- Transfer orbit phase 0.2 ~ 0.3 deg.;
- Drift orbit phase 0.1 ~ 0.2 deg.;
- Synchronous orbit phase 0.04 ~ 0.043 deg.;

B. Attitude Control Accuracy

- Transfer orbit phase 0.24 ~ 0.34 deg.;
- Drift orbit phase 0.17 ~ 0.24 deg.;
- Synchronous orbit phase 0.09 ~ 0.14 deg.;

C. Despin control accuracy < 0.03 deg.

Antenna pointing accuracy < 0.02 deg.

The satellite-ground loop control mode is adopted to this kind of satellite control system. Since 1988 this kind of satellite has been improved to applied communication satellite with four transponders and national beam antenna. And attitude maintain accuracy has been enhanced by improving the measure-control software to meet the user's demands [10]. By the end of 1990, China had successfully launched three second-generation communication satellites, and the first satellite's flying lifetime has been beyond the design lifetime.

### GEOSTATIONARY SATELLITE CONTROL [7]

#### (1) Development of Dual-spin Geostationary Satellite Control System

The first China geostationary experiment communication satellite STW-1 was successfully launched on April 8, 1984 [8]. Later in order to meet user's demands, Similar dual-spin satellites were launched, but antenna with national beam coverage was adopted instead of international wave. These satellites are the oblate ones with  $I_z/I_x > 1.0$ . Besides common components similar to ones used in international dual-spin satellite, an adaptive observer is adopted to process data from infrared earth sensor so as to enhance despin-lock direction accuracy. And it can make satellite run normally and lose little accuracy within the range from several to dozens thousands kilometer high. So the whole spin system may be regarded as one adaptive control system [9].

The meteorological satellite FY-2, which is to be launched, is a prolate satellite( its  $I_z/I_x < 1.0$ ) in transition orbit phase, so active nutation control is used ( shown in Fig 4.). In order to enhance the control accuracy and attitude determination accuracy, a liquid nutation damper made by Fokker, Holland and the dynamic balance mechanism self-developed are adopted in synchronous orbit phase.

#### (2) Development of Three-axes Stabilized Communication Satellite Control System

The three-axes control system used in medium and low orbit satellite had been well developed in BICE long time ago. To meet the demand of hi-capacity communication and broadcast satellite, now the three-axes stabilized satellite control system for synchronous orbit is being developed (Fig.5). The characteristics of this satellite

is as follows:

- Three-axes stabilized technique is adopted on all orbit phases including transfer phase;
- Solar panel and antenna are deployed once before ignition of apogee-motor;
- Bipropellant unified propulsion system is used.

Because the sloshing frequency of liquid in tank overlays the control system bandwidth during the ignition of apogee-engine, and the base-frequency of the solar panel is low and close to the bandwidth frequency, it is very difficult to meet both control stability and precision requirement in designing. By the cooperation of BICE and MBB, the controller used in this kind of control system has already been designed, and the practicability of the design has been verified and evaluated by mathematical simulation.

In orbit control design, apogee orbital transfer has been arranged into three steps ,and the design of ignition orbit phase has been optimized.

Meanwhile safety operating mode is also designed in control system.

#### CHARACTERISTICS OF CHINESE SPACECRAFT CONTROL SYSTEM DEVELOPMENT

##### (1). Control system being integrally developed

The development of Chinese spacecraft control system includes three fields:

The first field--research of control plant feature (Dynamics). It includes spacecraft structure, accessory flexibility dynamics, fuel-tank and liquid sloshing dynamics, multi-body dynamics, etc. In accordance with the feature of developing spacecraft, we have gradually formed a set of computer software .

The second field--research of control system(including sensors, controller and actuator), and research of control theory and simulation tech-

nology. These research purpose is to realize attitude and orbit determination, attitude and orbit control, program control,etc.

The third field -- research of measurement and control software and analysis of control system flight test results. By analyzing these results, the control system and measurement and control software can be improved.

##### (2) Propulsion system being wholly considered

We often regard propulsion system as an actuator in whole control system ( Normally it is divided into propulsion system and momentum exchange system). Thus although the complexity of control system is increased, it takes advantage of integral and optimal design and fault detection strategy.

##### (3) Reliability being highly stressed

From the beginning of prototype phase, reliability has been put in the first place, so system reliability redundancy design has been adopted. The feasible methods of reliability measure, system fault mode and effect analysis are put forward to satisfy the reliability performance requirement. During the period of control system technique implementation, the system reliability will be estimated and the design scheme be evaluated in stages. In order to maintain high reliability in control system, the component and raw material must be selected seriously and their quality must be confirmed strictly. According to the level of domestic electronic component, the component parts are sieved and aged. And the element and entire system composed by these components also must be assessed in operational environment. As a result, the performance of the control system which we developed has attained or exceeded the anticipated performance requirement.

#### CONCLUSION

With the development of Chinese space technology, spacecraft control technique , known as engi-

neering science, is advanced too. Now we are doing further research of spacecraft intelligent control technology, the guidance and navigation technique for spacecraft rendezvous and the application of adaptive control technique in spacecraft control system, etc [1].

In recent years, We have wide technological contact and cooperation with many countries. Here we express heartfelt thanks and we are looking forwards to more cooperation in the future.

#### REFERENCE

- [1] Zhou Guangrui "The Present and Development of Control Theory and Application of Space Technology in China" Aerospace Control, No. 4, 1990. (in Chinese)
- [2] Qiu Gang "Spacecraft Attitude Real-Time Determination System Based On Multiprocessor Distributed Architecture" 10th World Congress On Automatic Control, Germany July 27-31, 1987.
- [3] Wang Nanhua, et. al. "Real-time Diagnosis Expert System for Satellite Control system (SCRDES)" , Control Engineering No.6 ,1991. (in Chinese)
- [4] Yang Jiachi, Zhang Guofu and Sun Chenqi "Three-Axes stabilized Attitude Control System for Chinese Near Earth Orbit Satellite" VIII IFAC Symposium on Automatic Control in Space Oxford, UK July 2-6, 1979.
- [5] Chen Yiqing, et. al. "Digital Attitude Determination and Control System of Chinese Recoverable Satellite for Scientific Exploration and Technical Experiments" PISSTA, Nov. 6-8, 1989, Los Angals California, U.S.A. Vol.73, Advance in the Astronautical Science, A.A.S Publication
- [6] Wang Mihui "Attitude Control System of Polar-Orbit Meteorological Satellite" 10th IFAC Symposium Toulouse, FRANCE June 25-28, 1985.
- [7] Lu Zhendou "Two kinds Control mode of Synchronous Communication and Broadcast Satellite" China Space Technology, No.1 ,1990 (in Chinese)
- [8] Tu Shanchen,et. al. "Control System of The Chinese Geostationary Experimental Communication Satellite and Its Flight Results" 10th IFAC Symposium Toulouse, FRANCE Jun 25-28, 1985.
- [9] Zhou Guangrui and Yu Jiachun "The Adaptive observing Processor of earth acquisition message in Communication Satellite" Journal of Chinese Society of Astronautics No.2, 1989. (in Chinese)
- [10] Lu Zhendou, et. al. "Improvement in Attitude and Orbit Control Software for Chinese STW-2 Satellite" Proceeding of The Pacific Basin International Symposium On Advances in Space Science Technology and Its Application, Jun 7-10, 1987, Beijing, China.
- [11] Li Ye and Shao Hongqi "The Present and Future Chinese Communication Satellite" The Proceeding of 1991 Global Satellite Communication Symposium, May 28-31, 1991, Nanjing, China.
- [12] B.H Campbell and T.C. Coffey "Digital Attitude Reference System (DARS)" Navigation, Journal of the institute of Navigation, Vol.20, No.1, 1973.
- [13] H.Bittner, et. al. "The Attitude and Orbit Control Subsystem of the DFS Copernicus" 10th World Congress on Automatic Control Pre-prints, Vol.6, July 27-31, 1987 Munich, Germany.

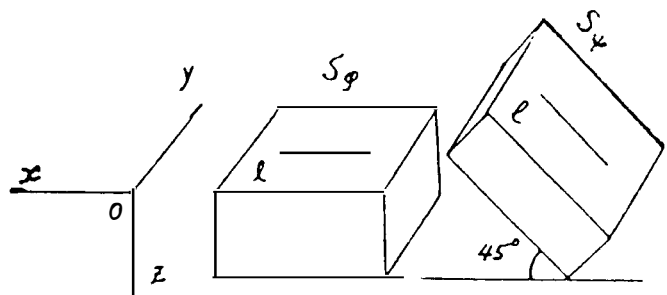


Fig.1 Installation Geometry of Sun Sensors

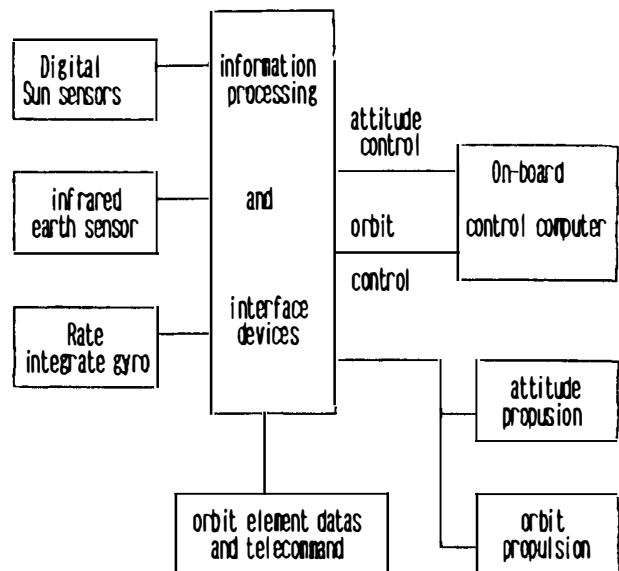


Fig.2 The principle block of The second generation recoverable satellite

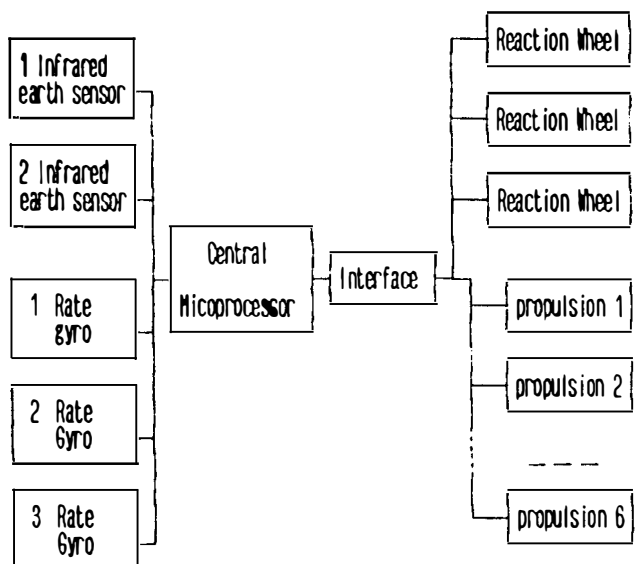


Fig.3 The Principle Block of meteorological satellite control system

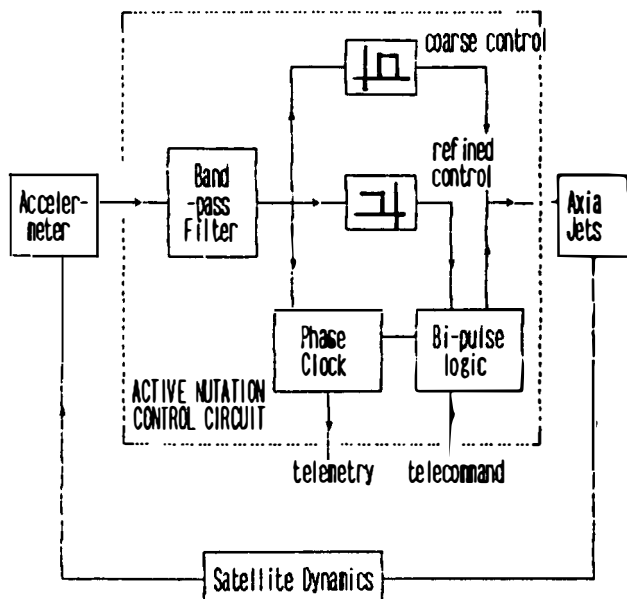
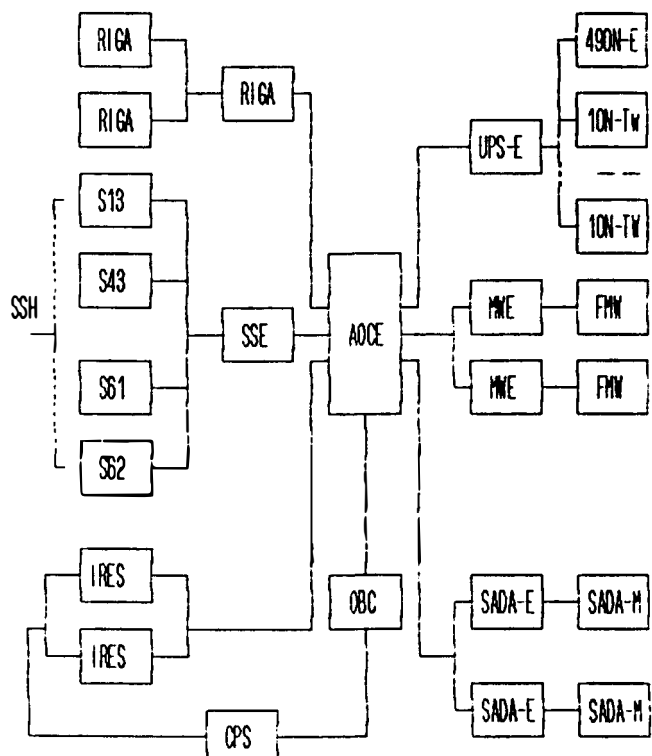


Fig.4 The structure Block of the active nutation control  
in the meteorological satellite FY-2



RIGA: Rate Integrating Gyro Assembly	CPS: Control Power Source
RIGE: Rate Integrating Gyro Electronics	UPS-E: LPS Electronics
SSH: Sun Sensor	90N-E: Apogee Motor
SSE: Sun Sensor Electronics	10N-TW: Thruster
IRES: Infrared Earth Sensor	MME: Momentum Wheel Elec.
AOCE: Attitude & Orbit Control Elec.	FMW: Fixed Momentum Wheel
OBC: On-Board Computer	SADA-E: SADA Electronics
	SADA-M: SADA Mechanism

Fig.5 The principle Block of new developed synchronous  
communication broadcast satellite control system

## ROBUST ATTITUDE CONTROL USING A CMG SYSTEM AND AN EXPERIMENT WITH A SIMULATION PLATFORM

A.Suzuki, H. Kurokawa and S. Kokaji

*Mechanical Engineering Laboratory, 1-2 Namiki, Tsukuba, Ibaraki, 305 Japan*

**Abstract.** A robust attitude control system was designed using exact linearization and robust model matching technique. High performance has been realized in rapid large angle rotation of a spacecraft under parameter uncertainty or changes. A pyramid type single gimbal CMG system was used as a control torquer. This CMG system has locally impassable singular points inside its working range. However, it was found that there is a global control method to avoid most of such points other than the neighborhood of the envelope. A platform which simulates a spacecraft's free rotation was constructed. Experimental results verified both control methods.

**keywords.** Linearization techniques, Robust control, Attitude control, CMG, Singularity avoidance, Steering law

### INTRODUCTION

For a future three axis attitude control of a spacecraft, rapid large angle rotation capability is required as well as high pointing accuracy. The local linearization method or Lyapunov function-based feedback can not be applied to such purpose. By the method of exact linearization (Isidori, 1985; Dwyer, 1984), a three axis attitude control system can be exactly linearized and linear control theory can be applied to get high accuracy even for rapid large angle rotation.

However, if there are modeling errors or parameter variation, the cancellation of nonlinear terms is no longer exact and the performance of the control system is not kept (Sastry, 1988). A spacecraft such as a space robot may have a modeling error and also change its moment of inertia largely as it moves. Thus robustness of the control system is important and several control methods have been proposed such as adaptive control and robust control. Robust model matching (RMM) is one of the design methods for a linear system with structured uncertainties (Eisaka, 1991). The RMM can assure arbitrarily low sensitivity to the structured uncertainty. Its advantage is that control response and its robustness are designed independently from each other. We applied the RMM to the linearized system of attitude control by exact linearization. The performance of the control system was evaluated by computer simulation and ground experiments.

Another important factor for large angle control is a powerful torquer. A single gimbal control moment gyro (CMG) system is one of the candidates. Among various system configurations, a four unit system of pyramid configuration is the most investigated. However, single gimbal CMG systems of no more than six units have locally impassable singular points other than the envelope of its working range (Kurokawa, 1988; Tokar, 1978). This implies that a usual gradient control for singularity avoidance may fail to avoid some of the singular points. However, there remains possibility that locally impassable singular states can be avoided with global control. Several researches (Kurokawa, 1985; Paradiso, 1990) aimed such global control. By further geometrical study after the previous studies (Kurokawa, 1988; Margulies 1978) and computer calculation of singular surface, we found that most of singular points other than those in the neighborhood of the envelope can be avoided by global control.

After developing robust control and singularity avoidance mainly by computer simulation, we carried out ground tests using a simulation platform. The experimental results verified the performance of the proposed robust control and the global CMG control.

In the next chapter, specification of the simulation platform is described. Also the attitude control using the pyramid type CMG system is briefly described. The following two chapters are for the robust control and the CMG singularity avoidance control with results of ground experiments.

## SIMULATION PLATFORM

A platform is constructed to simulate the motion of an artificial satellite under attitude control using a CMG system (Fig. 1). Its main frame is a truss structure made by iron pipes and bolt joints and this structure is so rigid that the center of the gravity hardly moves even when the attitude of the structure changes largely. The frame structure is suspended by a three axis gimbal mechanism using usual ball bearings. A usual ball bearing generates larger friction torque than an air bearing. However, a gimbal mechanism allows larger rotational angle than a spherical air bearing. The position of the center of the gravity is controlled using three balance adjusting mechanisms so that the gravitational torque can be ignored. The specification of the structure is shown in Table 1.

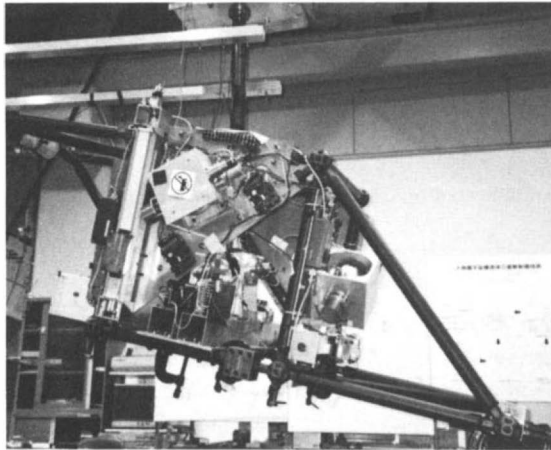


Fig. 1 Simulation platform

TABLE 1 Specification of the simulation platform

Attitude angle	Optical encoders	4 arcsec
	x & y axes : $\pm 30^\circ$ , z axis: $\infty$	
Angular velocity	Rate Gyros	0.1deg/sec
CMG gimbals angle	Optical encoders	0.005 deg
CMG	Flywheel speed	5000 rpm
	Angular momentum	5 Nms/unit
Controller	CPU(80386SX & 387SX, 16MHz)	
Platform	750x750x750mm, 240Kg	
	Inertia moment (33, 38, 43) Nms <sup>2</sup>	

The attitude controller has four single gimbal CMGs of pyramid configuration (Fig. 2), an onboard computer, three rotary encoders attached to the platform gimbal and three rate gyros. The specification is listed in Table 1. The block diagram of the attitude controller is shown in Fig. 3. The block of control law outputs desired torque for the attitude control and this is the input to the next block of steering law where rotation speed of the CMG gimbals are calculated.

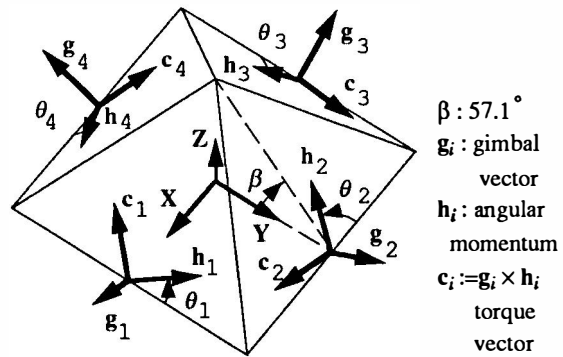


Fig. 2 Pyramid configuration

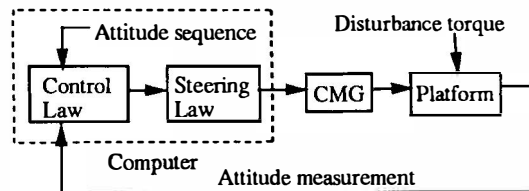


Fig. 3 Control block diagram

## ROBUST ATTITUDE CONTROL

In this section we describe robust attitude controller designed by exact linearization and robust model matching. In order to evaluate the robustness, we have carried out computer simulations and ground experiments.

### State Equations

An attitude of a rigid body is represented in several ways. We use the Euler quaternion  $\beta = [\beta_0, \beta_1, \beta_2, \beta_3]^t$ , because it has no singularity problems (the superscript t denotes transpose of a matrix). The quaternion is interpreted, as a rotation of angle  $\phi$  about an axis defined by a unit vector  $e = [e_1, e_2, e_3]^t$  with the following relations

$$\beta_0 = \cos(\phi/2), \quad \beta_i = e_i \sin(\phi/2), \quad i=1,2,3 \quad (1)$$

In this parametrization, the kinematic equations of the rigid spacecraft are represented as follows (Dwyer, 1984).

$$\dot{\beta} = \frac{1}{2} (\beta_0 \omega + \hat{\beta} \times \omega) \quad (2)$$

where  $\omega$  is the angular velocity of the spacecraft and  $\hat{\beta} = [\beta_1, \beta_2, \beta_3]^t$ . The dynamic equations are

$$I \ddot{\omega} = \tau - \omega \times I \omega \quad (3)$$

where  $I$  is the inertia matrix of a spacecraft and  $\tau$  is the control torque.

### Exact Linearization

Some class of nonlinear systems is transformed to an equivalent linear systems by coordinate transformation and nonlinear state feedback (Isidori, 1985). This exact linearization method can be applied to three axis attitude control (Dwyer, 1984). From Eq. (2) and (3), the state equations of the spacecraft attitude control are written as,

$$\begin{aligned}\dot{x} &= f(x) + g(x) \tau \\ &= \begin{bmatrix} \frac{1}{2} (\beta_0 \omega + \hat{\beta} \times \omega) \\ -I^{-1} \omega \times I \omega \end{bmatrix} + \begin{bmatrix} 0 \\ I^{-1} \end{bmatrix} \begin{bmatrix} \tau_1 \\ \tau_2 \\ \tau_3 \end{bmatrix}\end{aligned}\quad (4)$$

$$y = h(x) = [\beta_1 \ \beta_2 \ \beta_3]^t \quad (5)$$

where  $x = [\beta_1 \ \beta_2 \ \beta_3 \ \omega_x \ \omega_y \ \omega_z]^t$  is a state vector and  $y$  is an output vector. Differentiating  $j$ th output  $y_j$  with respect to time, we obtain

$$\dot{y}_j = \frac{\partial y_j}{\partial x} \dot{x} = L_f h_j(x) + \sum_{i=1}^3 L_{g_i} h_j(x) \tau_i \quad (6)$$

where  $L_f h(x)$  and  $L_g h(x)$  stand for the Lie derivatives of  $h$  with respect to  $f$  and  $g$  respectively. As  $L_{g_i} h_j(x) = 0$  for all  $i = 1, 2, 3$  and all  $x$ , the control torque  $\tau_i$  does not appear in Eq. (6). Therefore further differentiation of Eq. (6) leads to

$$\ddot{y}_j = L_f^2 h_j(x) + \sum_{i=1}^3 L_{g_i} L_f h_j(x) \tau_i \quad (7)$$

where  $L_f^2 h(x)$  stands for  $L_f(L_f h)(x)$  and  $L_g L_f h(x)$  for  $L_g(L_f h)(x)$ . This is written in vector form as

$$\begin{bmatrix} \ddot{y}_1 \\ \ddot{y}_2 \\ \ddot{y}_3 \end{bmatrix} = \begin{bmatrix} L_f^2 h_1(x) \\ L_f^2 h_2(x) \\ L_f^2 h_3(x) \end{bmatrix} + A(x) \begin{bmatrix} \tau_1 \\ \tau_2 \\ \tau_3 \end{bmatrix} \quad (8)$$

$$A(x) = \begin{bmatrix} L_{g_1} L_f h_1(x) & L_{g_2} L_f h_1(x) & L_{g_3} L_f h_1(x) \\ L_{g_1} L_f h_2(x) & L_{g_2} L_f h_2(x) & L_{g_3} L_f h_2(x) \\ L_{g_1} L_f h_3(x) & L_{g_2} L_f h_3(x) & L_{g_3} L_f h_3(x) \end{bmatrix} \quad (9)$$

If  $A(x)$  is nonsingular, the nonlinear state feedback law

$$\begin{aligned}\tau &= -A^{-1}(x) \begin{bmatrix} L_f^2 h_1(x) \\ L_f^2 h_2(x) \\ L_f^2 h_3(x) \end{bmatrix} + A^{-1}(x) \begin{bmatrix} v_1 \\ v_2 \\ v_3 \end{bmatrix} \\ \tau &= \omega \times I \omega + \frac{2}{\beta_0} I (\beta_0^2 \mu + \hat{\beta} \hat{\beta}^\top - \beta_0 \hat{\beta} \times \mu) \\ \mu &= v + \frac{1}{4} \omega^\top \omega \hat{\beta}\end{aligned}\quad (10)$$

yields the linear system

$$\ddot{y}_i = v_i \quad i = 1, 2, 3. \quad (11)$$

The matrix  $A(x)$  becomes singular only at  $\beta_0 = 0$ . Therefore this linearization is exact and global for positive value of  $\beta_0$ , i.e., rotating angle  $|\phi| < \pi$ . Applying the coordinate transformation as  $z = T(x) = [\beta_1, \beta_2, \beta_3, \dot{\beta}_1, \dot{\beta}_2, \dot{\beta}_3]$ ,  $z \in \mathbb{R}^6$ , the nonlinear system (4) and (5) are transformed into three separate single-input single-output linear systems as follows.

$$\dot{z} = \begin{bmatrix} 0 & \mathbf{E}_3 \\ 0 & 0 \end{bmatrix} z + \begin{bmatrix} 0 \\ \mathbf{E}_3 \end{bmatrix} v, \quad y = [\mathbf{E}_3 \ 0] z \quad (12)$$

where  $\mathbf{E}_3 \in \mathbb{R}^3$  is an identity matrix.

### Effect of Parameter Variation

There are modeling errors or parameter variation in a real system. In that case, the cancellation of nonlinear terms is no longer exact (Sastry, 1988). We evaluated the effect of parameter variation in the linearized system. Suppose the spacecraft's inertia matrix is different from a nominal value  $I_M$  but a real value  $I_R = I_M + \Delta I$ . The state equation of the real spacecraft is

$$\dot{x} = f_R(x) + g_R(x) \tau \quad (13)$$

while we modeled this as follows.

$$\dot{x} = f_M(x) + g_M(x) \tau \quad (14)$$

The system (13) can be written as

$$\begin{aligned}\dot{x} &= f_M(x) + g_M(x) \tau_i + \Delta f(x) + \Delta g_i(x) \tau_i \\ i &= 1, 2, 3\end{aligned}\quad (15)$$

where  $\Delta f(x) = f_R(x) - f_M(x)$ ,  $\Delta g(x) = g_R(x) - g_M(x)$ . These differences have the forms as follows.

$$\Delta f(x) = \begin{bmatrix} 0 \\ \Delta \tilde{f}(x) \end{bmatrix} \quad \Delta g_i(x) = \begin{bmatrix} 0 \\ \Delta \tilde{g}_i(x) \end{bmatrix} \quad (16)$$

Differentiating  $j$ th output  $y_j$  with respect to time, we obtain

$$\begin{aligned}\dot{y}_j &= L_{f_M} h_j(x) + L_{g_{M_i}} h_j(x) \tau + L_{\Delta f} h_j(x) + L_{\Delta g_i} h_j(x) \tau \\ &= L_{f_M} h_j(x)\end{aligned}\quad (17)$$

$$\begin{aligned}\ddot{y}_j &= L_f^2 h_j(x) + L_{\Delta f} L_{f_M} h_j(x) + L_{g_{M_i}} L_{f_M} h_j(x) \tau \\ &\quad + L_{\Delta g_i} L_{f_M} h_j(x) \tau\end{aligned}\quad (18)$$

As the linearization law is derived from the nominal model  $I_M$ , feedback torque is

$$\tau = (L_{g_{M_i}} L_{f_M} h_j)^{-1} (-L_f^2 h_j + v) \quad (19)$$

and the feedback system is written as follows.

$$\begin{aligned}\ddot{y}_j &= v + L_{\Delta f} L_{f_M} h_j \\ &\quad + L_{\Delta g_i} L_{f_M} h_j (L_{g_{M_i}} L_{f_M} h_j)^{-1} (-L_f^2 h_j + v)\end{aligned}\quad (20)$$

This is written in vector form as

$$\begin{aligned}\ddot{y} &= (\mathbf{E}_3 + B \Delta \tilde{g}(x) I_M B^{-1}) v + B \Delta \tilde{f}(x) \\ &\quad + B \Delta \tilde{g}(x) I_M B^{-1} \omega \times \hat{\beta} \times \omega + B \Delta \tilde{g}(x) \omega \times I \omega \\ &= (\mathbf{E}_3 + \alpha(x)) v + q(x)\end{aligned}\quad (21)$$

where  $\mathbf{E}_3 \in \mathbb{R}^3$  is identity matrix and

$$B = \begin{bmatrix} \beta_0 & -\beta_3 & \beta_2 \\ \beta_3 & \beta_0 & -\beta_1 \\ -\beta_2 & \beta_1 & \beta_0 \end{bmatrix} \quad (22)$$

Thus, in the exact linearization of the attitude control, the effect of the inertia moment variation is regarded as parameter changes  $\alpha(x)$  and the disturbance  $q(x)$  which are added to the linearized system inputs. Therefore the robust control theory for a linear system can be applied to obtain the robust attitude control system.

## Robust Model Matching

Robust model matching (RMM) is one of the design methods for a linear system with structured uncertainties (Eisaka, 1991). The principle of RMM is based on the concept of strict or approximate zeroing of the transfer functions from the equivalent disturbances to the output. The equivalent disturbances are the conceptual signals which represent the influence of parameter variation upon the state variables. The design procedure is as follows.

- step 1. Design a model matching controller which satisfies the specification
- step 2. Design the robust compensator

The equivalent disturbance  $q(s)$  is expressed as the linear combination of the measurable variables and input.

$$y^*(s) = G_{uy^*}(s) u + G_{qy^*}(s) q \quad (23)$$

$$q(s) = \begin{bmatrix} G_{qy}^{-1} & G_{qy}^{-1} G_{uy} \end{bmatrix} \begin{bmatrix} y^* \\ u \end{bmatrix} = M(s) \begin{bmatrix} y^* \\ u \end{bmatrix} \quad (24)$$

where  $y^*$  is all measurable variables and  $G_{uy^*}(s)$  and  $G_{qy^*}(s)$  are the transfer function from input  $u$  and disturbance  $q$  to  $y^*$  respectively. The ideal robust compensator  $R(s)$  is given as

$$R(s) = G_{qu}(s) \cdot M(s) \quad (25)$$

where  $G_{qu}(s)$  is a transfer function which satisfies the zeroing condition

$$W_{qy}(s) + W_{uy}(s) \cdot G_{qu}(s) = 0 \quad (26)$$

where  $W_{qy}(s)$  and  $W_{uy}(s)$  are the transfer function from  $q$  and  $u$  to output  $y$  of the control system designed in step 1). It is difficult to implement  $R(s)$  because it has a differentiator, hence low pass filter  $F(s)$  is added.  $F(s)$  must satisfy the conditions such that all elements of  $R(s) \cdot F(s)$  are proper, have a wide enough bandwidth to achieve the desired robust transient property and hold the internal model principle to achieve the steady-state property.

## Computer Simulations

A spacecraft's model of following inertia moment was used for design of controllers.

$$I = \begin{bmatrix} 33 & 0 & 0 \\ 0 & 38 & 2 \\ 0 & 0 & 43 \end{bmatrix} \quad (27)$$

Applying the coordinate transformation and nonlinear feedback law (10), nonlinear system (4) and (5) are transformed into the decoupled linear system (12). For each subsystem, we designed attitude controllers which has no steady position error, by usual model matching (MM) and robust model matching (RMM). A model transfer function from reference input to output was

$$G_{ry}(s) = \frac{1}{(s+1)^2} \quad (28)$$

Figure 4 and 5 show the structure of MM and RMM controllers respectively. Ideal robust compensator  $R(s)$  is

$$R(s) = [0 \ -s \ 1] \quad (29)$$

and we designed low pass filter  $F(s)$  as

$$\text{a) } F(s) = \frac{10}{s+10} \quad \text{b) } F(s) = \frac{100}{s+100} \quad (30)$$

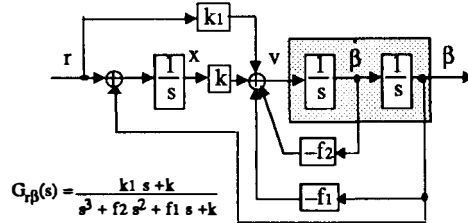


Fig. 4 The structure of MM controller

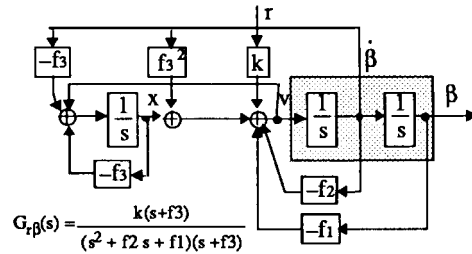


Fig. 5 The structure of RMM controller

Using these controllers, we carried out computer simulations. To evaluate the robustness, we changed the inertia moment as follows.

$$I = \begin{bmatrix} 308 & 0 & 0 \\ 0 & 43 & 40 \\ 0 & 0 & 313 \end{bmatrix} \quad (31)$$

Figure 6 shows the step response of the MM controller for 120 degree rotation about axis

$$e_r = (1/\sqrt{14}, 2/\sqrt{14}, 3/\sqrt{14})^T \quad (32)$$

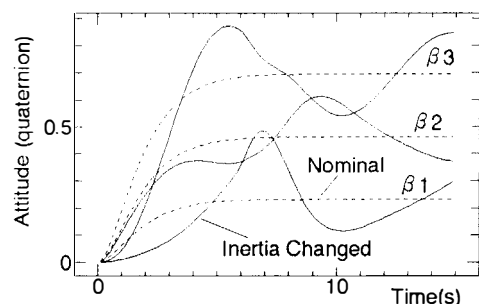


Fig. 6 The step response of MM controller

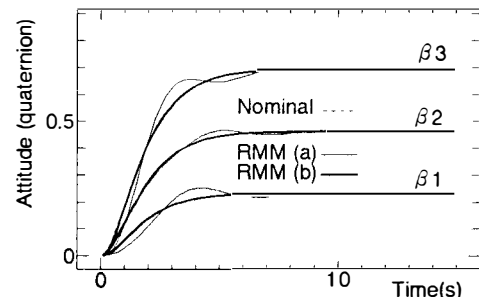


Fig. 7 The step response of RMM controller

For the nominal model, the attitude response was equal to the specified model  $G_{ry}(s)$ . For the inertia variation, however, the response changed largely. Figure 7 shows the response of the RMM controller. In the case using narrow bandwidth low pass filter (30a), the effect of inertia variation was not suppressed sufficiently. By using wide band filter (30b), the input-output behavior coincided with the nominal one.

### Ground Experiments

We implemented the controllers by MM and RMM for the simulation platform. A model transfer function from reference input to output  $G_{ry}(s)$  was the same as the computer simulation (28). The structure of MM controller is the same as that of computer simulation. Because of bias and noise of angular velocity sensors, we added new RMM compensator  $R_w(s)$  which suppressed disturbance caused by the sensors.

$$R_w(s) = [-s(s+2) \ s+2 \ 0] \quad (33)$$

$$F_w(s) = \frac{5}{s+5} \quad (34)$$

These control laws were installed on the onboard computer with sampling time of 10 msec.

Figure 8 and 9 show the step response of 15 degree rotation about the axis (32) for nominal and inertia changed systems. The response of MM controller has overshoot which seems to be caused by bias of angular velocity sensors. This overshoot converged, and steady performance of the MM controller is satisfied.

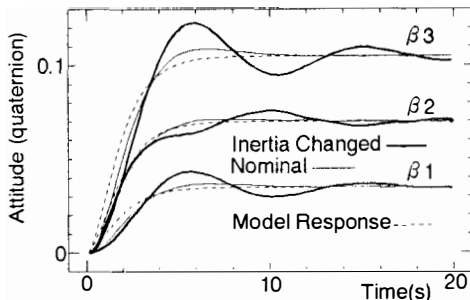


Fig. 8 The step response of MM controller

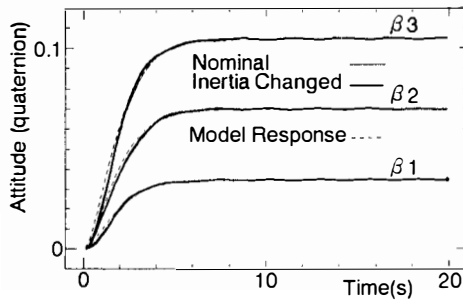


Fig. 9 The step response of RMM controller

In order to evaluate robustness, we installed additional mass. The inertia moment of simulation platform was changed to the following value.

$$I' = \begin{bmatrix} 103 & 0 & 0 \\ 0 & 49 & 23 \\ 0 & 0 & 106 \end{bmatrix} \quad (35)$$

The RMM controller suppressed the effect of inertia variations.

These results show that the robust attitude control is realized if torquers generate enough torque.

### GLOBAL SINGULARITY AVOIDANCE OF CMG

The total angular momentum vector,  $\mathbf{H}$ , of the pyramid type CMG system is a nonlinear function of the four gimbal angles,  $\theta_i$ 's (Fig. 2). Output torque,  $\mathbf{T}$ , generated by the gimbal motion is obtained as follows,

$$\mathbf{T} = -d\mathbf{H}/dt = -C \dot{\theta}, \quad (36)$$

where  $C$  is a Jacobian matrix and  $\dot{\theta}$  is a vector ( $d\theta_i / dt$ ).

To obtain a desired torque, gimbal motion,  $\dot{\theta}$ , is calculated generally as,

$$\dot{\theta} = -C^t(CC^t)^{-1}\mathbf{T} + k \omega_n, \quad C \omega_n = 0, \quad (37)$$

where the first term of the right is a pseudo-inverse solution of Eq. (36) and the second term is null motion which contributes null torque to Eq. (36). Calculation of this equation is the main body of the steering law in Fig. 3. In the experiments of the previous chapter, null motion was set zero, i.e.,  $k=0$ .

When the system is singular, i.e.,  $\det C=0$ , all the possible output torque only spans 2-dimentional space. This determinant,  $\det C$ , is an average of possible output, so it can be regarded as an index of the output capacity of the controller. To avoid degradation of the control performance, determinant must be kept as high as possible. This seems to be possible by a gradient method which determines the coefficient of null motion so that the determinant becomes larger. But even this method fails to avoid some class of the singular states.

Figure 10 illustrates the neighborhood of some singular states in the  $\theta$  space. The angular momentum is constant for each contour line, so the tangent vector is null motion. The null motion becomes two directional on the passable state ( $\theta_P$  in Fig. 10, called as hyperbolic (Kurokawa, 1985) or indefinite (Kurokawa, 1988)), while there is no null motion on the impassable state ( $\theta_I$ , called as elliptic or definite). This is explained by the quadratic form defined in the neigborhood of the singular states (Kurokawa, 1988). The gradient method avoids a passable state  $\theta_P$ , but it may fail to avoid the impassable one  $\theta_I$ , when such torque is desired as  $\mathbf{H}$  moves from  $\mathbf{H}-\Delta\mathbf{H}$  to  $\mathbf{H}+\Delta\mathbf{H}$  (path A in Fig. 10).

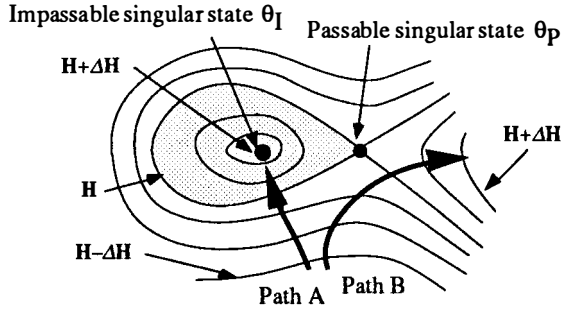


Fig. 10 Illustration of contour lines in the neighborhood of singular states as  $\mathbf{H}$  moves between  $\mathbf{H} \pm \Delta\mathbf{H}$ .

In order to avoid the state  $\theta_I$ , all the states in the hatched region must be globally avoided (selecting the path B for example). This region in the  $\theta$  space corresponds to a closed region in the angular momentum space. The surface of this region corresponds to either passable or impassable singular states. Curved triangle ABC in Fig. 11 is an example of cutting section of such a region obtained by a computer calculation. Global avoidance must be made before  $\mathbf{H}$  goes into this region.

Direct algorithm of this global avoidance is still under study now. Figure 11 explains a searching (try and error) method to find the branching point P in Fig. 11, which corresponds to the passable singular state  $\theta_P$  in Fig. 10, where appropriate selection of the path must be made to avoid the impassable region.

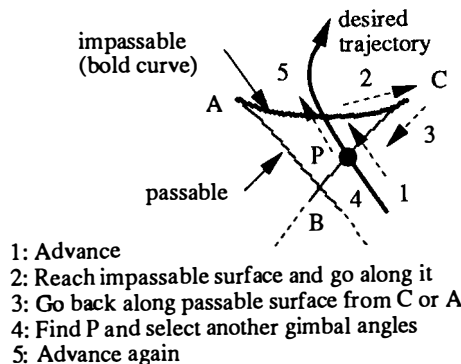


Fig. 11 Impassable region in the  $\mathbf{H}$  space and search method for global avoidance control

The effect of the global avoidance was evaluated by using the simulation platform. Figure 12 shows the results of pointing control when a constant disturbance torque was applied by the balance adjusting mechanisms. The CMG system generated counter torque and its  $\mathbf{H}$  went into the region in Fig. 11. Both the pseudo inverse control ( $k=0$ ) and the gradient control failed to avoid the region and the determinant went down to zero, while the global control succeeded to avoid. The global control was not realized as a real time calculation but implemented as a sequence control with off-line calculation only for this singular state. For an actual control, effective algorithm is required.

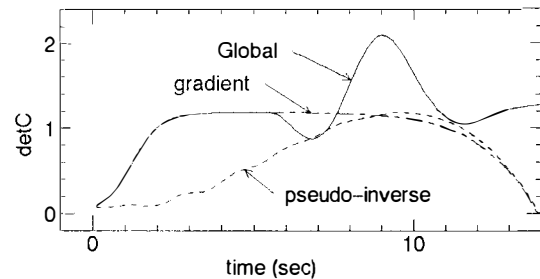


Fig. 12 Results of pointing control experiments.  
Initial  $\theta = (25, -25, 25, -25)$  (deg).

## CONCLUSION

Robust attitude control and global singularity avoidance control of CMG system are proposed and verified by computer simulation and ground experiments using a simulation platform. For the robust control, further study must be made to guarantee the stability of the control system. For the CMG control, effective algorithm must be developed.

## REFERENCES

- Dwyer T.A.W. III. (1984). Exact Nonlinear Control of Large Angle Rotational Maneuvers. *IEEE AC-29*, NO.9, 769-774.
- Eisaka T., Yanagita Y. and Tagawa R. (1991). Design of a robust electrical position servo based on dual model matching. *Int. J. Control.*, Vol.54, No.3, 497-515.
- Isidori,A. (1985). Nonlinear Control Systems. *Lecture Notes in Control and Information Sciences*. Springer-Verlag, New York.
- Kurokawa H. and Yajima N. (1988). A Study of CMG Systems - for Selection and Evaluation. *Proc 16th International Symposium on Space Technology and Science*. 1243-1249.
- Kurokawa H., Yajima N. and Usui S. (1985). A New Steering Law of a Single Gimbal CMG System of Pyramid Configuration. *Proc. 10th IFAC Symposium*. 251-257.
- Margulies G. and Aubrun J.N. (1978). Geometric Theory of Single-Gimbal Control Moment Gyro systems. *J. Astro. Science*. Vol.26, 159-191.
- Paradiso, J. A. (1991). A search-Based Approach to Steering Single Gimbaled CMGs. *CSDL-R-2261*.
- Sastry.S. S. and Kokotovic P.V. (1988). Feedback Linearization in the Presence of Uncertainties. *International Journal of Adaptive and Signal Processing*. Vol.2, 327-346.
- Tokar E.N. and Platonov V.N. (1978). Singular Surface in Unsupported Gyrodyne Systems. *Cosmic Research*. vol.16, No.5, 547-555.

## SPACECRAFT CONTROL ELECTRONICS - AN AUTOMATED MICROPROCESSOR BASED SPACECRAFT SYSTEM CONTROL FOR INTELSAT VII SATELLITES

S. Bangara\*, B. Chang\*, J.-L. Froeliger\*, K. Eriksson\*\*, T. McGuire\*\*, R. Steinberg\*\*\*  
and A. Habbak\*\*\*

\*International Telecommunications Satellite Organization, Washington DC, USA

\*\*Communications Satellite Corporation, Washington DC, USA

\*\*\*Space Systems/Loral, Palo Alto, California, USA

### ABSTRACT

As the in-orbit fleet of INTELSAT satellites continues to grow, it has become imperative to expand the automation of the spacecraft control and house keeping functions to increase flexibility and reliability of satellite operations. In order to safely and efficiently manage and operate a large number of satellites in orbit and to provide optimum communications service to its customers, INTELSAT has decided to expand on-board automation of the satellite house keeping tasks. This on-board automation is currently being implemented in the Spacecraft Control Electronics (SCE) of the Intelsat VII/VIIA series. This paper provides a description of the SCE architecture and the functions performed by the on-board processor system, together with the hardware and firmware design structure and the SCE testing philosophy.

### INTRODUCTION

INTELSAT presently operates a fleet of nineteen (19) satellites in synchronous orbit, consisting of thirteen (13) Intelsat V/VAs, five (5) Intelsat VIIs and an all K band Intelsat-K. The seven (7) Intelsat VII/VIIAs currently being manufactured by Space Systems/Loral would bring the number of satellites to operate to twenty-six (26) by the end of 1995. This new series can accommodate up to forty (40) channels to provide communication services in the C and Ku bands. The Intelsat VII/VIIA is a three axis stabilized satellite whose major housekeeping tasks have been implemented in a central and distributed microprocessor system, the SCE. The SCE performs the following functions: command and telemetry, attitude determination and control, safety system and fault protection, battery and thermal control, mechanism control and communication switching.

### SCE ARCHITECTURE

The INTELSAT VII/VIIA SCE is an extremely versatile and fully redundant on-board processor system that manages most satellite house keeping tasks. The SCE architecture is an integrated system to minimize the number of central processors while at the same time it is distributed to place Data Concentrator Units (DCUs) near

units being serviced. The SCE consists of two main central processors units (CPU) and eight remote DCUs as shown in Figure 1.

A MIL-STD-1553B serial data bus interconnects all elements of the SCE. Each central processor has its own data bus and each DCU interfaces with each central processor over its data bus. DCUs are distributed around the satellite to allow the SCE to efficiently service all satellite units and actuators. The DCUs are primarily under the control of the processor, which also controls the traffic across the 1553B data bus at a rate of 1 Mb/sec.

A majority of the house keeping functions are implemented in the CPU using the MIL-STD-1750A microprocessor. Ada is used as the high level source code.

The DCUs are implemented with TI-SBP9989 microprocessors, programmed in assembly language. The entire system is synchronized 16 times per second by the CPU over the 1553 data bus, thereby giving a basic CPU cycle time of 62.5 milliseconds. The nominal cycle time for the DCU processor is 1.667 milliseconds, to match the telemetry rate, and it is synchronized to the CPU cycle time of 62.5 milliseconds.

Although only one CPU and four DCUs are required for the mission, the two CPUs are

normally powered simultaneously, with one in control and the other one in hot stand-by. This also permits a transient-free switch over of the attitude control system to the redundant side using a special shadow mode.

Key features and advantages of the SCE are shown on Table 1. The SCE performs the following satellite functions:

- telemetry data acquisition and formatting
- command detection, authentication, decoding, distribution and execution
- attitude determination and control
- control safety system and fault protection
- automatic thermal control
- automatic battery charge management
- solar array position control
- antenna positioning mechanism control
- communications switching

The Intelsat VII/VIIA SCE is clearly an order of magnitude larger in scope, size and functionality than conventional control processors used in the past for communications satellites.

## SCE HARDWARE DESIGN

### OVERALL STRUCTURE

The DCUs and CPUs are built as stacks of trays, each tray performing a dedicated task. The trays of each unit connect to a flexible printed circuit board, the inter-module communication bus (IMCB), spanning the length of the unit. Each tray has a maximum of four 44-pin connectors which connect it to the spacecraft harness and to other trays in same unit.

Each unit has a DC/DC converter, connecting to the spacecraft bus, providing the various voltages required by the unit's circuitry. For each of the DCUs, only one of the redundant pair is normally powered at a time. The DCU power on and off functions are controlled by the CPUs.

### PROCESSOR HARDWARE

The main processor hardware consists of a MIL-STD 1750A CPU, 48k words of ROM, and 16k words of RAM, contained on three trays within the CPU. Four trays in the CPU contain circuitry for receiving, decrypting, and decoding spacecraft commands from the ground. One tray controls all communications over the associated 1553 bus. Another tray controls the processor and DCU configurations, including identifications of units that are powered on and in control, and the communication bus connections to each unit.

### DCU HARDWARE

Each DCU includes a "smart controller", based on a Texas Instruments SBP9989 microprocessor, clock generation and watch-dog timing circuitry, and a Bus Interface Unit, which is the DCU interface to the 1553 bus.

Other circuits which are common to the DCUs are the telemetry and command functions. These include digital status inputs, A/D convertor/control, analog multiplexer, temperature mux and sub mux for telemetry. Most of the command functions are performed by pulse command, relay command, column switch, row switch, row switch expansion, and multiple heater relay circuits, which are spread among the DCUs.

Circuits for specialized functions are included in each DCU. DCU-A includes the telemetry encoder. DCU-B has interfaces for the ADCS sensors and actuators, including the following:

**Serial Input:** DIRA, earth sensor, and digital sun sensor interfaces;

**Misc Command:** DCU-B internal circuitry;

**Wheel Control/CASS and Tachometer:**

Momentum wheel and Coarse Analog Sun Sensor (CASS) interface;

**Serial Output, Valve Coil Driver, and**

**VCD/Relay:** interfaces for thrusters and latch valves;

**Mag Torquer/MST:** interfaces to the magnetic torquer and Main Satellite Thruster (MST) control.

DCU-C includes stepper motor control and selection relays for the antenna positioning mechanisms. Both DCUs C and D include stepper motor control for the Solar Array Drive and relay control functions for the communications system switch drive matrix.

## SCE SOFTWARE DESIGN

The SCE software is coded in Ada plus a small amount of Assembler firmware for the processor, and Assembler for the DCU's. The CPU and the DCU firmware is single-threaded. Interrupts are used only when error conditions occur, thereby making debugging and measurement of overall throughput simpler. An overview of the SCE firmware structure is given in Figure 2.

### PROCESSOR FIRMWARE

The Processor firmware is partitioned into 7 logical segments: Battery, Thermal, Command, Telemetry, Attitude Determination and Control

System (ADCS), Control Safety System (CSS) and Operating System (OS).

The OS firmware provides tools and common routines for the rest of the firmware units. It consists of Subsystem Interfaces, Fault Detection, Subsystem Utilities, and the Power-Up tests. This unit also provides the scheduling of all the other firmware units, which is completed once every 62.5 msec (1/16 of a second per cycle).

The Battery and Thermal firmware are highly parameterized to allow test and operations personnel the capability to meet almost any type of contingency. There are a set of default parameters that allow the firmware to operate completely autonomously and only requires operational intervention when the parameters needed change.

The Command firmware allows for direct commanding of the satellite, autonomous commanding, and commanding with blocks of commands. The Command firmware allows turning on/off of discrete components, sending pulse commands, enabling/disabling of autonomous functions, uploading values into memory, and setting up block commands. Block commands can be executed through ground commands, or at some operator defined time (Time-Tagged Commands). Telemetry firmware provides both Normal and Dwell telemetry capabilities.

The ADCS firmware was converted from FORTRAN to Ada, retaining some of the heritage control loops. New and specialized control functions were incorporated where required. This firmware is highly specialized to make use of the Intelsat-VII sensors, DIRA, and thrusters. Exceptional care is taken to protect this firmware unit's variables from single event upsets (SEUs) to accommodate the many integrator and filters used throughout.

The control safety system (CSS) firmware monitors critical spacecraft functions and triggers on predefined conditions to "safe" the satellite if anomalous conditions occur. Some of the "events", "conditions", and actions to "safe" the satellite are commandable from the ground. This allows in-orbit adjustments to provide better control, prevent false triggering, and insure rapid response.

Fault Detection provides the 2-of-3 voting that is used for protecting data from Single Event Upsets (SEUs). Only critical data items are protected by 2-of-3 voting. A portion of the voted data is

"scrubbed" during each 1/16th of a second cycle to insure no SEUs have corrupted the data. The term 2-of-3 is used because the data items are stored into 3 separate locations in memory, and then compared to each other during the "scrubbing" process. If one of the values for an item is corrupted, it is overwritten by the value in the other two locations. In addition to the normal scrubbing, the most critical ADCS variables are also scrubbed immediately before use in the control loops.

### DCU FIRMWARE

The DCUs operate as peripheral processors, retrieving telemetry data and sending commands to the hardware. The four DCUs (A, B, C, D) collect normal telemetry using a pre-defined table that designates the information to be read. The DCUs also provide dwell, which allows telemetry data to be read at a faster rate, and memory readout, which allows the ground to examine the contents of memory. Command information is written into DCU memory by the CPU, then sent by the DCU to the appropriate output port.

The processor sends a broadcast pulse to the DCUs in every CPU cycle to keep the DCUs and the CPU synchronized. Each DCU interfaces with its own input and output circuits and other hardware. Some of the functions that are specialized by DCU are:

DCU A-Telemetry Encoder

DCU B-Earth Sensors, DSS, CASS, DIRAs,

Thrusters, Tachometer, Magnetic Torquer

DCU C-Switch Drive Matrix, APM, SADA

DCU D-Switch Drive Matrix, SADA

While DCU A, DCU C, and DCU D collect telemetry and process commands every 1.667 msec, DCU B completes reading input data, processing commands, collecting telemetry, and writing output data before the end of its 62.5 msec cycle. The processing for each DCU completes in 62.5 msec.

### SCE FUNCTIONS

#### TELEMETRY PROCESSING

The SCE provides the baseband portion of the satellite telemetry function. The data collection, processing, multiplexing, formatting and PCM encoding are all performed in the SCE. Spacecraft health, status and performance data are collected by the DCUs. The DCUs also perform signal conditioning and analog to digital conversion (A/D) locally. The coordination of sequential

data collection at the required intervals of 62.5 ms and the formatting of the data into telemetry frames are performed by the CPU. The telemetry encoding of the data onto baseband signals are achieved by DCU-A which receives the formatted data from the CPU. Both normal and dwell telemetry frames are generated simultaneously and independently. The implementation of command and telemetry functions by the SCE is shown in figure 3. A total of about 2000 telemetry parameters are in use including status bits. The general characteristics of the telemetry generated by the SCE are as follows:

Frame length: 256 bytes (8 bits/byte)  
Normal telemetry subcarrier frequency: 48 KHz  
Dwell telemetry subcarrier frequency: 72 KHz  
Modulation: PCM BPSK Coherent  
Coding: Bi-phase level-Manchester  
Data bit rate: 4800 BPS

## COMMAND PROCESSING

The overall command subsystem on the spacecraft provides for the reception, decryption, decoding and distribution of satellite commands. All baseband command functions are performed by the SCE as shown in Figure 3. The command subsystem consists of two separate command channels, individually accessible via unique command addresses. The command receiver outputs are sequentially sampled by the bit detectors in the SCE. Detection of a command subcarrier results in a lockup and subsequent detection of the BPSK/PCM command message. The message is error checked, the decoder address is verified and the data is routed to the CPU for decoding. Further address information is used for distributing the command data to the specific DCU which services the intended user. The command subsystem, which is operable at all times during the spacecraft life, is shown in Figures 4 and 5.

The basic command input to the processors can be either in plain text or enciphered text corresponding to clear or secure mode operation. In clear mode the plain text demodulated data passes directly through the mode switch, through the decoder address verification and bit error detection functions and to the CPU, bypassing the decryptor subassembly. Secure mode operation directs the cipher text demodulated data through the mode switch to and from the decryptor and to the CPU.

Commands are transmitted to the spacecraft at a data rate of 250 bits per second. Both command verification and command execution telemetry are transmitted as part of a minor frame of telemetry

data. Command execution telemetry is transmitted for two minor frames following the execution of the command.

A limited subset of valid commands affect the operation of the command processing subsystem directly by loading, queuing and/or executing stored commands. Stored commands are organized either as block commands or as time tagged commands. A separate set of commands effect the decryptor keys and variables. The remaining commands fall into various traditional command categories relay, pulse, internal etc. There are a total of about 1500 commands that have been allocated not including the memory load commands.

## ATTITUDE DETERMINATION and CONTROL FUNCTIONS

### Implementation of ADCS Functions in the SCE

The Intelsat VII/VIIA Attitude Determination and Control System (ADCS) is a flight proven, extremely reliable and easy to operate control system. Figure 6 shows the overall ADCS block diagram.

The CPU contains all of the control mode firmware to implement the ADCS requirements. DCU-B performs the interfacing functions between the CPU and the sensors and actuators. DCU-B is synchronized with the CPU using the broadcast message in the same manner as for the other DCUs. This is performed to synchronize the sensor/actuator data processing with the CPU operation.

The command system and application program in the CPU are used to select the ADCS mode (see Figure 7). The configuration and operating parameters have default values that either can be stored in programmable read only memory (PROM) or selected by ground command. This information is stored in RAM in the processor.

An overview of the ADCS firmware is shown in Figure 8. The ADCS modes are selected and initialized by either the separation switches, launch vehicle pulse commands, real time ground, or time-tagged, stored commands resident in the control processor. The ADCS application programs require the highest sampling rate of all application programs and they are the first scheduled task in each basic processing cycle (62.5 msec).

In addition to the mode dependent firmware tasks, the CPU can perform any of the following ADCS

related tasks in each basic cycle:

- store and execute thruster firing
- closed loop speed control for the wheels
- solar array drive mechanism control
- sensor data input and torque command output
- gyro bias estimation
- control safety system
- continuously operating 2-of-3 voting on RAM variables
- ground initiated self test

#### Attitude Control Sensors and Actuators

The following sensors are mounted on the Intelsat VII/VIIA spacecraft:

- Earth sensor: two scanning sensors, one active, the other available for redundancy. Each sensor provides roll and pitch information.
- Digital Integrating Rate Assembly (DIRA): the DIRA system (one gyro package and its associated electronics) provides position and rate information about each spacecraft axis. The gyro unit comprises four gyros (roll, pitch, yaw and a skew gyro) and their temperature control circuitry. The skew gyro provides redundancy if one of the other three gyros fails.
- Coarse Analog Sun Sensor (CASS): six independent (redundant) sun sensor optical heads provide an attitude measurement of the angular deviation of the sun line about roll/yaw and pitch/yaw axes.
- Digital Sun Sensor (DSS): two independent (redundant) optical heads and their associated electronic channel provides pitch and yaw errors relative to the sun line.

The following actuators are used to provide the necessary control and thrust torques:

- Momentum Wheel Assembly (MWA): two pitch momentum wheels (each one producing 61 Nmsec) and one yaw transverse momentum wheel (25 Nmsec) are mounted on the spacecraft. The normal operation mode uses the two pitch wheels mounted in V configuration; in case of failure of one of the two pitch wheels, the backup operation mode, or L mode, uses the remaining pitch wheel together with the transverse yaw wheel.
- Magnetic Torquers: two magnetic torquers are placed on the west and anti-earth face of the

satellite. When interacting with the earth magnetic field, these torquers create a dipole that is used to counter the effects of the solar pressure torques.

-Thrusters: twelve 22 N thrusters provide complete redundancy for all attitude and control modes, generating control torques about all three axes. A single 490 N Main Satellite Thruster (MST) provides the necessary velocity for apogee and perigee maneuvers.

#### Attitude Control Modes

Figure 9 gives an overview of all attitude control modes implemented in the Intelsat VII/VIIA series, with associated functions, sensors and actuators.

##### **Sun Acquisition Mode**

The Sun Acquisition (SA) mode damps residual rates and points the spacecraft -X axis towards the sun. When sun pointing the satellite rotates at 0.75 degree/second about the sun line, with the solar arrays facing the sun. Rates about other spacecraft axes are controlled to zero. Sensors used for SA are the CASS and the DIRA. Once in sun pointing mode, the DSS may be substituted for the CASS.

##### **Roll Earth Acquisition Mode**

The Roll Earth Acquisition (REA) mode is commanded from the sun pointing mode. REA damps the sun pointing roll rate and places the satellite XZ plane on the earth while tracking the sun. In addition to the CASS (or DSS) for pitch and yaw sensing, the REA uses the earth sensor for roll information. A loss of earth presence signal will cause the SCE to switch automatically to SA mode.

##### **Pitch Earth Acquisition Mode**

The Pitch Earth Acquisition (PEA) mode is commanded from the REA mode and searches for earth using the pitch rate. Using roll and pitch data from the earth sensor, the PEA points the satellite +Z axis at the earth nadir and tracks the earth. Yaw sensing is performed by the DIRA.

##### **Pitch/Yaw DIRA calibration**

This mode can be initiated from the REA. DIRA provides roll information and CASS (or DSS) provides pitch and yaw information to maintain the roll position constant and track the sun.

### All DIRA mode

This 3 axis DIRA control mode holds the spacecraft inertially fixed and allows it to be biased when desired.

### Main Satellite Thruster (MST) mode

The MST mode is designed to control the spacecraft attitude during Apogee Maneuver Firing (AMF) and Perigee Velocity Augmentation (PVA) orbit control maneuvers.

In addition to counteracting disturbance torques caused by the spacecraft center of mass motion, the MST controller stabilizes the solar array structural flexibility (the solar array is fully deployed at the time of these maneuvers) and the propellant slosh modes. The MST mode uses the DIRA for both rate and angle sensing on all axes and therefore relieves all earth and sun field of view constraints for the maneuvers. In the case of midnight launch injection it is possible to use the DSS in place of the DIRA for pitch and yaw sensing. In this case roll angle and 3 axis rate sensing is still provided by the DIRA.

### Normal On-Orbit Mode

The purpose of the on-orbit mode is to maintain pointing accuracy relative to the earth during normal operations.

Figure 10 presents a functional diagram of the on-orbit mode.

The scanning earth sensor provides roll and pitch information and the two pitch momentum wheels (in a V configuration) are the principal actuators. The wheels control short term roll and pitch errors, with the magnetic torquers providing long term roll and yaw momentum management. The torquers are driven by an on-board estimator that, with the momentum bias, allows yaw to be controlled through roll/yaw coupling. Thrusters automatically manage the pitch wheel momentum unloading.

The on-orbit control mode supports an attitude inversion. This is achieved by performing a wheel spin down, followed by a 180 degrees yaw maneuver and subsequent wheel spin up. Control of the satellite in inverted attitude is provided by gain changes in the observer and magnetic torquer controllers to compensate for the change in roll/yaw coupling due to orbit motion.

The on-orbit control mode also supports operation

in inclined orbits of up to 3 degree inclination. The V angle of the pitch wheels of 20 degrees is sufficient to allow for the yaw momentum storage to maintain the satellite pointing to the sub satellite point. A set of ground commanded dynamic trajectories are uploaded in the CPU to maintain pointing during inclined orbit operation.

### Station Keeping Mode

The Station Keeping (SK) mode provides three axis attitude stabilization during initial station acquisition, wheel spin up, north, south, east and west station keeping maneuvers, attitude inversion and station changes.

During maneuvers, the 22 N thrusters are used for attitude control while the wheels are maintained at their existing speed. The same topology is used for SK and MST with rate feedback from the DIRA. In Station Keeping, yaw attitude sensing is provided by the DIRA, while roll and pitch information is derived from the earth sensor. There is no time of day/time of year constraint for station keeping maneuvers.

Small velocity maneuvers for east and west longitude adjustment and eccentricity control can be performed in the normal on-orbit mode by using the time-tagged feature of the SCE to program commandable thruster on-times to be fired at dedicated times of the day.

### Backup Station Keeping Mode

The Backup Station Keeping mode is a contingency mode that can be used in the event of a double DIRA failure. It differs from the primary SK in that only position sensing is required. Roll and pitch errors are still provided by the earth sensor, with yaw derived from the CASS (or DSS) signal. The satellite local time when backup SK can be performed is constrained by the sun sensor position and field of view.

### Transition Mode

The purpose of the transition mode is to provide a safe and automatic transition from the station keeping mode to the normal on-orbit mode. The transition mode uses the spacecraft attitude and rates to compute a series of critically timed thruster pulses to damp any residual nutation. Roll and pitch positions are provided by the earth sensor and yaw position and 3 axis rates are provided by the DIRA.

### Shadow Mode

The purpose of the ADCS shadow mode is two fold:

- provide a transient free switching in normal control mode from one CPU to the other
- provide a means to verify proper operation of the control algorithms in the redundant CPU before placing it in control

An overview of the shadow mode is given in Figure 11.

The standby processor is configured to use the same control elements and gains as the one in control. Comparison of the normal mode telemetry between the shadow and the active CPU allows to verify the operational health of the redundant CPU/DCU-B pair from the SCE.

#### CONTROL SAFETY SYSTEM / FAULT PROTECTION

The Control Safety System (CSS) consists of continuously operating diagnostic and correction circuitry and processor based firmware that minimizes communications outages under anomalous conditions. Although CSS applications can be executed in all mission phases, its emphasis is significant during Perigee Velocity Augmentation (PVA) maneuvers, that are performed without command and telemetry capability.

The following independent monitors have been implemented in the CSS:

- a. CPU monitor (PVA)
- b. CPU monitor (on-orbit)
- c. DCU-B monitor (PVA and on-orbit)
- d. Earth sensor monitor (on-orbit)
- e. Thruster duration monitor (PVA and on-orbit)
- f. Thruster activation monitor (PVA)
- g. DIRA consistency monitor (PVA)
- h. Main Satellite Thruster injector temperature monitor (PVA)
- i. DIRA angle monitor (PVA)
- j. DIRA rate monitor (PVA)
- k. Under pressure monitor (PVA)
- l. Momentum wheel monitor (PVA)
- m. Over pressure (isolate regulator) monitor (PVA and on-orbit)
- n. Thruster duty cycle monitor (on-orbit)
- o. Latch valve monitor (all modes)
- p. Angle monitor (on-orbit)
- q. Earth sensor glitch monitor (on-orbit)

Most of the CSS monitors are resident in the CPU, with some resident in DCU-A, DCU-B and DCU-C.

Detections of anomalies by these monitor "watch dogs" will either place the satellite in a safe mode or will take a less severe action that is dependent on the present operational mode.

It is possible to individually override and/or inhibit by ground command any automatic function or switch over associated with these monitors. Once a monitor is tripped the entire function is bypassed until the monitor is reset.

#### THERMAL CONTROL

The SCE implementation of the automatic thermal control function is shown in Figure 12. The thermal control firmware is responsible for control of a number of heaters on the spacecraft. The DCUs gather the thermistor data as part of the normal telemetry data process. DCUs also contain the heater on/off control circuitry. All decisions for heater on/off control are made by the CPU, based on analysis of the selected thermistor data.

One heater control decision is made every two seconds by the thermal control firmware. The actual state of the heater relay is not checked by the firmware, so if the temperature is out of the deadband a control relay will be commanded to the proper state even if it is already in that state.

Functions selectable by ground command include enable/disable of the thermal firmware outputs, selection of temperatures for switching, and association of sets of thermistors with individual heaters. All heaters are also controllable by ground command.

#### BATTERY MANAGEMENT

The top level block diagram for battery management firmware is shown in Figure 13. The power subsystem on the satellite is controlled by redundant Power Control Units (PCU), which are serviced by the pair of DCUs nearby. The battery management firmware runs at all times on the CPU. The outputs may be disabled, and all functions performed by the automatic battery firmware may be performed by ground control.

Four control modes are used by the battery management firmware: eclipse, high charge rate, medium charge rate and trickle charge rate. Switching between modes is done automatically, based on parameters from the battery and integrated charge computed by the firmware. The charge rate sequence and charge rate mode switching conditions are selected by ground command. Default values are stored in ROM,

and are used if new values have not been commanded.

Some of the main features of the firmware control are: 1.) Monitoring of the solar array shunt current to determine if the satellite is in sunlight and enough charge is available for the required charge rate prior to switching to a new charge rate; 2.) Integration of the charge and discharge currents to determine when charge thresholds are crossed for switching modes; 3.) Automatic execution of safing functions when a specified battery temperature is reached in any mode.

The program supplies telemetry data continuously, for verification of proper operation. The states of the charge integration are monitored, as well as the various relays that control the system.

#### SOLAR ARRAY POSITION AND CONTROL

The CPU is responsible for driving both solar array wings of the spacecraft. The hardware interface between the CPU and the solar array drive is through DCU-C and DCU-D for north and south solar array drive respectively. Functions selectable by ground command include direction and slew rates for drive motion. In addition to the nominal drive motion of one revolution per day, programmable slew rates are provided for rapid orientation of the wing.

#### ANTENNA POSITION AND CONTROL

The CPU controls the Antenna Positioner Mechanism mounted on the spacecraft. There are a total of four Two-Axis Antenna Positioner Mechanism (TAAPM) and one Single Axis Antenna Positioner Mechanism (SAAPM) to reorient the Intelsat VII/VIIA antennas individually.

#### COMMUNICATIONS SWITCHING

The configuration and on/off status of the communications subsystem is fully controlled by the SCE. The telemetry and command interfaces in the DCUs perform all functions necessary for this control. Ordinary relay and pulse commands are used for on/off control of communications equipment, and for many switching and miscellaneous functions.

Most of the communications subsystem commands are "manual", i.e. controlled and timed by ground operations. The SCE does include an automatic RF blanking function, however, for some SSPAs. The SSPAs include a circuit and command input to allow the outputs to

be turned off momentarily to permit switching of the outputs without damage to the unit. Some switching commands to the SCE have an option to blank certain amplifiers while they are executed. If the option is selected, the CPU will energize the blanking function by a relay command, execute the selected command, and de-energize the blanking relay automatically, all as a result of the single command. This permits rapid reconfiguration of the communications system without risk of damage to any equipment.

The interface to the communications system also includes a set of switch commands that are controlled by a relay matrix called "switch drive matrix" commands. The types of switches that are controlled are shown in Figure 14. The switch drive matrix concept is depicted in Figure 15.

There are two separate switch drive matrices, one in DCU-C containing 32 columns and 14 rows, and one in DCU-D containing 32 columns and 9 rows. There is one relay for each column selection, split between the redundant DCUs of a pair. All relays can be switched by either DCU in a redundant pair. The row switches are redundant within a pair of DCUs, with the wiring starting at one DCU and ending at the other. The result is that a single failure of any one type can cause loss of only one row or one column in the matrix.

The main reasons for using the matrix approach are reduction of the required wiring between the DCUs and the communication equipment, and rapid reconfiguration of the communications subsystem for both failure recovery and traffic requirements.

#### **SCE TESTING**

##### TEST FLOW

There are four basic phases to the testing of the SCE: 1.) Sub-assembly or circuit testing; 2.) Unit level testing; 3.) Subsystem testing; 4.) Satellite level testing.

All components go through circuit testing. The CPU and the DCUs are each considered a unit, and all undergo unit level testing. The subsystem testing is oriented toward the ADCS functions, and only the CPU and DCUs A and B are tested as a subsystem. The full redundant SCE is used and tested through satellite level testing.

##### SUB-ASSEMBLY TESTING

All trays used in the SCE undergo some testing during and after assembly, including a few part value selection steps. The sub-assemblies are tested with an automated tester that includes a dedicated interface for each type of tray. This tests the trays independently, with measurement of all relevant electrical parameters, but no system-related data.

### UNIT TESTING

All SCE units proceed through the same test phases:

- a. Performance Tests
- b. Vibration
- c. Post-vibration performance test
- d. Thermal/Vacuum (including hot and cold performance)
- e. Post thermal vacuum performance test
- f. Electro-magnetic compatibility (EMC)
- g. Final functional test

The performance testing is different for the five units that comprise the SCE. There is a dedicated tester for the DCU-Bs and another for the CPUs that is used for each performance test, including the Thermal-Vacuum tests. DCUs A, C, and D are tested in two phases for each of the performance tests. The two phases consist of an ATE test followed by a functional test.

The Automatic Test Equipment repeats the tray tests with the trays bolted together to form a DCU. Each tray is tested individually, and only one tray is connected to the measurement equipment, i.e., rack of test equipment at a given time. The functions are tested using a special test memory unit that replaces the program in the DCU processor with a test program.

The separate functional test for DCUs A, C, and D is performed on another automated tester called the Metabyte Tester, with the DCU connected as it will be in flight. This test uses the DCU firmware instead of the test firmware, and tests function rather than electrical performance of each unit.

### SUBSYSTEM TESTING

SCE subsystem tests are performed to demonstrate performance of the attitude control modes as well as functionality and accuracy.

ADCS pointing performance is validated by an extensive series of Closed Loop Tests (CLT) using a spacecraft dynamic simulator. The Closed Loop Test Computer provides accurate simulation of the spacecraft dynamics including

rigid body and flexible modes, individual thruster uncertainty, magnetic fields, magneto torquer operation and simulated sensor signals (including sensor noise). Subsystem Closed Loop Tests are performed for each flight subsystem using two CPUs, two DCU-Bs and two DCU-As. In addition to testing all the control loops in all the modes, all features of the Control Safety System (CSS) are also verified at CLT level.

Functional tests of the ADCS, including tests that verify operation over temperature extremes and bus voltage variations, are performed on a three axis servo table. These tests also include functional verification of switching between redundant earth sensors, CPUs, DCU-Bs and momentum wheels. For each flight subsystem a full set of servo table tests are performed over temperature. These tests exercise the flight SCE units, together with the flight sensors (DSS, CASS, DIRA and earth sensors) and the flight momentum wheels.

### SYSTEM TESTING

After integration on the spacecraft, the SCE is tested at every major step of the integration and step flow. This includes:

- a. Integrated system reference performance tests
- b. Main body (horizontal) thermal vacuum tests
- c. Electromagnetic compatibility tests
- d. Electrostatic discharge tests
- e. Post dynamics performance tests
- f. Spacecraft thermal vacuum (vertical) tests
- g. Final integrated system reference performance tests
- h. Launch base tests

The system tests performed include:

- a. Command and telemetry functional
- b. Battery and thermal functional
- c. Command input and data bus timing
- d. Control safety system tests
- e. ADCS open and closed loop tests of all modes
- f. ADCS polarity tests

### **CONCLUSION**

The Intelsat VII/VIIA Spacecraft Control Electronics is a large and complex on-board processor system performing a variety of house keeping functions, including command and telemetry, attitude and orbit determination and control, control system safety and fault detection, battery management, thermal control, antenna and solar positioning control and communications switching.

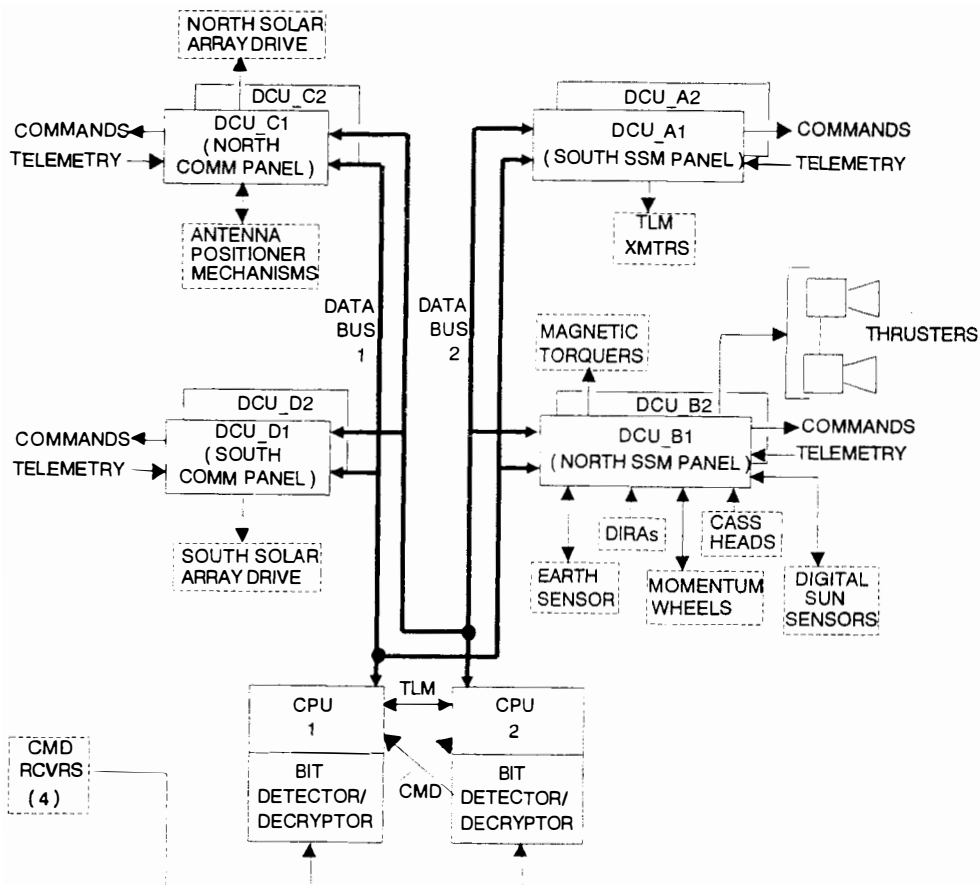
The high level of on-board automation and the extensive fault detection and protection system implemented in the SCE will benefit Intelsat to safely and efficiently operate the seven Intelsat VII/VIIA spacecraft that will be added to the already existing fleet of 19 satellites.

## ACKNOWLEDGMENTS

The authors would like to acknowledge all the individuals that have contributed to the Intelsat VII/VIIA SCE and this paper. While it is not possible to name everyone, the authors wish to acknowledge K. Raghunathan and R. Barto of INTELSAT.

Features	Advantages
Automatic Earth reference pointing control	Improved antenna pointing accuracy
Complete redundancy including dc/dc converters for high reliability	Higher satellite reliability
Complete cross-strapping for increased reliability	Higher satellite reliability
Distributed system for reduced harness weight	Increased weight margin
Modular/tray packaging for easy expansion or modification	Easy telemetry and command expansion
Time-tagged and uploaded block commands used to reconfigure the spacecraft using only one uploaded or time-tagged command	Reduced ground station activity
Single event upset protection	Protection against loss of communication links
Self test and diagnostics	Early indication of equipment operation problems
Memory readout on dwell telemetry	Verification of equipment operation
Reprogrammability of applications programs	In-flight failure recovery
Automatic battery charging	Reduced ground station activity
Automatic thermal control	Reduced ground station activity
Automatic execution of stored commands with hands-off operation provided	Reduced ground station activity
Automatic detection of loss of attitude control and switching to backup electronics or to safe mode.	Protects the satellite from catastrophic failures
Commercial test equipment can directly monitor and control the satellite or a panel via the MIL-STD_1553B data bus at 1 Mb/s rate	Reduces test time and protects schedule

Table 1: SCE Key Features and Advantages



CONTROL PROCESSOR = PROCESSOR/BIT DETECTOR

Figure 1: SCE BLOCK DIAGRAM

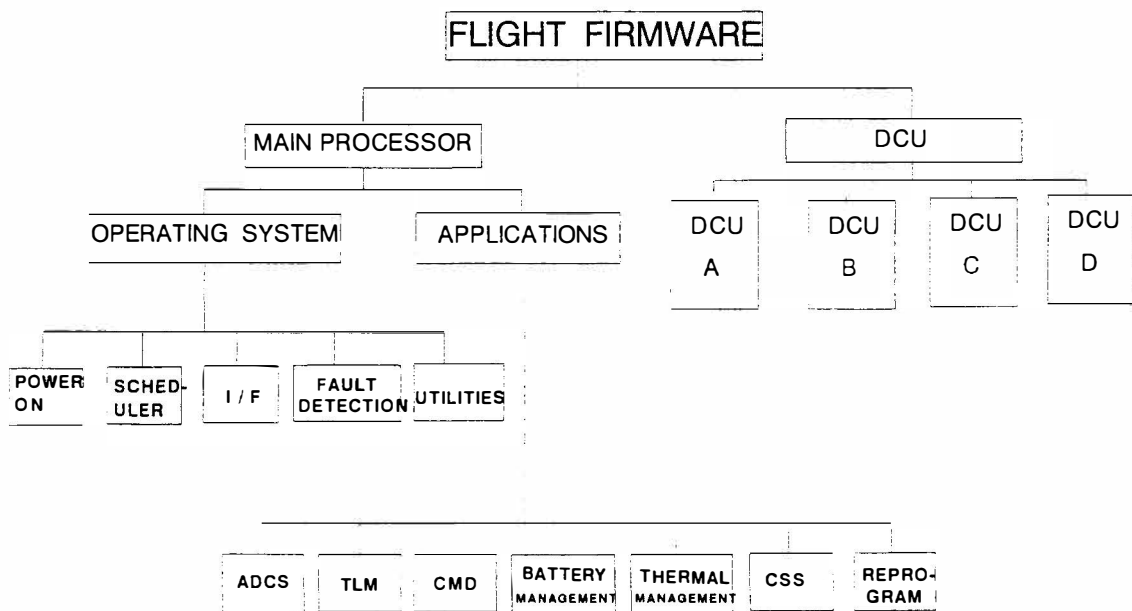


Figure 2: Firmware Structure Overview

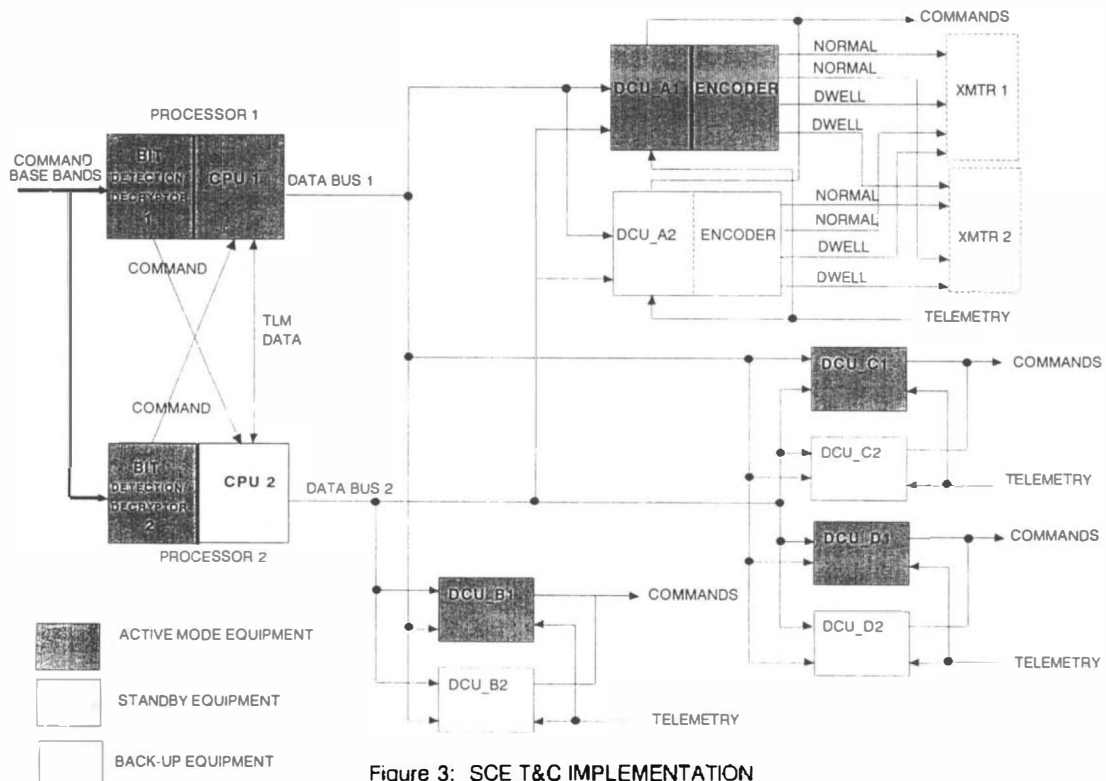


Figure 3: SCE T&C IMPLEMENTATION

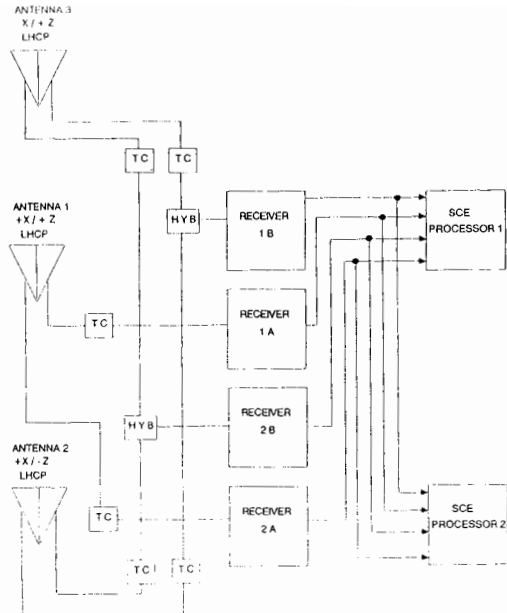


Figure 4: COMMAND SUBSYSTEM

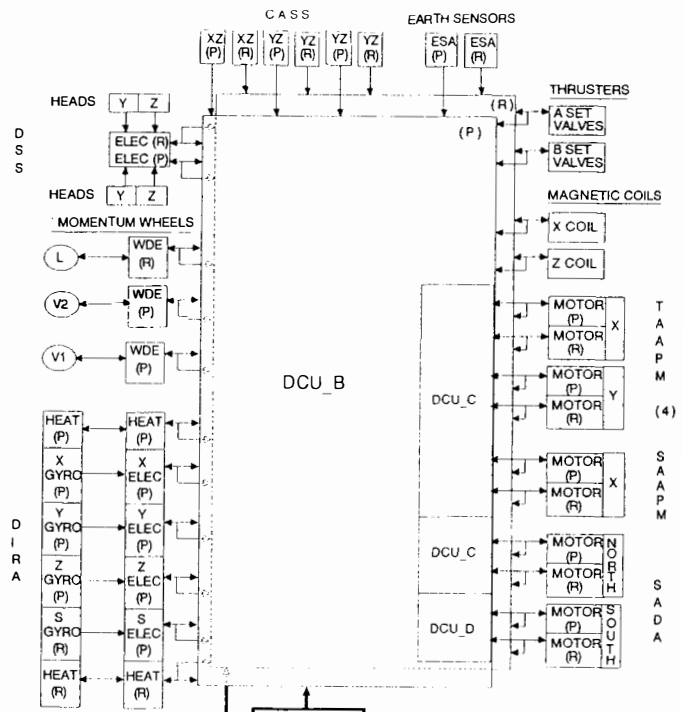


Figure 6: ADCS Block Diagram

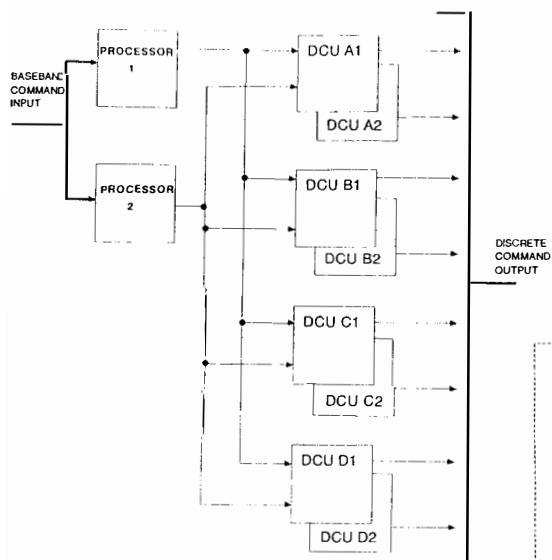


Figure 5: SCE COMMAND BLOCK DIAGRAM

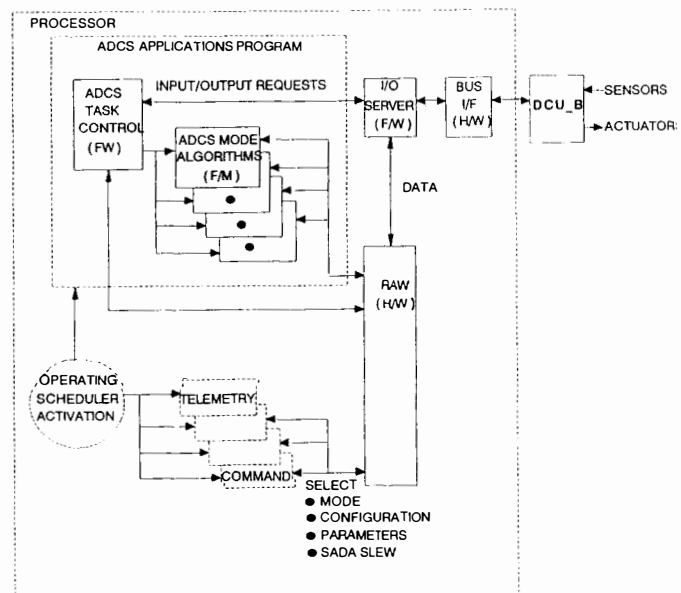


Figure 7: ADCS Processing Hardware and Firmware

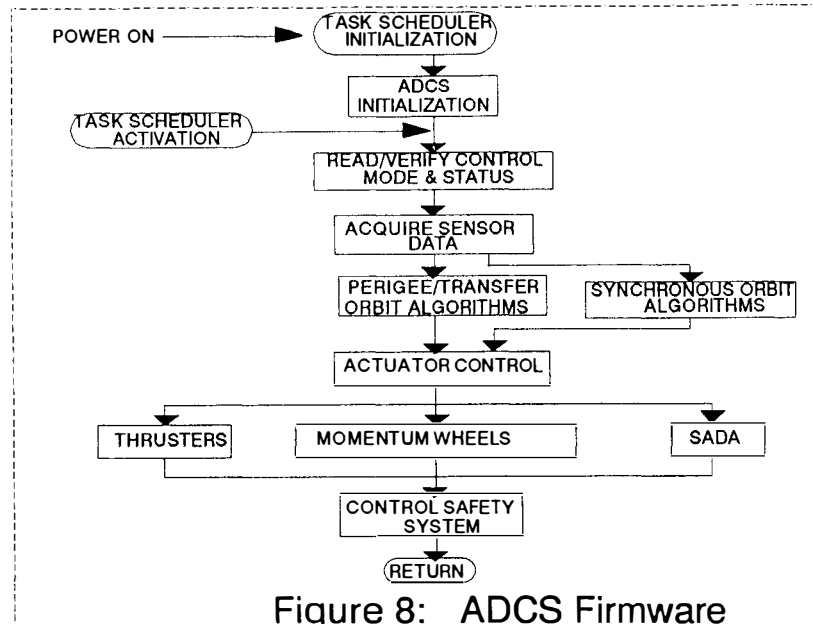


Figure 8: ADCS Firmware

Mode	Function	Nominal Sensors Position			Actuators All axes	Comments
		Roll	Pitch	Yaw		
Despin / Sun Acquisition	Damp tip-off rates and point - x axis at sun. Initiate roll rate.	CASS	CASS or DSS	CASS or DSS	Thrusters	Designed for worst-case initial rates.
Roll Earth Acquisition	Damp Sun acquisition roll rate and place Earth in XZ-plane.	ES	CASS or DSS	CASS or DSS	Thrusters	Requires correct Earth Sun geometry. ES scans must cut earth disk
Pitch Earth Acquisition	Search for Earth using pitch rate. Given Earth presence, point +Zaxis at Earth centroid.	ES	ES	DIRA	Thrusters	Pitch search used only if no Earth presence. Requires yaw DIRA calibration
Pitch / Yaw DIRA CAL	Maintains roll position and tracks the Sun.	DIRA	DSS or CASS	DSS or CASS	Thrusters	Prior to losing Earth presence pitch/yaw CAL may be initiated to continue tracking the Sun with either the CASS or DSS
All DIRA	Holds S/C fixed inertially and allows it to be biased when desired	DIRA	DIRA	DIRA	Thrusters	S/C attitude is initialized and roll, pitch or yaw maneuvers may be installed.
MST (includes PVA)	Controls attitude during main thruster firings.	DIRA	DIRA	DIRA	Thrusters	Same controller as SK mode. Full DIRA control for 6 am launch.
On-Orbit mode (includes L and V modes, inverted or inclined orbits ).	Wheels control roll and pitch errors. Magnetic momentum management opposes environmental torques.	ES	ES	—	Wheels Torquers Thrusters	Yaw error estimated by onboard observer. Thrusters used for wheel unloading. Does not use DIRA.

Figure 9: Attitude Control Modes

Mode	Function	Nominal Sensors Position			Actuators All axes	Comments
		Roll	Pitch	Yaw		
Stationkeeping	Controls attitude while applying orbit adjustment $\Delta V_s$ .	ES	ES	DIRA	Thrusters	Uses DIRA for rate feedback. Certain thrusters used to apply $\Delta V$ and off-modulated for control.
Transition	Used to transition from SK to On-Orbit mode. Damps residual momentum from thruster firings.	ES	ES	DIRA	Thrusters Wheels	Pitch goes directly to On-Orbit mode after firing 2 or 3 pitch pulses spaced $x$ sec apart. Roll - yaw momentum damped by commanded times thruster firings.
Backup Stationkeeping	Controls attitude while applying orbit adjustment $\Delta V_s$ .	ES	ES	CASS or DSS	Thrusters	Backup for double DIRA failure. Operation restricted to 6 am / 6 pm + - 1 hr.
Control Safety System	Disable control in emergencies. May be commanded or entered automatically if enabled and under specific conditions.	NONE	NONE	NONE	None	Disable thrusters and hold wheel speeds constant. In ground control, manual thruster firings and wheel speed biases can be commanded.

Figure 9: Attitude Control Modes (Continued)

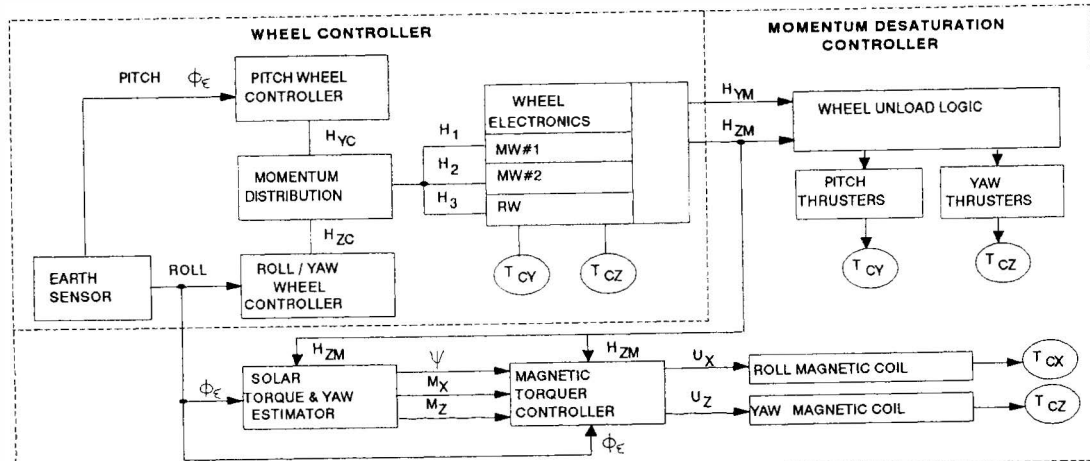


Figure 10: On-Orbit Functional Block Diagram

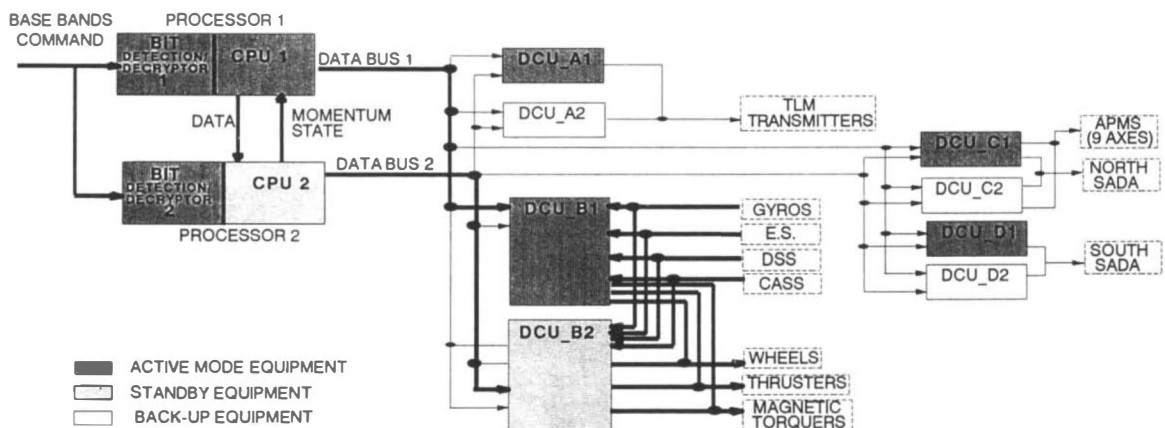


Figure 11: SCE ADCS SHADOW MODE

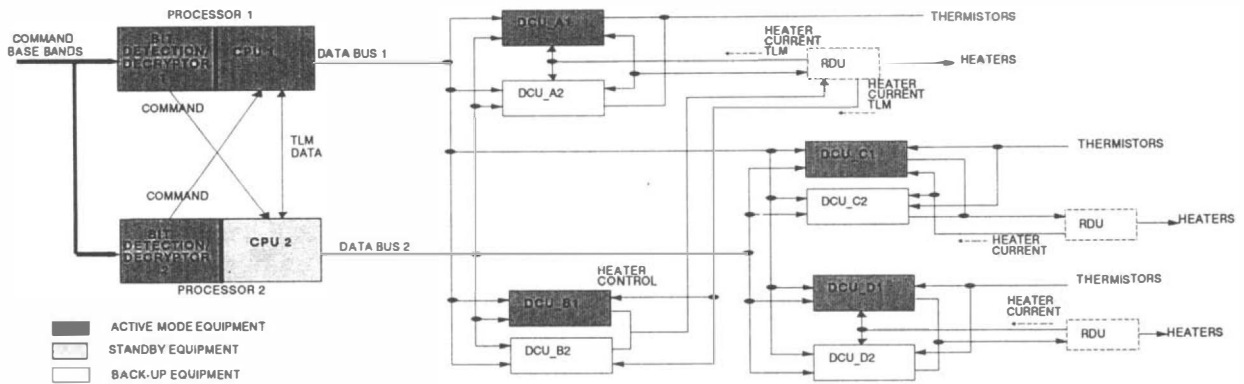


Figure 12: SCE AUTOMATIC THERMAL CONTROL IMPLEMENTATION

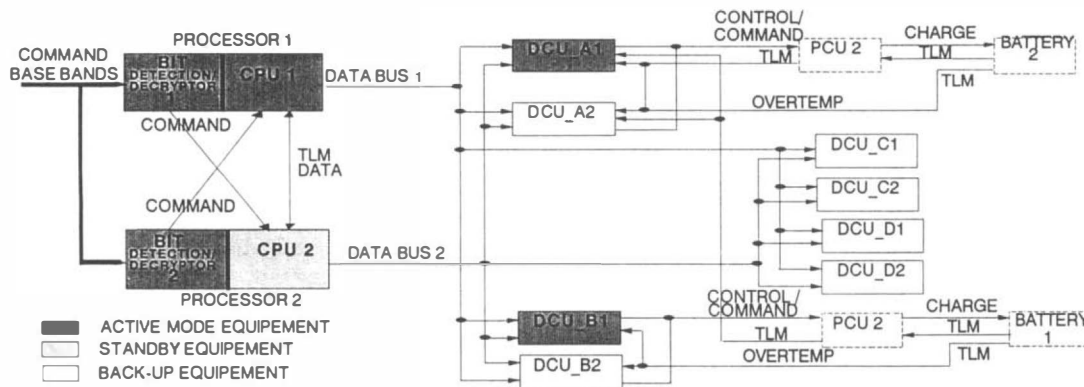


Figure 13: SCE AUTOMATIC BATTERY MANAGEMENT IMPLEMENTATION

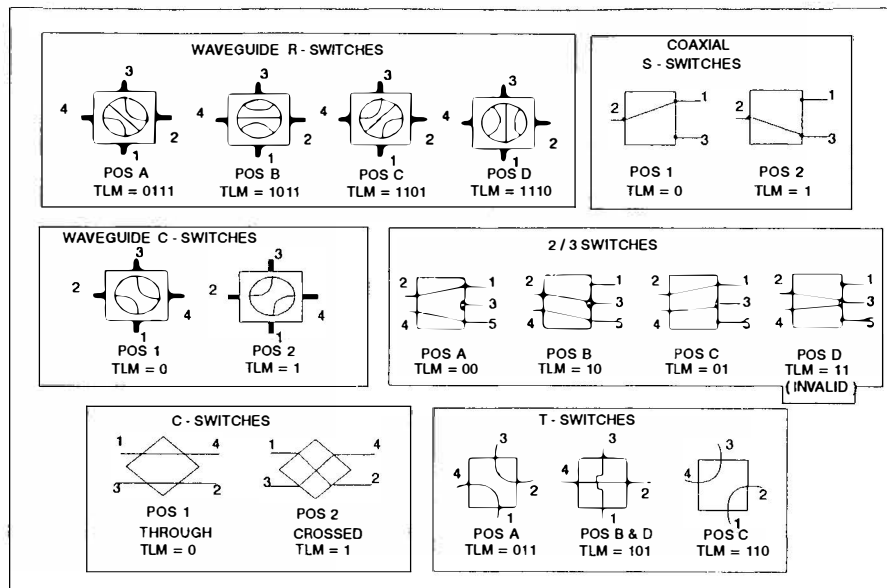


Figure 14: I7 Switches

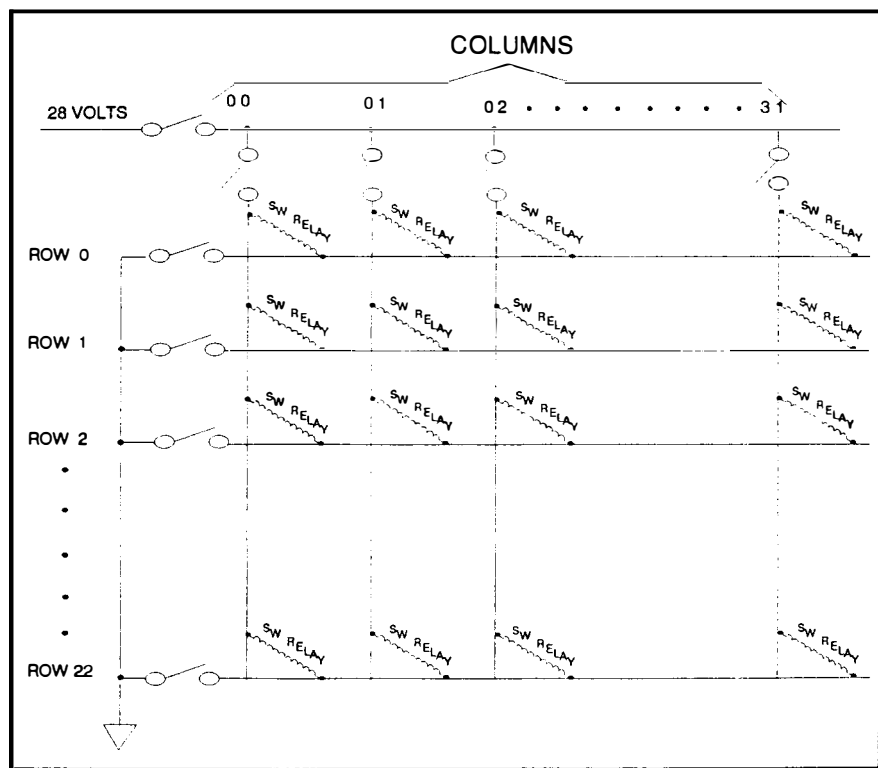


Figure 15: 17 Switch Driver Matrix Concept

# A RE-ENTRY CAPSULE CONTROL SYSTEM DESIGN FOR MICROGRAVITY EXPERIMENTS

A. Cavallo\*, G. De Maria\*, V. De Nicola\*\* and F. Ferrara\*\*

\*Dipartimento di Informatica e Sistemistica, Università degli Studi di Napoli "Federico II",  
Napoli, Italy  
\*\*Alenia Spazio S.P.A., Napoli, Italy

**Abstract.** CARINA is a new retrievable unmanned capsule designed by ALENIA SPAZIO under ASI (Agenzia Spaziale Italiana) contract. This paper deals with the operative attitude acquisition phase and the operative phase of its life cycle. In the operative phase the control system must assure microgravity requirements. Two different type of actuators are used for the two different phases: 20N hydrazine thrusters for the first, magnetic coils and a reaction wheel for the second, and, consequently, two control systems techniques are used. The former is based on a new discrete time modeling of the system due to the PWM-like behaviour of the thrusters and results in a discrete controller able to guarantee robustness against parameter uncertainties. The latter is a scheduling technique based on a LQR approach and guarantees the fulfilling of microgravity requirements. All the simulations, performed on the ESA-MIDAS dynamics simulator, take into account atmospheric drag, solar pressure and gravity gradient disturbances, and show the effectiveness of the adopted approach.

**Keywords.** Attitude and orbit control, Aerospace control, Guidance, Satellite control, Modeling.

## INTRODUCTION

The growing interest in microgravity processing aspects and both the need to answer to specific user's requirements and to organize flexible preparatory programs to the intensive utilization of large platforms or space stations, lead to the decision to develop autonomous systems with recovery capabilities. In this scenario ALENIA SPAZIO is studying, under ASI (Agenzia Spaziale Italiana) contract, a new retrievable unmanned capsule: CARINA.

The capsule life cycle can be divided into six phases, each with its own operative modes (Borriello and Ricciardi, 1991): 1) pre-launch phase; 2) launch phase; 3) operative attitude acquisition phase; 4) operative phase; 5) re-entry phase; 6) recovery phase. The operative modes are illustrated in Fig.1.

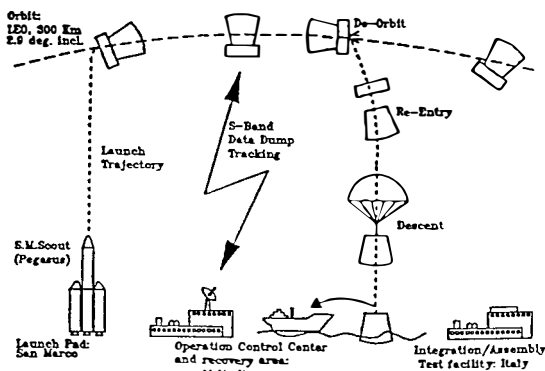


Fig. 1. CARINA mission scenario.

This paper deals with phases 3 and 4.

Phase 3 foresees the residual angular momentum reduction (despin), attitude acquisition by means of sun sensors and Earth sensor, and attitude manoeuvres in order to achieve the correct attitude for the beginning of phase 4. The actuators used during phase 3 are eight 20 N hydrazine thrusters.

The phase 4 has a nominal duration of 5 days with the capsule in a circular Low Earth Orbit (300 km) nearly equatorial (inclination 2.9°).

In order to assure the microgravity level requirements:

$10^{-5}$  g from 0 to 100 Hz,  $10^{-3}$  g above 100 Hz, a solution which foresees magnetic coils ( $100 \text{ As}\cdot\text{m}^2$  at the most) and a reaction wheel ( $10 \text{ mN}\cdot\text{m}$  at the most) has been examined.

Both the actuation systems considered exhibit peculiarities. The Hydrazine thrusters are ON/OFF devices with a fixed level of thrust and with a Minimum Impulse Bit which causes limit cycles. Magnetic coils and reaction wheels provide very low torque levels (about  $2 \text{ mN}\cdot\text{m}$ ). Such torques must be used in order to guarantee the microgravity requirements and the correct attitude towards the Earth for communication link. Moreover the closed-loop system must be robust with respect to environmental disturbances such as atmospheric drag and solar pressure.

In this paper the system (actuator plus plant) during phase 3 is modeled by a discrete time transfer function by using an approach based on the theory of PWM, with the pulselwidth playing the role of the control signal. This model enables the application of the classical linear control engineering to the design of a digital position servo.

As concerns phase 4, a different control strategy is adopted. Since magnetic coils and a reaction wheel are used, a continuous time model of the capsule dynamics is considered.

The controller has been designed by using a suitable gain scheduling strategy based on an LQR-type technique.

Simulations have been carried out by using the dynamics simulation code ESA-MIDAS, taking into account the environmental disturbances as atmospheric drag, solar pressure and gravity gradient.

## REFERENCE FRAMES AND CONFIGURATION OF CARINA CAPSULE.

In the following we will refer to three reference frames (Agrawal, 1986). The first one is the inertial reference  $X_0, Y_0, Z_0$  with the axes origin in the Earth's center (Fig. 2).

Another reference system used in the control system description during the operative phase, is the orbital frame X, Y, Z. The origin of this frame is the satellite center of mass (Fig. 2). The Z axis is parallel to and positive in the same direction of the vector joining the satellite center of mass to the Earth's center. The Y axis is normal to the satellite orbital plane and

positive towards the south. The X axis completes the right-handed orthogonal triad. This coordinate system is rotating about the Y axis, at the orbital rate of  $\omega_0$  rad/s. The last reference system used is the body reference system that, for the sake of simplicity, is taken coincident with the system of principal axes of inertia of the capsule. We utilize the Euler angles to define the attitude of the satellite with respect to the inertial or the orbital axes. The sequence of rotation used is z-y-x, and the rotation angles are indicated with  $\psi$ ,  $\theta$  and  $\phi$  respectively.

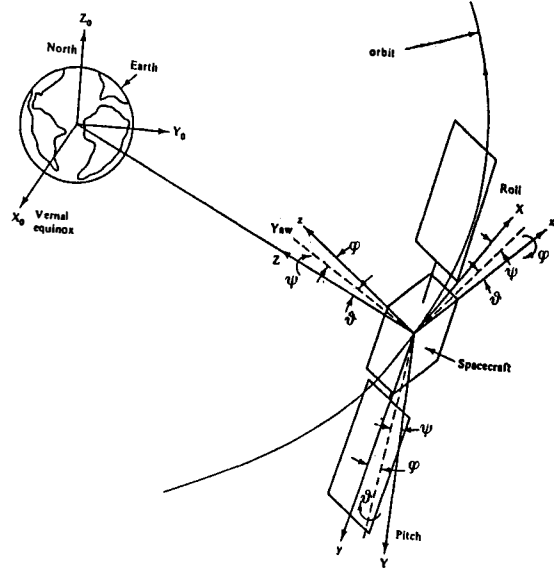


Fig. 2. Reference frames.

The present nominal configuration of the CARINA system is composed of two main parts (Borriello and Ricciardi, 1991):

- a re-entry vehicle (REV) being an Apollo/Gemini like capsule,
- an expendable service vehicle (SV) that provides resources to the overall system.

The REV supplies the accommodation to the payload and to the other subsystems performing functions strictly for the re-entry phase. The SV accommodates the propellant tank, batteries, thrusters for attitude control and sensors of the AOCS subsystem. The reference configuration is shown in Fig. 3. The total system mass is of 454 kg and the inertia moments are:  $I_{xx}=67 \text{ kg}\cdot\text{m}^2$ ,  $I_{yy}=I_{zz}=152 \text{ kg}\cdot\text{m}^2$ .

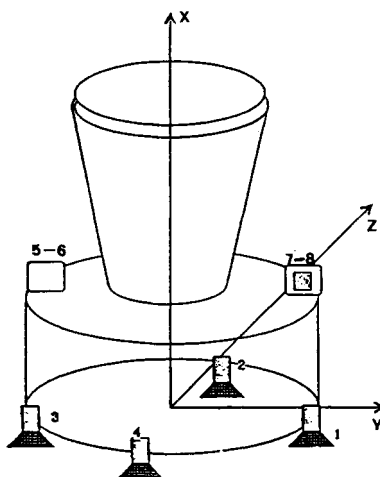


Fig. 3. Capsule configuration.

The actuators used to control the capsule during all the mission's phases, except during the operative phase, are hydrazine thrusters. This propulsion system is a hot gas system using hydrazine ( $N_2H_4$ ) as propellant. The hydrazine is stored in a diaphragm tank con-

taining also the pressuring gas (nitrogen). The hydrazine pressuring avoids sloshing in the tank which can disturb the microgravity during the operative phase. In Fig. 3 is visible the allocation of the eight 20 N thrusters and the propellant tank of the CARINA capsule. During phase 3 all the eight thrusters are used to obtain torques along the three axes of the capsule with arms of about 0.5 m. During the re-entry phase the four thrusters placed on the bottom plate are used in order to perform the necessary  $\Delta v$  manoeuvre.

During the operative phase we use as actuators two magnetic coils for yaw and roll control and a reaction wheel for pitch control. These actuators can be allocated in the SV. Coils can be wrapped along the inside wall of the SV in such a way to produce dipole moment along the body axes x and z; the wheel must be mounted on passive isolators to guarantee the  $\mu g$  environment in the SV with its spin axis along the y body axis.

#### PHASE 3: DESPIN.

Phase 3 starts with the residual angular momentum reduction.

In this phase we assume that flexibility of the capsule can be neglected. This assumption is valid when the control algorithm avoids excitation of flexible modes of the structure, i.e. generates frequencies well below the lowest resonance frequency, which is about 28 Hz. Then the rigid body dynamics equations with respect to the principal axes of inertia can be written as follows

$$\begin{aligned} T_x &= I_{xx} \dot{\omega}_x + \omega_y \omega_z (I_{zz} - I_{yy}) \\ T_y &= I_{yy} \dot{\omega}_y + \omega_x \omega_z (I_{xx} - I_{zz}) \\ T_z &= I_{zz} \dot{\omega}_z + \omega_x \omega_y (I_{yy} - I_{xx}) \end{aligned} \quad (1)$$

where  $\omega_x$ ,  $\omega_y$ ,  $\omega_z$  are the angular velocities,  $T_x$ ,  $T_y$  and  $T_z$  are the applied torques and  $I_{xx}$ ,  $I_{yy}$  and  $I_{zz}$  are the momenta of inertia.

Since, for the CARINA capsule, the x-axis is the symmetry and spin axis, the first equation in (1) is decoupled from the others. Generally the launcher cannot guarantee that the total angular momentum is aligned with the symmetry axis, then the despin phase does not only concern the velocity reduction about the x-axis, but also the reduction of the residual velocities about y and z-axes.

The first step is to reduce  $\omega_x$  and, being  $I_{zz}=I_{yy}$ , the first equation becomes  $T_x = I_{xx} \dot{\omega}_x$ . After this step  $\omega_x \approx 0$  and then also the remaining two equations can be considered purely inertial.

The actuators used in this phase are 20N hydrazine thrusters. These are typical ON/OFF devices characterized by a Minimum Impulse Bit (MIB) of 0.6 N·s. By considering the thrust level constant during the firing phase the MIB determines a minimum ON-time  $s_{min} = 0.03s$ .

Moreover there is a limitation on the OFF-time of 50 ms when the actuator works in off-modulation and of 500 ms in pulse-mode.

The characteristics of the selected actuators lead to a discrete time description of the Attitude and Orbit Control System (AOCS) which uses a sampling time  $T=1s$ . The modulation of the thrust is obtained by using a PWM (Pulse Width Modulation) technique. The PWM input ( $s \leq T$ ) is the width of the thrust time interval, the output is the thrust profile applied to the spacecraft. Taking into account the MIB characteristic of hydrazine thrusters, the block-diagram of the single axis open-loop system is represented in Fig. 4

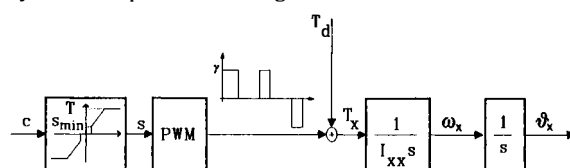


Fig. 4. x-axis open-loop system with actuators

where  $T_d$  represents external disturbances (atmospheric drag, solar pressure and gravity gradient) and the effects of the coupling among the axes, and  $\gamma$  is the torque applied to the capsule. The continuous system is described, in space state form, by

$$\dot{\mathbf{x}} = \mathbf{A} \mathbf{x} + \mathbf{b} T_d \quad (2)$$

where  $\mathbf{x} = (\theta_x \ \omega_x)^T$  and

$$\mathbf{A} = \begin{pmatrix} 0 & 1 \\ 0 & 0 \end{pmatrix}; \quad \mathbf{b} = \begin{pmatrix} 0 \\ \frac{1}{I_{xx}} \end{pmatrix}. \quad (3)$$

The discrete time description of the system in Fig. 4 can be easily obtained from (2)-(3). The input  $T_d(t)$  is the constant value  $\gamma$  [N·m] for the fraction  $|s|/T$  of each period, and zero for the remainder of each period. The pulselwidth is the magnitude of the control signal and is, therefore, positive. Negative control signals lead to negative torque. Then for each period we obtain

$$\mathbf{x}((k+1)T) = \exp(AT)\mathbf{x}(kT) + \int_{kT}^{kT+|s(k)|} \exp(A((k+1)T-\tau))\mathbf{b}\gamma sgn(s(k))d\tau \quad (4)$$

Rearranging eqn. (4), taking into account that from (3)

$$\exp(AT) = \mathbf{I} + AT \quad (5)$$

we obtain ( $T=1$  s)

$$\mathbf{x}(k+1) = \begin{pmatrix} 1 & 1 \\ 0 & 1 \end{pmatrix} \mathbf{x}(k) + \begin{pmatrix} 1 \\ 1 \end{pmatrix} \frac{\gamma}{I_{xx}} s(k) - \begin{pmatrix} 1 \\ 0 \end{pmatrix} \frac{\gamma}{2I_{xx}} |s(k)| s(k) \quad (6)$$

As the despin and rate damping phase is concerned we consider only the second equation of (6), which is linear in  $s(k)$  and decoupled from the first equation. Then a very simple controller can be designed in this phase. As in the performed manœuvres the axes can be considered decoupled, the model (2)-(3) is still valid for  $y$  and  $z$  axes.

Denoting with  $K_{vx}$ ,  $K_{vy}$  and  $K_{vz}$  the feedback velocity gains, the following values have been selected

$$K_{vx} = 1.675, \quad K_{vy} = K_{vz} = 3.8. \quad (7)$$

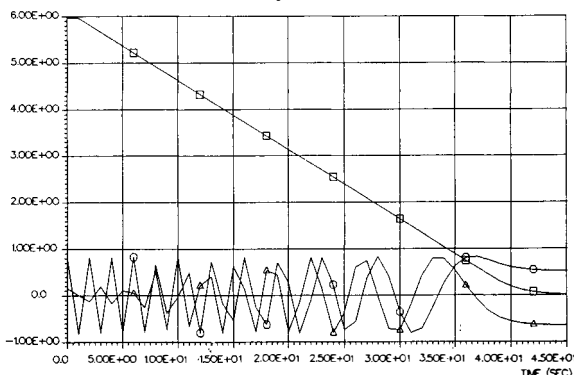


Fig. 5. Angular rates (despin).

In Fig. 5 the despin phase is depicted. From launcher specs the spin velocity about the  $x$ -axis is about 60 rpm and in the worst case about 6 rpm about the other axes. As it is shown in Fig. 5 only the  $x$ -axis is controlled. At the end of despin phase, residual angular velocities on  $y$  and  $z$  axes of about 5 rpm and -6.7 rpm, respectively, are obtained.

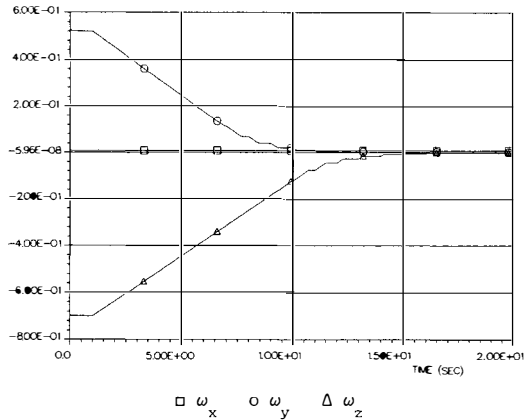


Fig. 6. Angular rates (rate damping phase)

In Fig. 6 the rate damping phase is illustrated. All the axes are controlled. Due to MIB characteristic of hydrazine thrusters, we have at steady state a limit cycles whose amplitudes are, for each axis:

$$\omega_x = 8.7 \cdot 10^{-3} \text{ rad/s}; \quad \omega_y = \omega_z = 3.3 \cdot 10^{-3} \text{ rad/s} \quad (8)$$

#### PHASE 3: OPERATIVE ATTITUDE ACQUISITION

Attitude acquisition is necessary for the CARINA system to assure the correct position with respect to both the trajectory and the Earth, before the beginning of the operational phase.

During this phase a sequence of rotations will be performed to acquire the desired attitude. Also in this phase, in order to decouple the rotational axes, we perform separate rotations on the  $x$ -axis, first, and then on  $y$  and  $z$  axes jointly. Then the discrete time model for each axis is that in eqn. (6).

Since during the attitude acquisition phase  $|s(k)|$  is well below  $T$ , due to a suitable selection of the controller, then in eqn. (6) we can retain only the linear term in  $s(k)$  and consider the square term in  $s(k)$  as a disturbance. Moreover we suppose that the computing time of the control signal can be neglected with respect to the sampling time  $T=1$  s.

The controller design can be accomplished by using a reference model which determines the desired attitude for each axis. We select the following model, which is referred, for the sake of simplicity, to the rotation about the  $x$ -axis:

$$\hat{\mathbf{x}}(k+1) = \begin{pmatrix} 1 & 0 \\ 0 & \lambda_2 \end{pmatrix} \hat{\mathbf{x}}(k) + \begin{pmatrix} 0 \\ 1 \end{pmatrix} w(k) \quad (9)$$

By denoting with  $e(k)$

$$e(k) = \mathbf{x}(k) - \hat{\mathbf{x}}(k) \quad (10)$$

and selecting

$$s_x(k) = \frac{I_{xx}}{\gamma} [(\lambda_2 - 1)x_2(k) + w(k)] \quad (11)$$

and

$$w(k) = (\lambda_1 - 1)e_1(k) \quad (12)$$

we obtain

$$e(k+1) = \begin{pmatrix} \lambda_1 & 0 \\ 0 & \lambda_2 \end{pmatrix} e(k) + \begin{pmatrix} \lambda_2 \\ 0 \end{pmatrix} x_2(k) \quad (13)$$

Then to design a stable closed-loop system it is sufficient to select  $\lambda_1$  and  $\lambda_2$  in order to guarantee the stability of the following system

$$\begin{pmatrix} e_1(k+1) \\ e_2(k+1) \\ x_2(k+1) \end{pmatrix} = \begin{pmatrix} \lambda_1 & 0 & \lambda_2 \\ 0 & \lambda_2 & 0 \\ (\lambda_1 - 1) & 0 & \lambda_2 \end{pmatrix} \begin{pmatrix} e_1(k) \\ e_2(k) \\ x_2(k) \end{pmatrix}. \quad (14)$$

Wide ranges of  $\lambda_1$  and  $\lambda_2$  inside the unit circle guarantee asymptotic stability of system (14). In order to avoid oscillating modes we select  $\lambda_1$  and  $\lambda_2$  such that the eigenvalues of the matrix in (14) are real and positive. Such an approach leads to a robust closed-loop system with respect to inertial and propulsive parameter uncertainties ( $I_{xx}$  and  $\gamma$ ). The stability robustness of dynamic system (14) has been tested by using the *boundary representation Theorem* (Cavallo, Celentano and De Maria, 1991). Space limitations does not allow us to prove the above statement.

For each axis we have selected

$$\lambda_1 = 0.98, \lambda_2 = 0.5. \quad (15)$$

In order to lower the amplitude of the limit cycle, due to the MIB, at steady state we select a lower value for  $\lambda_1$ :  $\lambda_1 = 0.8$ .

The actual controller results more complex than the one here proposed. Indeed, sensor data filtering and sensor signal conditioning are necessary to obtain the controller input illustrated, moreover high priority commands from ground stations or other on-board subsystem must be taken into account. Then it is realistic to introduce a sample period delay in the discrete time model. It is very simple to reformulate the problem in this case as above, obtaining a higher order system than (14), and to show that the same values of  $\lambda_1$  and  $\lambda_2$  (15) guarantee the stability of the closed-loop system.

In Fig. 7 and 8 angular positions and rates, respectively, are depicted for a single axis rotation of  $\pi$  rad. The simulations have been performed taking into account a sample period delay in computing the control signal, by using ESA-MIDAS detail simulator.

In Fig. 9 the pulse-width  $s(t)$  is depicted. The values of  $s(t)$  confirm that the term  $s(k)|s(k)|$  is negligible.

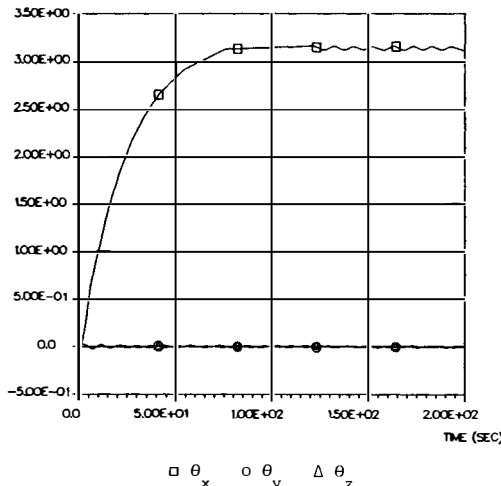


Fig. 7. Angular rotation about x-axis.

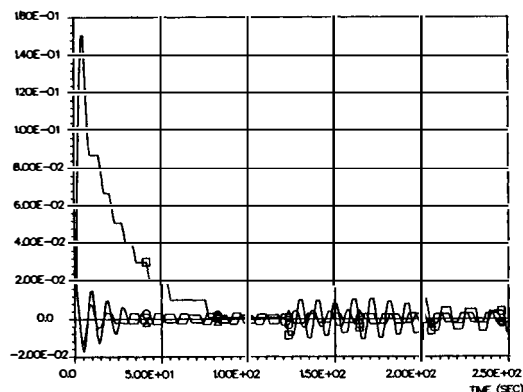


Fig. 8. Angular rates.

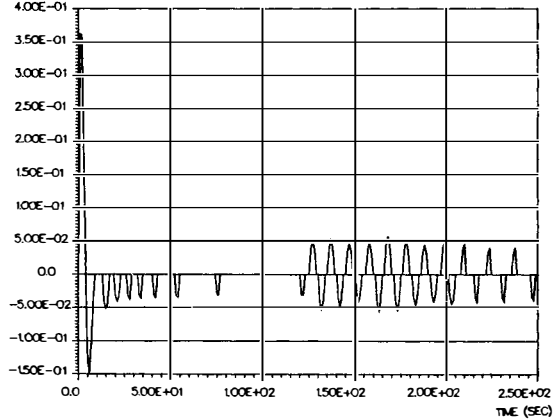


Fig. 9. Pulsewidth.

#### PHASE 4: OPERATIVE PHASE

In this phase the capsule control system has to guarantee the  $\mu g$  level requirements and the pointing of the antenna toward the ground station. This can be achieved regulating to zero the Euler angles between the orbiting frame and the body axes with the capsule nose in the upwind direction. Note that in this attitude the aerodynamic torques have a stabilizing effect due to the capsule shape.

The x and the z body axes (roll and yaw axes respectively) are controlled by magnetic coils as to produce dipole momenta that interacting with the Earth magnetic fields produce torques along the z and x axes. The y body axis (pitch axis) is controlled by a reaction wheel having the spin axis aligned with y (Collins and Bonello, 1973).

The control strategy adopted in this phase is based on a continuous time model of the capsule dynamics. We will show that the model can be written as

$$\dot{x} = A(x) x + B(x) u \quad (16)$$

where  $x = (\phi, \theta, \psi, \dot{\phi}, \dot{\theta}, \dot{\psi})^T$  is the vector of Euler angles and their derivatives and  $u = (A_x, V_y, A_z)^T$  where  $A_x, A_z$  are the dipole momenta along the x and z body axes respectively, and  $V_y$  is the input wheel voltage.

Eqn (16) can be derived from (1) as follows (Kaplan, 1976; Cornellisse, 1979):

$$\begin{pmatrix} \omega_x \\ \omega_y \\ \omega_z \end{pmatrix} = \begin{pmatrix} 1 & 0 & -\sin\theta \\ 0 & \cos\phi & \cos\theta \cdot \sin\phi \\ 0 & -\sin\phi & \cos\theta \cdot \cos\phi \end{pmatrix} \begin{pmatrix} \dot{\phi} \\ \dot{\theta} \\ \dot{\psi} \end{pmatrix} - \begin{pmatrix} \cos\theta \cdot \sin\psi \\ \cos\phi \cdot \cos\psi + \sin\phi \cdot \sin\theta \cdot \sin\psi \\ -\sin\phi \cdot \cos\psi + \cos\phi \cdot \sin\theta \cdot \sin\psi \end{pmatrix} \quad (17)$$

for a sequence of rotation z-y-x of  $\psi, \theta$  and  $\phi$  respectively.

$$\begin{pmatrix} T_x \\ T_y \\ T_z \end{pmatrix} = T_a + T_g \quad (18)$$

where  $T_g$  is the gravity gradient torque and  $T_a$  is the torque due to magnetic coils and reaction wheel.

$$T_g = 3 \omega_0^2 \begin{pmatrix} (I_{zz} - I_{yy}) \sin\phi \cdot \cos\phi \cdot \cos^2\theta \\ (I_{zz} - I_{xx}) \sin\theta \cdot \cos\theta \cdot \cos\phi \\ (I_{yy} - I_{xx}) \sin\theta \cdot \cos\theta \cdot \sin\phi \end{pmatrix} \quad (19)$$

From (1) and (17)–(19) we obtain

$$J(\xi)\dot{\xi} = -C(\xi, \dot{\xi}) - D(\xi)\dot{\xi} + E(\xi)\xi + T_a \quad (20)$$

where  $\xi = (\phi, \theta, \psi)^T$ , the matrix

$$C(\dot{\xi}, \ddot{\xi}) = C(\xi) \begin{pmatrix} \dot{\phi}^2 \\ \dot{\phi}\theta \\ \vdots \\ \dot{\psi}^2 \end{pmatrix} \quad (21)$$

takes into account Coriolis and centrifugal torques,  $J(\xi)$  is the total matrix of inertia,  $D(\xi)$  denotes torques depending on gyroscopic effects and  $E(\xi)$  torques depending on gravity gradient and attitude effects.  $T_a$  is the vector of applied torques and can be written as

$$T_a = \begin{pmatrix} 0 & 0 & -B_y \\ -B_z & K_w & B_x \\ B_y & 0 & 0 \end{pmatrix} \begin{pmatrix} A_x \\ V_y \\ A_z \end{pmatrix} = T_{BW}(\xi) \begin{pmatrix} A_x \\ V_y \\ A_z \end{pmatrix} \quad (22)$$

where  $K_w$  denotes the reaction wheel torque constant and  $(B_x, B_y, B_z)^T$  denotes the Earth-magnetic field expressed in body axes (Wertz, 1986).

By using the notations

$$E'(\xi) : E'(\xi)\xi = E(\xi) \quad (23)$$

$$Z^T(\dot{\xi}) = \begin{pmatrix} \dot{\phi} & 0 & 0 & 0 & 0 & 0 \\ 0 & \dot{\phi} & 0 & \dot{\theta} & 0 & 0 \\ 0 & 0 & \dot{\phi} & 0 & \dot{\theta} & \dot{\psi} \end{pmatrix} \quad (24)$$

$$\bar{B}(\xi) = J^{-1}(\xi) \quad (25)$$

the matrices  $A(x)$  and  $B(x)$  can be written as follows

$$A(x) = \left( \begin{array}{c|c} 0_{3 \times 3} & I_3 \\ \bar{B}(\xi) E'(\xi) & -\bar{B}(\xi) [C(\xi) Z(\dot{\xi}) + D(\xi)] \end{array} \right) \quad (26)$$

$$B(x) = \left( \begin{array}{c|c} 0_{3 \times 3} & \\ \bar{B}(\xi) T_{BW}(\xi) & \end{array} \right). \quad (27)$$

The control strategy adopted in this phase has been the following.

Select a set of points  $\xi^{(i)}$ ,  $i=1, \dots, n$  in a neighborhood of the desired attitude  $\xi=0$ . Such a selection defines a corresponding sequence of linear models

$$\dot{x} = A^{(i)}x + B^{(i)}u, \quad i=1, \dots, n \quad (28)$$

where

$$A^{(i)} = A(x^{(i)}), \quad B^{(i)} = B(x^{(i)}), \quad x^{(i)} = \begin{pmatrix} \xi^{(i)} \\ 0 \end{pmatrix}. \quad (29)$$

Note that, due to the small values of control signals and to the slow dynamics of the system, the angular rates  $\dot{\xi}^{(i)}$  can be neglected.

For each linear model an LQR controller has been designed. Finally a gain scheduling strategy has been adopted to select the appropriate controller at each step.

Simulations performed by using the ESA-MIDAS dynamic simulator (Figs. 10, 11), taking into account atmospheric drag, solar pressure and gravity gradient disturbances, show that such an approach guarantees the desired attitude acquisition fulfilling  $\mu g$  specs (Fig. 12).

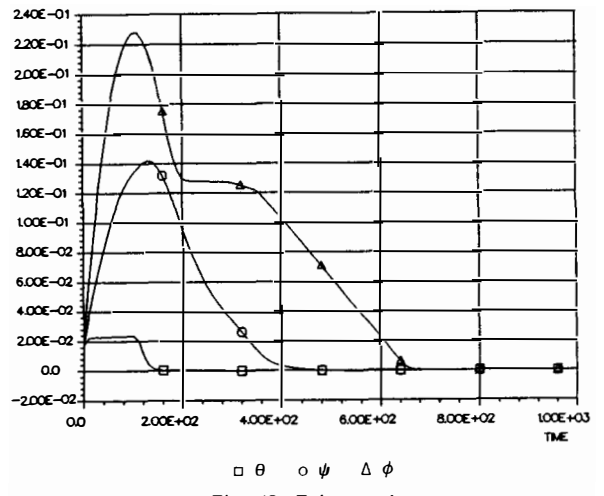


Fig. 10. Euler angles

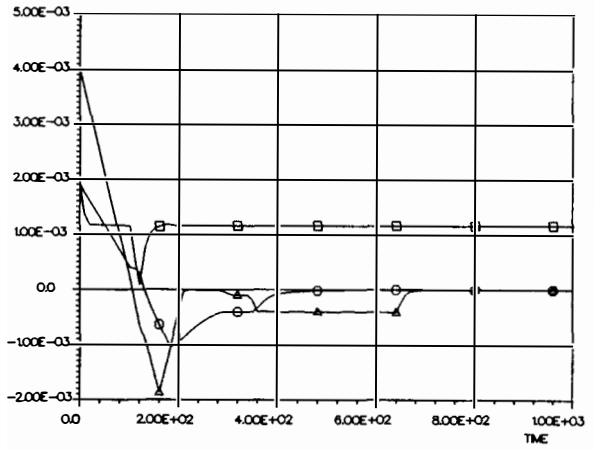


Fig. 11. Euler rates.

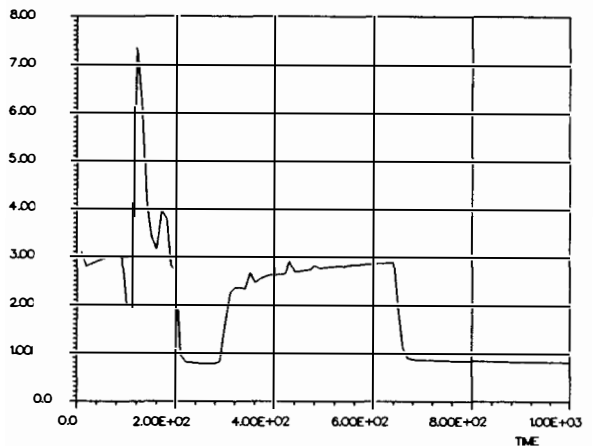


Fig. 12.  $\mu g$  level

## CONCLUSIONS

In this paper two different control strategies for two phases of the CARINA satellite mission have been presented.

The first one is based on a new discrete time approach to the design of controllers of satellites driven by thrusters, and exhibits robustness properties with respect to parametric uncertainties.

The second control policy uses a gain scheduling stra-

tegy based on a LQR-type technique to achieve accurate attitude and fulfill  $\mu g$  specs.

Two approaches have been studied for the CARINA project. In this paper the one that uses two magnetic coils and a reaction wheel has been presented. However the baseline of the CARINA program is to use three magnetic coils and a gravity boom. This configuration is the result of an economical trade-off.

Work in progress deals with the control signal limitations in this latter phase and is based on non-linear control techniques.

#### REFERENCES

- Agrawal, B. N. (1986). *Design of geosynchronous space-craft*. Prentice-Hall, London.
- Borriello, G. and Ricciardi, A. (1991). Technological development of an Italian re-entry capsule: CARINA. *Tech. Report ALENIA SPAZIO S.p.A.*
- Cavallo, A., Celentano, G. and De Maria, G. (1991). Robust stability analysis of polynomials with linearly dependant coefficients perturbations. *IEEE Trans. on Autom. Contr.*, AC-36.
- Collins, D.H. and Bonello, D.P.(1973). An attitude control system for Earth observation spacecraft. *AIAA Paper 73-854*, Key Biscayne, Fla.
- Cornellisse, J.W., (1979). *Rocket propulsion and space-flight dynamics*. Pitman Publish. London.
- Kaplan, M.H. (1976). *Modern spacecraft dynamics and control*. John Wiley & Sons, New York.
- Wertz, J. (1986). *Spacecraft attitude determination and control*. Reidel Pub. Comp., Dordrecht.

## ARIANE 5 DYNAMICS AND CONTROL

H. Klotz

*MBB/ERNO, Bremen, Germany*

### 1 Introduction

Along with the development of the ARIANE 5 launcher, as a support task to the Industrial Architect, a number of activities related to dynamics and control have been performed by MBB/ERNO, which can be grouped as follows, according to their different nature:

- Dynamic/kinematic analyses
- Definition of on-board control algorithms
- Development of a simulation program

The dynamic and kinematic analyses pertain to transition phases of the launcher, in particular lift-off, stage separation, as well as separation of payloads and supporting structures.

Control algorithms had to be defined for the operation of the upper stage, from burn-out until release of the last payload.

Finally, a dedicated program was developed for the simulation of the whole payload release phase, serving as a test bed for the on-board control algorithm.

This paper deals with the first two topics given above, describing the related activities and relevant results.

### 2 Dynamic Analyses

This section describes the activities related to the dynamic and kinematic analysis of transition phases of the launcher. These are, in the order of their occurrence during the mission:

- the lift-off phase, comprising the first six seconds after ignition,
- the separation between the lower stage and the upper composite (propulsive stage with payloads)
- the payload release phase, comprising the separation of up to three payloads, and of the supporting structures between the payloads.

The first and the last task are characterised by a high amount of statistical analysis. This was imposed by the respective requirements, which were formulated in terms of probabilities. The fact that for this purpose extensive Monte-Carlo simulations had

to be performed prohibited the use of general-purpose simulation tools. Instead, dedicated, custom-tailored simulation tools had to be developed.

The second task, instead, is more related to feasibility and optimization.

#### 2.1 Lift-Off Analysis

The major objective of the detailed analysis of the lift-off process was to verify that, under various wind conditions, and under consideration of the range of variation of various parameters, sufficient clearance is always available between the launch tower or platform on one hand, and the launcher on the other hand.

For this purpose, the lift-off process was simulated in detail, beginning with the ignition commands to the boosters, and ending when the launcher had reached an altitude of about 100 m.

For the simulation, effects of the following items had to be considered:

- Wind profile, i.e. wind velocity dependent on wind direction
- Aerodynamic properties of the launcher, considering also the effect of the launch equipment
- Elastic properties of the launcher (two bending modes) and their impact on measurement system and thrust application points
- Friction between booster skirts and platform
- Booster gimbal dynamics and gimbal control loop parameters
- Additional use of main engine gimbal for control

Clearance was analysed with regard to

- the booster nozzles in their platform holes
- the launcher with respect to tower, pylons and ropes
- some connectors to their sockets during the first centi- or decimeters

The study had to consider the variation of the nominal values within their ranges of uncertainty as well as the statistical variation of parameters described by their respective dispersions. Therefore the following approach was applied for the investigations:

First the nominal values to be used in the analyses had to be defined for those quantities subject to uncertainties, following the given requirements together with all available input data. This was achieved by impact assessments and a worst case analysis. With the resulting nominal data set, the following detailed analyses were performed:

- Sensitivity analysis, considering the influence of each individual input parameter on each output parameter
- Statistical analysis, considering the statistical distribution of the input parameters and evaluating statistically the output parameters, and
- Failure case analysis.

The approach used in the statistical analysis for the determination of envelopes is essentially the following: Within every simulation run, and for every altitude step, the clearance for the object under consideration - e.g. a booster nozzle - is determined in that way that the point of this object which comes closest to the forbidden region is identified, and the distance is taken as the clearance value. For the statistical evaluation, the values resulting from each calculation are sorted into sectors. Then for each sector the value with the required probability level is determined and taken as a point on the envelope.

In the following, some typical results of the statistical analysis are presented. Figure 1 shows a 3D-plot of the envelope of the nozzle, while in Figure 2 the clearance to the nozzle is shown for the worst case direction. Correspondingly, Figure 3 provides the large scale (up to 100m) envelope of the launcher. Finally, in Figure 4, the intersection of this envelope with the plane containing the launch tower is shown (with different margins).

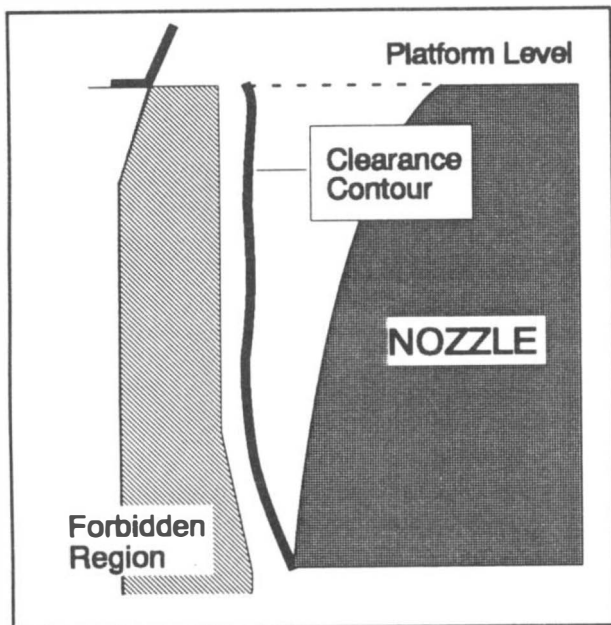


Figure 1: Envelope of nozzle in platform hole

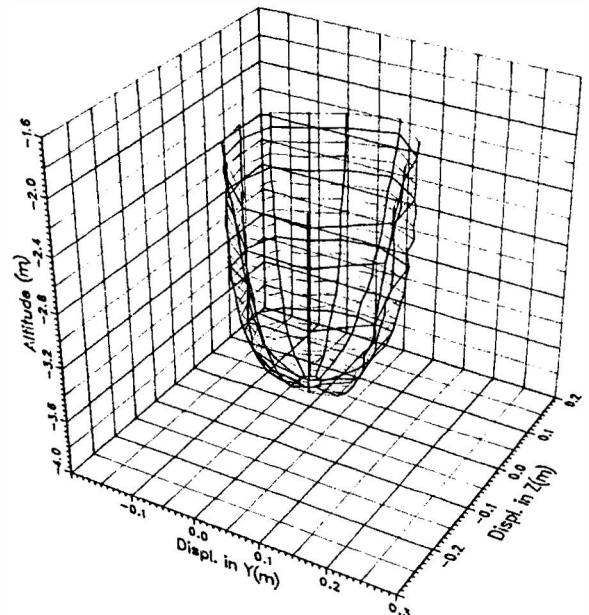


Figure 2: Worst case clearance contour

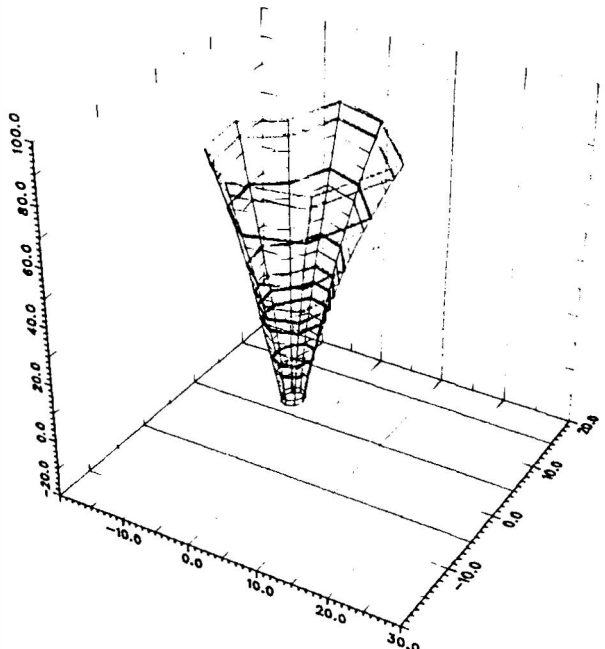


Figure 3: Large scale envelope

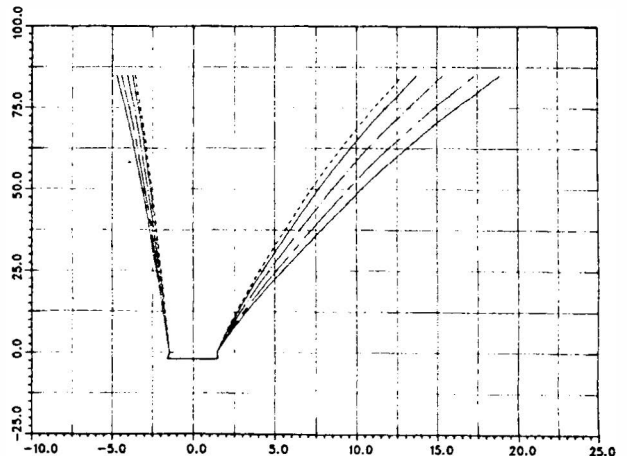


Figure 4: Clearance to tower

## 2.2 Stage Separation

This section deals with the investigation of the separation between the lower stage (EPC) and the upper composite (EPS + payloads). In this context, a very specific problem had to be solved, which has the following background:

After burn-out of the EPC main engine, proper separation of the upper stage is supported by ignition of separation rockets attached to the EPS. After separation, the rocket plume impingement generates a negative acceleration of the lower stage; the same effect occurs upon ignition of the EPS main engine, after burn-out of the separation rockets, at some distance from the lower stage. This in turn effects a migration of the residual propellants from the bottom to the top of the respective propellant tank. However, due to operational reasons, sloshing of propellant to the top of the tank has to be prevented, in order to avoid clogging of pressure ducts and thus jeopardizing a later reuse of the pressurisation system for deorbitation of the lower stage.

As a countermeasure for the propellant migration, auxiliary longitudinal thrusters are available on the lower stage.

The dynamics of the separation process can be controlled by the choice of essentially two free parameters, i.e.

- the time of physical separation (after ignition of separation rockets),  $t_{sep}$ , and
- the ignition time of EPS main engine,  $t_{ON}$

The above limitation must also hold in case of failure of one separation rocket. Such a failure will lead to a rotational motion around a transversal axis of the upper composite. In this case it has to be guaranteed, in addition, that clearance requirements between upper and lower stage are not violated.

As an optimisation criterion, a performance index is defined in terms of a mass figure which is linearly depending on  $t_{sep}$  and  $t_{ON}$ , with a penalty, in case of failure, depending non-linearly on the maximum rotation angle of the upper stage.

Thus, the problem to be solved can be formulated as follows:

Find a pair  $[t_{sep}, t_{ON}]$  such that the constraints on propellant migration and clearance are fulfilled, and the loss function is minimised.

Obviously such a problem, without consideration of performance, has either none, one, or an infinity of solutions. In the latter case a unique solution may be found by consideration of performance.

Since the problem could be reduced to a two-dimensional one, a graphic approach was applied for the solution of the optimization problem. For this purpose, the relevant domain of the  $t_{sep}/t_{ON}$ -plane was covered with a grid of about  $20 \times 20$  points.

For the determination of the relevant parameters, two simulation runs had to be performed for each pair of input parameters; one for the nominal and one for the failure case.

Figure 5 shows an example of a 3D plot of the propellant migration in the nominal case. In Figure 6 the principle of optimization is demonstrated. The curves for constant propellant migration (5m and 10m, respectively) intersect with the straight lines for the performance index. The optimum points are then found as the tangent points to the curves of constant propellant migration.

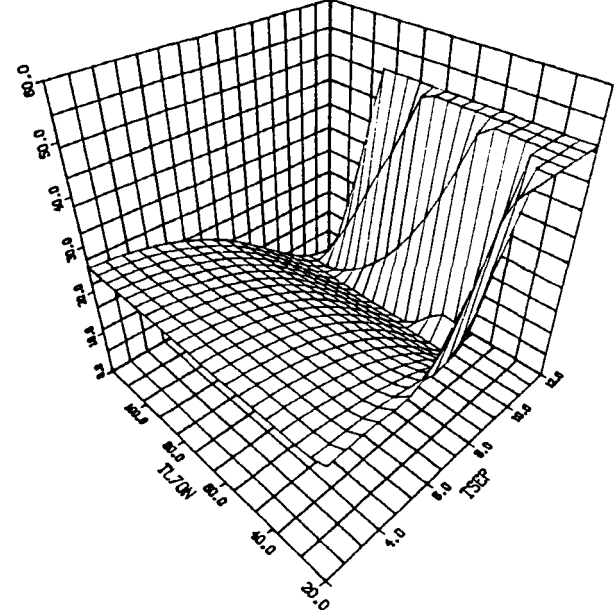


Figure 5: Propellant migration as a function of  $t_{sep}$  and  $t_{ON}$

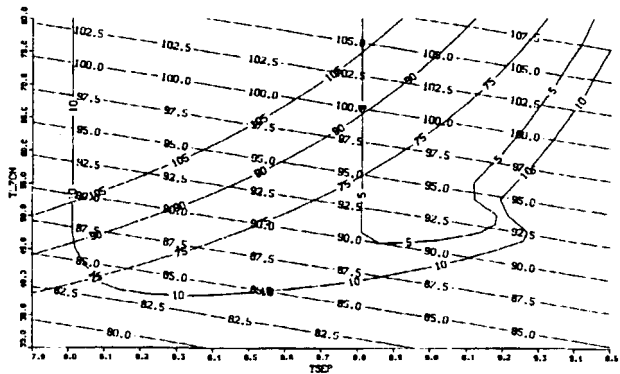


Figure 6: Optimization in the  $t_{sep}/t_{ON}$ -plane

As a consequence of the selected approach, about 800 simulation runs had to be performed per optimisation case. In fact, five different configurations had to be investigated. In addition, for each of these configurations, the number of separation rockets had to be varied (between 2 and 8), as well as the thrust level of the EPC longitudinal thrusters.

Therefore also for this task a dedicated tool was developed for simulation. A major problem was the adaptation of the integration interval while plume impingement forces were effective. This was due to the fact that the impingement force is given as a function of distance and angle, and thus of the system state vector itself. Here a careful optimisation of the

integration interval was necessary, in order to find a compromise between computation time on one hand and required accuracy on the other. Basically, the interval was kept small during plume impingement phases, and enlarged drastically during the coasting phase between burn-out of the separation rockets and the ignition of the EPS main engine.

### 2.3 Payload Separation

This task deals with the detailed investigation of the individual separation processes occurring during the payload release phase. These are, basically:

- the separation of payloads from the remaining upper composite in spinning or three-axis stabilized mode
- the separation of supporting structures between payloads (SPELTRA's) in three-axis stabilised mode

Different payload configurations had to be considered with different mass properties and different numbers of payloads, such that in total 27 different separation processes had to be investigated.

The objectives are dependent on the kind of separation:

For payload separations, requirements on the payload after release had to be checked. These pertain in particular to

- the relative velocity between the separating bodies
- the roll rate error
- the transversal rate (non-spinning case only)
- the roll angle (non-spinning case only)
- the longitudinal axis depointing (non-spinning case only)
- the angular momentum depointing (spinning case only)
- the nutation angle (spinning case only)

For SPELTRA separation, the only requirement to be checked was, besides the relative velocity, the clearance between SPELTRA and the payload below it.

As for lift-off, three types of analyses were performed, i.e. sensitivity analysis, statistical analysis, and failure case analysis.

The simulation of the individual separation processes contains the following model elements:

- Attitude: Non-linear rigid body dynamics
- Relative position: Linearized orbit equations (Clohessy/Wiltshire)
- Separation device:
  - Springs with given force/distance characteristics
  - Spring expansion process is modelled dynamically in detail, and separately for each spring

- Pyro release: Impulsive change of relative velocity and attitude rates.
- Clearance: Check of relative geometry between separating SPELTRA and remaining composite, providing the instantaneous points of closest approach.

Figure 7 shows the geometry used for clearance check. Due to rotational symmetry of SPELTRA and payload envelope, the clearance check can be reduced to a plane problem, after having identified the direction where the closest approach occurs.

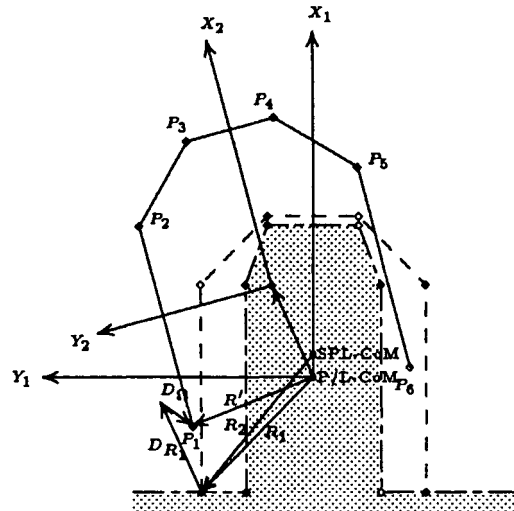


Figure 7: Geometry used for clearance check

In Figure 8, a typical evolution of the clearance vs. time is shown. (The clearance is set to a constant value after the SPELTRA lower edge has left the plane defined by the top of the payload envelope.)

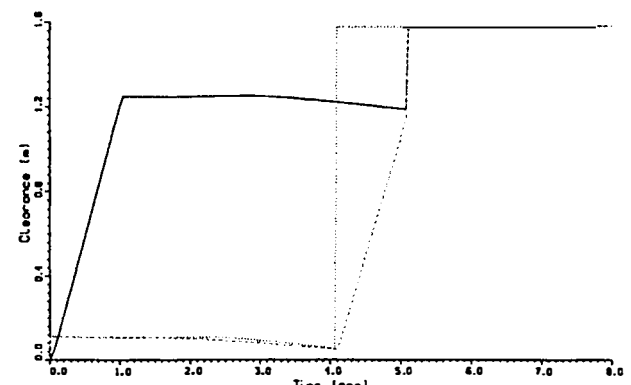


Figure 8: Clearance during SPELTRA separation

For the statistical analysis, the dispersions of the input parameters were given as Gauss or Rayleigh distributions, according to the nature of the quantity considered. Monte-Carlo simulations were applied extensively in order to generate a sufficiently representative set of outputs, allowing for the determination

of a 99% confidence interval. In case that the distribution of an output parameter showed a good correspondence with a known distribution, the confidence interval was determined by interpolation with a best-fit approximation.

This situation is shown for the nutation angle in Figure 9, which can be fairly approximated by a Rayleigh distribution.

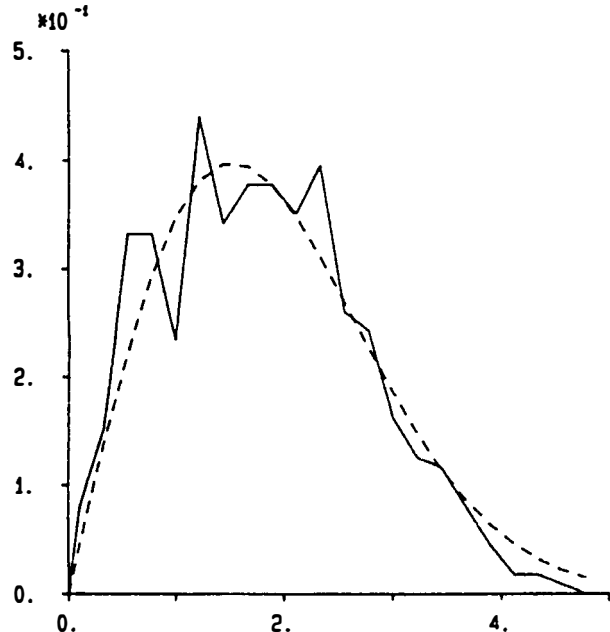


Figure 9: Distribution of nutation angle

In the frame of the failure case analysis, the case of a non-successful payload separation, such that the SPELTRA below had to be separated with the payload on top, was of particular interest. This was also investigated on a statistical basis.

### 3 Control Algorithm

All attitude and orbit control tasks between burn-out of the upper stage and the release of the last payload are performed autonomously by means of the on-board control algorithm. The complexity of this phase in terms of the necessary operations is illustrated in Figure 10, which shows a typical mission sequence for a triple payload launch. The elementary tasks of the control algorithm are the following:

- 3-axis stabilization of the upper composite
- slewing manoeuvres for proper orientation of the stage in release direction or for orbit manoeuvre execution
- orbit manoeuvres to achieve the required separation of apogee altitudes of the individual bodies
- spin-up/spin-down before and after spinning payload release
- nutation damping

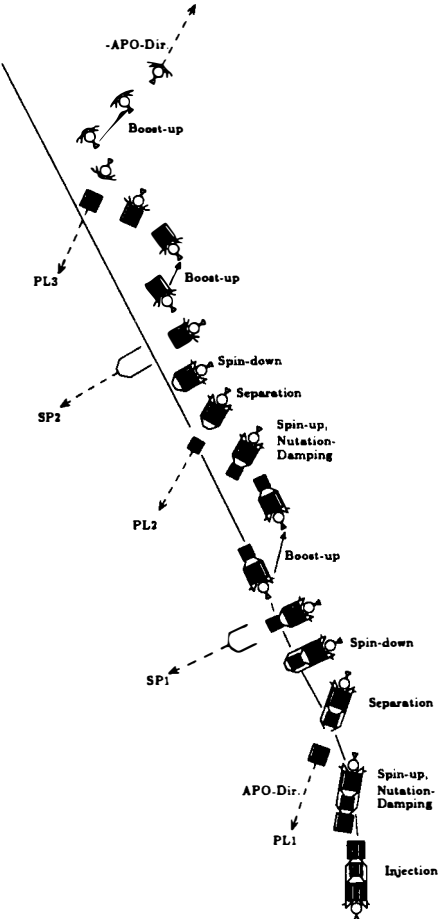


Figure 10: Typical mission sequence

As to the control system hardware, the stage is equipped with an Inertial Measurement Unit (IMU) and six thrusters.

The challenging problems the algorithm has to cope with are the following:

After each release the S/C mass properties are drastically changed. Besides the moments of inertia, also the dynamic unbalance will undergo considerable changes and may have a dispersion of up to several degrees. In connection with a high ratio of the moment of inertia about the transverse axis to that about the spin axis, this imposes problems for nutation damping and angular momentum control.

The release of the supporting structures, which cover the payloads over their full length, requires precise control of the transversal rates in order to guarantee clearance during the separation.

A further requirement is a sufficient separation of the apogee altitudes of all bodies. However, the accelerometer of the launcher is primarily designed for the powered flight. Therefore the resolution, which is determined by the least significant bit (LSB), is too low to use the measurement directly for the boost manoeuvres.

In order to overcome these difficulties, the following features are introduced into the control algorithm:

Firstly, an observer is used to estimate the dynamic unbalance of the composite after each separation of the payloads (in case of spinning release). Instead

of controlling the body axis, the rate of the principal axis and the angular momentum vector are controlled. Figures 11 and 12 illustrate the nature of the dynamic unbalance and how it affects the rate measurement. In Table 1, the algorithm for the reduced order observer is presented.

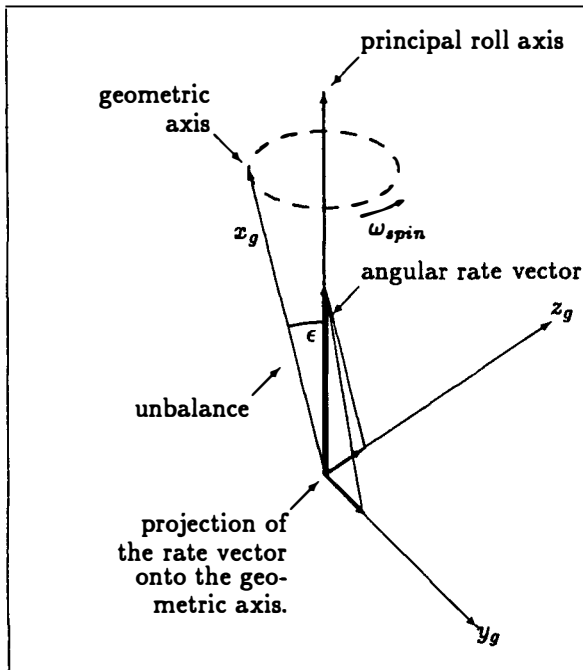


Figure 11: Transverse Components of  $\vec{\omega}$  in the Body Coordinate system (no nutation)

As to the changing mass properties: The controller is designed according to the Linear Quadratic Gaussian (LQG) approach. Since the system parameters vary after each release, the observer and controller gains (stationary solution of the Riccati equation) are stored as approximated functions of the changing moments of inertia and thruster forces.

Finally, a special filter of the inertial measurement unit (IMU) estimates the evolution of velocity between changes of the LSB.

The block diagram Figure 13 gives an overview of the overall control algorithm.

Typical results from the simulation of a release sequence are shown in Figure 14.

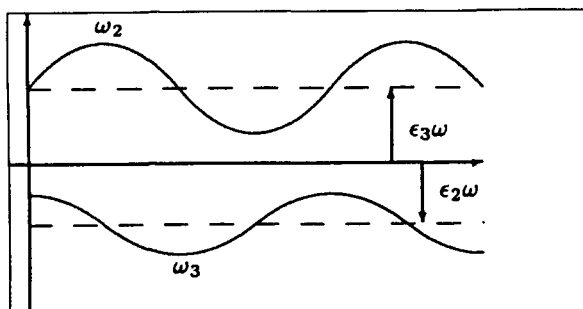


Figure 12: Measured Rate in the Body Axis System with Dynamic Unbalance

**INPUT:** IMU Measurement  $q_{IMU}$   
Compute the prediction error  $e$ :

$$e = \frac{2}{\Delta t} (q_{IMU,i} \Theta q_{IMU,(i-1)}) - \frac{\Delta t}{2} \cdot u_i - \dot{\omega}_{i-1} \quad (1)$$

Compute the correction term  $c$  by multiplying with the observer gain  $K_r$ :

$$c = K_r \cdot e \quad (2)$$

Compute the prediction for the linear state  $x_{i+1}$ :

$$\begin{bmatrix} \omega_1 \\ \omega_2 \\ \omega_3 \\ e_2 \\ e_3 \end{bmatrix}_{i+1} = \begin{bmatrix} 1 & 0 & 0 & 0 & 0 \\ 0 & 1 - \frac{\omega_n}{25} & -\omega_n \Delta t & -\omega_n \omega_s \Delta t & 0 \\ 0 & \omega_n \Delta t & 1 - \frac{\omega_n}{25} & 0 & -\omega_n \omega_s \Delta t \\ 0 & 0 & 0 & 1 & 0 \\ 0 & 0 & 0 & 0 & 1 \end{bmatrix} \times \begin{bmatrix} \omega_1 \\ \omega_2 \\ \omega_3 \\ e_2 \\ e_3 \end{bmatrix}_i + \begin{bmatrix} \Delta t \cdot I_1^{-1} & 0 & 0 \\ 0 & \Delta t \cdot I_2^{-1} & -\frac{\omega_n}{4} \Delta t I_2^{-1} \\ 0 & \frac{\omega_n}{4} \Delta t I_2^{-1} & \Delta t \cdot I_3^{-1} \\ 0 & 0 & 0 \\ 0 & 0 & 0 \end{bmatrix} \cdot \begin{bmatrix} N_1 \\ N_2 \\ N_3 \end{bmatrix} \quad (3)$$

Update the predicted state by the correction  $c$ :

$$\hat{x}_{i+1} = x_{i+1} + c \quad (4)$$

**OUTPUT:**  $\hat{\omega}_{i+1}$  and  $\hat{e}$

Table 1: Reduced Order Observer

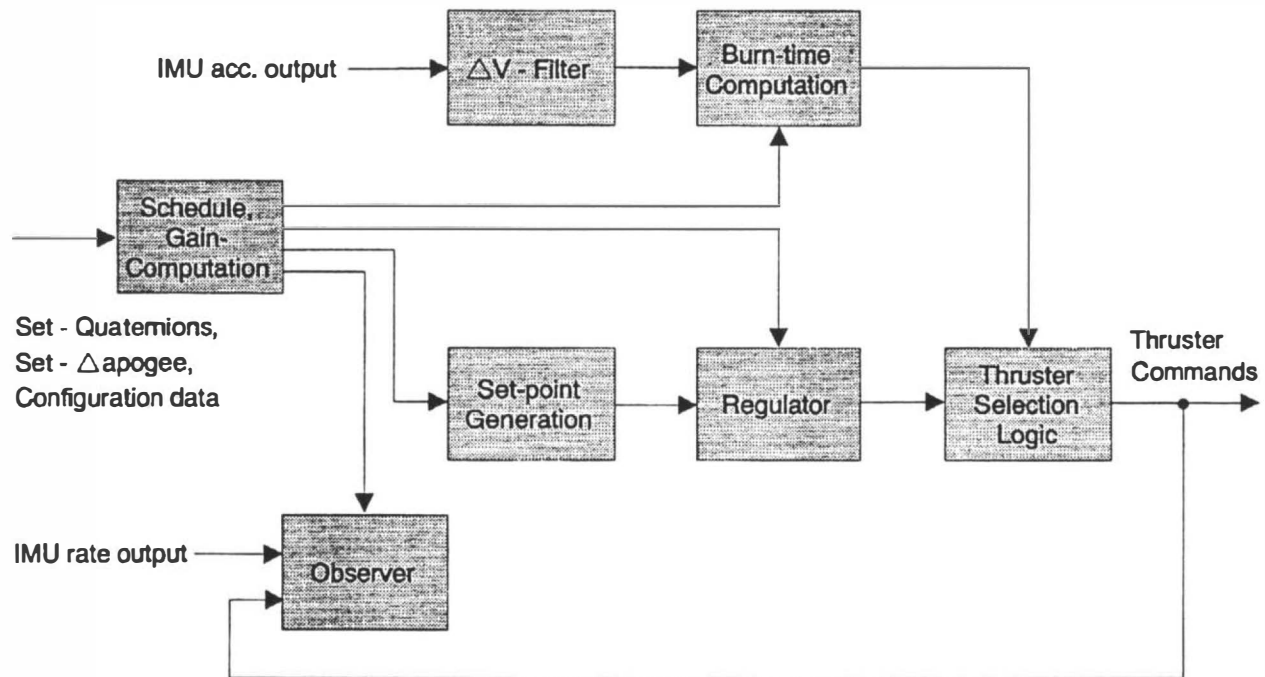


Figure 13: Block diagram of overall control algorithm

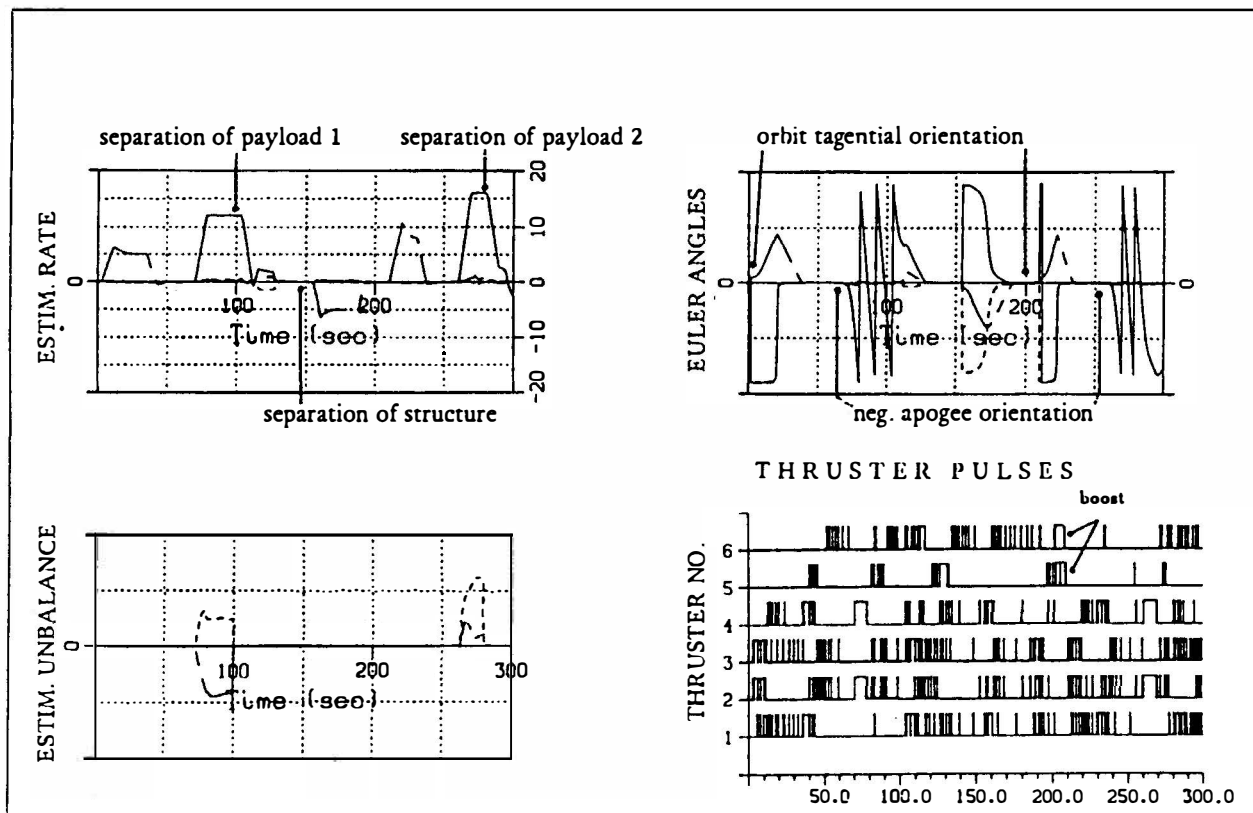


Figure 14: Simulation example

# OPTIMAL DIGITAL AUTOPILOT FOR SATELLITE LAUNCH VEHICLES DURING ATMOSPHERIC PHASE

M. Seetharama Bhat\*, B.S. Jaisimha\*\* and S.R. Vijayamohana Kumar\*\*

\*Department of Aerospace Engineering, Indian Institute of Science, Bangalore 560012, India

\*\*Vikram Sarabhai Space Center, ISRO, Trivandrum 695 022, India

**ABSTRACT** Digital autopilot is a closed loop tracking control system which aligns the launch vehicle in accordance with the guidance command. Controller is designed based on Linear quadratic regulator theory. Position and rate gyros are mounted on a flexible launch vehicle. Firstly, a dynamic output feedback control is designed by solving an equivalent optimal constant output feedback problem. An optimal output feedforward compensator is introduced in the outer loop to get tracking properties. Finally, a combined dynamic feedback - feedforward control is designed which is found to give better performance compared to two loop controller.

**Key Words:** Digital Autopilot; Launch Vehicle; Dynamic Output Feedback Control; Linear Quadratic Regulator Theory; Feedforward control.

## 1. INTRODUCTION

Design of controllers for launch vehicles has been attempted for over three decades. The autopilot is a closed loop servo (tracking) system designed not only to stabilize the vehicle but also to meet the prespecified performance specifications. This paper deals with a design of digital autopilot using the Linear Quadratic Regulator Theory (LQR) for the discretized model. The controller is designed for a multistage launch vehicle at an operating point (at Mach No. M = 1.8) corresponding to 30 secs into the flight which lies in a high dynamic pressure regime.

The conventional LQR theory relies on state variable feedback. The solution of LQR problem enables the determination of feedback gains by minimizing a quadratic performance index [1]. However, the most important drawback of the state variable feedback design is that it requires the measurement of all state variables. It may be noted that the optimal output feedback problem is a significant extension of the optimal quadratic "Complete state feedback" problem [2 - 6]. The use of quadratic performance index minimization criterion in the computation of feedback gain computation avoids the use of either adhoc tuning rules or the graphical design procedures. It yields a closed loop control law which is quantitatively derivable. In many practical problems, it may be difficult to either stabilize the system or to achieve the requisite performance or both, with constant output feedback. In such cases, the concept of low order controller comes into picture [3, 5 - 8]. The order of this compensator is less than or equal to the dimension of the state variables. The order of the controller is such that the overall closed loop system is asymptotically stable, while the performance is optimized to a satisfactory level.

The design of inner stabilization loop and outer tracking loop has been undertaken separately for a better understanding of the behavior of the closed loop system dynamics. The

realizable pitch autopilot involves the dynamic low order (first order) controller in the feedback as well as in the cascade path. The ubiquitous notch filter is not made use off in this case. The details of design procedure as well as some results of the simulation study are presented in Section 3.

## 2. MATHEMATICAL MODELING

The dynamics of the launch vehicle are typically represented by highly coupled nonlinear time varying differential equations [9 - 11]. These equations are not amenable for analysis or design of controllers. Therefore, a linearized time invariant model is derived for the controller design. Owing to the two plane of symmetry, decoupled equations of motion about pitch, yaw and roll axes are normally assumed in the controller design. The linearized model includes the effect of flexibility.

A well defined coordinate system is essential before one attempts to write any dynamical equation. The Fig. 1 clearly describes the coordinate system which will form the basis for the mathematical model developed. The control input is generated by SITVC system. The sensors are limited to position and rate gyros. Two rate gyros, one mounted forward of CG in the equipment bay and the other behind CG at the first-second interstage of a launch vehicle. The blended data from these two rate gyros (0.15:0.85) gives better performance in terms of least excitation of flexible modes [12].

A summary of equations [9,11] is given below. Apart from pitch, angle of attack and bending equations, the engine actuation dynamics is represented by a first order differential equation. This constitutes the mathematical model of the plant described by ten states viz.,  $\{\theta \dot{\theta} \alpha \dot{\alpha} q_1 \dot{q}_1 q_2 \dot{q}_2 q_3 \dot{q}_3 \delta\}$ , where the states 4 through 9 correspond to three generalized coordinates of bending modes and their time derivatives.

### Pitch Equation

$$\begin{aligned} I_{yy} \ddot{\theta} + C_{mq} \dot{\alpha} &= [C_{mq} - I_{yy} + m x_c (x_c + x_d)] \dot{\theta} \\ &+ [C_{mq} + m x_c v_{mo} + m_t v_{mo} x_{cg}] \dot{\alpha} \\ &+ \sum_{i=1}^3 [C_{mqi} - T_s (\phi'_{io} + x_c \phi'_{10})] q_i \\ &+ \sum_{i=1}^3 m x_c \phi'_{i0} q_i + [K_{ds} x_c] \delta; \end{aligned}$$

### Angle of Attack Equation

$$\begin{aligned} [m_t v_{mo} - C_{nq}] \dot{\alpha} &= -(m_t g \sin \theta_0) \theta + [C_{nq}] \\ &+ m_t (v_{xo} - x_{cg}) + m (x_c + x_d) \dot{\theta} \\ &- [C_{nq} + m v_{mo} + m_t v_{mo}] \dot{\alpha} + [K_{ds}] \delta \\ &- \sum_{i=1}^3 (T_s \phi'_{io} - C_{nqi}) q_i; \end{aligned}$$

### Bending / Structural Vibration Equation

$$\begin{aligned} m_i \ddot{q}_i &= [(-2 m_i \gamma_i \omega_i) - m_i] \dot{q}_i - [m_i \omega_i^2] q_i \\ &+ T_s \phi'_i(o) \sum_{j=1}^3 \phi'_j(o) q_j(t) \\ &- [K_{ds} \phi'_{io}] \delta - [C_{iq}] + m \phi'_{io} v_{mo} \\ &+ [C_{iq}] \dot{\theta} + [C_{iq}] \theta; \end{aligned}$$

### Position and rate gyros outputs

$$\begin{aligned} \dot{\theta}_m &= \theta + \sum \phi'_i(PG) q_i(t); \text{ and } \dot{\theta}_m = \theta + \sum \phi'_i(rq) q_i(t) \\ \text{or, } \dot{\theta}_m &= \theta + \sum (a \phi'_i(rq1) + b \phi'_i(rq2)) q_i(t) \end{aligned}$$

where,  $a, b$  are rate gyro blending ratios (0.15, 0.85). Together, the equations described above is considered sufficient for the present analysis. For definition of symbols, refer to [9, 13]. The linear time invariant model is given by

$$\dot{x} = A_C x + B_C u, \quad y = C x, \quad (1)$$

where  $x$  = state variables,  $y = [\theta_m, \dot{\theta}_m]$ ; ( $q = \theta$ ). The Eq. (1) is discretized to get,

$$x_{k+1} = A x_k + B u_k, \quad y_k = C x_k. \quad (2)$$

The open loop eigenvalues of the plant are:

$$\begin{aligned} -1.27 &\pm 113.05 i; \quad -0.83 \pm 57.51 i; \\ -0.41 &\pm 20.74 i; \quad -0.16 \pm 0.18 i; \quad -48.0; \quad -0.15. \end{aligned}$$

### 3. OPTIMAL CONTROLLER DESIGN

The objective of the controller design is to find the controller gains and parameters of the compensators such that attitude tracking is achieved with reasonable degree of stability.

The various types of controllers developed are as follows:

- First order dynamic feedback controller for stabilization.
- Addition of first order dynamic compensator in the cascade path to the controller in (a).
- Combined design of first order controllers each in both feedback and feedforward path.

The most important consideration in the design of controller is that it should be least complex. The optimal solution to the controller design depends strongly on the type of the controller, order of dynamic controller/ compensator and the performance index. For low order system, there exists some guideline in fixing the weighting matrices of the quadratic indices. But, such a guideline does not exist for a large order system. In the case of launch vehicle system, which is basically mechanical/inertia system, it is possible to alter the performance index so as to move the closed loop characteristics in a particular direction. It may be also noted that for many physical systems, it may not be possible stabilize the system and / or meet the minimal performance requirements with constant gain or dynamical controller with order less than critical number. It is extremely difficult to find such a critical number, but Kabamba et al [13] shows that it is possible to test whether a dynamical controller of given order can stabilize a system or not, through a homotopy operator.

The pitch plane dynamics of a launch vehicle along with the structural vibration is open loop stable at a flight time of 30 secs. In principle, a constant gain feedback controller (0th order dynamic controller) can provide stable operation. For the time being, only first order controllers have been envisaged. The design philosophy for getting three of the above said controller configurations are discussed in the sequel.

#### 3.1 Optimal Dynamic Output Feedback Controller

For ease of understanding and simplicity of design, a first order dynamic controller is designed in the inner feedback (FB) loop which is of the form:

$$z_{k+1} = D z_k + M y_k, \quad u_k = -(N z_k + K y_k) + r_{sk} \quad (3)$$

where,  $r_{sk}$  is the external input to the plant. The block diagram of the controller is given in Fig.2. Then, the LQR based optimal control problem is stated as in [5, 7] : \*Find the optimal feedback gains  $D, M, N$  and  $K$  so as to minimize the quadratic performance index (PI):

$$J = \sum_{i=0}^{\infty} [x_k^T Q x_k + u_k^T R u_k]; \quad Q \geq 0, \quad R \geq 0, \quad (4)$$

subject to the equations of motion (2) for obtaining a satisfactory transient response. Here, solution to an infinite time / stationary optimal control is obtained. On combining the Eqs. (2) and (3), the closed loop system can be represented as:

$$\begin{aligned} x_{k+1} &= (A - B K C) x_k - B N z_k + B r_{sk} \\ z_{k+1} &= D z_k + M C x_k, \end{aligned} \quad (5)$$

$$\text{or, } \begin{vmatrix} x_{k+1} \\ z_{k+1} \end{vmatrix} = \begin{vmatrix} A - B K C & -B N \\ M C & D \end{vmatrix} \begin{vmatrix} x_k \\ z_k \end{vmatrix} + \begin{vmatrix} B \\ 0 \end{vmatrix} r_{sk} \quad (6)$$

$$\text{or, } x_{sk+1} = A_s x_{sk} + B_s r_{sk}, \quad (6)$$

where  $A_s$  and  $B_s$  are defined suitably. The controller parameters  $K, N, M$  and  $D$  appear as coefficients of the state transition matrix of the closed loop system in (Eq. 6). In order to make these parameters amenable for computation a pseudo state equation is written as follows [5, 12]:

$$x_{sk+1} = (A_a - B_a F_b C_a) x_{sk} + B_r r_{sk}, \quad (7)$$

where,  $A_a, B_a, C_a$  can be written as

$$A_a = \begin{vmatrix} A & 0 \\ 0 & 0 \end{vmatrix}, \quad B_a = \begin{vmatrix} B & 0 \\ 0 & I \end{vmatrix}, \quad B_r = \begin{vmatrix} B \\ 0 \end{vmatrix},$$

$$F_b = \begin{vmatrix} K & N \\ -M & -D \end{vmatrix}, \quad C_a = \begin{vmatrix} C & 0 \\ 0 & I \end{vmatrix}.$$

For a regulator,  $r_{sk} = 0$ . The Eqs. (6,7) represent a single input,  $r$ -output system ( $r = 2$  in the present case), but the pseudo-state representation in Eq. (7) makes it appear as though it has two input and  $(r+1)$  - output system (the order of the controller  $n_c = 1$ ). The optimal dynamic controller design is now akin to the static controller design. The associated PI corresponding to closed loop system in Eq.(6) can be written as

$$J = \sum_{i=0}^{\infty} [x_k^T \begin{vmatrix} Q & 0 \\ 0 & 0 \end{vmatrix} x_k + u_k^T \begin{vmatrix} R & 0 \\ 0 & 0 \end{vmatrix} u_k],$$

$R = 1$ . On using Eq. (3) and trace operator, the Performance Index (PI) can be written as

$$J = \text{tr}[(Q_a + C_a F_b^T R_a F_b C_a) S],$$

where  $S$  is the steady state solution of the algebraic Riccati equation (in discrete version).

$$S = (A_a - B_a F_b C_a) S (A_a - B_a F_b C_a)^T + X_0, \quad (8)$$

and  $X_0 = I$  is an equivalent covariance matrix of the uncertainty in the initial condition  $x(0)$ . By making use of Lagrange multiplier matrix  $P$ , the optimal gain  $F_b^*$  is given by the necessary conditions for optimality as:

$$\begin{aligned} F_b^* &= -(R_a + B_a^T P B_a)^{-1} B_a^T P A_a S C_a^T (C_a S C_a)^{-1}, \\ P &= (A_a + B_a F_b^* C_a)^T P (A_a + B_a F_b^* C_a) + Q_a \\ &\quad + C_a^T F_b^{*T} R F_b^* C_a. \end{aligned} \quad (9)$$

The matrices  $P$  and  $S$  are symmetric and positive definite. For the existence of the solution, the regular conditions of controllability  $(A, B)$  and observability  $(A, Q)$  have to be met. The Eqs. (8,9) are coupled and nonlinear. No closed form solution can possibly be found. Approximate solutions can be obtained by either sequential method or gradient based iterative methods. The sequential methods are effectively used in computing the near optimal gains in [5, 12].

At this juncture, a brief discussion on the selection of weighting matrix 'Q' is in order. It may be recalled that degree of controllability is generally poor corresponding to the state variables representing the generalized coordinates of structural vibrations. Therefore, elements of the diagonal 'Q' corresponding to these states can be kept low. Such a selection reduces control effort and enables faster convergence of the sequential algorithm to the optimal value. While selecting  $Q$  and especially the off diagonal terms, it is desired that the dominant poles lie in the range of 4 to 8 rad/sec with reasonable damping properties at the end of reasonable fixed iterations. Also, the flexible mode eigen values of the closed loop system should be stable. After considerable trial and error, the matrix  $Q$  is selected as follows:

40.0	0	-85	0	-	-	0
0	1.0	-1.0	0	-	-	0
-85	-1.0	150.0	0	-	-	0
0	0	0	0.001	-	-	0
-	-	-	-	-	-	0
0	0	0	0	-	-	200.0

The resulting optimal gains are

$$\begin{vmatrix} -0.0244 & 0.0402 & 0.0506 \\ -2.5313 & -0.1639 & -0.3979 \end{vmatrix}$$

and the closed loop eigen values are given in Table 1. The unit impulse response (Figs. 3, 4) of the closed loop system is satisfactory. The maximum angle of attack is 0.31 degrees and the maximum exertion of the lateral accelerations on positive and negative sides are respectively 15.5 m/sec<sup>2</sup> and -11 m/sec<sup>2</sup> (not shown). The transients die down very quickly.

### 3.2 Tracking controller with the Addition of Dynamic Feedforward compensator

In principle, the autopilot demands that the output follow atleast a ramp input with finite error. Normally, only step response of the system is studied, as it is easy to interpret such a response and determine the necessary modifications in the iterative design procedure. The lag compensator is traditionally introduced in the cascade/forward path, to minimize the steady state error for the system having satisfactory transient response properties. The parameters of the compensator are then determined via adhoc tuning rules, which are very effective for low order stable systems. However, the introduction of lag filters may degrade:- 1) transient response, 2) gain and phase margins, 3) stability margins at the structural resonance frequencies. It is preferable to determine the parameters of the feedforward (FF) compensator via optimization technique as discussed above while maintaining the required transient properties. Firstly, the optimized FF compensator is introduced in the outer loop, while the previous computed optimal FB gain in the inner loop (Fig.5) is untouched. Here, coupling terms of the controller like  $D_{21}$ ,  $D_{12}$ ,  $M_f$ ,  $M_m$  are zeros, while they are nonzero for combined (FB+FF) controller.

The equation of motion for the system with the inner feedback loop is given by Eq. (6). The governing equations for the digital FF compensator is likewise written as

$$\begin{aligned} z_{fk+1} &= D_f z_{fk} + M_f e_k, \\ v_{fk} &= N_f z_{fk} + k_f e_k, \quad r_{sk} = v_{fk}, \quad (10) \\ e_k &= r_k - y_{fk} = r_k - C_r x_{sk} \end{aligned}$$

On combining Eq. (6) with Eq. (10) and simplifying, one gets,

$$\begin{aligned} \begin{vmatrix} x_{sk+1} \\ z_{fk+1} \end{vmatrix} &= \begin{vmatrix} A_s - B_s K_f C_r & B_s N_f \\ -M_f C_r & D_f \end{vmatrix} \begin{vmatrix} x_{sk} \\ z_{fk} \end{vmatrix} \\ &\quad + \begin{vmatrix} B_s K_f \\ M_f \end{vmatrix} r_k \end{aligned} \quad (11a)$$

$$\text{or, } x_{ak+1} = A_a x_{ak} + B_a r_k, \quad (11b)$$

where,  $A_a$  and  $B_a$  can be written accordingly. Here,  $y_{fk}$  is the measured value of the theta obtained from the gyro without passing through any signal processing filter. The Eq. (11b) has similar structure as in Eq. (7). The optimal gain parameters  $K_f$ ,  $N_f$ ,  $M_f$ ,  $D_f$  are determined so as to minimize a standard quadratic PI. The size of the  $Q$  matrix is  $12 \times 12$ . Normally, the weights corresponding to controller states are assumed to be zero. However, according to Anderson and Moore [1, Ch.9], one could shape the response properly, if the controller states are also weighted. However, the frequency shaped cost functional in [1] is based on the prespecified compensator, say, a notch filter, so that the introduction of filter does not effect the performance adversely. In

order to keep the order of the compensator low, the notch filters are not used here. Further, the notch filters are very sensitive to changes in the structural mode frequency. The low order compensator designed here is insensitive to the variation in modal frequency. The weightages corresponding to the states representing the modal deformation is kept low in the present case also. After lots of trial and error, the following simple diagonal weighting matrix,

$$Q = \text{diag} (0.1, 0.01, 0.1, 0.0001, 0.0001, 0.0001, 0.00001, 0.0001, 0.0001, 1.0, 0.01, 0.01)$$

is arrived at. If the controller state ( $z_{fk}$ ) is not weighted, then, the corresponding compensator pole will be located far to the left of s-plane (i.e., close to the origin in z - plane). This will make the cascade compensator in-effective. On the other hand, large controller state weighting will make the system sluggish or alternately, the larger associated state weighting will result in increased control activity. Both of these two are not desirable, and the Q-matrix used above is a sort of compromise solution.

The optimal gain of the inner loop is given by Eq.(10) and the corresponding gain elements of the cascade compensators in the outer loop are

$$F_f = \begin{vmatrix} -0.0687 & 0.0122 \\ -0.0472 & 0.9778 \end{vmatrix}.$$

The resulting closed loop eigenvalues are given in Table 1. With the introduction of outer loop, third bending mode poles have moved slightly to the right, whereas the first and second modes have moved to the left, which is desirable.

The simulation of the system response with regard to position gyro output (theta), angle of attack (alpha), pintel deflection (delta), and the first mode generalized coordinate for unit degree step input are given in Figs. 6 - 9 respectively. Even though the short period mode alone corresponds to under damped poles, the unit step response shows a over damped response. Such a response is possible for the continuous system of high order with the dynamic digital controller. Therefore, the design of controller based only on the requirement of pole placement of short period mode will not give satisfactory response. One has to check the step response at regular intervals of the sequential design procedure. The PI has to be modified at each of such instants. One has to watch the change in response of the closed loop system at each of such a trial and error selection of weightages as well as the sequential estimation of optimal gain.

### 3.3 Optimal Integrated Feedback-Feedforward Dynamic Controller Design

On examination of Fig.5, it can be seen that the position gyro measurement is used in the inner loop as well as outer loop in the constant gain feedthrough (the first element of K and  $K_f$  in Eq. 7 and Eq.10). More over, the FB and FF controllers are designed separately. There may be several advantages, if the FF controller and FB-controller gets the information from one another, i.e., these two are dynamically coupled. The controller proposed here in (Fig. 5), the measurements from position and rate gyros enter the coupled controller, while, the direct gain on q is used in the feedback path only, while, error between the reference and the position gyro goes through the forward/cascade path. The equations of motion are:

1 Airframe:  $x_{k+1} = A x_k + B u_k; u_k = -v_k + v_{fk}$

2 Feedback controller:

$$z_{k+1} = D z_k + D_{12} z_{fk} + M_\theta \dot{\theta}_{mk} + M_q \dot{\theta}_{mk};$$

$$v_k = N z_k + k_q \dot{\theta}_{mk}.$$

### 3 Feedforward controller:

$$z_{fk+1} = D_f z_{fk} + D_{21} z_k + M_f e_k + M_{fq} \dot{\theta}_{mk};$$

$$v_{fk} = N_f z_{fk} + k_f e_k; e_k = r_k - \theta_{mk}; \quad (12)$$

On combining the above equations, with  $z_{ak} = (z_k, z_{fk})$ , one gets,

$$\begin{vmatrix} x_{k+1} \\ z_{ak+1} \end{vmatrix} = \begin{vmatrix} A - BK_a C & BN_a \\ M_a C & D_a \end{vmatrix} \begin{vmatrix} x_k \\ z_{ak} \end{vmatrix} + \begin{vmatrix} B_a \\ M_f \end{vmatrix} r_k$$

$$M_a = \begin{vmatrix} M_\theta & M_q \\ -M_f & M_{fq} \end{vmatrix}, \quad D_a = \begin{vmatrix} D & D_{12} \\ D_{21} & D_f \end{vmatrix}, \quad B_a = \begin{vmatrix} B \\ 0 \end{vmatrix},$$

$$N_a = [-N \quad N_f], \quad K_a = [K_f \quad K_q]. \quad (13)$$

The equation (13) can be rewritten in a standard form, and the optimization is performed. Here, too the control states are weighted. The initial guess for the gain matrix is

$$F_a = \begin{vmatrix} 0.115 & 0.05 & 1.0 & -1.0 \\ -0.01 & 0 & 0.4 & 0 \\ 0 & -0.01 & 0 & 0.99 \end{vmatrix},$$

for which the closed loop system is stable, but have poor performance characteristics. The optimized gain is given by

$$F_a^* = \begin{vmatrix} -0.0550 & 0.0889 & 0.5950 & -0.6583 \\ 0.0537 & -0.0032 & 0.6903 & -0.3822 \\ -0.0054 & -0.0001 & -0.0032 & 0.8883 \end{vmatrix},$$

and the corresponding closed loop eigen values are in Table 1. The set of eigenvalues are very complex and it is very difficult to interpret the closed loop response in terms of the closed loop eigenvalues. The unit step response is given in Figs. 10-13. The step response is satisfactory.

### 4 CONCLUSIONS

This paper presents design philosophy for arriving at an optimal low order dynamic controller. The controller makes use of measurements from position and rate gyros. Firstly, a first order dynamic feedback (FB) controller is designed using linear quadratic theory. The design procedure is presented in a easily understandable, step by step, procedure. In order to get good tracking against step input, an optimal cascade compensator (FF) is included. A combined (FB+FF) is also designed for improved performance. The performance of the controllers are satisfactory.

**Acknowledgment:** The design of an optimal autopilot for launch vehicle was carried out at the Department of Aerospace Engineering, Indian Institute of Science, Bangalore under the sponsored program from Vikram Sarabhai Space Centre (VSSC), Trivandrum. Thanks are due to Dr. S. Srinivasan, E. Janardhana and other scientists at VSSC for many useful discussions.

### REFERENCES

1. B. D. O. Anderson and J. B. Moore: Optimal Control: Linear Quadratic Methods, Prentice-Hall Engle Wood Cliffs, NJ, 1990.

2. W. S. Levine and M. Athans: On the Determination of the Optimal Constant Output Feedback Gains for Linear Multivariable Systems, IEEE Trans. Automatic Control, Vol. AC-15, No.1, 1970, pp. 44-48.
3. J. O'Reilly: Optimal Low-order Feedback Controllers for Linear Discrete - Time Systems, In: Control and Dynamic Systems, Edited by C.T. Leondes, Academic Press, NY, V980, Vol. 16, pp. 335-367.
4. S. S. Choi and H. R. Sirisena: Computation of Optimal Output Feedback Controls for Unstable Linear Multivariable Systems, IEEE Trans. Automatic Control, Vol. AC - 22, No.1, 1977, pp. 134-136.
5. A. G. Sreenatha, M. Seetharama Bhat and S. K. Shrivastava: An Optimal Dynamic Output Feedback Controller for a Flexible Spacecraft, Optimal Control Applications and Methods, Vol.11, No.1, 1990, pp.51-66.
6. M. Seetharama Bhat, A. G. Sreenatha and S. K. Shrivastava: Robust Low Order Dynamic Controller for a Flexible Spacecraft, Proc. IEE, Part D: Control Theory & Applications, Vol.138, NO. 5, 1991, pp. 460 - 468.
7. M. Seetharama Bhat and A. G. Sreenatha: Design and Analysis of Longitudinal Autopilot for a Flexible Aircraft, Dept. of Aerospace Engg., IISc., Bangalore, India, Report No.AE/ADA/MSB-03.
8. H. C. Lester and D. F. Collins: Determination of Loads on a Flexible Launch Vehicle, NASA TND-2590, Feb. 1965.
9. A. L. Greensite: Analysis and Design of Space Vehicle Flight Control Systems, Spartan Books, NY, 1970.
10. M. Seetharama Bhat and S. K. Shrivastava: Preliminary Design of a Digital Autopilot for an Elastic Rocket, JATP, IISc., Bangalore, Jan. 1987, JATP-001.
11. C. V. Padmanabhan and T. V. Haridas: Autopilot Design for ASLV-D3, Part II: Flexible Body Control Design Methodology, Control & Guidance Division, VSSC, Trivandrum, Mar. 1990, Report No.VSSC/CGD/FCGD/08/90.
12. M. Seetharama Bhat, B. S. Jaisimha and S. R. Vijayamohana Kumar: Design and Analysis of Digital Autopilot for ASLV -Class of vehicles, Dept. of Aerospace Engg., IISc., Bangalore, June 1991, Report no. VSSC/IISc/AE/MSB-01.
13. P. T. Kabamba, R. W. Longman, and S. Jian-Guo: A Homotopy Approach to the Feedback Stabilization of Linear Systems, J. Guidance, Control Dynamics, Vol. 10, 1987, pp. 422-432.

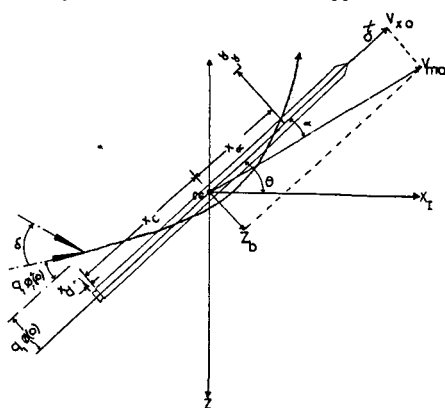


Fig. 1 Coordinate System

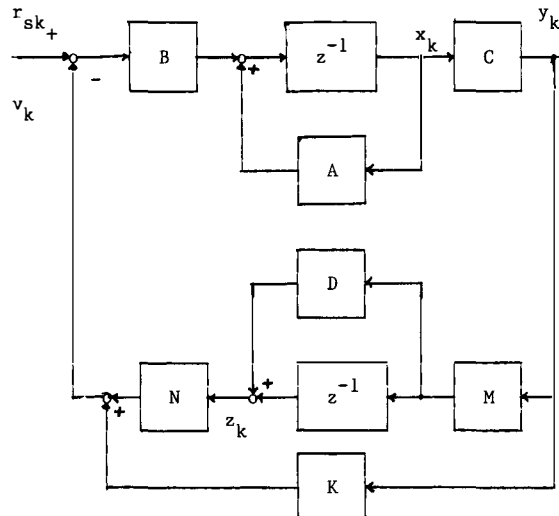


Fig. 2 Block diagram for feedback stabilization.

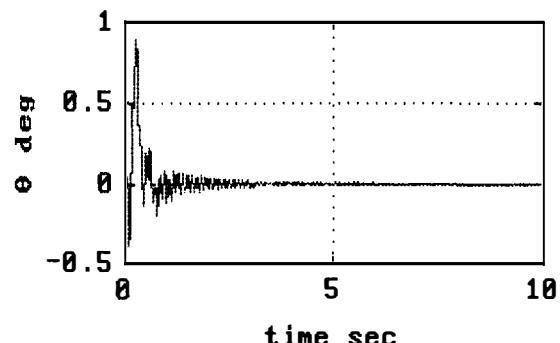


Fig. 3 Impulse Response for Dynamic FB Control

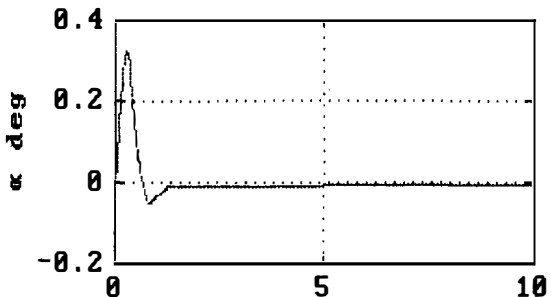


Fig. 4 Impulse Response for Dynamic FB Control

	FB Control only	FB+FF Control	Combined FB+FF
3rd Mode	$-2.91 \pm 111.5 i$	$-2.86 \pm 111.4 i$	$-5.61 \pm 108.2 i$
2nd Mode	$-0.83 \pm 57.2 i$	$-1.13 \pm 57.2 i$	$-1.29 \pm 58.2 i$
1st Mode	$-3.31 \pm 19.8 i$	$-2.63 \pm 20.8 i$	$-1.70 \pm 21.4 i$
Short Period Mode	$-3.92 \pm 5.24 i$	$-4.23 \pm 3.06 i$	$-2.45 \pm 6.7 i$
Drift Pole	-0.15	-0.15	-0.15
Actuator	-57.01	-57.07	-26.6 $\pm$ 6.7 i
FB Control	-22.45	-23.02	-11.59
FF Control	-	-0.79	-

Table 1. Eigenvalues of open loop and closed loop systems.

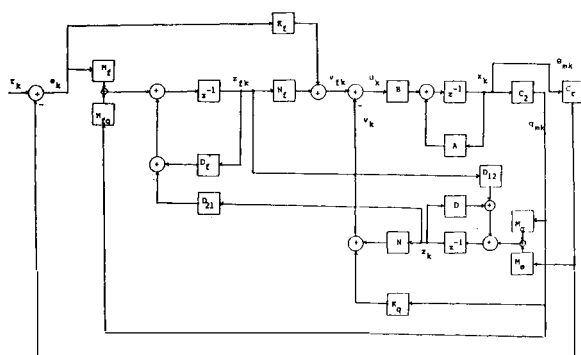


Fig. 5 Dynamic FB-FF Controller Configuration  
Step Responses for Dynamic FB+FF Control

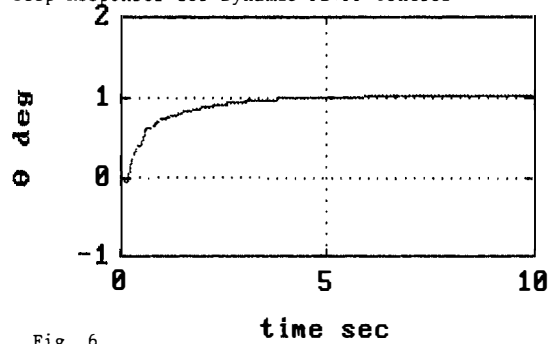


Fig. 6

Step Responses for Combined Dynamic FB+FF Control

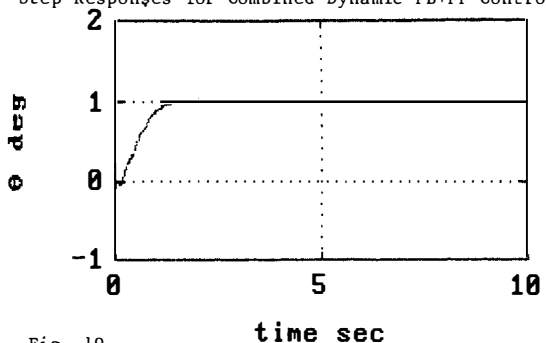


Fig. 10

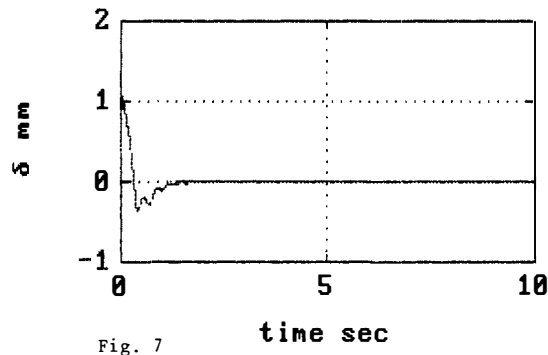


Fig. 7

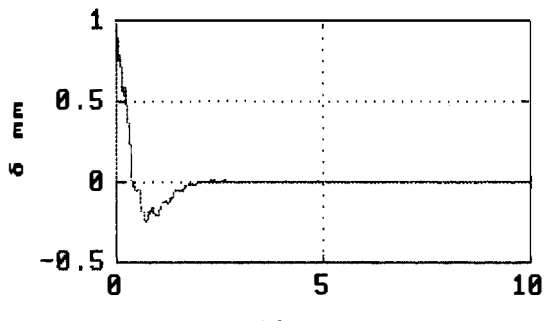


Fig. 11

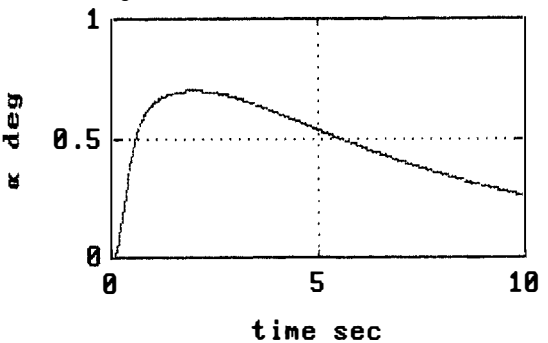


Fig. 8

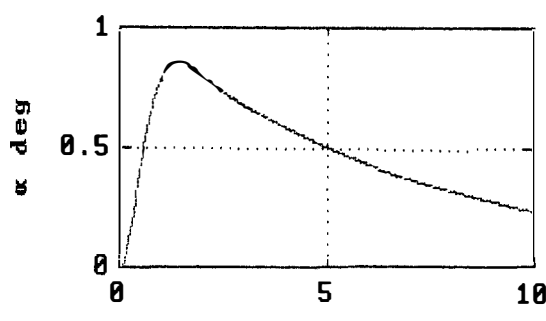


Fig. 12

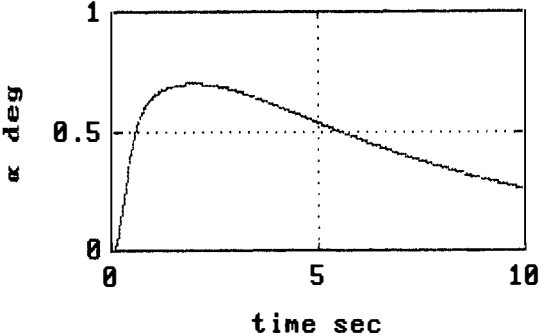


Fig. 9

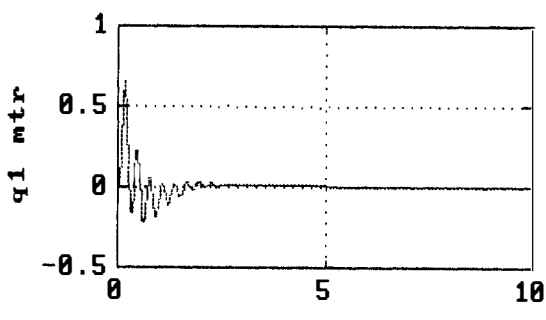


Fig. 13

## GRAVITY PROBE-B, A GYRO TEST OF GENERAL RELATIVITY IN A SATELLITE

F. Everitt, D. DeBra, P. Wiktor, J. Kasdin and Y. Jafry

*Stanford University, Department of Aero/Astro, Durand Building 028-B, Stanford, CA 94305, USA*

**Abstract.** Gravity Probe-B is the relativity gyroscope experiment being developed by NASA and Stanford University to test two extraordinary, unverified predictions of Albert Einstein's general theory of relativity. The experiment will check, very precisely, tiny changes in the directions of spin of four gyroscopes contained in an Earth satellite orbiting at 400-mile altitude directly over the poles. So free are the gyroscopes from disturbance that they will provide an almost perfect space-time reference system. They will measure how space and time are warped by the presence of the Earth, and, more profoundly, how the Earth's rotation drags space-time around with it. These effects, though small for the Earth, have far-reaching implications for the nature of matter and the structure of the Universe.

**Key words.** Satellite control; gyroscopes; drag-free control; control applications; actuators; helium thrusters; feedback control; angular measurement

### INTRODUCTION

Gravity Probe B is among the most thoroughly researched programs ever undertaken by NASA. This is the story of a scientific quest in which physicists and engineers have collaborated closely over many years. Inspired by their quest, they have invented a whole range of new technologies--technologies that are already enlivening other branches of science and engineering.

Why, after seventy years, do we still need to test Einstein's theory of general relativity? The answer is that although it is among the most brilliant creations of the human mind, weaving together space, time, and gravitation, and bringing an understanding of such bizarre phenomena as black holes and the expanding Universe, it remains one of the least tested of scientific theories.

General relativity is hard to reconcile with the rest of physics, and even within its own structure has weaknesses. Einstein himself was dissatisfied, and spent many years trying to broaden his theory and unify it with just one other branch of physics, electromagnetism. Modern physicists seeking wider unification meet worse perplexities. Above all, essential areas of general relativity have never been checked experimentally.

### The Problems of General Relativity and the Need for Further Tests:

The demolition work from negative experiments, valuable as it is, does not prove general relativity. If one asks for positive evidence, the story is in one view much better than it was, in another distinctly unsatisfactory.

The Einstein tests seem secure. The red-shift has been confirmed--notably in the elegant NASA program Gravity Probe A. The perihelion data have been strengthened, and supplemented by evidence from an astrophysical object, the Taylor-Hulse binary pulsar (though other astrophysical data from eclipsing binary stars conflict.) Starlight deflection is established, while a closely related new test, the Shapiro time delay experiment, based on radar ranging measurements to planets and spacecraft, has been executed very precisely. All of this indicates (what few physicists doubted) that Einstein was on the right track. Other more profound phenomena, however, remain untested. Save for some indirect evidence from the binary pulsar, no data exist on gravitational radiation. Even less is known about a vitally important relativistic effect "frame-dragging".

### DIRECTIONALITY IN SPACE-TIME

Gravity Probe B is designed to reveal--and check with high precision--two extraordinary consequences of general relativity, as seen by gyroscopes. What

is a gyroscope? The first, invented in 1852 by the French physicist J. B. L. Foucault, was an instrument for studying the Earth's rotation by means of a freely suspended flywheel. Since then gyroscopes have found many applications, especially in navigation, and many types exist. The ones for Gravity Probe B are not flywheels but electrically supported spheres, spinning in a vacuum. Others utilize the spins of atomic nuclei, circulating sound waves, even circulating laser beams. In all gyroscopes the underlying principle is that rotating systems, free from disturbing forces, should stay pointing in the same direction in space.

But what does "the same direction in space" mean? For Newton the answer was easy. Space and time were absolutes. A perfect gyroscope set spinning and pointed at a star would stay aligned forever. Not so for Einstein. Space-time is warped--and may even be set in motion by moving matter. A gyroscope orbiting the Earth finds two distinct space-time processes--frame-dragging and the geodetic effect--gradually changing its direction of spin.

#### Frame-dragging: Measuring the Rotation of Space-time:

In 1918, two years after Einstein formulated general relativity, W. Lense and H. Thirring calculated that according to the theory a rotating massive body should slowly drag space and time around with it!

Startling and far-reaching as Lense and Thirring's discovery was, any verification of frame-dragging seemed hopeless. Nothing happened until 1959 when Leonard Schiff of Stanford University (and independently George Pugh of the Defense Department) considered orbiting gyroscopes. On Schiff's calculations a gyroscope in polar orbit at 400 miles should turn with the Earth through an angle amounting after one year to 42 milliarc-seconds. This vitally important frame-dragging effect has never been seen. Gravity Probe B will measure it to a precision of 1% or better.

#### The Geodetic Effect - Measuring the Curvature of Space-time:

According to Einstein the Earth warps space-time. A second, much larger change in spin direction, the geodetic effect, follows from the gyroscope's motion through this space-time curvature. The phenomenon was foreshadowed in 1916 by W. de Sitter who predicted a minute relativistic correction to the complicated motions of the Earth-Moon system around the Sun--an effect finally detected in 1988 through an elaborate combination of lunar ranging and radiointerferometry data. For a gyroscope the predicted effect is a rotation in the orbit-plane of 6,600 milliarc-seconds per year--quite a large angle by relativistic standards! Gravity Probe B will measure this change to 1 part in 10,000 or better, the most precise quantitative check yet of any effect predicted by general relativity.

#### Gravity Probe B - Different Kind Of Experiment:

The Gravity Probe B instrument comprises four gyroscopes and a reference telescope sighted on Rigel, a bright star in Orion. In polar orbit, with the gyro spin directions also pointing toward Rigel, the frame-dragging and geodetic effects come out at right angles, each gyroscope measuring both. What do the two measurements signify, and how does Gravity Probe B differ from all previous tests of general relativity, positive or negative?

First, Gravity Probe B contrasts with earlier tests (redshift measurements apart) in being a physics experiment, not a disentangling of complex phenomena in stars or the solar system. Events are under the experimenter's control; disturbing effects are eliminated rather than calculated out; exact calibration checks can be performed on orbit to authenticate the results.

Second, Gravity Probe B supplies two new, very precise tests of relativistic effects on massive bodies. Relativity experiments form three groups, based respectively on clocks, electromagnetic waves, and massive bodies. Amazingly, except for the possible radiation drag in the binary pulsar, there is still only one secure positive result with massive bodies--perihelion precession. Yet such tests are crucial in exploring the differences between Einstein's and Newton's dynamics. Compare, for example, starlight deflection with the geodetic precession of a gyroscope, two effects often bracketed together since both check the curvature of space-time. Starlight deflection follows from the electromagnetic theory of light plus a special limiting case of Einstein's equations. The gyroscope effects, both frame-dragging and geodetic, follow from the conservation laws for massive spinning bodies derived from Einstein's full field equations--a critical element in the theory.

Third, most important, Gravity Probe B investigates the gravitational action of moving matter. Matter moving through space-time can be thought of as creating a new force--gravitomagnetism--which John Wheeler, dean of relativists, describes as being "as different from ordinary gravity as magnetism is from electricity." The frame-dragging measurement detects this force and fixes its scale. Commenting on its unverified status, Wheeler has said "It is hard to imagine a science so exposed for lack of evidence on a force so fundamental in the scheme of physics."

But to measure this extraordinary effect an extraordinary gyroscope is needed. The gyroscopes for Gravity Probe B have to provide a reference system stable to  $10^{-11}$  degrees/hour--a million times better than the best inertial navigation gyroscopes. Better, really. In inertial navigation many gyro errors can be quantified empirically and calibrated out. Not so in Gravity Probe B. Its gyroscopes have to be made stable absolutely.

Why, given the sophistication of modern gyroscope technology, is such a quest not absurd? In Gravity Probe B two factors--space and near zero temperature--transform the problem. The gyroscopes are suspended spinning spheres made of solid fused quartz. Electrically suspended gyroscopes have long been among the best inertial navigation instruments but ordinarily their performance is limited by support forces. Space, enhanced by "drag-free control", allows the support to be reduced to almost nothing. Low temperature operation greatly improves the mechanical stability of the instrument; and it also brings a means of shielding the gyroscopes against nongravitational disturbances and of reading their directions of spin.

#### Six Prerequisites to a Successful Relativity Mission:

Measurement of Schiff's two effects demands far more than placing a gyroscope in a satellite. Six distinct technical requirements have been simultaneously satisfied:

a drift-free gyroscope: a gyroscope having an absolute drift-rate (change in spin direction from nonrelativistic disturbances) less than  $10^{-11}$  degrees/hour

a gyro readout: a method for determining changes in spin angle to 0.1 millarc-second without disturbing the gyroscope

a stable reference: a means (telescope and mechanical structure) of referring the gyro readout to the guide star

a trustworthy guide star: a bright, properly located star whose motion with respect to inertial space is known

a technique for separating relativity effects: an orbit and a data processing method that together allow the frame-dragging and geodetic effects to be separated

a credible calibration scheme: a scheme of in-flight calibration tests to ensure that the gyroscopes--and the entire instrument--are free from errors that might masquerade as relativity signals

All six prerequisites are met. Hardest is the fourth, which goes beyond Gravity Probe B into the world of astrometry (the science of measuring star positions).

#### Simplicity in the Conceptual Design:

In conceptual layout, the Gravity Probe B instrument is simple. Its core is a block of fused quartz (a very stable glassy material), 21 inches long, bonded to a quartz telescope and containing within it four gyroscopes plus the drag-free proof masses described below. This gyro telescope structure is kept at high vacuum within a nine foot long cigar

shaped chamber ("the probe"), which is inserted into a large dewar vessel filled with 400 gallons of superfluid helium. The dewar maintains the instrument at a temperature of 1.8°K above the absolute zero and stays cold for two years. It is also the main structural element of the spacecraft.

Within the dewar, surrounding the probe, is a shield formed from superconducting lead foil which almost completely excludes the Earth's magnetic field. Thus, the gyroscopes operate (1) at low temperature (2) at low pressure (3) at low magnetic field (4) in the low gravity of space. These are four of seven "near zeros" that have been identified as hallmarks of Gravity Probe B. The other three characterize the gyro rotor.

The satellite orbit is polar, circular, at 400 mile altitude and coplanar with the line to the guide star, Rigel. The gyroscopes are aligned parallel to the telescope axis, two spinning clockwise and two counterclockwise, each gyroscope measuring both relativity effects. The difference in spin direction does not change the predicted effects; it does provide one of many validation checks on the experiment.

#### Drag-free and Roll: Two Symmetrizing Principles:

Low as the forces on the spacecraft are, they are not zero. Even at 400 miles, drag from residual atmospheric gases disturbs it, as does solar radiation pressure--the effect that pushes comets' tails away from the Sun. The consequent accelerations approach  $10^{-7}g$  (a ten millionth of the Earth's gravity)--tiny but harmful to gyro performance.

Pugh, in his independent proposal for a gyroscopic experiment, suggested a means for removing these accelerations, which was subsequently developed at Stanford and demonstrated in 1972 on the U.S. Navy's Triad transit navigation satellite. A proof-mass (in Gravity Probe B a quartz sphere identical to a gyro rotor) "floats" within an evacuated cavity near the spacecraft's center of mass. The proof mass, being shielded from external accelerations, tends to follow an ideal gravitational orbit; and by sensing its position and applying thrust forces to make the spacecraft chase after it, the satellite can be made drag-free. The mean acceleration on the gyroscopes is reduced to  $10^{-10}g$ ; their performance improves by a factor of 1,000.

Another powerful aid is roll. By skewering the spacecraft slowly (one revolution every ten minutes) about the line of Rigel, several disturbing forces on the gyroscopes--those from magnetic fields and residual gas, for example--are greatly reduced, and so are errors in the gyroscope and telescope readouts. These two symmetrizing principles, drag-free and roll, are crucial to Gravity Probe B.

#### Sophistication In Technology:

Simple in concept, Gravity Probe B nevertheless makes demands on technology that are exacting in the extreme. To

bring the experiment to its present state of readiness has taken years of research, advancing the frontiers in many areas--cryogenics, magnetics, quantum devices, telescope design, control systems, quartz fabrication techniques, metrology, and above all, gyroscopic technology.

#### A COHERENT FLIGHT PROGRAM

Gravity Probe B is expected to fly in 1995, thirty-five years after Schiff's work. That it signifies more theoretically now than in 1960 proves Schiff's acumen.

The concept is simple: a spinning sphere, a telescope, a star, each referred to the next, and the star to remote quasars. The execution has demanded a strenuous interdisciplinary collaboration between physicists and engineers at Stanford and elsewhere, sustained over many years.

Interdisciplinary research is sometimes conceived, narrowly, as a bringing together of fixed expertises for a new purpose. Gravity Probe B needs more; hence its long gestation period. This is a physics experiment testing one of the most abstruse of scientific theories, general relativity. Its success depends on new engineering ideas, many of which depend on new physics from another field, cryogenics. And throughout the process, invention has had to go hand in hand with continuing systems analyses of the total experiment, a steady interplay of physics, astronautics, and mechanical engineering.

Disciplines cross-fertilize. The dewar and the gyroscope each combine new physics and engineering principles, tailored for space. The thrusters for spacecraft pointing combine new mechanical and astronautical design principles. The porous plug and the instrument for measuring quartz homogeneity are engineering devices invented by physicists. The "Kalman" filter for processing relativity data is a physics function developed by engineers. Even mathematical techniques cross. Methods from nuclear physics theory have revolutionized the analysis of gyro performance. Methods from spacecraft orbital dynamics have simplified a correction to Schiff's formulae arising from the Earth's imperfect sphericity. But for Schiff's vision to become a flight program, ideas must be translated into hardware.

#### Demonstrated Technologies:

Every component technology of Gravity Probe B has now been demonstrated to precision consistent with flight requirements, some even in space.

#### Gyro fabrication

- flight-quality gyro rotors and housings
- roundness and homogeneity technology
- coating technology

#### Gyro suspension and spin

- 15,000 hours of low temperature run time
- high-speed spin
- simulated multi-level flight suspension system
- "low temperature bakeout" to final pressure

#### Gyro readout and low magnetic field

- precise London moment readout
- SQUIDS with submilliarc-second precision
- ultralow magnetic field shields

#### Telescope and pointing control system

- prototype telescope with submilliarc-second precision
- simulated pointing controller

#### Dewar technology

- porous plug demonstrated in 10-month hold-time dewar for the InfraRed Astronomy Satellite (IRAS) (launched 1983)
- Passive Orbital Disconnect Strut (PODS) to provide low heat leak support on orbit
- detailed thermal modelling
- neck tube design demonstrated

#### Spacecraft technology

- proportional helium thrusters
- drag-free control demonstrated in U.S. Navy's Triad satellite (launched 1972)
- helium slosh modeling

Integration, the elegant conjunction of these individual technologies into one experiment, is the next great challenge--and fascination--of Gravity Probe B.

## ORBIT CONTROL OF A RECALCITRANT SATELLITE

H. Boehnhardt\*,<sup>1</sup>, W. Peterhaensel\* and E.M. Soop\*\*

\*mbp Software and Systems, Dortmund, European Space Operations Centre ESOC, Darmstadt,  
Semerteichstr. 47-49, D-4600 Dortmund 1, Germany

\*\*European Space Operations Centre ESOC, Darmstadt, Robert-Bosch-Str. 5, D-6100 Darmstadt,  
Germany

**Abstract.** After the recovery of the OLYMPUS mission in mid August 1991 the orbit control of the satellite suffered from perturbations of daily attitude thruster firings. All orbital elements were affected in a dramatic way. Furthermore, additional constraints for the orbital correction manoeuvres arose from the attitude control mode applied and from the on-board hardware failures. The station keeping principles were adapted in order to cope with the recalcitrant behaviour of the OLYMPUS orbit. All orbit control operations were successfully performed by means of the ESOC PEPSOC software package which allows for both an almost automatic orbit calculation process and a suitable man-guided control of the optimum manoeuvre calculations.

**Keywords.** Geostationary satellites; orbit control; OLYMPUS; perturbations by attitude control; station keeping

### SHORT HISTORY OF THE OLYMPUS MISSION IN ORBIT

The telecommunications test satellite of the European Space Agency ESA, OLYMPUS, was launched on 12 July 1989 by an Ariane rocket from Kourou, French Guyana. It was positioned in geostationary height over the Earth equator ( $+/- 0.07$  deg latitude variation) at longitude  $19.0 +/0.07$  deg West. The routine station keeping operations of the satellite were started at ESOC Darmstadt in early August 1989. The dedicated mission ground station is located at Telespazio Fucino. Because of its colocation with other satellites (TDF-1, TDF-2 and TV-SAT-2) at 19 deg West, co-ordinated station keeping methods were applied up to August 1990 (Dreger and Soop, 1989; Boehnhardt, Dreger and Soop, 1990). Thereafter, the colocation at 19 deg West was resolved and the orbit of OLYMPUS was controlled according to normal station keeping principles for about nine months.

<sup>1</sup> now at: Universitäts-Sternwarte, Scheinerstr. 1,  
D-8000 München, Germany

During its in-orbit lifetime the spacecraft encountered some hardware failures (i.e. short circuit and blocking of the southern solar array, errors in the read-out of the Infra-Red Earth Sensors IRES) which had minor impacts on the orbit control of the satellite. However, on 29 May 1991 OLYMPUS went out of control of the Telespazio Fucino ground station and drifted eastward by about 5 deg per day. After two months and the completion of one full drift cycle around the Earth, a special appointed OLYMPUS rescue team was able to recover the mission and to bring OLYMPUS back into service at its nominal position at longitude 19 deg West (Wilkins, 1991). The station keeping deadbands of the mission were increased to  $+/-0.1$  deg both in latitude and longitude variation.

### ORBIT PERTURBATIONS AFTER THE RECOVERY

After the repositioning of OLYMPUS in mid August 1991 the orbit control suffered from strong perturbations due to daily attitude control and wheel dumping manoeuvres. Since the IRES provided erroneous data between about 0 and 5 hours UT each day, the satellite was put into so called Inertial Manoeuvre and Lock mode IML for attitude control during that part of the day. During IML mode the spacecraft thrusters (several hundreds of automatic thruster firings per day) were used to keep the satellite Earth-pointing, which caused considerable perturbations on the OLYMPUS orbit. The wheel dumpings - another type of automatic attitude thruster firings initiated by the on-board computer of the satellite - occurred in a almost regular daily sequence. However, an accurate prediction of the number of pulses fired on each main body axis and of the individual executions times was essentially not possible. The high rate of wheel dumping events (in total about 15 to 20 dumpings per day) was caused by the unbalanced torques on the satellite due to the blocked solar array.

An analysis of the OLYMPUS tracking data immediately after the repositioning has

shown that the IML perturbations were the dominant effects from the orbit control point of view. Compared to them, the wheel dumping operations and the natural perturbation forces could be neglected (about a factor of 4 and 14 times, respectively, smaller in size of their tangential components). The IML mode was used from the mission recovery up to 28 November 1991, while the wheel dumping manoeuvres continued also after the replacement of the IML mode by the so called Skew Pack Earth Attitude Reference mode SPEAR. They will remain a permanent perturbation source as long as the solar array is stuck.

#### The Orbit Determination And The IML Manoeuvre Estimation

As during the routine station keeping before the emergency on 29 May 1991, the OLYMPUS orbit calculations were performed by means of the ESOC software package PEPSOC during the mission recovery, the IML period and thereafter. Because of the strong and frequent perturbations on the satellite orbit during the IML period the following measures were taken by ESOC in order to allow for an appropriate orbit control of OLYMPUS from mid August to 28 November 1991:

- almost daily orbit determinations were performed with typical tracking intervals of about 1.7 days,
- almost hourly ranging and antenna pointing measurements from the Fucino ground station and two to four hourly ranging measurements from the VILSPA ground station were collected in order to provide enough tracking data over the relatively short time interval used for the PEPSOC orbit determination (on the average about 40 to 120 data points per run),
- in the orbit calculations the IML thruster firings were modelled by single burn dummy manoeuvres at the midpoints of the daily IML operations,
- the perturbations of the daily wheel dumpings were not taken into account for the OLYMPUS orbit calculations during the IML period.

Under these circumstances, the PEPSOC orbit determination and prediction process worked reasonably well, although the general accuracy of the results was reduced compared to the figures known from normal OLYMPUS station keeping. In particular, the day-to-day scattering in the solutions for the orbital elements was higher mainly because of the incomplete modelling of the orbit perturbations and because of the short tracking intervals with small measurements data sets (see Figs. 1a-g). Furthermore, the inclination determination suffered from the unfavourable observation geometry of OLYMPUS from the Fucino ground station which led to a factor of 194 between the error in the latitude position and the ranging error (for comparison, the corresponding along-track error from the eccentricity has a factor of 43 and that from the mean longitude of 18; see Soop, 1988, p. 126).

On the average, the net size of the IML manoeuvres per night was estimated to about 0.017 m/s in tangential westward

direction and to about 0.094 m/s in radial inward direction. The statistical mean scattering of the 87 manoeuvres estimated was 0.005 m/s and 0.031 m/s, respectively. The out-of-plane component could not be accurately determined with PEPSOC because of the short tracking interval applied (its mean value was found to be 0.18 m/s +/- 0.35 m/s in northern direction). However, the long term development of the inclination vector, obtained from the OLYMPUS orbit determinations during IML mode, deviated significantly from the drift motion under normal station keeping conditions (Fig. 1g). From the direction of the inclination vector drift the IML activities could undoubtedly be identified as origin for these OLYMPUS orbit perturbations, while from the amplitude of the drift deviation a net velocity increment of 0.15 m/s per day in northward direction was derived for the IML thruster firings. The actual IML manoeuvre sizes varied considerably from day to day and could only be predicted with moderate accuracy.

#### STATION KEEPING PRINCIPLES AND OPERATIONAL CONSTRAINTS

The daily IML manoeuvres made OLYMPUS to a recalcitrant satellite from the orbit control point of view. The unusual development of the OLYMPUS orbital elements is clearly depicted in Figs. 1a-g. Due to the IML operations, the station keeping strategy of OLYMPUS had to cope with

1. the strong and reversed longitude drift (about 14 times larger and in opposite direction to the natural West drift at longitude 19 deg West), which automatically reduced also the time interval between successive tangential manoeuvres (see Figs. 1a,f and Table 1),
2. the rapid increase of the eccentricity and the deviation from Sun-pointing perigee (see Figs. 1b,e),
3. the deviation of the inclination vector from its natural drift direction (see Fig. 1g),
4. no orbital manoeuvres during the daily IML periods,
5. the exclusive use of the South burn thrusters for the inclination correction manoeuvres because of the plume impingement of the North thrusters onto the damaged southern solar array.

It was usually not possible to perform the nocturnal longitude and eccentricity correction burns at the optimum midpoint times (i.e. shortly after midnight UT) because of the on-going IML operations. For safety reasons earlier execution times were chosen which on the other hand led to slightly higher eccentricity values than anticipated. The additional operational efforts for the OLYMPUS tracking and orbit determination were already discussed in the previous section.

#### Longitude And Eccentricity Control

The tangential manoeuvres of OLYMPUS were basically targeted such as to compensate on the first place for the IML mode induced East drift over the following

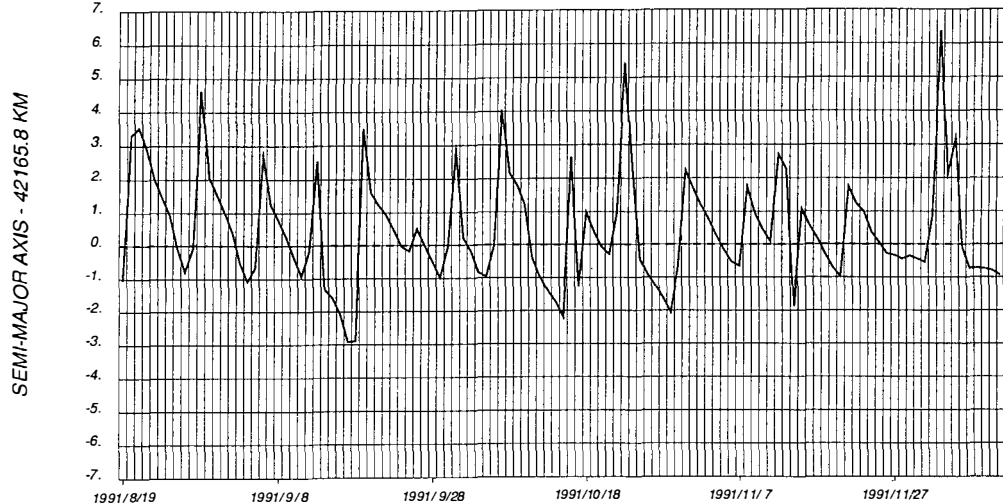
**TABLE 1 The OLYMPUS Station Keeping Manoeuvres during the IML Period from 20 August to 28 November 1991**

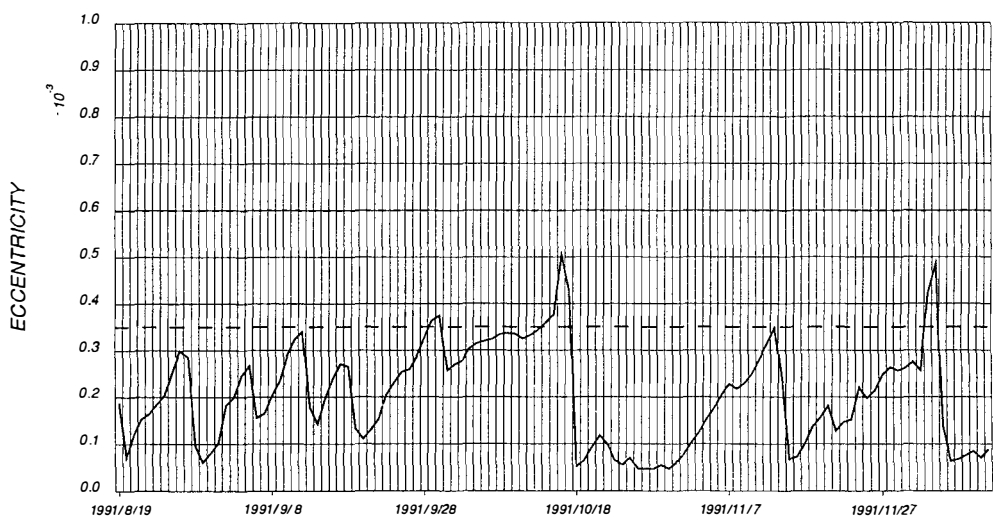
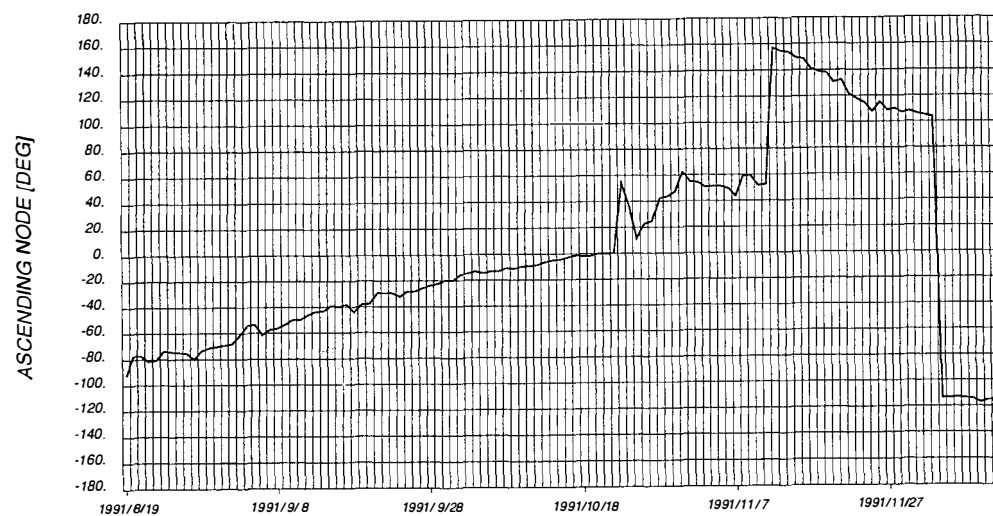
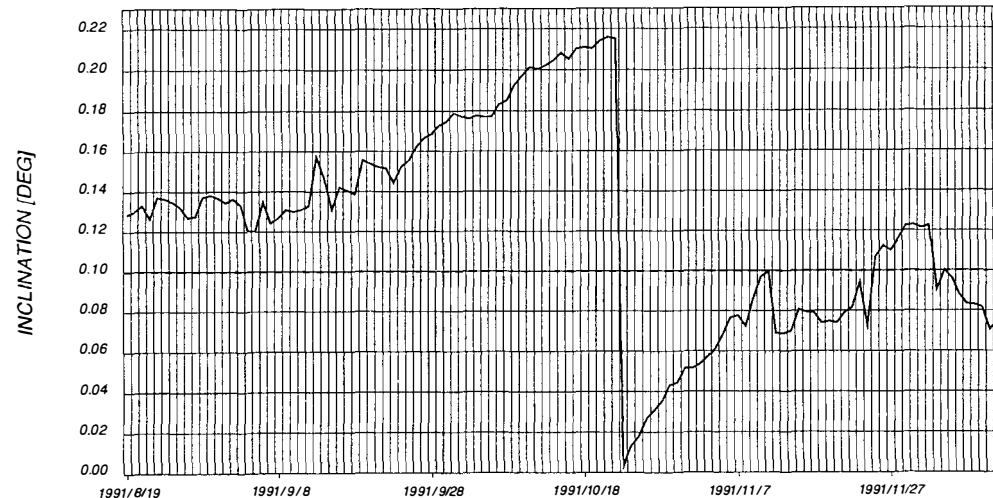
Manoeuvre Date	Midpoint Time (UT)	Thrust Direction	Size (m/s) Planned	Size (m/s) Obtained	Performance Degree (%)
1991/08/28	20:00:00	East	0.3288	0.3105	94.4
1991/08/29	12:03:33	West	-0.1505	-0.1439	95.6
1991/09/05	20:00:00	East	0.2748	0.2591	94.3
1991/09/06	07:58:02	West	-0.1325	-0.1204	90.9
1991/09/12	20:00:00	East	0.2761	0.2579	93.4
1991/09/13	10:44:13	West	-0.2449	-0.2181	89.1
1991/09/18	20:00:00	East	0.3244	0.3018	93.0
1991/09/19	12:50:15	West	-0.0820	---	---
1991/09/25	20:00:00	East	0.0600	0.0470	78.3
1991/09/30	20:00:00	East	0.3415	0.3254	95.3
1991/10/01	07:58:02	West	-0.2339	-0.2334	99.8
1991/10/06	20:00:00	East	0.3193	0.3529	110.5
1991/10/07	07:58:02	West	-0.1757	-0.1983	112.9
1991/10/10	20:00:00	West	-0.0615	-0.0595	96.7
1991/10/16	10:07:12	East	0.3394	0.3363	99.1
1991/10/17	11:45:27	West	-0.5618	-0.5636	100.3
1991/10/17	23:00:00	East	0.3850	0.3873	100.6
1991/10/21	21:00:00	East	0.0700	0.0699	99.9
1991/10/22	23:14:41	South	-11.5760	-11.8090	102.0
1991/10/24	10:00:00	West	-0.1866	-0.1876	100.5
1991/10/30	15:59:01	East	0.1773	0.1820	102.7
1991/11/07	21:56:18	East	0.1040	0.1084	104.2
1991/11/11	23:29:11	South	-7.3780	-7.7240	104.6
1991/11/14	08:11:46	West	-0.2629	-0.2714	103.2
1991/11/14	20:08:48	East	0.2503	0.2524	100.8
1991/11/20	22:06:51	East	0.1200	0.1240	103.3
1991/11/27	16:09:42	East	0.0320	0.0220	68.8

**Fig 1. The development of the mean orbital elements of OLYMPUS during the IML period**

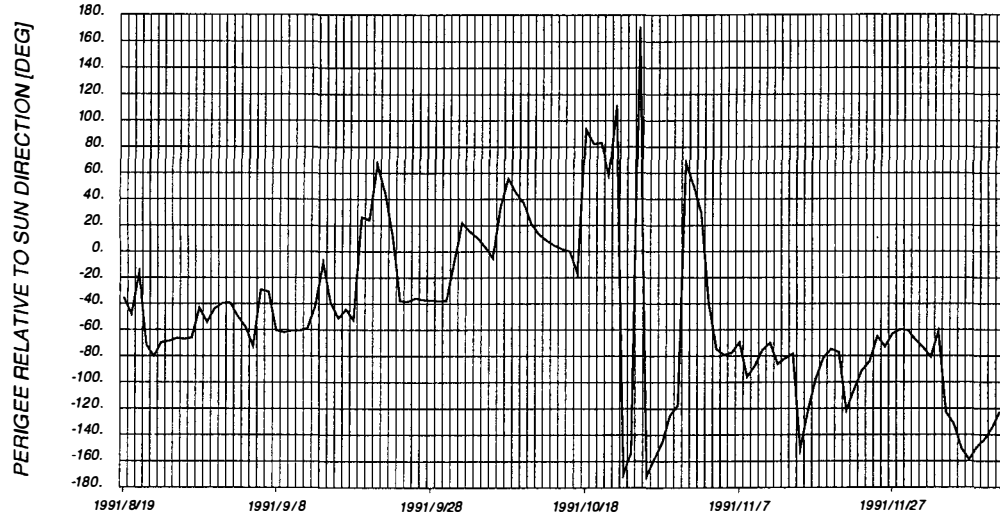
- la semi-major axis minus geostationary distance in km
- lb eccentricity
- lc right ascension of the ascending node in deg
- ld inclination in deg
- le perigee relative to Sun direction in deg
- lf minimum and maximum longitude per day in deg
- lg inclination vector (each square indicates the daily mean value of the inclination vector)

**1a**

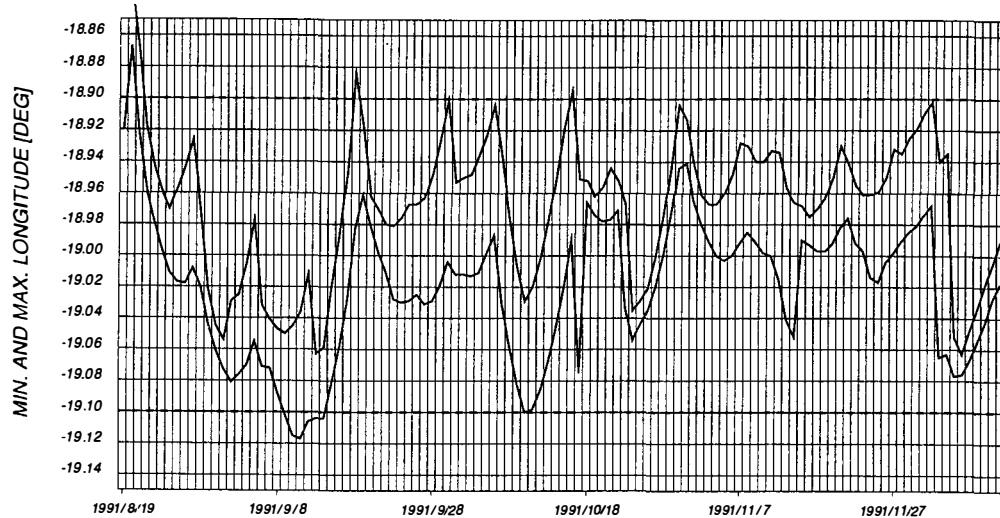


**1b****1c****1d**

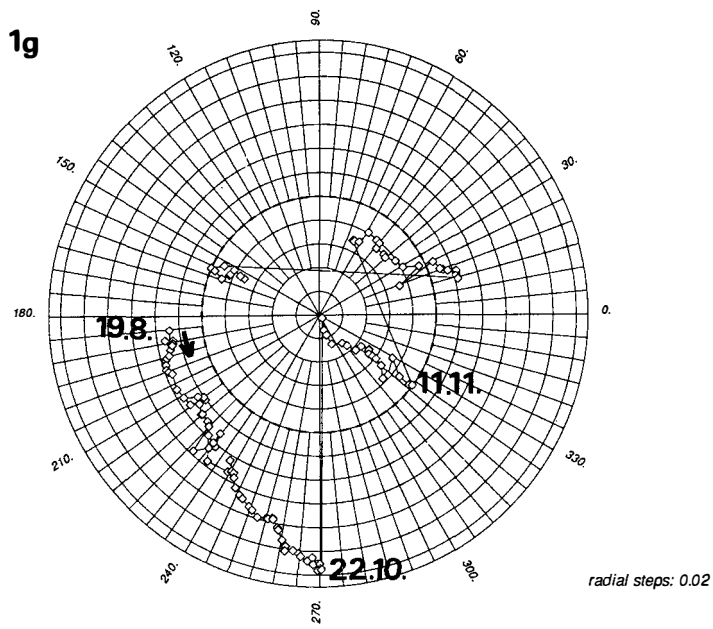
**1e**



**1f**



**1g**



about 7 to 10 days. They were in many cases also used to reduce the eccentricity close to zero over a few days after the manoeuvre execution. Therefore, predominantly multi-burn manoeuvres were performed on OLYMPUS (in total 7 two burn and 1 three burn manoeuvres). In that way it was possible to increase the time period with eccentricity below 0.0004 and simultaneously to reduce the amplitude of the daily longitude libration of the satellite. The latter consequence was advantageous for the longitude station keeping because it increased the longitude range available for the drift motion of the spacecraft.

In a few cases single burns were executed to correct or to reverse the longitude drift of OLYMPUS. The tangential manoeuvres preceding and succeeding the South burns on 22 October and 11 November 1991 were also implemented for compensating the anticipated cross coupling effects during the inclination manoeuvres.

The performance of the tangential manoeuvres (calculated by division of the estimated value of the burn through the planned size; see Table 1) were assessed by means of PEPSOC orbit determination. Therefore, it is certainly influenced by the unpredictably varying actual sizes of the IML manoeuvres during the tracking periods which covered the orbital manoeuvres. In fact, the sizes of the IML manoeuvres during these tracking intervals were set to fixed values predetermined from the preceding IML manoeuvre estimations (usually the mean value of these IML manoeuvre sizes were used). In particular, the low performance degree of small tangential manoeuvres may have suffered from the unknown actual size of the neighbouring IML operations. However, the mean performance of the OLYMPUS tangential manoeuvres during the IML mode period was of the order of that before the mission failure (95.8 % for the East burns and 98.9 % for the West burns; for comparison see Boehnhardt, Dreger and Soop, 1990).

Two longitude deadband violations occurred in the early phase of the station keeping in IML mode, i.e. between 9 and 14 September 1991 towards West and on 18 September 1991 towards East. In both cases, the window violations took place during a short time interval per day only and caused no hazards to the neighbouring spacecraft of OLYMPUS (TV-SAT-2 in the West, TDF-1 and TDF-2 in the East). The control centres of these satellites (GSOC Oberpfaffenhofen for TV-SAT-2 and CNES Toulouse for both TDFs) were informed about the OLYMPUS entries into their longitude windows, and they agreed to the proposed OLYMPUS operation sequences to solve the situation.

#### Inclination Station Keeping

During the recovery operations in the first half of August 1991 the inclination vector of the OLYMPUS orbit was put to an optimum starting value (inclination of 0.12 deg at right ascension of about 185 deg) for the expected following natural inclination vector drift. However, because of the daily IML thruster firings the inclination vector deviated significantly from the free drift motion, i.e. it remained above 0.1 deg amplitude (see Fig.

1g). Two out-of-plane manoeuvres were made with OLYMPUS during the IML period (see Table 1). On 22 October 1991 the OLYMPUS orbit inclination was reduced to about zero degree which for this date resembled the best inclination target value with respect to the constraints on the manoeuvre execution time and in order to achieve a maximum time interval for the succeeding inclination vector drift. The next inclination manoeuvre on 11 November 1991 was targeted in a very similar way like for the preceding out-of-plane burn. However, with this manoeuvre it was not possible to keep the OLYMPUS inclination below 0.1 deg for the rest of the IML period which ended on 28 November 1991. At the end of the IML period it was essentially impossible to bring the OLYMPUS inclination vector back to its nominal control area by a single South thrust because of the manoeuvre time constraints. Fortunately, the IML mode on OLYMPUS was replaced on 28 November 1991 by the more advantageous Skew Pack Earth Attitude Reference mode SPEAR which allowed also free orbit manoeuvring of OLYMPUS at the optimum midpoint times.

#### CONCLUSIONS

After the mission recovery the orbit control of OLYMPUS was very much complicated by perturbations and constraints arisen from the daily IML attitude thruster firings. By means of the PEPSOC software package for geostationary satellites ESOC was able to keep the OLYMPUS orbit under control at 19 deg West within acceptable limits for successful mission operations. Compared to the routine station keeping before the orbit failure, the orbit control of OLYMPUS required more frequent orbital manoeuvres and orbit determination processes. A careful man-guided targeting of the manoeuvre calculations was necessary, although the basic mission support made widely use of the automatic options of the PEPSOC software package.

The IML mode ended in late November 1991. However, even with the succeeding SPEAR mode OLYMPUS remained an unusual satellite from the orbit control point of view, since the perturbations produced by the daily wheel dumping operations prevail the accelerations by the natural perturbation forces at 19 deg West.

#### REFERENCES

- Boehnhardt, H., F. Dreger, E.M. Soop (1990). OLYMPUS Flight Dynamics Report Oct. 1989 - Sept. 1990, ESOC Darmstadt
- Dreger, F., E.M. Soop (1989). OLYMPUS Flight Dynamics Report No. 4 Vol. I, ESOC Darmstadt
- Soop, E.M. (1983). Introduction to geostationary orbits, ESA SP-1053, ESTEC Noordwijk
- Soop, E.M. (1987). Orbital control of geostationary spacecraft from dedicated control centres, ESA Bulletin 52, 42-46
- Wilkins, D. (1991). The OLYMPUS recovery "mission impossible?", Spaceflight 33, 384-386

# FUZZY LOGIC FOR CONTROL SYSTEMS

H. Ihara

*Space Systems Division, Hitachi Ltd., 216 Totsuka, Totsuka, Yokohama, Japan*

**Abstract.** Ever since fuzzy set theory was first proposed by Professor Zadeh, People in the control field have examined very carefully its applicability to the real world. Very few results of practical application were reported namely due to the difficulty of proving validity. One application to subway control in Japan awoke and encouraged people who had been expecting fuzzy logic. Control experts now cannot help considering its presence. Following the results shown from subway train control and crane control, the possibility of application to critical control, such as aerospace, is surveyed and discussed.

**Keywords.** Fuzzy control; Fuzzy system; Control applications; Artificial intelligence; Multiobjective optimization; Train control; Cranes; Aerospace control.

## INTRODUCTION

Since the early 1980s new technologies, some first proposed over twenty years ago, have been introduced into information processing and control disciplines. This phenomenon is largely due to the fast pace of evolution in computer science and Large Scale Integration (LSI) technologies. Knowledge engineering, fuzzy logic, and neural network techniques have been applied with great care to control systems although difficulties, such as instability and inconsistency, remain. Fuzzy logic seems most inadmissible to people in parts of the world other than the Far East. It is also said that people who are familiar with traditional analytical methods have a fundamental psychological barrier against the use of fuzzy logic. So, though it may seem strange, fuzzy logic has achieved more practical results in Japan than in other parts of the world (Teitelbaum,1990). Successful application of predictive fuzzy logic, which we developed, to the control of subway trains in Japan in 1986 validated its usefulness. Since then, fuzzy logic has been successfully applied to control systems in many plants and processes in order to achieve high product quality, high efficiency, and low energy consumption in spite of strong criticism by experts of traditional control technology. Examples of applications include water purification plants, controllers for rolling mills and

for blast furnaces in iron and steel plants, tunnel drilling equipment, ventilation controllers for highway tunnels, and more. Application to the information processing field, forecasting stock market trends for example, have followed. Fuzzy logic is now being applied to mass production of consumer goods in the home appliance, camera, and automobile industries. The list of successful applications of fuzzy logic is large and growing rapidly (Self,1990). Use of the term "fuzzy" has recently become fashionable to describe high quality, intelligent products in the marketplace. To future years, it would seem aerospace and astronautical engineers could no longer overlook the prominence which this discipline has achieved. Here, in this paper, the usefulness of fuzzy control systems are namely discussed with real data obtained, in the hope of finding some possible application in aerospace control.

## FUZZY CONTROL

I proposed the accompanying fig.1, which explained certain aspects of the human intelligence process, in 1980 in order to organize the research project on Artificial intelligence in Hitachi (Ihara,1985). Applying knowledge engineering to online control systems was one research issue of the project. It was apparently observed that human operators can control specific

systems through skill in the expression of linguistic variables similar to IF-THEN rules. Fuzzy set theory is useful for understanding the more complicated interactions in the fields shown in the upper left and the lower right quadrants of this figure. Some of these systems could not have been realized by conventional control technology due to the system complexity and time consuming work needed. Fuzzy logic was adopted as the solution. We proposed a "predictive fuzzy control" scheme which includes a feed-forward function in order to ensure the system stability though the general fuzzy system is a type of feedback scheme. The control rule of the general fuzzy control is written as follows;

IF  $x$  is  $A_i$  and  $y$  is  $B_i$   
THEN  $\Delta u$  is  $C_i$  ( $i=1, N$ )

On the other hand, that of the predictive fuzzy control is expressed as follows;  
If(  $U$  is  $C_i \rightarrow x$  is  $A_i$  and  $y$  is  $B_i$  )  
THEN  $u$  is  $C_i$  ( $i=1, N$ )

Complex control systems have been realized in Japan by applying fuzzy logic to problems in these quadrants.

#### RESULTS OF FUZZY CONTROL

Differences in control results between fuzzy logic and crisp logic are focused on here. A description of how control systems are built using fuzzy logic is beyond the scope of this paper. The controls of the subway train (Yasunobu, 1983) and the container crane (Yasunobu, 1986) are presented here for interesting examples. For detailed descriptions of these control schemes, please refere to the references.

#### Subway train control

An automatic train operation system using fuzzy logic was introduced to Sendai Municipal Transit Authority in 1986. Prior to this introduction, test runs were done with real trains at the subway of Sapporo city, Japan in 1982 as a part of the private research project on artificial intelligence. This result encouraged the people dedicated to planning subway train control at both Sendai municipality and Hitachi, Ltd. Careful examination was continued on the precisely tailored computer simulator of the subway system by the researchers. Performance indices, which were estimated concurrently, are train running time between stations, traceability of the target speed of each train, energy consumption of each train, safety within speed limits previously assigned, passenger comfort factors, and train stop error from the position assigned in front of the passenger's boarding position, as shown in Fig.2. Stop gap estimation from computer

simulations using established Proportional, Integral, and Derivative logic (PID) and Predictive Fuzzy Control logic (PFC) is shown in Fig.3. The left hand chart shows that PFC was superior to PID. The right chart shows that PFC could control the stop position almost as accurately as the operator. Fig.4 shows passenger's comfort by the number of commands to the driving motor or to the break system. The fewer control commands issued, the more comfortable the passengers feel because control commands cause forces which jar passengers. The train run curve using PFC shows very smooth operation. In addition to passenger comfort, the number of control commands affects the useful lifetime of the pertaining apparatuses. Power consumption is also improved, as shown in Fig.5. No control instability has been reported since commercial operation began in 1986.

#### Container crane control

The application to controlling container cranes was another interesting example although the system was not commercially realized for marketing. Validation tests were performed by applying a fuzzy controller to a one-half scale container crane in our test field. The total time spent moving containers affects directly the efficiencies of the cargo ship operation and the pier management. In addition, human operators require more than six months of training in order to develope the necessary skills. Performance indices, such as safety in restricted space, accurate container placement at pre-determined positions, elasped time for carrying each container from the pier to the ship's hold or visa versa, the amount of rope sway, and the operator's comfort. Fig.6 shows a schematic depiction of the system. Results using PID and PFC are shown in Figs. 7 and 8, respectively. It is apparent that operation time using PFC was shorter than that using PID. Also, swing angle of the rope was stabilized more quickly in Fig.8. Fig.9 shows how carring time and positioning accuracy using PFC and human expert were distributed. Operation by PFD was superior to human skill.

#### LESSONS LEARNED FROM APPLICATIONS

I have drawn the following lessons from my work on real applications (Ihara, 1991). Though there remain lessons to learn from future applications, I offer these with the hope that they might prove valuable to others in their efforts to apply fuzzy logic to real applications:

- 1) Designers should have a lot of design experience with basic control theory and with adaptive control applications.
- 2) Management should be enthusiastic about technological evolution.

- 3) Expertly skilled system operators should be involved in design and testing.
- 4) Target simulators for testing should be developed.
- 5) The relationship between the control cycle and the control time constant should be adequately understood.
- 6) The controller should be a microcomputer or similar processor based devices.
- 7) Controller action should be easily monitored in real time.
- 8) Control results should be easily recognizable.

Implicit in items 1 through 4 are necessary conditions on the development environment. Item 5 and 6 impose requirements for the hardware executing fuzzy logic. Item 7 and 8 pertain to system validation. We have already agreed that fuzzy logic can be effectively applied to problems in multivariable, nonlinear systems. These systems can be partitioned into the following two categories:

- 1) Systems which are complicated enough to obscure the control model. Systems in this category depend on a combination of many significant control variables, as well as on control variables which are highly nonlinear.
- 2) Systems in which the choice of control variables depend on system status.

While much has been accomplished in Japan using fuzzy logic, Development of these systems required approximations to optimum control using empirical methods. There remain areas for theoretical investigation. Among these, I think the following are most important:

- 1) Methods for optimizing membership functions for given applications.
- 2) Methods for optimizing the control cycle for given applications.
- 3) Methods for optimizing the control strategy for given applications.
- 4) Methods for approximating control models in order to improve predictive estimation.

## CONCLUSION

Applicability of fuzzy systems to control was discussed with the result of the practical applications. The fact that many kinds of products featuring fuzzy logic are being introduced into the marketplace seems to indicate that this is a promising breakthrough in the control arena. Theoretical proofs of fuzzy systems are desired to persuade those who are reluctant to apply fuzzy logic. Once a solid theoretical base has been established, systematic design criteria will be derived for non-linear, multi-object, time-variant, poorly-defined systems. We have found that one significant advantage over conventional crisp logic is that less computational power is needed for

on board controllers and onboard data processors in aerospace systems using fuzzy logic. Thus size, weight, and electrical power consumption are greatly reduced, which are most important for onboard space systems. Experimental trials are being conducted in the control of the space shuttle during reentry, control of spacecraft during rendezvous and docking, control of space robot motion, and control of helicopters during maneuvers. These trials are in critical areas in which further research and development is needed for their practical applications.

## REFERENCES

- Ihara,H.(1985).Overview of knowledge engineering at Hitachi,Ltd. Hitachi hyouron. Dec. pp.1-6(in Japanese)
- Ihara,H.(1991). Feasibility of fuzzy logic and neural networks to aerospace and aeronautics. Journal of the society of instrument and control engineers. Oct. pp.928-931 (in Japanese)
- Self,K.(1990). Designing with fuzzy logic. IEEE Spectrum. Nov. pp42-44 & 105
- Teitelbaum,s.(1990). Fuzzy. Los Angels times magazine. April. pp.24-28 & 41-42
- Yasunobu,S.,Miyamoto,S.and Ihara,H. (1983). Fuzzy control for automatic train operation system. 4th IFAC/IFIP/IFORS Conf. pp.33-39
- Yasunobu,S.and Hasegawa,T.(1986). Evaluation of automatic containercrane operation system based on predictive fuzzy control. Control theory and advanced technology(C-TAT),2.3. pp.419-432

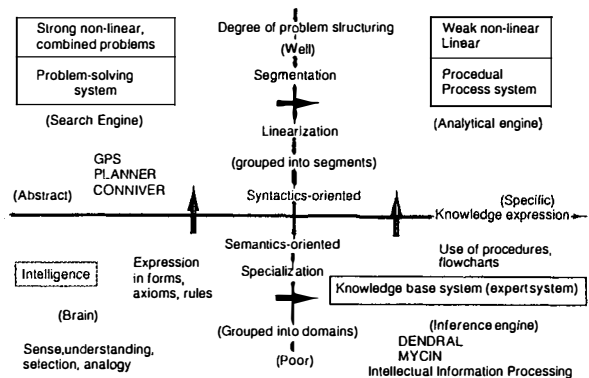


Fig.1. Category of Human Intelligence

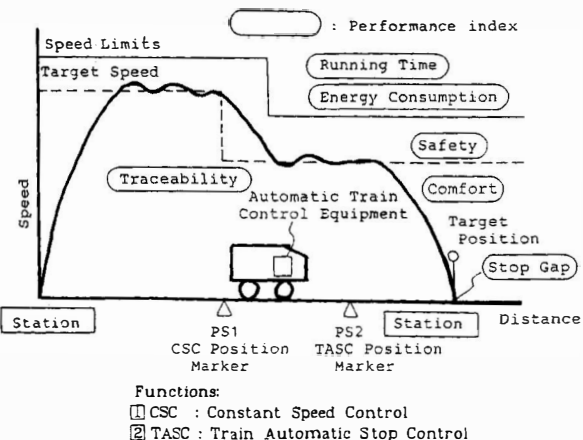
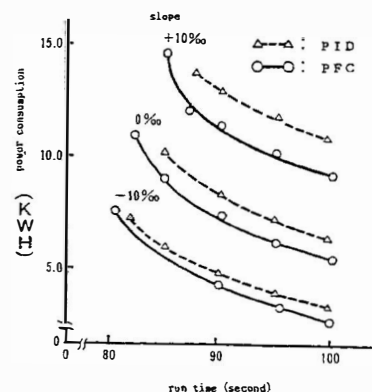


Fig.2. Control of Subway Train



PID VS PFC

Fig.5. Power Consumption

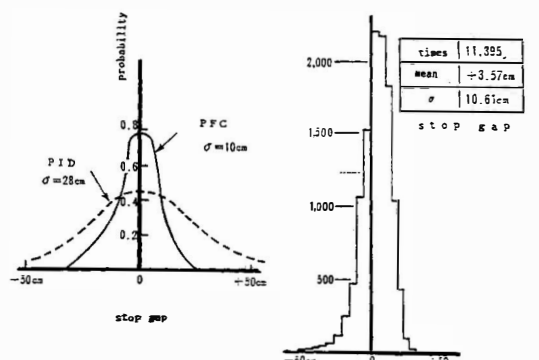


Fig.3. Gap Distribution of Train Stop

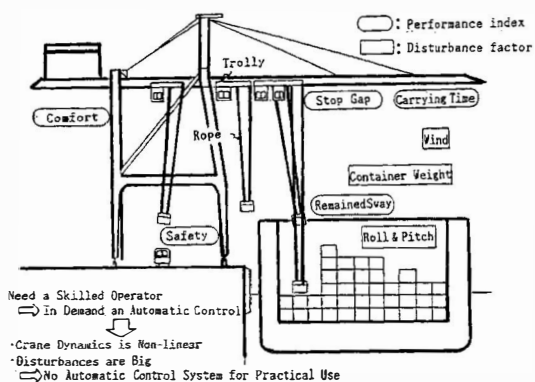


Fig.6. Control of Container Crane System

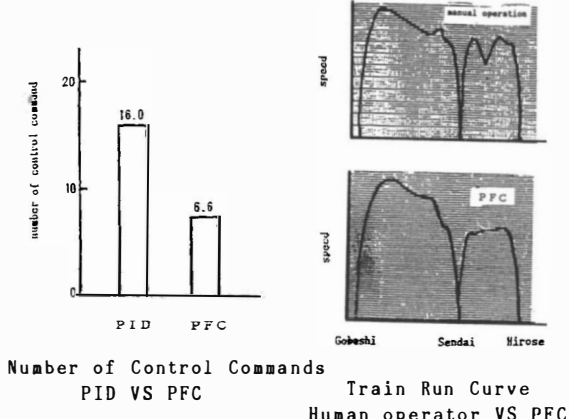


Fig.4. Passenger Comfort

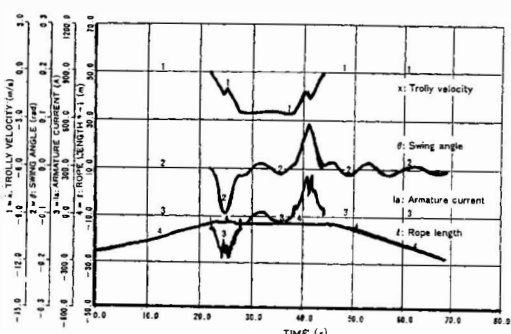


Fig.7. Control Result using PID

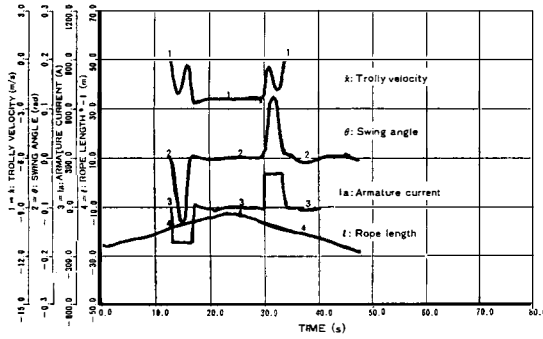


Fig.8. Control Result using PFC

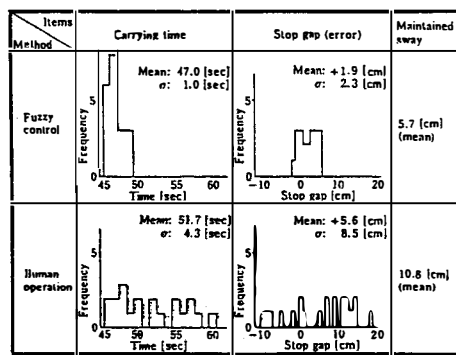


Fig.9. Control Result : Field Test

## USE OF AN EXPERT SYSTEM IN AUTONOMOUS ORBIT CONTROL

I.D. Kitching\*, R. Van't Veld\*, D. Taylor\* and S. Pallaschke\*\*

\*Space Engineering Europe, Kwikstraat 4, B-3078 Everberg, Belgium

\*\*ESA/ESOC/ECD, Robert-Bosch Str. 5, D-6100 Darmstadt, Germany

*Abstract.* Orbital Control (OC) is a vital aspect of every satellite mission. Traditionally, the process of OC and orbit determination (OD) has been very labour intensive. The analysis of the OD solution, the identification of anomalous behaviour and diagnosis of any problems that might occur, are all essentially made by the specialist. There is significant scope for the mundane and routine operations to be automated under software control, and for the experience and knowledge of the experts to be encapsulated in an Expert System.

The paper will discuss the role of Expert Systems in OC with an emphasis placed on the practical implications and benefits that such systems can offer. A prototype system, that has been developed to cover the areas of Initial OD of Geosynchronous Transfer Orbits and the routine phase of OD of Geosynchronous Orbits, will be presented.

*Keywords.* Satellite Control, Initial Orbit Determination, Automation, Expert Systems, Anomaly Diagnosis.

### INTRODUCTION

Orbital Control (OC) is a vital aspect of every mission, be it during the intense activity of the Launch and Early Orbit Phase (LEOP), the routine operations during the nominal phase, or the maintenance of satellites in atypical configurations (e.g. co-located or clustered satellites).

Traditionally, the process of orbit control has been very labour intensive, in that the results of orbit determination (OD) are analysed by the flight dynamicists who, with the aid of suitable software tools, evolve the orbit and plan manoeuvres to meet the orbit and attitude requirements. The analysis of the OD solution, the identification of anomalous behaviour and diagnosis of any problems that might occur, are all essentially made by the specialist, based on previous experience and supplemented by the knowledge of experts in the problem domain.

There is significant scope for the mundane and routine operations to be automated under software control, and for the experience and knowledge of

the experts to be encapsulated in an Expert System (ES) that can make reasoned judgements and decisions during the orbit control process with a minimum of external intervention. This would also enable less experienced operators to implement the process, freeing the experts to undertake more specialised tasks.

Each mission can be split into a number of phases such as LEOP, Transfer Orbit Phase, Commissioning and Validation Phase and Normal Operations Phase each of which can have different requirements for OD/OC support and place varying demands on the available resources. The use of an ES to assist in the operations can improve the efficiency of the process whilst freeing resources for use elsewhere.

The greatest benefit of an ES in OD/OC will occur during LEOP and Initial Orbit Determination (IOD). This is the mission phase which puts maximum demands on resources and uses facilities, some of which are not normally used during any other phase of the mission. During IOD there are a number of unknowns or uncertainties, such as the initial

injection state of the satellite from the launcher and observation calibration errors at the ground stations used only during LEOP. There are also problems such as lack of suitable ranging data due to visibility and priority constraints and the time critical aspects of the phase.

ESIOD (Expert System for Initial Orbit Determination) (Van't Veld and others, 1991) is a prototype system which has been developed to assess the applicability of Expert Systems to the problem domain of IOD. The purpose of the system is to evaluate the solution derived by the OD software. If the solution satisfies a number of predefined criteria, defined by the experts and contained in the Expert System Knowledge Base (KB), then the solution is designated as being valid and may be used for manoeuvre planning, antenna pointing prediction etc. If the solution fails any of the validity tests, then ESIOD attempts to locate the problem, and advises the operator of the remedial action required.

The paper will discuss the role of Expert Systems in OC/OD with an emphasis placed on the practical implications and benefits that such systems can offer. The prototype system, that has been developed to cover the areas of IOD of Geosynchronous Transfer Orbits and the routine phase of OD of Geosynchronous Orbits, will be presented.

## ORBIT DETERMINATION

The process of OD has, conventionally, involved continuous operator support, with the software packages involved being used essentially for only the numerically intensive parts of the process. Task scheduling, program execution, results analysis and anomaly investigation are all generally made by the operator which implies that the operator needs a high experience and skill level for the tasks involved or needs access to experts in the problem domain.

Although the critical aspects of OD are mission phase dependent, the basic steps are common:

- 1) At scheduled time intervals, pre-process the raw tracking (ranging and pointing) data. This can involve checking for data continuity and distribution, data reduction and ambiguity resolution.
- 2) Update the input parameter file(s) for the OD program. This will involve providing parameters such as initial estimates of any

unknowns which are being solved-for such as the satellite orbital elements or state vectors.

- 3) Execute the OD program. Typically, the orbit will be determined by a least-squares iterative method where a model of the orbit (including any relevant perturbations) is fitted to the tracking data.
- 4) Check that the solution has converged to a plausible orbit.
- 5) The determined orbit will then usually be evolved forward in time and used for operations such as manoeuvre planning or dead-band violation checks, in the case of geostationary spacecraft.

At each stage in the OD the operator will usually be required to perform some sort of evaluation of the program output to confirm its validity and take any appropriate action that is required.

A typical OD/orbit monitoring software package, PEPSOC (Portable ESOC Package for Synchronous Orbit Control), which has been developed by the European Space Agency (ESA) and is used by a number of organisations, consists of approximately 14 separate programs each of which require input and steering files, maintained by the operator. If the output from a particular program fails some predefined validity criterion then, apart from trivial cases, the operator will be required to seek expert advice.

Hence OC/OD can generally benefit from two enhancements; automation of mundane, non-specialised, repetitive tasks and from program output evaluation and decision making based on an ES.

The idealised system will be one which is operator independent except in the situations where an anomaly occurs which is outside the scope of the ES KB or where the criticality of the process demands human verification. This will provide benefits such as reduced operator and expert intervention, reduced demand on resources and improved reliability and flexibility.

## AUTOMATION OF FUNCTIONS

The use of an automated OC/OD system is most relevant for the Normal Operations Phase of a mission since this is normally where the routine operations will occur. During the early phases, such as LEOP, the short time scales involved and the

lack of repetitive operations, makes the use of an automated system less appealing.

Figure 1 shows a high level schematic of a task controller which would be suitable for a system such as PEPSOC and where the operational procedures follow a fixed and repetitive cycle of events. The functionality of each of the blocks is explained in the following sections.

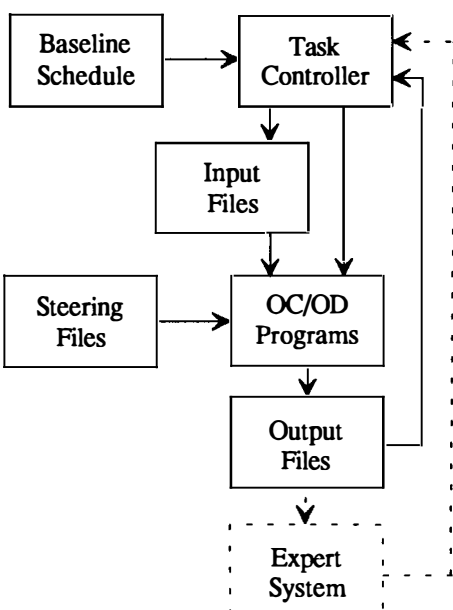


Fig. 1. Schematic of a Task Controller

### Baseline Schedule

The Baseline Schedule will contain a timetable of OC/OD events covering a complete cycle of operations. This will generally remain fixed during the mission. A schedule will exist for each satellite and will instruct the Task Controller when and which programs to execute, which input files require updating, the updated version of the input or the source from which the update should be obtained (e.g. the output from one program could form the input to another).

### Task Controller

The Task Controller performs the updating of input files and execute the various OC/OD processes as instructed from the schedule.

### Input Files

An input file will exist for each program within the system. The contents of the input files will be maintained by the Task Controller and will contain information relevant to the program in question

such as a time span over which data should be processed or initial estimates of solved-for parameters.

### Steering Files

The steering files contain input data which would not normally be changed, such as ground station information.

### OC/OD Programs

These are all the OC/OD programs contained within the system.

### Output Files

These are the output files from the OC/OD programs and may be used as input data for subsequent program runs.

Conventionally, it would be the responsibility of the operator to check the program outputs for validity and take any remedial action which is required. It is this role that the ES element is intended to replace.

## ROLE OF THE EXPERT SYSTEM

When the OC/OD process functions correctly, and no anomalies occur, the expertise required by the operator in the problem domain of OC/OD is minimal. However, when a situation occurs in which the solution or output from one the programs is invalidated in some way then, except for trivial situations (an invalid entry in an input file for example), it is likely that the operator will be required to seek the advice of an expert to solve the problem or provide recommendations. It is this role that the ES can fulfil.

The ES should be capable of fulfilling a number of basic functions to merit its inclusion in an operational system.

- 1) Interpret the data in the input and steering files to validate the input.
- 2) Assess the output of the OC/OD programs for anomalous results.
- 3) Diagnose problems that occur.
- 4) Update input files accordingly and rerun the programs until valid results are obtained.
- 5) If the problems are outside the scope of the system (KB) then indicate this to the operator together with any symptoms that have been identified.

As mentioned in the introduction, one of the areas of OC/OD where an ES would be of greatest benefit is for OD during the LEOP and the initial phases of a mission. A prototype ES has been developed to study this area.

### ESIOD

ESIOD, (Expert System for Initial Orbit Determination) is a prototype ES that has been developed by Space Engineering Europe under contract to ESA/ESOC (European Space Operations Centre) to assess the feasibility of a knowledge based approach in the IOD domain.

Initially, ESIOD was to cover the area of IOD for geosynchronous satellites but this was expanded to also encompass routine OD for geosynchronous satellites.

The purpose of ESIOD was to give automated support to the operator in assessing the plausibility of the solution from an OD. When an OD solution is considered invalid or when the input data to the OD software is not consistent, ESIOD diagnoses the anomaly and provides guidance to remedial actions with explanations of the reasoning. The recovery actions are monitored to optimise co-operative problem solving between the user and the system.

The ESIOD/OD software system is open loop in that the operator has to implement the recommendations rather than ESIOD automatically instigating the corrective actions.

If ESIOD determines that a solution is not plausible, but cannot identify the problem due to lack of knowledge in the KB, then this is indicated to the user as being outside the scope of the system and a list of all the symptoms that have been identified is given to enable the operator to perform external analysis of the problem.

### Global Data Flow

Figure 2 shows an overview of the data flow within the system.

The items above the dashed line represent the unmodified OD software, the tracking data file and the input and steering files for the OD software.

Before the OD I/O can be analysed by ESIOD it is converted into an intermediate format for ESIOD to read. This forms the ODIF (Orbit Determination Input File).

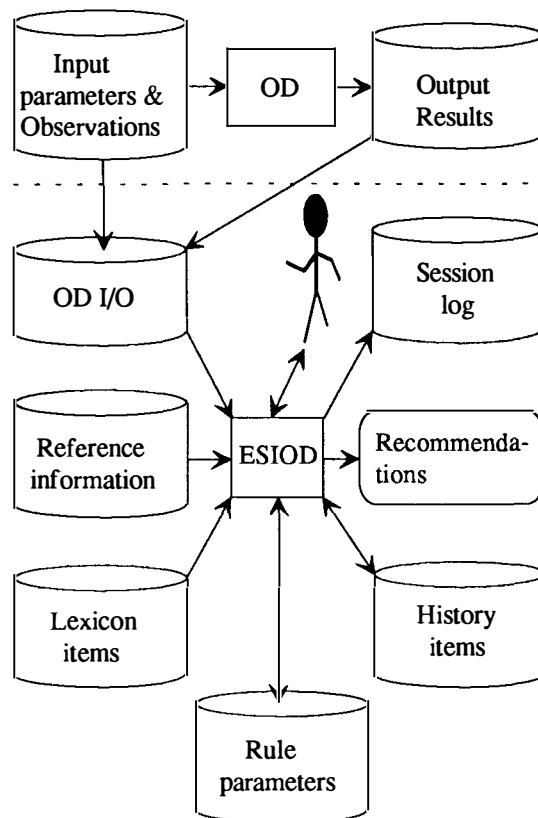


Fig. 2. ESIOD data flow

The other data files consist of:

- The RIF (Reference Information File) which is satellite dependent and contains information about the satellite which will not generally change.
- Rule parameters which are operator editable parameters used within the KB. The rule parameters can be used to fine-tune the system but should generally remain constant.
- Lexicon items used to explain terminology within the system.
- History items which contains symptoms and recommendations which have been identified or made from previous ESIOD runs for the same satellite.
- Session log which records all activity from the current session.

History items are used to avoid the same recommendations being made between consecutive runs, to check that the previous recommendation has been implemented and for a comparison of symptoms across runs where a particular problem cannot be identified from a single analysis.

### Inference Structure

Figure 3 shows the inference structure used within ESIOD.

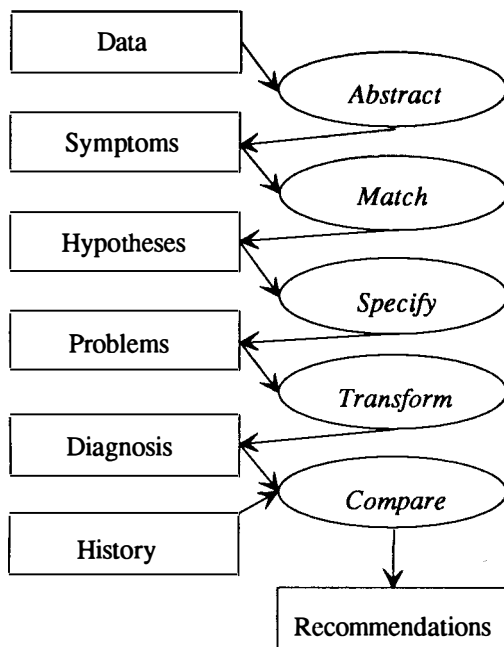


Fig. 3. ESIOD Inference Structure

The general inference structure is explained as follows.

Data or observations are *abstracted* from the ODIF and RIF into symptoms.

The symptoms are *matched* with the hypothetical problems that the system knows about.

The *specify* task ranks the hypothesis in order of those which are most likely.

The most likely problem is *transformed* into a diagnosis and associated recommendation.

The recommendation is *compared* with the history items to avoid repeated recommendations and then the final recommendation is presented together with all likely problems in a ranked order.

### Problem Taxonomy

The types of problems which the KB has been formed to identify are as follows:

- Input inconsistencies, i.e. invalid or erroneous entries in the ODIF. These are checked by comparison between the RIF and ODIF.

- Satellite transponder delay. This will be reflected in the measurements from all tracking stations and could be caused by an incorrect transponder delay in the input file or by the transponder delay not being solved-for during the OD run.
- Tracking station problems such range bias, time bias or noisy data. These are station dependent problems.
- Modelling problems such as atmospheric drag modelling error, solar radiation modelling error or manoeuvre modelling error. All of these errors may be caused by incorrect entries in the ODIF or by not solving for the parameters during the OD run. In the case of a manoeuvre modelling error an incorrect manoeuvre execution time may have been entered.

### Problem Symptoms

To diagnose the above problems, symptoms are abstracted from the ODIF and compared with those of the known problems. Each problem has a number of symptoms associated with it (some being common between problems) and within the problem each symptom carries a percentage weight where the sum of the percentage weights for all the symptoms of the problem equals 100. Therefore, if all the symptoms for a particular problem have been identified with full confidence then the problem will be identified as being 100 percent likely.

The majority of symptoms are abstracted from the data by numeric tests. These usually involve the residuals from the OD (the difference between the tracking data and the orbit model). For example the RMS of the residuals is tested against a predefined maximum (rule parameter) for a plausible solution and the number of rejected measurements (from the least-squares fitting process) is also compared against a maximum. These types of logical true/false black/white tests form the basis of the KB but lead to a very rigid system which would not work in practice unless each problem has a large number of symptoms and no one symptom carries a large percentage weight. To circumvent this problem fuzzy reasoning has been introduced to the tests.

### Fuzzy Reasoning

As an example, consider some symptom which has a numeric value,  $X$ , which is tested against a rule parameter,  $Y$ . For purely logical tests the symptom would be considered as existing if,  $X$  were equal to or larger than  $Y$ . For fuzzy reasoning a *symptom*

*confidence factor* (SCF), between the values of 0 and 1, is deduced by comparing the size of the deviation of  $X$  from  $Y$  as a function of the *symptom bandwidth* (SBW). This is shown in Fig. 4. The symptom percentage weight in the problem concerned is then multiplied by the SCF.

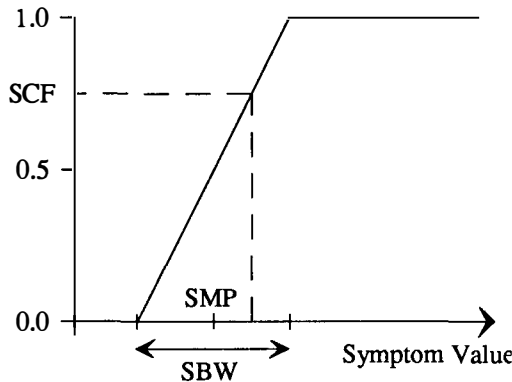


Fig. 4. Fuzzy Reasoning

The SBW is a fixed percentage (rule parameter) of the *symptom middle point* (SMP). In the above example, the SMP would be equal to  $Y$ . The SBW then would be, say, 20% of the SMP centred at the SMP. The uniform transfer function is then used to determine the SCF. In ESIOD the transfer functions are all linear but could in practice be made any shape for the symptom concerned.

#### Residual Trends

When diagnosing modelling problems in the OD, trends in the residuals as a function of time or satellite true anomaly are very import symptoms. At present, ESIOD makes no attempt to identify trends in the residuals but provides the operator with on-screen plots of the residuals and a selection of trends which are relevant to the problem solving. Like the numeric reasoning the trend identification also has associated confidence factors by enabling the operator to attribute more than one trend to a single plot. For instance, a residual plot might exhibit both a sinusoidal and a linear variation and so the operator could attribute a confidence of, say, 60% and 40% respectively to these trends.

#### System Testing

ESIOD has been tested against a number of artificially-produced test cases for a variety of erroneous and error free examples. The tests cases have a two-fold function. Initially they are used for system fine tuning by adjusting the rule parameters and they also serve as a training aid so that the

operator can become familiar with the identification of residual trends.

For the nominal (error free) test case, the solution is diagnosed as being acceptable without any additional operator assistance.

For the other test cases, problems such as station ranging biases and solar radiation modelling errors were diagnosed with confidences in excess of 50% and with differences between the next likely problem of typically several tens of percent.

ESIOD can also be used to diagnose cases outside the scope of the system but the problems diagnosed cannot be guaranteed to be correct. However, the symptoms which are identified are valid and can be used for external assessment of the problem.

## CONCLUSIONS

A clear need for automation and the use of Expert Systems in the area of Orbit Control and Orbit Determination has been identified. Significant manpower and time savings can be achieved by implementing an automated OC/OD system to perform the repetitive and mundane functions.

The use of an ES to provide confidence in the results from the numerically complex aspects of OC/OD and to aid in the diagnosis of problems and to provide recommendations for remedial actions has been demonstrated by the development of a prototype system to cover the areas of initial and routine orbit determination for geosynchronous satellites.

The system could be enhanced by incorporating automatic trend identification in the residuals plot analysis. This was not implemented as the goal of the project was to develop a prototype to demonstrate the applicability of Expert Systems to the OC/OD problem domain. This goal was achieved.

Also, in an operational scenario, the ES should be linked to the OC/OD software in a closed-loop manner so that the recommendations of the ES can be automatically implemented. This would reduce the operator involvement still further.

## REFERENCES

- Van't Veld, R., D. Taylor, I. D. Kitching, D. Rothwell, S. Pallaschke and M. Schaefer (1991). ESIOD: An Expert System for Initial Orbit Determination. *ESTEC AI Workshop*.

## THE UK MISSION MANAGEMENT AID PROJECT

H.J. Pipe

*MMA Project Office, Q153 Building, DRA Aerospace Division, RAE, Farnborough, Hampshire, GU14 6TD, UK*

**Abstract.** In the 21st century combat aircraft necessarily will be complex and sophisticated to counter aggressors, on land, sea, or in the air, anywhere in the world. Along with new and improved sensors and weapons, cockpit facilities are being enhanced, bringing more and varied information to be absorbed and handled by aircrew. In this environment, to optimise situational awareness and mission effectiveness, some form of computerised assistance will be needed. UK Industry and Government are collaborating in a Mission Management Aid (MMA) project, to investigate this problem, by rapid prototyping the functional requirements and examining the real-time interface between man and his intelligent aircraft; he must remain in command, but can delegate control when and where he wishes. This paper outlines the current work on the MMA, and covers the core topics of Sensor Fusion, Situation & Threat Assessment, Dynamic Planning, Tactical Response, and how the system might integrate into an aircraft.

**Keywords.** In-flight management; combat aircraft; advanced automation; artificial intelligence; man-machine interface; simulation.

### INTRODUCTION

Operational requirements for future military aviation such as the single-seat fighter, and battlefield helicopter, are becoming progressively more demanding. Traditional roles are being extended, and aircraft operating beyond the turn of the century will likely face increasingly hostile and more capable threats, both in the air and on the ground.

To meet this challenge avionics equipment is becoming more sophisticated and multi-functional, and integrated to form complex systems. In future, these might be managed by only a single crew, yet already aircrew can become overloaded during intensive combat.

To address the concept of a new class of support for a pilot, the Mission Management Aid Project was set-up in the late eighties. This research programme depends upon the collaboration of British Aerospace, GEC Avionics, GEC Sensors, Smiths Industries, and the Ministry of Defence, and draws on the combined expertise of staff seconded to form a multidisciplined team located on the Defence Research Agency site at Farnborough.

The Project is investigating the feasibility of a Mission Management Aid, the MMA, that would be installed in combat aircraft. By simulating the concept, on a network of computers, its functionality is being developed. This software prototyping environment allows rapid system investigations, and functional optimisation. Experimental man-machine interface work is helping to define Pilot requirements in an MMA equipped aircraft. Proving of system concepts will be extended naturally into trials in real-time using a pilot-flown Mission Capable Simulator.

Currently it is the aircrew who has thoroughly to understand the mission, its route and hazards, and try to make sense of all information, from whatever source, resolve ambiguities, and judge the best tactical response in any situation, be it air-to-air combat where a heads-up awareness is essential or in prosecuting a ground target. The MMA, by collating all information, is being designed to provide advanced tactical assistance, and control - if the pilot wishes, so that he can achieve an enhanced situation awareness and maintain this benefit when events change faster than human recognition. This will improve effectiveness and promote survivability.

## INTEGRATION OF THE MMA WITH FUTURE AIRCRAFT

To reach these objectives, the MMA must of course fully integrate with future aircraft systems. Figure 1 shows, simplistically, such base systems grouped with their Managers around a Pilot Interface Manager (PIM), supported by Health & Status Monitoring. The pilot exercises command via Controls and Displays. This forms a foundation for the MMA.

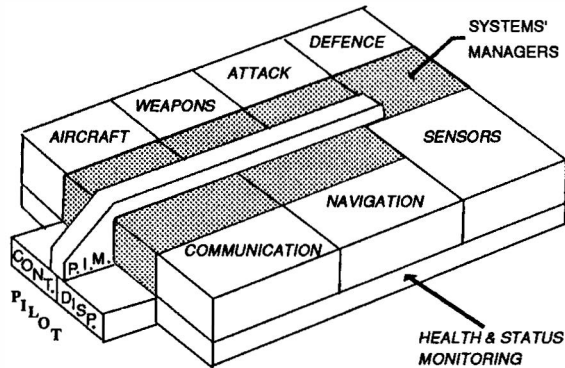


Fig. 1. Aircraft Base Systems

Some systems, like the Communications and Navigation Managers, probably will be expanded to support the MMA, and others added - such as a Sensors Manager, a Tactical Implementation Processor (TIP) and, for evading imminent disaster, a Reflex function. Besides these Support Functions, the PIM will expand and may become a central intelligent system, incorporating executive control over the systems managers, as shown in Fig. 2.

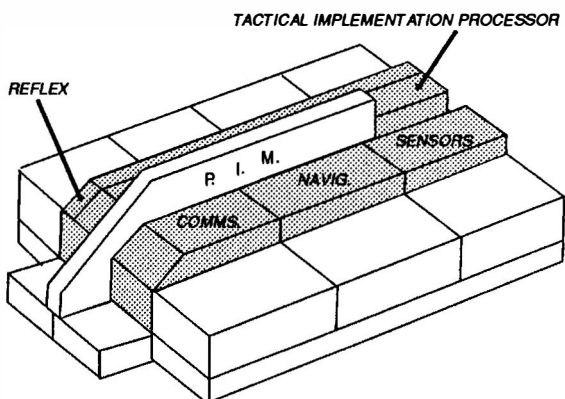


Fig. 2. MMA Support Functions

The MMA is likely to assume a top-level role, to augment the pilot, and itself is conceived to have Core Functions that perform Sensor Fusion, Situation Assessment, Planning and Tactical Routing, as shown in Fig. 3. In addition, a Displays & Controls Executive needs to handle information

exchange with the pilot, and this must seem natural and intelligent; indeed this ought to be tailored, when he boards his aircraft, to optimise cooperation between man and machine - the pilot of course will have ultimate control, but he can delegate tasks to

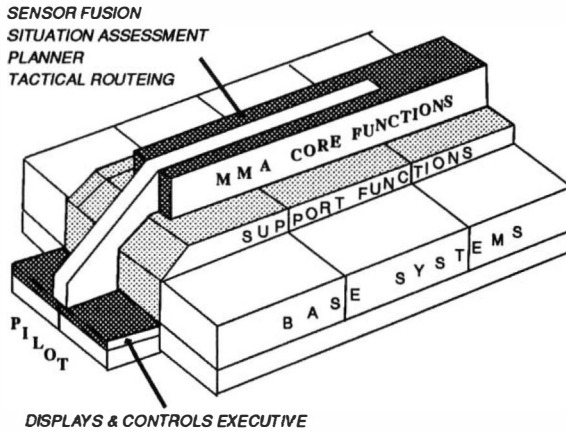


Fig. 3. Integration of the MMA

the MMA if he wishes.

## OPERATION OF THE MMA

Before take-off, to cross enemy territory, the MMA can confirm a proposed mission route, a section between waypoints, or compute an alternative to take account of new threats. At the same time, the Systems Managers will formulate their own agendas for mission activity.

During flight the aircraft continually assesses its environment and, as hostile military objects react to its presence, the MMA dynamically replans actions to suit, keeping calculated risks to a minimum while maintaining mission objectives, and advising the pilot appropriately with pertinent messages. The system also copes with housekeeping chores, and will be able to reconfigure facilities to bypass equipment faults. By using parallel processing, and redundancy, all MMA functions work simultaneously and systems can survive battle damage.

Freed of such tasks the aircrew can then make full use of the situational advantage given by the MMA, and augment it with his own cognitive abilities. Thus, by flying with a Mission Management Aid, the pilot and aircraft form a very effective combination.

## ARCHITECTURE OF THE MMA

In overview, the MMA Core Functions interact with the aircraft Base Systems (shown at the bottom of Fig. 4); and provide advice to the pilot, via the PIM, and/or direct control of the aircraft systems if and

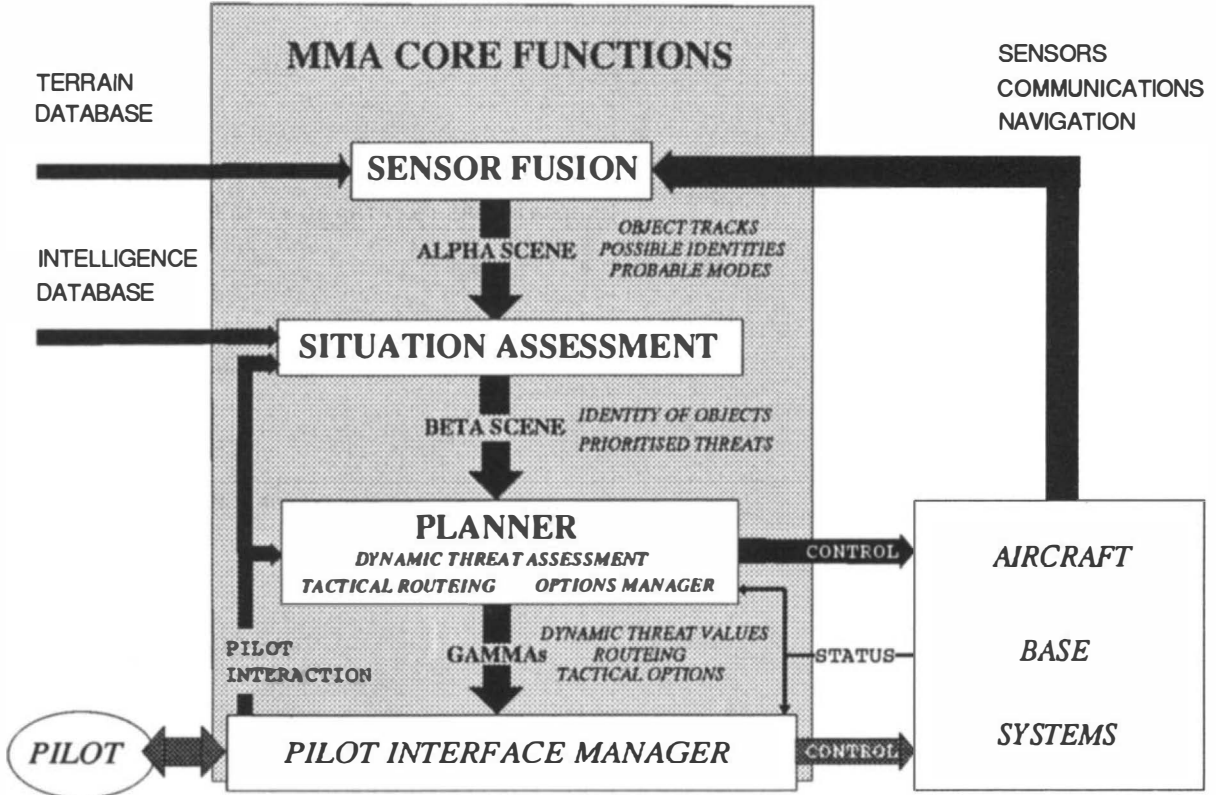


Fig. 4. The architecture of the MMA

when required by the pilot - he remains the ultimate decision maker and can delegate tasks to the MMA as appropriate. As a safety feature, and in the event of a catastrophic computer failure, reversion to the basic aircraft is always possible.

#### Sensor Fusion

Within the Core Functions of the MMA, Sensor Fusion is logically first. It handles observations of world objects by aligning data from various sources (sensors, communications, navigation) - which may have different accuracies, temporal and spatial reference frames - and resolves this information to provide correlated object tracks.

Using geographical knowledge from an onboard terrain database, and mission data loaded before take-off, with signature information obtained during flight, (from Radar and Infra-Red devices), the object tracks are then attributed with possible identities and probable modes of operation. This correlated view of the scenario is known as the Alpha Scene, a widespread view of all objects - including friendly forces.

#### Situation Assessment

This function takes the Alpha Scene and, with on-board intelligence about threat characteristics and

behaviour, identifies objects and their hostility towards the aircraft. If the pilot believes he has superior knowledge, he can interact with Situation Assessment to resolve ambiguities that might arise from the hypotheses generated, or to direct attention to a particular threat. This is the Beta Scene, local to the aircraft; a version of Alpha, that has been filtered to prioritise threat capability and intention, and also indicate friendly disposition.

#### The Planner

The Planner examines mission objectives against this scenario, proposes the best flight path and also gives tactical assistance in response to the dynamically changing local Beta Scene. The resulting options (Gammas) are available to the pilot, with the best one, Gamma\*, ready for automatic implementation.

In generating plans, account is taken of the current situation and available resources, such as weapons, fuel, countermeasures, and supporting aircraft.

In determining the route, various search strategies are used. The range and density of threats is of prime importance, and terrain screening from them - by flying low - is highlighted. Alternative routes are automatically evaluated against expected threat activity, fuel and time estimates, while keeping to

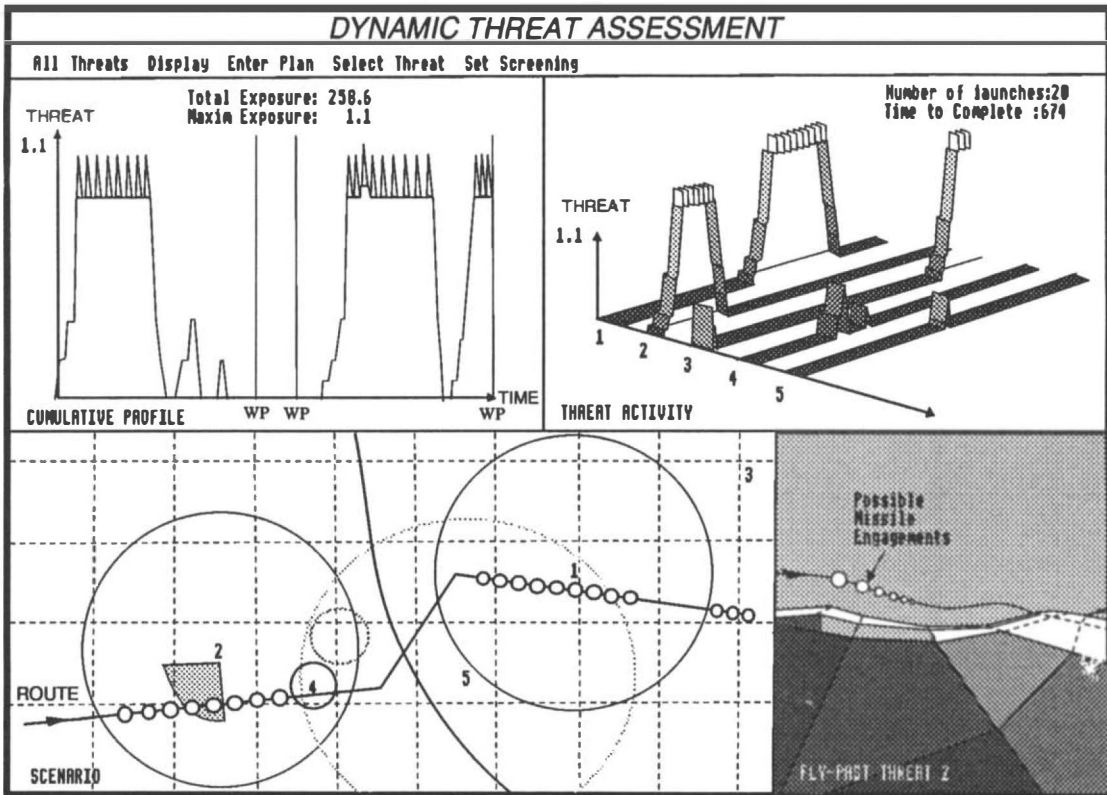


Fig. 5. Dynamic Threat Assessment ....engineering display\*

waypoint restrictions and other mission constraints, for example the time-on-target.

Within the Planner, three main functions exist:-

**Dynamic Threat Assessment** postulates the actions of hostile systems. Based on their "known" operational characteristics, the number and frequency of possible firings against the aircraft are calculated. Conceptually, for each threat, a profile of *activity level* against *time* is constructed and, for any route, a cumulative profile of all probable threat activities is developed.

As an example, the results of these computations, for ground-based threats, are shown in Fig. 5. The steps in the threat profiles indicate the expected system mode changes: from a baseline level of *surveillance*, via *acquisition*, and *tracking*, through to *illumination* when missile launches are imminent.

In predicting hostile responses, Dynamic Threat Assessment takes into account the reaction time of each system, the time required in each mode to achieve a firing solution, and the effects of terrain screening. Currently, as a pessimistic view is taken of enemy activities, the Planner dynamically minimises costs in a worst-case scenario.

**Tactical Routeing** provides an optimum course by

looking ahead through the local environment, taking account of the aircraft's performance, fuel and time constraints, as well as terrain-masked threats.

Path deviations are continually being evaluated against threat posture, in the context of the planned route, and refinements are achieved by balancing off-route costs against risks involved. Navigational instructions are generated automatically, and can control the flight.

An engineering display for observing the action of Tactical Routeing is shown in Fig. 6.

**The Options Manager** examines tactics against enemy actions, and recommends suitable responses.

For example against a missile attack, triggered by the warning of missile launch or approach, the Options Manager uses information from Situation Assessment about the appropriate hostile system and, with knowledge of the MMA aircraft's performance and resources, calculates the necessary *escape envelope*. This would take account of the kill zone of the threat, possible aircraft manoeuvres to break missile lock, use of countermeasures (chaff, flares, or electronic methods for example) or simply terrain screening. Figure 7 shows a snapshot of the activity of this function.

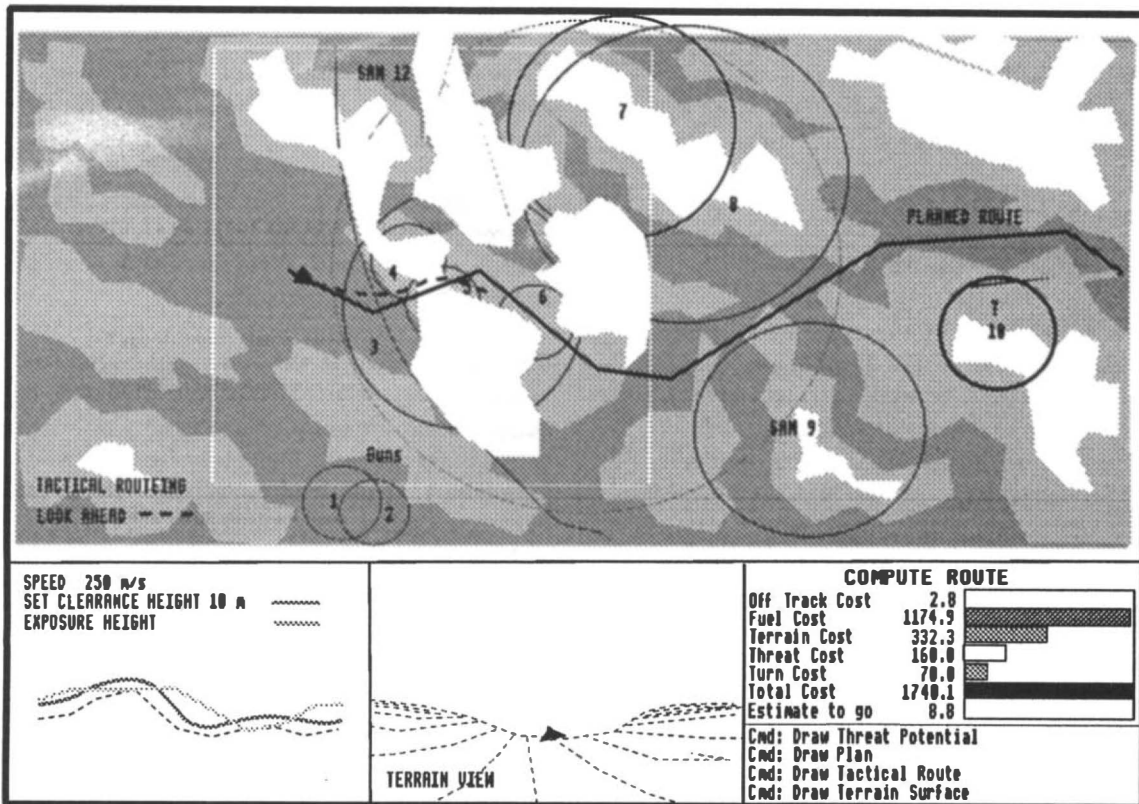


Fig. 6. Tactical Routeing...engineering display\*

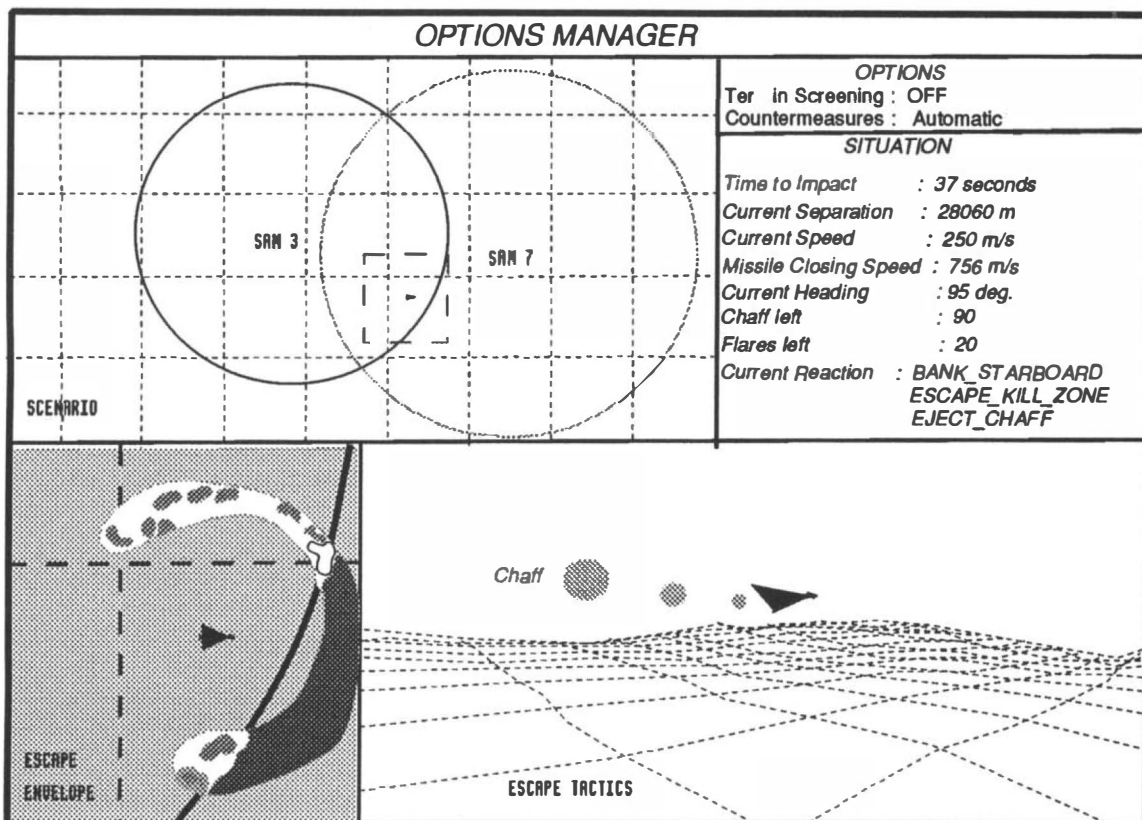


Fig. 7. Options Manager... engineering display\*

**\*Engineering Displays... Figures 5, 6, and 7.** It must be stressed that these diagrams are purely for engineering purposes only, during prototyping, to check the functional behaviour of the software modules. If any of this information is presented to the pilot, it would be severely edited and conveyed at the appropriate time, in such ways that are found to be acceptable from man-machine interface investigations into aircraft cockpit design.

These recommendations could be coupled into the aircraft's systems, to set-up automatic sequences and relieve the pilot of time-critical, split-second, actions. In an emergency situation, this is where a Reflex function is appropriate; this should improve survivability.

### MAN-MACHINE INTERFACE

The MMA will affect all the major avionic systems of future aircraft, as well as the pilot, and the relative level of authority between the pilot and the MMA (or its components) is of fundamental importance in the design of the overall system. It should be remembered that the MMA is intended to aid the aircrew. As such, it should relieve them of onerous tasks but permit them to carry out their preferred work, and that which is impractical to automate.

Clearly, the Pilot/MMA interaction is potentially very complex, and for effective use it must be designed carefully so as to be intuitive. The sharing of tasks with the MMA should be able to be tailored to pilot preferences, but is likely to be dynamically variable during flight. Also, the aircrew must be provided with the required information at the relevant time, but must not be overwhelmed; equally, they ought to have the opportunity to interrogate any function as far back as raw sensor data - but, as the MMA evolves and aircrew confidence in it grows, this should become unnecessary.

As an integral part of the Project, these interface aspects are being investigated both in the laboratory and in cockpit simulations. As this MMI work matures, the functions of the MMA are being combined with it, and the total system evaluated. This will lead into a series of tests and development in a pilot-flown mission-capable simulator.

### CONCLUDING REMARKS

Through this Project the concept of a Mission Management Aid is being developed and its functional requirements generated. Research is covering the MMA's need to assess all situations, to advise and decide on actions and reactions, and to controlling aircraft functions automatically if and when necessary, thus helping the pilot to complete a successful mission.

The Mission Management Aid brings together all avionics equipment into a total aircraft system. By being tailored dynamically in sympathy with human activities throughout a flight, it truly augments crew ability, giving much better situational awareness, better response, and increased effectiveness and survivability.

The interface between pilot and machine is being investigated in aircraft simulators, and confidence is growing in the emerging MMA. The Mission Management Aid thus is becoming a vital integral system for future aviation.

### BIBLIOGRAPHY

- Catford, J.R., and I.D.Gray (1989). Research into a Mission Management Aid. AGARD 49th Symposium of the Guidance & Control Panel, 10-13th October, Toulouse.
- Gibson, C.P., and Ms A.J.Garrett (1989). Towards a future cockpit - the prototyping and pilot integration of the Mission Management Aid. AGARD Conference on Situational Awareness in Aerospace Operations, 2-6th October, Copenhagen.
- Lovesey, E.J., and R.I.Davis (1991). Integrating machine intelligence into the cockpit to aid the pilot. AGARD Conference on Machine Intelligence for Aerospace Electronic Systems, 13-16th May, Lisbon.

## INFERRING OPERATOR INTENT AS A BASIS FOR AIDING IN MAN-MACHINE SYSTEMS

B. Hoshstrasser

285 Flowing Spring Trail, Roswell, GA 30075, USA

**Abstract** Intent interpretation by observing and explaining operator actions provides a powerful means of implicit communication between a human operator and a man-machine system. While not always required in an operational system, knowledge of the intentions of the user may be quite useful as a basis for providing assistance via an intelligent interface. Using a model of operator intent, intelligent assistance can be provided while leaving the operator in total control. Specifically, assistance can be offered through information management, error monitoring, and adaptive aiding. In addition, the intent model facilitates implicit communications between the human operator and intelligent planners and situation assessors, allowing the human to guide the reasoning of the intelligent aiding systems without the added burden of explicitly communicating with them. The basic design of the intent inferencer is described from a high level. Knowledge representation used in the intent inferencer is discussed more extensively.

**Keywords.** artificial intelligence, cognitive systems, man-machine systems, expert systems, adaptive systems, inference processes.

### WHY MODEL INTENTIONS?

The intentions of the operator of a complex system can be depicted as a set of plans and goals that describe what the operator is trying to achieve as defined by the capabilities and purpose of the system being manipulated. Operator support systems serving as an interface between a complex system and a human operator can greatly benefit from such a model of operator intent. Using the implicit communication provided by an intent model, we are able to provide assistance to the operator in three areas. First, we can assist the human by selecting appropriate displays of information for achieving his/her current plans and goals. Second, by having an understanding of what the human is trying to achieve, it is possible to recognize when an error occurs and provide assistance in correcting or compensating for the error. Finally, support is provided by an intelligent adaptive aider using the model of operator

intentions along with a model of human resource allocation to determine when help is needed in carrying out the tasks at hand.

Implicit communication of intentions is one of the greatest advantages of an intent inferencer in an intelligent man-machine system. It is particularly important in a time-limited domain when the explicit communication of intentions would be impossible due to time constraints. Expressions of intent are interpreted directly into the system by observing the human operator carrying out normal actions in the context of the complex system; the operator communicates by acting rather than through explicit speech-like acts. Implicit entry of intent is a valuable capability since it imposes no extra physical or mental workload on the operator, (i.e. - the operator doesn't have to explicitly tell the intent interpreter what he/she is doing), and it places no restrictions on possible activities.

Intent interpretation also supports implicit communication with integrated cooperative planning systems. The interpretation process results in the activation of plans and goals in the intent model which are passed on to the planners in the same way that a direct declaration of operator intent could be used to guide planner reasoning. Thus, the human operator is integrated into the aiding system as a cooperative planner. In this way, the other planning systems are focussed on the operator's objectives, rather than ignoring them as most automated planners do.

This paper will describe how inferred intent may be used to assist the operator, the design of the intent inferencer, and, finally, recent progress and future directions for the intent inferencer.

### USING THE INTENT MODEL FOR AIDING

A model of operator intentions serves as a basis for aiding both inside an intelligent man-machine interface and between intelligent subsystems.

#### Inside an Intelligent Interface

When intent is correctly inferred, the man-machine system has an accurate model of the current plans and goals of the operator. Using this model assistance can be provided to the human operator through information management, error monitoring, and adaptive aiding.

**Information management.** The goal of intelligent information management is to provide the information needed by the operator when it is needed, while eliminating any unnecessary or irrelevant information. An intelligent information manager can use operator intent to determine what information is needed by the operator to perform current tasks. The information manager has a knowledge base relating operator plans to specific pieces of information required for successful execution of those plans. Using this knowledge base and the active plans from the operator intent model, the information manager determines what information is needed by the operator to complete the current plans. The information requirements for all the active plans are combined into a single set of information requirements representing the total information needs of the operator. Then, the best displays and display formats to meet the aggregated information requirements can be determined.

In systems with multi-function, reconfigurable controls, the controls may also be configured by

the information manager. For example, many advanced aircraft have a complex, multi-level set of menus that the pilot must navigate to have access to certain controls. Based on the operator's intentions, the intelligent information manager can automatically select the necessary control menu for the pilot; relieving the pilot of the responsibility and workload associated with navigating a complex set of menus.

**Error monitoring.** Operator actions can be monitored for errors by evaluating the actions in the context of the current operator intent model. If a particular action is found to be inconsistent with the model of operator intentions, then that action is potentially an error. An error monitor can be designed to examine the operator's actions in terms of the current intentions and determine if that action has any serious consequences. An action can be classified as an error if the consequences of that action have a negative effect on the current plans (intentions) of the operator. Consequences can be of varying degrees, from negligible to, in some cases, life threatening. When a particular action is found to have serious consequences, the error monitor can recommend a course of action to compensate for the error.

**Adaptive aiding.** A representation of operator intentions given to an intelligent adaptive aider provides a means for supporting the operator by reducing workload. The adaptive aider, when authorized by the operator, can perform routine or procedural tasks without requiring any action on the part of the operator. This may be useful in situations where the operator is overloaded or simply does not want to be bothered with routine tasks. The adaptive aider can also carry out actions recommended by an error monitor to remediate an operator error.

The adaptive aider's decision of whether or not to provide assistance can be partially based on an estimate of the workload of the operator. A model of the operator's resource usage can be created directly from the intent model. Using the active plans in the intent model, a resource modeler estimates the level of use of the human operator's resources.

#### Between Intelligent Subsystems

A difficult problem in designing intelligent planners and situation assessors has been communicating the reasoning processes of the intelligent subsystem to the human in a form that the human can readily understand. Humans are understandably reluctant to accept the recommended actions from a planner or the

judgments of an assessor without a clear mapping of that output onto their own set of concepts about the domain in which they are operating. This issue is frequently approached as an explanation problem with respect to the human.

Correspondingly, the human has an explanation problem relative to the intelligent planner or assessor. For example, it is often difficult for the human operator to describe the complete set of interacting goals that define the problem space for an intelligent planner. The seemingly innumerable details of real world situations must be translated into the knowledge bases of the intelligent system to be usable as a basis for aiding. For a complex, dynamic domain such as tactical aviation, the ability of the operator to explain the situation to the intelligent system is highly constrained by both time and the expressiveness of a mostly graphical, non-textual interface.

Intent interpretation can solve these problems by providing a mechanism for both explicit and implicit communications with intelligent planners and assessors. Explicit communications allow the planner to propose plans and goals to the human operator and for the operator to accept or reject the planner's proposals. In addition, the operator can directly declare his intentions to the planner in the form of plans to be used or goals to satisfy. The proposals of the planner and declarations of the operator may be at various levels of abstraction or problem decomposition. This allows both the human and the planner to participate in the progressive formulation of plans while maintaining a mutual awareness of the evolution of the planning solution in the form of the model of intentions.

Intent interpretation also supports implicit communication with the planner. In highly dynamic situations, it is often easier for the operator to simply perform the steps of a plan and have the intent interpreter infer the plan from his actions. The plan is in turn interpreted as a method for achieving a goal. The interpretation process may result in the activation of plans and goals in the intent model which are passed to the planner in the same way that a direct declaration of operator intent is used to guide planner or assessor reasoning.

Plans which have been proposed by the planner can be implicitly accepted by the intent model in the same manner. If the operator begins to perform a plan that has been proposed, the intent interpreter can inform the planner that the plan was accepted. Plans are implicitly rejected only if the operator fails to act on the plans before they become inappropriate.

Modeling operator intentions provides a powerful communications mechanism between human operators, intelligent interfaces, and other intelligent subsystems. Next, the design of the intent interpreter will be described.

## DESIGN OF THE INTENT INTERPRETER

The intent inferencer or interpreter consists of two main parts: a Script-Based Reasoner and a Plan-Based Reasoner. Input to both is in the form of operator actions. The intent inferencer attempts to understand, or interpret, these actions based on its current model of the operator's intent and knowledge of the domain. An action is said to be explained if it is consistent with what was expected by or could be predicted from the current intent model.

### Plan and Goal Graph

The basis of the intent inferencer is a plan and goal graph that incorporates both domain knowledge and knowledge of system capabilities to define the possible set of plans and goals of the human operator in the context of the system. The plan and goal graph is constructed as a hierarchical, directed, acyclic graph. Each goal has one or more plans for satisfying that goal. These subplans are OR'ed together so that any one of the plans is individually capable of satisfying the goal. High level plans and subplans are carried out by satisfying a set of subgoals. Subgoals have an AND relationship; all subgoals must be satisfied to complete the parent plan. The children of leaf plans are actions. Some plans are sufficiently low level that they can be characterized by a single operator action; others require several actions to complete. Procedurally-oriented plans can have associated scripts specifying the actions necessary to execute the plan. The graph is organized hierarchically, much like a tree, but not exactly since nodes can converge as well as diverge; a particular subgoal may be required for carrying out, (at least partially), more than one parent plan.

The intentions of the operator are represented as dynamic instantiations of the static plans, goals, and scripts described by the plan and goal graph. Since the plan and goal graph represents all possible activities, only specific parts of the graph will be active at any one time.

### Script-Based Reasoner

A script is a loosely ordered set of actions that specifies the steps necessary to carry out a particular plan. Scripts represent learned, procedural knowledge and are used to recognize operator intent in stereotypical situations. Also, scripts provide a means for an adaptive aider to carry out routine tasks.

A script consists of a series of action/state pairs called events. An event is completed when either the action occurs or the state is achieved by some other means. Events are grouped into segments within the script. Segments impose order on the events which make up the script. Segments must be executed in order. The events inside a segment, however, may occur in any order. Inclusion of a specific event in the execution of a script may be either optional or required. Two types of segments are represented: cycles and blocks. The events inside a cycle may occur any number of times; the events in a block happen only once. Individual differences and variations in execution of scripts are accounted for using optional versus required events and loose ordering within script segments.

The Script Based Reasoner attempts to interpret operator actions as anticipated steps in the execution of an active script. If an operator action corresponds to an event in an open segment of a script, the event is marked as completed and the action is explained. All active scripts are searched, even if a match is found early on, since a particular action may occur in more than one of the active scripts. The termination conditions of each script are evaluated to determine if any of the scripts should be removed from the model of intent.

### Plan-Based Reasoner

If an action is not predicted by any of the active script instances, then plan-based reasoning attempts explanation of the action as a plan to satisfy one of the current goals of the operator. To do this, the Plan-Based Reasoner uses a knowledge base that is actually a static representation of the plan and goal graph for the given domain as nodes and links between those nodes. Each node represents a plan, goal, script, or action. Each link represents a particular relationship between two nodes. Constraints are placed on the links to provide a way to account for context. Instantiating a particular plan or goal may have side effects which include instantiating a script or removing plan and goal instances from the intent model which are in conflict with the newly inferred plans and goals of the operator. These side effects are also represented by links.

To explain an operator action through plans, the intent inferencer searches upward through its knowledge base, from the more specific nodes to the more abstract, to determine if the action was predicted by any of the active plans and goals of the human operator. This may require inferring instances of intermediate plans and goals to connect the action to a higher level plan or goal that is already active. Once an explanation has been found, instances of the new plans and goals used in the explanation will be invoked and incorporated into the current model of the operator's intent. Due to the hierarchical organization of the plan and goal graph and by considering active instances of nodes first in the explanation process, the search is biased toward mutual consistency with previously inferred intentions and the higher level goals of the operator. In doing so, we avoid the problems associated with typical plan recognition systems that consider the operator's plans in isolation, ignoring the more global, higher level intentions of the operator [Pollack, 1989].

## RECENT PROGRESS

The intent inferencer has been implemented in two versions. The first version was written in Lisp with an if-then rule knowledge base. Later, the intent inferencer was re-implemented in C++ for real time. The major difference between the Lisp-based and C++ versions is in the knowledge base. The newer, C++ version uses a concept map representation of the knowledge base.

Previously, if-then rules were used to express the knowledge required for intent interpretation. However, a more efficient system than symbol matching and chaining through if-then rules was needed for a real time implementation. The representation chosen is a concept map that is actually an implementation of the plan and goal graph. Not only does the concept map approach allow for a more efficient implementation of the intent inferencer, but it is also a more expressive representation, making it possible to enhance to our intent interpretation methodology.

### Knowledge Base Design

As stated earlier, the knowledge base for the Plan-Based Reasoner is a representation of the plan and goal graph as nodes and links. Nodes represent plans, goals, scripts, or actions; links represent semantic relationships between nodes. Several different kinds of links have been identified for the intent interpretation concept map.

Interpretation Links. Interpretation links describe the parent-child relationships that exist among the nodes in the plan and goal graph. When a lower level plan (or goal) can be interpreted as supporting a higher level goal (or plan), they are linked. The interpretation links are analogous to the if-then rules in the previous intent interpreter knowledge base design. Constraints are placed on interpretation links to account for context. Constraints determine if the link is practical to consider as an explanation given the current situation and provide a means for the intent inferencer to disambiguate possible explanations.

Mutual Exclusion Links. Some nodes in the network cannot simultaneously be active. Mutual exclusion links allow for removal of nodes from the intent model when new, conflicting intentions are inferred. For example, in the domain of aviation, an aircraft cannot simultaneously descend and climb to a new altitude. If the previous intent was to descend, but the pilot has now commanded a climb, the intention to climb replaces the intention to descend.

Mutual exclusion links do not have to be absolute exclusions based on node type. Exclusions can be constrained so that nodes are mutually exclusive only under certain conditions.

Script Links. Script links connect procedural plans to scripts. Scripts describe a prescriptive set of actions that must be performed to carry out a plan. An example of a script link is a pointer from a plan about preparing for takeoff to a script that represents the checklist of steps that need to be executed prior to takeoff.

Expectation Links. Expectation links can be used to guide the future reasoning of the Plan-Based Reasoner. Certain nodes will cause us to anticipate that other nodes will be active in the near future. By considering the expected nodes first, we can guide the search of Plan-Based Reasoner, thus increasing the speed of the intent inferencing process, and the accuracy as well.

The following types of links are actually specializations of the Expectation Link.

Co-Dependency Links. There may be some nodes that support each other; we would usually expect to see these nodes coexist. The child goals of a plan immediately come to mind as an example since all goals must be satisfied before the parent plan is completed.

When a plan is inferred, the co-dependency links could be used to determine which of the child goals has not yet been satisfied. Those goals could

then be activated, or put into an anticipated state. An integrated adaptive aider could monitor the posted co-dependent goals and assist the operator by executing the necessary actions to satisfy the goals when the operator is too busy to do so. A further advantage to posting the unachieved goals is that they could be used to guide the efforts of integrated intelligent planners towards achieving the operator's goals.

Timing/Ordering Links. For some nodes, there is an implied ordering or timing that is not explicit in the plan and goal graph itself. In the past, we have used constraints to enforce ordering. Some of this knowledge can be seen in constraints on the interpretation links. A node may be constrained such that it cannot become active unless another node has previously been completed or achieved. This kind of knowledge is not always obvious in the knowledge base. Careful study of the knowledge base is required before the ordering dependencies can be identified. By the explicit use of timing or ordering links, we can make domain knowledge more apparent in the implementation of the knowledge.

Alternatively, timing or ordering links could be used to suppress nodes which are not possible given the current situation.

### Advantages of the Concept Map Design

One of the major advantages of this design is the added richness of the representation. Using the various link types identified above, we can extend the capabilities of our intent inferencer. Expectancy based reasoning can be introduced into the part of the intent inferencer that has, until now, used causal attribution exclusively to interpret intentions.

Consistency of representation is another advantage of the concept map design. By using links to replace if-then rules and side effects, the knowledge base is much more homogeneous and therefore, easier to understand as well as maintain.

Concept mapping has been shown to be a good method for knowledge acquisition and knowledge engineering. Domain experts can readily be taught concept mapping techniques [McNeese 1990]; it is a natural way to represent complex situations and interactions. Domain experts can play a key role in constructing the plan and goal graph, providing the knowledge engineer and domain expert with a shared, mutually understood starting point for further knowledge elicitation. Further, by examining the knowledge base/concept map, the domain expert is able to verify that the knowledge

engineer has captured an accurate representation of the information provided by the expert. From a validation perspective, concepts represented in the concept map can be used as test points. In addition, major decisions that can be made using the knowledge base/concept map are visible.

Knowledge engineering suggests that the concept map representation of intentions is, in fact, a closer representation of human cognitive processes than the original design. The original design lacked some of the expressiveness needed to more accurately reflect operator intentions in complex systems. Domain experts have been readily able to identify mutual exclusion, co-dependency, and order dependent relationships among the concepts represented in the plan and goal graph. These relationships may be directly translated to link types inside the intent inferencer's knowledge base.

By implementing this richer, more accurate model of intentions, better support can be provided to the operator through an intelligent interface. A variety of different links between concept nodes can be used to enrich the support given the operator in the following ways:

- A resource model can use expectation links to anticipate operator activities and predict future workload.
- Expectation and script links can guide the adaptive aider in deciding what activities can be pursued to help the operator when assistance is indicated.
- An error monitor can use co-dependency links to recognize errors of omission. Ordering links can help in identifying errors of omission or task sequencing errors.
- An intelligent information manager can use expectation links to select displays to help the operator anticipate his or her next activity. In many cases, knowing what activity to pursue next is the hardest problem facing the operator of a complex system.

To date, interpretation and mutual exclusion links have been fully implemented. Script links have been designed, but not yet implemented. Work has begun on the design of some of the expectation link types.

## CONCLUSIONS

The intent inferencing methodology and knowledge base design described here have been demonstrated as an effective paradigm for

inferring operator intent in dynamic, strongly contextual domains. The resulting intent model is used in intelligent interfaces to provide assistance to the operator through information management, error monitoring, and adaptive aiding. The intent model also provides a means of communication with and direction to cooperative planning systems.

## REFERENCES

- Fishbein, M. and Ajzen, I. (1975). *Belief, Attitude, Intention, & Behavior: An Introduction to Theory and Research*. Reading, MA: Addison-Wesley.
- Hoshstrasser, B.D. and Geddes, N.D. (1989). OPAL operator intent inferencing for intelligent operator support systems. V.L. Shalin and G.A. Boy (Eds.), *Proceedings of the IJCAI-89 Workshop in Integrated Human-Machine Intelligence in Aerospace Systems*, 53-70. Detroit, MI.
- Hoshstrasser, B.D. (1991). A concept map approach for representing intentions of human operators of complex systems. *Proceedings of the IJCAI-91 Workshop W.4 Agent Modelling for Intelligent Interaction*, 86-92. Sydney, Australia.
- McNeese, M.D., Zaff, B.S., Peio, K.J., Snyder, D.E., Duncan, J.C., McFarren, M.R. (1990). *An Advanced Knowledge and Design Acquisition Methodology: Application for the Pilot's Associate*. AAMRL-TR-90-060. Armstrong Aerospace Medical Research Laboratory, Wright-Patterson Air Force Base, Ohio.
- Pollack, M.E. (1989). Plan Recognition Beyond STRIPS (Extended Abstract). *Proceedings of the Second AAAI Workshop on Plan Recognition*. Detroit, MI.
- Rouse, W.B., Geddes, N.D., & Curry, R.E. (1987). An architecture for intelligent interfaces: Outline of an approach to supporting operators of complex systems. *Human-Computer Interaction*, 3(2), 87-122.
- Schank, R., & Abelson, R. (1977). *Scripts, Plans, Goals, and Understanding*. Lawrence Erlbaum Associates, Inc: Hillsdale, NJ.

## AI-DEMONSTRATORS FOR THE ROSAT AND D2-MISSIONS

C. Sielaff\*, R. Küke\*, G. Ohlendorf\*, D. Heyland\*\*, R. Timm\*\*\*, Dr. Reinelt† and H. Koenemann††

\*Deutsche Aerospace ERNO Raumfahrttechnik GmbH, PO Box 10 59 09, D-2800 Bremen, Germany

\*\*DLR, Linder Höhe, D-5000 Köln 90, Germany

\*\*\*ESA/ESTEC, Postbus 229, Keplerlaan 1, NL-2200 AZ Noordwijk, The Netherlands

†DLR/GSOC, Münchener Str. 20, D-8031 Oberpfaffenhofen, Germany

††DARA, Königswinterer Str. 522 - 524, D-5300 Bonn 3, Germany

**Abstract.** Two studies for proving the feasibility of AI-applications for space are presented. AI-systems that provide support in the areas of diagnosis and scheduling are deployed in operation centers and integrated with the operational environment.

**Key Words.** AI-applications for space; Diagnosis; Scheduling, Integration with operational environment

### 1. INTRODUCTION

Up to now, most of the AI-applications for space have been tested and demonstrated only by using specific test data or in a simulated test environment. Now, ERNO performs two studies which demonstrate the capabilities of AI-applications in real operational environments using real spacecraft data:

In the study TIKON, "Technologien für die Intelligente Kontrolle von Raumfahrzeugen", ERNO develops an integrated system for the demonstration of the operations support capabilities of AI-applications where ROSAT is the demonstration mission.

(TIKON is under contract of by DARA and is supported by DLR/GSOC)

The two most important components of TIKON will be:

- MARS (Mission Activities and Resources Scheduler), an AI-based mission scheduling tool developed by ERNO, used in TIKON for the planning and scheduling of the ROSAT pointing and observation activities;

- CONNEX (CONnectionist EXpert system), an expert system shell, developed by ERNO, used in TIKON for the fault diagnosis for the ROSAT AMCS and the ROSAT DHS.

These AI-components will be embedded into a "classic" software environment, which provides the communications between ROSAT, the user and MARS and CONNEX.

In the study COMPASS, "COMputer-based PAyload Operations Support System", ERNO ports and adapts the above mentioned expert system shell CONNEX to a Macintosh portable computer which will then be connected to the D2 ground support equipment either at the GSOC or at the MUSC. (COMPASS is under contract of ESTEC and led by DLR).

The COMPASS system will be used to monitor the HOLOP telemetry data during the D2-mission in order to demonstrate the support capabilities of a diagnosis expert system to the ground crew, and eventually thereby also to the on-board crew, by inferring hypothesis about possible HOLOP faults in case the HOLOP

telemetry shows off-nominal behaviour.

The following sections briefly describe the two studies. The technical bases of them, namely the two AI-applications MARS and CONNEX are described in separate annexes.

## 2. TIKON

The overall objectives of TIKON comprise the adaptation, enhancement and development for space-applications of the following AI-techniques:

Intelligent monitoring and control, i.e.

- intelligent system surveillance and diagnosis of failures and faults
- autonomous identification of recovery operations in case of failures

Knowledge-based mission planning and scheduling, i. e.

- planning of action sequences for payload and subsystem operations, and spacecraft manoeuvres
- scheduling of these actions in accordance with the given mission constraints (e.g. resources, due dates etc.)
- integration of planning and scheduling
- replanning and rescheduling

Virtual Operations Handbook, i.e.

- intelligent procedure execution support
- event-driven retrieval of documentation
- advanced text and graphics documentation (e.g. hypertext and hypermedia)

Integration of AI-systems and conventional data-processing, i.e.

- knowledge consistency for the different knowledge-based systems
- operations coherence, e.g. intelligent interplay between failure diagnosis, documentation on recovery operations and rescheduling.
- interface aspects for AI-system/AI-system and AI-system/ conventional system communication

Advanced MMI-techniques, i.e.

- intelligent, priority-driven display
- knowledge-based enhanced sensor feedback (e.g. translation of sensor data into graphics which are easily understandable by the operator).

This goal shall be achieved by setting up a demonstration system. This system shall combine the listed AI-techniques into an integrated functional unit and shall serve to

- test and refine the AI-techniques;
- demonstrate their applicability to space.

For the latter objective the demonstration system must operate in a real or simulated space-mission environment, which would either be related to the space segment (i.e. spacecraft) or the ground sequent (i.e. a ground control center). For TIKON, the ground segment has been chosen as demonstration environment, i.e. the TIKON demonstration system will resemble an advanced operator's workstation in a spacecraft control center.

It is clear that not all these goals can be achieved in one step. So, as the first step of the long journey to a complete system, a "minimum TIKON" has been defined consisting of

- a TM/TC interface to connect TIKON to either a real spacecraft or to a spacecraft simulator;
- a diagnosis system (based on CONNEX);
- a scheduler (based on MARS);
- a Human Computer Interface;
- a communication manager connection all these modules.

An overview of the "minimum" TIKON system is shown in figure 1.

This system will be connected to the ROSAT simulator at DLR/GSOC and will be tested and evaluated by the ROSAT operation team.

The definition of the different modules of TIKON has been derived together with DLR/GSOC personnel to provide for realistic operational (and functional) requirements. This way, the "minimum"

TIKON" shall become the starting point

for a (complete) ground operations support system where AI-technologies are applied when they are appropriate to solve operational problems

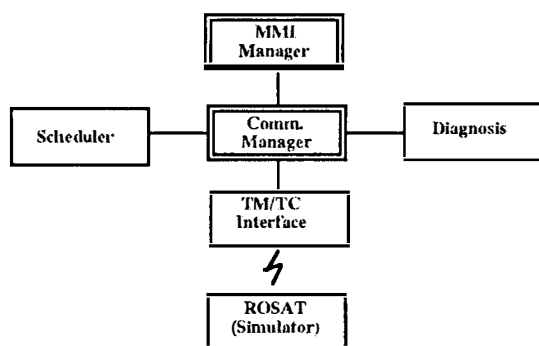


Fig. 1. Overview of the TIKON System

### 3. COMPASS

Payload design, implementation and operation in COLUMBUS, the European contribution to the International Space Station Freedom, which is intended for 30 years of operation, is a challenging task for all experts involved. There are many new and still unsolved problems resulting from the long life-time and from special operational and logistic requirements. These problems are:

- Knowledge Conservation

Normally, it takes several years from the idea for a payload until its first flight. During this time, there are already some changes in the personnel responsible for design and operation. Regarding an intended time of payload operations in the magnitude of years rather than days, it is clear, that some experts will retire or leave the space community in this period. Their knowledge must be kept alive, not only in huge piles of paper which tend to become unreadable or un-understandable for newcomers.

- In-orbit Integration and Test

Today, integration and test of a payload take some months, requires a large number of experts, and needs a complex ground support system consisting of simulators, special check-out equipment, normal workshop equipment such as tools, instruments, etc. For COLUMBUS, it is foreseen to integrate and test new payloads on-

board the spacecraft where all the resources, manpower and technical resources, are very restricted.

- In-orbit Maintenance, Re-configuration and Repair

The today's approach for most of the payloads is "shot and forget", mainly because the mission time and resources are too restricted and the mission schedule is too dense to allow for repair activities in case of problems. In COLUMBUS, the crew will be responsible to maintain their ability for scientific work. Faults in payloads have to be identified and repaired on-board, because the transport capabilities will be very restricted.

To all these problems, diagnosis expert systems provide if not an answer, so at least a step in the right direction. Recognizing these chances, many space-companies and national and international Space Agencies started investigations on the use of expert systems for spacecraft systems, subsystems and payloads.

Some years ago, ERNO started the design of an on-board diagnosis system for COLUMBUS subsystems. This system had to fulfil at least the following requirements:

- it shall use only the informations coming directly from the sensors for the diagnosis;
- it shall be able to handle incomplete and even partly wrong symptoms arising from
  - defect sensor;
  - slowly evolution of faults;
  - incomplete or faulty knowledge bases;
- it shall provide for early warnings of gradually evolving faults;
- it shall be able to handle multiple faults;
- it shall not use probabilistic data, because no statistics are available;
- the knowledge acquisition shall be done by the domain experts, not by knowledge engineers;
- it shall fit into the very restricted computer resources available on-board.

These requirements, and especially the last

one, led to the development of CONNEX, described in a separate annex.

The requirements for payload diagnosis are very similar to those of subsystem diagnoses with the following extensions:

- the user (payload operator, scientist, etc.) must be able to enter his/her observations into the expert system either initiatively or on system request;
- it must be possible to define weights for the connections to represent the different degrees of "criticality" of different symptoms for different anomalies.

With these extensions, CONNEX was successfully used to perform payload diagnosis in the ESA/ESTEC study named "COMputer-based PAyload operations Support System for COLUMBUS; COMPASS". CONNEX was complemented with a configurable pre-processing and with tools for an event (anomaly-) driven selection and presentation of recovery procedures and supporting documentation. The COMPASS system was implemented mainly on a SYMBOLICS UX1200 and on a Sun SPARC station; an environment not fulfilling the requirement of minimum resource needs.

In the follow-on activity, starting now, the technological prototype COMPASS will be upgraded and simplified -as far as the resource needs are concerned- to become an operational prototype. COMPASS II will run on a Macintosh (portable) computer.

This COMPASS II system will then be tested by connecting it to the ground infrastructure of the D2-mission (end of January/begin of February '93) and by supporting the (ground) operations of the HOLOP payload by listening and diagnosing the Telemetry of HOLOP (see figure 2).

The next envisaged step is then to divide the COMPASS system into the diagnostic kernel and the user interface and to implement the diagnostic kernel directly into a payload electronic. The idea behind this approach is, that each (complex enough) payload shall be equipped with its own diagnostic system, where all these

systems can be operated using one on-board portable computer as interface to the crew.

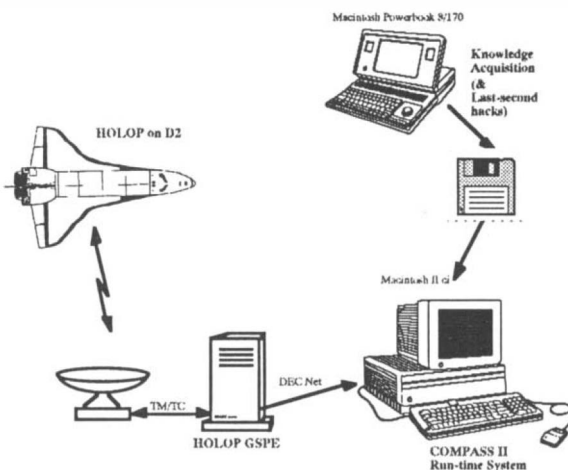


Fig. 2. COMPASS II Configuration

## ADVANCED CONTROL SYSTEM FEATURES OF THE SPACE STATION REMOTE MANIPULATOR SYSTEM

M.E. Stieber\* and C.P. Trudel\*\*

\*Canadian Space Agency, Space Station Project Office, R-105 Montreal Road, Ottawa, Ontario, Canada

\*\*Spar Aerospace Limited, Advanced Technology Systems Group, 9445 Airport Road, Brampton, Ontario, Canada

**Abstract:** The Space Station Remote Manipulator System (SSRMS) is part of Canada's contribution to Space Station "Freedom". This large manipulator will be used during the assembly and operation of the station to perform tasks such as the assembly of truss segments and pressurized modules, berthing the Shuttle Orbiter, and positioning EVA astronauts as well as the Special Purpose Dexterous Manipulator. This paper provides an overview of the role and configuration of the SSRMS and discusses the major SSRMS payload handling requirements. The SSRMS control systems and its operating modes are described, with focus on the Force/Moment Accommodation and the Artificial Vision systems. The utility of these advanced features is illustrated by simulation and test results

**Keywords:** Robots, Space Station, force control, vision systems.

### INTRODUCTION

The joint development, operation and utilization of Space Station "Freedom" (SSF) is a cornerstone of the U.S., European, Japanese and Canadian space programs. Fig. 1 shows the configuration of the Station after completion of 17 assembly missions. Robot manipulators will play a key role during the in-orbit assembly of the Station and for its external maintenance and servicing. The Canadian Mobile Servicing System (MSS) has been assigned a predominant role in satisfying these functions on SSF which requires a versatile system with the capability to manipulate a wide range of objects at a number of different operating locations on the station. This role is described by Werstiuk, Gossain (1987).

The MSS features two manipulator systems which can work together or independently of each other: the Space Station Remote Manipulator System (SSRMS) to handle large payloads, shown in Fig. 1 and 2, and the Special Purpose Dexterous Manipulator (SPDM) for small payloads and dexterous tasks, shown in Fig. 3. The dual-arm SPDM is an important element for the external maintenance of the Station, significantly reducing the requirements for Extra-Vehicular Activity (EVA). The control system concepts for the SPDM are similar to those for the SSRMS. More detail on the role and design of the SPDM is provided by Hunter (1991).

This paper focuses on the SSRMS which is manifested on the third flight of the Shuttle Orbiter to the Station, currently planned for March 1996.

We will describe the configuration of the SSRMS and some of its SSRMS payload handling requirements. The control systems concepts of the SSRMS will be discussed in some detail. The utility of two advanced control features, Force/Moment Accommodation (FMA) and the Artificial Vision Function (AVF) will be illustrated by simulation and test results.

## SPACE STATION REMOTE MANIPULATOR SYSTEM (SSRMS)

### SSRMS Configuration

Fully extended as shown in Fig. 2, the SSRMS measures roughly 17 m including a Latching End Effector (LEE) at each end. The LEES are designed to attach to payloads and to serve as a base for the SSRMS when attached to a station-mounted Power Data Grapple Fixture (PDGF). Power, data and video will be passed through the SSRMS for the operation of the SPDM and to support the keep-alive, telemetry and command requirements of payloads.

The SSRMS will operate most of the time from a Mobile Base System/Mobile Transporter which can translate along the Space Station truss structure. However, the symmetric arrangement of the joints and LEEs enables either end of the SSRMS to function as the base or tip and permits the SSRMS to relocate itself by stepping from one PDGF to another. PDGFs are placed strategically on the station allowing the SSRMS access to areas which are beyond its reach from its Mobile Base System.

The SSRMS has seven joints arranged anthropomorphically in clusters of three at each end, acting as "wrist" and "shoulder" respectively, and one central joint acting as an "elbow". All joints are of identical design and have a range of travel of +/- 270 degrees. The kinematic redundancy provided by the 7 joints increases the operational flexibility and helps to avoid arm configurations near kinematic singularities.

### SSRMS Payload Handling Performance

Examples of the tasks performed by the SSRMS are the assembly of station truss segments and the attachment of pressurized modules, the positioning of EVA astronauts, and the berthing of the Shuttle Orbiter when it visits the station. The maximum payload mass for the SSRMS is 116,000 kg which is representative of a loaded Shuttle Orbiter. In

order to ensure adequate controllability for the manipulation of large payloads, very low drift rates and precise control of the joints at very low velocities are required.

Assembly and berthing operations require accurate positioning of payloads of all sizes within the tolerance or capture range of the respective berthing mechanisms. The resolution of the SSRMS tip motion is required to be better than 1 cm / 0.01 degrees which allows precise positioning and alignment of payloads in manual operating modes when suitable visual cues are available to the operator, or in automatic modes when a vision system is used as will be discussed later. The open-loop positioning accuracy of the SSRMS is specified at 4.5 cm / 0.7 degrees (RMS).

## SSRMS CONTROL SYSTEMS

### Overview

The SSRMS control system and human interface philosophy is based on the proven concepts of the Shuttle RMS (Ravindran, Doetsch 1982) which have been extended to incorporate a number of new and advanced features.

The SSRMS can be operated from any of the Multipurpose Application Consoles (MPAC) in the pressurized environment of the Space Station or from a Shuttle Aft Flight Deck Workstation while the Shuttle is berthed to the station. The present MSS design does not preclude remote control of the SSRMS from the ground via an RF link from the Space Station Control Center although currently no requirement for ground control of the MSS or SSRMS has been baselined.

Fig. 4 provides an overview of the SSRMS control system functional concept. This concept allows the SSRMS to be operated in a number of human-in-the-loop or automatic modes. Although resolved motion operation is the principal means of payload manipulation, joint-by-joint operation is also available in both the human-in-the-loop and automatic modes.

In the Manual Augmented (resolved rate) human-in-the-loop mode of operation, the operator commands translational and rotational velocities of a Point-of-Resolution (POR) using a translational and a rotational hand controller, each with 3 degrees of freedom. These handcontrollers are similar to those used to control the RMS on the Shuttle Orbiter. In addition to camera views and/or

direct views of the operation, feedback displays available to the operator at the MPAC include POR position/orientation and velocities, joint positions and rates, and force-moment sensor measurements.

In the automatic resolved motion modes, the POR is commanded toward a target position and orientation along "straight-line" trajectories. The target may be specified by the operator, or a series of pre-stored targets may be called up to produce an automatic sequence of motions. Alternatively, the Artificial Vision Function (AVF) can be used to provide real-time target position and orientation in an automatic tracking mode.

In both the manual and automatic POR modes, the inverse kinematics of the manipulator are used to resolve the POR rate commands into joint rate commands or joint position commands, or both. The joint commands are sent to each of the joint servos to effect the POR motion. In addition, an arm plane change capability utilizes the kinematic redundancy of the SSRMS to reposition the elbow without moving the POR.

A number of control features may be invoked in conjunction with the various operating modes to enhance the capabilities of the SSRMS, e.g. Force/Moment Accommodation (FMA) and Position/Orientation Hold Selection (POHS) on uncommanded POR degrees of freedom.

The computer architecture used to implement the control systems of the SSRMS is described in more detail by Stieber, Laurenzio, Fung (1991). We will now focus on the FMA and the Artificial Vision Function of the SSRMS which represent significant advances relative to the Shuttle RMS.

#### Force/Moment Accommodation

Large space manipulators such as the SSRMS can exert significant loads at their interfaces, for instance in constrained motion situations during berthing operations. In those situations the FMA control feature of the SSRMS can be invoked in order to automatically limit the SSRMS tip forces and moments. In other operational scenarios such as EVA support or berthing to an active berthing mechanism, the FMA feature can be used to actively limp the SSRMS by setting very low force/moment limits for the FMA. Tests have shown that FMA can considerably increase crew productivity during assembly and ORU changeout operations.

Fig. 5 shows a functional block diagram of the FMA system. The representation of the "barrier" in Fig. 5 indicates the fundamental nonlinearity of contact dynamics but is somewhat symbolic because in reality there are 3 translational and 3 rotational degrees of freedom to consider, and in the case of multiple points of contact even the static relationships between displacement and reaction forces/moments can be quite complicated. The combined stiffness of the manipulator and the "barrier" acts as a gain factor in the feedback loop and it is hence not surprising that a high combined stiffness can give rise to dynamic stability problems.

The reaction forces are measured with a 6-axis force-moment sensor at the tip of the SSRMS and fed back into the arm control system via a nonlinear compensator. The FMA modifies the commands originating from handcontrollers or auto-sequences such that selected force/moment limits are not exceeded. The axes along or about which FMA is active can be selected by the operator either from the MPAC keyboard or during the operation using handcontroller commands ("hot stick"). The force/moment limits can be chosen in the ranges of 0 to 445 N / 407 Nm respectively. The FMA system has a relatively low bandwidth and is hence not effective to control impact loads.

Fig. 6 shows the results of a laboratory test demonstrating the effectiveness of the FMA. In the test, a fixed interface is grappled by an experimental robot with a 0.5 inch offset in alignment normal to the end effector longitudinal axis prior to grapple. The end effector forces and moments required to align the end effector to the fixed interface are shown without FMA and with FMA active. The forces and moments are seen to be significantly reduced with FMA active. A spike in the moment curve during a rapid change in load (impact) demonstrates the low bandwidth characteristic of the FMA mentioned above.

#### Artificial Vision Function

Fig. 7 shows a block diagram of the AVF. A key element is the Artificial Vision Unit (AVU) which processes video images from SSRMS-mounted cameras or Space Station external cameras in real time to extract the position, orientation, and velocities of target patterns with respect to the camera or reference targets in the field of view. This information can be displayed to the operator, used to track objects with pan-and-tilt mounted cameras or to control the SSRMS in one of the

AVF supported control modes. This latter capability plays a key role for the automation of SSRMS operations on the Station.

The feasibility of using the AVF for automatic payload berthing operations has been demonstrated for the full range of SSRMS payloads by simulations. Fig. 8 shows the scenario and initial conditions for a simulation of automatic berthing of the Shuttle Orbiter to the Space Station Pressurized Berthing Adapter (PBA). For this operation the SSRMS has relocated itself to a PDGF mounted on the U.S. Laboratory Module. Prior to berthing, the SSRMS has captured the approaching Shuttle and arrested its motion relative to the Station.

For the simulation of the berthing operation it is assumed that the PBA is equipped with a boresight camera and that the Shuttle displays a suitable visual target. The lightweight and slender SSRMS is modelled as a chain of flexible bodies while the Station and the Shuttle are represented as rigid bodies. The SSRMS simulation model also includes the dynamics of the servomechanisms and gearboxes in the joints. The AVU is modelled as an ideal sensor with a processing delay.

Fig. 9 shows how the translational and rotational displacements converge toward the capture range of the berthing mechanism (3 in / 1.5 degrees RMS). The initial conditions were chosen such as to trigger oscillations in the SSRMS: translational offset [-3 1 -1.5] ft, rotational offset [15 12 10] degrees, all velocities zero. The motion is relatively slow in order to avoid excessive excitation of oscillations in the SSF/SSRMS/Shuttle dynamic system which has a natural frequency below 0.01 Hz. It takes about 15 minutes before the Shuttle is positioned within the capture envelope. This is comparable with the timeline for a manually controlled berthing operation. The parameters of the control algorithm are varied as a function of the SSRMS payload, and for smaller payloads much more rapid convergence is achieved.

## CONCLUSIONS

The SSRMS fulfils a critical role in the assembly, maintenance and servicing of Space Station Freedom. This role demands the capability to precisely manipulate even very large payloads such as the Shuttle Orbiter. The SSRMS control systems support a number of different manual and automatic modes of operation. Force/Moment Accommodation and the Artificial Vision Function represent advanced control system features which enhance the operational flexibility and the potential automation of the SSRMS. The application of those features was illustrated by simulation and test results related to berthing operations and ORU changeout.

## ACKNOWLEDGEMENTS

The authors wish to thank their colleagues at the Canadian Space Agency and at Spar Aerospace Ltd. who have contributed to the development of the SSRMS Control Systems.

## REFERENCES

- Hunter, D. G. (1991). The Space Station Freedom Special Purpose Dexterous Manipulator. *Proc. IEEE National Telesystems Conference*.
- Ravindran, R., K. H. Doetsch (1982). Design Aspects of the Shuttle Remote Manipulator Control. *Proc. AIAA Guidance and Control Conference*.
- Stieber, M. E., D. A. Laurenzio, P.T.K. Fung (1991). Control System Architecture of the Mobile Servicing System. *Proc. 42nd IAF Congress*.
- Werstiuk, H. L., D.M. Gossain (1987). The Role of the Mobile Servicing System on Space Station. *Proc. IEEE Int. Conf. on Robotics and Automation*.

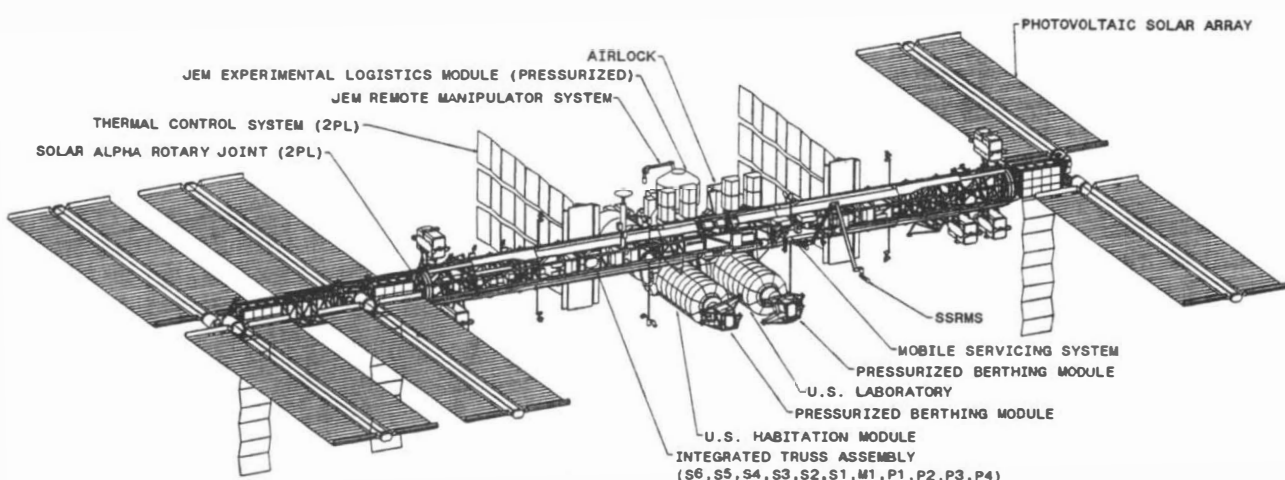


Fig. 1: Space Station *Freedom* (Permanently Manned Capability planned for 1999)

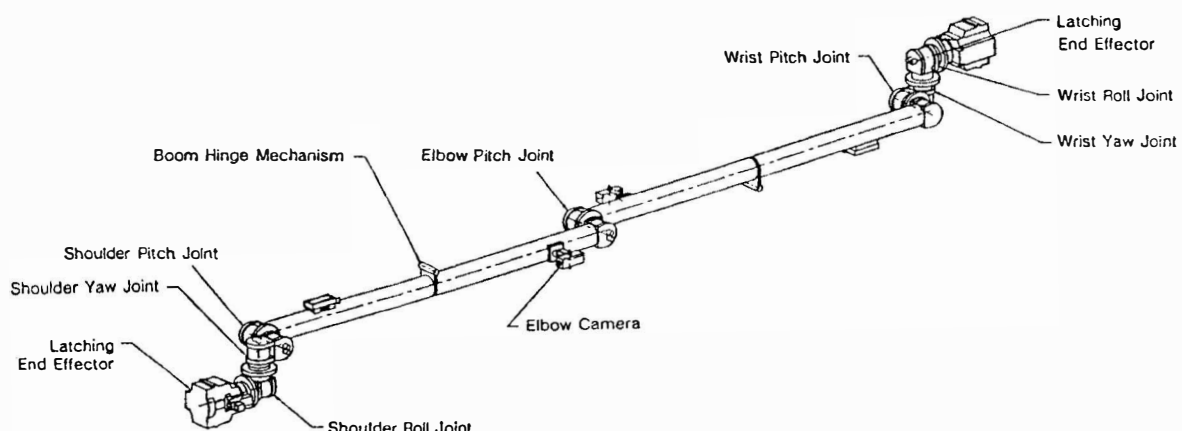


Fig. 2: Space Station Remote Manipulator System (SSRMS)

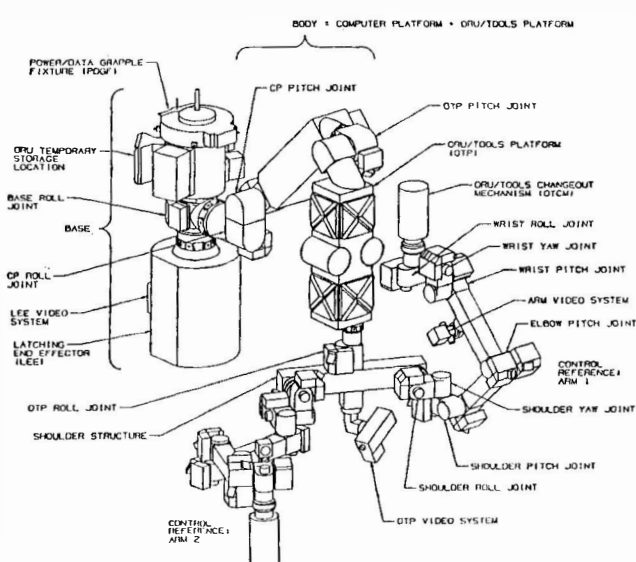


Fig. 3: Special Purpose Dexterous Manipulator (SPDM)

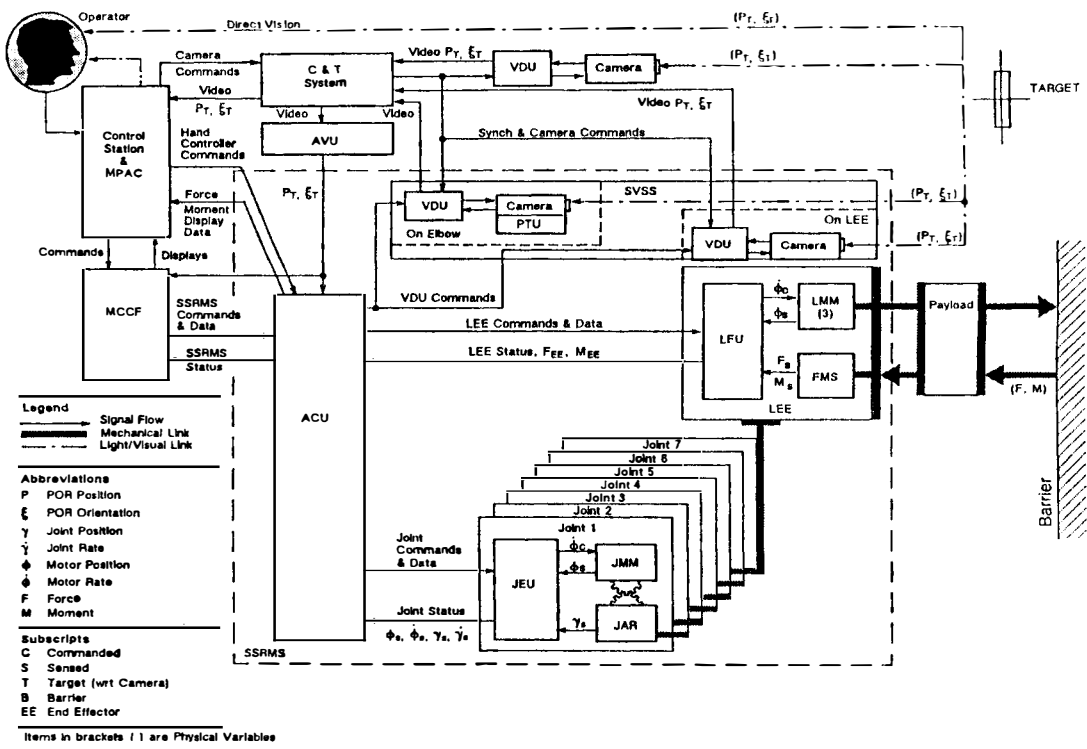


Fig. 4: SSRMS Control Systems

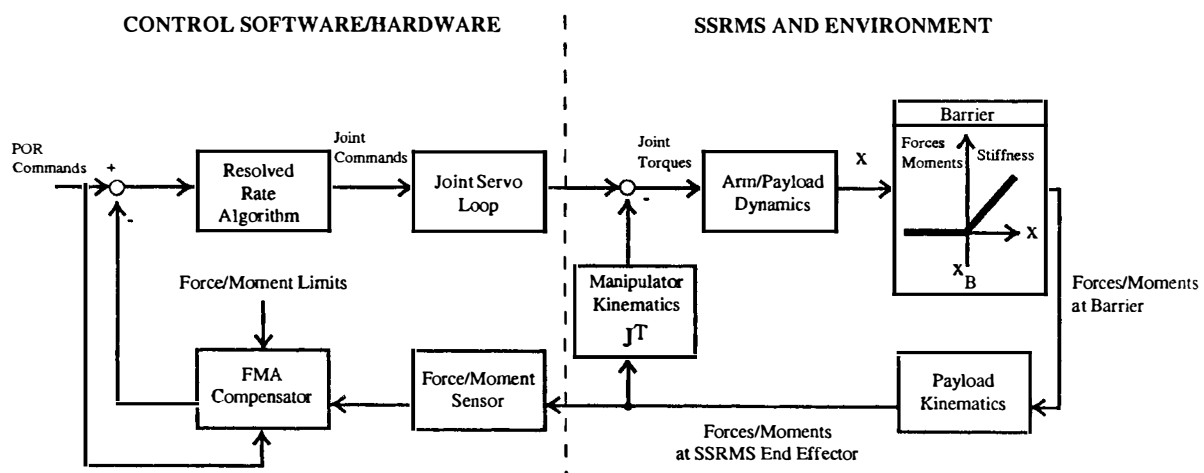


Fig. 5: SSRMS Force/Moment Accommodation

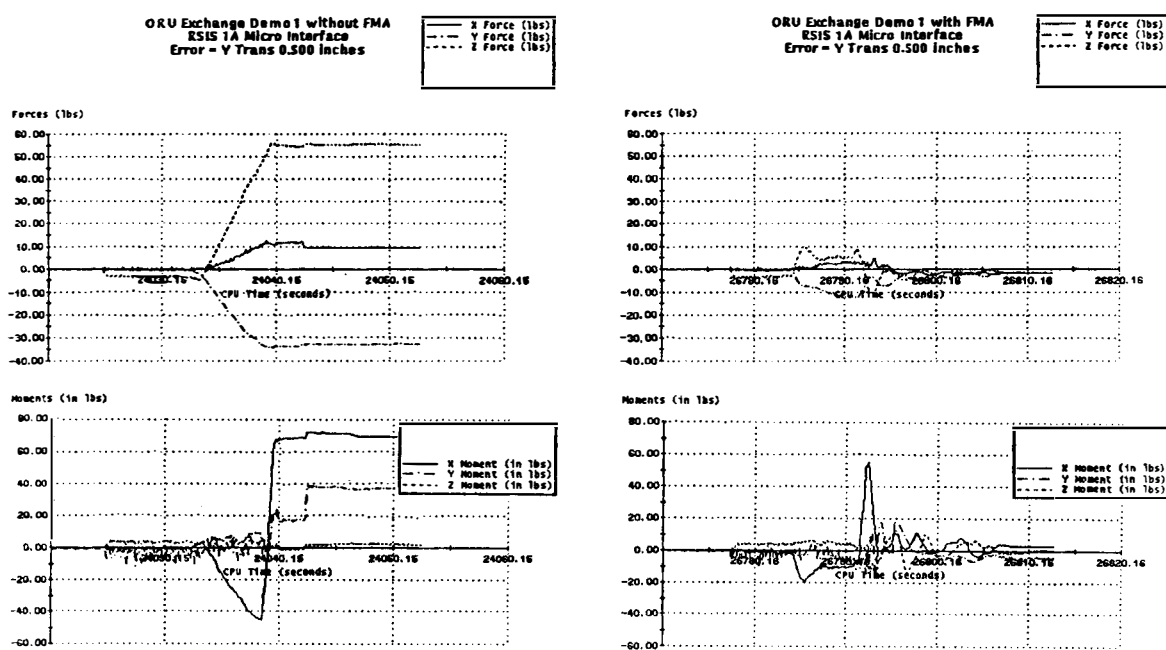


Fig. 6: Laboratory Test Results for Force/Moment Accommodation

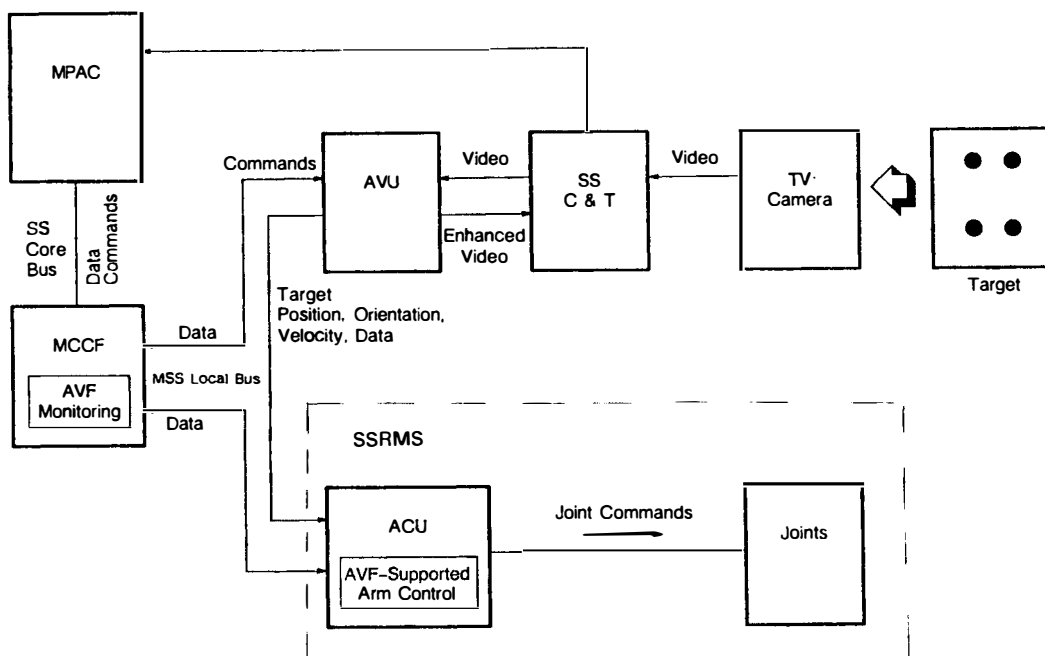
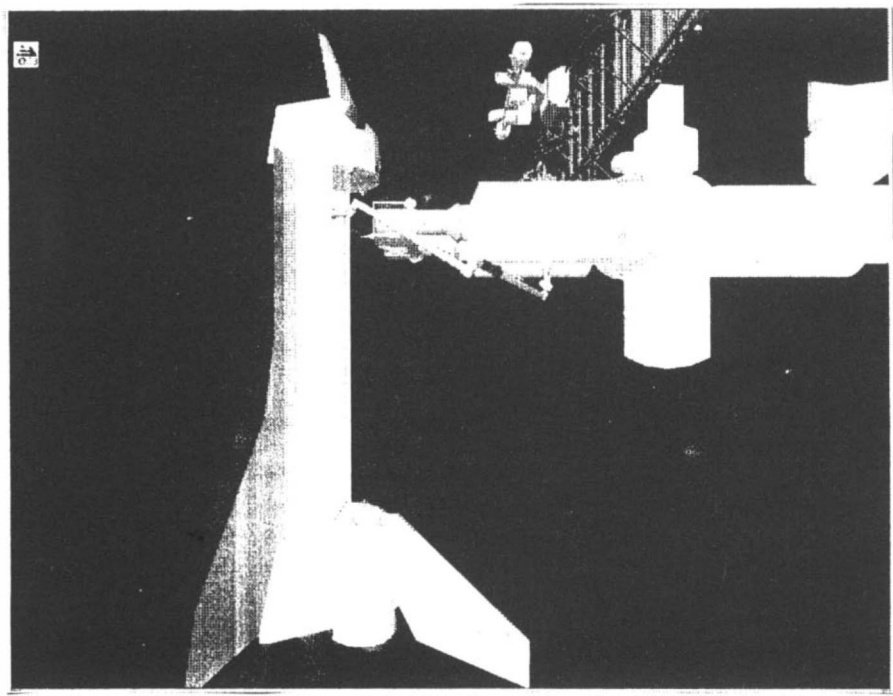
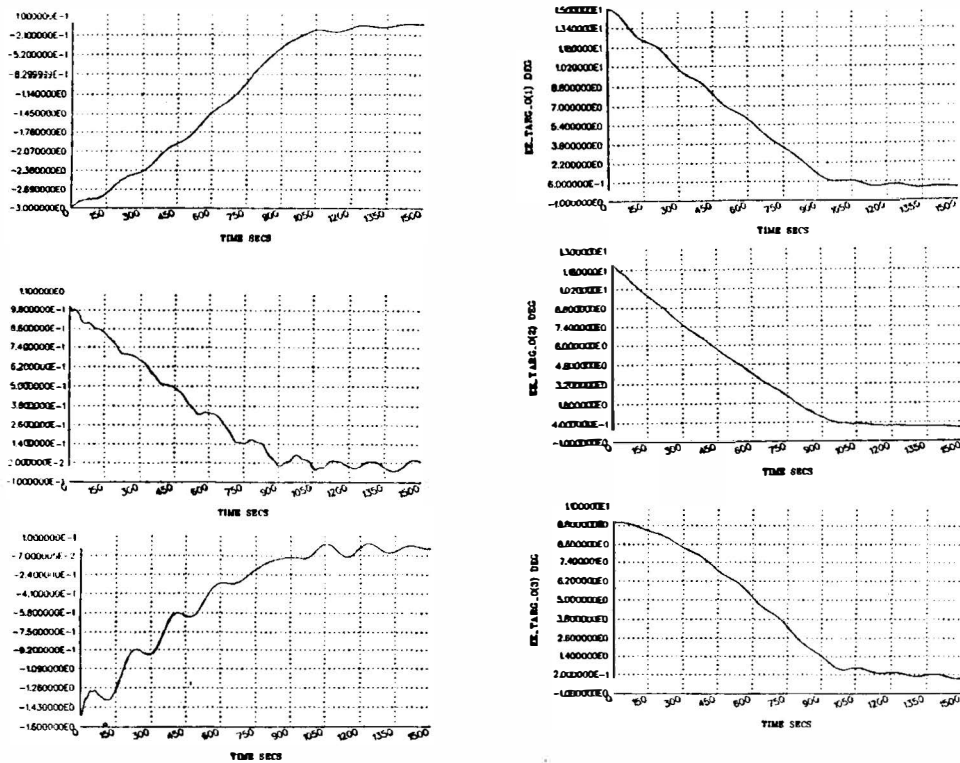


Fig. 7: Artificial Vision Function (AVF)



**Fig. 8: Shuttle Berthing Operation using SSRMS**



**Fig. 9: Simulation of Automatic Berthing of the Shuttle using AVF**

## EFFICIENT ADAPTIVE CONTROL OF A TWO-ARMED FREE-FLYING ROBOT

D.R. Meldrum

*Department of Electrical Engineering, Stanford, CA 94305, USA*

**Abstract:** This paper presents a new efficient adaptive inverse dynamics controller for achieving precise manipulation of an unknown object by a multi-armed mobile-base robot. This is a difficult control problem that must address many topics such as coordinated control, redundant degrees-of-freedom (mobile base), and identification of the unknown object parameters. Previous methods address these issues except the parameter estimates do not converge. They also require inversion of Generalized Jacobian matrices which is computationally intensive. The new control method presented in this work incorporates a sequential hybrid estimation algorithm into the generalized inverse dynamics control structure. With sufficient excitation, the parameters converge to their true values. Efficiency of the adaptive control algorithm is enhanced by using a new efficient algorithm for inverting the Generalized Jacobian matrices. The entire adaptive control algorithm is described and plans for experimental verification are discussed.

**Keywords:** space robotics, adaptive control, inverse Jacobian, cooperative control, parameter identification.

### INTRODUCTION

Robotic manipulation of unknown objects whether in a space or industrial environment requires an efficient adaptive controller. An adaptive controller is necessary to identify the dynamic properties of the unknown object and to sense changes in the system dynamics. Efficiency of the control and identification algorithms is necessary to achieve a high bandwidth and hence better, real-time performance. The efficiency of the adaptive controller becomes even more important when controlling a mobile-base robot with multiple manipulators. Additional issues that must be addressed include the reaction forces and moments imparted to the base from the motion of the manipulators (similar to the attitude control problem for a satellite) and coordinated control of the multiple manipulators.

It is generally found that adaptive control algorithms for these problems are complex and computationally intensive. Adaptive control methods based on the well known computed torque control law [5] require the inversion of the system inertia matrix [6] and exact linearization of the nonlin-

ear plant [5]. These adaptive controllers yield global asymptotic stability in plant state error but are only locally stable in parameter error [6]. The computed torque controller has been implemented on a mobile-base multiple-manipulator robot in [8] but the method requires inversion of a large Jacobian matrix and is *not* adaptive. Current control methods for dealing with a mobile base require application of conservation of momentum constraints at the base and the pseudo-inversion of a large, complex generalized Jacobian [11, 17, 18, 19]. One exception is the inverse dynamic adaptive control method developed and implemented by Vincent Chen [4] on a two-armed free-flying robot. Chen's controller allows for thruster control at the mobile base; however, since the controller is based on trajectory tracking error, the unknown parameters in the system converge but not necessarily to their true values. The algorithm is also computationally intensive because it requires explicit inversion of the Jacobian and generalized Jacobian matrices.

The new adaptive control algorithm presented in this paper provides improvements in two areas:

a different adaptation scheme is implemented in the inverse dynamics controller to achieve true parameter identification and a new computationally efficient technique is presented for computing the inverse of the Jacobian and generalized Jacobian matrices. Global asymptotic stability holds in both the state and parameter error. The ultimate goal is to improve the tracking, robustness, and parameter identification performance over previous results [4, 8].

After setting the background with a description of Chen's inverse dynamics adaptive controller, the new adaptation scheme which is based on a sequential hybrid estimation algorithm [3] will be presented. Next the efficient technique for computing the inverse Jacobian and inverse generalized Jacobian will be described. This is a critical step in real-time implementation of the controller because it is computationally intensive and it is the only thing that is changed when switching from one control mode to the next. The implementation of the new adaptive controller on a two-armed free-flying robot is discussed in the final section.

## THE ADAPTIVE CONTROLLER

The adaptive control algorithm developed in this research is based on an inverse dynamics adaptive controller by Bayard and Wen [1], the generalized inverse dynamics adaptive controller by Chen [4] and the sequential hybrid estimation algorithm by Canudas de Wit and Aubin [3]. Primary features of the new algorithm are numerous. The framework provided by Chen's algorithm [4] (which is a generalization of the Bayard and Wen algorithm [1]) yields multiple arm control that does *not* require closed-kinematic-chain equations of motion, the capability of performing task-space control, a modular structure which makes it easy to add or delete bodies from the system being controlled (called "system concatenation"), and precise trajectory following in the presence of uncertainty in the payload mass properties. It also provides stable predictable behavior via the impedance concept whether or not the manipulators and payload are in free-space or in contact with the environment [16]. Incorporation of the sequential hybrid estimation algorithm into the inverse dynamics controller yields an efficient technique for estimating the *true* values of the unknown system parameters. Before describing the adaptive controller, the robot model and parameters will be defined.

## Robot Model

The dynamic model for a robot manipulator is:

$$\tau = \mathcal{M}(\mathbf{q})\ddot{\mathbf{q}} + \mathbf{C}(\mathbf{q}, \dot{\mathbf{q}})\dot{\mathbf{q}} \quad (1)$$

where  $\mathbf{q}$ ,  $\dot{\mathbf{q}}$ , and  $\ddot{\mathbf{q}}$  are respectively the manipulator joint position, velocity, and acceleration  $n \times 1$  vectors,  $\tau$  is an  $n \times 1$  vector of joint torques,  $\mathcal{M}(\mathbf{q})$  is an  $n \times n$  symmetric positive definite mass matrix, and  $\mathbf{C}(\mathbf{q}, \dot{\mathbf{q}})$  is an  $n \times n$  matrix of centripetal and Coriolis functions. If  $\mathbf{x}(0)$  represents

the position of the end-effector, then the forward kinematic transformation from joint space to task space is

$$\mathbf{x}(0) = \mathbf{G}(\mathbf{q})$$

where  $\mathbf{G}(\mathbf{q})$  is a nonlinear vector-valued function. The corresponding transformations from joint space to task space for velocity and acceleration are

$$\mathbf{V}(0) = \mathbf{J}(\mathbf{q})\dot{\mathbf{q}} \quad (2)$$

$$\alpha(0) = \mathbf{J}(\mathbf{q})\ddot{\mathbf{q}} + \mathbf{J}'(\mathbf{q})\dot{\mathbf{q}} \quad (3)$$

where  $\mathbf{J}$  is the  $m \times n$  Jacobian matrix,  $m$  is the number of task space coordinates,  $n$  is the number of joint space coordinates or the number of links in a serial multi-link manipulator,  $\mathbf{V}(0)$  is the end-effector velocity, and  $\alpha(0)$  is the desired end-effector acceleration. Thus, given the desired task space trajectories  $\mathbf{x}(0)$ ,  $\mathbf{V}(0)$ , and  $\alpha(0)$ , the desired joint space trajectories are found as follows:

$$\mathbf{q} = \mathbf{G}^{-1}(\mathbf{q})\mathbf{x}(0) \quad (4)$$

$$\dot{\mathbf{q}} = \mathbf{J}^{-1}(\mathbf{q})\mathbf{V}(0) \quad (5)$$

$$\ddot{\mathbf{q}} = \mathbf{J}^{-1}(\mathbf{q})[\alpha(0) - \mathbf{J}(\mathbf{q})\dot{\mathbf{q}}] \quad (6)$$

where  $\mathbf{J}^{-1}$  denotes the generalized inverse of  $\mathbf{J}$ . An efficient technique for inverting the Jacobian is described in the Jacobian Inversion Section.

## Inverse Dynamics Adaptive Control

The generalized inverse dynamics adaptive control algorithm developed by Chen [4] is shown below primarily to show the structure of the controller used in this research. Note that this controller differs from the computed torque method in that the mass matrix,  $\mathcal{M}(\mathbf{q})$ , does *not* premultiply the proportional-derivative terms.

Control Law:

$$\tau_{cmd} = \mathbf{Y}(\mathbf{q}, \dot{\mathbf{q}}_d, \ddot{\mathbf{q}}_d)\hat{\theta} + \mathbf{J}^T(\mathbf{q})(\mathbf{K}_{V_x}\dot{\tilde{\mathbf{x}}} + \mathbf{K}_{P_x}\tilde{\mathbf{x}})$$

where

$$\begin{aligned} \mathbf{Y}(\mathbf{q}, \dot{\mathbf{q}}_d, \ddot{\mathbf{q}}_d)\hat{\theta} &= \hat{\mathcal{M}}(\mathbf{q})\ddot{\mathbf{q}}_d + \hat{\mathbf{C}}(\mathbf{q}, \dot{\mathbf{q}}_d)\dot{\mathbf{q}}_d \\ \dot{\tilde{\mathbf{x}}} &= \mathbf{J}(\mathbf{q})\dot{\mathbf{q}} \end{aligned} \quad (7)$$

Adaptive Law:

$$\begin{aligned}\dot{\boldsymbol{\theta}} &= \boldsymbol{\Gamma}^{-1} \mathbf{Y}^T (\mathbf{q}, \dot{\mathbf{q}}_d, \ddot{\mathbf{q}}_d) \mathbf{J}^{-1}(\mathbf{q}) (\dot{\tilde{\mathbf{x}}} + c\tilde{\mathbf{x}}) \\ \dot{\mathbf{K}}_{V_x} &= \frac{1}{\delta} (\dot{\tilde{\mathbf{x}}} + c\tilde{\mathbf{x}}) \dot{\tilde{\mathbf{x}}}^T\end{aligned}$$

where  $\mathbf{x}$  represents the vector of *task*-space variables, which may include joint angles, endpoint positions, payload positions, and any other quantity that satisfies the condition in Equation (7). The Jacobian,  $\mathbf{J}(\mathbf{q})$ , in Equation (7) is the Generalized Jacobian which relates joint rates to any velocities in the system. Simply by changing this Generalized Jacobian matrix it is possible to change from one control mode to another; for example, from end-point control to object control [4]. The adaptation scheme updates the physical parameter vector,  $\boldsymbol{\theta}$ , and the velocity feedback gain,  $\mathbf{K}_{V_x}$ . The position feedback gain,  $\mathbf{K}_{P_x}$ , does not need to be updated. The adaptive gains which are based on trajectory tracking errors are:  $\boldsymbol{\Gamma}$ , a positive-definite diagonal parameter update gain matrix;  $\delta$ , a scalar velocity feedback update gain; and  $c$ , a scalar relative weighting between the velocity and position errors. For more explicit details of the controller see [1, 4].

Via Chen's "system concatenation" method [4] it is possible to easily handle multiple manipulator systems. Typically when multiple manipulators grasp a single object, the complete system consists of at least one closed-kinematic chain. Analysis of closed-kinematic chains is very difficult. In the system concatenation method each system is modeled individually and then concatenated together to form a single open-chain model of the entire system. To achieve zero relative motion between each manipulator gripper and its grasp points, a controller task is added via an appropriate Generalized Jacobian. With this method it is very easy to add (delete) manipulators and payloads to (from) the system without changing the controller for the entire system. Only the Jacobian needs to be changed as the robot system changes and as various robot tasks are requested [4].

With the adaptive controller described above it is possible to capture and manipulate an unknown object with a multi-armed mobile-base robot [4]. But since the adaptation is based on trajectory tracking errors, the parameter estimates do not necessarily converge to their true parameter values. The other complication with this algorithm is that the various forms of the Jacobian, the Generalized Jacobians, must be inverted in real-time. This is a computationally intensive, order ( $n^3$ ) step where  $n$  is the number of degrees of freedom. In the next few sections a new identification scheme is employed in the inverse dynamics

control structure and a method for efficiently computing the Jacobian inversion in order ( $n$ ) steps is shown.

## Parameter Identification

A sequential hybrid estimation algorithm similar to [3] is used in the generalized adaptive task space impedance controller to identify the dynamic properties of the manipulator and/or an unknown object. The new contributions are that the identification may be performed in a joint space, end-point space, or task space environment. In previous methods this was not the case [3]. Another improvement is that by using this identification scheme *true* parameter identification is achieved. In previous work [4] the parameters do not converge to their *true* values since the goal is to merely minimize tracking error.

The algorithm developed by Canudas de Wit and Aubin [3] is as follows. Rewrite the robot dynamics equation (1) in a form which is linear in the unknown physical parameters,  $\boldsymbol{\theta}$  (mass, inertia, link lengths):

$$\boldsymbol{\tau} = \mathbf{Y}(\mathbf{q}, \dot{\mathbf{q}}, \ddot{\mathbf{q}}) \boldsymbol{\theta}$$

or

$$\begin{pmatrix} \tau_1 \\ \tau_2 \\ \vdots \\ \tau_n \end{pmatrix} = \begin{pmatrix} y_{11}^T & y_{12}^T & \cdots & y_{1n}^T \\ & y_{22}^T & \cdots & y_{2n}^T \\ & & \ddots & \vdots \\ & & & y_{nn}^T \end{pmatrix} \begin{pmatrix} \theta_1 \\ \theta_2 \\ \vdots \\ \theta_n \end{pmatrix}$$

where  $\mathbf{Y}(\mathbf{q}, \dot{\mathbf{q}}, \ddot{\mathbf{q}})$  is an  $n \times n_\theta$  upper-triangular information matrix. By exploiting the upper-triangular structure of the  $\mathbf{Y}$  matrix, it is possible to estimate the unknown parameters link by link. For example, link  $n$  depends only on the parameter vector  $\theta_n$ , link  $n - 1$  depends only on  $\theta_{n-1}$  and  $\theta_n$  and so on.

The  $i$ th parameter vector is estimated as follows:

$$\begin{aligned}\dot{\hat{\theta}}_i &= P_i y_{ii} e_i \quad \forall i = n, n-1, \dots, 1 \\ e_i &= \tau_i - \sum_{j>i}^n y_{ij}^T \theta_j^0 - y_{ii}^T \hat{\theta}_i\end{aligned}$$

where  $\theta_j^0$  represents the estimate of  $\theta_i$  obtained in the pass corresponding to link  $j$  for all  $j > i$  and  $P_i$  is an  $n_\theta \times n_\theta$  matrix. The estimation algorithm which is performed link by link is exponentially convergent provided that the information vectors are persistently exciting. For details see [3].

To achieve true parameter estimates in the inverse dynamics controller, the sequential hybrid estimation algorithm just defined is used as the new adaptation scheme. It replaces the previous

one stated above in the Inverse Dynamics Adaptive Control Section but with an important modification. It is desirable to be able to specify not only joint trajectories but any *task* space trajectory. As stated before, this is achieved through the Generalized Jacobian as in Equation (7). Applying this transformation to the information matrix yields:

$$\mathbf{Y}_x(\mathbf{q}, \dot{\mathbf{q}}_d, \ddot{\mathbf{x}}_d, \ddot{\mathbf{x}}_d) = \mathbf{J}^{-T}(\mathbf{q}) \mathbf{Y}(\mathbf{q}, \dot{\mathbf{q}}_d, \dot{\mathbf{q}}_d, \ddot{\mathbf{q}}_d)$$

Once this transformation is made, the identification algorithm proceeds as shown above. The adaptation for the velocity feedback gain remains the same.

Looking at the *task* space inverse dynamics controller and the identification scheme it is clear that the inverse Jacobian transformation is ubiquitous. In the next section an efficient method for inverting the Jacobian is presented.

## Jacobian Inversion

Typically the Jacobian matrix relates joint velocities to end-point velocities. The standard Cartesian-space control is achieved by using this Jacobian. The Generalized Jacobian relates joint velocities to other velocities of the system (see Equation (7)). An example is a Generalized Jacobian that relates the *relative* velocity between a manipulator gripper and the payload grasp point. In this case, the *task* is to control the *relative* motion between the gripper and the grasp point. The inversion of the Jacobian and Generalized Jacobians typically requires order ( $n^3$ ) operations where  $n$  is the number of degrees of freedom in the system. However, using a technique developed by Guillermo Rodriguez of the Jet Propulsion Laboratory for inverting inertia matrices, [13, 14] a new algorithm has been developed that reduces the number of operations required to compute the inverse Jacobian to order ( $n$ ) [9, 10]. By formulating the  $n$ -link robot equation as a spatially recursive algorithm in the form of a filtering and smoothing problem, this approach makes it possible to factor and invert the Jacobian efficiently. Solutions to this problem for the singular case [9], the redundant degrees-of-freedom case, and the mobile base case have been solved [10]. These are very general results that may be used for any dynamic system composed of rigid serial links. The techniques may be easily extended to flexible link dynamic systems via a finite element approach to the problem and by treating the non-actuated joints appropriately [7].

The Jacobian matrix as defined in equation (8) may be factored into the following form [13]:

$$J = B^* \phi^* H^*. \quad (8)$$

where the “spatial transition operator”  $\phi^*(k+1, k)$  is the Jacobian which transforms velocities across a link,

$$\phi(k+1, k) = \begin{pmatrix} \mathcal{I} & \tilde{l}(k+1, k) \\ 0 & \mathcal{I} \end{pmatrix} \quad (9)$$

and the “state-to-output map”  $H(k)$  is defined as  $H(k) = h^T(k)$  where  $h(k) \in \mathbb{R}^6$ . Thus the matrices  $H^* = \text{diag}[H^T(1) \dots, H^T(n)]$ ,  $B^* = [\phi^T(1, 0), \dots, 0]$  and

$$\phi = \begin{pmatrix} \mathcal{I} & 0 & \dots & 0 \\ \phi(2, 1) & \mathcal{I} & \dots & \vdots \\ \vdots & \vdots & \ddots & 0 \\ \phi(n, 1) & \phi(n, 2) & \dots & \mathcal{I} \end{pmatrix}$$

See [13, 9, 10] for more detailed definitions.

In order to invert the Jacobian matrix, it is useful to first form the symmetric positive definite relation,

$$(J^* J) = H \phi B B^* \phi^* H^*$$

If the manipulator is nonredundant and nonsingular, then

$$(J^* J)^{-1} = (\mathcal{I} - L)^* D^{-1} (\mathcal{I} - L)$$

where  $L$  is a lower triangular matrix (causal operator),  $D$  is a diagonal matrix (memoryless operator) and  $\mathcal{I}$  denotes the identity matrix. This relationship may be implemented in an order ( $n$ ) recursive algorithm which is actually a Kalman filter and Bryson-Frazier smoother [9, 10].

If the robot is at a singular configuration or if the robot has redundant degrees of freedom (e.g. a robot with a mobile-base), the pseudoinverse of the Jacobian is:

$$(J^* J)^\dagger = (\mathcal{I} - L)^* D^\dagger (\mathcal{I} - L)$$

where  $D^\dagger$  is the pseudoinverse of the diagonal matrix  $D$  [15]. The recursive implementation of this algorithm is now a filter/smooth algorithm [9, 10] which yields the least squares solution to the problem:

$$\dot{q}_{LS} = \arg \min_{\dot{q}} = \frac{1}{2} \|V(0) - J \dot{q}\|^2.$$

These algorithms are easily modified to be useful for any generalized Jacobians as specified in equation (7).

Implementation of the order ( $n$ ) inverse Jacobian algorithms makes it possible to achieve higher bandwidth control of the robot system. The Jacobian inversion arises in all types of robot control problems and was previously a very computationally intensive and limiting step.

## CONCLUSIONS

A new adaptive controller has been developed that is computationally efficient, truly identifies the unknown parameters in the system, achieves precise end-point trajectory tracking and easily is reconfigured to handle changes in a modular system. A sequential hybrid estimation algorithm [3] has been modified and incorporated into the generalized inverse dynamics control algorithm developed by Chen [4] to achieve these results. Computational efficiency of the adaptive control algorithm is achieved via a new recursive algorithm that inverts various Generalized Jacobian matrices in only order ( $n$ ) computations whereas previous methods require order ( $n^3$ ) computations.

To demonstrate the features of this new algorithm the adaptive control scheme is currently being tested on a two-armed free-flying robot in the Aerospace Robotics Laboratory at Stanford University. The goals in these robot experiments are to demonstrate that the new algorithms developed above improve the control bandwidth of the system and truly identify the mass, center of mass and inertia of an unknown payload being manipulated under dual arm control. For the results of these experiments see [10].

## ACKNOWLEDGEMENTS

This research is supported by the NASA Graduate Student Researchers Fellowship Program under Grant NGT-50431 and by the Zonta International Amelia Earhart Fellowship Program.

## REFERENCES

- [1] D.S. Bayard and J.T. Wen, "Robust Control for Robotic Manipulators—Part II: Adaptive Case," Jet Propulsion Laboratory Engineering Memorandum EM 347-87-204, February 1987.
- [2] A.E. Bryson, Jr. and Y.C. Ho, *Applied Optimal Control*, Blaisdell Publishing Co., 1969.
- [3] C. Canudas de Wit and A. Aubin, "Robot Parameter Identification via Sequential Hybrid Estimation Algorithm," *Proc. of the 1991 IEEE Int. Conf. on Robotics and Automation*, pp. 952-957.
- [4] V. Chen, "Experiments in Nonlinear Adaptive Control of a Free-Flying Space Robot," *Ph.D. Thesis, Stanford University*, 1992.
- [5] J.J. Craig, *Introduction to Robotics*, Addison-Wesley Publishing Co., Reading, MA, 1989.
- [6] J. Craig, P. Hsu, and S. Sastry, "Adaptive control of mechanical manipulators," *1986 IEEE Conference on Robotics and Automation*, pp. 190-195, San Francisco.
- [7] A. Jain and G. Rodriguez, "Spatial operator approach to under-actuated manipulator kinematics and dynamics," *Proc. of the 1991 Automatic Control Conference*, pp. 2045-2050.
- [8] R. Koningstein, "Experiments in Cooperative-Arm Object Manipulation with a Two-Armed Free-Flying Robot," *Ph.D. Thesis, Stanford University*, October 1990.
- [9] D.R. Meldrum, G. Rodriguez, and G.F. Franklin, "Efficient control with an order ( $n$ ) recursive inversion of the Jacobian for an  $n$ -link serial manipulator," *Proc. of the 1991 American Control Conference*, pp. 2039-2044.
- [10] D.R. Meldrum, "Indirect Adaptive Control of Multi-Link Serial Manipulators using Kalman Filtering and Bryson-Frazier Smoothing," *Ph.D. thesis, Stanford University*, August 1992.
- [11] E. Papadopoulos and S. Dubowsky, "On the dynamic singularities in the control of free-floating space manipulators," *Proceedings of the Winter Annual Meeting of the American Society of Mechanical Engineers*, DSC-Vol. 15, pp. 45-52, San Francisco, December 1989.
- [12] G. Rodriguez, "Kalman filtering, smoothing, and recursive robot arm forward and inverse dynamics," *JPL Publication 86-48*, 1986. Also in *IEEE Journal of Robotics and Automation*, Vol. RA-3, No. 6, Dec. 1987.
- [13] G. Rodriguez and K. Kreutz, "Recursive mass matrix factorization and inversion: an operator approach to open- and closed-chain multibody dynamics," *JPL Publication 88-11*, 1988.
- [14] G. Rodriguez, K. Kreutz, and A. Jain, "A spatial operator algebra for manipulator modeling and control," *1989 IEEE Intl. Conference on Robotics and Automation*, pp. 1374-1379.
- [15] G. Strang, *Linear Algebra and its Applications*, Third Edition, Harcourt Brace Jovanovich, Publishers, 1988.
- [16] S. Schneider, "Experiments in the dynamic and strategic control of cooperating manipulators," *Ph.D. Thesis, Stanford University*, September 1989.
- [17] Y. Umetani, K. Yoshida, "Resolved motion rate control of space manipulators with generalized Jacobian matrix," *IEEE Trans. on Robotics and Automation*, Vol. 5, No. 3, pp. 303-314, June 1989.
- [18] K. Yoshida, Y. Umetani, "Control of space free-flying robot," *Proc. of 29th IEEE Conf. on Decision and Control*, pp. 97-102, 1990.
- [19] K. Yoshida, R. Kurazume, Y. Umetani, "Dual arm coordination in space free-flying robot," *Proc. of 1991 IEEE Int. Conf. on Robotics and Automation*, pp. 2516-2521.

# DYNAMIC CONTROL OF SPACE MANIPULATORS HOLDING FLEXIBLE PAYLOADS: ANALYSIS AND EXPERIMENTAL VALIDATION IN THE ONE D.O.F. CASE

D. Alazard and J.P. Chrétien

CERTIDERA, 2 Avenue E. Belin, Toulouse, France

**Abstract:** A robust dynamic control scheme to drive a complex payload with a flexible manipulator is presented. Force, rate and position control loops are first tuned in the case of an inert payload, which mass may vary in an arbitrary range. A simple representation of the dynamics of more complex payloads (including typically flexible appendages) is then introduced to analyze, with the help of a formal calculus tool, the stability of the various control loops according to the basic parameters describing the payload. Linear Quadratic control solutions taking into account explicitly the payload dynamics are also considered and discussed. An experimental mock-up is used to illustrate some remarkable behaviors of the closed loop system.

**Keywords:** SPACE MANIPULATORS — DYNAMIC CONTROL — FLEXIBLE MEMBERS  
— COMPLEX PAYLOAD — ATTITUDE CONTROL — EXPERIMENT

## Introduction

Space manipulators have three main features which make them quite different from terrestrial ones : the first one is the lack of a fixed base, so that reaction forces and torques on the vehicle supporting the manipulator give birth to complex combined dynamics ; the second one is the zero-g environment, which allows a mass ratio between the manipulator and payload very low ; the third one is (for the time being) the absence of productivity requirements, which allows to operate at a low rate of displacement. However, the payload mass may vary on a very wide range, a fact that the control system must take into account.

Space manipulators already flying and new ones being currently planned are basically designed to access a working space as large as possible, so that the control system primarily appears as similar as those implemented for industrial robots, with a major concern about the position control of the end effector and payload ; it would seem therefore quite straightforward to reuse the know-how as is and to build up an architecture combining trajectory generation in Cartesian space and low level position servo loops tuned on an estimation of the inertia seen by each joint. However, and due to the abovementioned aspects, these manipulators appear also as very thin sets of articulated members creating forces and torques between two massive bodies : the concepts of dynamic control, in which the motion of the payload is a consequence of the forces and torques which are applied to it by the manipulator, appear as an

interesting solution to the control problem, which has been often proposed in theoretical papers for the control of terrestrial manipulators, but has seldom been used on a large scale in industry because of the difficulty to apply really the calculated forces/torques in each joint with geared electric drives. A great part of the papers published on the subject deal with some kind of compensation of the linear coupling terms in the mass matrix and the non-linear terms appearing quadratically in the equations of motion, in order to achieve a decoupled control of the dynamics of the manipulator, even in the case of flexible members, but little attention has been devoted to the problem where the payload is itself a dynamically complex object, for which the concept of dynamic control seems necessary.

This paper is divided in four sections. The first one summarizes, in the one d.o.f. case, the dynamic control scheme presented in a previous paper ([1]) in which the control synthesis is split up in two subproblems : one is the design of the manipulator control system in such a way that the force control at the interface between the end effector and the payload is as good as possible (the factors limiting the performances being basically the compliances, either located in the joints or distributed in the members, and the in-joint friction) ; the other one is the design of a control of the payload assuming that the force/torque at the interface is precisely controlled : on the example of a simple payload having only mass and inertia, we proposed an architecture building up the position control loop in three steps from the inner force control level through an intermediate rate control loop.

The second section introduces a flexible mode into the payload. The use of a formal calculus tool allows to

---

This work has been performed under contracts granted by C.N.E.S. — Centre Spatial de Toulouse (France) under the technical management of M. Maurette

express the various transfer functions as depending literally in dynamic parameters characterizing the payload. The interactions between the payload flexible mode and the manipulator flexible mode are then better understood, and the frequency ranges in which control of the payload dynamics are possible are identified, as well as the maximum damping achievable with the robust control structure designed for the rigid payload case.

In the third one, control solutions taking into account explicitly the payload dynamics are considered: a linear quadratic (LQ) control law is established to control the spring-mass system rate from force measurements at the interface, and the relationships between the performance index and the effectiveness of the control is discussed.

In the last one, these theoretical analyses are validated on an experimental set-up dedicated to control/structure interaction, named SECAFLEX [2]. Comparisons between simulations and experiments on the set-up, are presented.

## 1 Control design

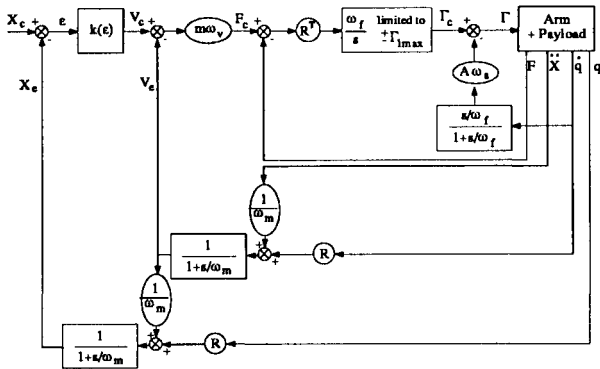


Figure 1 Dynamic control scheme (one d.o.f. case)

Notations:

- $X_c$  : desired Cartesian position (m)
- $X_e$  : estimated Cartesian position (m)
- $k(\epsilon)$  : non-linear position gain (cf equ.1)
- $V_c$  : desired Cartesian velocity (m/s)
- $V_e$  : estimated Cartesian velocity (m)
- $m$  : mass of the payload (Kg)
- $\omega_v$  : rate loop gain (rd/s)
- $F_c$  : desired force at the interface (N)
- $R$  : total arm length (m)
- $\omega_f$  : force loop gain (rd/s)
- $\Gamma_c$  : desired torque (Nm)
- $A$  : inertia of arm seen from the joint ( $Kg.m^2$ )
- $\omega_a$  : damping gain (rd/s)
- $\Gamma$  : drive torque (Nm)
- $F$  : measured force (N)
- $\ddot{X}$  : measured acceleration at the interface ( $m/s^2$ )
- $\dot{q}$  : measured joint velocity (rd/s)
- $q$  : measured joint position (rd)
- $\omega_m$  : estimation filters cut off frequencies(rd/s)

The proposed control scheme is shown on figure 1 in the mono-dimensional case. The various considerations which have led to this synthesis are widely detailed in [1] in which the multi-dimensional version is presented. We simply mention that this scheme allows to control the force at the interface between the end effector and the payload as well as its Cartesian velocity or position. The force control loop tuning depends only on the manipulator design features in terms of electric mode (located in the joint drive) and flexible modes (also located in the joint but mainly distributed along the beam). So, a force detector (or a six d.o.f. wrist detector in the general case) located at the interface is needed but the loop structure is very simple and robust: the controller is a pure integrator of which the gain (i.e. the bandwidth)  $\omega_f$  is tuned to cut off the undesirable modes completed by a dissipative inner loop built on the joint rate. In order to get a force loop with a static gain equal to one and a response independent of the rate, this joint rate feedback is filtered with a high-pass filter tuned according to the bandwidth  $\omega_f$ . The kinematic transformation between Cartesian space and joint space appears inside this loop and the transpose of the Jacobian matrix is needed to express the Cartesian force as a joint torque.

Inside the bandwidth  $\omega_f$ , the manipulator can be considered as a pure force generator. Under this assumption, a Cartesian proportional-derivative controller is sufficient and robust. The rate loop gain depends on the payload mass (inertia) and is tuned inside the force loop bandwidth. In the same way, the position loop gain is tuned inside the rate loop bandwidth  $\omega_v$  but is corrected by a non-linear term (equation 1) according to the drive torque limitation  $\Gamma_{max}$  in order to generate admissible set-point shapes.

$$\epsilon = K^{-1}(V_c) = \left( \frac{1}{\omega_x} + \frac{(m.R + A/R).|V_c|}{2.\Gamma_{max}} \right).V_C \quad (1)$$

Payload Cartesian position and velocity estimation are both made by the mixture of two complementary measurements:

- an inertial measurement provided by an accelerometer (and a set of gyroscopes in the multi-dimensional case) located at the interface. This exteroceptive detector is needed to take into account the manipulator flexible modes in case of high frequency solicitations.
- a joint measurement provided by tachometer and position sensors to obtain, after the kinematic and geometric transformations, a good estimation of payload velocity and position respectively in case of low frequency solicitation or in quasi-static case.

This compound measurement is achieved by a high-pass filter on inertial measurement and a low-pass filter on joint measurement.

**NUMERICAL APPLICATION.** The arm has a total length of 6 m, a mass of 80 kgs and its flexibility is represented by a 30.000 Nm/rd local stiffness located in the middle of the arm (that corresponds to a free

mode frequency about 30 rd/s). The loop gains tuning in terms of bandwidth is the following:

mass (kg)	125	1.000	16.000
$\omega_a$ (rd/s)	2.	2.	2.
$\omega_f$ (rd/s)	4.	4.	4.
$\omega_v$ (rd/s)	1.	0.7	0.2
$\omega_x$ (rd/s)	0.4	0.28	0.07
$\omega_m$ (rd/s)	1.	1.	1.

Table 1 Gain tuning

## 2 Closed loop behavior with a flexible payload

In order to get a simple approximation of a complex payload (as for instance a flexible appendage) in the framework of a mono-dimentional study, we replace the punctual mass by a spring-mass system. In addition of the total mass  $m$ , two new parameters are introduced (cf fig 2):

- $\omega_e = \sqrt{\frac{k_p}{m_2}}$  : frequency of the payload cantilever mode.
- $\lambda = \frac{m_1}{m}$  : rigid mass ratio.

The arm, the payload and all kinematic, dynamic and geometric parameters are displayed on figure 2.

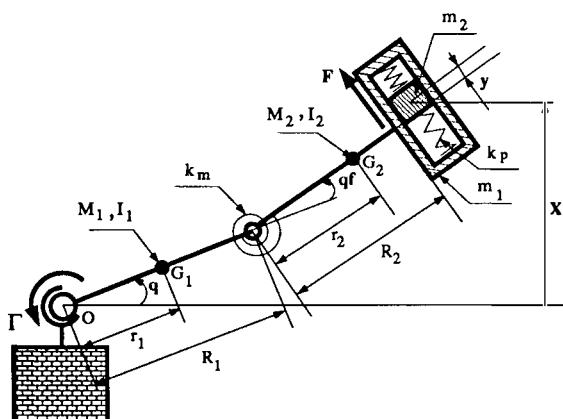


Figure 2 One d.o.f model of the arm holding a flexible payload

The control law presented in the previous section has been tested with the help of a simulation tool for various parametric configurations of the payload. The parametric variations which have been considered (cf. table 2) allows to place the payload mode frequency inside or outside the bandwidths of the three loops.

m (kg)	125 - 1000 - 16000
$\lambda$	0.1 - 0.5 - 0.9
$\omega_e$ (rd/s)	0.05 - 0.1 - 0.5 - 1 - 10 - 20

Table 2 Parametric variations

The simulation results are also presented in [1]. We briefly recall that:

- the force loop becomes unstable for low masses as soon as the cantilever frequency  $\omega_e$  is inside the force loop bandwidth  $\omega_f$  and this instability is more and more pronounced as the rigid mass ratio is low;

- for the rate loop, the parametric range leading to instabilities is more complex and not continuous. We have noticed the damping effect of the rate loop which stabilizes the payload flexible modes located inside the force bandwidth, but other instabilities appear for higher frequencies and reveal some interactions between the manipulator mode and the payload mode. These phenomena are also very sensitive to the mass ratio, so that the interpretation is not easy;
- the position loop behavior is roughly the same as the rate loop one.

In order to analyze in greater detail these behaviors and to specify the influence of each payload parameter on the loops stability, a formal calculus tool has been used. This tool (MACSYMA) allowed us to express, directly from the literal expression of the Lagrangian, the different open loop transfers functions as a function of these three parameters ( $\lambda$ ,  $m$  et  $\omega_e$ ) and to follow the poles evolution through the control feedbacks.

The main results only are presented here, in a synthetic form, because formal calculus tools provide a great amount of results which are not readily usable. The readers will refer to [3] for full details. The three specific open loop transfer functions between available measurements and drive torque read:

$$\frac{\dot{q}}{\Gamma}(s) = K_p \cdot \frac{(s^2 + \Omega_m^{j2}).(s^2 + \Omega_p^{j2})}{s.D(s)} = \frac{N_q(s)}{s.D(s)} ; (K_p > 0)$$

$$\frac{F}{\Gamma}(s) = -K_f \cdot \frac{(s^2 - \Omega_m^{i2}).(s^2 + \omega_i^2)}{D(s)} = \frac{N_f(s)}{D(s)} ; (K_f > 0)$$

$$\frac{\ddot{X}}{\Gamma}(s) = -K_\gamma \cdot \frac{(s^2 - \Omega_m^{i2}).(s^2 + \omega_e^2)}{D(s)} = \frac{N_\gamma(s)}{D(s)} ; (K_\gamma > 0)$$

with:

$$D(s) = (s^2 + \omega_m^2).(s^2 + \omega_p^2)$$

As we can see, the common denominator and the various numerators are products of two second order polynomials, which describe respectively the manipulator flexible mode and the payload flexible mode. The payload zero and the arm zero in transfer functions  $\frac{F}{\Gamma}$  and  $\frac{\ddot{X}}{\Gamma}$  are then quite decoupled, because:

- $\omega_l = \sqrt{\frac{k_p}{m_{eq}}}$ , with  $\frac{1}{m_{eq}} = \frac{1}{m_1} + \frac{1}{m_2}$ , is the payload free mode frequency,
- $\omega_e = \sqrt{\frac{k_p}{m_2}}$ , is the payload cantilever mode frequency,
- $\Omega_m^i = \sqrt{\frac{k_m \cdot (R_1 + R_2)}{M_2 \cdot r_2 \cdot R_1 \cdot R_2 - (M_2 \cdot r_2^2 + I_2) \cdot R_1}}$ , corresponding to real symmetric roots, is the frequency of manipulator mode seen from the interface (non-minimum phase zero).

All the poles and the others zeros depend on both manipulator and payload parameters. But if the two flexible modes are frequencyly decoupled, then  $\omega_p$  and  $\Omega_p^j$  tend towards the two specific payload frequencies;  $\omega_l$  and  $\omega_e$  respectively, and  $\omega_m$  and  $\Omega_m^j$  tend towards the free and the cantilever manipulator modes frequencies seen from the joint assuming the payload is rigid. So we will assign:

- $\omega_p$  to the free frequency of the payload flexible mode

- $\omega_m$  to the free frequency of the arm flexible mode
- $\Omega_p^j$  to the cantilever frequency of the payload flexible mode seen from the joint
- $\Omega_m^j$  to the cantilever frequency of the arm flexible mode seen from the joint

In addition of these considerations, an ordering relationship between these frequencies is checked on all the parametric range:

$$\Omega_p^j < \omega_p < \omega_l \quad (2)$$

This allows us to plot the root loci of the successive feedbacks.

## 2.1 Inner damping loop

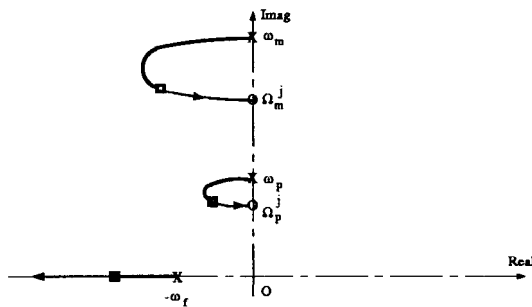


Figure 3 Root locus of the damping loop

The corresponding closed loop transfer is:

$$\frac{\dot{q}}{\Gamma_c}(s) = \frac{N_q(s).(s + \omega_f)}{s.[(s + \omega_f).D(s) + A.\omega_a.N_q(s)]} = \frac{N_q(s).(s + \omega_f)}{s.D_5(s)}$$

Then:

$$\frac{F}{\Gamma}(s) = \frac{N_f(s).(s + \omega_f)}{D_5(s)}$$

The damping effect of the rate feedback is clearly shown: the distribution of alternating poles and zeros along the imaginary axis due to the co-location of the drive and the tachometer guarantee the stability of the loop for any parametric configuration.

## 2.2 Force control loop

The open loop transfer to be considered is then:

$$\frac{F}{\varepsilon_f}(s) = \frac{R.\omega_f.N_f(s).(s + \omega_f)}{s.D_5(s)}$$

with a negative loop gain:  $-K_f.R.\omega_f$

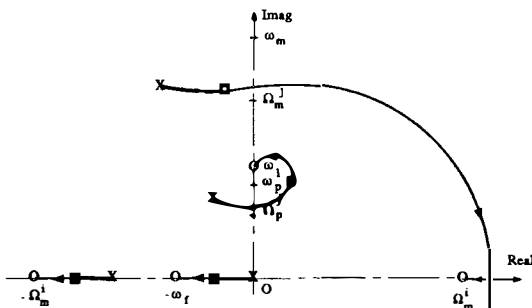


Figure 4 Root locus of the force loop

The closed loop is given by:

$$\begin{aligned} \frac{F}{F_c} &= \frac{R.\omega_f.N_f(s).(s + \omega_f)}{s.D_5(s) + R.\omega_f.N_f(s).(s + \omega_f)} \\ &= \frac{R.\omega_f.N_f(s).(s + \omega_f)}{D_6(s)} \end{aligned}$$

and then:

$$\frac{\dot{q}}{F_c} = \frac{R.\omega_f.N_q.(s + \omega_f)}{s.D_6(s)} ;$$

$$\frac{\ddot{X}}{F_c} = \frac{R.\omega_f.N_\gamma.(s + \omega_f)}{D_6(s)}$$

Due to the ordering relation 2, the payload mode branch may cross the imaginary axis, depending on the loop gain  $\omega_f$ . This possibility of instability depends also on the inner loop tuning  $\omega_a$ . Fig. 9 displays the damping  $\xi$  of the flexible payload mode according to both parameters  $\lambda$  and  $\omega_e$  for a mass of 125 Kg in the case of nominal (rigid) tuning. We can notice that the instability is well pronounced for low mass ratios and low frequencies  $\omega_e$  located inside the control bandwidth. For higher frequencies ( $8.\text{rd/s} < \omega_e < 12.\text{rd/s}$ ) the instability appears for medium value of  $\lambda$ . This is quite in accordance with the results obtained by simulations.

## 2.3 Rate control loop

The open loop transfer is now:

$$\frac{V_e}{\varepsilon_v}(s) = m.R.\omega_v.\omega_f.(s + \omega_f) \cdot \frac{s.N_\gamma(s) + R.\omega_m.N_q(s)}{s.(s + \omega_m)D_6(s)}$$

The roots of the numerator can be considered as the closed loop poles of the following open loop transfer:

$$\frac{N^*}{D^*}(s) = \frac{(s^2 + \Omega_m^{j2}).(s^2 + \Omega_p^{j2})}{s.(s^2 - \Omega_m^{i2}).(s^2 + \omega_e^2)}$$

with the negative loop gain  $-R.\omega_m.K_q/K_\gamma$ . The corresponding root locus is:

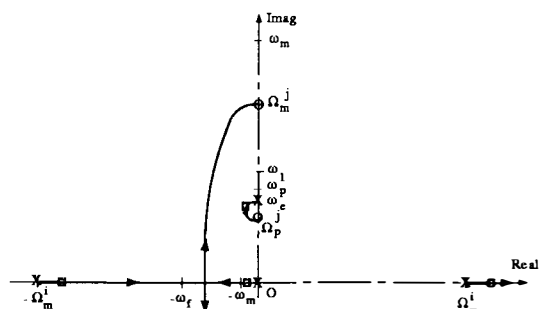


Figure 5 Zero locus of rate loop

For the proposed parametric variations and the nominal value of  $\omega_m$ , it is easy to check that  $\omega_e$  is very near to  $\Omega_p^j$ , so the final distribution of the numerator roots is not quite different from the denominator  $D^*(s)$  ones. That seems sound when it comes to control  $\dot{X}$  and allows us to plot the root locus of the rate loop.

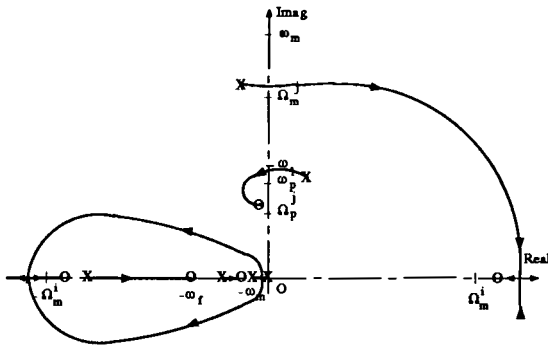


Figure 6 Root locus of rate loop

Relationship  $\omega_l > \omega_e$  ensures a stabilizing effect for the payload pole, but the evolution of this root locus according to the payload parameters reveals two kinds of coupling between the different poles of the system:

- coupling between the manipulator pole and the payload pole (cf Fig 8.c), which appears when  $\omega_e$  is near the natural manipulator frequency: for high mass ratios, the payload pole is attracted in the right half plane by the real zero while the manipulator pole is attracted by the payload zero.
- coupling between the manipulator pole, the payload pole and the rigid pole (cf Fig 8.b). For low values of  $\lambda$  and on a large range of cantilever frequency ( $0. < \omega_e < 12. \text{rd/s}$ ), the payload pole is attracted as above in the right half plane but the manipulator pole is then sent to the stable real negative axis while the rigid pole is attracted by the payload zero.

Moreover some parametric configurations lead to multiple order poles and it is no more possible to plot the payload mode damping characteristic as it was done for the force loop, and in order to specify the frequency ranges in which this control scheme is possible, the minimum damping of the rate loop has been plotted according to both parameters  $\lambda$  and  $\omega_e$  in the case of a mass of 125.Kg (cf fig. 10). Two range of instability can be distinguished:

- for middle frequency ( $2. < \omega_e < 12. \text{rd/s}$ ) and for any value of  $\lambda$ .
- for very low frequencies ( $1. < \omega_e < 2. \text{rd/s}$ ). The minimum damping presents a maximum for middle value of the mass ratio, but is negative for very low values ( $\lambda \leq 0.1$ ).

### 3 Linear Quadratic control

The nominal rate loop was initially designed in the case of a rigid payload and was tuned according to the only available dynamic parameter of the payload  $m$ . In the previous section we have seen that the disturbance introduced by a possible flexible mode of the payload could destabilize this loop. So it is interesting to evaluate the achievable performances if we suppose that some measurements of this disturbance (typically  $y$  et  $\dot{y}$  on figure 2) are available to build the rate loop (under the assumption of a perfect force control). In this line, a L.Q. feedback of the controlled state  $\dot{X}$  and states describing the payload dynamics  $y$  and  $\dot{y}$

has been investigated in agreement with the following block diagram.

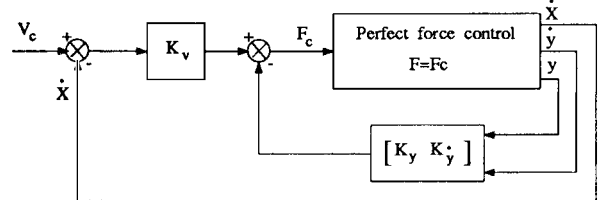


Figure 7 Feedback of the payload dynamics in the rate loop

The computation of the three gains has been done in a literal way and assumes that the three payload parameters  $m$ ,  $\lambda$  and  $\omega_e$  are also known.

The open loop can be suitably represented by a spring-mass system and then described by the well-known state representation:

$$\begin{aligned}\dot{\underline{X}} &= \begin{bmatrix} 0 & \frac{k_p}{m_1} & 0 \\ 0 & 0 & 1 \\ 0 & -\frac{k_p}{m_{eq}} & 0 \end{bmatrix} \underline{X} + \begin{bmatrix} \frac{1}{m_1} \\ 0 \\ -\frac{1}{m_1} \end{bmatrix} F ; \\ \underline{X} &= [\dot{X} \quad y \quad \dot{y}]^T\end{aligned}$$

or transfer function representation:

$$\begin{aligned}\frac{\dot{X}}{F}(s) &= \frac{1}{m_1} \cdot \frac{s^2 + \omega_e^2}{s.(s^2 + \omega_l^2)} ; \\ \frac{y}{F}(s) &= \frac{1}{m_1} \cdot \frac{1}{s^2 + \omega_l^2} .\end{aligned}$$

The performance index weights only the output  $\dot{X}$  and the input command  $F$ :

$$I = \int_0^\infty (q \cdot \dot{X}^2 + r \cdot F^2) dt$$

with:  $q = m \cdot \omega_q$  and  $r = \frac{1}{m \cdot \omega_r}$ . (The weights have been written in order to have an index homogeneous to an energy).

The closed loop eigenvalues are given by the Hamiltonian matrix  $\mathcal{H}$  and then the gain matrix  $[K_v \quad K_y \quad K_y]$  can be easily found by eigenvalues assignment.

The computation of the characteristic polynomial of  $\mathcal{H}$  gives:

$$\begin{aligned}\det(sI - \mathcal{H}) &= s^2 (s^2 + \omega_l^2)^2 - \frac{\omega_r \cdot \omega_q}{\lambda^2} (s^2 + \omega_e^2)^2 \\ &= \mathcal{P}^- \cdot \mathcal{P}^+ \\ \text{with : } &\bullet \mathcal{P}^+ = s(s^2 + \omega_l^2) + \frac{\sqrt{\omega_r \cdot \omega_q}}{\lambda} (s^2 + \omega_e^2) \\ &\bullet \mathcal{P}^- = s(s^2 + \omega_l^2) - \frac{\sqrt{\omega_r \cdot \omega_q}}{\lambda} (s^2 + \omega_e^2)\end{aligned}$$

The polynomial  $\mathcal{P}^+$  contains the stable roots and then represents the closed loop characteristic polynomial.

The two tuning parameters ( $\omega_q$  and  $\omega_r$ ) of the L.Q. controller lead to closed loop eigenvalues which are given by the transfer:

$$\frac{s^2 + \omega_e^2}{s.(s^2 + \omega_l^2)}$$

looped with a gain:  $\frac{\sqrt{\omega_r \cdot \omega_q}}{\lambda}$ . We recognize the open loop transfer:  $\frac{\dot{X}}{F}(s)$ , which means that the L.Q. control feedbacks only the state  $\dot{X}$  and doesn't use the two others state components to optimize the proposed criterion. So by identification:

$$K_y = 0 ; K_{\dot{y}} = 0 ; K_v = m \cdot \sqrt{\omega_r \cdot \omega_q}$$

The rate loop provided by this technique is exactly the same than the previous one built in the rigid case. The equivalent bandwidth is:

$$\omega_v = \sqrt{\omega_r \cdot \omega_q}$$

and does not depend upon the two "flexible" parameters of the payload:  $\lambda$  and  $\omega_e$ . That means the payload flexible mode cannot be considered like a disturbance and must be take into account in the performance index. Then it can be shown that the gain  $K_v = m \cdot \sqrt{\omega_r \cdot \omega_q}$  is kept, and so, stays independent of the both weightings on the states  $y$  and  $\dot{y}$ .

#### 4 Experimental validation

The experimental set-up SECAFLEX [2] is a two d.o.f. planar flexible manipulator controlled by electric gear drives applying torques on very flexible beams of metal; in order to be representative of zero-g environment, this manipulator is supported on air-bearings. These specific features make it appropriate of future space manipulator dynamics and control. To validate the previous analysis, only one joint is needed, but three mock-ups of dynamic paylaod have been built up:

- a spherical tank partially filled with water representative of sloshing phenomena.
- an horizontal pendulum to validate the pendular approximation which is currently used to describe liquid sloshing.
- a spring-mass system as previously described and which is the most suited to reflect the parametric variations considered in simulation.

The experimental illustration of theoretical concepts often raises some practical problems which affect the correlation between simulations and experiments. The most important difficulty met here is the friction located in the joint gear and in the spring-mass system guidance. The in-joint static and viscous friction has been a subject for detailed modeling and for a efficient mechanism of compensation which are related in an other paper [4]. Good results have been achieved in the rigid case (figure 11). In flexible case however the natural damping of the spring-mass system hides the expected unstable behaviors. On the other side, due to the gravity acting on the experiment, the sloshing mode of the tank half filled reveals the same property as the flexible mode with a lower damping ratio and allows a better illustration of the theoretical concepts. For tank filling between 0 and 50%, the slosh may be correctly approximated by a transverse mode which frequency reads, under the assumption of small deflection:

$$\omega_e = \sqrt{\frac{g}{R_s}}$$

with

- $g$  :  $9.81 \text{ m/s}^2$  ;
- $R_s$  : ray of the sphere (20 cm) .

Variations on rigid mass ratio only are possible with this device, but its natural frequency  $\omega_e$  about  $7.\text{rd/s}$  is just located between the force loop bandwidth and the natural free frequency of the arm flexible mode. In order to compare this parametric configuration with the previous 3-D characteristics, the various pulsations of the experimental closed loop system are given:

• arm natural free frequency	: 12.rd/s
• $\omega_f ; \omega_a$	: 3.rd/s
• $\omega_v$	: 2.5 rd/s
• $\omega_x$	: 0.55 rd/s
• $\omega_m$	: 0.5 rd/s

For a half filled tank, the equivalent mass ratio is 0.66 and the total mass is 25 Kgs. The dynamic slosh is just located in a unstable area. Figure 12 shows the corresponding experiment. The total mass is the same than in the rigid case (figure 11), but the control is now destabilized by the payload mode. This behavior in agreement with the previous analysis is well performed on both simulation and experiment results which present a good correlation on various responses.

#### 5 Conclusions

The dynamic control scheme built in the rigid case, able to control any rigid mass/inertia, is not robust w.r.t. the possible payloads flexible modes. Main instability problems appear for low masses and mass ratios. This configuration is extreme among the parametric variation range which has been chosen very wide and so very penalizing. The force loop and the rate loop behaviors are then quite different.

The first one becomes unstable as soon as the cantilever payload frequency is inside its bandwidth and particularly for very low masses and very low mass ratio. That can be suitably explained by the difficulty to control force and torque applied on low masses and inertias.

The stability issues understanding of the second one is more intricate because of some interactions between the manipulator and the payload flexible modes. Inside the force loop bandwidth and for middle or high rigid mass ratio, the payload mode is damped according to the co-location theorem: the force control loop applies precisely the force at the interface where the Cartesian velocity is measured and provides active damping. For very low mass ratios, that is no more the case, but we have to consider that the rate loop gain  $m \cdot \omega_v$  is not tuned to the real rigid mass:  $\lambda \cdot m$ . For the cantilever frequencies outside the force loop bandwidth, co-location is no more guaranteed: the payload becomes instable even for important mass ratios while the manipulator mode is stabilized.

A L.Q. control assuming that some measurements of payload deflections are available has been investigated for the rate loop. This technique appears very disappointing because it does not feed back these new mea-

surements and so, provides the same structure control than the one built in the rigid case. This particular feature is related to the performance index which only takes into account the velocity at the interface and disappears if we consider the Cartesian position control. More detailed developments could be carried on in this way.

The experimental validation have led some practical problems. Friction modeling investigations have been required to simulate the observed real phenomena. Then, compensation mechanisms have been introduced to satisfy the non-dissipative assumption. The equivalence between the sloshing mode of a spherical tank and a flexible mode provides good results even in the case of a dynamic payload. In order to describe experimentally a more important parametric range, further considerations will be focused on the spring-mass system improvement.

## References

- [1] P. Carton, J.P. Chrétien, and M. Maurette. Simulation and control of space manipulators bearing complex payloads. In *Automatic Control in Aerospace, Proceedings of the XIth IFAC Symposium, Tsukuba, Japan*, July 1989.
- [2] J.P. Chrétien. SECAFLEX : an experimental set-up for the study of active control of flexible structures. In *American Control Conference*, volume 2, pages 1397–1402, Pittsburgh, Pa, June 21–23 1989.
- [3] D. Alazard and J. P. Chrétien. Stratégie de commande dynamique pour la manipulation de charges utiles complexes. Rapport Final 4/7717a(texte), b(planches), CNES/DERA, Juin 1991.
- [4] S. Gomes and J.P. Chrétien. Dynamic modelling and friction compensated control of a manipulator joint. In *IEEE Robotic and Automation Proceedings*, Nice, May 10-15 1992. IEEE. To be published.

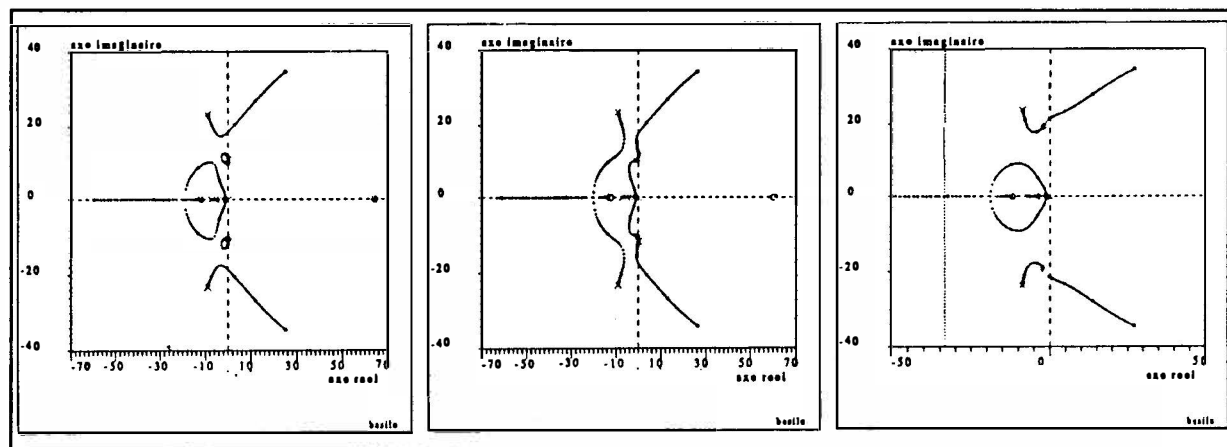


Fig 8.a :  $\lambda = 0.75; \omega_e = 10 \text{ rd/s}$

Fig 8.b :  $\lambda = 0.65; \omega_e = 10 \text{ rd/s}$

Fig 8.c :  $\lambda = 0.6; \omega_e = 18 \text{ rd/s}$

Figure 8 : Rate loop root locus :  $m = 125 \text{ Kg}$

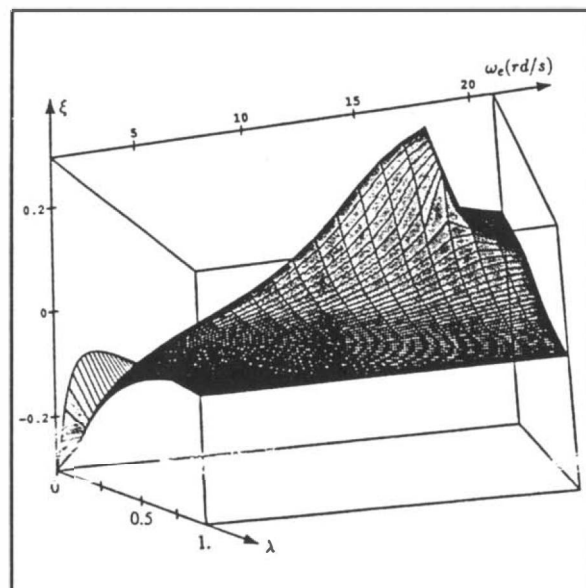


Figure 9 Damping of the payload flexible mode  $\xi$  : force loop ;  $m = 125 \text{ Kg}$

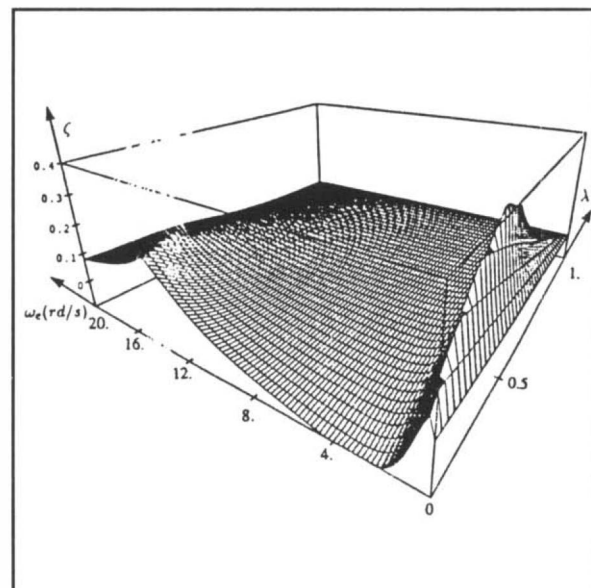


Figure 10 Minimum damping  $\zeta$  of the rate loop ;  $m = 125 \text{ Kg}$

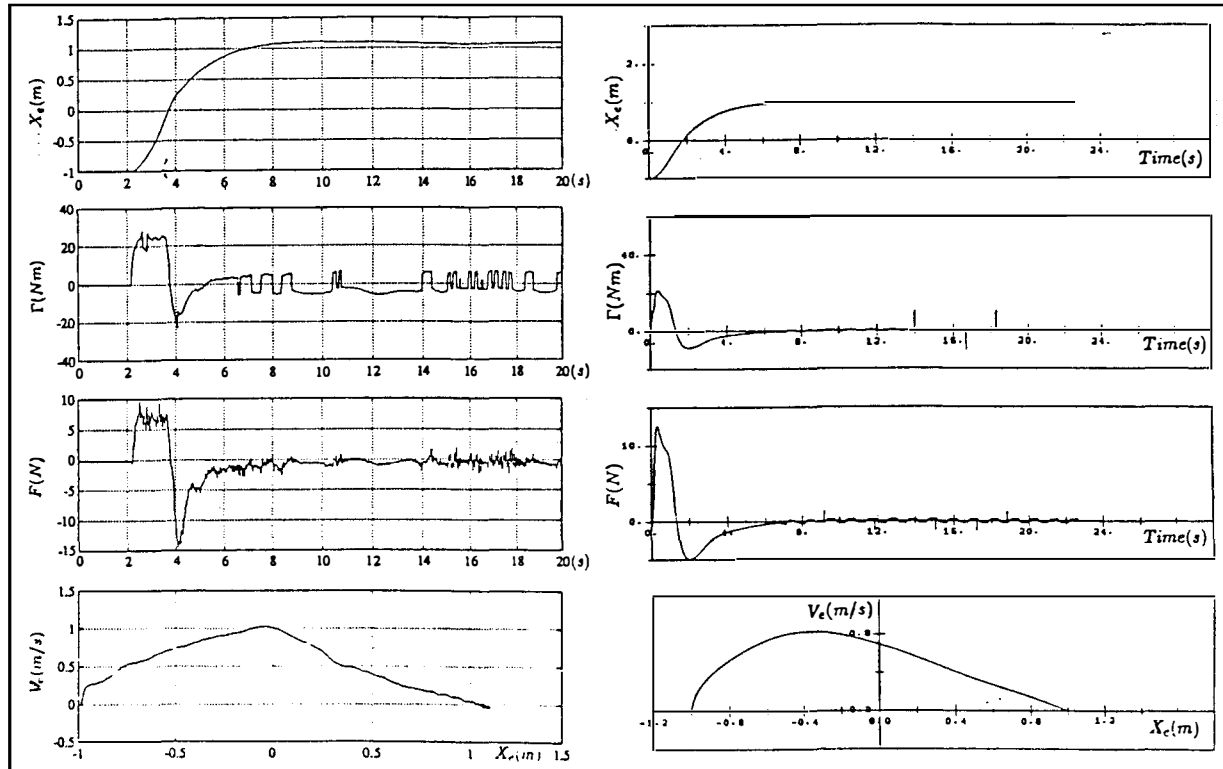


Fig 11.a : Experiments

Figure 11 : Rigid payload ;  $m = 25Kg$  (Position control loop)

Fig 11.b : Simulations

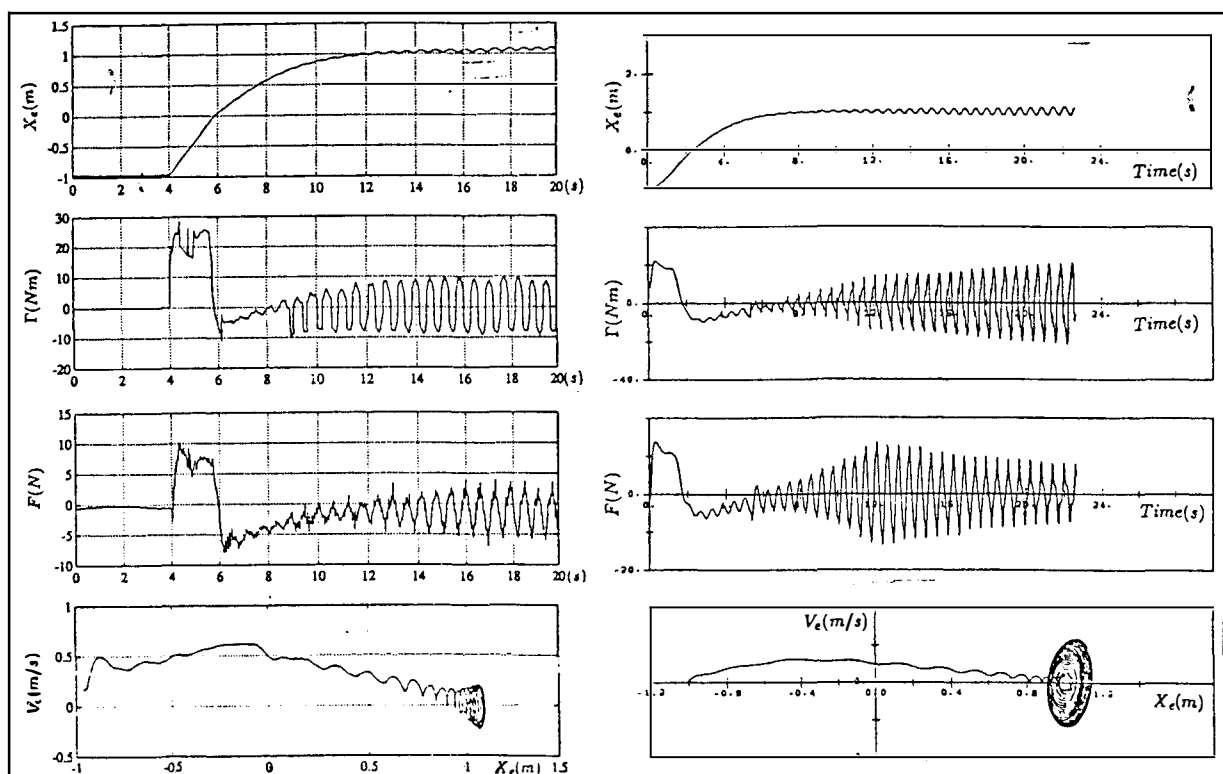


Fig 12.a : Experiments

Figure 12 : Dynamic payload ;  $m = 25Kg$ ;  $\lambda = 0.66$ ;  $\omega_e = 8rd/s$  (Position control loop)

Fig 12.b : Simulations

Figure 12 : Dynamic payload ;  $m = 25Kg$ ;  $\lambda = 0.66$ ;  $\omega_e = 8rd/s$  (Position control loop)

## KNOWLEDGE BASED CONTROL WITH 3D VISION FOR AUTONOMOUS ROBOTIC TASKS

St. Wienand\*, E. Ersü\*, F. Grünewald\* and J. Matthiesen\*\*

\*ISRA Systemtechnik GmbH, Mornewegstr. 45A, 6100 Darmstadt, Germany

\*\*Technische Hochschule Darmstadt, Institut für Regelungstechnik, Fachgebiet Regelsystemtheorie  
und Robotik, Schloßgrabenstraße, 6100 Darmstadt, Germany

**Abstract:** Multiple knowledge based environment modelling and sensor information processing systems have been proposed. However only few systems have really been implemented with real hardware. This paper mainly describes the results of the EXAMINER II project which is currently performed for the national space agency DARA. An action planning and multi-sensorial knowledge based environment modelling system which uses a 3D vision system is designed and demonstrated on a real robotic system.

**Keywords:** Knowledge Based Control, Robots, Sensor Data Fusion, Environment Modelling, 3D Vision

### INTRODUCTION

One of the major tasks in developing more advanced space robot control systems is to augment the autonomy of the systems. This is very important in order to be able to also solve problems like maintenance and repair of satellites or to serve unmanned or partly unmanned spacecrafts. One important subtask is the perception which is responsible for modelling the environment of the system as closely as possible to reality and interpreting it.

If a system which shall be autonomous to some degree approaches a spacecraft which is in a status not completely known in order to maintain or to repair it, the most important action which has to be done first is to solve the question "How does the environment look like?". It is essential for the safety of the system, because without knowing about the environment it is not possible to plan any safe operation.

However as the environment is highly structured in the sense that in principle all possible objects and a nominal status of the environment is known a priori some assumptions can be made which make the solution of those questions easier.

The paper describes how these types of environmental information can be used in order to solve the perception task. A knowledge based system is presented which uses multisensor fusion to obtain the required model information. One major source of information is a stereo object recognition vision system which is the essential part of the multi-sensorial system.

Following the definition of the baseline of the project an overview over the system is given where also the planning part (=task decomposition and execution) is shortly described. Then the knowledge base, the 3D vision and model generation module are described in more detail, as they mainly contribute to the solution of the task stated above.

### BASELINE OF EXAMINER II

The major goal of this project which is named EXAMINER II is to design a multisensorial knowledge based environment modelling system which is able to detect the status of its environment by various sensors and to monitor the execution of tasks using this model.

3D vision, 2D vision and distance sensors are the main sources for sensor information. Sensor data fusion techniques which are themselves model based are used to get more abstracted information. The system builds a 3D model of its environment.

The manipulator and the sensor data acquisition modules are both controlled by action planning modules which plan sub-tasks and execute actions. They use the environment model and on-line sensor information in order to take decisions and act on changes in the environment. Tactile sensor information is used additionally to the geometrical sensors which are used by the environment modelling task.

It is assumed that this environment is structured, that means that all objects and their possible attributes relevant for action planning are principally known to the system. The task of the system is now to detect the real state of the environment. This also includes the generation of parts of this model where a priori model is missing or where it is detected that the a priori model does not meet the reality.

The demonstration task for this system is the inspection and servicing of a partly damaged satellite. The main goal of EXAMINER II is to model the actual state of the satellite, assuming that it has been damaged somehow without knowing what really has happened.

The project is based on two other projects, EXAMINER I which was performed also for the national space agency DARA and WISMO which was realised for robot control system industry.

In EXAMINER I (Kegel, 1990) a real-time system which is able to break down high level commands to motion primitives, where also sensor feedback is used to determine systems states was developed. It follows an object oriented approach of a task decomposition system where information about what to do with objects is stored with the objects themselves. This kind of planning and representation of plans proved to be well suited for low level action planning.

WISMO (Simon, 1991), a knowledge based assembly and task planning system, is also a real-time system which is able to plan and execute assembly tasks. It follows the object oriented approach only for the environment modelling. The procedural knowledge is represented in a rule based approach. This makes the system very flexible for different application areas. WISMO's structure and knowledge representation scheme are the guideline for the project presented here.

In EXAMINER II the principles of both systems are combined in order to solve the complex task of environment modelling by sensor data with an acceptable amount of effort. It is important that there is a realisation on a real robotic test bed as many of the practical problems arise from the properties of real sensors and cannot be simulated in a realistic way.

## SYSTEM OVERVIEW

### Hardware Architecture

In Figure 1 the system hardware structure is shown. It consists of a net of several computers and control systems linked together via an Ethernet connection.

The planning and MMI are implemented on a SUN workstation. Also the main part of the knowledge base is held on this computer. The model generation is implemented on a separate PC which also holds part of the knowledge base.

The execution level is implemented on another PC. It holds the low level action planner and all execution modules. It sends commands to the robot controller, the gripper controller and the collision avoidance which are all themselves separate computer systems. The vision system is a VME-bus based system which performs the whole image processing part of the system.

The following sensor equipment is used:

- Two cameras on the gripper
- Two scene cameras
- One medium range distance sensor on the robot gripper
- One 6 dimensional force torque sensor in the wrist of the robot
- An optical taxel array in the gripper fingers
- A gripping force sensor

The first three sensors are mainly used for the model generation task described in this paper. The last 3 sensors are mainly used for sensor controlled motions and for the lower level action planners.

### Information processing architecture

In Figure 2 the general architecture of the system is shown. It is similar to many other knowledge based systems, however it reflects the fact that the system is a hybrid system with both knowledge based and non knowledge based sub-systems which work together. All information is stored in the knowledge base, but the way of access to the information is different for the different kinds of modules.

The planning part of the system shown on the left side plans actions and executes them. The sensor signal processing part on the right side extracts information from the available sensor signals. The

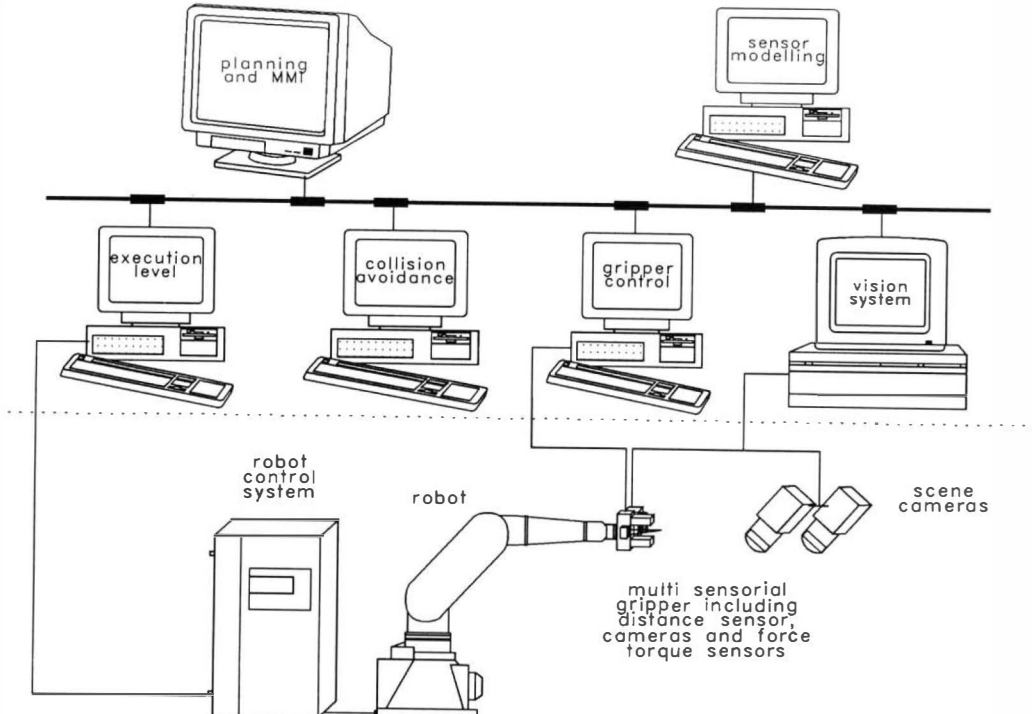


Fig. 1 Hardware structure

knowledge base in the middle to which the other modules communicate contains all information necessary for the system.

Further within the system three main layers can be distinguished. The bottom layer consists of all processing modules which are hardware specific. This is on the planning side the execution control which mainly consists of the conventional robot control system and some supervisory modules. It coordinates the actions of the different control systems.

The sensor information processing on this level consists of several modules which process the information of all the sensors in the system

The action planning module on the planning side is able to decompose commands into actions which are specific to this dedicated system environment. It knows how the system hardware can be used, what objects are in the system and how they can be handled. It follows a pre-defined action plan, checking the result of each of its actions using sensor information in a pre-defined way. It is able to react on changing environment, but these reactions are already foreseen in the plan.

It is a knowledge based system in which an object oriented approach is used. As the objects and the actions can be directly related to each other, very effective planning is possible. This advantage is paid with the disadvantage of less flexibility in planning. However the possible actions on this level are very much restricted by the capabilities of the real hardware anyway.

The action planner uses as sub-system a collision avoidance module which is able to plan collision free paths in the 3D environment. This module uses a special representation of the environment where all objects which might be possible obstacles for the motion of the robot are transformed into the configuration space of the robot. Then a potential field method is used to generate a collision free path to a given goal position. Due to the special implementation of the system this can be done in a very short time.

The 3D vision module on the sensor processing side is a non knowledge

based system which is able to extract 3D information from 2D image processing results. This module is discussed in more detail later in this paper.

The upper layer is completely knowledge based and not system specific, as it works on a higher abstraction level. On the planning side this is a high level task planner which is able to decompose tasks formulated in a command given to that module into actions (=sub-tasks) which the low level action planner can process.

Due to the higher flexibility a rule based approach was chosen. The main difference to the action planner is that the plans are no more pre-defined explicitly, but the system has to generate them with the help of its rule set and all other information from the knowledge base.

The model generation module on the sensor information processing side is in principle very similar to the task planner, although it uses a different set of rules another set of actions. This module is described in more detail later in this paper.

Communication within the system is done via both the knowledge base and via commands and messages. For each of the modules an interface language is defined through which it can be accessed. As the operator has access to all modules, these languages

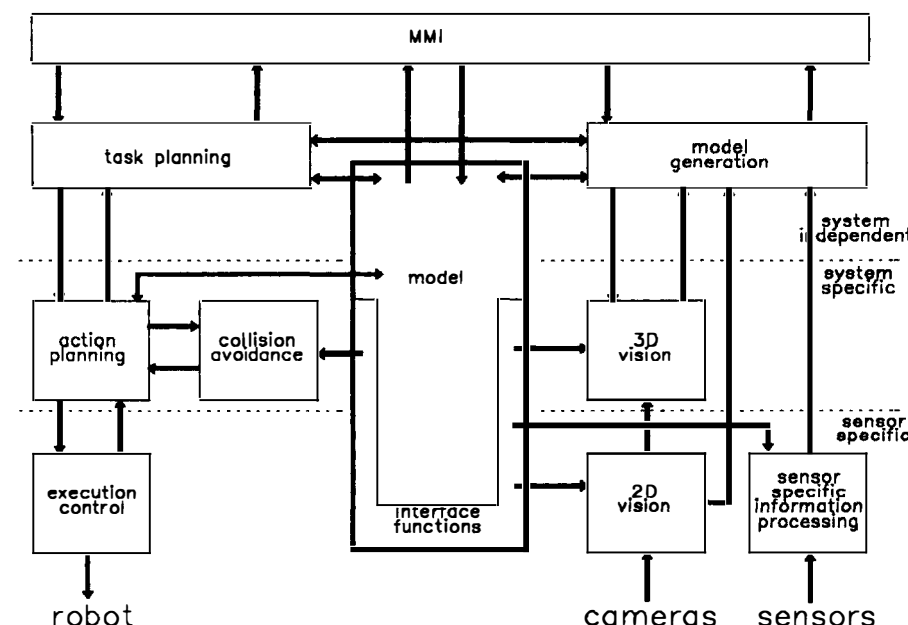
Fig. 2 General system architecture

separately. The outputs of those modules are either values or vectors representing the current sensor readings. Those modules are distributed over different computer systems and they are sampled at very different rates or on request. They are all collected in the knowledge base where an "image" of the current sensor values is stored. This layer is completely algorithmic, although these modules also require information from the knowledge base.

Vision plays a specific role in this context. As it is a sensor system it is situated on the lowest level in the hierarchy of the control system. On the other hand one image can be processed in various ways in order to get different kinds of information. This information processing can be a very complicated process itself which can also be model based.

The vision system is - from the point of view of the control system - a number of different sensors sensing different properties of the environment. Therefore the interface to the vision system is much more complicated than to other sensors, which are in most cases only able to measure one specific item.

In the middle layer the information processing is system specific but not directly hardware specific.



together define the interface language of the system.

The lower level modules (including the action planner) on the planning side also use sensor information directly. This can be done because they do not require a very high abstraction level. The advantage is that this kind of communication is faster than indirect communication via the knowledge base.

Further a communication link between the task planner and the model generator exists where they can exchange commands directly. This capability is essential for the way how the system works. As the model extraction module is himself a kind of a planning module it plans both sensor actions but also robot actions in order to obtain the required information. On the other hand the task planning module also generates commands for the model extraction in order to resolve information missing in the knowledge base but required to solve a given task.

#### THE KNOWLEDGE BASE

The central role in a knowledge based system plays the knowledge base itself (Fig. 3). The information in it has to be both detailed enough for the lower level modules and abstract enough for the higher level modules and for presentation to the operator. The information must be presented to each level in the appropriate way.

This is achieved by using the frame concept for representing the information in the knowledge base. There are three types of frames which can be used:

- type frames containing descriptions of frame classes
- object frames containing descriptions of objects
- rule frames containing descriptions of rules as they are also formalized in frames.

Frame slots can also contain procedures how to get an information instead of an information itself. By this mean it is possible to define also frames with partly unknown information. During execution this information can be resolved by performing the procedure which may be the generation of a task for another module of the system.

Further it allows the information to be stored distributed. This avoids large data streams between the knowledge base and sub-modules of the system. Example: It is not necessary to keep the explicit model for recognition of an object by vision in the central knowledge base. Instead this model can be kept in the vision system. In the central knowledge base only the name of the model and a procedure how to get has to be stored.

There are different ways how the modules interface the knowledge base. The knowledge based modules like the task planning, the action planning and the model generation have direct access to the knowledge base.

The other modules interface the knowledge base via interface functions. They define both the kind of information which is exchanged and its abstraction level. The information is presented to each caller in an appropriate form. The same is true for the information added to the model vice versa.

The definition of the model interfaces highly influence the capabilities of the system as they define the information available for the system and is therefore a very important step in the development process.

The knowledge base is structured in the sense that it can be divided into several knowledge domains describing different aspects of the system and its environment on different levels. As the kind of information in the those domains are different also different approaches are used to represent the knowledge. In general for factual, relational and causal knowledge an object oriented approach is used whereas operational knowledge and the meta knowledge is represented in rules.

Further the knowledge base is distributed. The information is stored where it will be used. However there is a central part of the knowledge base which at least contains the information where a certain piece of information is located and how it can be accessed.

To obtain an environment model is the purpose of the system. Therefore this part of the knowledge base is now described in more detail.

#### The Environment Model

The environment model is meant to be the basis for the task and action planning modules and also for

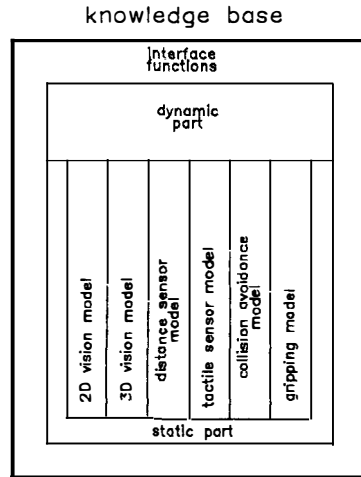


Fig. 3 Structure of the knowledge base

the environment generation module. Those modules plan actions in an uncertain (= not completely known) environment.

Therefore the model not only contains a priori knowledge but also knowledge derived from sensor information processing. This has some consequences:

- Inaccurate and incomplete models: Unprecise measurements or sensor signal noise results in erroneous or incomplete geometric data.
- Non repetitive path: As the actions which have to be performed in order to execute a task are not known a priori, the system cannot expect to meet exactly the same situation two times.

This leads to some requirements for the environment model:

- Efficiency: It is necessary to find an efficient representation of the information both with respect to access time and amount of data, as the kind of information the information processing modules require might be very different.
- Representation of uncertainty: As data is uncertain this uncertainty has to be modelled in order to let the system know about it.

- Completeness and extendability: The model structure must be complete in the sense that all necessary information is represented in some way and it must be extensible in the sense that new information can be added.

The environment model consists of a dynamic and a static part.

In the dynamic part the current state of the environment is represented. It contains actual states of objects (e.g. door open/close), their relations (e.g. object is gripped/is on the table) and actual geometric attributes like position and orientation.

As the goal is to use the model for planning repair tasks, it cannot be assumed that the initial state of this model is completely known. Moreover it is possible that it changes uncontrolled (not controlled by the system itself). Therefore the task of EXAMINER II is to determine the status of this dynamic model from the available sensor information.

The dynamic part is also updated by the execution modules when they change something in this environment.

The static part contains information which does not change. This part is in some way the "experience" of the system. It contains mainly knowledge about objects – geometric models, procedures to get special properties, how the objects can be used and other attributes relevant for the system.

It is now clear that one representation for an object is not enough. Different kinds of information and models are required. In the frame-structured knowledge base the various representations are stored in different slots of the frame.

It would be preferable to store information which depends on another information in form of a rule or an algorithm how to derive the required information. However this way is not practical in all cases because sometimes it is extremely expensive or complicated to formulate such a rule or algorithm. Therefore a mixed way is chosen. If possible such a rule is derived, if not the different representation is stored explicitly.

There is an important distinction between two ways of modelling an object, the sensor independent and the sensor dependent modelling.

The sensor independent model of an object contains all information about it used by the modules which do not process themselves sensor information. These are for example all planners and the operator interface.

It contains various properties of the objects which are relevant for the information processing modules. It also contains different descriptions of the same object for different purposes. A good example for that is the 3D representation of the object. In order to plan a collision free robot path a 3D model of all objects in the environment is required. This model is basically a description of the outer envelope of the objects. For gripping an object another type of 3D model is required. It describes the gripping interfaces and their geometry. For displaying the object to an operator again another type of 3D description is required which is a volume model which is very detailed compared to the one used for 3D object recognition by vision. Due to this fact for each application an appropriate model is derived from the general 3D description of the system.

Sensor specific modelling is required, although the basic environment model has to be sensor independent. This comprises both the modelling of the sen-

sor itself and the modelling of objects with respect to the specific sensor

A sensor model comprises all properties of a sensor which are relevant for its use and for the processing of its data.

Sensor specific models of objects are necessary because different sensors "see" the same thing in different ways. An ultrasonic sensor is able to perceive surfaces in a specific way (depth information, low angular resolution, limited angular deviation of the surface allowed). A vision system sees the same surface completely different (high angular resolution, in 2D no depth information).

For the sensors the object has different properties. This has to be modelled, either by adding to the sensor model rules what the sensor will see in dedicated situations (which is rather difficult) or by adding to the environment model information what a specific sensor will be able to see.

Those sensor specific models cannot only be derived from the geometric description of an object, although a model of the geometry is necessary. Additional information is required describing the special properties of a sensor with respect to an object. Nevertheless this model should be organized in a way where it is possible to derive all sensor specific models from one sensor independent model and the appropriate sensor specific information.

There are two basic approaches for sensor specific modelling:

- Explicit geometric model with additional sensor specific information: The sensor specific information is kept together with the geometric model. The sensor specific model is derived from the geometric model and the sensor specific information by an interface module on request of a specific sensor data processing module.
- Explicit sensor data model for specific sensors: For each sensor a specific model is generated and stored. This generation can be done automatically or with system operator support. Each sensor specific data processing module can directly access its own model. The various models can be stored in a distributed way in order to speed up access times. However provisions have to be made in order to keep the models consistent.

In the system discussed mainly the method of explicit representation is used in order to be able to store the information in a distributed way and in order to speed up the information processing.

#### SENSOR INFORMATION PROCESSING

It is one of the most important tasks of the system to keep the environment model as close to the real state as possible. Therefore the system has also the capability of updating and even adding new information to this model in order to achieve this goal.

These functions are sensor information processing functions. They are activated when the system detects "unforeseen" situations during the execution of the action plans.

There are two levels of this sensor information processing, the sensor dependent processing and the sensor independent processing.

In this system a multi-sensorial approach is made to solve this task, as using more than one physical sensor makes it possible to use a system design

which relies on the definition of "logical sensors". This makes sensor information processing on higher levels independent from the physical sensor which is a great advantage with respect to the flexibility of the information processing.

#### Sensor dependent information processing

In a multisensorial system it is very important that the functions of all sensors can be controlled from upper levels of the control system. Therefore it can be distinguished between sensor specific sensor information processing and sensor independent information processing.

Sensor specific information processing is mainly determined by the physical possibilities of the sensor itself. The same is true for the logical interface (possible sensor commands and parametrizations). However it is very important that all potential capabilities of the sensor are fully exploited. This comprises also all possible configurations and parametrizations, including the possibility to send specific sensor models to the sensors.

From the statements above it can be derived that a kind of a sensor command language has to be defined for the perception system also for the sensor dependent part in order to be able to use those sensors in a flexible way. This language defines the capabilities of the sensor system for the higher level control system and perception functions.

#### Sensor independent information processing

The purpose of the sensor independent information processing is to merge the complementary, redundant or partial, and/or repetitive informations from:

- the various sensors (instantaneous perception of the environment)
- the a priori knowledge (the static part of the model)
- the previous environment model

into one consistent model of the environment around the robot.

The input for this module are high level sensor tasks ("perception" tasks). The output of this module are sub-tasks, which can be both commands to the lower level sensor processing modules or to the lower level task planning modules.

This module is itself a kind of a planner which is able to plan sensor actions in order to resolve some required information. Typically this information cannot directly be accessed by one sensor action or it cannot be assumed that this is possible (If this would be the case this would be a task for the sensor specific information processing).

The knowledge to be processed in this module is very similar to a task planner. However it is able to process a special type of tasks, namely sensor data processing tasks. Further the type of sub-tasks is different. Its knowledge is represented in the form of rules. The premisses of those rules are composed of the current state of the environment and the information required. The conclusions are again sub-tasks.

This function can be activated by the operator by specifying a command (e.g. "inspect area") or by a planning module when it detects some unforeseen situation.

#### 3D vision

As the information required in the model is basically 3D, also a 3D sensor is required. In this system this is mainly a 3D vision system, although the distance sensor in conjunction with the 2D vision information is also used to obtain or to verify 3D information.

The 3D system consists of a real time vector-extractor which converts the iconic grey-level image onto a CAD like description of the contours. The result is a vector-list. Afterwards a model based segmentation procedure extracts attributed symbols such as corners, straight lines, blended lines and closed contours. Based on this symbolic representation a stereo vision module finds the best match between several model objects and the image contours. Models are also represented as contours, i.e. by their symbolic representations.

The scene which will be analysed is visible at least by two cameras. Due to the analysis of these two images it is possible to determine the 3 D position of this objects. The processing is based upon the determination of the 3D location of object features like e.g. corners.

This vision system is the most powerful "physical sensor" within the system because it is able to determine most of the important attributes of an object within its environment. The task mentioned above form the core of the multisensorial system. In fact the 3 D vision system plays the role of several logical sensors simultaneously, depending on the type of information it is asked.

Acting as an "object recognizer" it is located on a higher level of the information processing hierarchy than it is when it is acting as a "feature extractor". In the first case it is used by the higher level modules as a source for the (abstracted) information whether a specific object is there and where it is. In the second case it is used as an information source for a low level information about the presence or absence of a line.

#### CONCLUSION

In this paper an architecture for a hybrid system was presented which is able to obtain parts of an unknown environment model. Besides the main modules of the system are described in more detail.

In future two main aspects will be investigated in more detail. The first one is the correspondence between the environment model obtained by sensor data processing and the information requested by the planning tasks. The second one is the question how one can deal with less structured environment.

#### REFERENCES

- Kegel G. (1990). Erhöhung der Systemautonomie von Robotersystemen durch multisensorielle Informationen und Nutzung einer Wissensbasis. Dissertation 1990, TH Darmstadt
- Matthiesen J., H. Tolle, E. Ersü and S. Wienand (1992). Sensorinformationsverarbeitung und Planung in einem autonomen Steuerungssystem für Wartungs- und Reparaturaufgaben in der Raumfahrt. Fachtagung Automatisierung, Dresden, spring 1992
- Simon W. (1991). Untersuchungen zu einer intelligenten und lernfähigen Robotersteuerung für die Montageautomatisierung. Dissertation 1991, TH Darmstadt

## SHARED FORCE/POSITION CONTROL FOR REDUNDANT ROBOT MANIPULATORS

R. Kline-Schoder, J.-N. Aubrun and M. Wright

*Lockheed Research Laboratory, O/92-30, B/250, 3251 Hanover St., Palo Alto, CA 94304, USA*

**Abstract:** The design and use of redundant robot manipulators has presented numerous challenging control problems. The two most important are the position and force control of the end effector. Solutions to both of these control problems are needed so that robot manipulators can be used in their most flexible configurations. This paper presents a position control algorithm which is based on an iterative search and a force controller which uses standard control design techniques. It then suggests that these two control algorithms can be combined to yield a shared force/position controller. The shared controller has the properties of an impedance controller and can be implemented in a pair of 80386-based computers for a robot manipulator with seven joints. Results of a computer simulation of a planar, two-joint robot manipulator are presented and show the functionality of the developed shared force/position control algorithm.

**Key Words:** *robot control, force control, position control, iterative methods*

### Introduction

Control of robot manipulators has been a topic of research for many years. One aspect of the control of robot manipulators which has proven to be particularly elusive is the efficient (from an implementation standpoint) shared force/position control for the end effector. Solving the pure position control problem (i.e., the real time calculation of joint angles, given desired end effector position and orientation) for redundant robots has been studied and adequate solutions are used in common practice. Useful end effector force control algorithms, on the other hand, have not yet been developed or implemented for realistic systems (i.e., robot manipulators with greater than two or three degrees of freedom). Combining force and position control in a shared sense to achieve impedance control has also only been studied in a very simplified manner. Shared force/position control is necessary for the

many tasks which require precise interaction between a robot and the environment. Examples include: insertion tasks (for connectors), surface following (for inspection), multiple arm coordinated motion (for manipulating extended bodies), and object definition (for determining inertia properties and/or categorization). Furthermore, shared force/position control provides a mechanism for the smooth transition between pure position control and pure force control. This is advantageous from an implementation point of view, for it can minimize the number of different operational states of the robot. Members of the Lockheed Palo Alto Research Laboratory have designed and built a robot which has two, seven degree-of-freedom manipulator arms. This robot is used as a test bed for both high level task management algorithm development and unique robot control system implementation. The result of research with this hardware has been the development of a new shared force/position control algorithm which can be implemented on a pair of 80386-based, IBM compatible computers.

Current descriptions of shared force/position control algorithms tend to treat this subject either with overly simplistic examples or with unrealistic computational demands (see [1]). The shared force/position control algorithm which is most often quoted is the operational space approach introduced by Khatib [2]. This method performs a feed-forward calculation in order to compensate for all of the manipulator dynamics such that the manipulator appears as a unit mass on a unit spring. While this approach is theoretically sound, a major drawback, which is related to implementation, makes the algorithm virtually useless for a complicated robot. This implementation difficulty arises in the real time calculation of the robot dynamics, which involves nonlinear, coupled, differential equations. Other researchers ([3] and [4]) have concentrated on solving the problem of transitioning from purely position control to purely force control. These methods promise to reduce

the amplitude of initial contact forces but do not address the more fundamental issue of implementing a flexible and robust shared force/position algorithm, which will effectively overcome the difficulties involved with transition. Direct attempts at implementing impedance control for redundant systems have been made recently. The algorithm described in [5] promises to overcome many of the difficulties associated with redundant manipulators. However, to make the implementation computationally manageable, the controller must be simplified to a stiffness controller, which has the effect of reducing the advantages of the impedance control scheme. Finally, some researchers have tried to augment impedance control methods with acceleration controllers [6] [7]. This idea begins to approach the operational space method of eliminating manipulator dynamics with feed-forward commands and requires only slightly less computational power than the Khatib algorithm.

This paper describes the hardware and software configuration of the Lockheed robotics test bed and discusses the requirements for shared force/position control. The algorithm which has been developed to implement shared control on the robot makes use of an iterative kinematic solver (coupled with a joint angle position controller) to achieve Cartesian end effector position control and a simple torque feed-forward calculation to achieve force control. Shared force and position control is accomplished by weighting the force and position errors in a Cartesian, body-fixed coordinate frame. Choosing the appropriate weights allows switching between pure force and position control, or a shared combination of the two. This configuration behaves like an impedance controller, where the system is equivalent to a spring, pulling the end effector towards the work plate and ensuring contact. Further, this control algorithm has been simulated with a simple computer model to provide experience with the method and to predict expected performance.

## System Description

The robotics test bed at the Lockheed Research Laboratory consists of two, seven degree-of-freedom (DOF) manipulator arms and a two DOF vision platform for mounting a video camera. Figure 1 shows a front view line drawing of the test bed. The manipulator arms were purchased from Robotics Research Corporation and contain the required motors, gears, resolvers, and torque sensors for controlling the position of the joints relative to each other. Lockheed has assembled the necessary electronics to power the motors and to condition the signals from the sensors for feedback control. Inner-loop torque control

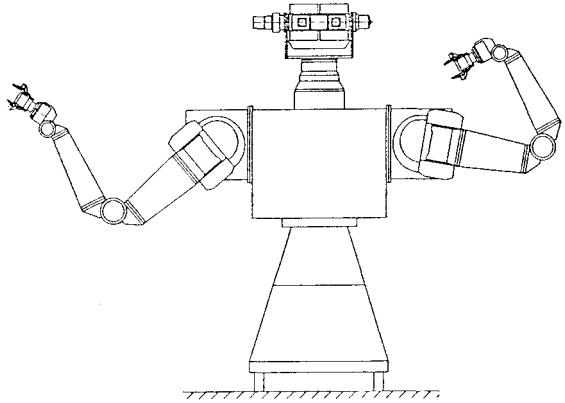


Figure 1: Schematic Diagram of Robotics Test Bed

is implemented in analog electronics and outer-loop position and force control are implemented in two 16 MHz, 80386-based computers for all seven joints.

The requirement for the implementation of position and force control comes from desired operational characteristics of the manipulator arms. Obviously, position control is necessary to orient the arms relative to inertial space in order to perform numerous simple tasks which require uncontrolled interaction with the environment external to the manipulator (e.g., picking up objects from one place and positioning them somewhere else). Manipulator force control is needed when precise interaction between the manipulator and the environment is required. Examples of these tasks include: connector insertion, surface following for inspection, multiple arm, coordinated motion for manipulation of extended rigid bodies, and the determination of mass properties used for categorization and identification. Shared force/position control arises whenever transitions from free end effector boundary conditions to constrained boundary conditions are expected. This situation occurs when a manipulator approaches a surface against which the interaction force between the manipulator and object must be regulated. The transition from no interaction force to the desired interaction force must occur in a smooth fashion, minimizing impact forces and eliminating the chance for an instability to arise.

## Position Control

The position control problem can be stated simply as the determination of the necessary joint angles as a function of time to achieve the desired end effector path and orientation. The difficulty in implementation results from the fact that the kinematic equations which transform from joint angles to end effector position and orientation are nonlinear. Only specific manipulator designs have

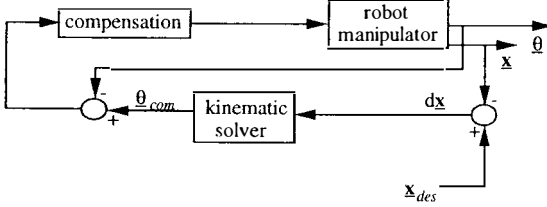


Figure 2: Block Diagram of the Position Control Architecture

closed-form solutions for the inverse of this nonlinear transformation. Redundant manipulators have the added difficulty of accounting for multiple solutions to the same problem and choosing the most appropriate solution from the set of possible solutions. Numerous solutions to the inverse kinematics problem exist. The solution described in this paper is an iterative search algorithm based on Newton's Method and was chosen for its flexibility and compatibility with the force control solution presented later.

A block diagram of the position control algorithm is shown in Figure 2. The end effector position is denoted by  $\underline{x}$ , which is a  $6 \times 1$  vector of three Cartesian coordinates of the end effector location and three measures of the orientation of the end effector (in our case, we used three direction cosines from the matrix relating the orientation of a reference frame fixed in the end effector to an inertial frame). The goal of the position controller is twofold: 1) to determine the values of the joint angles required to position the end effector in inertial space (i.e., the kinematic solver) and 2) to determine the joint motor torques required to achieve the relative joint angles determined from the result of the kinematic solver calculations (i.e., the position servo for the joint angles). While the implementation of the position servo for the joint angles is not trivial, an elegant solution has been implemented by [8] and will not be discussed any further. The kinematic solver takes errors in the Cartesian position and orientation of the end effector,  $d\underline{x}$ , and generates commands to the joint angle position servo.

The kinematic solver is based on an iterative search algorithm which uses Newton's method. The relationship between the end effector position and orientation  $\underline{x}$  and a set of joint angles  $\underline{\theta}$  is nonlinear and has been derived for the hardware described above by Levinson [9].  $\underline{\theta}$  represents an  $n \times 1$  vector of joint angles, where  $n$  represents the number of manipulator joints. The equations can be summarized in the following notation:

$$\underline{x} = f(\underline{\theta}), \quad (1)$$

which represents a set of six, coupled, nonlinear,

kinematic equations. Variations in the values of  $\underline{x}$  as a function of variations in the joint angles can be expressed as a  $6 \times n$  matrix known as the Jacobian and is denoted as

$$\frac{d\underline{x}}{d\underline{\theta}} = \frac{\partial f(\underline{\theta})}{\partial \underline{\theta}} = J(\underline{\theta}). \quad (2)$$

Multiplying Equation 2 by  $d\underline{\theta}$ , one derives the equation relating variations in the end effector position and orientation to changes in the joint angles as

$$d\underline{x} = J(\underline{\theta}) d\underline{\theta}. \quad (3)$$

Equation 3 can be inverted by employing the pseudoinverse to yield the following expression:

$$d\underline{\theta} = [J^T(\underline{\theta}) J(\underline{\theta})]^{-1} J^T(\underline{\theta}) d\underline{x}. \quad (4)$$

With Equation 4 as a basis, the iterative algorithm used to solve for the joint angles given a desired end effector location proceeds as follows:

1. Evaluate  $d\underline{x} = \underline{x}_{des} - \underline{x}$ .
2. Let  $\underline{\theta}^* = \underline{\theta}$ , the current joint angles.
3. Evaluate  $J(\underline{\theta}^*)$ .
4. Determine  $d\underline{\theta}^*$  from Equation 4, substituting  $\underline{\theta}^*$  for  $\underline{\theta}$  in the expression.
5. Let  $\underline{\theta}^* = \underline{\theta}^* + k d\underline{\theta}^*$ , where  $k$  is a constant, convergence parameter.
6. Evaluate  $\underline{x}^*$  from Equation 1, substituting  $\underline{\theta}^*$  for  $\underline{\theta}$  in the expression.
7. If  $\|\underline{x}^* - \underline{x}_{des}\| < \epsilon$ , where  $\epsilon$  is a small number, let  $\underline{\theta} = \underline{\theta}^*$ , else return to step 4.

This procedure is effective and has proven to be easy to implement for a manipulator with seven joints on a single 80386-based computer.

## Force Control

The force control problem centers on determining the required joint torques to achieve the desired end effector/environmental interaction forces. A block diagram of this control problem is shown in Figure 3. This figure shows that joint torques are applied to the manipulator arm, resulting in a  $6 \times 1$  vector of three end effector forces and three moments, denoted by  $\underline{F}$ . Force control is achieved by comparing a commanded force vector with the force values measured by a six DOF force/torque sensor (i.e., forming the force error) and determining the required changes in the end effector forces to drive the errors to zero (i.e., filtering the force errors with some compensation). The changes in the end effector forces are transformed into joint

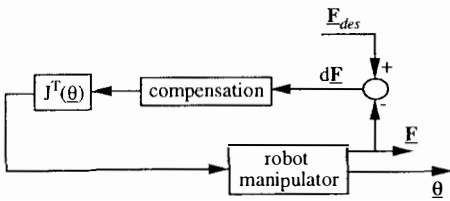


Figure 3: Block Diagram of the Force Control Architecture

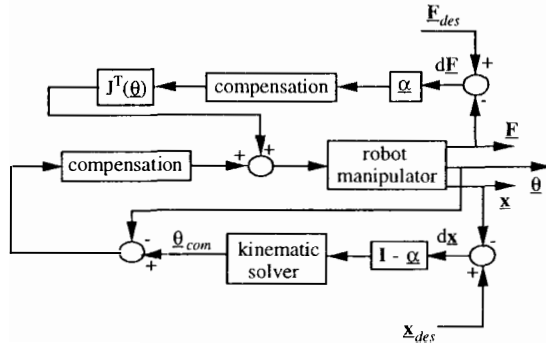


Figure 4: Block Diagram of the Shared Force/Position Control Architecture

torques by applying the Jacobian (see [1]) shown in Equation 2. Implementation of this algorithm is extremely straightforward and requires no extraordinary computational power, even for a robot manipulator with greater than seven joints.

### Shared Force/Position Control

A shared force/position controller can be implemented by combining the results of the previous two sections. A block diagram of the controller architecture is shown in Figure 4. The architecture is essentially the parallel combination of the position and force control architectures discussed previously. The only additions are matrix multiplications of the position and force error vectors by  $I - \underline{\alpha}$  and  $\underline{\alpha}$ , respectively.  $\underline{\alpha}$  is a matrix with diagonal elements which range from 0 to 1 and which determine the ratio of force and position control for each axis of the end effector. A value of 0 corresponds to pure position control and a value of 1 corresponds to pure force control. Therefore, position and force control can be combined in any one of the six end effector axes by varying the diagonal elements of  $\underline{\alpha}$ . One issue that needs to be raised at this point concerns the design of the force and joint angle compensation controllers. If a diagonal element of  $\underline{\alpha}$  does not exactly equal 0 or 1, interaction between the two controllers is inevitable. If both of the compensation laws contain an integrator, the shared controller will be unstable due to the parallel combination of integrated

signals. Care must be taken to design compatible compensation laws for each of the position and force control loops when they are used in a shared mode. This control architecture behaves like an impedance controller, where the impedance of the manipulator arm is varied by changing the diagonal elements of  $\underline{\alpha}$ , effectively determining the ratio of the manipulator force to position. This method can be used to control the transition from unconstrained position control to partially constrained force control by either limiting the speed of approach of the end effector or by adjusting the diagonal elements of  $\underline{\alpha}$  to change the impedance of the manipulator. The implementation of this shared force/position control algorithm is a rather simple addition of the separate force and position controllers discussed previously. This algorithm can be implemented in two 80386-based computers, one to perform the kinematic solver and force control calculations and one to perform the joint angle compensation calculations.

### Computer Simulation

A simple, planar, two degree-of-freedom robot manipulator has been modelled and the behavior simulated on a digital computer. The manipulator is controlled with the shared force/position control algorithm derived previously. The simulation models the motion of the two DOF manipulator moving over a sinusoidally varying surface with a constant speed and controlling the force applied by the end effector to the surface. The results of the simulation are shown in Figure 5. The figure shows the position of the end effector and the force applied by the end effector to the surface over which it is moving. The results show that the position of the end effector moves in the unconstrained direction in a manner consistent with the commanded motion (i.e., a constant speed). Further, Figure 5 shows that the end effector applies a force to the surface in the constrained direction which is within 5% of the commanded force over the entire range of unconstrained motion. These results emphasize the functional behavior of the shared force/position controller presented above.

### Conclusions

Position and force control for robot manipulators is required in order to provide the manipulator with full functionality. Position control is used to command the position and orientation of the manipulator end effector relative to some fixed reference frame. Force control is used to command the interaction forces and torques from a manipulator end effector on to the environment external to the manipulator. A shared force/position controller is

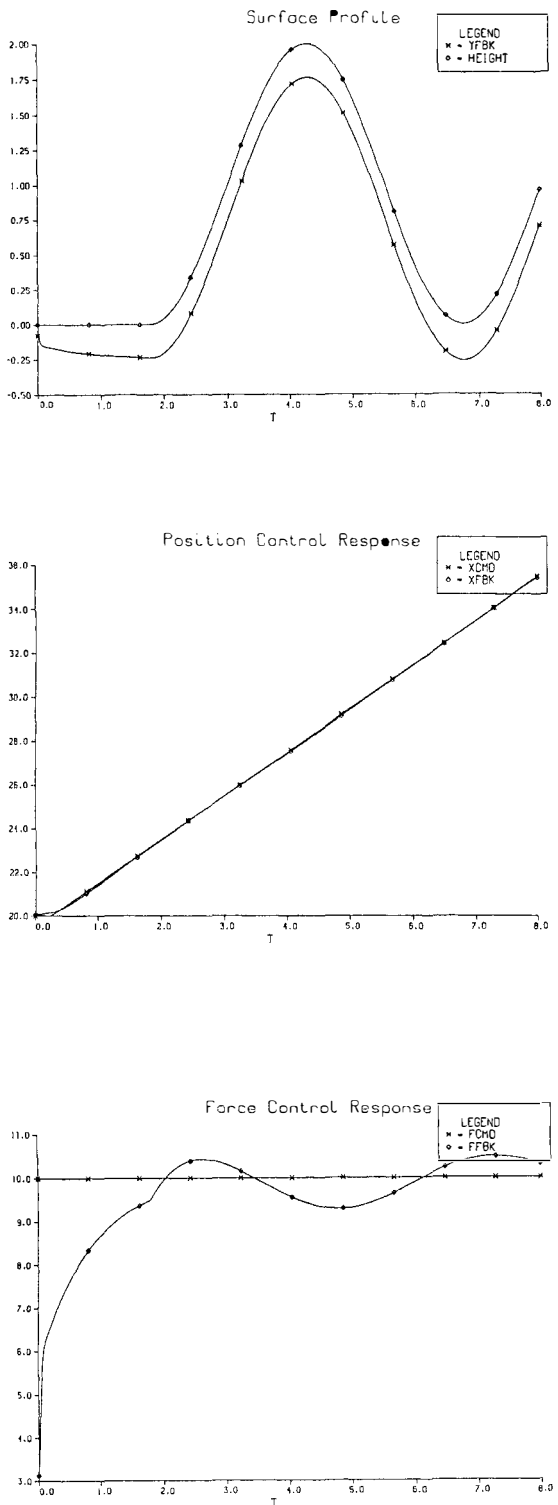


Figure 5: Computer Simulation Results of Shared Force/Position Controller

used to regulate the transition from unconstrained position control to constrained force control. The position control for redundant robot manipulators can be achieved with the derived kinematic solver algorithm. The algorithm is based on an iterative search, using the end effector position error and employing the variation of the nonlinear relationships between end effector position and the current joint angles to changes in the joint angles (i.e., the Jacobian). The derived force control algorithm uses a standard compensation design and the transformation between errors in end effector force and the desired joint torques. The shared force/position controller combines the two separate controllers in such a way that by varying a parameter between 0 and 1, any combination of force or position control can be achieved for any of the end effector degrees of motion. The algorithms are simple enough to be implemented in two 80386-based computers for a manipulator with seven degrees-of-freedom. A computer simulation of a simple, 2 degree-of-freedom robot has shown that the proposed shared force/position control algorithm is effective at achieving the desired operational functionality of the robot manipulator.

## References

- [1] Craig, J. (1989). *Introduction to Robotics: Mechanics and Control*, Addison-Wesley Publishing Company.
- [2] Khatib, O. (1987). A Unified Approach for Motion and Force Control of Robot Manipulators: The Operational Space Formulation. *IEEE Journal of Robotics and Automation*, Vol. RA-3, No. 1.
- [3] Walker, I. (1990). The Use of Kinematic Redundancy in Reducing Impact and Contact Effects in Manipulation. *Proceedings of the 1990 IEEE Conference on Robotics and Automation*, Cincinnati, OH.
- [4] Mills, J. (1990). Manipulator Transition To and From Contact Tasks: A Discontinuous Control Approach. *Proceedings of the 1990 IEEE Conference on Robotics and Automation*, Cincinnati, OH.
- [5] Newman, W., M. Dohring (1991). Augmented Impedance Control: An Approach to Compliant Control of Kinematically Redundant Manipulators. *Proceedings of the 1991 IEEE Conference on Robotics and Automation*, Sacramento, CA.
- [6] Komada, S., K. Ohnishi, T. Hori (1991). Hybrid Position/Force Control of Robot Manip-

- ulators Based on an Acceleration Controller. *Proceedings of the 1991 IEEE Conference on Robotics and Automation*, Sacramento, CA.
- [7] Liu, G., A. Goldenberg (1991). Robust Hybrid Impedance Control of Robot Manipulators. *Proceedings of the 1991 IEEE Conference on Robotics and Automation*, Sacramento, CA.
- [8] Sahinkaya, Y., M. Wright, B. Leonard, T. McGinnis (1990). Development of an Intelligent Controller for a Two-Axis Camera Vision Platform. *Proceedings of the 1990 American Control Conference*, Boston, MA.
- [9] Levinson, D. (1990). The Use of Autolev for Kinematic Analyses of Robots. *Proceedings of the 1990 AIAA Guidance, Navigation, and Control Conference*, Portland, OR.

## ADAPTIVE AND EVOLUTIONARY ROBOTICS - A NEW ARCHITECTURE FOR LEARNING-BASED AUTONOMOUS SPACE ROBOT

T. Tanabe and S. Nakasuka

*Department of Aeronautics, University of Tokyo, Bunkyo-ku, Tokyo, Japan*

**Abstract.** A learning-type, hierarchical architecture for an autonomous robot management and control system is proposed. The upper task planner generates a sequence of robot movements which achieves the given objectives and the lower task executor realizes them in the robot movements using sensor feedbacks. At the executor level, some operational parameters, which dictate how the robot should move in response to the sensor information, are learned, which together with the sensor feedbacks compensates for the gaps between the robotic world and the real world. At the task planning level, learning of macro operators is performed. The system as a whole provides the adaptability to the environmental changes or new situations, and also realizes the evolutional growth of the versatility. Preliminary laboratory experiments using two manipulators and some cameras for block construction tasks have been performed, which indicates that the proposed architecture is promising.

**Keywords.** Autonomous System; Space Robots; Learning Systems; Parameter Tuning; Macro Planning.

### INTRODUCTION

It has been widely recognized that autonomous system will be required in the future space systems and operations where manned participations or teleoperations are difficult and not cost-effective. In the field of space robotics, too, the development of autonomous systems architecture will be a key issue in order for them to be really helpful in achieving various sophisticated space activities.

When architecting robot systems under the conventional design philosophy such that almost all the robotic movements are "hard-coded" before real operations, the following problems will be inevitable. Firstly, robustness to various changes in the environment, such as failures of some joints or changes of camera relative position, which may occur during the actual operations, is quite limited. And secondly, control software becomes lengthy, complex and not-easy-to-check type program, and moreover, "bugs" or algorithmic errors cannot be removed without elaborate human inspections. These drawbacks seem to come from the fact that such type architecture only utilizes an a priori knowledge about the system and environment, and has little capability to modify or adapt itself to various real time changes.

"Learning type" approach has been applied in various ways to compensate for these drawbacks. In Liang, Chang and Hackwood(1989) and Tanabe and Yoshikawa(1990), the transformation formula from camera frame to robot frame is updated during actual operations using Kalman filtering and least square method respectively. In Miller(1989), Neural Networks are utilized in on-line fashion to obtain information as to the mappings from the robotic commands to the actual effects and also its inverse transformation. Rangwala and Dornfeld(1989) also employs Neural Network to tune operational parameters of manufacturing robots. In these literatures, learning is a parametric one utilized mainly to compensate for the real time change of the environment, the system itself and the relationships between them.

The learning of this type, however, cannot acquire "structural knowledge" such as the knowledge about how to generate a sequence of basic movements to achieve certain sophisticated tasks. This so called "task planning" has been attracting many researchers in the field of artificial intelligence (Nilsson, 1980, Camarinha-Matos, 1987, Minton and colleagues, 1990). In these studies, basic movements are represented as "operators" in such various forms as precondition-add-delete lists, frames, semantic networks, procedural net-

works or production rules, and a sequence of operators to achieve high level tasks are searched for logically, not in interactions with the real world. The combinatorial explosions of the search space is one of the major difficulties in this line, and learning of macro operators has been proposed as one approach to this problem(Iba, 1989, Tanaka and Mitchell, 1991). Though, as Brooks (1990) criticized, the real world is too complicated to be modeled by a logical world, these task planning methodologies can be said useful or even indispensable in the abstract planning level if the lower level of the system can manage the "gaps" between the generated task plans and the real world.

We have combined the above two types of learning to construct an autonomous, hierarchical robot management and control architecture. Implemented with two type learning capabilities, the system is, as a whole, expected to exhibit adaptive as well as evolutional features. Preliminary laboratory experiments for block construction tasks have been performed, and the results indicate that the proposed architecture is quite promising.

In the next section, this architecture is explained in detail, followed by the descriptions of the laboratory experiment. The two learning mechanisms are explained in detail in the context of our experimental setups. Finally, the experimental results are given.

### LEARNING-BASED ROBOT CONTROL ARCHITECTURE

Figure 1 describes the overall architecture of our robot control system. The solid lines with arrows show the nominal information flows and the dotted lines show the flows which are triggered when a certain learning activity is required. Each numbered arrow indicates the following information flow.

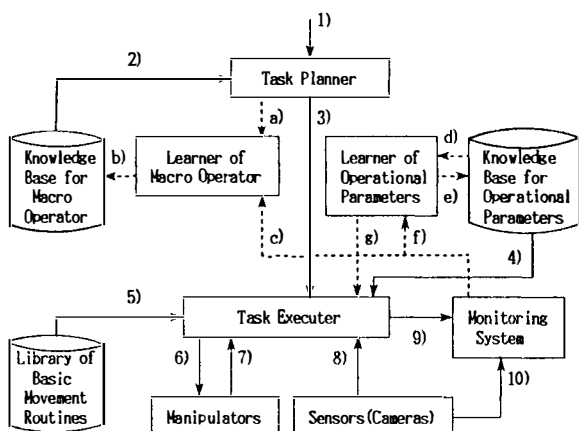


Fig.1. Architecture of learning-based autonomous robot control system.

A certain high level task command is input from man or other upper level systems (1).

"Task Planner" interprets it into a sequence of low level basic robot movements (3) by referring to the knowledge base of macro operators (2). If the task planner cannot find a corresponding macro operator for the given task, it generates the sequence by logical search using the basic and macro operators. Each time a useful sequence is found, it triggers the "Learner of Macro Operator"(a), which generalizes the generated sequence using Explanation Based Learning (EBL) to construct a new macro operator and stores it in the knowledge base (b).

"Task Executer" receives this sequence and realizes each basic movement one by one in manipulators (6,7) using the sensor infomation (8) and operational parameters (4). Library of basic movement routines is utilized (5) to interpret abstract level commands into actual, lower level ones to the manipulators. The operational parameters mean such changeable parameters that dictate the way the manipulators move in response to the commands and sensor information. Examples are a transformation matrix from robot frame to sensor frame (Tanabe and Yoshikawa, 1990) or a cutting speed for a certain industrial robot (Rangwala and Dornfeld, 1989).

"Monitoring System" monitors the output of "Task Executer"(9) and the actual movement of the robot (10), and provides information on command-effect relationships to the other subsystems. When it detects a gap between the anticipated effect of a certain robot command and the actual one, it triggers the parameter adjustment mechanism (f) or macro re-learning mechanism (c) to restore the consistency. The re-tuned operational parameters and macro operators are stored in the knowledge base again (e,b).

As discussed in many literatures, planning in abstract, logical world alone cannot be applied to the real world problems because of the gaps between these two worlds. In our architecture, this problem is solved to some extent by the hierarchical configuration. The basic movements at the task planning level are not such elementary movements of manipulators as "change the joint angle by a certain degree" or "close the grip at the current position", but a kind of "goals" of small subtasks such as "grasp the No.3 object" or "joint the two blocks grasped by the two manipulators." The lower level, that is the Task Executer in our system, is responsible for achieving the specified subgoals. The gaps between the two worlds are compensated for in this level by the sensor feedbacks and, if the gaps are large, retuning the operational parameters. It is, therefore, important how to set the abstract level of the movements

used in the task planning. They must be abstract enough not to be disturbed by the gaps between the two worlds, but at the same time they must be elementary enough to provide the planning flexibility. In our laboratory experiment, the basic movements are selected with these considerations.

It is expected that this architecture has the following strong features.

- 1) The operational parameters can always be kept up-to-date, which provides the first level adaptability to the change of the system and the environment.
- 2) Even if more drastic changes occur or completely new tasks are ordered, the system tries to meet with the task command, though the planning process take some time. This provides the second, higher level system adaptability.
- 3) The system is evolutional, that is, the learned knowledge further enhances the adaptability and versatility of the system itself.
- 4) The macro planning is performed recursively, which makes possible the generation of high level sophisticated task sequences.

### LABORATORY EXPERIMENT OF BLOCK CONSTRUCTION TASKS

#### Overview of the Experimental Setups

The proposed architecture is examined in the laboratory experiment for block construction tasks. The experiment system consists of two five degree of freedom manipulators, one monochrome and one color CCD cameras, and a set of processors. The overall configuration of the hardware system is described in Fig.2. Task Planner, Learner of Macro Operator and Knowledge Base for Macro Operator in Fig.1 are implemented in LISP, and the other subsystems are coded in C language.

Figure 3 describes the block construction task performed in our experiment. In the initial situation, several raw blocks with different colors are placed on the table. Each row block has the shape described in the right part of Fig.3. The four pins at the top of it can be inserted into the tail of another one, connecting the two blocks. The human operator orders the robotic system to joint them into a long, straight pole with a prescribed color sequence. The robotic system, after acquiring the position-color relationships of the raw blocks with a color camera, plans the sequence of movements, and then executes it with the visual feedbacks. The detailed descriptions are given below.

#### Basic Movements

The basic movements used at the task planning level are selected with the previously mentioned

considerations as follows;

*PICK(hand,color,grasped-position)*: picks-up the raw blocks of "color" using "hand(left or right)" manipulator. The grasped position on the raw blocks are specified as either "upper" or "lower".

*JOIN(hand)*: connects two blocks grasped by the two manipulators with "hand(left or right)" over the other manipulator.

*CHANGE-GRASPED-POSITION (hand,length)*: changes the grasped position of "hand(left or right)" manipulator by "length(integer)" unit. Positive "length" means the upward direction and negative "length" means the downward.

*FREE(hand)*: releases "hand" manipulator from the blocks.

For JOIN operation, visual feedbacks are used to compensate for the uncertainties in the positions and directions of the grasped raw-blocks. The other movements are performed in a rather feed-forward fashion. For PICK operation, the color camera provides information on the rough posi-

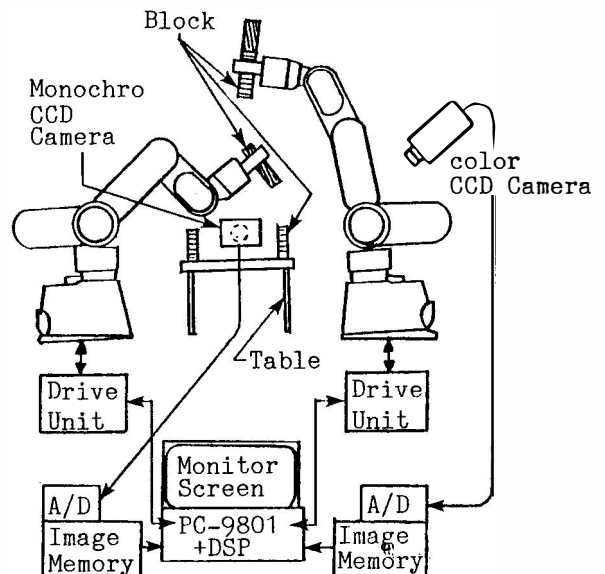


Fig.2. Hardware setups for block construction experiment.

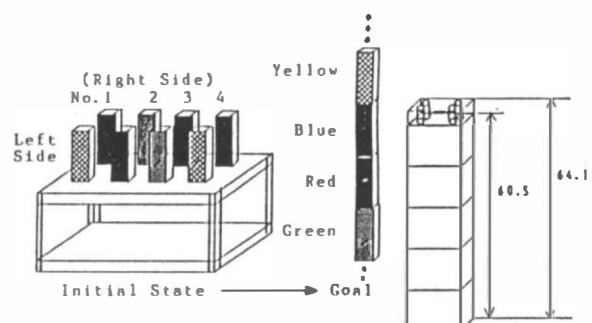


Fig.3. Block construction task overview.

tion of each colored raw-block, which is then utilized by the Task Executer to move the manipulator grip. There is no need to precisely prescribe the grasped block position and direction relative to the manipulator grips, because such uncertainties can be compensated for in JOIN operation.

### Visual Feedback

In JOIN operation, visual feedback using the image of the monochrome camera is performed as in Fig.4. In the experimental set-ups, the location where JOIN operation is performed is nearly fixed, and the camera is set in front of it so that it can view both the blocks rather two-dimensionarily. This location is selected so that the uncertainties in the grasped block position and direction may be stuffed only in the directions on this focal plane, and therefore the visual feedback is needed only in two dimension. The three degrees of freedom of manipulators are enough for this objective. At first, the contour of the lower block is extracted from the image, then the target position of the upper block is set in the image frame, aligned with the lower one with a small gap( $d$ ). Secondly, visual feedback is performed to reduce the difference ( $\Delta\theta, \Delta\xi, \Delta\eta$  in Fig.4) by sending the following control inputs to the upper manipulator.

$$\underline{\Delta p} = A \underline{\Delta q}, \quad \underline{\Delta p} = \begin{bmatrix} \Delta x \\ \Delta y \\ \Delta \phi \end{bmatrix}, \quad \underline{\Delta q} = \begin{bmatrix} \Delta \xi \\ \Delta \eta \\ \Delta \theta \end{bmatrix}$$

$\Delta x, \Delta y, \Delta \phi$  : incremental control inputs in the direction of x,y-coordinates and about the pitch-axis of the manipulator frame.

*A matrix* : influence coefficient matrix between incremental manipulator control inputs and ma-

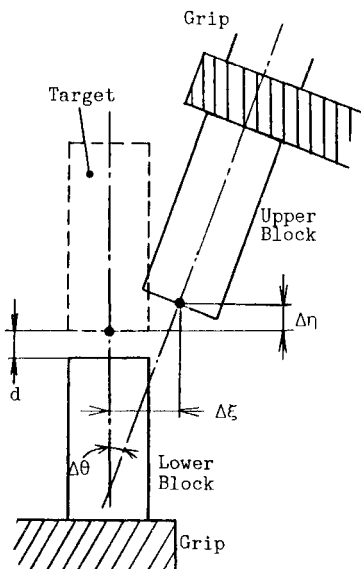


Fig.4. Image frame used for visual feedback.

nipulator grip movements in the image frame.

After several iterations can reduce the difference between the target and actual positions in the image frame below a certain tolerance value, the upper manipulator moves the block downward along the direction of the block axis until the two blocks are connected. The value for the gap ( $d$ ) between the lower block and the target position of the upper block must be made as small as possible to ensure the successful connection, but it must also be large enough to discriminates the two objects during the visual feedback. Considering these effects, in our experiment the value of three pixels is utilized.

### Operational Parameters

The matrix  $A$  dictates how the manipulator should move in order to achieve a certain movement of the grasped block in the image frame, and is different for the left and right manipulators. We consider these  $A$  matrices as operational parameters because they may be changed according to the way how the manipulator grasps the block, or by possible anomalies such as unintentional camera movements or some failures in the manipulator drive unit. They are estimated using a simple least square formulation;

$$A = PQ^T(QQ^T)^{-1}$$

$$P = (\underline{\Delta p_1} \ \underline{\Delta p_2} \ \dots \ \underline{\Delta p_n})$$

$$Q = (\underline{\Delta q_1} \ \underline{\Delta q_2} \ \dots \ \underline{\Delta q_n})$$

$\underline{\Delta p_i}$  :  $i_{th}$  command inputs to the manipulator

$\underline{\Delta q_i}$  :  $i_{th}$  movement of the grasped block in the image frame

In order to obtain the matrices  $P$  and  $Q$ , the manipulator is moved some times in such a set of directions that minimizes the estimation error. During the visual feedback, when the Monitoring System detects a large discrepancy between the anticipated movement of the block ( $\underline{\Delta q}$ ) and the actual one in the image frame, the estimation process of matrix  $A$  is re-initiated. By this way, matrix  $A$  can be kept up-to-date at any time.

### Task Planning

Task planning is performed using the STRIPS-like representations (Nilsson, 1980) of the basic movements(operators); that is, preconditions (the restrictions on the situation at which the operator can be applied), add-list(the features added after the operator application) and delete-list(the features deleted after the operator application). Task Planner searches exhaustively for an appropriate sequence of basic movements and their parameters which achieves the given objectives. A

search tree is generated in breadth-first manner, in which only the operators whose preconditions are satisfied by the state of each node are applied to that node. As can easily be inferred, this strategy gives rise to the problem of combinatorial explosion of the search space. This problem is solved to some extent in our system using the macro learning method explained in the next section.

### Macro Learning

When a certain objective is achieved by a sequence of basic movements, "Learner of Macro Operator" is triggered to transform the sequence into a new macro operator. In order to enhance the usefulness of the macro, EBL(Explanation Based Learning) type generalization procedure(Mitchell, Keller, and Kedarnath-Cabelli, 1986) is employed. Macro generation is done in the following manner.

- (1) The operator sequence from the initial state to the goal state is extracted from the search tree.
- (2) All the constants concerning the manipulators and colors in the operator sequence are replaced with variables.
- (3) Using the preconditions, add and delete-lists of each operator, this sequence of movements is simulated in the computer again. During the simulation, if an operator orders that some variables must satisfy the preconditions in order for that operator to be applicable, then such preconditions are stored. If the preconditions are already satisfied as a logical consequence of the previous operators, they need not be stored. Add-list and delete-list are updated at each operator application in a incremental manner.
- (4) A macro operator is registered in the form of preconditions, add-list and delete-list (the same representation as the basic operator), and the sequence of operators. Add-list and delete-list are the ones obtained after the final operator application in (3), and the preconditions are the list of stored preconditions in (3).

The generated macro operator can be used in the same way as the basic operators for task planning. They can also be one operator in the operator sequence for another new macro, so the macro generation can be performed recursively. Macro operators with many constants in the preconditions could rarely be applied because such preconditions are satisfied only in quite specific states. Such type macros are even harmful because they add computation time for matching process which will fail in almost any time. The generalization procedure by changing constants into variables is, therefore, quite important to refine the "raw" macros into frequently applicable,

useful operators.

## RESULTS OF LABORATORY EXPERIMENTS

### Effect of Macro Learning

In order to examine the effect of macro learning, the following procedure is performed. The task planning and macro learning is first done for small problems, that is, the construction of two span block, then three span block, four span block, and so on. The macro operators generated during the smaller problems are utilized for later, larger problems.

Figure 5 shows the comparison of the search space(the number of nodes in the search tree) for the case that (1) macro learning is not performed and (2) performed. In (2), the macro operators generated in the smaller problems can be utilized for problem solving, which drastically reduces the search space. Moreover, the divergence rate of the search space as the problem size grows is much less when using the macro learning. (3) shows the cumulative sum of (2), which means the total search space required for generation of macro operators in smaller problems plus the search space for solving the specific problem. The comparison between (1) and (3) indicates that the macro learning can reduce the computation load even including the time required for learning.

### Actual Block Construction Example

Figure 6 shows photographs of block construction sequence for one example problem; six blocks with different colors are placed on the table which are

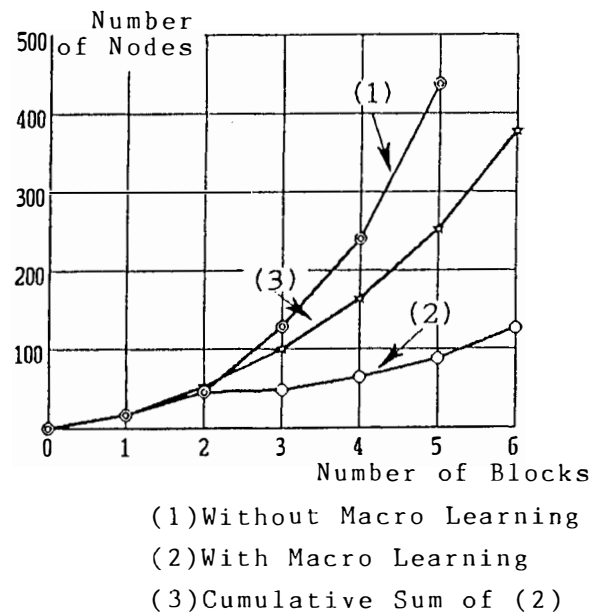


Fig. 5. Comparison of the number of nodes in the search tree.

to be connected into one pole with a prescribed color sequence. In order to make it clearer, the contours of the blocks are emphasized in the photographs. The first photo shows the very first movement; the left manipulator grasps the yellow raw blocks. The second one shows the situation when the visual feedback is performed to align the two blocks. Generally, several (three to five) iterations are needed for alignment. The last photo shows the final stage of the sequence; the sixth block is just connected to the five-length pole.

## CONCLUSIONS

A learning-based, hierarchical architecture for a robot control and management system is proposed. The key idea is that the executor has the ability to compensate for the gaps between the logic world and the real world by using sensor feedbacks and re-tunings of the operational parameters. With this aidings, the upper level can employ various useful techniques developed in AI logic fields such as macro planning or explanation based learning.

In our current system, the preconditions, add-list

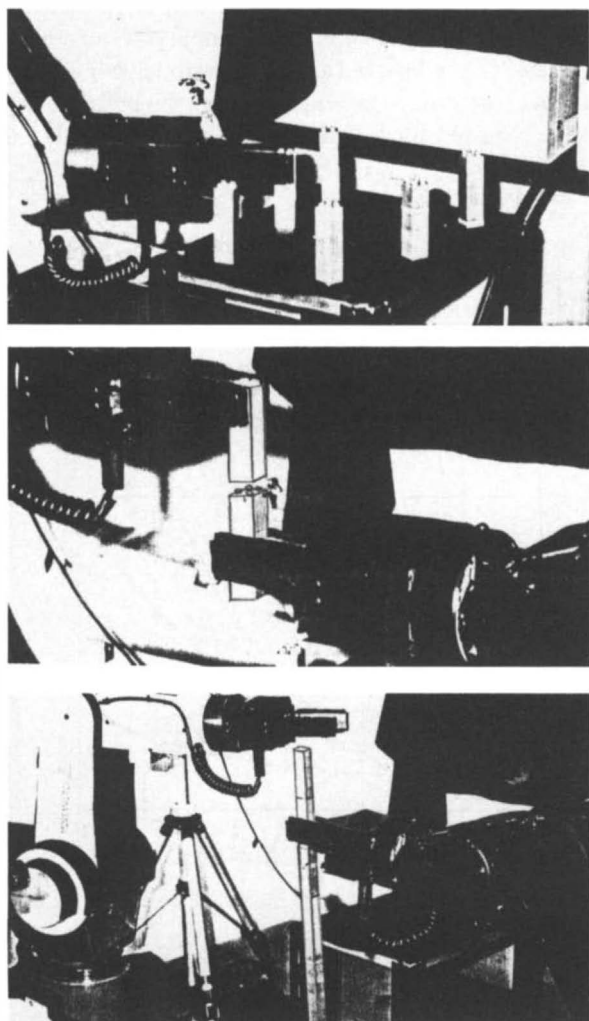


Fig.6. Block construction example.

and delete-list of the basic operators are coded by human beforehand and fixed during the actual operations. One way to further enhance the adaptability of the system is to add the ability to re-write these attributes from the sensor information if necessary((c) in Fig.1). For example, such a case may occur that a certain operator causes a collision of two blocks which cannot be predicted, and therefore the preconditions of the operator must be modified. The difficulty in achieving this lies in transforming the sensor information into the linguistic form which has some generality. We are now continuing research in this line.

## REFERENCES

- Brooks,R.A.(1990).Elephants don't play chess. *Robotics and Autonomous System*, 6, 3-15.
- Camarinha-Matos,L.M.(1987).Plan generation in robotics. *Robotics*, 3, 291-328.
- Iba,G.A.(1989).A heuristic approach to the discovery of macro-operators. *Machine Learning*, 3-4, 285-318.
- Liang,P., Chang,Y.L., and Hackwood,S. (1989). Adaptive self-calibration of vision-based robot systems. *IEEE Trans. Systems, Man, and Cybernetics*, SMC19-4, 811-824.
- Miller III,W.T.(1989).Real-time application of neural networks for sensor-based control of robots with vision. *IEEE Trans. Systems, Man, and Cybernetics*, SMC19-4, 825-831.
- Minton,S., Carbonell,J.G., Knoblock,C.A., Kuokka,D.R., Etzioni,O., and Gil,Y.(1990). Explanation-based learning: A problem solving perspective. In J.G.Carbonel (Ed.), *Machine Learning*. MIT/Elsevier. pp.63-118.
- Mitchell,T.M.,Keller,R., and Kedar-Cabelli,S. (1986). Explanation-based generalization: a unifying view. *Machine Learning*, 1-1, 47-80.
- Nilsson,N.J.(1980).*Principles of Artificial Intelligence*. Morgan Kaufmann, San Mateo.
- Rangwala,S.S.,and Dornfeld,D.A.(1989). Learning and optimization of machining operations using computing abilities of neural networks. *IEEE Trans. Systems, Man, and Cybernetics*, SMC19-2, 299-314.
- Tanabe,T.,and Yoshikawa,S.(1990). Autonomous space robot concept with learning capabilities - laboratory demonstration of peg-in-hole by bi-arm. *Preprints of the 41st Congress of IAF*, IAF-90-028.
- Tanaka,T.,and Mitchell,T.M.(1991). Embedding learning in a general frame-based architecture. In N.G.Bourbakis (Ed.), *Applications of Learning and Planning Methods*. World Scientific Publishing Co..pp.3-34.

## TASK-LEVEL PROGRAMMING WITH COLLISION AVOIDANCE FOR AUTONOMOUS SPACE ROBOTS

P. Adolfs and J. Matthiesen

TH Darmstadt, Control Systems Theory and Robotics Laboratory, Schlossgraben 1, D-6100 Darmstadt, Germany

**Abstract.** The reasons for integrating collision avoiding path planning into a task-level programmable multi-sensor robot system are put forward. The underlying system architecture and the specific approaches for environment modelling, task planning and path planning are discussed. Task planning is performed using a rule based expert system and a frame representation of relevant environment data. Path planning is based on a configuration-space approach with a fast new algorithm for obstacle transformation. Results gained from experimental laboratory work are presented and show some advantages and problems of the entire system.

**Keywords.** robots; task-level programming; collision avoidance.

### INTRODUCTION

In this paper two major problems of orbital robot system autonomy, facilitated task-level programming and real-time collision avoiding path planning are discussed and an integrated solution is put forward. Task-level specification of system behaviour is a key issue serving the reduction of data transfer bandwidth requirements. The underlying idea is that when manipulating within the space environment a ground or astronaut operator merely has to state the system's handling objectives in a more or less abstract fashion leaving the planning of details and the entire execution train to the control system. One necessary feature of a partly autonomous action planner is the ability to generate collision-free trajectories for the manipulator including the consideration of real-time varying environments. Extensive theoretical and experimental lab work has shown collision avoiding path planning in a cluttered environment to be a considerable problem of its own. The existence of a real-time path planner therefore greatly alleviates the burden the general robot control system's strategic and planning level has to carry. Alternative approaches suggest disjunct use of the workspace by separate manipulators (Cheng, 1991) and tackle the problem of single manipulator collision avoidance by explicit environment and task design. Comparable approaches (Lozano-Perez, 1989) have only limited real-time capabilities or have so far not been demonstrated in an integrated system featuring task-level programming.

### SYSTEM DESIGN

The functionality of the entire system has been distributed on a server and a client level named in analogy to the X-windows terminology (Nye 1989) for modularity reasons. Major benefit of this subdivision scheme is that improvements can be added on either side of the layer interface without interfering with the other side's integrity. The task-level programming features belong to the strategy and planning (S&P) "client" level and have been tested with an existing system for knowledge based assembly shortly sketched in the following section. Collision avoidance is considered a feature of general use and was consequently integrated into the action execution "server" level.

#### Task-level programming

The aim of using a higher language task specification of programming language is to facilitate the man-machine communication by adapting the machine's level of data processing in some sort to the common way humans think. Computers need formal languages to process and can only work on a restricted vocabulary. Humans on the contrary like to express their intentions individually and can handle multiple modes of expression and even syntactically wrong sentences. For the purpose of high level commanding a multi-sensor robot system we defined a formal language frame permit-

ting the usage of near to natural language constructs with a simple syntax and individual wording. We call the task-level commands "operations" whereas the more primitive actor motions or sensor functions are referred to as "(elementary) actions". An "operation" consists of three elements answering the following questions:

a) What is to be done? - the **operator**, b) Which tool shall be used? - the **grasped object** and c) Where is the focus of attention for this operation? - the **target object**. Thus, an operation reads e.g. "put, probe\_1, freezer". A series of operations is put into a list called the Assembly Plan or Operation Plan. This list is given to the S&P modules for processing. These modules have to bridge the gap between the action and the command level. The action level integrates a number of services provided for the S&P layer such as elementary robot and gripper motions configurable with parallel sensor (eg. force-) control and observation modes. When a motion finishes, a batch of current sensor data (e.g. wrist forces/torques, robot & gripper positions, grip force and object presence/slip information) are gathered and preprocessed. Together with action state information (e.g. that a motion was stopped due to contact detection) this batch is transferred back to the S&P level.

The coarse task-level operations are split up by the S&P modules into a series of subordinate actions according to the initial state and the intermediate sensor data readings. This subdivision answers to a) Which component (actor/sensor) will carry out the following action?, b) Which specific action type is necessary? and c) Which are the appropriate parameters for the action? Following the action execution its result must be classified based on the sensor readings and execution state information. If a deviation from the intended course of execution is detected, corrective measures have to be taken. This means, the selection of the next action is based on the intermediate state generated.

The problems involved include logical planning and classification. We used expert system technology to further structure the S&P level. One key aspect in conjunction with expert systems is the separation of knowledge from the knowledge processor or inference engine. The knowledge is subdivided twofold into factual vs. strategic on the one hand and static vs. dynamic or time-varying on the other. Static factual knowledge subsumes the naming, fixed characteristics and hierarchical structure of the environment objects. Dynamic facts comprise position information, system generated symbolic states and information about mechanical and logical object interconnections subject to change due to robot handling. Strategic knowledge is represented as production rules of the form

IF (the robot is in approach position of probe\_1)  
and (the gripper is closed)

THEN (open the gripper)

The set of conditions and actions implemented for system control, planning and classification adapts the application independent forward chaining rule processing mechanism to the problem domain.

## Implementation

The task-level robot programming system WISMO developed at TH Darmstadt (Simon, 1991) features frame-based hierarchical object modelling and a production rule based cyclic planning and execution control algorithm. Rules are used in every step of this cycle: manipulator/sensor action type selection, parameter calculation, system state classification after action execution and environment model updates. The system thus emulates a planning-acting-perception cycle. The WISMO architecture is shown in Fig. 1.

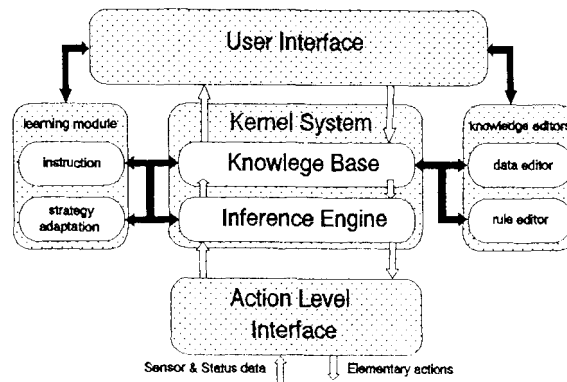


Fig. 1: WISMO architecture (Simon 1991)

A WISMO environment object is represented as a collection of positions relative to a reference coordinate frame in work space together with appropriate handling information. The positions are of predefined type (eg. denoting reference to world or object coordinates, defining tool corrections or part-of relations) in order to enable automatic algorithmic handling. The manipulation states of robot, gripper and objects are expressed using a predefined set of symbolic attribute-value pairs that the system classification component is able to deal with. Data reduction was achieved by superimposing a class hierarchy and an inheritance scheme for positions and attributes.

Knowledge transfer to WISMO is performed in three steps: First, a rough outline of the course of action is laid down as a list of operations, e.g. "mate, peg\_1, hole\_3". In a second step, the objects involved have to be modelled and their relevant position and attribute data have to be obtained. Thirdly, the operator interactively specifies which

concrete manipulator actions he wishes the system to perform given the operations. A recording module memorizes the initial symbolic system state and the actions/parameters commanded and transforms both into action and parameter planning rules which consequently enable the system to reperform the planning shown by the human instructor. Another positive aspect lies in the instruction mode's basic strategy to fasten the strategies told only to the classes of the objects involved. By this means basic substrategies like peg-in-hole mating or screwing must be instructed only once and are automatically remembered by the system given a similar problem. Using this simple machine learning approach the tedious process of manually filling the system's rule base is reduced.

### Collision avoidance

A very important feature of a task-level programmable robot system is autonomous collision-free path planning. Such a component frees the task planner from geometrical considerations concerning the robot's movement: Provided that such a component exists, it is sufficient to command target configurations with respect to the given task, for example the position of an object which should be grasped. The path-planner computes automatically a movement which guides the system to the target position.

However, in order to render the problem handable, the following classification of the overall manipulator movements is advantageous: For objects which have to be handled, we define a pre-position from which the grip configuration can be approached collision-free under all circumstances (Kegel, 1990). Then, the manipulator movements decompose into three parts: gross motions between pre-positions, fine motions between pre-positions and grip positions and, finally, the gripping act itself.

In order to ensure the flexibility of such a robot system especially in dynamically varying environments the path planner has to work online. Therefore on the one hand the internal model of the environment has to be updated whenever a change occurs and on the other hand the computation of the further movement must be very fast. To attain this goal an internal model of the environment is described in configuration-space (c-space), which is the space of all kinematically possible configurations of the robot. All configurations which cannot be reached without collision between robot and an environment obstacle are marked as forbidden. Main advantage of the c-space model is a fast collision-test for the robot which can be performed by a single read access to the c-space.

Due to this fact a very efficient path-planning is possible. Unfortunately, the transformation of objects given in work-space coordinates into c-space needs much computational expense. In order to reduce this time considerably some special algorithms were developed, which are described in more detail in the next section.

### Representation of environment

Mapping objects given in work-space coordinates into c-space is a very time-consuming task, especially when considering the complex shape of the robots links not only by simple envelope-bodies. Most approaches use recursive algorithms (Gouzenes, 1984), which start at the first link of the robot and determine the collision interval when moving the link. To avoid this on-line collision check we developed a new method. Therein the correspondence between work-space and c-space is stored in a look-up-table, which is called OCMEM-table. This concept is based on a discretization of work-space as well as c-space into elementary cells. Figure 2 shows all the positions  $V_a(e)$ , which can not be reached by the robots tool-center point (TCP) without a collision between the robot and such an elementary cell  $e$ . Thereby the orientation of the robots hand and a possible load is fixed and the TCP is defined as the intersectionpoint of the three hand-axes. Thus a TCP-position complemented by the kinematic state corresponds to a specific shape of the robot. To store the correspondence between  $e$  and  $V_a(e)$  in a look-up-table is the basic idea of OCMEM. Because the table entry does not depend on the actual environment but only on the size of the elementary cells, the table can be calculated with an off-line procedure.

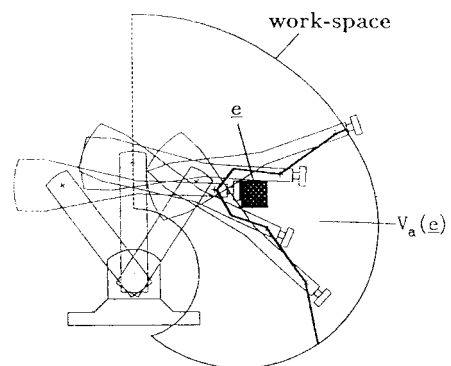


**Fig. 2:** The elementary work-space cell  $e$  causes the not collision-free reachable region  $V_a(e)$  (=OCMEM lookup-table) in c-space.

For mapping an object  $O$  in real-time to c-space in the first instance it has to be discretized into elementary cells like

$$O = \{ e_1, e_2, \dots, e_m \}$$

In the next step the OCMEM table is applied to every cell  $e_i$  and the corresponding forbidden regions in c-space are superposed. Thus the not collision-free reachable region  $C(O)$  with respect to the object  $O$  is calculated via

$$C(O) = V_a(e_1) \cup V_a(e_2) \cup \dots \cup V_a(e_n).$$

The principle of this transformation is illustrated in fig. 3. The object  $O$  is discretized into 3 elementary cells (a). The OCMEM table contains for each elementary cell  $e_i$  the non-reachable c-space regions  $V_a(e_i)$  (b), which are superposed to get the whole forbidden part of the c-space  $C(O)$ . Because

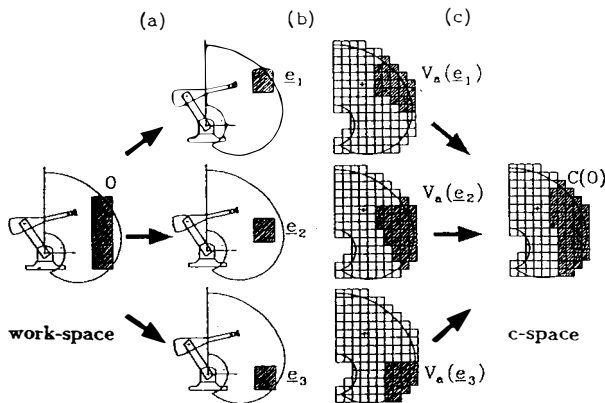


**Fig. 3:** Mapping the object  $O$  to c-space. (a) Discretization of object  $O$ . (b) Determination of the forbidden c-space regions for each elementary-cell. (c) Superposition of these regions.

of rotational symmetry with respect to the z-axis the TCP-position is described using cylindrical coordinates  $(r, \phi, z)$ . With a dimension of the elementary cell  $e$  of  $5\text{cm} \times 5\text{cm} \times 2^\circ$  the size of the OCMEM table would be in the range of 100 Megabytes, which today cannot be realized on standard hardware. To make this concept applicable to an industrial robot system some special techniques have to be used in order to reduce the size of the OCMEM table as well as to speed up the mapping. Therefore the symmetry of the workspace according to the z-axis is used, which results in a considerable reduction of size. For the example discussed above we achieve a reduction factor of 180. By additionally using a difference-coding technique which is described in (Adolphs, 1990) a very short mapping time is achieved.

By using this approach all objects, whose position is known before the robot movement starts, can be mapped to the c-space. This task can be performed in a few seconds. But moreover changes in the environment which occur while the robot is moving have to be considered for the internal model. For this purpose an extension of the OCMEM-concept described so far for moving obstacles was developed which cannot be discussed here. A description is given in (Adolphs, 1992).

## Path-planning

The shortly discussed method for modelling obstacles into the c-space is well suited to apply many of the well-known global path-planning methods. To achieve fast computation we developed a special path-planning algorithm which is based on the distance-field approach, but includes some heuristical motivated enhancement.

Low computational expense is reached by utilization of special limitations. These limitations are:

1. Restriction to two directions for searching the path
  - (a) random search within a  $r, z$ -slice of c-space
  - (b) search in  $\phi$ -direction
2. Priority on finding one possible path, not necessarily the optimal one.

This results in a very fast algorithm which is able to find semi-optimal paths. It is specially appropriate to meet the online requirement.

Fig. 4 illustrates the principles of this MINPOT algorithm in more detail. The figure shows a 2-dimensional  $z, \phi$ -slice with constant  $r$ -coordinate in the c-space described in cylindrical coordinates. This simplification is made for better illustration only, all the algorithms are implemented for three dimensions (including the  $r$ -coordinate). The hatched area denotes the non-reachable regions in c-space. Starting at the target cell (T) a distance field is generated within the target sector. The cells with the same  $\phi$ -coordinate as the target cell (target sector) get a distance value, which describes the distance to the target cell. Thus the neighbouring cells get the value 1, the neighbours of these cells the value 2 and so on. The generation of the distance field in that manner is related to the type (a) search discussed above.

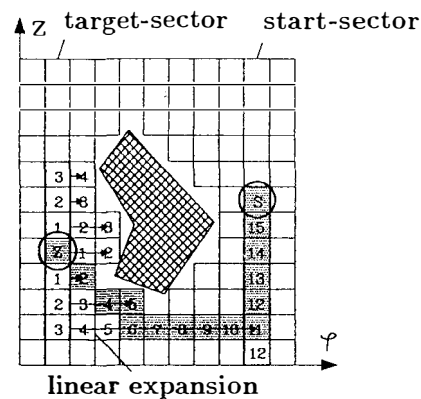


**Fig. 4:** Basic idea of MINPOT-algorithm.

Every cell that gets a distance value while expanding the field serves as a starting cell for a linear

expansion in  $\phi$ -direction. For the example of fig. 4 the linear expansion is successful in the third step of expansion, because the start-sector is reached first in this case. Now the generation of the distance field continues beginning with the cell in the start-sector which was reached first.

For more complex environments the algorithm has special strategies for the case that the startsector cannot be reached in the first step: Additional sectors for expansion of the distance field are located between start- und target-sector automatically.

The path can be found by following the negative gradient of the distance field starting with the start-cell. The path found is highlighted in fig. 4 by the grey area.

### Sensor-systems

Besides the fast algorithms for modelling and path-planning, sensor systems are needed which are able to survey the environment in real time. To limit the hardware expense of such systems we use a hierarchical classification of the objects: objects whose position in the environment is fixed are modelled in advance. Thus the sensor systems can concentrate on changes within the work-cell. As an example for demonstrating the real-time capabilities of the path-planning module an infrared-radar sensor was integrated, which surveys a table. When an additional obstacle is put on the table this sensor determines the current position of the object and sends the geometrical data of this obstacle to the path-planning processor. The robot avoids such obstacles automatically without interrupting its motion.

### Integration

One main aspect of the work presented in this paper is the integration of task-planner and path planner in a modular manner. Fig. 5 shows how this integration was realized. The task planner generates commands which are classified in the following way:

- (1) motion commands with collision avoidance for gross motions
- (2) motion commands without collision avoidance for fine motions
- (3) gripper and/or manipulation commands

Gross motions (1) which implicate long sweeps to a target configuration are given to the path planner first. It generates a sequence of intermediate points which describe the collision free path. Commands of type (2) are transferred directly to the RCM 3D commercial robot control unit. Com-

mands belonging to the third type are sent to and are autonomously executed by the gripper control unit.

By means of integrating sensors into the system the environment can be monitored online: information about the objects handled is generated by the gripper sensors and fed back to the task planner. On the other hand, sensors surveying the work space directly provide the path planner with data for updating its internal world model.

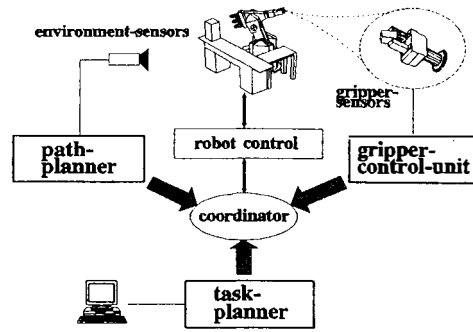


Fig. 5: System hardware structure

### Experiments

The entire system has been verified in ground-based experiments and continues to be used. In the course of system build-up a MANUTEC R3 robot connected to a Siemens RCM-3D control unit was augmented by the components discussed (cf. Fig.5). For the sake of modularity task planner, path planner, gripper-control unit and coordinating unit are implemented on separate hardware. This permits modifying the setup with respect to the specific task. For instance, the adaptation to different grippers (we used a parallel jaw gripper and a three-fingered gripper as well) or different sensors for surveying the environment is possible.

### Task specification

The modelling and instruction scheme proposed turned out to be effective in a series of lab setups including the handling of a satellite mock-up (Matthiesen 92) and several small assemblies. The time for implementing an assembly consisting of 60 operations, 12 objects and including strategies such as tool handling and screwing was about two weeks. Students unfamiliar with the robot-environment and the expert system approach were able to use the system after about a week of training. Experience showed, however, that by instruction in general too many simple rules are generated. This results from the underlying assumption that every planning step has its own specific reason which in fact turns out to be rarely true. Debugging large rule domains is time consuming and requires a

degree of expertise the target system user is not expected to own. Taking into account, in addition, that planning rules represent links of a decision graph we will further investigate into using a graph representation for planning.

Some difficulty also arose from the approach not to bother the instructor with the situation specific interpretation of sensor data. One way to cope with this requirement we went is to use standard attributes for classifying the situation such as the symbolic robot position and gripper state (open, closed, object gripped etc.). However, the evaluation of any action's success is tricky on such premises and further work has to be invested in this area.

Finally, the geometrical modelling should be supported by CAD techniques and in the same step more geometrical object information should be supplied in order to enable more complex sensor data interpretation and knowledge based updates of the collision avoiding path planner's object database.

#### Path-planner

The algorithms for modelling the environment and path-planning were implemented on a INTEL i860 processor running with 32 MHz. Using this processor the calculation of internal world model as well as path-planning is accelerated by a factor of 10-15 with respect to a former implementation on 80386 (16 MHz) hardware.

A reasonable compromise between low computation time and accuracy could be achieved by a size of elementary cells of 5cm x 5cm x 2°, which was evaluated with a lot of simulations. The mapping of an additional obstacle into the c-space model need 50-100 msec. depending on the size and the position of the object. A global path-planning with respect to whole model of environment can be performed in 15-100 msec.. Thereby the computation time highly depends on the length of the path which has to be computed. Fortunately the time for path-planning does not increase for more complex environments. It depends on the path-length and the size of elementary cells only.

#### CONCLUSION

An autonomous multi-sensor robot system was discussed which can be programmed using task-level instructions. In this context the capability to automatically generate collision-free robot trajectories complemented with suitable environment obstacle sensing and local dexterity by using flexible multi-sensor grippers plays an important role.

#### ACKNOWLEDGEMENT

This work was partly supported by DFG (collision avoidance) and partly performed in a project sponsored by DARA and headed by ISRA Systemtechnik GmbH. The authors are grateful for this support.

#### REFERENCES

- Adolphs, P., D. Nafziger (1990). A method for fast computation of collision-free robot movements in configuration-space. IEEE Int. Workshop on Intell. Robots and Systems, Tokyo.
- Adolphs, P., H. Tolle (1992). Collision-free real-time path-planning in time varying environment. IEEE Int. Conf. on Intell. Robots and Systems, Raleigh, USA.
- Gouzenes, L. (1984). Strategies for solving collision-free trajectories problems for mobile and manipulator robots. The Int. Journal of Robotics Research, Vol.3, No. 4.
- Cheng X., D. Kappey and J. Schloen (1991). Elements of an Advanced Robot Control System for Assembly Tasks. 5th int. Conf. on Advanced Robotics, Pisa.
- Kegel, G. (1990). Erhöhung der Autonomie von Robotersystemen durch multisensorische Informationen und Nutzung einer Wissensbasis. Dissertation, TH Darmstadt, Fachgebiet Regelsystemtheorie und Robotik.
- Lozano-Perez T., J.L. Jones, E. Mazer and P.A. O'Donnell (1989). Task-Level Planning of Pick-and-Place Robot Motions, IEEE Computer, March 89, pp 21-29.
- Nyc, A. (1990). X Protocol Reference Manual for X Version 11, O'Reilly & Associates, Inc., Sebastopol, CA.
- Simon W. (1991). Untersuchungen zu einer intelligenten und lernfähigen Robotersteuerung für die Montageautomatisierung. Dissertation, TH Darmstadt, Fachgebiet Regelsystemtheorie und Robotik, published in VDI-Series 20: "Rechnerunterstützte Verfahren", Nr. 47.
- Matthiesen J., H. Tolle, S. Wienand, E. Ersü (1992). Sensorinformationsverarbeitung und Planung in einem autonomen Steuerungssystem für Wartungs- und Reparaturaufgaben in der Raumfahrt. Fachtagung Automatisierung, Dresden.

## MODELLING AND CONTROL OF A HERA JOINT

R.J. Gorter\*, A. van Swieten\*\*, A. Veltman\* and P.P.J. van den Bosch\*

\*Control Laboratory, Department of Electrical Engineering, Delft University of Technology, P.O. Box 5031,  
2600 GA Delft, The Netherlands

\*\*Attitude Control Group of Fokker Space and Systems, P.O. Box 12222, 1100 AE Amsterdam-Zuidoost,  
The Netherlands

**Abstract.** HERA is a space robot with elastic joints and flexible limbs. This paper describes the modelling and control of the HERA joints. Based on analytical studies and measurements, a dynamic model for the joints is presented, which can be used, together with the HERA equations of motions, to simulate HERA operations. The torque characteristics of the Brushless DC motor are studied and based on measurements a Harmonic drive model, valid during forward and backward drive, is presented. This gear model includes the Harmonic drive flexibility, load-dependent friction and hysteresis.

A derived control design model has been used to investigate the influence of the joint flexibility and limb flexibility on HERA performance. The performance limitations of decentralized joint control under motor velocity and/or joint position feedback are studied as function of the lowest structural resonance frequency and the lowest anti-resonance frequency. It has been pointed out how the performance limitations and the selection of the controller gains can be based on these frequencies.

**Keywords.** Brushless DC, Harmonic drive, Simulation, Control design and Flexibility

### INTRODUCTION

The HERmes Robot Arm, HERA, will be used during missions of the European spaceplane HERMES. The primary purpose of HERA is to support the servicing missions of HERMES to the Columbus Man-Tended Free-Flyer. HERA's task will be exchange of Orbital Replaceable Units (ORU's), support of astronaut extra vehicular activity and inspection of outer surface of spacecrafts. The low mass and the requirement of relocatability, i.e. HERA must be able to step over from one base point on the Columbus Free-Flyer to another, are the key design goals for HERA [1]. HERA is a symmetrical manipulator and consists of two, long flexible limbs, connected by an elbow and at each limb end a wrist with an attached end-effector. The arm has seven identical joints of which three are placed in each wrist and one is placed in the elbow. Each joint contains a Brushless DC motor, a motor driver, a brake, a Harmonic drive gearbox, a combined motor velocity and commutation sensor and a joint shaft position sensor.

#### Modelling

In order to support the design and analysis with respect to control and verification of operations, accurate simulations of complete HERA tasks are necessary. This demands both detailed mathematical modelling of the multi-body flexible HERA structure and a high computational speed, to be able to simulate HERA operations of 20 minutes within reasonable computer time. A set of non-linear ordinary differential equations, with cross-coupling and nonlinear effects resulting from dynamic interaction among the links of the robot arm has been derived. [2] These equations are necessary, but not sufficient, to represent the dominant dynamics of HERA, since they do not fully include the important

interactions with the joint. In this paper a simulation model for the joint will be presented which include the dominant characteristics of the joint. The effects of the joint flexibility, friction, current and power limiters on HERA operations and control design are studied with the simulation model.

#### Control

Due to the amount and complexity of centralized decoupling control laws and the limitations of the on-board computing power of HERA, decentralized joint control will be used. The HERA system control level generates trajectories for each independent joint controller. Each joint controller must be robust enough to handle coupling effects and inertia variations. In this paper the consequence of the joint and limb flexibility on a single joint controller will be shown.

### MODELLING

#### Brushless DC motor

HERA is provided with a 13 pole-pair, two-phase Brushless DC motors in the joints. For HERA, the Brushless DC motor offers the following advantages; small size, small weight, no sparks and carbon dust from brushes, reliability and potentially high efficiency. A Brushless DC motor requires a specific motor driver, phase current controller and rotor sensing for commutation to compensate for the absence of brushes.

In a Brushless DC motor the flux linkage between the rotor permanent magnets and the stator currents is position dependent. Therefore the inverter drive signals are synchronized to the position sensor output signals so that

synchronisation between the stator phase currents and the rotor flux is ensured. When square-wave phase currents are applied, the developed motor torque is not constant, i.e. the motor torque will contain a ripple. Low levels of torque ripple are desirable in order to minimize speed fluctuations and to avoid excitation of the HERA limb resonance frequencies. In [3] it has been shown that, under the assumption that the phase current wave forms can be impressed flawless, the torque ripple can be minimized by selecting an optimum combination of flux linkage and the phase current waveforms. In the ideal case, when the compensating, and therefore sinusoidal shaped, phase feed currents are impressed flawless, the electromagnetic torque is constant and no torque ripple exists. Then a Brushless DC motor can be described by a linear relation between motor current  $\{I_m\}$  and motor torque  $\{T_m\}$  equal to a brush DC motor;  $T_m = K_m \cdot I_m$  with  $K_m$  the motor constant in [Nm/A].

### Motor model

A mathematical model of the motor, consisting of equations for the electrical and mechanical dynamics together with a model of the motor driver, have been derived. ([4]) Figure 1 shows, for maximum motor speed, the simulated current in one phase when the top-current controller must impress a sinusoidal shaped phase current, which reduces the torque ripple. When the phase current reaches the current setpoint the top-current controller switches off the phase voltage (off-state) till the next signal of a oscillator (at 20kHz) switches the phase voltage on (on-state). The back-emf (electro motive force) will oppose the increase of the phase current during the on-state while the back-emf will decrease the motor current during the off-state. The current ripple depends on the applied voltage, the electrical time constant of the motor and the motor velocity. Also the mean value of the motor current is less than the current setpoint because only the top-current reaches the current setpoint.

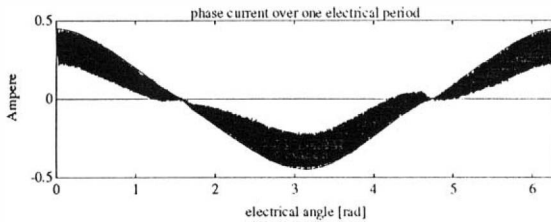


**Fig 1.** Phase current over one electrical period.

$$T_m = K_m \cdot (1 - A \cdot \dot{\theta}_m) \cdot \{1 + (B \cdot \dot{\theta}_m) \cdot \cos(4 \cdot 13 \cdot \theta_m)\} \cdot I_m \quad (1)$$

In practice accurate control of the phase currents, in particular at higher motor speed, is not possible. As a result torque ripple exist even with an optimum combination between the phase currents and flux linkages. The current deviation will result in a torque ripple with a lowest frequency component of four times the electrical frequency as can be seen from fig. 2. Because the mean current is less, also the mean torque will differ. The torque ripple and deviation can be simulated by eq.(1) when it is assumed that both effects are related linearly to the motor velocity  $\{\dot{\theta}_m\}$ . Because the constants do not depend linearly on the motor velocity the obtained values are worst case estimates and only valid in the velocity work region of the motor ( $0 \leq \dot{\theta}_m \leq 20 \text{ rad/s}$ ). Equation (1), which will be used in the simulation model and is a simplification of the motor model, describes the relevant characteristics of the motor and is

much more economical in the use of CPU time than the complete motor model. The constant  $A$ , indicates the deviation of the torque (30% at maximum motor velocity) and the constant  $B$  indicates the torque ripple amplitude. (16.5% top-top ripple at maximum motor speed).

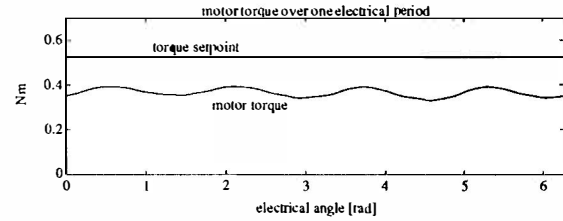


**Fig 2:** motor torque over one electrical period.

### Harmonic drive

The Brushless DC motor is connected in line with a Harmonic drive. A Harmonic drive is a compact, high ratio gear mechanism, whose utility for (space) robots derives from their compact design, high torque transmission and negligible backlash. However the Harmonic drive also introduces torsional flexibility into the joint which should be considered during the control design. A Harmonic drive consists of a rigid circular-spline, an elliptical wave-generator and a non-rigid flexspline.

A Harmonic drive can be described by a torsion-spring system between the input and output axis. Instead of backlash a Harmonic drive has a soft-windup characteristics. The torsional stiffness relation  $\{C(\theta_m/N_h - \theta_j)\}$  between the Harmonic drive deformation (the difference between the motor angle on output level  $\{\theta_m/N_h\}$  and the joint angle  $\{\theta_j\}$ ) and the Harmonic drive deformation torque  $\{T_d\}$  can be described by a piece-wise linear stiffness function, representing the hardening of the torsional stiffness for larger output torques of the Harmonic drive. When the output torque is increased from zero to a certain level and then decreased to zero again, deformation does not return to zero due to the hysteresis loss in the Harmonic drive.

### Gear model

The Harmonic drive can be described by the following set of equations. When the Harmonic drive is friction free, the torque exerted by the Harmonic drive on the joint axis  $\{T_j\}$  is equal to the Harmonic drive deformation torque  $\{T_d\}$  and the torque exerted on the motor axis  $\{T_{mot}\}$  equal to the deformation torque divided by the gear ratio.  $\{T_d/N_h\}$ .

$$\begin{aligned} J_m \cdot \ddot{\theta}_m &= T_m - T_{mot} \\ J_g \cdot \ddot{\theta}_j &= T_{out} - T_{load} \\ T_d &= C \cdot (\theta_m / N_h - \theta_j) \\ T_j &= T_d - T_{fric\ out} \\ T_{mot} &= T_d / N_h - T_{fric\ mot} \end{aligned} \quad (2)$$

where:  $T_m$  Motor torque [Nm]

$T_{load}$  Load torque on joint-output axis [Nm]

$T_d$  H. d. deformation torque [Nm]

$T_{mot}$  H. d. torque on motor axis [Nm]

$T_j$  H. d. torque on joint-output axis [Nm]

$T_{fric\ out}$  Friction on joint-output axis [Nm]

$T_{fric\ mot}$  Friction on motor axis [Nm]

$C$	H. drive stiffness function	[Nm/rad]
$\theta_m$	Motor angle	[rad]
$\theta_j$	Joint angle	[rad]
$J_j$	Motor axis inertia	[kgm <sup>2</sup> ]
$J_g$	Joint axis inertia	[kgm <sup>2</sup> ]
$N_h$	H. drive ratio = 121	

### Friction model

The friction model is based on Harmonic drive measurements done by Fokker Space and Systems. During the design tests an external spring has been wound-up and released with constant velocities. The test results are valid during forward drive, when the joint axis is driven by the motor axis and during backdrive, when the motor axis is driven by the joint-output axis. The gearbox tests showed that the friction torque is dominantly determined by the joint-output torque and depends linearly on the joint-output torque. Further is found that the efficiency of the Harmonic drive under load conditions is almost equal during forward drive and backward drive. The velocity-dependent friction is quite weak and fully submerged in a friction term that is completely wave generator-position related. The gearbox tests showed that the traditional, commonly postulated ([5]), linear dynamic friction model with a static and a dominant dynamic friction component appears not to be valid for HERA.

The friction model, derived during forward drive tests, has the following form:

$$T_{fric} = T_{per} \cdot \sin(2 \cdot \theta_j / N_h) + T_{stat} \cdot \text{sign}(\dot{\theta}_j) + \alpha \cdot T_j \quad (3)$$

where:  $\alpha$  load-friction coefficient .25  
 $T_{per}$  periodic position dependent 10 [Nm]  
 $T_{stat}$  static friction coefficient 15 [Nm]

The periodic position dependent friction  $T_{per} \cdot \sin(2 \cdot \theta_j / N_h)$  and the static friction  $T_{per} \cdot \text{sign}(\dot{\theta}_j)$  act on the motor shaft. The periodic position dependent friction is periodic with half a turn of the wave generator. This is equal to one tooth displacement of the flexspline relative to the circular spline. The periodic position dependent friction is thus a tooth friction. The load friction  $\alpha \cdot T_j$  acts on the joint axis. The efficiency of the gearbox during forward drive, when the static friction and the tooth friction are neglected, is equal to  $T_j / (N_h \cdot T_{mot}) = 1/(1+\alpha) = 0.8$ .

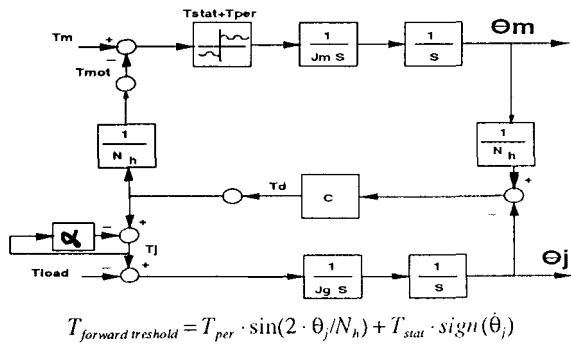


Fig 3. Harmonic drive friction model during forward drive

During back drive the velocity direction will change while the output torque is still in the same direction. The friction model presented in eq. (3) is no longer valid. For a proper energetic friction model it is at least necessary to change the sign of the load-friction term. When it is assumed that during forward and backward drive the load-friction depends linearly on the joint side, then during back drive the load-friction should be equal to  $-\alpha \cdot T_j$ . The Harmonic drive efficiency is then equal to  $(N_h \cdot T_{mot})/T_j = (1-\alpha)$ . Because it is found that the efficiency of the gearbox is equal for forward and backward drive it can be concluded that with a joint-side dependent friction the friction coefficient  $\alpha$  must change between forward and backward drive.

However a much better interpretation is obtained when it is assumed that the load-friction depends linearly on the driven side. During backdrive the motor axis is driven by the joint axis and with a driven side dependent friction the friction will be equal to  $\alpha \cdot T_{mot}$ . Then the efficiency of the gearbox during backdrive is now  $(N_h \cdot T_{mot})/T_j = 1/(1+\alpha)$  and is equal to the efficiency during forward drive. Not only the load-friction coefficient  $\alpha$  is now constant, but also the hysteresis in the gearbox can be explained with the aid of the driven side dependent load-friction.

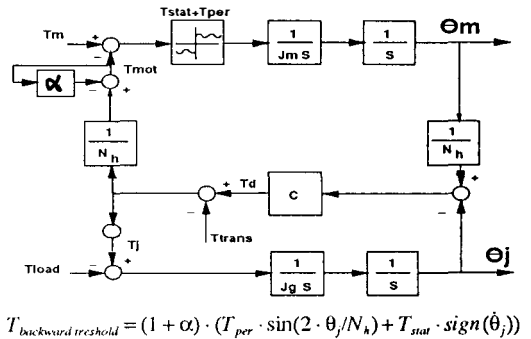
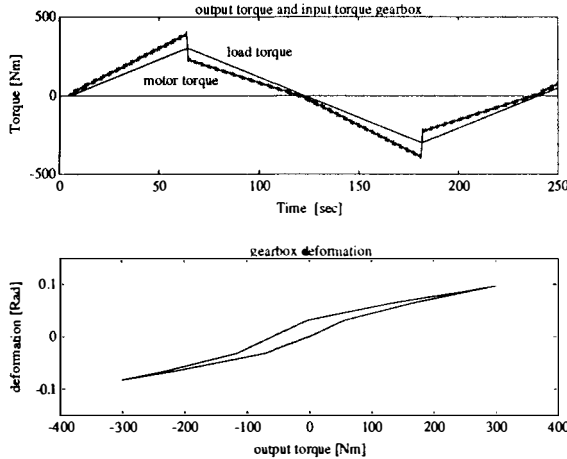


Fig 4. Harmonic drive friction model during backward drive

Figure 3 and 4 show block-diagrams of the Harmonic drive with the driven-side dependent friction during forward and backward drive. Although the stiffness function  $\{C(\theta_m/N_h - \theta_j)\}$  is kept constant, is the gearbox seen at the joint side stiffer during backward drive than during forward drive. Figure 3 and 4 also show that the threshold torque (the torque which must be exerted on the motor or joint axis before the motor axis will turn) differs for forward drive and backward drive, which is in agreement with the test results.

The test results show that during the transient between forward and backward drive the output torque and the deformation are constant and that the friction changes step-wise. In the model described so far, by the direction change of the load-friction the output axis will be accelerated. Therefore in the presented model a transient torque has to be introduced which represents the internal deformation in the gearbox, and keeps the output torque and deformation constant during a change in drive direction. This term,  $T_{trans}$ , which only changes when the joint axis velocity changes direction, can be calculated based on the observation that the deformation, stiffness and output torque are constant during such transients. From forward to backward drive  $\alpha \cdot T_j$  must be added to  $T_{trans}$  and from backward to forward



**Fig 5.** Harmonic drive during forward and backward drive when an external spring is wind-up and released

$\alpha \cdot T_j$  must be subtracted of  $T_{\text{trans}}$ . With the presented model the hysteresis is automatically introduced into the Harmonic drive, as can be seen from fig 5.

## CONTROL

A design model of a one degree of freedom flexible planar manipulator with payload, representative for a fully stretched HERA, has been used to study the joint performance limitations as function of the lowest eigen-frequencies of this manipulator. The behaviour of the dominant closed-loop eigen-values, which are related to the eigen-frequencies of the joint and limb, has been based on the root-locus method. The design has been done in two steps, first the limb is considered as ideal rigid bodies and only the influence of the internal gearbox flexibility on the joint control has been considered. Secondly, the limb are considered to be flexible and the influence of the flexible modes of the limb on the joint control has been investigated.

The decentralized joint controller has to perform the tracking and disturbance rejection tasks of the joint control level simultaneously. The most important HERA joint performance requirements are the desired velocity settling time (1 second) and the demand that the motor-gear vibrations shall be damped with a damping ratio of at least 1. According to these requirements the dominant closed loop poles must be on the negative real axis and the real part of the closed loop must be smaller than -4. The desired closed-loop bandwidth is thus 4 rad/s. Since in the HERA approach no decoupling strategy is available the motion of each joint affects each other joint. For the necessary disturbance rejection it is desired to keep the controller gains as high as possible. Two general types of disturbances will be considered during the design: an internal torque disturbance acting on the motor axis and an external disturbance acting of the joint axis. The main disturbance rejection requirement is that the ripple on the output torque due to internal disturbances shall not exceed 2% of the output torque.

## Design model

In the rigid limb linear design model the joint is modelled by a torsion spring between the motor and a gear-load, representing the mass of the limb and payload. Due to the fast current control loop the transfer function between motor torque and current command is essentially a pure gain, the motor is therefore modelled as a linear torque actuator. This

model representation is shown in fig 6. During the design it is assumed that the motor inertia  $J_m$  and spring stiffness  $C$  are constant and that the gear-load inertia  $J_g$  is variable and can be any inertia in the enormous range for which the joint is designed. (Min. 0.17 Kgm<sup>2</sup>, max. 3.6 10<sup>6</sup> Kgm<sup>2</sup>)

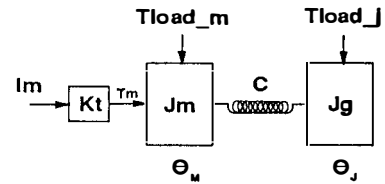


**Fig 6.: Rigid limb design model representation**

The rigid limb model is described by eq.4. where all values are equivalent output values. To obtain the equivalent output values the motor torque constant must be multiplied with the gearbox ratio and the motor inertia must be multiplied with the square of the gearbox ratio. Note that only the motor current  $I_m$  is a steersignal,  $T_{\text{load}_j}$  and  $T_{\text{load}_m}$  are the disturbances acting on the joint axis and motor axis, respectively. With the two sensors in the joint the motor velocity  $\dot{\theta}_m$  and the joint position  $\theta_j$  can be measured.

$$\begin{aligned} J_m \cdot \ddot{\theta}_m + C \cdot \dot{\theta}_m - C \cdot \dot{\theta}_j &= K_t \cdot I_m - T_{\text{load}_m} \\ J_g \cdot \ddot{\theta}_j - C \cdot \dot{\theta}_m + C \cdot \dot{\theta}_j &= -T_{\text{load}_j} \end{aligned} \quad (4)$$

where:	$K_t$	Motor constant	465 [Nm/A]
	$J_m$	Motor inertia	176 [Kgm <sup>2</sup> ]
	$J_g$	Gear-load inertia	[Kgm <sup>2</sup> ]
	$C$	Gearbox stiffness	2*10 <sup>5</sup> [Nm/rad]
	$I_m$	Motor current	[A]
	$T_{\text{load}_j}$	Load on joint axis	[Nm]
	$T_{\text{load}_m}$	Load on motor axis	[Nm]

## Eigen-frequencies.

For the control design it is useful to recognize the three different eigen-frequencies in the design model.

- The first eigen-frequency is the joint eigen-frequency  $\omega_j$  which is the resonance-frequency of the mass-spring system shown in fig 6.
- When the gear-load inertia  $J_g$  in fig 6. is fixed the motor inertia  $J_m$  will oscillate with the motor eigen-frequency  $\omega_m = \sqrt{C/J_m}$ .
- When the motor inertia is fixed the gear-load inertia will oscillate with a gear eigen-frequency  $\omega_g = \sqrt{C/J_g}$ .

The eigen-frequency of the joint is:  $\omega_j = \sqrt{\omega_m^2 + \omega_g^2}$ . Figure 7 shows the three eigen-frequencies over the complete allowed inertia range for the joint.

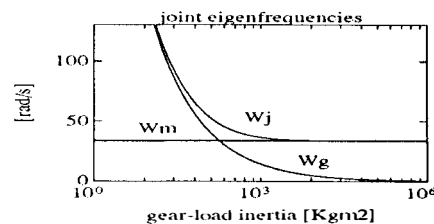


**Fig 7.: Joint eigen-frequencies in rad/s**

## Resonance behaviour.

Figure 8 shows the open-loop Bode magnitude diagrams for a joint connected to a rigid limb and to a flexible limb. This paragraph focuses on the rigid limb case. The strong antiresonance ( $\omega_g$ )/resonance frequency ( $\omega_j$ ) phenomenon [5] exhibited in fig 8. is typical for the motor-Harmonic drive combination. When the motor current is applied with a frequency equal to  $\omega_g$ , the motor will not rotate and behaves like a node. The gear-load inertia is not affected by the anti-resonance frequency and will rotate undisturbed. In the neighborhood of  $\omega_g$  it is not possible to control the Harmonic drive deformation with the motor.

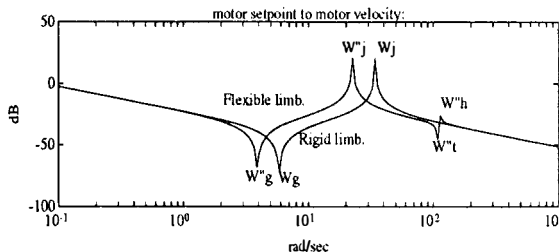


Fig 8. Open loop Bode diagrams

## Design

A motor-velocity control loop will be considered first, because joint-position feedback only, with low-order controllers, will not asymptotically stabilize the closed-loop. The transfer-functions from the motor current to motor velocity is described by eq. (5).

$$\frac{\theta_j}{I_m} = \frac{K_m \cdot (s^2 + \omega_g^2)}{J_m \cdot s \cdot (s^2 + \omega_j^2)} \quad (5)$$

### P-controller.

Figure 9. shows the root locus for the open loop transfer-function from motor current to motor velocity for three different ratios  $\omega_g / \omega_j$ . For the three cases when the proportional gain goes to infinity the bandwidth of the closed-loop goes to  $\omega_g$  and the damping of the motor-gearbox vibration will be minimal.

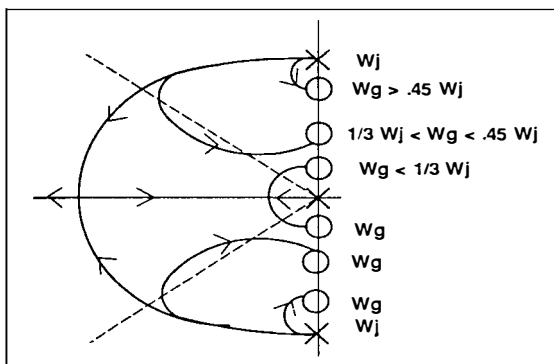


Fig 9.: Illustration of performance limitations of Proportional feedback for different ratio  $\omega_g / \omega_j$

For small proportional gain the closed-loop pole related to the rigid motion is on the negative real axis. When  $\omega_g / \omega_j < 1/3$ , i.e. for large payloads, and the proportional gain is increased one of the eigen-values related to the joint vibration meets the eigen-value related to the rigid motion and both break away from the real axis converging to  $\omega_g$  on

the imaginary axis. This break away point is located at  $1.1 \cdot \omega_g$  from the origin and is equal to the maximum bandwidth which can be obtained with a P-controller.

Figure 9 shows that the poles related to joint vibrations become critically damped for certain proportional gains. For  $\omega_g / \omega_j > 1/3$ , the eigen-values related to the joint vibrations are no longer able to reach the real axis and it is not possible to provide a critically-damped motor-gearbox vibration independent of the proportional gain. A further distinction can be made between well damped motor-gear vibration (damping ratio  $> 0.6$ ) and badly damped motor-gear vibration. In [6] it is shown that for badly damped joint vibrations ( $\omega_g / \omega_j > 0.45$ ) the best possible damping of the vibration modes is obtained when the rigid mode is located at approximately  $2/3 \cdot \omega_g$ . However the eigen-values in the badly damped region are very sensitive to variations in feedback gain and in practice it will be hard to obtain the maximum damping.

### PI-controller.

An advantage of a PI-controller compared with a P-controller is that the integrating action will drive the steady state velocity error due to static load-disturbances to zero. The representation for the used PI-controller is given by eq. (6). Two parameters have to be selected, the proportional gain  $P$  and the integration time constant  $\tau_i$ .

$$\frac{I_m}{\theta_{se} - \theta_m} = P \cdot \left( 1 + \frac{1}{\tau_i \cdot s} \right) = P \cdot \left( \frac{s + 1/\tau_i}{s} \right) \quad (6)$$

Figure 10 shows that when the zero in  $-1/\tau_i$  is too far into the left half plane, or equivalent when the integration time of controller is too fast, the poles in the origin will directly move to the zeros related to  $\omega_g$ . Then it is not possible to obtain a critically damped motor velocity response. When the integration time is slower the zero moves to the origin. Figure 10 shows that by selecting a proper proportional gain and integration time constant the rigid mode and motor-gear vibrations become critically damped. Analyses show that therefore the ratio  $1/\tau_i$  to  $\omega_g$  must be smaller than 0.2. For an increasing proportional gain  $P$  the poles out of the origin will move to zero of the PI-controller and the root-loci will meet the negative real axis at approximately  $0.57 \cdot \omega_g$ , being the maximum closed loop bandwidth with a PI-controller. Similar to the P-controller, when the ratio  $\omega_g / \omega_j$  is too large, the poles related to  $\omega_j$  move directly to the zero related to  $\omega_g$ . It is calculated that for a PI-controller this ratio border is 0.44 and the integration action thus improves the damping capability of the controller.

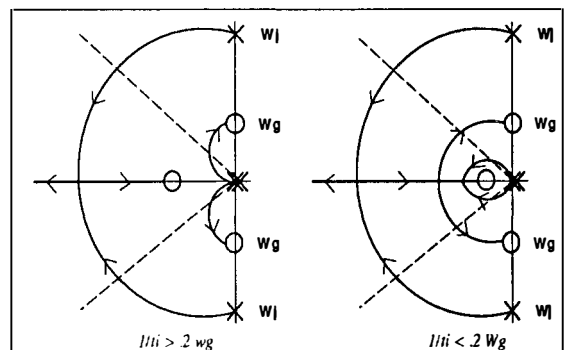


Fig 10.: Illustration of the selection rules for a PI-regulator parameters

## Disturbance rejection.

Although with a PI-controller the steady state velocity error due to static disturbances to zero will be zero, still a position error due to both type of disturbances will be introduced. The steady state gains from stepwise disturbances to joint position is  $\tau_s/P \cdot K_p$ . The flexibility, combined with the desired servo performance, limit the increase of the regulator gains and thus the decrease of the steady state error.

The controller is not capable to suppress frequency dependent disturbances in the neighbourhood of the  $\omega_g$ . For this frequency surrounding the controller can not control the spring deformation and thus the output torque due to the anti-resonance behaviour of the joint. In the neighbourhood of  $\omega_g$  the disturbance on the motor axis are not suppressed i.e. they introduce a ripple on the output torque. Therefore it is important to reduce the motor torque ripple and tooth ripple of the gearbox as much as possible.

## Velocity control of flexible limb.

Beside that the joint controller must perform the joint control task, i.e. control the motion of the rigid-body of the limb, it must also suppress, as good as possible the vibrations in the limb. The Bode diagram shown in fig 8 indicates the difference between the rigid limb and a limb with one bending mode. Compared with a rigid limb the joint vibration frequencies are decreased and higher eigen-frequencies, related to the limb vibration are added. When the root locus is drawn below by fig 8, it can easily be shown that the behaviour of the dominant eigen-values can still be described by the lowest resonance and anti-resonance frequencies and that the influence of the higher mode on this behaviour is small. The same design rules and bandwidth limitation rules are valid, only the magnitude of  $\omega_g$  and  $\omega_i$  are decreased compared with the rigid limb case and they can no longer directly be related to the pay-load.

Figure 8 shows that resonance ( $\omega_{r,h}$ ) and anti-resonance ( $\omega_{a,h}$ ) frequencies related to the bending mode of the limb are close to each other. This indicates that under feedback the eigen-values related to the flexible mode of the limb quickly converge to the anti-resonance frequencies of the limb. The maximum possible damping of the limb mode is small. However the vibration frequency of the limb is high compared with maximum possible closed loop bandwidth and therefore the effect of the flexible mode on the response will be small after the response time.

## Cascade control.

So far only velocity control has been considered. When exact positioning of the joint is necessary, a cascade control structure can be used. Investigations show that due to the flexibility a cascade control structure is not necessary stable, the controller gains have to be selected properly. The controlled joint will have an undesirable small stability margin with proportional feedback of the joint position only. To increase the stability margin the outer-loop must contain a controller with a well selected differentiating factor (phase-lead network). The controller gains selection rules and the maximum possible bandwidth as function of the lowest eigen-frequencies can be found similar as in the previous paragraph with the aid of root locus plots of the closed inner-loop.

## State feedback.

State-feedback controllers, based on a fourth-order reconstruct model similar to eq.(4) has been investigated and good performance is possible with a rigid limb. When one flexible mode is taken into account, the system becomes unstable due the limb vibration mode. Fourth order models are found to be inaccurately for state feedback because of the truncation error and observation spillover due to the neglected limb modes ([7]). Therefore state feedback is no good control strategy for the HERA joint.

## CONCLUSIONS

For the HERA a joint simulation model is derived. The influence of the motor driver on the torque characteristics of a Brushless DC motor has been investigated. In practice adequate control of the phase currents at higher motor speed is not possible and the resulting deviation results in a torque ripple. A relation, which includes the velocity dependency of the motor torque characteristics has been presented and will be used to simulate the motor behaviour. Based on measurements a Harmonic drive model, with a driven side dependent friction has been introduced. To simulate the transient between forward and backward drive, a transient torque was introduced, representing the internal deformation of the gearbox, yielding an accurate model including hysteresis.

It has been shown that the performance limitations and selection of joint output feedback controllers gains can be described by the lowest structural resonance frequency and the lowest anti-resonance frequency, i.e. the eigen-frequency which will be found when the motor is locked. This anti-resonance frequency defines the maximum possible controller bandwidth.

More advanced controllers than joint output feedback controllers are sensitive for instability due to spillover, related to the limbs flexibility. Their practical use for HERA is small.

## REFERENCES

- [1] Schoonejans, P. and G. Andre. (1990). The Hermes Robot Arm: Advances in Concepts and Technologies. *Proceedings of 41th IAF Congress*, 184-195.
- [2] Ellenbroek, M. and M. Lent. (1990). Efficient simulation of a flexible space manipulator arm. *Proceedings of the first national congress*, Netherlands, 167-191.
- [3] Bolton, H.R. and R.A. Ashen. (1984). Influence of motor design and feed-current waveform on torque ripple in Brushless DC drives. *IEE Proceedings*, Vol131, no3, 82-90.
- [4] Gorter, R.J.A., "Modelling and Control of a HERA joint" Master thesis 1992, Delft University of Technology, Control Laboratory, dep. of Electrical Engineering, doc. A92.011 (593)
- [5] Sweet L.M. and M.C. Good. (1985). Redefinition of the Robot Motion-Control Problem. *IEEE Control Systems Magazine* august, 18-25.
- [6] Cetinkunt, S. and W. Book (1990). Performance limitations of joint variable-feedback controllers due to manipulator structural flexibility. *IEEE Transaction on robotics and automation*, vol.6,no.2, 219-231
- [7] Kamoh, H., S. Tzafestas, H. Lee and H.G. Kalat. (1986). Modelling and control of flexible robots arms. *Proceedings of 25th conference on decision and control*, Athens, 1866-1870.

## DEVELOPMENT OF AN AUTONOMOUS ONBOARD CONTROL SYSTEM FOR RENDEZVOUS AND DOCKING

J.M. Pairo\*, W. Fehse\*\* and A. Getzschmann\*\*\*

\*MATRA Marconi Space, Toulouse, France

\*\*ESA/ESTEC Noordwijk, The Netherlands

\*\*\*MBB/ERNO Bremen, Germany

**Abstract :** The Rendezvous and Docking System Pre-Development Programme, started in 1989 and concluded in 1992, is an early proof-of-concept of an autonomous RVD onboard system for the various potential European scenarios. On the basis of Hermes and Columbus requirements and baselines, a generic concept of an autonomous onboard GNC system for RVD including interaction of human operators has been defined. The technological items (RV sensors, docking mechanism, GNC processor mockups, and onboard software) have been tested, using existing facilities (EPOS, DDTF). The developed concepts are described, the test results are discussed, and recommendations for future development are given.

### 1 - INTRODUCTION

On the basis of Hermes and Columbus requirements and baselines, a generic concept of an autonomous onboard Guidance, Navigation and Control (GNC) system for Rendezvous and Docking (RVD) including interaction of human operators has been defined. Aboard the chaser vehicle the rendezvous and docking tasks are performed by two subsystems: the RV-Control System, performing the GNC and the Mission and Vehicle Management (MVM) Functions, and the Docking/Berthing System (DBS).

The GNC functions include:

- the generation of the required state values, i.e. position, attitude, and related velocities, to achieve a desired trajectory (guidance),
- the determination of the vehicles actual state (navigation),
- the calculation and generation of forces and torques to achieve the required state (control),

The MVM functions include:

- the sequencing of operations, i.e. trajectory, attitude, station keeping manoeuvres to implement a particular

approach or departure strategy (mission management),

- the assignment of hardware and software items to a particular operation (vehicle management),
- the detection of transgression of safety boundaries of state, the failure of H/W and S/W items and their replacement and the initiation of contingency operation sequences where necessary (FDIR).

The docking/berthing functions include:

- the reception and capture,
- the attenuation,
- the retraction and mechanical alignment and
- the structural latching.

The execution of all these functions is considered as nominally performed by an autonomous onboard system. However, human operators on either the chaser or target vehicles or on ground must have the possibility to supervise and interact with the system in nominal and contingency cases. The particular aspects of man and automatic system interfaces and interactions are collected under the term Man-in-the-Loop (MIL). In particular the interaction of human operators with the

automatic GNC and MVM system are of importance for the overall RVD system concept.

The RVD System Pre-Development Programme addresses all GNC and MVM functions, the man-in-the-loop aspects concerning those functions and the so called front end functions of the docking mechanism. The latter ones are the dynamic functions of the mechanism, which provide the transition from relative alignment and rate conditions due to the GNC performance prior to contact up to the conditions required for engaging the structural connections. A strong interrelation exists between GNC and docking mechanism performance. The required reception range and attenuation capabilities of the docking mechanism are determined by the relative position accuracy and by the linear and angular rates left at switch off of the GNC system, plus drift rates built up due to disturbances. A balance must be found between GNC and docking mechanism needs.

## 2 -SCOPE OF ACTIVITIES IN THE RVD-PDP

The RVD Pre-Development Programme has been based on the availability of a large number of technological items, which were developed in previous technology contracts by ESA and by national agencies in Europe.

After collection of the relevant requirements and concepts already available in the Hermes and Columbus projects and definition of the concepts for GNC, MVM, MIL and DBS to be pursued in the RVD-PDP, five major development lines had to be followed:

- development of a RV-control S/W (non-real time) and of a simulator modelling its environment including the onboard data management architecture,
- real time closed loop verification with the software of one control mode implemented in a breadboard of the onboard processor ,
- RV-sensor testing in realistic motion and illumination environment on the 'real world testbed' EPOS,
- investigation of crew interaction with the automatic system on a graphic interaction simulator,

- testing of a scaled down model of a docking mechanism on the docking dynamics testbed DDTF.

## 3 -THE REFERENCE RVD SCENARIOS

The basic RV control system to be developed and tested under the RVD-PDP was required to be suitable to form the basis of RVD onboard systems for the cases of :

- RVD of Hermes with the Columbus Free Flyer
- Rendezvous to berthing of the Free Flyer with the Space Station Freedom
- RVD of Hermes with Freedom

In order to provide sufficient flexibility for potential changes or future needs of the Hermes and Columbus projects, it was decided to investigate also the approach to sun-pointing target and the approach along R-bar in addition to the standard V-bar approach pursued by the two projects at the time of implementation of the RVD-PDP.

Multiple approach strategies, modes, and trajectories have been thus developed to accommodate the different approach and docking/berthing scenarios. For example, there is one strategy for rendezvous and docking of Hermes to the Columbus Free Flyer in an Earth-pointing attitude, another strategy when Columbus is in a Sun-pointing attitude, another strategy for rendez-vous and proximity operations of Columbus with the Space Station Freedom for berthing, etc, as shown in fig 3-a.

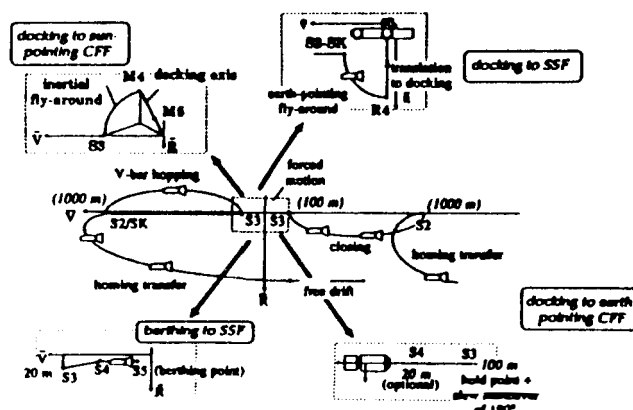


Fig 3-a Various European Rendezvous Scenarios

#### 4 - OVERALL RENDEZVOUS STRATEGY

The Chaser establishes a TM link with the target, acquires the GPS Information needed to enable relative GPS positioning, and then first performs a homing phase using relative GPS positioning to control to the S2 point which is co-planar and several hundred meters in trail with the target. Then the chaser closes to the S3 point (at about 150 m), using either V-bar hopping or forced translation. The Chaser position is controlled with respect to the EP local orbital frame. At S3, an optical-based guidance system, using a CCD camera to register the relative positions of the retroreflectors illuminated by the Chaser flashing laser, provides navigation to allow closure on the docking/berthing boresight to 20m and then into docking when desired. Inside 20m the laser/CCD camera proximity sensor can additionally provide attitude angles, and for docking scenarios, the chaser controls the relative position, attitude, and velocity of the two docking ports in the target docking port reference frame, controlling closure to effect a soft (order of the cm/sec) docking. For an Earth-pointed target, the S3 to docking approach is performed along the V-Bar. For an inertially pointed target, a circular fly-around would be performed, using relative GPS navigation, until final alignment for acquisition of the target spacecraft docking axis by the laser proximity sensor.

The position-velocity trajectory followed by the Chaser during closure has been specifically designed to ensure, as far as feasible, a collision-free approach. As long as the relative velocity is higher than the final docking velocity, the chaser will drift-to-miss the target in case it has to shut itself off. At a few metres, the Chaser relative velocity has been reduced to about around 2 cm/sec, and this is maintained to contact, ensuring a soft docking (back-up thrusters can arrest all forward motion in the event of a system fault or significant docking axis misalignment). The overall duration of the final docking phase from 100m is about 40 minutes.

More details can be found in [1].

#### 5 - THE ONBOARD RVD CONTROL SYSTEM

The RV Control System, allowing the control of the chaser spacecraft during RV and proximity with a target spacecraft, including nominal approach, retreat and contingency

operations, is composed of the following elements:

- sensors, actuators
- a RV control on-board software (dedicated to the management of the RVD system, and to the elaboration of torques and forces for spacecraft attitude and position control)
- a Guidance, Navigation and Control (GNC) computer (on which a part of the RV control on-board software is due to run)
- a real-time bus (allowing real-time exchanges between the sensors/actuators and the GNC computer)
- a system computer

The overall hardware architecture and redundancy concept is shown in fig 5-a. A failure detection, isolation and recovery (FDIR) strategy has been implemented for the completion of the RV mission according to the assumed fail-operational/fail-safe redundancy concept. Three levels of FDIR have been considered: built-in test equipment, low level FDIR applying to equipment information, and high level FDIR responsible for the monitoring of spacecraft parameters. More details can be found in [1].

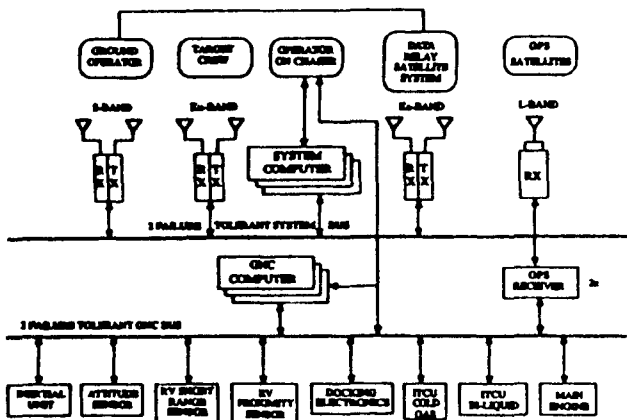


Fig 5-a RV Control System Architecture

#### 6 - THE RV CONTROL SOFTWARE

On the software side, figure 6-a illustrates the RVD system software architecture, showing the grouping of rendezvous functions into System Functions and GNC Functions. This

partitioning was selected to accommodate the stringent safety and reliability requirements. The System Functions include the following :

- Vehicle Configuration Management : Checks the availability of required equipment prior to any mode change
- Phase and Mode Management : Schedules and manages the various rendezvous modes as the rendezvous progresses through the different phases to the final docking and departure.
- TM/TC Interface (I/F) : Manages vehicle-to-vehicle and vehicle-to-ground communications
- High-level Failure Detection, Isolation and Reconfiguration (FDIR) : checks state vector estimations from the GNC against pre-defined nominal trajectories, and inhibits the thrusting when outside of approach corridor.

The GNC functions include the following elements:

- Execution of GNC algorithms;
- Algorithm Management : Schedules the GNC algorithms depending upon the phase mode;
- Real-time Bus I/F : sensor data acquisition and actuator commanding;
- Low-level FDIR : hardware failure detection routines and built-in tests.

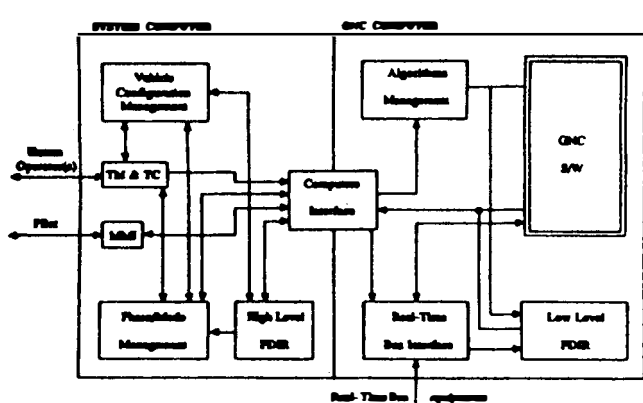


Fig 6-a : RV Control s/w architecture

## 7 - DEVELOPMENTS AND TESTS

### 7.1 - Closed Loop Testing of the RV-Control System with ROSS

All of the relative navigation and control algorithms for automatic rendezvous, closure,

proximity operations, and capture have been defined under ESA and CNES contracts.

A simulation tool for the validation of the GNC concept setup for rendezvous and proximity operations has been designed and developed. This tool, the Rendezvous Onboard System Simulator (ROSS), includes models for the rendezvous control (RVC) software (both GNC and MVM tasks), and additionally includes the simulation of a complete environment, called the rendezvous verification software (RVV), including:

- a set of models for the simulation of the equipments aboard the chaser spacecraft (sensors, actuators) and aboard the target spacecraft;
- models of the spacecraft orbital motion and attitude dynamics, including the main external perturbations (absolute and differential air drag, plume impingement by thrusters,...);
- models of the interfaces between the on-board rendezvous control system and the operators candidate to the mission control, i.e. the Hermes pilot, the target operator (FSS only) and ground operators;
- the simulation control system, including TM/TC handling and a set of facilities for data control and archiving.

The ROSS, thus including both the RVC and the RVV, has been designed so as to be executed in real-time if needed. Additionally, the structure of the tool is such that the implementation of the software over separate computers is possible:

- one GNC computer, including all GNC and a part of MVM tasks;
- one System computer, including the remaining MVM tasks;
- one environment computer, including the complete RVV

The complete MVM software is table driven (parameterised) to allow easy adaptations to future RVD mission changes or modifications. In order to be independent from the target machine, a Virtual Operating System (VOS) has been developed, acting as a small software layer between the application software and the target machine operating system.

Figure 7.1-a illustrates the architecture of ROSS.

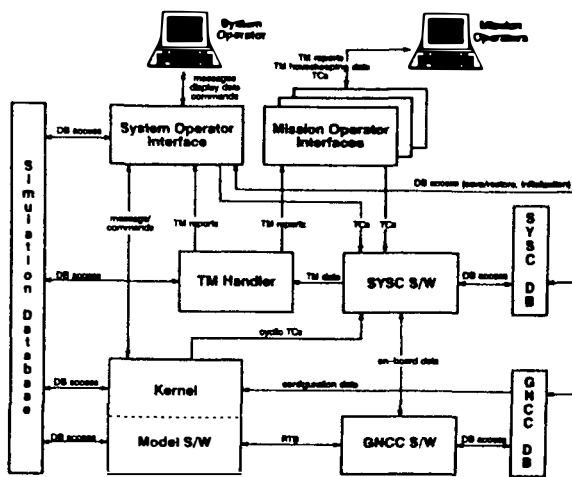


Figure 7.1-a : ROSS Architecture

ROSS is coded in C, and implemented on SUN workstation.

A closed-loop test campaign was performed with ROSS, where the nominal European RVD scenarii (Hermes docking at earth pointing MTFF, and MTFF berthing at SSF) have been simulated in order to check the correct system autonomy (nominal sequencing of the modes and phases, and the management of resources) and the GNC system performances by comparison with the assessments made during the development phase. In addition, hard and soft failures on almost all the sensors and actuators involved in the GNC have been simulated and their effect onto the autonomous system performance has been analysed in order to check the robustness of the active and passive safety concepts.

Thanks to these tests, the feasibility of the autonomous GNC and MVM concept was demonstrated in a simulated but highly realistic environment. ROSS allowed to show that the performances of the GNC system were in line with the requirements. ROSS also showed that some parameters needed to be revised in order to cope with transient effects, the frequency concept and other effects coming from previously unconsidered effects.

It has been shown that the FDIR concept satisfies the (FO)/FO/FS requirements for all the cases studied. Though, future work is required to achieve a higher autonomy for isolation of ambiguous failures beyond the

scope of the concept which was the baseline for ROSS.

In addition to the ROSS development, for the final 20m of approach, the GNC software was additionally coded in Ada and successfully real-time tested on the ESA Advanced Guidance and Control Processor (breadboard of RV GNC processor).

## 7.2 MIL Tests

The definition of candidate concepts for human operator (H.O.) intervention was performed taking into account the RV and Proxops strategies, the onboard system, the RV Control tasks and the capabilities of the different operators. This led to the concept of the H.O. supervisory control capability, which includes intervention in MVM and also involvement in GNC tasks. In addition to this supervisory control concept, two intervention capabilities in the GNC have been analysed: manual control (accelerations are directly commanded by the pilot via joysticks) and manual state update (correction/replacement of a biased/failed RVS by the operator).

For the definition of the RVD-PDP display concept, the Hermes cockpit concept was used as reference.

The verification of the concept for intervention into MVM tasks was performed with a combination of two simulators, i.e. the ROSS, which provided the telecommand interface and the Flight display, and the Rendezvous Simulator for Man In the Loop (RVSIMIL), which provided the Navigation displays (see fig 7.2-a).

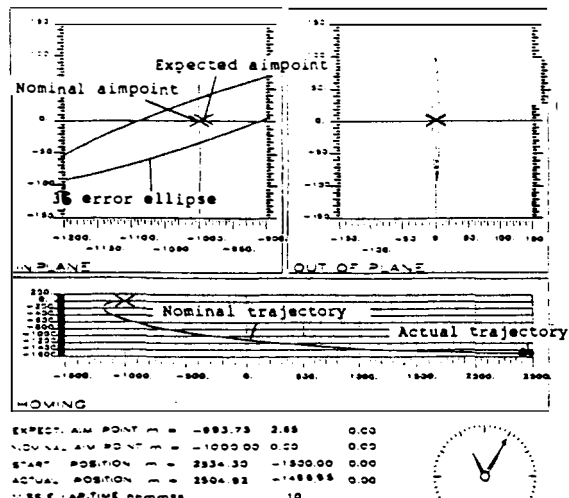


Fig 7.2-a Example of RVSIMIL Display

The verification of the intervention concept into the GNC tasks was done with the real-time Man-In-the-Loop Simulator (MILS) at Aerospatiale, Cannes. This latter was concentrated on the last 100 m.

The tests have demonstrated that the proposed concept combining two displays (a Flight Display with TM data, messages and TC interface, and a Navigation Display with graphical illustration of trajectories) provides a suitable Man-Machine Interface (MMI) for intervention in automatic RVD. It provides an adequate monitoring capability either for nominal and contingency cases, as well as command access to the automatic system in case of active intervention.

This was verified by successful human operator intervention into MVM for which some cases of phase or mode sequence change were tested. But the number of contingency strategies that could be implemented in RVD-PDP was low, and in a further stage, the contingency conditions must be identified in more detail and back-up strategies defined.

For the intervention in GNC, it came out that the 6 DOF manual control was possible when navigation data is available, but should be limited to 3 DOF only (position or attitude) when navigation data are not available. Also, for manual state update, a 6DOF RV sensor bias correction could be performed with low effort.

More details can be found in [3].

### 7.3 RV-Sensor Closed Loop Testing

In recent years development activities for rendezvous sensors have been started by ESA and national agencies in Europe. Within the PDP, three short range camera sensor breadboards have been available for testing, which are

- a short range sensor developed by MATRA with CNES R&T fundings (MATRA patent),
- a short range sensor developed by MBB under ESA R&T fundings,
- a short range sensor developed by SAAB with Sweden national fundings.

The sensors have been tested on EPOS (European Proximity Operation Simulator) developed by DLR-Germany with ESA and RFA fundings. This facility is formed by

- a gantry robot, which simulates the chaser motion,

- a three axes turn table, which simulates the target attitude
- sun simulators, which simulate the effects of the sun for two cases
  - a) sun illuminates the target
  - b) sun is in the field of view of the sensor

The EPOS is shown in Figure 7.3-a

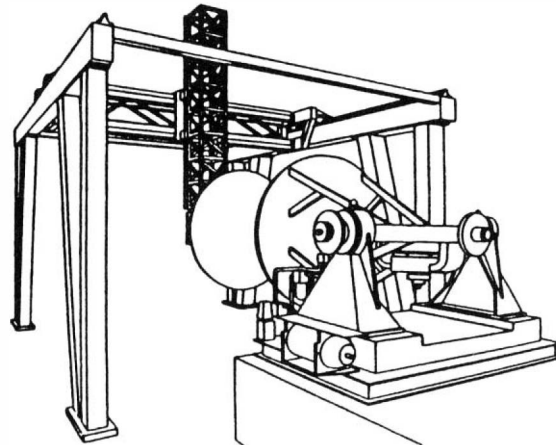


Fig 7.3-a: EPOS

The objective of the tests were to identify the impacts (if any) due to relative kinematics characteristics between the sensor head and the target pattern, and to presence of sun on the performances and functional capabilities of the sensors. The tests have been performed over a range from 0 to 10 meters with lateral and vertical displacements of +/- 1.5 meters and velocities up to 200 mm/s. The range, linear velocities and angular rates were varied during the tests. For illumination aspects, tests have been performed with sun illuminating the target, sun in the field of view (for the sensors which could accept it), and reflecting surfaces in the vicinity of the target reflectors.

In the operating range tested, the three sensors met the motion requirements, and the sensor noise remained under the desired limits under a wide spectrum of motion conditions. Sensors were able to track target motions well beyond the expected conditions in orbit. Distinctions between the various tested sensors characteristics could be also observed through these tests, for example related to the impact of the respective size of the target patterns on the range and relative attitude measurement noise, or related to the improvements brought by some internally implemented error compensation processings to improve the linearity.

To sum up, the sensor tests yielded valuable information on the sensor behaviour under motion and illumination conditions, and the sensor error model within the GNC simulations performed in parallel within the RVD-PDP could be validated, particularly for what concerns noise.

More detailed results can be found in [2]

#### 7.4 Docking dynamics investigations

While the final approach was investigated in detail from a GNC point of view, a test campaign on contact dynamics has been performed. Prior to this campaign, a functionnally representative mock-up of the most promissing concept for a future DBS FE for RV missions between manned spacecraft has been designed and developed by SENER-Spain and integrated on the existing Docking Dynamics Test Bench available at Matra (developed iunder CNES contract).

This DDTF has been designed to perform a highly representative relative 6 DOF motion between the docking interfaces of two rendezvousing spacecraft. This is achieved thanks to an active loop based on a 6-axes force/torque detection, mathematical modelling of the vehicles orbital motion and attitude dynamics, and a 6 degree of freedom servo motion. This 6 DOF relative motion is basically realized by accomodating the docking interface of one of the spacecraft (the target S/C in the present cases) on a six axes table driven by six electric screw-jacks. The other spacecraft interface (the chaser one) is fixed in the laboratory frame. The six axes loads detection is based on six mono-axis force transducers .

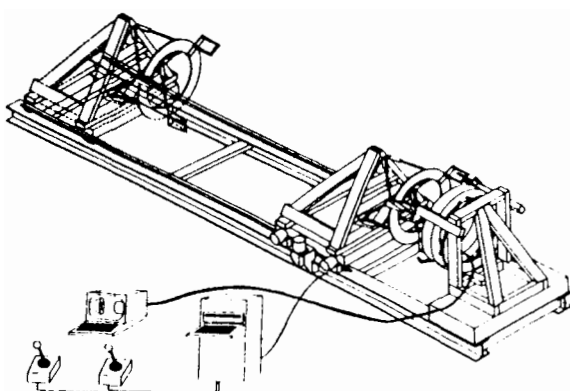


Fig 7.4-a Docking Dynamics Test Facility

Since this DDTF was initially designed for experimentation with docking mechanism

dedicated to full automatic missions, the DBS FE tested here had to be scaled down (0.5).

The tested DBS mock-up is composed of two halves. The halve mounted on the target vehicle is totally passive, while capture latches are implemented on the active half mounted on the chaser spacecraft. The passive half is composed of a ring on which different sets of guiding petals can be implemented in different configurations. The active half consists in an interface ring, an attenuation stage, a docking ring on which guiding petals are implemented, and capture latches which can be implemented either on the interface ring or on the docking ring. The attenuation stage is composed of 6 dampers where the stiffnesss and the damping coefficient are tunable. The latches are driven by stepper motors and their capture range and velocities are also tunable.

In addition, a fully software simulation tool called Docking Simulation Programme (DSP) developed by Aeritalia-Italy in a previous ESA contract has been available for results comparison.

A large amount of tests have been performed, allowing investigations on:

- mission dependant spacecraft inertias
- initial misalignement and kinematical conditions
- DBS FE guiding stage characteristics (3 and 4 petals, petals inclination, shape and orientation, petals friction)
- DBS FE attenuation stage stiffness and damping characteristics
- DBS capture stage characteristics (latches location, actuation strategy wrt to contact time)

The conclusions and recommendations that can be derived from this test campaign are numerous.

The main overall conclusion is that the European front-end concept (alignment by petals, passive attenuation system, capture before contact and retraction by capture latches) has been demonstrated, and its robustness against contact conditions, mission scenarios and configuration changes, has been shown.

Much was learned or clarified through the tests and analyses performed concerning the front-end functions, the contact conditions and the contact dynamics. Concerning the front-end functions, the number of petals does not affect the contact loads, and the petals should

be implemented according to system/configuration constraints, but small inclination/shape angles should be favoured. For the attenuation system, the concept of a passive one with loads below 4000 N, and deformations below 15 mm and small lateral and angular excursions has been demonstrated. For capture/retraction, it is recommended to make capture before contact, and wait before starting retraction with low velocities. It can also be concluded that malalignments affect the petal length and the capture range and span, but have little influence on the dynamics.

This test campaign also showed that the DDTF allowed to iterate the investigations on GNC with the work on the DBS FE. The DDTF also performed correct gravity compensation of the docking port flexible part, and allowed to investigate different capture strategies based on capture conditions computed by the DDTF. In addition, though a scaling down was needed, the DDTF scaled up results proved to be reliable when compared with corresponding DSP simulations results. Indeed, the test results have been validated by comparison with a software tool (the ESA Docking Simulation Programme), showing very good similarity between the hard and the software tests.

## 8 CONCLUSIONS

Within the RVD-PDP, a generic concept of an autonomous onboard GNC system for RVD including interaction of human operators has been defined.

It was the opportunity to reassess overall system aspects. For example, the location of the intermediate points S2 and S3 were reconsidered, and their respective lower limits reduced to 200 m and 50 m for safety reasons. Consequences on the overall timing and fuel consumption could be derived.

An RV Control System, representative of Hermes and CFF, which allows testing of the fail-operational and fail-safe transitions, and which provides additional margin for further investigation was developed.

The GNC and System computers have been filled with the GNC and MVM software, and verification of the RV Control System started.

In addition to this, a concept for Man Machine Interface to support human operator intervention into automatic RVD manoeuvres

was developed and verified via ROSS, RVSIMIL and MILS. The concept for the human operator role foresees intervention into MVM and GNC tasks. For more ambitious monitoring and intervention concepts, the need for the operator assistant tools was identified.

Besides, testing of sensor equipment and docking mechanism is a first step, from a technological point of view. The final on ground step, i.e. testing of the RV Control System at higher integration levels, including onboard software, onboard computer and RV sensors under motion and illumination conditions is still necessary for final validation.

Europe has now reached a situation where the key elements of the autonomous Rendezvous and Docking technology are now ready to support ambitious space programmes. Though, it is necessary to first finalize the proof-of-concept activity via on-ground and in-orbit activities. Indeed, EPOS and DDTF facilities should be used for integration and on ground demonstration of a complete RVD system, which should be followed by an in-orbit demonstration of the RVD hardware (essentially, the RVsensor) and software (operations, relative navigation with GPS) under real operational constraints.

## REFERENCES

- [1] J.M. Pariot & al.  
"Development of GNC System for Rendezvous, Major Results of the RVD Pre-Development Programme" - ESA International GNC Conference, Noordwijk 1991
- [2] A. Tobias & al.  
"Rendezvous Sensor Performance Requirements & Validation on a Motion Simulation Facility" - AIAA/AAS Astrodynamics Conference, August 1992
- [3] D. Wilde & al.  
"Man Machine Interface for Automatic Rendezvous & Docking maneuvers" - ESA Workshop - Spacecraft GNC Systems : Software for Design and Implementation - Noordwijk, Oct 1992.

# EVALUATION OF AUTONOMOUS GNC STRATEGIES FOR THE ROSETTA INTERPLANETARY MISSION<sup>1</sup>

C. Champetier\*, P. Regnier\*, J.B. Serrano\*\* and J. de Lafontaine\*\*\*

\*MATRA Marconi Space, 31 rue des Cosmonautes, 31077 Toulouse Cedex, France

\*\*GMV S.A., Isaac Newton s/n (PTM), 28760 Tres Cantos, Madrid, Spain

\*\*\*ESTEC-WK Division, Keplerlaan 1, Postbus 299, 2200 AG-Noordwijk, The Netherlands

## ABSTRACT

This paper presents the most recent results obtained in the frame of the ESA study on "Autonomous and Advanced Navigation Techniques", part of the Technology and Research Programme of ESA. New guidance, navigation and control (GNC) concepts applicable to the near-comet phases of the ROSETTA mission have been investigated and detailed performance results obtained with a complete simulation software tool are described here. This paper is focused on the evaluation and performance assessment of GNC concepts applicable to the descent and landing phase of the mission, including the following points :

- Attitude and Articulation Control System (AACS) concepts for a multibody spacecraft (Section 3) ;
- autonomous spacecraft trajectory Guidance, Navigation and Control concepts for the descent phase, including the open-loop and the guided subphases (Section 4) ;
- touch down control concepts (Section 5)

The introduction presents the study assumptions, Section 2 is dedicated to the description of the software tool and the simulated models, and a synthesis with further recommendations are discussed in Section 6.

## 1 INTRODUCTION

### 1.1 Context

The ROSETTA mission, cornerstone of the long term scientific ESA program, aims at performing a rendezvous with and landing on a comet nucleus to bring back to Earth a scientifically meaningful sample of its subsurface. It is an illustrative example of the kind of problems that should be overcome for the successful accomplishment of a deep space mission.

This paper presents the most recent results obtained in the frame of the ESA study on "Autonomous and Advanced Navigation Techniques" (AANT study), which is part of the ESA Technology and Research Programme related to the ROSETTA mission. This study, spread over two years, concerns the GNC system design for the proximity operations near a comet. The three major stages of the study are the GNC analysis and performance assessment supported by closed-loop simulations (Phase 1), the GNC system design with elaboration of a cost and development plan (Phase 2), and GNC software prototyping and implementation on a real-time test bench (Phase 3). The key points discussed in this paper are related to the first part of the study which ended this year.

<sup>1</sup> The results presented in this paper have been obtained in the frame of the ESA contract 8808/90/NL/PM

### 1.2 ROSETTA mission description

The baseline scenario for the near-comet phases of the ROSETTA mission is summarized hereunder (Ref. 1).

After a 41-month cruise-to-comet phase during which only small orbit control maneuvers are performed, the near-comet operations are initiated. The first critical operation is the detection of the comet, with stringent requirements on the Narrow Angle Camera pointing stability. Depending on the nucleus size, albedo and Sun illumination angle, the detection by means of the spacecraft imaging system takes place from  $6.10^5$  km to  $3.10^6$  km from the comet. In the worst case, a minimum time of 3 days is left to the ground segment to process the sky images for comet identification and to optimize the rendezvous maneuvers.

The comet approach phase from 300 000 km (first rendezvous maneuver) to close vicinity of the nucleus (130/35 km) lasts 33 days. Three or four maneuvers are foreseen to reduce the relative velocity down to 25 m/s at 5000 km and 2 m/s near the nucleus. The approach trajectory is designed to optimize the observability of the relative position/velocity of the spacecraft (bias approach) and to minimize the damage due to impacts of debris (low velocity).

Once the spacecraft enters the gravity field of the nucleus, the comet observation phase is initiated. In order to achieve a global mapping of the comet (21 days duration), the spacecraft is injected into a comet polar orbit compatible with a good illumination angle, or optionally comet stationary (hovering) and quasi-inertial points are used. During this phase, an overall mapping of the illuminated part of the comet will be performed in order to determine a preliminary topography of its surface and to recognize candidate landing area of scientific interest.

After the global mapping phase, potential landing sites are identified from ground image processing. The spacecraft is then injected into an optimized elliptical orbit (typ. with a periapsis of 5-10 kms) for detailed mapping of the candidate landing area. A period of 18 to 37 days is allocated to this phase.

The open-loop descent phase is then initiated from a low altitude Descent Preparation Orbit used to achieve the relative phasing of the spacecraft with the landing site while intensive ground tracking accurately reconstructs the dynamical state of the spacecraft. After one or two revolutions on this orbit, a deorbiting maneuver command is uplinked to the spacecraft and executed at the pre-selected time. The resulting homing orbit brings the spacecraft to a position and velocity that allows the use of the on-board instruments to synchronize the spacecraft motion with that of the landing site and initiate the

autonomous final guided descent. At about 1 km altitude, a (typically) 1 m/s vertical descent is initiated.

The vertical velocity at touch down is reduced to 10 cm/s and the residual kinetic energy is dissipated into shock absorbers. Due to the weak gravity field (typically 70  $\mu\text{g}$ ), the low spacecraft stability margins (static stability angle less than 20 deg), and the poor knowledge of the comet surface characteristics, the GNC system must ensure an active stability at touch down to prevent from tipping over in case of local surface irregularities and sliding in case of icy slope. After being completely stabilized, anchoring is performed as soon as possible and the ground communication is established for monitoring the on-comet operations.

The investigation of Autonomous GNC concepts applicable to the observation phase for spacecraft navigation and comet parameters identification has already been presented in previous publications (Refs. 2, 3, 4) along with the critical issue of detecting and avoiding dangerous debris.

The AACCS concepts applicable to the fine pointing of a camera in the comet detection phase have been evaluated by closed loop simulations under a complex real world modelization (multi-body spacecraft, flexibilities, dry friction), and associated results are presented in Ref. 4.

### 1.3 Spacecraft and GNC Instruments

The baseline spacecraft design (Ref. 1) is based on the reuse of the Mariner Mark II (MMII) module developed for CASSINI and CRAF missions under NASA/JPL responsibility. An optimum concept leading to minimum modification of the baseline MMII is shown on Fig.1. The spacecraft consists of three main modules :

- the cruiser, its scan platform and High Gain Antenna (based on MMII) used in all phases except reentry ;
- the lander carrying the sampling devices and left on the comet after departure ;
- the aerocapsule attached on the side of the MMII and carrying the sample container back to Earth.

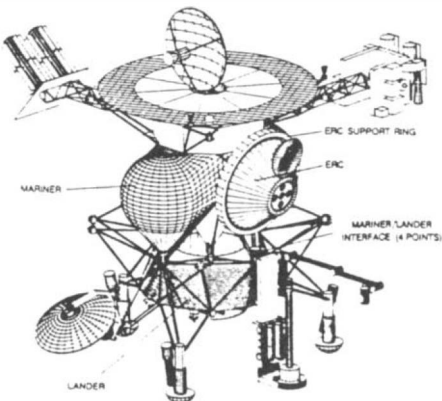


Fig. 1 : The ROSETTA spacecraft configuration

Table 1 identifies the candidate navigation instruments also used for scientific purposes (cf Ref. 5). The imaging system (e.g. Narrow and Wide Angle Cameras) and the Star and Target Tracker are used for the comet detection and mapping. They provide the ground with images from which the main characteristics of the comet (shape, gravity field, rotation) are identified. The inertial lines-of-sight to natural landmarks located on the comet surface constitute the main information used for this purpose.

INSTRUMENTS	MEASUREMENTS
Imaging System (cameras)	<ul style="list-style-type: none"> <li>• LOS to the comet optical center in the camera frame,</li> <li>• comet apparent diameter,</li> <li>• contour extraction (limb tracking),</li> <li>• LOS to natural landmarks,</li> <li>• light curve.</li> </ul>
Star and Target Tracker	<ul style="list-style-type: none"> <li>• inertial stars referenced LOS to the comet optical center,</li> <li>• comet apparent diameter,</li> <li>• optical center tracking.</li> </ul>
Laser	<ul style="list-style-type: none"> <li>• range and range rate,</li> <li>• surface roughness,</li> <li>• surface normal unit vector,</li> <li>• 3D topographic map correlation.</li> </ul>
Radar	<ul style="list-style-type: none"> <li>• range and range rate,</li> <li>• surface roughness,</li> <li>• surface normal unit vector.</li> </ul>
Doppler Instrument	<ul style="list-style-type: none"> <li>• relative velocities along three squinted beams.</li> </ul>

Table 1 : Spacecraft Navigation Instruments

Only the surface instruments (radar and laser) are used for spacecraft navigation during the descent phase. In addition, the use of an artificial landmark tracking system is envisaged. The characteristics of these instruments are precised hereafter :

- Artificial Landmark System, from ROSETTA System Definition Study :
  - Angular Error : a few degrees below 30 kms, 1° below 3 kms,
  - Operating Range : 30 kms,
  - Measurement Frequency : 1 Hz.
- Laser Range Finder, from CALS (Ref. 5) :
  - Operating Range : from 10 m to 15 kms for the range, 3 kms for the relative attitude, roughness and 3D topography measurements,
  - Accuracy : about 20 cms for the range ; other measurements are derived from scanning an area and performing a least square estimation to compute the relative attitude and roughness ; expected performance : 3° and 20 cms,
  - Measurement Frequency : 1 Hz for the range, a few seconds for the relative attitude and roughness depending on the scanned area. The 3D topography measurement update is expected to be around 200 s (needs correlation technique),
  - Scanning Squint : from 0 to 4° (controlled),
  - Beam Divergence : 40  $\mu\text{rad}$ ,
  - Scanning Pointing Accuracy : 8  $\mu\text{rad}$ .
- Radar Microwave Instrument, from CALS (Ref. 5) :
  - Operating Range : from 10 m to 500 kms for the range and range rate, 15 kms for roughness, 3 kms for relative attitude and Doppler velocity,
  - Measurements Accuracy : about 1% down to 10 kms and 20 cms at low altitude in range, a few mm/s in Doppler velocity, the relative attitude must be constructed from 3 range measurements along three squinted beams (expected accuracy : <1° down to 200m), the roughness accuracy is expected to be about 10 cms,
  - Measurements Resolution : 25 cms in range and roughness, <1° down to 400 m and <4° down to 50 m in relative attitude, <1 cm/s in Doppler velocity,
  - Measurement Frequency : 1 Hz,
  - Squint Angle : 2°,
  - Beamwidth : 0.4°.

All surface measurements are available with 20° of LOS-normal angle.

The candidate AOCS sensors for the descent phase and their nominal characteristics are precised hereafter :

- 4 Fiber Optics Rotation Sensors (gyros) : of the type NASA DRIRU II (drift of 0.003°/h) or SPOT 4 (drift of 0.01°/h), bandwidth around 10 Hz,
- 3 Accelerometers : range 0 – 0.1 g, threshold 10<sup>-6</sup> g
- Optical Encoders at each articulation (2 for the HPSP and 2 for the HGA). Expected angular accuracy : 0.05°,
- Radio Frequency Sensors for the HGA and the MGA : angular accuracy of 0.01°.

One of the expected output of the study is the precise specification on the class of gyros to be boarded on the spacecraft in order to fulfil the pointing and stability requirements.

The candidate AOCS actuators and their nominal characteristics are the following :

- one bipropellant 400 N articulated main engine for maneuvers of more than 1 m/s,
- 24 hydrazine 10 N thrusters for maneuvers less than 1 m/s and coarse attitude control,
- 24 hydrazine 0.2 N thrusters for fine attitude control ,
- cold gas 20 N thrusters for on-comet operations,
- 2 biliquid 70 N thrusters for stabilization during sampling in case of anchoring failure,
- 4 skewed reaction wheels (26 Nms, 0.4 Nm) (TBC),
- Direct Drive or Stepping Motors at articulations.

Here again, the need for the low level thrusters against a reaction wheels control system must be assessed.

## 2 DEVELOPED SOFTWARE TOOL AND SIMULATED MODELS

### 2.1 Software Tool

A large part of the Phase 1 of the study has been devoted to the design, development and validation of a software tool named as AANTool which purposes are to assess the performance of selected GNC concepts for each mission phase in a realistic environment, to specify the GNC instruments, to select baseline and optional GNC concepts for trade-offs at system level and to prepare an easy implementation of the application software on a real time test bench. Furthermore, AANTool has been designed in a way to be easily applicable to other deep space missions. Therefore its main characteristics are the compactness (one software for all mission phases to optimize the use of common datas and the development of the environment software), modularity (clear separations between different processes), flexibility (different spacecraft, measurements configurations and types of analyses are possible), and a friendly user's interface (file driven structure, postprocessing). The detailed architecture and capabilities of AANTool are described in Refs 4 and 6. Its functional definition is shown on Fig. 2 and its basic capabilities in Table 2.

SIMULATION OF GNC OPERATIONS FOR :	TYPE OF ANALYSIS	SIMULATED BODIES	SIMULATED DoFs	REMARKS
AACS (in detection and observation phases)	TS, MC	Spacecraft Comet	All DoF (*) Rotation	spacecraft traj. and comet rotation have no impact on GNC analyses
OBSERVATION PHASE	TS,MC,CA	Spacecraft Comet	Trajectory Rotation	not yet implemented in AANTool
EJECTION PHASE	TS,MC,CA	Ejected Device Comet	Traj. + Att. Rotation	not yet implemented in AANTool, in house software for CA
OPEN-LOOP DESCENT PHASE	TS,MC,CA	Spacecraft Comet	Trajectory Rotation	TS and MC are performed inside the Guided Descent Branch of AANTool
GUIDED DESCENT PHASE	TS, MC	Spacecraft Comet	All DoF (*) Rotation	s/c traj. and att. separated for analysis, but all DoFs for validation
ON-COMET PHASE	TS, MC	Spacecraft Comet	All DoF (*) Rotation	comet rotation motion is stationary (constant inertial rotation vector)

(\*) = trajectory + attitude + articulations + flexibilities + fuel sloshing

TS = Time Simulation, MC = Monte-Carlo analysis, CA = Covariance Analysis

Table 2 : Synthesis of AANTool Capabilities

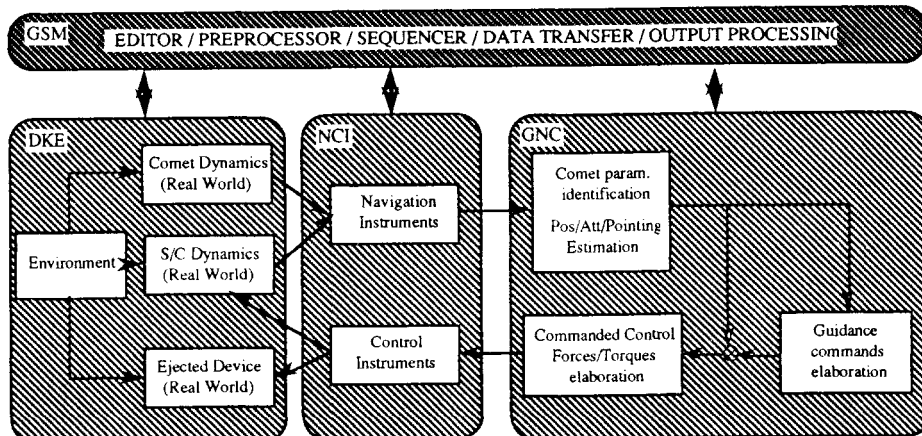


Fig. 2 : AANTool Functional Definition

## 2.2 Simulated Models

Complex models representative of the Dynamics, Kinematics and Environment (DKE) and the Navigation and Control Instruments (NCI) have been developed and implemented in AANTool (Refs. 4, 6). They include among others the simulation of comet dynamics with the rotational motion of an ellipsoidal shaped body under the effects of external torques (outgassing), an irregular gravity field based on harmonics coefficients of an homogeneous body plus additional mascons, and a non flat fractal discretized surface limited area (Fig. 4). The simulation of the spacecraft dynamics includes a central body, a 2 axis articulated antenna directly attached to it, a 2 axis articulated platform at the end of a boom attached to the central body, a 2 DoFs flexibility at the boom linkage point, 2 pendulums for liquid sloshing effects, and three landing legs with dampers (Fig. 3).

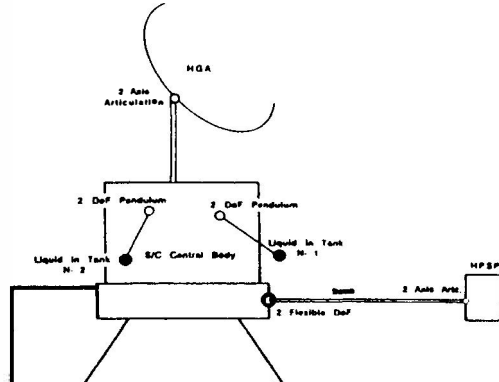


Fig. 3 : Spacecraft Simulated Model

The simulation of the environment includes actions of the comet gravity (forces and gravity gradient torques), comet outgassing and solar pressure forces and torques, Sun and Third Bodies gravitational forces, propulsive forces and torques (by thrusters, reaction wheels and articulation motors), and comet surface reaction forces in a two steps procedure (first for the rigid spacecraft with pads dampers, and then for the flexible and articulated spacecraft) which allow to simulate many on-comet situations, as shown on Fig. 5 (anchoring and sampling effects are also included).

All the GNC instruments cited in section 1.3 have been modeled with quite complex and non linear functions such as quantization, pulse width modulation, harmonics terms, dry friction, comet optical center and apparent diameter computation). In particular, the modelization of the surface measurements (radar and laser) has been carefully developed : the altitude measured by the Radar Microwave Instrument is derived from the mean range of 100 rays traced inside its wave cone, while its relative attitude measurement is constructed from the altitudes measured on three squinted wave cones (i.e. 300 rays are traced). The scanning process of the Laser Instrument has also been simulated with ray tracing techniques : a least square estimation technique is applied on the individual ranges of 100 rays traced inside its FOV in order to derive the informations of altitude, mean slope and roughness (mean and min-max values). A dichotomy technique is used to find the intersection of each ray with the discretized surface modelized near the landing site. These models are very representative of the real measurements and therefore errors induced on the spacecraft navigation and attitude control are very realistic in order to perform a relevant performance analysis.

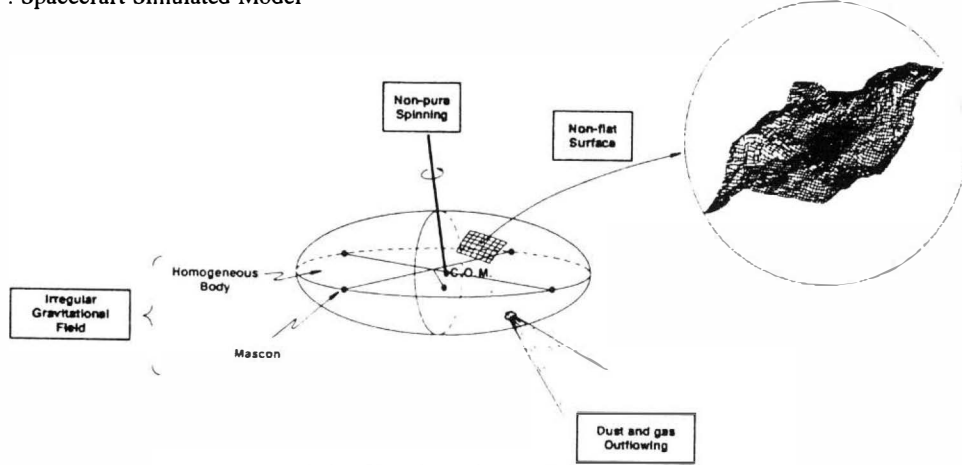


Fig. 4 : Simulated Comet Models

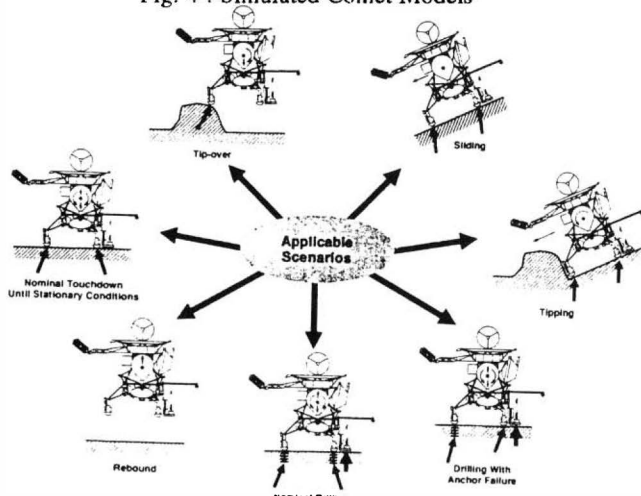


Fig. 5 : AANTool Applicability for the on-comet phase

### 3 ATTITUDE AND ARTICULATION CONTROL SYSTEM PERFORMANCE ANALYSIS

#### 3.1 Objectives and Requirements

The primary objective of the AANT study concerning the AACCS is to investigate, elaborate and trade AACCS configurations and algorithms for multi-body spacecraft compatible with the detection phase and the near-comet phases of the ROSETTA Mission.

This objective has been met in two steps. In the first step, candidate AACCS configurations and concepts were designed and preliminary performance analyses in terms of robustness and disturbances rejection performed using simple models and classical design tools such as MATLAB. In a second step, detailed performance analyses and validation of the proposed schemes have been carried out by closed loop simulations using more realistic models of the spacecraft dynamics, environment and instruments implemented in AANTool.

The AACCS analyses have been carried out for the detection, observation and descent phases, but here only the results obtained in the descent phase are presented (see Ref. 4 for the other phases). During this phase, the AACCS must autonomously control the spacecraft attitude and the HPSP pointing direction with respect to the comet surface from inertial measurements (gyros), surface normal measurements (radar or laser), using an on-board propagated comet kinematic and shape model, and HPSP pointing commands generated by the trajectory navigation function of the on-board GNC system. Two kinds of AACCS requirements apply : first the spacecraft attitude must be measured and controlled with respect to the normal to the comet surface at the landing site in order to optimize the contact of the landing legs, the rotation around the normal vector being unconstrained (except for thermal reasons). Then the instruments must be pointed with given specifications on the accuracy and stability depending on the kind of measurements performed. Any error in the instruments pointing direction will affect not only the measurements accuracy but also the trajectory navigation based on the reference or estimated pointing direction, which in turn may introduce additional errors in the pointing commands. A simple analysis to numerically derive these effects has been performed (Ref. 7) according to the kind of comet surface (rough or smooth) and the pointing strategy (biased or vertical pointing direction) :

- instruments pointing accuracy requirement :
  - estimation : 2 mrad over the descent duration (typ. 1 h),
  - control : 4 mrad over the descent duration ;
- spacecraft attitude measurement and control accuracy requirement wrt the surface normal at the landing site :
  - from 3 kms vertical and up to 3 kms horizontal distance : 5°,
  - from 50 m altitude and a few meters horizontal error : measurement accuracy : 1°, control accuracy : 2°, maximum attitude rates : 0.1 °/s ;
- HGA Earth pointing accuracy requirement : 0.18°.

In order to make the performance assessment easier but still representative of the real GNC system, the analyses have been carried out separately for the spacecraft trajectory navigation and control (reported in Section 4), and for the attitude control concepts, but taking into account disturbances introduced by the thruster control system (i.e. misalignment torques).

#### 3.2 Selected AACCS Architectures

Three basic AACCS architectures, one baseline and two options, have been selected to cover as much as possible all the system choices relevant to interplanetary missions, including ROSETTA.

The first one is the baseline ROSETTA configuration derived from the Mariner Mark II. In this architecture, the scientific instruments and the comet sensors required for navigation (laser, radar, cameras) are located on the high precision scan platform which is gimballed around two axes. Accelerometers and Sun Acquisition Sensor are located on the main bus. The High Gain Antenna (HGA) and the Medium Gain Antenna (MGA) are mounted on the same gimballed mechanism. The attitude of the bus does not have stringent measurement/control requirements (typically 0.5° during maneuvers). On the contrary, the platform which supports the scientific and navigation instruments must be pointed with a high level of accuracy/stability. For this purpose, the gyros are mounted on the platform. The attitude measurement issued from the gyros is updated with a collocated star sensor. The antennas pointing errors in tracking mode are detected by RF sensors located at the focus of the antenna. The absolute attitude of the bus is determined from the platform attitude measurement and the encoders located at the platform articulation axes. The absolute attitude of the antennas (required for Earth acquisition) is determined from the platform attitude measurement, the platform encoders and the encoders placed at the HGA/MGA articulation axes.

In Option 1 configuration, the HGA is no longer articulated, but fixed to the bus, while the MGA remains articulated. The interest for studying such an architecture, apart from the system point of view, is that it may be selected for other interplanetary missions not involving a landing, and furthermore it imposes specific constraints on the bus attitude control which do not appear in the other AACCS concepts. The control of the bus in the platform-mounted gyros configuration has been designed taking into account these most stringent constraints.

In Option 2 configuration, The NAC (and eventually the WAC) and the gyros are mounted on the bus. The fine pointing of the cameras (NAC during detection, and eventually WAC and NAC during observation) is performed by the bus attitude control. This option is of interest because the pointing stability is enhanced by the high inertia of the bus. The HGA/MGA must then be articulated as communications must be preserved during the descent phase. In order to cover as much as possible all the AACCS design choices, the articulated platform has been kept in this option. The idea is that some scientific instruments or low resolution camera may require low level of pointing performance during the observation and descent phases, and so can be mounted on a gyro-free platform. The pointing performance of the platform in such an architecture has been assessed.

#### 3.3 Attitude and Articulation Control Concepts

In order to evaluate the proposed AACCS architectures, two basic control concepts have been investigated (Fig. 6) :

- control concept A : platform-mounted gyros, applicable to the baseline and Option 1 architectures,
- control concept B : bus-mounted gyros, applicable to the Option 2 AACCS architecture.

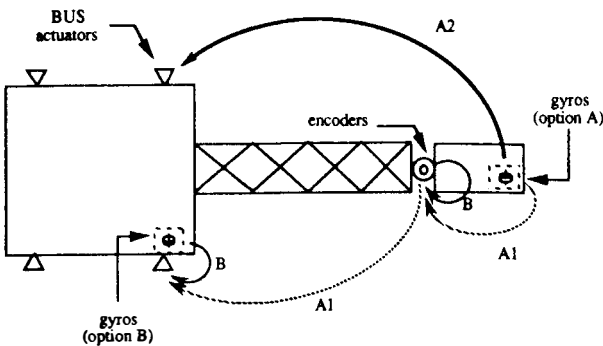


Fig. 6 : The candidate AACCS control concepts

Actually, two control concepts of type A referred to as A1 and A2 have been proposed :

#### A1) Unblocked articulation stepper motor

The platform attitude is controlled by feeding back the gyro measurements on the motor commanded angular rate, while the bus attitude is controlled by feeding back the encoder measurements on the wheels or the thrusters.

#### A2) Blocked articulation stepper motor

In this concept, the command of the stepper motor is blocked to a given value. The platform attitude is controlled by feeding back the gyro measurements on the wheels or thrusters of the bus, as if the platform was fixed with respect to the bus ; the stiffness of the motor combined with the high inertia of the bus is expected to be sufficient to allow for a precise pointing. However, this concept is more dedicated to the detection phase and has not been applied to the descent phase.

In concept B, the bus attitude is controlled by feedback of the gyro measurements on the wheels or thrusters, while the platform pointing is estimated via the encoders measurements and controlled by the articulation motors.

### 3.4 Selected Control Laws

Linear and decentralized control laws have been designed for the attitude control of the bus, the platform and the antenna, from simple one axis models, and robustness (gain and phase margins) and accuracy (control bandwidths) design goals.

For the platform and the bus, there exists one controller for each control concept cited above, plus one single controller for concept A2. In addition, special features have been implemented for specific cases (e.g. integrator terms for rate ramps, filter for the bus in the descent phase). The antenna has a single controller with an optional integrator term.

The controllers are mainly composed of constant gains, lead compensation terms or second (and fourth) order filters. The obtained open-loop bandwidths at 0 dB range from 0.05 Hz for the bus in concept A1 to 0.18 Hz for the antenna with the integrator term.

### 3.5 AACCS Concepts Detailed Performance Analysis in the Descent Phase

#### 3.5.1 Evaluation Method

The objectives of the simulations performed with AANTool (for all mission phases) are to solve GNC trade-offs which could not be demonstrated before, to assess the performance and robustness of the selected concepts and

to precise the instruments specifications. The simulations campaign has been organized accordingly in a precise logic presented hereafter.

Three different levels of parametric analyses, which must establish the dependence of some given performance objectives (pointing stability, landing accuracy, fuel consumption,...) on system parameters have been performed. The system parameters have been divided into three groups :

- Environmental Fixed Parameters,
- Technological Fixed Parameters,
- Controllable Parameters.

The Environmental Fixed Parameters are constraints imposed by the environment, such as comet characteristics (kinematics, dynamics, mass,...) or environmental disturbances (solar pressure, comet outgassing). The Technological Fixed Parameters are constraints imposed by the technology, such as capabilities and performance of instruments or initial conditions, dispersion and knowledge errors. The Controllable Parameters are those that can be selected by the GNC system designer such as GNC concepts, strategies and algorithms, parameters of the GNC algorithms (filter gains, controllers transfer functions coefficients), types and combinations of measurements.

The overall objectives of the parametric analyses are to :

- A) select the Controllable Parameters that will optimize the performance objectives for given typical Fixed Parameters,
- B) determine the sensitivity of the performance to the Environmental Fixed Parameters,
- C) determine the sensitivity of the performance to the Technological Fixed Parameters, identify the critical ones and specify their admissible operational range.

These general objectives correspond to the three levels of simulation : levels A, B, C, level A (selection of the Controllable Parameters) being the top level presented in this paper in sections 3.4, 4.3 and 5.3.

#### 3.5.2 Simulations Assumptions

The performance analysis of the AACCS concepts for the descent phase are based on time simulations of the platform pointing and the bus attitude control, the spacecraft being submitted to a typical force profile (introducing misalignment and compensation torques). As said before, the spacecraft navigation is not simulated together with the attitude control in order to uncouple as much as possible the complex environment of the descent phase. Therefore the platform pointing is commanded towards the real Selected Landing Site (SLS) instead of being computed by the trajectory estimation function. Furthermore, because of the high frequency of the attitude simulation (about 20 Hz) and the large duration of the descent, only two portions lasting about 2 mns have been simulated starting at high (2800m) and low (180m) altitudes (Fig. 7).

The main assumptions for the level A analyses (selection of Controllable Parameters for typical Fixed Parameters) concerning the numerical values of the important parameters to be considered for the simulation of AACCS operations in the descent phases are the following (all noise standard deviation are  $1\sigma$ ) :

- comet characteristics : medium size (equivalent radius of 3 kms), density  $0.8 \text{ g/cm}^3$ , rotation period 10 hrs ;

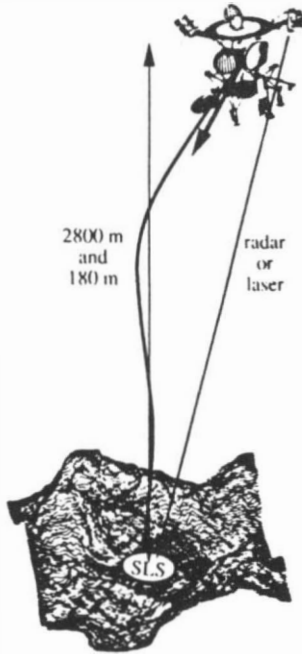


Fig. 7 : AACCS Simulation in the Descent Phase

- external perturbations : solar pressure, comet outgassing, Sun tidal acceleration ;
- gyros (SPOT 4) : misalignment angles of  $0.01^\circ$ , scale factor error of  $10^{-5}$ , drift error of  $0.01^\circ/\text{h}$ , quantization step of  $4.26 \cdot 10^{-6} \text{ rad/s}$ , PSD of  $3.761 \cdot 10^{-15} \text{ rad}^2/\text{s}^2/\text{Hz}$  ;
- RF sensors : white noise of  $0.022^\circ$  ;
- optical encoders : white noise of  $0.05^\circ$ , quantization step of  $0.0003^\circ$  ;
- stepper motors (SAGEM) : stiffness of  $1200 \text{ Nm/rad}$ , viscous damping of  $35 \text{ Nm/rads}^{-1}$ , quantization step of  $1.83 \cdot 10^{-6} \text{ s}$ , dry friction of  $0.3 \text{ Nm}$ , noise torque of  $4.47 \cdot 10^{-5} \text{ Nm}$  ;
- thrusters :  $1\text{ON}$  thrust, MIB of  $50\text{ms}$ , 4 thrusters on each spacecraft side, torques are assumed to be realized with 2 or 4 thrusters and a lever arm of  $1\text{m}$  ;
- radar and laser instruments : misalignment angles of  $0.01^\circ$ , measurement errors as indicated in Section 1.3.

### 3.5.3 Simulations Results

The specific objectives of the AACCS simulations for level A in the descent phase were to evaluate and trade-off the following concepts :

- platform mounted (concept A1) versus bus mounted (concept B) gyros,
- inertial versus surface normal relative bus attitude control,
- surface normal filtering process with or without on-board comet model.

The level A results are shown on Table 3. The first four rows specify the chosen controllable parameters (e.g. control concept) and the first two columns list the performance objectives and their associated requirements :

- P01** HGA pointing control error,  
**P02** platform pointing control error over 1 hour, without gyros updating,  
**P03** bus attitude control error with respect to the real SLS normal or the Z inertial axis (depending on the control mode : inertial or relative),  
**P04** filtered SLS normal estimation angular error,  
**P05** torques fuel consumption.

The fifth and sixth rows correspond to some fixed parameters which are of crucial importance for the AACCS performance : the presence of model errors in the filtering process and the type of comet surface : ellipsoid or discretized. The performances shown may be considered as  $3\sigma$  values. The cases where the performance does not meet the requirement have bolded borders. The table is divided in two parts corresponding to the results obtained for the high and low altitudes environments.

A part of level C simulations have been performed : the influence of the type of comet surface on the AACCS performance has been assessed as well as the effect of comet model errors in the surface normal measurements filtering process. Furthermore a simulation with fuel sloshing and HPSP boom flexibilities has shown that with the numerical values assumed for the analysis, no degradation of the AACCS performance is foreseen.

Figure 8 shows an illustration of the chaotic thruster control during the guided descent for the relative mode (control with respect to the estimated surface normal at high altitude).

AACCS Configuration		A1	A1	A1	A1	A1	A1	B	B	B	B
surface instrument	radar	laser	radar	radar	radar	radar	laser	radar	radar	radar	laser
bus attitude control (Absolute or Relative)	R	R	R	R	A	R	A	R	R	A	A
comet model	Yes	Y	Y	N	Y	Y	Y	Y	N	Y	Y
model errors	No	N	Y	/	Y	Y	Y	Y	/	Y	Y
type of surface	Ellipsoid	E	E	E	E	Discretized	D	E	E	E	D

Performance Objective	Reqt	SIMULATION RESULTS AT HIGH ALTITUDE											
		0.18°	0.09°	0.08°	0.1°	0.17°	0.03°	0.12°	0.05°	0.05°	0.015°	0.05°	0.05°
P01	0.18°	0.09°	0.08°	0.1°	0.17°	0.03°	0.12°	0.05°	0.05°	0.015°	0.05°	0.05°	0.05°
P02	4 mrad	0.7 mrad	0.7 mrad	1 mrad	2 mrad	0.4 mrad	1 mrad	1.5 mrad	2 mrad	0.8 mrad	1.5 mrad	2 mrad	0.8 mrad
P03	5°	0.6°	0.46°	0.7°	10°	0.3°	17°	0.6°	0.6°	0.09°	0.6°	0.6°	0.09°
P04	No Rqt	0.5°	0.14°	< 0.5° after 60s	N.A.	< 0.5° after 60s	17.5°	< 0.5° after 60s	N.A.	< 0.5° after 60s	110 g	130 g	60 g
P05	No Rqt	140 g	135 g	200 g	60 g	60 g	580 g	110 g	130 g	60 g			

Performance Objective	Reqt	SIMULATION RESULTS AT LOW ALTITUDE											
		0.45°	3.5 mrad	0.6°	0.02°	0.23°	0.015°	1 mrad above 50m	0.5 mrad above 50m	10 mrad	0.02°	2.9° > 80m	2.9° < 20m
P01	0.18°	Not Available	N.A.	0.9° > 50m 3.5° < 50m	7° at 20 m	0.035°	0.6° > 80m 2.9° < 20m	N.A.	N.A.	N.A.	0.02°	2.9° > 80m 4.2° at 20m	2.9° > 80m 4.2° at 20m
P02	4 mrad			4 mrad	7° at 20 m	0.035°	0.6° > 80m 2.9° < 20m	N.A.	N.A.	N.A.	0.02°	2.9° > 80m 4.2° at 20m	2.9° > 80m 4.2° at 20m
P03	5°			3.5 mrad	2.1° at 120m 7.5° at 20m	2.6° at 140m 9.2° at 20m	0.6° > 80m 6° at 20m	N.A.	N.A.	N.A.	0.02°	2.9° > 80m 4.2° at 20m	2.9° > 80m 4.2° at 20m
P04	No Rqt			0.9° > 50m 3.5° < 50m	2.1° at 120m 7.5° at 20m	2.6° at 140m 9.2° at 20m	0.6° > 80m 6° at 20m	620 g	21 g	250 g	620 g	21 g	250 g
P05	No Rqt			0.6° > 50m 3.2° < 50m	2.1° at 120m 7.5° at 20m	2.6° at 140m 9.2° at 20m	0.6° > 80m 6° at 20m						20 g

Table 3 : AACCS Simulations Level A Results for the Descent Phase

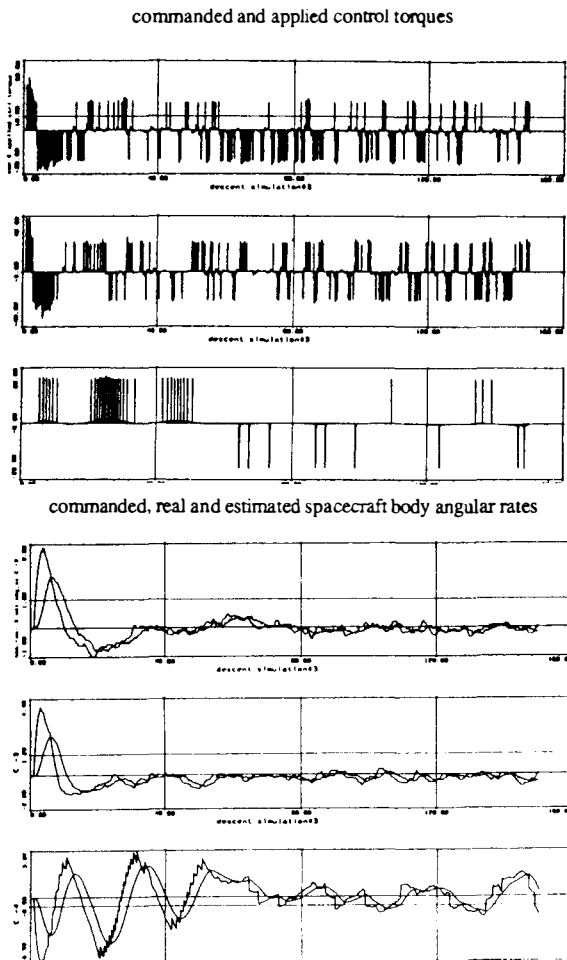


Fig. 8 : Thruster Attitude Control in the Descent Phase

### 3.5.4 Synthesis and Recommendations

The synthesis of AACs simulations results for the descent phase can be divided into three specific points :

- on the surface normal measurements filtering process :
  - the performance is not too much dependent on the instrument used. This is due to the fact that the radar and the laser have quite the same range errors at low altitude ( $< 3$  kms) ; although the relative attitude computation is then more precise with the laser (least square estimation technique) than with the radar (three squinted beams), the discretization of the surface erases this difference ;
  - the surface normal filtered estimation angular error is as shown on Fig. 9. Estimation errors at high altitude are due to surface irregularities and those at low altitude to surface sensors measurements bias and noise in range (here 20 cm) ; this graph has been extrapolated from simulation outputs at low and high altitudes with and without the comet surface discretization. It shows that there is a minimum attainable estimation error of the surface normal of about  $2^\circ$  at 200 m. Actually these values depend on the comet surface characteristics (size of irregularities) and the surface sensors performance. However their variation with these factors should not be large enough to modify the conclusions of the analysis ;
  - the presence of errors in the on-board comet model of the filtering process does not modify the long term estimation performance. Indeed the initial divergence introduced by model errors are compensated for in about 60s.

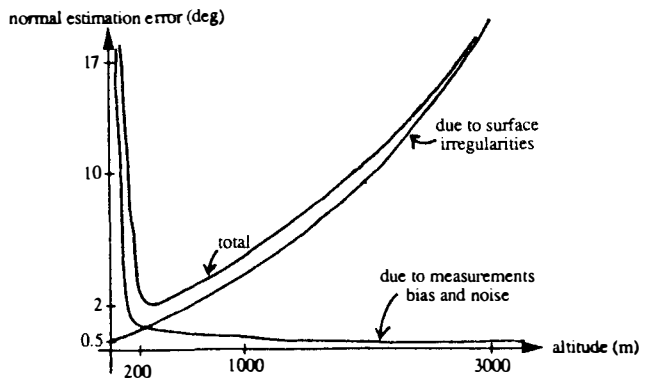


Fig. 9 : Surface Normal Angular Estimation Error

- on the bus attitude control concept :
  - the control relative to the comet surface normal without using an on-board comet model has required a lower bandwidth which has largely degraded the performance ;
  - with an on-board comet model, the performance of the bus attitude control relative to the surface normal comes from the normal filtering estimation angular error which is described above (from  $2^\circ$  at 200m to  $17^\circ$  at 10m and 3kms). Therefore the specification ( $2^\circ$  below 50m,  $5^\circ$  above) can not be fulfilled except around 200m altitude ;
  - the accuracy of the inertial bus attitude control depends on the level of misalignment torques induced by the trajectory control system and on the AACs configuration (i.e. location of gyros) which affects the bus attitude estimation error. Therefore its best performance ( $0.02^\circ$ ) is obtained with concept B (bus mounted gyros) at low altitude and its minimum performance is  $0.3^\circ$  for concept A1 at high altitude.
  - the inertial bus attitude control is much smoother than the one relative to the surface (Fig. 8), therefore the corresponding fuel consumption is 10 times lower and the HGA pointing accuracy 4 times better.
- on the AACs configuration : there is no large performance discrepancy between the two possible spacecraft architectures (bus or platform mounted gyros and articulated HGA), except that gyros which are collocated with the pointing instruments produce a better pointing performance which in turn improves the spacecraft navigation performance.

Given these results the following recommendations can be given :

- The concept of bus relative attitude control with respect to the estimated comet surface normal at the selected landing site during the entire guided descent phase should be rejected because of its expected high consumption (about 15 kgs for one hour) and bad performance (up to  $17^\circ$  attitude control error for the bus at low and high altitudes, and up to  $0.6^\circ$  pointing error for the HGA) ;
- The proposed control concept consists in the following GNC operations :
  - from the initiation of the descent down to an altitude of about 200m : the spacecraft attitude is smoothly controlled with respect to the quasi-inertial reference of the surface estimated normal at the selected landing site, based on the ellipsoidal comet model, the estimated position of the SLS and the on-board estimated comet rotational motion. During that time, the surface normal measurements with either the radar or the laser are filtered using the on-board comet model, and the local normal at the SLS is

estimated, producing an angular estimation error as shown on Fig. 9 ;

- at about 200m altitude, the normal measurements filtering process is stopped because the estimation error is expected to have reached its minimum attainable value. The last estimation of the local normal at the SLS is stored and is used as the new quasi inertial reference corrected of the comet estimated rotation for the bus attitude control. That is, a slew maneuver of the bus brings its attitude from the previously roughly estimated surface normal reference towards the newly filtered surface normal reference ;
- from about 200m down to landing, the bus attitude is controlled with respect to the previously estimated surface normal, without processing the normal measurements from either the radar or the laser.

The advantages of this control concept are the following :

- it ensures the minimum attainable bus attitude control error, composed of the comet surface normal estimation error of about  $2^\circ$  at 200m, and the absolute bus attitude control error of less than  $0.5^\circ$  ;
- the control is smoother, which improves the pointing accuracy of the HGA ( $< 0.03^\circ$ ) and surface instruments ( $< 0.5$  mrad) and reduces the fuel consumption (about 1.5 kgs for one hour) ;
- this concept is robust and safe with respect to surface measurements failures because it is not directly dependent on the instruments outputs ;
- the bus attitude control is possible down to a few centimeters from the comet surface because surface measurements are not necessary under about 200m altitude. Furthermore the expected residual angular rates are about  $0.01^\circ/\text{s}$ , ten times lower than the specification.

Complete levels B and C simulations should also prove the interest for this strategy since any environment or surface sensors performance degradation does not pollute the spacecraft attitude control but only the normal measurements filtering process.

The baseline spacecraft architecture (platform mounted gyros) is recommended because it improves the instruments pointing accuracy which affects the surface normal estimation error and the spacecraft navigation error.

## 4 AUTONOMOUS GNC CONCEPTS FOR THE DESCENT PHASE

In this section are reported the investigation and performance analysis of Guidance, Navigation and Control concepts applicable to the descent phase for the spacecraft trajectory only (but including instruments pointing issues), the AACCS analyses being uncoupled in a first step (Section 3).

### 4.1 Objectives and Requirements

The descent and landing scenario is as shown on Fig. 10. The open-loop descent is initiated at the Descent Initiation Point on the Descent Preparation Trajectory . At this point, a deboost maneuver is commanded in order to start a ballistic arc encountering the normal to the surface at the Selected Landing Site (SLS) at about 1 to 3 km from the surface. Then, the guided descent is initiated. First the spacecraft is synchronized with the selected landing site using cruiser 10N gas thrusters. Finally, a final descent along the normal to the surface is performed, the vertical commanded landing velocity being typically 1m/s up to 100-200m altitude where it is reduced to 10cm/s.

The objectives of the GNC analyses were to investigate and analyse flexible and robust GNC strategies for the open-loop descent (i.e. type of orbit for descent preparation, trade-off of different conditions at the Synchronization point) and the guided descent (i.e. type of measurements to be processed, navigation filter, guidance and control concepts) in order to achieve a safe landing on a scientifically meaningful landing site. The available navigation instruments and associated measurements are those described in Section 1.3.

This phase of the mission is a very critical one, due to the poorly known environment and perturbations, comet complex rotational dynamics and irregular topography. Therefore the selected GNC system must be robust enough to cope with these a-priori unknown external conditions. The associated requirements are the following :

- horizontal position error relative to the SLS at the synchronization point :  $< 100$  m (3 sigma),
- horizontal position error at landing wrt the SLS :
  - 20m in case of Laser Assisted Navigation,
  - 50m in case of Landmark Assisted Navigation,
  - 200m in case of Unassisted Navigation ;
- horizontal velocity at landing :  $< 1$  cm/s,
- vertical velocity at landing :  $< 10$  cm/s.

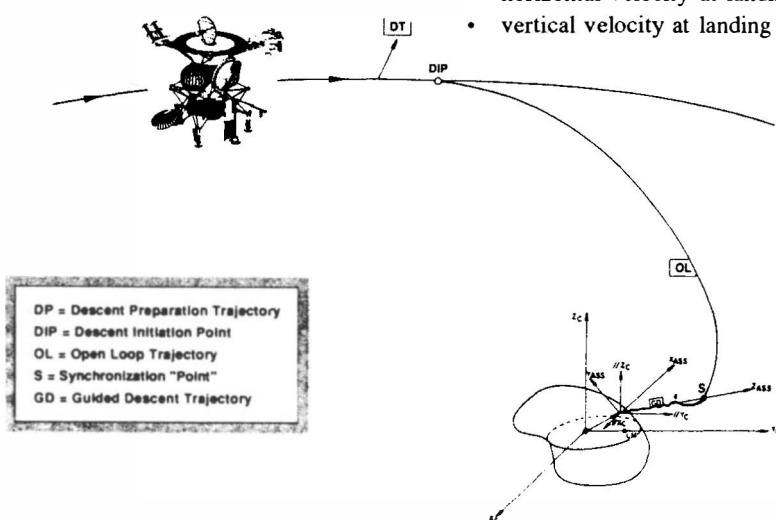


Fig. 10 : Descent and Landing Scenario

## 4.2 Selected GNC Strategies and Concepts

For the open-loop descent, the different GNC strategies which have been investigated consist in Descent Preparation elliptic orbits or hold points or inertial station points, followed by either an elliptic, hyperbolic, or vertical arc. In addition, four open-loop terminal states concepts were investigated corresponding to the possible navigation strategies of the guided descent, with characteristics as low and high altitudes, low and high descent velocities and minimum covariance matrix at synchronization point.

Four navigation strategies have been selected for the guided descent phase :

- Laser assisted navigation (LSN). A 3D-topographic map of an area around the SLS is constructed on the ground during the detailed mapping phase and stored in the on-board computer. During the guided descent, a small area is periodically (every few minutes) scanned with the laser mapper (Fig. 12). The correlation of the obtained topography map with the on-board one permits the estimation of the relative horizontal position of the spacecraft with respect to the SLS. This strategy is very attractive because of the very accurate obtained information. Two options appear from a guidance point of view : a continuous descent down to touchdown (LSN1) and a descent with intermediate hold points (LNShp) to construct the topography maps and, eventually, to select a more appropriate landing site.

- Radar navigation (RN). At the beginning of the guided descent, the comet surface is scanned by the radar instrument in a vertical direction. The scanning is performed until an area with roughness compatible with a safe landing is found. Then the landing site (SLS) is updated to this autonomously selected new site (ASLS). The drawback of this concept comes from the fact that the roughness measurement is not very accurate (standard deviation of the range measurements is provided by the radar) and also from the loss of information on the spacecraft relative horizontal position.

- Landmark assisted navigation (LN). In this option, some information on the spacecraft horizontal position relative to the SLS is available on-board from the LOS measurement provided by the artificial landmark tracker or by the camera used to track natural landmarks (if

appropriate illumination conditions are ensured). If an artificial landmark is used, it must be ejected from the spacecraft and delivered to the comet surface before initiating the descent. Preliminary performance assessment in terms of dispersion at impact has been investigated in the frame of the AANT study (Ref. 4).

- Unassisted navigation (UN). In this concept, the GNC system does not rely on any natural or artificial external reference on the comet surface and must perform the descent without any measurement of the spacecraft relative horizontal position with respect to the SLS (Fig. 11). This back-up strategy is selected for a rough landing near a SLS or for landing anywhere on the comet when no landing site has been selected. It is the simplest one : it involves neither the mass penalty and the complexity of an artificial landmark nor the image / radar / laser processing requirements. On the other hand, the major drawback comes from the large errors at landing which depend on the uncertainty in the comet characteristics.

Information on the range and relative velocity of the spacecraft with respect to the comet surface as well as on the normal to the surface at SLS is available from the radar measurements for all the navigation strategies.

Guidance concepts have been designed to force the spacecraft on the reference trajectory applicable to the navigation strategies cited above. Constant position, constant velocity, exponential braking or constant braking laws are combined with specific parameters in order to realize a corridor acquisition and a final descent guidance phases. Hold points acquisition and landing site update concepts are also possible.

Different state vector estimation concepts (measurement processing without prediction, linear observer and Kalman filter) have been investigated in terms of complexity and performance and at the end the linear observer concept has been selected. Pseudo-measurements of the state vector are constructed using available ones and comet on-board models and an adequate on-board state propagation model using the comet gravitational field estimated parameters is used. The gains of the linear observer are computed before hand using steady state gains of a continuous Kalman filter.

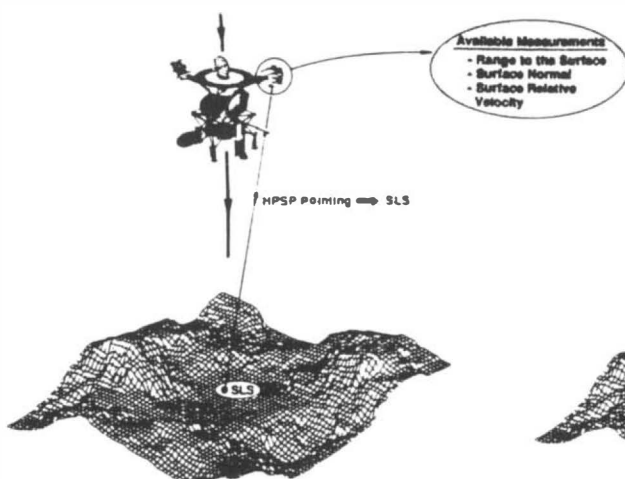


Fig. 11 : Unassisted Navigation

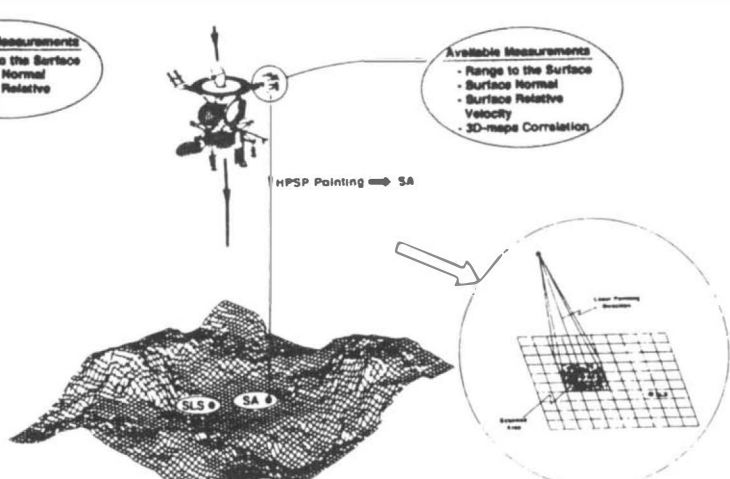


Fig.12 : Laser Assisted Navigation

### 4.3 GNC Concepts Detailed Performance Analysis

The evaluation method followed to analyse the selected GNC concepts was the same as for the AACs analyses (Section 3.4.1), with the three levels A, B and C of parametric analyses which only the first is reported here.

#### 4.3.1 Open-loop Descent Results

Table 5 presents the trade-offs results for the Descent Preparation orbit design, obtained from a covariance analyses performed with AANTool. Dispersion and knowledge errors in position and velocity obtained at the synchronization point at 1500 m altitude with a vertical velocity of 1 m/s are shown for different types of orbits and de-boost maneuvers. The best performance (about 85 m in dispersion and knowledge, 1 sigma) is reached for the 20 kms x 6 kms polar elliptic orbit with a de-boost maneuver at the periapsis. A performance improvement is achieved when the SLS is on the comet nucleus equator, thus enabling the use of an equatorial orbit. The requirement of 100m, 3 sigma, is not fulfilled due mainly to the initial errors at the DIP (about 50 m in dispersion and knowledge).

#### 4.3.2 Guided Descent Results

Detailed numerical analyses of the selected GNC concepts presented in Section 4.2 have been performed by Monte-Carlo simulations with AANTool in order to demonstrate the feasibility of those concepts in terms of navigation and control errors in accuracy and velocity at landing. In particular, the analyses have revealed the :

- influence of open-loop terminal state concepts on the GNC performance,
- influence of using hold points on the laser based navigation performance,
- validity of the guidance concepts,
- trade-off between the laser and radar measurements,

- evaluation of the relative velocity estimation based on Doppler measurements and on-board comet models,
- trade-off between using the commanded or measured acceleration and HPSP pointing direction in the estimation process,
- trade-off between the four navigation strategies,
- most appropriate GNC concept for the guided descent depending on spacecraft environment, instruments characteristics and landing site location.

Three main analyses are presented here : first, the trade-off between the possible descent initial conditions (Table 4) for the Laser and Radar Assisted Navigation (LSN and RN) strategies has been answered (Table 6).

Concept	S1	S2	S3	S4	
Selected	$h_s$	700 m	600 m	1500 m	2500 m
Data	$(V_r)_s$	-2 m/s	-0.5 m/s	-1 m/s	-2 m/s
	$(V_H)_s$	1.46 m/s	1.50 m/s	0.80 m/s	0.77 m/s

$h$ : altitude

$V_r$ : vertical velocity in the SLS-frame

$V_H$ : horizontal velocity in the SLS-frame

Table 4 : Open-loop terminal states concepts

The measurements used are the Doppler, laser altimeter, laser scanning (relative attitude and min/max roughness) and the laser correlation for the LSN case. The performance obtained are quite similar for the different envisaged concepts. However due to the lower fuel consumption, and because the guided descent is long enough to compensate for the initial knowledge errors, the S3 concept is recommended for the LSN strategy. Concerning the RN strategy, concept S1 is recommended because the ASLS is much closer to the initial landing site (result not shown in the table) due to the fact that the initial knowledge and dispersion matrices are smaller than for the S2 concept.

Open Loop Terminal State Concept 3																	
Descent Preparation Strategy	Orbits											Hold Point	Inertial Station Point				
	20 Km x 20 Km equatorial orbit	20 Km x 20 Km polar orbit	20 Km x 6 Km polar orbit				20 Km x 6 Km equatorial orbit										
De-boost Radius	20 Km	20 Km	6 Km	6 Km	6 Km	6 Km	6 Km	6 Km	6 Km	6 Km	6 Km	Hold Point	Inertial Station Point				
Fuel consumption	0.80 m/s	0.404 m/s	0.926 m/s	0.434 m/s	0.297 m/s	1.12 m/s	1.035 m/s	0.987 m/s									
Transfer time	4.93 h	8.2 h	0.69 h	1.64 h	8.21 h	0.55 h	0.69 h	0.69 h									
Dispersion (1 $\sigma$ )	Radial	456 m	118 mm/s	917 m	247 mm/s	68 m	27 mm/s	142 m	43 mm/s	906 m	245 mm/s	59 m	26 mm/s	64 m	26 mm/s	65 m	26 mm/s
	Down-track	415 m	34 mm/s	829 m	37 mm/s	52 m	15 mm/s	104 m	12 mm/s	826 m	36 mm/s	47 m	17 mm/s	44 m	14 mm/s	55 m	17 mm/s
	Cross-track	72 m	9 mm/s	116 m	35 mm/s	20 m	6 mm/s	29 m	5 mm/s	115 m	34 mm/s	19 m	6 mm/s	42 m	12 mm/s	21 m	6 mm/s
Knowledge (1 $\sigma$ )	Total	620 m	123 mm/s	1241 m	252 mm/s	87 m	32 mm/s	178 m	45 mm/s	1231 m	250 mm/s	77 m	32 mm/s	88 m	32 mm/s	88 m	31 mm/s
	Radial	423 m	110 mm/s	896 m	243 mm/s	64 m	28 mm/s	142 m	46 mm/s	896 m	243 mm/s	54 m	25 mm/s	63 m	28 mm/s	64 m	28 mm/s
	Down-track	386 m	33 mm/s	817 m	37 mm/s	51 m	15 mm/s	103 m	13 mm/s	818 m	37 mm/s	46 m	17 mm/s	41 m	13 mm/s	51 m	15 mm/s
	Cross-track	66 m	8 mm/s	114 m	35 mm/s	19 m	5 mm/s	30 m	6 mm/s	114 m	35 mm/s	18 m	5 mm/s	40 m	12 mm/s	20 m	6 mm/s
	Total	577 m	115 mm/s	1219 m	248 mm/s	84 m	33 mm/s	178 m	48 mm/s	1219 m	248 mm/s	74 m	31 mm/s	85 m	33 mm/s	85 m	33 mm/s

Table 5 : Trade-offs results of different open-loop strategies

Navigation strategy		LSN1			LSN2			RN1			RN2		
Open Loop Terminal state concept		S3			S4			S1			S2		
Fuel consumption (Kg)*		3.23	0.59	3.28	4.50	0.41	4.52	4.07	0.68	4.13	3.79	0.72	3.85
Landing Accuracy (m)	East*	6.1	3.9	7.2	7.5	3.6	8.3	0.1	0.3	0.3	2.1	1.8	2.8
	North*	4.3	2.6	5.0	6.0	2.9	6.7	-2.8	0.3	2.9	0.1	2.2	2.2
Landing velocity (mm/s)	East*	7.0	5.1	8.7	-7.6	5.0	9.1	-0.1	2.7	2.8	0.2	5.3	5.3
	North*	-1.3	2.5	2.8	-1.0	2.8	3.0	1.4	2.2	2.6	2.4	3.2	4.0
	Vertical*	106.3	4.2	106.4	106.6	5.1	106.7	108.0	0.1	108.0	106.1	0.4	106.1

\* Mean values, random values (1 $\sigma$ ) and total RMS values respectively

Table 6 : Trade-offs results of open-loop terminal states concepts

The second analysis concerns the performance assessment of the Radar Assisted Navigation strategy with autonomous landing site update according to the roughness measurement for different comet topography conditions : a small flat area found after some surface scanning (the ASLS may be tracked as a landmark), a large flat area found after some surface scanning (the ASLS can not be tracked as a landmark), a large flat area found just after starting the guided descent (early LS update) and no flat area found before landing (i.e. Unassisted Navigation strategy). Results are illustrated on Fig. 13 where the landing accuracy with respect to the real value of the actual ASLS (located at the origin of the East / North frame) and the landing dispersion (i.e. location of the ASLS relative to the GSLS) are plotted with the same scale. The conclusions are that a very good landing accuracy is achieved even if the flat area is not tracked as a landmark (4m x 3m, 3 sigma) and that landing dispersions are about the same (about 80m x 125m, 3 sigma) for large and small areas after some surface scanning. However the early LS update degrades the landing performance. This analysis shows the better performance of the RN strategy compared to the Unassisted Navigation, assuming the roughness measurement is good enough for landing site on-board selection.

The third analysis focused in this paper concerns the trade-off between the different GNC concepts :

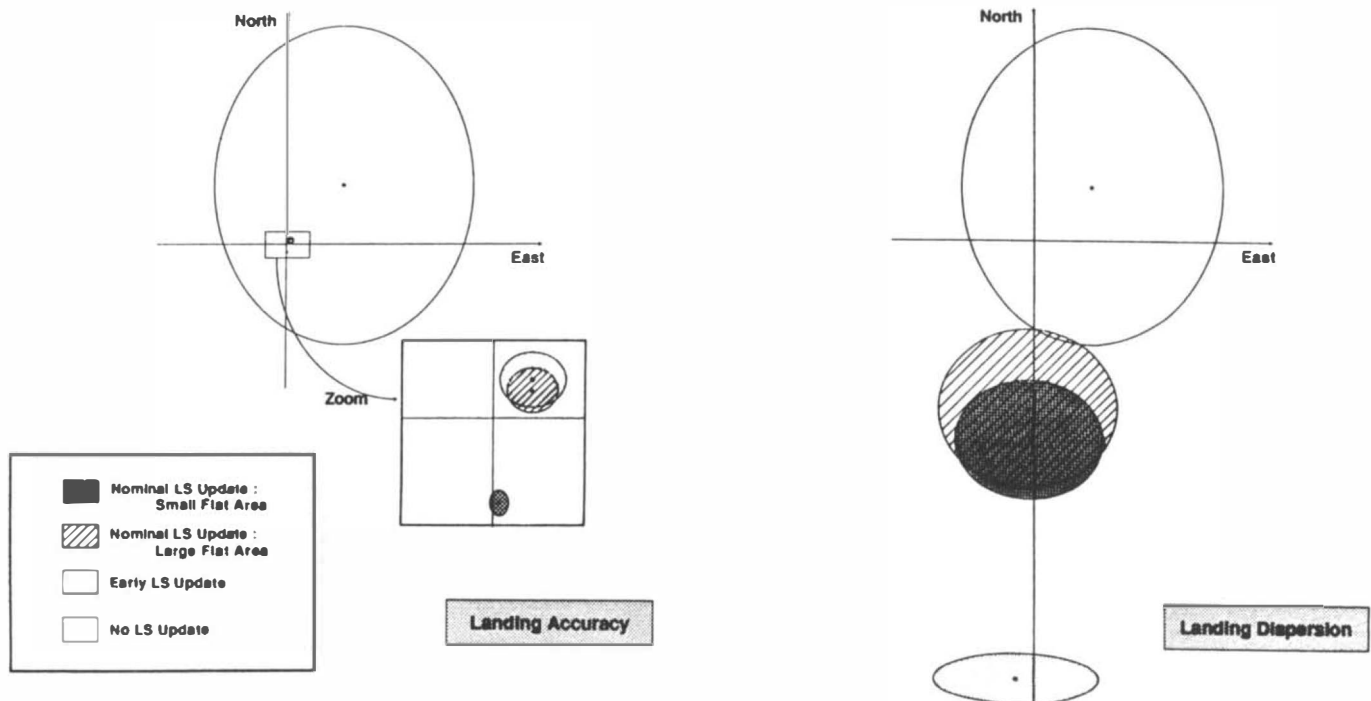


Fig. 13 : Radar navigation performance for different comet topography conditions

Navigation strategy		LSN1			RN1			UN			LN1			LSNh <sub>p</sub>		
Flight time		~1800 sec			~900 sec			~900 sec			~1800 sec			~3600 sec		
Fuel consumption (Kg)*		3.23	0.59	5.0	3.33	0.19	3.9	4.09	0.57	5.8	2.93	0.16	3.41	5.32	0.44	6.64
Landing Accuracy (m)	East*	6.1	3.9	17.8	1.3	0.8	3.7	19.8	44.4	183	4.2	10.1	34.5	7.5	4.2	20.1
	North*	4.3	2.6	12.1	0.9	0.7	3.0	19.5	50.1	189.8	5.8	8.5	31.3	8.1	1.7	13.2
Landing velocity (mm/s)	East*	7.0	5.1	22.3	4.2	3.9	15.9	4.6	4.9	19.3	7.3	5.5	23.8	7.4	5.1	22.7
	North*	-1.3	2.5	8.8	3.1	3.4	13.3	2.1	5.2	17.7	6.8	2.1	13.1	-1.7	2.7	9.8
	Vertical*	106.3	4.2	118.9	107.8	0.1	108.1	106.4	4.3	119.3	105.1	3.6	115.9	105.5	3.2	115.1

\* Mean values, random values ( $1\sigma$ ) and total RMS values respectively

Table 7 : Trade-off results of navigation strategies

- laser assisted navigation with the S3 open-loop terminal state concept (LSN1),
- radar search navigation with the S1 concept (RN1) (assuming a large flat area),
- unassisted navigation with the S1 concept (UN),
- landmark assisted navigation with the S3 concept (LN1),
- laser assisted navigation with the S3 concept and with an hold point at 500m altitude during 30mn (LSNh<sub>p</sub>).

The results are presented in Table 7 (landing accuracy is given with respect to the ground or autonomously selected landing site when applicable, i.e. for the RN strategy). The horizontal error at landing is about (3 sigma) 21m for the LSN (24 for the LSNhp), 5m for the RN (but with a dispersion of 156m), 230m for the UN and 46m for the LN. The vertical velocity error with respect to the reference value of 10cm/s is less than 2cm/s and the horizontal velocity error less than 2.5cm/s in all cases. The hold point keeping accuracy is about 12m and 8m in horizontal and vertical position, and 20mm/s and 4mm/s in horizontal and vertical velocity.

Other analyses have shown that a descent strategy with no open-loop phase degraded the performance in landing accuracy and fuel consumption, while the use of an equatorial orbit for the Descent Preparation trajectory has shown a very small performance improvement.

#### 4.4 Recommendations

The conclusion output from the previous results is that the Laser Assisted Navigation Concept starting at 1500m altitude and 1m/s vertical velocity after an open-loop descent initiated by a de-boost maneuver at the periapsis of a polar equatorial orbit should be selected as the baseline GNC concept for the descent phase. With this strategy, all the landing requirements (scientific and safety) are fulfilled with respect to the ground selected landing site. However this GNC concept involves an expensive mission cost due to the use of the laser instrument and the associated on-board 3D map correlation techniques involved for measurement processing.

A first optional strategy, the Radar Assisted Navigation strategy, is proposed. With this strategy, the safety and degraded accuracy landing requirements are fulfilled with respect to the on-board selected landing site, but not the scientific ones. However, this strategy corresponds to a low cost spacecraft architecture without the laser instrument but with possibly the need for an improved radar roughness accuracy.

The second optional strategy which is proposed is the Radar Unassisted Navigation strategy. With this strategy, the degraded accuracy landing requirements are fulfilled with respect to the ground selected landing site, but the scientific and safety requirements are not ensured. However, this strategy corresponds to the lowest cost spacecraft architecture.

### 5 TOUCHDOWN CONTROL

As concerns the on-comet GNC operations, the following points have been investigated in the study :

- touchdown control : concepts for controlling and monitoring the touchdown,
- stabilization of the spacecraft on the comet : methods for controlling the tipping over and the sliding of the spacecraft while standing on the comet,
- sampling operations : monitoring and control of nominal and back-up sampling modes,
- on-comet attitude and pointing : methods for Earth recovery after an eclipse,
- multi-landing : strategies for immediate take-off and re-landing in case of contingency.

In this paper, only the touchdown control and the related performance assessment are discussed. The reader can refer to Refs. 3, 4, 8 for a more detailed presentation of the other GNC analyses concerning the on-comet operations.

#### 5.1 Assumptions and Requirements

The basic requirements on the GNC system for the on-comet phase are recalled hereafter :

- After landing, the spacecraft must be actively controlled in position and attitude in order to prevent any unsafe event (rebound, tip-over, sliding).until the spacecraft is safely anchored to the surface soil,
- Sampling operations must be monitored and an active control in position and force must be applied in case of any non nominal event (anchoring failure),

- Furthermore, the spacecraft inertial attitude must be known at all time to an accuracy allowing the recovery and tracking of the Earth by the HGA.

The main assumptions applicable to the GNC operations for the on-comet phase are the following.

Spacecraft architecture : the assumptions listed in Section 3 are applicable, in particular the mass of the spacecraft around 2600 kg, the maximum inertia about  $7500 \text{ kg m}^2$ . The spacecraft center of mass height above the legs end-points is about 2m and the distance between two legs of 2m. Only the baseline AACs architecture is investigated for the on-comet phase.

Sensors and actuators : in addition to the nominal equipments already mentioned in Section 1.3, contact sensors may be available on each landing leg in order to independently detect the contact with the comet surface. The three accelerometers mounted on the spacecraft central body may also serve for touchdown detection. As concerns actuators, a cold gas thrusters propulsion system must be used during the on-comet operations in order not to pollute the landing site. The available thruster level is 30N with an Isp of 60s offering a complete 3-axis force and torque control, and two 70N thrusters mounted on the top of the spacecraft in order to provide a downwards force in case of non nominal events during sampling operations.

The numerical conditions under which the GNC system must meet the above mentioned requirements are the following :

- spacecraft landing vertical downwards velocity : 10 cm/s,
- spacecraft lateral dispersion velocity at landing : a few cm/s (1cm/s TBC),
- spacecraft maximum angular rate at landing :  $0.1^\circ/\text{s}$ ,
- spacecraft maximum angular alignment error wrt the surface normal at landing :  $3^\circ$ ,
- drilling operation maximum force and torque : 100 N and 10 Nm,
- comet surface characteristics : friction coefficient from 0.1 to 0.9, maximum roughness of 50 cms.

#### 5.2 Selected Control Concepts

As under low gravity field and/or high surface friction conditions, the weak natural stability of the spacecraft is not sufficient to ensure a safe passive touchdown (e.g. tipover in case of pad blocking on the irregular surface) or to prevent rebound, active control concepts have been proposed for the touchdown.

A first control concept assumes the availability of contact sensors information. The cold gas thrusters are used to generate torques for controlling the spacecraft attitude and to press the lander towards the comet surface. The controlled variables in rotation (angular rate and attitude of the spacecraft with respect to the comet surface) are not directly measured, but can be reconstructed from the gyros measurements and the estimation of the comet rotational dynamics.

In this concept, the control strategy depends on the number of pads at contact. When only one pad rests on the surface, a torque is created along the axis defined by the other pads in such a way to rotate the spacecraft in the

right direction, while the angular rates around the other axes are controlled to zero. At the same time, a force along the bus axis towards the comet surface is created to preserve the contact of the resting pad. When two pads are resting on the ground, the torque is created along the axis joining the two contact points. When the three pads are in contact, the force along the bus axis is maintained until the complete stabilization of the spacecraft (see Figure 14).

The previous scenario of the active touchdown assumes the availability of the footpad's contact sensors information, which affects the robustness of the control, since the sensors are located far from the GNC calculator, and the information needs to be uplinked. So, the investigation of a back-up scenario which requires less hardware is recommended. The following approach is proposed :

- at contact, the surface reaction force contributes to the accelerometers measurements, in addition to the forces created by the thrusters. In order to distinguish both, it is proposed to cut off the GNC system just before the contact, so only the reaction force remains.
- once the first footpad touchdown is detected, a thrust is performed along the bus axis, towards the comet surface so as to increase the reaction force. Then, the friction force which stabilizes the spacecraft in translation is proportionally increased. The control force is applied within the surface delimited by the pad ends, which guarantees the stability in rotation whatever are the pads at contact, and so the robustness of the design.

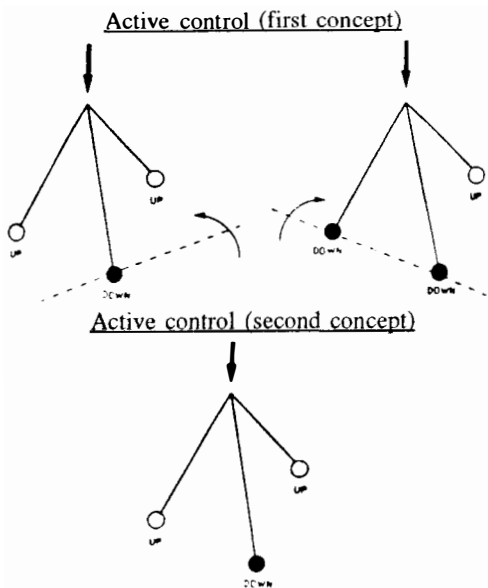


Fig. 14 : Touchdown Control Concepts

### 5.3 Touchdown control concepts detailed performance analysis

The analyses of the touchdown control concepts are based on time simulations of the spacecraft attitude and position dynamics and control starting at an altitude of less than 1m (i.e. about 3 m for the spacecraft center of mass) from the comet surface, with a vertical downwards velocity of 10 cm/s. Nominally, the spacecraft attitude is assumed to be aligned with the surface normal at the selected landing site. This means that for example, if the

surface has a mean slope of 30° with respect to the local vertical, the spacecraft is also tilted of 30° with respect to the local vertical.

It is assumed that there is no control operation in attitude and position (i.e. no actuation at all) until the contact of one pad with the comet surface is detected by either contact sensors or the accelerometers measurements. However the possible dispersions induced by the spacecraft control system are introduced in the form of initial errors in spacecraft angular alignment with respect to the surface normal and errors in lateral velocity. The simulations have been performed with numerical values for these initial errors (respectively up to 20° and 5 cm/s) much higher than the specified ones (resp. 3° and 1 cm/s) in order to well differentiate their effects on the different control concepts.

The control concepts have been simulated with a non rotating comet, an ellipsoid comet model (flat surface) and no external perturbations. However the surface slope has been made varying from 0° to 30° and the friction coefficient from 0.1 to 0.9. Indeed, the primary objective of the simulations is to trade-off the different control concepts in presence of the main disturbing effects (surface slope and friction) and therefore other secondary sources of perturbation could be neglected.

The performance objectives associated to the GNC simulations for the touchdown analysis are the following:

- PO1** tranquillization time after touchdown,
- PO2** fuel consumption,
- PO3** HGA pointing control error.

Simulation results are shown on Table 8. The first row specifies the control concept, the four next rows give the selected fixed parameters and their associated variations and the last three rows list the performance objectives, their associated requirements and the obtained values. The performances shown may be considered as 3 $\sigma$  values. The cases where the performance does not meet the requirement have bolded borders.

### 5.4 Synthesis and Recommendations

The synthesis of GNC simulations results for the touchdown control is the following.

- With no control, the spacecraft rebounds as the pads contractions become negative because the spacecraft center of mass has an upwards velocity and the comet gravity is too low to counteract it (an optimization of the landing pads spring and damper characteristics could change this but the robustness of the system would be very low) ;
- The semi-active and active control concepts ensure permanent contact of the landing pads on the comet surface for all envisaged conditions (even a touchdown with 50° of initial angular misalignment is feasible but the tranquillization time would be very important because of the sliding velocity generated by the control) ;
- the active control concept gives a smaller tranquillization time but the fuel consumption is increased because of the additional torque control ;
- the HGA pointing is very much disturbed at touchdown : 0.2° maximum offset for a nominal touchdown.

control concept		no control	semi-active control						active control					
comet surface slope (deg)	any	0	0	0	0	30	30	0	0	0	0	30	30	0
comet surface friction coefficient	any	0.1	0.1	0.1	0.9	0.1	0.1	0.1	0.1	0.1	0.9	0.1	0.1	0.1
spacecraft initial angular error (deg)	any	0	20	20	20	0	20	0	20	20	20	0	20	0
spacecraft initial lateral velocity (cm/s)	any	0	0	5	5	0	5	0	0	5	5	0	5	0
Performance Objective	Reqt	SIMULATIONS RESULTS												
PO1 (s)	No reqt	rebound	13	53	56	70	18	63	13	48	54	48	18	63
PO2 (kg)	No reqt		1.3	5.3	5.9	7.3	1.8	6.2	1.3	9.8	10.5	9.5	1.9	7.8
PO3 (deg)	0.18		0.15	0.9	0.9	0.9	0.25	1	0.15	0.9	0.9	0.9	0.25	1

Table 8 : Trade-offs results of the control strategies at touch down

From these results, the following recommendations can be given :

- The control of the touchdown is mandatory in order to avoid unsafe events like rebound and sliding in all environments.
- The semi-active control is recommended for the following reasons :
  - there is no need for contact sensors as additional hardware. The touchdown is detected by a step of 0.5 mg in the accelerometers measurements,
  - if the landing initial conditions are nominal, the expected performance of the semi-active control concept is 15s of tranquillization time and less than 1.5 kg of fuel consumption,
  - a complete 30N cold gas thrusters configuration is not needed since no control torques are applied, but only a 60N downwards vertical force generated by two opened thrusters located at the top of the spacecraft (may be standard hydrazine thrusters since only upwards thrusters are used).
- The HGA pointing control is not compliant with the specification during the touchdown. The HGA could be roughly controlled using the gyros and encoders measurements during the touchdown and then a search mode is initiated with the RF sensors after spacecraft tranquillization.

## 6 CONCLUSIONS

During the phase 1 of the AANT Study, different GNC strategies and concepts applicable to the near comet phases of the ROSETTA mission (i.e. detection, observation, ejection, descent and landing and on-comet operations) have been defined after a detailed review and critical analysis of GNC requirements and assumptions.

The algorithms corresponding to the selected GNC strategies and concepts, but also to detailed models of the real world (comet and spacecraft definition and dynamics, instruments) have been designed, developed and integrated in a dedicated software tool (AANTool) for performance assessment and trade-offs. This software can be viewed as a "phase B" simulation software which could serve other deep space programmes with only few updates thanks to its completeness and flexibility.

Based on intensive simulations campaigns, baseline GNC concepts and alternatives have then been selected for

more detailed functional design in Phase 2 and performance evaluation of the on-board software on a real time test bed in Phase 3 of the study.

## ACKNOWLEDGEMENTS

The simulation tool "AANTool" has been developed by INISEL ESPACIO (Spain). We acknowledge Mr Lluis Cabre and Ms Maria Balaguer for their participation to this development.

## REFERENCES

- ROSETTA/CNSR System Definition Study, Final Report MATRA ESPACE, January 1991, *ESA Contract 8228/89 /NL/SK*.
- Advanced GNC Concepts and Techniques for an Interplanetary Mission, C. Champetier, P. Regnier, J. de Lafontaine, February 1991, *14<sup>th</sup> Annual AAS Guidance and Control Conference*.
- Autonomous and Advanced GNC Techniques for the Interplanetary ROSETTA Mission, C. Champetier, J. B. Serrano, J. de Lafontaine, June 1991, *First International Conference on Spacecraft Guidance, Navigation and Control Systems*.
- Autonomous and Advanced Navigation Techniques Study, Phase 1 Summary Report MATRA MARCONI SPACE, August 1992, *ESA Contract 8808/90/NL/PM*.
- Study and Design of a Comet Approach and Landing System, October 1991, Executive Summary Officine Galileo, *ESA Contract 7988/88/NL/PB(SC)*.
- AANTool : a Software Tool for the Design and Analysis of Deep Space Autonomous GNC Systems, C. Champetier, P. Regnier, J.B. Serrano, L. Cabre, J. de Lafontaine, August 1992, *ESA Workshop Spacecraft Guidance Navigation and Control Systems – Software for Design and Implementation*.
- Autonomous and Advanced Navigation Techniques Study, Attitude and Articulation Control System. Part 1 : Analysis. *Technical Note MATRA S414/NT/75.90*, Issue 1, May 6, 1991, *ESA Contract 8808/90/NL/PM (SC)*
- Autonomous and Advanced Navigation Techniques Study, On-comet operations. Part 1 : GNC analyses. *Technical Note MATRA S414/NT/80.90*, Issue 2, April 1992, *ESA Contract 8808/90/NL/PM (SC)*

## AUTONOMOUS ON-COMET OPERATIONS ASPECTS OF THE ROSETTA MISSION

K. Schilling, H. Roth and B. Theobold

Fachhochschule Ravensburg-Weingarten, Postfach 1261, D-7987 Weingarten, Germany

**Abstract.** The aim of the ROSETTA-mission is to return pristine material from a comet to Earth. In particular during the phase near and on the comet, spacecraft operations have to be performed autonomously in a rather uncertain environment. This paper studies for the on-comet phase the operations constraints, and analyses an adaptive control concept for the sampling of cometary materials from the scarcely known soil. The adaptive control algorithm identifies during sampling the crucial parameters characterizing the cometary soil and the spacecraft's subsystem performances. According to these measurements it initiates an adaption of the drill's penetration rate and of the AOCS cold gas thrusting activities. This technique has been assessed in computer simulations and exhibited advantages regarding the reliability of operations as well as in the efficient use of the limited S/C-resources.

**Key words.** Spacecraft Operations, Autonomous Systems, Space Robotics, Adaptive Control, Mission Analysis.

### INTRODUCTION

The aim of the ROSETTA-mission is the return of pristine cometary material to Earth for detailed investigations with extensive laboratory equipment. From these experiments the scientists expect to gain further insight about the origin and the formation processes of our solar system. The scientific importance of this mission led to its selection as one of the four cornerstones in the scientific programme of the european space agency (ESA).

According to the current plannings a launch in December 2002 will lead to an encounter of comet Hartley-2 in February 2008 and an Earth return in November 2010. But a requirement for the mission design is still to provide sufficient flexibility to accommodate a change of the target comet (due to scientificly even more favourable opportunities or due to potential launch delays). In order to avoid active -and thus very risky- periods near perihel the comet encounter will take place at a distance between 5 and 6 AU. This means the signal propagation delay will be about 40 minutes (one way) and ground control interaction is very limited during this critical period.

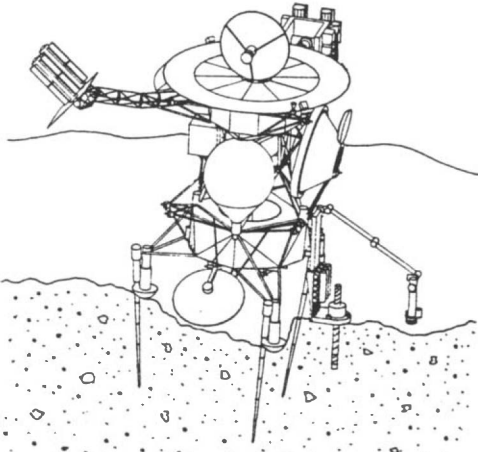


Figure 1: The spacecraft configuration during on-comet operations with deployed anchors and drill equipment.

Thus challenging requirements regarding autonomous on-board reaction capabilities exist. In addition the knowledge on expected cometary environments is not very detailed. The broad variation range for the comet characteristics will only be narrowed during comet approach, when during the observation phase the orbiting spacecraft will transmit actual measurements from remote sensing instruments. Unfortunately the mechanical properties of the soil, determining the sampling scenario, can hardly be derived from

these measurements and will still vary in a broad band. Thus the on-comet operations require strategies to quickly adapt control actions to actual sensor data, gained during the sampling process.

## SCENARIO OF THE ON-COMET PHASE

After landing, in the nominal operations sequence the spacecraft is stabilized via cold gas thrusting, and it should autonomously reestablish as quickly as possible the communication link with the ground control centre, which will be lost during the final descent. Then first information about the landing site will be transmitted, to allow on ground a quick assessment of the actual situation. Meanwhile the spacecraft must autonomously (due to the signal propagation delay) handle the interaction with the uncertain environment and the maintenance of the radio link despite disturbances.

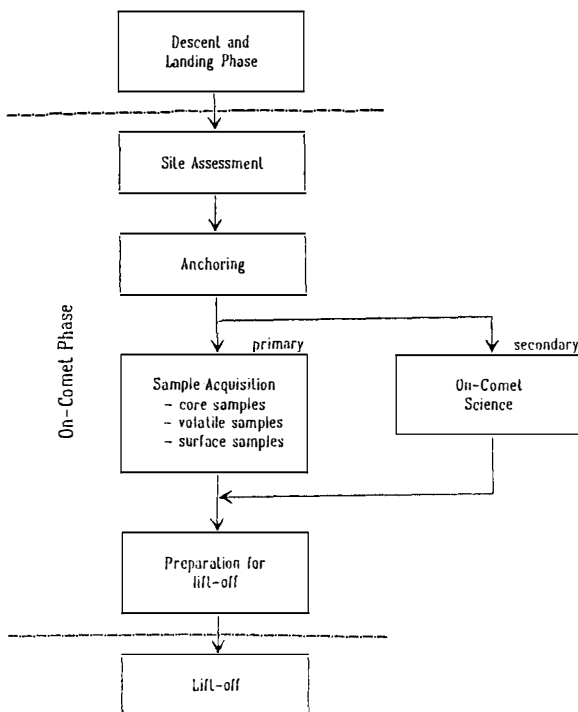


Figure 2 : Schematic of the on-comet operations flow

If the location is considered appropriate so far, a test anchor equipped with accelerometers and temperature sensors is used to obtain first data on the mechanical properties of the subsurface layers. If these data are satisfactory according to scientific and technical criteria, the anchors will

be deployed, in order to provide a stable fixation for the on-comet operations, in particular for the sampling. The sample acquisition system (SAS) should then collect three types of samples :

- **core sample** : to document the stratigraphic soil properties to a maximum depth of 3 m; mass: ca. 10 kg
- **volatile sample** : volatile gases, expected to be bound in the ice of the comet's interior; mass: up to 100 g
- **surface sample** : samples from different surface locations in the reach of the SAS; mass : up to 5 kg.

To perform these tasks the actual version of the SAS consists of the following three parts:

- **Drilling System**, including the drilling table (to be lowered to the surface after landing) and sampling tubes, to be successively introduced into the borehole,
- **Robotic Arm**, to feed the sampling tubes into the drilling system and to bring the acquired samples into the return capsule's storage container,
- **Surface Sampling Device**, to be handled by the robotic arm in order to collect surface pieces.

In particular when the core sample is acquired via drilling, the reaction forces and torques must be accommodated. There are layers of varying resistance and hard pieces embedded in fluffy material to be expected. Thus during peak load periods the anchors should be supported by cold gas thrusting to provide the required stability. There is a quick reaction capability necessary to prevent any sinking or side movement, as this would cause the drill to jam. Because the core sample is of highest scientific importance, all measures must be undertaken to avoid such a jamming.

To comply with the uncertainties of the cometary environment, there have back-up scenarios been elaborated for extreme situations. Thus the landing site might be considered not suitable, either because there is no chance to access the pristine amorphous ice of the core, or if the carrying capacity of the surface is not sufficient. In this case there is a capability foreseen to move to a second site.

If in a worst case due to hard soil no anchoring is possible, two core and one volatile sample can be acquired with a corer of smaller diameter and at a higher penetration rate. For this emergency sampling the limits for thermal disturbance of the samples (less than 5 K above surface temperature) must be relaxed. The vertical counterreaction force to drilling will then be provided by the thrusters.

In order to acquire sufficient mass in case of low density materials, there is a capability foreseen to compress the samples and to repeat sampling operations.

### COMETARY SOIL MODEL

The current cometary models were mainly derived from astronomical observations and the spacecraft fly-bys at Comet Halley in 1986. In addition experiments to produce comet analogue material were performed at the vacuum chamber of DLR Cologne in order to derive characteristic material properties. This provided significant improvements in the understanding of comets. "However, despite all the efforts, the composition, the inner structure and the evolutionary processes of comet nuclei are still a matter of wide uncertainty and they will remain a field of scientific debate..."(Stöffler/Schwehm 1989, p.17).

Table 1: Expected variation bands of typical physical/mechanical parameters of comets (redrawn from Stöffler/Schwehm, 1989).

Parameter	Range
Fraction of refractory dust	0 - 100 %
Porosity of refractory surface material	0 - 95 %
Porosity below dust mantle	10 - 80 %
Density of dust mantle	0.005 - 2.2 g/cm <sup>3</sup>
Density below dust mantle	0.1 - 1.5 g/cm <sup>3</sup>
Grain size of monophase grains	0.001 - 100 μm
Grain size of multiphase grains and composite aggregates	1 μm - 1 m
Compressive strength of bulk samples	10 <sup>-4</sup> - 10 <sup>2</sup> MPa

Variations of the irradiation environment during the perihel passages in comet's orbit should have caused an evolution of different layers close to the surface. A very porous and nonhomogenous surface structure must be expected, including loose dust material, boulders, pebbles and areas of exposed lower layers. Nevertheless potential save landing locations can be modelled in a first engineering approach as follows :

- dust layer : cohesionless material with a density between 0.005 and 2 g/cm<sup>3</sup>; thickness up to 1m
- crust layer: thin (few centimeter), hard (cohesion up to 4 MPa, Young's modulus up to 10 GPa) material formed by solar irradiation,
- nucleus : hard (cohesion obtained in the laboratory between 1 and 4 MPa ; Young's modulus up to 800 MPa) and brittle material at low temperature.

### EFFECTS OF PHYSICAL AND ENGINEERING PARAMETERS

For ROSETTA on-comet operations typical parameters to be identified on-board in order to optimize the sampling / AOCS coordination will be cometary soil properties like size, hardness, cohesion and stiffness of the different layers, because they are influencing the forces and torques caused by the drill. In the following table the different parameters affecting the on-comet operations are summarized.

Table 2: Identification of characteristic parameters influencing the on comet phase.

Item	Parameter	Effect
Cometary Properties	cohesion	<ul style="list-style-type: none"> <li>- reaction forces of anchors</li> <li>- drilling forces and torques</li> <li>- landing pad creeping</li> <li>- crust fragmentation</li> </ul>
	Young's modulus	<ul style="list-style-type: none"> <li>- shearing stress</li> <li>- tilting of S/C</li> </ul>
	internal angle of friction	<ul style="list-style-type: none"> <li>- footpad sinking</li> <li>- shear stress</li> <li>- soil resistance</li> </ul>
	adhesion factor	<ul style="list-style-type: none"> <li>- anchor uplift capacity</li> </ul>
	soil stratigraphy	<ul style="list-style-type: none"> <li>- force and torque profile of drilling</li> <li>- anchor stability</li> </ul>
	comet dynamics	<ul style="list-style-type: none"> <li>- thermal control (day/night cycle)</li> <li>- data transmission (contact periods)</li> </ul>
Drilling Equipment	drill rotation rate	<ul style="list-style-type: none"> <li>- sample heating</li> <li>- torques</li> </ul>
	pushing force	<ul style="list-style-type: none"> <li>- causes vertical force to be accommodated by anchors, AOCS</li> <li>- sample heating</li> <li>- sample acquisition time to reach given depth</li> <li>- power requirement</li> </ul>

Anchors	forces caused by gravity, comet dynamics, antenna movements, drilling, robot arm motion, motor vibrations, activation of gas pockets, etc.	spacecraft stability
AOCS	sensor resolution selection of thruster combination reaction time duration of thrusting	<ul style="list-style-type: none"> <li>- recognition of tilting</li> <li>- effectivity of attitude change counterreaction</li> <li>- jamming avoidance of drill</li> <li>- counterreaction tuning</li> </ul>

Item	Characteristic Parameter	Parameter influenced by
Spacecraft Resources	data transmission rate cold gas propellant available power thermal control	<ul style="list-style-type: none"> <li>- antenna pointing accuracy</li> <li>- power allocation</li> <li>- comet dynamics / link geometry</li> <li>- landing manoeuvre fuel consumption</li> <li>- anchor stability</li> <li>- maximum forces generated by drilling</li> <li>- coordination of operational activities</li> <li>- comet dynamics (day/night)</li> <li>- power consumption</li> </ul>

## COMPUTER SIMULATION FRAMEWORK

In order to investigate technologies to deal with these challenging autonomy problems, exemplarily an adaptive control algorithm was analysed in this context. As the core sampling by drilling is the most critical period, this phase was selected

for the computer simulation. The parameters to be considered are listed in table 3.

Table 3 : Simulated adaptive control scenario

Parameter Type	Specific Parameter
Optimisation Criteria	<ul style="list-style-type: none"> <li>- attitude stability (primary)</li> <li>- duration of drilling (secondary)</li> </ul>
Models	<ul style="list-style-type: none"> <li>- drill / soil interaction</li> <li>- mechanical properties of soil layers</li> <li>- simplified spacecraft structure</li> </ul>
Measurements	<ul style="list-style-type: none"> <li>- ideal gyros</li> <li>- force sensors (between pad/soil, drill (vertical direction))</li> <li>- torque sensors (between pad/soil)</li> </ul>
Control Actions	<ul style="list-style-type: none"> <li>- cold gas thruster (24 x 30 N)</li> <li>- hydrazin thruster (2 x 70 N)</li> <li>- drill feed velocity</li> </ul>

In order to perform meaningful simulations, models of the following spacecraft components have been implemented :

- drill equipment, in order to evaluate the resulting forces and torques dependent on soil properties and pushing force/drill rotation rate,
- finite element model of Lander structure, to couple the generated force at the drill with the resulting forces and torques at each of the three anchors,
- attitude control system, to generate for the desirable counterreaction the optimum approximation within the range of available thrusters,
- anchors, to determine the actual fixation capacity from a given stress/strain relationship,
- spacecraft dynamics, to deal with the situation that the anchors are teared off.

The simulation tool was already designed in a modular way to support future extensions. Thus as soon as more detailed models regarding the interactions between anchors/drill and the soil are available the implemented models can be easily updated. Further improvements of the simulation environment should also address

- thermal control aspects,
- limitations of available power,
- data transmission requirements.

## ADAPTIVE CONTROL CONCEPT FOR CORE SAMPLING

The task of the adaptive control concept is to coordinate reactions of the SAS, the anchors and the AOCS according to the actual soil properties. As attitude stability is a prerequisite for drilling, it must prevent rotational as well as translatorial movements to avoid damage to the drill.

This requires decision strategies working autonomously on-line to induce appropriate drill and AOCS reactions to achieve an optimum between the spacecraft resources and the required operations time. The control action is modeled with respect to the characteristic soil parameter : cohesion  $c$  and Young's modulus  $E$ .

The related values have to be identified during drilling in order to adapt the control strategies and controller parameters (Aström/Wittenmark, 1989).

The essential sensor inputs are provided with respect to attitude by accelerometers and gyroscopes (to determine tilting or sliding of the spacecraft). For lift-off or critical limits detection there are force- and torque- sensors at the pads / anchors and at the drill foreseen. In addition there are in the SAS sensors to measure

- the penetration depth of the drill,
- the voltage  $u$  of the penetration motor and
- the temperature at the tip of the drill.

The AOCS means to react are control units like thrusters and reaction wheels. The effect of the reaction wheels is too small to deal with the torques and forces (generated by drilling) exceeding the capabilities of the anchors. As soon as the anchors are teared off and the spacecraft is in a free movement, the usual attitude control laws regarding stability are active. In this case the reaction wheels are included for control in a nominal manner.

In the current stage of simulations, limitations in the sensor resolutions and delays in the dynamics of actuators have not been taken into account.

Figure 3 depicts the identification / adaption scheme and Figure 4 shows the interconnections and interfaces of the control concept explained in more detail in the following.

The mission management provides the supervising frame for the adaptive controller operations. This includes estimations regarding most appropriate nominal penetration rates and drill rotation rates

(according to soil properties derived from anchoring measurements).

The optimal value for the drill rotation rate  $n$  will depend on the soil parameters. For example for hard material the rotation should be higher than for soft soil. However, at the beginning of the drilling process the soil parameters at the drill point are unknown. The determination of the initial value will be a typical task of the supervising mission management. After identification of the real soil parameters the mission management has to adapt and optimize the value of the rotational velocity.

Before the on-line identification of the soil parameters with succeeding adaption of the drill controller parameters begins, the initial values of the controller parameter must be defined. At the beginning of the identification procedure a nominal desired value for the drill pushing force  $F_r$  nominal has to be chosen. It should be high enough to provide a small penetration rate but small enough such that no anchor tearing off results at the beginning. The anchor capability limits are not known at the beginning of the drill process. But a first hint can be expected from anchoring. In order to be on the safe side, it will be a better procedure to start with a pushing force too small than too high. But it is a great advantage of the adaptive control concept that after the starting phase all further information about the soil characteristics, required for control, is directly acquired from the on-going drill process.

After convergence of the identification and adaption algorithms, the desired nominal value of  $F_r$  can be increased. But care must be taken, that the resulting force  $F_r$  pushing down the drill into the soil does not exceed the anchor capabilities. Anchor tearing off would be recognized by measuring the forces and torques at the pads together with the attitude measurement signals. In case the anchors are still fixed in the ground the forces do not cause a recognisable attitude change.

Critical situations will occur if there are sudden changes in the soil characteristics. Expected changes derived from anchoring measurements can be anticipated by adaption of  $F_r$  through the supervising mission management. Otherwise it is possible, that the force  $F_r$  will exceed the maximum force to be compensated by the anchors.

Possible reactions are

- to activate thrusters to support the anchors for spacecraft stability purposes or
- to lower the drill pushing force  $F_r$ .

The adaptive control algorithm should initiate an optimum combination of both activities.

As soon as one of the force sensors indicates lift-off, supported by the attitude sensors showing rotational or translatorial movements, the feed velocity has to be immediately reduced by decreasing the desired value of the pushing force  $F_r$  nominal. In this case one or more anchors are teared out or got loose. To maintain a stable attitude in such situations, it is necessary to fire suitable thruster combinations for pressing down the spacecraft.

If all anchors are teared out, the dynamics of the spacecraft has to be taken into account. In this case the nominal attitude controller comes into

action. After stabilisation of the spacecraft by the attitude controller, drilling without anchoring must continue. For the remainder the drill forces and torques have to be compensated by the AOCS solely.

Thus, in all cases the drill controller is working as an underlaying control loop optimizing the drilling process according to the measured soil parameters, for an anchored spacecraft as well as for a free moving vehicle.

By the adaptive control concept anchors, sample acquisition system and cold gas thrusters are coordinated and support each other. This results in increased capabilities to guarantee spacecraft stability. Thus the reliability and efficiency of spacecraft operations during the on-comet phase will be significantly increased.

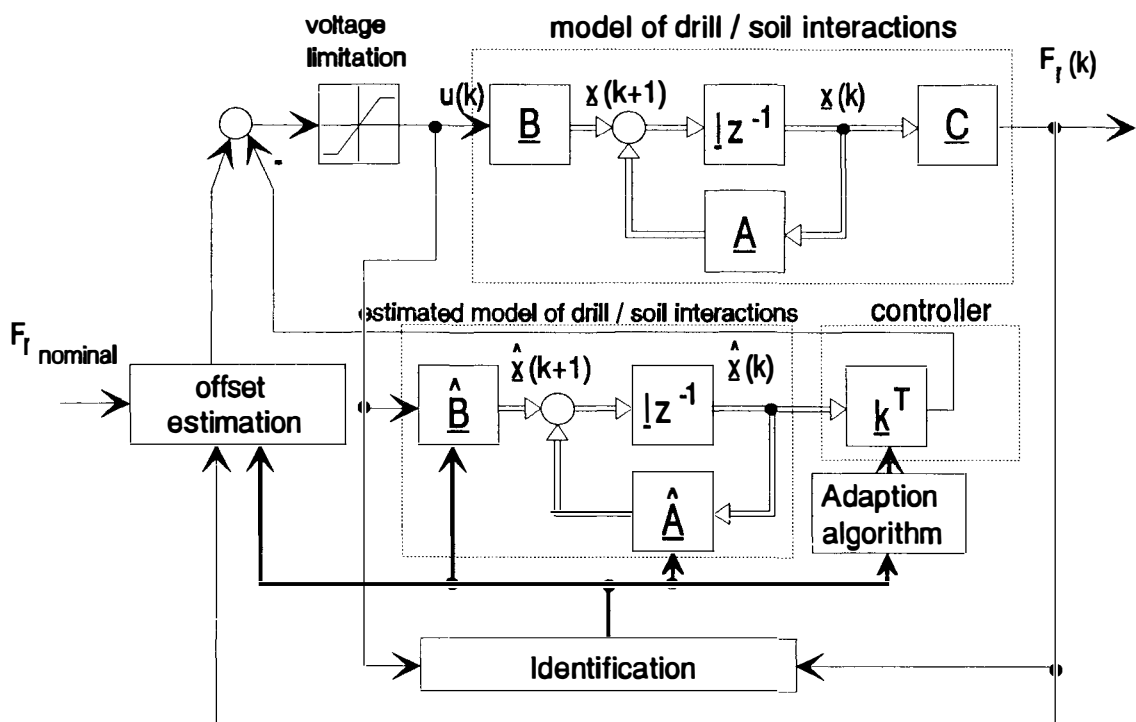


Figure 3 : Identification / adaption scheme

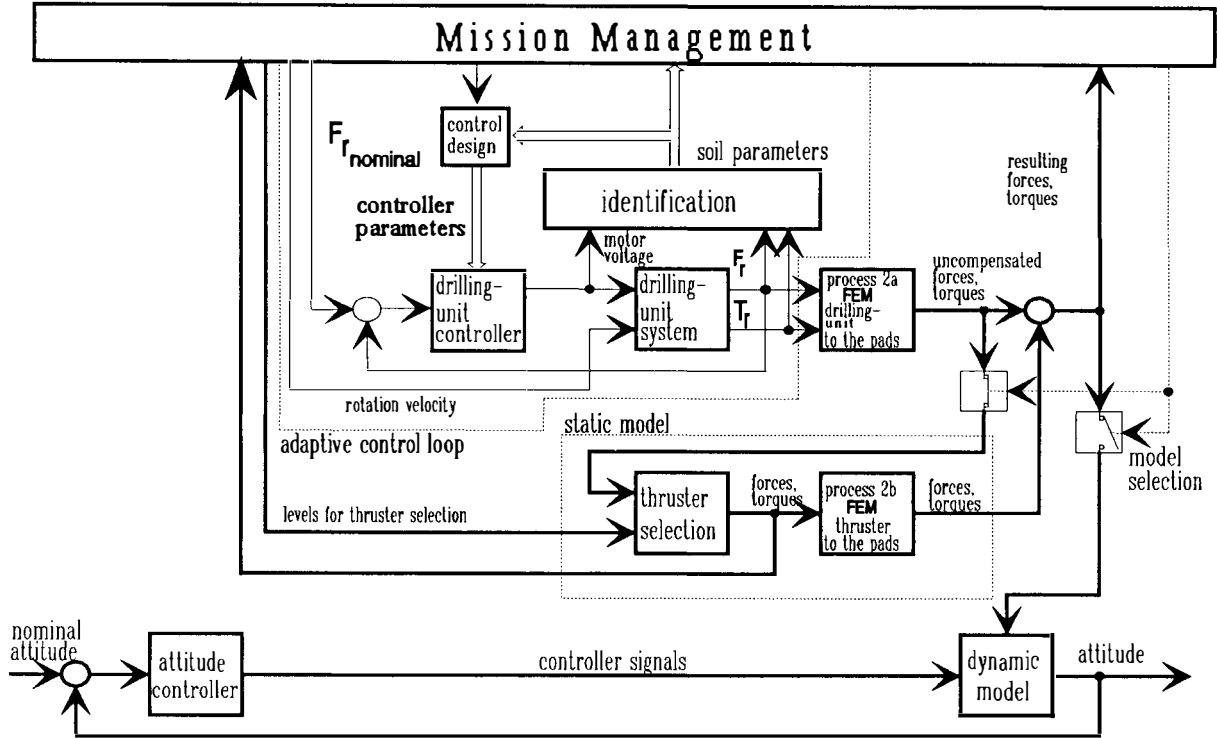


Figure 4 : Adaptive control concept

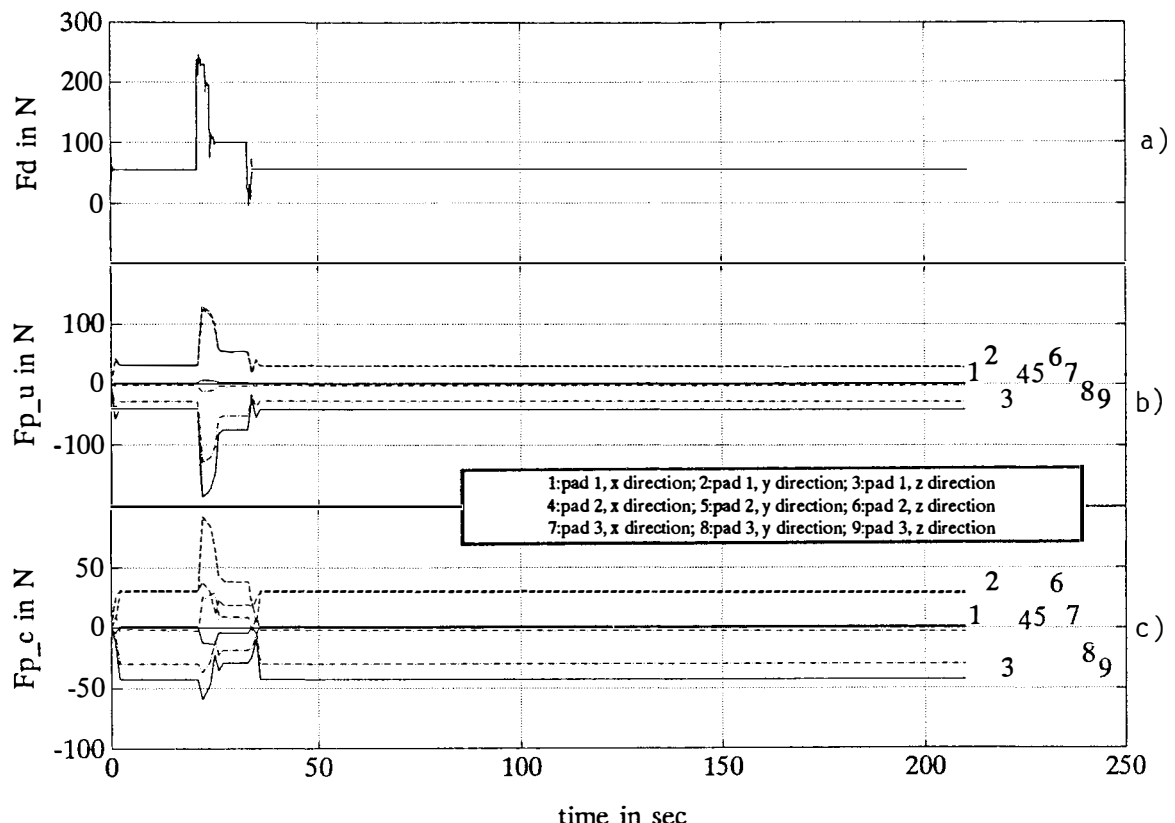


Figure 5 : Simulation of occurring forces, when the drill encounters hard material inclusions embedded in a softer environment : a) at the drill location, b) at the anchors (3-d force vectors) without counterreaction thrusting, c) at the anchors, when adaptive thrusting is provided.

## SIMULATION RESULTS

In simulations the adaptive control algorithm was tested on soil parameters varying in the admissible range. The results were very encouraging, showing that this controller can even handle sudden, abrupt changes in material properties within acceptable limits. The worst case regarding peak loads occurs, when the drill encounters in a soft material layer a hard inclusion. The resulting force profiles are given in figure 5. Figure 5 a) displays the force resulting at the drill location. Figure 5 b) shows the forces acting on the anchors, when no counterreaction via thrusters is initiated. In the displayed situation there results a tearing off of the anchors, as the maximum sustainable force of 150 N is exceeded. Figure 5 c) exhibits the remaining forces (within the capabilities of the anchors), when the algorithm activates in parallel the thrusters of the AOCS.

The comparison of 5b) and 5c) shows that thruster compensation leads to significantly smaller acting peak forces and torques at the anchors. Thus only a short thrusting period can avoid tearing off of the anchors, preserving their counterreaction capabilities as main contribution to future spacecraft stability.

Further comparisons were performed with a conventional PI-controller. In the situation of figure 5 it lead to unacceptable oscillations throughout the hard layer, while the adaptive controller quickly adapts to the new soil parameters, causing only quickly damped oscillation for the short initial period. Also for the other situations compared the adaptive scheme was preferable.

## SUMMARY

The aim of this paper was to analyse the constraints for autonomous ROSETTA on-comet operations. In particular for the very demanding period of core sampling it was shown that adaptive control methods can provide interesting contributions to support spacecraft autonomy capabilities.

The results of this paper are

- the development of an integrated anchor/drill/AOCS operations concept, to improve reliability and resource consumption efficiency,
- first analyses on the drill control regarding transitions between the different soil layers.

Regarding the application of adaptive control technology in the field of spacecraft autonomy of interest are

- capabilities to adapt to actual measurements,
- a very attractive performance for scarcely known environments,
- applicability of engineering standards on the verification of algorithms (important in case of high quality assurance requirements).

As assessed at the concrete example of ROSETTA on-comet operations, adaptive controls provide an interesting approach to enable autonomous spacecraft reactions in an uncertain environment.

## Acknowledgements

Part of this work has been elaborated in an ESA contract. We thank J. de Lafontaine and E. Bornschlegl for their comments and support during that study.

## REFERENCES

- Aström,K.J./Wittenmark,B.  
Adaptive Control  
Addison-Wesley 1989.
- Bornschlegl, E.  
ASDMS : An Autonomous Spacecraft Data Management System  
Preparing for the Future 2 (1992). 4 - 6.
- Eiden,M.J./Coste,P.  
The Challenge of Sample Acquisition in Cometary Environment  
ESA Journal 15 (1991), 191 - 211.
- Lafontaine,J.de  
Autonomous Spacecraft Navigation and Control for Spacecraft Landing  
to appear in J.Guidance, Control and Dynamics.
- Matra Espace/JPL/Dornier GmbH/BAe/Aeritalia  
ROSETTA - System Definition Study - Final Report, 1991.
- Schilling,K.  
Simulation of ROSETTA On-Comet Operations  
Annales Geophysicae, in press.
- Schwehm,G./Langevin, Y. (eds.)  
ROSETTA/CNSR A Comet-Nucleus Sample-Return Mission  
ESA SP-1125, Noordwijk, June 1991.
- Stöffler, D., G. Schwehm (eds.)  
Physics and Mechanics of Cometary Materials  
ESA SP-302, Noordwijk 1989.

# A DEVELOPMENT METHODOLOGY FOR SPACE A&R CONTROL SYSTEMS

P. Putz\* and A. Elfving\*\*

\*Department of Space Robotics, Dornier GmbH, Friedrichshafen, Germany

\*\*Robotics Section, ESA/ESTEC, Noordwijk, The Netherlands

**Abstract.** In an effort to support the development of flexible space Automation and Robotics (A&R) systems, the European Space Agency ESA has begun to establish an A&R Control Development Methodology (CDM). The CDM encompasses guidelines for the design of control systems to accomplish inter-project unification (for the parallel development of systems with common functionality) and intra-project traceability (to account for evolving requirements and technological capabilities for a given A&R system). The CDM calls for a phased analysis and development approach to progress from user requirements to hardware and software implementations. A main focus is on a systematic structure of the requirements in order to clearly separate functional, application, operational, and implementational influences. Prime constituents are a solution independent Activity Analysis framework, a Functional Reference Model as the generic logical model of A&R control system architectures, a scheme to capture the function allocation decisions for given operational modes, and guidelines for deliverables and reviews throughout the different phases. Work along the CDM can be very well supported by existing computer-aided software engineering (CASE) tools.

**Keywords.** Hierarchically intelligent control; control architectures; reference models; control system synthesis; control system requirements analysis; robots; software tools.

## INTRODUCTION

### Motivation

Several space programs currently planned and under development define the need for quite complex and sophisticated Automation and Robotics (A&R) capabilities (e.g. internal automation and servicing of orbiting laboratories, platform external servicing, surface mobility and sample acquisition for planetary exploration). Design driving requirements for the resulting A&R systems are to account for evolving needs and technological capabilities for life times of up to 30 years (International Space Station), to meet very high safety and reliability demands, and to be realized within tight budgetary and time constraints. This implies high operational flexibility and built-in growth potential with controlled cost and risk. Other typical constraints are procurement and development by multi-disciplinary and multi-national teams involving (re-using, if possible !) multi-vendor hardware and software.

There is wide agreement on the central importance of the A&R control subsystem to enable such quality and flexibility. Also the control subsystem involves several disciplines (control engineering, dynamics, simulation, computer hardware, software, human operations, etc.). Yet, while each of these disciplines per se is certainly highly mature in terms of widely accepted methods and tools, their systematic coordination in a system engineering sense has remained somewhat unsatisfactory. Crucial questions such as how to account for the interrelation of control concept design and A&R system design (design for automation !), the appropriate incorporation of control analysis into the required procedures such as Software Engineering Standards, or the optimal inclusion of human operations analysis so far mainly have been resolved in an ad-hoc fashion in space projects. Moreover, there has been concern from the Space Agencies that too little transfer of results among parallel A&R projects or from one generation of a system

to the next has been taking place. In a scenario of shrinking budgets, this necessarily becomes an issue of prime interest.

In recognition of these facts, the European Space Agency ESA has initiated the development of guidelines and principles for the design of A&R systems in general and control systems in particular (Elfving and Kirchhoff, 1991). The main output of the respective program (Dornier, 1990 and 1992) is the so called A&R Control Development Methodology (CDM) as a concise yet comprehensive framework for guiding the design creativity to the common benefits of developers and users.

### Purpose and Benefits

The purpose of the CDM is to capture principles and rules for designing A&R control implementation architectures within a simple overall structure, using unified and unambiguous terminology, and above all maintaining traceability between solution independent requirements and final realizations. This traceability is really at the core of the CDM effort. It has been a central premise to establish a systematic method which gives rise to A&R systems driven by actual requirements (what has to be done) instead of potential capabilities (what can be done).

It shall be possible to assess the impact of evolving requirements or technological capabilities on the final product. This is a prerequisite for a truly open and extendible system which allows interfacing and possible re-use of modules from different system generations or from different applications and which supports the partitioning of development among different teams, ideally allowing each to bring in their best expertise and available equipment.

The expected benefits from applying the CDM hence are higher quality products which are easily maintainable and extendible, allow better project control during the development process, and

can be realized in less time and for less overall system development cost.

It shall be stressed that, even though all of the preceding arguments have originally been raised within the space A&R context, many of the same problems are also expected to be of key importance in the development of terrestrial A&R control systems (e.g. for industrial manufacturing automation). In that sense, the potential benefits of the CDM should also apply to this much larger "market".

### Structure of the Paper

The remainder of the paper is structured as follows: an overview of the major CDM steps will be given first. The subsequent chapters will treat these steps and their key constituents in more detail: the hierarchical activity analysis, the analysis of functional requirements with the Functional Reference Model, the analysis of operational requirements, the design and production phase. The concluding summary will also briefly refer to prototype application examples currently underway.

### OVERVIEW OF THE CDM

The CDM above all defines a life cycle model for the A&R control subsystem. A life cycle model breaks the overall system analysis and design process into clearly defined individual steps or phases which are delimited by verifiable milestones. This serves to separate different and independent influences, but also allows for a controlled project management where the contributions of different specialist teams can be systematically coordinated. One widely accepted life cycle model (for software development) underlies the various software engineering standards such as BSSC (1991).

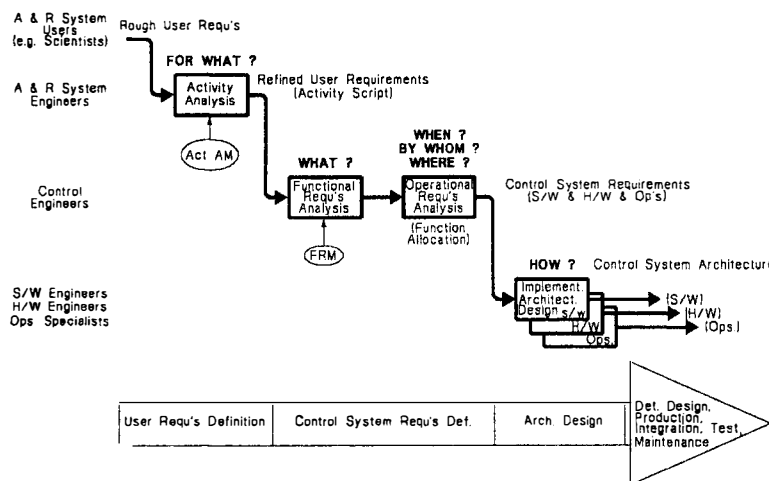


Fig. 1. Main Steps of the CDM

When introducing a life cycle model for the A&R control subsystem, two important issues should be accounted for: the A&R subsystem is part of a larger A&R system (which also includes the electromechanical A&R devices such as robots or dedicated automation mechanisms), and in itself it is a complex hybrid of computer hardware, software, and "brainware" (human operations such as the manual control in teleoperation). Thus, a CDM has to resolve both the correct incorporation of the control life cycle into the overall A&R system life cycle and the appropriate coordination of the contributing component disciplines (such as the control software development "sub-lifecycle").

A key lesson learnt in most system engineering life cycles is the paramount importance of the requirements analysis phase. Indeed, this is the area where the most significant decisions are taken, and where mistakes have the most dramatic effects on overall cost and time. This is especially true in control engineering, and thus the CDM places its main focus on a careful and systematic structure of the initial steps. The later phases (from software design onwards) are barely treated since by then, the well understood and practiced techniques are considered fully sufficient.

Fig. 1 illustrates the main steps of the CDM in a simplified fashion. The first step is called Activity Analysis. It is part of the User Requirements Definition phase, where the overall A&R problem is formulated. Its input is the user provided top level A&R system requirements specification. A first key message of the CDM is that already the user requirements need to be refined in a systematic (hierarchical) structure. The proposed output from this step is a so called Activity Script, a semi-formal and fairly detailed prescription of the process which has to be automated by the A&R system (key question: FOR WHAT do I need automation and control?).

The next phase is the refined analysis of the (control) subsystem requirements. Another key CDM concept is that this should be separated into two individual steps: Functional Requirements Analysis (purely stating WHAT control functions have to be performed) and Operational Requirements Analysis (specifying for each desired mode of operation WHEN, BY WHOM, and WHERE these control functions need to be executed). The specific meaning of these questions will be clarified in the respective chapter later on. In any case, this amounts to an allocation of the identified control functions to what we call different possible domains (preparation or utilization, human or machine, even on ground or in orbit). The output of this phase are the control subsystem requirements, already split up into control hardware, control software, and control operations parts.

The last step identified in Fig. 1 is the Implementation Architecture Design which, for the software part, coincides with the well known S/W Architectural Design phase. The point of the CDM is that also control hardware and control operations shall be "designed" to the same level in this step. The big difference to the preceding requirements analysis phase is that only design starts to say HOW the required functions are going to be realized. While it is mandatory that requirements be solution independent, design introduces the actually proposed mechanisms and concepts for implementation. This involves the specific processors, bus systems, real time operating system services, algorithms, software communications schemes, operational procedures, etc. This fundamental dualism between requirements analysis and solution design has also been expressed by calling the requirements the Logical Model of the control subsystem, whereas the design is its Physical Model.

The remaining phases after Implementation Architectural Design are not shown in Fig. 1 any more, since they are considered the "conventional" steps of Detailed Design, Production, Integration, Testing, and finally Delivery and Maintenance. This appears to be so well known that it is not discussed within the CDM context.

Note that the individual steps will typically be performed by quite different teams. The A&R system users (microgravity scientists for an automated orbiting laboratory) write the original User Requirements. The structured refinement by Activity Analysis is a task of A&R system engineers (because it also gives rise to requirements for other A&R subsystems besides control!). The Control Subsystem Requirements will be analyzed by control engineers, while the final Design is the domain of the respective specialists (computer hardware engineers, software engineers, operations specialists, etc.). Of course responsibility "comes back" as integration and testing moves higher up in the system hierarchy (up to the final acceptance tests by the users).

The CDM is not limited to just prescribing a phased development, but for each of the shown steps it offers non-trivial support in the form of generic architecture schemes (reference models), guidelines on their use, and even computer based tool assistance. Two key CDM contributions are shown in Fig. 1: the Activity Analysis Method (ActAM) and the Functional Reference Model (FRM). They will be introduced in later chapters.

What has to be stressed here is the deeper reason for separating analysis steps like this. It is exactly this separation (with the well defined responsibilities within the individual steps) which is expected to provide the desired traceability: the many requirements, constraints, and arbitrary decisions involved are introduced in a modular fashion, such that their effect is clearly located within the life cycle and also the impact of changing circumstances (e.g. evolving requirements or new applications) is traceable. One could overlay iteration loops over Fig. 1 for system updates. The influences considered to be more volatile are put into later steps: if the available implementation technology changes "slightly" (e.g. more sophisticated control algorithms become feasible), development only has to be re-done from Implementation Architecture Design on (with the same subsystem requirements !). If technology evolves such that a more sophisticated operational scenario becomes feasible (e.g. more functions are located on-board rather than on ground, or more machine intelligence is employed to take over previously human functions), the iteration picks up at Operational Requirements Analysis. One only has to go back to Functional Requirements Analysis or even Activity Analysis if new functions are identified (e.g. because of a growth of the application scenario). The key point is that all of these potential updates remain within the unified framework of the Functional Reference Model and do not violate the underlying control system structure. This is what provides openness, growth potential, and re-useability.

#### HIERARCHICAL ACTIVITY ANALYSIS

##### The Activity Analysis Method (ActAM)

The Activity Analysis step of the CDM shall produce refined user requirements suitable for further system and subsystem analysis. "Suitable" really means that even the user requirements possess a structure which enables a traceable transition to modular solutions. What this implies for Activity Analysis is shown in the left half of Fig. 2. In order to formulate user requirements on the A&R system, one shall first analyze the process to be automated. This analysis shall result in a hierarchical description of A&R system activities to be performed. We propose a three layer hierarchy of activities: the very top level A&R Missions represent the highest level of activity for which an A&R system is responsible (e.g. "SERVICE a life Science Experiment", "REPAIR a satellite"). Each A&R Mission can be decomposed into Tasks defined as the highest level activity performed on a single subject (e.g. "OPEN a door", "DISCONNECT a utility line", "INSTALL a sample in a processing furnace"). Finally, each task shall be decomposeable into Actions (e.g. "GRIP a sample container", "EXTRACT the container from the furnace", "MOVE the container to the freezer"). A&R missions, tasks, and actions can be formulated as commands with associated attributes which specify the particular circumstances.

The key concept is that this structured activity analysis shall only be driven by the process requirements and not by any particular automation solution. This is why the definition of the activity layers and the individual activity commands is A&R solution independent (a SERVICE can be done by any cooperation of robots and astronauts, an OPEN could be performed by a dedicated door drive or by a robot, a GRIP can be executed by a general purpose gripper or a dedicated tool, etc.). This is meant to

force system engineers to identify what the process really needs, and only in a later step to decide how to realize it.

The actual Activity Analysis Method (ActAM) outlined in Dornier (1992) goes beyond merely formulating what has to be done in terms of A&R Missions, Tasks, and Actions. It also proposes the relationship to A&R system design which is seen to be an iteration of activity decomposition, system capability identification, and comparative evaluation. This shall prevent Activity Analysis from prescribing activities for which no solution exists. This issue will not be refined here any more, however.

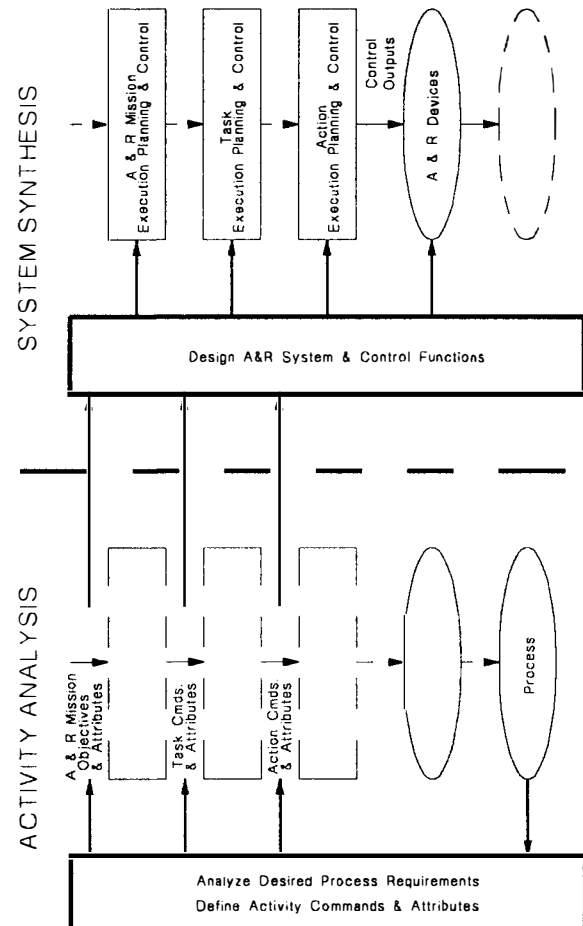


Fig. 2. Activity Analysis and System Synthesis

##### The Activity Scripting Language (AcSL)

The hierarchical activity analysis procedure outlined above can easily be seen to serve more than the purpose of user requirements formulation. We also consider it an important means for the development and optimization of operational scenarios, a common language for A&R system users, operations planners, developers, and managers. Thus, in order to account for the desired unambiguity, we have defined a semi-formal Activity Scripting Language (AcSL). AcSL shall not be "yet another robot programming language", but a guideline on typical A&R Missions, Tasks, and Actions. Indeed, AcSL is a scripting language and not an executable language (since execution belongs to the much later implementation phase). The point is that, no matter how exotic the application might be, at the level of tasks and especially actions it will require more or less the same vocabulary of activities (reflecting the fact that at the bottom of any automation system there are only so many capabilities ...).

Dornier (1992) lists AcSL frameworks for typical space A&R activities and how to specify them unambiguously (like templates to be filled out during Activity Analysis). This comprises some 15 A&R missions, 20 tasks and 25 actions. Each activity is defined by

initial conditions, termination conditions, boundary conditions, possible non-nominal situations and associated relief strategies, and attributes specifying the relevant configuration of the environment (e.g. required accuracies or maximum expected uncertainties). First applications have already demonstrated that it may seem uncommon and painful to describe the user requirements to such detail, but this effort greatly pays off in later phases. It is also a surprisingly potent tool to bridge the communication gap between the different parties (with their different backgrounds and terminologies) involved in the early phases.

It shall be briefly mentioned that the Activity Analysis is also the input to the overall A&R system analysis and design phase (Elfving and Kirchhoff, 1991). This is not treated in the CDM since it goes beyond the control domain, but obviously the same principles employed here will also be of benefit in the wider context.

#### FUNCTIONAL REQUIREMENTS ANALYSIS

The second major step of the CDM is the analysis of functional requirements for the A&R control system based upon the refined user requirements (Activity Script). Note that at this point the main decisions on the overall A&R system have already been taken (in a step not pertaining to the CDM). That is, the A&R devices have been designed and represent the "plant" to be controlled (cf. right half of Fig. 2). What needs to be found is the requirements on the A&R control subsystem.

The key concept at this point is to start with a purely functional analysis of the requirements. In the definition of the CDM, a function is the description of a duty to be performed in terms of its given input information, boundary conditions, and expected output. A function only says WHAT has to be done, strictly independent of HOW and BY WHOM. Typical control functions (on different hierarchical layers) are servo control, inverse kinematic transformation, path interpolation, path planning, force/torque sensor data processing, etc. All of these can be specified without saying how they are done (using which algorithm) or by whom they are performed (the same function can be realized in software for one operational mode and by a human in the next, such as path planning in teleoperation!).

The reason for analyzing the control functions first is the desired uniform structure of the control architectures. The claim simply is that even the most diverse applications use the same fundamental control functions, but in possibly quite different realizations. Only by uncovering the essential functions can one appreciate the commonalities or differences among individual control systems.

#### The Functional Reference Model (FRM)

In order to maintain the desired traceability to the activities identified in the user requirements, the control functions will be cast in the same overall structure (see Fig. 2), that is a three layer hierarchy responsible for achieving A&R missions, tasks, and actions. One of the central contributions of the CDM is to provide a general framework (logical model) for all A&R control functions. Since this shall serve as a reference for all possible applications, it has been called Functional Reference Model (FRM). The FRM is meant to be the essential functional and information architecture of general A&R control systems, independent of particular applications, operational scenarios, and implementations.

The top level view of the FRM is shown in Fig. 3. Just like the Activity Analysis scheme, the FRM consists of three hierarchical layers of control functions. The overall A&R control system is responsible for reaching a global goal, the A&R Mission

Objectives. These are successively broken down into sub-goals: the tasks and actions, each handled by control functions on the appropriate layer (whence the names of the control layers), until the elementary "control outputs" can be issued to the A&R devices (e.g. currents to the joint motor drives). It is important to note that the criterion for layer separation in the FRM is derived from the activities to be performed by the A&R system (from the problem domain) and not from an implementation structure (the solution domain): the FRM layers are not necessarily identical to the A&R device / subdevice hierarchy (where one A&R system may consist of several robots or dedicated automation facilities, and one robot of an arm, a mobile base, a gripper, etc.) or to a hierarchy of decentralized control stations. This would violate the application and implementation independence of the FRM.

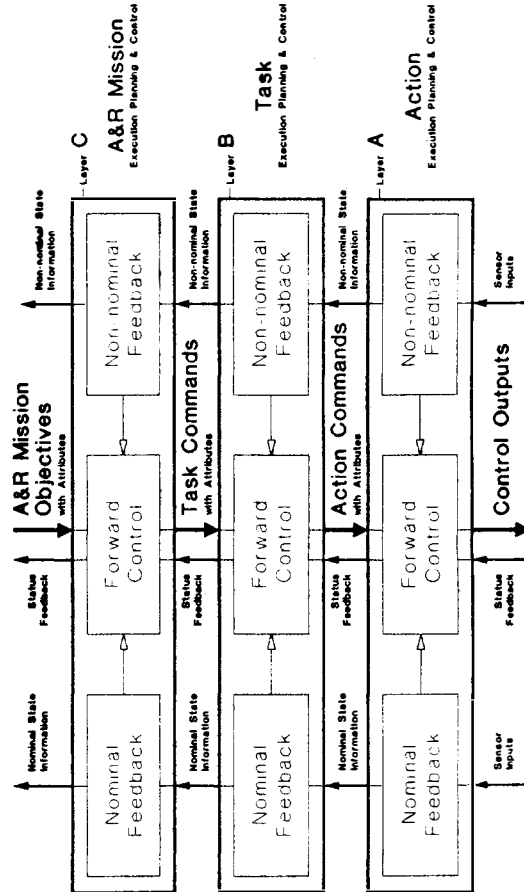


Fig. 3. Functional Reference Model (FRM) for A&R Control Systems

The second structuring scheme of the FRM is a clear separation into "vertical" branches of control based on the concept of feedback. The center branch is called Forward Control (FC). FC functions are responsible for activity decomposition, execution planning, and control by taking the most appropriate a-priori information known to each layer into account. FC functions could potentially exist without feedback, amounting to "blind" feedforward control action without regard to the actual effects on the controlled system. Obviously this cannot consider any modeling imperfections and disturbances, such that feedback is introduced. The left branch of the FRM consists of Nominal Feedback (NF) functions for refinement and update of a-priori knowledge ("world models") based on the actual, but essentially expected, evolution of the process and consequently formulation of controlled adjustments of the FC. By FC and NF, "cascaded" control loops are closed on action, task, and A&R mission layers and are equipped with everything necessary for the "nominal" course of events.

Besides FC and NF, the FRM foresees a third branch of "Non-Nominal Feedback" (NNF) functions responsible for the monitoring of discrepancies between actual and allowable states in both the FC and NF functions (because of the actual, but essentially unexpected, evolution of the process), diagnosis of their origins, and generation of directives (including recovery strategies and constraints) for FC. The NNF functions are thus reserved for "contingency" or "rescue" cases that are only triggered by irregularities not accounted for in the nominal FC / NF loop. The separation of NF and NNF is chosen in order to stress the high importance of safety and reliability especially in space applications, and to underline the fundamental difference in purpose and possible realization. Note that it is a subjective matter of definition for each particular application what is nominal and what not, but once this decision is taken, there will have to be an independent treatment of "exceptions". Thus, a simple system would have a very constrained set of nominal situations and would break into NNF in situations which might be perfectly nominal for more sophisticated systems.

Dornier (1992) gives a much more refined definition of the FRM. This not only amounts to a careful specification of the information flow among the function modules shown in Fig. 3 (distinguishing between commands, attributes, state information, status feedback, updates, etc.), but it also refines FC, NF, and NNF to a level where the commonly expected functions such as joint servo control, path interpolation, etc. are identified. The underlying study has also shown how the most common control methods can indeed be accommodated in this general architecture.

It shall be acknowledged that the concept and structure of the FRM have been heavily and beneficially influenced by the NASREM architecture developed at the US NIST (Albus, McCain, and Lumia, 1989). Indeed, Dornier (1990) started with an analysis of NASREM and similar control architectures. There were, however, several features which finally determined ESA to develop an "own" reference model: NASREM was considered too application and implementation oriented (its layers are bound to the A&R device structure, its Global Data System is an implementation issue), the World Modeling and Global Data System concepts appeared too unstructured and potentially ambiguous. Non-Nominal Feedback was not found as an integral part of the reference model, there was no apparent development method around the NASREM architecture, elaboration of details in higher layers was not available yet. It is true, however, that there are more similarities than discrepancies between the FRM and NASREM and much of the original "NASREM spirit" is very much visible in the CDM work.

#### How to Use the FRM for Functional Requirements Analysis

For given user requirements (activity analysis) of a control application, the functional requirements shall be derived in a hierarchical fashion according to the FRM framework. The resulting functional architecture (logical model) is called the Application Architecture (AA) since it is specific for the given problem (yet still solution independent!). The difference between the (specific) AA and the (generic) FRM is that functions from within the FRM which are not needed for the application are deleted, refinements beyond the FRM level of detail can be added, and the project specific nomenclature can be introduced where the application is concerned (the control system terminology should be kept from the FRM, however!). Despite these differences, the general architecture of the AA is that of the FRM, such that the commonalities among different applications become immediately apparent. At this point, the right half of Fig. 2 is complete: the necessary functions for the A&R control subsystem are defined in a highly structured fashion, exactly compatible with the structure of the Activity Analysis, and therefore traceability is made possible.

Dornier (1992) discusses more practical aspects on generating an AA. After all, this is the most critical step in the overall life cycle. For instance, upon A&R system design, the mapping between activities and A&R devices is fixed (e.g. it is defined that an INSTALL task is always done by a robot, while some OPEN tasks may be also performed by an "active" door mechanism - depending on the task attributes). This is taken into account in the AA by showing the individual control concepts for each action and task (e.g. which sensors are involved, what feedback scheme such as position control / impedance control / force control is chosen, etc.). An important issue is the support of the functional analysis step by computer tools. Dornier (1992) reviews several widely known methods appropriate for this phase such as Structured Analysis (SA) or Structured Analysis and Design Technique (SADT). The examples given there use SA with the TeamWork CASE tool which was found extremely adequate. It is clear, however, that the CDM is not bound to any one such tool or method.

#### OPERATIONAL REQUIREMENTS ANALYSIS

The third major step of the CDM according to Fig. 1 is the analysis and incorporation of the operational requirements on the A&R control subsystem. Operational requirements are understood as defining the desired modes of operation, namely the circumstantial fashion (especially w.r.t. the extent of human involvement) in which the control functions are to be performed. The underlying idea is that even in modes as different as "telemanipulation" and "automatic task program execution with online planning", the same fundamental control functions (from the FRM !) are involved, but allocated in quite different ways to humans and machines (software). Hence the "operational" view is considered independent of the functional view: functions for the same application simply shift their allocation as one goes from manual control to automatic control.

In other words, operational requirements are defined precisely by specifying the allocation of the control functions to the following domains: preparation or utilization (WHEN are the control functions performed?), human or machine (BY WHOM are the control functions performed?), and (for space applications) on ground or on board (WHERE are the control functions performed?). This brings in the key questions answered at this step (see Fig. 1).

The most fundamental operational decision is taken by specifying WHEN the functions are performed. Functions are allocated to Utilization if they are used during the actual A&R system operation in order to achieve the A&R mission objectives. The character of the utilization functions determines much of the flexibility, power, and convenience available during operation. For instance, a typical telemanipulation only provides low level machine functions (joint or cartesian level servo control) for utilization, the higher level utilization functions (such as path planning for obstacle avoidance) must be performed by the human operator in order to reach the A&R mission objectives. This has the advantage of high flexibility, but the drawback of intensive human involvement and strong skill requirements. On the other hand, a task level automatic system provides relatively high machine functions for utilization (all of the Action and Task Layers) with lower human skill requirements but normally less flexibility. The successful operation within a utilization domain requires appropriate prior Preparation functions. These are also from within the FRM framework and "prepare" or enable the utilization domain for all anticipated nominal and non-nominal situations (such as the typical "off-line programming" defining action sequence plans, world models, object lists, etc.). Note that utilization / preparation is not necessarily the same as on-line / off-line: a teach-in sequence involving the actual robot on-line is preparation and not utilization because it does not directly serve the mission objectives in a productive scenario.

The second operational decision is much more self-explanatory: specifying BY WHOM the functions are performed (for both preparation and utilization). Typically, functions are allocated to humans if they require low bandwidth but high intelligence and intuition (poorly structured problems), and they are allocated to machines (hardware and software) if they require high bandwidth, reliability, and data volumes, but low intelligence (well structured problems).

For space applications, a key decision to be captured during operational requirements analysis is WHERE control functions are performed. Those being allocated on board are very "expensive" since they are subject to all of the space qualification and budget constraints. This is not only true for software, but also for humans on board: their time is so valuable that it can only be spent for the most essential duties. Thus, only the functions with the tightest control bandwidth requirements will be put on board. The situation is more relaxed on ground, where there are fewer implementation constraints. On the other hand, the impact of the up/downlink communication channels (capacity, delays, loss of signal periods) on control performance has to be considered. With evolving computer technology, the expected tendency is that more and more control functions can be put into on-board software, and only the highest supervision loops are closed over the ground.

Since the three domains explained above are mutually independent, there are eight possible combinations for the allocation of each control function in a given mode (e.g. human ground preparation or on-board machine utilization). As a guideline, Dornier (1992) shows examples of the allocation patterns for the most common operational modes.

The Operational Requirements Analysis step consists of identifying the functional allocations. This can be supported by the same CASE tools (e.g. using the control flow constructs of SA/RT). The result is the final control subsystem requirements definition including the functional requirements from Step 2 and the operational requirements from Step 3. Because of the allocation, they are already grouped into requirements for control software, control hardware, and human control operations (on ground and on board).

#### DESIGN AND PRODUCTION

The fourth and last step of the CDM in Fig. 1 is the Implementation Architecture Design. This is shown separate for control hardware, control software, and human control operations (based upon the distinct requirements after Step 3) and is under the responsibilities of the respective specialists within a project. For the software part this corresponds to the Architectural Design phase (BSSC, 1991) for which well established methods and tools exist. This is where the actual implementation decisions are taken on HOW the control functions are going to be realized (programming language, algorithms, data structures, real time communication mechanisms, etc.). The result is the control software architecture, a physical model of the control subsystem. The main point is that, because of the tight connection to the preceding steps, this still exhibits the underlying FRM structure and thus provides the desired modularity, openness, extensibility, and interchangeability.

The subsequent phases (Detailed Design, Production, Integration, Test, Maintenance) are not specifically covered in the CDM any more since they are well understood and supported by excellent methods and tools. A possibly novel feature of the CDM is to treat the branch of human operations in just the same way as the hardware and software parts: procedures need to be established, refined, trained, demonstrated with the actual system.

#### CONCLUSIONS

We have outlined the major steps of a newly developed A&R Control Development Methodology. Because of the page limit, treatment has been very condensed and we refer to Dornier (1992) for details and prototype application examples. The main feature of the CDM is a disciplined system engineering approach with clear phases. The phases exhibit built-in traceability due to the separation and distinct accommodation of independent influences. A main focus is on solution independent requirements analysis resulting in a functional architecture or logical model of the control system. For this purpose, the CDM offers an Activity Scripting Language (AcSL) and a Functional Reference Model (FRM) structured into implementation independent hierarchical layers. Operational requirements are treated as conditions on the allocation of the identified control functions. Powerful CASE tools can be employed to support the analysis and design steps.

The introduction has spelled out the expected benefits of the CDM approach. We believe it supports intra-project evolution because the impact of evolutionary changes is decoupled and traceable. It supports inter-project unification because it is based on general reference models which expose the functional commonality among different applications and implementations, and because it leads to common terminology, modularization, and ultimately compatible interfaces.

First demonstration applications of the CDM have been begun. A prototype control system for a planned Spacelab A&R mission has been designed (Putz and Elfving, 1992). Many lessons have been learnt, but the overall experience was highly positive. AcSL and FRM have shown very beneficial in the difficult phase of extracting the relevant user requirements and "translating" them to control functions and architectures.

Further plans call for getting even more experience by building implementations. When the guidelines in the CDM are mature enough, one can think of "automating" some of them by providing specially tailored computer tools which take over much of the routine work in analysis and design. The main ideas of the CDM are certainly not specific to A&R control, and there will be efforts to extend them for even wider applications.

#### REFERENCES

- Albus, J.S., H.G. McCain, and R. Lumia (1989). NASA/NIST Standard Reference Model for Telerobot Control System Architecture (NASREM). NIST Technical Note 1235.
- BSSC (ESA Board for Software Standardisation and Control) (1991). ESA Software Engineering Standards. Doc. Nr. ESA-PSS-05-0.
- Dornier (1990). Evaluation of Standards for Robot Control System Architectures (Control Techniques). FSA Contract 8009/88/NL/JG Final Report.
- Dornier (1992). Baseline A&R Control Development Methodology Definition Report. ESA Contract 9292/90/NL/JG Report.
- Elfving, A., and U. Kirchhoff (1991). Design Methodology for Space Automation and Robotics Systems. ESA Journal, 15, 149 - 164.
- Putz, P., and A. Elfving (1992). Using the ESA CDM to Design the Control Architecture of the "Bioscreening with Robotics" Columbus Precursor Experiment. Proc. 2nd Int. Symp. on Artificial Intelligence, Robotics, and Automation in Space (i-SAIRAS), Toulouse, Sept. 30 - Oct. 2, 1992.

# RENDEZVOUS AND BERTHING BETWEEN COLUMBUS FREE FLYING LABORATORY AND SPACE STATION FREEDOM

W. Wöhlike

Deutsche Aerospace, ERNO Raumfahrttechnik GmbH, Hünefeldstr. 1-5, D-2800 Bremen 1, Germany

**Abstract:** One of the major goals of the European Columbus project is to perform experiments and processes in a very low microgravity environment. It is therefore the intent to provide a Free Flying Laboratory (Free Flyer) which will be serviced at the Space Station Freedom (Freedom) and by the spaceplane Hermes.

For servicing at Freedom, the Free Flyer performs a Rendezvous and Berthing (RvB), which is mainly driven by safety requirements, in particular the demand for collision avoidance.

A short interpretation of these requirements is given in order to find a strategy which enables the determination of a safe approach and departure trajectory. This strategy is mainly based on the estimation of the so-called safe region, which defines the relative velocity and angular rates with respect to the distance between the two vehicles. Two estimation algorithms are discussed, one for the determination of the safe region for large distances between chaser and target, and one which is particular suitable for the last meters during final approach and close distances during departure. Both algorithms take the vehicle shapes and dimensions of Freedom and Free Flyer into account.

The adjustment of the arrival time is realized by a transfer manoeuvre between hold points and a station keeping manoeuvre in hold points. Each of the transfer manoeuvres is subdivided into the phases: velocity acquisition, constant velocity, constant braking, and exponential braking.

Finally the RvB scenario is outlined involving the phases: nominal approach and nominal departure.

**KEYWORDS :** Free Flyer, Rendezvous Scenario, Safe Trajectory, Collision Avoidance.

## 1 Introduction

The Free Flyer five year mission, see the detail description in [1], encompasses the Free Flyer launch by ARIANE 5, ten microgravity cycles with intermediate Hermes visits, and RvB with Freedom.

For RvB with Freedom the Free Flyer shall be de-

signed to support a flight dynamic concept of a safe trajectory. This concept shall provide the capability to allow, at any time during the proximity operations within the Freedom Command and Control Zone (CCZ), the shutting off of the Free Flyer propulsion system, resulting in a trajectory which avoids any possibility of collision with Freedom.

The implementation of all RvB related functions to perform a safe approach and departure shall be one-failure-tolerant. Moreover, after any failure in the RvB related equipment it shall be possible to activate the two failure tolerant safe abort command resulting immediately in a propulsion shut off and a drift away from Freedom.

The following paper is subdivided into three major parts. The first one deals about the fundamental RvB dynamic in coplanar orbits. The second one deals about the safe region, the selection of a reference trajectory, and the transfer concept. With these results the complete RvB scenario can be established.

## 2 Fundamentals

### 2.1 RvB in Coplanar Orbits

This section describes the dynamic of two orbiting spacecrafts (S/C) in a spherical earth gravity gradient field with a potential

$$U = -\frac{\mu}{|\mathbf{R}_o|}, \quad (1)$$

the earth gravitational constant  $\mu$  and the vector  $\mathbf{R}_o$  between the earth and the S/C centre of mass (c.o.m.). The gravitational acceleration due to the given gravitational potential (1) and an additional disturbance acceleration  $\mathbf{a}_o$  at the S/C target position  $\mathbf{R}_o$  is given by the following equation:

$$\ddot{\mathbf{R}}_o = -\frac{\mu}{R_o^3} \mathbf{R}_o + \mathbf{a}_o. \quad (2)$$

For the chaser S/C the equation

$$\ddot{\mathbf{R}} = -\frac{\mu}{R^3} \mathbf{R} + \mathbf{a} \quad (3)$$

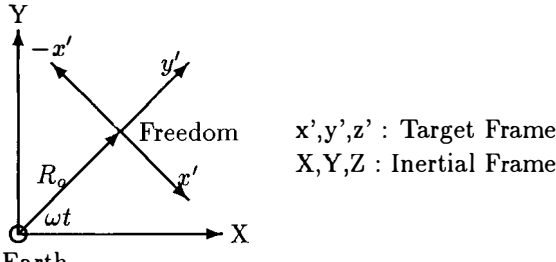


Figure 1: Freedom Coordinate System

is defined. The difference between equation (3) and (2) defines the acceleration  $\ddot{\mathbf{r}}$  between target and chaser:

$$\ddot{\mathbf{r}} = -\frac{\mu}{R^3} \mathbf{R} + \frac{\mu}{R_o^3} \mathbf{R}_o - (\mathbf{a} - \mathbf{a}_o) . \quad (4)$$

With  $r \ll R_o$  the equation (4) can be stated in the following form:

$$\ddot{\mathbf{r}} = -\frac{\mu}{R_o^3} [\mathbf{I} - 3 \frac{\mathbf{R}_o \mathbf{R}_o^T}{R_o^2}] \mathbf{r} + (\mathbf{a} - \mathbf{a}_o) . \quad (5)$$

The equation describes the RvB dynamic in the inertial frame. To achieve an universal algorithm for any target S/C orientation a transformation between the inertial coordinate system and the target one is necessary and defined as

$$\mathbf{r} \stackrel{\text{def}}{=} \mathbf{T} \mathbf{r}' , \quad (6)$$

with the transformation matrix  $\mathbf{T}$  and the existence of its inverse  $\mathbf{T}^{-1}$ . Furthermore, the equation (5) can be stated with the definition (6) and the additional transformation of the disturbance acceleration

$$\mathbf{a} \stackrel{\text{def}}{=} \mathbf{T} \mathbf{a}' \quad (7)$$

w.r.t the target frame in the following form:

$$\ddot{\mathbf{r}}' = -\frac{\mu}{R_o^3} [\mathbf{I} - 3 \frac{\mathbf{T}^{-1} \mathbf{R}_o \mathbf{R}_o^T \mathbf{T}}{R_o^2}] \mathbf{r}' - \mathbf{T}^{-1} \ddot{\mathbf{T}} \mathbf{r}' - 2 \mathbf{T}^{-1} \dot{\mathbf{T}} \mathbf{r}' + (\mathbf{a}' - \mathbf{a}'_o) . \quad (8)$$

This equation describes the features of the rendezvous dynamic in a spherical earth gravity gradient field.

## 2.2 Freedom Coordinate System

The Freedom target coordinate system, see figure 1, is defined by the vector

$$\mathbf{R}_o \stackrel{\text{def}}{=} \begin{bmatrix} \cos(\omega t) \\ \sin(\omega t) \\ 0 \end{bmatrix} R_o \quad (9)$$

between the earth c.o.m. and the target c.o.m, the transformation

$$\mathbf{T} \stackrel{\text{def}}{=} \begin{bmatrix} \sin(\omega t) & \cos(\omega t) & 0 \\ -\cos(\omega t) & \sin(\omega t) & 0 \\ 0 & 0 & 1 \end{bmatrix} \quad (10)$$

between the inertial frame and the target reference frame, the angular velocity

$$\omega \stackrel{\text{def}}{=} \sqrt{\frac{\mu}{R_o^3}}, \quad (11)$$

and the disturbance acceleration

$$\Delta \mathbf{a} \stackrel{\text{def}}{=} \mathbf{a}' - \mathbf{a}'_o \quad (12)$$

between Freedom and Free Flyer with respect to the target reference frame. With the definitions (9)-(12) equation (8) can be written in the following form:

$$\begin{aligned} \ddot{\mathbf{r}}' = & -\omega^2 \begin{bmatrix} 0 & 0 & 0 \\ 0 & -3 & 0 \\ 0 & 0 & 1 \end{bmatrix} \mathbf{r}' - \\ & 2 \begin{bmatrix} 0 & -\omega & 0 \\ \omega & 0 & 0 \\ 0 & 0 & 0 \end{bmatrix} \dot{\mathbf{r}}' + \Delta \mathbf{a} \end{aligned} \quad (13)$$

To achieve a state vector form the equation (13) is separated into components:

$$\ddot{r}'_x - 2\omega r'_y = \Delta a_x, \quad (14)$$

$$\ddot{r}'_y - 3\omega^2 r'_x + 2\omega r'_z = \Delta a_x, \quad (15)$$

$$\ddot{r}'_z + \omega^2 r'_z = \Delta a_x. \quad (16)$$

With the subsequent definitions of the components

$$x \stackrel{\text{def}}{=} r'_x, \quad (17)$$

$$y \stackrel{\text{def}}{=} r'_y, \quad (18)$$

$$z \stackrel{\text{def}}{=} r'_z, \quad (19)$$

and the equations (14) - (16) the state vector equations are given as :

$$\dot{x} = \dot{x}, \quad (20)$$

$$\dot{y} = \dot{y}, \quad (21)$$

$$\dot{z} = \dot{z}, \quad (22)$$

$$\ddot{x} = 2\omega \dot{y} + \Delta a_x, \quad (23)$$

$$\ddot{y} = 3\omega^2 y - 2\omega \dot{x} + \Delta a_y, \quad (24)$$

$$\ddot{z} = -\omega^2 z + \Delta a_z. \quad (25)$$

A cross coupling between x,y motion and z motion is not given by the above equations. Therefore a separation into two systems is possible. The equations (20),(21),(23),and (24) are summarized to the matrix equation

$$\begin{bmatrix} \dot{x} \\ \dot{y} \\ \dot{z} \\ \ddot{y} \end{bmatrix} = \begin{bmatrix} 0 & 0 & 1 & 0 \\ 0 & 0 & 0 & 1 \\ 0 & 0 & 0 & 2\omega \\ 0 & 3\omega^2 & -2\omega & 0 \end{bmatrix} \begin{bmatrix} x \\ y \\ \dot{x} \\ \dot{y} \end{bmatrix} + \begin{bmatrix} 0 & 0 \\ 0 & 0 \\ 1 & 0 \\ 0 & 1 \end{bmatrix} \begin{bmatrix} \Delta a_x \\ \Delta a_y \end{bmatrix} \quad (26)$$

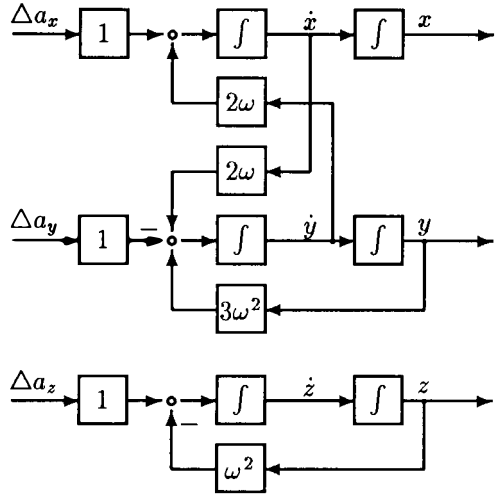


Figure 2: Struture Diagram of the relative Orbit Dynamic

or shorter with the related defintions to equation

$$\dot{\mathbf{x}}_1 = \mathbf{A}_1 \mathbf{x}_1 + \mathbf{B}_1 \mathbf{u}_1. \quad (27)$$

Similar the equations (22) and (25) are combined into equation

$$\begin{bmatrix} \dot{z} \\ \ddot{z} \end{bmatrix} = \begin{bmatrix} 0 & 1 \\ \omega^2 & 0 \end{bmatrix} \begin{bmatrix} z \\ \dot{z} \end{bmatrix} + \begin{bmatrix} 0 \\ 1 \end{bmatrix} \Delta a_z \quad (28)$$

or the equation

$$\dot{\mathbf{x}}_2 = \mathbf{A}_2 \mathbf{x}_2 + \mathbf{B}_2 \mathbf{u}_2. \quad (29)$$

The structure diagram , see figure 2, represents the separation between the in-plane and out-of-plane dynamic clearly. Equation (26) and (27) are well known as Clohessy-Wiltshire linearized differential equations.

### 2.3 Special Solution

The homogenous solution  $\Delta\mathbf{a} = 0$  of the time invariant linear State Vector Equations (27) and (29) are calculated via the LAPLACE inverse transformation:

$$\mathbf{x}_i(t) = \phi_i(t - t_o) \mathbf{x}_o \quad (30)$$

with

$$\phi_i(t - t_o) \stackrel{\text{def}}{=} \mathcal{L}^{-1}\{(s\mathbf{I} - \mathbf{A}_i)^{-1}\} \quad (31)$$

for  $i = 1, 2$ . The matrices

$$\begin{aligned} \phi_1(t - t_o) = & \\ \begin{bmatrix} 1 & 6\omega(t - \frac{1}{\omega}s) & \frac{4}{\omega}s - 3t & \frac{2}{\omega}(1 - c) \\ 0 & 4 - 3c & -\frac{2}{\omega}(1 - c) & \frac{1}{\omega}s \\ 0 & 6\omega(1 - c) & 4c - 3 & 2s \\ 0 & 3\omega s & -2s & c \end{bmatrix} & \end{aligned} \quad (32)$$

and

$$\phi_2(t - t_o) = \begin{bmatrix} c & \frac{1}{\omega}s \\ -\omega s & c \end{bmatrix} \quad (33)$$

are stated with  $c \stackrel{\text{def}}{=} \cos(\omega t)$  and  $s \stackrel{\text{def}}{=} \sin(\omega t)$  and are known as transition matrices. The solution of the homogenous systems are generated by multiplication of the transition matrix with the initial state vector:

$$\begin{aligned} x(t) = & \sin(\omega t)(\frac{4}{\omega}\dot{x}_o - 6y_o) - \frac{2}{\omega}\cos(\omega t)\dot{y}_o \\ & + (6\omega y_o - 3\dot{x}_o)t + (x_o + \frac{2}{\omega}\dot{y}_o) \end{aligned} \quad (34)$$

$$\begin{aligned} y(t) = & \frac{1}{\omega}\dot{y}_o \sin(\omega t) + \cos(\omega t)(\frac{2}{\omega}\dot{x}_o - 3y_o) \\ & + 4y_o - \frac{2}{\omega}\dot{x}_o \end{aligned} \quad (35)$$

$$\begin{aligned} \dot{x}(t) = & 2\dot{y}_o \sin(\omega t) + (4\dot{x}_o - 6\omega y_o)\cos(\omega t) \\ & + 6\omega y_o - 3\dot{x}_o \end{aligned} \quad (36)$$

$$\begin{aligned} \dot{y}(t) = & \sin(\omega t)(3\omega y_o - 2\dot{x}_o) \\ & + \cos(\omega t)\dot{y}_o \end{aligned} \quad (37)$$

$$z(t) = \cos(\omega t)z_o + \frac{1}{\omega}\dot{z}_o \sin(\omega t) \quad (38)$$

$$\dot{z}(t) = -\omega z_o \sin(\omega t) + \dot{z}_o \cos \omega t \quad (39)$$

The above equations are the fundamental basis for the following safe trajectory concept.

## 3 Safe Trajectory Concept

### 3.1 Approach/Departure Quadrant

Considering the equations (34) and(35) with  $\dot{x}_o = 0$  and  $\dot{y}_o = 0$  :

$$x(t) = 6y_o(\omega t - \sin(\omega t)) + x_o \quad (40)$$

$$y(t) = y_o(4 - 3\cos(\omega t)) \quad (41)$$

For  $t \geq 0$  the terms in the brackets are greater than zero. Four quadrants are considered for drift away:

Quadrant1  $x > 0 \quad y > 0$  drift in +x

Quadrant2  $x < 0 \quad y > 0$  collision risk

Quadrant3  $x < 0 \quad y < 0$  drift in -x

Quadrant4  $x > 0 \quad y < 0$  collision risk

A drift in direction of the Freedom is unacceptable in regard to the safe trajectory concept for collision avoidance. Therefore, quadrant 1 or 3 can only be selected.

In quadrant 1 the Free Flyer orbit altitude is higher than the Freedom one. This difference in orbit altitude is necessary for a drift away in +x direction. For long term safety it is important, that this difference will not be compensated by the differential air drag effect. Under the assumption of equal air densities, the ballistic number of the Free Flyer in quadrant 1 has to be greater than the Freedom one.

A similar argumentation for quadrant 3 leads to a Free Flyer ballistic number of less than the one of Freedom.

In its nominal orientation the ballistic number of the Free Flyer is lower than the Freedom one, so

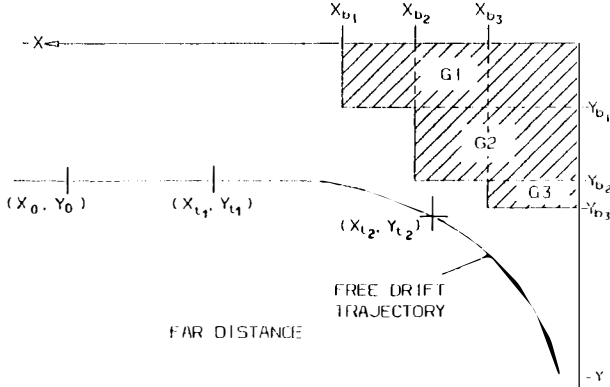


Figure 3: Collision Detection Model 1

that a propulsion shut off in quadrant 3 ensures a drift away in  $-x$  direction. Therefore quadrant 3 is selected for the approach and departure trajectory.

### 3.2 Trajectory Selection

During the approach phase the Free Flyer transfer velocities shall be selected in such a way, that after a propulsion shut off in quadrant 3 no collision will occur.

A collision will only occur, if one point  $x(t), y(t), z(t)$  for  $t > 0$  of the free drift trajectory defined by the equations (34)-(39) and the initial condition  $x_o, y_o, z_o, \dot{x}_o, \dot{y}_o, \dot{z}_o$  will be in the configuration region of Freedom, described by  $x_{Bi}, y_{Bi}$  and  $z_B$  in figure 3.

The values to define the border of the region  $x_{Bi}, y_{Bi}, z_B$  are selected in such a way, that a violation of this border by the Free Flyer c.o.m. in an arbitrary attitude leads to a collision, i.e. the Free Flyer is assumed to be a sphere.

A mathematical formulation of this conservative algorithm is given by the definition of the safe region  $\mathcal{SR}$ :

$$\begin{aligned} (x_o, y_o, z_o, \dot{x}_o, \dot{y}_o, \dot{z}_o) \in \mathcal{SR} \Rightarrow \forall_{t>0} \\ [(x(t) < x_{b1}) \vee (y(t) < y_{b1})] \wedge \\ [(x(t) < x_{b2}) \vee (y(t) < y_{b2})] \wedge \\ \dots \\ [(x(t) < x_{bn}) \vee (y(t) < y_{bn})] \wedge \\ [(|z(t)| < z_{b1})] \end{aligned} \quad (42)$$

If all points of the selected trajectory  $x(t), y(t), z(t), \dot{x}(t), \dot{y}(t), \dot{z}(t)$  are elements of the safe region, the trajectory is defined as element of the safe trajectory set  $\mathcal{ST}$

$$\begin{aligned} \forall_{t>0} (x(t), y(t), z(t), \dot{x}(t), \dot{y}(t), \dot{z}(t)) \in \mathcal{SR} \\ \Rightarrow (x(t), y(t), z(t), \dot{x}(t), \dot{y}(t), \dot{z}(t)) \in \mathcal{ST} \end{aligned} \quad (43)$$

A refinement of this collision detection algorithm 1 is necessary in the very close vicinity of Freedom. In

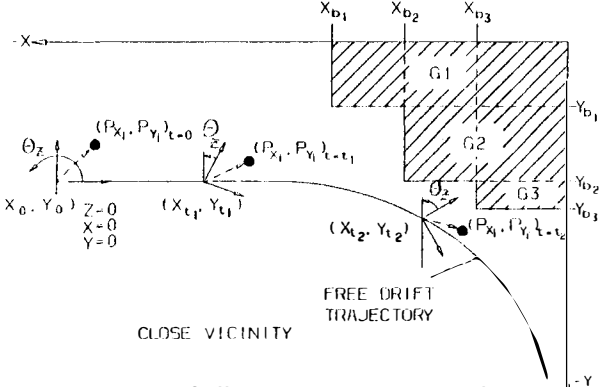


Figure 4: Collision Detection Model 2

this case, however, the Free Flyer surface is modelled as a set of grid nodes, see figure 4. Each of these grid nodes will be projected into the orbit plane. A violation of one of these projection of a grid nodes with the in-plane configuration region of Freedom leads to a collision detection.

The mathematical formulation is given by the following alternative definition of the safe region:

$$\begin{aligned} (x_o, y_o, z_o, \dot{x}_o, \dot{y}_o, \dot{z}_o, \theta_{x_o}, \theta_{y_o}, \theta_{z_o}, \dot{\theta}_{x_o}, \dot{\theta}_{y_o}, \dot{\theta}_{z_o}) \\ \in \mathcal{SR} \Rightarrow \forall_{t>0} \forall_{i=1,2,\dots,m} \\ [(\mathcal{P}_{x_i}(x, y, \theta_x, \theta_y, \theta_z)_{(t)} < x_{b1}) \vee \\ (\mathcal{P}_{y_i}(x, y, \theta_x, \theta_y, \theta_z)_{(t)} < y_{b1})] \wedge \\ [(\mathcal{P}_{x_i}(x, y, \theta_x, \theta_y, \theta_z)_{(t)} < x_{b2}) \vee \\ (\mathcal{P}_{y_i}(x, y, \theta_x, \theta_y, \theta_z)_{(t)} < y_{b2})] \wedge \\ \dots \\ [(\mathcal{P}_{x_i}(x, y, \theta_x, \theta_y, \theta_z)_{(t)} < x_{bn}) \vee \\ (\mathcal{P}_{y_i}(x, y, \theta_x, \theta_y, \theta_z)_{(t)} < y_{bn})] \wedge \\ [(|z(t)| < z_{b1})] \end{aligned} \quad (44)$$

If all points of the selected trajectory  $x(t), y(t), z(t), \dot{x}(t), \dot{y}(t), \dot{z}(t), \theta_{x_o}, \theta_{y_o}, \theta_{z_o}, \dot{\theta}_{x_o}, \dot{\theta}_{y_o}, \dot{\theta}_{z_o}$  are elements of the safe region, the trajectory is defined as element of the safe trajectory set  $\mathcal{ST}$

$$\begin{aligned} \forall_{t>0} (x(t), y(t), z(t), \dot{x}(t), \dot{y}(t), \dot{z}(t), \theta_{x_o}, \theta_{y_o}, \theta_{z_o}, \dot{\theta}_{x_o}, \dot{\theta}_{y_o}, \dot{\theta}_{z_o}) \in \mathcal{SR} \\ \Rightarrow (x(t), y(t), z(t), \dot{x}(t), \dot{y}(t), \dot{z}(t)) \in \mathcal{ST} \end{aligned} \quad (45)$$

With this advanced selection algorithm the safe trajectory set can be identified or the safety of a selected trajectory will be investigated.

Special events, as thruster open failures, measurement errors, control errors etc. are investigated as a change of the initial conditions. A limitation of such errors is a major design demand.

The demand of minimum propellant is not of major interest for this scenario, because collision avoidance and adjustment of the arrival time are overriding. In so far a minimum propellant demand can only be implemented by a minimum distance between safe trajectory and v-bar, see figure 6.

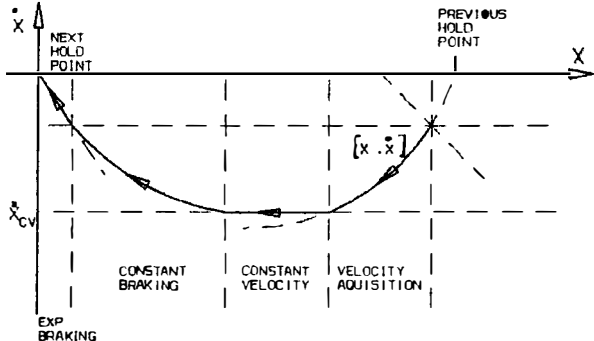


Figure 5: The Transfer between Hold Points illustrated in the Phase Plane.

### 3.3 Transfer on the Trajectory

The velocity control strategy for a transfer on the trajectory is subdivided in the two major elements:

- Transfer between Hold Points.
- Station Keeping in Hold Points.

The transfer between hold points is illustrated in figure 5. The initial starting point  $[x_0, \dot{x}_0]$  may be anywhere in the phase plane, nominally close to station keeping of the previous hold point. The predefined trajectory is subdivided into: the velocity acquisition, constant velocity, constant braking, and exponential braking. For each of these phases a special control algorithm is developed. The interception of the acquisition trajectory can take place either during constant velocity, constant braking, or the exponential braking branch.

Station keeping in hold points is necessary to adjust the arrival time or to cover special operational constraints as e.g. a grappling failure. Special algorithms have been investigated in order to minimize the propellant consumption during a station keeping for up to 24 h, or during grappling.

## 4 RvB Scenario

The RvB scenario including proximity operations is illustrated in figure 6 and is subdivided into the nominal approach and departure.

### 4.1 Nominal Approach

The proximity operations are started when the Free Flyer has completed the plane and phase correction manoeuvres and has entered the control box S1, see figure 6.

The Free Flyer will drift from S1 to S1A due to the difference in orbital velocity of the two vehicles. Only attitude control is performed for this 'drift-by'. When S1A is reached, the first burn of the Hohmann transfer to a so-called hold point S2 is executed. During the final phase of the transfer, deviations from the nominal Hohmann trajectory

will be corrected using bi-propellant thrusters with 22 N thrust level. Position determination is performed by the Differential Global Positioning System (DGPS). The transfer time from S1 to S1A is about 3 orbit revolution (270 min) and from S1A to S2 is about 50 min.

During the whole transfer from S1 to S2 the Free Flyer will be pointed with the -x axis in the velocity direction to enable firing with the higher thrust (400 N) at S1A. The solar arrays rotational axis extends perpendicular to the orbit plane.

The hold point S2 is located 1 km ahead of the Freedom and 20 m below its v-bar. In S2 the Free Flyer will be reoriented with its minus x-axis pointing nadir. The solar arrays rotational axis is still maintained perpendicular to the orbit plane. From S2 onwards four of the five thruster branches will be inhibited. The chosen Free Flyer attitude results in an efficient use of the 22 N bi-propellant thrusters, leading to minimum propellant consumption. Presently, the Free Flyer station keeping time at S2 is assumed to be 90 min maximum with a position accuracy of  $\pm 15m$  in x-direction,  $\pm 10m$  in y-direction (out of plane), and  $\pm 50m$  in z-direction (v-bar).

After station keeping the Free Flyer performs a transfer from the hold point S2 to the hold point S3, which is located 100 m ahead of the Freedom and 20 m below its v-bar. During this transfer the Free Flyer position control is characterized by the use of 22 N hot gas thrusters, a control limit cycle with lower deviation and an advanced navigation using DGPS and the RvB sensors located on the Free Flyer. The transfer time will be about 50 min. At the hold point S3 station keeping of up to 60 min will be performed with a position accuracy of  $\pm 5m$  in x- and y-direction and  $\pm 10m$  in z-direction.

During the last transfer from the hold point S3 to the grappling point S5 the Free Flyer will rise its orbit between S3 and S4 from  $\pm -20m$  to  $\pm -17m$ . At S4A the transfer velocity is reduced to be compliant with the collision avoidance requirement.

At S5 the Free Flyer will perform a station keeping of less than 5 minutes. During this time the Free Flyer will be grappled by Freedom's remote manipulator and the rendezvous will be terminated. After grappling, the Free Flyer solar arrays and antenna mast will be retracted and the manipulator will move the Free Flyer to its final docking position with the laboratory docked to a logistic node of Freedom.

### 4.2 Nominal Departure

After completion of the Free Flyer servicing and P/L resupply/reconfiguration at Freedom, the Free Flyer will be transferred from the logistic node to the grapple point. After system activation and de-

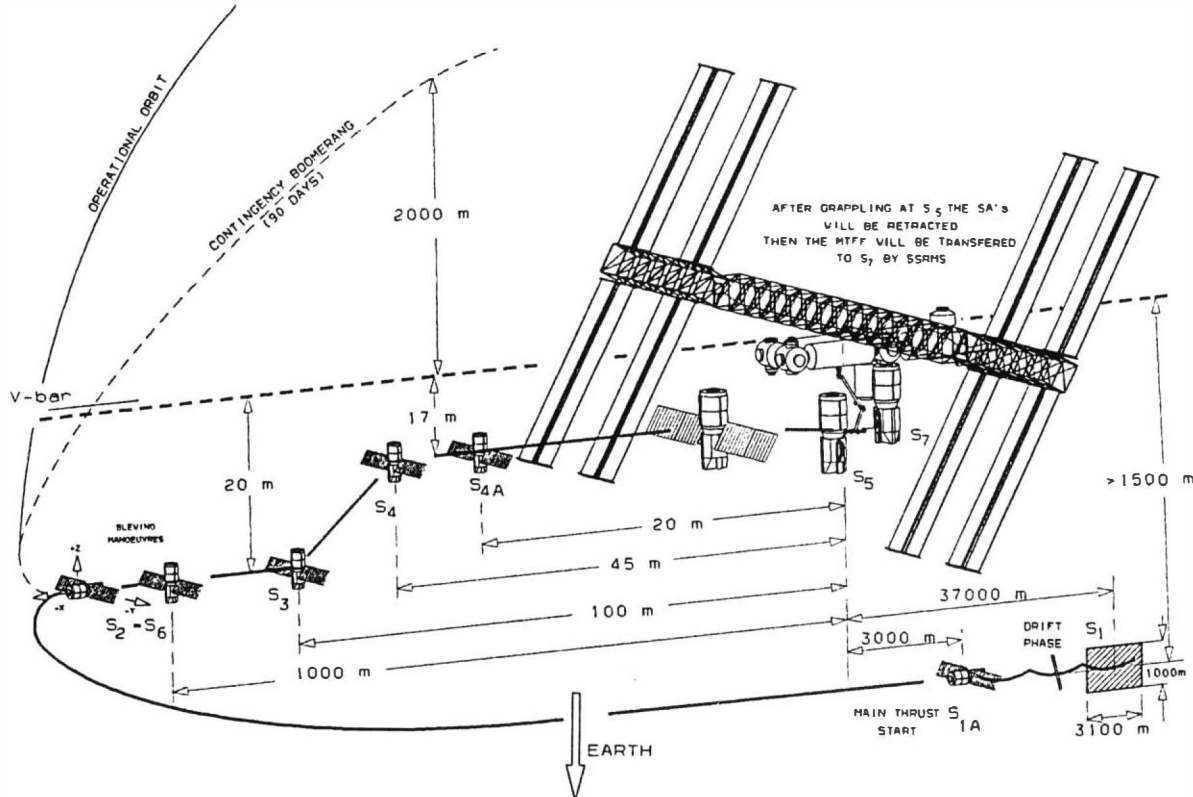


Figure 6: RvB Scenario between Free Flyer and Freedom

ployment of the solar arrays and antenna the Free Flyer will be released from the manipulator arm such, that the free Flyer c.o.m. will be about 15 m below the v-bar. The natural drift will lead to a separation of the two vehicles of about 500m per orbit revolution in +v-bar direction of Freedom. After two or three drift orbits a thrusted pulse will be applied to approach the hold point S6. Station keeping will be performed similar to the station keeping at S2. After a final system checkout and calibration the station keeping will be terminated by initiating an orbit transfer manoeuvre into the operational orbit.

## 5 Conclusion

The defined method allows the selection of a safe trajectory, which provides, at any time during proximity operation within the Freedom CCZ, the capability to shut off the propulsion system resulting in a Free Flyer drift away without any possibility of collision. This method can be used generally for rendezvous in coplanar orbits.

After Free Flyer propulsion shut off, the attitude might be uncontrolled. As long as the orbit altitude is lower than the one of Freedom, the drift away con-

tinues. In the case, that the uncontrolled Free Flyer has a higher ballistic number, the differences in the orbit altitude decreases, resulting after crossing the v-bar in a Free Flyer reapproach to Freedom.

Presently, this effect cannot be totally excluded, but on the other hand it is plenty of time, several hours, to initiate an escape manoeuvre by Freedom.

## 6 Acknowledgement

This paper as presented here refers to the proposal B/L 1990 and has been performed under the contract of ESA. Valuable information has been obtained from colleagues, in particular Mr. Dr. W. Schnetzer, Mr. J. Rohlfsen, Mr. J. Sommer, and Mr. D. Wilde.

## References

- [1] Wilfried Wöhleke Mission Characteristics and Microgravity Environment of the Columbus Free Flying Laboratory, 39. Congress of the Hermann Oberth Society, Garmisch Partenkirchen, 1990

# SYNTHESIS OF ROBUST MULTIVARIABLE CONTROLLERS FOR LARGE FLEXIBLE STRUCTURES

Cher-Hiang Goh and G. Grübel

DLR German Aerospace Research Establishment, Institute for Flight Systems Dynamics,  
D-8031, Oberpfaffenhofen, Germany

**Abstract**— In this paper, the design of robust multivariable controllers for flexible structures with collocated actuators and sensors is considered. The method exploits the positive realness property of the flexible structure and involves a novel guidance for selecting the weighting matrices for the states and the control inputs, as well as for the covariance matrices of the process and the measurement noise in an *LQG* approach. Depending on the choice of design parameters, the resultant full-order compensator is guaranteed to be either positive real or strictly positive real. The method is applied to the DLR flexible test structure to demonstrate its capability.

**Keywords**— Robust multivariable control; positive real synthesis; linear optimal control; vibration control; large space structures.

## 1 Introduction

The design of controllers for complex systems such as flexible space structures, is inevitably performed on simplified models whose parameters are known only approximately. The resulting compensators, when operating in a real environment, are required to retain the properties they are designed to have, foremost of which is the closed-loop stability. It is well known that a flexible structure with collocated actuators and sensors remains positive real despite the uncertainties in the system parameters (Bals, 1989; Joshi, 1989). It is thus advantageous if this system property can be used when designing the compensator. The rationale of applying a strictly positive real compensator for the collocated flexible structure is based on the fact that the interconnection of a positive real system with a strictly positive real compensator in a negative feedback configuration, will guarantee the closed-loop to be asymptotically stable in the sense of Liapunov. In this paper, we also provide a simpler Liapunov-function proof to show the sufficiency of the closed-loop stability in the presence of plant perturbations.

There are several approaches in synthesizing positive real compensators in the literature (Bals, 1989, 1991; Coville *et al.*, 1991; Hyland, 1985; Jacobus, 1990; McLaren, 1987; Safonov *et al.*, 1987).

A direct approach using parameter optimization within a suitably parametrized positive real controller structure has been developed and successfully applied to the control of flexible structures in (Bals, 1989, 1991). Here the behaviour of the (low-order) controllers is directly linked to the (high-order) plant model via multicriteria optimization.

The optimal projection approach (Hyland, 1985; Jacobus, 1990) requires solving four coupled Liapunov/Riccati equations by some sophisticated numerical methods such as the continuation homotopy techniques. The approach is complex and numerically demanding. The equations

are derived from the necessary conditions of the optimality and therefore the solution needs further validation. Nevertheless, the approach has been applied successfully to controlling of flexible structures and it can handle low-order strictly positive real compensator synthesis as well. A drawback is that the existence question of the solution is not answered before the design is carried out.

Recently there has been some interests to design a strictly positive real compensator within the  $H_\infty$  framework (Coville *et al.*, 1991; Safonov *et al.*, 1987). The method proposed by Coville (1991) designs a compensator that is positive real only within a particular frequency region of interest while treating the robustness issue at other frequencies via the small gain theorem. This approach is not suitable for the large space structures where the uncertainties can occur basically at all frequencies. The approach suggested by Safonov *et al.* (1987), is to perform a bilinear transformation of the plant and design a compensator for this transformed plant. The compensator designed will be transformed back to obtain the real compensator. Obviously, the physical meaning of the system will be lost in the transformation process and it is not clear as how to choose the weighting functions for the transformed plant in the  $H_\infty$  framework. To our knowledge, no real system has been designed with this methodology yet.

The approach taken by McLaren *et al.* (1987) relies on the separation principle. It first determines a state feedback gain matrix via either the pole placement or the linear quadratic approach, followed by a specific observer design using the so-called  $\alpha$ -shift technique. The value of  $\alpha$  is selected so as to ensure the strictly positive realness of the resultant compensator. It can be proved that a larger value of  $\alpha$  will result into a dynamic compensator with a lower gain. The question of what value of  $\alpha$  is "good" is not clear.

Since it is known that the modern *LQG/LTR* approach gives no guarantee that the resultant observer-based dynamic compensator is asymptotically stable (Joshi, 1989),

it seems to be even more difficult to achieve a compensator that has the structural property of being strictly positive real exploiting the positive realness property of the plant. In the sequel, we develop a synthesis methodology to construct a positive real (or better a strictly positive real) compensator from the plant by properly selecting the weighting matrices for the states and control efforts and the covariance matrices for the process noise and the measurement noise in the *LQG* approach. It is also implied in the sequel that a stabilizing observer-based dynamic compensator with the strictly positive real property always exists for a positive real plant such as the flexible structure. Interestingly, the idea of using the weighting matrices as control design parameter has also been proposed by Mukhopadhyay (1987) to improve stability robustness using constrained optimization techniques.

This paper is organized as follows. In section 2, the design problem is formulated. The method is then outlined and stated in form of theorems in section 3. In section 4, an application example using the DLR flexible structure is illustrated and the controller performance evaluated. Finally, we give our conclusive remarks in section 5. All the proofs are in the appendices.

## 2 Design Problem Formulation

Consider a multivariable linear system in minimum realization form

$$\dot{x} = Ax + Bu + v \quad (1)$$

$$y = Cx + w, \quad (2)$$

where  $x \in R^n$  is the state,  $v \in R^n$  is the process noise,  $u \in R^m$  is the control input,  $y \in R^m$  is the measured output and  $w \in R^m$  is the measurement noise. It is assumed that the process noise and the measurement noise are uncorrelated.

An observer-based dynamic compensator which consists of a linear quadratic state regulator and an estimation filter can be represented as:

$$\dot{x}_c = Ax_c + Bu + H(y - Cx_c) \quad (3)$$

$$u = -Kx_c, \quad (4)$$

with  $x_c \in R^n$  being the estimated state. The state feedback gain matrix  $K$  of the *LQ* regulator and the gain matrix  $H$  of the estimation filter are determined as to minimize the quadratic performance index

$$J = \frac{1}{2} \lim_{t_f \rightarrow \infty} \frac{1}{t_f} \mathcal{E} \int_0^{t_f} [x^T Q x + u^T R u] dt. \quad (5)$$

The performance index is an expectation cost under the influence of the process noise and the measurement noise.

From the *LQG* theory, the matrices  $K$  and  $H$  can be determined by solving two (decoupled) algebraic Riccati equations (Joshi, 1989) :

$$XA + A^T X - XBR^{-1}B^T X + Q = 0 \quad (6)$$

$$YA^T + AY - YCTW^{-1}CY + V = 0, \quad (7)$$

such that  $X = X^T > 0$ ,  $Y = Y^T > 0$ . The matrices  $K$  and  $H$  are then given as:

$$K = R^{-1}B^T X \quad (8)$$

$$H = YC^TW^{-1}. \quad (9)$$

The matrices  $Q = Q^T \geq 0$ ,  $R = R^T > 0$ , are the state and control weighting matrices whereas the matrices  $V = V^T \geq 0$ ,  $W = W^T > 0$ , are the covariance matrices of the

process and the measurement noise.

Generally, with an arbitrary choice of the matrices  $Q, R, V, W$ , the observer-based dynamic compensator can not be guaranteed to be strictly positive real. Hence, the design problem is how to select the free matrices  $Q, R, V, W$  for a given positive real system  $(A, B, C)$  in order to achieve a strictly positive real dynamic compensator  $(A - BK - HC, H, K)$ .

## 3 Robust Control Synthesis Method

**Lemma 3.1:** Let a square transfer matrix  $G(s)$  be strictly proper and have poles only in  $\text{Re}(s) < 0$ . If  $(A, B, C)$  is a minimal realization of  $G(s)$ , then  $G(s) = C(sI - A)^{-1}B$  is positive real if and only if there exist a positive definite matrix  $P$  and a matrix  $L$  such that (Popov, 1973)

$$PA + A^T P = -LL^T$$

$$PB = C^T.$$

This is also known as the Kalman-Yakubovich Lemma .

**Definition 3.2:**  $G(s) = C(sI - A)^{-1}B$  is strictly positive real if in addition to the above, the matrix  $L$  is of full rank, i.e.  $LL^T$  is positive-definite symmetric (Anderson, 1968).

A strictly positive real compensators has a unique robustness property which can be formulated in the following theorem.

**Theorem 3.3 :** If a strictly proper, strictly positive real compensator is used with a given strictly proper, positive real plant in a negative feedback configuration, then the closed-loop system is guaranteed to be asymptotically stable. (Proof in Appendix A)

It is to note that this theorem applies to any positive real compensators, not necessarily being the same order as the design model. The proof in the Appendix A is simpler than given in (Popov 1973) and uses only the Lyapunov Stability Theory for linear time invariant systems. It is immediately obvious that, closed-loop stability remains guaranteed as long as the plant remains positive real despite of parameter variations.

It is sometimes of interest to design such controllers in a decentralized manner such that proper fault detection mechanisms can be used to guarantee the closed-loop stability under actuator/sensor failures.

Given a strictly proper plant  $(A, B, C)$  with positive real property, then it satisfies the Kalman-Yakubovich Lemma with a matrix  $P = P^T > 0$  and a matrix  $M = M^T \geq 0$ . The synthesis procedures for designing robust multivariable controller in the *LQG* approach as formulated in section 2. can then be summarized in the following theorems and corollary:

**Theorem 3.4:** The negative feedback full-order *LQG*-controller designed for a strictly proper, positive real system  $(A, B, C)$  is guaranteed to be positive real, if the four weighting matrices as in section 2. are selected as  $R = R^T > 0$ ,  $Q = Q^T = M + PBR^{-1}B^TP \geq 0$ ,  $W = R$  and  $V = P^{-1}MP^{-1} + P^{-1}C^TR^{-1}CP^{-1}$ . (Proof in Appendix B)

As free design parameter remains only the matrix  $R$ , whereas the matrices  $Q, V, W$  are computed from the design model  $(A, B, C)$  and its positive real property  $P, M$ . In practice, the two algebraic Riccati equations in the *LQG* approach need not to be solved and the controller parameters  $K$  and  $H$  are determined as  $K = R^{-1}B^TP$

and  $H = P^{-1}C^T R^{-1}$ . Though the strict positive realness of the full-order compensator can not be proved, it is a stabilizing one as the closed-loop poles, i.e. the eigenvalues of the matrix  $(A - BK)$  and  $(A - HC)$  are made stable by the *LQG* approach.

**Theorem 3.5:** The negative feedback full-order *LQG*-controller designed for a strictly proper, positive real system  $(A, B, C)$  is guaranteed to be strictly positive real, if the four weighting matrices are selected as  $R = R^T > 0$ ,  $Q = Q^T = \hat{Q} + PBR^{-1}B^TP$  with  $\hat{Q} = \hat{Q}^T > 0$ ,  $W = R$  and  $V = P^{-1}MP^{-1} + P^{-1}C^TR^{-1}CP^{-1}$ . (Proof in Appendix C)

The design parameters are thus only the control weighting matrix  $R$  and the matrix  $\hat{Q}$ . In practice, only one algebraic Riccati equation needs to be solved and the controller parameters  $K$  and  $H$  are determined by  $K = R^{-1}B^TP_1$  and  $H = P^{-1}C^TR^{-1}$ . Here the strict positive realness of the full-order compensator is guaranteed. One can also use the matrix  $\hat{Q}$  to take into account the spillover effects of truncated modes based on the singular perturbation approach (Joshi, 1989).

**Corollary 3.6:** The negative feedback full-order *LQG*-controller with prescribed degree of stability  $\alpha (\alpha > 0)$ , designed for a strictly proper, positive real system  $(A, B, C)$  is guaranteed to be strictly positive real, if the four weighting matrices are selected as  $R = R^T > 0$ ,  $Q = Q^T = \hat{Q} + PBR^{-1}B^TP$  with  $\hat{Q} = \hat{Q} > 0$  (for  $A \rightarrow A + \alpha I$ ),  $W = R$  and  $V = P^{-1}MP^{-1} + P^{-1}C^TR^{-1}CP^{-1}$ . (Proof in Appendix D)

In a regulator design with prescribed degree of stability, i.e. all regulator poles are to the left of  $-\alpha$ , the designer has greater freedom in specifying the control objectives meaningfully. In this paper, this corollary is not used for the design example, but only stated here for completeness.

Following the above procedures one yields a robust multivariable controller for a positive real plant. The method synthesizes an observer-based compensator that is of the same order as the plant and model reduction techniques such as the balanced-realization truncation or the optimal hankel-norm approximation can be used to obtain lower complexity controllers. However, strict positive realness of the reduced-order compensator may no more be guaranteed. We have recently developed a new model reduction method for strictly proper, strictly positive real systems which preserves the strict positive realness property in the reduced-order system. The results will be reported elsewhere.

Since the triple  $(A, B, C)$  is assumed to be controllable and observable, the set of the  $n$ -th order stabilizing controllers is non-empty. In the case of a positive real system, it is obvious from the above synthesis method that the set of the  $n$ -th order strictly positive real dynamic compensators is also non-empty. This observation thus answers the question of the existence of a stabilizing strictly positive real observer-based compensator for a positive real plant. This is in strong contrast to the approach taken in (Hyland, 1985; Jacobus, 1990), where the existence question of the solution is not satisfactorily answered.

For the sake of brevity, we did not include an  $n$ -th order matrix inequality equation which is useful in approximately computing the  $H_\infty$ -norm related to a particular disturbance attenuation problem. Such approximation is useful as the closed-loop system is of order  $2n$  and the  $H_\infty$ -norm computation requires a eigenvalue solution of matrix with dimension  $4n$ . This may be a formidable task for high order models of flexible structures.

## 4 Design Example

### 4.1 Description of the DLR Flexible Structure

The plant to be controlled is a hanging plate experiment at DLR (Bals, 1989; Schäfer and Lange, 1988). Fig. 1 shows the test set-up for the homogenous thin plate (mass = 66kg, height = 2.75m, width = 1.50m). The plate has very small structural rigidity because of its small thickness (2mm). The plate is suspended vertically by two light parallel wires to minimize static deformations due to gravity. This configuration approximates closely the totally free boundary conditions encountered in many spacecraft systems. The reference structures for the sensors and actuators are realized by a precision measurement support system, which can be assembled from basic elements such as rails and slides, where the test device can be attached to. Two supporting structures are provided which are completely decoupled from each other: one for the actuators and one for the sensors. For the study here, the system is configured with two collocated actuator/sensor pairs positioned as shown in Fig. 2. The actuators provide maximum output of 0.1 N.

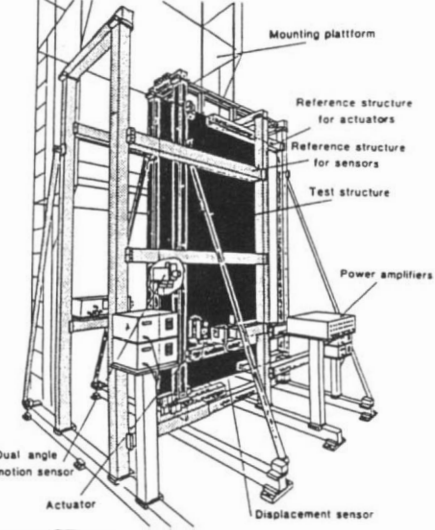


Fig. 1 The hanging plate test set-up

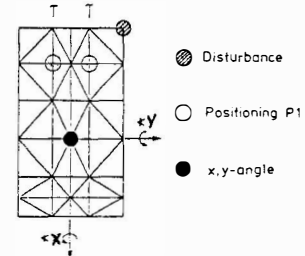


Fig. 2 The actuator/sensor position

Table 1. : The 20 vibration modes of the DLR plate

mode	$\Omega_i$ rad/sec	$\xi_i$	mode	$\Omega_i$ rad/sec	$\xi_i$
1	0.99511E+0	0.005	11	5.70006E+1	0.005
2	1.46561E+0	0.005	12	6.95847E+1	0.005
3	4.83737E+0	0.005	13	7.61079E+1	0.005
4	1.23294E+1	0.005	14	9.12207E+1	0.005
5	1.34928E+1	0.005	15	9.83542E+1	0.005
6	2.74695E+1	0.005	16	1.01407E+2	0.005
7	3.01332E+1	0.005	17	1.17394E+2	0.005
8	4.07051E+1	0.005	18	1.30978E+2	0.005
9	4.83668E+1	0.005	19	1.35705E+2	0.005
10	4.98611E+1	0.005	20	1.37721E+2	0.005

The system model of the flexible structure is a 40th-order linear system with 2 inputs and 2 outputs. The inputs are the two force actuators and the outputs are the rate measurements from the two sensor locations. The mode frequencies are obtained via finite element method. The damping of the modes does not result from the finite element analysis and is assumed to be 0.5% for all modes (Bals, 1989; Schäfer and Lange, 1988). The numerical values are shown in the Table 1.

In the following designs, a 4-th order model containing the first two modes of the evaluation model is used for synthesis to demonstrate the effectiveness of the design methodology. The 40-th order model is used for time response evaluation assuming a disturbance of 0.1 N with duration 0.5 sec acts on the top-right corner of the plate (see Fig. 2).

## 4.2 Design 1: ( R )

In this approach the matrix  $R$  is chosen to be  $0.005I$ .

The disturbance response in Fig. 3 indicates that the disturbance is well attenuated when compared to the open loop behaviour. In Fig. 4 the notches of the sensitivity function ( $S$ ) implies that the 2 modes of the design model are being attenuated. The complementary sensitivity function ( $T$ ) also shows no vibration peaks and one can proceed with the high authority design for controlling the positions of the flexible structure. The compensator has a phase lead-lag characteristic as seen in Fig. 9. In this design the first 2 modes are taken as design model  $G_r$  whereas the next 18 modes are considered as error model  $\Delta G = G_o - G_r$  to assess the robustness of the design. The sufficient condition for which the compensator  $G_c$  is robustly stabilizing the closed-loop under additive uncertainty is  $\bar{\sigma}(\Delta G) < (1/\bar{\sigma}G_c(I + G_rG_c)^{-1})$  for  $0 \leq \omega < \infty$ , where  $\bar{\sigma}$  denotes the largest singular value. Evaluating the robustness of the design from Fig. 10, shows that modes 3,4 and 5 violate the conservative sufficiency test for robustness in the presence of additive uncertainty. However, the controlled structure with the compensator is asymptotically stable by closed-loop analysis. In an iterative process of choosing matrix  $R$ , it is found that this design parameter has restricted influence on the system responses. Nevertheless, the design approach is simple and achieves good performance. It is remarked here that the approach has also been used to design 10-th order compensator and the system exhibits also good performance.

## 4.3 Design 2: ( Q and R )

By using the  $R$  matrix obtained in design 1., we converge very fast to obtain matrix  $Q$  for designing the observer-based compensator. The final matrices are selected as  $R = 0.006I$  and  $\hat{Q} = \hat{Q}^T = 20 \times \text{diag} [1, 3, 1, 1]$ .

The disturbance response is shown in Fig. 6. Comparing it with Fig. 3 indicates that the disturbance attenuation is faster than in design 1 but with slight increase in control effort. The compensator has a low pass filter characteristic with the steady state gain of about 42 dB as seen in Fig. 9. It rolls off with a rate of 20db per decade as it is usually the case with observer-based compensator design. The notches from the sensitivity function ( $S$ ) in Fig. 7 indicates vibration suppression at those particular frequencies. Again, the conservativeness of using singular values to assess the robustness is visible in Fig. 10 where violation of the test occurs at the modes 3,4,5,9 and 10. However, the closed-loop is asymptotically stable as being proved in **Theorem 3.3**.

## 5 Conclusions

In this paper a robust multivariable controller synthesis methodology is developed for positive real plants such as the collocated flexible structures. It is concluded that by exploiting the positive real property of the collocated flexible structure, one can select the various weighting matrices in a special way such that the resultant compensator is either positive real, or strictly positive real. An application using the method to the DLR flexible structure is illustrated. The techniques developed here also offers great potential to investigate future structure/control interaction problem (Bals *et al.*, 1991; Lim and Junkins, 1989; Sco *et al.*, 1990).

## References

- Anderson, B.D.O. (1968).* A simplified viewpoint of hyperstability, *IEEE Trans. Auto. Contr.*, **AC-13**, 292-294.
- Bals, J. (1989).* Aktive Schwingungsdämpfung flexibler Strukturen, *Doctoral Dissertation*, Universität Karlsruhe.
- Bals, J., G. Grübel *et al.* (1991).* Flows between Structural Control Designs by Examples of the Extendable and Retractable Mast, *Proc. of Int. Symp. on Active Materials and Adaptive Structures*, Alexandria, VA.
- Bals, J (1991).* A Hyperstability/Multiobjective Optimization Approach for Active Flexible Structures *Proc. of 1st. IFAC Symposium on Design Methods of Control Systems*, Zurich.
- Coville, A., H. Abou-Kandil and P. Costal (1991).* Hyperstability and Small Gain: A Unified Approach in the  $H_\infty$  Frame, *Proc. ECC*, France, 2266-2271.
- Hyland, D.C. and D.S. Bernstein (1984).* The Optimal Projection Equations for Fixed-Order Dynamic Compensation, *IEEE Trans. Auto. Contr.*, **AC-29**, 1034-1037.
- Hyland, D.C. and D.S. Bernstein (1985).* The Optimal Projection Equations /Maximum Entropy approach to Designing Low-order, Robust Controllers for Flexible Structures, *Proc. of the 24th IEEE CDC*, 745-752.
- Jacobus, M., D.S. Bernstein *et al.* (1990).* Design of Strictly Positive Real Fixed Order Dynamic Compensators, *Proc. of the 29th CDC*, Honolulu, Hawali, 3492-3495.
- Joshi, S.M. (1989).* Control of Large Flexible Space Structures, *Lecture Notes in Control and Information Science*, **131**, Springer Verlag Berlin, Heidelberg.
- Lim, K.B. and J.L. Junkins (1989).* Robustness Optimization of Structural and Controller Parameters, *J. of Guidance, Control and Dynamics*, **12**, 89-96.
- McLaren, M.D. and G.L. Slater (1987).* Robust Multivariable Control of Large Space Structures using positivity, *J. of Guidance, Control and Dynamics*, **10**, 393-400.
- Mukhopadhyay, V. (1987).* Stability Robustness Improvement Using Constrained Optimization Techniques, *J. of Guidance, Control and Dynamics*, **10**, 172-177.
- Ogata, K. (1970).* Modern Control Engineering, *Prentice-Hall*, Inc., U.S.A.
- Popov, V.M. (1973).* Hyperstability of Control Systems, *Springer Verlag*, Berlin.
- Safonov, M.G., E.A. Jonckherre *et al.*, (1987).* Synthesis of Positive Real Multivariable Feedback Systems, *Int. J. Control*, **45**, 817-842.
- Schäfer, B.E. and T. Lange (1988).* Dynamic and Control Experiments of Large Space Structures at DFVLR, *Control Theory and Advanced Technology*, **4**, 91-119.
- Scott, K., Hunziker, R.H. Kraft *et al.* (1990).* Optimization of Linear Controlled Structures, *Proc. ACC*, 854-859.
- Slater, G.L., Q. Zhang and A. Bosse, (1989).* Robustness with Positive Real Controllers for Large Space structures, *Proc. AIAA Guidance, Navigation, and Control Conference*, Boston, MA, 932-941.

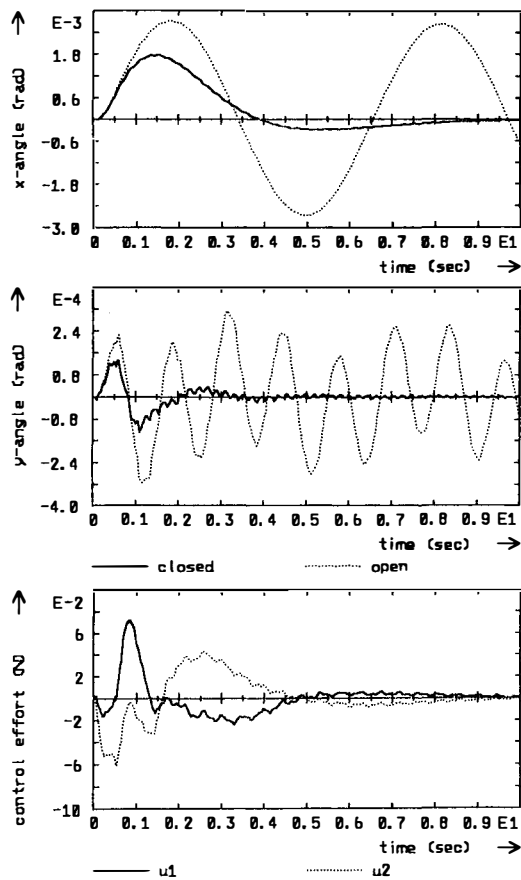


Fig. 3 The disturbance time response (  $R$  )

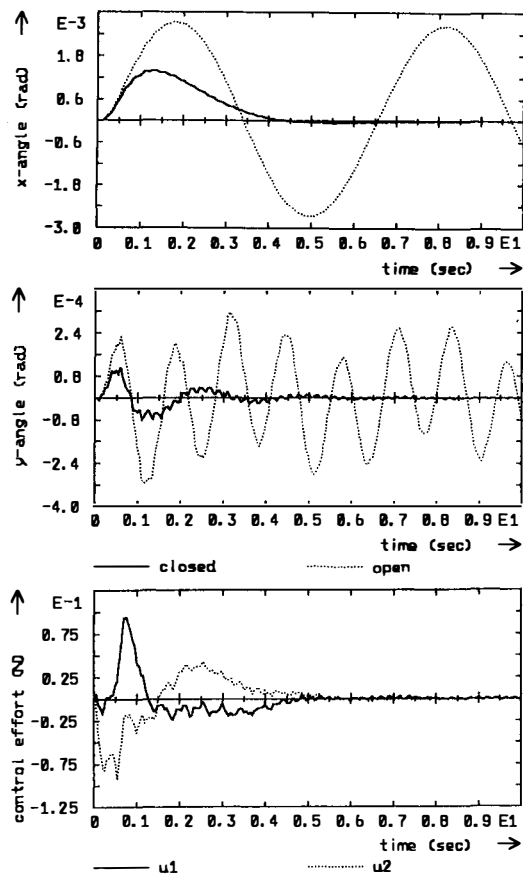


Fig. 6 The disturbance time response (  $Q$  &  $R$  )

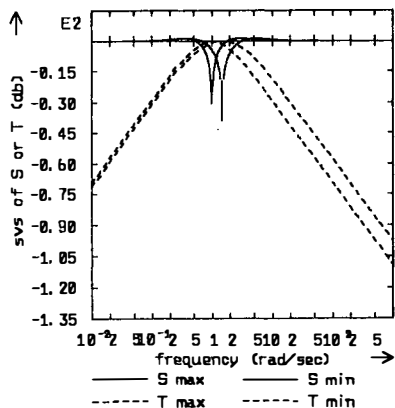


Fig. 4 The closed-loop property (  $R$  )

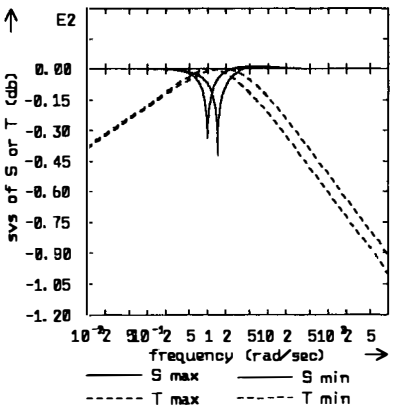


Fig. 7 The closed-loop property (  $Q$  &  $R$  )

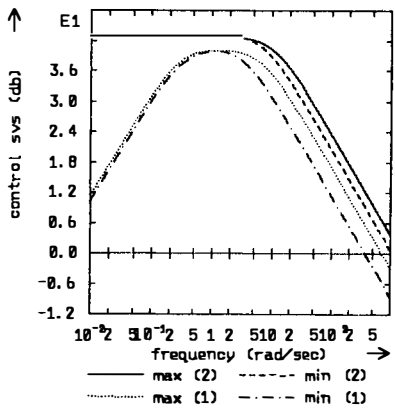


Fig. 9 The controllers (Design 1 & 2)

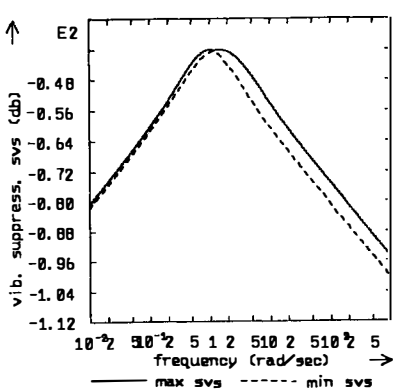


Fig. 5 The vibration suppression (  $R$  )

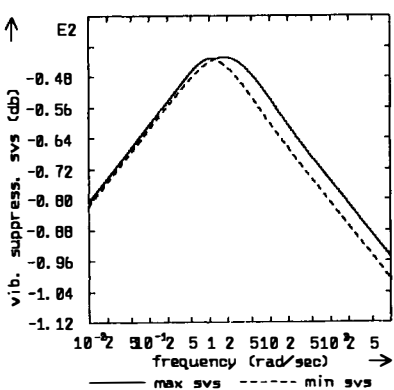


Fig. 8 The vibration suppression (  $Q$  &  $R$  )

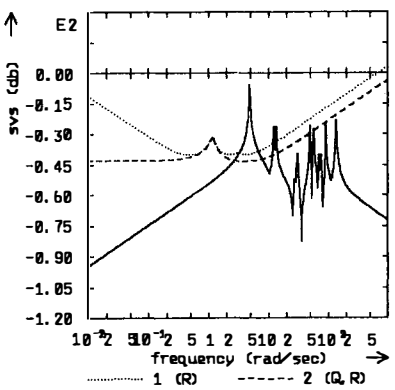


Fig. 10 The robustness test

### Appendix A: Proof of Theorem 3.3:

Given that the plant with the triple  $(A, B, C)$  is positive real and the controller with the triple  $(A_c, B_c, C_c)$  is strictly positive real, then due to Kalman-Yakubovich Lemma, there exist a matrix  $P = P^T > 0$  and a matrix  $M = M^T \geq 0$  such that

$$PA + A^T P = -M$$

$$PB = C^T,$$

and a matrix  $P_c = P_c^T > 0$  and a matrix  $M_c = M_c^T > 0$  such that

$$P_c A_c + A_c^T P_c = -M_c$$

$$P_c B_c = C_c^T.$$

As the compensator is in the negative feedback configuration, then the Lyapunov equation for the closed-loop system will be:

$$\bar{P}\bar{A} + \bar{A}^T\bar{P} = -\bar{M},$$

with the closed-loop stability matrix  $\bar{A} = \begin{bmatrix} A & -BC_c \\ B_c C & A_c \end{bmatrix}$ .

It is known from the Lyapunov Stability Theory that the existence of a  $\bar{P} > 0$  for a given  $\bar{M} > 0$  or  $\bar{M} \geq 0$  (if it is permissible), is a necessary and sufficient condition for the asymptotic stability of  $\bar{A}$ . It is obvious that the matrix  $\bar{P} = \bar{P}^T = \begin{bmatrix} P & 0 \\ 0 & P_c \end{bmatrix} > 0$  and the matrix  $\bar{M} = \bar{M}^T = \begin{bmatrix} M & 0 \\ 0 & M_c \end{bmatrix} \geq 0$  satisfy the closed-loop Lyapunov equation and thus the asymptotic stability of the closed-loop is assured. The choice of  $\bar{M} \geq 0$  is permissible here since the time derivative of the Lyapunov function can not be identically zero except at the origin, i.e.  $[x^T \ x_c^T] \bar{M} \begin{bmatrix} x \\ x_c \end{bmatrix} = x^T M x + x_c^T M_c x_c$ , vanishes only at  $x = 0$  and  $x_c = 0$  (Ogata, 1970). It is remarked that the proof using the hyperstability concept yields the same conclusion (Popov, 1973). ■

### Appendix B: Proof of Theorem 3.4:

The system  $(A, B, C)$  is positive real and hence satisfies the Kalman-Yakubovich Lemma with  $P = P^T > 0$  and a matrix  $M = M^T \geq 0$ , i.e.

$$PA + A^T P = -M$$

$$PB = C^T.$$

Rewriting the first equation as:

$$PA + A^T P - PBR^{-1}B^T P + M + PBR^{-1}B^T P = 0$$

and its dual form  $P^{-1}A^T + AP^{-1} = -P^{-1}MP^{-1}$  as

$$\begin{aligned} &P^{-1}A^T + AP^{-1} - P^{-1}C^T R^{-1}CP^{-1} + \\ &P^{-1}MP^{-1} + P^{-1}C^T R^{-1}CP^{-1} = 0. \end{aligned}$$

Then it is straightforward to observe that these two equations are the algebraic Riccati equations related to the full-order controller design using the LQG approach, if the weighting matrices are chosen as  $R = R^T > 0$ ,  $Q = Q^T = \hat{Q} + PBR^{-1}B^T P \geq 0$ ,  $W = R$  and  $V = V^T = P^{-1}MP^{-1} + P^{-1}C^T R^{-1}CP^{-1} \geq 0$ . The positive-definite symmetric solutions of the algebraic Riccati equations are  $X = X^T = P$ ,  $Y = Y^T = P^{-1}$  and the state feedback gain matrix and the estimator gain matrix can be determined as  $K = R^{-1}B^T P$  and  $H = P^{-1}C^T R^{-1}$ .

The positive realness of the controller with the triple  $(A - BK - HC, H, K)$  is ascertained by showing that the controller satisfies the Kalman-Yakubovich Lemma with  $P_c = P_c^T > 0$  and  $M_c = M_c^T \geq 0$ . First it is established that  $P_c = P$ . This is easy as due to the system positive real property  $PB = C^T$ , one yields  $P_c H = PP^{-1}C^T R^{-1} = C^T R^{-1} = PBR^{-1} = K^T$ . Next it remains to show the existence of  $M_c$ , i.e.

$$\begin{aligned} &P_c(A - BK - HC) + (A - BK - HC)^T P_c \\ &= P(A - BK - HC) + (A - BK - HC)^T P \\ &= P(A - BK) + (A - BK)^T P - PHC - C^T H^T P \\ &= P(A - BK) + (A - BK)^T P - K^T C - C^T K \\ &= P(A - BK) + (A - BK)^T P - 2PBR^{-1}B^T P \\ &= -M - 4PBR^{-1}B^T P = -M_c \leq 0, \end{aligned}$$

as  $M \geq 0$  and  $PBR^{-1}B^T P \geq 0$ . ■

### Appendix C: Proof of Theorem 3.5:

Rewriting the algebraic Riccati equation for the regulator as

$$P_1 A + A^T P_1 - P_1 B R^{-1} B^T P_1 + \hat{Q} + P B R^{-1} B^T P = 0$$

and the dual form of  $P^{-1}A^T + AP^{-1} = -P^{-1}MP^{-1}$  as

$$\begin{aligned} &P^{-1}A^T + AP^{-1} - P^{-1}C^T R^{-1}CP^{-1} + \\ &P^{-1}MP^{-1} + P^{-1}C^T R^{-1}CP^{-1} = 0. \end{aligned}$$

It is easy to observe that these two equations are the algebraic Riccati equations related to the full-order controller design using the LQG approach, if the weighting matrices are chosen as  $R = R^T > 0$ ,  $Q = Q^T = \hat{Q} + PBR^{-1}B^T P > 0$  ( $\hat{Q} > 0$ ),  $W = R$  and  $V = V^T = P^{-1}MP^{-1} + P^{-1}C^T R^{-1}CP^{-1} \geq 0$ . The positive-definite symmetric solutions of the algebraic Riccati equations are  $X = X^T = P_1$ ,  $Y = Y^T = P^{-1}$  and the state feedback gain matrix and the estimator gain matrix can be determined as  $K = R^{-1}B^T P_1$  and  $H = P^{-1}C^T R^{-1}$ .

The strictly positive realness of the controller with the triple  $(A - BK - HC, H, K)$  is ascertained by showing that the controller satisfies the Kalman-Yakubovich Lemma with  $P_c = P_c^T > 0$  and  $M_c = M_c^T \geq 0$ . First we prove that  $P_c = P_1$ . Similar to 3.3.1, it is shown that due to  $PB = C^T$ , we have  $P_c H = P_1 P^{-1}C^T R^{-1} = P_1 B R^{-1} = K^T$ . Next it remains to show the existence of  $M_c$ , i.e.

$$\begin{aligned} &P_c(A - BK - HC) + (A - BK - HC)^T P_c \\ &= P_1(A - BK - HC) + (A - BK - HC)^T P_1 \\ &= P_1(A - BK) + (A - BK)^T P_1 - P_1 H C - C^T H^T P_1 \\ &= P_1(A - BK) + (A - BK)^T P_1 - K^T C - C^T K \\ &= P_1(A - BK) + (A - BK)^T P_1 - \\ &\quad P_1 B R^{-1} B^T P - P B R^{-1} B^T P_1 \\ &= P_1(A - BK) + (A - BK)^T P_1 + P_1 B R^{-1} B^T P_1 \\ &\quad + P B R^{-1} B^T P - (P_1 + P) B R^{-1} B^T (P_1 + P) \\ &= -\hat{Q} - (P_1 + P) B R^{-1} B^T (P_1 + P) = -M_c < 0, \end{aligned}$$

as the matrix  $\hat{Q} = \hat{Q}^T > 0$  and  $(P_1 + P) B R^{-1} B^T (P_1 + P) \geq 0$ . ■

### Appendix D: Proof of Corollary 3.6:

If a prescribed degree of stability  $\alpha > 0$  is imposed on the design of the regulator, i.e. the real part of every eigenvalue of  $(A - BK)$  is less than  $-\alpha$ . Then the full-order compensator is again guaranteed to be strictly positive real. In this case, the matrix  $P_1$  is solved in the following equation:

$$P_1(A + \alpha I) + (A + \alpha I)^T P_1 - P_1 B R^{-1} B^T P_1 + \hat{Q} + P B R^{-1} B^T P = 0,$$

and the controller can be shown to be strictly positive real as it satisfies  $P_c H = K^T$  and

$$\begin{aligned} &P_c(A - BK - HC) + (A - BK - HC)^T P_c \\ &= \vdots \\ &= -\hat{Q} - 2\alpha P_1 - (P_1 + P) B R^{-1} B^T (P_1 + P) \\ &= -M_c < 0. \end{aligned}$$

(For brevity, this part of the proof is only sketched). ■

## DIRECT NUMERICAL DESIGN OF REDUCED ORDER CONTROLLERS FROM EXPERIMENTAL DATA

R.D. Irwin, W.G. Frazier and J.R. Mitchell

*Department of Electrical and Computer Engineering, Stocker Center, Ohio University, Athens, Ohio 45701, USA*

**Abstract** An iterative numerical algorithm for designing robust controllers using experimental data models is presented. This numerical approach has several advantages over standard analytical approaches. First, design constraints of many types can be specified. Also, the controller order is pre-specified by the designer. Finally, no analytical model of the system to be controlled is required; instead, experimental frequency response data can be used. The algorithm has been successfully applied to the design of a controller for disturbance rejection and vibration suppression in a flexible structure test facility. This application involved satisfying a variety of design goals, resulted in a low order controller, and experimental data were used as the sole plant model.

**Key Words** aerospace control; controllers; computer aided design; frequency response; numerical methods

### INTRODUCTION

Research in control design has focused almost exclusively on the problem of designing controllers for systems that are described by analytical models. Here analytical models include those that are derived from empirical considerations and measurements but that yield finite dimensional linear state space or transfer function matrix models. The most serious problem with many modern design techniques is the fact that the resulting controllers have order at least as great as that of the plant model. In extreme cases in which the plant model order is very high this characteristic can lead to the total failure to generate a controller due to numerical limitations of the design algorithms. Robust control techniques combined with model reduction techniques may offer no relief due to either their own numerical difficulties or to the fact that it is impractical to achieve a sufficient degree of robustness to compensate even for modeling error.

This paper promotes the pragmatic approach of designing reduced order controllers using iterative numerical techniques applied to frequency response data models. Advantages of this approach include the freedom to simultaneously specify design constraints of many types, the ability to constrain the controller order, and the elimination of the need to derive an analytical model. The major disadvantage of the numerical approach is the lack of existence results. This lack of theoretical

framework for the existence of controllers which meet the desired design goals or for algorithm convergence must be weighed without undue prejudice against the limitations of analytical techniques which typically encompass only one or two design goals and which require analytical models. For example, recent results on mixed H-infinity/H<sub>2</sub> controller design must at this point be considered as numerical techniques, since the set of equations that must be solved to obtain such a controller must be solved iteratively. Similar statements can be made concerning mu-synthesis. Our philosophy is that once a numerical approach is deemed necessary or desirable for any reason, the controller design should include as many realistic design goals as can be accommodated within the framework of the particular numerical method to be used. Hence, a better alternative to analytical techniques may be a completely iterative approach.

This paper presents a simple numerical approach to the design of controllers for linear, time-invariant, multivariable systems. The organization of the paper is as follows. First, the basis of the numerical algorithm for achieving the design constraints is presented. The results of application to, and implementation in, a large space structure test facility are then presented. Finally, conclusions are drawn regarding the algorithm effectiveness and future research directions are indicated.

## CONSTRAINT IMPROVEMENT ALGORITHM

Let the set of  $L$  inequalities

$$(1) \quad f_k(\omega_j; s) > c_k(\omega_j) \quad \forall \omega_j \in \Omega_k \quad k = 1, 2, \dots, L,$$

define desired closed loop design constraints, where each  $c_k: \Omega_k \rightarrow R$  is defined according to the desired shape of  $f_k$ , and  $s$  is a vector of controller parameters. Denote the violations of Eq. (1) by  $v_j(s)$ ,  $j = 1, 2, \dots, N_v$ , where  $N_v$  is the total number of violations. It follows (dropping the dependence on  $s$  for brevity) that the gradient of each  $v_j$  is given by

$$g_j = \frac{\partial v_j}{\partial s} = \left[ \frac{\partial v_j}{\partial s_1} \frac{\partial v_j}{\partial s_2} \dots \frac{\partial v_j}{\partial s_p} \right]^T. \quad (2)$$

In the application reported in this paper,  $s$  contains the elements of a state-space representation of the controller and the  $f_k$  are singular value robustness and performance measures. The controller parameters are updated by

$$s^{(m+1)} = s^{(m)} + \epsilon^{(m)} d^{(m)} \quad (3)$$

where  $\epsilon$  is the step length and  $d$  is the parameter update vector.

### Choice of Direction Vector

A fundamental result from optimization theory is that to improve a violation  $v_j$  a parameter correction vector  $d$  must be chosen with the property  $g_j^T d > 0$ . Since, in general, there are many violations to be improved at any one iteration,  $d$  should be chosen to satisfy  $g_j^T d > 0 \quad j = 1, 2, \dots, N_v$ . A sufficient condition for such a direction to exist is that the system

$$[g_1 \ g_2 \ \dots \ g_{N_v}]^T d = w \quad (4)$$

be consistent, where

$$w = [w_1 \ w_2 \ \dots \ w_j \ \dots \ w_{N_v}]^T \quad (5)$$

and  $w_j > 0$  for  $j = 1, 2, \dots, N_v$ . This is a  $N_v$  by  $P$  system of linear equations. In practice Eq. (3) is almost always underdetermined because there are usually more free parameters than violations. Hence, there may be many solutions. The singular value decomposition [4] is used to obtain the solution having minimum 2-norm.

Although the above development indicates a general

technique for choosing an acceptable correction vector, it does not indicate how to choose the precise entries of  $w$  for good algorithm performance. Since it is desired to improve all the violations simultaneously, it seems reasonable to choose  $w$  such that each of violations is considered to be equally important (Mitchell, 1972).

### Choice of Step Size

Once the correction vector  $d$  is chosen at each iteration, it is necessary to determine a satisfactory step length. The choice of step length is based upon maintaining closed loop stability, maintaining open loop controller stability, and improvement of the violated constraints. In order to satisfy the requirement that the closed loop system remain stable at each iteration using only frequency response data at a finite number of points (as opposed to a mathematical model) the multivariable Nyquist criterion [6] is employed. Although not a reliable indicator of relative stability margins, it has proven effective for maintaining closed loop stability during algorithm execution. Open loop controller stability (desirable in most applications, e.g., when loop failure is possible) is maintained by simply monitoring the controller's pole locations. The final requirement for the step length, improvement of the violated constraints, cannot always be achieved. This is usually caused by one of the constraints reaching a local minimum or by two or more constraints reaching a condition of local opposition. At this point the algorithm is usually terminated. If the resulting design is not acceptable, another initial controller should be considered.

## APPLICATION TO THE ACES FACILITY

The original motivations for the development of the numerical approach to design were the extreme requirements faced in the Active Control Evaluation for Spacecraft (ACES) program and the Control Structure Interaction Phase I Guest Investigator (CSI/GI) program. One of the goals of these programs was to assess the effectiveness of various controller design approaches for large space structure control and vibration suppression using the NASA Marshall Space Flight Center ACES facility as a common test bed. Many of the difficulties encountered in the ACES and CSI/GI programs were due to the lack of high fidelity analytical models. Another problem encountered by those investigators who used "same order" controller design techniques such as LQG-based or H-infinity techniques was that of being unable to implement their controllers within the computational

constraints of the facility control computer.

### Overview of Facility

The ACES test facility is shown in schematic form in Fig. 1. The facility is intended for the study of line-of-sight (LOS) and vibration suppression control issues as they pertain to flexible aerospace structures. The primary element of the facility structure is a spare Voyager magnetometer boom measuring approximately 15 meters in length and weighing about 2.5 kilograms. The objective of the control design is to maintain the centroid of the reflected laser beam at the center of the photodetector in the presence of base motion disturbances imparted by the base excitation table (BET). This geometry mimics an on-orbit telescope with the primary and steerable secondary mirrors separated by a flexible mount and with base motion disturbances from crew motion, thruster firings, or other sources.

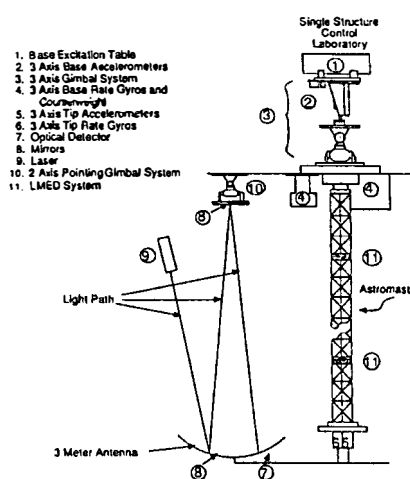


Fig. 1 The ACES Test Facility.

Two selected subsets of sensors and actuators were considered: (1) The image motion compensation (IMC) components, consisting of the two-axis photodetector and the two-axis pointing gimbal torque motors and (2) the Advanced Gimbal System (AGS) and base gyro components, consisting of the two-axis AGS and two of the gyros mounted at the base plate. The control computer of the facility takes data at 50 hertz and has a fixed computational delay of one sample period.

A typical experimental open loop frequency response for the IMC subsystem is given by Fig. 2, where it can be seen that the dominant characteristic is the pendulum effect of the gimbal. Very little interaction with the flexible structure is

apparent, although a gimbal support arm mode at about 12.5 hertz can be seen. The three other IMC responses are similar, with the cross axis elements having significantly lower gain at all frequencies. The fact that the IMC gimbals do not interact heavily with the structure has led many investigators to model the overall ACES control problem as the IMC system subject to output disturbances only. What has been ignored by all but one investigator is the fact that the BET induces significant disturbance torques at the gimbal/support arm interface. These disturbance torques appear as input disturbances. Thus, since the controller will always lie in the feedback path instead of the forward path, it is not sufficient to maintain the loop gain at a high level. Instead, it is necessary that the gain of the controller itself be maintained at a high level in order to achieve disturbance rejection.

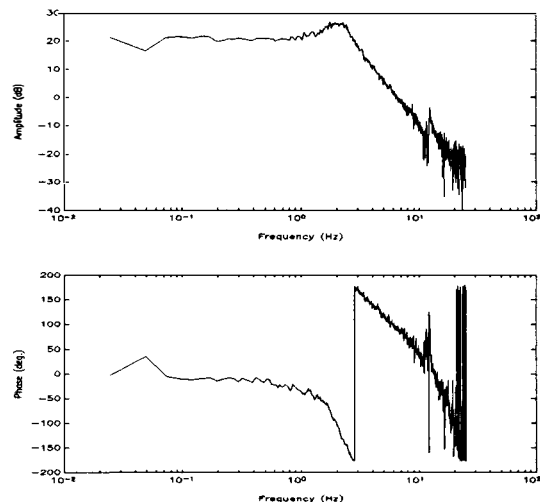


Fig. 2 Experimental Frequency Response from y-Axis IMC Gimbal to x-Axis LOS Error.

A typical AGS/base gyro frequency response is shown in Fig. 3, where the bending phenomena are clearly seen. What is not apparent in the magnitude plot is the effect of the pendulum mode at about 0.16 hertz. Damping or rejecting this mode is critical to the goal of reducing the LOS error.

### Design Philosophy

The basic design philosophy is to use the AGS (x and y axes only) with feedback from the base gyros to dampen the pendulum modes and the bending modes of the boom while using the IMC gimbals with feedback from the LOS error to maintain the laser beam at the center of the detector. Analysis of Fig. 2 indicates that achieving significant

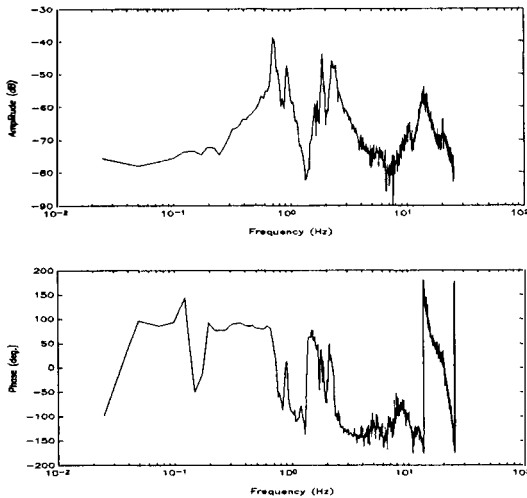


Fig. 3 Experimental Frequency Response from y-Axis of AGS to y-Axis Base-Gyro.

bandwidth in the IMC-LOS loops is difficult due to the large phase lag introduced by the computational delay. Therefore, any increase in the damping of the higher frequency bending modes of the structure should have a significant impact on overall performance. Since the IMC gimbals have very little impact on the base gyros, the IMC-LOS subsystem was designed independently of the AGS-base gyro subsystem.

Assume the closed loop configuration in Fig. 4 for each subsystem. Define

$$R_{IMC}^o(e^{j2\pi fT}) = [I + GK(e^{j2\pi fT})]_{IMC}, \quad (6)$$

$$R_{IMC}^i(e^{j2\pi fT}) = [I + KG(e^{j2\pi fT})]_{IMC}, \quad (7)$$

$$V_{IMC}^o(e^{j2\pi fT}) = [I + (GK(e^{j2\pi fT}))^{-1}]_{IMC}, \quad (8)$$

$$V_{IMC}^i(e^{j2\pi fT}) = [I + (KG(e^{j2\pi fT}))^{-1}]_{IMC}, \quad (9)$$

$$R_{AGS}^o(e^{j2\pi fT}) = [I + GK(e^{j2\pi fT})]_{AGS}, \quad (10)$$

$$R_{AGS}^i(e^{j2\pi fT}) = [I + KG(e^{j2\pi fT})]_{AGS}, \quad (11)$$

$$V_{AGS}^o(e^{j2\pi fT}) = [I + (GK(e^{j2\pi fT}))^{-1}]_{AGS}, \quad (12)$$

and

$$V_{AGS}^i(e^{j2\pi fT}) = [I + (KG(e^{j2\pi fT}))^{-1}]_{AGS}. \quad (13)$$

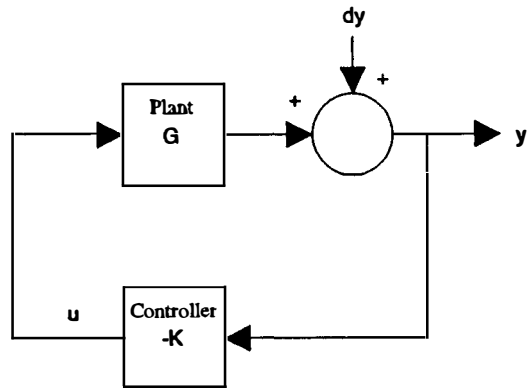


Fig. 4 Feedback Configuration for ACES Facility.

Using Eq. (6) to Eq. (13) the closed loop design constraints are defined as given in Table 1, where  $\sigma_{\min}$  denotes the minimum singular value of a matrix. The last constraint is intended to decrease the impact of the pendulum mode on the LOS. The other constraints on the return differences provide stability robustness to unstructured additive uncertainties in the plant model. The constraints on the inverse return differences provide stability robustness to unstructured multiplicative uncertainty in the plant model and also provide performance improvements by preventing large peaks in the closed loop frequency response. Discussion of the relationship of these constraints to the stability robustness and performance of multivariable systems is given in Safanov, Laub, and Hartman (1981).

Table 1: Constraint Values.

Constraint	Initial	Final
$\sigma_{\min}[R_{IMC}^o] > 0.5 \quad f \in (0, 25)$	0.23	0.51
$\sigma_{\min}[R_{IMC}^i] > 0.5 \quad f \in (0, 25)$	0.23	0.51
$\sigma_{\min}[V_{IMC}^o] > 0.6 \quad f \in (0, 25)$	0.28	0.61
$\sigma_{\min}[V_{IMC}^i] > 0.6 \quad f \in (0, 25)$	0.28	0.61
$\sigma_{\min}[R_{AGS}^o] > 0.6 \quad f \in (0, 25)$	0.36	0.60
$\sigma_{\min}[R_{AGS}^i] > 0.6 \quad f \in (0, 25)$	0.36	0.60
$\sigma_{\min}[V_{AGS}^o] > 0.7 \quad f \in (0, 25)$	0.36	0.67
$\sigma_{\min}[V_{AGS}^i] > 0.7 \quad f \in (0, 25)$	0.36	0.67
$\sigma_{\min}[R_{IMC}^o] > 18 \quad f = 0.15$	10.00	14.10

To implement the algorithm, expressions for the gradients of these constraints were needed and were calculated by a technique similar to that presented in Newsom and Mukhopadhyay (1985).

Next, initial controllers were designed for the IMC-LOS loops and for the AGS-base gyro loops by using one-loop-at-a-time graphical techniques and the experimental data. The controller for each subsystem was 10<sup>th</sup> order. It should be noted that recently developed high fidelity models are 50<sup>th</sup> order for the AGS-base gyro loops (Medina, 1991). Design techniques such as LQG and H-infinity would yield (not counting weighting) controllers of at least 50<sup>th</sup> order. In the design of the initial controllers the effects of cross-axis coupling were ignored, except for the determination of absolute stability. As a result, the constraints were not satisfied as can be seen by comparing the entries in Table 1.

### Numerical Results

The multivariable design was then performed (taking cross-axis coupling within each subsystem into account) using only experimental data with the algorithm described previously. Implementation was on an Intel 80386-based personal computer. To illustrate the results of the algorithm, Fig. 5 and Fig. 6 show the frequency response (as calculated from the open loop experimental data) of the singular values of  $R^o_{IMC}$  for the initial and final controllers, respectively.

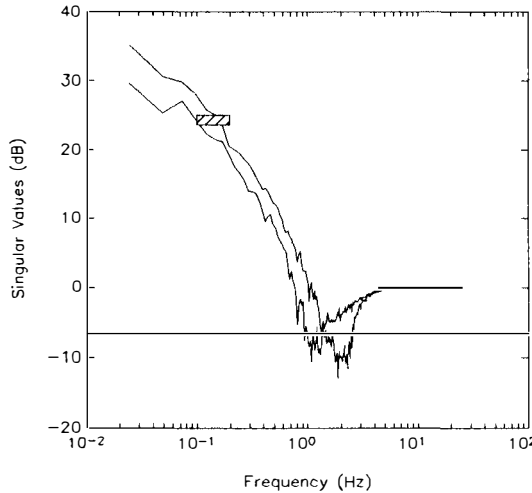


Fig. 5  $R^o_{IMC}$  Initial Singular Value Response.

The final values of the constraint functions are given in Table 1. The constraints for the AGS subsystem were not satisfied. This is because the algorithm reached a point such that these constraint functions were in a condition of local opposition with one another.

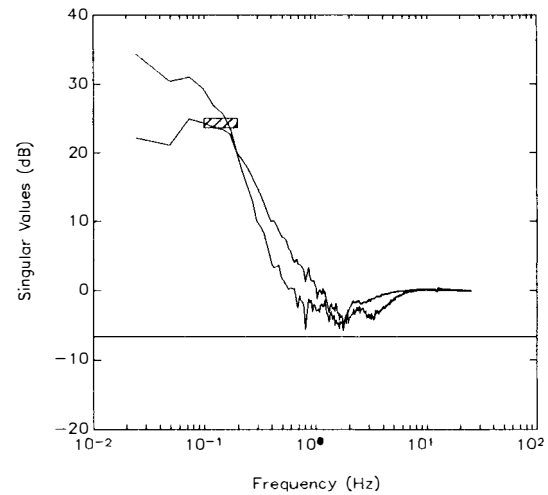


Fig. 6  $R^o_{IMC}$  Final Singular Value Response.

### Experimental Results

The controller was then implemented at the ACES facility. The open loop x-axis LOS error due to an x-axis BET disturbance (intended to simulate spacecraft crew motion) is shown in Fig. 7.

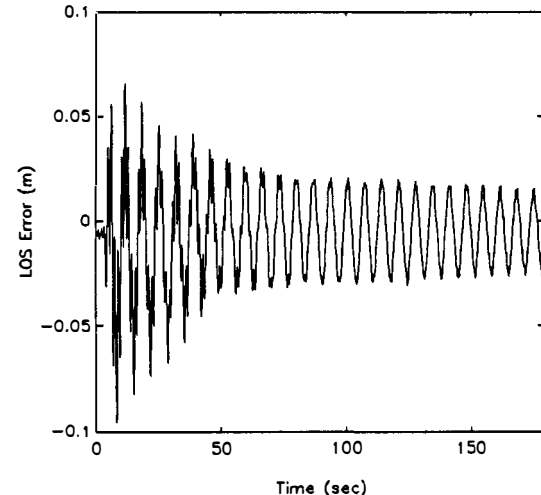


Fig. 7 Experimental Open Loop x-Axis LOS Error.

The dominant behavior in the response is the lightly damped pendulum mode. After closing only the IMC-LOS loops, the effect of the pendulum mode is reduced considerably as Fig. 8 reveals. However, the bending mode continues to have a large impact. After closing the IMC-LOS loops and the AGS-base gyro loops the effect of the pendulum mode is further reduced and the effect of

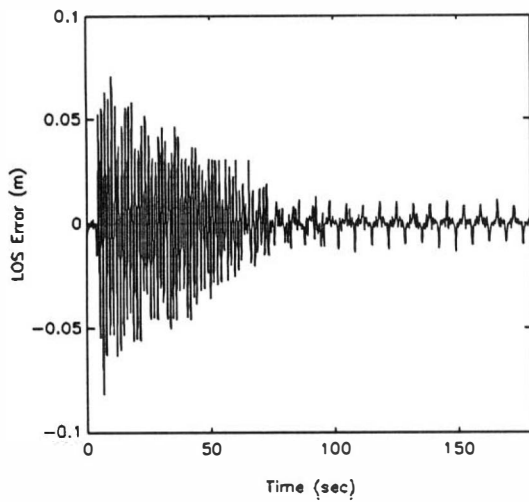


Fig. 8 Experimental x-Axis LOS Error with only IMC-LOS Loops Closed.

the bending mode almost eliminated as shown in Fig. 9. Although not shown, similar results were obtained when the same disturbance was applied to the y-axis of the BET.

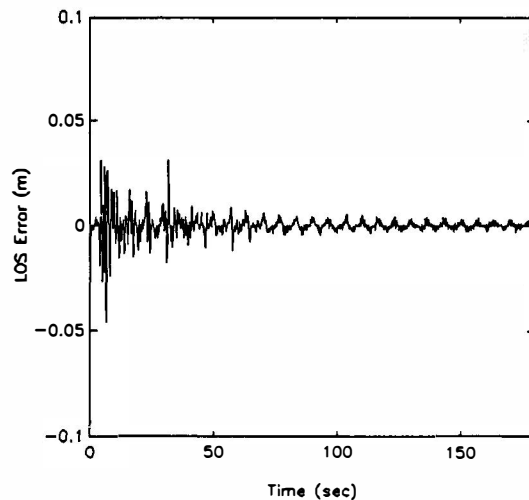


Fig. 9 Experimental x-Axis LOS Error with all Loops Closed.

## CONCLUSIONS

A simple numerical approach to the design of robust controllers has been presented. The technique has the advantages of (1) yielding a controller of designer-specified order, (2) allowing the specification of multiple design constraints, and (3) having no requirement that an analytical model be available.

The technique has been applied to the control of the

NASA ACES facility using experimental frequency response data as the only model. The resulting controller was implemented in the ACES facility and achieved very significant performance improvements.

Ongoing efforts include the application of the numerical approach to the NASA CSI ground test facility and the use of properties of unstructured performance and robustness measures to obtain enhanced algorithm performance.

## REFERENCES

- Medina,E. (1991), *Multi-input, Multi-output System Identification from Frequency Response Samples with Applications to the Modeling of Large Space Structures*, M. S. Thesis, Ohio University.
- Mitchell,J.R. (1972), *An Innovative Approach to Compensator Design*, Ph.D. dissertation, Mississippi State University.
- Newsom,J.R. and V. Mukhopadhyay (1985), "A Multiloop Robust Controller Design Study Using Singular Value Gradients," *Journal of Guidance, Control and Dynamics*, vol. 8, no. 4, pp. 514-519.
- Safonov,M.G., A.J. Laub, and G. L. Hartman (1981), "Feedback Properties of Multivariable Systems: The Role and Use of the Return Difference Matrix," *IEEE Transactions on Automatic Control*, vol. AC-26, no. 1, pp. 47-65.

## THE NASA-LaRC CONTROLS-STRUCTURES INTERACTION (CSI) TECHNOLOGY PROGRAM

J.R. Newsom and W.W. Anderson

*NASA Langley Research Center, Hampton, VA 23665, USA*

**Abstract.** The integration of active control systems for controlling the structural dynamics of flexible spacecraft can significantly benefit performance. Recognizing the potential improvement for future spacecraft, NASA has an ongoing Controls-Structures Interaction (CSI) technology program whose objective is to develop and validate the technology needed to integrate active control systems and flexible structures to meet the requirements of future space missions. The CSI program is a multicenter program involving research teams from NASA's Langley Research Center (LaRC), Jet Propulsion Laboratory (JPL), and Marshall Space Flight Center (MSFC). The JPL is focusing on optics-class missions and the MSFC is focusing on astrophysics missions. The purpose of this paper is to describe the ongoing activities at the LaRC, which are of a theoretical, ground test, and flight test nature, with focus on applications to spacecraft with multiple interacting pointing systems, large space radiometers, Space Station Freedom, and the Space Shuttle Remote Manipulator System (RMS).

**Keywords.** Control System Design, Structural Control, Space Vehicles, Satellite Control, Optimization

### INTRODUCTION

Conventional spacecraft attitude and pointing control system design begins with a mathematical model of the vehicle that includes specific structural characteristics along with selected sensor and actuator locations. Typically the structure has been optimized from a stiffness point of view so as to raise modal frequencies as high as possible within weight and load constraints, and the actuator locations have been selected based on required subsystem arrangements and local structural stiffness considerations. Based on attitude control, pointing and slewing requirements, specific control hardware and control-law architecture are then selected and a procedure to determine control gains invoked. Analyses and simulations are then used to assess performance with respect to requirements, and iterative redesigns are developed, if required.

This technique works well if the frequencies of the structural modes of vibration are high relative to the closed-loop control system frequencies, as dictated by pointing requirements and the disturbance environment. However, as spacecraft are growing larger, or weight limitations are limiting stiffness, vibration frequencies are decreasing. Also, as attitude and pointing control requirements are growing more stringent, closed-loop frequencies are increasing. The result is the necessity to control structural vibration modes. In this situation the spacecraft design team must have the methodology to design a system which meets performance and remains stable. The overall goal of this methodology is to not only meet pointing performance and stability requirements, but also to optimize the structure by relying on control for stiffness or damping enhancements, and in so doing optimize structural parameters such as weight, strength, or stiffness.

The methodology associated with meeting these requirements and taking advantage of these opportunities is known as controls-structures interaction (CSI) methodology and is the subject of intense research interest, fostered by a NASA-sponsored program (ref. 1). The overall goal of this program is to advance CSI technology to the point where it can be used in practical spacecraft design for future vehicles. Efforts are focused on developing design techniques for the simultaneous optimization of the control system and the structure, and on validating these techniques using ground and flight test articles. This paper describes the LaRC activities within the NASA CSI Program with emphasis on recent accomplishments.

#### PROGRAM ORGANIZATION

The efforts at the LaRC are organized into four areas: studies of mission needs for CSI technology; development of integrated analysis and design methods; development of ground test articles and techniques to validate the analytical methods; and development of flight test articles to verify analysis and ground test results. These efforts rely on in-house activities, supplemented by out-of-house contracts and grants. An Analytical Design Methods (ADM) Team and a Ground Test Methods (GTM) Team contain the majority of in-house people and activity. These two teams each have personnel from both controls and structural-dynamics disciplines and are collocated in a building containing the laboratory that houses the CSI ground test articles. The out-of-house activities are partially funded through a Guest Investigator Program, conducted jointly with the Air Force Phillips Laboratory (ref. 2). The organization is managed by a program office, the CSI Office, which directly manages the missions needs and flight test activities, and provides technical objectives to the ADM Team and the GTM Team. These teams report administratively to parent control and structural-dynamics discipline organizations.

#### MISSION BENEFITS USING CSI TECHNOLOGY

In order to provide focus for the research efforts of the program, studies quantifying the benefits of CSI technology for certain missions have been undertaken. A geostationary platform (GEOPLAT), the Shuttle Orbiter Remote Manipulator System (RMS), an

evolutionary Space Station Freedom, and a multipayload platform, such as the Upper Atmosphere Research Satellite (UARS) spacecraft, have been studied to date.

#### GEOPLAT Study (ref. 3)

A platform (fig. 1) at geostationary orbit, housing one or more large scanning radiometers, allows a continuous view of the same area of the Earth, and can meet many of the objectives of NASA's Mission-to-Planet-Earth, such as a continually updated precipitation map of the Earth. However, the needed spacial resolution at the Earth's surface and the distance from geostationary orbit combine to form stringent diffraction-limit and pointing requirements for the radiometer. The diffraction limit results in large antenna diameters; the large antennas, launched into geostationary orbit, result in light weight and, thus, low-frequency structures; the high pointing resolution, combined with the disturbances associated with scanning, results in the need for a high-gain and, therefore, high-frequency control system. This means that in order to meet mission goals, structural modes must be controlled, and, thus, CSI design techniques must be used. This study examined these issues and showed (fig. 2) that, with CSI technology, antennas up to 80 meters in diameter could be used and requirements met, while antenna performance would be unacceptable for diameters above 20 meters without the benefit of the new capability. The CSI technology benefit, from this study, is that significantly larger antennas could be used with improved performance.

#### Shuttle RMS Study (ref. 4)

The Shuttle Orbiter RMS is a long, flexible, and lightly damped robotic arm. This lightly damped characteristic often increases the time which astronauts use to accomplish various tasks. A study was done to quantify the benefit of increasing the closed-loop damping of the RMS on the time required to assemble Space Station Freedom (using a design current at the time). A baseline assembly scenario was first developed and, then, timeline analyses were used to determine required RMS usage. A Charles Stark Draper Laboratory simulation of the RMS was used to estimate individual maneuver times using  $\pm 1$  inch residual oscillations as the definition of

maneuver completion (fig. 3). The study showed that by increasing damping by a factor of 3, cumulative settling time for assembling Freedom could be reduced from 10 hours to 2 hours (fig. 4). This benefit was considered significant and was one reason behind the initiation of a joint effort (discussed later) between LaRC and the Johnson Space Center (JSC) specifically aimed at improving RMS damping.

#### Evolutionary Space Station Freedom Study (Ref. 5)

An evolutionary Space Station Freedom (fig. 5) will have significant onboard activities that provide disturbance inputs to the spacecraft. These include crew activity (exercise, EVA, IVA, console operations, centrifuge operation), control system activity, and operations of the Freedom RMS and its transporter. While the pointing requirements of the station itself are minimal (5-degree accuracy with 2.5-degree stability), there are candidate attached payloads with pointing requirements as low as 0.15 arc-sec. accuracy and .02 arc-sec. stability and a microgravity requirement of 1 micro-g quasi-steady (below .1 Hz), with linear relief to 1000 micro-g for transient accelerations of 100 Hz and above. The study modeled an evolutionary station, developed a simulation, and examined a variety of approaches to minimize errors in the pointing and micro-g levels caused by disturbances. These approaches included isolating disturbance sources (treadmill or centrifuge); active and passive vibration suppression of the base structure, using piezoelectric, momentum, and thrust actuators, and passive damping materials; and isolation and vibration compensation of the payloads. The conclusions of the study were: isolating disturbances, such as the treadmill, was effective (9.3 dB reduction in pointing jitter and 49 dB reduction in micro-g level); active damping of the base structure was beneficial, but limited by practical cost and complexity in suppressing selected modes excited by a certain disturbance; passive damping was effective in accommodating multi-disturbances; payload isolators were very effective for reducing high-frequency jitter; and an active gimbal system was a must for experiments requiring precision pointing.

#### Multi-Payload Platform Study

Current methods for assessing the ability of a multi-payload platform, such as the Upper Atmosphere Research Satellite (UARS), to meet payload pointing requirements are based on open-loop structural responses of each payload to disturbances from all other payloads. The total response is estimated, in a worst-case sense, by adding absolute values of the responses. Structural modification to alter the frequency of an offending mode, or a change to a payload to alter its disturbance input to the base structure, is used to cure any problems. These methods are conservative and work best when the spacecraft is stiff relative to the control system bandwidth and when disturbances and performance requirements are low. The intent of this study is to apply CSI techniques to analytical models of a UARS class spacecraft to assess the value of these techniques for application to larger, more flexible, multi-payload platforms planned for the future.

The particular control technique is a feed-forward technique referred to as Mirror Motion Compensation (MMC). A rigid-body MMC scheme has been implemented on the GOES-I/M spacecraft currently being built for NASA and NOAA (ref. 6). The current study extended the GOES MMC concept to also compensate for structural flexibility effects and analytically demonstrated the technique on the UARS. Figure 6 shows results of pointing error at one of the UARS instruments due to a disturbance resulting from scanning of another UARS instrument. The MMC technique is seen to reduce pointing jitter by a factor of 5. However, studies indicated that the effectiveness of the MMC technique is very sensitive to precise knowledge of the structural frequencies that are being compensated. Further research is needed to reduce this sensitivity.

#### INTEGRATED ANALYTICAL DESIGN METHODS

At LaRC, an Analytical Design Methods (ADM) Team has been constituted with the goal to conceive and develop methodology for spacecraft design which incorporates CSI technology. The emphasis has been on methods for the simultaneous design and optimization of a spacecraft's control system and structure, and the translation of these methods into algorithms and computational tools for

practical integrated computer-aided design. The approach has been to define four classes of spacecraft, each of increasing complexity, and address the classes sequentially. These classes are: (I) a beam-like backbone structure requiring vibration suppression; (II) Class I with small-angle articulating payloads; (III) nonlinear Class I (large-angle maneuvers); and (IV) general nonlinear problem with robotic arms and large-angle articulated payloads. At this point, research results are available for Class I only.

For Class I, an optimization-based formulation of the problem has been chosen, wherein a set of design variables are selected that optimize a performance metric, subject to a set of constraints (fig. 7). The unique feature of this is that both control and structural variables are included in the metric, the constraints, and the design variables. Three specific approaches to the optimization-based formulation are being pursued. These are: (1) "CSI-Design" (ref. 7), the principal thrust of the ADM Team, involving in-core structural analysis, control design, and parametric optimization; (2) system decomposition into a structures portion and a controls portion, and subsequent optimization using global sensitivity equations (ref. 8); and (3) an out-of-house effort using Boeing's Integrated Analysis Capability (ref. 9), a database management system which communicates with separate structures, controls, and optimization modules. Results from two studies using the CSI-Design methodology will be discussed to illustrate the benefits of integrated design, but first it is necessary to cover the issue of what type of control-design technique is best suited for this application.

To determine this, three techniques were compared: (1) Linear-Quadratic-Gaussian (LQG) control; (2) static- (SDC) and dynamic-dissipative control (DDC); and (3) H-Infinity optimal control. The comparisons were made by designing, implementing, and testing control laws for the Langley CSI Evolutionary Model (CEM) shown in figure 8. This test article (ref. 10), subsequently described in more detail, has a 62-bay central truss (10-inch bays) with two side booms, two towers, and a 16 ft. diameter reflector. The structure is suspended using two cables as shown in figure 8. Accelerometers and air-jet force actuators are collocated at eight points on the structure. Table 1 (ref. 11) lists a comparison of the closed-loop damping ratios for the first ten of the test article's structural modes for the

three techniques. The DDC approach provided the best active damping and was chosen for the following two studies. Further work on dynamic-dissipative compensation is covered in reference 12.

#### Generic Geostationary Platform (GGP) Model Study

The first study using the CSI-Design methodology (ref. 7), focused on a 10-bay, 30-meter long truss structure (fig. 9) with two flexible radial-rib antennas of 7.5 and 15 meters in diameter, one at each end and assumed to be fixed to the truss during operation. A three-axis control-moment-gyro (CMG) system with attitude and rate sensors, collocated at the center-of-mass of the structure, was assumed for control. Nine structural design variables were formulated by dividing the truss lengthwise into three sections and allowing the outer diameters of the longeron, batten, and diagonal truss tubes to vary. Two more variables are the outer diameters of the antenna support members, bringing to 11 the total number of structural design variables. For the control system, the elements of the gain and compensator matrices were used as design variables. Constraints were placed on average control power and structural mass, and upper and lower bounds on tube size to accommodate manufacturing realities and prevent buckling and overstress. Table 2 contains the results of applying the CSI-Design methodology to this problem for a performance metric which was the weighted sum of total plus closed-loop pointing performance. A sixth-order dynamic dissipative controller was used. An initial design, based on rigid-body performance, was first obtained. Then, a control-optimized design was performed, resulting in a 30% increase in controlled performance, but also an 18% increase in total mass because of increased actuator mass. An integrated design was next carried out, which resulted in a four-fold increase in controlled performance with little change in total system mass, the result of lightening the structure in favor of larger actuators. These results demonstrate that the integrated design produces a better design by a large margin over the conventional approach.

#### CSI Evolutionary Model (CEM) Study

The second study using the CSI-Design methodology (ref. 7) focused on the CEM (fig.

8), previously described briefly. An integrated controls-structure design was obtained by minimizing the steady-state average control power in the presence of white noise input disturbances at actuators No. 1 and 2 (located at the end of the main bus nearest to the laser tower), with a side constraint on the steady-state rms position error at the laser detector (60 ft. above the structure) for reasonable steady-state pointing performance, and a constraint on the total mass to have a fair comparison with the Phase-0 design. To perform the design, the truss structure was divided into seven sections, three for the main bus, and one each for the two towers and two horizontal booms. The effective areas of the truss-section longerons, battens, and diagonals were selected as the structural design variables. Both static and dynamic dissipative controllers were used in the integrated design. The six remaining actuators (Nos. 3-8) were used in the design, along with velocity signals obtained by processing the accelerometer outputs. Using a constraint on the rms pointing error of 2.4 inches at the laser detector and a constraint on the total mass of 19.2 slugs (nominal mass of Phase-0 CEM), a control optimized design was performed first (with fixed structural design variables), and then an integrated design. Table 3 gives the results of these designs. The integrated design approach shows a 40-43% reduction in control power over the control optimized design while meeting pointing and mass constraints. Again, these results demonstrate that the integrated design - allowing combined structural and control optimization - produces a much improved design.

The methodology of this study has been used to redesign the Phase-0 CEM (designated as the Phase-1 CEM). The test article has been rebuilt according to the optimized design parameters and, as of the writing of this paper, testing is being conducted to experimentally evaluate the integrated design methodology.

#### GROUND TEST METHODS

At LaRC, a Ground Test Methods (GTM) Team has been constituted with the goals of conceiving and developing ground test methodology for flexible spacecraft and validating the analytical methodologies developed for design of such vehicles. Numerous investigations of ground test methods have been undertaken including

methods of suspension which best simulate zero-g, methods of combining full-scale components and sub-scale components, and methods of combining physical and computer models. Ground test articles provide the focus for validation of these methods as well as for validation of the advanced analytical CSI methodologies. These articles include representative structure, control computers, sensors and actuators, and data acquisition and recording systems. Two major test articles developed at Langley are the Mini-Mast Testbed and the CSI Evolutionary Model (CEM), previously described. They have been used for in-house purposes and as part of an out-of-house Guest Investigator Program.

#### Mini-Mast Testbed (fig. 10)

This test article is a 20-meter long generic truss, deployed vertically and cantilevered from its base on a rigid foundation. The truss has three graphite/epoxy member types: longerons; battens that form the triangular cross-sections; and diagonals in the beam face planes. These members are connected by titanium corner joints. The beam has 18 bays which are deployable, two bays at a time. Various accelerometers, rate gyros and noncontacting displacement sensors are located along the beam. Three torque-wheel actuators are mounted orthogonally at the top of the beam. The sensors and actuators are connected via fiber-optic cables to a control computer and data recording equipment. The Mini-Mast has five structural modes below 10 Hz: two bending modes at 0.86 Hz; a torsion mode at 4.2 Hz; and a pair of bending modes at 6.1 Hz. There are 113 modes (local diagonal modes) above these and below the second torsion mode at 22.9 Hz.

As a precursor effort, to assure that the Mini-Mast facility was ready for out-of-house use, an in-house investigation was conducted (ref. 13). The effort used systems identification theory to determine the design model and then LQG theory to design the closed-loop controller. Torque-wheel actuators and displacement sensors were used. Closed-loop damping of 30 percent of critical was demonstrated, 10 times more than the three-percent passive damping of the basic structure. Excellent agreement between simulated and actual test data allowed certification of the facility for use by guest investigators.

The initial Guest Investigator Program conducted by NASA used the Mini-Mast (in addition to the Active Control Technique Evaluation for Spacecraft (ACES) at NASA-MSFC) as its test articles. Selected guest investigators were provided resources and

technical support to test their methods on the hardware. Five universities and three companies were involved. Results of their investigations are given in reference 2. Table 4 is from this reference and is included for summary purposes.

#### Langley CSI Evolutionary Model (CEM)

(ref. 10; fig. 8)

This is the current test article for CSI testing. As the name implies, the test article will evolve over time in terms of size, complexity, and capability. The Phase-0 CEM, previously discussed briefly, has a 62-bay central truss (10-inch bays) with two booms, two towers, and a 16 ft. diameter reflector. The booms project 10 bays to each side and provide the mounting point for the two suspension cables. One tower has 11 bays and a laser source mounted on top; the second tower has four bays and a simulated antenna reflector attached to it. The reflector also has a mirrored surface to reflect the laser to a ceiling mounted target located 60 ft. above the model. The CEM has six "rigid-body" modes: three near 0.15 Hz, involving horizontal translation and rotation; two near 0.73 Hz, involving vertical bouncing; and one at 0.90 Hz, involving compound pendulum dynamics in a vertical plane. Flexible modes begin at about 1.5 Hz. Analytical models predict 81 modes below 50 Hz. Variable-thrust, bi-directional, compressed-air thrusters (ref. 14), with good response out to 10 Hz, are the primary control actuators. There are four groups of four thrusters. Twenty-eight servo accelerometers, with good response up to 300 Hz, are the primary control sensors with eight angular-rate sensors and 195 piezo-film accelerometers available. A VAX 3200 and a Cyber 175 are available for control law testing and data handling.

In addition to the two uses mentioned previously, significant studies using line-of-sight (LOS) pointing as the measure of performance have been conducted. Typical tests consist of 10 seconds of excitation followed by either free-decay or closed-loop control. As indicated in figure 11, the test and simulated LOS pointing are qualitatively in very

good agreement, although some quantitative differences are apparent. This indicates that control law design for flexible structures using finite element derived design models (tuned by system identification tests) is quite viable. The performance of the controller can be described in terms of the LOS pointing error decay rates. The damping is increased from less than 1% to more than 10% between open- and closed-loop, respectively. While this limitation in damping was partially due to actuator saturation, the stability margin of the high gain controller limited performance. Present and future research is emphasizing the use of active structural members and combined active/passive damping to increase the performance of high gain controllers.

## FLIGHT TEST ARTICLES

Plans exist for several CSI flight-test articles, from a moderate experiment in the middeck of the NASA Space Shuttle to an extensive orbital free-flyer dedicated solely to CSI investigations. Two of these will be discussed here: the Middeck Active Control Experiment (MACE); and the Shuttle Remote Manipulator System (RMS) Damping Enhancement Experiment.

#### Middeck Active Control Experiment (MACE)

(ref. 15)

The MACE test article (fig. 12) has been designed to capture the physical characteristics of a class of multibody platforms in a small-scale package. It will be carried into space in several Space Shuttle Orbiter middeck lockers, assembled by the crew into a variety of configurations, and used for testing a set of relatively simple to relatively complex controller implementations. The initial configuration for MACE consists of a segmented straight tubular bus, with members connected by universal joints, and a two-axis pointing/tracking payload at each end. Also to be included is an active member consisting of a square Lexan rod with piezoelectric ceramics and surface bonded strain gauges mounted on the sides. Torque wheels and rate gyros will be located at the test article center-of-gravity. The test article will be 1.7 meters in length when assembled and will have its first flexible mode below 2 Hz. Experiments will be conducted by the crew on several separate days. These experiments will include open-loop identification and closed-loop attitude control and pointing of the basic configuration with

attached test payloads. Characterization data will be downlinked and processed by ground-based system identification algorithms. Control system parameters will then be derived and uplinked to the MACE experiment computer. An estimated flight date for MACE is 1994.

#### Shuttle Remote Manipulator System (RMS) Damping Enhancement Experiment

The Shuttle Orbiter RMS is a very lightly damped system, with the result that considerable crew time is often wasted waiting for vibrations to damp down to acceptable values. The LaRC and JSC are conducting a joint effort examining alternative ways of enhancing damping and the operational value of these enhancements. A four-task program was initiated in 1989. Task I, an examination using simulation, of control-computer, control-law modifications (software only) has been completed by LaRC (ref. 16). This task showed small gains in damping (10 to 30 percent gain) associated with feeding back analog joint-tachometer signals. Task II, an examination, using simulation, of hardware, as well as software modifications, has been completed. This study determined that a modification consisting of adding a three-axis RMS tip position acceleration measurement was needed. This enhancement improved the damping level by a factor of three (fig. 13) and reduced joint torques by a factor of two following Shuttle thruster firings. Task III of this effort involves using the Shuttle Engineering Simulator (SES) at JSC to evaluate the operational value of the damping enhancements. Based on this evaluation, a decision to modify an RMS flight unit and test it in space (Task IV) will be made.

#### CONCLUDING REMARKS

The CSI efforts to date have demonstrated the utility and benefits of the application of this technology to a variety of NASA missions, including geostationary platforms, the Shuttle RMS, an evolutionary Space Station Freedom, and multipayload platforms such as the UARS. The research has examined different approaches to optimized controls/structures design of these vehicles and is proceeding with an in-house version, CSI-Design. This tool has been shown to result in significant improvements in the controlled performance of

simulated large flexible spacecraft and experimental ground test articles and has been applied to the redesign of the CEM. Ground test experiments are being conducted to evaluate the integrated design approach. Following these analytical and ground test activities, extensive flight activities are possible, depending on resource availability - the MACE test article and the enhancement of the RMS being the two most probable.

An important aspect in this program has been the multidisciplinary nature of the organization: pulling together people from two different disciplines and getting them to work together. This has worked well by developing technical teams, with specific separate roles. The teams (Analytical Design Methods and Ground Test Methods) have personnel from both disciplines, are collocated in a common area, have their activities managed by the applicable line managers from the parent controls and structures organizations, and are coordinated by a special office. This office, the CSI Office, is designated to be the focal interface at LaRC for the program, its reporting, and its advocacy. The Office also manages all flight activities and special CSI programs as they arise.

#### REFERENCES

1. Newsom, J. R.; Layman, W. E.; Waites, H.B.; and Hayduk, R.J.: The NASA Controls-Structures Interaction Technology Program. NASA TM-102752, October 1990.
2. Smith-Taylor, R.; and Tanner, S. E.: The Controls-Structures Interaction Guest Investigator Program - An Overview and Phase I Experimental Results. Paper Presented at the 14th Annual AAS Guidance and Control Conference. Keystone, Colorado, Feb. 1991
3. Control-Structures-Interaction (CSI) Technologies and Trends for Future NASA Missions. NASA CR-187471, December 1990.
4. Lamb, B. A.; and Nowlan, D. R.: Benefits of Control-Structure Interaction (CSI) Technology to Space Station Assembly by Flexible Robotic Systems (RS). NASA CR-187523, November 1989.

5. Pak, Y.; and Yu, C.: Benefits of CSI Technology to the Operation of Space Station - Final Technical Briefing. Contract NAS1-18763, May 5, 1991.
6. Chu, P. Y.: Slew Disturbance Compensation for Multiple Spacecraft Payloads. Paper AAS 89-369, August, 1989.
7. Maghami, P. G.; Joshi, S.M.; and Lim, K. B.: Integrated Controls-Structures Design: A Practical Design Tool for Modern Spacecraft. Proceedings of the ACC, June 1991.
8. Woodard, S. E.; Padula, L. P.; Graves, P. C.; and James, B. B.: A Multidisciplinary Approach to Optimization of Controlled Space Structures. Paper presented at the Third Air Force/NASA Symposium on Recent Advances in Multidisciplinary Analysis and Optimization, San Francisco, September 24-26, 1990.
9. Hunziker, K.S.; Kraft, R. H.; Kosut, R. J.; and Armstrong, E. S.: Optimization of Linear, Controlled Structures. Proceedings of the ACC, May 1990, pp. 854-859.
10. Belvin, W. K.; Horta, L. G.; and Elliott, K. B: The LaRC CSI Phase-0 Evolutionary Model Testbed-Design and Experimental Results. NASA Technical Memorandum 102762, January 1991.
11. Lim, K. B.; Maghami, P. G.; and Joshi, S. M.: A Comparison of Controller Designs for an Experimental Flexible Structure. Proceedings of the ACC, June 1991.
12. Joshi, S. M.; and Maghami, P. G.: Dynamic-Dissipative Compensator Design for Large Space Structures. Paper presented at the AIAA GN&C Conference, New Orleans, August 1991.
13. Montgomery, R. C.; and Ghosh, D.: Active Control Test on the Mini-Mast. Proceedings of the NASA-UCLA Workshop on Computational Techniques in Identification and Control of Flexible Flight Structures, Lake Arrowhead, California, November 2-4, 1989, pp. 19-22.
14. Jacot, A. D.; Bushnell, G. S.; and Anderson, T. M.: Bi-Directional Thruster Development and Test Report. NASA Contractor Report 182013, February 1990.
15. Miller, D. W.; de Luis, J.; and Crawley, E. F.: Dynamics and Control of Multipayload Platforms: The Middeck Active Control Experiment (MACE). IAF Paper 90-292, Oct. 1990.
16. Scott, M. A.; Gilbert, M. G.; and Demeo, M. E.: Active Vibration Damping of the Space Shuttle Remote Manipulator System. Paper presented at the AIAA Guidance & Control Conference, New Orleans, August 1991.

TABLE 1 Predicted Closed-Loop Damping Ratios  
of CEM Structural Modes

Mode #	freq. (Hz)	LQG	DDC	H-inf
1	0.15	0.251	0.361	0.008
2	0.15	0.294	0.330	0.013
3	0.15	0.381	0.370	0.016
4	0.73	0.281	0.247	0.009
5	0.75	0.051	0.071	0.008
6	0.87	0.080	0.084	0.013
7	1.47	0.029	0.070	0.016
8	1.74	0.027	0.239	0.023
9	1.88	0.016	0.045	0.018
10	2.29	0.005	0.007	0.005

TABLE 2 Integrated Design of the GGP Model  
(Dynamic Dissipative Controller)

	Controlled Performance	Structural Mass	Actuator Mass	Total Mass
Initial Design	1.00	1.00	1.00	1.00
Control-Optimized Design	1.30	1.00	1.45	1.18
Integrated Design	4.03	0.66	1.44	0.97

TABLE 3 Integrated Design of the CSI Evolutionary Model

	RMS Displacement	Control Power
Open Loop (Phase-0)	22.54	0.00
Open Loop (Phase-1)	18.34	0.00
Control-Optimized (S) Design	2.4	7.11
Control-Optimized (D) Design	2.4	6.41
Integrated Design (S)	2.4	4.21
Integrated Design (D)	2.4	3.64

TABLE 4 Phase I Guest Investigators

University/Industry	Principal Investigator	Primary Thrust
Arizona State	Dr. B. Wie	Collocated/Noncollocated Controllers
Boeing Aerospace	Dr. M. Chapman	Nonlinear Math Modeling
Cal Tech	Dr. J. Doyle	Noncollocated Controller Design
University of Cincinnati	Dr. R. Allemand	System ID and Controller Design
Dynamic Engineering	W. Reed	Passive & Active Suspension Design
Harris Corporation	Dr. D. Hyland	Noncollocated Controller Design
MIT	Dr. W. Vander Velde	Sys ID & Fault Detection & Isolation
Purdue	Dr. R. Skelton	Noncollocated Controller Design

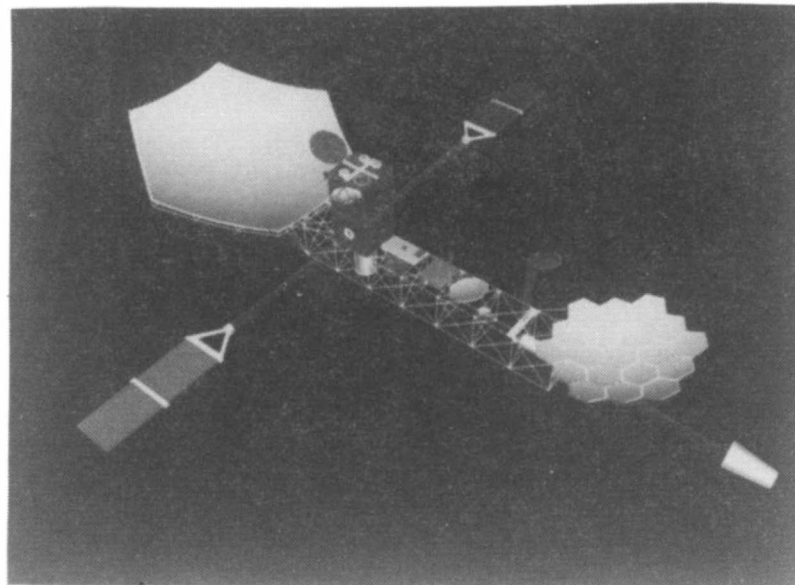


Fig. 1. Representative Geostationary Science Platform

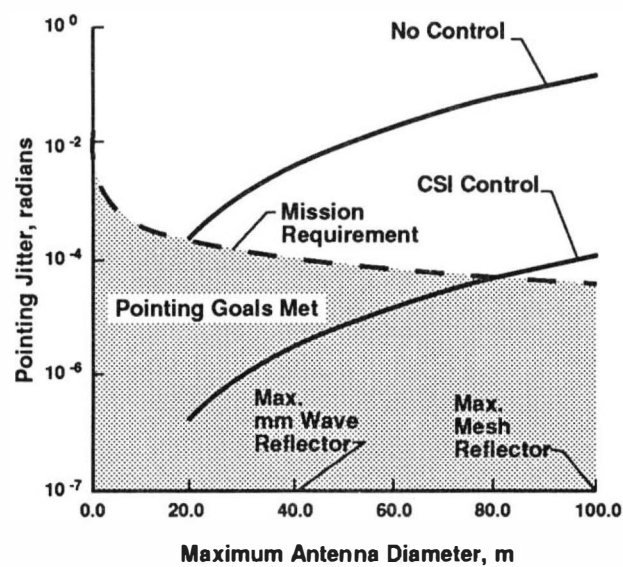


Fig. 2. CSI Methodology Pointing Performance Improvements

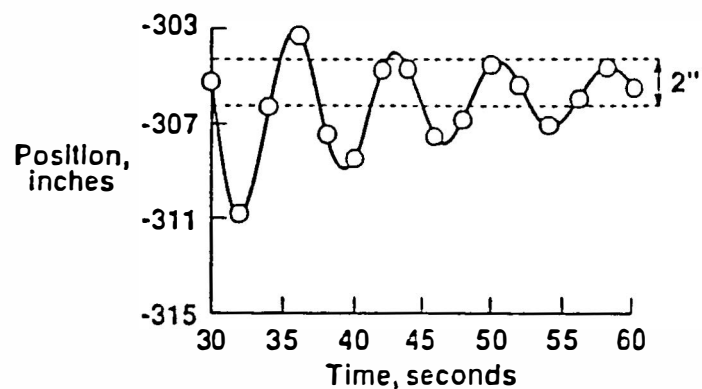


Fig. 3. Simulated Shuttle-RMS Response

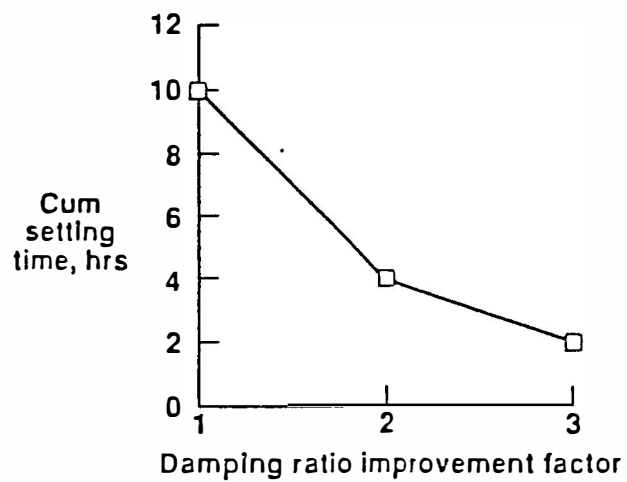


Fig. 4. Increased RMS Damping Benefit

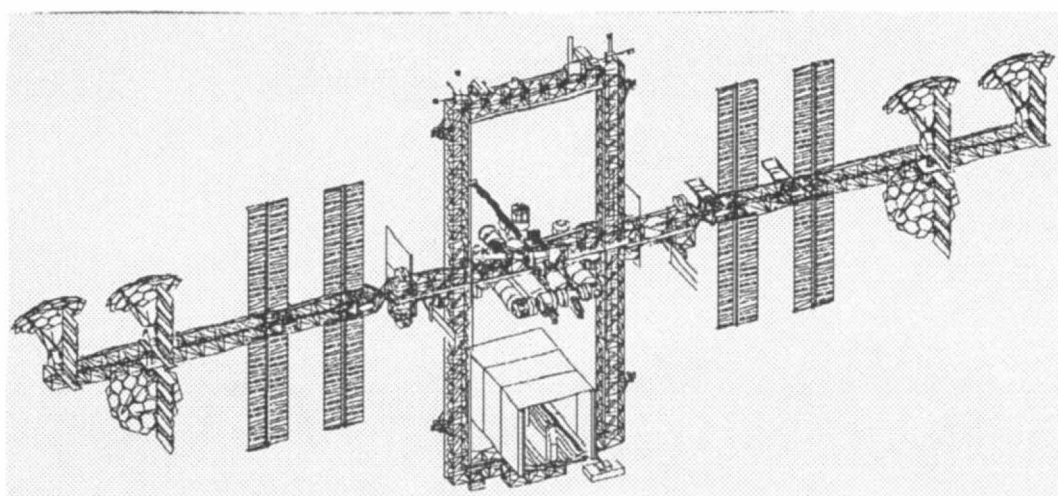


Fig. 5. Evolutionary Space Station Freedom Configuration

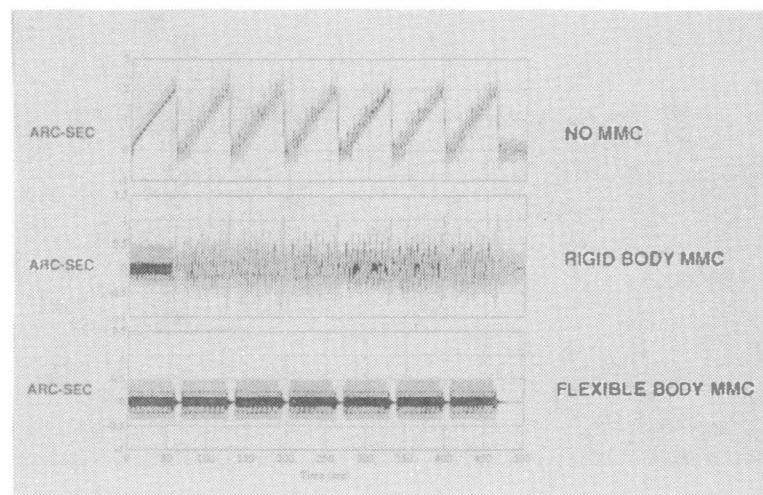


Fig. 6. Simulated UARS Pointing Error Improvement

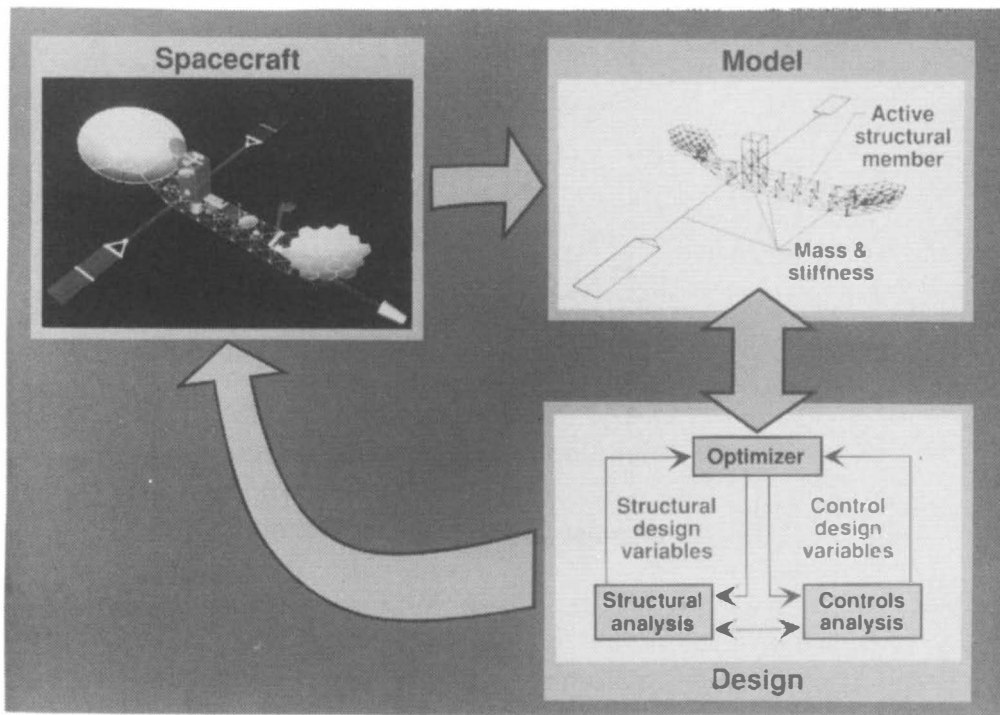


Fig. 7. Integrated Design Methodology

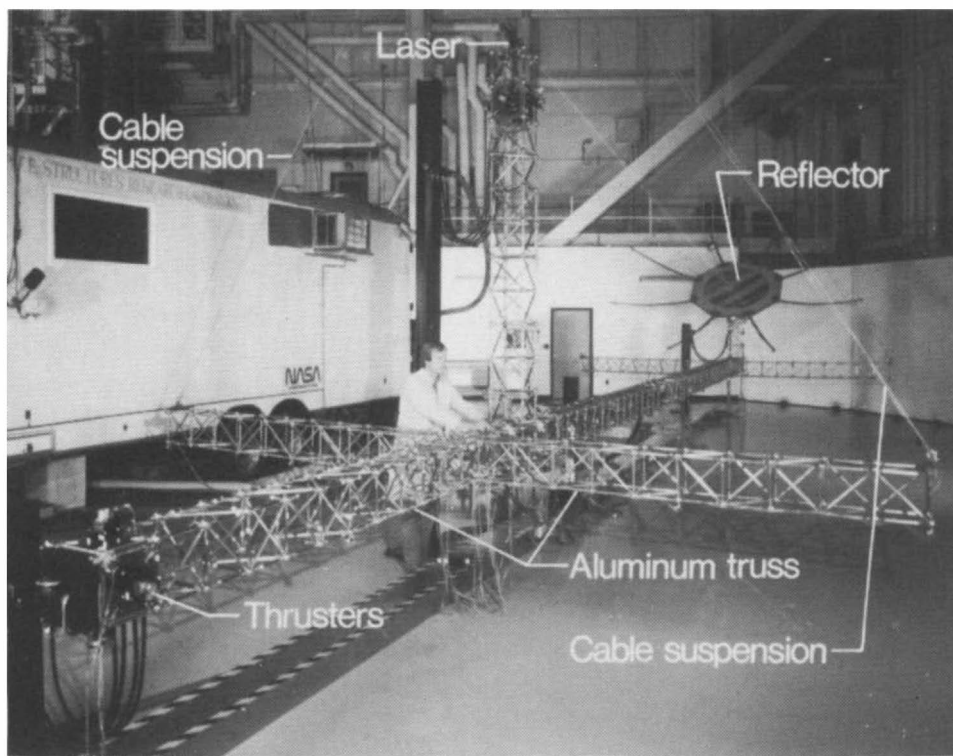


Fig. 8. LaRC Phase-Zero Evolutionary Test Article

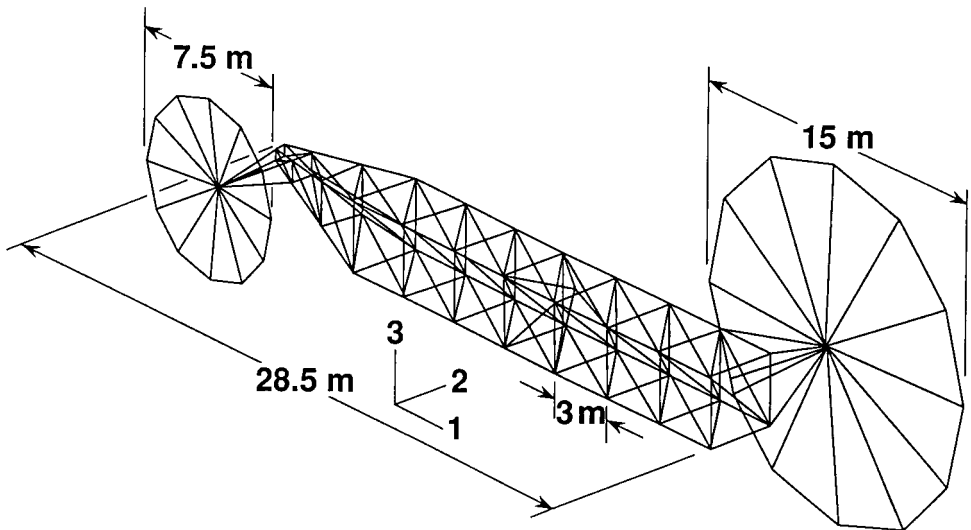


Fig. 9. GEOPLAT Configuration used in Integrated Design Study

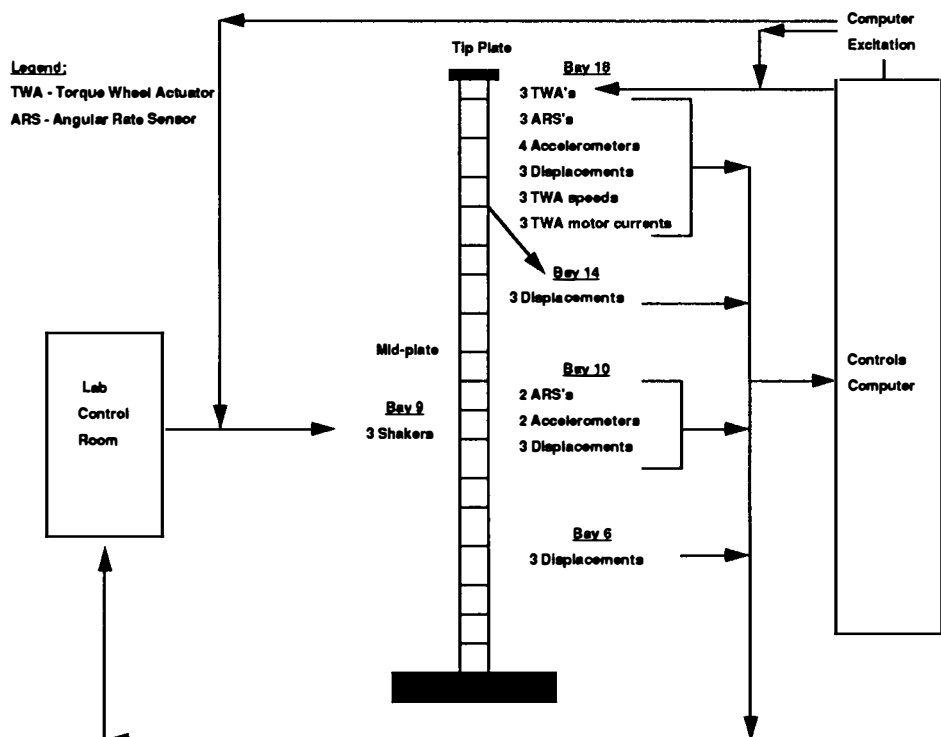


Fig. 10. Mini-Mast Testbed

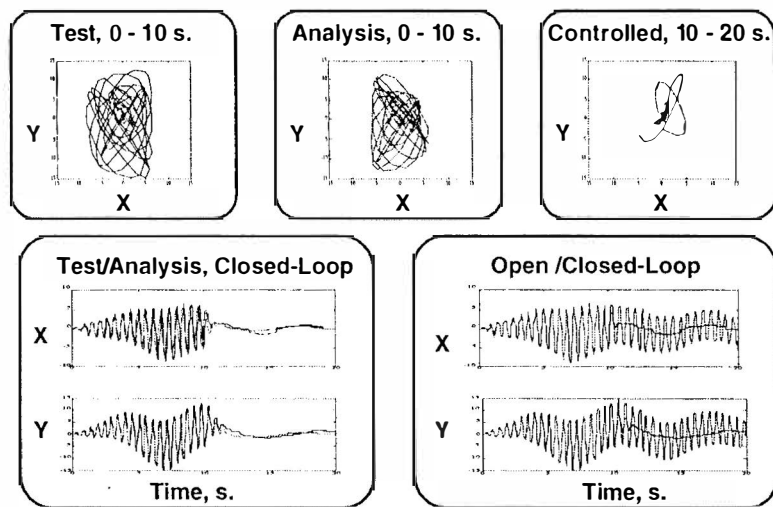


Fig. 11. LOS Results for Phase-0 CEM

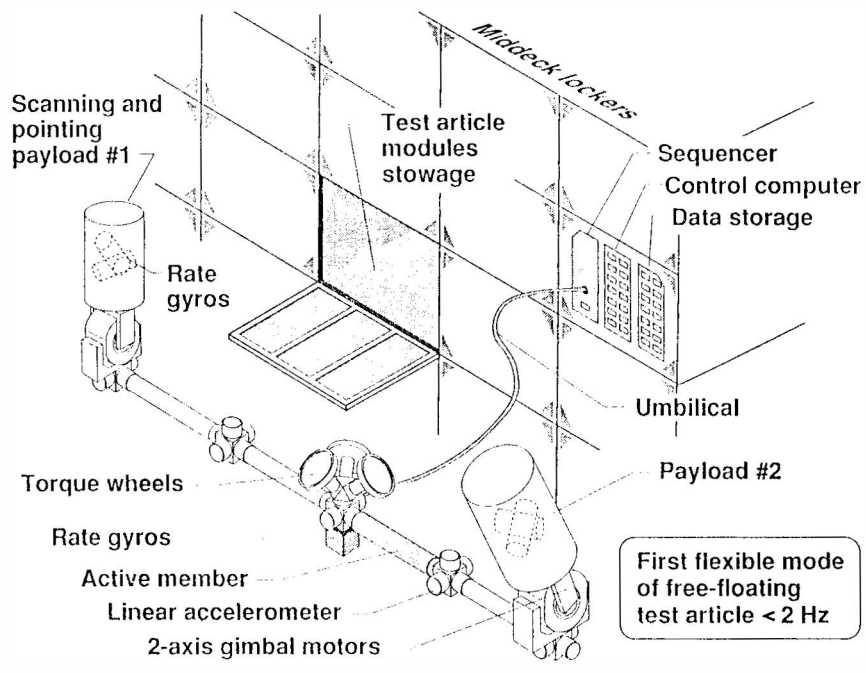


Fig. 12. Middeck Active Control Experiment Configuration (MACE)

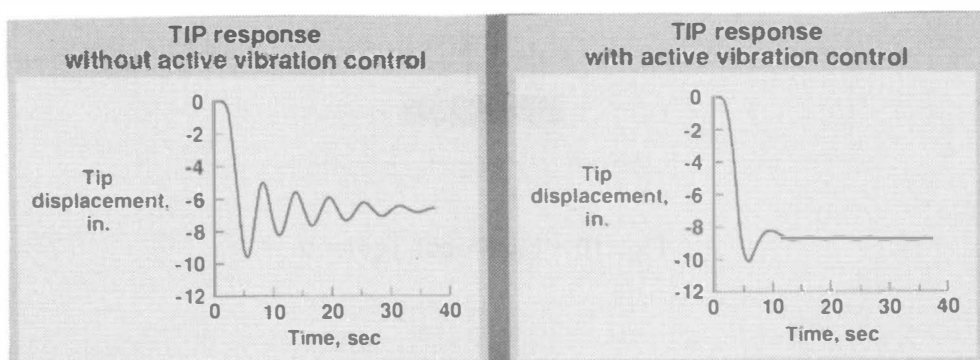


Fig. 13. RMS Open and Closed-loop Response

## DYNAMIC ALIGNMENT OF GIMBALLED AND FIXED SUBSYSTEMS ON FLEXIBLE HELICOPTERS

W.H. Boykin

*System Dynamics Incorporated, Gainesville, Florida, USA*

**Abstract:** Effectiveness of helicopter weapon systems depends on dynamic alignment of weapons to day/night target acquisition sensors. Dynamic misalignment in this high vibration, structural flexure environment is large. A method has been developed to utilize ring laser gyros in the alignment of fixed and gimballed weapons to target acquisition sensors.

**Keywords:** alignment, boresight, helicopters, flexure, inertial

### INTRODUCTION

A key element in helicopter weapon system effectiveness is the accuracy of boresight alignment of target acquisition sensors to each other and to the various weapon systems. Helicopters impart relatively high vibrational disturbances to instruments used for dynamic alignment and control, as well as large structural flexures between weapon system elements when compared to the required boresight alignment accuracies.

Current US helicopter weapon systems are aligned via alignment tools which are not part of the helicopter. They are arranged on or near the helicopter in order to determine, by optical collimators, the orientations

of the various subsystems relative to the tools. Differences in orientation of the subsystems relative to the design orientation imposed by the tool are stored in a computer for boresight corrections during the use of the weapon subsystem.

Now that inertial devices are beginning to be used on weapons as well as the target acquisition sensors' precision gimbals, it is natural to consider the use of these inertial devices for both control and alignment. Advantages of such "internal" alignment systems over "external" alignment systems are:

(1) dynamic alignment errors may be determined throughout the mission via the inertial devices mounted on the

subsystem,  
(2) greater precision in the alignment estimates is possible, and  
(3) the manpower intensive "external" alignment job is eliminated by automation.

This paper presents a new approach to an alignment algorithm which consists of:  
(1) attitude matching estimation via strapdown generation of attitude measurement errors without a master inertial measurement unit, and (2) optimal estimation of the chain of alignment error contributors in concert with the total, end-to-end, boresight error estimate.

Simulations were used to test the dynamic alignment algorithm for ring laser gyros. The subsystems to be aligned to each other are:

- (1) gimballed radar to gimballed electro-optical sensors,
- (2) inertial navigation system to electro-optical sensors,
- (3) turreted gun to electro-optical sensors,
- (4) missile seekers to gimballed radar, and
- (5) rocket wing stores to gimballed electro-optical sensors.

There are two types of alignments: gimbal-to-gimbal, and fixed-to-gimbal. In the gimbal-to-gimbal case the measurements expressed in terms of the alignment errors are of the order of ten milliradians so that linear design methods are natural. Fixed-to-gimbal alignments involve large angles between subsystems so that "extended" methods would be needed except for the

availability of independent measurements via the resolver/encoder chain.

The flexure modes of the helicopter were determined from test data and NASTRAN models updated via test data. The flexure modes excited by helicopter control inputs and wind gusts along with the structural "offset" due to gun reaction forces are of relative large amplitudes and low frequencies. Rotor harmonics induce higher frequency modes but at lower amplitudes.

The elements of the dynamic alignment algorithm is presented. A strict limitation in its design was that there will be no special maneuvers performed at any time. Good alignment must be achieved under hover conditions. With only low level motion inputs inertial instrument biases can result in large alignment errors. The ring laser gyro considered has acceptable imperfection for the band pass filter approach herein.

It is well known that data latency has also produced large alignment errors from the use of attitude matching algorithms. The dynamic alignment algorithm includes compensation for asynchronous data sampling.

#### MISALIGNMENT PROCESS

Misalignments of significance range between 0.5 and 20 milliradians, and typically the larger misalignments are associated with the lower frequencies of motion. Some

misalignments are constant over the hours of the mission.

Fig. 1 illustrates one of the subsystem alignment pairs: a target acquisition sight (TAS) and a gun (GUN).

The constant misalignments are not shown. They are: the tilts of the TAS ( $\underline{\epsilon}_s$ ) and GUN ( $\underline{\epsilon}_g$ ) elevation axes, and the structural tilt ( $\underline{\epsilon}$ ) between the base of the TAS and the base of the GUN. There are also misalignments which affect the measurements, namely, the misalignments ( $\underline{\epsilon}_s$  and  $\underline{\epsilon}_g$ ) of the gyro packages relative to the GUN tube and the TAS telescope, and the resolver misalignments. The later are included in the resolver biases.

The resolvers measure the angles

TAS elevation	$E_s$
TAS azimuth	$A_s$
GUN elevation	$E_g$
GUN azimuth	$A_g$

and

platform roll  $\delta_p(1)$   
 platform pitch  $\delta_p(2)$   
 platform yaw  $\delta_p(3)$ .

Deformations, to be estimated, are denoted by  $\underline{\delta}$ .

#### TRUTH MODEL

The true misalignment is computed from the end-to-end total rotation which is defined in terms of the above true rotational elements and misalignments.

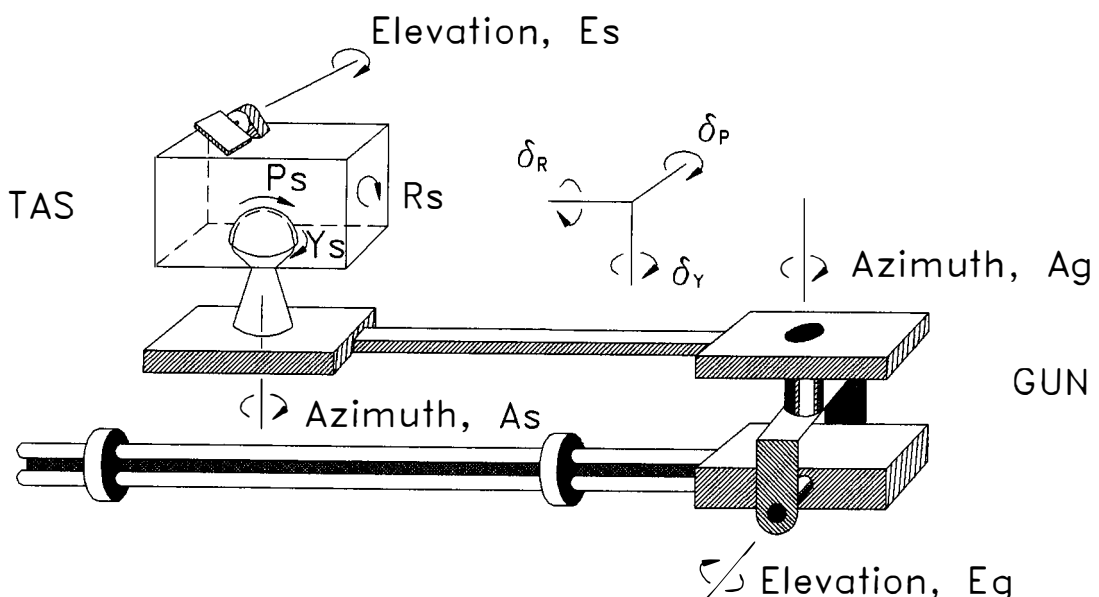


Fig. 1. Systems to be aligned.

Here direction cosines are used and denoted by "C". The chain of 'true' rotations are defined by:

$$\begin{aligned} {}^{\text{Is}}\mathbf{C}^{\text{Es}}(\underline{\epsilon}_{\text{S}}) * {}^{\text{Es}}\mathbf{C}^{\text{Eso}}(\text{Es}) * {}^{\text{Eso}}\mathbf{C}^{\text{P}}(\underline{\iota}_{\text{S}}) * {}^{\text{P}}\mathbf{C}^{\text{As}}(\underline{\delta}_{\text{P}}) * {}^{\text{As}}\mathbf{C}^{\text{Aso}}(\text{As}) \\ * {}^{\text{Aso}}\mathbf{C}^{\text{Ag}}(\underline{\epsilon} + \underline{\delta}) * {}^{\text{Ag}}\mathbf{C}^{\text{Ag}}(-\text{Ag}) * {}^{\text{Ag}}\mathbf{C}^{\text{Ego}}(-\underline{\iota}_{\text{g}}) * {}^{\text{Ego}}\mathbf{C}^{\text{Eg}}(-\text{Eg}) \\ * {}^{\text{Eg}}\mathbf{C}^{\text{Ig}}(\underline{\epsilon}_{\text{g}}) = {}^{\text{Is}}\mathbf{C}^{\text{Ig}} \approx \mathbf{I}_{3 \times 3} - \Delta_{\text{T}} \end{aligned} \quad (1)$$

where, for the small misalignment angles between the TAS and GUN,  $\Delta_{\text{T}}$  is the "skew" matrix of the total misalignment vector  $\underline{\delta}_{\text{T}}$ . That is,

$$\Delta_{\text{T}} = \begin{vmatrix} 0 & -\delta_{\text{T}3} & \delta_{\text{T}2} \\ \delta_{\text{T}3} & 0 & -\delta_{\text{T}1} \\ -\delta_{\text{T}2} & \delta_{\text{T}1} & 0 \end{vmatrix}$$

In this truth model the gimbal angles Es, As, Ag, and Eg are true angles and have no measurement imperfections. The misalignments are also true and are to be estimated. In the estimation process to follow the estimator cannot separate a gimbal (or resolver) rotation misalignment from a measurement imperfection. Such separations are not of practical importance since only the total needs to be used in misalignment corrections in the fire control computer. If a resolver bias (or equivalently a misalignment about the resolved gimbal axis) is present, it must appear in both the truth model's misalignments and affect the resolver measurements. Mutual orthogonality of all gimbal and gyroscope axes leads to the a simple analysis. All misalignments are relative to the conditions of GUN and TAS alignment and orthogonality. Thus, misalignments about axes

of rotation are thought of as resolver biases: there is no gimbal rotation misalignment.

#### THE MEASUREMENTS AND THEIR FILTER MODELS

Measurements are provided by two tri-axes of gyroscopes and two resolver chains. Each gyroscope package measures the inertial (L) angular velocity of the body to which it is attached. The angular velocity measurements are denoted by:

(TAS)  ${}^{\text{L}}\underline{\omega}^{\text{Is}}$

(GUN)  ${}^{\text{L}}\underline{\omega}^{\text{Ig}}$

The measurements are modeled as follows. The resolver measurement vector is written in terms of the resolver measurements from the "truth" relationship Eq. (1):

$$\begin{aligned} z_R = \underline{\delta}_{\text{T}} - \underline{\epsilon}_{\text{S}} - [\text{Es}] * \underline{\iota}_{\text{S}} \\ - [\text{Es}] [\underline{\delta}_{\text{P}}] [\text{As}] * (\underline{\epsilon} + \underline{\delta}) \\ + [\text{Es}] [\underline{\delta}_{\text{P}}] [\text{As}] [-\text{Ag}] * \underline{\iota}_{\text{g}} \\ + [\text{Es}] [\underline{\delta}_{\text{P}}] [\text{As}] [-\text{Ag}] [-\text{Eg}] \\ * \underline{\epsilon}_{\text{g}} \end{aligned} \quad (2)$$

where  $z_R$  is the de-skew of the measurement matrix:

$$Z_R = [E_S] [\delta_p] [A_S] [-A_g] [-E_g]$$

The measurements are modeled as follows. The angular velocities are differenced to form the "strapdown" filter measurement:

$$\begin{aligned} Z_{\text{STRAP}} &= {}^{\text{Ig}}\underline{\omega}^{\text{Is}} = {}^L\underline{\omega}^{\text{Is}} - {}^L\underline{\omega}^{\text{Ig}} \\ &= d \underline{\delta}_T / dt + {}^L\Omega^{\text{Ig}} \underline{\delta}_T + b \quad (3) \end{aligned}$$

The misalignments  $\underline{\delta}_T$ ,  $\underline{\epsilon}_S$ ,  $\underline{\epsilon}_T$ ,  $\underline{\epsilon}_G$ , and  $\underline{\epsilon}_G$  are not all treated as state variables. Some of the estimates are linear combinations of the chosen state variables. Thus, the measurement model matrix,  $H_m$  contains parameters of the F-matrix in the system:

$$\begin{aligned} \dot{X} &= F X + G u \\ Z &= H_m X \end{aligned} \quad (4)$$

The total misalignment  $\underline{\delta}_T$  is not separable from the gyro package misalignment  $\underline{\epsilon}_S$ , since the total true misalignment  $\underline{\delta}_T$  contains it and the resolver chain does not encompass it. Thus,  $\underline{\delta}_T$  is not sight "tube" to gun "tube" true alignment as it should be, but includes the gyro package misalignments with respect to the "tubes". We are only interested in the "tube" to "tube" misalignments so that the  $\underline{\epsilon}_S$  and  $\underline{\epsilon}_G$  misalignments must be removed from  $\underline{\delta}_T$ , which is composed of a mean value  $\underline{\delta}_{Tm}$  and a variable part  $\underline{\delta}_{Tv}$ . The variable part is estimated independently via the process consisting of the "strapdown" measurement of Eq. (3) with a bandpass filter state model.

Since the TAS and GUN can move over large angles relative to each other, we can also perform independent estimates of the constant misalignments  $\underline{\epsilon}_S$ ,  $\underline{\epsilon}_T$ ,  $\underline{\epsilon}_G$  and  $\underline{\epsilon}$ .

The independently estimated total variable misalignment  $\underline{\delta}_{Tv}$  and the constant misalignments are used in Eq.(2) as if they were measurements in order to form a new combining measurement:

$$\begin{aligned} Z_{\text{COMB}} &= Z_R - \underline{\delta}_{Tv} \\ &- \underline{\epsilon}_S + [E_S]^* \underline{\epsilon}_T \\ &- [E_S][\delta_p][A_S][-A_g]^* \underline{\epsilon}_G \\ &- [E_S][\delta_p][A_S]^* \underline{\epsilon} \\ &= [E_S][\delta_p][A_S]^* \underline{\delta} \end{aligned} \quad (5)$$

where  $\underline{\epsilon}_S$  includes  $\underline{\delta}_{Tm}$  and intentionally excludes  $\underline{\epsilon}_S$  and  $\underline{\epsilon}_G$ .

The measurements and the measurement model for the estimation of the constant misalignments  $\underline{\epsilon}_S$ ,  $\underline{\epsilon}_T$ ,  $\underline{\epsilon}_G$  and  $\underline{\epsilon}$  involve the gyro measurements. Since large angles are involved the linearization used in Eq. (3) cannot be used. The nonlinear expression is:

$${}^L\underline{\omega}^{\text{Is}} = {}^{Is}\mathbf{C}^{\text{Ig}}_{\text{TRUE}} {}^L\underline{\omega}^{\text{Ig}} + {}^{\text{Ig}}\underline{\omega}^{\text{Is}} \quad (6)$$

During the estimation of the constant misalignments the TAS and GUN are held at fixed but widely separated positions. In this case  ${}^{\text{Ig}}\underline{\omega}^{\text{Is}}$  is zero and with

$${}^{Is}\mathbf{C}^{\text{Ig}}_{\text{TRUE}} = {}^{Is}\mathbf{C}^{\text{Ig}}_m (\mathbf{I} - \mathbf{Y})$$

Eq. (6) may be written:

$$\begin{aligned} \underline{\omega}^{\text{Is}} &= {}^{\text{Is}}C^{\text{Ig}}_m (\underline{\omega}^{\text{Ig}} - \gamma \underline{\omega}^{\text{Ig}}) \\ &= {}^{\text{Is}}C^{\text{Ig}}_m \underline{\omega}^{\text{Ig}} \\ &\quad + {}^{\text{Is}}C^{\text{Ig}}_m \Omega^{\text{Ig}} \gamma \end{aligned}$$

This result provides the measurement model for estimation of the constant misalignments:

$$\begin{aligned} \underline{z}_{\text{tilts}} &= ({}^{\text{Is}}C^{\text{Ig}}_m)^T (\underline{\omega}^{\text{Is}} \\ &\quad - {}^{\text{Is}}C^{\text{Ig}}_m \underline{\omega}^{\text{Ig}}) \\ &= -\Omega^{\text{Ig}} \gamma \end{aligned} \tag{7}$$

where

$$\begin{aligned} \gamma &= \underline{e}_{\text{Is}} - [E_{\text{Is}}]^* \underline{r}_{\text{Is}} \\ &\quad + [E_{\text{Is}}][\delta_p][A_{\text{Is}}][-\underline{A}_{\text{Ig}}]^* \underline{r}_{\text{Ig}} \\ &\quad - [E_{\text{Is}}][\delta_p][A_{\text{Is}}]^* \underline{\epsilon} \end{aligned}$$

The measurement matrices for the three processes from Eq. (3) to (7) are therefore:

$$H_{\text{ms}} = \begin{vmatrix} (a^2 - b)I - a\Omega \\ aI - \Omega \\ \Omega - (a + \kappa)I \\ I \end{vmatrix}$$

where  $I$  = identity;  $a$ ,  $b$  and  $\kappa$  are filter parameters;  $\Omega = {}^L\Omega^{\text{Ig}}$

$$H_{\text{mt}} = \begin{vmatrix} \Omega \\ -\Omega [E_{\text{Is}}] \\ -\Omega [E_{\text{Is}}][\delta_p][A_{\text{Is}}] \\ \Omega [E_{\text{Is}}][\delta_p][A_{\text{Is}}][-\underline{A}_{\text{Ig}}] \end{vmatrix}$$

### combine

$$H_{\text{mc}} = [E_{\text{Is}}][\delta_p][A_{\text{Is}}]$$

### STATE MATRICES

The state or F-matrices as in Eq. (4) which correspond to each of the three processes are basically low pass or high, band pass filter models.

### strapdown

$$F_s = \begin{vmatrix} -aI & -I & I \\ bI & [0] & [0] \\ [0] & [0] & -t_H \end{vmatrix}$$

### tilts

$$F_t = \begin{vmatrix} -t_L I & kI \\ [0] & -t_L I \end{vmatrix}$$

where  $t_L I$  matches the low (L) end of the bandpass  $/b$ . The high (H) end  $t_H$  cutoff is as large as practicable considering the measurement noise. The state matrix for estimating the dynamic structural bending misalignment  $\underline{\delta}$  is the same as the "strapdown" estimation for the total misalignment  $\underline{\delta}_{\text{I}}$ .

### RESULTS

Fig. 2 is a typical of result without the bias offset. All results were obtain via simulations of helicopter rigid body and deformation motion. Gyro imperfections as specified by the vendor are included.

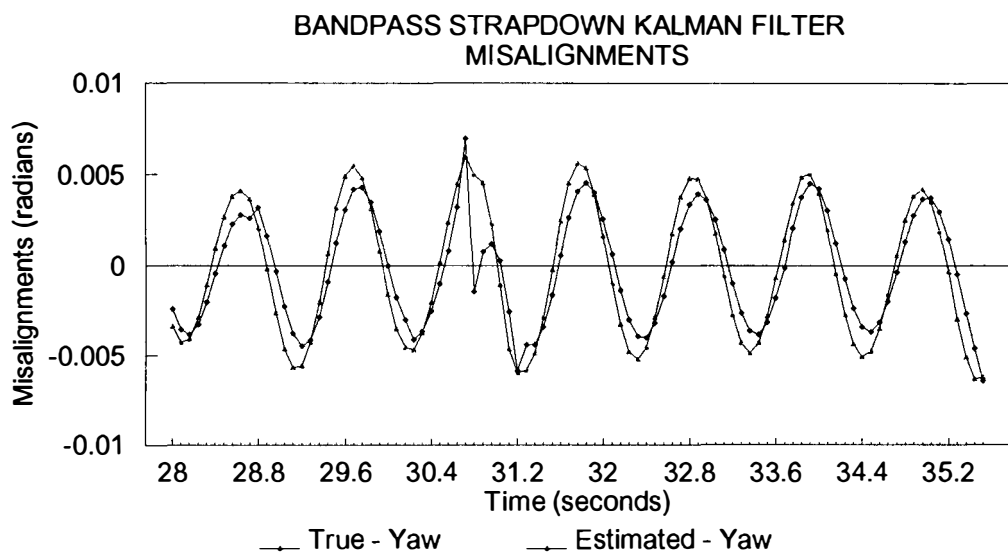


Fig. 2. Yaw axis estimated and true total misalignment.

### CONCLUSIONS

Numerous technical papers have been written on "transfer" alignment, which aligns a slave inertial navigation system to a master, aligns both translational and rotational states. Sutherland (1968) provides us with an early paper on the subject. Bar-Itzhack (1985, 1988) has a number of papers on the subject which clarifies various aspects of the problem.

The problem of aligning attitudes of two bodies with flexure in between has received little attention. Walrath (1990) has developed a technique which provides a limited capability to align non-gimballed bodies with flexure in between.

Boykin (1983) was successful in the use of a non-autonomous approach to estimate resolver biases and gimbal tilts of a target acquisition system. External landmarks were used.

Herein a technique has been presented which provides

alignment of gimballed subsystems with flexure of the structure between the subsystems. This approach apparently provides good estimates of both total misalignment (as in Walrath) and component misalignments over a wide range of bending

frequencies with low levels of helicopter rigid body motion. Eq. (1) provides the "truth" model from which the "true" misalignments are computed.

This approach allows for a back-up mode of operation in the case that the gun (or other weapon) has a gyro failure in the middle of a mission. The component misalignments can be used to reduce boresight errors since they are largely constant.

Further work must be done to thoroughly examine the performance boundaries of this approach. A sensitivity

simulation analysis is planned.

#### REFERENCES

- Bar-Itzhack, I.Y. and Vitek, Y. (1985). The enigma of false bias detection in a strapdown system during transfer alignment. AIAA J. Guidance and Control, 8, 175-180.
- Bar-Itzhack, I.Y. and Goshen-Meskin, D. (1988). Identity between INS position and velocity error equations in the true frame. AIAA J. Guidance and Control, 11, 590-592.
- Boykin, William H., Hobson R.W., and Nicholls, G.D. (1983). Estimation of TADS resolver errors and gimbal misalignments. System Dynamics Incorporated, Technical Report 83-8, June 1983.
- Sutherland, A.A., Jr. (1968). The kalman filter in transfer alignment of inertial guidance systems. AIAA J. Spacecraft, 10, 1175-1180.
- Walrath, C. (1990). ISBMS test and demonstration final report. Westinghouse Electronic Systems Group Report, July 24, 1990.

## MODAL CHARACTERIZATION OF THE ASCIE SEGMENTED OPTICS TEST BED: NEW ALGORITHMS AND EXPERIMENTAL RESULTS

A. Carrier and J.-N. Aubrun

*Lockheed Palo-Alto Research Laboratory, 3251 Hanover Street, B/250, O/92-30, Palo-Alto, CA 94304, USA*

**Abstract.** New frequency response measurement procedures, on-line modal tuning techniques, and off-line modal identification algorithms are developed and applied to the modal identification of the Advanced Structures/Controls Integrated Experiment (ASCIE), a generic segmented optics telescope test-bed representative of future complex space structures.

The frequency response measurement procedure uses all the actuators simultaneously to excite the structure and all the sensors to measure the structural response so that all the transfer functions are measured simultaneously. Structural responses to sinusoidal excitations are measured and analyzed to calculate spectral responses. The spectral responses in turn are analyzed as the spectral data become available and, which is new, the results are used to maintain high quality measurements. Data acquisition, processing, and checking procedures are fully automated.

As the acquisition of the frequency response progresses, an on-line algorithm keeps track of the actuator force distribution that maximizes the structural response to automatically tune to a structural mode when approaching a resonant frequency. This tuning is insensitive to delays, ill-conditioning, and nonproportional damping. Experimental results show that it is useful for modal surveys even in high modal density regions.

For thorough modeling, a constructive procedure is proposed to identify the dynamics of a complex system from its frequency response with the minimization of a least-squares cost function as a desirable objective. This procedure relies on off-line modal separation algorithms to extract modal information and on least-squares parameter subset optimization to combine the modal results and globally fit the modal parameters to the measured data. The modal separation algorithms resolved modal density of 5 modes/Hz in the ASCIE experiment. They promise to be useful in many challenging applications.

**Keywords.** *modal characterization; system identification; flexible structures; segmented optics*

### INTRODUCTION

Active control for large flexible structures has been the object of 15 years of research, yet because of the lack of experimental demonstrations traceable to actual developments, it has not been implemented in a single space mission. Much work has been done on not so large and not so complex flexible structures. As a result, numerically tractable and numerically robust procedures and algorithms for modeling and high performance control of truly large and complex systems are lacking. Precision segmented reflectors are major examples of systems where the size and the complexity issues arise. The Keck Ten Meter Telescope, soon to be operational on mount Mauna Kea in Hawaii, is one of them. The Keck primary mirror is composed of 36 hexagonal segments. The control system uses 108 actuators and 162 sensors to maintain the segments optically aligned. The Keck structure has 150 modes below 50 Hz with a modal density as high as 25 modes/Hz. Regrettably, the Keck telescope will not benefit from structural control technology.

To address the challenges specific to the active control of precision segmented optics, and to the active control of complex flexible structures in general, the Lockheed Palo-Alto Research Laboratory designed and built the Advanced Structures/Controls Integrated Experiment (ASCIE). The ASCIE test-bed emulates a telescope with a segmented mirror. Its seven-hexagonal-segment primary mirror is mounted on a lightweight flexible truss structure. The six peripheral segments are actively controlled by 18 electromagnetic precision actuators. 24 position sensors measure the relative displacements between the segments. The ASCIE segmented optics and support structure have 50 modes below 50 Hz. The ASCIE control hardware [5] which has been designed to meet the strict requirements for precision control of segmented optics, has demonstrated segment alignment performance down to 60 nanometers rms. Using a non validated Finite Element Model and worst case control design techniques, a factor of 3 to 5 improvement in segment alignment bandwidth was achieved over classical control techniques, and vibration attenuation in 25 out of 28 controlled modes was experimentally demonstrated [1],[2].

The objective of the present work is to develop a dynamic model of ASCIE from experimental input output data. The objective is two fold. One objective is to test how accurately the dynamic behavior of complex systems like ASCIE can be predicted by Finite Element Analysis (one to one comparison between the Finite Element and the identified models requires careful system identification to extract all the natural modes of the system including those with relatively low response). The other is to develop a control design model. This model will be used to test how much improvement in segment alignment bandwidth, and structural vibration suppression is achievable using an identified versus a FEM model. This paper reports on experimental results in modeling ASCIE.

Our work was to explore new excitation techniques for data acquisition using sinusoidal test signals, and new algorithms for extracting modal information from the non-parametric frequency response test data.

The data acquisition process we tested is classical, but the way we implemented it is not. Steady state responses to sinusoidal excitations were analyzed to determine the system admittance matrix at a given frequency, and frequency sweep was used to determine the non-parametric system admittance matrix over a grid of frequencies. System non-linearities were handled via harmonic analysis. But, what is new, at each frequency, a system inversion was approximately realized to achieve good signal to noise ratio. In addition, the principal system admittance gains and associated input and output patterns were determined. This approach yields some important and inherently multivariable properties of the system being tested, namely the modal frequencies, the modal dampings, and what is new, the mode shapes because, at a resonant frequency, the maximum system admittance gain is obtained when the actuator inputs are combined so as to excite a pure mode. Dwells in both spatial and spectral domains are performed which is critical to the modal identification of complex symmetric lightly damped structures, since for such structures tuning to the resonant frequency alone fails to isolate closely spaced modes.

When the acquisition process was completed, a parametric modal model was fitted to the full non parametric measured system admittance matrix, and new algorithms based on low rank matrix approximation, or on convex and quadratic optimization techniques were used to carry one step further the identification of the modal parameters started during the data acquisition process. The algorithms are used repeatedly. Each time they are called, they extract one or several dominant natural modes from the non parametric response over a prespecified frequency range. To identify a mode, they use the modal information contained in the maximum system admittance gain and its associated input and output patterns, and the consistency of this modal information over any specified frequency range to give accurate modal parameters free to the extent possible from the contributions of the nearby modes.

The paper is organized as follows. Section 2 de-

scribes the ASCIE high modal density flexible structure that was used to demonstrate the new modeling techniques. Section 3 briefly describes the data acquisition procedure. Section 4 illustrates the application of on-line modal testing to the ASCIE experiment. Section 5 illustrates the application of off-line modal analysis, and model refinement via parameter optimization, to the modal identification of ASCIE.

## ASCIE TEST-BED

The ASCIE emulates a f/1.25 Cassegrain telescope. Its seven-hexagonal-segment primary mirror is mounted on a light-weight flexible truss structure. The six peripheral segments are actively controlled in three degrees of freedom by 18 linear electromagnetic precision actuators. 24 Kaman position sensors (4 per actively controlled segment) are used to measure the relative displacements between the segments and generate commands for the actuators to keep the segments optically aligned, the central segment acting as a reference.

**Non Colocated sensing:** The edge inductance sensors measure the relative positions of the primary mirror segments. The central segment, instead of the support structure which lacks dimensional stability, is used as a reference. The edge sensors have a 60 nanometer rms resolution below 5 Hz, and a large measurement range ( $\pm 1$  mm) to accommodate the initially large segment misalignments. A laser optical system, not described, is used for initial calibration and system alignment. In future works, this system will also be useful for optical scoring.

**Actuation:** The actuators have been specially designed at Lockheed [5] to meet the strict resolution, dynamic range, smoothness of operation and bandwidth requirements for precision control of segmented optics. When driven in force mode, their bandwidth is 140 Hz. Each actuator is instrumented with an automatic system providing force offloading to reduce power dissipation.

**Colocated sensing:** Each segment alignment actuator is instrumented with a colocated Kaman inductance position sensor. Each sensor has a 60 nanometer rms resolution below 5 Hz, and a measurement range of  $\pm 1$  mm.

**Truss structure:** The structure was designed and optimized to emulate a large telescope structure while being able to support the mirror segments in a 1-g environment. Its modal distribution contains several dense clusters and is fundamentally different from the well-spaced distribution of beamlike structures.

### Real-time processing and data acquisition:

The ASCIE computer and graphic set up includes an Array Processor, a mini computer, two PCs, and an input/output unit. The Array Processor is an AP-120B, a 12 MFlops machine with 64K of internal memory from Floating Point Systems, fully programmable from the Harris-800 mini computer. The Array Processor is the main computational unit and it is responsible for real-time control processing,

signal generation, and real-time Direct Memory Access data transfers to a 256 Kbytes internal memory block residing on the Harris-800 mini computer. The Harris-800 and the PCs are used to monitor the ASCIE experiments via graphical displays of the Kaman sensor readings, the actuator commands, and the mirror segment piston and tilt misalignments. The input/output unit is composed of 32 16 bit-analog to digital and 18 16 bits-digital to analog converters.

### DATA ACQUISITION

Steady state responses to sinusoidal excitations are measured and analyzed to determine the system admittance matrix at one frequency, and frequency sweep is used to determine the system admittance matrix over a grid of frequencies. The frequency response measurement procedure uses all the actuators to simultaneously excite the structure, and all the sensors to simultaneously measure the structural responses. The transfer functions in all degrees of freedom are measured in a single path. The spectral responses are analyzed as the spectral data become available, and the results are used to excite the system preferentially according to its principal gains and corresponding principal actuator force vectors. The mean-squares force input is adjusted to maintain a given mean squares displacement response. This excitation technique maintains high quality measurements and avoids the problems associated with system ill-conditioning.

### ON-LINE MODAL TESTING

On-line modal testing consists in experimentally isolating the modes of a system to measure their characteristics. It was first proposed by Lewis and Wrisley [3]. It requires tuning the polarities and the relative magnitudes at one frequency of several shakers located at discrete points on the structure to produce a pure mode response. Classical modal tuning techniques require a lot of instrumentation, expensive data acquisition systems, and they can be difficult to implement. Experimental factors such as measurement non-collocated with the excitations, delays, non-proportional damping, lack of orthogonality of the mode shapes in high modal density regions, and ill-conditioning affect these techniques or make them fail. This section presents an effective on-line modal testing technique relatively insensitive to the above experimental factors which was developed to perform limited modal surveys on ASCIE.

The approximate modal tuning objective is to maximize the root-mean-squares displacements for a given root-mean-squares force excitation. It is a generalization of the gain concept used for single-input single-output systems. It requires tuning the relative phases and the relative magnitudes of the various sine forces to maximize the response. Only a preliminary measurement of the transfer function matrix and a singular value analysis of this matrix are needed to find the force vector that maximizes the response at a given frequency. Gain tuning can therefore easily and reliably be achieved experimentally.

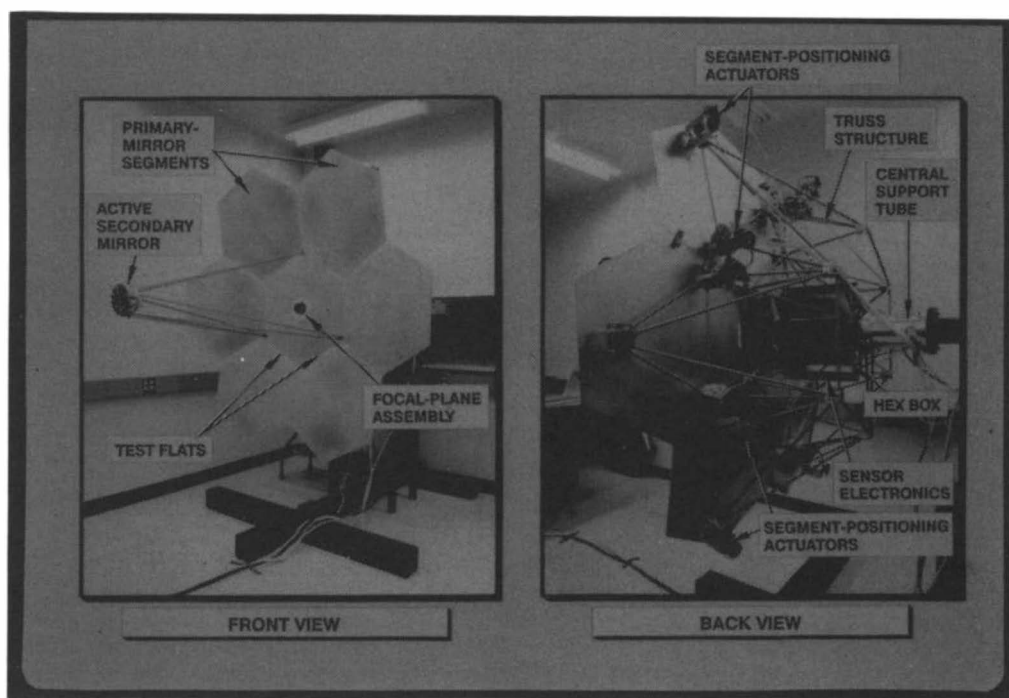


Figure 1: ASCIE test-bed

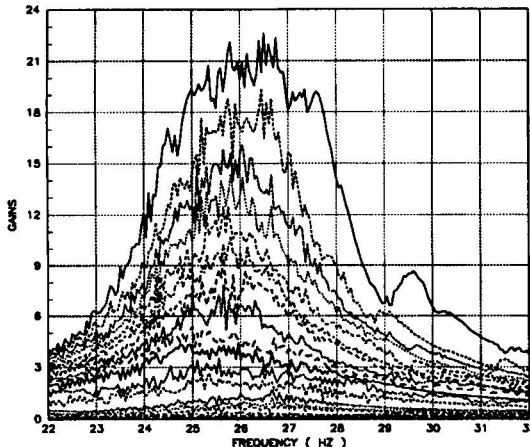


Figure 2: ASCIE non-collocated frequency response in high modal density region

For lightly damped systems, at a resonant frequency, the maximum admittance gain is obtained when the actuator forces are combined so as to excite a pure mode. Gain and modal tuning are therefore nearly equivalent. This is the theoretical basis for our modal tuning procedure.

The tuned force and response vectors at a resonant frequency yield the mode shapes at the actuator and sensor locations respectively. To isolate the target mode, the polarities and relative magnitudes of the actuator forces must be adjusted according to the mode shape at the actuator locations and a linear combination of all the responses must be taken according to the mode shape at the sensor locations. Once the target mode is isolated, a frequency sweep can be performed to measure its modal characteristics.

The effectiveness of this procedure is illustrated in Figure (2) and Figure (3). The ASCIE admittance matrix from the 18 mirror segment actuators to the 24 edge position sensors (Figure (2)) is measured between 22 and 33 Hz. The singular value decomposition of the admittance matrix at 27 Hz is then computed to extract the mode shape information of the dominant mode around this frequency. This mode shape information in turn is used to isolate the corresponding mode as explained above, and a single-input single-output sine sweep is performed. Figure (3) shows the resulting measured modal response. The phase curve shows that the phase drops by 180 degrees as the sweep passes through the resonant frequency as it should for a pure mode response. The modal frequency and the damping ratio of the isolated mode, obtained by curve fitting the modal response, are 26.9 Hz and 3.3% respectively.

#### DYNAMIC CHARACTERIZATION OF ASCIE

With a small number of sensors and actuators, it is experimentally impossible to isolate all the modes of

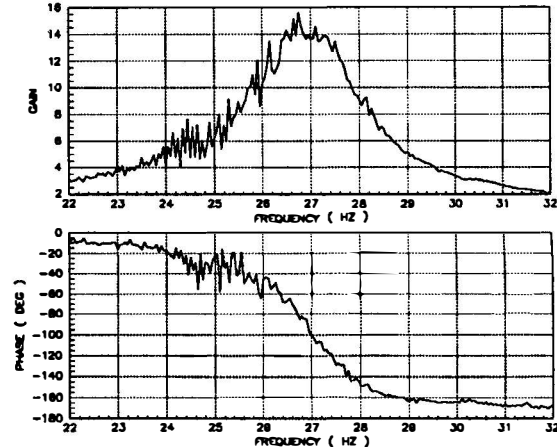


Figure 3: Frequency response of dominant mode around 27 Hz extracted by on-line modal tuning

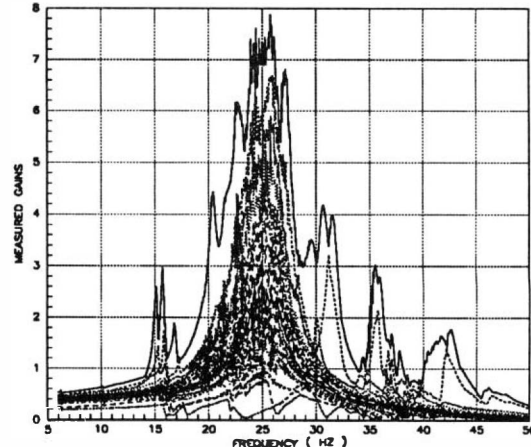


Figure 4: Measured collocated frequency response of ASCIE

the complex ASCIE structure. Analytical techniques that can determine the modal properties of the structure without isolating the modes must be used. This section illustrates the application of analytical techniques specially developed to construct a modal representation of the ASCIE segmented optics and support structure from its measured collocated response. Figure (4) shows the principal gains of this response between 6 and 50 Hz.

#### Approach

The characterization is treated as a curve fitting problem in the frequency domain. The error criterion is the least-squares difference between the theoretical and the measured frequency responses. Its minimization is treated as a classical two step initialization-least squares optimization problem. However because of the complexity of the present problem, a lot of effort is devoted to the initialization procedure: the main idea consists in isolating the modes according to their spectral and spatial separation to estimate

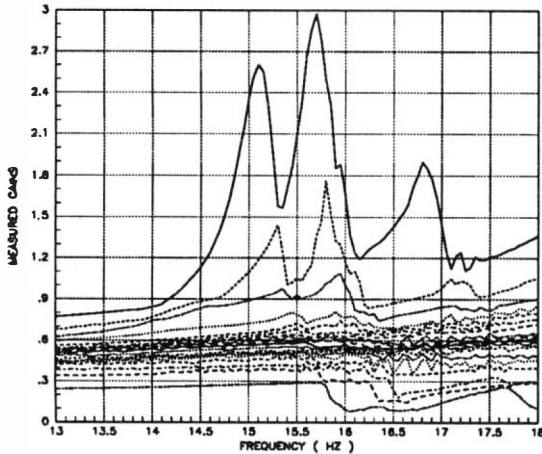


Figure 5: Measured collocated frequency response of ASCIE between 13 and 18 Hz

their dynamic characteristics.

#### Spectral Partitioning

The spectral partitioning is performed by visual inspection of the frequency response: the dominant modes with similar frequencies are grouped together. Accordingly the ASCIE collocated frequency response is partitioned over 6 frequency ranges: 1 to 13 Hz, 13 to 18 Hz, 20 to 29 Hz, 28 to 33 Hz, 33 to 39 Hz, and 39 to 50 Hz.

#### Analytical Modal Separation

On each frequency range, an analytical modal separation algorithm [4] is used iteratively to extract the non-parametric frequency response of one or several modes at a time from the measured frequency response. This algorithm operates like the gain-based modal tuning technique of the previous section: it extracts modes on the basis of the dominance of their response in some frequency range around their resonant frequencies. Extracting a single mode response involves determining the proper distribution of excitation forces and the proper linear combination of the measured responses (that is the mode shapes at the actuator and the sensor locations respectively) as in on-line modal tuning. Similarly, extracting a multiple mode response involves determining multiple distributions of excitation forces and multiple linear combinations of the measured responses. Figure (6) illustrates a single application of the analytical modal separation algorithm to extract the modal response of the 4 dominant natural modes of the ASCIE segmented optics and support structure between 13 and 18 Hz from its collocated frequency response (Figure (5)). The frequency response of the residual system (Figure (7)) clearly illustrates that the modal response of the dominant modes is well extracted.

#### Extracting Modal Properties from Non-Parametric Modal Responses

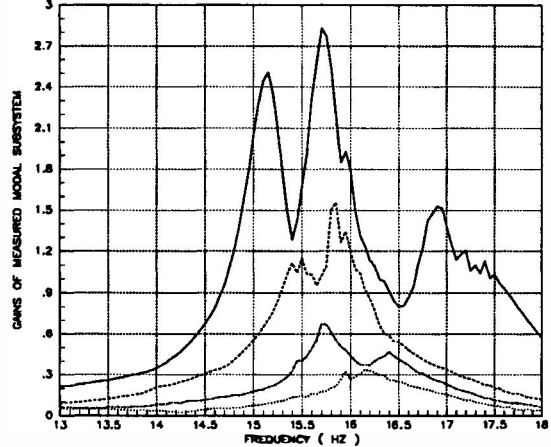


Figure 6: Non parametric frequency response of ASCIE 4-mode model between 13 and 18 Hz

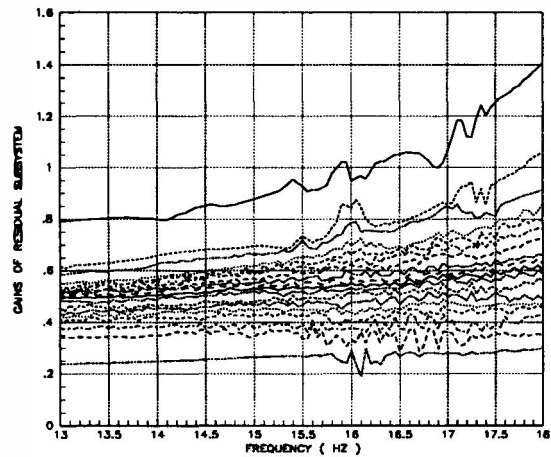


Figure 7: Residual ASCIE frequency response between 13 and 18 Hz after the estimated modal response of a 4-mode model is removed

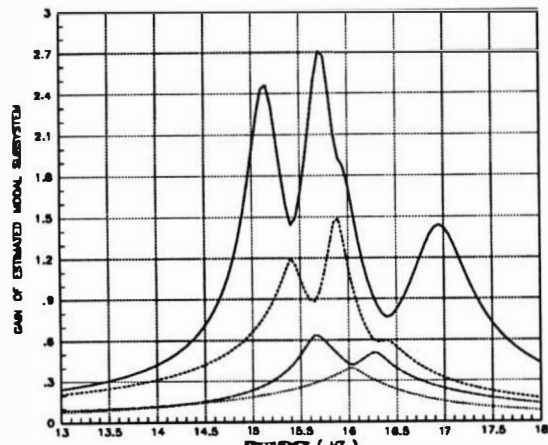


Figure 8: Calculated ASCIE 4-mode model frequency response between 13 and 18 Hz

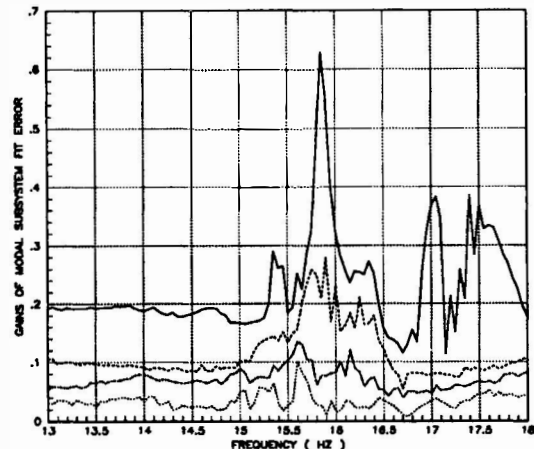


Figure 9: ASCIE optimal modal response fit error between 13 and 18 Hz

Each non-parametric modal response is analyzed to estimate the dynamic characteristics of the modes it contains. Non-parametric modal responses are simple, involving only a few modes, so that their analyses can be carried out effectively. Special numerical algorithms [4] are used for this purpose. Figure (8) for instance is the result of applying these algorithms to the non-parametric modal response of Figure (6). It shows the calculated frequency response of a theoretical 4 mode model.

#### Optimization of Theoretical Model Constructed from Modal Subsystems

Once all the non-parametric modal responses have been analyzed, the characteristics of all the modes in each frequency range are combined to build a linear state-space modal representation of ASCIE. This modal representation is then tuned to best predict the measured frequency response in the least-squares sense. A Newton-Raphson optimization algorithm is used to carry out this task. However because the op-

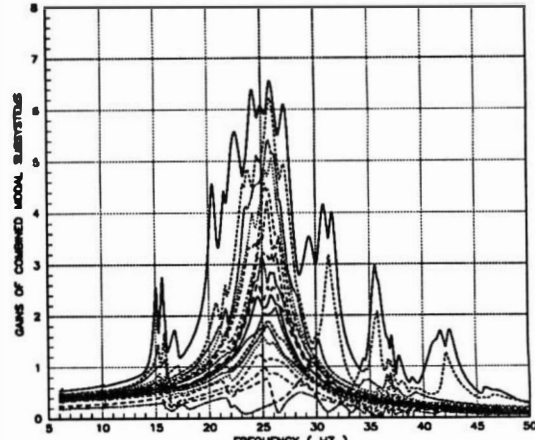


Figure 10: Calculated collocated frequency response of ASCIE

timization involves several thousands modal parameters, it is not carried out in the usual vector form. Instead, the structure of the identification problem is exploited to break down the optimization problem into two linear least-squares problems which are solved explicitly, and a non-linear least-squares problem of relatively small size involving only the modal frequencies and the damping ratios of the predicted modes. All three optimization problems are solved successively and iteratively.

Figure (10) shows the principal gains of the optimal model obtained by globally tuning a 50-mode model to the measured ASCIE collocated frequency response. In this case, 4024 modal parameters were optimized, and 324 transfer functions were fitted simultaneously. Figure (11) compares some local results, namely the measured and the calculated frequency responses for one collocated actuator sensor pair. The only significant difference between the two responses is around the 50 Hz boundary: it corresponds to the contributions of the unmodeled modes outside of the frequency range being analyzed.

Figure (12) gives the modal frequency and damping ratio histograms corresponding to the identified 50-mode model. It shows that modal clusters with as many as 5 modes/Hz have been resolved.

## CONCLUSION

In this paper, system identification techniques specially developed to characterize the dynamics of complex structures from frequency response data are applied to ASCIE. Multiple excitations at a single frequency are used to acquire the frequency responses. At each frequency, the system is excited preferentially according to its principal gains to avoid the problems associated with system ill-conditioning. Spectral and spatial separation are used concurrently in on-line modal tuning techniques, and off-line modal separation techniques. These techniques can isolate pure modal responses in high modal density clusters for estimating their characteristics. These estimated

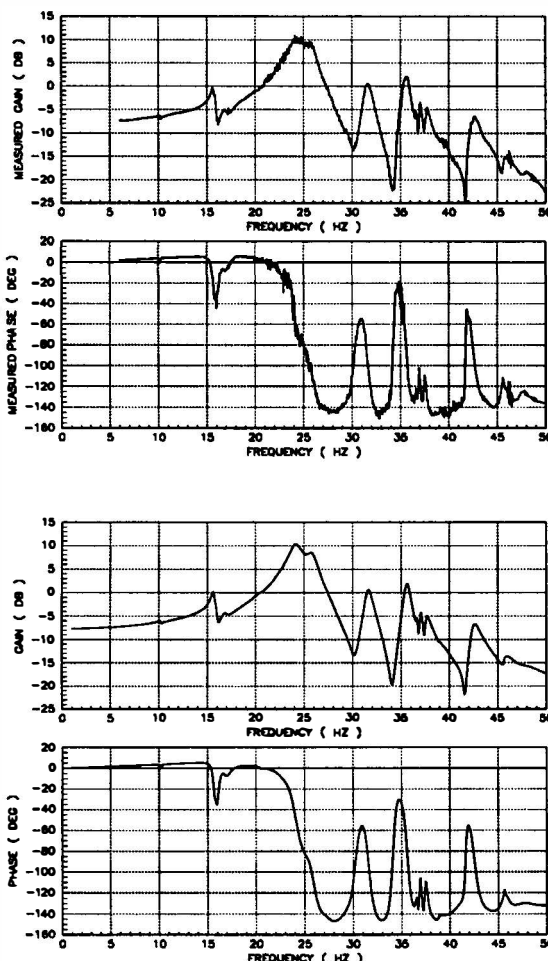


Figure 11: Example of collocated transfer functions showing excellent agreement between predicted and measured responses

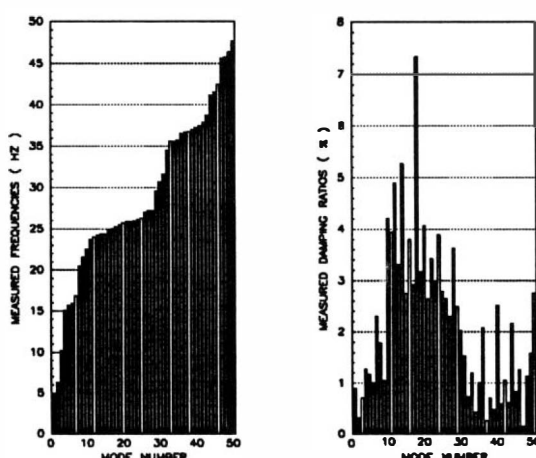


Figure 12: Modal frequencies and damping ratios of ASCIE 50-mode model

modal characteristics can be combined to construct a linear model and to initialize a frequency domain multi-level least-squares optimization procedure. The optimized model matches accurately the measured responses and meets the requirements for high performance control design.

## ACKNOWLEDGEMENTS

The authors would like to thank Ernie Perez, Paul Reshatoff, and Don Zacharie for their outstanding technical support.

## References

- [1] Carrier A., 'Modeling and Shape Control of a Segmented-Mirror-Telescope', Stanford University PhD Thesis, Department of Aeronautics and Astronautics, March 1990.
- [2] Carrier A., Bryson A., Aubrun J. N., ' $H_\infty$  Control Design for the ASCIE Segmented Optics Test-Bed: Analysis, Synthesis, and Experiment', Proceedings of the 4th NASA/DoD CSI Technology Conference, Orlando, Florida, November 1990.
- [3] Lewis R., Wrisley D., 'A system for excitation of pure natural modes of complex structures', Journal of Aerospace Sciences, Vol. 17, No. 11, pp705-722, November 1950.
- [4] Carrier A., Aubrun J. N., 'Modal Characterization of the ASCIE Segmented Optics Test-Bed: New Algorithms and Experimental Results', Proceedings of the 5th NASA/DoD CSI Technology Conference, Lake Tahoe, Nevada, March 1992.
- [5] Lorell K., Aubrun J.-N., Zacharie D., Perez E., 'Development Of A Precision , Wide-Dynamic-Range Actuator For Use In Active Optical Systems', Proc. 23rd Aerospace Mechanisms Symposium, pp. 139-156, 1989.
- [6] Stroud R., Smith S., Hamma G., 'MODALAB - A New System of Structure Dynamic Testing', The Shock and Vibration Bulletin, No. 46, pp. 153-175, August 1976.
- [7] Asher G., 'A Method of Normal Mode Excitation Utilizing Admittance Measurements', Proceedings of the National Specialists' Meeting on Dynamics and Aeroelasticity, pp. 69-76, Fort Worth, Texas, November 1958.
- [8] Ibanez P., 'Force Appropriation by Extended Asher's Method', presented at the SAE Aerospace Engineering and Manufacturing Meeting, San Diego, CA, December 1976.
- [9] Ryan R. and al., Dynamic Testing for Large Systems', NASA TM-78307, Sept. 1980.

## ACTIVE STRUCTURAL CONTROL ON THE ASCIE TESTBED

R.J. Kline-Schoder

*Lockheed Research Laboratory, O/92-30, B/250, 3251 Hanover Street, Palo Alto, CA 94304, USA*

**Abstract:** The use of an integrated line-of-sight and structural control system for regulating the panel tilt of a single panel of the ASCIE test bed is discussed. Two actuators are used: one for relatively low bandwidth, large amplitude panel motions and another for relatively high frequency, small amplitude structural control. A finite element model of the system is developed and is used for designing the control law. The control algorithm is based on robust synthesis techniques and is implemented on a digital computer. Experimental results show that the robust control algorithm achieves a bandwidth which is comparable to the first structural frequency of the system and far exceeds the performance of a simple integral controller.

**Key Words:** *automatic control, control applications, digital control, laboratory techniques, modal control, robust control*

### Introduction

As space structures become larger in size and smaller in mass, interaction between the main payload and the support structure becomes more likely and less tolerable. This situation most commonly arises when the main payload of the spacecraft is actively controlled and the payload control system applies reaction forces to the support structure. These control forces can, in turn, excite structural vibrations in the support structure which may ultimately limit payload performance. This phenomenon has been termed control/structure interaction (CSI) and is the focus of much current research. Members of the Lockheed Palo Alto Research Laboratory have built a test bed known as the Advanced Structures/Control Integrated Experiment (ASCIE) in order to

investigate the application of novel control techniques to the CSI phenomenon. The ASCIE test bed simulates a 2 m diameter Cassegrain telescope with a segmented primary mirror. The six mirror segments are actively controlled with three actuators per segment and are mounted on a lightweight, flexible support structure. Numerous methods for achieving segment alignment and shape control have been implemented. However, all of the the methods have been limited by induced structural vibrations.

One proposed method of solving this CSI problem is to include active structural members in the support structure in order to actively apply damping to unwanted structural vibrations. Active structural control is presently the focus of significant research resources. To date, no single method of active structural control has proven to be effective in all configurations and applications. Many research efforts have focused on the analytical development of control algorithms and use computer simulation to judge the efficacy of the proposed method [1]–[3]. Members of the Jet Propulsion Laboratory (JPL) have designed and built an active structural member [4] and have used this hardware in conjunction with various laboratory test articles [5][6]. The JPL team has achieved promising results using an impedance matching approach which uses the actuator as a mass/spring/damper, tuned to match the impedance of the structure. Matching the structural impedance with the active member theoretically is the most efficient method for removing energy from the vibrating structure. The JPL laboratory experiments have shown that this method works well for particular

structures and specific hardware configurations. Other local feedback methods have also been investigated [9]. Preumont, *et al.*, used a relatively simple feedback algorithm with commercially available piezoelectric actuators. These controllers use a series force measurement, add 90 deg of phase, and apply a control force proportional to this measurement. The results are quite good from the local control standpoint; however, the general applicability for reducing global structural vibrations has yet to be demonstrated. Other researchers have applied modern control techniques to the structural control problem [7][8]. These methods have been shown to be effective; however, the formulation can be complex and the robustness of the designs can be low. Finally, a hierarchical approach has been proposed [10] which attempts to include knowledge of the entire structure while retaining the flavor of a colocated control system design.

This paper describes the experimental setup used to test various methods of structural control on an ASCIE sub-cell. The sub-cell has been fitted with a version of the JPL actuator mentioned earlier. The piezoelectric actuator serves as one of the support members and can be used to alter the dynamic characteristics of the structure. The sub-cell has been modelled using finite element methods and is shown to possess many of the key characteristics of the complete ASCIE structure (*i.e.*, virtually identical structural frequencies, similar modal density, and the CSI phenomenon). A simple, one degree of freedom, panel-tilt control system has been implemented, which exhibits bandwidth limitation due to structural interaction with the control system. Various methods of altering the dynamic behavior of the structure have been implemented on the test sub-cell. The methods include simple, colocated, velocity feedback, impedance matching of the actuator to the structure, and a design based on the  $H_\infty$  paradigm. All of these methods have previously been shown to be effective in certain structures. The most effective method for the ASCIE sub-cell experiment has been the controller designed using robust synthesis (*i.e.*,  $H_\infty$ ) techniques. The development of this controller is discussed in the remainder of this paper. Results of laboratory

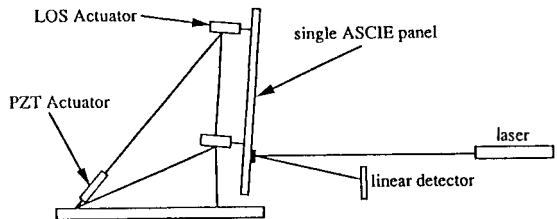


Figure 1: Schematic Diagram of Experimental Setup

experiments with the  $H_\infty$  control system show significant improvement in system response and bandwidth.

## Experimental Hardware

The complete ASCIE is an operational test bed which contains a seven-segment, actively controlled primary mirror, which is 2 m in diameter. The primary mirror is supported by a light, flexible space truss attached to a central rigid tube which acts as the metering reference. A hexagonal box surrounding the central tube constitutes the base structural element upon which the six identical segment sub-cells are attached. Each of the six segments is controlled in piston and tilt by three linear actuators. The current research considers one of the six identical segments, removed from the complete test bed, and mounted on a bench as shown in the side view of Figure 1. The single segment contains two actuators, a line-of-sight (LOS) actuator and the active structural piezoelectric actuator. The single LOS actuator is used to control the tilt of the panel relative to the table and the piezoelectric actuator is used to provide active structural control. The tilt angle is measured with a laser which shines on a mirror mounted to the panel and whose return beam illuminates a single axis photo detector.

To aid in the control system design, a finite element model (FEM) of the system was developed using ASTRO, a proprietary program developed at Lockheed. The model

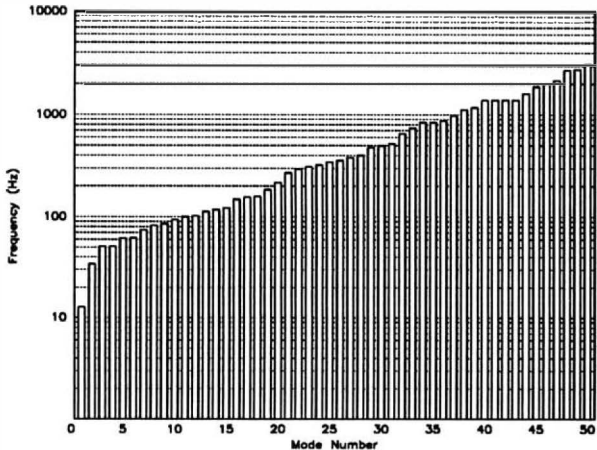


Figure 2: Histogram of FEM Modes

consisted of approximately 150 nodes which were used to describe the structural dynamics of the test article. A histogram of the first 50 modes is shown in Figure 2. The figure shows that the fundamental mode is approximately 13 Hz and that the modal density is quite high (which is typical of ASCIE-like structures). In order to verify the accuracy of the model, a single-input-single-output (SISO) transfer function was generated using the LOS actuator as the input and the panel tilt as the output. A comparison of the measured data and a transfer function derived from the FEM is shown in Figure 3. This figure shows that the FEM is accurate in predicting the fundamental mode of the system; however, significant differences exist for frequencies above 60 Hz. This situation is quite common when attempting to model complicated structures. It is well known that the implications of this inaccuracy for control system design are rather severe. The design of a control system for a plant with significant modelling errors can be extremely difficult. One of the advantages of robust control synthesis techniques (*i.e.*,  $H_\infty$ ) is that the controller can be de-sensitized to certain modelling errors. With this in mind, a control system was developed using  $H_\infty$  design tools.

### Control Law Discussion

The emergence of robust control synthesis techniques (see [11]) has provided control

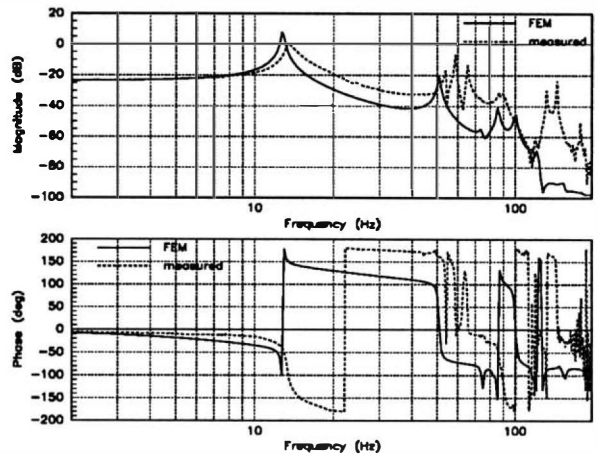


Figure 3: Measured and FEM-derived SISO Transfer Functions

system designers with additional tools for the development of multi-variable controllers. These techniques provide the capability to simultaneously input information describing modelling error sources and required performance and stability characteristics directly into the control system formulation and to derive optimum controllers based on these data. The inclusion of this information tends to yield controllers which are less conservative and which can provide greater robustness and performance than those based on modern or classical techniques.

The current research made use of these characteristics of  $H_\infty$  control law design: exploiting the capability to explicitly shape both the low and high frequency closed-loop plant dynamics and shape the required frequency response of the control actuators. The desired open-loop low frequency response, as is the case for most control systems, is high gain, which serves to reject disturbances through the cross over region. Open-loop high frequency behavior must roll off at a sufficiently high rate in order to minimize the possibility of spill over of unmodelled dynamics. The required frequency response of the control actuators consists of low frequency inputs from the LOS actuator and high frequency control authority from the piezoelectric, structural actuator. These characteristics of the control system dynamics and actuators are

conveniently prescribed using frequency domain descriptions. The resultant  $H_\infty$  control law, based on an 8 mode model, consisted of 27 states. This controller was reduced, using singular perturbation methods, to a 20 state controller before being discretized for implementation in a digital computer.

## Experimental Results

A series of tests were performed with the experimental hardware to determine the efficacy of the previously-described control algorithm. The test consisted of performing a step response of the closed-loop system to an initial panel tilt error. The control algorithm was programmed in C, was implemented on an 80486-based computer, and ran with a sample rate of 500 Hz. The computer read the measurement of the panel tilt angle through an analog-to-digital converter, calculated the desired commands for the LOS and piezoelectric actuators, and output the required signals with digital-to-analog converters.

In order to perform an initial system test and to provide an excellent example of the controls/structures interaction phenomenon, a simple integral control system was implemented. This controller ignored the presence of the active structural element and provided a baseline for comparison of the behavior of the  $H_\infty$  controller. The results of this experiment are shown in Figure 4. This figure shows both the time history of the regulated panel tilt angle and the control effort required to achieve the given time history. The time history of the panel tilt angle shows that the initial angle is reduced to a noise limited value in approximately 0.4 seconds. The transient response is rather oscillatory at the fundamental mode of the plant and clearly shows interaction between the control system and the structure.

The results of the integrated design of a structural and alignment control system designed with  $H_\infty$  techniques is shown in Figure 5. This figure shows the time history of the regulated panel tilt angle and the required forces from the LOS actuator and piezoelectric actuator to achieve the shown angle time history. The basic idea was to use the LOS actuator to provide the large forces and large excursions

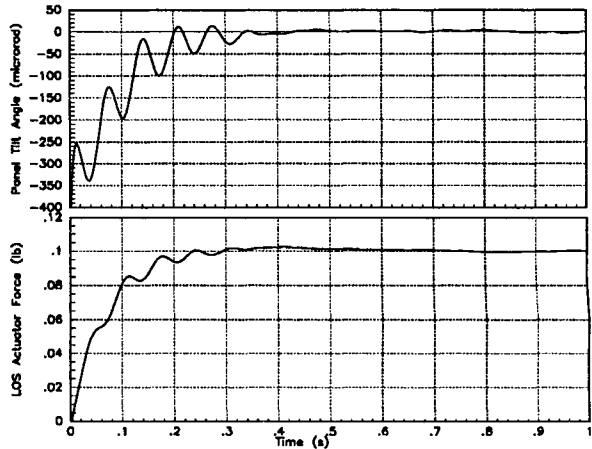


Figure 4: Step Response of SISO Integral Controller

required to achieve the gross panel motion and to use the piezoelectric actuator to control the structural modes of the system. The time response of the panel tilt angle behaves like a critically damped, second-order system with a bandwidth of approximately 7 Hz, which compares quite well with the first fundamental mode of the system. Further, the  $H_\infty$  controller bandwidth is also significantly higher than the bandwidth achieved from the pure integral control algorithm. The actuators also behave as would be expected: the LOS actuator provides the low frequency, high amplitude forces required for the gross motion of the panel and the piezoelectric actuator provides the high frequency, low amplitude forces for structural control.

## Conclusions

Interaction between supporting structures and control system actuators result in decreased system performance and difficult structural control problems. Active structural members have been suggested as a possible means of adding damping to certain structural modes, thereby reducing the chance of spill over and increasing the performance of systems which exhibit control/structure interaction (CSI). Previous researchers have used these active structural members in a local force or impedance feedback mode. This paper discusses an application of robust sythe-

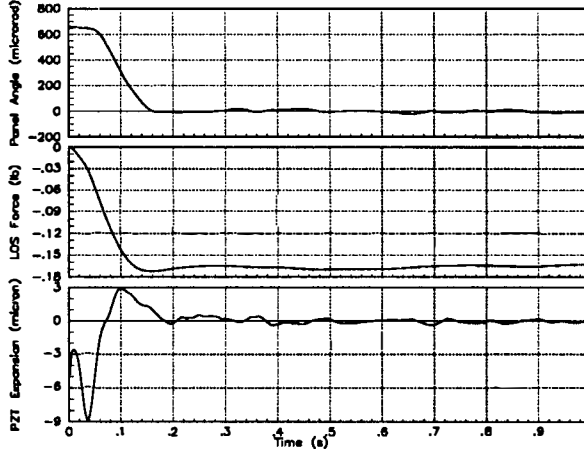


Figure 5: Step Response of Robust Controller

sis techniques in the development of an integrated structural and line-of-sight (LOS) control algorithm. A finite element model of a test article was developed and used to derive an  $H_\infty$  control law which was implemented on a digital computer. The test article consisted of a single panel of the ASCIE test bed which contained an active structural member. A LOS actuator was used to provide the large amplitude, low frequency gross motion to regulate the panel tilt and a piezoelectric actuator was used to achieve high frequency, small amplitude structural control. The results of laboratory experiments show that the  $H_\infty$  control law achieved closed-loop system response bandwidth comparable to the open-loop lowest structural frequency and which far exceeded the performance of a simple integral controller.

### Acknowledgments

The author would like to acknowledge the role played by Dr. Abbas Emami and Nassar Kharish and Mr. Thomas Holmes all of Systems Control Technology, Inc. Their role in developing the robust control algorithm and performing the necessary robustness evaluations were key to the successful completion of this research. In addition, the efforts of Messrs. Ted Havas and Michael Wright of the Lockheed Research Laboratory in the development of the finite element model of the test article are greatly appreciated. With-

out their results, the control system could not have been designed.

## References

- [1] Balas, M. (1982). Some Trends in Large Space Structure Control Theory: Fondest Hopes; Wildest Dreams. *IEEE Transactions on Automatic Control*, Vol. AC-27.
- [2] Meirovitch, L., H. Baruh, H. Oz (1983). A Comparison of Control Techniques for Large Flexible Structures. *AIAA Journal of Guidance, Navigation, and Control*, Vol. 6, No. 4.
- [3] Hu, A., L. Taylor, R. Singh (1991). Special Class of Nonlinear Damping Models in Flexible Space Structures. *AIAA Journal of Guidance, Navigation, and Control*, Vol. 14, No. 1.
- [4] Anderson, E., D. Moore, J. Fanson (1990). Development of an Active Member Using Piezoelectric and Electrostrictive Actuation for Control of Precision Structures. *Proceedings of the 31st AIAA SDM Conference*.
- [5] Chen, G., B. Lurie, B. Wada (1989). Experimental Studies of Adaptive Structures for Precision Performance. *Proceedings of the Thirtieth AIAA SDM Conference*.
- [6] Fanson, J., B. Lurie, J. O'Brien, C-C. Chu, R. Smith (1991). Identification and Control of the JPL Active Structure. *Proceedings of the 32nd AIAA SDM Conference*.
- [7] Fanson, J., C-C. Chu, R. Smith, E. Anderson (1990). Active Member Control of a Precision Structure with an  $H_\infty$  Performance Objective. *Proceedings of the AIAA Dynamics Specialist Conference*.
- [8] Peterson, L. (1991). Optimal Projection Control of an Experimental Truss Structure. *AIAA Journal of Guidance, Navigation, and Control*, Vol. 14, No. 2.

- [9] Preumont, A., J.-P. Dufour, C. Malekian (1992). Active Damping by a Local Force Feedback with Piezoelectric Actuators. *AIAA Journal of Guidance, Navigation, and Control*, Vol. 15, No. 2.
- [10] Hall, S., E. Crawley, J. How (1991). Hierarchic Control Architecture for Intelligent Structures. *AIAA Journal of Guidance, Navigation, and Control*, Vol. 14, No. 3.
- [11] Stein, G., J. Doyle (1991). Beyond Singular Values and Loop Shapes. *AIAA Journal of Guidance, Navigation, and Control*, Vol. 14, No. 1.

## A POINTING AND CONTROL ARCHITECTURE FOR LARGE OPTICAL AEROSPACE SYSTEMS

P.S. Shirley\*, R.L. Van Allen\*\* and S.M. Seltzer\*\*\*

\*US Air Force, Phillips Laboratory, Space Experiments Directorate, Kirtland AFB, New Mexico, USA

\*\*Van Allen Associates, Woodbridge, Virginia, USA

\*\*\*Consultant, Huntsville, Alabama, USA

**Abstract.** Important new advances in laser optics and recent space pointing demonstrations have enabled the United States Strategic Defense Initiative Organization (SDIO) to propose control strategies for large space based laser systems which utilize existing technologies and approaches. System performance, which has always been stressing from a control perspective, is now apparently within the state-of-the-art. The objective of this paper is to explain the nature of the technology advances and examine the control system implications for improving the feasibility and performance of systems such as large Space Based Laser platforms.

**Keywords.** Satellite control; vibration control; laser beam control; hierarchical systems; uncooled optics; precision pointing; target tracking.

### INTRODUCTION

It appears that H.G. Wells, the futuristic author of the late 19th and early 20th century, was well ahead of his time when he wrote of Directed Energy Weapons in his highly popular novel *The War of the Worlds*:

*It is still a matter of wonder how (they) were able to slay men so swiftly and so silently. Many think that in some way they were able to generate an intense heat... This intense heat they project in a parallel beam against any object they choose by means of a polished parabolic mirror of unknown composition... Whatever is combustible flashes into flame at its touch, lead runs like water, it softens iron, cracks and melts glass, and when it falls upon water, incontinently that explodes into steam...*

This description illustrates a concept that had not come of age in 1898 when he wrote of Martians and their tools of destruction, but appears to be well within the grasp of technologists today. Over the decades since Wells wrote of such exotic weaponry, progressive steps have been taken which have advanced state-of-the-art in optics, laser device performance, and satellite system development.

In recent years the United States Department of Defense has spent a considerable amount of effort in designing a large Space Based Laser (SBL) platform. The purpose of the laser system is to search out and destroy strategic ballistic missiles which have been launched at the U.S. or her allies. As the world situation has changed, the primary mission of the space laser has been altered to include missile defense over limited theatres of operation and accidental launches of existing missile forces. In either scenario, the goal of pinpoint "speed of light" defense remains a desirable vision for defense planners.

### THE PROBLEM STATEMENT

For any Directed Energy Weapon platform, the primary requirement is to deliver the necessary laser beam irradiance at the target. Beam irradiance is defined as:

$$I(r) = B/R^2 \sin \theta_a \exp(-r^2/2R^2\sigma_T^2)$$

$$\sigma_T = (\sigma_j^2 + \sigma_D^2)^{0.5}$$

$I(r)$  Beam Irradiance at Target (Watts/Meter<sup>2</sup>)

$B$  Laser Brightness (Watts/Steradian)

$R$  Range to Target (Meters)

$\theta_a$  Target Aspect Angle (Radians)

$r$  Radial Distance at Target Plane from Optical Axis (Meters)

$\sigma_T$  Total Laser Beam Divergence (Radians)

$\sigma_D$  Beam Divergence Due to Obscurations and Wavefront Aberrations (Radians)

$\sigma_j$  Dynamic Laser Pointing Error (Radians)

The translation of this equation into space qualified hardware has been the challenge that has faced the SBL weapon system developers. Early research focused on generating sufficient laser brightness by developing lasers at an appropriate wavelength with high beam quality, and developing large mirrors to use as an exit aperture to decrease the beam spot size at the target.

SDIO has demonstrated through the development of a chemical laser (termed "Alpha") that it can repeatedly generate a high-quality megawatt-class laser beam, confirming their ability to produce weapon-level beams with a space-operable laser. This hydrogen fluoride chemical laser operating at 2.8 microns, has validated the technology, computational methods and fabrication processes

necessary for the scaling of these devices to the power levels required for strategic defense. As well, innovations in optics manufacturing techniques have led the way to the development of the 4-10 meter aperture telescopes required, such as the LAMP 4 meter segmented mirror. This technology appears to be well in hand.

Given these advances, the challenge then moves to delivering this energy to the target. To do so requires a sophisticated beam control subsystem to transfer the beam from the device to the primary mirror system, as well as an Acquisition, Tracking, and Pointing (ATP) subsystem to perform very precise pointing and targeting functions under dynamic slew conditions. Thus the system engineer is challenged with minimizing the dynamic HEL beam pointing errors,  $\sigma_j$ .

#### Beam Control/ATP

The configuration for a generic SBL platform is shown in fig 1. The purpose of the beam control and ATP subsystems is to (i) control the high energy beam from the laser device to the output of the projection telescope, (ii) deliver the beam to a specific point on the target, and (iii) maintain it there until target kill is effected.

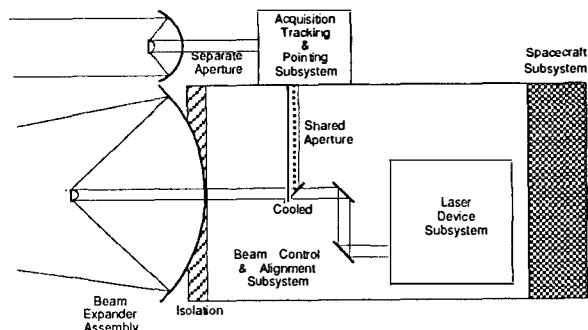


*fig 1 Generic SBL Platform*

The ATP functions are to acquire the target, maintain precision track during the High Energy Laser (HEL) engagement, locate the aimpoint on the target, and maintain the aimpoint until target negation. This subsystem utilizes passive and active sensors to image the target and infer track information. Imaging sensors may utilize plume imagery, hardbody fiducials, target range, and a priori target information to determine the location of the beam spot and the desired aimpoint. Multiple track files are maintained in a central fire control computer for automatic sequencing and time-optimal control. The sensors can be located at either separate aperture (adjacent to the main telescope) or shared aperture (looking through the main aperture) locations. Track accuracies of 0.1 pixel and boresight maintenance of 0.5-1.0 mrad are typical performance requirements. The aimpoint is required to be located and maintained within a specified vulnerable area on the target.

Beam control architectures are constructed to maintain alignment of the high energy beam as it propagates through the system and to minimize the amount of optical jitter caused by onboard disturbances. The key performance goal for jitter is typically expressed as some fraction of the HEL spot size at the target and is selected to maximize kill

efficiency of the entire SBL platform (e.g. 1/4-1/5 of a spot size). Primary pointing and jitter disturbances are coolant flow in the optical elements (high frequency, moderate amplitude), laser device gain generator disturbances (high frequency, low amplitude), and thrust imbalance (low frequency, high amplitude).

Boresight maintenance and precise pointing of the laser beam (as commanded by the ATP system) is accomplished by precision high bandwidth steering mirrors, inertial sensing devices, and an articulated telescope front end. Pointing precision is attained with combined fine/coarse steering mirrors with followup commands to the (isolated) frontend controller. The state of the art for inertial sensors is approximately 40 nanoradians noise equivalent angle (NEA) while the recent development of kilohertz-class steering mirrors allow the implementation of "hundreds" of hertz alignment loops. Microradian-level boresight sensing requires the use of temperature insensitive optical elements and low drift steering components.

Jitter control on the spacecraft is accomplished via active or passive isolation of the pointer front end from the laser device rear end and by implementing high bandwidth alignment loops. The optical alignment loops sample the beam train from the device to the output of the telescope (i.e. the secondary mirror of the telescope) and so are "end-to-end" optics controllers. The actual implementation of the pointing controller may involve both large-throw (coarse) and high bandwidth (fine) steering mirrors to provide adequate dynamic range. Other steering mirrors may also be required for translation control between the spacecraft and telescope segments. Isolation systems proposed for SBL platforms have routinely demonstrated 40-60 decibels of reduction in transmission of disturbance forces to the telescope front end. The combined jitter control system typically achieves performance estimates of a fraction of a  $\mu$ radian.

A high bandwidth alignment loop is implemented on the platform and acts as an inner loop controller for the lower bandwidth outer track loop. Track loop bandwidths are limited by delays associated with the round trip time of laser illuminator pulses to the target and by the illuminator/sensor repetition rates. Loop bandwidths of a few hertz are typical. Dynamic lag in the presence of accelerating targets is minimized by the use of rate "aiding" commands to the front end controller; thus the tracker is actually minimizing track deviations about a "nominal" flight which is being commanded by the fire control computer.

The precision pointing function for the SBL is accomplished through the use of the precision steering mirrors (point ahead, aimpoint designation, small angle slew) and the articulated front end (large angle slew). A key technical requirement is associated with the highly accurate position measurements (fractions of a  $\mu$ radian) over a very wide dynamic range (milliradians for steering mirrors, degrees for front end slew). Optical jitter induced during large angle slew is sensed and compensated by the end-to-end optical alignment loop.

Control system design has been severely stressed by the need to move the large platform mass quickly and with great precision, and to reduce the effects of platform

vibration disturbance sources. The major satellite disturbances are due to (i) coolant flow through all the high power optics, (ii) mass imbalance effects due to laser effluent discharge, and (iii) platform controller (e.g., thrusters, control moment gyros (cmg's)) inputs to the large structure. The approach to meeting these requirements has involved development of high torque, low noise cmg's, or reaction wheels and advanced techniques for passive and active mechanical isolation. High bandwidth alignment and stabilization loops have required new designs for high acceleration cooled steering mirrors and for feedforward adaptive noise cancellation techniques. The integrated control design thus is very complex and has required simultaneous breakthroughs in many design disciplines for successful implementation.

## ADVANCES

### The Relay Mirror Experiment

On February 14, 1990, the SDIO launched a mirror-carrying satellite known as the Relay Mirror Experiment (RME) from Cape Canaveral AFS, Florida. The specific objective of the RME was to validate the stabilization, tracking, and pointing technologies at performance levels required for SDI missions through a credible demonstration of a space-based relay mirror system.

The primary equipment for the RME consisted of three major elements: a free-flying satellite and two ground systems (see fig 2). As the spacecraft flew overhead, the two ground systems simultaneously tracked and illuminated it with two separate laser systems. A green laser beacon was used from one site, and a blue laser beacon was used from the other. On board the satellite, a bisection tracker acquired both beacons and controlled steerable mirrors to accomplish fine tracking of the two cooperative beacons. Once the line-of-sight to both of the ground sites was stabilized, a third infrared laser was relayed between the two sites via the orbiting satellite.

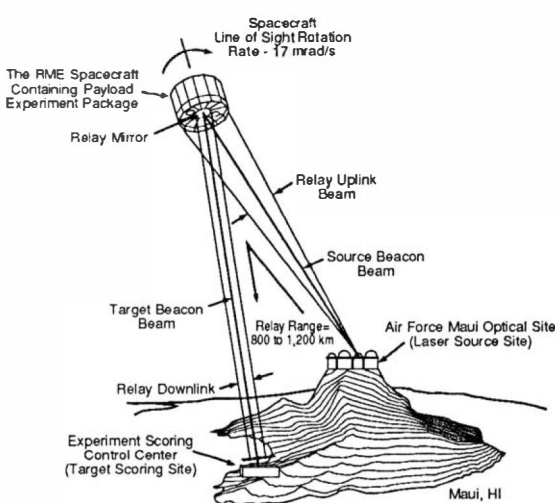


*fig 2 Relay Mirror Experiment Demonstration*

The RME demonstrated that a laser can be accurately relayed to a satellite 450 kilometers above the earth and back to a 3-meter target on the ground, achieving pointing accuracy that was 16 times better than the goal experiment

designers set out to reach. The line-of-site stabilization that was achieved was 2.3 times better than planned. The spacecraft's simple attitude control subsystem performed at sufficient levels of accuracy to support the laser beam relay. There is every reason to believe that the technology exploited in RME can be extended to simultaneous control of all three attitude angles, as is required for SBLs.

### Uncooled Optics

Another area within the High Energy Laser (HEL) community in which advances have been made has been uncooled high powered optics. The benefits of using uncooled optics are easily understood when you review the many disadvantages associated with the use of cooled optics within the beam train. The mass of the associated cooled optics, when compared with conventional non-cooled mirrors, is much higher and much more voluminous. The associated plumbing required to flow the coolant through the mirrors occupies valuable space and complicates the system design and development, leading to concerns regarding reliability. Perhaps most significant is the fact that the coolant flow induces jitter onto the line of sight to the target by vibrating the coolant lines, optical benches, and the mirrors themselves. These disturbances can easily remain undetected, resulting in potentially significant uncorrected errors as the beam is propagated towards the target.

Over the last few years SDIO has sponsored research into the development of HEL capable uncooled optics. Low absorption, highly reflective coatings have been fabricated and tested which can handle the intense power associated with the HEL. Potential payoff is expected with up to a two to three fold reduction in satellite platform weight. Furthermore, one of the primary sources of beam jitter, vibrations due to coolant flow, will be eliminated. This demonstrated technology will be capable of providing low risk uncooled optics for future SDIO space demonstrations.

### Component Developments

High bandwidth precision steering mirror developments over the last ten years have resulted in the demonstration of "large" (10-40 cm) steering mirrors with effective open loop bandwidths near a kilohertz. Uncooled high bandwidth mirrors and alignment loops were demonstrated in the space environment on the RME program. Alignment performance of less than a microradian has been routinely obtained in systems with 300 hz loops. Uncooled components and high bandwidth controllers can now be baselined for SBL systems because of the development of the very high efficiency coatings.

### SBL PLATFORM STUDY

To understand the implications of the technology advances, a simple SBL platform design was generated to illustrate system performance gains which might be obtained. This generic SBL concept includes the subsystems that are traceable to future systems: laser payload element, beam expander section, beam control and optical alignment subsystem, pointing and tracking subsystem, and spacecraft controller subsystem. It is assumed that the laser payload element design is derived from the existing

laser technology which is available, such as the Alpha laser system, and will consist of a Laser Gain Generator (LGG) and a Laser Fuel Supply System (LFSS). For this study we will use a 4 meter beam expander section which is rigidly mounted to the spacecraft structure. The secondary mirror and Auto Alignment System (AAS) sensor will be suspended via a support structure mounted forward of the beam expander. The beam control and optical alignment subsystem will use uncooled optics. For simplicity, the pointing and tracking functions will be performed via a single passive sensor system known as the Acquisition Tracker and Pointer (ATP). The spacecraft will utilize Reaction Control System (RCS) thrusters to perform the coarse pointing of the vehicle. We assumed that the spacecraft would be on the order of 50,000 pounds. This seemed reasonable given the uncooled optics advances which promise large weight savings. The overall satellite layout is assumed to be as shown in fig 3.

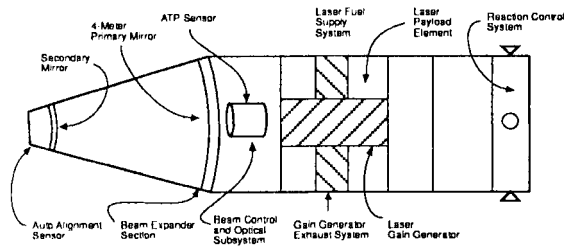


*fig 3 Satellite Concept*

#### Satellite Control Design

To assist in illustrating the performance gains of this notional spacecraft, we used as simple a control system as possible. For this SBL design a hierarchical controls approach was followed. The spacecraft provides a reasonable platform upon which a very accurate optical beam pointing system is mounted. It is felt that the platform must provide pointing accuracy on the order of a milliradian, stabilized for a number of seconds of time during the laser firings.

The two major design drivers for any control system are (1) the reference that the controller is attempting to follow and/or stabilize against, and (2) the disturbances (and noise) associated with the process.

In the case of this SBL concept, the reference is a rapidly accelerating test object moving across the field of view. It is assumed that the test object is accelerating when it is first perceived by the optical field of view. The entire issue of how the test object gets there is entirely ignored in this study.

Some of the expected disturbances, of which there are many, are addressed briefly here:

**LFSS Blowdown System.** Dynamically, this consists of high pressure gases moving around corners as they journey from the high pressure tanks to the inlet of the laser gain generator.

**LGG.** This machinery provides a broad frequency band of disturbances which change over time.

**Gain Generator Exhaust System (GGES).** This system takes the expanding gases from the gain generator and

expels them overboard from the spacecraft into free space, leading to potential thrust imbalances.

**Beam Control System.** The motion of the fast steering mirrors and beamwalk mirrors are another source of dynamic disturbance.

One can continue this list by including the motion of the secondary mirror, the cooler associated with the AAS and the ATP sensor, the dynamics of the moving spacecraft, the firings of the RCS jets, and such subtle disturbances as gravity gradients, aerodynamic drag, and various solar effects. The system must perform in a highly stressing environment.

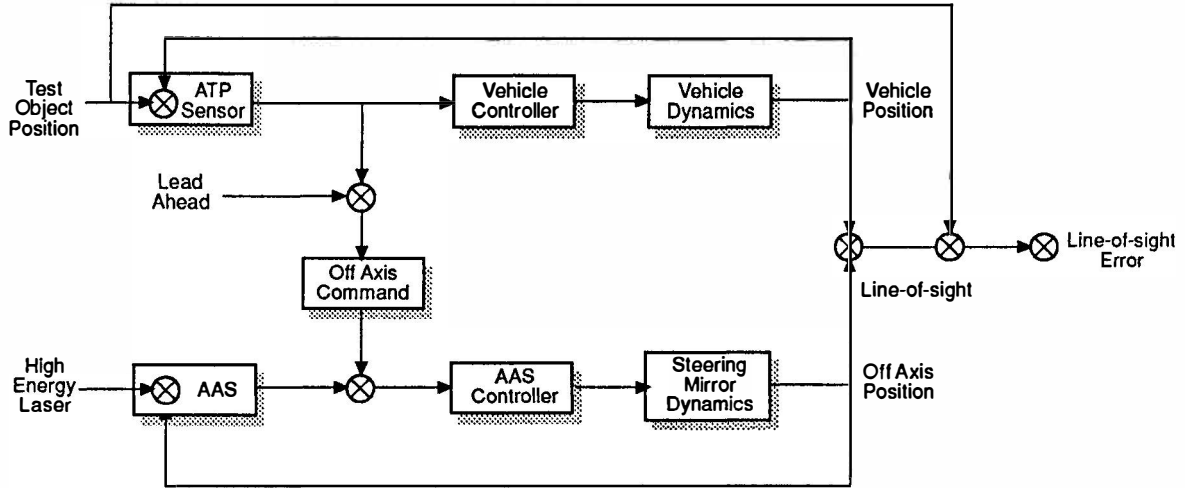
Given that the system contains an uncooled optics system, it is assumed that the two most dynamically important disturbances are the GGES thrust imbalance and the laser gain generator disturbance. The thrust imbalance is modeled as a deterministic force of 4.94 lbs acting upon the spacecraft structure. The laser gain generator disturbance was modeled as a stochastic Power Spectral Density (PSD) and was scaled from previously collected data to account for the spacecraft mass.

The technology breakthroughs discussed earlier have impacted the design of the control system in several ways. Specifically:

(i) the deletion of coolant flow as a jitter source allows the designer to tie the beam expander and satellite aft end together as an integrated optical system (i.e. not isolated from each other). This aspect of the design permits the telescope to be hardmounted to the spacecraft and allows large angle pointing to be performed via spacecraft slew. A high bandwidth alignment loop (see (ii) below) remains an important part of the architecture to compensate for disturbances. (ii) the development of kilohertz steering mirrors allows the implementation of the high bandwidth alignment loops and consideration of some relaxation on spacecraft controller requirements. For example, the use of thrusters for the vehicle controller can be baselined given the feeling that sufficient error rejection capability exists for compensation of rapid slew operations. If this proves to be incapable, it can be augmented hierarchically with a reaction wheel or control moment gyro system.

Figure 4 shows the resultant integrated control design for the notional SBL system. The tracking concept is a separate aperture sensor which is boresighted to the HEL optical path via an extended Reference Transfer System (RTS) device. Track errors generated by the ATP system are used to drive the spacecraft directly through the spacecraft controller. Residual pointing errors against thrusting targets will likely be larger than acceptable due to thruster implementation in the spacecraft controller, so the track error will also be used in an open loop fashion to offset the AAS high bandwidth alignment loop. The line of sight to the target then is controlled to an effective bandwidth associated with the alignment steering mirror. This control architecture is traceable to typical SBL configurations. Bandwidths of several hundred hertz for alignment control, and on the order of 0.2-2 hertz for the spacecraft control, are achievable.

As mentioned earlier, a simple RCS system was used within the vehicle controller. The RCS thrusters for the



PS 01370 WD 20

*fig 4 Satellite Control Design*

spacecraft were sized in the following manner. From engagement simulations, the maximum relative angular acceleration of the test object was determined to be  $1.0 \text{ mrad/s}^2$ . We assumed a spacecraft moment of inertia of  $220,000 \text{ sl-ft}^2$ , which would require a torque of  $220 \text{ ft-lb}$  acting on the spacecraft. It is expected that the GGES thrust imbalance will be on the order of  $4.94 \text{ lb}$ , acting on the spacecraft structure with a moment arm of  $4.62 \text{ ft}$ , producing a torque of  $23 \text{ ft-lb}$ . Thus the pitch and yaw control thrusters must have a torque capability of  $243 \text{ ft-lb}$  to overcome the test object acceleration and the thrust imbalance. With selected moment arms of  $17.1 \text{ ft}$ ,  $12\text{-lb}$  thrusters can provide a pitch and yaw torque of  $290 \text{ ft-lb}$ .

## SIMULATION/ANALYSIS RESULTS

### Simulation Description

A control system simulation was constructed for this SBL concept to gain insight into the nature of the various

disturbances and predict system pointing performance.

The spacecraft is modelled as a rigid body for this study, though a flexible body model will likely be generated for advanced analyses.

The vehicle controller consists of inputs from position and rate sensors driving the RCS thrusters. The values for the PD compensation are derived from past SBL studies. The AAS alignment loop was modelled as a  $100 \text{ hz}$  type 1 control loop with a mirror resonance at  $1200 \text{ hz}$ , typical of a piezo drive fast steering mirror. Control loop inputs are allocated for random disturbances on the spacecraft and the

optical system, and for deterministic test object motion. The integrated control simulation is illustrated in fig 5.

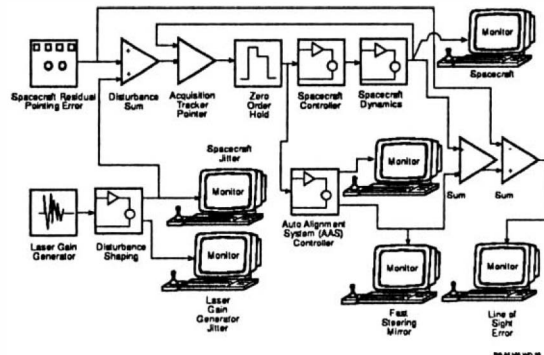


*fig 5 Integrated Control Simulation*

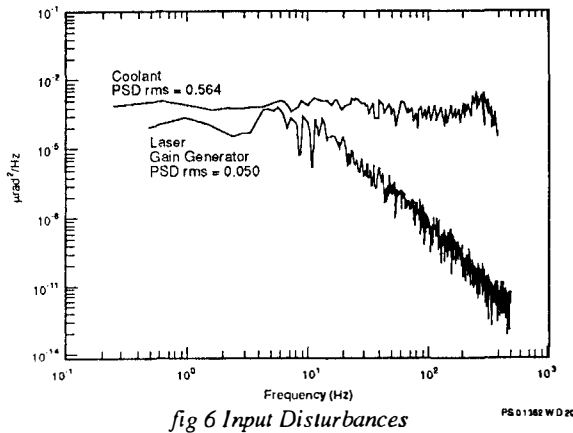
### Results

The control simulation was used to investigate system performance in the presence of random disturbances and expected target trajectories. Random force and jitter PSDs were obtained and used to drive either the spacecraft (i.e. sensed by the ATP system) or the alignment loop (sensed

by the AAS sensor). Residual pointing errors from separate spacecraft control analysis provided deterministic target following error inputs to the ATP system.

SBL structural dynamic response studies have predicted the coolant disturbance to be the primary high frequency jitter source. In early SBL configurations using cooled optics, this in turn drove the requirement for advanced vibration isolation systems and multiple levels of optical compensation. In current SBL designs, all of the optical train mirrors are uncooled, therefore this major jitter source is not of concern. The next

largest predicted disturbance is associated with the laser device gain generator operation. Both disturbances are shown in fig 6.



These two jitter sources, along with the deterministic thrust imbalances, were used in the simulation to predict system performance and to illustrate the performance gain which is realized by deleting the coolant requirement. The LGG force was converted to optical acceleration and position via assumed system moment of inertia and physical dimension data. The coolant jitter was arrived at by using the force frequency spectra from reference documents and scaling the double integral to representative jitter values that have been measured. Input and residual jitter from the simulation runs is shown in table 1.

Table 1 Simulation Results

	Input Jitter	Residual Error
LGG Disturbance Only	50 nrad	5 nrad
LGG+Coolant Disturbances	564 nrad	308 nrad

The corresponding PSDs are shown in fig 7.

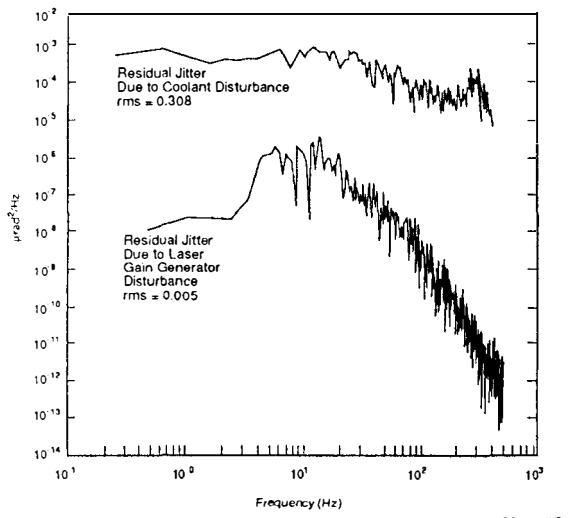


fig 7 Residual Line-of-sight Jitter

The results indicate that significant gains are obtained in the line of sight stabilization through the elimination of the coolant flow. Other studies and design tradeoffs to improve system performance will be pursued and include:

- sizing the controller deadband to maximize mission lifetime, yet still provide acceptable pointing performance,
  - selecting the bandwidth and type of the alignment loop to provide jitter rejection and removal of following error from dynamic targets,
  - spacecraft slew vs fine/coarse steering slew requirements.
- These variations to the design parameters will likely be reported on in future papers.

### Conclusions

Jitter from traditional SBL disturbance sources should not be a problem for a system designed as indicated above. Significant gains in system performance will likely be obtained through the use of uncooled optics and a similar approach to hierarchical control.

### SUMMARY

Taking the above factors into account, the current control architecture for the space laser platform reduces to a relatively simple hierarchical control set with the spacecraft providing large angle coarse pointing and the laser payload providing fine pointing control. The two loops are interconnected via an offload from fine pointing to the satellite control which increases the effective dynamic range against accelerating or maneuvering targets. Pointing precision of less than a microradian is expected based on results from system simulations.

These results show significant advances that clearly indicate that the technology to field a SBL system is well in hand. By implementing techniques and control schemes that have evolved over the last few years, SDIO has achieved a less complex, lower risk, and higher probability approach to achieving their technical objectives.

### REFERENCES

- Ball Aerospace Systems Group, Applied Technology Associates, Inc., and USAF Phillips Laboratory (March 1992). Program Summary for SDIO. Relay Mirror Experiment and Wideband Angular Vibration Experiment.
- R & D Associates Systems Engineering Division, and Cambridge Research. (February 1987). USAF AFWL TN85-61. Structural Dynamic Response of a Space Based Laser System.
- USAF Systems Command Phillips Laboratory News Release Number 91-53 (July 15, 1991). News Media Tour Alpha.
- USAF Systems Command Phillips Laboratory News Release Number 91-28 (April 23, 1991). Relay Mirror Experiment Ends.
- Wells, H.G. (1898). The War of the Worlds.

## MODELING AND CONTROL OF A SPACECRAFT WITH MANOEUVRABLE FLEXIBLE BEAMS

G. Ambrosino\*, G. Celentano\*, F. Garofalo\* and L. Verde\*\*

\*Dipartimento di Informatica e Sistemistica, Università degli Studi di Napoli "Federico II", via Claudio 21,  
I-80125 Napoli, Italy

\*\*Centro Italiano Ricerche Aerospaziali, Via Maiorise - 81043 Capua (CE), Italy

**Abstract.** A model of a spacecraft consisting of a rigid platform with manoeuvrable flexible appendages is obtained by the application of a finite element method. The model is used both for detailed simulations and for the synthesis of a control algorithm which enables maneuvering of the flexible appendages without inducing elastic vibrations. A numerical example is presented.

**Keywords.** Modeling; finite element method; vibration control; aerospace control; tracking systems.

### Introduction

The current concepts of complex interplanetary spacecraft generally foresee the presence of light and flexible beamlike appendages to handle external payloads. The onboard control system is entrusted with the complex tasks of guaranteeing accurate positioning of the platform in an inertial space and maneuvering the appendages suppressing their elastic vibrations.

A mathematical model for accurate simulation of the large motions of the overall system and concurrent small deformations of the elastic beam, which explicitly accounts for the coupling effects between these two dynamic behaviours, is a valuable tool for many purposes, like for instance, structural verification of the hybrid structure, design of the actuators for platform attitude control, beam orientation and load manipulation, design and performance evaluation of control algorithms, planning of operations.

In this paper we focus our attention on modeling and control of a hybrid interconnected system made up of a rigid platform connected to a maneuvering beamlike appendage; the appendage, in turn, is connected to a rigid end effector by a spheric joint (see Fig. 1). The dynamics of such a structure are, in principle, described by a set of ordinary and partial differential equations.

Two commonly used approximations of such a system include finite element models and modal expansion models (e.g. Meirovitch and Kwak, 1990; Meirovitch, 1988; Ho and Herber, 1985; Hughes, 1973).

The former have the inconvenience of the high dimensionality of the approximating model; the latter seem to be better suited for the evaluation of the free response of a flexible system and hence cannot be conveniently used for the case of controlled system. In this paper we present a methodology for the generation of a model based

upon finite element and lagrangian methods. The proposed approach has been successfully used by the authors for modeling flexible manipulators (Ambrosino, Celentano and Garofalo, 1991). It allows the designer to obtain a low order model, accurate at low frequencies. For sake of notational simplicity, we shall be concerned only with planar motions with a single appendage, although the concepts and developments presented here are quite general and can be readily applied to the spatial case with multiple appendages.

### System Description

The main feature of the proposed approach is that the flexible beam is divided in  $n$  elements, the shape of each of them being described, at each instant, by its elastic strain. This hypothesis is realistic if the inertia forces, acting on the  $i$ -th element and due to the distributed mass of the element, are negligible with respect to all the forces exerted by the remaining part of the structure on the extrema of the element itself. This can be considered as a straightforward extension of the De Saint Venant principle.

The system here considered is that shown in Fig.1. It is made up of:

- a rigid platform  $A$  characterized by a mass center  $G_A$ , mass  $M_A$  and polar moment of inertia  $I_A$  with respect to  $G_A$ ;
- a flexible beam  $B$  connected, through an actuated rotary joint, to point  $P$  of the platform on one end, and to an end-effector on the other end; the beam is divided in  $\nu$  elements; the  $i$ -th one is characterized by a length  $l_i$ , a Young's modulus  $E_i(z_i)$ , a mass density  $m_i(z_i)$ , and a moment of inertia  $I_i(z_i)$ ,  $z_i$  being the curvilinear abscissa along the  $i$ -th element;

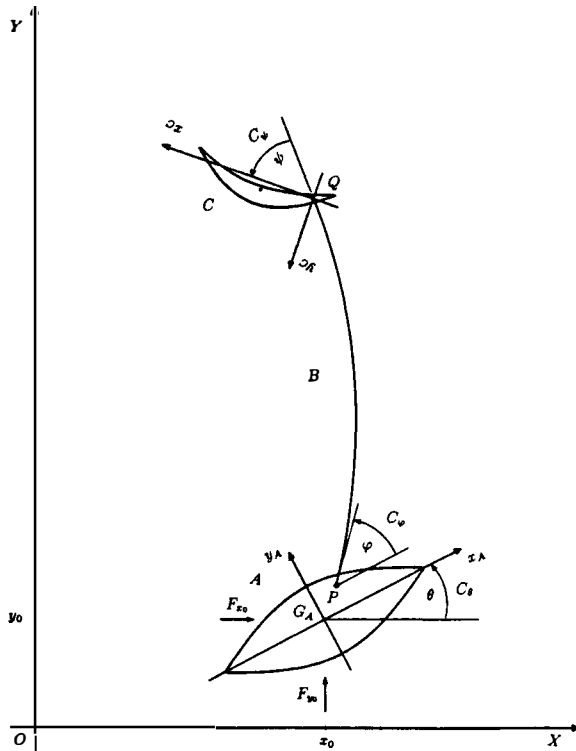


Figure 1: The System and the Reference Frames.

- a rigid payload  $C$  hinged to the beam at the point  $Q$ , characterized by a mass center  $G_C$ , mass  $M_C$  and polar moment of inertia  $I_C$  with respect to  $G_C$ .

To describe the motion, we introduce a set of inertial axis  $Oxy$ , a set of body axis  $G_Ax_Ay_A$  coinciding with the principal axis of the rigid platform and a set of end-effector axis  $Qx_Cy_C$  parallel to the principal axis of the end-effector.

With respect to these coordinate frames (see Fig. 1), the system configuration is described by:

- the lagrangian coordinates  $x_0, y_0$ , and  $\theta$  of  $A$  with respect to  $Oxy$ ;
- the lagrangian coordinate  $\varphi$  of  $B$  with respect to  $A$ , and  $\psi$  of  $C$  with respect to  $B$ ;
- the lagrangian coordinates  $\gamma_1, \epsilon_1, \dots, \gamma_\nu, \epsilon_\nu$  related to the elements of length  $l_1, \dots, l_\nu$  in which the beam has been divided and representing their flexural slopes and flexural displacements (see Fig. 2).

In what follows the coordinates of  $P$  with respect to  $G_Ax_Ay_A$  will be indicated with  $(x_{AP}, y_{AP})$ , while the coordinates of  $G_C$  with respect to  $Qx_Cy_C$  will be  $(x_{CG_C}, y_{CG_C})$ .

The spacecraft is actuated by

- a force  $F_0$  and a torque  $C_\theta$  with respect to  $G_A$  acting on the platform  $A$ . The force  $F_0$  has components  $F_{0x}$  and  $F_{0y}$  in the inertial reference frame;
- joint torques  $C_\varphi$  and  $C_\psi$  due to joint actuators placed in  $P$  and  $Q$  respectively;

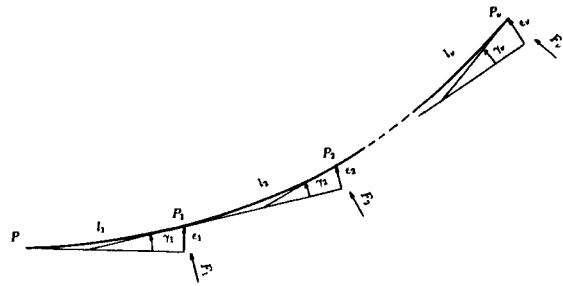


Figure 2: Schematic Representation of the Flexible Appendage.

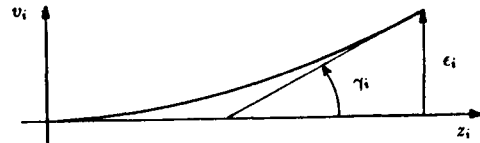


Figure 3: The Flexural Deformation.

- a system of point forces  $F_i, i = 1, \dots, \nu$ , acting orthogonally to the beam at points  $P_i$  (see Fig. 2).

The flexural deformation  $v_i(z_i, t)$  (see Fig. 3) of the  $i$ -th element of the beam can be described in terms of shape functions as

$$v_i(z_i, t) = r_i(z_i)\epsilon_i(t) + s_i(z_i)\gamma_i(t) \quad (1)$$

where the functions  $r_i(z_i)$  and  $s_i(z_i)$  can be derived by the equation of the elastic strain

$$\frac{d^2}{dz_i^2} \left[ E_i(z_i) I_i(z_i) \frac{d^2 r_i(z_i)}{dz_i^2} \right] = 0 \quad (2a)$$

$$\frac{d^2}{dz_i^2} \left[ E_i(z_i) I_i(z_i) \frac{d^2 s_i(z_i)}{dz_i^2} \right] = 0 \quad (2b)$$

subject to

$$r_i(0) = 0, \quad \left. \frac{dr_i}{dz_i} \right|_{z_i=0} = 0$$

$$r_i(l_i) = 1, \quad \left. \frac{dr_i}{dz_i} \right|_{z_i=l_i} = 0 \quad (3a)$$

$$s_i(0) = 0, \quad \left. \frac{ds_i}{dz_i} \right|_{z_i=0} = 0,$$

$$s_i(l_i) = 0, \quad \left. \frac{ds_i}{dz_i} \right|_{z_i=l_i} = 1 \quad (3b)$$

In the case of  $E_i(z_i)I_i(z_i) = \text{const}$  along the  $i$ -th element, the previous equations are satisfied by (Meirovitch, 1988)

$$r_i(z_i) = \frac{3z_i^2}{l_i^2} - \frac{2z_i^3}{l_i^3} \quad (4a)$$

$$s_i(z_i) = \frac{z_i^3}{l_i^2} - \frac{z_i^2}{l_i}. \quad (4b)$$

By indicating with  $q = [x_0, y_0, \theta, \varphi, \psi, \gamma_1, \epsilon_1, \dots, \gamma_\nu, \epsilon_\nu]^T$  the  $n$ -vector of lagrangian coordinates, one can evaluate the overall kinetic energy  $T$  and elastic energy  $U$  as functions of  $q$  and  $\dot{q}$ . Knowledge of the kinetic and potential energies is tantamount to specifying the lagrangian  $\mathcal{L}$  of the system given by

$$\mathcal{L}(q, \dot{q}) = T - U. \quad (5)$$

By using results of the variational calculus, the governing dynamic equation for the system are derived through the Lagrange equation

$$\frac{d}{dt} \frac{\partial \mathcal{L}}{\partial \dot{q}_j} - \frac{\partial \mathcal{L}}{\partial q_j} = \mathcal{F}_j, \quad j = 1, \dots, n \quad (6)$$

where  $\mathcal{F}_j$  are the generalized nonconservative forces.

## The Mathematical Model

### Kinetic Energy Computation

The kinetic energy for the overall system is obtained by computing the kinetic energy of each part of the structure and then summing over all the elements.

#### Kinetic Energy of the Rigid Platform

The kinetic energy of the rigid platform  $A$  is simply given by

$$T_A = \frac{1}{2} M_A (\dot{x}_0^2 + \dot{y}_0^2) + \frac{1}{2} I_A \dot{\theta}^2. \quad (7)$$

#### Kinetic Energy of the Beam

The kinetic energy of the  $i$ -th element of the beam is given by

$$T_{B_i} = \frac{1}{2} \int_0^{l_i} m_i(z_i) (\dot{x}_i^2(z_i) + \dot{y}_i^2(z_i)) dz_i \quad (8)$$

where  $x_i(z_i)$  and  $y_i(z_i)$  are the coordinates of the generic point of the  $i$ -th link in the inertial coordinate frame. They can be evaluated, at each time instant, in terms of the lagrangian coordinates, as

$$x_i(z_i) = x_{P_{i-1}} + z_i \cos \theta_i - v_i(z_i) \sin \theta_i \quad (9a)$$

$$y_i(z_i) = y_{P_{i-1}} + z_i \sin \theta_i + v_i(z_i) \cos \theta_i \quad (9b)$$

where

$$\theta_i = \theta + \varphi + \sum_{h=0}^{i-1} \gamma_h \quad \gamma_0 = 0 \quad (10a)$$

$$x_{P_i} = x_i(l_i) \quad y_{P_i} = y_i(l_i), \quad (10b)$$

for all  $i = 1, \dots, \nu$  and with

$$x_{P_0} = x_0 + x_{AP} \cos \theta - y_{AP} \sin \theta \quad (11a)$$

$$y_{P_0} = y_0 + x_{AP} \sin \theta + y_{AP} \cos \theta \quad (11b)$$

where  $P_0 = P$ .

#### Kinetic Energy of the Payload

The kinetic energy of the payload can be computed as

$$T_c = \frac{1}{2} M_C (\dot{x}_{G_C}^2 + \dot{y}_{G_C}^2) + \frac{1}{2} I_C \dot{\alpha}^2 \quad (12)$$

where

$$x_{G_C} = x_{P_\nu} + x_{CG_c} \cos \alpha - y_{CG_c} \sin \alpha \quad (13a)$$

$$y_{G_C} = y_{P_\nu} + x_{CG_c} \sin \alpha + y_{CG_c} \cos \alpha \quad (13b)$$

$$\alpha = \theta + \varphi + \psi + \sum_{h=1}^{\nu} \gamma_h. \quad (13c)$$

The total kinetic energy  $T$  of the overall structure is given by

$$T = T_A + \sum_{h=1}^{\nu} T_{B_h} + T_C \quad (14)$$

By algebraic manipulation, which can be performed by a symbolic manipulation language, the total kinetic energy of the structure can be rewritten as function of  $q$  and  $\dot{q}$  in the form

$$T = \frac{1}{2} \dot{q}^T M(q) \dot{q}. \quad (15)$$

### Potential Energy Computation

The potential energy of the overall structure is simply the elastic energy associated with the elastic beam.

It is clear that the flexural deformation  $v_i(z_i, t)$  of the  $i$ -th element of the beam, given by (1) with (3) and (3), exactly describes the static deformation of a clamped uniform link subject to a terminal load. In this case the deformation parameters  $\gamma_i$  and  $\epsilon_i$  are related to the external load—shear force  $S_i$  and bending moment  $M_i$ —through the relationship

$$\begin{pmatrix} S_i \\ M_i \end{pmatrix} = K_i \begin{pmatrix} \epsilon_i \\ \gamma_i \end{pmatrix} \quad (16)$$

where  $K_i$  is the stiffness matrix of the  $i$ -th link. The elastic energy of the  $i$ -th element can be computed as the elastic component of the work done by external forces. Hence

$$U_i = \frac{1}{2} S_i \epsilon_i + \frac{1}{2} M_i \gamma_i = \frac{1}{2} (\epsilon_i \ \ \gamma_i)^T K_i \begin{pmatrix} \epsilon_i \\ \gamma_i \end{pmatrix} \quad (17)$$

It is worth noting that, no matter how complex the link shape is, this approach enables the exact evaluation of the elastic energy in static situations, provided that matrices  $K_i$  are correctly evaluated. This fact can be conveniently used in order to treat complex beam shapes without increasing the number of lagrangian coordinates.

As regards the computation of matrix  $K_i$ , for the case of uniform beam elements, it is simply given by

$$K_i = \begin{pmatrix} \frac{12E_i I_i}{l_i^3} & -\frac{6E_i I_i}{l_i^2} \\ -\frac{6E_i I_i}{l_i^2} & \frac{4E_i I_i}{l_i} \end{pmatrix} \quad (18)$$

For the case of complex beam shapes, it can be numerically evaluated with the aid of commercial CAD packages like *NASTRAN*.

Obviously the potential energy of the overall structure will be given by

$$U(q) = \sum_{h=1}^{\nu} U_h(q). \quad (19)$$

## The Dynamical Model

By using (15) and (19), the lagrangian function (5) can be obtained as function of  $q$  and  $\dot{q}$ . In order to use expression (6) to derive the equations of the motion, it is necessary to express the generalized forces  $F_j$  in terms of the actual ones. This can be obtained from the virtual work  $\delta W$  corresponding to a virtual displacement  $\delta q = [\delta q_1, \dots, \delta q_n]^T$ . Since the components  $F_{ix}$  and  $F_{iy}$  in the inertial reference frame of the force  $F_i$  can be expressed as

$$F_{ix} = F_i \sin \theta_i \quad (20a)$$

$$F_{iy} = -F_i \cos \theta_i \quad (20b)$$

we have

$$\begin{aligned} \delta W = & F_{x_0} \delta q_1 + F_{y_0} \delta q_2 \\ & + C_\theta \delta q_3 + C_\varphi \delta q_4 + C_\psi \delta q_5 \\ & + \sum_{i=1}^{\nu} \sum_{j=1}^n F_i \left( \sin \theta_i \frac{\partial x_{P_i}}{\partial q_j} - \cos \theta_i \frac{\partial y_{P_i}}{\partial q_j} \right) \delta q_j \end{aligned} \quad (21)$$

By indicating with  $u = [F_{x_0}, F_{y_0}, C_\theta, C_\varphi, C_\psi, F_1, \dots, F_\nu]^T$  the vector of actual forces, the dynamical model of the overall system can be obtained in compact form as

$$A(q)\ddot{q} + B(q, \dot{q})\dot{q} + Cq = D(q)u \quad (22)$$

## Controller Design

To illustrate the controller design philosophy it is worth partitioning the vector of lagrangian coordinates in two subvectors, the first one  $q_a = [x_0, y_0, \theta]^T$  associated with the lagrangian coordinates of the platform and the other one,  $q_b = [\varphi, \psi, \gamma_1, \epsilon_1, \dots, \gamma_\nu, \epsilon_\nu]^T$ , associated with the lagrangian coordinates of the appendage.

With this notation and on the base simple physical considerations, system (22) can be rewritten as

$$\begin{pmatrix} A_a(q) & A_{ab}(q) \\ A_{ab}(q) & A_b(q) \end{pmatrix} \begin{pmatrix} \ddot{q}_a \\ \ddot{q}_b \end{pmatrix} +$$

$$\begin{pmatrix} B_a(q, \dot{q}) & B_{ab}(q, \dot{q}) \\ B_{ba}(q, \dot{q}) & B_b(q, \dot{q}) \end{pmatrix} \begin{pmatrix} \dot{q}_a \\ \dot{q}_b \end{pmatrix} + \begin{pmatrix} 0 & 0 \\ 0 & C_b \end{pmatrix} \begin{pmatrix} q_a \\ q_b \end{pmatrix} = \begin{pmatrix} I & D_{ab}(q) \\ 0 & D_b(q) \end{pmatrix} \begin{pmatrix} u_a \\ u_b \end{pmatrix} \quad (23)$$

where, obviously,  $u_a = [F_{x_0}, F_{y_0}, C_\theta]^T$  and  $u_b = [C_\varphi, C_\psi, F_1, \dots, F_\nu]^T$ .

We assume that the objective of the control is that of computing the control forces  $u_a$  and  $u_b$  capable of changing the orientation angle  $\varphi$  of the appendage and  $\psi$  of the end-effector in accordance with a given desired behaviour  $\hat{\varphi}(t)$  and  $\hat{\psi}(t)$ , without inducing movements of the platform or elastic vibrations of the appendage. This means that the controller should track a state trajectory specified by  $\dot{q}_a(t) = 0$ ,  $\ddot{q}_b(t) = [\dot{\varphi}(t), \dot{\psi}(t), 0, \dots, 0]^T$ .

We propose to evaluate both the control signals  $u_a$  and  $u_b$  as the sum of two parts: the first one, feedforward, which should track, as close as possible, the desired trajectory; the second one, closed-loop, driving to zero the state errors.

Let first consider the problem of synthesizing the control signal  $u_b$ . It will have the form

$$u_b(t) = u_{b0}(t) + u_{bc}(t) \quad (24)$$

$u_{b0}(t)$  being the feedforward part. By assuming that the control action  $u_a$  is able to maintain the rigid platform fixed at the desired position  $\dot{q}_a(t)$ , the open loop control  $u_{b0}(t)$  should satisfy

$$A_b(\hat{q})\ddot{\hat{q}}_b + B_b(\dot{\hat{q}}, \hat{q})\dot{\hat{q}}_b + C_b\hat{q}_b = D_b(\hat{q})u_{b0}(t) \quad (25)$$

so that we can assume

$$u_{b0}(t) = D_b^\dagger(\hat{q}) \left[ A_b(\hat{q})\ddot{\hat{q}}_b + B(\hat{q}, \dot{\hat{q}})\dot{\hat{q}}_b + C_b\hat{q}_b \right] \quad (26)$$

where  $D_b^\dagger = (D_b^T D_b)^{-1} D_b^T$  denotes the pseudoinverse matrix of  $D_b$ .

As regards the control  $u_a$  acting on the platform, consistently with the previous considerations, it will have the form

$$u_a(t) = u_{a0}(t) + u_{ac}(t) \quad (27)$$

Once  $u_{b0}(t)$  has been evaluated, the feedforward component  $u_{a0}(t)$  can be evaluated as

$$A_{ab}(\hat{q})\ddot{\hat{q}}_b + B_{ab}(\dot{\hat{q}}, \hat{q})\dot{\hat{q}}_b = u_{a0}(t) + D_b(\hat{q})u_{b0}(t) \quad (28)$$

Obviously the ability of signal  $u_{a0}(t)$  to maintain the platform in the desired fixed position depends, to a large extent, on how close the actual appendage trajectory corresponding to the signal  $u_{b0}(t)$  is to the desired one and on the initial state error  $q(t_0) - \dot{q}(t_0)$ ,  $\dot{q}(t_0) - \ddot{q}(t_0)$ . This is the reason for adding to both the feedforward controls a feedback component.

For what concerns  $u_{ac}(t)$ , it can be obtained by means of three decoupled PD controller as

$$u_{ac} = \begin{pmatrix} h_{x_0}(x_0 + \tau_{x_0}\dot{x}_0) \\ h_{y_0}(y_0 + \tau_{y_0}\dot{y}_0) \\ h_\theta(\theta + \tau_\theta\dot{\theta}) \end{pmatrix} \quad (29)$$

The technique used for tuning the parameters  $h_{x_0}, \tau_{x_0}, h_{y_0}, \tau_{y_0}, h_\theta, \tau_\theta$  of the *PD* controllers is that described in Ambrosino, Celentano and Garofalo, 1988. Based on the knowledge of the maximum possible error between the true and the assumed dynamics, this technique guarantees that the tracking error  $e_a = q_a - \hat{q}_a$  remains bounded and tends to an arbitrarily small neighbourhood of the origin with a dynamics described by

$$\ddot{e}_a + L_1 \dot{e}_a + L_2 e_a = 0 \quad (30)$$

where  $L_1$  and  $L_2$  are diagonal matrices that can be arbitrarily prescribed by the designer.

Finally the feedback component of signal  $u_b$  is computed as a state feedback of the form

$$u_{bc} = L_c(t) \begin{pmatrix} q_b \\ \dot{q}_b \end{pmatrix} \quad (31)$$

where the gain matrix  $L_c(t)$  can be computed with an optimal control technique, as suggested in (Meirovitch and Kwak, 1990), with reference to the system

$$\dot{x} = \begin{pmatrix} 0 & I \\ A_b^{-1} C_b & A_b^{-1} B_b \end{pmatrix} x + \begin{pmatrix} 0 \\ A_b^{-1} D_b \end{pmatrix} u_{bc} \quad (32)$$

where  $x = [q_b, \dot{q}_b]^T$ .

## Numerical Example

In order to illustrate the modeling approach and the control design procedure described in the previous section, a simulated example with a spacecraft consisting of a rigid platform and a flexible appendage without end-effector has been carried out.

The mass of the platform is 500kg, while its mass moment of inertia about the mass center is 200kg m<sup>2</sup>. The coordinates of the hinge point  $P$  with respect to the platform axis are ( $x_{AP} = 0, y_{AP} = .50m$ ). As regards the flexible appendage, it was assumed 10m long, with uniform distributed mass of 2kg/m, and constant value  $EI = .228 \times 10^5$  kg m<sup>2</sup>. The inertial reference frame was assumed coincident with the principal axis of the platform at the desired position. Finally, two actuator forces were assumed to act on the appendage at  $z = l/2$  and  $z = l$ ,  $l$  being the total beam length, so that, for the construction of the model, the appendage was divided into two elements.

The manoeuvre consists of slewing the appendage through an angle  $\varphi$  of 90°, so that  $\dot{q}_b = [\dot{\varphi}(t), 0, \dots, 0]^T$ . Fig. 4 gives the time behaviour of  $\dot{\varphi}(t)$ .

Two different situations were considered in the simulations. The first one assumes that only a joint torque at point  $P$ , generated by means of an ideal *PD* controller, attempts to track the desired behaviour of  $\dot{\varphi}(t)$ , while no other control actions are exerted (uncontrolled case). The second one (controlled case) considers the presence of both

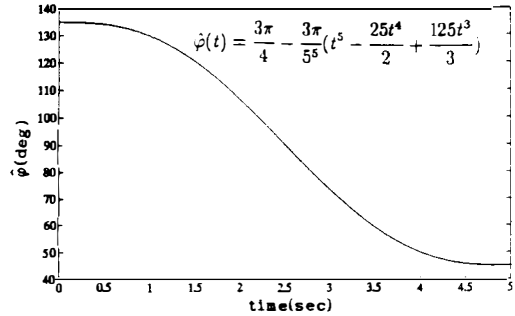


Figure 4: Time History of the Desired Appendage Maneuver.

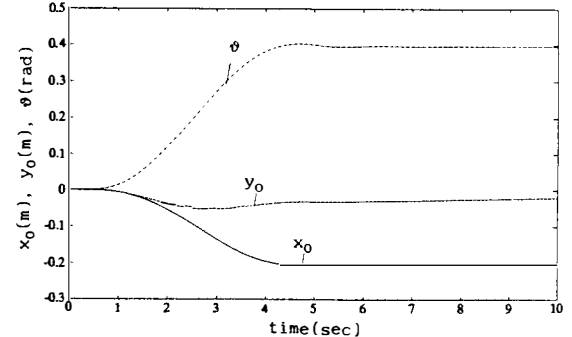


Figure 5: Time History of the Platform lagrangian Coordinates: Uncontrolled Case.

feedforward and feedback control actions as described in the previous section. Fig. 5 and Fig. 6 show the time history of the platform lagrangian coordinates for the uncontrolled and controlled case, respectively. Fig. 7 and Fig. 8 show the total flexural deformation  $\Delta$  of the appendage measured at the tip, without and with control, respectively.

For what concerns the tuning of the feedback control parameters, the *PD* parameters of the component  $u_{bc}$  as in (29) were chosen so as to guarantee a time constant of the error dynamics (30) less than 666 msec. Finally, as the time varying terms of the coefficient matrices in (32) turned out to be small compared to the constant terms, the gain matrix  $L_c$  was assumed to be constant and computed on the basis of the values of the coefficient matrices at the final instant of the desired trajectory. For these calculations we choose as weighting coefficient matrices  $Q$  and  $R$  of the standard  $LQ$  problem  $Q = \text{diag}[10^4, 5 \times 10^3, 3 \times 10^4, 40, 200, 50, 3, 30, 2, 20]$  and  $R = \text{diag}[10, 2, 3]$ .

## Conclusions

The equations of the motion of a spacecraft consisting of a rigid platform and a reorienting flexible appendage with a moving rigid end-effector has been derived by means of a finite element method together with a lagrangian approach. These equations are non-linear and time-varying. The model was used for the design of a controller enabling a desired manoeuvre of the appendage and guaranteeing both the suppression of its elastic vibrations and accurate positioning of the plat-

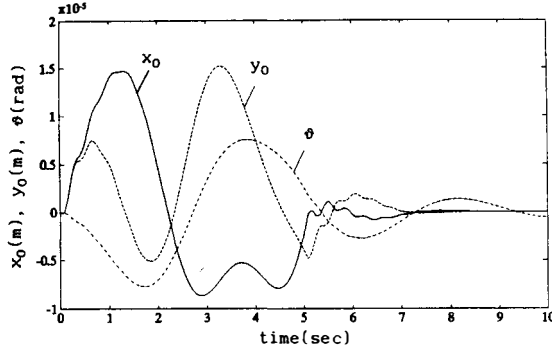


Figure 6: Time History of the Platform lagrangian Coordinates: Controlled Case.

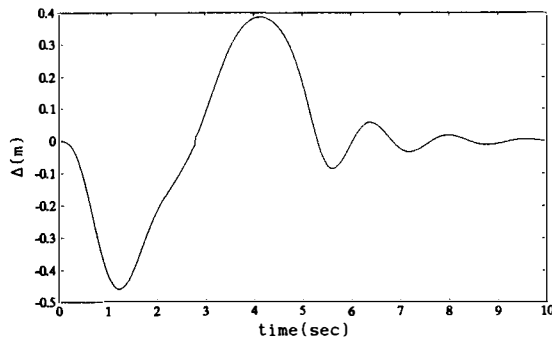


Figure 7: Time History of the Tip Displacements: Uncontrolled Case.

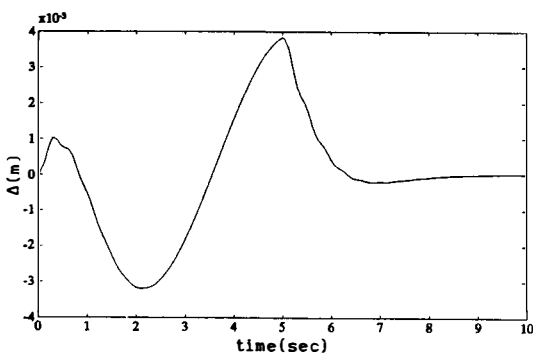


Figure 8: Time History of the Tip Displacements: Controlled Case.

form.

The proposed control strategy splits the control action in two parts: the first one guaranteeing the optimal maneuvre of the appendage without elastic vibrations, the second one providing the positioning of the platform. Each control action consists of a nominal part, feedforward, obtained with a “pseudo-inverse problem technique”, and a feedback part which is a continuous function of the tracking error.

## References

- Ambrosino, G., Celentano, G., and Garofalo, F., “Dynamic simulation of a planar flexible boom for Tokamak in-vessel operations,” *Fusion Technology*, vol. 18, 1991.
- Ambrosino, G., Celentano, G., and Garofalo, F., “Adaptive tracking control of industrial robots,” *ASME J. Dynam. System Measurement and Control*, vol. 110, 1988.
- Ho, J.Y.L. and Herber, D.R., “Development of dynamics and control simulation of large flexible space systems”, *J. of Guidance and Control*, Vol.8, May-June 1985.
- Hughes, P.C., “Dynamics of flexible spinning spacecrafts”, *Proc. XXIV Congress of the International Astronautical Federation*, Baku, USSR, Oct.1973.
- Kane, T.R., Likins, P.W., and Levinson, D.A., *Spacecraft Dynamics*, McGraw- Hill, New York, 1983.
- Meirovitch, L., *Computational Methods in Structural Dynamics*, Sijthoff and Noordhoff, The Netherlands, 1988.
- Meirovitch, L. and Kwak, M.K., “Dynamics and control of spacecrafts with retargeting flexible antennas”, *J. of Guidance and Control*, Vol.13, March- April 1990.

## GENERAL ACTIVE MICROMOTION ATTENUATOR

J.P. Granier\*, A. Frey\*\* and D. Barat\*\*

\*Microdynamics and Accuracy Pointing, Dynamics and Automatics Department, CNES, 18 Avenue Edouard Belin,  
31055 Toulouse Cedex, France

\*\*Ecole Supérieure d'Electricité, Plateau du Moulon, 92192 Gif-sur-Yvette Cedex, France

**Abstract :** This paper presents the one axis test bench of the microdynamic and accuracy pointing laboratory of the CNES and the preliminary results of a decoupling system which uses an inertial control mass to assume the decoupling function of a proof mass. The objective of this test bench is to compare on the same realisation, different types of control law in term of robustness versus external disturbances or modelling errors. The ability of real time implementation and the tuning facility will also be evaluated during this study.

**Keywords :** Digital control , Robustness , Acceleration control , Decoupling, Damping

### INTRODUCTION :

The next generation of high resolution pointing systems needs an accurate angular control as well as the new microgravity payloads needs some degree-of-freedom control, in order to suppress the effects of the on-board ambient acceleration levels.

The design of such experiments is very dependent on the environment at the interface with the spacecrafts. The specifications of the systems should be less stringent with a quiet interface.

The aim of our R&D approach is to define new concepts of isolation and pointing systems by carrying on on-ground experimental tests on simple demonstrative breadboards.

The CNES is developing a demonstrator of an isolation system named GAMMA (General Active MicrMotion Attenuator) which uses the effect of action-reaction on an inertial hanging mass to control the linear acceleration along one degree-of-freedom of a proof mass which represents an experiment.

### The GAMMA PROJECT :

The objective of the GAMMA project is to compare different types of discrete acceleration control laws implemented on a real-time processor using a demonstrator.

The criteria of comparison will be :

- the Applicability
- the Decoupling results
- the Robustness to variations of model knowledge or external disturbances
- the Compatibility with the real time control and the available control bandwidth
- the Tuning facility

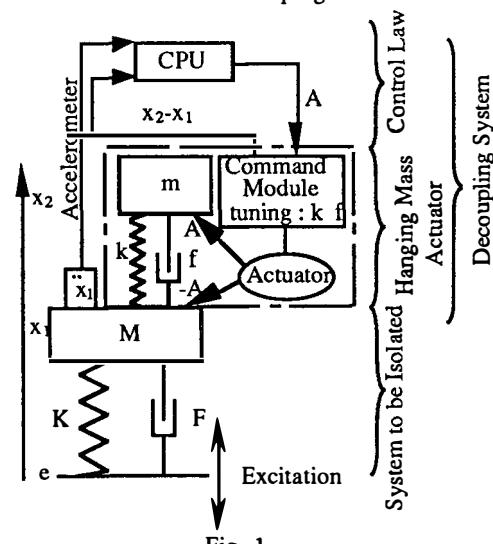
All the characteristics of the system to be isolated and the decoupling system should be adjustable as the excitation system in order to evaluate the robustness of the different types of control laws.

The control laws to be tested will be :

- Modal Control
- Linear Quadratic Optimal Control
- $H_\infty$  Control
- Predictive Control

### The GAMMA TEST BENCH :

The GAMMA test bench is made up of three parts (Fig. 1). The first part is the system to be isolated from external disturbances. It's represented by a proof mass hanging on a system which can provide a tuning mechanical stiffness and damping.



The characteristics of this system are :

Mass M : 40 kg  
 m : 1 kg  
 Stiffness K: 5 to 50 Hz  
 k: .5 to 5 Hz  
 Damping F: 0.01 to 1  
 f: .05 to 1

The excitations are provided by vibration exciter BRÜEL&KJAER (type 4814) which is controlled in acceleration by the BRÜEL& KJAER vibration exciter controller (type 1050).The disturbances provide by this system are described in Fig. 2

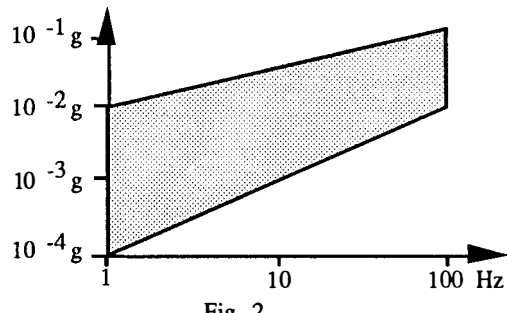


Fig. 2

The second part is the decoupling system is composed by a hanging mass actuated by a linear motor without any mechanical stiffness or damping and an electronic command module . The electronic command module computes an equivalent electronic stiffness and damping in fonction of tuning indicators. It uses a position capacitive detector which has a resolution less than .1 micrometer. It also applies the command given by the CPU to the decoupling system.

The third part is the Control Process Unit which collects the informations of the isolated mass acceleration and the relative position between the isolated proof mass and the mass of the actuator. It computes the right command to apply to the decoupling system in order to compensate the disturbances produced by the calibrated vibration exciter. The real time computer is based on an architecture using a microprocessor M68020 (25 MHz).

#### The GAMMA CONTROL DESIGN :

To obtain a decoupling gain and a damping coefficient corresponding with specifications, there are two solutions ; the first one is to change the equivalent stiffness and damping , the second one is to change the equivalent mass and damping.The advantage of the second versus the first solution is a better rejection of direct disturbances applied to the mass to be isolated . This disturbances can be generated by an experiment itself which should be fixed to the proof mass.We have chosen this solution which have an other advantage . In fact, the decoupling system may be added to an existing platform or structure and doesn't need to be taken in account at the beginning of the design of the mount.

With such a principle of isolation system, this study evaluates the applicability of new automatics methods on this concept.

The general structure of the control laws is a feedback computed from the acceleration of the isolated mass , the relative position of the actuator and the

command of the process because there is a direct transmission in the system. In fact we suppose they are the only measurable parameters of a real system to isolate. To complete these informations we use a state observer which is design by the KALMAN method. The estimated state will be used by the different types of controller we want to evaluate.The general block diagram is represented by the Fig. 3.

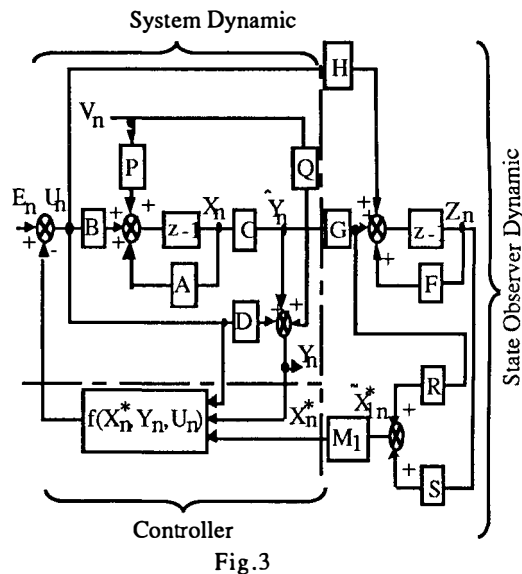


Fig.3

where :

$E_n$  is equal to zero , the system is a regulator  
 $U_n$  is the force applied to the system  
 $Y_n$  is the acceleration of the isolated system  
 $X_n^*$  is estimated state of the whole system  
 $V_n$  is the disturbance

The system is also given by the state representation Eq. (1) and Eq. (2)

$$\dot{X} = AX + BU + PV \quad (1)$$

$$\ddot{X}_1 = CY + DU + QV \quad (2)$$

with:

$$X = \begin{pmatrix} x_1 \\ \dot{x}_1 \\ x_2 - x_1 \\ \dot{x}_2 - \dot{x}_1 \end{pmatrix}$$

$$A = \begin{pmatrix} 0 & 1 & 0 & 0 \\ \frac{K}{M} & \frac{F}{M} & \frac{k}{M} & \frac{f}{M} \\ 0 & 0 & 0 & 1 \\ \frac{K}{M} & \frac{F}{M} & -k\frac{M+m}{Mm} & -f\frac{M+m}{Mm} \end{pmatrix} \quad B = \begin{pmatrix} 0 \\ \frac{1}{M} \\ 0 \\ \frac{M+m}{Mm} \end{pmatrix}$$

$$P = \begin{pmatrix} 0 & 0 \\ \frac{K}{M} & \frac{F}{M} \\ 0 & 0 \\ \frac{K}{M} & \frac{F}{M} \end{pmatrix} \quad C = \left( \frac{K}{M} \quad \frac{F}{M} \quad \frac{k}{M} \quad \frac{f}{M} \right) \quad D = \left( \frac{1}{M} \right)$$

$$\text{and } Q = \left( \frac{K}{M} \quad \frac{F}{M} \right)$$

This system is detectable and controllable, so we can use the estimated state to impose a dynamic which respects the specifications.

The KALMAN discret estimator is design by using two measurements, the relative displacement between the two mass and the acceleration of the proof mass which is integrated twice to obtain the variation of the proof mass position. The KALMAN discret filter estimates the disturbances and the velocities of the two mass.

An example has been chosen with a system to isolated which has the following characteristics :

$$\begin{aligned}K &= 162875 \text{ N/m} \\F &= 3.55 \text{ Ns/m} \\M &= 40 \text{ kg}\end{aligned}$$

which represents a resonance frequency of 10 Hz and a resonance of 57 db.

The decoupling system has the following characteristics :

$$\begin{aligned}k &= 157.91 \text{ N/m} \\f &= 17.769 \text{ Ns/m} \\m &= 1 \text{ kg}\end{aligned}$$

which represents a cut off frequency of 2Hz and no resonance

The ponderations used to obtain the KALMAN estimator are :

$$\begin{pmatrix} 10^{-3} & 0 & 0 & 0 \\ 0 & 10^{-3} & 0 & 0 \\ 0 & 0 & 10^{-3} & 0 \\ 0 & 0 & 0 & 10^{-3} \end{pmatrix} \text{ on the estimation of } \begin{pmatrix} \dot{x}_1 \\ \dot{x}_2 - \dot{x}_1 \\ v \\ \ddot{v} \end{pmatrix}$$

$$\text{and } \begin{pmatrix} 5 \cdot 10^{-10} & 0 \\ 0 & 10^{-4} \end{pmatrix} \text{ on the measurement of } \begin{pmatrix} \int \int \ddot{x}_1 \\ x_2 - x_1 \end{pmatrix}$$

This estimator has been tested until 20Hz and has given excellent results .

#### CONTROL SYNTHESIS :

For the control there is three main constraints : the limitation of the displacement of the control mass which is peak to peak of 10 mm (Fig 4 shows the efficiency of the decoupling mass on the acceleration of the proof mass), the maximal force the linear motor can apply which is 40N and the objective of a maximal rejection of the disturbances on the proof mass. All the discretisation is made with a sampling frequency of 500 Hz which can provide a control until 50 Hz.

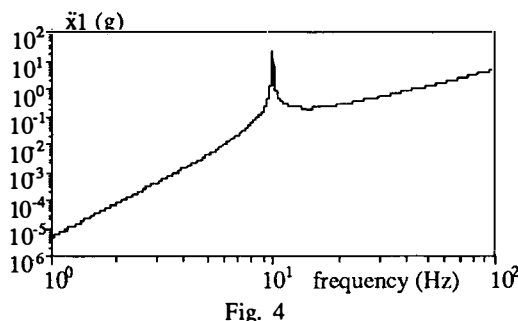


Fig. 4

We can notice that this system isn't very efficient at low frequency , this is due to the little range of displacement allowed to the decoupling mass.

The first objective is to damp the resonance and the second one is to provide a decoupling gain.

#### QUADRATIC METHOD

The quadratic method has been used for the possibility of taking into account different criteria on the acceleration of the proof mass , on the relative displacement and on the command. The ponderations used for this case are : 1 for the acceleration term , 1000 for the displacement and 0 for the command because the linear motor can provide 40 N which is enough for such a control with a bandwidth control less than 100 Hz.. We have just to verify the limit is not reached.

The Simulation results are presented below on Fig. 5 which gives the efficiency of the decoupling system on the dynamic of the proof mass versus the acceleration disturbances (a- represents the initial system and b- the same system with the activation of the isolating mass).

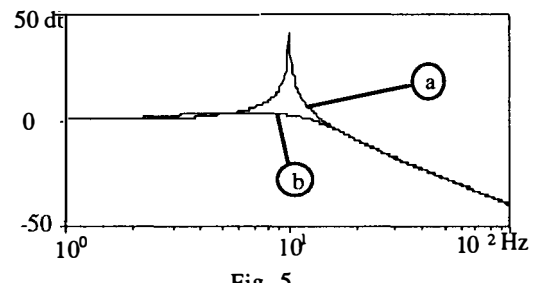


Fig. 5

The Fig. 6 presents the effect of the decoupling system on the relative displacement. The upper curve is with the activation of the decoupling system.( units m/(m/s^2) )

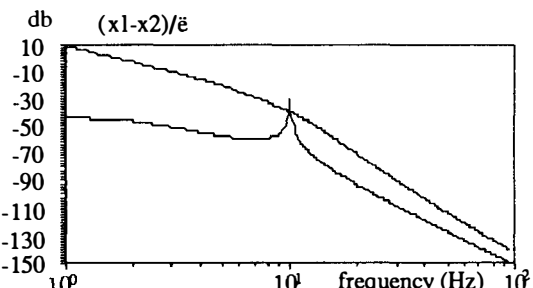


Fig. 6

On Fig. 7 , we have the representation of the command versus the acceleration disturbances. units(N/(m/s^2))

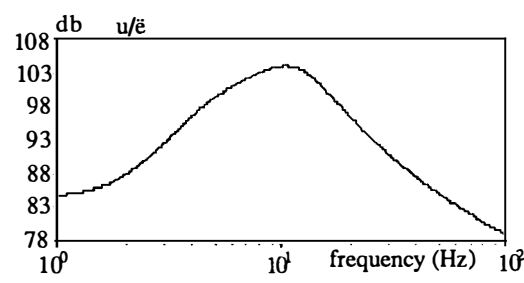


Fig. 7

**Conclusions :** The quadratic method is appropriate to take into account the different criteria but the tuning in term of rejection in the frequency domain is very difficult to appreciate. On an other hand, the correctors we obtain are simple and may be design on the sampling model .They have a degree equivalent of the degree of the system . So it is very easy to implement such correctors on the CPU.

#### MODAL METHOD

The modal method has been used for having a more easier tunability of the rejection in the frequency domain. The simulation results present on Fig. 8 the rejection of acceleration disturbances ( a-without any control and b-with control) The two modes of the isolated system (b) are fixed to :

- 1Hz with a damping factor of 0.9
- 50 Hz with a damping factor of 0.81

These damping factor are design to avoid to important gain at low frequencies.

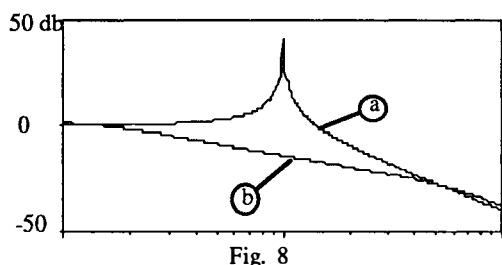


Fig. 8

The Fig 9 ( units m/(m/s<sup>2</sup>) )presents the displacement which is necessary to complete such an isolation . We remark that it is more important at low frequency this is due to a mimimum efficiency of the decoupling mass at low frequencies.The difference is about 20 db.

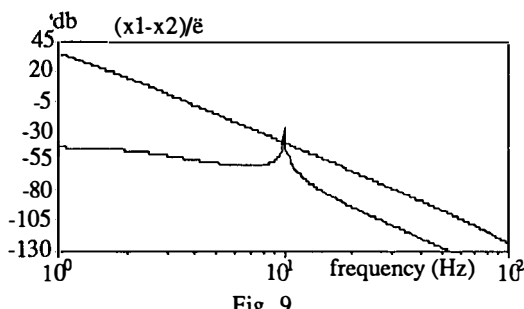


Fig. 9

The Fig. 10 , we have represented the evolution of the command versus the acceleration disturbances . An important increasing of command can be notice at low frequency in comparaison with Fig. 7.

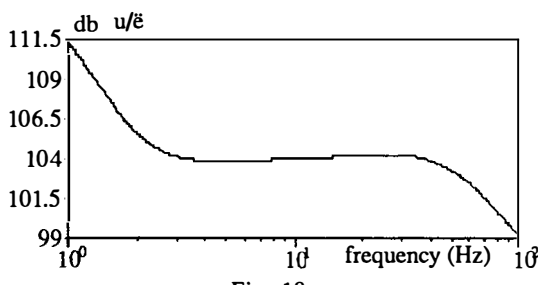


Fig. 10

**Conclusions :** The modal method is well appropriate to adjuste the frequency response but this tuning is made regardless of consequences on displacement and on the command. It is possible to design the corrector by using the sampling model and it easy to implement it on the CPU.

#### CONCLUSIONS

The GAMMA concept needs only the knowledge of the dynamics of the system to isolate and the actuator with margins which will be estimated versus the robustness of the control design . An other advantage is that the decoupling system may be added to an existing platform and doesn't need to be taken into account at the beginning of the platform definition. It may be very usefull for damping modes which appears after the conception.

The control using accelerometric feedback is equivalent of increasing artificially the proof mass . One of this consequence is to have a better rejection of external disturbances which can appears directly on the platform.

Such a test bench will provide a very interesting comparaison basis between different types of modern automatics methods related to the same application.The evaluation on the test bench will begin soon.

We can notice that the two methods we have presented have difficulties for the tuning in different domains . The H $\infty$  design proposes solutions to solve this problem . So it will be the next approach we want to investigate.

#### REFERENCES

1. J.K. HAVILAND, T. W. LIM, W. D. PILKEY and H Politansky,"Control of Linear Dampers for Large Space Structures", AIAA Guidance, Navigation, and Control Conference Monterey, CA Aug 17-19 1987
- 2 G DUC , "Robustesse des Systemes Multivariables" 1990, Ecole Supérieure d'Electricité, GIF-SUR-YVETTE 91192 FRANCE
- 3 T. A. POSBERGH and S. DAHL, "A Control Formulation for the Damping of Structures by Vibration Absorbers",AIAA-91-2607-CP
- 4 J.F. MAGNI and C. CHAMPETIER, "BASILE, Commande Modale" CERT BP 4025 TOULOUSE 31055 FRANCE
- 5 J. MASSE , J.F. BONNANS and G. LAUNAY,"BASILE la Commande Optimale", mai 1991, INRIA ROCQUENCOURT. FRANCE

## NEW METHODS FOR NEW CHALLENGE IN SPACECRAFT CONTROL DESIGN

M.C. Charmeau and P. Pelipenko

*Centre National d'Etudes Spatiales, 18 Avenue Edouard Belin, 31055 Toulouse Cedex, France*

**Abstract** A review of the new problems encountered in space control, essentially due to structural interaction with flexible modes and complex dynamics of multi-payload satellites, has confirmed that classical control methods turn out to have shortcomings. Modern techniques of control, from Linear Quadratic to  $H_\infty$  methods, have been studied in order to determine whether they are well suited to this class of problems. The most promising ones were tested on simplified models to verify coarsely their feasibility and performances. In parallel, a purpose-built software tool combining Computer Aided Design for automatics and symbolic manipulation of dynamic equations is being developed to help control designers faced with these new problems.

**Keywords** satellite attitude control, control system design, computer-aided system design, robust control, simulation, software tools.

### INTRODUCTION

New space control requirements impose stringent technological constraints which make space control problems more and more difficult to solve: spacecraft systems have grown larger, platforms and payloads often need independent pointing, and control-structure interaction can no longer be ignored as structural modes and control frequency bands overlap.

In the same time, on board systems require higher performances in precision (particularly for Earth observation), bandwidth (pointing systems) and robustness (equipment perturbations, uncertainty of flexible modes), for platform attitude control as well as for instrument pointing.

Classical control techniques begin to show their limits and are not efficient enough to meet these new requirements and constraints. But new promising methods have appeared recently in the domain of automatic control. Some of them have been well-known for a few years (Linear Quadratic Methods, Pole placement, Predictive control, Adaptative control,...) but have not yet come into practical use. Others ( $H_\infty$ ,  $\mu$ synthesis,...) are in the development process and seem promising for a lot of various applications.

In 1990, CNES felt the opportunity to start an R&D action with the objective of promoting the synergy between the automatic community and the space industry. CNES and MATRA MARCONI SPACE consulted most of the French laboratories working in

the field of advanced automatics in order to determine which techniques could be applicable to space control problems. A parallel action aimed to develop, in collaboration with CERT<sup>0</sup> and AEROSPATIALE, a powerful Computer Aided Design (CAD) tool well suited to control design of multibody flexible systems that could help the user to implement these new automatics methods. This tool combines the multibody dynamics program JAMES with the CAD control synthesis software BASILE, and special functions have been added to take into account the specificity of complex spacecraft control design.

The first part of this paper sets out the main results of the MATRA/CNES study (Champetier, 1991) and the second part explains the principle of the new CAD tool that is currently under development.

### SPACE APPLICATION OF ADVANCED AUTOMATICS

The first part of the R&D action concerning the application of modern automatics methods in space control was composed of three phases :

- . make the state of the art of the problems encountered in space applications
- . review and analyse the "modern control techniques"

<sup>0</sup> CERT : Centre d'Etudes et de Recherches de l'Ecole Nationale Supérieure de l'Aéronautique et de l'Espace à Toulouse - section automatique.

. assess the appropriate methods with simplified dynamic models in order to verify coarsely their feasibility and performances.

In this paper we will discuss briefly about the first point to show the classes of problems encountered in space domain and next we will develop the approach of SPOT attitude control problem treated with multivariable techniques.

### Identification of problems and needs

In order to cover a large spectrum of applications, many project teams were consulted :

- earth observation projects (SPOT family)
- scientific satellites (SOHO, FIRST, ROSETTA, ...)
- telecommunication and relay satellites (EUTELSAT family, DRS, ...)
- fine pointing (SILEX, GOMOS, ...)

For each application, limitations concerning the command approach used (most of the time "classical") were analysed, keeping in mind the possibility of the alternative use of modern control techniques.

Among all problems identified, the most critical points were :

- observation satellites : in normal mode, the main difficulty in terms of attitude control, is the dynamic coupling between flexible panels and the central body, associated with a high pointing accuracy requirement (lots of modes in and out AOCS<sup>1</sup> bandwidth, uncertainty margins on frequencies and damping factors, time variant frequencies/inertias). Complexity due to non controllable cantilever modes coupled with SADM<sup>2</sup> harmonics. Complexity due to a low frequency sampling. In orbit control mode (control by thrusters), additional problems are caused by non linear command (frequency modulation) coupled with large panel modes. We can also note the problems due to the colocation of movable payloads and satellite control. We can add for high pointing accuracy mission specifications the necessity to filter the dynamic perturbations transmitted by the platform to the payload.
- fine pointing systems : problems in this class of applications, when embarked on satellites, are the interface specifications between platform control and payload control, and their integration in the definition of control laws. Technological constraints are to be taken into account (dry friction, non linearities, ...). The fact that some of the instruments are to be mounted at the extremity of flexible supports add complexity to platform and payload dynamics.
- communication and relay satellites : problems are there less complicated by the fact that pointing requirements are weaker than for observation missions. We can still recall the problems of solar array flexible modes and liquid sloshing during orbit correction maneuvers. We can also highlight the

relay satellites problems, due to large inertia antenna moving and interacting with the platform control.

• scientific projects : control problems, for this class, are specific of the type of application. A constant problem is the rejection of dynamic perturbations coming to the payload interface from data storage units and dry friction of reaction wheels. For performance requirements in a limited frequency band, frequency shaping techniques can be considered for the control concept.

Next table sums up the critical points and shows how modern control techniques could respond to the classes of problems encountered.

TABLE 1 Classification of Problems

CLASS	CRITICAL POINTS	NEEDS
classical AOCS optimisation	. command saturation . non linearity . robustness . reject of internal dynamic perturbation	. multivariable robust control . non linear control . frequency shaping
fine pointing	. high control bandwidth . perturbations reject . technological constraints	. non linear control . adaptive/predictive control . multivariable control
multi-body systems	. configuration evolution . large spectrum of perturbations	. centralised / decentralised control . robust or adaptive control . multivariable control

After the review of control problems encountered in space projects, some representative themes have been selected to assess coarsely the applicability of modern control techniques.

The selected themes were :

- fine pointing of instruments : control in presence of important dry friction and application of non linear predictive control.
- SPOT attitude control in fine pointing mode, application of LQG/LTR methods and frequency shaping and of  $H_\infty$  control to take into account the multi-actuator (wheel + SADM) problem.

In this paper we will focus on SPOT attitude control because it includes many generic problems like internal perturbations compensation, multi-axis coupling, or not well known flexibilities.

The following results concern a first approach to the problem consisting in working on a simplified model of the satellite dynamics.

### SPOT 4 Attitude Control

<sup>1</sup> AOCS : Attitude and Orbit Control System

<sup>2</sup> SADM : Solar Array Drive Mechanism

The problem is here to control the attitude of a low sun-synchronous satellite. Control laws must be performant enough to maintain satellite angular position within the requested pointing precision. Perturbations are external (gravity gradient, aerodynamic pressure, solar pressure) and internal (flexibility of solar generator, SADM harmonics, moving equipments).

SPOT 4 actual control is based on a classical proportional/derivative feedback, already used on SPOT 1, 2 and SPOT 3. But specific difficulties have appeared because of a new larger solar array and have led to significant modifications of the attitude control system.

Classical Control. The general architecture of control loops is presented here.

The currently used control law is a proportional / derivative control associated with a positive lag shift network. Seven flexible modes have been included in the control band to maintain a good bandwidth (1 Hz) and gains were tuned to satisfy all solar array angular positions. The main problem comes from the presence of a 7th flexible mode at 1.05 Hz, which must be integrated in the control band to assure the stability of the system. An important positive phase shift is used for this reason, leading to a bandwidth of 1.8 Hz.

A significant problem is the perturbation rejection, more particularly the SADM perturbations rejection, nominally ensured by the control wheels. The rejection function shows bad performances (0 dB) at a frequency corresponding to the first flexible mode of the solar array on pitch axis. The SADM motor presents an harmonic frequency near this mode, so the pitch wheel is inefficient to control it. An active control of SADM has been introduced to attenuate this effect without degrading performances and stability. The SADM control formerly proposed and that has been considered here generates a rate control equal to the estimated pitch rate, amplified and filtered by a second order filter.

The classical analysis of stability and robustness of control loops has been done axis by axis, without the use of multivariable robustness analysis methods. The problem is in this case to find the parameters configuration which defines the "worst cases".

The SADM control tuning is complicated by the fact that it strongly depends on the principal loop (AOCS). The SADM must not be slaved to the low frequency angular motions of spacecraft during attitude homing phases.

In order to prove that advanced automatics could provide interesting solutions to this kind of problems, multivariable robust control techniques have been selected for control laws synthesis and tested on a SPOT 4 simplified model :

- LQG/LTR with frequential shaping for multi-axis coupling study (without SADM control)
- $H_\infty$  for multi-actuator study (wheels & SADM)

### LQG Techniques Application

Different applications of Linear Quadratic methods have been developed on multi-axis SPOT attitude control (LQ, LQG, LQG/LTR, frequency shaping). The very good robustness properties of LQ method have been restored by LQG/LTR, when LQG was leading to insufficient phase margins.

The LTR study has shown that it was possible to use, in the estimator synthesis, the model noise weighting on a state variable corresponding to a particular flexible mode to increase robustness relatively to this mode.

Frequency shaping has permitted to achieve the design by strong filtering outside control bandwidth. The comparison between classical and LQ methods leads to some remarks :

- LQG/LTR techniques ensure very good robustness performances, but the gain with respect to classical methods is not very appreciable because of the worst case gain tuning in classical approach. The systematisation of robust multivariable control laws synthesis is interesting to note.
- the real gain introduced by such methods comes from the perturbation rejection properties and high frequency noise : for a similar bandwidth, the perturbation rejection is increased of a 2.2 factor, and the cutting in frequency is faster.
- The order of the LQG/LTR controller with a 5 modes model is approximately 16. The addition of frequency shaping increase the order to 19 (classical controller of 6th order). Model reduction methods

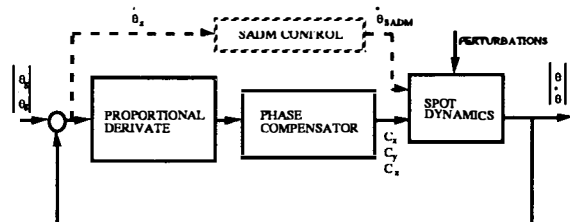


Fig. 1. Structure of SPOT 4 Attitude Control

would be interesting to be tested.

- An adaptation of controller must be done to take into account the panels rotation in satellite axes. Some solutions must be studied to analyse the impact on the on-board computer.
- The synthesis (made here in continuous domain) must be done directly in discrete domain to avoid stability and robustness impacts of 8Hz sampling period.

### Reaction Wheels and SADM Control with $H_\infty$ Method

$H_\infty$  methods offer a general context for frequential formulation of objectives relatively to performances (bandwidth, perturbations reject) and robustness (structured : model parameters variation, or unstructured : model variation inside a frequential shape) of multivariable systems. These objectives are formulated in terms of  $H_\infty$  norm minimization of

proper transfer matrices build from system transfer matrix and filters which define performances and robustness criterias. This norm minimization uses advanced mathematics aspects. Some toolboxes (MATLAB, BASILE, ...) are available to help to solve these mathematical problems.

The study has developed next points :

- $H\infty$  methodology, in relation to habitual concepts of classical techniques users.
- optimization problem definition of a controller with this formalism.
- preliminary resolution elements for problem optimization, to really understand mathematical behaviour of synthesis tools.

Methodologies adapted to synthesis tool have been applied. Two reference methodologies have been used:

- MSC (Mixed Sensitivity problem Configuration) which is close to classical approach : frequency specifications and robustness analysis via phase and gain margins.
- SCC (Standard Compensation Configuration) which represents a similar approach to LQG method in its formulation and can be interpreted as a second step for a robust refinement.

The development of such approaches has presented some problems due to numerical conditioning, problems in cost functions definition, algorithm selections ...

The preliminary results are very attractive by the fact that thanks to a combined methodological approach, frequency domain and LQG techniques lead to a performant and robust controller.  $H\infty$  method seems promising for the future to solve space projects control problems. CNES effort for the future phases of the study will focus on the more detailed evaluation of such methods ( $H\infty$  and  $\mu$ synthesis) applied to complete satellite models to verify in details the use of robust command methods on SPOT example.

## A NEW CAD TOOL

When faced with problems of control-structure interaction, the control designer has to perform coupled control and dynamic analyses, even at early stages of the design process. On a satellite like SPOT 4, the platform can still be considered as rigid for attitude control synthesis and only solar arrays or payloads have to be modelized as flexible bodies. The issue is not the same on large space structures for which a control structure optimization may be necessary: an iterative process has then to take place between the structure design from finite element model and the control system design. (Stornelli and co-workers, 1991).

In the case of new generation Earth observation satellites or scientific multi-payload satellites, the difficulty comes from the fact that there are many flexible modes sensitive to control action. The following questions come into mind:

- is active control of these modes necessary?
- is a classical control technique appropriate or would a modern method be more adequate?

- is global control better than local control?

To answer these questions, several models of the dynamics are needed: at first very simple ones for preliminary studies, then more representative linearized ones for detailed analyses and controller design, and a complete non-linear model for validation, verification of simplification hypotheses and performance evaluation through simulations.

Many programs are now available to study the dynamics of flexible multi-body systems (such as ADAMS, DADS, ESA-MIDAS, or TREETOPS) but most of them are limited to simulation and the model equations cannot be easily used for analyses. However, to achieve control design, an appropriate tool can be very helpful to compute the dynamic equations, simplify and linearize the model and perform control synthesis and validation.

CNES, in collaboration with CERT and AEROSPATIALE has undertaken an R&D study to combine the multibody program JAMES with the CAD control synthesis program BASILE (Imbert, 1991).

JAMES was developed by AEROSPATIALE (Garnier, Rideau, 1989), for their own use, to compute analytically the dynamic equations of mechanical systems. Based on symbolic manipulation, it uses MAPLE mathematical manipulation language and a library of matricial operations specially developed to keep compact expressions in the equations.

A system can be described as a set of rigid and flexible bodies connected by joints. Forces and torques can be applied at user-defined points. There is no need for numeric values at this stage. The dynamic equations are automatically computed and can be simplified by the user with the help of several functions (factorisation, linearization,...).

It is then possible to generate a FORTRAN-, C-, or ADA- simulator from the mass matrix, the second member and the force vector of the system. As it is directly derived from the symbolic equations of the studied system, such a simulator is particularly efficient and well-suited to parameter changes. Even the number of flexible modes can be given as a parameter and changed between simulations.

BASILE, developed by INRIA has a library of functions and routines that can be used interactively or into user-built programs. Among these functions can be found all basic tools needed for classical control such as transfer functions manipulation or Bode and Black diagrams, and more specific ones for filtering, optimal control, pole placement, robust control,...

BASILE also provides numerical integration routines for simulation and optimization.

To transfer easily JAMES's outputs into BASILE, an interface was developed by AEROSPATIALE. Linearized equations of the dynamics are put in state

space form to be used directly for control analyses with BASILE.

### How Can this Tool be Helpful?

To design the attitude control system of a satellite with many flexible modes - some of them being in the control band - and with particularly stringent attitude requirements, several stages are necessary.

At first, a simplified model of the system has to be built, from results of finite element analysis generally. If too many flexible modes are making the model too large and difficult to study, a model reduction is advisable. Decoupling of axes may be interesting, but is not always possible.

Linearised equations are preferred to perform control synthesis.

When control laws have been chosen, they have to be validated by simulation to estimate their performances. This can be done on the simplified linear model to optimize the control laws, but the best estimations can be done only on a complete non-linear model.

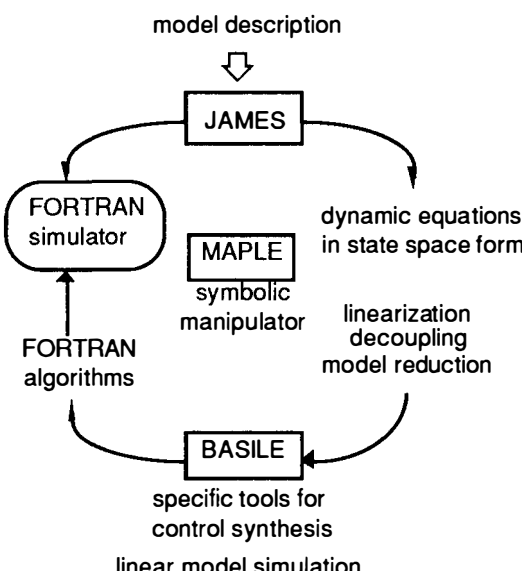


Fig. 2. Principle of the CAD Tool

JAMES handles tree-like systems of rigid or flexible bodies. A description of the geometry and modal characteristics of the satellite has to be entered into JAMES. Each body is defined by its number of modes (which can remain symbolic) and the points and joints that are linked to it. Numerical values can be assigned to some of the parameters describing the system in order to simplify the expressions (if they are equal to zero or identity, for example), but all the others parameters are defined by their names. They are for each body:

- mass, tensor of inertia,
- vector between the reference point of the body and its center of mass,
- participation factors in translation and rotation and deformation at the points for flexible bodies,...

Forces and torques are applied to the system at the joints or at specific points that the user has defined in a formal way. No numerical value is necessary at that stage.

The computation of the dynamic equations lasts a few seconds and gives the result in the following form:

$$M(p)\dot{q} = S(p,q) + Lq + Kp + F(p,q),$$

where p and q are respectively the position and velocity parameters,

M(p) is the mass matrix,

S(p,q) is the second member of Coriolis and centrifugal forces,

L is the damping matrix,

K is the rigidity matrix and

F(p,q) is the vector of external forces.

This equation can be linearized and converted into:

$$\begin{cases} \dot{x} = Ax + B_1 u_1 + B_2 u_2 \\ y = C_1 x + C_2 \dot{x} \end{cases}$$

with  $x = \begin{pmatrix} p \\ q \end{pmatrix}$ ,

$u_1$  vector of command,

$u_2$  vector of perturbations,

$C_1$  and  $C_2$  observation matrices,

which is conventional automatic control terminology.

A FORTRAN translation of the equations gives to the user the possibility to calculate the numerical values of the A, B and C matrices and the ability to change them easily when necessary.

The system can be then transferred into BASILE and is ready for further simplifications and analyses.

Once the equations have been linearized, the model may not yet be simple enough to perform control synthesis as soon. One could wish to try a model reduction.

No model reduction method seems to be superior to the others, since the results depend on the model to which the method is applied. Several algorithms were translated into BASILE functions by CERT and the choice has been left to the user who can compare the results:

- internal balancing theory,
- modal reduction,
- component cost analysis.

Decoupling of axes or parts of the model is attractive as single input single output theory is simpler than multi-variable theory and easier to put into practice. Decoupling criteria are being studied and will be introduced among BASILE's tools if they prove to be useful.

### Command Algorithms

In addition to BASILE's functions, several new modules were written by CERT to give a larger choice to the user.

- computation of control algorithms by LQ, LQG, LQG-LTR methods,
- robust control algorithm using positivity,
- multi-input multi-output (MIMO) stability criteria by singular value method.

As it is very easy to develop new procedures in BASILE, future improvements are foreseen. If the  $H_\infty$  method application studies lead to promising results, the corresponding tool will be transferred into BASILE.

#### Validation and Simulation

Two types of simulation are possible: a simulation with the simplified linear model which was used for control synthesis, and a simulation with a "complete" model, more or less representative of the real dynamics.

The first simulation can be performed with BASILE special functions and is very fast. It is a good tool for preliminary validation.

The complete simulation needs the specific FORTRAN simulator that is generated by JAMES. Control algorithms are translated into FORTRAN code and can be linked to the dynamics simulation program. A real validation tool is then available.

#### CONCLUSION

CNES R&D automatics program aims at promoting the new techniques that will become necessary to meet tomorrow's challenges in satellite and payload control. Taking into account advanced automatics theory will be made easier by setting up from now on close links between laboratories and industry, and by preparing versatile software tools suitable from the very first design phases of space control systems.

The positive preliminary results of the MATRA/CNES study let us hope that new control methods will help to solve the emerging difficulties due to the interaction between control, structure dynamics and payload motion.

The concerted action between CNES, CERT and AEROSPATIALE is leading to the development of a software tool especially intended to answer these new problems. The application field of such a tool will be very large, ranging from satellite attitude control to robotics.

Studies are going on to determine precisely what performances can be expected when using  $H_\infty$  and  $\mu$ synthesis method for the stabilization of a typical Earth observation satellite.

#### Acknowledgment

We express our gratitude to the MATRA MARCONI SPACE, AEROSPATIALE Cannes and CERT teams who have achieved, under CNES contracts, the studies without which this paper could not have been issued.

#### REFERENCES

- C. Champetier, E. Desplats and P. Pelipenko (1991). Modern control techniques for spacecraft AOC/GNC systems. Proc. First ESA Internat. Conf. on 'Spacecraft Guidance, Navigation and control Systems', ESTEC, Noordwijk, The Netherlands, 4-7 June 1991 (ESA SP-323, december 1991), pp. 483-490.
- C. Champetier, E. Desplats, B. Frapard, P. Regnier (1991) Application des Techniques Modernes de Contrôle dans le Domaine Spatial. Rapport Final CNES/MATRA n° 896/CNES/90/0778/00
- C. Garnier and P. Rideau (1989). Gemmes: a new tool for dynamic modelling. Proc. International Conference: 'Spacecraft Structures and Mechanical Testing', Noordwijk, The Netherlands, 19-21 october 1988, (ESA SP-289, january 1989), pp. 149-154.
- Imbert, N. (1991). Etude relative au développement d'un outil général de conception et de validation des lois de commande d'attitude pour les véhicules spatiaux. Rapport final CNES/DERA n°3/7728, CERT
- Stornelli, S. and co-workers (1991). Control strategies for space systems. Proc. First ESA Internat. Conf. on 'Spacecraft Guidance, Navigation and control Systems', ESTEC, Noordwijk, The Netherlands, 4-7 June 1991 (ESA SP-323, december 1991), pp. 475-482.

## LOCALIZATION OF STRUCTURAL FLAWS USING CROSS TRANSFER FUNCTION ZEROS

G.D. Shepard\* and J.A. Lepanto

*The Charles Stark Draper Laboratory, 555 Technology Square, Cambridge, Massachusetts, USA*

*\*also Department of Mechanical Engineering, University of Massachusetts, Lowell, Massachusetts, USA*

**Abstract.** Frequency based localization is a technique which locates structural flaws by monitoring changes in transfer function pole and zero frequencies. This technique has been successfully applied to isolate simulated structural flaws in a modal database representation of a spacecraft using transfer function poles and driving point zeros. However, the number of usable frequencies and, therefore, the achievable spatial resolution, was limited by high modal density and narrow excitation bandwidth. In this paper, the feasibility of improving spatial resolution by incorporating the zeros of cross transfer functions is demonstrated. The frequency based procedure was developed specifically to support structural health monitoring in an environment that is less than ideal for modal testing. For spacecraft on-orbit, testing to detect structural flaws is constrained by the limited availability of sensors and excitation sources, and by the requirement for minimal impact on mission operations. Frequency based localization is well suited for this application, since measurements of input forces and modal frequencies only are required. This greatly reduces the requirements for sensors and data acquisition compared to localization techniques that rely on measurements of mode shapes.

**Keywords.** localization, system integrity, structural flaws, transfer functions, poles, zeros, health monitoring

### INTRODUCTION

Frequency based localization is a procedure whereby flaws in a structure can be isolated by monitoring changes in the transfer function pole and zero frequencies associated with the global modes of the structure. An advantage of this particular localization technique is that it provides reliable results using data from sparsely placed sensors.

Previous results have demonstrated that frequency based localization using transfer function poles and driving point zeros can be successfully applied to isolate structural flaws in a complicated spacecraft that is modelled by a large modal database (Shepard and Lepanto, 1991). The example structure was the Space Station Freedom (SSF), which proved to be a stressing case for the localization procedure due to high modal density, a narrow bandwidth of excited frequencies, and the fact that most of the frequencies were small

multiples of the fundamental frequency. As a result, the number of usable frequencies, and therefore, the achievable spatial resolution, limited our success to the localization of flaws which were distributed over one or two bay portions of the truss.

However, it was hypothesized that the resolution of more subtle flaws should be possible by increasing the number of usable frequencies through the use of cross transfer function zeros; i.e. zeros of the transfer functions that relate the response at one location on the structure to the input force at another location.

The goal of the research described below was to take the first step in validating this hypothesis by demonstrating the feasibility of incorporating cross zeros in the localization procedure. The inclusion of cross transfer function zeros required an extension of the analysis and calculations used in the SSF example, and thus returned us to the

"proof of concept" stage of development. Therefore, the large, complicated database for the SSF model was abandoned in favor of a simple beam model. This choice of a tractable finite element model proved crucial to our success.

#### EFFECT OF FREQUENCY SEPARATION ON LOCALIZATION ACCURACY

The procedure for frequency based localization of flaws in a structure requires a solution to the following system of equations:

$$[\text{MRM}] \left\{ \frac{dk}{k} \right\} = 2 \left\{ \frac{d\omega}{\omega} \right\} \quad (1)$$

where MRM is the modal reference matrix for the structure,  $(dk/k)$  is the stiffness discrepancy vector, and  $(d\omega/\omega)$  is the frequency discrepancy vector (Shepard and Milani, 1988). The rows of the MRM correspond to the mode frequencies; the columns correspond to the macro-elements into which the structure is divided for localization.

The accuracy of this localization procedure is highly sensitive to the numerical conditioning of the MRM for the structure. As more frequencies are included in the localization procedure, the orthogonality of the row space of the MRM becomes a concern. Each row of the MRM relates structural discrepancies to the change in a particular pole or zero frequency. The elements of each row are constructed from the pole or zero mode shape that corresponds to the particular pole or zero frequency. If two mode shapes are very similar, the corresponding row vectors will be nearly parallel, and the MRM will be poorly conditioned.

Omitting the special case of repeated eigenvalues (which is unlikely to occur in the case of a complicated, unsymmetrical, engineering structure), the mode shape vectors of two adjacent frequencies become increasingly parallel as the frequency separation decreases. To see this, consider a structure with a dynamical matrix  $B(s)$

$$B(s) \dot{X}(s) = F(s) \quad (2)$$

The structural response to an input at node  $j$  is determined by the transfer function vector  $h_j$  of the transfer function matrix  $H(s) = B(s)^{-1}$ ,

$$h_j = \frac{a_j}{|B(s)|} \quad (3)$$

where  $a_j$  is the  $j^{\text{th}}$  column of the adjoint matrix  $\text{Adj } B(s)$ . The mode vector of a pole, a driving point zero, or a cross zero is obtained by substituting the mode frequency into  $a_j(s)$ . For a lightly damped structure, these mode vectors will be closely approximated by substituting the resonant and antiresonant frequencies which correspond to the pole and zero frequencies. Clearly, the  $a_j(s)$  mode vectors for any two closely spaced frequencies become increasingly parallel as the frequency separation approaches zero.

The need to avoid closely spaced frequencies suggests a simple strategy for selecting candidate frequencies. Starting with the driving point transfer function, the first step is to select poles which are adequately separated in frequency from adjacent poles. Next select the driving point zeros which are centered between the adequately spaced poles. Finally, for each case where the driving point zero is not centered between a particular pair of adequately spaced poles, choose instead a cross zero from a transfer function between the input force and some node other than the driving point.

Poles and zeros selected in this manner will be most likely to improve the numerical conditioning of the MRM because closely spaced frequencies are avoided. These modes will also be the easiest to identify since they will produce the most dominant resonant and antiresonant responses on the frequency response plots. The strategy will also minimize the number of sensors because it makes maximum use of response data measured at the single driving point (poles, driving point zeros), and utilizes response data from other points (cross zeros) only when necessary. The inclusion of cross zeros in the localization procedure greatly increases the number of candidate zeros, and therefore increases the chances of finding a suitable zero between every pair of adequately spaced poles.

#### CALCULATION OF CROSS TRANSFER FUNCTION ZEROS

The computation of transfer function cross zeros and the associated cross zero vectors can be accomplished by solving a non-symmetric eigenvalue problem. This eigenvalue problem can be formulated either in physical coordinate space or in a reduced modal coordinate space (Henderson, 1991). The eigenvalues and eigenvectors computed in reduced modal space are approximations to those computed in the physical space eigenproblem. The level of agreement of

the two formulations is dependent on the number of modes retained after truncation. In the case of the reduced beam model, the modal space method resulted in excellent agreement with the NASTRAN computation of the driving point zeros. Note that only the driving point zeros can be computed using NASTRAN.

## FREQUENCY CORRECTION FACTOR FOR CROSS ZEROS

The use of cross transfer function zero frequencies for frequency based localization introduces a complication which does not occur for pole or driving point zero frequencies. The cross zero eigenanalysis yields a set of cross zeros (eigenvalues), a set of corresponding cross zero mode shapes (eigenvectors), and, for each cross zero frequency, an input force (Lagrange multiplier). After structural modification (i.e. in the presence of a structural flaw), all of these quantities are changed. It has been shown (Shepard and Milani, 1988) that the effect of structural change on an eigenfrequency is a first order effect, whereas the effect of structural change on modal shape is a second order effect and can be ignored. In the case of cross zeros, however, we have found that the effect of structural change on the driving force is of first order, and cannot be ignored.

The easiest way to account for the effect of the driving force is to think of it as a local structural modification at the driving point. Since we are dealing with lightly damped structures - zero damping in the limit - the driving force (as well as the change in the driving force) must be harmonic, and either in-phase or out-of-phase with the displacement at the driving point. For a given cross zero frequency  $\omega$ , driving point amplitude  $x$ , and driving force  $f$ , the driving force can be modeled by the addition of a small trim mass

$$m_C = \frac{f}{\omega^2 x} \quad (4)$$

or a trim stiffness (tied to ground)

$$k_C = \frac{f}{x} \quad (5)$$

depending on whether the driving force is in-phase or out-of-phase, respectively, with the driving point displacement. The fractional change in the driving point force ( $\frac{df}{f}$ ) can then be characterized as

a local structural change  $\left(\frac{dm_C}{m_C}\right)$  or  $\left(\frac{dk_C}{k_C}\right)$ , depending on the phase. It has already been established that the effect of structural changes on frequency changes is of first order. By viewing force changes as structural changes, it is clear that force changes, like structural changes, have a first order effect on frequency changes.

As an example of the preceding cross zero strategy, consider the case where the driving force  $f = k_C x$  is out of phase with the driving point displacement  $x$ . The equation for a particular cross zero frequency,  $\omega$ , will be an expanded form of a typical row of Eq. (1)

$$\frac{v_1}{V} \frac{dk_1}{k_1} + \dots + \frac{v_C}{V} \frac{dk_C}{k_C} + \dots + \frac{v_n}{V} \frac{dk_n}{k_n} = 2 \frac{d\omega}{\omega} \quad (6)$$

where  $v_C = \frac{1}{2} k_C x^2$  and  $V' = V + v_C$ . In this equation, the term involving  $k_C$  accounts for the effect of the driving point force on the cross zero frequency  $\omega$ . All of the other terms on the left hand side of the equation refer to frequency changes caused by stiffness changes in the elements of the structure. Rearranging Eq. (6)

$$\frac{v_1}{V} \frac{dk_1}{k_1} + \dots + \frac{v_n}{V} \frac{dk_n}{k_n} = \left(1 + \frac{v_C}{V}\right) 2 \frac{d\omega}{\omega} - \frac{v_C}{V} \frac{dk_C}{k_C} \quad (7)$$

The left hand side of Eq. (7), which accounts for the effect of structural changes on the cross zero frequency, is now in the standard form used to compute the row elements of the MRM. Note that the frequency change  $\frac{d\omega}{\omega}$  and the cross zero driving force change  $\frac{dk_C}{k_C}$  are measured on the structure, and the structural change weighting factor for cross zeros  $\frac{v_C}{V}$  is computed from the nominal model of the structure.

When the cross zero driving force is in phase with the driving point displacement, the stiffness correction term on the right hand side of Eq. (7) must be replaced by a mass correction term:

$$\frac{v_1}{V} \frac{dk_1}{k_1} + \dots + \frac{v_n}{V} \frac{dk_n}{k_n} = 2 \frac{d\omega}{\omega} + \left(1 - \frac{t_C}{T}\right) \frac{t_C}{T} \frac{dm_C}{m_C} \quad (8)$$

where  $t_C = \frac{1}{2} m_C x^2$ . Again,  $\frac{d\omega}{\omega}$  and  $\frac{dm_C}{m_C}$  are measured on the structure, and  $\frac{t_C}{T}$  is computed

from the nominal model of the structure.

## FREQUENCY BASED LOCALIZATION PROCEDURE

The first step in the procedure for localization using cross zeros was to develop a finite element model of a simple beam. This model, shown in Fig. 2, contained 22 nodes and 21 beam elements. All of the modal frequencies out to 600 Hz were initially considered as candidates for localization. The MRM was then assembled using NASTRAN for all of the pole, driving point zero, and cross zero frequencies: 20 poles, 20 driving point zeros, 232 cross zeros. The zeros were computed by assuming an input force at node 92. The cross transfer function zeros were computed at each of 21 locations (nodes) on the beam. For localization, the structure was partitioned into 21 macro-elements, where each macro-element corresponded to one of the NASTRAN beam elements. The resulting MRM was a 272 x 21 matrix.

The next step was to choose *usable* pole, driving point zero, and cross zero frequencies based on the requirements for adequate modal separation. Frequencies were eliminated accordingly, and the MRM was reduced to a 40 x 21 matrix. The numerical conditioning of the row and column spaces for this reduced MRM was evaluated (Lepanto, 1989), and additional rows were removed, yielding a 21 x 21 MRM. This MRM was numerically well conditioned in accordance with the criteria established in our previous research.

The final step in the procedure was to perform the localization. Once a well conditioned MRM was determined, the stiffness of a selected element in the NASTRAN model was increased to simulate a flaw, and the frequencies that characterized the flawed model were obtained from NASTRAN analysis. The frequency discrepancy vector,  $\left\{ \frac{d\omega}{\omega} \right\}$ , was calculated for the usable pole, driving point zero, and cross zero frequencies. A modified frequency discrepancy vector,  $\left\{ \frac{d\omega}{\omega} \right\}'$ , was calculated by adding the frequency correction factor for each cross zero to the vector  $\left\{ \frac{d\omega}{\omega} \right\}$ . Finally, the stiffness discrepancy vector was calculated according to Eq. (1):

$$\left\{ \frac{dk}{k} \right\} = [MRM]^{-1} 2 \left\{ \frac{d\omega}{\omega} \right\}' \quad (9)$$

## APPLICATION OF FREQUENCY BASED LOCALIZATION TO NASTRAN MODEL OF A SIMPLE BEAM

Two types of examples were used to investigate the applicability of cross transfer function zeros for frequency based localization. The first three examples served to establish a benchmark for the beam model. Although the NASTRAN model of the beam was less complicated than the SSF model used previously, the beam model resulted in a 21 x 21 MRM, whereas the largest usable MRM in the SSF examples was 12 x 12. Therefore, the first step was to determine whether the increased size of the MRM introduced any numerical complications in the localization procedure. The fourth example demonstrated the feasibility of including cross zeros in the localization process.

### Benchmark Study for Beam Model

The objective of this benchmark study was to establish that the localization procedure is not compromised numerically when large modal reference matrices are used. The first example used a 21 x 21 MRM that contained only poles and driving point zeros of the beam model. The numerical conditioning for the row and column spaces of this MRM was evaluated and was judged to be acceptable according to the criterion previously established for a smaller MRM. Fig. 3 shows the percent change in stiffness that was localized in each beam element when a 5% increase in stiffness was simulated in beam element 16. Note that the results of this localization are characterized by considerable noise, despite the fact that the numerical conditioning of the MRM had been judged to be adequate. Although the results suggest that the stiffness change is in the portion of the structure containing element 16, the results are not conclusive and this localization cannot be considered successful.

Revisiting the numerical conditioning for the column space of the MRM, it was determined that columns 9 and 13 might not be sufficiently orthogonal to insure good numerical conditioning of the larger MRM. To test this possibility, column 9 was removed from the MRM, reducing it to a 21 x 20 matrix, and the localization was repeated. The results of this second example are given in Fig. 4, where the noise level is greatly reduced and the change in stiffness is isolated to element 16. In the third example, column 13 was removed from the MRM instead of column 9.

The results of the third localization are shown in Fig. 5. Once again, there is a significant reduction in noise compared to the first example, and the change in stiffness is isolated to element 16.

These three examples indicate that as more rows and columns are added to the MRM, the localization procedure becomes increasingly sensitive to the numerical conditioning of this matrix.

#### Feasibility Study for Cross Transfer Function Zeros

Based on the three examples described above, to assure acceptable numerical conditioning, it was determined that the 21 x 20 MRM should be used in the example to evaluate the feasibility of using cross zeros for localization. Therefore, in the fourth example, column 13 was removed from the original 21 x 21 MRM, and two of the driving point zeros were replaced with two cross zeros. The resulting MRM included 14 pole frequencies, 5 driving point zero frequencies, and 2 cross zero frequencies. Figure 6 shows the percent change in stiffness that was localized in each beam element when a 5% increase in stiffness was simulated in beam element 16. This localization is successful and the results are comparable to those achieved using only pole and driving point zero frequencies (Fig. 5).

## CONCLUSIONS

The goal of this study was to demonstrate the feasibility of incorporating cross transfer function zeros in our frequency based localization procedure. We have met this goal by extending our previous analysis. In doing so, we established that two issues are crucial if cross zeros are to be successfully included for localization. First, a correction factor must be applied for each cross zero in the frequency discrepancy vector to account for the effect of the driving force. Second, as the MRM gets larger, the localization procedure becomes increasingly sensitive to the numerical conditioning of the column and row spaces for this matrix. The resolution of more subtle flaws requires more usable frequencies and more macro-elements for the structure, which correspond to additional rows and columns, respectively, in the MRM. Therefore, as we include more cross zeros in the localization procedure and attempt to isolate flaws in smaller segments of the structure, the criteria for acceptable numerical conditioning of

the MRM must be reevaluated.

## REFERENCES

- Henderson, T. (1991). Computation of cross transfer function zeros. Charles Stark Draper Laboratory memorandum EGC-91-174.
- Lepanto, J. A. (1989). Numerical conditioning for frequency based localization. Charles Stark Draper Laboratory memorandum SS-88-07.
- Shepard, G. D. and J. Milani (1990). Frequency based localisation of structural discrepancies. Mechanical Systems and Signal Processing, 4(2), 173-184.
- Shepard, G. D. and J. A. Lepanto (1991). Application of frequency based localization to identify structural flaws in flexible spacecraft. IFAC Workshop in Dynamics and Control of Flexible Aerospace Structures, Huntsville, Alabama, USA.

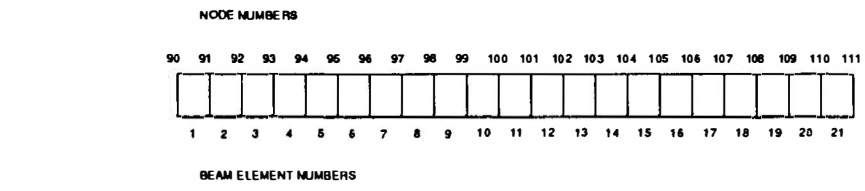


Fig 1. Beam model.

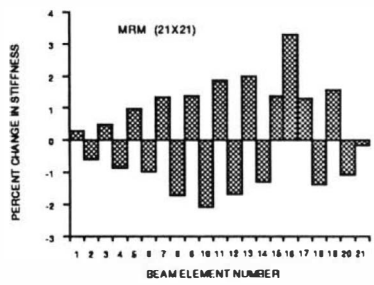


Fig 2. Localization of 5% increase in stiffness of element 16 using poles and driving point zeros.

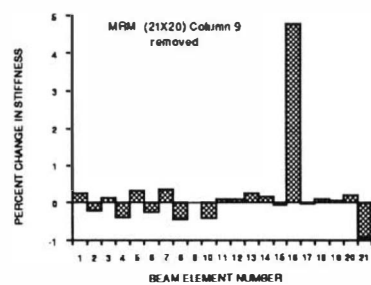


Fig 3. Localization of 5% increase in stiffness of element 16 using poles and driving point zeros.

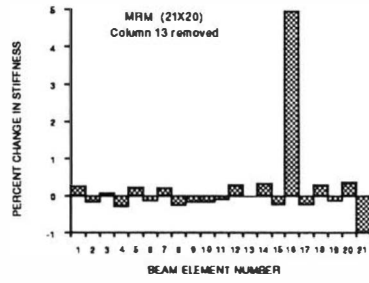


Fig. 4. Localization of 5% increase in stiffness in element 16 using poles and driving point zeros.

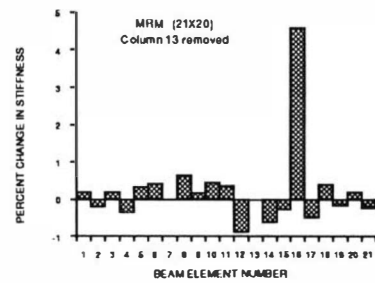


Fig. 5. Localization of 5% increase in stiffness of element 16 using poles, driving point zeros, and cross zeros.

## FEATURE RECOGNITION OF TWO-DIMENSIONAL OBJECT SCENES USING CONTOUR CURVATURE REPRESENTATION

S. Udomkesmalee

*Jet Propulsion Laboratory, California Institute of Technology, 4800 Oak Grove Drive,  
Mail Stop 198-326, Pasadena, CA 91109, USA*

**Abstract.** The contour curvature representation of object shapes yields a scale- and/or rotation-invariant model-matching technique for object recognition problems. General characteristics associated with the proposed curvature function are discussed. In addition, an algorithm for computing the curvature function and recognizing object shapes is derived, and numerical results confirming the feasibility of shape recognition based on the proposed algorithm are shown. Finally, a general feature-tracking formulation for celestial bodies, such as comets and asteroids, is presented.

**Keywords.** Pattern recognition; contour curvature; feature extraction; Fourier transform; least-squares estimation.

### INTRODUCTION

Although the analytical groundwork for understanding two-dimensional object images (Duda and Hart, 1973; Horn, 1986) has been established, a generic autonomous vision system (autonomous tracker) for guidance, navigation, and control applications in aerospace has not yet been realized. With growing complexities in the flight missions and science experiments of deep space exploration, the need for developing intelligent autonomous systems for space exploration has become critical in order to optimize flight operation and performance. In this paper, we present the use of contour curvature for shape recognition, which represents an appropriate step toward realizing autonomous feature-recognition systems for closed-loop tracking applications. By incorporating model-matching operations for an object's boundary points (the operations can be accomplished via one-dimensional functional representations instead of the typical two-dimensional correlation templates), we potentially optimize onboard memory/processing and the ground/operator interface.

The idea of using curvature functions for object recognition has been suggested (Perkins, 1978; Segen, 1983; Shirai, 1975). However, these past explorations did not fully exploit the rotation-invariant and similarity-in-scale characteristics of contour curvature. In this paper, the use of contour curvature for shape recognition is reexamined. A more robust definition of the curvature function, in terms of function differentials instead of the usual approximation by angle differences between chords drawn from a center point to a fixed distance on either side, is employed. In addition to the spectrum-based methodology for model matching, the method for extracting scale and rotation information about objects from the curvature function is presented.

Because the proposed robust algorithm for computing the curvature function based on a cubic polynomial curve-fitting scheme directly provides an edge-smoothing effect which could be required for objects with rough surfaces such as comets or asteroids, we present a formulation to handle partial viewing of target features with unknown scale and rotation.

### CONTOUR CURVATURE REPRESENTATION

A two-dimensional object shape can be represented simply in terms of boundary points. This set of points can be described parametrically by

$$T(x,y) = \{x(s), y(s)\}, \quad (1)$$

where  $s$  represents the tracing distance along the boundary curve  $T(x,y)$ ; see Fig. 1. Thus, the curvature function of the curve  $T$  defined on the  $xy$ -plane is given by

$$C(s) = (d^2x/ds^2)^2 + (d^2y/ds^2)^2. \quad (2)$$

Furthermore, assuming that the first- and second-order derivatives of  $y(x)$  and  $x(y)$  exist, it can easily be shown that

$$\begin{aligned} C(s) &= [d\psi/ds]^2 = [D_x^2 y]^2/[1+(D_x y)^2]^3 \\ &= [D_y^2 x]^2/[1+(D_y x)^2]^3, \end{aligned} \quad (3)$$

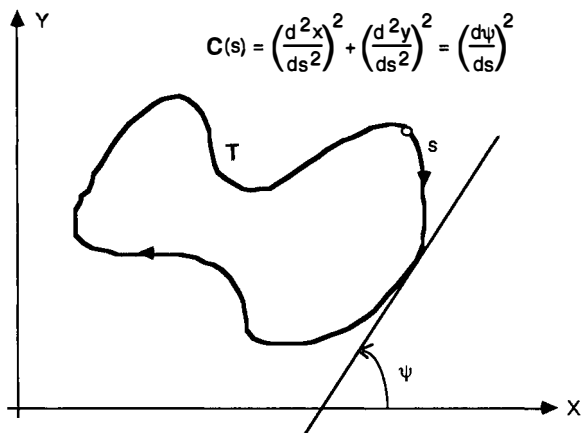


Fig. 1. Graphical Description of Contour Curvature.

where  $D_x y = dy/dx$ ,  $D_x^2 y = d^2y/dx^2$ ,  $D_y x = dx/dy$ ,  $D_y^2 x = d^2x/dy^2$ .

Note that  $C(s)$  has the following properties:

*Periodicity:*  $C(s+nS) = C(s)$ ;  
 $n = 0, 1, 2, \dots$  and  $S$  denotes the perimeter.

*Rotation Invariance:*  $C[R_\theta T(x,y)] = C[T(x,y)] = C(s)$ ;  
 $R_\theta$  is the rotation operator.

*Similarity:*  $C[T(rx,ry)] = C(rs)$ .

The obvious periodicity characteristic of the curvature function permits the starting point, i.e., zero value of the perimeter variable  $s$ , to be defined anywhere along the boundary curve. This means one need not fix a starting point, nor major axes, for geometrical feature extraction or recognition. The periodicity of  $C(s)$  also allows an efficient matching of curvature data by exploiting the shift-invariant property of the discrete Fourier transform.

The rotation-invariant and similarity-in-scale properties of  $C(s)$  authenticate the use of contour curvature as the geometrical representation of objects. By normalizing the parameter  $s$  to the object's perimeter  $S$ , a one-dimensional, scale- and rotation-invariant representation of an object shape is achieved. This new perspective on the curvature function is invaluable. By virtue of bypassing the standard time-consuming operation of matching the object to all possible scale and orientation forms, we can now achieve 1-D representation of any 2-D object image, irrespective of scale and orientation, in less time than ever thought possible.

By examining the curvature function  $C(s)$ , geometrical features such as lines, corners, and circular arcs can be extracted; see Fig. 2. Curve segments corresponding to lines produce zero curvatures; circles produce constant curvatures ( $1/R^2$  where  $R$  is the radius); and corners mean sharp peaks in the curvature function; see Fig. 3.

Furthermore, information regarding the object orientation ( $\theta$ ) can be estimated by comparing differences in the curvature angles ( $\psi$ ) of the object and a reference (model) at the same point along the boundary. This can be achieved by estimating the linear shift between the image and model. The detailed algorithm for estimating  $\theta$  is described in the next section.

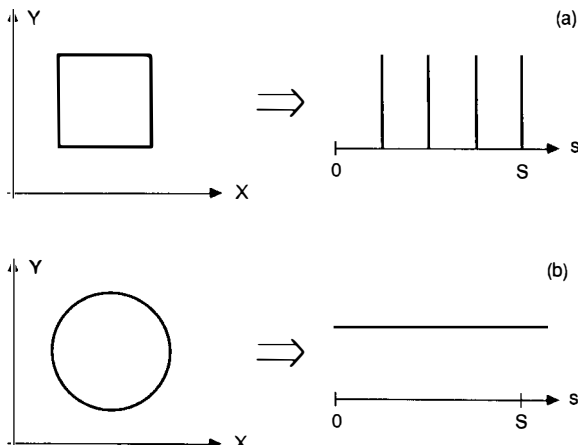


Fig. 2. Curvature Function of (a) a Square and (b) a Circle.

## COMPUTATION OF THE CURVATURE FUNCTION

Given a set of  $xy$ -pairs representing the boundary points in proper sequence (by tracing along the boundary points), the contour curvature, Eq. (2), which is based on some neighborhood points, can be estimated by using the expression in Eq. (3). Because of the closed-curve characteristic, there is a portion of the function which contains points where  $y(x)$  would be multi-valued while  $x(y)$  would be single-valued and vice-versa. In this situation, it is necessary to use that function description (either  $y(x)$  or  $x(y)$ ) which remains single-valued. Let's consider the case where  $C(s)$  at  $(x_k, y_k)$  point is computed from  $y(x)$ :

$$\tilde{y}_i = a\tilde{x}_i + b\tilde{x}_i^2 + c\tilde{x}_i^3; \quad i = k-M, \dots, k, \dots, k+M; \quad (4)$$

where  $\tilde{x}_i = x_i - x_k$ , and  $\tilde{y} = y_i - y_k$ .

Here, a least-squares technique can accurately estimate  $C(s)$  given a few neighborhood points ( $\pm M$ ) around the center point. Thus, it can be shown that the curvature at  $(x_k, y_k)$  is simply

$$C(s_k) = 4a^2/[1+b^2]^3. \quad (5)$$

The least-squares solution for coefficients  $[a, b, c]$  for the  $2M+1$  data points centered at  $(x_k, y_k)$  can be shown to be

$$\hat{a} = (A_{11}\Sigma\tilde{x}\tilde{y} - A_{21}\Sigma\tilde{x}^2\tilde{y} + A_{31}\Sigma\tilde{x}^3\tilde{y})/\Delta, \quad (6)$$

$$\hat{b} = (-A_{21}\Sigma\tilde{x}\tilde{y} + A_{22}\Sigma\tilde{x}^2\tilde{y} - A_{32}\Sigma\tilde{x}^3\tilde{y})/\Delta, \quad (7)$$

$$\hat{c} = (A_{31}\Sigma\tilde{x}\tilde{y} - A_{32}\Sigma\tilde{x}^2\tilde{y} + A_{33}\Sigma\tilde{x}^3\tilde{y})/\Delta, \quad (8)$$

where

$$\Delta = A_{11}\Sigma\tilde{x}^2 - A_{21}\Sigma\tilde{x}^3 - A_{31}\Sigma\tilde{x}^4, \quad (9)$$

$$A_{11} = \Sigma\tilde{x}^4\Sigma\tilde{x}^6 - \Sigma\tilde{x}^5\Sigma\tilde{x}^5, \quad (10)$$

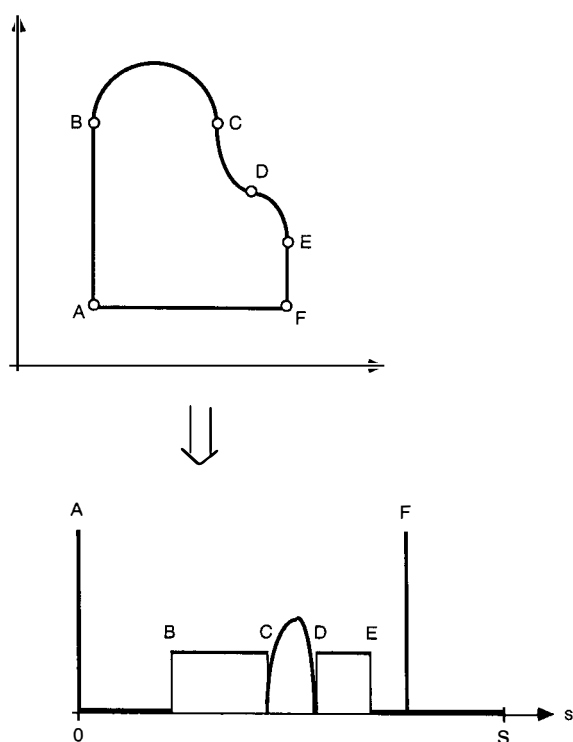


Fig. 3. Curvature Function of a Complex Geometrical Shape.

$$A_{21} = \sum \tilde{x}^3 \sum \tilde{x}^6 - \sum \tilde{x}^4 \sum \tilde{x}^5, \quad (11)$$

$$A_{31} = \sum \tilde{x}^3 \sum \tilde{x}^5 - \sum \tilde{x}^4 \sum \tilde{x}^4, \quad (12)$$

$$A_{22} = \sum \tilde{x}^2 \sum \tilde{x}^6 - \sum \tilde{x}^4 \sum \tilde{x}^4, \quad (13)$$

$$A_{32} = \sum \tilde{x}^2 \sum \tilde{x}^5 - \sum \tilde{x}^3 \sum \tilde{x}^4, \quad (14)$$

$$A_{33} = \sum \tilde{x}^2 \sum \tilde{x}^4 - \sum \tilde{x}^3 \sum \tilde{x}^3. \quad (15)$$

The parameter  $s$  and  $\psi$  at  $(x_k, y_k)$  can be computed recursively:

$$s_k = s_{k+1} + \sqrt{1 + \hat{a}^2} |x_{k+1} - x_k|, \quad (16)$$

$$\psi_k = \tan^{-1}(\hat{a}). \quad (17)$$

Note that when  $C(s)$  must be computed from  $x(y)$ , the above set of Eqs. (4)-(17) can still be applied by simply interchanging  $x_i$  and  $y_i$ .

Since we must choose between the function definition of either  $y(x)$  or  $x(y)$  for calculating  $C(s)$ , a criterion that can accommodate several changes of direction (this is typical of noisy-edge images) inside the  $2M+1$  window must be established. Let's define the gradient arrays  $\{\dot{x}_k\}$  and  $\{\dot{y}_k\}$  by

$$\dot{x}_k = \begin{cases} 1 & \text{if } x_{k+1} > x_k \\ 0 & \text{if } x_{k+1} = x_k \\ -1 & \text{if } x_{k+1} < x_k \end{cases}, \quad (18)$$

$$\dot{y}_k = \begin{cases} 1 & \text{if } y_{k+1} > y_k \\ 0 & \text{if } y_{k+1} = y_k \\ -1 & \text{if } y_{k+1} < y_k \end{cases}. \quad (19)$$

Based on  $\{\dot{x}_k\}$  and  $\{\dot{y}_k\}$ , the overall directional changes in  $x$  and  $y$  at  $s_k$  can be summarized by

$$\dot{X}_k = \sum_{k-M}^{k+M} \dot{x}_i, \quad (20)$$

$$\dot{Y}_k = \sum_{k-M}^{k+M} \dot{y}_i. \quad (21)$$

Thus the axis that provides the minimum number of directional changes is selected as the independent axis, i.e., at  $s$ , use  $y(x)$  if  $|\dot{X}_k| \geq |\dot{Y}_k|$ , and use  $x(y)$  if  $|\dot{X}_k| < |\dot{Y}_k|$ .

Another unique situation that must be addressed is the  $90^\circ$  corner that aligns with the  $xy$ -axes. To avoid the averaging effect at the multi-valued point of the least-squares polynomial, Eq. (4), a small perturbation ( $\delta$ ) can be added to those series of points inside the  $2M+1$  window; see Fig. 4. Furthermore, any curled-back point inside this window should be discarded as a bad data point.

Finally, the parameter "s" is critical for accurate estimation of an object perimeter ( $S$ ). Since the boundary edges are quite sensitive to the digitization error introduced by integer pixel values, the boundary curve can be further smoothed by replacing the next boundary point by the estimated values ( $\hat{y}_{k+1}$ ) based on the polynomial fit at  $(x_k, y_k)$ , i.e.,

$$\hat{y}_{k+1} = \hat{y}_k + \hat{a}(x_{k+1} - x_k) + \hat{b}(x_{k+1} - x_k)^2 + \hat{c}(x_{k+1} - x_k)^3. \quad (22)$$

Because of the availability of  $\{\hat{a}, \hat{b}, \hat{c}\}$ , this smoothing step can be achieved with minimal computational cost during the proposed curvature-function calculation. Furthermore, the use of smoothed boundary points  $\{\hat{x}_k, \hat{y}_k\}$  is preferred over the raw boundary point  $\{x_k, y_k\}$  in terms of robustness and noise-suppression aspects.

## MODEL-MATCHING METHOD

The proposed curvature function  $C(s)$  is well-suited for image interpretation predicated on the knowledge-based technique (Symosek and colleagues, 1987), where symbolic image features are matched with a database organized by a set of rules to produce meaningful results. However, objects with similar low-level features or objects without distinct features (lines, corners, and circular arcs) readily recognized in the curvature function, would require a matching technique of comparing various models with image curvatures to determine the object class.

Let  $C_R(s)$  be a perimeter-normalized curvature function of a reference model and  $C_I(s)$  be a computed normalized curvature function, i.e.,  $C_R(s)$  is sampled to match the number of discrete points in  $C_I(s)$ . Since  $C_I(s)$  could have a different starting point from  $C_R(s)$  because they could be different in orientation, matching  $C_I(s)$  with  $C_R(s)$  could be achieved by a circular shift of the  $C_I(s)$  sequence by  $\sigma$ , where  $\sigma$  is computed from the following minimization criterion:

$$J_R = \min_{\sigma} \sum [C_R(s) - C_I(s+\sigma)]^2. \quad (23)$$

This operation can be done in  $N^2$  time for each model. However, by finding the smallest  $L^2$  norm in the Fourier domain, the fast Fourier transform (FFT) algorithm can be employed. (Note that the FFT algorithm accomplishes the equivalent minimization task of Eq. (23) in  $N \log N$  time.) Furthermore, exploiting the shift-invariant property of the power spectrum,  $C_R(s)$  and  $C_I(s)$  can be matched independent of  $\sigma$ , i.e.,

$$J_R = \sum [P_R(\omega) - P_I(\omega)]^2, \quad (24)$$

where  $P_R(\omega)$  and  $P_I(\omega)$  represent the power spectrum of  $C_R(s)$  and  $C_I(s)$ .

Thus, given a finite number of models to be matched with the input image, the model that produces the smallest  $L^2$  norm, Eq. (24), is selected. In addition, the circular shift  $\sigma$  can be easily computed, realizing that

$$\mathcal{F}\{C(s+\sigma)\} = e^{j\omega\sigma} \mathcal{F}\{C(s)\}. \quad (25)$$

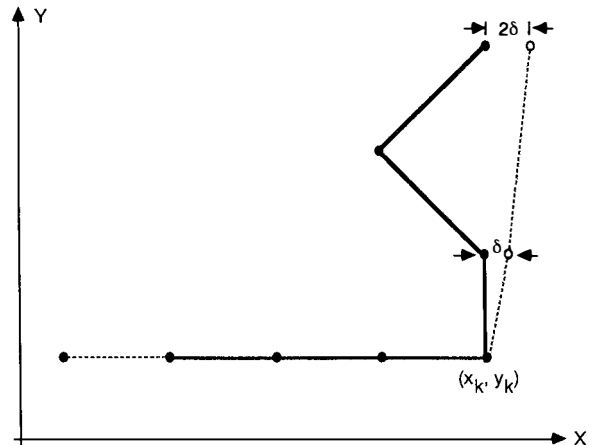


Fig. 4. The Perturbation Technique for a Multi-valued Function Region.

Therefore, if  $\phi_R(\omega)$  represents the phase of the selected model, and  $\phi_I(\omega)$  represents the phase of the object,  $\sigma$  satisfies

$$\phi_R(\omega) = \pm\phi_I(\omega) - \omega\sigma. \quad (26)$$

Note that the sign ambiguity in  $\phi_I(\omega)$ , which is easily resolved, stems from the fact that boundary tracing of the object can be in the opposite direction of model boundary tracing. Based on Eq. (26), the amount of shift  $\sigma$  can easily be estimated from a few data points taken from the Fourier plane. Once  $\sigma$  is known, the object orientation can be estimated from the curvature angles:

$$\hat{\theta} = \psi_R(s) - \psi_I(s+\sigma^*). \quad (27)$$

Note that the definition of  $\psi$  is translation-invariant, and the ambiguity interval of  $\psi$ , as configured in Fig. 1, is  $180^\circ$ . Therefore, any orientation above  $180^\circ$  will be folded back to the  $0^\circ$ - $180^\circ$  range. However, if the origin of the xy-axes lies inside the object boundary, then a full  $360^\circ$  range can be realized. Thus, the object shape can be reconstructed, given the curvature function pair of  $C(s)$  and  $\psi(s)$ ; this topic will be addressed in future work.

Finally, the scale factor ( $r$ ) can be computed from the calculated perimeters of object and model, i.e.,

$$\hat{r} \approx S_I/S_R. \quad (28)$$

## NUMERICAL RESULTS

Digitized images (128 by 128 frames) of two object shapes (A and B) are used; see Fig. 5. The object images are rescaled and rotated, boundary points are traced, and the corresponding curvature functions are computed with  $M = 3$ ; see Figs. 6 and 7. Note that Figs. 6 and 7 are plotted with a line plotter, and the object shapes shown at the top of Figs. 6(a), 6(b), 7(a), and 7(b) only approximate the digitized images since the outlines connect pixel-midpoints instead of tracing around the square pixels. However, the curvature functions are computed based on the correct digitized images.

The scale- and rotation-invariant characteristics are demonstrated in Figs. 6 and 7. Scale-invariant plots of  $C(s)$  are achieved by the suggested perimeter-normalization technique; 128 equally spaced points along the  $s$ -axis are achieved by means of a linear interpolation technique. Furthermore, these numerical results compare reasonably well to the theoretical curvatures shown in Fig. 3, with the exception of small ambiguities (noise) due to digitization of object images and the smoothing aspect of the cubic least-squares fit; and these ambiguities do not affect the proper positioning of the distinct features.

Finally, the model-matching technique based on the power spectrum (see Fig. 8) and the estimated scale ( $r$ ) and orientation ( $\theta$ ) are summarized in Table I. Thus, the discrimination between the two objects can be easily achieved using the computed cost ( $J$ ). Furthermore, the predicted scale and orientation match the actual values almost exactly. The scale factors are predicted according to Eq. (28) using the estimated perimeters. For the orientation estimates, the computed angle differences are averaged over a particular segment -- the AB segment (as shown in Figs. 6 and 7). In our example it can be shown that the best results are achieved using a line segment. It should be noted that the scale and orientation estimates for the case where the model and the input are mismatched are irrelevant, and thus omitted.

## AUTONOMOUS FEATURE-TRACKING APPLICATIONS

The planetary mission, such as the Comet Rendezvous Asteroid Flyby (CRAF), which was designed to explore

and survey the physical properties and chemical composition of a comet and an asteroid, requires an autonomous tracking operation of a high level in order to achieve its science objectives. By requiring the spacecraft tracking instruments to rapidly and accurately point to any particular feature on the comet/asteroid, a conventional mo-

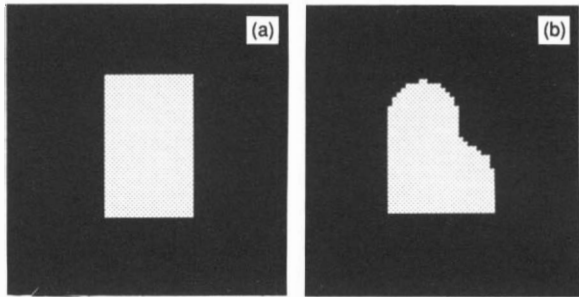


Fig. 5. Top Views of (a) Object A and (b) Object B.

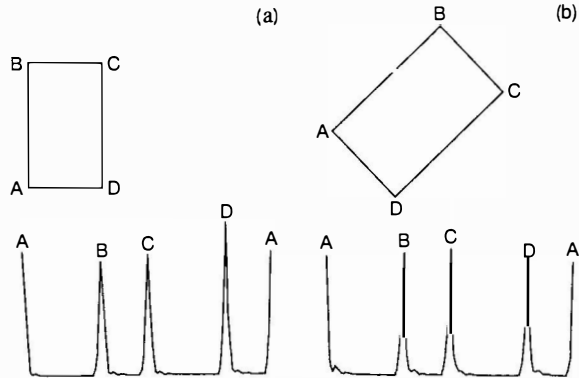


Fig. 6. Computed Curvature Functions of Object A at (a)  $r = 1$ ,  $\theta = 0^\circ$  and (b)  $r = 1.2$ ,  $\theta = 45^\circ$ .

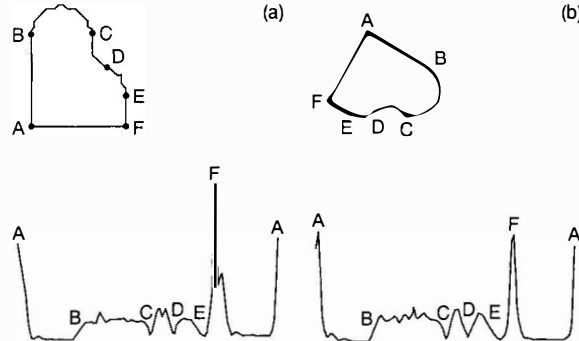


Fig. 7. Computed Curvature Functions of Object B at (a)  $r = 1$ ,  $\theta = 0^\circ$  and (b)  $r = 0.8$ ,  $\theta = 120^\circ$ .

Table 1. Classification Results and Scale/Orientation Estimates

INPUT MODEL	Object A	Object B
	$r = 1.2$ $\theta = 45^\circ$	$r = 0.8$ $\theta = 120^\circ$
Object A $r = 1.0$ $\theta = 0^\circ$	$J = 0.039$ $\hat{r} = 1.21$ $\hat{\theta} = 45.1^\circ$	$J = 1.872$
Object B $r = 1.0$ $\theta = 0^\circ$	$J = 0.849$	$J = 0.025$ $\hat{r} = 0.785$ $\hat{\theta} = 119.8^\circ$

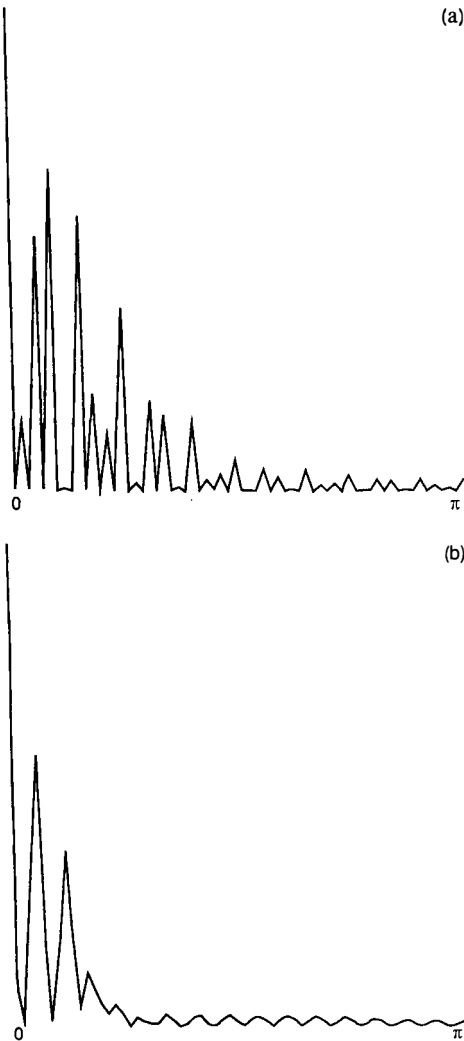


Fig. 8. Curvature Power Spectrum of (a) Object A and (b) Object B.

saicking approach, which is very slow and requires handling of an enormous amount of data, is no longer practical. The additional requirement of properly identifying the planetary features during orbit allows accurate determination of spacecraft attitude and position relative to the target, thus permitting autonomous navigation to optimize space mission control operation.

Fig. 9 depicts an artist's rendering of the CRAF spacecraft orbiting the nucleus of Comet Tempel-2; it also depicts asteroid 951 Gaspra and planetary features of Venus. These types of imagery can be expected for CRAF tracking applications. Thus, the tracking algorithm must be able to quickly handle changes in the scale, rotation, aspect angles, and illumination of the scene. Furthermore, not only is continuous viewing not available due to comet dust/coma and time-sharing of the science camera, only portions of reference features, e.g., craters and limbs, may be apparent during viewing. None of the currently used target detection and recognition algorithms (Casasent, 1987) is applicable for this type of tracking application.

The proposed contour curvature methodology could be modified for CRAF applications. However, the image-processing aspect, which primarily involves background suppression, contrast/edge enhancement, cluster detection, boundary tracing, and segmentation, will not be addressed. Our primary focus in this paper is on the basic foundation of the recognition process -- geometrical representation of objects and recognition algorithms -- and the low-level classification dealing only with object shapes and outlines.

Hence, given a series of one-dimensional curvature functions (open contours can be generated) extracted from various features in a given scene,  $\{C_i(s), i = 1, 2, \dots, N\}$ , the following algorithm can be employed for identifying desired features:

*Step 1. Line, corner, and curve screening:* Given some *a priori* specifications on the feature of interest, undesired elements of the sequence  $\{C_i(s), i = 1, 2, \dots, N\}$  can be filtered out by specifying acceptable thresholds for  $C_i(s)$ . For example, if the line features are desired,  $C_i(s)$  must be near zero, and for elliptical craters,  $C_i(s)$  can be bounded by upper and lower limits.

*Step 2. Partial Curvature Matching:* Even if  $C_i(s)$  is an open contour, we can still match  $C_i(s)$  to some selected model  $C_R(s)$  by

$$J_R = \min_{(\tau, \sigma)} \sum_{0 < \tau \leq 1} (C_R(s) - C_j(\tau[s+\sigma]))^2; \quad (29)$$

Thus, by forcing  $C_i(s)$  and  $C_R(s)$  to have the same number of discrete points,  $C_i(s)$  can be matched to some segment along  $C_R(s)$ .

*Step 3. Detection Criterion:* Since  $J_R$  also provides a measure of closeness between  $C_i(s)$  and  $C_R(s)$ , the simplest criterion would be to select the model that yields the smallest  $J_R$ . Note that  $J_R$  should also be normalized by some factor to prevent numerical biases caused by large curvature values. More work is required in this area. Moreover, formulation for the detection criterion at this step can easily be extended to include general statistical decision theory (Blackwell and Girshick, 1954) or even fuzzy mathematics (Zadeh, 1965).

*Step 4. Model Update:* Once the desired feature is detected in a given scene, it is beneficial to update the model  $C_R(s)$  for future use by the correctly identified  $C_i(s)$ . This added intelligence is essential to the designing of autonomous vision systems. Thus, we can envision a knowledge-based system capable of using actual observations in a particular application to evolve *a priori* representation of object shapes (e.g., lines, rectangles, ellipses) to a more complex geometry that also includes various indentations and distortions along the outlines.

Note that shape distortions due to viewing an object from different angles could be parameterized for relatively planar features such as craters and riverbeds. For 3-dimensional sensitive features such as comet/asteroid limb features, a number of  $C_R$  models would be required for various viewing perspectives. This would not be quite as troublesome as it would appear to be, since  $C_R$  is merely a 1-dimensional function and could be parameterized or compressed for efficient memory storage.

## CONCLUSION

The advantages of using contour curvature for shape recognition are overwhelming. In comparison to the widely used Hough transform (Hough, 1962) and modified Hough transform (Ballard, 1981), the curvature function provides a one-dimensional representation of object geometry that allows immediate deduction of lines and corner and circular arc features without having to analyze a multi-dimensional transform space for each particular shape, as in the case of the Hough transform. Furthermore, in addition to achieving scale- and/or rotation-invariant model-matching, the proposed algorithm makes information in regards to objects' scales and orientations readily available.

The problem of not having a closed contour due to occlusion or partial viewing has been addressed. Continuing research into the applications of the proposed curvature function is needed. In addition, the advantages of being able to reconstruct object shapes from the curva-

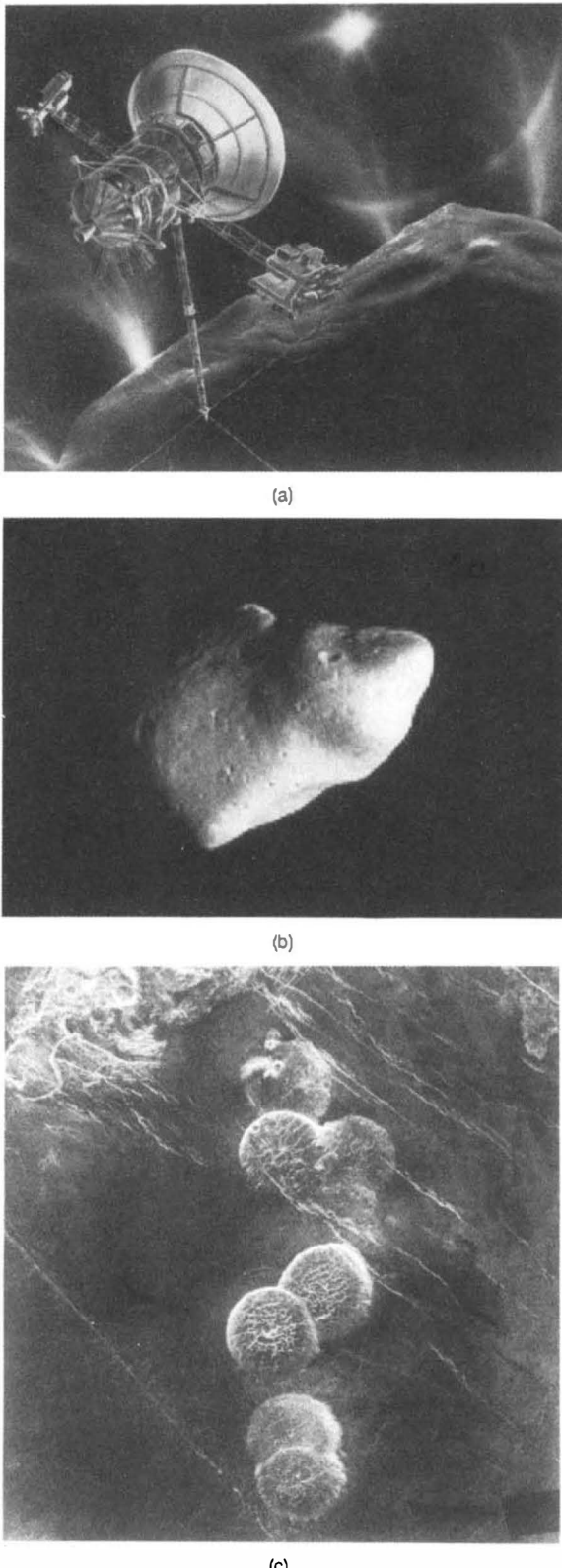


Fig. 9. Feature-tracking Applications: (a) Comet Rendezvous Asteroid Flyby (CRAF) Mission, (b) Asteroid 951 Gaspra, and (c) Planetary Features of Venus.

ture function  $C(s)$  used in conjunction with the curvature angle  $\psi(s)$  should be explored.

In conclusion, the proposed methodology is the most practical and efficient concept for recognizing features and object shapes given a broad spectrum of two-dimensional object images.

#### ACKNOWLEDGMENTS

This research was partly performed at the Jet Propulsion Laboratory, California Institute of Technology, under a contract with the National Aeronautics and Space Administration.

#### REFERENCES

- Ballard, D. H. (1981). Generalizing the Hough transform to detect arbitrary shapes. *Pattern Recogn.*, 13(2), 111-122.
- Blackwell, D., and M. A. Girshick (1954). *Theory of Games and Statistical Decisions*. John Wiley & Sons, New York.
- Casasent, D. (1987). Electro-optic target detection and object recognition. In *Proc. SPIE*, Vol. 762 (electro-optical imaging systems integration). Society of Photo-optical Instrumentation Engineers, Bellingham, Washington. pp. 104-125.
- Duda, R. O., and P. E. Hart (1973). *Pattern Classification and Scene Analysis*. John Wiley & Sons, New York.
- Horn, B. K. P. (1986). *Robot Vision*. MIT Press, Cambridge, Massachusetts.
- Hough, P. V. C. (1962). *Methods and means for recognizing complex patterns*. U.S. Patent 3,069,654. Office of Public Affairs, Patent and Trademark Office, Washington, D.C.
- Perkins, W. A. (1978). A model-based vision system for industrial parts. *IEEE Trans. Comput.*, C-27, 126-143.
- Segen, J. (1983). Locating randomly oriented objects from partial view. In *Proc. SPIE*, Vol. 449 (3rd Int. Conf. on Robot Vision and Sensory Controls), Part 2. Society of Photo-optical Instrumentation Engineers, Bellingham, Washington. pp. 676-684.
- Shirai, Y. (1975). Edge finding, segmentation of edges and recognition of complex objects. In *4th Int. Joint Conf. on Artificial Intelligence*. Morgan Kaufmann Publishers, Inc., San Mateo, California. pp. 674-681.
- Symosek, P., D. Panda, S. Yalamanchili, and W. Wehner III (July 1, 1987). Knowledge-based vision for space station object motion detection, recognition, and tracking. In *Proceedings of the Workshop on Space Telerobotics*, JPL Publication 87-13, Vol. 2. Jet Propulsion Laboratory, Pasadena, California. pp. 9-18.
- Zadeh, L. A. (1965). Fuzzy sets. *Inform. and Control*, 8, pp. 338-353.

# THE POINTING STABILITY OF THE HUBBLE SPACE TELESCOPE AND PROPOSED CONCEPTS FOR THE POINTING CONTROL OF THE NEXT GENERATION SPACE TELESCOPE (NGST)

P.Y. Bély\*,<sup>1</sup> and B.S. May\*\*

\*Space Telescope Science Institute, 3700 San Martin Drive, Baltimore, MD 21218, USA

\*\*Department of Civil Engineering, The Johns Hopkins University, Baltimore, MD 21218, USA

## Abstract

The on-orbit pointing performance of the Hubble Space Telescope is presented. Essentially all of the line of sight jitter is due to a rigid body motion of the main body of the satellite by reaction against its flexible solar arrays. Jitter caused by internal vibration is negligible. NGST, HST's possible successor, is a much larger observatory which will require a gain of an order of magnitude in pointing stability. It is shown how the use of a high orbit, changes in the telescope configuration, and the incorporation of active optics can bring about such an improvement.

**Keywords:** Space Astronomical Observatories; Active Optics; Pointing Control Systems; Wavefront Sensing.

## Introduction

Astronomical observations from the ground are severely affected by atmospheric turbulence and transparency which degrade images and limit the spectral coverage. From the very start of the space program, astronomers found great advantage in observing from outside the atmosphere. The first astronomy missions which explored the spectral bands unobservable from the ground (UV, IR and X-ray) were enormously productive. In the optical range as well, a space telescope offers enormous advantages, providing resolution unattainable from even the best observatory sites on earth. This combination of high resolution and broad spectral coverage is the apanage of space, and the motivation behind the NASA/ESA Hubble Space Telescope (HST) and future astronomical space observatories.

The resolution of a telescope with an aperture of diameter  $D$ , and operating at the wavelength  $\lambda$ , is given by the Rayleigh criterion  $1.22\lambda/D$ . Thus, the larger the aperture and the shorter the wavelength (e.g. UV), the more accurate the pointing and tracking of a telescope need to be in order not to degrade the quality of the image. Typically, a diffraction-limited space telescope will have to track one to two orders of magnitude more precisely than the atmospheric-limited ground equivalent. This has been one of the main challenges for HST, as it will also be for its envisaged successor, the Next Generation Space Telescope (NGST).

In this paper we examine how HST has met its pointing stability requirements and, building on this experience, propose approaches to meet the challenges posed by its successor.

## State of the art: the Hubble Space Telescope

Heir of surveillance spacecraft and twenty years in the making, the Hubble Space Telescope represents, in many aspects, the culmination of current engineering technology. This is particularly embodied in the telescope's pointing quality, the goals of which were the highest ever set for an astronomical telescope or civilian spacecraft. The pointing specifications for HST were based on the criteria that line of sight tracking errors should not degrade the image size of its diffraction-limited optics by more than 10%, translating into a stability of 0.007 arcseconds over a 24 hour period.

To achieve this goal, the basic philosophy was to rely on an essentially passive system and to isolate as much as possible the heart of the observatory from thermal and mechanical disturbances. The optical telescope assembly (OTA), which contains the telescope proper, the fine guidance system and the science instruments, is kinematically mounted inside the Space Support Module (SSM) which protects the OTA from orbital thermal variations. All the main active devices (reaction wheels, mobile antennae and tape recorders) are installed on the outer body. The only active elements on the OTA are those indispensable to the operation of the science instruments (beam

<sup>1</sup> Affiliated to the Astrophysics Division, Space Science Department, European Space Agency.

switcher, filter wheels) and the fine guidance system (star selectors).

Pointing is accomplished through movement of the spacecraft as a whole using reaction wheels, and is designed around a double feedback loop (Dougherty et al, 1982). The principal loop operates at 40 Hz and relies on inertial attitude sensing by gyroscopes. The second loop, operating at 1 Hz, senses the changes in the line of sight by measuring the position of two stars in the field surrounding the target, and corrects any drift in the inertial sensing.

Before launch, all active components were individually tested and modified as required to suppress potential sources of vibration. Finally, a system level test aimed at verifying the intrinsic "quietness" of HST was performed on the fully assembled spacecraft (except for the solar arrays), by suspending it from an isolating air bag and exercising all active components. Since it was not possible to measure the optics directly, the line of sight jitter was derived from accelerometer data. This test indicated that the pointing stability on orbit would meet the specifications.

#### On-orbit tracking performance of HST

HST pointing jitter is routinely measured using telemetry data from the gyros and the Fine Guidance System (FGS), but this measurement is limited to about 20 Hz and does not represent the true image motion seen by the scientific instruments. To obtain a more complete picture, a dedicated test was executed in January 1992 using the High Speed Photometer (HSP), which is capable of a very high sampling rate. A bright star (known to have no short term variability) was placed on the edge of a large aperture of the HSP and the flux integrated and recorded every millisecond. The flux fluctuates as the star moves in and out of the unocculted portion of the aperture and is a direct measure of the line of sight jitter caused either by the motion of HST as a whole or by internal vibrations affecting the optical train. The test had a sensitivity on the order of 0.2 milliarcsecond and covered frequencies up to 500 Hz (Nyquist frequency). Typical results of the test can be summarized by Figure 1 which is a plot of the power spectra of jitter versus time in one of the test segments and by Figure 2 which is a synthesized spectrum incorporating the maximum amplitudes measured at frequencies above 10 Hz.

Based on the results of the dedicated test and previous investigations, it can be inferred that HST's line of sight jitter has three main sources:

1. **Rigid body motion of the telescope.** This is the largest contributor by far. This results from the body of the spacecraft reacting against the oscillation of the very flexible solar arrays, which although very light, can represent up to 6% of the total inertia of the satellite depending on orientation. Most of the effect occurs at a frequency of 0.1 Hz, the fundamental mode of solar arrays in pitch and yaw. However, there is still significant power in the second solar array mode, which is an in-plane vibration with a frequency of 0.6 Hz and other modes up to about 2.5 Hz. These modes are impulsively excited every time the telescope is slewed to a new target, and a stabilization period of 100 seconds must be allowed before normal opera-

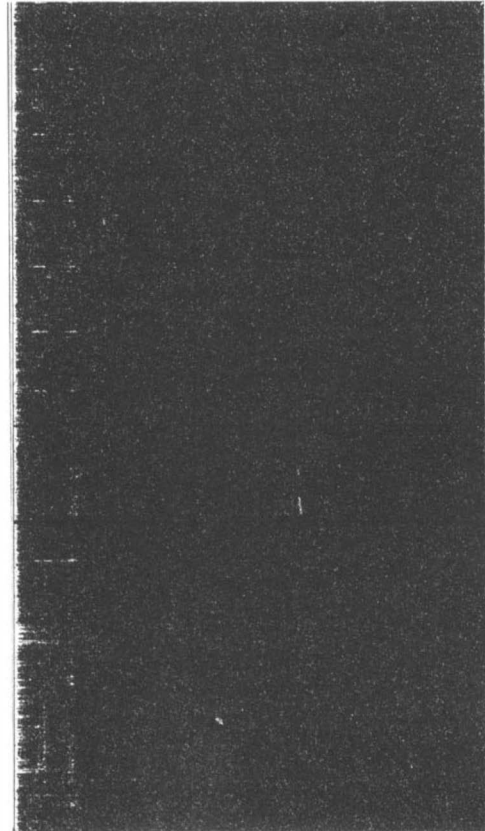


**Fig. 1.** This "image" is formed by stacking up the power spectra of the line of sight jitter over 1 second duration similar to the lines of a video image. Time runs vertically, and the duration of the test segment shown here is 639 seconds. The horizontal axis is frequency, extending from 0 at left to 500 Hz at right. The grey scale is proportional to the amplitude of the jitter, with white representing higher jitter. Most of the jitter occurs at frequencies lower than 10 Hz, but one can observe temporary excitations in the 20-30 Hz range and at about 60 Hz. There is also a trace at about 300 Hz which is an excitation created by the tape recorder.

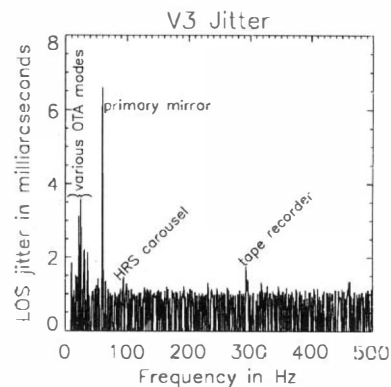


**Fig. 2.** Upper envelope of the power spectrum of the jitter experienced during the test. Frequencies less than 10 Hz are not shown. Specific features have been identified using the pre-launch computer model of HST.

tion can resume. Unfortunately, excitation of these modes also occurs at every passage from orbital day to orbital night and vice versa. This phenomenon, which was vastly underestimated in the design stage, is due to the thermal shock in the rods and deployment drum system supporting the solar array blankets. The pointing control soft-

ware has been tuned to minimize the effect, but the disturbance typically still reaches 200 milliarcseconds peak to peak, well above what is scientifically tolerable. More seriously, the effect often leads to a temporary loss of guide stars which interrupts observations for about 5 minutes.

2. *Flexible modes within the telescope.* Particularly noticeable are the vibration of the primary mirror tilting on its support (about 60 Hz), and various modes in the structure supporting the optics (primarily from 10 to 30 Hz). These modes appear to be excited by shocks induced by the solar arrays or possibly by thermal creaks within the outer structure (SSM). The corresponding vibrations are of very low amplitude (a few milliarcseconds), are quickly damped (in 1 second or less), and have virtually no effect on observations.
3. *Internal excitations propagating to the optical train.* In principle any active device on board such as reaction wheels, antennas, and tape recorders, as well as the mechanisms of the guiding systems and science instruments, are potential excitors. It is difficult to separate the influence of the reaction wheels from the background excitation created by the solar arrays because they are always operative and constantly changing speed. But of the other devices, only two could be identified: (i) the hunting of a filter/grating wheel in the High Resolution Spectrograph (HRS) which produces very momentary excitations around 90 Hz, and (ii) the differential gear in the tape recorder reels winding system which induces a continuous vibration in the 300 Hz frequency range while in use. In both cases, the amplitude of the corresponding line of sight jitter is barely detectable (1 to 2 milliarcseconds) and in practice negligible.

In conclusion, it can be said that HST's "passive" design philosophy which relied on minimizing internal and external excitations and on stiffening the structure to avoid interaction was essentially successful. If it currently fails to meet the original specifications, this is because of an oversight in the implementation of that philosophy regarding the solar arrays.

On the other hand, this failure points out the intrinsic limitation of this design philosophy: it is not resilient. Because it is difficult to fully test spacecraft in their operational environment before launch, enough flexibility should be incorporated to cope with potential diversions of the design parameters.

It is sad to realize that the two major technical problems of HST, the error in the primary mirror figure and the solar array disturbances, would be well within the corrective range of active optics now available for modern optical systems.

#### The Next Generation Space Telescope (NGST)

The Next Generation Space Telescope, planned for launch early in the next century, is intended to be a successor to the Hubble Space Telescope with improved light-collecting power, spectral coverage and spatial resolution. The scientific potential and technical aspects of this telescope have been reviewed in Bély, Burrows and

Illingworth (1989), and its importance has been identified most recently by the "Bahcall Report" (1991).

NGST will be more than just a large scale version of HST. The current baseline for NGST calls for a filled 8 meter aperture, passively-cooled, and diffraction-limited resolution for its entire spectral range, from the far UV (120 nm) to the near IR (10  $\mu\text{m}$ ). Diffraction-limited imaging in the UV requires a pointing stability of about 0.5 milliarcsecond which is an order of magnitude higher than HST's. To meet this challenging goal, we propose to build on HST's heritage, while augmenting its design philosophy as follows.

- Move to a *high earth orbit* in order to minimize the level of external torques and disturbances, and thus reduce the demand on the pointing control system.
- As in HST, maximize the *structure stiffness* in order to keep the natural frequencies of the spacecraft's main body well above the frequency range of most of the excitations.
- Use *active optics* to compensate for any remaining error in the line of sight.

#### High Earth Orbit

High earth orbits (geosynchronous or higher) offer overwhelming advantages for astronomical observatories in space (Neill et al, 1989). Long exposures can be accomplished without interruption and the absence of occultation by the earth allows an efficiency approaching 100% (compared to about 30% for low earth orbit). Because the earth subtends a small angle, baffling can be minimal. Heat input from earth albedo is also greatly reduced, permitting the telescope to be passively cooled down to the 100 K range for IR work.

High orbits are also very advantageous from the point of view of pointing stability. The thermal load is essentially constant, resulting in excellent dimensional stability. Gravity gradient and aerotorque are almost nonexistent, considerably reducing the demand on the pointing control system. Figure 3 illustrates this point by comparing the torques due to gravity gradient, aerodynamic and solar radiation for a spacecraft of NGST's size at various orbits.

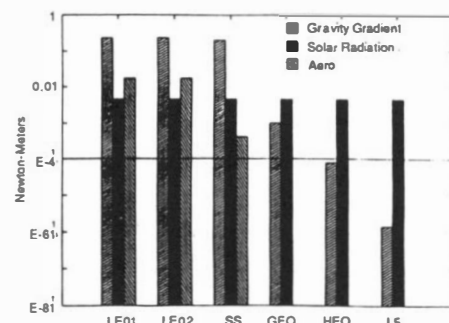


**Fig. 3.** Torques due to gravity gradient, aerodynamic and solar radiation for a spacecraft of NGST's size at various orbits. LEO1 and LEO2 are two typical low earth orbits of 600 km altitude with 28 and 5 degree orbit inclination respectively. SS is a sun-synchronous orbit of 900 km altitude, GEO a circular geosynchronous orbit, HEO a 4 day orbit at 100 000 km altitude (thus beyond the Van Allen belt), and LS is the Lagrangian point of the earth/moon system.

In high orbits the total torque is reduced by almost two orders of magnitude compared to low earth orbit. The earth's magnetic field cannot be used to dump reaction wheel momentum, but saturation can be avoided altogether by optimizing the sequence of observations in order to balance the direction of the solar pressure over time.

#### High stiffness structure

Our approach for obtaining a structure with high stiffness in spite of the large dimensions of NGST is as follows:

- Reduce the overall length of the telescope by relaxing the requirements concerning baffling against sun, moon and bright earth. As explained above, this is possible with little observational impact due to the selection of a high orbit.
- Use a single integrated structure instead of the "double structure" of HST. This design loses the protection and isolation offered by the outer shell, but this is not a serious drawback in the more benign environment of high earth orbit.
- Eliminate all appendages such as orientable solar arrays and antennae which inevitably have very low natural frequencies.

An artist's view of our proposed implementation is shown in Figure 4. The solar arrays are body-mounted and the communication antennae might possibly be of the phased-array type. Figure 5 shows the compactness of the proposed NGST design.

To verify that a minimum stiffness goal similar to that of HST could be met, the dynamic behavior of the supporting structure has been studied using the Algor finite-element code. The model is composed of the main structure truss, with lumped masses representing the outer shield, primary and secondary mirrors, scientific instruments, and space support equipment. The structure was optimized to lead to a fundamental frequency above 15 Hz while minimizing the overall mass. Various configurations were investigated, including a tripod type mount for the secondary mirror, and the best solution was found to be the truss shown in Figure 6. The first five mode shapes and frequencies of the main structure truss are listed in the following table.

Mode	Frequency (Hz)	Mode shape
1	15.5	ovalling
2	16.4	ovalling
3	17.0	torsion
4	17.6	bending/ovalling
5	17.8	bending/ovalling

With this design, the total mass of the observatory is 15 700 kg, including 3025 kg for the truss structure. The moment of inertia is 150 000 kg-m<sup>2</sup> around the line of sight and 428 000 kg-m<sup>2</sup> in the perpendicular direction. This compares very favorably to HST, which has a total mass of 11 000 kg, and a moment of inertia of 31 000 kg-m<sup>2</sup> around the optical axis and 78 000 kg-m<sup>2</sup> in the perpendicular direction.



Fig. 4. Artist view of NGST.

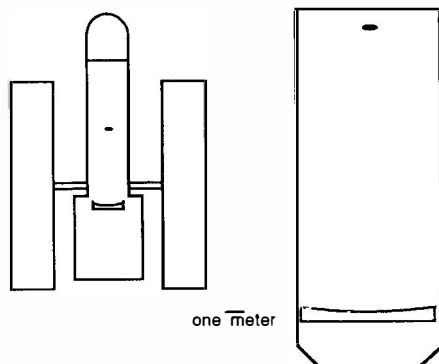


Fig. 5. HST and the proposed NGST shown at the same scale.

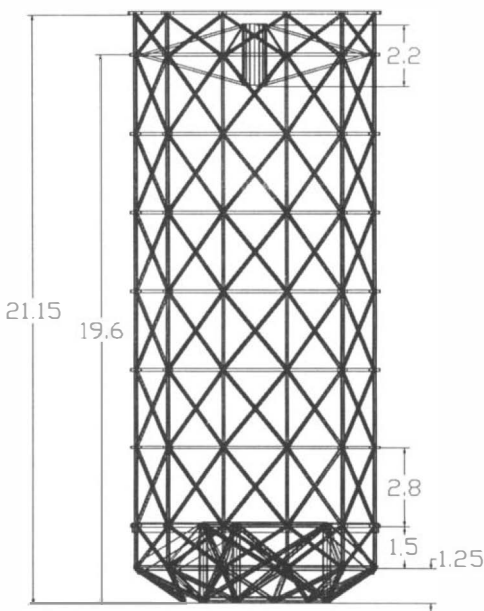


Fig. 6. Main structure truss.

### Active optics

The benefits of incorporating active optics in demanding optical systems increase dramatically as size augments. Stringent controllability of an "optical bench" weighing several tons is no longer necessary, since the light beam can easily be redirected through the active steering of one of the optical elements. The requirements on the support structure and associated positioning system are therefore greatly relaxed, and the structure can be allowed to deform and mispoint beyond the overall tolerance. Hence, the pointing control becomes a two-tiered system, composed of coarse "body pointing" for general targeting coupled with "beam steering" for fine correction of line of sight errors.

Active optics is typically accomplished by inserting an additional optical element dedicated to beam steering. For NGST, however, we propose to make the secondary mirror active so as to reduce the number of reflections in the system. The size of the secondary mirror is sufficiently small (30 cm) to allow such tip/tilt control at the low bandwidth considered, particularly if a "reactionless" system is used.

Concerning line of sight error measurement, it is essential that the light used for the guiding system travel through the main (science) optics, in order to capture all internally-induced drift and jitter. But this leads to a potentially fundamental problem because of the intrinsically small field of NGST. One must make sure that the faint stars found in the least dense fields (typically 17 to 19 th magnitude) are adequate for position sensing at the sampling rate required by the control system, so as not to limit observations to fields possessing bright guide stars.

The position of a star is found by collecting a statistically significant number of photons so as to pinpoint the centroid of the point spread function with the required level of accuracy. The noise equivalent angle (NEA) of a centroiding system is given by  $NEA = \sigma_{ES}/G$ , where  $\sigma_{ES}$  is the noise on the error signal and  $G$  is the error signal gain (i.e the slope of the excursion/error signal transfer function). In an imaging type sensor (such as a quadrant detector or a CCD), the error signal for each sensing direction is of the type  $ES = (A - B)/(A + B)$ , where  $A$  and  $B$  are the photon counts in each of the measuring areas.

Therefore, the error signal noise is given by

$$\sigma_{ES} = \sqrt{\left(\frac{\partial ES}{\partial A}\sigma_A\right)^2 + \left(\frac{\partial ES}{\partial B}\sigma_B\right)^2},$$

where  $\sigma_A$  and  $\sigma_B$  are the photon noise of each set of counts  $A$  and  $B$ , which at the null are proportional to  $\sqrt{N}$ .

Performing the differentiation and substituting, the new expression for the noise equivalent angle is found to be

$$NEA = \frac{1}{G\sqrt{N}}.$$

For a diffraction-limited image, the sensor gain can be shown to be

$$G = \frac{16 D}{3\pi \lambda},$$

where  $\lambda$  is the wavelength used for guiding and  $D$  the telescope primary mirror diameter.

The total photon count  $N$  coming from a guide star of magnitude  $m_v$  during an integration time  $t$  is:

$$N = 1.7 \times 10^7 \times 10^{-0.4m_v} \Delta\lambda A\tau\epsilon t$$

where  $\Delta\lambda$  is the bandpass of the detector in Angstroms,  $A$  the area of the entrance aperture in square meters,  $\tau$  the transmission of the optics, and  $\epsilon$  the detector quantum efficiency.

Using the above formulation, Figure 7 gives the noise equivalent angle of the guiding system as a function of the integration time for various diameters of the guiding field. This plot was based on a star population density at the galactic pole (most sparse star distribution) as determined from the Soneira-Bahcall model for the galaxy and assumes that three stars are needed on average in the field to guarantee a good probability of finding at least one guide star. Typical values of 1500 Å for the bandpass, 50% for the detector efficiency and 0.6 for the optics transmission have been assumed.

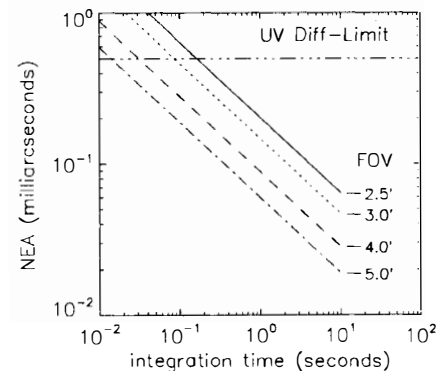


**Fig. 7.** Noise equivalent angle of the guiding system vs integration time, for various values of the field of view (FOV)

Using this plot one can determine that a guiding field of about 3.5 arcminutes in diameter is enough to guarantee a noise equivalent angle of better than 0.5 milliarcseconds while allowing a sampling rate of at least 20 Hz. Such a field diameter appears to be quite acceptable from the points of view of optical aberrations, baffling and physical size at the focal plane.

### Conclusion

This preliminary study has shown that two central issues behind achieving the pointing stability goal of NGST appear resolvable:

- despite its size, the telescope structure can be made stiff enough to be above the frequency range of internal disturbances,
- the sensing of line of sight errors necessary for the use of an active optics system can be done on field stars with full sky coverage and a high enough sampling rate.

It now remains to be verified that the proposed concept is valid at the system level. This will be performed with an end to end computer simulation including optics, structural modes, sensors and control system, and is the goal of the next phase of our studies.

### Acknowledgements

Out thanks to Olivia Lupie and William Haile for major contributions in the analysis of HST jitter data, and to David Wilkinson who assisted in the finite element calculations. The Johns Hopkins University Space Grant Consortium provided partial funding for this work.

### References

Dougherty, H., K. Tompetrini, J. Levinthal, and G. Nurre, (1982). *Space Telescope Pointing Control System*, Journal of Guidance, AIAA, Vol 5, 4.

Bély, P. Y., C. Burrows and G. Illingworth, (1989), *The Next Generation Space Telescope*, Proc. NASA/STScI Workshop, Baltimore, Md.

Bahcall, J.N. (1991), *The Decade of Discovery in Astronomy and Astrophysics*, National Academy Press.

Bahcall, J.N., R.M. Soneira, (1981), *Predicted star counts in selected fields and photometric bands: applications to galactic structure, the disk luminosity function, and the detection of massive halo*, The Astrophysical Journal Supp., Vol 47, p357-401.

Neill, J.P., P. Bély, G. Miller, A. Spigler, (1989), *Orbital Sites Tradeoff Study*, Proc. NASA/STScI Workshop on "The Next Generation Space Telescope", Baltimore, Md.

## CONTROL STRUCTURE INTERACTION IN LONG BASELINE SPACE INTERFEROMETERS

J. Spanos, Z. Rahman, C. Chu and J. O'Brien

*Jet Propulsion Laboratory, California Institute of Technology, Pasadena, California, USA*

**Abstract.** By avoiding the effects of earth's atmosphere, space interferometers offer significant improvements in optical performance over their ground based counterparts. Since the resolving power of an interferometer is proportional to the length of its baseline, very long baselines have been proposed for space flight. However, the longer the baseline the more flexible the spacecraft which in turn implies a less benign vibration environment. In this paper the problem of structural vibration is dealt with a multi-layer control approach which includes structural quieting, disturbance isolation, and active optical control. The approach is validated in the laboratory and experimental results obtained for the disturbance rejection of each control layer are presented.

**Keywords.** Control technology; control applications; laboratory techniques; flexible structures; active damping; vibration isolation; optical interferometers.

### Introduction

The angular resolution and astrometric accuracy of ground based telescopes and interferometers are greatly limited by the earth's atmosphere. This is attributed to the fact that earth instruments must resolve objects despite wavefront phase distortions introduced by atmospheric turbulence. For astrometry, there are important advantages in using interferometers over telescopes and these have been discussed by Colavita et al (1991a). The Orbiting Stellar Interferometer (OSI) shown in Figure 1 is the first conceptual interferometer targeted to achieve 10 micro-arcsec angular accuracy and 5 milli-arcsec imaging resolution from space (Colavita et al, 1991a).

OSI is a large space truss carrying three interferometers with baselines ranging from 1 to 18 meters. Figure 2 shows the optical train of a single interferometer. Star light reaches each of the two collecting telescopes at locations 1 and 1' and after following duplicate paths through the structure the two legs combine at bend 9. The interfering beams are then sent into a fringe tracker which detects the difference in the pathlength traveled by each beam, and an angle tracker which measures the angular difference of the two beams (i.e., wavefront tilt). The optical elements shown in Fig. 2 are rigidly attached to the truss except for

- (i) the light collecting siderostat mirror at station 1 which is capable of rotating in two orthogonal directions (i.e., azimuth and elevation),
- (ii) the reactionless fast steering mirror at bend 4 which also articulates in two degrees of freedom, and

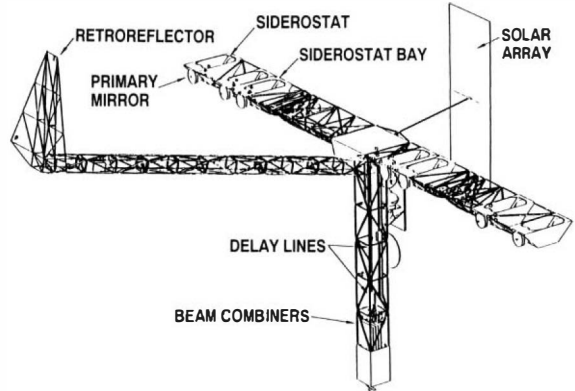


Figure 1. Orbiting Stellar Interferometer (OSI).

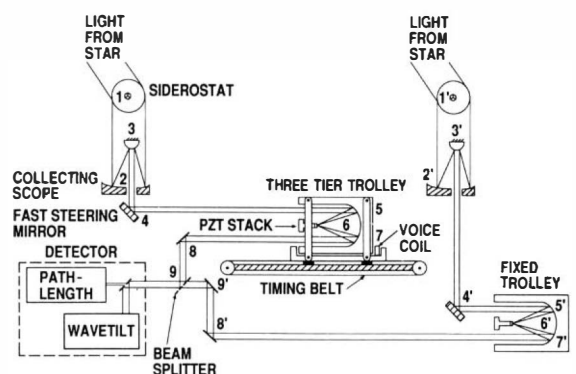


Figure 2. Interferometer optical train.

- (iii) the three-tier trolley at bends 5,6,7 which consists of a timing belt, a voice coil actuator, and a fine motion reactionless piezo-electric actuator.

The optical performance of the interferometer depends on how well wavefront tilt and optical pathlength variations are regulated to zero. In OSI pathlength control is achieved by feedback loops wrapped around the three trolley actuators and fringe tracker while wavefront tilt control is achieved by feedback loops involving the siderostat, fast steering mirror, and angle tracker.

It is important to consider how interferometer performance is related to control system performance. The astrometric error variance of an interferometer (angle in radians) is given by  $\sigma = \lambda / (\sqrt{2n} \pi B V)$  where  $\lambda$  is the wavelength of light,  $B$  the baseline length between the two siderostats,  $n$  the number of photons collected, and  $V$  the fringe visibility (Colavita et al, 1991a). With the baseline length selected, the only other quantity that affects optical performance is fringe visibility. This can take values in the interval (0,1) and the closer it is to unity the smaller the astrometric error will be. The maximization of the fringe visibility is the ultimate objective of the control system.

Clearly, placing an interferometer in space eliminates the performance problems associated with atmospheric effects but a new problem emerges: *structural vibration*. The space truss on which all optical elements are attached is likely to be light weight, lightly damped, and highly flexible by comparison to the relatively stiff and massive ground-based structures. On-board disturbances originating from reaction wheels and tape recorders can set the optical train into large amplitude vibrations deteriorating fringe visibility and thereby threatening the successfull operation of the interferometer.

In order to maintain optical performance despite a flexible structure and a stressing vibration environment, a recent study (Laskin and San Martin, 1989) found that a multi-layer control system architecture combining active and passive damping, disturbance isolation, and high bandwidth control of optical pathlength and wavefront tilt would be necessary. In this paper the multi-layer concept is demonstrated experimentally on a ground facility known as the JPL Phase B interferometer testbed (Eldred and O'Neal, 1991). The performance obtained from each control layer is presented in terms of the achieved vibration attenuation as seen by the pathlength measurement sensor.

### **The JPL Multi-Layer Control Concept**

Future optical class spacecraft will be required to operate in the nanometer-level vibration regime. On board disturbances amplified by the resonant dynamics of the structure may result in vibration amplitudes well into the micron range. The idea behind using multiple control layers to attenuate vibrations is illustrated in Figure 3. The disturbance signal is intercepted

- (i) at the source,

- (ii) in the path between the disturbance source and the optical elements, and
- (iii) at the optical elements.

Intercepting the disturbance signal at the source is accomplished with a blend of passive and active isolation control. The concept of passive isolation is based on separating the noise source from the structure by a soft spring so that the disturbance is significantly attenuated as it passes through the interface. In essence, a large amount of the vibration energy that would otherwise pass through to the structure is stored as strain energy in the spring. Active isolation is the application of feedback control to reduce disturbance transmission beyond that achieved with the passive soft mount. This is a local control system since the objective of the isolation layer is to measure and compensate for the disturbance signal right at the source.

The component of the disturbance getting past the isolation layer can be intercepted on its way to the optical elements by means of the structural quieting layer. In the context of this paper structural quieting refers to passive and active dampers located throughout the structure and capable of dissipating the vibrational energy. The objective of this layer is to make the structure be as quite as possible. The passive dampers may be fluidic viscous devices converting vibrational motion into heat while active dampers perform similarly by dissipating energy across electrical resistors. At JPL the most utilized active damper is a piezoelectric actuator with an integral force feedback loop. The importance of this layer cannot be understated since, in addition to dissipating vibrations, it provides the low authority control layer necessary to enable robust implementation of the other two layers.

The remaining part of the disturbance is intercepted by the optical control layer. This consists of fast steering mirrors for wavefront tilt control and delay lines for pathlength control. Optical control can be viewed as another isolation layer since one of its primary functions is to actively isolate the disturbance from its most critical target. The articulation of optical elements can be carried out at bandwidths well over 100 Hz and, as a result, this layer represents the highest level of control authority on optical performance. However, the structure has several lightly damped modes in this frequency range and control-structure interaction becomes an issue. To avoid significant performance degradations and more importantly closed loop instability it is imperative that the optical control layer operate in concert with the other layers and particularly with the structural quieting layer.

In order to demonstrate the three layer control concept in the laboratory, the Jet Propulsion Laboratory has developed an experimental ground facility known as the Phase B multi-layer testbed (Figure 3). This is an eight foot tall precision truss structure cantilevered at the base and equipped with an optical motion compensation system. A detailed description of the Phase B testbed is given by Eldred and O'Neal (1991).

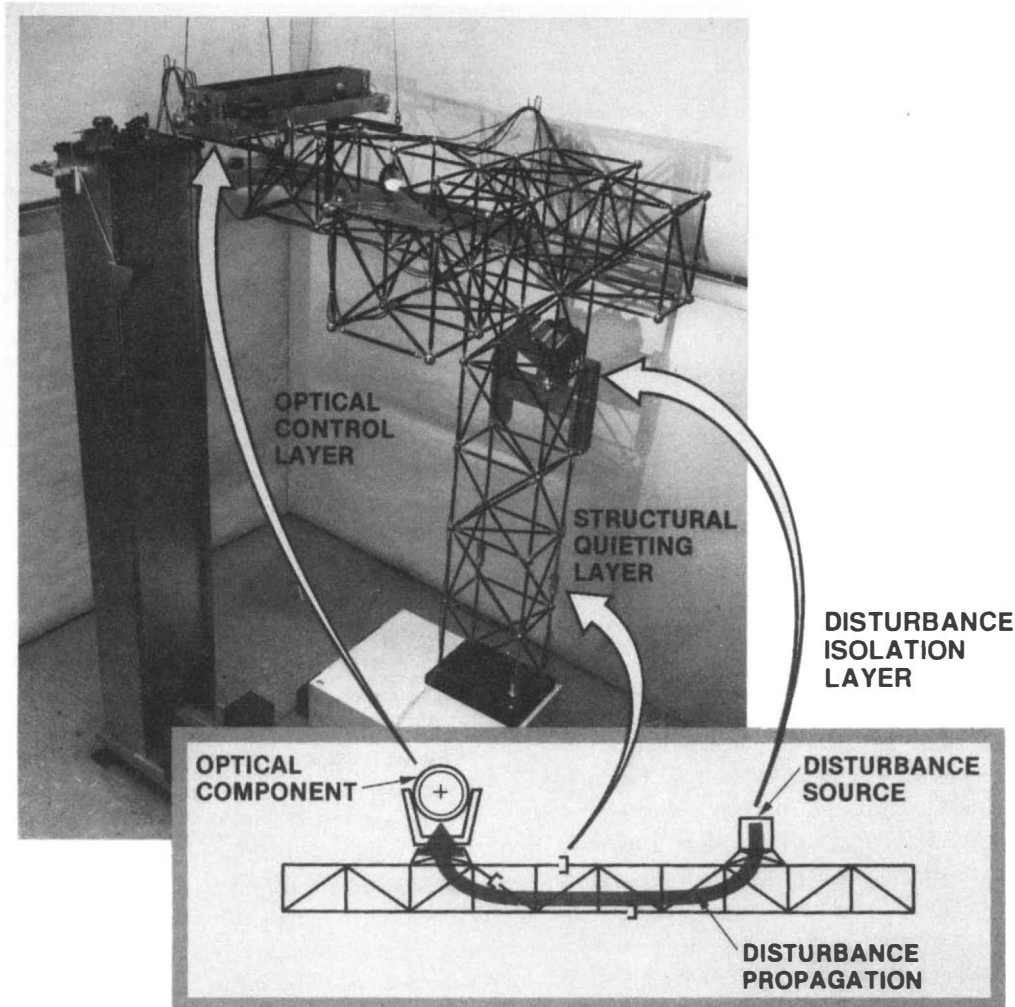


**Figure 3.** The multi-layer control concept and its experimental demonstration on the JPL Phase B testbed.

### Structural Quieting

The structural quieting layer on the Phase B testbed is represented by the passive and active members shown in Figure 4. A problem of considerable importance in the design of this layer is the placement and tuning of dampers. The damping introduced by imbedding these devices into the structure is effective at reducing the peak responses in the vicinity of resonant frequencies. This not only enhances the disturbance attenuation of the system, but also allows for the implementation of more aggressive control strategies to achieve greater performance.

The effectiveness of viscous elements in introducing damping is a function of several variables, including their number, their location in the structure, and their physical parameters (i.e., the stiffness and damping coefficients). This is known as the damper placement and tuning problem. A standard approach for the placement problem is based on heuristic kinetic and strain energy distributions. This approach is relatively effective if the goal is to provide damping improvement in selected structural modes. A more systematic approach is to pose the general optimal damper placement/tuning problem as follows:

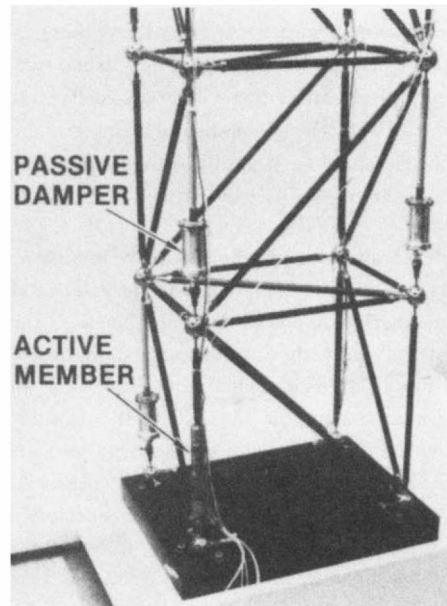


**Figure 4.** Structural quieting elements imbedded into the truss structure.

$$\min_{K \in \mathcal{K}} \min_{B \in \mathcal{B}} \mathcal{J}_{cost}(B, K)$$

where  $\mathcal{J}_{cost}(B, K)$  is defined as the optimal performance metric with damper locations  $B$  and stiffness and damping parameters  $K$ . Two types of performance metrics are typically considered. The first one is the maximization of modal damping in selected structural modes. The process involves solving an eigenvalue problem for a given damper configuration with corresponding stiffness and damping coefficients and determining the modal dampings achieved. The second type of criterion is to minimize the  $H_2$ -norm of selected transfer functions. The transfer function of interest here is the disturbance transmission from noise source to optical pathlength.

The damper placement and tuning problem is a joint “continuous+discrete” optimization problem. The selection of locations ( $B$ ) for placement is a “discrete” combinatorial optimization problem while the selection of values for  $K$  (tuning) is a continuous mathematical programming problem (Milman and Chu, 1992).

The combinatorial optimization problem is known to be difficult due to the fact that the potential number of candidate locations for placement ( $N$ ) will be large in a large space structure. However, relatively few passive devices ( $n$ ) may be available or even necessary. In general,  $N \gg n$ , and the total number of combinations,  $\frac{N!}{n!(N-n)!}$  is usually quite large. Therefore, it is impractical, if not impossible to attempt an exhaustive search. In this paper, a simulated annealing strategy (Kirkpatrick et al, 1983) was used to solve the combinatorial optimization problem.

The structural quieting layer on the Phase B testbed consisted of 4 passive dampers (Honeywell D-Struts) and 4 piezoelectric active members. The passive dampers were in existence prior to imbedding them into the structure and their stiffness and viscous damping coefficients could not be tuned. For the active members, integral force feedback was used to close each of the 4 colocated local loops where the gain of each loop was tuned individually.

The criterion used for placing the active and passive dampers is a mixture of the methods mentioned above. Some members were placed using the kinetic/strain energy distribution method to maximize damping in key structural modes. The remaining members were optimally placed by minimizing the  $H_2$  norm of the transfer function from the disturbance input to optical pathlength output. The result is shown in Figure 5. The resonant peaks of almost all modes below 100 Hz were considerably attenuated. System identification using transfer function curve fitters (Spanos, 1991) revealed that the damping in the major modes was increased to better than 5% of critical. For comparison purposes the modal damping ratios of the system without the structural quieting layer ranged from 0.1% to 1% of critical.

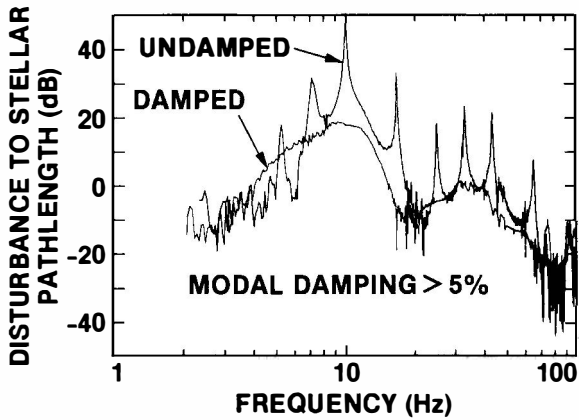


**Figure 5.** Disturbance attenuation due to the structural quieting layer.

### Disturbance Isolation

The fixture shown in Figure 6 represents the disturbance isolation layer on the the Phase B testbed. The disturbance source was a proof-mass shaker suspended on an accordion type flexure which in turn was rigidly attached to the truss structure. The corner frequency of the soft mount was measured at 3 Hz with natural damping on the order of 12% of critical. An active stage consisting of a voice coil actuator and an LVDT displacement sensor was added in parallel with the soft mount. Active control experiments using positive position feedback (PPF) were successfull in reducing the corner frequency of the isolator by a factor of 2 over the passive system. This translated into approximately 10 dB performance improvement in the 1-10 Hz frequency range.

With the structural quieting layer on, the transfer function from disturbance source to optical pathlength was measured with and without the isolator. The experimental results in Figure 7 show the improvement in optical performance when the PPF loop is closed. An order of magnitude improvement in disturbance rejection over the hard mount is evident up to 100 Hz with the exception of

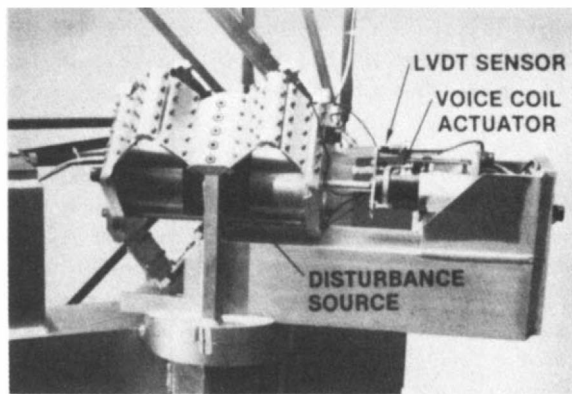


**Figure 6.** Disturbance isolation fixture on the JPL Phase B multi-layer testbed.

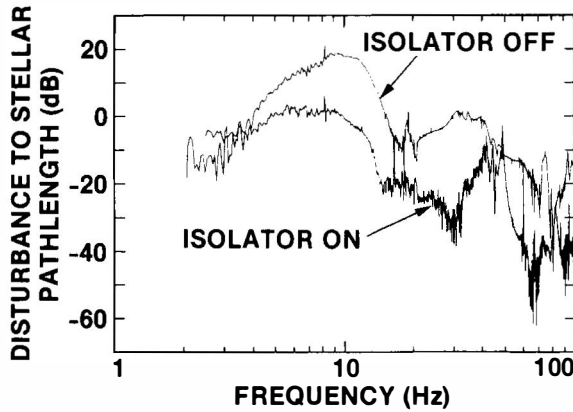


**Figure 7.** Disturbance attenuation due to the isolation layer.

the 40-50 Hz region. In this narrow band the accordion flexure no longer acts like an ideal spring but exhibits lightly damped resonances corresponding to undesired surge modes.

### Optical Control

The optical compensation system on the Phase B testbed is contained in a rectangular shaped trolley, and attached firmly on top of the truss structure. It represents a two-tier version of the OSI trolley in Figure 2 and has been described in detail by Colavita et al (1991b).

The system was designed to capture the interaction between structural flexibility and optical pathlength as would occur in a space based interferometer. The optical configuration shown in Figure 8 represents an extreme case where the laser beam bounces off mirrors located on opposite ends of the truss structure. Vibrational motions of the mirrors in the path of the laser beam change the

length of the optical path and this change is measured interferometrically by a fringe detector. Control is provided by a coarse motion voice coil actuator (6 mm stroke) and a fine motion piezoelectric actuator (30  $\mu\text{m}$  stroke, 10 nm resolution). Early experiments with the optical control layer were reported by O'Neal and Spanos (1991).

The frequency response functions (FRF) for the two-input one-output system were measured with the aid of a Fourier analyzer. Sine sweep and band limited white noise excitations were used to identify the system dynamics. The effects of noise were reduced via spectral averaging and the FRF's were obtained with high coherence levels.

The FRF from PZT actuator to optical pathlength did not show the characteristic resonant behavior of a flexible structure due to the fact that the mass of the PZT driven mirror is quite small and its motion is momentum compensated. It was found that while the magnitude response is relatively constant at frequencies below 1 kHz, the phase response drops linearly with a constant slope corresponding to 70 microseconds of pure time delay. This delay was attributed to hysteretic behaviour of the actuator as well as to the digital nature of the pathlength measurement.

The FRF from voice coil (VC) actuator to optical pathlength was significantly affected by structural flexibility. The magnitude response before and after the structural quieting layer was installed is shown in Figure 9. Clearly, structural quieting enhances system damping presenting the optical control designer with a more benign system to control. The dominant peak at 0.7 Hz is due to the flexure that attaches the moving part of the trolley to its base. All other peaks in the frequency response function correspond to structural modes of the truss. Parametric

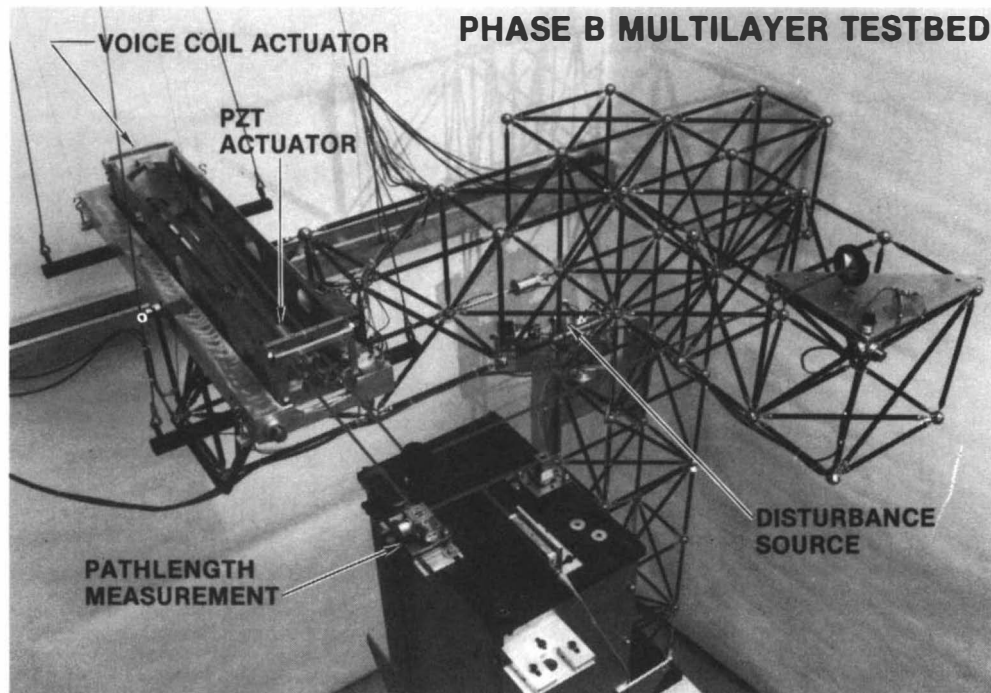


**Figure 8.** The optical compensation system on the JPL Phase B multi-layer testbed.

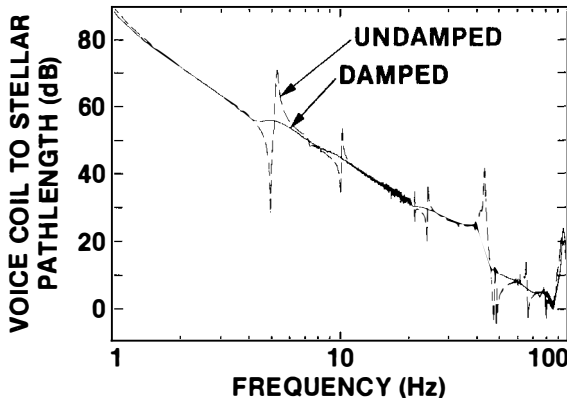


**Figure 9.** Frequency response function from voice coil actuator and optical pathlength sensor before and after the structural quieting layer was installed.

transfer function identification via complex curve fitting (Spanos, 1991) revealed the presence of a nonminimum phase zero at 85 Hz which represents an upper bound on the bandwidth of the voice coil loop.

The block diagram of the two-input one-output optical control system is shown in Figure 10. The output of the PZT controller drives both the PZT actuator and the voice coil controller. The objective of this configuration is to desaturate the small stroke PZT actuator in the low frequency range where the disturbance signals tend to have large amplitudes. Classical control system design techniques (Bode, 1945) were used to shape the open loop response in the frequency domain. Here it is important to note that, unlike most modern control design methods, this design methodology does not require an explicit parametric model of the plant. The FRF measurement can be used directly to synthesize robust controllers.

The loop transfer function of the system is

$$L = K_1(1 + K_2G_2)$$

The objective is to design the two compensators  $K_1(s)$  and  $K_2(s)$  such that the closed loop system is stable and the total loop gain  $|L|$  is as large as possible over the largest achievable bandwidth. The design requirements are placed on  $|L|$  since the disturbance rejection is inversely proportional to  $|L|$  at frequencies where  $|L|$  is much larger than unity. The following three properties can be easily deduced:

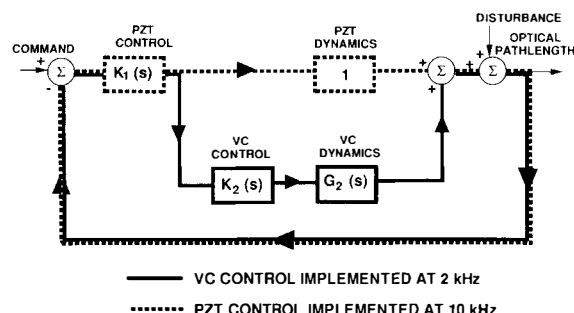


**Figure 10.** Optical control system architecture.

1. When  $|K_2G_2| \gg 1$ ,  $|L| \approx |K_1K_2G_2|$

2. When  $|K_2G_2| \ll 1$ ,  $|L| \approx |K_1|$

3. When  $|K_2G_2| = 1$ ,  $|L| \approx \phi |K_1|$

where  $\phi = -\pi + \text{angle}(K_2G_2)$  and  $\text{angle}(K_2G_2)$  is the phase angle (in radians) of  $K_2G_2$  at the frequency where  $|K_2G_2| = 1$ . When the voice coil loop gain is large, the total loop gain is the product of the voice coil and PZT loop gains. The total loop gain approaches the PZT loop gain as the voice coil loop gain becomes much smaller than unity. The third property states that at the voice coil loop gain crossover frequency the total loop gain is the product of the PZT loop gain and the phase margin  $\phi$  associated with  $K_2G_2$ .

With the above under consideration, the control laws were designed one loop at a time. First, the voice coil controller was designed to stabilize the system assuming that it is driven directly by the laser pathlength measurement (i.e.,  $K_1(s) = 1$ ) and the PZT actuator is disconnected. The compensator was a twenty second order filter with a cross-over frequency at 33 Hz. The PZT controller was a third order filter of the low pass type. Figure 11 shows the frequency response of the loop transfer function  $L$  and PZT transfer function  $K_1$ . The effects of the various time delays including those due to computer implementation of the controllers were taken into account. The frequency responses are clearly in agreement with the three properties described earlier. At high frequencies the total loop gain approaches that of the PZT while at low frequencies  $|L|$  gets a 60 dB boost from the voice coil loop gain. A closed loop bandwidth of 500 Hz was achieved. This was limited primarily by digital implementation time delay, actuator phase lag, and high frequency noise.

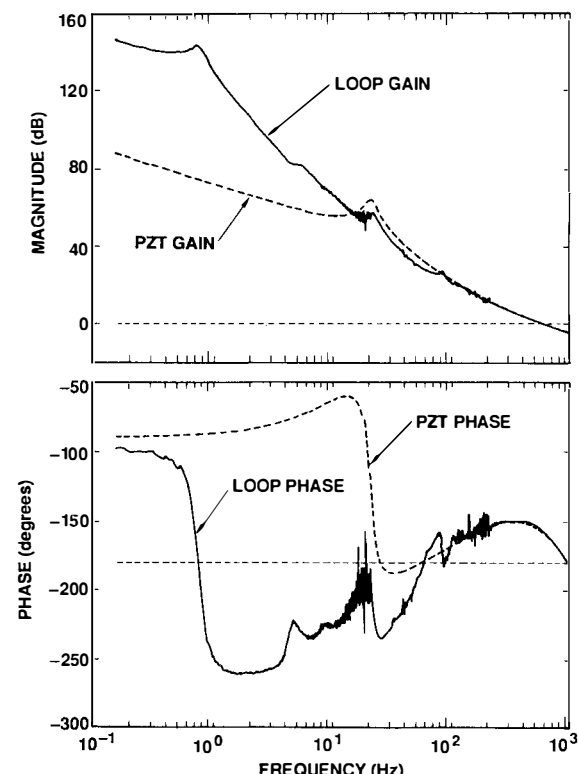


**Figure 11.** Optical control system loop shapes.

Both control laws were discretized using the bilinear transformation and prewarping was used to match them to their analog counterparts at the respective gain crossover frequencies. The low bandwidth voice coil controller and the high bandwidth PZT controller were implemented at 2 kHz and 10 kHz respectively. The phase lags associated with the zero order hold and the computational delay were modelled as pure time delays since the sampling frequencies of both controllers are much higher than their respective bandwidths.

Two closed loop experiments were carried out. Both were conducted with the structural quieting layer and disturbance isolation layer in place. The first experiment involved two types of disturbances: laboratory noise forcing the 0.7 Hz trolley mode and a shaker induced sinusoid at 7.3 Hz. The open loop time history was recorded for the first 5 seconds at which time the control loop was closed and the time history was recorded for an additional 5 seconds. The data are plotted in Figure 12. The two disturbance components are evident during the first 5 seconds while the optical pathlength variation is shown to be stabilized at the 5 nanometer level RMS. The second closed loop experiment involved the measurement of the transfer function from disturbance source to optical pathlength. The open and closed loop measurements are shown in Figure 13. The optical controller provides nearly 70 dB of disturbance rejection at 10 Hz and about 20 dB rejection at 100 Hz. These attenuation levels are in excellent agreement with the total loop gain shown in Figure 11.

### Summary and Conclusions

Control structure interaction has been identified as a key technology required to enable future optical class space missions such as long baseline interferometry. In this paper a three layer control approach involving disturbance isolation, structural quieting, and optical control was successfully demonstrated in the laboratory. The experimental results were given in terms of the disturbance transmission function from noise source to optical pathlength.

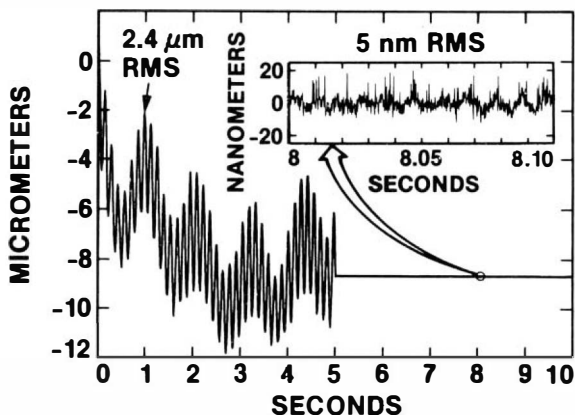


**Figure 12.** Optical pathlength response to laboratory ambient disturbance and shaker induced sinusoidal excitation. The control loop is closed after 5 seconds.

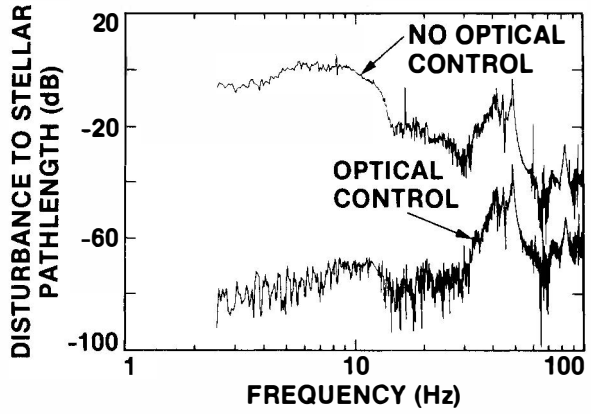


**Figure 13.** Disturbance attenuation due to the optical control layer.

Figure 14 summarizes the results and shows how each layer implemented successively lowers the disturbance transmission function. Assuming that a band-limited white noise disturbance excites the structure with energy uniformly distributed over 1–100 Hz and that the multi-layer controller achieves a normalized pathlength variation equal to 1 nanometer RMS, the attenuation factor achieved by each layer is

- (i) structural quieting: 6
- (ii) disturbance isolation: 6
- (iii) optical control: 139

The multi-layer control system enables a 5100:1 disturbance reduction. Clearly, the biggest contributor to performance is the optical control layer. However, the structural quieting layer was the catalyst that enabled a robust high bandwidth optical control system design by introducing modal damping on the order of 5% of critical to the most dominant structural modes. An equally important result obtained on the Phase B multi-layer testbed is the stabilization of optical pathlength at the 5 nanometer level which indicates that interferometry is feasible on a flexible structure.

### Future Work

Additional work is needed in the areas of disturbance isolation, high frequency structural quieting, and momentum compensated optical actuators.

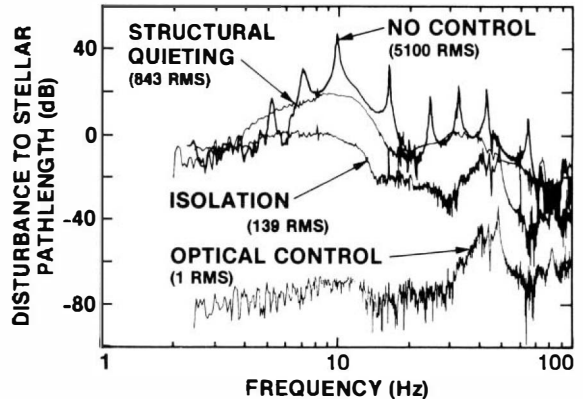


**Figure 14.** Comparison of each control layer in terms of disturbance attenuation.

In the disturbance isolation area a new single-axis fixture is currently under development at JPL which combines a passive and an active stage. Particular attention will be paid to the problem of surge modes in the passive stage and the proper blend of displacement and force feedback in the active stage. A multi-axis unit of the Stewart platform type is also under consideration as this allows full six degree of freedom isolation. The performance of these devices will be demonstrated on the Phase B testbed as well as on a larger scale interferometer test bed currently under development at JPL.

The problem of introducing large amounts of damping in the high frequency range (i.e., in modes with frequencies greater than 100 Hz on the Phase B testbed) appears to be considerably more difficult due to high modal density and localization. Finite element models used by optimal damper placement and tuning algorithms are not sufficiently accurate at high frequencies and this makes the problem even more difficult. High frequency structural quieting appears to be a research area largely untapped.

The interaction between the optical control layer and the structure can be minimized by utilizing momentum compensated actuators. Reactionless delay lines and fast steering mirrors are undesirable because of the added system complexity, increased power consumption, and more importantly the added mass. However, the reaction mass does not need to be as large as the prime mass and a trade can be made on the basis of performance gained versus overall cost.

### Acknowledgements

This research was performed at the Jet Propulsion Laboratory of the California Institute of Technology under a contract with the National Aeronautics and Space Administration sponsored by the Office of Aeronautics and Space Technology. The authors wish to thank Dr. Robert Laskin for reviewing the manuscript and the entire JPL

CSI team for their contribution to this work. Thanks are also due to Dr. Mark Colavita for information on interferometric issues.

### References

- Bode, H. W., *Network Analysis and Feedback Amplifier Design* Van Nostrand, NY, 1945.
- Colavita, M. M, Shao, M., and Rayman, M. D., "OSI: Orbiting Stellar Interferometer for Astrometry and Imaging," Applied Optics, Special Section on the Williamsburg Space Optics Conference, 1991a.
- Colavita, M. M. et al, "Prototype High Speed Optical Delay Line for Stellar Interferometry" SPIE Proc. on Active and Adaptive Optical Systems, Vol. 1542, San Diego, CA, July 22-24, 1991b.
- Eldred D. B., and O' Neal M. C., "The JPL Phase B Testbed Facility" Proc. of the ADPA/AIAA/ASME/SPIE Conference on Active Materials & Adaptive Structures, Alexandria, VA, Nov. 4-8, 1991.
- Kirkpatrick, S., Gelatt, C. D., and Vecchi, M. P., "Optimization by Simulated Annealing," *Science*, Vol. 22, pp. 671-680, May, 1983.
- Laskin, R. A., and San Martin, M., "Control/Structure System Design of a Spaceborne Optical Interferometer," Paper AAS-89-424, AAS/AIAA Astrodynamics Specialist Conference, Stow, Vermont, Aug. 7-10, 1989.
- Milman, M. H. and Chu, C. C., "Optimization Methods for Passive Damper Placement and Tuning", 1992 AIAA Guidance, Navigation, and Control Conference, Hilton Head, SC, August 12-14, 1992.
- O'Neal, M. C. and Spanos, J. T., "Optical Pathlength Control in the Nanometer Regime on the JPL Phase B Interferometer Testbed," SPIE Proc. on Active and Adaptive Optical Systems, Vol. 1542, San Diego, CA, July 22-24, 1991.

## CONTROL AND METROLOGY ISSUES IN LONG-BASELINE STELLAR INTERFEROMETERS

M.M. Colavita and M. Shao

*Jet Propulsion Laboratory, California Institute of Technology, Pasadena, CA 91109, USA*

### Abstract

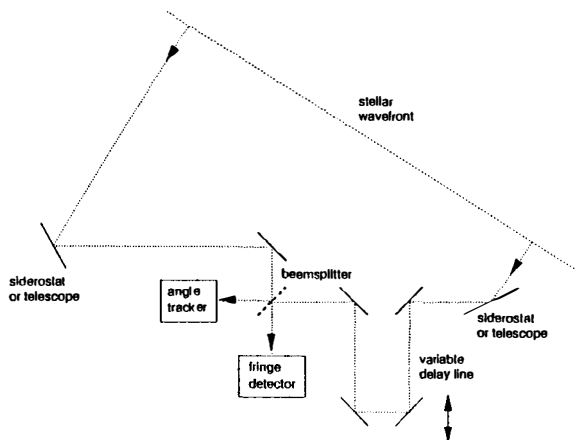
The field of optical stellar interferometry has seen tremendous growth in the past few years, as technology catches up with the requirements established by the science goals and the operating environment. Presently, several ground-based interferometers are in operation, and a number are in the development or planning stages. In addition, serious studies of space-based interferometers are in progress. The control challenges in optical interferometry on the ground pertain mostly to offsetting the deleterious effects of the Earth's atmosphere—the fundamental limitation to ground-based astronomy—and to compensating for Earth rotation. In space, away from the atmosphere, in addition to the control challenges associated with large space structures, there are metrology challenges to enable high-accuracy astrometry and imaging. The required level of metrology,  $\sim 10\text{--}100$  picometers, pushes the current state of the art.

**Keywords:** stellar interferometry, adaptive optics, space optics, laser metrology, computer control, control applications, stochastic systems.

### 1 Introduction

Optical stellar interferometry is the coherent combination of the light from a stellar source received by two or more spatially-separate apertures in order to obtain information about the source structure or position. The separation of the apertures is called the baseline, and one of the advantages of interferometry is that the baseline length can be much larger than the diameter of a filled-aperture telescope. For the case of a telescope, diffraction-limited resolution is inversely proportional to telescope diameter, while for an interferometer, resolution is inversely proportional to baseline length. Thus, with the long baselines possible with an interferometer, very high angular resolutions can be achieved. For application to astrometry—the measurement of stellar positions—the simple geometry

Figure 1: Schematic of an optical interferometer.



of an interferometer gives it a number of advantages over a conventional telescope.

Figure 1 gives a schematic of a simple two-element optical interferometer. Light is collected by two small telescopes or siderostats, and directed via relay mirrors to a beamsplitter where the light is combined. A variable optical delay line is inserted into one arm of the interferometer. In order to detect fringes, i.e., for the light to combine coherently, several conditions must be met: 1) The pathlengths of the light from the stellar wavefront to the combining beamsplitter via each arm of the interferometer must match to within the coherence length of the light, typically  $\sim 1 \mu\text{m}$ . This is accomplished by controlling the optical delay line. 2) The wavefront tilts of the beams when they are combined must be matched to within their diffraction limits. This is accomplished by controlling fast-steering mirrors in the optical train. 3) For a ground-based interferometer, the presence of atmospheric turbulence requires that optical pathlength and wavefront tilt be corrected on time scales of  $\sim 10$  ms for a visible-wavelength interferometer; this requirement does not apply for a space interferometer.

While stellar interferometry has a long history, the advent of computers for Real-time control and automation, and the maturation of detector and controlled-optics technology, has enabled re-

liable and scientifically-productive instruments to be built. The Mark III interferometer on Mt. Wilson (Shao et al. 1988) has been operational since 1986, and has generated scientific results in several areas of astronomy (cf. Shao and Colavita 1992). In addition to other current or planned ground-based interferometers, two of the next-generation 8–10 m telescope projects: the European Southern Observatory’s Very Large Telescope (VLT) and the Keck I and Keck II telescopes on Mauna Kea, will include interferometric operation. Finally, the important science that could be done with an astrometric interferometer in space led the National Research Council’s Astronomy and Astrophysics Survey Committee (1991) to recommend an Astrometric Interferometer Mission, and several serious studies of space interferometers are in progress.

Both ground and space interferometers pose interesting control and metrology problems. The problems for ground-based interferometers typically relate to compensating for atmospheric turbulence and Earth rotation, while the problems for space interferometers, away from the effects of the Earth’s atmosphere, relate to the control of large space structures and to precise metrology of the instrument to allow for high-accuracy astrometry and imaging.

## 2 Ground-Based Interferometry

### 2.1 Pathlength Control

For a typical ground-based interferometer, the light-collecting telescopes or siderostats are fixed to the earth, while optical delay lines, as in Fig. 1, are used to equalize the pathlengths in each arm—essentially, to “point” the interferometer. For long baselines, the optical delay lines must move rapidly to correct for Earth rotation; a 400 m baseline interferometer requires two delay lines which can each vary the optical path by up to 15 mm/s. However, to avoid blurring of the optical interference pattern, the delay line must follow the programmed position and rate to an accuracy of  $\sim 10$  nm rms in the presence of the mechanical noise induced by the rapid motion.

Figure 2 shows a schematic of a delay line developed at JPL for a next-generation ground-based interferometer (Colavita et al. 1991). The basic optical assembly is a cat’s eye retroreflector, which returns an optical beam parallel to the input direction, but displaced in position. The cat’s-eye assembly is suspended above a rolling cart using a low-resonant-frequency flexure suspension for noise isolation, and the rolling cart uses large-diameter wheels to reduce bearing noise. The cat’s eye uses a short-travel piezoelectric transducer (PZT) on its focus mirror, and a voice-coil motor which drives

Figure 2: Schematic of a delay line developed at JPL for a next-generation optical interferometer.

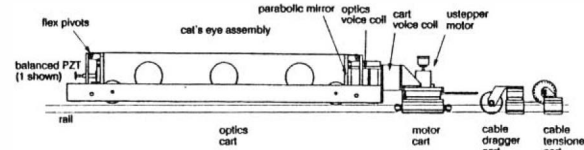
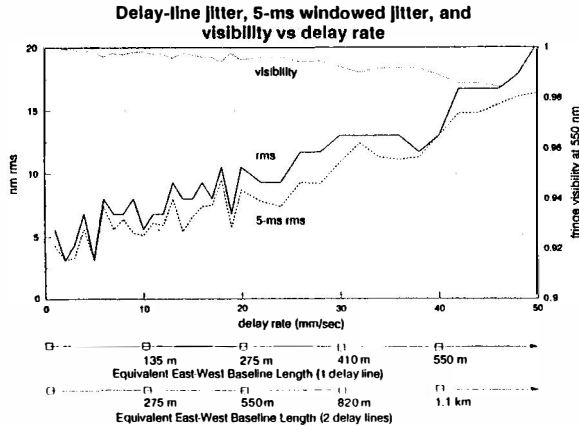


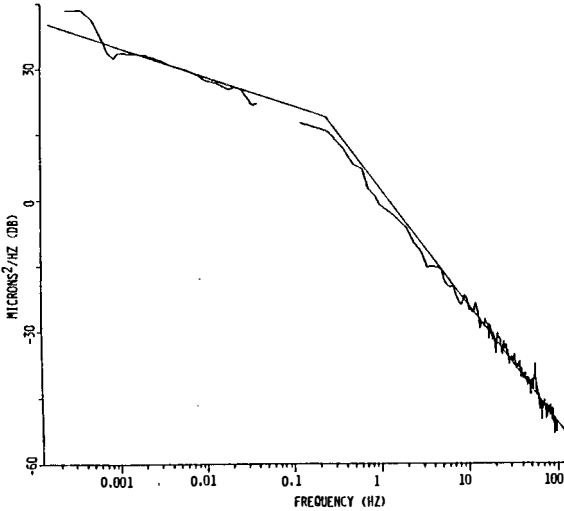
Figure 3: Optical path jitter as a function of delay rate for the new delay line.



the entire cat’s-eye assembly relative to the rolling base. A second cart contains a friction drive using a microstepper motor. This cart drives the optics cart using a second voice-coil motor, which provides isolation from motor disturbances.

The real-time control system is the key to the operation of the delay line. There are 4 actuators in the system (from fine/high-bandwidth to coarse/low-bandwidth): PZT, optics-cart voice coil, motor-cart voice coil, and microstepper motor. The overall position of the delay line is sensed using a laser interferometer, while two eddy-current sensors measure the positions of the two voice-coil actuators. Effectively, the actuators in the system are controlled such that each actuator is used to keep the next finer actuator within its dynamic range, e.g., the optics-cart voice coil is used to keep the PZT centered. As implemented, bandwidth separation is used such that each actuator and its controller appear as an inner loop in the controller for the next coarser actuator. The controllers are implemented using a VME-based control system with 68030 single-board computers; the fastest sampling rate (for the PZT) is 4 kHz. Figure 3 shows the achieved rms optical path jitter of the delay line as a function of delay rate; the high-frequency jitter remains below 10 nm rms for rates to  $\sim 30$  mm/sec, which represents a factor of  $\sim 40$  improvement over the delay line used in the Mark III interferometer.

Figure 4: Measured power spectrum of optical path fluctuations using the Mark III interferometer and a 12 m baseline.



## 2.2 Fringe Tracking

Atmospheric turbulence, which imposes random phases on the incident stellar wavefront, is the fundamental limitation to ground-based interferometry. At visible wavelengths, the transverse spatial scale of turbulence is  $\sim 10$  cm, while the time scale of turbulence is  $\sim 10$  ms. One effect of the short time scale is that the position of the optical delay line must be updated at time scales of  $\sim 10$  ms in order to follow the motion of the interference pattern (fringe) (cf. Greenwood 1977).

Thus, modern interferometers typically use a white-light fringe tracker to follow the atmospheric motion. The tracker measures the phase of the white-light fringe by using coherent demodulation of the fringe pattern, or other method; the phase is then used to control the delay-line position. Generally, astronomical objects are not very bright, and the photon-noise in estimating the fringe position is the major limitation. For  $N$  total detected photons per aperture per coherent integration time ( $\sim 10$  ms), the error standard deviation of an optimal phase estimator is  $1/(\sqrt{N}V)$  rads rms, where  $V$  ( $\leq 1$ ) is the fringe contrast. A 4-bin phase estimator, as is used on the Mark III interferometer (Shao et al. 1988), is suboptimal by  $\sqrt{4/\pi}$ . Typically,  $\geq 100$  photons per coherent integration time are required for acceptable performance, which sets a limit on the minimum brightness of the fringe-tracking source. Figure 4 shows a power spectrum of the atmospheric phase fluctuations as measured with the Mark III interferometer; the characteristic  $f^{-8/3}$  and  $f^{-2/3}$  asymptotes are typical of results in turbulence theory.

## 2.3 Angle Tracking

As mentioned earlier, the beams of light from the two collecting apertures of the interferometer must

be parallel to each other in order to obtain high-contrast interference. In addition to mechanical errors in the telescope drive mechanisms, atmospheric turbulence introduces tilts into the wavefronts which must be tracked out, and all interferometers implement at least a low-bandwidth angle-tracking servo. As mentioned above, the transverse spatial scale of the turbulence-induced phase errors is  $\sim 10$  cm at visible wavelengths for a typical astronomical site. This length is referred to as the Fried length  $r_0$ , and is the aperture diameter over which the incident phase front is approximately flat. To first order, interferometers are limited to subapertures of this size in order to work coherently. However, much of the error introduced by turbulence takes the form of wavefront tilts. A fast tilt-tracking servo can allow the use of apertures of diameter  $\sim 3r_0$  with the same fringe contrast as an interferometer using  $r_0$ -sized apertures and a slow tilt servo. The division between "slow" and "fast" is the typical atmospheric coherence time  $\tau_0$ ,  $\sim 10$  ms at visible wavelengths. An ideal knife-edge centroid algorithm (as implemented, for example, with a quad cell) has an error standard deviation of  $(3\pi/16)/\sqrt{N}$  waves rms, where  $N$  is the number of detected photons from one aperture; to estimate phase to 1/15 of a wave requires  $\sim 80$  photons, which again places a constraint on object brightness. More sophisticated angle trackers can use a Kalman filter and an optimal centroid estimator to optimize performance given the atmospheric turbulence statistics and the estimator photon noise (Clark et al. 1986).

## 2.4 Adaptive Optics and Advanced Techniques

While tilt correction allows the use of apertures up to  $3r_0$ , to use still larger apertures requires the use of adaptive optics to correct for wavefront aberrations (cf. Hardy 1991). An adaptive optics system consists of several components: a deformable mirror, a wavefront sensor, and a reconstructor. The deformable mirror, which is located at an image of the telescope primary, typically uses a thin mirror which is driven by a number of electrostrictive actuators; the spacing of the actuators typically corresponds to  $\sim r_0$  in the compressed beam. To drive the deformable mirror, an estimate of the wavefront phase is required. The wavefront sensor typically measures local wavefront tilts, while the reconstructor takes an array of wavefront tilts, and, conceptually, integrates them to obtain the wavefront phase, which is then used to drive the deformable mirror. Originally developed for military uses, adaptive optics is beginning to see application in astronomy for single-telescope imaging (cf. Rousset et al 1990).

In addition to the challenges associated with the low photon flux of astronomical objects, adap-

tive optics can pose significant computational burdens. If  $t$  is the vector of wavefront tilts, then the wavefront phase vector  $\phi$  can be estimated by a matrix multiply, viz.  $\phi = Rt$ , where  $R$  is an  $M \times M$  reconstruction matrix, where  $M$  is the number of actuators in the deformable mirror. For correction at visible wavelengths, this reconstruction is required at  $\tau_0$  rates (faster for observation of low-earth-orbit satellites), and systems developed for military applications have typically used special-purpose hardware. The trend in astronomy has been to apply adaptive optics at longer wavelengths, where both the time scale of the required correction is slower and the number of actuators required of the deformable mirror is less; a major goal is to reduce the cost of systems to a level affordable by astronomers.

Fighting the effects of atmospheric turbulence is the major challenge for ground-based interferometry, and the discussion above is only a brief introduction to some of the issues involved. For a more detailed discussion of advanced techniques, as well as an overview, see Shao and Colavita (1992).

### 3 Space-Based Interferometry

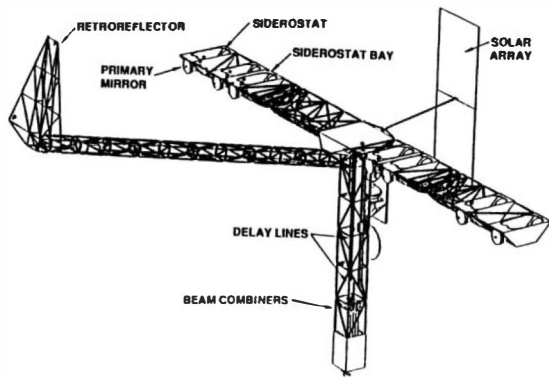
The advantages of space for astronomical observations are well known. However, from the perspective of interferometry, the major gain in going to space is not the increase in transparency, but rather the elimination of atmospheric turbulence, so that the many compromises associated with interferometry on the ground are unnecessary. However, space introduces challenges of its own. One is the stabilization of large space structures. To enable high sensitivity, it is necessary that the structure be stable to the diffraction limit of the interferometer baseline. If the structure is not stable, then short exposures, as are required on the ground, are necessary to freeze the motion of the interference fringes, and much of the advantage of going to space is lost.

The elimination of atmospheric turbulence not only greatly increases the sensitivity of an interferometer, but allows measurements which are not possible from the ground. One of these is astrometry with accuracies of  $10 \mu\text{as}$  ( $50 \times 10^{-12}$  rads) over wide angles. However, to achieve such accuracies requires precise metrology of the instrument geometry.

Two interferometers have been studied seriously for a future space mission:: POINTS (Precision Optical Interferometer in Space) (Reasenberg et al. 1988) and OSI (Orbiting Stellar Interferometer) (Gershman et al. 1991). Below, the OSI instrument will be described to illustrate some of the issues involved.

OSI uses 3 interferometers arranged collinearly

Figure 5: OSI point design with an 18 m maximum baseline.



on a single spacecraft. Each of the three interferometers is similar in operation to a ground-based interferometer, with articulating siderostats and optical delay lines. Two of these interferometers track bright guide stars to establish the spacecraft orientation; as the three interferometers are assumed collinear, only 2 spacecraft rotations are important. Using the information from the guide interferometers, the third interferometer, which would observe the dim science object, is stabilized so that it can use a long coherent integration time to increase sensitivity. Figure 5 shows one point design of the OSI concept which uses an 18 m maximum baseline on a deployed structure. The total mass is  $\sim 3800$  kg, and the spacecraft would be launched into a 900 km sun-synchronous orbit by an Atlas IIAS/Centaur. A second point design currently being considered uses a 7 m maximum baseline, for launch using an Atlas IIA.

#### 3.1 Structural Control

The stabilization of the third interferometer can be accomplished by attitude control of the entire spacecraft, as with HST. However, by using the delay line of the science interferometer, its fringe position can be stabilized by feeding forward from the guide interferometers to the delay position. The error in the fringe position for an interferometer can be written

$$\epsilon = \vec{B} \cdot \hat{s} - x, \quad (1)$$

where  $\vec{B}$  is the interferometer baseline,  $\hat{s}$  is the unit vector to the source, and  $x$  is the delay-line position. Thus, errors in fringe position can be corrected by changing  $B$  (attitude control) or by varying  $x$  (delay-line control).

One advantage of using optical delay lines for synthetic stabilization of the spacecraft is that very high control bandwidths can be achieved. This high-bandwidth control can also be used for suppression of spacecraft vibrations, which can be a concern for large space structures. Table 1 shows the results of a simulation conducted for the 18 m

Table 1: Simulation results for induced vibrations (pathlength errors) into the OSI structure by 4 HST-type reaction wheels with different vibration suppression techniques.

base structure	$\sim 750$ nm rms
+ passive dampers	$\sim 75$ nm rms
+ isolation of reaction wheels	$\sim 30$ nm rms
+ 250 Hz pathlength control	$\sim 3$ nm rms
or + 1 kHz pathlength control	<1 nm rms

OSI point design. The vibration source was modeled as several HST-type reaction wheels mounted to the structure. The various table entries show the residual vibration remaining after application of various suppression strategies. To avoid smearing of the interference fringe, residual pathlength errors of less than 10 nm rms are required. As seen from the table, passive techniques can be used to reduce the vibration from 750 nm rms for the case of the reaction wheels hard-mounted to the spacecraft structure to 30 nm rms. Pathlength control, by feeding forward from the guide interferometers sensing the spacecraft vibrations to the delay position of the science interferometer, provides the additional suppression required to meet the vibration requirements. The JPL CSI program (Layman 1990) is concerned with the development of technologies for the quieting of such large space structures.

### 3.2 Laser Metrology

OSI uses laser metrology to monitor relative motions of the instrument. The metrology system has two parts. There is an external metrology system which measures the distances between retroreflectors mounted to each siderostat and retroreflectors mounted on a metrology structure; the metrology structure is at the far left in Fig. 5. In addition, there is an internal metrology system which measures internal pathlengths through the instrument. Essentially, the external metrology system monitors the relative baselines, defined by the vectors connecting the siderostat retroreflectors— $B$  in Eq. (1)—while the internal metrology system monitors the delay-line positions (and other internal delays)— $x$  in the same equation. While this monitoring is important for attitude control, so that the attitude sensed by the guide interferometers accurately reflects the attitude of the science interferometer, it is crucial for high-accuracy astrometry, the primary science goal of OSI.

Interferometers measure stellar positions by measuring the delay position at which the interference fringe is found. If one knows the baseline vector  $B$ , the fringe position gives the angle between the baseline and the star. Thus, precise knowledge of the baseline vector is crucial. With

an 18 m maximum baseline, and a requirement for 10  $\mu$ as( $50 \times 10^{-12}$  rad) astrometry, the endpoints of the interferometer baseline must be known to an accuracy of 1 nm. A detailed error analysis, which accounts for propagation of errors from linear measurements to three-dimensional positions, leads to requirements for linear metrology accuracy of  $\sim 100$  picometers—less for a shorter-baseline instrument. While such resolution can be achieved with a laser metrology system, obtaining accuracy at these levels in the presence of systematic error sources is challenging. As an example, surface errors in the faces of a retroreflector will change the measured distance as the retroreflector articulates about its vertex with siderostat rotation. These errors can easily exceed the allowed error budget, and will require careful calibration. The development of calibration methods for all systematic error sources, and the demonstration of these methods in the lab, is one of the goals of ongoing research in space interferometry.

## 4 Conclusion

The control challenges associated with interferometry on the ground pertain mostly to compensation for Earth rotation and atmospheric turbulence. Long-baseline interferometers require high-speed delay lines which can maintain low vibration levels in the presence of significant mechanical noise; this is accomplished using cascaded actuators and a high-speed digital control system. Most of the challenges associated with atmospheric turbulence pertain to efficiently using the limited flux from the astronomical source. However, the application of adaptive optics to phase the apertures of next-generation interferometers presents challenges in computation and implementation, efficient use of scarce photons, and, from the astronomer's perspective, the reduction in cost below that of military-funded systems. In space, the control challenges move away from compensation of atmospheric turbulence to compensation of structural vibrations. Space interferometers using optical delay lines can exploit the high bandwidth with which pathlength can be controlled to synthetically stabilize a large space structure without requiring high-bandwidth actuation of the structure itself. In space, with the elimination of atmospheric turbulence, high-accuracy astrometry is now possible over wide angles. However the achievement of the desired science goals requires the development of three-dimensional laser metrology systems with accuracies beyond the current state of the art.

## 5 Acknowledgments

This work was performed at the Jet Propulsion Laboratory, California Institute of Technology, un-

der a contract with the National Aeronautics and Space Administration.

## References

- [1] L. D. Clark, Jr., M. Shao, and M. M. Colavita. A photon-camera star tracker for stellar interferometry. *Proc. SPIE*, 627:838–845, 1986.
- [2] M. M. Colavita, B. E. Hines, M. Shao, G. J. Klose, and B. V. Gibson. Prototype high speed optical delay line for stellar interferometry. *Proc. SPIE*, 1542:205–212, 1991.
- [3] National Research Council. *The Decade of Discovery in Astronomy and Astrophysics*. Wash. DC: Natl. Academy Press, 1991.
- [4] R. Gershman, M. D. Rayman, and M. Shao. A moderate space mission for optical interferometry. In *42nd Congress of the International Astronautical Federation*, 1991. paper no. IAF-91-421.
- [5] D. P. Greenwood. Bandwidth specification for adaptive optics systems. *J. Opt. Soc. Am.*, 67:390–393, 1977.
- [6] J. W. Hardy. Adaptive optics—a progress review. *Proc. SPIE*, 1542:2–17, 1991.
- [7] W. E. Layman. Control structure interaction (CSI) technology. In P. Y. Bely, C. J. Burrows, and G. D. Illingworth, editors, *The Next Generation Space Telescope*, pages 263–269. Space Tel. Sci. Inst., 1989.
- [8] R. D. Reasenberg, R. W. Babcock, J. F. Chandler, M. V. Gorenstein, J. P. Huchra, et al. Microarcsecond optical astrometry: An instrument and its astrophysical applications. *Astron. J.*, 32:1731–1745, 1988.
- [9] G. Rousset, J. C. Fontanella, P. Kern, P. Gigan, F. Rigaut, P. Léna, C. Boyer, P. Jagourel, J. P. Gaffard, and F. Merkle. First diffraction-limited astronomical images with adaptive optics. *Astron. Astrophys.*, 230:L29, 1990.
- [10] M. Shao and M. M. Colavita. Long-baseline optical and infrared stellar interferometry. *Annu. Rev. Astron. Astrophys.*, 30:in press, 1992.
- [11] M. Shao, M. M. Colavita, B. E. Hines, D. H. Staelin, D. J. Hutter, K. J. Johnston, D. Mozurkewich, R. S. Simon, J. L. Hershey, J. A. Hughes, and G. H. Kaplan. The Mark III stellar interferometer. *Astron. Astrophys.*, 193:357–371, 1988.

# A NEW TRAJECTORY OPTIMISATION TOOL (ALTOS) APPLIED TO CONVENTIONAL LAUNCHERS

G. Lecohier and K. Mehlem

*Mathematical Studies Section, European Space Research and Technology Center, ESA, Noordwijk, The Netherlands*

**Abstract:** ALTOS is a newly developed Advanced Launcher Trajectory Optimisation Software. This new tool can be characterised by its three main features: Modelisation of the ascent vehicle, of the ascent trajectory and of constraints, 3DoF ascent trajectory simulation , 3 DoF ascent trajectory optimisation based on the direct collocation and direct multiple shooting method. In this present paper, the results obtained with ALTOS for conventional launchers such as Ariane 5 are presented together with the experience gained during the study of the operation and the performance characteristics of the tool.

**Keywords:** Simulation, Optimisation, Direct Collocation , Direct Multiple Shooting , Launcher, Ascent Trajectory

## 1.0 Introduction

In the design of a new conventional launcher one of the key issues is the most appropriate trajectory lifting the maximal payload mass into the desired orbit. For this type of problem, a variety of design, modelling and optimisation tools have been developed in the past. The ALTOS software is a new efficient development; the name stands for Advanced Launcher Trajectory Optimisation Software which is applicable to conventional launchers and to advanced winged and air-breathing spaceplanes. For a given launcher configuration and for selected flight control laws the first task of this tool is to simulate the 3 DoF ascent trajectory. However, the main task is to determine the flight control laws which allow to lift the maximum payload mass into the desired orbit, while satisfying a variety of path and boundary constraints along the ascent trajectory.

When applied to conventional launchers, the ALTOS software operation is divided into three parts: modelisation, simulation and optimization. These three aspects are accessible to the ALTOS user through a powerful user interface which contains state-of-the-art nested menus presented in a graphical environment. In the modelisation process the ALTOS user will have to describe the launcher propulsion system such as boosters and main engine mass flow, the environmental characteristics such as launch site, atmosphere and winds, the launcher configuration mass properties and the launcher aerodynamics. In addition to these data, the ascent trajectory constraints have to be selected. The ALTOS software has been designed such that the most common conventional launcher path and boundary constraints are selectable. Among them one can find for example the heat load, the dynamic pressure, ground station visibility, intermediary and final orbit characteristics, etc. For the simulation process, the user will have to describe the control laws in terms of pitch and yaw angle time history. The optimization methods which have been implemented are based on the direct optimization

methods; these are the direct collocation method and the direct multiple shooting method.

In the present paper the results obtained with ALTOS for an generic Ariane 5 configuration will be presented. First it is shown how the launcher has been modelled and how the different trajectory path and boundary constraints have been introduced and treated by ALTOS. In the next step, the simulated ascent trajectory are presented using the initial guess and optimal control strategy. The next section deals with the optimisation methods used within ALTOS. Finally, the last part of the paper will present the experience gained concerning the operation and the performance characteristics of the tool.

Note that the data presented in this paper under the name Ariane 5 data do not correspond to the latest Ariane 5 data and are in some areas are incomplete. For that reason, the payload optimal values and the optimal trajectories presented in this paper are only valid with respect to the input values to the ALTOS software.

## 2.0 Modelisation of Conventional Launchers/Trajectories

The modelisation of the ascent trajectory of a conventional launchers can be divided into four main sections namely the environmental models, the vehicle models, the trajectory modelisation with its path and boundary constraints, the control models.

Before detailing the models required within ALTOS, we will first introduce the "Phase" and the "Stage" concept. A "Phase" is a period of the ascent trajectory with constant modelling characteristics. A phase transition occurs at a change in the propulsion systems activity, at an instantaneous change in the launcher total mass (jettisoning of an empty stage), at a change in the control strategy, when a boundary constraint has to be met or when a path constraint has to be activated or deactivated. The "Stage" concept is

related to the vehicle in the sense that it corresponds to the propulsion staging. The functioning of each launcher stage contains thus one or more phases.

The environmental model allows the user to specify the central body parameters relevant for the ascent trajectory such as the gravitational factor, the J2 coefficient, the equatorial radius, the flattening coefficient. Also included in this model are the launch pad location, the atmospheric and wind models. The atmospheric data which are mandatory for realistic ascent trajectories are the pressure for further calculation of the thrust, the air density for calculation of the aerodynamic force or of the dynamic pressure and the velocity of sound for Mach number computation. These data can be given as function of the altitude and latitude but will be considered as time independent as conventional ascent trajectories last only a few hundred minutes.

The vehicle model is one of the driving parts within the ALTOS software. The main characteristic of a launcher is its mass dependency on time. The vehicle masses are divided into dry and propulsion masses. The dry masses are either transported up to target orbit or are released at the end of a phase. The propulsion systems are defined through specific impulse and the nozzle exit area, burning time, and either thrust or mass flows (propulsive and none propulsive). As these latter functions can only be given in tabulated form, the interpolation type has to be specified. Beside the mass properties of the launcher, the aerodynamic properties for each stage configuration have to be detailed. For axis-symmetric conventional launchers, the aerodynamic coefficient ( $C_a$ ,  $C_n$ ) or ( $C_d$ ,  $C_l$ ) are given as function of the angle of attack only.

The radial position, geocentric longitude, geocentric latitude and their inertial rate of change augmented by the mass rate are the seven state variables used for ascent trajectory modelling. This trajectory specification is completed after definition of the different path and boundary constraints which are active at the different phases of the ascent. ALTOS comprises the most commonly used boundary and path constraints for conventional launchers. These are limitations imposed on states, dynamic pressure, heat flux, bending moment, accelerations, walking impact path, tracking station visibility, controls, flight path azimuth, velocity-altitude/dynamic pressure, target orbit, etc.

Within ALTOS, the attitude and hence the thrust direction of a conventional launcher is controlled by pitch and yaw angles. The control strategies applied within a phase for the pitch are either constant pitch, constant pitch rate, gravity turn or optimisable pitch. The control law applied for the yaw angle are either constant yaw or optimisable yaw. Optimisable control means that the control value is optimisable at a given set of time points within the phase. The control value between these time points is calculated by piecewise linear interpolation.

### 3.0 Optimisation Methods

The optimal ascent trajectory problem even with multiple phases can be formulated in the form of a continuous optimal control problem (OCP). The classical indirect methods that solves the OCP problem were not selected for ALTOS; these methods give more accurate solutions and fast, but at the price of complex mathematical pre-analysis and of associated boundary values problems that are difficult to solve

especially when the optimal solution structure is not well known.

For these reasons direct optimisation methods were implemented in ALTOS. These methods are less accurate but have the capability to handle numerous complex constraints. The basis of the direct optimisation method is the transformation of the continuous optimal control problem into a non linear programming problem (NLP), i.e. a finite dimensional optimisation problem. Two different methods transforming the OCP into NLP are implemented. These are - a direct collocation method called TROPIC (Well, 1989) and - a direct multiple shooting method called PROMIS (Well, 1989). In these methods, the optimized control laws are not calculated as continuous differentiable function of time. Their values are only calculated over a predefined set of time points along the ascent trajectory. Between these time points, the controls are interpolated by piecewise linear functions. In the same manner, the path constraints are not treated as continuous functions but are evaluated over a other user-predefined set of time points.

### 4.0 Ascent Trajectory Simulation

To simulate the ascent trajectory dynamic, the formulation of the equations of motion of a mass point in a gravitational field were derived in geocentric coordinates. The equations are presented below, where (g) represents the contribution of the gravity field restricted to the first zonal term and (a) expresses the contribution of the external accelerations on the launcher due to the thrust, lift and drag. The control angles influence the ascent trajectory through thrust, lift and drag forces.

$$\dot{r} = v_r \quad (\text{EQ } 1)$$

$$\dot{\phi} = v_\phi / r \quad (\text{EQ } 2)$$

$$\dot{\lambda} = v_\lambda / (r \cos \phi) - \Omega_E \quad (\text{EQ } 3)$$

$$v_r = v_\phi^2 / r + v_\lambda^2 / r + g_r + a_r \quad (\text{EQ } 4)$$

$$v_\phi = (-v_r v_\phi - v_\lambda^2 \tan \phi) / r + g_\phi + a_\phi \quad (\text{EQ } 5)$$

$$\dot{v}_\lambda = -(v_r v_\lambda + v_\phi v_\lambda \tan \phi) / r + g_\lambda + a_\lambda \quad (\text{EQ } 6)$$

To fully describe the launcher behaviour a seventh equation of motion that describes the time dependency of the launch vehicle mass  $m$  is mandatory. This seventh equation describes all the mass flows of the different propulsion systems and also mass jettisoning during the ascent.

A Runge-Kutta integrator of order 4-5 has been implemented in ALTOS such that the full ascent trajectory can be reconstructed via a 3 DoF integration once the control profile has been specified by the ALTOS user (initial guess) or determined by the optimisation process (optimal solution).

### 5.0 Modelisation of an Ariane type Launcher

To illustrate the capability of ALTOS, a generic Ariane5/Hermes optimisation problem is presented. The objective is to determine the optimal payload mass that can be launched

from Kourou into a target orbit of 70x340 km, 28.5 deg inclination.

The control of the ascent trajectory is performed via pitch and yaw control. The ascent is segmented into 5 phases. The first phase lasts 5 s during which the launcher performs vertical lift-off. The second phase lasts 10 s. In this phase, the launcher performs a steering manoeuvre in form of a pitch turnover at constant rate. The value of the pitch rate is to be calculated by the optimisation process. The pitch should be constant in the third phase the duration of which has to be determined by the optimisation process. But at the end of the phase, a zero incidence angle in pitch is imposed so that the angle between the relative flight path angle and the pitch vanishes and that a gravity turn or a zero incidence flight can follow in the fourth phase. The zero angle of incidence is flown to reduce the aerodynamic bending loads. The gravity turn stays active until jettisoning of the 2 P230 solid boosters. During all these phases, the yaw should be constant at 60 degrees. In the fifth phase pitch and yaw have to be optimized. Three path constraints are active for this ascent:

- the dynamic pressure  $q < 40300 \text{ Pa}$ ,
- the heat flux  $1.705 \times 10^{-7} \sqrt{\rho v^3_{rel}} = \Phi_h \leq 75 \text{ kw/m}^2$
- a velocity-altitude constraint ;  
if  $v_{rel} \leq 5.35 \text{ km/s}$  then altitude  $h < 130 \text{ km}$   
otherwise altitude  $h < 100 \text{ km}$

The final boundary constraints are given by the target orbit parameters and by the safe impact of the H155 after phase 5 into the Pacific Ocean at least 200 km from the coast.

The launcher is considered to have 2 stages. The propulsion systems are 2 P230 solid boosters and the H155 main engine whose characteristics are given in the first table and the mass flows in fig. 1&2.

## 6.0 Trajectory Optimisation

The problem described above was first optimised by TROPIC. The optimised solution was then refined using the PROMIS optimizer. Table 2 lists the targeted and the achieved values for the constraints and the payload.

These results were obtained by simulation using the control laws derived by both optimisation processes. The TROPIC optimal solution was achieved using 19 collocations nodes. Among them 7 were placed on the 5th phase where the controls are optimisable. The sparse nodding is the reason for the discrepancies between the targeted values and the obtained values. In fact, in the TROPIC method, the state variables between two collocation nodes are approximated by polynomial functions. Looking to the fig. 1 & 2, one can see that the resulting mass flow is irregular with some abrupt variations. These variations can only be taken into account by a denser collocation noding especially in the area where one may expect non-smooth behaviour in a state variable. This option has a serious penalty. By increasing the number of collocation points, one also increases drastically the size of the optimisation problem and thus the computational time. Although TROPIC has its drawbacks, it is already of considerable help as the resulting solution provides the structure of the optimal controls.

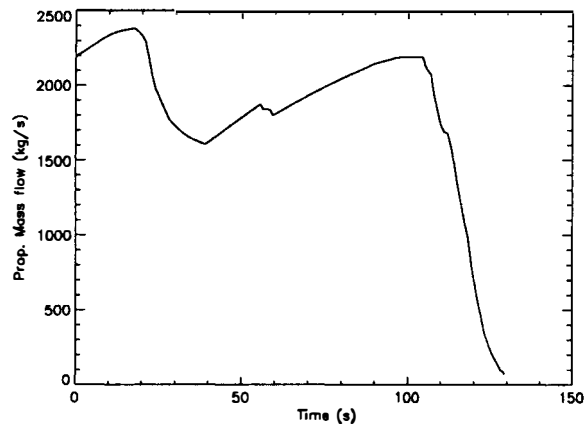


Fig1: P230 Propellant mass

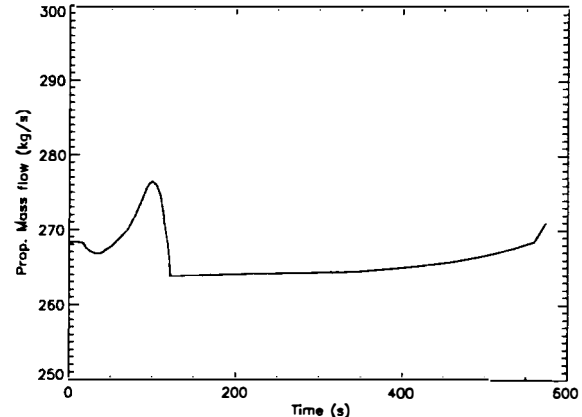


Fig2: H155 Propellant mass flow

TABLE 1. Engine characteristics

	2*P230	H155
Mass Jettisoned (kg)	71404 at $t=129.17 \text{ s}$	14944 at $t=574 \text{ s}$
Burned Prop. mass (kg)	471415	152815
Burned No Prop (kg)	3893	52
Total mass burned (kg)	475308 at $t=129.174 \text{ s}$	152877 at $t=574 \text{ s}$
Isp prop in vacuum (s)	271.21	430.11
Burn Time (s)	129.17	574
Nozzle Exit Area ( $\text{m}^2$ )	2 * 6.366	2.504
Active in phase	1-2-3-4	1-2-3-4-5

TABLE 2. Optimal results for restricted problem

	Target	Tropic	Promis
Mass perigee	optimal	22908	22307
apogee	70	68.03	70.14
inclination	340km	614.8	344.80
dynamic pressure	28.5 deg $<40300 \text{ Pa}$	28.51 $t=64 \text{ s}$	28.5 $t=64 \text{ s},$ $q=38535 \text{ Pa}$
Heat flux	$<75 \text{ kw/m}^2$	max = 56	max = 73.9
altitude	$<130 \text{ km}$	135	125.7
vel- alt	if $v > 5.35$	if $v > 5.35$	if $v = 5.35$
	$h < 100 \text{ km}$	$h = 119.0$	$h = 100.02$

This solution was then used as initial guess for a PROMIS run. PROMIS is based on a direct multiple-shooting method, so the right hand side of the state equations is fully active during the optimisation process. For phase 1, 2 and 3, single shooting meshes were considered, two shooting meshes were placed in phase 4 and 5. In phase 5, where the control parameters are optimisable, we placed 4 control nodes. This sparse noding leads to a non-smooth pitch profile (see fig. 5) when linear control interpolation is used. A jump in the control profile is also noticeable at t= 129.17 s as the connect conditions were not imposed in the controls at the phase transition occurring at the jettisoning of the P230 boosters (fig. 5 & 6). This connect condition was switched off on purpose for comparative reasons with reference cases. The simulation results obtained with the PROMIS optimal control laws show no violation of the path constraints (see fig. 7 & 8). There is only a small overshoot in the apogee altitude. This could be refined by requiring a greater accuracy of the optimal solution. The accuracy was fixed to 5. 10-4 in the present run and corresponds to 20 kg payload mass and to 2 km altitude.

The altitude, inertial velocity, the two control variables pitch and yaw, the heat flux and the dynamic pressure are the six variables which are plotted over time in fig. 3 to 8.

## 7.0 Some ALTOS Specifics

Before starting any optimisation procedure, the ALTOS user should carefully define a consistent conventional launcher model especially in term of propulsion and masses. In this task, the user will however get help from the software if he runs the ALTOS initialisation tasks where numerous consistency checks are performed.

Due to the ALTOS special design it has been found that the best strategy to solve a complex problem is by adopting a gradual approach. First, solve the boundary problem where all the path constraints are switched off. Once a solution is found, solve an extended problem by adding one or two path constraints. This procedure is repeated until the full constrained problem is achieved. This method has two advantages, a) it is easier to solve the problem when the shape of the trajectory and the structure of the controls are not known and b) this way avoids inconsistent problem definition.

While optimising a given problem, it was found more convenient to start the optimisation process with the TROPIC optimizer (based on the collocation method) which accepts more crude initial guesses. The state variable values have only to be acceptable and within the state box constraints at the collocation nodes. The optimal controls obtained with TROPIC are then used to determine the full trajectory by the trajectory simulator. The evaluation of the obtained trajectory is left to the ALTOS user. If the trajectory is violating several constraints path and/or boundary constraints, it is usually recommended to restart the optimisation process by adding some collocation nodes in critical areas namely where the collocation errors are the largest. This process is left to the user's judgement but he has to be aware that an increase of the number collocation nodes will result in a larger CPU time. Once an "acceptable" TROPIC optimal solution has been achieved, it is recommended to refines it using the

PROMIS optimizer. The switch from one optimisation method to the other is straightforward for the user who has only to activate the corresponding menu.

Since PROMIS is based on the direct multiple shooting method so that the equations of motion are fully integrated within the optimisation process, it leads directly to realistic trajectories. However, once an optimal PROMIS solution is found, it is necessary to check by simulation the path if the path constraints are acceptable within the constraints nodes. If violations occur between two path constraint nodes it is recommended to shift or add a path constraint node at the time point where this phenomena occurs. After this, it is necessary to repeat the PROMIS process. Experience shows that only few iterations are required to find a fully acceptable solution.

## 8.0 Conclusion

The ALTOS software is a powerful tool when applied to conventional launcher problems with numerous complex constraints. As most of the conventional launcher constraints can be treated by the software, the trajectory design of new conventional launchers such as Ariane 5 can be performed.

The two optimization methods available within the software are complementary. The direct collocation optimiser (TROPIC) is most efficient when dealing with smooth (slowly varying) state dynamics. However in more complicated cases, TROPIC already provides the structure of the optimal controls even with few collocations nodes. By using the direct multiple shooting method (PROMIS) which insures that the right hand side of the equations of motion are fully taken into account within the optimisation procedure it is possible to refine the TROPIC solution. Although the path constraints in the direct methods are only evaluated on a restricted set of time points, practice shows that by judicious placement of these path constraint nodes, acceptable solutions can be found.

The associated 3DoF simulation tool is useful in case of trajectory validation, of auxiliary calculations and of a priori or a posteriori control strategy evaluation.

While using ALTOS the user is helped by the software thanks to a powerful associated graphical user interface where all the important problem features can be displayed and thanks to instructive error messages or help menus for better understanding of conflictual situations.

## 9.0 Acknowledgement

The authors would like to thank the MBB and DLR team members who developed the ALTOS software under ESA contract. Their valuable advice in introducing the authors in the ALTOS problematics have helped them to appreciate the wide range of opportunities offered by the software.

## 10.0 References

- Well, K., D., Kraft, C., Jaensch and K., Schnepper (1989)  
ALTOS Technical Report TR1 : Survey paper on trajectory optimisation methods, ESA contract no. 8046/88/nl/jg
- Buhl, W., K. Ebert, H. Wolff (1992) ALTOS Technical Report TR2 : Modelization, ESA contract no. 8046/88/nl/jg
- Well, K., K. Ebert, and others (1992) ALTOS user's manuel, ESA contract no. 8046/88/nl/jg
- Palmer, A.S. (1991) Arian 5 data , private communication.

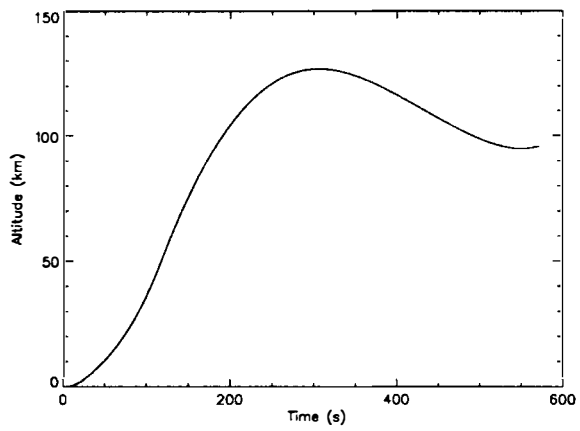


Fig 3. Altitude profile

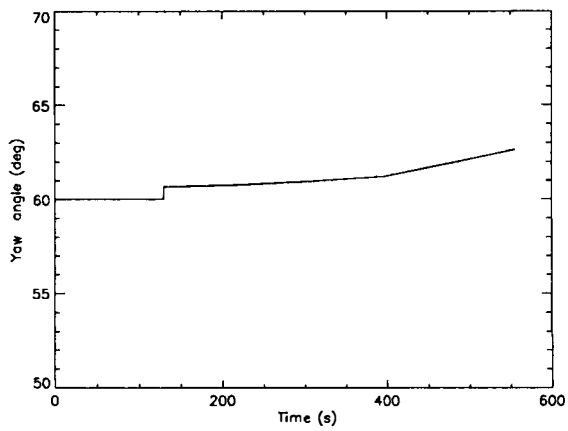


Fig 6. Second Control - Yaw profile

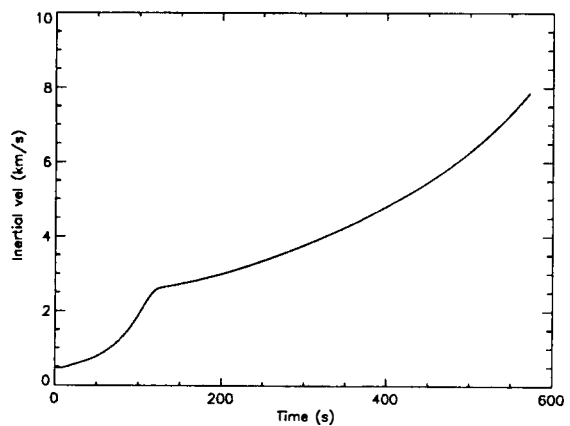


Fig 4. Inertial velocity profile

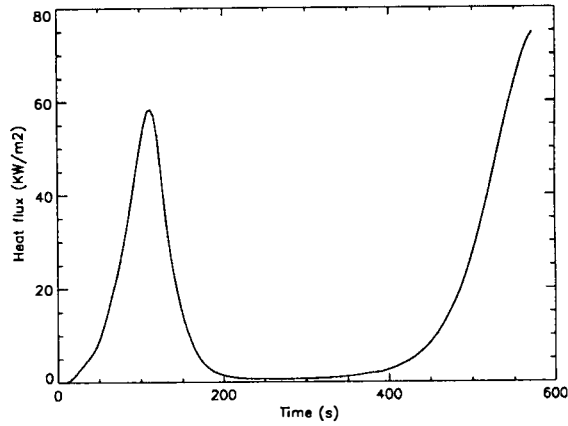


Fig 7. Evolution of the Heat flux

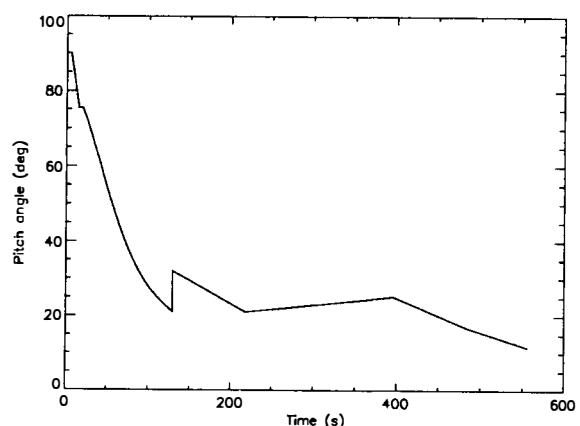


Fig 5. First control - Pitch profile

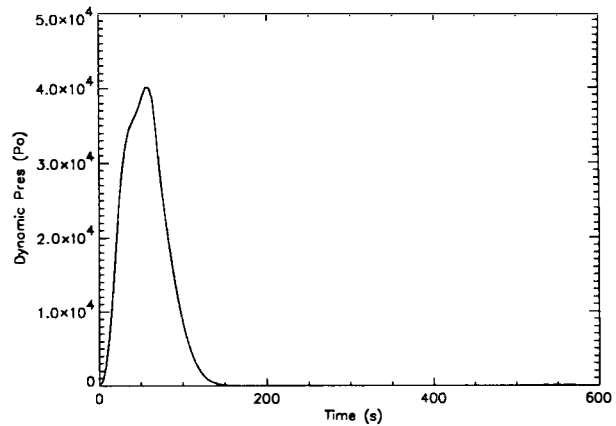


Fig 8. Evolution of the Dynamic pressure

# GUIDANCE AND TRAJECTORY OPTIMIZATION UNDER STATE CONSTRAINTS - APPLIED TO A SANGER-TYPE VEHICLE

R. Bulirsch and K. Chudej

*Lehrstuhl für Höhere und Numerische Mathematik, Sonderforschungsbereich 255, Transatmosphärische Flugsysteme,  
Technische Universität München, Postfach 20 24 20, D-8000 München 2, Germany*

**Abstract:** Complex real-life optimal control problems are usually subject to control and state inequality constraints. In generalization of earlier results of Maurer we present necessary conditions which hold if interior point conditions hold on active state constrained subarcs. These conditions are useful for an appropriate handling of piecewise defined model functions, derived e.g. from given table data. In addition we state a theorem giving information on the existence of contact points for ascent or descent optimization problems of point mass models of space vehicles or aeroplanes under dynamic pressure limits. These results are applied to the ascent optimization of a Sänger-type lower stage.

**Keywords:** optimal control; state inequality constraints; bang-bang controls; singular controls; interior point conditions; existence of contact points; multipoint boundary-value problem; multiple shooting method; space vehicle.

## 1. INTRODUCTION

The paper addresses the solution of complex optimal control problems with multidimensional control functions encountered e.g. in aeronautics and astronautics. These practical problems are often subject to control and state constraints. Often some quantities of the given model are only available as table data and must be approximated by suitable functions. Here in general the following problem arises: The convergence of the applied direct or indirect methods to solve the problem numerically depends crucially on the global differentiability properties of the used approximation functions, if no other precautions are taken. But the amount of work to construct a global approximating  $C^r$ -function rises enormously if  $r$  is large. A well known precaution consists in stopping the integration of the initial value problems at the in general isolated points of lower differentiability order. This leads to the preservation of the high order of the used integration method and the introduction of additional interior point conditions. We present here, in a slight generalization of earlier results of Maurer, necessary conditions which hold, if an interior point condition has to be fulfilled while a state constraint is active on a subarc.

In addition, we present a theorem giving information on the existence of state constrained subarcs and contact points for ascent and descent problems of point mass models under dynamic pressure constraints.

## 2. MATHEMATICAL MODEL

The space vehicle considered here is the lower stage of a two-stage Sänger type vehicle, with a turbo and ramjet engine in the lower stage and a conventionally rocket-propelled upper stage (c.p. e.g. Koelle and Kuczera, 1990). The whole system will be launched horizontally and will be able to deliver into orbit either a manned shuttle type upper stage or an unmanned cargo unit. The lower stage is winged and capable of performing cruising flights due to its airbreathing engines. Due to its importance on the resulting flight path a dynamic pressure constraint is considered in the problem formulation.

In order to obtain the detailed switching structure of the solution the problem is transformed into a multipoint boundary-value problem with jump conditions. Due to its complicated structure, a good first approximation of state and especially adjoint variables is needed to start the multiple

shooting algorithm. This first approximation is computed by a special direct collocation method which solves a nonlinear programming version of the original optimal control problem (von Stryk, 1991). So in fact an efficient hybrid approach is used (von Stryk and Bulirsch, 1992; von Stryk 1992).

The following notation is used:

#### State Variables

$v$	velocity
$\gamma$	path inclination
$\chi$	azimuth inclination
$h$	altitude
$\Lambda$	geographical latitude
$\theta$	geographical longitude
$m$	mass
$x = (v, \gamma, \dots, m)^T$	

#### Control Functions

$C_L$	lift coefficient
$\mu$	bank angle
$\delta$	mass flow
$\varepsilon$	thrust angle
$u = (C_L, \mu, \delta, \varepsilon)^T$	

#### Other Important Quantities

$a$	speed of sound
$D, L$	drag and lift force
$C_D, C_L$	drag and lift coefficient
$f$	right hand side of o.d.e.
$F$	reference area
$g$	gravitational acceleration
$H$	Hamiltonian
$I_{sp}$	specific impuls (turbo/ramjet)
$J$	performance index
$\lambda$	adjoint variables
$Ma$	mach number
$Q$	switching function
$q$	dynamic pressure
$r_0$	Earth's radius, $R = r_0 + h$
$T$	thrust force (turbo/ramjet)
$t$	time
$t_{engine}$	switching time of engines
$t_{staging}$	separation time
$\varrho$	atmospheric density
$\omega$	angular velocity

The objective of the optimization is to minimize the fuel consumption of the lower stage, i.e.

$$\min -m(t_{staging}) \quad (1)$$

s.t. the following constraints: The equations of motion of a point mass in a flight path oriented coordinate system over a spherical and rotating Earth with no wind in the atmosphere (see e.g. Miele, 1962) are used to describe the position and velocity of the space craft.

$$v = \frac{[T(v, h) \delta \cos \varepsilon - D(v, h; C_L)]}{m} - \quad (2)$$

$$\begin{aligned} \dot{v} &= -g(h) \sin \gamma + \omega^2 R \cos \Lambda (\sin \gamma \cos \Lambda - \\ &\quad - \cos \gamma \sin \chi \sin \Lambda) \\ \dot{\gamma} &= \frac{[T(v, h) \delta \sin \varepsilon + L(v, h; C_L)] \cos \mu}{mv} - (3) \\ &\quad - \left[ \frac{g(h)}{v} - \frac{v}{R} \right] \cos \gamma + 2 \omega \cos \chi \cos \Lambda + \\ &\quad + \omega^2 \cos \Lambda (\sin \gamma \sin \chi \sin \Lambda + \\ &\quad + \cos \gamma \cos \Lambda) \frac{R}{v} \\ \dot{\chi} &= \frac{[T(v, h) \delta \sin \varepsilon + L(v, h; C_L)] \sin \mu}{mv \cos \gamma} - (4) \\ &\quad - \cos \gamma \cos \chi \tan \Lambda \frac{v}{R} + \\ &\quad + 2 \omega (\sin \chi \cos \Lambda \tan \gamma - \sin \Lambda) - \\ &\quad - \omega^2 \cos \Lambda \sin \Lambda \cos \chi \frac{R}{v \cos \gamma} \\ \dot{h} &= v \sin \gamma \quad (5) \\ \dot{\Lambda} &= \cos \gamma \sin \chi \frac{v}{R} \quad (6) \\ \dot{\theta} &= \cos \gamma \cos \chi \frac{v}{R \cos \Lambda} \quad (7) \\ \dot{m} &= -\frac{T(v, h)}{g_0 I_{sp}(v, h)} \delta \quad (8) \end{aligned}$$

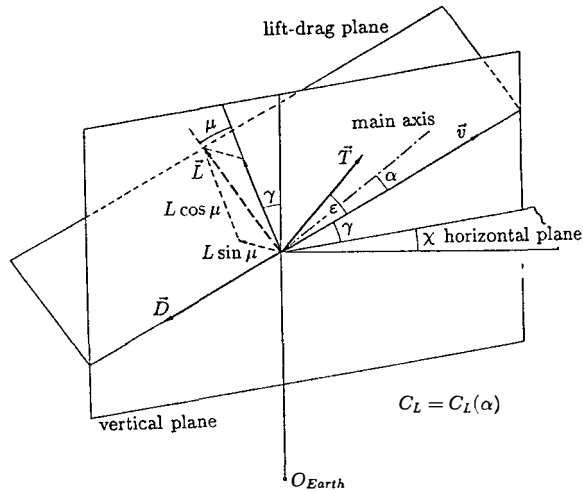


Fig. 1 State and Control Variables

The thrust model is based on tabular data<sup>1</sup> of the maximum thrust  $T(v, h)$  and the specific impuls  $I_{sp}(v, h)$  of a turbo and ramjet engine, which are approximated by  $C^\infty$ -functions through a nonlinear least squares approach. For more details see Bulirsch and Chudej (1991).

The used drag and lift model consists of a Mach-dependent quadratic polar<sup>1</sup>.

$$\begin{aligned} L(v, h; C_L) &= q(v, h) F C_L \\ D(v, h; C_L) &= q(v, h) F C_D(Ma; C_L) \\ C_D(Ma; C_L) &= C_{D_0}(Ma) + k(Ma) C_L^2 \end{aligned}$$

<sup>1</sup>Data from SFB 255, TU München and MBB, Deutsche Aerospace, München, Germany.

The following abbreviations are used:  $q(v, h) = 0.5 \varrho(h) v^2$ ;  $Ma = v/a(h)$ . More details about the formulas for  $\varrho(h)$ ,  $a(h)$  and  $g(h)$  are given in Chudej (1992).

The following control constraints on the linear control throttle setting  $\delta$  and the non-linear control  $C_L$  hold:

$$0 \leq \delta \leq 1 ; |C_L| \leq C_{L,max} \quad (9)$$

Due to its importance on the flight path the dynamic pressure  $q$  is constrained:

$$S(x) := q(v, h) - q_{max} \leq 0 \quad (10)$$

The used boundary conditions prescribing a horizontal launch at Kourou or Europe and the separation conditions of the two stages are omitted here due to the lack of space.

The engine switching point  $t_{engine}$  is described by

$$\underline{v} \leq v(t_{engine}) \leq \bar{v} ; \underline{h} \leq h(t_{engine}) \leq \bar{h}.$$

In summary, the following *optimal control problem* has to be solved:

Find the optimal engine switching point  $t_{engine}$ , the optimal staging time  $t_{staging}$  and piecewise continuous control functions  $u : [0, t_{staging}] \rightarrow U \subset \mathbb{R}^k$ , such that the performance index

$$J[u] = \varphi(x(t_{staging})) \quad (11)$$

is minimized s.t.

$$\dot{x} = f(x, u) , \quad f : \mathbb{R}^{n+k} \rightarrow \mathbb{R}^n \quad (12)$$

$$r_1(x(0)) = 0 , \quad r_1 : \mathbb{R}^n \rightarrow \mathbb{R}^{p_1} \quad (13)$$

$$r_2(x(t_{staging})) = 0 , \quad r_2 : \mathbb{R}^n \rightarrow \mathbb{R}^{p_2} \quad (14)$$

$$\tilde{N}(x(t_{engine})) = 0 , \quad \tilde{N} : \mathbb{R}^n \rightarrow \mathbb{R}^{\tilde{p}} \quad (15)$$

$$C(x, u) \leq 0 , \quad C : \mathbb{R}^{n+k} \rightarrow \mathbb{R}^c \quad (16)$$

$$S(x) \leq 0 , \quad S : \mathbb{R}^n \rightarrow \mathbb{R}^s \quad (17)$$

### 3. NECESSARY CONDITIONS OF CALCULUS OF VARIATIONS

We present here the necessary conditions of optimal control theory (see e.g. Bryson and Ho, 1975; Jacobson, Lele and Speyer, 1971; for a rigorous proof and an extension to multidimensional controls and multidimensional state constraints see Norris, 1973; Maurer, 1976, 1979a) which lead to a multipoint boundary-value problem. Due to the limited space we restrict the presentation to one state constraint ( $s = 1$ ) and one interior point constraint ( $\tilde{p} = 1$ ) both of order one (for the definition of the order of a function with respect to an o.d.e. system see e.g. Jacobson, Lele and Speyer 1971; Hamilton 1972; Maurer 1976). For some

technical assumptions (e.g. the Slater condition) which are, however, for practical problems sometimes partly hard to verify, we refer the reader to Maurer (1976, 1979a).

The dynamic pressure constraint<sup>2</sup> is of first order since

$$S(x) = q(v, h) - q_{max} \quad (18)$$

$$S^1(x, u) = \frac{\partial q}{\partial v} \dot{v}(x, u) + \frac{\partial q}{\partial h} \dot{h}(x). \quad (19)$$

Therefore, the augmented Hamiltonian  $H(x, u, \lambda, \eta) = \lambda^T f(x, u) + \eta^T S^1(x, u)$  is introduced. The adjoint variables  $\lambda$  satisfy the Euler-Lagrange-Equations

$$\frac{d\lambda}{dt} = -\frac{\partial H(x, u, \lambda, \eta)}{\partial x}. \quad (20)$$

Moreover,  $\eta$  satisfies  $\eta(t)S(x(t)) = 0$  on  $[0, t_{staging}]$ . The optimal controls  $u$  satisfy the minimum principle for all admissible controls  $u^*$  with respect to the augmented Hamiltonian.

$$u = \arg \min_{u^*} H(x, u^*, \lambda, \eta) \quad (21)$$

$$H(x, u, \lambda, \eta) = \text{const on } t \in [0, t_{staging}]. \quad (22)$$

**Theorem 1** (boundary subarc of the state constraint (e.g. Jacobson, Lele and Speyer, 1971; Maurer, 1976))

Suppose  $[t_a, t_b]$  is a boundary subarc of  $S$ , i.e.  $S = 0$  on  $[t_a, t_b]$ . Then the following jump and sign conditions hold:

$$\lambda^T(t_a^+) = \lambda^T(t_a^-) - \kappa^T S_x(t_a), \kappa \geq 0 \quad (23)$$

$$\lambda^T(t_b^+) = \lambda^T(t_b^-) \quad (24)$$

$$\eta \geq 0 ; \dot{\eta} \leq 0 \quad (25)$$

**Theorem 2** (contact point of the state constraint (e.g. Jacobson, Lele and Speyer, 1971; Maurer and Heidemann, 1975))

Suppose  $t_c$  is a contact point of  $S$ , i.e.  $S(t_c) = 0$ . Then the following jump condition holds:

$$\lambda^T(t_c^+) = \lambda^T(t_c^-) - \kappa^T S_x(t_c), \kappa \geq 0 \quad (26)$$

**Theorem 3** (interior point condition, state constraint inactive (e.g. Bryson and Ho, 1975))

Suppose  $N(x(t_i)) = 0$  and  $S(x(t_i)) < 0$ . Then the following jump condition holds:

$$\lambda^T(t_i^+) = \lambda^T(t_i^-) - \hat{\kappa}^T N_x(t_i) \quad (27)$$

The following statement combines Theorem 1 and 3 giving information how to modify eq. (27) on state constrained arcs, and is a slight generalization of Maurer (1979b) to multidimensional controls.

---

<sup>2</sup>Load factor limits can be treated analogously.

*Theorem 4* (interior point condition, boundary subarc of the state constraint)

Suppose that  $t_1 \in ]t_a, t_b[$  and  $N(x(t_1)) = 0; S = 0$  on  $[t_a, t_b]$ . Then the following jump condition holds in addition to eqs. (23,24):

$$\lambda^T(t_1^+) = \lambda^T(t_1^-) - \bar{\kappa}^T S_x(t_1) - \hat{\kappa}^T N_x(t_1) \quad (28)$$

Suppose  $\exists j: (S^1)_{u_j} \neq 0$  then  $\bar{\kappa} = -\hat{\kappa} \frac{(N^1)_{u_j}}{(S^1)_{u_j}}$ . (29)

Modified statements hold, if the order of the state constraint or the interior point condition are different from one.

This theorem is then applied to the Sänger type lower stage, where, due to the approximation of the functions  $C_D(Ma)$  and  $k(Ma)$ , the following interior point conditions of order one hold:

$$N_1(x(t_1)) = \frac{v}{a(h)}|_{t_1} - const = 0.$$

Several authors (e.g. Jacobson, Lele and Speyer, 1971; Hamilton, 1972; Maurer and Heidemann, 1975; Maurer, 1977) formulated theorems about the existence of contact points and boundary subarcs of state constraints of optimal control problems with one dimensional control functions. This approach can be transferred to the optimal control problem of the point mass model considered here with a multidimensional control function.

#### *Theorem 5* (existence of contact points)

Consider an optimal control problem described by the state differential equations (2-8) of a point mass model for a payload optimal ascent (1) and a dynamic pressure constraint (10). Suppose  $t_c$  is a contact point of the dynamic pressure constraint  $q \leq q_{max}$  then the Lagrange-parameter of Theorem 2 is  $\kappa = 0$ , if  $|C_L(t_c^-)| < C_{L,max}$ ,  $|C_L(t_c^+)| < C_{L,max}$  or  $\delta(t_c^+) = \delta(t_c^-) = 1$ .

#### *Corollary 6*

As a consequence no nontrivial contact points exist in the above mentioned case for payload optimal ascents of a point mass model under a dynamic pressure limit.

This is a very useful statement which discards a whole class of switching-structure-candidates for the optimal control problem.

A detailed investigation and application of the above mentioned minimum principle to the ascent optimization problem of chapter 2 shows that there exist several different competing control laws on boundary subarcs of the dynamic pressure constraint. These can be separated into two main groups, either with maximum thrust or with singular thrust. Figure 2 shows a detailed

picture of one boundary arc which is divided into subarcs with optimal controls of both main groups (see also Bulirsch and Chudej, 1991). The appearance of singular boundary arcs is also reported by Seywald (1991) for the related problem of a two-dimensional range optimization for a supersonic aircraft under dynamic pressure limits.

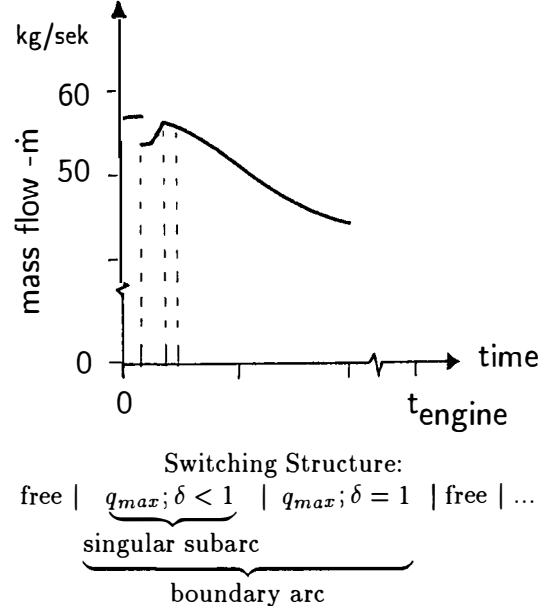


Fig. 2 Dynamic Pressure Boundary Arc (Detail)

#### 4. MULTIPONT BOUNDARY-VALUE PROBLEM

In summary, the set of all necessary conditions leads to a multipoint boundary-value problem with jump conditions of the following type:

Find the n-dimensional vector function  $z(t)$  and the parameters  $\tau_1, \dots, \tau_s, t_{staging}$  satisfying

$$\dot{z}(t) = F(z(t)) = \begin{cases} F_0(z(t)) & \text{if } 0 < t < \tau_1 \\ \vdots \\ F_s(z(t)) & \text{if } \tau_s < t < t_{staging} \end{cases}$$

$$\begin{aligned} r_i(z(0), z(t_{staging})) &= 0 & 1 \leq i \leq \bar{n} \\ r_i(z(\tau_{j_i}^-), z(\tau_{j_i}^+)) &= 0 & \bar{n} < i \leq n+s \\ j_i &\in \{1, \dots, s\} \end{aligned}$$

where  $F$  is a combination of the right hand sides of the state and adjoint equations and some so-called trivial equations of type  $\dot{\sigma} = 0$  for each jump parameter  $\sigma$ .

This multipoint boundary-value problem with jump conditions is solved by the multiple shooting method (e.g. Bulirsch, 1971; Stoer and Bulirsch, 1983; Oberle, 1982; Hiltmann, 1990). Extrapolation methods or high order Runge-Kutta-Fehlberg methods with step size control are used as initial

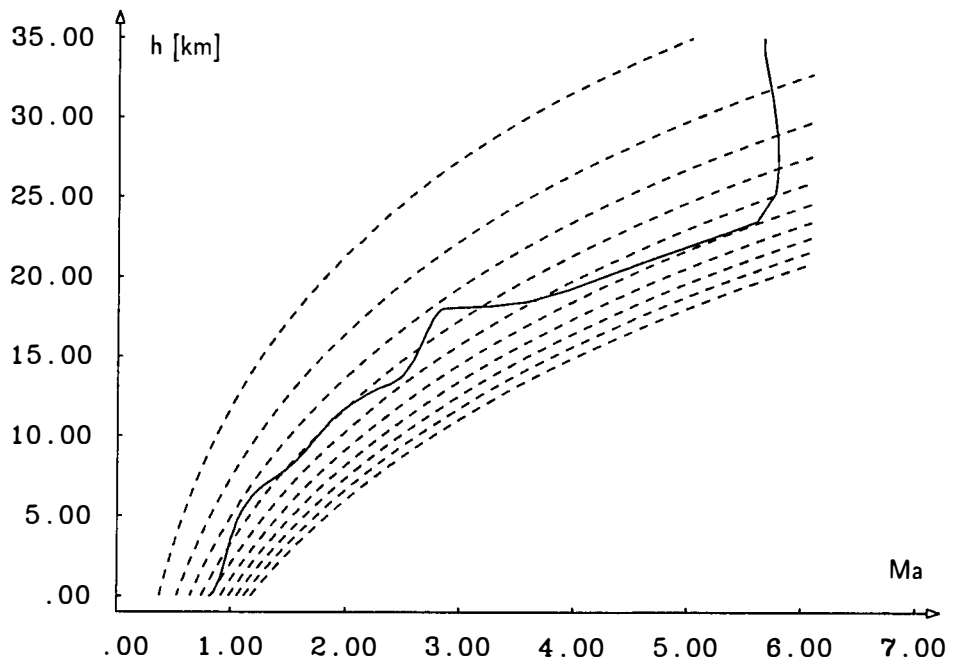


Fig. 3 Velocity-Altitude Diagram

value problem solvers. After a solution is obtained an a posteriori check of the additional sign conditions is made.

### 5. THE HYBRID METHOD

Nevertheless, the construction of an appropriate initial trajectory to start the multiple shooting method is even for the unconstrained case a difficult and time consuming problem. In particular no precise enough information about the adjoint variables is available. Therefore, a recently developed method was used which combines a special direct collocation method with the multiple shooting algorithm. Based on the approximate solution of the optimal control problem provided by a special direct collocation method initial estimates for the adjoint variables  $\lambda$  can be also obtained from the Lagrange multipliers of the nonlinear programming problem obtained via parametrization of the optimal control problem and using collocation techniques. By this fusion of direct and indirect methods, one can benefit from the large domain of convergence of the direct method and the high accuracy provided by the multiple shooting method. On the other hand, the disadvantage of direct methods, namely that these numerical solutions are sometimes not optimal, does not play a role if checked by an indirect method afterwards. Moreover, direct collocation is a very efficient method since no integration of differential equations is to be carried out; the right hand sides of the differential equations are to be fulfilled

only piecewise. For more details see von Stryk and Bulirsch (1992) and von Stryk (1991, 1992).

### 6. CONCLUSION

For the ascent optimization problem of an air-breathing lower stage of a two-stage space vehicle numerical solutions were computed by the multiple shooting method. Therefore, detailed information is provided with respect to the optimal switching structures, including maximum and singular thrust arcs and the appearance of boundary arcs of the considered state constraint. These practical computations were supported by an extension of known theoretical statements to the complex optimal control problem encountered here. In addition Theorem 5 includes a statement for a case where the Hamiltonian is allowed to be non-regular for this optimal control problem with mixed linear and nonlinear control functions. This may be of some interest from a theoretical point of view. The given necessary conditions for interior point conditions on active state constrained subarcs are getting more and more important for realistic and complex optimal control problems with piecewise defined model functions derived from table data. On the other side, the treatment of these complex optimal control problems is a lot easier when the multiple shooting method is combined with a special direct collocation method, thus giving a reliable and efficient hybrid method.

## 7. ACKNOWLEDGEMENT

This work was partly supported by the Deutsche Forschungsgemeinschaft (DFG) through the SFB 255 Transatmosphärische Flugsysteme.

## 8. REFERENCES

- Bryson, A.E. and Y.-C. Ho (1975). *Applied Optimal Control*, 2nd ed. Hemisphere Publishing Corp., Washington, D.C.
- Bulirsch, R. (1971). *Die Mehrzielmethode zur numerischen Lösung von nichtlinearen Randwertproblemen und Aufgaben der optimalen Steuerung*. Report der Carl-Cranz-Gesellschaft e.V., Oberpfaffenhofen, Germany. Reprint (1985) Mathematisches Institut, TU München, Germany.
- Bulirsch, R. and K. Chudej (1991). *Ascent Optimization of an Airbreathing Space Vehicle*. Proc. of the AIAA Guidance, Navigation and Control Conference. New Orleans, Louisiana, Paper-No. AIAA-91-2656, 520-528.
- Chudej, K. (1992). Optimal Ascent of a Hypersonic Space Vehicle. In R. Bulirsch, A. Miele, J. Stoer, K.H. Well (Ed.). *Proc. of the Conf. on Optimal Control, Oberwolfach, 1991*. Birkhäuser, Basel. (to appear). [Report des SFB 255: Transatmosphärische Flugsysteme. No. 10, Mathematisches Institut, TU München, Germany, 1991.]
- Hiltmann, P. (1990). *Numerische Lösung von Mehrpunkt-Randwertproblemen und Aufgaben der optimalen Steuerung mit Steuerfunktionen über endlichdimensionalen Räumen*. Dissertation, Mathematisches Institut, TU München, Germany.
- Jacobson, D.H., M.M. Lele and J.L. Speyer (1971). New Necessary Conditions of Optimality for Control Problems with State-Variable Inequality Constraints. *J. Math. Anal. Appl.*, 35, 255-284.
- Koelle, D.E. and H. Kuczera (1990). *Sänger Space Transportation System*. 41st IAF-Congress, Dresden, Germany, Paper-No. IAF-90-175.
- Maurer, H. (1976). *Optimale Steuerprozesse mit Zustandsbeschränkungen*. Habilitation, Mathematisches Institut, Universität Würzburg, Germany.
- Maurer, H. (1977). On Optimal Control Problems with Bounded State Variables and Control Appearing Linearly. *SIAM J. Control and Optimization*, 15, 345-362.
- Maurer, H. (1979a). Differential Stability in Optimal Control Problems. *Appl. Math. Optim.*, 5, 283-295.
- Maurer, H. (1979b). *On the Minimum Principle for Optimal Control Problems with State Constraints*. Report No. 41, Rechenzentrum der Universität Münster, Germany.
- Maurer, H. and U. Heidemann (1975). Optimale Steuerprozesse mit Zustandsbeschränkungen. In R. Bulirsch, W. Oettli and J. Stoer (Ed.). *Proc. of the Conf. on Optimization and Optimal Control, Oberwolfach, 1974*. Lecture Notes in Mathematics 477. Springer, Berlin.
- Miele, A. (1962). *Flight Mechanics I, Theory of Flight Paths*. Addison-Wesley, Reading, Massachusetts.
- Norris, D.O. (1973). Nonlinear Programming Applied to State-Constrained Optimization Problems. *J. Math. Anal. Appl.*, 43, 261-272.
- Oberle, H.J. (1982). *Numerische Berechnung optimaler Steuerungen von Heizung und Kühlung für ein realistisches Sonnenhausmodell*. Habilitation, Report M-8310, Institut für Mathematik, TU München, Germany.
- Seywald, H. (1991). *Optimal Control Problems with Switching Points*. Report NASA-CR 4393. Virginia Polytechnic Institute and State University, Blacksburg, Virginia.
- Stoer, J. and R. Bulirsch (1983). *Introduction to Numerical Analysis*, 2nd ed. Springer, New York, New York.
- von Stryk, O. and R. Bulirsch (1992). Direct and Indirect Methods for Trajectory Optimization. *Annals of Operations Research*. (to appear). [Report des DFG-Schwerpunktprogrammes: Anwendungsbezogene Optimierung und Steuerung. No. 271, Mathematisches Institut, TU München, Germany, 1991.]
- von Stryk, O. (1991). Ein direktes Verfahren zur näherungsweisen Bahnoptimierung von Luft- und Raumfahrzeugen unter Berücksichtigung von Beschränkungen. *Z. angew. Math. Mech.*, 71, 6, T705-706.
- von Stryk, O. (1992). Numerical Solution of Optimal Control Problems by Direct Collocation. In R. Bulirsch, A. Miele, J. Stoer, K.H. Well (Ed.). *Proc. of the Conf. on Optimal Control, Oberwolfach, 1991*. Birkhäuser, Basel. (to appear). [Report des DFG-Schwerpunktprogrammes: Anwendungsbezogene Optimierung und Steuerung. No. 322, Mathematisches Institut, TU München, Germany, 1991.]

## ASCENT GUIDANCE FOR AN AEROSPACE PLANE

K.D. Mease\*

*Department of Mechanical and Aerospace Engineering, Princeton University, Princeton, NJ 08544-5263, USA*

**Abstract**—A single-stage vehicle using airbreathing propulsion holds promise for a more economical delivery of payloads to orbit. The utility of the vehicle is contingent on having a guidance capability for flying a near minimum-fuel ascent trajectory. The challenges in ascent guidance are identified via an analysis of the guidance problem relative to that for the U.S. Space Shuttle. Feedback guidance logic for the hypersonic phase of a near-minimum-fuel ascent trajectory is described. The two-time-scale nature of the vehicle translational dynamics allows the translational state space to be decomposed approximately into an invariant slow manifold and an invariant foliation of fast manifolds. Robust near-optimal guidance is synthesized as a composite of the minimum-fuel control on the slow manifold—as determined by the dynamic pressure and heat rate constraints—and a fast control for robust tracking of the slow manifold in the presence of atmospheric disturbances and modeling errors. The tracking control is designed using feedback linearization and the bandwidth-limited variable structure control method. Simulations indicate the effectiveness of the guidance logic.

**Keywords**—Aerospace Plane; Trajectory Guidance; Singular Perturbations; Feedback Linearization; Variable Structure Control.

## Introduction

The term aerospace plane refers here to a class of horizontal takeoff, single-stage-to-orbit vehicles that use primarily airbreathing engines to accelerate to orbital velocity. The flight envelope is defined by dynamic pressure, acceleration, and heat rate limits. The viability of the vehicle depends critically on the capability of guiding it along a fuel-efficient ascent path within the flight envelope.

In this paper, results from previous studies are brought together to analyze the aerospace plane ascent guidance problem and describe a partial solution. Based on available aerospace plane aerodynamic and propulsion models,<sup>1</sup> the minimum fuel ascent trajectory is presented. The guidance problem is then assessed relative to that of the U.S. Space Shuttle.

While the combined significance and uncertainty of the aerodynamic forces poses a difficult guidance problem, the two-time-scale structure in the translational dynamics under the minimum-fuel ascent control program simplifies the problem. This structure was postulated in [2] and has been verified<sup>3</sup> for the aerospace plane model mentioned above. The hypersonic arc of the minimum-fuel ascent trajectory up to Mach 23 lies approximately on a reduced-order slow manifold in the translational state space; for this

arc, the optimal control program is dictated by local concerns—fuel performance and safety constraints—and not by the objective of reaching the target orbit.<sup>2</sup>

The guidance problem is further simplified by the constraint boundary tracking feature of the minimum-fuel ascent. The optimal hypersonic arc lies on the lower boundary of the flight envelope established by dynamic pressure, acceleration and heating constraints.<sup>2-4</sup> This feature suggests treating the ascent guidance problem during the hypersonic phase as a constraint boundary tracking problem.<sup>3</sup> Robust, near minimum-fuel constraint boundary tracking logic<sup>5</sup>—designed using a blend of singular perturbations, optimal control, feedback linearization, and variable structure control—is described and demonstrated by simulation.

## Modeling

We consider ascent in the equatorial plane. Defining velocity relative to an inertial frame with origin at the earth's center, assumed nonaccelerating, and orientation fixed with respect to the celestial sphere, the translational state equations, in an inverse square central gravity field, are

$$\dot{E} = \frac{VR_T(\alpha, \pi; E, r, \gamma)}{m} \quad (1)$$

$$\dot{in} = -f(\alpha, \pi; E, r, \gamma) \quad (2)$$

\* Assistant Professor

$$\dot{r} = V \sin \gamma \quad (3)$$

$$\dot{\gamma} = \frac{R_N(\alpha, \pi; E, r, \gamma)}{mV} - \left( \frac{\mu}{r^2} - \frac{V^2}{r} \right) \frac{\cos \gamma}{V} \quad (4)$$

where  $E = \frac{1}{2}V^2 - \mu/r$  is the specific energy,  $m$  is the vehicle mass,  $r$  is the radial distance of the vehicle center of mass from the earth's center, and  $\gamma$  is the flight path angle that defines the direction of the inertial velocity.  $V$  is viewed as a function of  $E$  and  $r$ , and  $\mu$  is the gravitational parameter.

The aerodynamic and propulsion forces are blended into control-to-force maps

$$R_N = R_N(\alpha, \pi; E, r, \gamma) \quad (5)$$

$$R_T = R_T(\alpha, \pi; E, r, \gamma) \quad (6)$$

Similarly, the control-to-fuel flow rate map is defined as

$$f = f(\alpha, \pi; E, r, \gamma) \quad (7)$$

An available model<sup>1</sup> and the 1976 U.S. Standard Atmosphere<sup>6</sup> or perturbations thereof are used to construct the control-to-force and control-to-fuel flow rate maps.

The controls are the angle-of-attack ( $\alpha$ ) and the throttle vector ( $\pi$ ). For conceptual simplification, we assume there are distinct linear throttles for a ramjet, a scramjet, and a rocket engine. The use of angle of attack as a control requires some discussion. In the model employed here, engine performance does not vary with angle of attack. It is more likely, however, that the engine performance will be highly sensitive to angle of attack. An extreme case is where engine performance dictates the angle of attack and the vertical lift must be controlled by varying the bank angle. Except in the discussion, the coupling between angle of attack and engine performance is neglected here.

The outputs of interest are the dynamic pressure  $q$  and the convective heat transfer rate  $Q$ , given by

$$q = \frac{1}{2}\varrho V_{\text{air}}^2 \quad (8)$$

$$Q = \frac{C}{\sqrt{r_n}}(1 - g_w)\sqrt{\varrho}V_{\text{air}}^3 \quad (9)$$

where  $\varrho$  is the atmospheric density;  $V_{\text{air}}$  is the air relative velocity;  $r_n$  is the nose cap radius of curvature at the stagnation point; and  $g_w$  is the ratio of wall to free stream enthalpy, taken here to be 0.05. A value of the constant  $C$  of  $1.876 \times 10^{-8}$  yields<sup>7</sup> the heat rate in BTU/ft<sup>2</sup>/sec, if  $\varrho$  is in slugs/ft<sup>3</sup>,  $V_{\text{air}}$  is in ft/sec and  $r_n$  is in ft.

## Minimum-Fuel Ascent

The target is a low earth orbit. Taking a circular orbit as a specific example, the final conditions are

$$E(t_f) = -\mu/2r_{LEO}; r(t_f) = r_{LEO}; \gamma(t_f) = 0 \quad (10)$$

where  $r_{LEO}$  is the radius of the target orbit and  $t_f$  is the free final time. Achieving a particular position on

the orbit is not considered here as part of the ascent guidance problem. To ensure the safety of the vehicle and crew, dynamic pressure and heat rate constraints are imposed in the form

$$q \leq q_{\max} \quad (11)$$

$$Q \leq Q_{\max} \quad (12)$$

An acceleration constraint is not imposed since the unconstrained accelerations are reasonable for the models employed here. There is also a lower bound on the final vehicle mass due to the finite fuel supply. The control constraints are that angle of attack has lower and upper bounds, and each throttle has a lower bound of zero and an upper bound of unity.

The ascent problem is to determine a piecewise continuous control program  $u = (\alpha, \pi)$  on  $[t_0, t_f]$  that takes the vehicle from the initial state to the target orbit without violating the constraints. The control programs that solve the ascent problem make up the feasible control set. The minimum-fuel ascent problem is to determine the feasible control program that minimizes fuel mass consumed.

A representative minimum-fuel trajectory<sup>3,4</sup> is shown in Fig. 1. In [4], the dynamic pressure limit is  $q_{\max} = 1260$  psf below Mach 1 and increases linearly to 2000 psf by Mach 3. The dynamic pressure limit above Mach 3 is 2000 psf.<sup>3,4</sup> The heat rate is constrained<sup>3</sup> not to exceed 400 BTU/ft<sup>2</sup>s. The maximum heat rate is high relative to that of the Shuttle, since active cooling is assumed. The target orbit<sup>3</sup> is circular at an altitude of 100nm (185km).

## Ascent Guidance Problem

The nominal guidance objective is to fly the minimum-fuel trajectory, i.e., maximize performance. Flying the minimum-fuel trajectory, however, means flying on constraint boundaries, i.e., with no safety margin. Given the modeling uncertainties, the guidance logic must provide a compromise between performance and safety. The modeling uncertainties are bookkept as uncertainties in the control-to-force maps, the control-to-fuel flow rate map, and the output maps. The specific sources of uncertainty that contribute to the errors in these maps are the following. The relations, at a given point in time and space, between the altitude and the ambient atmospheric variables, such as density, pressure, temperature and speed of sound, are uncertain; the atmosphere model, such as the 1976 U.S. Standard, on which the guidance logic is based predicts at best average ambient conditions. Also the computation of  $\vec{V}_{\text{air}}$ , at a given point in space and time, requires knowing the inertial velocity of the air at that point. The atmospheric velocity has a component due to the earth's rotation and a component due to the earth-relative atmospheric motion, i.e., the wind. The latter component is the most uncertain.

Before discussing the aerospace guidance problem further, the Space Shuttle ascent guidance<sup>8,9</sup> is reviewed for purposes of comparison. A representative ascent trajectory is shown in Fig. 1. During the first stage of ascent, the solid rocket boosters (SRBs) and the three main engines accelerate the vehicle to about Mach 4. The sequence vertical climb–pitchover maneuver– gravity turn comprises the nominal flight path. This flight path is the most fuel efficient compromise between drag and gravity losses that does not violate the lateral aerodynamic load constraints. The nominal flight path is determined prior to the launch day, based on the monthly mean wind. Inertial attitude commands consistent with the nominal path are preprogrammed into the onboard computer(s) as functions of the air-relative speed. A few hours before launch, winds are measured using balloons. If the differences from the mean are not too large, they are accommodated by closed-loop load relief. Lateral accelerations are measured and, by gimbaling the SRBs, maintained at safe levels. For large deviations from the mean winds, the nominal trajectory is reprogrammed or the launch is postponed. Axial acceleration is kept below 3 g's by a preprogrammed throttling back of the main engines around the peak in dynamic pressure.

The Space Shuttle jettisons its SRBs at around Mach 4 and 140,000 ft (43 km). Then linear tangent steering is used to fly along a near minimum-fuel path to orbit while accelerating until the main engine cutoff at a speed of roughly 23,000 ft/s. At separation of the SRBs, the aerodynamic force accounts for less than 2% of the total force, so that only the thrust and gravitational forces need be considered subsequently. Under the assumptions of uniform gravity and flat earth, the minimum-fuel steering program, for a given thrust magnitude program, is for the tangents of the thrust angles to vary linearly with time. The constants in the linear steering laws are chosen such that specified altitude, speed, flight path angle, and orbit plane are achieved at the time of main engine cutoff. Following separation of the external tank, the orbital maneuvering system supplies the required orbit insertion burns, again based on linear tangent steering.

The distinctive features of an aerospace plane—horizontal take- off, structural constraints different from those of the Shuttle, and airbreathing engines—lead to a much different minimum-fuel flight path. Greater drag losses are accepted in order to achieve better engine performance. The aerospace plane accelerates to Mach 3 at maximum dynamic pressure except for the initial transient/citePow91. Although the aerospace plane structure will not be as sensitive to lateral aerodynamic loads as the Shuttle and other rocket launch vehicles, engine performance and attitude control may restrict the range of angle of attack.

The period during which the aerospace plane accelerates from Mach 3 to Mach 23 is referred to here (somewhat incorrectly) as the hypersonic phase.

The acceleration is achieved by ramjet and scramjet propulsion. The optimal ramjet/scramjet performance is typically achieved by flying at full throttle and at maximum dynamic pressure or maximum heat rate, whichever is more restrictive. The ramjet to scramjet switch at Mach 6.9 is readily determined from the optimality conditions. Thus the challenge for guidance is to develop steering logic that yields fuel-efficient yet safe ascent. The vehicle during this phase climbs from 50,000 to 150,000 ft, thus remaining well within the atmosphere. Aerodynamic force is considerable and cannot be neglected. Linear tangent steering is not a good approximation of the minimum-fuel program. Thus a different guidance logic is required for the hypersonic phase of the aerospace plane ascent.

At the point when the scramjet begins to lose effectiveness in further accelerating the aerospace plane, the minimum-fuel strategy is to increase the angle of attack in order to increase lift and climb out of the atmosphere. We refer to this ascent phase as the climb- out phase. The climb-out trajectory, powered by the rocket engine, is reminiscent of a gravity turn, and is followed by a coast to orbital altitude and an insertion burn into the specified target orbit. Even though the altitude at the initiation of the climb-out is comparable to the altitude at which the Shuttle begins linear tangent steering, the aerodynamic force is not negligible due to the near orbital speed.

## Time-Scale Structure

A consequence of the hypothesis that  $r$  and  $\gamma$  change faster than  $E$  and  $m$ —an extension of the energy state hypothesis used in aircraft dynamics—is that the translational state space has a particular manifold structure. There is an isolated two-dimensional, control dependent, invariant slow manifold and an invariant foliation of two-dimensional fast manifolds, each of which intersects the slow manifold transversely. This hypothesis for the aerospace plane dynamics was put forth and studied in [2]. For the models employed here, it has been verified that the dynamics of the reduced-order subsystems, obtained through a first-order approximation of the slow manifold and a zeroth-order approximation of the fast foliation, combine to provide an adequate description of the original dynamics during the hypersonic phase.<sup>3</sup>

Given the manifold structure, the control  $u = (\alpha, \pi)$  can be considered a composite of slow and fast components,  $u = u_s + u_f$ , where  $u_f$  is zero on the slow manifold, and each component can be designed separately. In the following, the first-order approximation of the slow manifold and the zeroth-order approximation of each fast manifold are used, but in referring to them we simply use slow manifold and fast manifold, respectively. The dynamics on the slow manifold are given by Eqs.(1,2), supplemented by the two al-

gebraic relations, between the state and control variables, that define the slow manifold. The dynamics on a fast manifold are given by Eqs.(3,4) with energy and mass constant to zeroth-order. Values of the state variables on the slow manifold are denoted by the subscript “*s*”.

## Guidance Logic for Hypersonic Phase

In this section, guidance logic<sup>5</sup> for the hypersonic phase is described that yields robust near-minimum-fuel performance and robust safety with respect to modeling uncertainty. This guidance logic has evolved through several previous studies.<sup>2,3</sup>

### Minimum-Fuel Slow Controls

The minimum-fuel slow controls at each point on the slow manifold are given by<sup>2,3</sup>

$$\alpha_s^*, \pi_s^* = \arg \max \left[ -\frac{dE}{dm} \right] = \arg \max \left[ \frac{VR_T}{mf} \right] \quad (13)$$

This control law, together with the two relations defining the slow manifold, specify, for each pair  $(E_s, m_s)$ , the optimal controls and the values of the fast variables  $r_s$  and  $\gamma_s$ . In fact, using the relation between  $r$  and  $\alpha$  on the slow manifold, one can maximize the function given above by choosing the throttles and the radial distance, rather than the throttles and the angle of attack. Eq.(13) leads to optimal throttle and engine switching logic [2, 3]. For our models, we find that the minimum-fuel slow control program is to use full throttle for the active engine mode and a radial distance dictated by safety constraints (dynamic pressure or heat rate). The unconstrained optimal value of  $r_s$  violates at least one of the safety constraints.

Given the uncertainty in  $R_T$  and  $f$ , one could assume a probability distribution for the errors and replace the function being maximized with its average over the uncertainty. This is probably the best way to establish the switching conditions between engine modes. The optimal throttle setting should be full throttle independent of the error. Regarding the optimal radial distance, the uncertainties in the output maps are the important ones, since the constraints determine the optimum. There is a trade-off between performance and safety. Performance considerations dictate averaging over the uncertainty; safety considerations dictate biasing  $r_s$  in the direction of safety by an amount commensurate with the uncertainty in the relevant output map. Detailed vehicle knowledge is required to make the appropriate design decision.

### Robust Fast Controls

Only the angle of attack is used to control the fast dynamics during the hypersonic phase. Since the

minimum-fuel program on the slow manifold is to use full throttle for the optimal engine mode, leaving room for a fast component in the throttle would entail backing off from this program. Whereas performance was the primary concern in designing the slow controls, safety is the primary concern in designing the fast control.

The logic for the fast component of the angle of attack results from feedback linearization and variable structure control. Based on the zeroth-order singular perturbation approximation, the guidance problem for the fast dynamics is reduced to a regulation problem on a constant energy and mass plane. Replacing the fast state pair  $(r, \gamma)$  with either  $(q, \dot{q})$  or  $(Q, \dot{Q})$  and introducing an appropriate control transformation,<sup>3</sup> the fast dynamics are exactly linearized. Control logic for regulating to  $(q_{\max}, 0)$  or  $(Q_{\max}, 0)$  is designed by introducing an integral state variable  $z$ , where  $\dot{z} = q - q_{\max}$  or  $Q - Q_{\max}$ , and constructing a bandwidth-limited variable structure control for the third-order linear system.

The variable structure control is designed to establish an attracting (sliding) plane in the three-dimensional state space on which the desired set point is asymptotically stable. By using linear control in a small boundary-layer around the sliding plane, the high gain and chattering behavior of the ideal variable structure control is eliminated. Based on estimated bounds on a nonlinear, nonautonomous disturbance to the nominally linear dynamics, the parameters of the variable structure control law are determined such that the boundary-layer is globally attracting in a finite time and such that, once in the boundary layer, the state is driven to a trapping neighborhood of the desired set point in a finite time. Further details can be found in [5] and the references therein.

## Simulations

The effectiveness of the feedback guidance logic is indicated by simulating the hypersonic ascent phase. The initial values of the state variables are consistent with a speed of Mach 3, a dynamic pressure of 2000 psf, a mass of 280,000 lbf and a flight path angle of zero.

The atmospheric model used in the guidance logic is an exponential approximation of the U.S. Standard Atmosphere. The errors in the atmospheric model introduce errors in the control-to-force, control-to-fuel flow rate and output maps. The safety constraints are  $q_{\max} = 2000 \text{ psf}$  and  $Q_{\max} = 400 \text{ BTU}/\text{ft}^2/\text{sec}$ . Since the state variables  $E$ ,  $r$ , and  $\gamma$  are defined with respect to an inertial frame, we assume they can be accurately determined from inertial measurements. We further assume the mass is accurately known by measuring the fuel flow rate. We also assume that the outputs  $q$  and  $Q$  are measured directly without error. The values of the control design parameters have not

been fine-tuned. Various balances between performance and safety could be achieved.

Fig.(2) shows the guided flight through a nonstationary atmosphere in which a sequence of density pulses is superimposed on the stationary Standard Atmosphere. The solid curves show the behavior of the variable on the left axis; the dashed curves show the behavior of the variable on the right axis. There are two 20% density increases with pulse-width 50 sec: one beginning at 250 sec, the other at 700 sec. There are two 10% pulses, with pulse-width 25 sec: an increase at 350 sec and a decrease at 625 sec. Although the guidance decisions are based on an inaccurate atmosphere model, the active constraint boundary is accurately tracked. Compared with the ascent in the unperturbed Standard Atmosphere, the vehicle mass at the initiation of the climb out phase is reduced by about 3%. To generate the rapid flight-path-angle adjustments that are necessary to follow the time-varying altitude of the dynamic pressure and heat rate constraints, somewhat large angle-of-attack values are required. The largest angle-of-attack values are required when the dynamic pressure has dropped and lift is harder to produce. The largest angle-of-attack values produce axial loads that are at most 1.5 g's.

## Conclusions

In accelerating from supersonic to near orbital speed, an aerospace plane experiences aerodynamic forces that are large and cannot be modeled accurately. The linear tangent steering used by the U.S. Space Shuttle for the same acceleration phase is not valid, because it only produces a near minimum-fuel ascent when aerodynamic forces are negligible.

The two-time-scale and constraint boundary tracking nature of the aerospace plane ascent under the minimum-fuel control program facilitates the development of guidance logic. The two-time-scale nature of the translational dynamics allows the corresponding state space to be decomposed approximately into an invariant slow manifold and an invariant foliation of fast manifolds. Robust near-optimal guidance has been synthesized as a composite of the minimum-fuel control on the slow manifold—as determined by the dynamic pressure and heat rate constraints—and a fast control for robust tracking of the slow manifold in the presence of atmospheric disturbances and modeling errors. The tracking problem has been solved as a family of regulation problems on the fast foliation, using the feedback linearization methodology and a bandwidth-limited variable structure controller. Simulations indicate the effectiveness of the guidance logic.

## Acknowledgment

This research was supported by the NASA Langley Research Center under Grant NAG1-907.

## References

- [1] Shaughnessy, J.D., Pinckney, S.Z., McMinn, J.D., Cruz, C.I., and Kelley, M.-L., "Hypersonic Vehicle Simulation Model: Winged-Cone Configuration," NASA TM 102610, Nov. 1990.
- [2] Corban, J.E., Calise, A.J., and Flandro, G.A., "Rapid Near-Optimal Aerospace Plane Trajectory Generation and Guidance," *Journal of Guidance, Control and Dynamics*, Vol.14, No.6, 1991, pp. 1181-1190.
- [3] Van Buren, M.A., and Mease, K.D., "Aerospace Plane Guidance Using Time-Scale Decomposition and Feedback Linearization," *Journal of Guidance, Control and Dynamics*, Vol. 15, No. 5, 1992.
- [4] Powell, R.W., et al, "Ascent Performance of an Air-Breathing Horizontal-Takeoff Launch Vehicle," *Journal of Guidance, Control and Dynamics*, Vol.14, No.4, 1991, pp. 834-839.
- [5] Mease, K.D. and Van Buren, M.A., "A Nonlinear Geometric Synthesis of Aerospace Plane Ascent Guidance Logic," IFAC Nonlinear Control System Design Symposium, Bordeaux, France, June 24-26, 1992.
- [6] Anon., *U.S. Standard Atmosphere, 1976*, National Oceanic and Atmospheric Administration, NASA and United States Air Force, Washington, DC, Oct. 1976.
- [7] Tauber, M.E. and Yang, L., "Performance Comparison of Maneuvering Vehicles Returning from Orbit," AIAA Paper 87-2490, 1987.
- [8] McHenry, R.L., Brand, T.J., Long, A.D., Cockrell, B.F., and Thibodeau III, J.R., "Space Shuttle Ascent Guidance, Navigation, and Control," *J. Astronautical Sciences*, Vol. 27, No. 1, pp. 1-38, 1979.
- [9] Schleich, W.T., "The Space Shuttle Ascent Guidance and Control," AIAA Paper No. 82-1497, 1982.

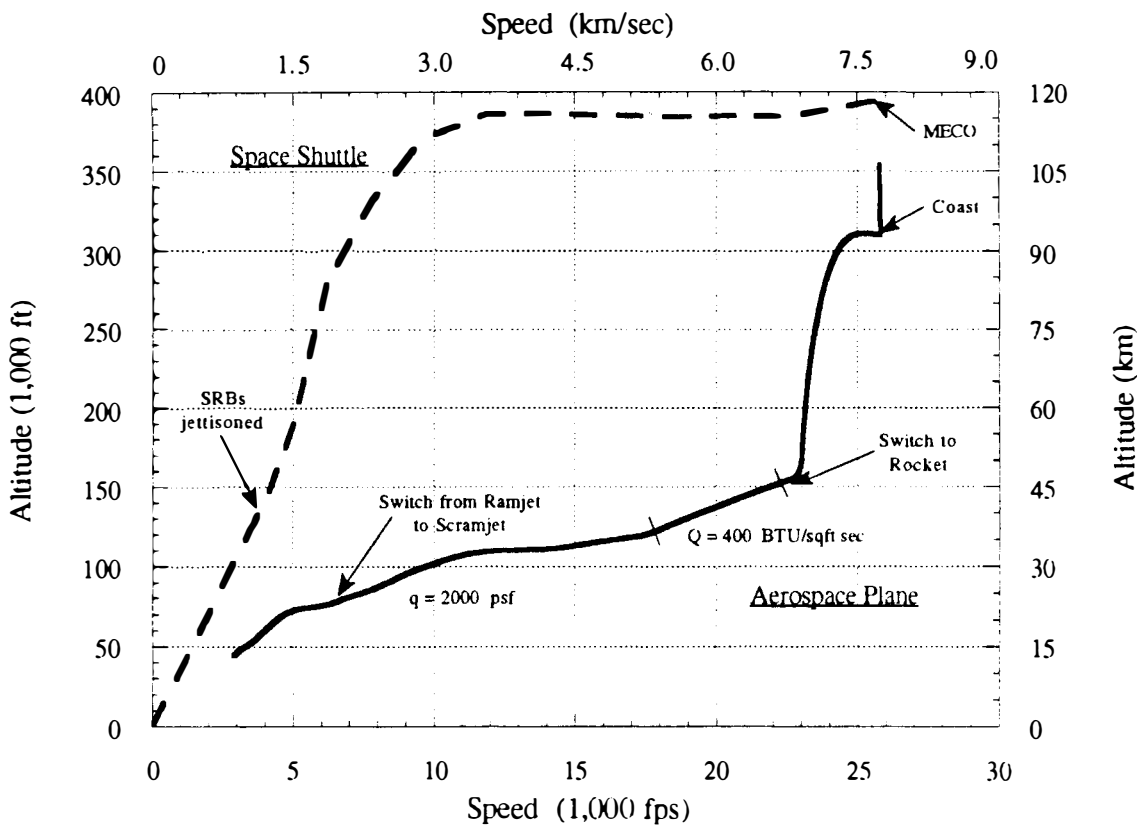


Fig. 1 Minimum-Fuel Ascent of Space Shuttle and Aerospace Plane

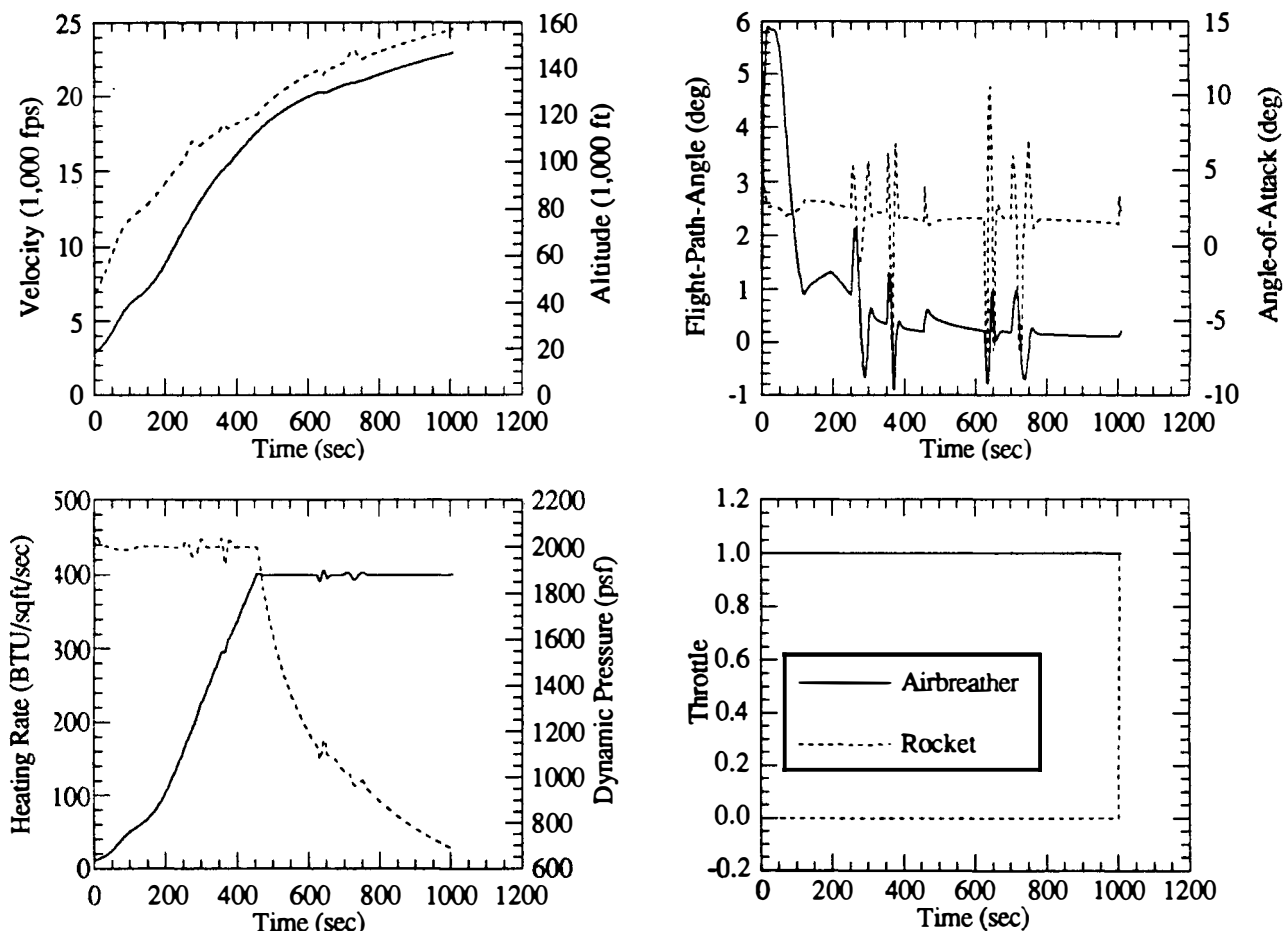


Fig. 2 Simulated Time Histories of State Variables, Outputs, and Controls for Guided Ascent through Atmospheric Disturbances.

## ON ASCENT GUIDANCE OF A HYPERSONIC VEHICLE

W. Grimm

*Institute of Flight Mechanics and Control, University of Stuttgart, Forststraße 86, D-7000 Stuttgart 1, Germany*

**Abstract.** A guidance for flight in the vertical plane is designed for a hypersonic aircraft. The objective is to maximize the final vehicle mass on the flight to a specified altitude and speed. The aircraft tracks a reduced model extremal of the remaining flight path. “Reduced” means to regard the flight path angle as a control. Real-time capability is achieved by a simplified solution of initial value problems on the computation of a reduced model extremal. Simulations illustrate the performance of the guidance method.

**Keywords.** guidance systems; optimal control; feedback control; hypersonic vehicles; reduced models.

### NOMENCLATURE

$b$	fuel flow, $b = b(h, V, \eta)$
$C_L$	lift coefficient
$D$	aerodynamic drag, $D = D(h, V, n)$
$g$	acceleration of gravity, $g = g(r)$
$h$	altitude
$m$	mass
$n$	load factor
$q$	dynamic pressure, $q = \rho(h) \cdot V^2/2$ , where $\rho(h)$ denotes air density
$r$	distance to the center of earth, $r = R_0 + h$ , where $R_0 = 6378$ km is the radius of earth
$S$	wing reference area
$T$	thrust, $T = T(h, V, \eta)$
$V$	velocity
$\gamma$	flight path angle
$\delta$	latitude
$\eta$	power setting

### INTRODUCTION

In view of the limited performance of previous onboard computers, many aircraft guidance methods are based on “reference flight paths”. A traditional concept is the “energy state method”, which is also applied to hypersonic aircraft (Corban, Calise, Flandro, 1991): The vehicle tracks an energy state extremal, which minimizes fuel consumption on the way to a specified terminal energy. Reference altitude and power setting maximize the ratio of energy rate and fuel consumption. However, this simple

result is only valid if the terminal manifold is a constant-energy locus.

To be free in the choice of boundary conditions one needs a full state extremal. The aircraft is guided by “neighboring optimal feedback control” in the environment of the reference trajectory (Bock, Krämer-Eis, 1981; Kugelmann, Pesch, 1990). The approach is valid in a certain neighborhood of the precomputed extremal. The validity domain must be estimated in off-line simulations.

Because of the progress in both computer technology and nonlinear programming methods one can consider on-line optimization of flight paths. This option is suitable for abort cases or a deviation from the planned course such that “local” guidance schemes would fail. To comply with real-time conditions one will avoid sophisticated integration methods like high-order Runge-Kutta formulae with variable step-size. For instance, an approximate solution of the equations of motion is obtained by collocation with a given partition of the time interval. The combination with optimal parameterized control is called “direct collocation” - an optimization method which is also considered for guidance of hypersonic aircraft (Bradt, Jessick, Hardtla, 1987). Since the state history is parameterized as well as the control history, one gets a lot of parameters.

To avoid this drawback the guidance in this paper uses an explicit solution of the differential equations. Similar to the energy state method the state vector is “reduced” in the sense of Singular Perturbations.

Flight path angle is treated as a control, whereas altitude is kept in the state vector. An integration formula tailored to the special structure of the “reduced system” speeds up the computation of the optimal reference trajectory. First experiments with fighter aircraft were promising (Grimm, 1986), and the application to hypersonic aircraft is obvious.

### THE DYNAMICAL MODEL

The aircraft is considered as a point mass moving over a nonrotating earth with a constant heading of 180° (flight to the south at constant longitude). The equations of motion are

$$\dot{\delta} = -\frac{V}{r} \cos\gamma, \quad (1)$$

$$h = V \sin\gamma, \quad (2)$$

$$\dot{V} = \frac{T - D}{m} - g \sin\gamma, \quad (3)$$

$$\dot{\gamma} = \frac{g}{V} \left( n - \left( 1 - \frac{V^2}{gr} \right) \cos\gamma \right), \quad (4)$$

$$\dot{m} = -b. \quad (5)$$

The controls are the load factor  $n$  and the power setting  $\eta$ . In terms of propulsion technology  $\eta$  is the “fuel-to-air ratio” normalized by the stoichiometric value. For the calculations in this paper  $\eta$  is bounded between 0.5 and 1.8:

$$0.5 \leq \eta \leq 1.8 \quad (6)$$

The maximum lift coefficient induces a state dependent upper bound on  $n$ . The lower bound is set to 0:

$$0 \leq n \leq \frac{qSC_{L,max}(M)}{mg} \quad (7)$$

To allow a load factor of unity it is necessary that

$$1 \leq \frac{qSC_{L,max}(M)}{mg}. \quad (8)$$

The gravitational acceleration  $g$  is altitude dependent:

$$g = \mu/r^2 \quad \text{with } \mu = 3.986 \times 10^{14} \frac{m^3}{s^2}$$

The drag is modelled by a Mach number dependent parabolic drag polar:

$$D = qS(C_{D0}(M) + K(M) \cdot C_L^2)$$

Since the load factor is considered to be the aerodynamic control,  $C_L$  is only a shorthand for the expression

$$C_L = \frac{nm}{qS}.$$

Thrust is the product of dynamic pressure and the “thrust coefficient”  $c_T$ :

$$T(h, V, \eta) = q \cdot c_T(M, \eta)$$

Regarded as a vector thrust is assumed to be aligned with velocity.

The fuel flow  $b$  has a similar structure as  $T$ :

$$b(h, V, \eta) = q \cdot c_b(M, \eta)$$

The dynamic pressure limit is

$$q \leq 71.8 \frac{kN}{m^2}. \quad (9)$$

Constraints (8) and (9) represent the upper and lower boundary of a corridor in the  $(M, h)$ -diagram, which contains the set of admissible  $(M, h)$ -pairs (dashed lines in Fig. 1,  $(M, h)$ -diagram). The set of  $(M, h)$ -pairs satisfying (8) with the equal sign is called “loft ceiling”. The model functions  $C_{D0}$ ,  $K$ ,  $C_{L,max}$ ,  $c_T$  and  $c_b$  are taken from a generic, horizontal-takeoff, single-stage-to-orbit configuration (Shaughnessy and co-workers, 1990). A cubic-spline representation of the model was provided and used by Cliff and Well (1991).

### DESIGN OF A NEAR-OPTIMAL GUIDANCE

#### The Optimal Control Problem

The objective is to design a state dependent guidance algorithm, which generates a near-optimal trajectory in the sense of the following optimal control problem:

Maximize  $J[n, \eta] = m(t_f)$  subject to (P)

- the equations of motion (1) - (5),
- given initial values for  $\delta, h, V, \gamma, m$ ,
- the terminal conditions  $h(t_f) = h_f, M(t_f) = M_f$ ,
- the control constraints (6), (7) and
- the state constraint (9).

#### The Reduced Problem

Using optimal feedback control for  $n$  and  $\eta$  one would obtain the exact extremal of (P). Optimal feedback control means to solve (P) continuously for each current state and take the initial value of  $n$  and  $\eta$  as control command. For real-time purposes the respective extremal of (P) is computed with a dynamic model, which results from (1) - (5) after a reduction in the sense of Singular Perturbation Theory (SPT). Solving (P) with the “reduced model” yields the “reduced solution”. For details see Ardema (1983).

The reduction made in this paper is such that  $\gamma$  is considered as a control. Following the SPT-formalism the original control  $n$  is eliminated by the condition

$$\dot{\gamma} = 0 \Rightarrow n = (1 - \frac{V^2}{gr}) \cos \gamma. \quad (10)$$

Thus, the actual control  $n$  is replaced by the “pseudo-control”  $\gamma$ . The “reduced problem” can be stated as follows:

Maximize  $J'[\gamma, \eta] = m(t_f)$  subject to  $(P')$

- the equations of motion (1), (2), (3), (5),
- given initial values for  $\delta_0, h_0, V_0, m_0$ ,
- the terminal conditions  $h(t_f) = h_f, M(t_f) = M_f$
- the control constraint (6) and
- the state constraints (8), (9).

Note that in differential equation (3)  $n$  is replaced by (10). Also note that control constraint (7) disappears since  $n$  is eliminated. The reduced model does not account for load factor limitations. To keep the reduced solution in a domain, where at least  $n = 1$  is possible, constraint (8) is added.

#### The Reduced Solution

The reduced problem  $(P')$  is solved via control parameterization. The controls  $\gamma$  and  $\eta$  are modelled as piecewise constant functions to a given partition

$$\{t_i = \tau_i \cdot t_f \mid 0 = \tau_0 < \tau_1 < \dots < \tau_m = 1\}$$

of the time interval. State constraints (8), (9) are enforced at each grid point  $t_i$ . Thus, the optimal control problem  $(P')$  is converted into a nonlinear program, which is solved by Sequential Quadratic Programming (Kraft, 1988). The optimization program calls for solutions of initial value problems with system (1), (2), (3), (5) and given controls  $\gamma(t)$  and  $\eta(t)$ . The solutions are approximated in the following way. The model functions for thrust and drag are set up in a form that the equations of motion of the reduced model take the form

$$\dot{\delta} = -\frac{V}{r} \cos \gamma, \quad (11)$$

$$\dot{h} = V \sin \gamma, \quad (12)$$

$$\dot{V} = \sum_{i=0}^2 c_i(h, \gamma, \eta) \cdot V^i, \quad (13)$$

$$\dot{m} = \sum_{i=0}^2 d_i(h, \gamma, \eta) \cdot V^i. \quad (14)$$

In each subinterval  $[t_{i-1}, t_i]$  of the parametrization grid  $h(t)$  is replaced by the constant  $h(t_{i-1})$ . Since  $\gamma$  and  $\eta$  are constant in  $[t_{i-1}, t_i]$ ,  $c_i$  and  $d_i$  become constants in  $[t_{i-1}, t_i]$ . This allows a closed-form solution of (11) - (14) in each subinterval. Using partial derivatives of the solution formula the gradients of cost function and constraints can be obtained accurately. The usual loss of correct digits on numerical differentiation is avoided. The computation of gradients is about as much expensive as the computation of the

trajectory itself (On numerical differentiation the expense is multiplied by the number of parameters.).

#### Overall Structure of the Feedback Guidance

Let  $(\delta_0, h_0, V_0, \gamma_0, m_0)^T$  denote the current state of the aircraft. The guidance algorithm proceeds in two steps:

1. The “reduced problem”  $(P')$  is solved with the initial state  $(\delta_0, h_0, V_0, m_0)^T$ . The solution techniques are described in the previous section.
2. Let  $\gamma^0(t)$  and  $\eta^0(t)$  denote the solution of  $(P')$ . The power setting command is simply  $\eta^0(0)$ . The load factor is derived from

$$\dot{\gamma} = C \cdot (\gamma^0(0) - \gamma_0)$$

with an appropriate gain factor  $C$ . Substituting  $\dot{\gamma}$  by (5) yields the load factor command:

$$n = (1 - \frac{V^2}{gr}) \cos \gamma + \frac{CV}{g} \cdot (\gamma^0(0) - \gamma_0) \quad (15)$$

The command is simply cut off at the bounds if it violates constraint (7).

#### Implementation Aspects

1. The SPT-formalism suggests to derive the load factor command with the help of the costates of the reduced solution. This was found to be better than feedback formula (15) in the case of fighter aircraft (Grimm, 1986). Although estimates of the costates are easily obtained here, formula (15) with  $C = 0.15$  yields better results in this application.
2. Ideally, the reduced solution is updated on each call of the guidance algorithm. In practice the slowly varying solution of  $(P')$  is only updated at a small frequency. To keep computation time small update intervals up to 20 sec are permitted. After each update the time to the next update is selected under consideration of the number of iterations required on getting the last solution.
3. When the vehicle approaches the desired terminal conditions, the guidance algorithm is replaced by a simple terminal guidance to accurately hit the terminal values. The terminal guidance must be switched on at a moment when the target altitude  $h_f$  is still reachable with load factors constrained by (7). Otherwise the terminal manifold is missed. Since the reduced solution does not know that  $\gamma$  cannot be changed arbitrarily, it is not a suitable reference in the last seconds.

#### SIMULATION RESULTS

Three examples with increasing flight duration are chosen. In all cases the initial state is given by  $\delta(0) = 0.83$ ,  $h(0) = 22.9$  km,  $M(0) = 2.55$ ,  $\gamma(0) = 0$  and

**TABLE 1 Terminal Values of the Simulations**

example	1	2	3
$M_f$	7	10	12
$h_f$ [km]	29	32	35
$t_f$ [sec]	126	402	747
$t_f^0$ [sec]	153	401	639
$m_0 \cdot m_f$ [Mg]	8.53	16.06	22.35
$m_0 \cdot m_f^0$ [Mg]	7.95	14.69	20.82

$m(0) = 130$  Mg,  $M_f$  and  $h_f$  are the prescribed terminal values in (P) and (P'), respectively. Simulation means to integrate Eqs. (1) - (5) with the controls given by the guidance algorithm in the previous section. Earth rotation  $\omega_E$  is considered, too; Eqs. (1) - (5) are augmented by the necessary  $O(\omega_E)$ -terms.

In all cases the initial state is given by  $\delta(0) = 0.83$ ,  $h(0) = 22.9$  km,  $M(0) = 2.55$ ,  $\gamma(0) = 0$  and  $m(0) = 130$  Mg.  $M_f$  and  $h_f$  are the prescribed terminal values in (P) and (P'), respectively. Simulation means to integrate Eqs. (1) - (5) with the controls given by the guidance algorithm in the previous section. Earth rotation  $\omega_E$  is considered, too; Eqs. (1) - (5) are augmented by the necessary  $O(\omega_E)$ -terms.

As mentioned previously a terminal guidance is activated on approaching the terminal manifold. However, the terminal guidance law becomes undefined at the terminal point itself. The simulation is stopped at the moment, when the estimated time-to-go is less than the size of the next integration step. In a last Euler step (stepsize = estimated time-to-go) the final state is estimated. The final values  $t_f$  and  $m_f$  in Table 1 are obtained in this way.  $t_f^0$  ( $m_f^0$ ) is the estimated flight time (final mass) of the first reduced solution, which belongs to simulation time  $t = 0$  and has the same initial state as the simulation itself. As can be seen from Table 1,  $m_f^0$  is always larger than  $m_f$ . This is expected, since  $n$  is less than one in the reduced model (see (10)). So the reduced model produces less drag and needs less fuel to accelerate.

The reduced solution is determined by “single-shooting”: On solving an initial value problem the integration procedure runs from 0 to (the respective estimate of) the final time without interior stops. It is well known that with single-shooting the convergence domain of an optimization method shrinks as final time grows. This effect also occurs in examples 1-3. While convergence is no problem in example 1, the reduced solution must be updated each 1.25 sec at the beginning of example 3. The update interval must be kept so small to generate a reduced solution with the results of the previous one. The combination of parameterized optimal control and “multiple shooting” (Bock and Plitt, 1984) would lead to a larger

convergence domain. This is the recommendation to overcome convergence difficulties for large final times.

Fig. 1 depicts example 3. The  $(h, M)$ -diagram contains the simulated trajectory (solid line) and the first reduced solution (dotted line), which lies on the  $q_{max}$ -boundary between Mach 6.5 and 9.2. The peak touching the “loft ceiling” (defined by constraint (8)) is a peculiar feature of the reduced solution. The peak occurs around Mach 6 in other examples, too. So it must be inherent to the vehicle model. The peak reappears in flattened form in the simulated flight path.

The dotted line in the  $\eta$ -diagram is the  $\eta$ -history of the *first* reduced solution.  $\eta$  is modelled as a piecewise constant function in the reduced solution. So the jumps indicate the parameterization grid of the reduced solution. The solid line is the power setting command of the simulated flight path. It is the initial value of the reduced solution which starts at the respective simulation time. The steplike shape indicates the update intervals of the reduced solution. Altogether, the  $\eta$ -curve of the guided solution (solid line) looks like a delayed response to the first reduced solution (dotted line). At  $t \approx 680$  sec the guidance algorithm is replaced by a terminal guidance.  $\eta$  is set to the mean value along the last reduced solution. The time-to-go is estimated from the remaining Mach number difference  $M_f - M$ . The load factor is such that the target altitude  $h_f$  is reached within the estimated time-to-go.

According to (15) the load factor is determined by the condition that  $\gamma$  (solid line in the  $\gamma$ -diagram) follows the reference flight path angle  $\gamma^0(0)$  (dashed line in the  $\gamma$ -diagram).  $\gamma^0(0)$  is the initial value of  $\gamma$  of the reduced solution. As the reduced solution is updated,  $\gamma^0(0)$  exhibits the behavior shown in Fig. 1. Each jump in  $n$  indicates an update of the reduced solution. Note that the update interval is enlarged to 20 sec after the initial phase. For decreasing update intervals  $n(t)$  converges to a smooth function. This can be seen at the first 50 sec with an update interval of 1.25 sec. The upper bound of  $n$  given by (7) (dashed line in the load factor diagram) is never reached. The lower bound 0 is taken in the first seconds. Although the vehicle can produce zero lift with small angles of attack, a positive lower bound on  $n$  may be desirable. Also note that the significant variations in the initial phase are due to the choice of the initial state near the “loft ceiling” (8).

## CONCLUSIONS

The subject of the present paper is a guidance which is based on a reduced model optimization of the remaining flight path (“reference trajectory”, “reduced solution”). On the computation of the reference trajectory initial value problems with the

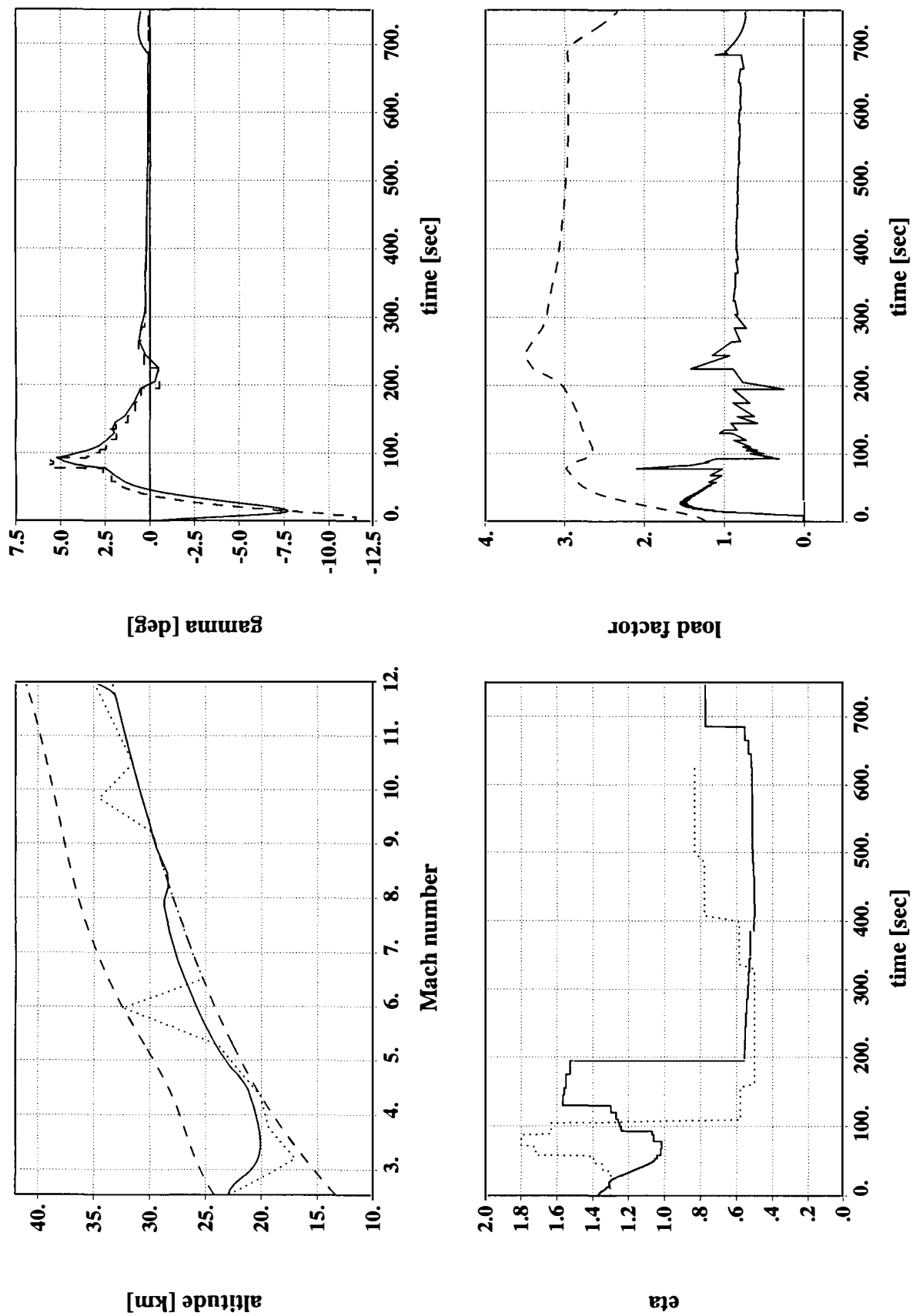


Fig. 1. Simulated trajectory of example 3.  
solid line: simulated trajectory; dotted line: first reduced solution; dashed line:  $q_{max}$ - and  $C_{L,max}$ -boundary  
(1st diagram), reference flight path angle (2nd diagram), upper bound of the load factor (4th diagram).

reduced model are solved in a simplified manner. Thus, the computation of the reference trajectory becomes real-time feasible. Large final times require multiple-shooting technique to achieve convergence on the computation of the reference trajectory.

The guidance produces admissible solutions in the sense that given terminal conditions and state constraints are satisfied. The lift command becomes a smooth function of time if the reference trajectory is updated frequently enough.

The “reduced solution” is not a good reference, when the estimated time-to-go shrinks to zero. The reduced model does not account for bounds on variations of the flight path angle. A terminal guidance must be switched on as long as the terminal conditions are actually reachable with admissible lift commands.

The concept is applicable to problem formulations where payoff index and terminal conditions are functions of final latitude, altitude, Mach number and mass. The paper presents trajectories with constant longitude. An extension to three dimensions is not yet developed. A comparison of the simulations in this paper with fuel optimal trajectories would be desirable.

#### ACKNOWLEDGEMENT

The author would like to thank Dr. E.M. Cliff from Virginia Polytechnic Institute for providing the aircraft model in simulation-ready form.

#### REFERENCES

- Ardema, M.D. (1983). An introduction to Singular Perturbations in nonlinear optimal control. In M.D. Ardema (Ed.), *Singular Perturbations in Systems and Control*, CISM Courses and Lectures No. 280. Springer, Wien - New York. pp. 1-92.
- Bock, H.G., and Krämer-Eis, P. (1981). An efficient algorithm for approximate computation of feedback control laws in nonlinear processes. *ZAMM*, 61.
- Bock, H.G., and Plitt, K.J. (1984). A multiple shooting algorithm for direct solution of optimal control problems. *9th IFAC World Congress*, Budapest, Hungary.
- Bradt, J.E., Jessick, M.V., and Hardtla, J.W. (1987). Optimal guidance for future space applications. *AIAA Guidance, Navigation, and Control Conference*, August 17-19, Monterey, Ca..
- Cliff, E.M., and Well, K.-H. (1991). Energy-heading transients in atmospheric flight guidance for air-breathing hypersonic vehicles. *AIAA Third International Aerospace Planes Conference*, Dec. 3-5, Orlando, Fl..
- Corban, J.E., Calise, A.J., and Flandro, G.A. (1991). Rapid near-optimal aerospace plane trajectory generation and guidance. *J. Guidance, Control & Dynamics*, 14(6), 1181-1190.
- Grimm, W. (1986). A numerical approach for on-line guidance of aircraft. *25th IEEE Conference on Decision & Control*, Athens, Greece.
- Kraft, D. (1988). *A Software Package for Sequential Quadratic Programming*. DFVLR-FB 88-28, German Aerospace Research Establishment.
- Kugelmann, B., and Pesch, H.J. (1990). New general guidance method in constrained optimal control, part 1: numerical method. *J. Optimization Theory and Applications*, 67(3), 421-435.
- Shaughnessy, J.D., Zane Pinckney, S., McMinn, J.D., Cruz, C.I., and Kelley, M.-L. (1990). *Hypersonic Vehicle Simulation Model: Winged-Cone Configuration*. NASA TM 102610.

# NON LINEAR ATTITUDE CONTROL LAW OF A SPACE PLANE APPLICATION TO HERMES

F. Jouhaud

Systems Department, Office National d'Etudes et de Recherches Aérospatiales, ONERA,  
29 avenue de la Division Leclerc, BP 72, 92322 Chatillon Cedex, France

**Abstract.** A non linear attitude control law has been synthesised for the early reentry trajectory of a space plane, in the transition domain corresponding to low dynamic pressure, where it is necessary to pass from full thruster control to full aerodynamic control.

The principle of this attitude control law is based on the "task oriented control" technique. It consists in first selecting an objective or task. In second, a decoupled dynamic is chosen for the evolution of the real value of that objective toward its desired value. From this desired dynamic, it is then computed the corresponding momentum to apply to the space vehicle. This desired momentum is finally obtained by a proper combination of aerodynamic control deflections and thruster ignition.

This new attitude control law has been applied to Hermes space plane and checked from the point of view of respect of output versus time templates for canonical inputs in the transition domain. This check has been done in nominal conditions but also with aerodynamic modelling errors and turbulence. In addition, simulations of the whole early reentry, including first bank maneuver, has been lead in order to evaluate thruster consumption and aerodynamic control activity.

**Keywords.** Aerospace control - Non linear control systems - Space vehicles.

## INTRODUCTION

This article has for object the synthesis of a non linear attitude control law in the transition domain of a space plane reentry trajectory. This domain corresponds to low dynamic pressure, where it is necessary to switch from full thruster control to full aerodynamic control.

The principle of this attitude control law will be based on the "task oriented control" technique. This consists in first selecting an objective or task, here attack angle, side slip and aerodynamic bank angle. In second, we have to choose a decoupled dynamic for the evolution of the real value of that objective toward a desired value (provided by guidance or human pilot). From this desired dynamic, it can be computed the corresponding needed angular acceleration, which is directly connected to the momentum applied to the space vehicle. This desired momentum will be finally obtained by a suitable combination of aerodynamic control deflections and thruster ignition.

## SPACE PLANE FLIGHT DYNAMICS

### Reference Frames and Notations.

This study was supported by ESA/CNES.

- 4 different frames will be used to represent the space plane motion :
- . inertial geocentric frame ( $C, x_i, y_i, z_i$ ), with the  $z_i$ -axis along the Earth pole axis, toward North and  $C$  is the Earth center(see Fig. 1),

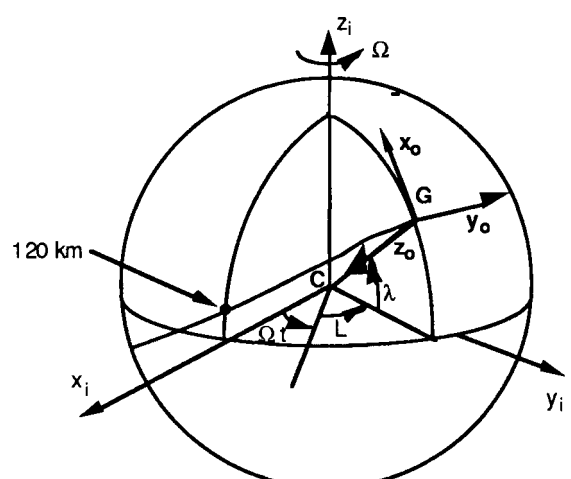


Fig. 1 -Inertial frame and spheric coordinates

- . local Earth frame attached to the space plane ( $G, x_o, y_o, z_o$ ) with  $x_o$  toward North,  $y_o$  toward East

and  $\mathbf{z}_0$  along descending vertical, G is the center of mass of the vehicle (see Fig. 2),  
 . body frame ( $O, \mathbf{x}, \mathbf{y}, \mathbf{z}$ ), with O at the rear of space plane and  $\mathbf{x}$  toward its nose (see Fig. 2 and 4),  
 . aerodynamic frame ( $O, \mathbf{x}_a, \mathbf{y}_a, \mathbf{z}_a$ ) with  $\mathbf{x}_a$  along the airspeed vector  $\mathbf{V}_a$  (see Fig. 3 and 4), such that:

$\mathbf{V}_a = \mathbf{V} - (\Omega_E \wedge \mathbf{CG}) - \mathbf{V}_w$   
 where  $\mathbf{V}$  is the inertial speed,  $\mathbf{V}_w$  the wind vector, and  $\Omega_E = \Omega_E \mathbf{z}_1$  is the Earth rotation vector ( $\Omega_E = 7.29212 \cdot 10^{-5} \text{ rad/s}^{-1}$ ).

The Earth is considered as an oblate ellipsoid, with  $r_{eq} = 6378,142 \text{ km}$  radius at Equator and  $r_p = 6356,611 \text{ km}$  radius at poles.

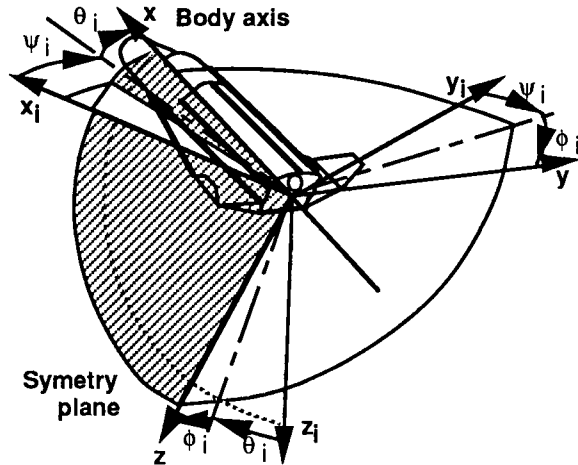


Fig. 2 - Body and inertial frames

$$\begin{aligned}\begin{bmatrix} \mathbf{x} \\ \mathbf{y} \\ \mathbf{z} \end{bmatrix} &= \mathbf{M}_{bi}(\psi_i, \theta_i, \phi_i) \begin{bmatrix} \mathbf{x}_i \\ \mathbf{y}_i \\ \mathbf{z}_i \end{bmatrix} \\ \begin{bmatrix} \mathbf{x}_o \\ \mathbf{y}_o \\ \mathbf{z}_o \end{bmatrix} &= \mathbf{M}_{oi}(L, \lambda) \begin{bmatrix} \mathbf{x}_i \\ \mathbf{y}_i \\ \mathbf{z}_i \end{bmatrix} \\ \begin{bmatrix} \mathbf{x}_a \\ \mathbf{y}_a \\ \mathbf{z}_a \end{bmatrix} &= \mathbf{M}_{ao}(\chi_a, \mu_a, \gamma_a) \begin{bmatrix} \mathbf{x}_o \\ \mathbf{y}_o \\ \mathbf{z}_o \end{bmatrix} \\ \begin{bmatrix} \mathbf{x}_a \\ \mathbf{y}_a \\ \mathbf{z}_a \end{bmatrix} &= \mathbf{M}_{ab}(\alpha, \beta) \begin{bmatrix} \mathbf{x} \\ \mathbf{y} \\ \mathbf{z} \end{bmatrix}\end{aligned}$$

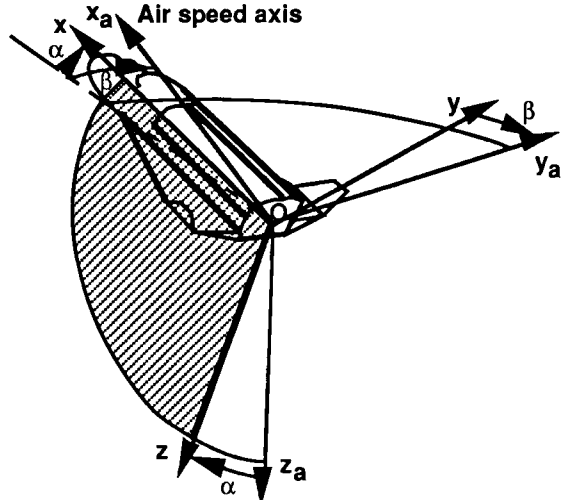


Fig. 4 - Aerodynamic and body frames

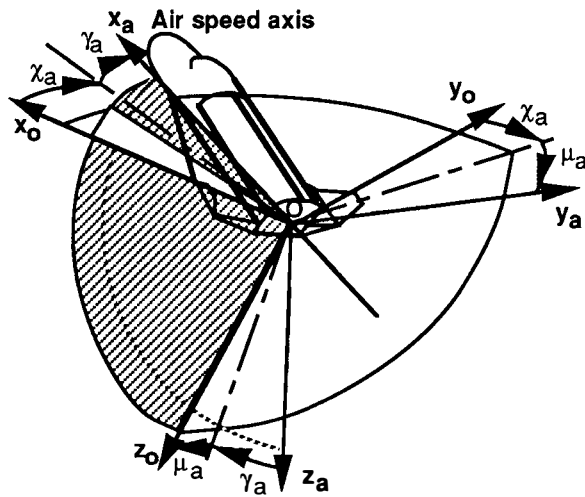


Fig. 3 - Aerodynamic and local frames

Figures 1 to 4 show how are defined :

- longitude L and latitude  $\lambda$ ,
- inertial azimuth  $\psi_i$ , pitch  $\theta_i$ , roll  $\phi_i$ ,
- aerodynamic heading angle  $\chi_a$ , slope  $\gamma_a$ , bank angle  $\mu_a$ ,
- angle of attack  $\alpha$  and side slip angle  $\beta$ .

Between all the reference frames, we have the following relations:

### Equations of Motion

With previous notations, the equations of motion are :

$$\begin{aligned}\overset{\circ}{\mathbf{r}} &= \mathbf{V} && \text{kinematic relation (7)} \\ \overset{\circ}{\mathbf{V}} &= \mathbf{g} + \frac{\mathcal{F}_a + \mathcal{F}_r}{m} && \text{dynamic equation (8)} \\ \overset{\circ}{\lambda} &= \mathbf{A}(\Omega) \lambda && \text{quaternion evolution (9)} \\ \overset{\circ}{(\mathbf{I} \Omega)} &= \mathcal{M}_a + \mathcal{M}_r && \text{momentum equation (10)} \\ \overset{\circ}{m} &= \sum_{i=1}^{nr} \delta r_i \overset{\circ}{m}_i && \text{mass consumption (11)} \\ \overset{\circ}{\delta a} &= \tau^{-1} (\delta ac - \delta a) && \text{servos dynamic (12)} \\ \overset{\circ}{\delta r} &= f_r(t, \delta r, \delta r_C) && \text{thrusters dynamic (13)}\end{aligned}$$

where :

- .  $\mathbf{r}$ ,  $\mathbf{V}$  are the inertial position and velocity in cartesian coordinates,
- .  $\lambda$  are the quaternions associated with  $\psi_i, \theta_i, \phi_i$ ,
- .  $\Omega = [ \Omega_x \ \Omega_y \ \Omega_z ]^T$  : inertial rotation vector in body frame,

$$\mathbf{A}(\Omega) = \begin{bmatrix} 0 & -\Omega_x & -\Omega_y & -\Omega_z \\ \Omega_x & 0 & \Omega_z & -\Omega_y \\ \Omega_y & -\Omega_z & 0 & \Omega_x \\ \Omega_z & \Omega_y & -\Omega_x & 0 \end{bmatrix} \quad (13)$$

- .  $m$  : mass of the space plane,
- .  $I$  : inertia matrix in body frame,
- .  $\mathbf{g}$  : gravity vector including J2 term,
- .  $\mathcal{F}_a$ ,  $\mathcal{M}_a$  : respectively aerodynamic force and momentum, depending on aerodynamic controls  $\delta_a = [\delta_l, \delta_m, \delta_n]$  (for pitch, roll and yaw)
- .  $\mathcal{F}_r$ ,  $\mathcal{M}_r$  : respectively thruster force and momentum depending on thruster controls  $\delta_r$ .

$$\mathcal{F}_r = \sum_{i=1}^{nr} \mathcal{F}_{ri} \delta_{ri}, \quad \mathcal{M}_r = \sum_{i=1}^{nr} \mathcal{M}_{ri} \delta_{ri} \quad (14)$$

where  $\mathcal{F}_{ri}$  and  $\mathcal{M}_{ri}$  are respectively the force and momentum of  $i^{\text{th}}$  thruster,  $\delta_{ri}$  is the relative thrust varying between 0 and 1.

We define the thrust control vector  $\delta_r$  as  $\delta_r = [\delta_{ri}]_{i=1, nr}$  with mass consumption  $m_i$  and dynamic friction with delay for ignition and cut-off.

The computation of these forces and momentum requires the following quantities, all related to the state vector of the space plane :

- altitude  $h = ||\mathbf{r}|| - r_{eq} \left[ 1 + \left( \frac{r_{eq}^2}{r_p^2} - 1 \right) \frac{z_i^2}{||\mathbf{r}||^2} \right]^{-\frac{1}{2}}$
- atmosphere characteristics at altitude  $h$  : air density  $\rho$  and sound celerity  $c_s$  given by NOAA 76 standard atmosphere,
- dynamic pressure  $\bar{q} = \frac{1}{2} \rho ||\mathbf{V}_{all}||^2$
- Mach number  $M = \frac{||\mathbf{V}_{all}||}{c_s}$
- attack angle  $\alpha$ :  $\tan \alpha = \frac{\mathbf{V}_{a.z}}{\mathbf{V}_{a.x}}$
- side slip angle  $\beta$ :  $\tan \beta = \frac{\mathbf{V}_{a.y}}{\sqrt{(\mathbf{V}_{a.x})^2 + (\mathbf{V}_{a.z})^2}}$
- local rotation vector  $\omega = \Omega - \Omega_o = [p \ q \ r]$   
 $\omega$  is the rotation vector of the body frame relatively to the local Earth frame and is expressed in the body frame.
- $\Omega_o$  is the rotation vector of the local Earth frame relatively to the inertial frame.
- latitude  $\lambda$ :  $\tan \lambda = \frac{z_i}{\sqrt{x_i^2 + y_i^2}}$
- longitude  $L$ :  $\tan(L + \Omega_E t) = \frac{y_i}{x_i}$
- aerodynamic slope  $\gamma_a$ :  $\tan \gamma_a = - \frac{\mathbf{x}_a \cdot \mathbf{z}_o}{||\mathbf{x}_a \wedge \mathbf{z}_o||}$
- aerodynamic heading  $\chi_a$ :  $\tan \chi_a = \frac{\mathbf{x}_a \cdot \mathbf{y}_o}{\mathbf{x}_a \cdot \mathbf{x}_o}$
- aerodynamic bank angle  $\mu_a$ :  $\tan \mu_a = \frac{\mathbf{y}_a \cdot \mathbf{z}_o}{\mathbf{z}_a \cdot \mathbf{z}_o}$

For the test maneuvers, the initial position and velocity are kept fixed in order to respect a fixed value of dynamic pressure. For simulations of early reentry trajectory, the integration began at the

altitude of 120 km and finished at a 2000 Pa dynamic pressure.

## TASK ORIENTED ATTITUDE CONTROL LAW FOR TRANSITION

### Closed Loop

We decide to choose as "objectives" to be controlled the 3 angles  $\alpha$ ,  $\beta$  and  $\mu_a$  which are directly connected to the acceleration applied to the space plane.

Rewriting equations 7 to 10 in state vector form yields the non linear system :

$$\begin{cases} \dot{\mathbf{x}} = \mathbf{f}(\mathbf{x}, \delta) \\ \mathbf{z} = \mathbf{g}(\mathbf{x}) \end{cases} \quad (15)$$

where  $\mathbf{x} = [\mathbf{r}, \mathbf{V}, \lambda, \Omega]$ ,  $\delta = [\delta_a, \delta_r]$  and  $\mathbf{z} = [\alpha, \beta, \mu_a]$

We want to realize  $\mathbf{z}(t) \rightarrow \mathbf{z}_d(t)$

We can see, as  $\mathbf{z}$  doesn't depend directly on control  $\delta$ , that  $\mathbf{z}_d$  is not reachable at once. In order to let appear the influence of  $\delta$  on  $\mathbf{z}$ , we have to derive twice  $\mathbf{z}$  versus time :

$$\begin{cases} \cos \beta \ddot{\alpha} \approx \Omega \mathbf{y}_a + \Omega \dot{\mathbf{y}}_a \\ \quad + \frac{\mathbf{V}_a \cdot \dot{\mathbf{z}}_a}{\mathbf{V}_a} - \frac{\mathbf{V}_a \cdot \mathbf{z}_a}{\mathbf{V}_a} \frac{\mathbf{V}_a \cdot \mathbf{x}_a}{\mathbf{V}_a} + \sin \beta \ddot{\alpha} \dot{\beta} \\ \ddot{\beta} \approx -\Omega \mathbf{z}_a - \Omega \dot{\mathbf{z}}_a \\ \quad + \frac{\mathbf{V}_a \cdot \dot{\mathbf{y}}_a}{\mathbf{V}_a} - \frac{\mathbf{V}_a \cdot \mathbf{y}_a}{\mathbf{V}_a} \frac{\mathbf{V}_a \cdot \mathbf{x}_a}{\mathbf{V}_a} \\ \ddot{\mu} \approx \Omega \mathbf{x}_a + \Omega \dot{\mathbf{x}}_a - \sin \beta \ddot{\alpha} \\ \quad - \cos \beta \ddot{\alpha} \dot{\beta} - \omega_0 \cdot \dot{\mathbf{x}}_a \end{cases} \quad (16)$$

with :

$$\mathbf{V}_a = \dot{\mathbf{V}} - (\Omega \mathbf{E} \wedge \mathbf{V})$$

(as wind vector is supposed to be not known by attitude control, its derivation is omitted),

$$\begin{cases} \dot{\mathbf{x}}_a = \cos \beta \dot{\alpha} \mathbf{z}_a + \dot{\beta} \mathbf{y}_a + \Omega \wedge \mathbf{x}_a \\ \dot{\mathbf{y}}_a = -\sin \beta \dot{\alpha} \mathbf{z}_a - \dot{\beta} \mathbf{y}_a + \Omega \wedge \mathbf{y}_a \\ \dot{\mathbf{z}}_a = -\cos \beta \dot{\alpha} \mathbf{z}_a + \sin \beta \dot{\alpha} \mathbf{y}_a + \Omega \wedge \mathbf{z}_a \end{cases} \quad (17)$$

The relation (14) can be rewritten in vector form :

$$\mathbf{z} = \mathbf{A}(\mathbf{x}) \mathbf{z} + \mathbf{B}(\mathbf{x}) \quad (18)$$

As  $\mathbf{z}$  depends directly on  $\delta$ , through equation (10)

we can choose  $\mathbf{z}$  as far as we respect the physical constraints on  $\delta$ . In the present study, we have taken for  $\mathbf{z}$  the following value:

$$\mathbf{z} = \mathbf{K}_1 (\mathbf{z}_d - \mathbf{z})$$

$$+ \mathbf{K}_2 (\mathbf{z}_d - \mathbf{z}) + \mathbf{K}_3 \int_0^t (\mathbf{z}_d - \mathbf{z}) dt \quad (19)$$

which means that the "output"  $\mathbf{z}$  follows the "input"  $\mathbf{z}_d$  according to a third order transfer.

In order to have decoupled objectives, **K1**, **K2** and **K3** have a diagonal form. The values of these gain matrix are chosen, in accordance with capability of the vehicle, for ensuring a good trade off between accuracy and stability.

The role of the integral term is to suppress long term errors in the realization of  $\mathbf{z}_d$ , in particular in presence of modelling errors. But for large amplitude maneuver, or large modelling errors, this integral term can have too large value, and then a threshold function is applied to it.

As **K1**, **K2** and **K3** were chosen for regulation purpose near a quasi-constant desired objective  $\mathbf{z}_d$ , for large variation of the objective we use then a "pre-control" that filters the order  $\mathbf{z}_c$  (from guidance law or human pilot) to obtain a  $\mathbf{z}_d$  compatible with the available level of momentum.

### Pre-control

In hypersonic conditions, it is supposed that the orders coming out of guidance are in fact orders on attack angle  $\alpha_c$  and on roll rate  $\dot{\mu}_{ac}$  (with side slip angle  $\beta_c=0$ ). They are transformed by a first order filter to the desired values  $\alpha_d$ ,  $\beta_d$ ,  $\dot{\mu}_{ad}$ , and  $\ddot{\mu}_{ad}$  by integration. The time constants of the first order filters are chosen in accordance with both dynamics and specifications.

At this point, we have seen how to pass from order on objective  $\mathbf{z}_c$  to a desired objective  $\mathbf{z}_d$ , from this  $\mathbf{z}_d$  to the second derivative of objective  $\mathbf{z}^{\circ\circ}$  using (19) and then from  $\mathbf{z}^{\circ\circ}$  to the desired momentum  $\mathcal{M}_d$  using (10). We have finally to do the repartition between aerodynamic and thruster momentum and compute the corresponding controls to complete the attitude control law as can be seen on the recapitulative diagram or Fig. 6.

### Desired Momentum Partition

For the repartition between aerodynamic and thruster part of the momentum, the following algorithm, based on the value of the dynamic pressure  $\bar{q}$ , was selected :

- .1) for  $\bar{q} \leq \bar{q}_0$  : thrust control alone,  
 $\delta_l = \delta_m = 0$ ,  $\delta_r$  of longitudinal equilibrium ( $M = 0$ )  
if  $(||\mathbf{z} - \mathbf{z}_d|| \geq \text{Threshold1} \text{ or } (||\mathcal{M}_d|| \geq \text{Threshold2}))$   
then  $\delta_r$  minimizes  $||\mathcal{M}_d - \mathcal{M}_r(\delta_r)||$  according to paragraph below,
- .2) for  $\bar{q} \geq \bar{q}_1$  : aerodynamic control alone,  
 $\delta_r = 0$   
 $\delta_a$  minimizes  $||\mathcal{M}_d - \mathcal{M}_a(\delta_a)||$  with method detailed in paragraph below,
- .3) for  $\bar{q}_0 \leq \bar{q} \leq \bar{q}_1$  : combination of thrust and aerodynamic control,  
 $\delta_a$  minimizes  $||\mathcal{M}_d - \mathcal{M}_a(\delta_a)||$ , and

if  $||\mathcal{M}_d|| \geq \text{Threshold3} (\bar{q})$  then  $\delta_r$  minimizes also  $||\mathcal{M}_d - \mathcal{M}_r(\delta_r)||$

The threshold number 3 is a rough estimation of maximum level of aerodynamic momentum. Then thrusters act only when aerodynamic control is insufficient. When it occurs, the total momentum is also demanded to thrusters. Indeed, due to their impulsive working, the thruster controls meet difficultly low level momentum. The aerodynamic controls act more rapidly and will adapt the aerodynamic momentum when, after the delay of thrusters, the thruster momentum will raise.

### Aerodynamic Momentum Realization

We seek  $\delta_a$  which minimizes  $||\mathcal{M}_d - \mathcal{M}_a(\delta_a)||$  using Newton's iterative method. It is clear that without constraints on  $\delta_a$  this minimum would correspond to  $\mathcal{M}_d = \mathcal{M}_a(\delta_a)$ .

Finally, as there is a delay in the realisation of this desired  $\delta_{ad}$  corresponding to  $\mathcal{M}_d$ , we take into account the first order evolution of aerodynamic controls (12) in computing the following order  $\delta_{ac}$  for the servos :

$$\delta_{ac} = (1 - K_4)^{-1} (\delta_{ad} - K_4 \delta_a)$$

where 1 is the identity matrix and  $K_4$  a diagonal gain matrix.

### Thruster Momentum Realization

The simplified, although general, thruster selector adopted here, consists in making a repartition of the  $2^n$  possible combinations of  $n$  thruster based on the angular sector of the momentum created by each combination. Then for a particular desired momentum  $\mathcal{M}_d$ , we determine first the corresponding angular sector and the associated subset of combinations. Then this subset, with a reduced number of items, is sequentially explored to find the combination which lowers  $||\mathcal{M}_d - \mathcal{M}_r(\delta_r)||$ .

The angular separation of momentum is based on angle  $\theta$  and  $\chi$  of the spheric representation of the momentum in body frame :

$$\mathcal{M} = \begin{bmatrix} L = ||\mathcal{M}|| \cos \theta \cos \chi \\ M = ||\mathcal{M}|| \sin \theta \cos \chi \\ N = ||\mathcal{M}|| \sin \theta \sin \chi \end{bmatrix}$$

## RESULTS

### Perturbation Causes

There were 2 kinds of perturbation causes considered : variation of aerodynamic coefficients and presence of wind turbulence.

set of longitudinal aerodynamic errors : mainly 20% loss of efficiency on longitudinal aerodynamic controls

. set of lateral aerodynamic errors : up to 30% loss of efficiency on lateral aerodynamic controls

turbulence is modelled as a stochastic wind vector  $V_w$ , with standard deviation about 55 m/s and length of correlation about 20 km.

### Test Maneuvers

The test maneuvers, depicted in Fig. 2, were a negative step of  $3^\circ$  of angle of attack  $\alpha$ , and a positive step of roll rate  $\dot{\mu}_a$  of  $6^\circ/\text{s}$ .

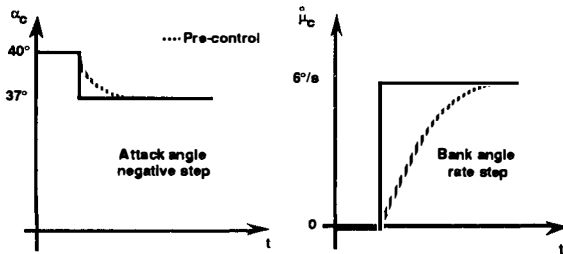


Fig. 5 - Test maneuvers.

Both maneuvers have been conducted at six control points of the early reentry trajectory corresponding to the following values of the dynamic pressure : 1, 100, 450, 500, 950 and 1700 Pa.

Then both maneuvers, for all 6 control points have been lead in the following conditions :

- . nominal,
- . wind turbulence only,
- . set of longitudinal modelling errors,
- . longitudinal errors and turbulence,
- . set of lateral modelling errors,
- . lateral errors and turbulence,
- . longitudinal and lateral combined errors and turbulence.

With the actual sets of gains and thresholds of the law, we obtained a good compliance of responses to canonical inputs to specified templates, as can be seen on Fig. 7 and 8 for maneuvers with longitudinal errors and turbulence.

### Early Reentry Simulations

These simulations have been made in order to evaluate the propellant consumed by thrusters, and the energy required to move the aerodynamic controls.

The activity of aerodynamic controls is expressed in a very simplified form by computing the time integral of the sum of the absolute value of the angular speed of all aerodynamic controls :

$$\text{"activity"} = \int_{t_0}^{t_f} ||\delta \omega|| \, dt$$

The simulations have been realized with the same sets of perturbation causes than for the test maneuvers. The resulting propellant consumption of thruster and the aerodynamic control activity are indicated in TABLE 1.

TABLE 1 Thruster consumption

	Thruster Consumption (kg)	"Activity" (1000°)
nominal	33.3	1.7
turbulence	31.6	2.5
longitudinal	45.8	9.0
longi. + turbulence	41.7	6.4
lateral	33.3	3.1
lateral+turbulence	33.1	3.3
combined	38.0	5.1

### CONCLUSION

A non linear closed loop attitude control law has been synthesised for the transition domain between thruster and aerodynamic control, for the early reentry of a space plane, corresponding to low dynamic pressure.

The principle of this attitude control law is based on the "task oriented control" technique. It consists in ensuring the respect of a desired objective or task, which was here attack angle, side slip and aerodynamic bank angle. Thus we obtain a non linear closed loop control, which depends very little on the type of actuator used.

This new attitude control law has been checked from the point of view of respect of time templates for test maneuvers ( $3^\circ$  attack angle and  $6^\circ/\text{s}$  roll rate step) at various points of the early reentry trajectory, corresponding to different dynamic pressures covering all the transition domain (from 1 to 2000 Pa). In addition, simulations of the whole early reentry, including first bank maneuver (from 0 to  $90^\circ$ ), has been lead in order to evaluate thruster consumption and aerodynamic control "activity".

The test maneuvers and the early reentry simulations have been done in the following conditions :

- . nominal,
- . wind turbulence (up to 55 m/s of standard deviation) only,
- . set of longitudinal modelling errors (decrease of pitch aerodynamic control efficiency by 20%),
- . longitudinal errors and turbulence,
- . set of lateral modelling errors,
- . lateral errors and turbulence (decrease of lateral aerodynamic control efficiency up to 30%),
- . longitudinal and lateral combined errors and turbulence.

For the test maneuvers, we have found a good compliance with specified time templates.

In the early reentry simulations the thruster consumption attained 46 kg and aerodynamic activity 9000°.

Finally, it is believed, that this new structure of attitude control law would be convenient for the whole reentry trajectory (probably with some slight improvements, as gains adaptation in function of Mach number and altitude).

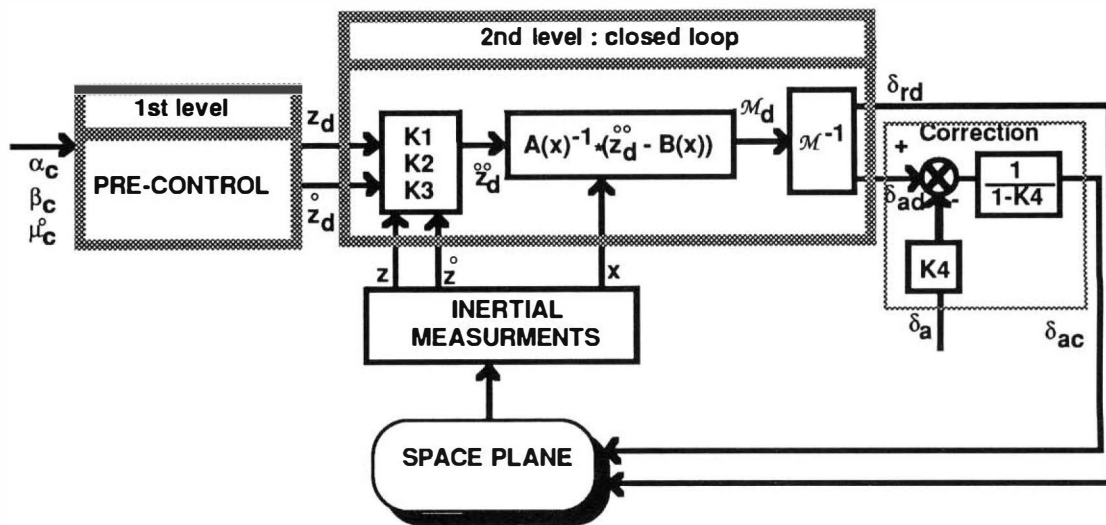


Fig. 6 - Task objective control

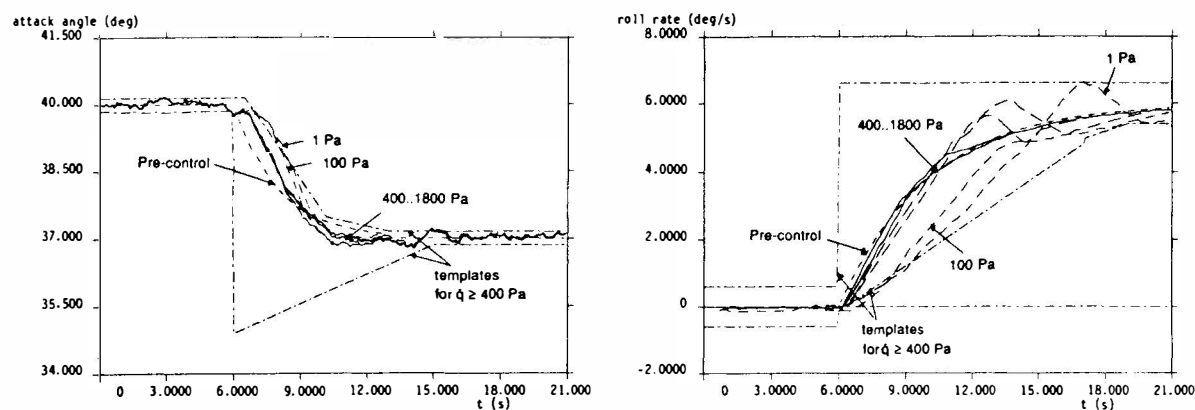


Fig. 7 - Test maneuvers with turbulence

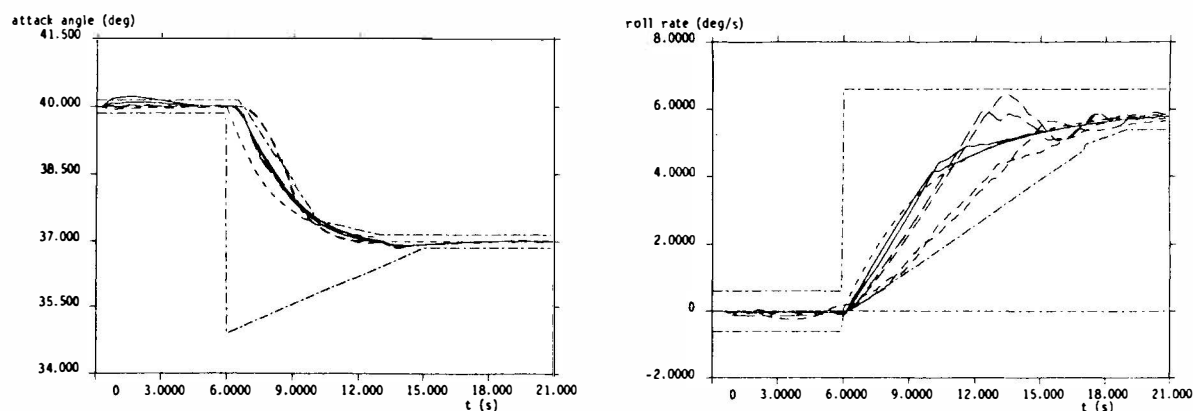


Fig. 8 - Test maneuvers with longitudinal errors

## STAR PATTERN RECOGNITION SENSOR OF THE ASTRO TYPE

Ch. Elstner, D. Ratzsch and W. Skarus

Jena-Optronik GmbH, Göschwitzer Str. 33, D-6905 Jena-Göschwitz, Germany

**Abstract.** A Star Pattern Recognition Sensor (SPRS) system has been designed for autonomous, all stellar attitude determination. The system consists of three optical heads, including the CCD camera, three image processors and an attitude determination processor. The first system, the ASTRO 1, was realized from 1984 to 1987 and launched in November 1989 to the Russian MIR space station. This paper will present in-orbit test results. Currently, the advanced ASTRO 1M system is under development. First tests with the engineering model have been done. The accuracy of the centroid calculation for a single star has been investigated under laboratory conditions. It was found to vary from 3 to 7 arcseconds, depending on track rates. Performance of attitude determination has been tested using real stars. Under the conditions of constant Earth motion an accuracy of about 2 arcsec was obtained.

**Keywords.** Sensors; Attitude control; Angular measurement; Image processing; Identification; Star sensor; Star pattern recognition

### INTRODUCTION

As large-area charge coupled devices (CCDs) became available, efforts commenced to create worldwide a new generation of star sensors with better sensitivity and accuracy performance (Hopkinson and colleagues, 1987; Salomon, 1979; Stanton and colleagues, 1987). First star sensors of this new generation were applied in missions of the late eighties, like such as ROSAT (Lange, 1986), GRANAT, and ASTRO-C. They were used as components of attitude measurement systems and as reference for scientific payloads, but in all applications as so-called star trackers, that means, they determine the star coordinates only. In the star tracker mode the potential possibilities of a star sensor are not completely utilized. Considering the inertial character of the natural fixed-star sky, a direct attitude determination by star pattern recognition is possible and was realized in our Star Pattern Recognition Sensor (SPRS) systems of the ASTRO type.

### THE SPRS ASTRO 1

Our first Star Pattern Recognition Sensor system - the ASTRO 1 - was designed and manufactured

from 1984 to 1987 for a Russian customer. It consists of three optical heads, three image processing units, an attitude determination unit, and a manager & interface unit (Fig. 1).

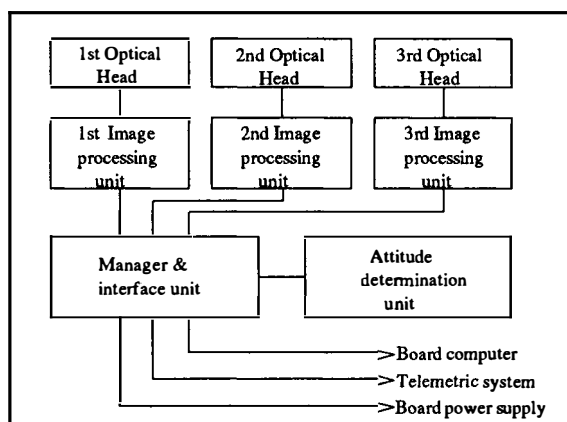


Fig. 1. Structure of the SPRS ASTRO 1

An optical head has a 5.3 x 8 degree field of view (FOV) imaged by a 1.4/100 mm lens on a 520 pixels by 580 pixels CCD array. Moreover, the optical head includes the electronics to drive and read out the CCD, thermoelectric cooler, sunshade, shutter and power supply. The whole CCD readout data are digitized by an 8-bit A/D converter and transmitted to the image processing unit.

The image processing unit saves the bright pixels, containing the star images, interpolates to find the image centroids and transforms the coordinates of the star images into a unit invariant coordinate system. The coordinates and brightness values of up to 7 stars are sent to the attitude determination unit. The order of the output stars is determined by their relative brightness. Star images that include saturated pixels or other defects are marked and of less importance in the following processes. One optical head and the coupled image processing unit form a channel.

The attitude determination unit identifies the stars delivered by up to three channels by comparing the angular distances with the data of a system internal star catalog. Structure and content of the catalog are optimally tailored to the tasks to be solved. It contains about 8500 stars so that the FOV of an optical head is, on average, covered by ten catalog stars.

The 1st flight unit of the ASTRO 1 system was launched on the KVANT 2 module to the Russian MIR space station on 26 November 1989 (Fig. 2). In accordance with the schedule the observations in 1990 and 1991 were done without on-board utilization of the attitude determination unit. This unit is planned to be used in May 1992.

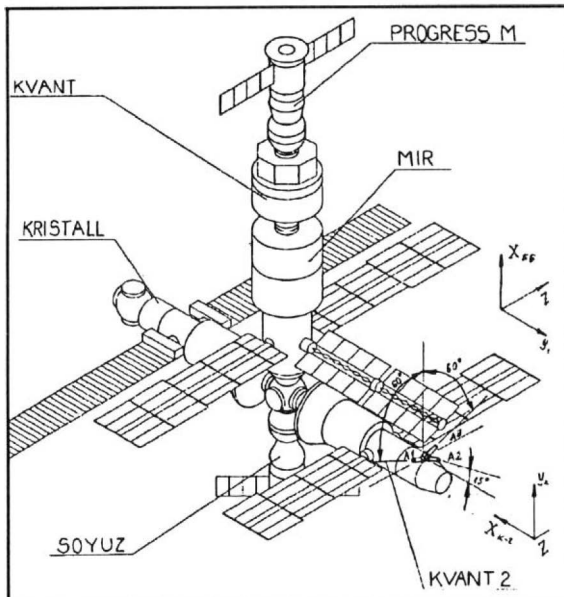


Fig. 2. ASTRO 1 installation on MIR space station  
A<sub>n</sub> indicates the optical heads

In 1990 the system was tested in order to determine its in-orbit performance. For this purpose, the ASTRO 1 data from several observations were transmitted by telemetry to Earth. Investigations of the data were made both by Jenoptik GmbH and by the Institute for Space Research of the Russian Academy of Science, Moscow.

### Test Data Processing

For presentation in this paper an observation dated April 1990 has been selected. This observation was taken in inertial orientation of the MIR space station (angular rate less than 20arcsec/sec) and includes 334 cycles. There were no disturbances caused by Sun, Earth or Moon so that all three channels registered stars within their FOV. The integration time during the observation was about 1.0 second.

### Probability of Star Detection

An important prerequisite for successful attitude determination is a high probability of detecting three or more stars within the sensor FOV. Taking into account the FOV size, this requires a sensitivity of the optical heads being down to the 6.3 magnitude.

To determine the realized sensitivity of the ASTRO 1 optical heads, the stars recorded were identified. Figure 3 shows the star content of the 1st channel during the observation mentioned above, Table 1 the results of identification. N in Table 1 is the number of the cycles of observation which include the concerned star. Pay attention to the fact that the values given in table 1 do not describe the dimmest stars detectable because only the seven brightest stars are put out by the image processing units.

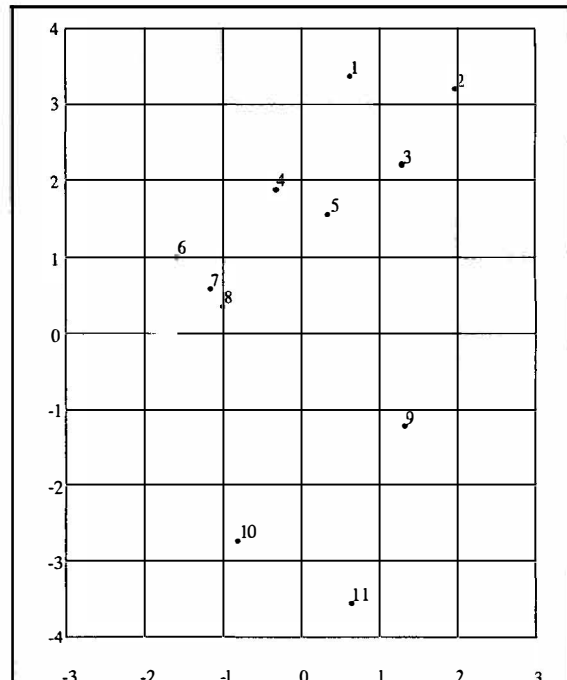


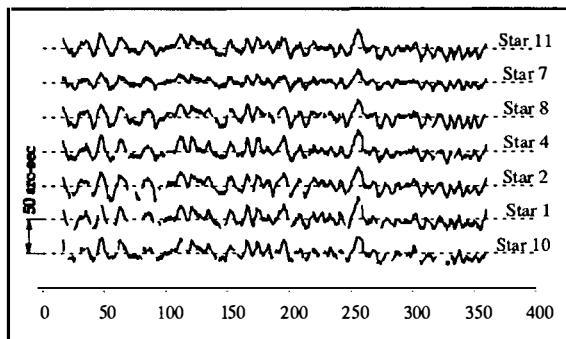
Fig. 3. Stars registered in the 1st channel

**TABLE 1 Identified Stars in 1st Channel**

Star	SAO number	Right ascension	Declination	$m_v$	SP	N
1	85016	17h19m46s	25°32'49"	5.3	A2	298
2	84951	17h14m38s	24°51'01"	3.2	A2	315
3	84948	17h14m10s	26°03'46"	7.0	K0	69
4	85005	17h19m01s	27°17'35"	7.1	M0	321
5	84958	17h15m35s	27°08'40"	6.8	K0	18
6	85028	17h21m08s	28°46'02"	6.3	F8	8
7	85001	17h18m26s	28°49'58"	5.8	K0	334
8	84983	17h17m12s	28°55'23"	7.1	M0	321
9	84812	17h04m24s	28°41'29"	8.1	M0	22
10	65810	17h07m39s	31°13'07"	6.6	K2	290
11	65716	16h59m55s	30°56'25"	3.9	A0	334

### Star Image Position Accuracy

Although the MIR station was held in inertial orientation during taking the observation there was a residual motion demonstrated in Fig. 4 for the X-coordinates of some stars within the FOV of the 1st channel.

**Fig. 4. Residual motion of MIR space station**

Caused by the residual motion of the MIR station the accuracy of a single star image position could not be estimated in a direct way. So the average distances between two stars each and the standard deviation of the measurements were calculated. Table 2 shows the values of the standard deviation for the 1st channel. Only distances have been considered that are found more than 20 times in the observation.

The average standard deviation amounts to 3.7 arcsec. The maximum values appear if star 2 is included. This effect results from a decreasing performance of the centroid algorithm for large star images. Under the assumption of independence of both centroid calculation for the various stars and each star coordinate you can estimate an accuracy of about 1.6 arc-sec for the X coordinate and 2.1 arcsec for the Y coordinate. (The used CCD array has pixels sized 18µm x 24µm.)

**TABLE 2 Standard Deviation of Star Distances**

	1	2	3	4	7	8	9	10	11
1	-	3.0	3.5	3.5	4.3	3.8	-	3.1	4.3
2	3.0	-	5.8	4.8	5.6	3.9	-	4.0	4.6
3	3.5	5.8	-	3.4	3.9	3.6	-	3.6	3.2
4	3.5	4.8	3.4	-	3.4	3.8	2.5	3.6	3.7
7	4.3	5.6	3.9	3.4	-	2.8	3.1	3.6	3.8
8	3.8	3.9	3.6	3.8	2.8	-	3.3	3.8	3.6
9	-	-	-	2.5	3.1	3.3	-	-	2.7
10	3.1	4.0	3.6	3.6	3.6	3.8	-	-	3.3
11	4.3	4.6	3.2	3.7	3.8	3.6	2.7	3.3	-

(all values given in arcsec)

### Accuracy of Attitude Determination

As mentioned above, the attitude determination was not realized on-board the MIR station in case of the utilized observation. So it has been simulated by using the data transmitted by the telemetry system and the complete Engineering model of ASTRO 1 that also includes the attitude determination unit. Because of the residual motion of the station, an exact reference for determination of accuracy was, even in this case, not available. So the average angular distances  $\beta_{ij}$  between the Z-axis (line of sight direction) and  $\gamma_{ij}$  between the X axis of the optical heads and the standard deviation of the measurements were calculated. It was assumed that the alignment of the optical heads is fixed during the observation time. The results are given in Table 3.

**TABLE 3 Standard Deviation of Axis Distances**

angle	average value	standard dev.
$\beta_{12}$	82.5521 deg.	3.1 arcsec.
$\beta_{13}$	119.9565 deg	7.7 arcsec
$\beta_{23}$	82.4834 deg	2.6 arcsec
$\gamma_{12}$	32.904 deg	57 arcsec
$\gamma_{13}$	60.045 deg	14 arcsec
$\gamma_{23}$	33.356 deg	21 arcsec

The improvement of the realized accuracy results from the fact that by utilization of multiple stars for attitude determination effects of random errors can be roughly reduced by the square-root of the number of stars being identified.

### THE SPRS ASTRO 1M

Currently, an improved SPRS - the ASTRO 1M - is under development (Elstner, 1990; Elstner, 1991).

It is intended for the attitude measurement and control system of the Russian satellites of the SPEKTR type which shall carry out astrophysical research in various regions of the electromagnetic spectrum in the middle and late nineties.

The ASTRO 1M system consists of three optical heads, an electronic and a power supply unit (Fig. 5). The electronic unit comprises a multiplexer module, three image processing modules, and two attitude determination and interface modules each. One attitude and one interface module will stand by as redundant units.

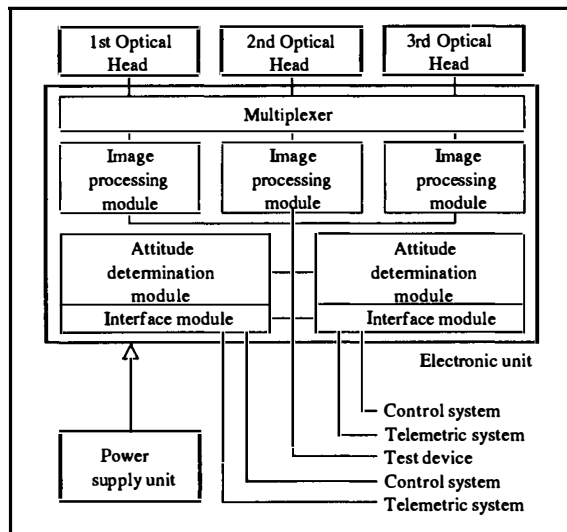


Fig. 5. Structure of the SPRS ASTRO 1M

#### Star Image Position Accuracy

One channel of the ASTRO 1M engineering model was tested on the star sensor test facilities of MBB/Ottobrunn (Ziegler, 1990) to determine the accuracy of centroid calculation for one single star. For this purpose, the optical head was mounted on a two-axis air bearing turntable whose angular position can be measured with an accuracy of 0.36 arcsec. A multiple star simulator was used to stimulate the optical head.

Pointing mode test. To measure the pointing performance 1000 positions statistically distributed within the FOV were selected. At each position the results of 20 consecutive measurements were taken and stored to calculate both bias error and noise equivalent angle (NEA). The results of the pointing mode test are shown in Table 4.

Scanning mode test. The performance in scanning mode was tested by moving in X direction along several selected lines covering the FOV. The results of the scan mode test are shown in Table 4.

TABLE 4 Star Image Position Accuracy

Pointing mode	BIAS X ( $1\sigma$ )	2.1 arcsec
	BIAS Y ( $1\sigma$ )	3.0 arcsec
	NEA X ( $1\sigma$ )	0.5 arcsec
	NEA Y ( $1\sigma$ )	0.4 arcsec
Scanning mode in X direction	Standard deviation X	4.2 arcsec

\* scan rate: 300 arcsec / sec

#### Accuracy of Attitude Determination

Although one channel was tested under laboratory conditions, additional tests have been done to investigate the performance of the entire SPRS system with real stars. For this reason, we took some observations at the Thüringer Landessternwarte "Karl Schwarzschild Observatorium" in Tautenburg. The three optical heads of the ASTRO 1M were mounted on a special mounting support with fixed alignments of  $3 \times 120$  degrees in azimuth and an angle of 15 degrees between their Z axis and the zenith. This arrangement is a compromise between minimization of atmospheric effects and the pairwise coupling of the channels to improve the accuracy of attitude determination. The mounting support is Earth-fixed and so the constant Earth rotation causes the stars to drift smoothly through the FOV of the optical heads. Figure 6 shows a plot of a typical observation including autonomous initial attitude determination. There are three phases of work:

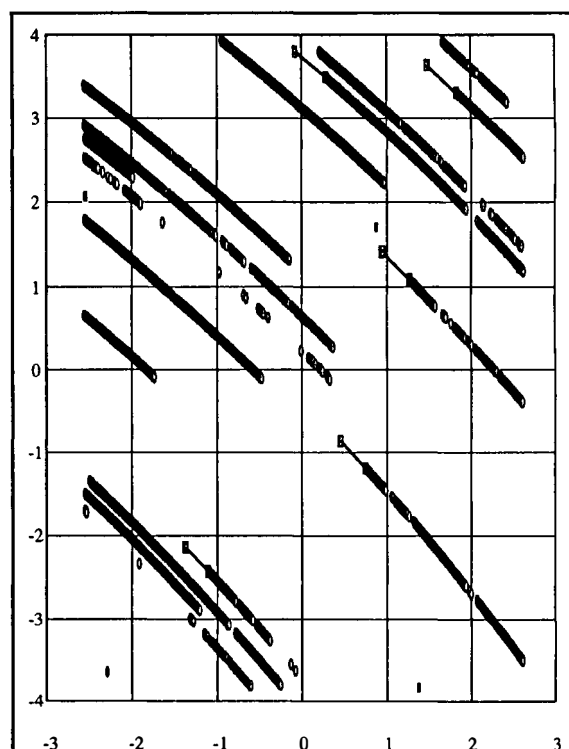


Fig. 6. Stars registered during observation

A - The first 10 to 20 cycles after power-on are used for opening the shutter and optimizing the integration time. Stars registered during phase A are shown in Fig. 6 as rectangles.

B - The last cycle of phase A is used for autonomous attitude determination. This process takes in worst case 5 minutes. During phase B no cycles are generated.

C - The initial attitude is found and has to be verified by the next cycle. From this point of time, the SPRS works with a nominal data update rate of 2 seconds each.

Stars that were identified in initial attitude determination are marked with a line during phase B.

Data processing of ASTRO 1M attitude data has been done by computation of ideal path of the sensors Z axis through the celestial sphere and of the residuals between measured and ideal positions. Figure 7 shows the results of such calculations for an observation of about 1350 cycles. The calculated  $1\sigma$  values amount to 1.2 arcsec in right ascension and 1.5 arcsec in declination.

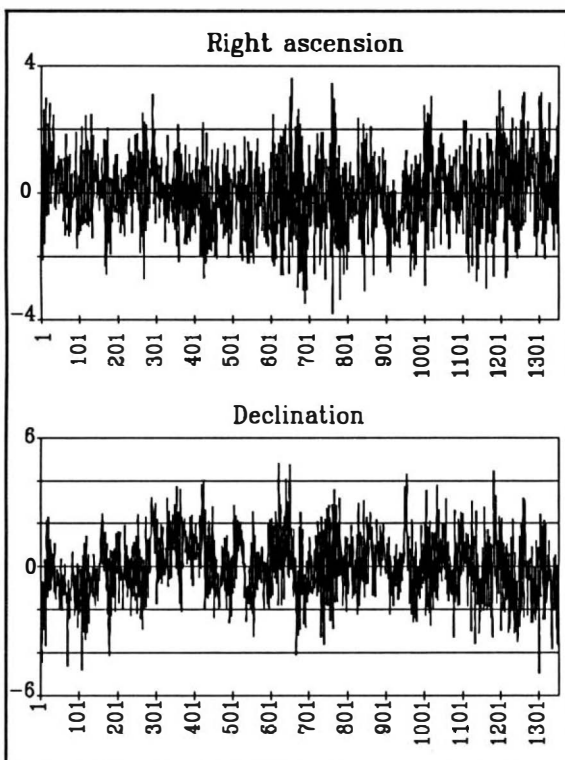


Fig. 7. Accuracy of attitude determination

## CONCLUSIONS

Test results presented in this paper demonstrate in-orbit performance of the SPRS system ASTRO 1, used on the MIR space station, and of the ASTRO 1M system, derivated from on-ground observations. It was shown that it is possible to identify star pattern and calculate attitude.

Test of accuracy both of star image centroid and attitude is difficult and connected with a high effort in test facilities. Centroid accuracy can be estimated under laboratory conditions in a wide range, but performance and accuracy tests of star pattern recognition and attitude determination in a variety of conditions are possible only by utilization of the natural fixed star sky.

## REFERENCES

- Elstner, Ch., W. Müller, and W. Skarus (1990). ASTRO 1M - a new system for determination of orientation of spacecrafts. 41st Congress of the International Astronautical Federation, paper IAF-90-335
- Elstner, Ch., G. Lichtenauer, and W. Skarus (1991). ASTRO 1M - a new system for attitude determination in space. SPIE Vol. 1478 Sensors and Sensor Systems for Guidance and Navigation, 150 - 159.
- Lange, G., B. Moßbacher, and D. Purl (1986). The ROSAT star tracker. SPIE Vol. 627 Instrumentation in Astronomy VI, 243 - 253
- Salomon, P. M. (1979). Charge-coupled device (CCD) trackers for high accuracy guidance applications. SPIE Vol. 203 Recent Advances in TV Sensors and Systems, 130 - 141
- Stanton, R. H., J. W. Alexander, E. W. Dennison, T. A. Glavich, and L. F. Hovland (1987). Optical tracking using charge-coupled devices. Optical Engineering, Vol. 26 No. 9, 930 - 938
- Ziegler, F. (1990). Präzisionssternsensor für die Lagemessung von wissenschaftlichen Satelliten. Zeitschrift für Flugwissenschaften und Weltraumforschung, 14, 391 - 399

# AUTONOMOUS STAR TRACKER DEVELOPMENT

R.W.H. van Bezooijen

*Lockheed Palo Alto Research Laboratory, 3251 Hanover Street, Palo Alto, CA 94304, USA*

**Abstract.** The attitude control, pointing control, and navigation systems of future advanced spacecraft will be characterized by a high degree of autonomy, very high accuracy, efficient commandability, and fast fault recovery. These characteristics are incompatible with the constraints of conventional star trackers which mandate a-priori definition and careful preparation of each on-board attitude fix, and only work if attitude uncertainties are small. With the availability of a highly-efficient, non-iterative star pattern recognition algorithm, accurate CCD star trackers, fast microprocessors, and high density memory chips, it is now feasible to build an Autonomous Star Tracker (AST) capable of determining its attitude rapidly and reliably without having any a-priori attitude knowledge. The Lockheed Palo Alto Research Laboratory is developing an AST prototype that will use the true sky to demonstrate its capabilities. In addition to being capable of attitude acquisition, the AST is designed to also perform autonomous attitude updating and to provide attitude information continuously. The paper describes a number of functions that are enabled or enhanced by the AST, including: gyroless/cheap-gyro attitude control, attitude safing, fast fault recovery, autonomous acquisition of celestial targets by space-borne astronomy telescopes, autonomous optical navigation, precision pointing to terrestrial targets, and uncalibrated attitude acquisition. In addition, an overview of the star pattern recognition algorithm is provided, a thorough, computer simulation program using a 248,516 star catalog is described, and simulation results are presented. These simulations show that an anti-blooming capable AST with an 11.3 degree FOV diameter, a 4148 guide star database, and a MC68030 class microprocessor performs an attitude acquisition in 0.6 seconds with a success rate of 99.25%. Raising this number to 100% should be achieved easily by selecting the guide stars more carefully.

**KEYWORDS.** Intelligent sensors, star trackers, pattern recognition, attitude determination, autonomous systems, space vehicles, optical navigation, inertial navigation, fault recovery, position determination.

## INTRODUCTION

The attitude control, pointing control, and navigation systems of future advanced spacecraft will be characterized by a high degree of autonomy, very high accuracy, efficient commandability, and fast fault recovery. These characteristics are incompatible with the constraints of conventional star trackers which mandate a-priori definition and careful preparation of each on-board attitude fix, only work when attitude uncertainties are small, and, for some applications, require a human operator for closing the loop. In addition to being incapable of fulfilling the needs of future spacecraft systems, conventional star trackers are currently costly to use due to their lack of intelligence, which necessitates the expenditure of significant human, ground software, uplink, on-board storage, and telemetry resources.

With the availability of a robust, highly efficient star pattern recognition algorithm (van Bezooijen, 1989a and 1989b), accurate CCD cameras, fast microprocessors, and high density memory chips, it is now feasible to build an Autonomous Star Tracker (AST) capable of determining its attitude rapidly and reliably without having any a-priori attitude knowledge. In the past, analysis was used to show that an AST with a field of view measuring 11.3 degrees in diameter, a 10 arcsec (1 sigma) spatial accuracy, an all-sky database of some 4,100 guide stars, and an MC68000 class microprocessor, is capable of determining its attitude in approximately 1 second with a success rate very close to 100% (van Bezooijen, 1986 and 1989a).

The Lockheed Palo Alto Research Laboratory is currently developing an AST prototype that incorporates the aforementioned star identification algorithm. This AST is designed to operate in three different modes. In the "acquisition mode," the tracker is required to determine its attitude without having any a-priori attitude knowledge. In the "update mode," it is provided with its expected attitude and its attitude error and is requested to return its measured attitude. The AST will output its attitude continuously at frequencies up to 10 Hz when operating in the "continuous mode".

In addition to building and testing the AST prototype, the research program also involves the evaluation of different guide star selection algorithms and the development of a reliable

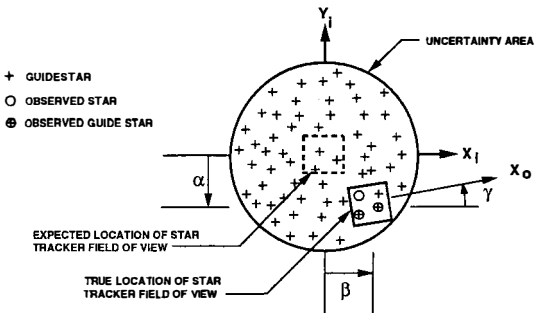


Fig. 1. Attitude Determination Problem.

computer simulation program needed for predicting the AST performance. This paper describes a number of AST applications, outlines the development approach, gives an overview of the star identification algorithm, describes the simulation program, and presents computer simulation results.

The computer simulations are performed for an AST with an 11.3 degree FOV diameter (FOV area of 100 square degrees). This FOV is sufficiently large to ensure fast and reliable star identification at the cost of a moderate amount of memory, and it is small enough for achieving a high AST accuracy. While reducing the amount of memory required, ASTs with a larger FOV have many disadvantages, including: (1) higher probability of interference from the Sun, the Earth, and the Moon, (2) more complex optical design, (3) increased optical distortion, (4) more difficult to accommodate on the spacecraft, and (5) lower accuracy. In addition, a preliminary analysis shows that, for a constant focal ratio, the integration time does not decrease with an increase in the FOV. Going from a circular to a more practical square FOV is expected to have a negligible effect on the performance. In the following, the AST with the 11.3 degree FOV diameter is called the "Reference AST".

The attitude determination problem requiring star identification is illustrated in Fig. 1. Due to attitude errors, the coordinate system associated with the star tracker ( $X_0, Y_0, Z_0$ ) deviates from its expected inertial orientation ( $X_i, Y_i, Z_i$ ). Employing

geometric and brightness criteria, the star identification algorithm determines which of the stars observed by the tracker (the "observed stars") correspond to which of the a-priori selected "guide stars". If at least two of the observed stars are guide stars, and these stars are correctly identified, the attitude about all three axes (angles  $\alpha$ ,  $\beta$ , and  $\gamma$ ) can be computed. The area in which the guide stars are selected, referred to as the "uncertainty area," needs to be sufficiently large to ensure that it will include the field of view of the star tracker. In the case of the AST acquisition mode, the uncertainty area covers the entire sky. As is illustrated by Fig. 1, some of the guide stars within the FOV of the STR may not be observable, while some of the observed stars may be non-guide stars. The recognition algorithm needs to be sufficiently robust to cope with this situation.

## APPLICATIONS

Applied to high-precision space-borne astronomy telescopes, the AST (co-boresighted with the telescope) allows automation of target acquisition. Following a slew to a new target, the AST, operating in the update mode, provides its, and hence the telescope's attitude, down to an error that is small relative to the field of view of the Fine Guidance Sensor (FGS). This allows the FGS to acquire its tracking star(s) used for pointing control, following a correction of the post-slew pointing error. Relative to other automated acquisition methods (van Bezoijen, Lorell, and Powell, 1985), the AST eliminates the need for ground selection and on-board storage of guide stars around each target (in addition to the tracking stars).

Used for updating the attitude of gyro-based attitude control systems, the AST eliminates the need to perform ground selection and on-board storage of guide stars for each planned update. Operating in the update mode, the AST performs an attitude fix upon request from the attitude control system. Since there is no penalty for performing frequent updates, the AST can be used either to improve accuracy, or to reduce cost by allowing the use of cheaper, less accurate gyros. Because the AST can provide its attitude continuously, it would be possible to eliminate gyros in a number of cases.

The AST is also ideally suited for updating the attitude of strapdown inertial navigation systems. Due to the absence of an inertial platform, these systems need more frequent attitude updates to maintain navigational accuracy. In addition to being able to perform updates at the desired frequency, the all-sky capability of the AST eliminates the need to reorient the vehicle for updates.

Operating in its acquisition mode, the AST will allow fast recovery from faults that cause a loss of attitude knowledge. This is important for systems where outages are very costly, or where a loss of attitude could lead to catastrophe if not remedied quickly. The Space Infrared Telescope Facility (SIRTF) and the Cassini planetary spacecraft are examples of spacecraft where an AST could be used to avert catastrophe.

Following a fall-back to the safe mode operated from ROM, SIRTF (Eisenhardt and Fazio, 1988) must be kept in a safe attitude relative to Sun and Earth in order to avoid damage to the cryogenically cooled telescope. This can be accomplished by bringing the telescope axis perpendicular to the sun line with the aid of the Sun Sensor, next use the AST (co-boresighted with the telescope) to determine the attitude about the sun line, and then point the telescope to either the ecliptic North or South Pole following a roll about the sun line. The 100,000 km orbit selected for SIRTF makes it impractical to use an Earth sensor for performing the safing function. Being able to acquire targets efficiently is an added benefit of using the AST on SIRTF.

In the case of Cassini (Draper, 1988), the quick fault recovery enabled by an AST would reduce the length of the critical time intervals associated with Saturn orbit insertion, Titan Probe release, and the Titan fly-by targeting burns needed for gravity assist. This reduction in critical time translates directly into a reduced probability of catastrophic failure.

Used on planetary spacecraft (e.g., Cassini) the AST could perform autonomous optical navigation. Being performed on the ground, optical navigation is currently hampered by long delay times.

Following separation from the Space Station, the Assured Crew Return Vehicle (ACRV) must be placed in the correct attitude for

a collision avoidance maneuver. The AST would enable the ACRV to achieve this attitude within the limited time available.

Combined with a GPS receiver, the AST enables autonomous, high-precision pointing to terrestrial targets as is required for laser communication and efficient ground observation. Assuming a 1 arcsec accuracy for the newest generation CCD trackers, it should be feasible to point to terrestrial targets with a better than 20 m accuracy from an altitude of 500 km.

An AST, integrated with a device for measuring the direction of the local vertical (e.g., a three-axis accelerometer) enables planetary rovers to determine their position autonomously. To achieve this, the AST is used to determine the inertial direction of the local vertical. Given the time of the star field observation and the inertial direction of the local vertical, the position of a vehicle on Mars can be computed to an accuracy of a few hundred meters.

## DEVELOPMENT APPROACH

The AST research program depicted in Fig. 2 involves three main activities: guide star database generation, creation of a computer simulation program for predicting the AST performance, and demonstration of the AST performance using a prototype and the true sky. The simulation program is described in a separate section.

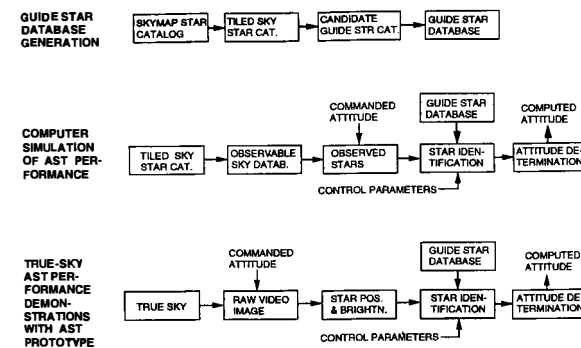


Fig. 2. AST Development Approach.

**Guide Star Database Generation.** The guide star database needed for performing star identification consists of: (1) The position and predicted AST brightness of the selected guide stars, and (2) All pairs of guide stars having a mutual angular distance less than a certain value, typically chosen to be equal to the greatest FOV dimension. The guide stars are obtained from the SKYMAP version 3.3 star catalog (McLaughlin, 1989) which has been compiled primarily for the purpose of satellite attitude determination and provides 622 bytes of information for each of its 248,563 stars.

We can either assume the AST magnitude of the guide stars to be the same as the visual magnitude given in the catalog, or we can translate the visual magnitude of the stars to the AST magnitude using the spectral response of the AST and the spectral star information provided by the catalog. In the former case we can either accept a large error in the predicted AST magnitude of the guide stars, or we have the option to minimize this error by adding an optical filter to the AST to bring its spectral response closer to that of the V filter.

Having larger magnitude errors makes star identification more difficult and necessitates a higher guide star density. Addition of a filter makes guide star selection and identification easier at the cost of a reduced AST sensitivity. Currently, translation of the visual to AST magnitude is not implemented. However, further research should be performed to determine the accuracy of V to AST magnitude translation, given the spectral information available in the SKYMAP star catalog.

Guide star database generation is performed using the following steps: (1) Conversion of the single-file SKYMAP catalog on 9 track tape to 100 files on Macintosh readable Teac (150) tape, (2) Extraction of the necessary star data, (3) Organization of the stars into a tiled-sky catalog, (4) Creation of a candidate guide star catalog, (5) Guide star selection, and (6) Formation and sorting of guide star pairs. The data currently extracted for each star at step (2) consists of its SKYMAP record number, epoch 2000.0 right ascension and declination, position error, proper motion and visual magnitude.

The sky has been partitioned into 110 slightly overlapping tiles to allow efficient generation of the candidate guide star catalog, the guide star database, the observable sky database, and the observed stars. Within each tile, the stars of the tiled-sky catalog are sorted in sequence of increasing visual magnitude. The tiles overlap each other by at least 0.7 degrees, which permits a tile by tile generation of the candidate guide star catalog. In this catalog, each candidate is accompanied by a list of its close neighbors out to a distance of 0.35 degrees. This structure facilitates rapid guide star selection using one of the selection algorithms.

The tiles are sized such that an AST can never extend into more than 4 tiles, provided its largest FOV dimension is less than 16 degrees. This is achieved by arranging the tiles into 5 declination bands per hemisphere and partitioning each band in an appropriate number of tiles. The core area (i.e., area minus overlap border zone) of the first band, extends to 16.2 degrees from the pole and comprises one tile, the "polar cap". The core width of the second, third, fourth and fifth bands is 16.4, 20.7, 18.4, and 18.3 degrees, respectively. These bands are partitioned into 6, 12, 18, and 18 tiles along constant right ascension lines.

In the tiled-sky catalog, the number of stars in the core area of the tiles ranges from a low of 1024 to a high of 5033, while the number of stars in the border area of the tiles ranges from 78 to 407. It was found that a total of 797 stars (0.32%) lack visual magnitude information. Using the core stars with defined visual magnitude, an integrated star density model is generated for each tile. This density model assumes that the log of the integrated star density is a linear function of the magnitude, and a least squares fit is employed to establish the two model parameters. Using the model, a "model magnitude limit" is established per tile. At this limit the number of stars according to the model equals the number of stars in the tile. It ranges from 9.28 to 9.80 magnitude.

Generation of the candidate guide star catalog requires definition of a close neighbor radius value and an upper magnitude limit, defined as a delta relative to the aforementioned model magnitude limit. Using 2.5 for the magnitude delta and 0.35 degrees for the close neighbor radius, a candidate guide star catalog comprising a total of 16,603 candidates is generated. The density of the candidates varies roughly from 0.23 per square degree to 0.82 per square degree. The selection of guide stars and the generation of the guide star pairs is covered in the simulation section.

The need for a catalog with the depth of SKYMAP is illustrated by the fact that even if there were no error in the predicted AST magnitude and the SKYMAP catalog were 100 % complete down to the model magnitude limit, the faintest guide star candidates could have unknown close neighbors with a brightness up to 10% (2.5 magnitude) of that of the candidate.

**AST Prototype.** Since the simulations can only approximate the truth, suffer from some statistical uncertainties, and cannot possibly account for all parameters involved, it is absolutely necessary to validate the AST performance using a proof-of-concept or prototype model. Using this prototype, a large area of the sky will be mapped and the raw video data will be stored on disk or tape. In the lab, each of the frames thus obtained can be further processed and used to test the star identification capability of the AST. Following verification of its star identification capabilities using true sky images in the lab, its capabilities will be demonstrated in real time at an observatory.

The AST prototype and its Support Equipment will be assembled from the following commercially available components: (1) A thermoelectrically cooled CCD camera head with a NuBus interface board for a Macintosh II computer, associated software, and a camera lens adapter, (2) A 35 mm f/1.4 and a 50 mm f/1.2 camera lens, and (3) A computer controlled telescope with equatorial wedge and tripod.

The anti-blooming capable CCD camera will be equipped with a 1024x1024 pixel CCD that is used in a Frame Transfer mode, implying a sensitive area of 512x1024 pixels. Equipped with the 35 mm lens, the FOV can be selected within the range from 10x10 to 10x20 degrees. The integration time will be approximately 1.1 s using a V filter and the smallest FOV, and will be much shorter without this optical filter. With the 50 mm lens, the FOV can be selected within the range from 7x7 to 7x14 deg. The larger aperture allows a reduction of the integration

time to 0.4 s with the V filter in place. A Macintosh IIci computer will be used to control the camera, store the video data, and perform the star identification.

The CCD camera will be mounted in a piggyback fashion to a computer controlled 8", f/6.3 Meade LX200 telescope enabling efficient mapping of the sky.

## STAR IDENTIFICATION

Star identification is achieved using a star pattern recognition algorithm. The objective of this algorithm is to find the largest group of stars within the the star field observed by the AST that matches a group of guide stars. The brightest observed stars are picked for the identification process. Although the simulations allow the use of up to 12 stars, 8 is a more typical number. The anti-blooming capability of the CCD camera is exploited to ensure that the desired number of stars can be obtained, even if a very bright star is present. The recognition algorithm assumes that a group of observed stars matches a group of guide stars if all of the following criteria are met:

1. The measured angular distance of each pair of observed stars matches the predicted angular distance of the corresponding pair of guide stars to within the distance tolerance ( $t_{dis}$ ).
2. The measured magnitude of each of the observed stars matches the predicted magnitude of the corresponding guide stars to within the magnitude tolerance ( $t_{mag}$ ).
3. The geometry of the group of observed stars is not the mirror image of that of the group of guide stars.

In the above, the angular distance of a star pair is defined as the angle between the two stars of the pair. In practice, the "vector distance" between two stars is used as a measure of the angular distance. The vector distance is defined as the linear distance between the stars, assuming that the stars are located on a celestial sphere with unit radius.

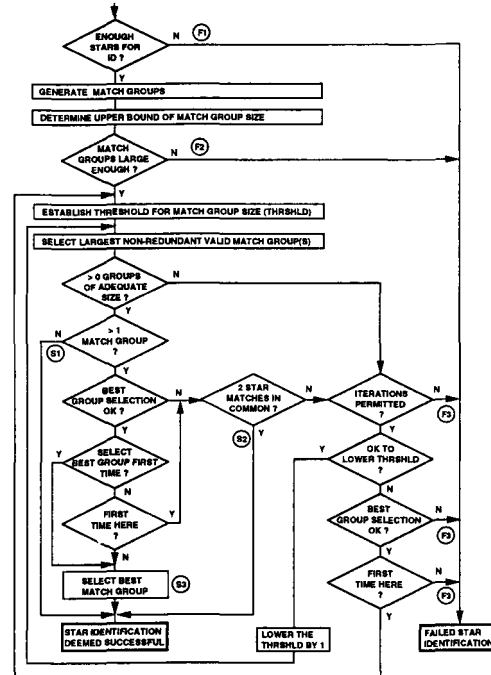


Fig. 3. Recognition Algorithm Flow Diagram.

A high level flow chart of the star pattern recognition algorithm is depicted in Fig. 3. First it is checked if a sufficient number of stars is available to enable successful identification. For the acquisition mode this number needs to be at least 3. If a sufficient number of observed stars is available for identification, match groups are generated (see first box). This match group generation process is clarified using the example shown in Fig. 4. In this example, 8 observed stars (O1 through O8) are available for identification. Four of the 8 stars are guide stars, namely observed stars O1, O2, O4, and O7 which are equal to guide stars G14, G26, G51, and G3 respectively. We will assume that the observed brightness of the 4 observed guide stars deviates less than  $t_{mag}$  from their predicted values, while the measured 6 distances between the observed guide stars deviates less than  $t_{dis}$  from their predicted values.

Following generation of all observed star pairs (28 for the example shown in Fig. 4), it is checked which pairs of guide stars match each of the observed star pairs. To make this checking efficient, all guide star pairs are stored in the AST guide star database in sequence of increasing angular distance. We start with checking if the pair consisting of O1 and O2 matches any guide star pairs, and find that guide star pair G14-G26 is among its matching guide star pairs. This latter match results in the formation of two "match groups," j and k, where match group j consists of a "kernel star match" made up of O1 and G14 and one member, being the kernel of match group k.

As a result of the match, the arrays identifying the observed and guide stars corresponding to the kernel of match groups j and k are updated, resulting in:  $OMAT(j) = 1$ ,  $GMAT(j) = 14$ , and  $OMAT(k) = 2$ ,  $GMAT(k) = 26$ . In addition, the array that keeps track of the number of members associated with the kernel of each match group is updated, resulting in:  $NASS(j) = 1$  and  $NASS(k) = 1$ . Also, the array that identifies the match group associated with each member of a match group is updated, resulting in  $MAT(j,1) = k$ , and  $MAT(k,1) = j$ .

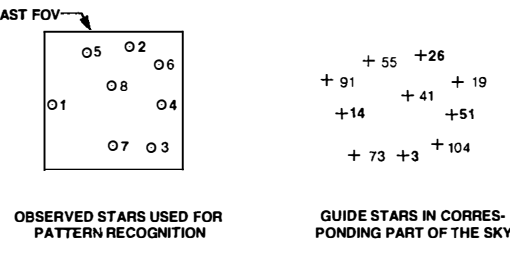


Fig. 4. Example of Matching Star Patterns.

We now have a means to find the observed and guide stars that correspond to member 1 of match group j; these are given by  $OMAT(MAT(j,1)) = 2$  and  $GMAT(MAT(j,1)) = 26$ . The array values as obtained are shown in Table 1, assuming that j and k are match groups 10 and 11 respectively. The two match groups are also depicted in Fig. 5.

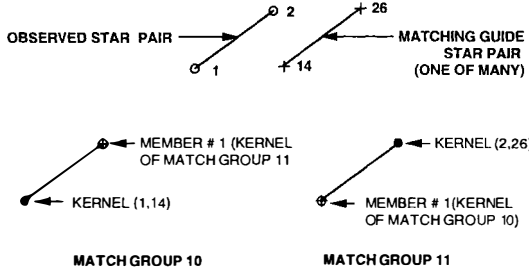


Fig. 5. Match Group Generation.

When we check which guide star pairs match observed star pair O1-O4, it is found that guide star pair G14-G51 is one of the matching guide star pairs. As a result, a member is added to match group 10, while a new match group (41) having O4, G51 as its kernel is created. This match results in the following array updates:  $NASS(10) = 2$ ,  $MAT(10,2) = 41$ ;  $OMAT(41) = 4$ ,  $GMAT(41) = 51$ ,  $NASS(41) = 1$ , and  $MAT(41,1) = 10$ . Processing of observed star pair O1-O7 results in the addition of a third member to match group 10.

After having processed all 28 observed star pairs all initial match groups (typically 7000 for the reference AST) have been generated. The array values for the 4 match groups with kernel star matches O1, G14; O2, G26; O4, G51; and O7, G3, are shown in Table 1. Because of false matches, each of these four groups typically has more members than the 3 shown.

The upper bound for the size of valid match groups is determined next (second box in flow diagram) by evaluating the NASS vector. In order to have a valid match group of i star matches (1 kernel plus i - 1 members), we need to have at least i match groups with i - 1 or more members as may be seen from the example of Fig. 4 where i = 4. If the upper bound of the match group size is less than the minimum value required (3 or 4 for the acquisition mode), star ID failure is reported.

In the next step, the threshold for the match group size is established (third box). This threshold is one of the control

TABLE 1 List of Initial Match Groups

Match Group	Kernel Match		Numb. of Members	Match Groups associated with Members of Match Group i		
	Obs. Star	Guide Star		First Member	Second Member	Third Member
i	$OMAT(i)$	$GMAT(i)$	$NASS(i)$	$MAT(i,1)$	$MAT(i,2)$	$MAT(i,3)$
10	1	14	3	11	41	57
11	2	26	3	10	41	57
41	4	51	3	10	11	57
57	7	3	3	10	11	41

parameters of the star pattern recognition algorithm. It is usually set at the upper bound of the match group size minus 2. All match groups that are smaller than the threshold are eliminated in the following operation (included in fourth box). In addition to the elimination of these small match groups, which are likely to be spurious, it is also necessary to eliminate each member of a remaining match group that is associated with a match group that has been eliminated.

The remaining match groups are then validated, an operation where it is checked if each of the angular distances between the members of the match groups satisfies the distance tolerance. For the example of match group 10, these distances are indicated by dashed lines in Fig. 6. Next, redundant groups are eliminated which is followed by eliminating match groups where the pattern of guide stars is the mirror image of the pattern of observed stars. In the example shown in Fig. 4, match groups 11, 41, and 57 are redundant. Finally, the largest remaining match group(s) are extracted.

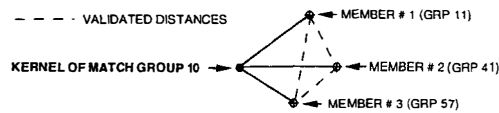


Fig. 6. Match Group Validation.

If the size of the extracted group(s) is insufficient, iterations are permitted, and it is allowed to lower the threshold, the process is repeated starting with the thresholding of the initial match groups. If only one non-redundant valid match group of sufficient size is left, the star identification is deemed to be successful. If there are multiple non-redundant match groups, there are three possibilities: all of them are correct, at least one of them is correct, or they are all faulty.

The probability of the first of these possibilities to occur is fairly high because it frequently happens that one of the angular distances does not match because of a large attitude error of one of the observed guide stars. This case can be salvaged by checking if all match groups have 2 star matches in common as is shown in the flow diagram. If there are no two common star matches, it can be attempted to find a solution by lowering the threshold, or by selecting the "best group", either immediately (select best group first time = Y), or if all else fails.

The RSS value of the distance errors is currently used as the criterion for finding the best match group. The group with the lowest value is selected as the correct match group.

## SIMULATION PROGRAM

An overview of the simulation is shown in Fig. 7. A simulation run consists of: (1) Generation of the guide star database, (2) Generation of the observable sky, (3) Evaluation of the star identification performance at the prescribed sky locations, and (4) presentation of the simulation results. The parameters used to simulate the reference AST case are shown in Table 2. The numbers quoted below are for the AST reference case, while compute times are valid when using a Mac IIci.

**Guide star database.** The guide stars are selected from the candidate guide star catalog using the specified guide star density, the close neighbor acceptance criteria, and the specified selection mode as inputs. Stars with close neighbors will be accepted as guide stars only if the integrated magnitude of

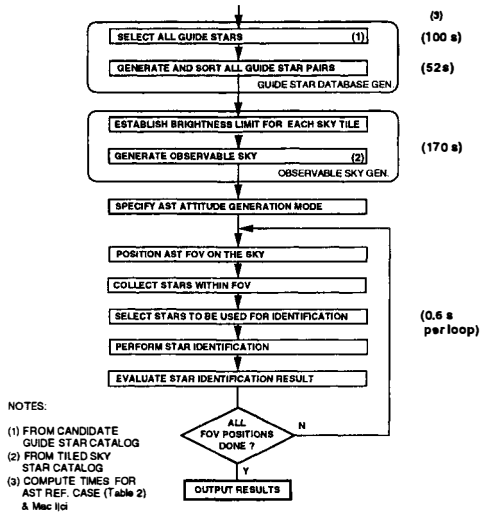


Fig. 7. Simulation Overview.

neighbors closer than a specified distance (close disturbing star radius) exceeds the guide star magnitude by the specified margin (close disturbing star magnitude margin). Currently, the required number of guide stars per tile is obtained by simply picking the brightest qualifying stars. The distribution of the guide stars obtained this way is not very uniform and better methods are being developed. Given the guide star pair distance limit, all guide star pairs are generated and sorted in sequence of increasing angular distance.

TABLE 2 Parameter Values for Reference AST

Operation	Parameter Description	Parameter Value
Guide Star Database Generation	FOV Shape	: Circular
	FOV Area	: 100 square degrees
	Guide Star Density	: 10 per AST FOV
	Close Disturbing Star Radius	: 240 arcsec
	Close Dist. Star Magnitude Margin	: 2.5 magnitudes
	Guide Star Selection Mode	: Brightest Stars
Observable Sky Database Generation	Guide Star Pair Distance Limit	: 11.3 degrees
	Catalog Completeness	: 95%
	Catalog Reliability	: 95%
	Catalog Magnitude Error	: 0.0 magnitude
	AST Sensitivity Limit	: 7.5 magnitude
	AST Magnitude Error	: 0.3 magnitude (1 $\sigma$ )
	AST Spatial Accuracy per axis	: 10 arcsec (1 $\sigma$ )
	Star Clumping Factor	: 3x mean density
	Time from Guide Star (GS) Epoch	: 10 years
	Magnitude Threshold for Observable Stars	: 0.42 mag above faintest reach. GS
Star Identification Testing	Magnitude Margin relative to Threshold	: 0.77 magnitude
	Magnitude Limit for Close Star generation	: 4.0 mag above faintest GS in tile
	FOV Positioning Mode	: Prescribed, all sky
	FOV Positioning Pitch	: 0.0475 deg (for 10,000 positions)
	AST Dynamic Range	: 5 magnitudes
	AST Saturation Range	: 5 magnitudes
	Number of Stars used for ID	: 8 (brightest, unsaturated)
	Limit to Number of Saturated Stars	: 3
	Tolerance on Guide Star Pair Distance	: 37 arcsec
	Relaxed Distance Tolerance	: 37 arcsec
	Tolerance on Guide Star Magnitude	: 0.77 magnitude
	Number of identified stars needed	: at least 3 for success
Star ID Confusion Handling	Initial Threshold for Match Group Size	: 2 below maximum value
	Limit to match grp size (kernel+members)	: 11
	Star ID Confusion Handling	: Select best group if all else fails
	Iterations permitted ?	: yes

It takes 100 s to select the 4148 guide stars for the reference AST case. The faintest guide stars have a 6.3 visual magnitude. A highly efficient algorithm enables generation and sorting of all 82,316 guide star pairs in just 52 s. This speed allows the amount of AST ROM needed for storing the guide star database to be reduced from 552 Kbytes to 42 Kbytes for applications where an attitude acquisition delay of some 60 s can be tolerated.

Observable Sky Generation. The objective of this operation is to generate the AST magnitude and "true" sky position of all stars brighter than the AST threshold. The magnitude and position are computed by combining the error contributions of the AST and the catalog, making it possible to compute these parameters only once per simulation run. The threshold for each tile is established by specifying it relative to the faintest reachable guide star. Guide stars within the area that covers the tile and extends up to a FOV diameter distance beyond the edge of the tile are defined as being reachable.

For the reference AST, the threshold is set at 0.42 mag, which gives a randomly selected guide star a 99% probability of exceeding this threshold, given a magnitude error of 0.3. If the

AST sensitivity limit is brighter than the threshold, the threshold is replaced by the sensitivity limit. Magnitude errors will be generated for all stars down to the AST threshold magnitude plus a sufficiently conservative margin. In the case of the reference AST, this margin is set at 0.77 magnitude, implying that all stars having at least a 1% probability of exceeding the AST threshold are considered.

The guide stars are processed first. A fraction of the guide stars is made non-observable at random to account for a non-perfect catalog reliability. For the reference AST case, 198 of the 4148 guide stars were eliminated because of this reason. Because of the incompleteness and limited depth of the star catalog, additional "unknown" close stars are generated randomly within the close disturbing star area of the remaining guide stars. The magnitude limit for these stars is specified relative to the faintest guide star in the tile, while their density can be biased using a "clumping factor" different from 1 to reflect the fact that most stars are members of multiple systems. Seven hundred and fifty unknown close disturbing stars were generated for the reference AST case and added to the 350 known ones.

The guide star position errors include the effect of the star position error in the catalog, the contribution of the AST, the effect of uncompensated proper motion, and the effect of any close disturbing stars. The latter effect is incorporated by computing the combined centroid location. The guide star magnitude errors are generated randomly using the combined 1  $\sigma$  value of the catalog and AST contributions and accounting for close disturbing neighbors.

Next, magnitude errors are randomly assigned to all non guide star catalog stars down to the aforementioned conservative limit. All stars with a "true" AST magnitude brighter than the AST magnitude threshold are retained. For the reference AST case, a total of 6,360 of these stars were collected. Additional observable stars are generated randomly to account for the imperfect catalog completeness. A total of 537 of these stars were generated for the reference AST case. The catalog completeness used for the simulation is modeled as a function of the magnitude. This model is obtained by evaluating the curve describing the logarithm of the integrated density of the stars in each tile versus magnitude and postulating that this relation should be linear.

It takes 170 seconds to generate the 10,847 observable stars of the reference AST case. Among them are 3,950 guide stars.

Star Identification Testing. The test sequence consists of positioning the AST FOV on the sky, collection of the observable stars within the FOV, selection of a subset of these for identification use, star identification, and evaluation of the identification result. The FOV can be positioned using the prescribed, all-sky method, the prescribed single position method, or the all-sky random method. The first method, which allows up to 10,000 evenly distributed positions covering the entire sky is the most useful as it represents a very systematic way for detecting problematic sky areas. Having detected these difficult spots, the single position method can be used to diagnose the identification failures.

Following collection of the observable stars within the FOV, it is attempted to select the desired number for identification use (8 for the reference AST). The selection of these stars is influenced by the dynamic range constraint, the AST anti-blooming capability (defined in terms of a saturation range), and the number of stars allowed to be in saturation. In addition to the desired number of ID stars, the tolerance on the guide star pair distance, the relaxed distance tolerance (applicable when performing the match group validation), and the magnitude tolerance need to be provided to the star pattern recognition algorithm. For the reference AST case the tolerances are selected such that the probability of meeting each of these tolerances is 99%. It is also necessary to specify how to resolve star ID confusion cases (more than one final match group) and whether or not to allow iterations.

The average time needed for performing one loop is 0.6 s for the AST reference case. The high speed is made possible, among other things, by storing the guide star database and the observable sky database in RAM.

## RESULTS

The simulations show that the AST, operating in its acquisition mode, is capable of successfully identifying the stars within its FOV in 9,927 out of 10,000 cases. It performs the identification in just 0.57 seconds on the average, with a minimum of 0.23 and a maximum of 2.70 s, assuming use of Mac IIci equivalent computer. The AST was incapable of identifying the star field in 64 cases (failed ID), while there were 9 cases where the AST erroneously deemed the identification successful (false ID). The result is shown in the first row of table 3.

TABLE 3 Simulation Predictions of AST Performance

Parameters used for Star ID		ID Results <sup>1</sup>			ID Compute Time <sup>2</sup>			Needed Array Space				
Select Iterat.	Match Group	Magn. Toler.	Success	Failed	False	Mean	Min.	Max.	(s)	(s)	(s)	(Kbyte)
Best OK?												
Group												
1st x?												
no	yes	11	0.77	9,927	64	9	0.57	0.23	2.70	520		
yes	no	11	0.77	9,925	66	9	0.57	0.23	1.70	304		
yes	no	6	0.77	9,925	66	9	0.57	0.23	1.68	214		
yes	no	6	2.00	9,869	103	28	1.19	0.33	5.63	310		

1) For a total of 10,000 evenly distributed FOV locations, covering the entire sky

2) Using a MC68030 class microprocessor running at 25 Mhz

The majority of the failures (55) are due to having less than 3 guide stars among the observed stars, clearly an indication that a more sophisticated guide star selection method is needed. Identification of 17 of the 170 cases with 3 guide stars among the observed stars was unsuccessful (4 of the 17 were false IDs). There was only one case where identification was unsuccessful with more than 3 guide stars (4) among the observed stars. An investigation of this case showed that one of the 4 guide stars had an out of tolerance magnitude, thus reducing the number of usable guide stars to 3. The value of selecting the best match group to resolve ambiguity is illustrated by the fact that this method raised the number of successes by 17. However, this method was also responsible for 4 of the 9 false identifications.

Of the 9936 cases that were deemed successful by the star pattern recognition algorithm, there were 8732 cases with only one final match group (5 of them were false), 1183 cases with multiple final match groups that all had 2 star matches in common, and 21 multiple final match groups where the best match had to be picked.

The simulations show a maximum of 8,184 initial match groups, from which it can be deduced that the recognition algorithm needs 520 Kbytes of array space. By prohibiting iterations, this array space can be reduced to 304 Kbytes, as there is no need to preserve the matrices associated with the initial match groups. A simulation showed that not allowing iterations (see Fig. 3) increased the number of failed identifications by only 2, while no additional false identifications occurred. The results of the latter simulation are shown in the second row of table 3. Avoiding iterations had the additional benefit of reducing the maximum compute time from 2.7 to 1.7 seconds.

A further reduction of array space can be achieved by limiting the maximum match group size to 6, instead of 11, which allows the space needed for the MAT matrix (see Identification section) to be cut in half to 90 Kbytes, implying that the needed total array space can be reduced to 214 Kbytes. According to the simulations (third column of table 3) the reduction in the cap has no impact on the identification performance. However, limiting the number of identified stars to 6 (instead of 8) impacts the accuracy of the computed spacecraft attitude somewhat.

In some applications (e.g., the ACRV) the AST has been dormant for a long time prior to its use. Consequently, there may be a substantial error in the AST sensitivity. To determine the performance of an AST with unknown sensitivity, the star brightness was effectively eliminated from the recognition algorithm by opening up the tolerance to 2 magnitudes. As may be seen in row 4 of table 3, this uncalibrated AST retains a very high success rate of 98.69%, which will most likely increase to 100% through use of a more sophisticated guide star selection algorithm. Elimination of the star brightness in the recognition algorithm does impact the compute time and the needed array space as may be seen from table 3.

The number of observed stars used for the star pattern recognition has an impact on the star identification success rate,

the false identification rate, and the compute time, as well as the required array space. Four simulation runs were performed where the number of stars used for recognition was varied from 6 to 12. The result is shown in Fig. 8, from which it may be seen that it is fairly optimal to use 8 stars for the identification. Having a larger number of stars makes it easier to falsely match a subgroup of them with a group of non corresponding guide stars. Actually, as might be expected, the observed false match probabilities of 0.09, 0.17, and 0.25% correspond very well with the number of triplets for 8, 10, and 12 stars, which are equal to 56, 120, and 220 respectively.

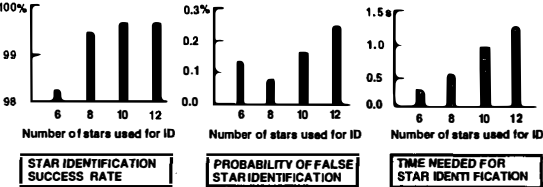


Fig. 8. Sensitivity to Number of Stars used for ID

## CONCLUSIONS AND ACKNOWLEDGEMENTS

Using realistic simulations, it has been shown that an Autonomous Star Tracker with an 11.3 degree FOV diameter, a spatial accuracy of 10 arcsec (1 sigma), a brightness accuracy of 0.3 magnitude (1 sigma), a database of 4148 guide stars, a highly efficient non-iterative star pattern recognition algorithm, and an MC68030 class microprocessor running at 25 Mhz, will be capable of determining its attitude in approximately 0.6 s without having any a-priori attitude knowledge. It can do so with a demonstrated success probability of 99.25%, while the probability of false identification is less than 0.1%.

Failures are caused by an insufficient number of guide stars in certain parts of the sky due to the use of a very simple guide star selection method. This problem can be remedied easily by using a more sophisticated selection algorithm. Therefore, it is expected that an AST with an improved guide star database will achieve a 100% success rate. The potential of a perfect success rate is enabled by anti-blooming capable CCDs that make it possible to eliminate failures caused by a lack of dynamic range (van Bezooijen, 1989a and 1989b).

A very high success rate of 98.69% is retained when the star brightness is not used for star pattern recognition, implying that the AST will function, even if a sensitivity calibration is not available, as may be the case for certain applications (e.g., the ACRV). Because of the high mechanical stability of CCD trackers, geometrical re-calibrations are probably not required. The success rate for the non-calibrated AST is expected to reach 100% once an improved guide star database has been generated.

The author gratefully acknowledges the Astronomical Data Center at the NASA Goddard Space Flight Center for providing the SKYMAP star catalog. He also would like to thank Paul Reshatoff and Ted Havas for their outstanding technical support.

## REFERENCES

- Draper, R.F. (1988). The Mariner Mark II Program. Paper AIAA 88-0067, AIAA 26th Aerospace Sciences Meeting, Reno, Nevada, Jan 1988.
- Eisenhardt, P., and G.G. Fazio (1988). The SIRTIF concept and its realization. NASA Ames Research Center, Moffett Field, CA, Nov 17, 1988.
- McLaughlin, S.F. (1989). SKYMAP Star Catalog, version 3.5. National Space Science Data Center, Goddard Space Flight Center, Greenbelt, Maryland.
- van Bezooijen, R.W.H., K.R. Lorell, and J.D. Powell (1985). Automated star pattern recognition for use with the Space Infrared Telescope Facility (SIRTF). Xth IFAC symposium on automated control in space, Toulouse, France, June, 1985.
- van Bezooijen, R.W.H. (1986). Success potential of automated star pattern recognition. Paper AIAA-86-0254, AIAA 24th Aerospace Sciences Meeting, Reno, Nevada, Jan 6-9, 1986.
- van Bezooijen, R.W.H. (1989a). Automated Star Pattern Recognition, Ph.D. Dissertation, Stanford University, Stanford, California.
- van Bezooijen, R.W.H. (1989b). A Star Pattern Recognition Algorithm for Autonomous Attitude Determination, XIth IFAC Symposium on Automatic Control in Aerospace, Tsukuba, Japan, July, 1989.

## IMPINGEMENT CALCULATIONS FOR ULTRA-LOW DENSITY HELIUM THRUSTERS

Y.R. Jafry<sup>\*1</sup>, J. Vanden Beukel<sup>\*\*</sup>, I.D. Boyd<sup>\*\*\*</sup> and D.B. DeBra<sup>†</sup>

<sup>\*</sup>Space Science Department, ESA/ESTEC, Noordwijk, The Netherlands

<sup>\*\*</sup>Lockheed Missiles and Space Company, Sunnyvale, California, USA

<sup>\*\*\*</sup>Elloret Institute, Palo Alto, California, USA

<sup>†</sup>Stanford University, Stanford, California, USA

**Abstract** A new semi-empirical thruster plume model is presented based on recent experimental and numerical (Direct Simulation Monte Carlo) studies. The results are unique in that they pertain to unprecedently low flow rates (nozzle Reynolds numbers below 200). The model is used in computing the impingement forces acting on a spacecraft solar panel emersed in a thruster plume. The time-varying impingement effects due to changes in surface temperature were found not to be a serious limitation on the thruster calibration accuracies for the GP-B and STEP spacecraft. This suggests that both spacecraft could yield useful aeronomic data through monitoring of the thruster activity of the drag-free control systems.

**Key words** spacecraft control, helium thruster plumes, impingement, rarefied nozzle flows, plume measurements, DSMC simulations, aeronomy

## INTRODUCTION

GP-B (Gravity Probe B) and STEP (Satellite Test of the Equivalence Principle) are two proposed space-based experiments in basic physics, scheduled for launch at the end of the decade. Both will utilize *drag-free* spacecraft in 600 km polar orbits around the earth. By monitoring the activity of the drag-free compensators, it will be possible to obtain *in situ* drag measurements from which variations in density and winds may be observed with unprecedented resolution ( $\approx 80$  km, spatially;  $\approx 10$  seconds, temporally).

The accuracy of the estimation of the drag force will depend on the accuracy to which the thrust system can be calibrated. Each spacecraft will have about 18 thrusters distributed around the vehicle. The thrusters will be electromagnetically-actuated proportional devices utilizing boil-off helium from the spacecraft cryogenic systems as the propellant. On-orbit calibration procedures are envisaged (Wiktor, Jafry & DeBra, 1992), after which the largest source of uncertainty may be due to the time-varying effects of impingement of the thruster plume gas on spacecraft surfaces. In order to investigate this, an extensive experimental and

numerical study was performed.

The plume experiments were considered necessary because of the extremely low densities of the flows compared with conventional spacecraft attitude control jets. The nozzle Knudsen number ranges from 1 to 0.01 across the dynamic range of the thruster (0.05 mN to 5 mN). This corresponds to nozzle Reynolds numbers ranging from 1 to 160. By comparison, a typical spacecraft attitude control thruster which develops, say, 1 N, operates at a nozzle Reynolds number of around 1000.

It is well known that for very low densities the nozzle and plume expansions can not be adequately modeled using continuum theory (Bird, 1980). Consequently, we performed both experimental and numerical (DSMC, Direct Simulation Monte Carlo) studies, then generated a semi-empirical plume model based on the combined results. Using this new plume model, impingement effects were computed using standard free molecular flow theory.

## PLUME EXPERIMENTS

Figures 1 and 2 contain schematics of the experimental layout and the nozzle design. The measurements of local mass flux (i.e., the product  $\rho V$ ) were performed using a helium mass spec-

<sup>1</sup> formerly at Stanford University where this work was supported under NASA Contract No. NAS8-36125.

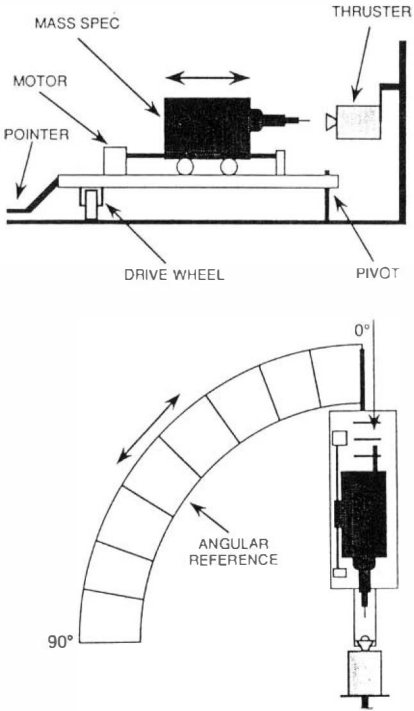


Fig. 1. Experiment schematic.

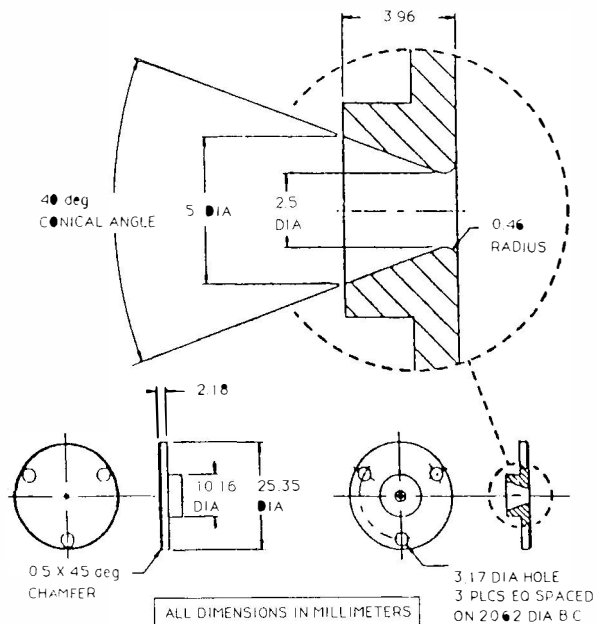


Fig. 2. Nozzle geometry.

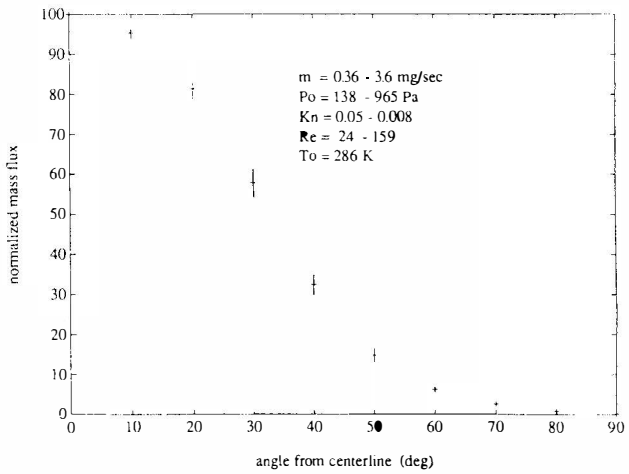


Fig. 3. Nominal plume shape

trometer (Jafry & Vanden Beukel, 1992; Jafry, 1992).

Figure 3 shows the range of experimentally observed plume shapes for nominal flow rates ranging from 0.36 mg/sec to 3.6 mg/sec and radial distances (measured downstream from the nozzle exit) ranging from 2 cm to 14 cm. The abscissa represents the angle,  $\phi$ , measured from the plume centerline, and the ordinate contains the *normalized angular mass flux*,  $f(\phi)$ , which is defined as the local mass flux divided by the mass flux on the centerline at the same radial location. This normalisation is appropriate because it was not possible to obtain a direct calibration from the spectrometer reading to the mass flux. The crosses represent the mean plume shape (averaged over a range of flow rates and radial locations), and the vertical bars represent deviations from the mean, which include "real effects" caused by the variation in flow rate and location, in addition to experimental errors. From these results, it is concluded that the far-field plume shape does not vary significantly with either radial location or flow rate, for flow rates around the nominal.

Figure 4 shows how the mass flux on the plume centerline varies with distance from the nozzle. Included in the plots are the 'best' inverse-square fits to the data. (the curve-fits were optimized in the 'least-squares' sense). It is evident that the inverse-square model is an appropriate description. This is in accordance with the 'expanding bubble' (or 'source-flow') model whereby, for collisionless expansion at a constant velocity, the far-field axial density decay would follow an inverse-square profile (Simons, 1972).

Our experimental data is unique in that there is no other plume data for thrusters operating in such a rarefied regime. Typically, past measurements have been performed at much higher flow rates where the continuum model is

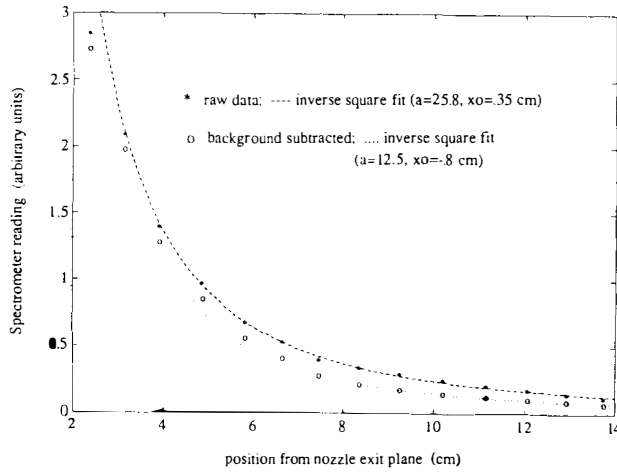


Fig. 4. Axial mass-flux profile

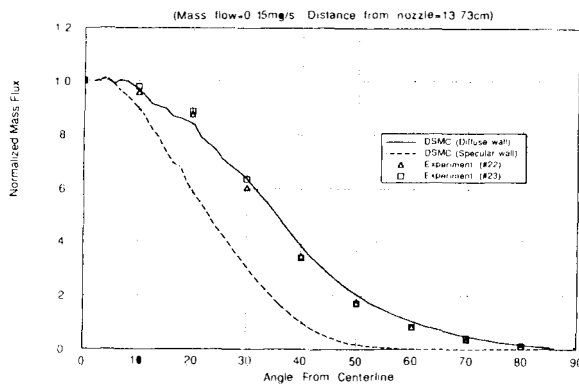


Fig. 5: Comparison between experiment and DSMC results.

valid (Dettleff, Boettcher, Dankert, Koppenwallner & Legge, 1986; Lengrand, 1984; Lengrand, Allégre & Raffin, 1982; Legge & Dettleff, 1986; Lengrand, Allégre & Raffin, 1976).

## DSMC COMPUTATIONS

In parallel with the experimental data, we performed some DSMC computations for identical flow rates and geometries used in the experiments. Figure 5 compares the plume shapes from experiment and from DSMC computations for a mass flow of 0.15 mg/sec ( $Kn=0.1$ ). The computations were performed for both diffuse and specular reflection between the gas particles and the nozzle walls (results for both cases are shown in the figure). In general, the computations for diffuse interaction matched the experimental data very well. This was observed for all flow rates around the nominal. This supports the current belief that medium energy helium interacts diffusely with metallic surfaces (Hurlbut, 1988).

Our computations are unique in terms of the high degree of rarefaction, and because they have been generated from stagnation all the way out to the far-field of the plume. By comparison, previous numerical work has tended to focus on higher density flows in the immediate vicinity of the nozzle lip (Campbell, 1989; Hueser, Melfi Jr., Bird & Brock, 1986; Nelson & Doo, 1988; Penko, Boyd, Meissner & DeWitt, 1991).

## COMPOSITE MODEL

To perform impingement calculations, we need to know local values of density, velocity, and temperature throughout the plume. These can be obtained by combining the measured plume shapes with the DSMC computations and with measurements of thrust and total mass flow.

### Density and velocity

Assuming that the velocity is essentially constant in the far-field plume (confirmed by our DSMC results) then the local density,  $\rho$ , is related to the corresponding value on the centerline,  $\rho'$ , according to

$$\rho = \rho' f(\phi) \quad (1)$$

where  $f(\phi)$  is the normalized angular mass flux obtained from the plume experiments. The mass flow,  $\dot{m}$ , and thrust force,  $F$ , due to particles crossing an arbitrary control surface are given by

$$\dot{m} = \int \rho (\mathbf{U} \cdot \mathbf{n}) dA \quad (2)$$

$$F = \int \rho (\mathbf{U} \cdot \mathbf{k})(\mathbf{U} \cdot \mathbf{n}) dA \quad (3)$$

where  $\mathbf{U}$  is the velocity vector,  $\mathbf{n}$  is the normal to the control surface, and  $\mathbf{k}$  is the direction in which we wish to evaluate the force. Assuming that the plume flow is *conical* (confirmed by experiments), then the mass flow and thrust can be evaluated over the control surface defined by a hemispherical shell of radius  $r$ , where  $r$  is the polar distance measured downstream from the nozzle exit. Whence,

$$\dot{m} = 2\pi r^2 u_r \rho' \int_0^{\pi/2} f(\phi) \sin \phi d\phi \quad (4)$$

$$F = 2\pi r^2 u_r^2 \rho' \int_0^{\pi/2} f(\phi) \sin \phi \cos \phi d\phi \quad (5)$$

where  $u_r$  is the (constant) radial speed ( $\mathbf{U} \cdot \mathbf{n} = u_r$ ). The force has been evaluated in the direction of the plume centerline ( $\mathbf{U} \cdot \mathbf{k} = u_r \cos \phi$ ). The specific impulse,  $I_{SP}$ , is obtained from the ratio of  $F$  and  $\dot{m}$ .

$$I_{SP} = \frac{F}{\dot{m} \times g} = \frac{u_r}{g} \times \frac{\int_0^{\pi/2} f(\phi) \sin \phi \cos \phi d\phi}{\int_0^{\pi/2} f(\phi) \sin \phi d\phi} \quad (6)$$

Rearranging gives

$$u_r = I_{SP} \times g \times \frac{\int_0^{\pi/2} f(\phi) \sin \phi d\phi}{\int_0^{\pi/2} f(\phi) \sin \phi \cos \phi d\phi} \quad (7)$$

which gives the radial velocity in terms of the  $I_{SP}$  and the plume shape. Performing the integrations for the nominal far-field plume obtained from the experiments yields

$$u_r \approx I_{SP} \times g \times 1.21 \quad (8)$$

Using our measured value for the  $I_{SP}$  ( $\approx 145 \pm 5\%$ ), Eq. 8 yields a speed of 1720 m/s for the nominal plume. Rearranging Eq. 4 gives

$$\rho' = \frac{\dot{m}}{2\pi r^2 u_r} \times \frac{1}{\int_0^{\pi/2} f(\phi) \sin \phi d\phi} \quad (9)$$

which, for the nominal far-field plume, becomes

$$\rho' \approx \frac{\dot{m}}{2\pi r^2 u_r} \times 5.0 \quad (10)$$

where the mass flow is given by

$$\dot{m} = \frac{F}{I_{SP} \times g} \quad (11)$$

Equations 1, 8, 10, and 11 can be solved to give the local velocity and density, at any plume location  $[\phi, r]$ , corresponding to a given thrust.

## Temperature

The temperature in the plume is related to the *distribution function* of the molecules in the plume. Legge (1988) demonstrates that an *ellipsoidal distribution function* is a reasonable approximation in the far-field plume beyond the freezing surface. The “freezing surface” is the boundary in the plume beyond which the flow is so rarefied that the streamlines remain straight. It coincides with the boundary where continuum theory breaks down. For the GP-B thruster plumes, the DSMC results reveal that the freezing surface is within a few millimeters from the nozzle, hence Legge’s ellipsoidal distribution function should be valid thereafter. This model consists of a *skewed Maxwellian distribution* in which the temperature in the direction parallel to the streamlines,  $T_{||}$ , is different from the temperature in directions perpendicular to the streamlines,  $T_{\perp}$ . The parallel temperature,  $T_{||}$ , is forever equal to the temperature at the freezing surface, and the perpendicular temperature decreases with distance from the freezing surface according to

$$T_{\perp} \approx T_{||} \cdot \left( \frac{r_f}{r} \right)^{1.5} \quad (12)$$

where  $r_f$  is the distance from the nozzle to the freezing surface. We can approximate  $T_{||}$  by the

temperature at the nozzle exit. Assuming that the effective Mach number at the exit is about 2.7 (Jafry, 1992) then the exit temperature – and hence  $T_{||}$  – is about 90 K. Introducing the *parallel speed ratio*,  $S_{||}$ , defined as

$$S_{||} = \frac{u_r}{\sqrt{2RT_{||}}} \quad (13)$$

then for  $T_{||}$  equal to 90 K and  $u_r$  equal to 1720 m/s, we have  $S_{||}$  approximately equal to 3. As Legge concludes, for parallel speed ratios in excess of 4, the impingement forces based on the ellipsoidal distribution are very close to those based on a conventional Maxwellian distribution with the temperature equal to  $T_{\perp}$ . Hence, for all intents and purposes, it is concluded that the gas in the far-field plume for the GP-B thruster can be described using a conventional Maxwellian distribution with a temperature which varies with distance from the nozzle, according to

$$T \approx 90 \cdot \left( \frac{r_f}{r} \right)^{1.5} \quad (14)$$

## IMPINGEMENT CALCULATIONS

Since the proposed GP-B and STEP space-craft will have many thrusters, impingement of thruster gas with solar panels is probably unavoidable.

Ideally, one would like to make direct experimental measurements of the impingement forces. Many investigators have performed such experiments with conventional thrusters (Lengrand, Allégre & Raffin, 1982; J. Allégre & Lengrand, 1986; Rogers, Allégre, Raffin & Lengrand, 1988). However, with the GP-B thrusters the impingement forces are too small to be accurately measured, so we must rely on modeling.

Typically, the distance between a thruster and a solar panel is about 1 m. At this distance, the mean-free-path of the plume gas ranges from 20 m to 2000 m over the range of thrust levels; so it is reasonable to model the impingement process as free-molecular, for which exact results exist.

The exact expressions for the normal pressure,  $P$ , and shear stress,  $P_t$ , acting on a surface element emersed in a Maxwellian gas under the assumptions of free molecular flow, are given by (Kogan, 1969)

$$\begin{aligned} P = & \frac{\rho_{\infty} V^2}{2S^2} \left[ \left( \frac{2 - \alpha_n}{\sqrt{\pi}} S_{\theta} + \frac{\alpha_n}{2} \sqrt{\frac{T_w}{T_{\infty}}} \right) e^{-S_{\theta}^2} \right. \\ & + \left( \left( S_{\theta}^2 + \frac{1}{2} \right) (2 - \alpha_n) + \frac{\alpha_n}{2} \sqrt{\pi \frac{T_w}{T_{\infty}}} S_{\theta} \right) \\ & \times (1 + \text{erf}(S_{\theta})) \left. \right] \end{aligned} \quad (15)$$

vestigate the consequences on the impingement forces.

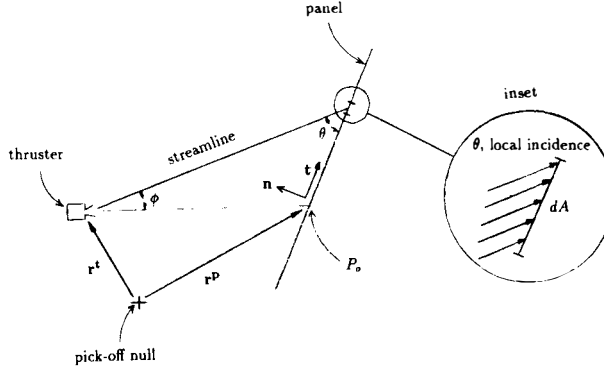


Fig. 6. Impingement schematic.

$$P_t = \alpha_t \frac{\rho_\infty V^2}{2\sqrt{\pi}} \frac{\cos \theta}{S} \chi(S_\theta) \quad (16)$$

where

$$S \triangleq V \sqrt{\frac{m}{2kT_\infty}} \quad (\text{speed ratio}) \quad (17)$$

$$S_\theta \triangleq S \sin \theta \quad (18)$$

$$\text{erf}(x) \triangleq \frac{2}{\sqrt{\pi}} \int_0^x e^{-s^2} ds \quad (19)$$

$$\chi(x) \triangleq e^{-x^2} + \sqrt{\pi} (1 + \text{erf}(x)) \quad (20)$$

and  $\theta$  is the incidence angle which is defined as the angle between the bulk velocity vector,  $\mathbf{V}$ , and the plate tangent (Fig. 6). The ' $\infty$ ' subscript refers to conditions in the plume, for which  $\rho$ ,  $V$ , and  $T$  can be determined from the plume model described above. For a surface element, the net normal force and shear force are obtained by multiplying  $P$  and  $P_t$ , respectively, by the elemental area  $dA$ . A complete body (solar panel) can be considered as comprising of a number of plate elements.

The symbols  $\alpha_n$  and  $\alpha_t$  are the normal and tangential momentum accommodation coefficients, defined here as

$$\alpha_n \triangleq \frac{P_{n_i} - P_{n_r}}{P_{n_i} - P_{n_w}} \quad (21)$$

$$\alpha_t \triangleq \frac{P_{t_i} - P_{t_r}}{P_{t_i}} \quad (22)$$

where  $P_{n_i}$  and  $P_{n_r}$  are the components of momentum, *normal* to the surface, of the incident and reflected particles, respectively;  $P_{t_i}$  and  $P_{t_r}$  are the components of momentum, *tangential* to the surface, of the incident and reflected particles, respectively;  $P_{n_w}$  is the normal momentum of the reflected molecules which have reached thermal equilibrium with the surface at temperature  $T_w$ . By varying the values of the accommodation coefficients and the surface temperature, we can in-

## Results

For a typical thruster impinging on a typical solar panel, computations at nominal values of  $T_w = 300$  K,  $\alpha_n = 0.6$ , and  $\alpha_t = 1$ , reveal that the net thrust may be reduced in magnitude by 13% and shifted in orientation by 5 degrees; the net moment about the spacecraft mass center may be altered by 6%, and a couple with a magnitude of 7% of the total moment is introduced about the line-of-action of the net force (a feature that is not physically possible for a thruster acting alone).

These impingement effects can vary by  $\pm 22\%$  as the accommodation coefficients are varied from 0 to 1 for  $\alpha_n$  (specular to diffuse), and 0 to 1.2 for  $\alpha_t$  (the value in excess of unity suggests diffuse reflection with significant "backscattering" (Liu, Sharma & Knuth, 1979)). These variations are relatively large, and could severely diminish the quality of the aeronomy data. However, it is reasonable to expect that after the spacecraft has adapted to the orbital environment (i.e., when the initial outgassing and contamination processes are complete), then any changes in the surface properties would be much less extreme.

Having accounted for gross changes in surface properties, then the next largest source of variations in impingement forces will be due to spacecraft temperature fluctuations. Computations reveal that for temperature variations of  $\pm 100$  K about the nominal (taken to be 300 K), the impingement forces will vary by 3%; and for extreme temperature swings of  $\pm 200$  K, the corresponding variations in impingement forces will be about 9%.

The above results are, however, conservative since they are based on a chosen thruster/panel pair for which there is a relatively high degree of impingement. Not all thruster/panel combinations will interact to the same degree. Prudent design will strive to minimize such interactions.

## CONCLUSIONS

Experiments have been performed to determine the shape of the plumes emanating from the GP-B and STEP thrusters. The experimental data is supported by DSMC numerical computations; and together, the data sets provide the basis for a complete plume model. These results are unique because they pertain to nozzle flow regimes well below the continuum limit.

Assuming that the surface properties do not undergo large changes after initial adaptation to

the orbital environment, then the largest variations in thrust due to impingement will be associated with surface temperature fluctuations, and will be limited to about 3%.

## References

- Bird, G. A. (1980). Breakdown of continuum flow in freejets and rocket plumes. In *Progress in Astronautics and Aeronautics*, AIAA. 12th International Symposium on Rarefied Gas Dynamics, Charlottesville, Virginia.
- Campbell, D. H. (1989). Nozzle-lip effects on argon expansions into the plume backflow. *Journal of Spacecraft and Rockets*, 26(4), 285–292.
- Dettleff, G., Boettcher, R. D., Dankert, C., Koppenwallner, G., & Legge, H. (1986). Attitude control thruster plume flow modeling and experiments. *Journal of Spacecraft and Rockets*, 23(5).
- Hueser, J. E., Melfi Jr., L. T., Bird, G. A., & Brock, F. J. (1986). Rocket Nozzle Lip Flow by Direct Simulation Monte Carlo Method. *Journal of Spacecraft and Rockets*, 23(4), 363–367.
- Hurlbut, F. C. (1988). Particle surface interaction in the orbital context: A survey. In *Progress in Astronautics and Aeronautics – Rarefied Gas Dynamics: Space-Related Studies*, Pasadena, California. 16th International Symposium on Rarefied Gas Dynamics, AIAA.
- J. Allégre, M. R. & Lengrand, J. C. (1986). Experimental study of the plume impingement problem associated with rocket stage separation. *Journal of Spacecraft and Rockets*, 23(4), 368–372.
- Jafry, Y. R. (1992). *Aeronomy coexperiments on drag-free satellites with proportional thrusters: GP-B and STEP*. PhD thesis, Stanford University, Stanford, California.
- Jafry, Y. R. & Vanden Beukel, J. (1992). Ultralow density plume measurements using a helium mass spectrometer. *Journal of Vacuum Science and Technology*. Accepted for publication.
- Kogan, M. N. (1969). *Rarefied Gas Dynamics*. New York: Plenum Press.
- Legge, H. (1988). Modeling free molecular plume flow and impingement by an ellipsoidal distribution function. In *Progress in Astronautics and Aeronautics – Rarefied Gas Dynamics: Space-Related Studies*, AIAA. 16th International Symposium on Rarefied Gas Dynamics, Pasadena, California.
- Legge, H. & Dettleff, G. (1986). Pitot pressure and heat-transfer measurements in hydrazine thruster plumes. *Journal of Spacecraft and Rockets*, 23(4), 357–362.
- Lengrand, J. C. (1984). Plume impingement upon spacecraft surfaces. 14th International Symposium on Rarefied Gas Dynamics, Tsukuba Science City, Japan.
- Lengrand, J. C., Allégre, J., & Raffin, M. (1976). Experimental investigation of underexpanded exhaust plumes. *AIAA Journal*, 14(5), 692–694.
- Lengrand, J. C., Allégre, J., & Raffin, M. (1982). Underexpanded free jets and their interaction with adjacent surfaces. *AIAA Journal*, 20(1), 27–28.
- Liu, S. M., Sharma, P. K., & Knuth, E. L. (1979). Satellite drag coefficients calculated from measured distributions of reflected helium atoms. *AIAA Journal*, 17(12), 1314–1319.
- Nelson, D. A. & Doo, Y. C. (1988). Simulation of multicomponent nozzle flows into a vacuum. In *Progress in Astronautics and Aeronautics – Rarefied Gas Dynamics: Space-Related Studies*, AIAA. 16th International Symposium on Rarefied Gas Dynamics, Pasadena, California.
- Penko, P. F., Boyd, I. D., Meissner, D. L., & DeWitt, K. J. (1991). Pressure measurements in a low-density nozzle plume for code verification. AIAA. 27th Joint Propulsion Conference.
- Rogers, A. W., Allégre, J., Raffin, M., & Lengrand, J. C. (1988). Thruster plume impingement forces measured in a vacuum chamber and conversion to real flight conditions. In *Progress in Astronautics and Aeronautics – Rarefied Gas Dynamics: Space-Related Studies*, AIAA. 16th International Symposium on Rarefied Gas Dynamics, Pasadena, California.
- Simons, G. A. (1972). Effect of nozzle boundary layers on rocket exhaust plumes. *AIAA Journal*, 10(11).
- Wiktor, P., Jafry, Y. R., & DeBra, D. B. (1992). On orbit thruster calibration with applications to Gravity Probe B. Accepted for presentation at the 12th IFAC Symposium on Automatic Control in Aerospace, Ottobrunn, Germany.

# ON ORBIT THRUSTER CALIBRATION WITH APPLICATIONS TO GRAVITY PROBE B

P. Wiktor, Y. Jafry and D. DeBra

*Hansen Laboratories, GP-B, Stanford University, Stanford, CA 94305-4085, USA*

**Abstract:** A general procedure to determine accurately the true relationship between the commanded and the actual force output of a set of thrusters is presented. This relationship is determined from data generated from a spacecraft while it is on orbit. On orbit thruster calibration measures the true outputs of the thrusters in the actual space environment in which they operate. The feasibility of the calibration technique is verified by a digital simulation of the Gravity Probe B (GP-B) spacecraft dynamics. GP-B is an Earth orbiting experiment which will test several aspects of general relativity. A set of 18 proportional thrusters generates forces and moments for three degree of freedom attitude and three degree of freedom drag free translation control of the GP-B spacecraft. A total of 108 parameters are needed to characterize the magnitude and direction of both the force and moment outputs of the 18 thrusters. The ability to calibrate these parameters to an accuracy of better than 1% is demonstrated.

**Keywords:** recursive least squares, system identification, satellite control, force control, estimation, actuators, propulsion, thrusters.

## 1 Introduction

Large control coupling forces can result if a spacecraft's thrusters are not calibrated properly. Let's say a pure translation force is commanded with an improperly calibrated thruster system. If there is a scale factor mismatch between the thrusters then a torque could be inadvertently produced in addition to the translation force. For Gravity Probe B (GP-B) [7, 9] with a scale factor mismatch of only 10% this may be the largest torque disturbance on the spacecraft [6].

Accurate thruster calibration is necessary for an Aeronomy co-experiment on GP-B as well. Variations in drag of the upper atmosphere will be determined by monitoring the commands to the thrusters. The accuracy of the drag measurement is directly related to how well the thrusters can be calibrated [3].

It is difficult to accurately calibrate the thrusters on the ground prior to flight. Ground calibration is limited by: the low vacuum pressure ( $< 10^{-4}$  torr) required [1, 2]; the low force levels ( $< 1 \text{ mN}$  peak) which have to be measured for GP-B [1, 2, 5]; uncertainty in the direction of thrust output [5]; uncertainty in the on orbit thruster operating temperature and pressure and finally, uncertainty

in the exact effect of plume impingement on the thruster output [3].

This paper describes a general technique for on orbit thruster calibration. This technique is verified using a detailed six degree of freedom nonlinear simulation of the spacecraft dynamics [3]. The simulation incorporates closed loop attitude and translation control systems and a mass trim system. The principal purpose of the mass trim system is to reduce disturbances on the spacecraft caused by mass imbalances [10]. It is used here to generate the reference forces for thruster calibration. The impact that thruster calibration has on spacecraft operations is discussed in the final section.

## 2 Calibration Technique

### 2.1 Problem Definition

The resulting force,  $\mathbf{F}_c$ , on the spacecraft due to a set of thruster commands,  $\mathbf{T}_c$ , is,

$$\mathbf{F}_c = A\mathbf{T}_c. \quad (1)$$

In general  $\mathbf{F}_c$  is a  $6 \times 1$  vector composed of three components of force and three components of moment. The  $n \times 1$  vector,  $\mathbf{T}_c$ , consists of the

thrust commands to the  $n$  thrusters. The  $6 \times n$  thruster configuration matrix,  $A$ , contains information on the output direction and magnitude of each thruster. The first three elements of the  $i^{\text{th}}$  column of  $A$  give the magnitude and direction of the  $i^{\text{th}}$  thruster's force output. Similarly the last three elements give the magnitude and direction of the moment output. The goal of thruster calibration is to identify the  $6 \times n$  coefficients of  $A$ .

In the next subsection we define how much data is needed to calibrate the thrusters even under the ideal conditions of no measurement noise and no external disturbances. A general technique is developed in the subsequent subsection to calibrate the thrusters in spite of real world sensor noises and force disturbances.

## 2.2 Calibration Technique, No Noise

To calibrate the thrusters a set of experiments,  $k = 1, \dots, m$ , is performed. In each experiment a calibration force,  $\mathbf{F}_c(k)$ , is exerted on the spacecraft and the closed loop spacecraft attitude and translation control systems issue a set of thruster commands,  $\mathbf{T}_c(k)$ , to compensate this disturbance. If the controller is working perfectly and there are no other disturbances on the spacecraft then the thrusters exactly compensate the calibration force,

$$\mathbf{F}_c(k) = A\mathbf{T}_c(k). \quad (2)$$

By performing  $m$  experiments with  $m$  different calibration forces, the following matrix relationship can be formed:

$$[\mathbf{F}_c(1) \dots \mathbf{F}_c(m)] = A[\mathbf{T}_c(1) \dots \mathbf{T}_c(m)]. \quad (3)$$

To calibrate the thrusters we solve (3) for  $A$ . The matrix,  $[\mathbf{T}_c(1) \dots \mathbf{T}_c(m)]$ , must be square and full rank for  $A$  to exist and be unique in (3). In this case  $A$  is given by,

$$A = [\mathbf{F}_c(1) \dots \mathbf{F}_c(m)][\mathbf{T}_c(1) \dots \mathbf{T}_c(m)]^{-1}. \quad (4)$$

We now state a fundamental requirement which must be satisfied in order to calibrate the thrusters:

**Requirement 2.1** *In order to calibrate the thrusters, the thrust command vectors,  $\mathbf{T}_c(k)$ , must span both the row space and nullspace of the thruster configuration matrix,  $A$ .*

This is easy to see. The matrix,  $A$ , has  $n$  columns. If  $r_A$  is the rank of  $A$ ,  $\text{rank}(A) = r_A$ , then the dimension of the row space is  $r_A$  and the dimension of the null space is  $n - r_A$ . The row space and null space of a matrix are orthogonal complements of each other [8]. As stated above, for  $A$  to exist and be unique the matrix,  $[\mathbf{T}_c(1) \dots \mathbf{T}_c(m)]$ , must be square,  $m = n$ , and full rank,  $\text{rank}([\mathbf{T}_c(1) \dots \mathbf{T}_c(m)]) = n$ . In other words the vectors,  $\mathbf{T}_c(k)$ ,  $k = 1, \dots, n$ , must span

the entire  $n$  dimensional input space of  $A$ . This means that they must span both the  $r_A$  dimensional row space as well as the  $n - r_A$  dimensional null space of  $A$ .

The significance of Requirement 2.1 is that it explicitly defines the set of calibration forces,  $\mathbf{F}_c(k)$ , and thruster commands,  $\mathbf{T}_c(k)$ , required to calibrate the thrusters. Let's say that the pseudoinverse,  $A^\dagger$ , of  $A$  is used for control [11],

$$\mathbf{T}_c(k) = A^\dagger \mathbf{F}_c(k). \quad (5)$$

The resulting thruster commands,  $\mathbf{T}_c(k)$ , are exclusively in the row space of  $A$  [8]. From this fact and Requirement 2.1 the following two important conclusions follow:

1. *The calibration forces,  $\mathbf{F}_c(k)$ , must span the entire column space of the thruster configuration matrix,  $A$ .* In physical terms this means that in order to calibrate the thrusters, calibration forces must be generated in all possible output directions of the thruster system. For GP-B this means that independent calibration moments must be generated about the yaw, pitch and roll axes and translation forces must also be generated along three mutually perpendicular axes. To see this consider what happens if the calibration forces do not span the entire column space of  $A$ . In this case there exists a calibration force,  $\mathbf{F}_c(3)$ , which is a linear combination of two other calibration forces,

$$\mathbf{F}_c(3) = \alpha_1 \mathbf{F}_c(1) + \alpha_2 \mathbf{F}_c(2). \quad (6)$$

Premultiplying (6) by  $A^\dagger$  and using (5),

$$\mathbf{T}_c(3) = \alpha_1 \mathbf{T}_c(1) + \alpha_2 \mathbf{T}_c(2), \quad (7)$$

we see that the thrust command vector,  $\mathbf{T}_c(3)$ , is also a linear combination of two other thrust command vectors,  $\mathbf{T}_c(1)$  and  $\mathbf{T}_c(2)$ . The matrix,  $[\mathbf{T}_c(1) \dots \mathbf{T}_c(m)]$ , formed from these vectors therefore is not full rank and can not be inverted to solve for  $A$  in (4).

2. *Thruster commands,  $\mathbf{T}_n(k)$ , in the null space of  $A$  are required to calibrate the thrusters.* The pseudoinverse (5) does not generate any null space components,  $\mathbf{T}_n(k)$  [8]. Therefore to satisfy Requirement 2.1, these null space components must be added to the thruster control (5),

$$\mathbf{T}_c(k) = A^\dagger \mathbf{F}_c(k) + \mathbf{T}_n(k). \quad (8)$$

In physical terms, generating null space commands is equivalent to calibrating the thrusters against each other. Even though the null space commands do not produce an external output force, they push and pull against each other and useful information for thruster calibration is obtained. Theoretically there is

no limit to the number of thrusters which can be calibrated using this scheme. The null space components for thruster calibration are completely compatible with the need to dump helium gas for temperature control [10].

### 2.3 Calibration Technique, With Noise

The following assumptions were made in the last subsection:

- The calibration force,  $\mathbf{F}_c(k)$  is known exactly.
- The calibration force is the only force exerted on the spacecraft.
- The closed loop attitude and translation control systems command the thrusters to perfectly cancel the calibration force.
- The thruster coefficients do not change with time. In other words,  $A$  is constant.
- There are no thruster biases or unmodeled mass properties offsets.

Naturally none of these assumptions are valid in the real world. A more realistic model is developed in this section. This model is used to develop a calibration technique which can calibrate the thrusters in spite of sensor noise, disturbance forces, unmodeled mass properties offsets and thruster biases.

To account for errors we recast (3) as a state estimation problem with the measurement equation,

$$\mathbf{F}_c(k) = T_c(k)\mathbf{a}_w(k) + \mathbf{v}_m(k) + \mathbf{b}. \quad (9)$$

The coefficients in the matrix,  $A$ , are now ‘strung out’ into the vector  $\mathbf{a}_w(k)$  and the thrust command vector,  $\mathbf{T}_c(k)$  is formed into the matrix  $T_c(k)$  [10]. The measurement noise,  $\mathbf{v}_m(k)$ , accounts for external disturbances on the spacecraft as well as errors in measuring the calibration force,  $\mathbf{F}_c(k)$ . The vector,  $\mathbf{b}$ , accounts for steady state disturbances on the spacecraft due to thruster biases and mass properties offsets. The vectors,  $\mathbf{a}_w(k)$ , in (9) are time varying thruster coefficients. These are modeled as a mean value,  $\mathbf{a}$ , plus zero mean white process noise,  $\mathbf{w}(k)$ :

$$\mathbf{a}_w(k) = \mathbf{a} + \mathbf{w}(k). \quad (10)$$

Substituting (10) into (9) results in the following measurement equation:

$$\mathbf{F}_c(k) = T_c(k)\mathbf{a} + \mathbf{v}(k). \quad (11)$$

The measurement noise,  $\mathbf{v}(k)$ ,

$$\mathbf{v}(k) \stackrel{\text{def}}{=} T_c(k)\mathbf{w}(k) + \mathbf{v}_m(k) + \mathbf{b}, \quad (12)$$

now accounts for variations in the thruster coefficients,  $\mathbf{w}(k)$ , as well as the original measurement noise,  $\mathbf{v}_m(k)$ . The covariance of  $\mathbf{v}(k)$  is

$$V(k) \stackrel{\text{def}}{=} E\{[\mathbf{v}(k) - \mathbf{b}][\mathbf{v}'(k) - \mathbf{b}]'\} \quad (13)$$

$$= T_c(k)W(k)T_c'(k) + V_m(k) \quad (14)$$

where  $W(k)$  is the covariance of  $\mathbf{w}(k)$  and  $V_m(k)$  is the covariance of  $\mathbf{v}_m(k)$ .

The goal of thruster calibration is to estimate the mean value,  $\mathbf{a}$ , of the true thruster coefficients,  $\mathbf{a}_w(k)$ . Since the mean values do not change with time they can be modeled by the state equation,

$$\mathbf{a} \stackrel{\text{def}}{=} \mathbf{a}(k+1) = \mathbf{a}(k). \quad (15)$$

The thruster calibration problem can now be stated as follows: given the state equation (15) together with the measurement equation (11) estimate the mean values of the thruster coefficients,  $\mathbf{a}$ . The solution is the Kalman filter which in this case reduces to weighted recursive least squares due to the time invariant state equation, (15). From the Kalman filter the state estimate,  $\hat{\mathbf{a}}$ , is given by,

$$\hat{\mathbf{a}}(k+1) = \hat{\mathbf{a}}(k) + K(k)[\mathbf{F}_c(k) - T_c(k)\hat{\mathbf{a}}(k)], \quad (16)$$

where the Kalman gain,  $K(k)$ , is

$$K(k) = M(k)T_c(k)[V(k) + T_c(k)M(k)T_c'(k)]^{-1}, \quad (17)$$

and the estimation error covariance matrix,  $M(k)$ , is

$$M(k+1) = M(k) - K(k)T_c(k)M(k). \quad (18)$$

The rate of convergence of the Kalman filter depends on the proper choice of the process and measurement noise covariance matrices,  $W(k)$  and  $V(k)$ . For optimal convergence, the values of  $W(k)$  and  $V(k)$  used in the filter should match the actual covariances of these noises. For a discussion on how to choose  $W(k)$  and  $V(k)$  properly see [10].

### 2.4 Generating Calibration Forces

There are many ways of generating calibration forces on the spacecraft. In this subsection we discuss the calibration forces which can be generated by a mass trim system. Centrifugal forces can be generated by offsetting the mass properties of a rolling drag free spacecraft like GP-B. These ‘static experiments’ can only generate calibration forces in four directions, the two translation directions normal to the spacecraft roll axis and moments about pitch and yaw. To satisfy Requirement 2.1 so that the thrusters can be calibrated, translation forces along the roll axis and roll moments must also be generated. These are generated by sinusoidal ‘dither experiments’ along and around the roll axis.

### 2.4.1 Static Experiments

The GP-B spacecraft rolls slowly (1 revolution/10 minutes) about its longitudinal axis. A drag free [4] translation control system commands the thrusters to force the roll axis to pass through the pick-off null of the translation control proof mass. If the center of mass of the spacecraft does not fall on the roll axis, then the thrusters must generate a body fixed control force to take out the centrifugal force caused by the mass imbalance. Similarly an attitude control system commands the thrusters to keep the direction of the roll axis inertially fixed. If the roll axis does not coincide with a principal axis of inertia of the spacecraft then the thrusters must generate a constant pitch or yaw torque to compensate the resulting moment. A mass trim system can be used to offset the center of mass and a principal axis of inertia of the spacecraft; the thrusters can therefore be calibrated against the resulting known forces and moments. We wish to generate calibration forces,  $\mathbf{F}_c$ , using known offsets of the mass trim system to generate data for the measurement equation (11),  $\mathbf{F}_c = T_c \mathbf{a} + \mathbf{v}(k)$ . The next subsection describes mass center offsets and the subsequent subsection deals with offsets of a principal axis of inertia.

**Center of Mass Offsets** The centrifugal force,  $-(m_D \mathbf{p}^{d/v} + m_R \mathbf{p}^{r/v})\omega_3^2$ , due to offsets of the centers of mass of the main body of the spacecraft,  $\mathbf{p}^{d/v}$ , and mass trim system,  $\mathbf{p}^{r/v}$ , relative to the pick-off null of the translation control system are offset by the thruster force,  $T_c \mathbf{a}$ , plus unmodeled disturbances,  $\mathbf{v}$ :

$$-(m_D \mathbf{p}^{d/v} + m_R \mathbf{p}^{r/v})\omega_3^2 = T_c \mathbf{a} + \mathbf{v}, \quad (19)$$

where  $\omega_3$  is the roll rate of the spacecraft [Table 1].

The mass,  $m_D$ , and the location of the center of mass,  $\mathbf{p}^{d/v}$ , of the main body of the spacecraft are not likely to be known very accurately. To get rid of the dependence on these terms we define the calibration force,  $\mathbf{F}_c(k)$ , as the difference between the centrifugal force corresponding to two different mass trim positions,

$$\begin{aligned} \mathbf{F}_c(k) &\stackrel{\text{def}}{=} -m_R[\mathbf{p}^{r/v}(k+1) - \mathbf{p}^{r/v}(k)]\omega_3^2 \\ &= [T_c(k+1) - T_c(k)]\mathbf{a} + [\mathbf{v}(k+1) - \mathbf{v}(k)]. \end{aligned} \quad (20)$$

The dependence on  $m_D \mathbf{p}^{d/v}$  drops out since this term remains unchanged from time  $k$  to  $k+1$ .

Equation (20) is in the form of our measurement equation, (11), however the ‘measurement noise’,  $[\mathbf{v}(k+1) - \mathbf{v}(k)]$ , can be quite large due to the time varying external disturbances on the spacecraft. Since the *average* external disturbance in body axes is small we minimize the measurement noise by offsetting the mass trim system for at least one orbit period and using the *average* thruster commands for that period in the measurement equation, (20).

**Principal Axes of Inertia Offsets** We use the same technique of taking the difference between successive averaged measurements to calibrate the thrusters against principal axes offsets as we used for center of mass offsets. The only difference is that the calibration forces,  $\mathbf{F}_c(k)$ , are yaw and pitch moments induced by changing the orientation of a principal axis of inertia of the spacecraft.

The calibration forces for a principal axis of inertia offset are,

$$\mathbf{F}_c(k) = \begin{bmatrix} -{}^s I_{32}^{R/r}(k+1) + {}^s I_{32}^{R/r}(k) \\ {}^s I_{31}^{R/r}(k+1) - {}^s I_{31}^{R/r}(k) \\ 0 \end{bmatrix} \omega_3^2, \quad (21)$$

where  ${}^s I_{32}^{R/r}$  and  ${}^s I_{31}^{R/r}$  are two cross products of inertia of the mass trim system relative to the spacecraft. For small angular displacements,  $\theta_1$  and  $\theta_2$ , of the mass trim system, these terms can be approximated in terms of the principal axes of inertia,  ${}^r I_{11}^{R/r}$  and  ${}^r I_{33}^{R/r}$ , of the mass trim system [10]:

$$\begin{aligned} {}^s I_{32}^{R/r} &\approx \theta_1({}^r I_{11}^{R/r} - {}^r I_{33}^{R/r}) \\ {}^s I_{31}^{R/r} &\approx \theta_2(-{}^r I_{11}^{R/r} + {}^r I_{33}^{R/r}) \end{aligned} \quad (22)$$

### 2.4.2 Dithering Experiments

For small displacements of the mass trim system the acceleration of the spacecraft,  $\ddot{\mathbf{p}}^{d/n}$ , relative to inertial space times the mass of the spacecraft,  $m_D + m_R$ , equals the force applied to the spacecraft by the thrusters,  $T_c \mathbf{a}$ , the mass trim system,  $-m_R \ddot{\mathbf{p}}^{r/d}$  and external disturbances,  $\mathbf{v}$ :

$$(m_D + m_R)\ddot{\mathbf{p}}^{d/n} = T_c \mathbf{a} - m_R \ddot{\mathbf{p}}^{r/d} + \mathbf{v}, \quad (23)$$

where  $\ddot{\mathbf{p}}^{r/d}$  is the acceleration of the mass trim system relative to the main body of the spacecraft and  $\mathbf{v}$  incorporates unmodeled disturbances. In (23)  $m_D$  and  $m_R$  are the mass of the main body of the spacecraft and the mass trim system respectively. By rearranging terms, (23) can be written in our standard measurement equation form, (11), with the calibration force,

$$\mathbf{F}_c \stackrel{\text{def}}{=} (m_D + m_R)\ddot{\mathbf{p}}^{d/n} + m_R \ddot{\mathbf{p}}^{r/d}. \quad (24)$$

Given a sinusoidal dither of the mass trim system at a frequency of  $\omega_d$ , the amplitude of the accelerations,  $|\ddot{\mathbf{p}}^{d/n}|$  and  $|\ddot{\mathbf{p}}^{r/d}|$ , can be determined from the position amplitudes,  $|\mathbf{p}^{d/n}|$  and  $|\mathbf{p}^{r/d}|$ :

$$|\mathbf{F}_c| = \{(m_D + m_R)|\mathbf{p}^{d/n}| + m_R|\mathbf{p}^{r/d}|\}\omega_d^2. \quad (25)$$

To calculate accurately the amplitude of the calibration force,  $|\mathbf{F}_c|$ , in (25) we need to ‘pick out’ the amplitudes of the spacecraft and mass trim motions,  $|\mathbf{p}^{d/n}|$  and  $|\mathbf{p}^{r/d}|$ , at the dither frequency,  $\omega_d$ , from data which is corrupted by sensor noise and external disturbances. We use synchronous demodulation to zoom in on the amplitudes specifically at

dither frequency. Synchronous demodulation and its subsequent low pass filtering is equivalent to the discrete Fourier transform,  $\mathbf{z}(w_d)$ , of a time domain signal,  $\mathbf{z}(qT_s)$ , at a specific frequency,  $w_d$ , and bandwidth,

$$\mathbf{z}(w_d) \stackrel{\text{def}}{=} \frac{1}{n} \sum_{q=1}^n \mathbf{z}(qT_s) e^{-(i\omega_d qT_s)}. \quad (26)$$

The variable,  $T_s$ , in (26) is the sample frequency and  $n$  is the number of samples of the signal,  $\mathbf{z}(qT_s)$ .

The dither frequency,  $\omega_d$ , must be chosen carefully to minimize measurement noise. It should be well below the translation and attitude control system bandwidths [Table 1] so that these control systems have enough time to compensate the disturbances caused by the mass trim system. The dither frequency must not coincide with any other disturbance frequency or structural mode and it must be high enough to produce a large enough calibration signal. Taking these considerations into account we chose the mass trim translation and roll dither frequencies listed in Table 1.

### 3 Simulation Verification

We verified the calibration technique using two separate computer programs. The dynamics of the spacecraft were simulated using a Fortran program [3] and the thrusters were then calibrated in Matlab [10].

#### 3.1 Simulation Results

We calibrated the *cart\_cg* [10] configuration of 18 non-opposing thrusters with the locations of the thrusters not known exactly. The force and moment output of each thruster (6 coefficients per thruster) were calibrated for a total of  $6 \times 18 = 108$  thruster coefficients. The parameters used for simulation are summarized in Table 1.

The simulation program was run both with and without aerodynamic drag.

**Without Drag:** After 96 experiments the estimated thruster coefficients converged to their true values with an error of 0.27% RMS. The RMS calibration error is defined as  $(\text{RMS})_{\text{error}} \stackrel{\text{def}}{=} \sqrt{\frac{1}{n} \sum_{i=1}^n (\hat{a}_i - a_i)^2}$ , where  $n$  is the number of thruster coefficients,  $a_i$  are the true thruster coefficients and  $\hat{a}_i$  are the estimates of those coefficients.

**With Drag:** We only obtained enough data for 48 experiments with aerodynamic drag. With a peak drag level of 0.1 mN, the calibration converged with an error of 1.05%. The convergence rates with and without drag are almost identical however. This means that with 96 experiments the

parameter	value
spacecraft mass	$m_D = 2000 \text{ kg}$
spacecraft inertia	$I^{D/d} = \text{diag}(1077, 1077, 1185) \text{ kg} \cdot \text{m}^2$
mass trim mass	$m_R = 50 \text{ kg}$
mass trim inertia	$I^{R/r} = \text{diag}(39, 39, 78) \text{ kg} \cdot \text{m}^2$
s/c roll freq.	$\omega_3 = 2\pi/600 \text{ rad/sec}$
s/c orbit freq.	$\omega_o = 2\pi/(97.7 \times 60) \text{ rad/sec}$
m/t trans. freq.	$\omega_d = 10\omega_3 \text{ rad/sec}$
m/t roll freq.	$\omega_d = 2.5\omega_3 \text{ rad/sec}$
trans. control b/w	0.5 rad/sec
roll control b/w	0.06 rad/sec
attitude b/w	3. rad/sec
sample time	$T_s = 1 \text{ sec}$
peak aero. drag	0.1 mN

Table 1: Thruster calibration simulation parameters. Abbreviations: m/t  $\Rightarrow$  mass trim, s/c  $\Rightarrow$  spacecraft, b/w  $\Rightarrow$  bandwidth.

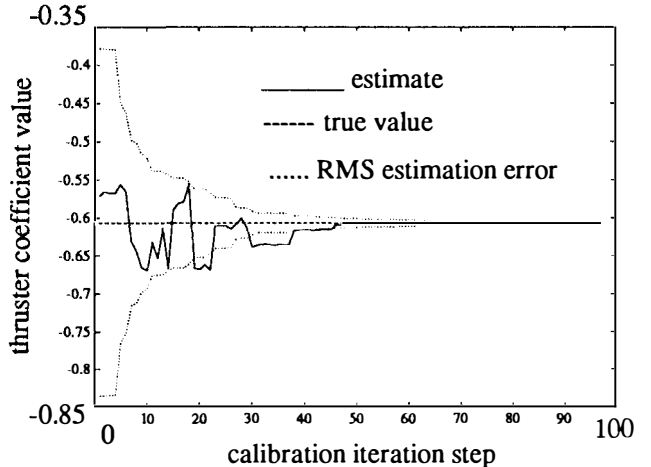


Figure 1: Calibration convergence of a typical thruster coefficient.

calibration with drag would converge to roughly the same accuracy as the no drag calibration (0.27%).

Figure 2 is a 3-D plot of the thruster coefficient estimation errors,  $\hat{a}_i - a_i$ , ( $i = 1, \dots, 108$ ), for all 108 thruster coefficients. This plot serves as a visual confirmation that the calibration algorithms do in fact converge on 108 individual thruster coefficients.

### 4 Practical Considerations

On orbit thruster calibration will influence spacecraft design, operations, telemetry, attitude control, translation control, temperature control, thruster control and on orbit processing requirements. Here is a list of some of the implications of on orbit thruster calibration:

**Time** It takes at least five full days to gather enough data (96 experiments) to calibrate 18 thrusters (108 coefficients) to an accuracy of better than 1%. For each static experiment, the mass

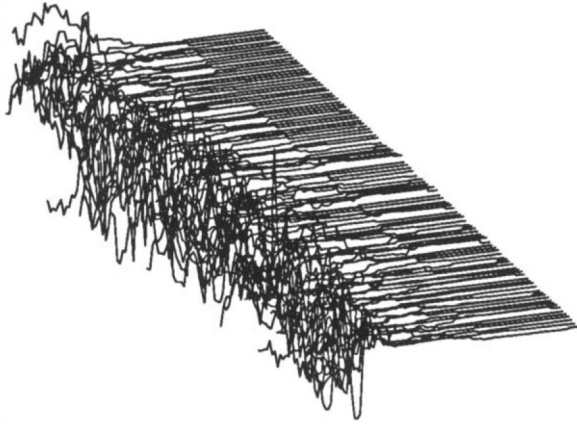


Figure 2: 3-D plot of thruster coefficient estimation errors, for all 108 coefficients.

trim system must be moved and then the thruster commands must be averaged for at least ten spacecraft roll periods which is approximately one orbit period. At least ten periods are required for each dither experiment. This takes 10 minutes for translation dither along the roll axis and 42 minutes for rotational dither around the roll axis.

**Data** It takes at least 17.3 megabytes of data to calibrate 108 thruster coefficients to an accuracy of better than 1%. The data is sampled every second to avoid aliasing the control signals caused by the response of the spacecraft to atmospheric density variations which, according to D.B. DeBra, are expected to have a magnitude of 10% of the nominal drag level at a frequency of 0.1 Hz. By doing some on orbit data processing, the amount of data which has to be sent down to the ground via telemetry reduces to 6.2 kilobytes. The on orbit processing involves time averaging for static experiments and synchronous demodulation for dither experiments.

## 5 Conclusion

The feasibility of calibrating the GP-B thrusters on orbit has been verified using a digital computer simulation of the spacecraft dynamics. The ratio of output force and moment (6 coefficients) to the commanded output was determined to an accuracy of better than 1% RMS for 18 individual thrusters (108 coefficients total). A Kalman filter based calibration technique has been developed which does not depend on any specific way of generating calibration reference forces. The estimates of the thruster coefficients generated by the Kalman filter converge to the true values in spite of zero mean disturbances, sensor noises and steady state biases. At least five full days and 17.3 megabytes of data are required to calibrate 18 thrusters to better than 1% accuracy. The effect of thruster calibration on GP-B science gyro drift is negligible so thruster calibration could be done at any time

during the GP-B science mission; however it is appropriate to do the calibration early on in the mission for the aeronomy co-experiment and for proper evaluation of the attitude and translation control systems.

## References

- [1] J.S. Bull. Precise attitude control of the Stanford relativity satellite. *Stanford University Ph.D. Thesis*, SUDAAR 452, 1973.
- [2] J-H Chen. Helium thruster propulsion system for precise attitude control and drag compensation of the Gravity Probe B satellite. *Stanford University Ph.D. Thesis*, SUDAAR 538, 1983.
- [3] Y.R. Jafry. Aeronomy coexperiments on drag-free satellites with proportional thrusters: GP-B and STEP. *Stanford University Ph.D. Thesis*, 1992.
- [4] B.O. Lange. Control and use of a drag-free satellite. *Stanford University Ph.D. Thesis*, SUDAAR 194, June 1964.
- [5] K-N Lee. The design of a wide dynamic range helium thuster for Gravity Probe B. *Stanford University Ph.D. Thesis*, 1992.
- [6] B.W. Parkinson and Kasdin J.N. Twenty milliarcsec pointing system for the rolling GP-B spacecraft. *11<sup>th</sup> Annual AAS Guidance and Control Conference*, February 1988.
- [7] L.I. Schiff. Motion of a gyroscope according to Einstein's theory of gravitation. *Proceedings of the National Academy of Sciences*, 46(871), 1960.
- [8] G. Strang. *Linear Algebra and its Applications*. Harcourt Brace Jovanovich, Inc., 1989.
- [9] J.P. Turneaure, C.W.F. Everitt, and B.W. Parkinson. The Gravity Probe B Relativity Gyroscope Experiment: Approach to a flight mission. *Proceedings of the Fourth Marcel Grossman Meeting on General Relativity*, 1986.
- [10] P.J. Wiktor. The design of a propulsion system using vent gas from a liquid helium cryogenic system. *Stanford University Ph.D. Thesis*, June 1992.
- [11] P.J. Wiktor and D.B. DeBra. The minimum control authority of a system of actuators with applications to Gravity Probe B. *14<sup>th</sup> Annual AAS Guidance and Control Conference*, February 1991.

# TOWARDS A FULLY AUTOMATIC FLIGHT FOR PASSENGER AIRCRAFT AND SPACE AND EARTH REFERENCE SYSTEMS

M.J. Pélegrin

c/o CERT, B.P. 4025, 31055 Toulouse Cédex, France

**Summary** - The first subject concerns Aeronautics. If the number of planes increases at 4.5 % per year (freight aircraft : 8 %) the Air Transport System should become fully automatic from take-off to landing. This includes both the automatization of the plane (which is closed to be effective) and the Air Traffic Control, a much more difficult problem to solve some aspects of the problems are detailed in the presentation, namely an automatic system for all the motions of aircraft on the ground, from the exit of the landing runway to the gate and then to the threshold of the take-off runway.

The second subject concerns Space. The tremendous progress in range measurements means that the previous concept of the rigid body Earth is vanishing : crust tides, non-stationarity of the rotation vector... should be taken into account and injected in the analysis of data coming from satellites. Some recent acquisitions in this domain are recalled in the presentation.

## Keywords -

- 1 - Overall Safety - Vigilance - Flight Management Systems (FMS) - Cooperative Rendez-vous - SSR Mode S - 4D Trajectory.
- 2 - Earth rigidity - Clocks stability - Earth motion - Universal Times - Tides (maritime and crust) - 3-body problem - Precession - Nutation.

## I - TOWARDS A FULLY AUTOMATIC FLIGHT

My first comment will concern aeronautics. It's a pleasure for me to find several papers dealing with aeronautics in this symposium.... certain persons in this audience know why !

My comment will be provocative-it states that :

"Commercial planes which will be built in years 2010 will be certified fully automatic ... or they will not be !". Let me say first, that does not mean that there will be nobody on board as technical crew<sup>1</sup>. This

is a very critical subject which involves both technical and human problems. Let me first enumerate some technical problems.

a) The overall safety of a plane, when it is used according to specifications which have been verified during the certification and when it is guided (Air Traffic Control) in a safe way is of the order of  $5 \cdot 10^{-8}$  per hour of flight.

The "human safety" for a wealthy person - this is the case for pilots, they have 2 medical examinations per year- is only  $10^{-6}$  per hour. This is why there are two pilots on board and this is why it is

<sup>1</sup> fully automatic Metro's are in operation at the present time ; the first one in Lille, France, has

functioned perfectly since 1983 ? nobody has complained about the lack of conductor or supervisor on board

unacceptable to have only one pilot on board, at least in the present concept of the cockpit<sup>1</sup>.

b) there is one catastrophic mid-air collision every 3 years over Europe/USA. It can result from ATC error and/or pilot error. The present number of commercial planes is 7500. It is expected that this number will double around 2008-2010 and triple around 2015-2020 [1]. Could we imagine that one mid-air collision per year would be accepted by the population? Certainly not.

Then the safety of the Air-Transport System (the aircraft plus its guidance through the ATC) must be improved by at least a factor 3. Note that the main difficulty will probably come up from the ATC.

c) progress is written in the genetic patrimony of man. Systems always evolve in the way of more automatization : we have to accept that fact. Safety is winning in this evolution.

But the operator is more and more kept out of the system. Systems work better and better ; operator intervention is rarer and rarer... His attention is less and less sollicited. And, if he has to intervene, he is faced with the complex degraded system: is he able to understand in a few seconds what the state of the system is ?

Pilots are now regularly authorized to sleep on board... under certain conditions (not both at the same time).

d) let us consider now a commercial routine flight on a modern aircraft, as every day thousands exist.

For planes built from 1978 - 1980 we can say that a flight is a sequence of automatic sub-phases, manually engaged by the pilot, a few hundred feet after take-off to landing.

---

<sup>1</sup> a single pilot could be accepted if the plane is equipped with an automatic system which will ensure its recovery ... after the death of the pilot. According to physicians it is very rare that death occurs suddenly without any advice (of the order of minutes). We can imagine a red button in the cockpit, to be pressed "if the pilot feels that death is arriving soon".

The automatic recovery system is technically feasible today.

For very recent planes, those equipped with an FMS (Flight Management System) the engagement of subphases can be made automatically, moreover the use of sub-phases may be overpassed and the FMS may directly optimize a sub-phase which could be "the climb to the assigned FL". At landing the control of plane on the center of the runway, as well as the breaking, could be fully automatic.

Does that mean that the crew has nothing to do on board ? Certainly not at the present time : the flight profile stored in the FMS is a "nominal" flight profile ignoring other traffic ; it is rare, very rare that the real flight is the replica of the "ideal flight plan" of the FMS ; the Control (en-route and terminal area) gives instructions to the planes in order to avoid conflicts ; The main action of the action of the crew is to assimilate these instructions which come up at random and must be executed without delay. Hence, the full automatization of a flight will necessary included automatic transfer of instructions to the FMS or AP even if ATC is not fully automatized. The two problems : automatization of the flight itself and automatization of the AT management could be considered as two independant problems. At the terminal area the problem is tied to the airport capacity (take-offs, landings, ground motions, vortex traces, even in some cases-terminal building gates).

To conclude this first approach concerning a fully automatic flight it is necessary to automatize from one part :

- the taxiing before take-off and after landing
- the acceleration on the runway
- the rotation and the very initial attitude of the plane after take-off,

and from a second part :

- the Air Traffic Control, the plane being taken in charge from the break release to touch down
- the dialog between the ground computers and the cockpit (automatic data link).

### Taxiing

I am fully convinced that manual control of the plane from the gate to the runway

threshold by using the engines to move the plane will be abandoned within 10 to 15 years for the following reasons :

- fuel economy, mainly to reduce pollution (a "small" aircraft consumes about 360 kg/h of fuel when taxiing...),

- noise reduction ; the present regulation (FAR 36 chapter 3) will gradually be reinforced; continuous noises under a given threshold are not taken into account, it is probable that in the near future such noises will be comptabilized and the taxiing with the engines of many aircraft on the airport will no longer be accepted,

- ageing of components, namely engines, even at idle state, and carbon breaks (they wear out more when they are cold than hot. When taxiing prior to landing, they are in a "cold state").

Under bad weather conditions the ground motion of planes is slowed down ("ground" radars do not "see" the planes everywhere on the taxiways or manoeuvres areas). Planes are authorized to move leg-by-leg between crossings.

Automatic ground motion will become a necessity and if we assume that planes will be moved by tractors (as those presently used for movement from the gates to a remote position from which the plane can move by itself everywhere on the airport except on the runways, then the motions could be controlled by a centralized computer which will monitor all the traffic, like trains are now controlled by a central computer in many parts of the world [2].

The difficult part of this tractor system is the rendez-vous between the tractor and the plane once it has left the runway under manual or automatic control.

I may suggest a solution as illustrated in Fig. 1. It does not imply that flight is fully automatized and I think that it will be implemented long before the full automatization of a flight is a reality. It consists of an ensemble of two vehicles A and B. In this solution the plane is supposed to be clutched by its front landing gear, other versions clutch the plane through its main landing gear, but in all versions the principle is the same :

vehicle A is a heavy and powerful automatic tractor, vehicle B is a light vehicle with power limited to its own motion. It can navigate with regard to A but it is equipped with sensors which can recognize at a given distance the landing gear of the plane to catch.

The rendez-vous which must be performed without stopping the plane, in the version described here, is performed as follows :

Vehicle (A + B tied) moves toward the plane in a straight portion of the taxiway ; at a given distance, of the order of 100 m, (A + B) are stopped ; after confirmation that overall configuration is correct (that is, the plane has passed sensors located on the runway, its speed is correct - 5 kts) then A liberates B and sends it towards the plane ; B navigates first with regard to A then looks for the front landing gear of the plane which is coming in front of it ; when the distance reaches a given value, the motion of B is inverted such that the plane approaches B ; then B catches the landing gear, becomes passive, is driven by the plane, sent a message to A confirming the correct clutch between the plane and B. Then A navigates in such a way that a smooth rendez-vous between (B + plane) and A is performed. Note that this last rendez-vous is "cooperative" ; it must be so because it concerns the connexion of two moving bodies of let say 150 T for the plane and something like 25 to 30 T for vehicle A. On the contrary, the rendez-vous between the plane and B, which is not cooperative, is such that a percussion between the plane and the light vehicle B is acceptable<sup>2</sup>.

I could not comment anymore on this system for which the faisability phase is engaged. I mentioned it just to point out that the Air Transportation System could soon be fully automatized from "gate to gate".

Then to ensure full automatic flight two subphases must be finally automatized :

- the acceleration on the runway
- the rotation and initial stabilized attitude.

I will be brief on these two sub phases.

---

<sup>2</sup> French Patent n° 91 05129 to be extended to foreign countries. For information apply to the author.

When accelerating on the runway, the plane behaves like an automobile in the first hundred meters, then to a hybrid between an automobile and a plane when lift appears and finally like a plane once the wheels have quit the runway. As far as I know, there is no automatic pilot for an automobile. This is a new problem, a difficult one because, due to acceleration, the vehicle is governed by highly non-linear equations. In addition, the plane cannot be aided by an ILS as it is, when landing in an automatic mode, except for alignment on the center of the runway thanks to the localizer beam.

During these two sub-phases, the plane will use its Inertial Systems (INS) to monitor the rotation and the initial climb.

Fully automatic flight will necessitate automatization of these two sub phases. It is a difficult task which will lead to additional equipment on board but there is no technological gap even with the present technology.

Certainly the most difficult part will be the automatization of the ATC and the automatic link between ground stations and planes.

You are certainly aware that an automatic link is forecast for 1997 - 1998, first in connection with the MODES - SSR (Monopulse Secondary Radar). Europe will probably be covered by such radars between 1995 - 1998. In the meantime, dedicated satellites are being studied and they are expected to become operational at the end of the century. As you know, digital VHF is, already used through ARINC<sup>3</sup> and SITA<sup>4</sup>, on an automatic mode but only for companies usage.

Messages for the ATC - Plane communications are not yet standardized. They will be soon. Ground communication network is a major part of the ATC's future : this is a necessity to get full advantage of SSR-MODES namely the "anti-garbling" by calling planes at will (S is for *selective* address) ; the messages routing will be a fall out of the radar network.

---

<sup>3</sup> ARINC : Air Radio Incorporated.

<sup>4</sup> SITA : Société Internationale des Transmissions Aéronautiques

It would take too long to talk about the future ATC ; let's summarize the situation like this :

The present ATC will certainly be unable to control the traffic when it will be twice that of today. However, the full automatization is not forecast before 2015 (and most experts think that this is an optimistic date). Man will still be in the loop for a long time and man will be responsible -not the computers radar network !

I am glad to mention that recently experiments have been conducted successfully. In october 1991 a joined project between the UK-CAA and EUROCONTROL demonstrated a "world-first" use of the Mode-S data link in a realistic ATS environment using the BAC 1-11 research aircraft of DRA-BEDFORD, UK.

Two scenarios were flown. In the first the R/T channel was used for all communications between the air traffic controller and the pilot. In addition to this standard communication protocol, through the ARINC 429 data bus in the aircraft was, via the Mode-S data link, automatically interrogated from the ground. In this way the ATC system on the ground could constantly check the status of the flight director, auto pilot and auto throttle instruments against the clearances given by the controller. Moreover it was observed that simply displaying the basic down linked aircraft data to the controller e.g. air speed, aircraft heading, etc, led to a considerable reduction in use of R/T because questions like : "what is your heading ?", etc. were not necessary any more.

In the second scenario the controller sent all ATC clearance via the data link to the aircraft. They were displayed in the cockpit on an experimental screen and subsequently acknowledged by the pilot pushing a button. This acknowledgement was sent down to the ground system via the data link and the controller was advised accordingly. However there was no connection between the data link and the flight control instruments in the aircraft. The R/T channel was constantly available for specific pilot requests and emergencies and indeed had to be used during one of the demonstration flights.

From an ATS point of view this scenario was less realistic than the first as the data link communication took far more time than acceptable for time critical clearances such as altitude and/or heading changes. Nevertheless it clearly demonstrated the capabilities of the data link and some of its current limitations.

Nowadays controllers are aided by computers ; what they have on there screen is not the radar video but synthetic data coming from a computer (the "best" estimated position <sup>5</sup> and some data concerning this flight). The En-Route controller -as well as the approach one- have an automatic conflict detection which gives warning if a conflict may happen between 2 and 3 minutes.

The Approach controller is informed of the sequence of landing long before the landings occur. In case of too short separation between two planes, they can request a delay of the second plane or an acceleration of the first <sup>6</sup>. The computer, which has mathematical models of most of the planes, checks if the modification is acceptable i.e. feasible by accelerating or decelerating the plane according to the "Company rules" (which are also stored in the computer) ; if not, the controller will look for a trajectory modification and will first try to modify the "angle of interception the ILS axis".

All these 4-D trajectory modifications are proposed by the controller and checked by the computers. In the near future we can reasonably think that these modifications will be automatically initiated by the computer and unique acceptable landing sequence for the next 15 to 20 mn will be presented to the controller for decision. No large difficulties are expected for that type of automatization.

The main problem lies in the "sector division" of the air space (I am not referring to the overall partition of the airspace ; the new partition for VFR and IFR flights is gradually implemented in all countries ; it has been implemented in France last April 2nd). A controller is in

---

<sup>5</sup> Most of the time a plane is seen by more than one radar

<sup>6</sup> Systems MAESTRO in France (Paris), COMPAS in Germany (Frankfurt) and, in test, à Descent Adviser in Denver (Colorado).

charge of an airspace which has been defined in such a way that 15 to 18 aircraft can be present simultaneously. This is a maximum ; if the adjacent sector is prepared to deliver an additional plane to the sector when it is such loaded, the controller refuses it ! ... and delicate situations arise (the plane can be asked to make a circle -"a 360°"- or more, before entering the next sector...)

The trends are to evaluate the possibility of forgetting the sector partition and to have the same controller supervising a plane from take-off to landing. Obviously a controller will control several flights. These problems are not as yet solved but it seems that optimization algorithms to control the traffic would be simpler to derive. It would be a global <sup>7</sup> real time control ; this is mainly a mathematical problem. To initiate it, I think that we have to forget about the present way of achieving optimality inside a sector (en Route control) optimization is made in the controller brain and it is quite good. Many attempts have been made to analyze the reasonning process in the controller's mind. No success (Neuronal networks are much too poor at the present time ; the only certitude is that the controller does not use a (parallel) sequence of decisions). At the company level, cost indexes are used to estimate the penalization which results from deviations with regard to the "ideal flight plan" - a plan which assumes that the plane is alone in the sky but which complies with present rules : airways and flight levels - Cost indexes are presently a mixture of additive parameters (fuel consumption, sometime fuel consumption squared, additional time of flight, velocity deviation...) weighed by coefficients which are set up by the company staff ; they can be adjusted when necessary. What I am suggesting is to look for a unique commonly accepted penalization index, for each type of aircraft. The, optimization could be done by the computer and complete equality for the airlines operators should be achieved. This penalizing index is derived from the flight envelopes of the aircraft (in fact, a collection of flight envelopes according to the present mass of the aircraft ; only one load factor  $n = 1$  can be considered ; for

---

<sup>7</sup> global with regard to a dense area such as North Western Europe/Southern Europe/USA etc ...

climb and descent phases, an optimum configuration taken as the basic configuration).

Let's give weight 1 at this optimum commonly accepted flight state (altitude, velocity or Mach). Any deviation from this state induces a penalization even though it lead to a smaller consumption. The airline has established its schedule according to the optimum state ; if velocity is reduced for AT management reasons, schedules will no longer be satisfied, thence a penalization should be accounted for. It, probably, will not be too important.

We can then imagine that, starting from the Z, V flight envelope with the optimum state specified and quoted 1, we draw contour lines around that point for iso-penalization<sup>8</sup> (see Fig. 10).

All these data can be stored in a processor - Let us now suppose that the airline wants to modify the optimum state for any reason (for ex. in order to compensate for a late departure and try to arrive on time) - In that case, the airline may send a message to the AT Center saying "the optimum setting for that particular flight is  $Z_2 V_2$  (instead of  $Z_q V_q$ )". We then have to assume that, again, a commonly accepted algorithms stored in the processor, will automatically re compute the iso-penalization contours ; this new set of data will be used for global optimization.

I think that only global optimization may solve the problem if traffic is increasing as forecast. It will need unique-commonly-accepted penalization indexes to run the global optimization process. In addition, to maintain a certain degree of flexibility, choice of the optimum state (crise phase) for a particular flight can be specified by the airline ; a commonly-accepted algorithm will automatically recompute the penalization indexes.

I hope to have convinced you that the automatic plane could be a reality in the next 15 - 20 years even if ATC is not yet, at that time, fully automatized.

---

<sup>8</sup> adding a 3 axis "penalization index", contour-lines are the section of the penalization index surface by planes parallel to Z, V plan ; this surface is tangent to the Z, V plan at the optimum flight state.

This is not a sanction about man, this is the result of logical considerations dominated by the safety requirements. Man will stay on board, in the cockpit ... at least during the transition period ! He will have a very delicate task because unexpected failures (this means : non-listed failures) will still happen with a very low probability and the comprehension of the new state of the machine after an uncorrected failure will be hard to understand quickly by this "operator". However, man has designed the fully automatic system and his presence on board will probably help in the comprehension of a failure and thus contribute to improve the system for the future.

## 2. SPACE AND EARTH REFERENCE SYSTEMS

Now I am passing to the second subject which concerns Space : the reference coordinate systems. Right now you have noticed that there are several reference coordinate systems. Everybody is concerned : but do we really know what we are talking about ? The Aerospace community is deeply involved in these problems. Thanks to SPOT-1 (Feb. 1986), SPOT-2 (Jan. 1990), ERS-1 (European Remote Sensing Satellite) (July 1991)<sup>9</sup> and the future SPOT-3, 4 and 5 which are programmed, the demand for finer and finer detail analysis of the pictures taken by these satellites calls for precise definition of reference systems.

Distance measurements within one meter over thousands of km raise the problem of reference systems in which the objects are placed (ground fixed or mobile systems, maritime objects or vehicles, aircraft, satellites). Rigidity no longer exists, everything is "deformable" in a non-elastic way. This is equally true for the Earth.

Let us start with the so well known time notion ; who has questioned himself about this ? During the agricultural period, some ten thousand years ago, time was related to the apparent sun motion ; uniform or regular time had no meaning. Nothing was in favor of a time which is not attached

---

<sup>9</sup> ERS-1 has a side looking radar which is not affected by clouds.

strictly to the sun motion, whatever the regularity is.

Then mathematics arrived and the need for something which evolves "linearly" or "uniformly" (what is the meaning of these terms ?) rose up. Some time after clocks were invented .... and Astronomy became a real science : astronomy needed time measurements, clocks needed to be adjusted over a long period of time on celestial motion, two interrelated problems.

What is the present situation ?

This is a bad compromise but nothing better could be imagined. What are the constraints ? Time should be uniform, time should round off the day (for everybody), the year for specialists.

The conventional clocks based upon the local gravity reset daily or from time to time has lead the way to atomic clocks, the stability (..uniformity) of them may be kept as better than  $10^{-12}$  (... what does that mean ?).

But the course of the Earth around the sun is far from a circle or even from an ellipse, apparent sun velocity varies during the year. Kepler knew that and arrived at the fundamental (good) approximation of the planet motions.

The compromise I was referring to a few minutes ago is the following one : man wants a time which evolves regularly, synchronized on the Earth's motion. This one can be easily detected by the position of the sun at the meridian of the observer. The fact that nothing is circular in the universe makes that an "intermediate time" should be arbitrarily defined : it is defined as the motion of a pseudo-sun which would rotate around the Earth (apparent motion) on a circle and would coincide at least twice a year with the true sun. This is the time we used, a time which is represented by atomic resonance of cesium atoms, a very stable time. But, with this time the sun does not pass at its maximum daily height at 12 H 00 (local time). For 1961 (Fig. 2) it was 16 mn in advance in Nov. 3rd or 14 mn late (Feb. 11th). Exact coïncidence arrived 4 times during the year (Ap. 15th, June 14, Sept. 1st, Dec. 26th) [3].

We have said that time should be a "uniform" parameter for everybody. In differential equations concerning the motions due to gravity (on the Earth or around the Earth) we need a time attached to the Earth's rotation (which is not constant...). We start from the "Universal Time 1" UT1 which is related to the sideral mean time. Atomic clocks are assumed to give the most uniform time IAT (International Atomic Time). UT1 and IAT behave as indicated Fig. 3. Then we define a "local time" CUT (Coordinated Universal Time) which is as uniform as IAT but which is always within  $\pm 0,5$  second with regard to UT1 :

$$\begin{aligned} |\text{CUT} - \text{IAT}| &= n \\ \text{seconds (exactly)} & \\ |\text{CUT} - \text{UT}| &< 0,5\text{s} \end{aligned}$$

The times of corrections (temps) are irregular, last correction has been made on Dec. 31st 1990.

IAT was officially adopted in 1971 ; it is broadcast on a world-wide basis for systems synchronization by LORAN C (when available) and, more and more, by GPS (which has a world-wide coverage). The variations UT1 - IAT indicate the irregularities of the Earth's rotation (air mass motions, relative motion between the mantle and the core, tides...).

Let's come back to the coordinate system problem and start with Poincaré's three-body problem, stated in 1889 and still without a theoretical solution. It concerns 3 rigid bodies which interact with each other according to Newton's law [4].

It can be stated through the accelerations of each body :

$m_j$  is the mass of each body  
 $r_{ji}$  is the vector body  $j$  to body  $i$  (centers of mass).

The system momentum is constant ; the plane perpendicular to the momentum and containing the inertial center, is fixed in a Galilean reference system.

The 2-body problem has an exact solution which was known before the Poincaré's era.

The motion of the vector  $r_{12}$  is the one where body 1 is considered as fixed with a

mass  $m_1 + m_2$ . If the origin is taken as the center of mass of the 2 bodies, then

$$\overline{r_1} = - \frac{m_2}{m_1 + m_2} \overline{r_{12}}$$

$$\overline{r_2} = + \frac{m_1}{m_1 + m_2} \overline{r_{12}}$$

Perfect rigidity does not exist, bodies are, at least, elastic. Moreover if we consider the Earth as one of these bodies we know that it is not a rigid body nor an elastic one because of :

- the huge mass of the Oceans which by their motions (tides)<sup>10</sup> modify the inertial momentum of the Earth and induce overloads on the bottom, which, in turn, induce earth crust deformations.

- the crust tides, on the surface of the Earth, due to planet attraction (mainly lunar). The surface of the Earth thus varies like the surface of the ocean with an amplitude of 30 cm (any point of the surface of the earth is so varying by 60 cm in altitude in approximately 23 hours) with regard to the center of mass of the Earth which is assumed to be fixed within less than 10 cm.

- the load of the atmosphere on the surface of the Earth ; under a High Pressure Area the forces on the ground are higher than under a Low Pressure Area ; computations show that a local deformation appears. In anyway the mass of the atmosphere (something equivalent to 2,50 m of crust) though it rotates at the same angular velocity as the Earth on average, is not rigidly tied to it.

- the tectonic plate motions (1 cm or more per year is the relative motion of plates in some areas) modify the local loads and thus induce also deformations ; the state of the volcanic activity (there are about 200

---

<sup>10</sup> tides are mainly due to the moon attraction ; the "open tide", let's say in the middle of the Atlantic Ocean, is of the order of  $\pm 50$  cm. If higher tides arise along the sea shore, in certain locations, it is only due to "bassin effect" resulting of the local profile of the coast. In some points of Brittany tides may reach 15 m.

volcanoes in activity over the world) also modifies the profile of the Earth's crust.

It is then important to deal separately with the gravitational perturbations and the non-gravitational ones, i.e. the above mentioned perturbations. For the first one we should use inertial reference coordinate systems, or references related to them (which implies the knowledge of the motion of the reference systems with regard to a pure inertial reference system). For the second one, we can use any grid system, well defined with regard to the Earth, assuming that the rotation vector of the Earth is known in the grid used.

Most of these phenomena which were presented as the consequences of external perturbations are also modifying the mass repartition in the Earth which induces perturbations both to the Earth and to the initial causes (normally, planet perturbations). Obviously these modifications are of much lower order. May I recall that Poincaré was the promoteur of chaos : he demonstrated that if we consider two systems which interact, each other and a perturbation due to a 3rd system, then the whole system may go to instability on an unpredictable manner ... this is chaos.

Let's come back to the rigid body problem; if no theoretical solution exists we can look for approximations, namely in particular cases.

The solar system is a particular case :

The absolute regularity of the planets has been accepted until Poincaré and for the great majority of humans it can be considered as a good acceptable assumption. Poisson's (1781 - 1840) theorem states that great axis of the planets motions (or any intercelestial body) are constant even if gravitational perturbations due to other bodies interact.

If rigidity does not exist, full stability neither exists. Let's come back to the Earth alone or, better to the Earth-moon compound. According to the big-bang theory, the sun was created 15 G years ago, the Earth 4.5 G years, as to the moon its birthday is not yet clearly established ; it seems proved that it is not a part of the Earth which should have been ejected,

but, merely, an accretion phenomena . The fact that its own rotation is exactly equal to its revolution period around the Earth is due to a non-uniform distribution of masses inside its crust.

There are many phenomena which dissipate<sup>11</sup> Earth-moon energy (the deep space density is not null) and consequently, if every thing were constant (sun, mass namely) the Earth would come closer and closer to the sun. The surface temperature of the Earth is not constant -a lot has been said recently on this very important subject. Let's note that at the present time it is assumed that the "level" of the oceans is increasing by 15 cm per century. This is mainly due to the fusion of continental glaciers (the polar table account for less than the continental glaciers) and to the dilatation of water due to temperature rise. It results important modification in the mass repartition within the surface of the Earth.

From the system Earth-moon taken alone, the energy dissipation resulting from the tides slows down the rotation of the Earth (as well as the one of the moon around the Earth which, consequently, goes very slowly to closer and closer orbits). As you remember probably, the duration of the "civil day" was shortened by 1 s on Dec. 31st, 1990, in order to absorb the delays which were accumulated previously<sup>12</sup>.

Let's arrive now at the motion of the Earth with regard to a galilean or inertial reference.

The earth is approximately an ellipsoïd with a flattening of 0,0033 ; this is a rough approximation for the problems we are dealing with.

Galileo (1564-1642) said that it rotates and rotates around the sun : the earth was no longer the center of the Universe. Its rotation is complex, even if we restrict the Universe to 3 bodies, the Earth, the sun and the moon. Note that if we assume that the sun attraction is the same when the moon is between the Earth and the sun and when it is at the opposite side, then the

---

<sup>11</sup> solar wind, mainly protons, may furnish energy to the planet

<sup>12</sup> At the precambrian, some 500 million years ago the earth rotated in 15 hours.

vector earth/moon would have a Keplerian motion. This approximation no longer copes with the measurements made every day with instruments installed both on the Earth, on satellite or ... on the moon.

The orbital plane of the Earth rotates around the sun in 26.000 years (more precisely : the precession (in longitude), per Julian century, will be for year 2000,0 : 5029,0966 arc seconds) : this is the *precession* effect ; it is due to the Earth flattening. The orbital plane of the moon rotates in 18 2/3 year and oscillates 5 to 5.3° with regard to the ecliptic, this is the *nutation* effect ; both effects can be easily represented by the trace of the rotational Earth vector on a plane perpendicular to the ecliptic (Fig. 4) the trace is made of a circle (described in 26000 years) surrounded by a perturbation the period of which is 18 2/3 years (see Table I).

As a consequence the polar star (Alpha polaris) which seems to be fixed in the sky (in fact is presently located at 1° from the Earth vector) will be at the closest position in year 2015 : 1/2° but in 5500 years the "polar star" will be Alpha Cephei.

Winter is defined like the time at which the sun passes at the minimum height in the sky but this is not the time at which the Earth is at the closest point of the sun ; this time, called the perihelion, is presently on Jan. 6th. There is no connexion between the winter solstice and the perihelion of the Earth (Fig. 5).

Unfortunately, as we have already said, the Earth rotational vector is not constant in direction and module ! Below the crust there is the magma which is a high viscosity fluid; it does not rotate at the same angular velocity as the Earth this is an important source of perturbation. On the crust there is differential motions in the oceans and above the crust, the atmosphere motions induce perturbations. Fig. 11 indicates how the duration of the day has varied between 1820. An unexpected and inexplained slowing down period appeared between 1870 and 1900 (the duration of the day increased by 10 ms) ; an acceleratory period appeared between 1900 and 1940.

At the present time, thanks to atomic clocks very small variation could be

measured and it appears that daily variations (order : microseconds) are superimposed to semi yearly and yearly variations From these facts -no rigidity, no stability- it results that any reference system can only be arbitrary and temporary.

For the present time, three surfaces (or volumes) are commonly used :

1 - the topographic surface : this is the interface between "the Earth" and the "atmosphere"

2 - the geoïd which is a mathematical surface corresponding to a iso-potential from which the gravity parameter  $g$  is derived :

$$g = \text{grad } W = \text{grad } (V + \phi)$$

$W$  is the potential which is composed of two terms  $V$  and  $\phi$  ( $V$  gravitational potential,  $\phi$  acceleration due to the Earth rotation) the local gravity parameter  $g\phi$  at latitude  $\phi$  is given by the Clairaut equation (1743) with a still acceptable accuracy :

$$g\phi = g_a \left[ 1 + \left( \frac{5}{2} \frac{w_a^2}{g_a} - \alpha \right) \sin^2 \phi \right]$$

where :  $g_a$  is the gravity parameter at equator

$\alpha$  the earth flattening

$\alpha$  was taken as 1/297 and since 1926 is taken as 1/296,7.

3 - the "Earth ellipsoid" which is a simple (this is a revolution ellipsoid) -and useful- approximation of the geoid. Fig. 6 indicates the distances between the ellipsoid and the geoid.

Note that there is a difference (within 1 m) between the geoid and the mean level of the oceans.

To describe the solar system, including its artefacts -we are concerned...- we use celestial reference systems. Directions are related to stars or radio-sources it is not assumed that these objects are fixed. These systems are centered on the sun,

more precisely at the center of mass of the solar system. Inertial systems are often used they constitute a very good approximation of a Galileo system.

For space mechanics, the one which we use to design and control a satellites, quasi-inertial systems are used : they are systems parallel to inertial systems but the origin is subjected to non-uniform motion with regard to a galilean system.

At last, the model used must not induce errors greater than the one resulting from the measurements. The recent technologies such as VLBI (Very Large Base Interforemetry) or laser telemetry, have given a strong motivation to geodesists and astronomers to look for better models.

A few words about satellite trajectories.

The rough altitude of the shuttle is of the order of 400 km ; it's very close to the Earth (radius : 6378140 m) ; many satellites are between 800 and 8000 km ; stationary satellites are roughly at 36000 km ; the moon is roughly at 384000 km).

It is rarely acceptable to assume that the satellite is describing an ellipse around the Earth, the center of mass of which being a focus of the ellipse. However, it can be accepted, as a first approximation, if lunar perturbations are computed and surimposed to the ellipse.

Normally the system Earth-moon is taken as the central force generator neglecting the rotation around the sun. At a given time and for a short period of time (a few second or some minutes according to the accuracy looked for), it can be assumed that locally the motion is keplerian (the velocity of the center of mass is supposed constant). The satellite trajectory can then be made of the succession of arcs of ellipses which would result from this approximation (see Fig. 7). Many other approximations are used, for example the osculatrice approximation which consists in assuming that a time  $t$ , perturbations stop ; for a short time the real motion stay very close to the "osculatrice" ellipse (the term osculatrice is not correct, strickly speaking).

It's not too difficult to write a program complying with these assumption and it's easy to imagine other types of approximation and their programmation. This is the way the 3-body problem is considered as solved today.

The GPS shows clearly that the absence of a mathematic solution to the 3-body problem -and, a fortiori, to the n-body problem- leads to an impossibility of predicting the trajectories of the 18 satellites used in this system-. Let say a word about GPS satellites ephemeris.

As you know, satellites are sending messages on a continuous basis ; these messages give the identity of the satellite, its position in a world wide reference system called WGS 84 and the time (with an accuracy of  $10^{-11}$  s with regard to the Universal Time) at which the first digit of this message has been broadcast. If a vehicle can receive 4 satellites at the "same time"<sup>13</sup>, the distances to 3 satellites can be computed and hence the coordinates with regard to an Earth system of reference. (Fig 8). To cope with the accuracy of the measurements (which are, essentially, time intervals) it is necessary to refresh the ephemeris which are stored in the memory of the satellite every 3 or 4 hours. This means that the approximate solution for the 3-body-problem is acceptable only for a time interval of 3 to 4 hours.

The absolute accuracy of measurement is of the order of 10 cm according to the present state of the refreshment of ephemeris<sup>14</sup>.

The reference systems are numerous. Let us restrict the problem to the case concerning the determination of coordinates of points on the Earth.

<sup>13</sup> 3 Satellites would be sufficient if the vehicle carries a clock set at the Universal Time with an accuracy of  $10^{-11}$  seconds. Only atomic clocks can do that and they have to be reset from time to time (energy in GPS). With 4 satellites a conventional quartz clock can be used in the vehicle.

<sup>14</sup> this accuracy is reached when the code P is used (military code). For public use (code C/A) the ephemeris are voluntarily degraded and the precision is of the order of 10 m for short measurement to 1 m with a continuous measurement.

I will not comment on the classical geodesy, I will just mention that the origin of this system does not coincide with the center of mass of the Earth (absolute deviation of the vertical at the "fundamental point"). The bias is in the order of 100 m.

Let's detail a little more the system using satellites. Dynamics equations are derived from the motion of the space vehicle. The Earth system is defined as follows :

- origin : center of mass of the Earth determined from the harmonic expansion of the Earth potential.
- scale : very close to 1 ; it is derived from the fundamental constants GM and C (gravity and light velocity).
- orientation : result from the specification at a given time the rotation parameters of the earth.

The longitude origin is correlated with the ascending node of the orbit ; it is normally fixed as the longitude of one of the stations.

The CIO (Conventional International Origin) results from the following assumption, generally accepted by the scientific community : the motion of the center of mass of the Earth, with regard to the mean crust, is constrained within a sphere of less than 1 dm diameter.

A true Earth reference system (CIO - BIH) is defined as follows :

- origin Co : the CIO ; the "z axis" is the real rotation vector. Fig. 9 gives the deviation of the vector between 1978 - 80.
- x-axis : in the Greenwich true meridian plan passing by Co, Pv (true pole) and Go (Greenwich). Gv is defined as the intersection of this plan and the true equator ; the x-axis is CoGv.
- y-axis such that the Oxyz is direct.

A third reference system is also defined, is the "true celestial reference system". This is the one which is used to measure the position of satellites. This system should be loosely tied to earth in order not to be sensitive to the non-gravitational causes

(pole motions) but equations relating this system to an earth reference system should exist and should be simple.

To define it a new assumption is made : the Earth momentum and the instantaneous rotational vector are quasi co-linear (in fact this misalignment corresponds to a few centimeters difference at the pole).

It is used by the IERS (International Earth Rotation Service).

Origin : Co

z-axis : true pole axis

x-axis : intersection of the true equatorial plane (perpendicular to the instantaneous rotational Earth vector) and the true ecliptic plane  
y-axis such as Oxyz is direct.

From these data, we arrive at the following accuracies :

- when using the conventional geodesical system it is accepted that two points on the Earth are located within 10 meters (inside a system the accuracy is better ; it is 3 m at  $1\sigma$  in the French system).

- when using Doppler measurements on satellite transit with the DMA ephemeris accuracy better than 1 m (50 cm if simultaneous measurements are achieved or if final data is extracted from a continuous recording of, say, several minutes<sup>15</sup>).

- when using laser measurements on satellites LAGEOS.

an accuracy of 10 cm may be achieved

- when using VLBI pointed at deep space radio source an accuracy of 1 cm may be achieved.

It is surprising to note that in the last case mentioned the origin of the Earth system may be chosen quite arbitrarily. In fact, the origin is placed at one of the VLBI station...

---

<sup>15</sup> due to reduction of the ionospheric errors and reduction of the receiver noise

## REFERENCES

- [1] LOTOS Report (1991). "Flying Ahead. A view of the Future for Civil Aeronautics", CEC, DGXII, Brussels.
- [2] Pélegrin, M. (1991) SAATMAS - Système Assurant Tous les Mouvements d'Avions au Sol. Patent n° 91 05129.
- [3] Zarrouati, O. (1987). Trajectoires spatiales, CNES (F)
- [4] Poincaré., Les Méthodes Nouvelles de la Mécanique Celeste (3 tomes 1892, 93, 99) Reprinted by Dover Publications Inc. (1957).
- [5] Ph. Hartl and al., (1986). GPS Overview and Present Status, AGARD - CP - 40.

TABLE I

### Solar System Data

- |    |   |
|----|---|
| 1. | Gauss constant<br>$k = 0,01720209895 = \frac{2}{365,2569}$                                      |
| 2. | Speed of light<br>$c = 299792458 \text{ m s}^{-1}$  |
| 3. | Earth equatorial radius<br>$a = 6378140 \text{ m}$  |
| 4. | Earth geopotential ellipticity<br>$J_2 = 0,00108263$  |
| 5. | Mass of the Earth<br>$M = 5,974 \exp 24 \text{ kg}$   |
| 6. | Gravitational constant<br>$G = 6,672 \cdot 10^{-11} \text{ m}^3 \text{ kg}^{-1} \text{ s}^{-2}$ |
| 7. | Ratio Lunar mass/Earth mass<br>$\mu = 0,01230002$   |
| 8. | Precession per Julian century for J 2000,0<br>$p = 5029,0966 \text{ arc sec}$                   |
| 9. | Obliquity ecliptic for J 2000,0<br>$\varepsilon_0 = 23^\circ 26' 21'' 448$                      |

10. Nutation constant for J 2000,0  
 $N_0 = 9'' 2109$
11. Flatening-off of the Earth at the poles  $f = 0,00335281 = \frac{1}{298,257}$
12. Heliocentric gravitation  
 $GS = 1,32712438 \exp 20 \text{ m}^3\text{s}^{-2}$
13. Ratio Sun mass/Earth mass  
 $S/M = 332946,0$
14. Sun mass  
 $S = 1,989 \exp 30 \text{ kg}$
15. Earth half great axis (orbit)  
1,076711 a.u.  
152,1 exp 6 km
16. Earth half small axis  
0,983289 a.u.  
147,1 exp 6 km
17. Mean dist earth-sun  
1.000000 a.u  
149.6 exp 6 km
18. Sideral revolution period  
1,00004 tropic year  
365,256 days
19. Mean orbital velocity  
29.79  $\text{km.s}^{-1}$
20. Excentricity  
0,0167
21. Sun diameter  
1392 000 km
22. Center of mass (Earth - Moon)  
(from center of Earth)  
4666 km

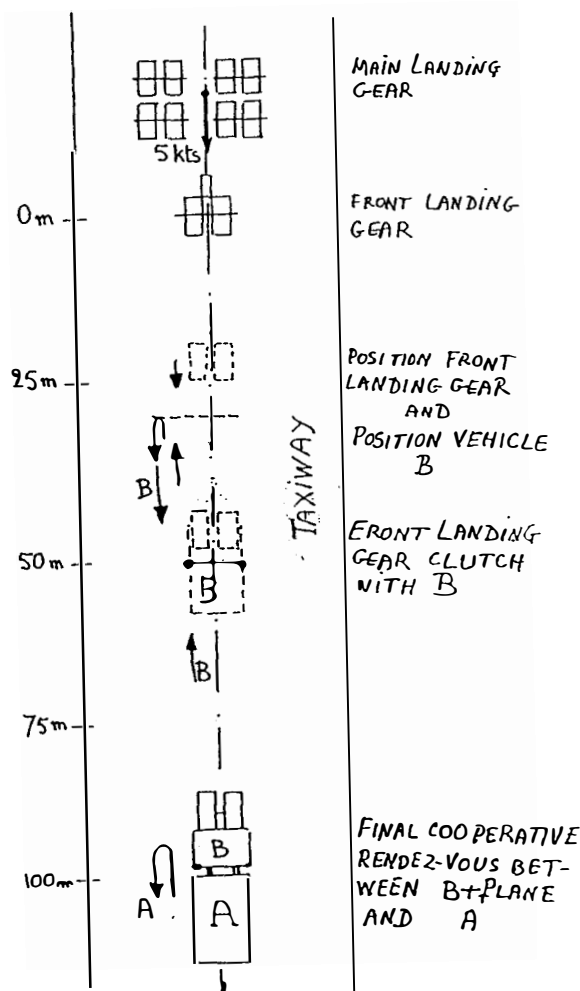


Fig. 1 - Dual tractor subsystems (SAATMAS Project)

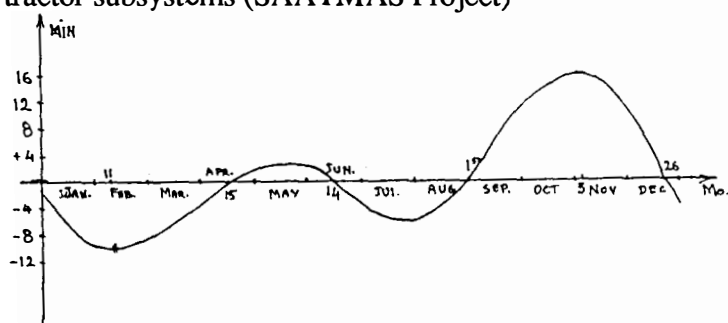


Fig. 2 - Civil meantime vs Solar Civil Mean Time

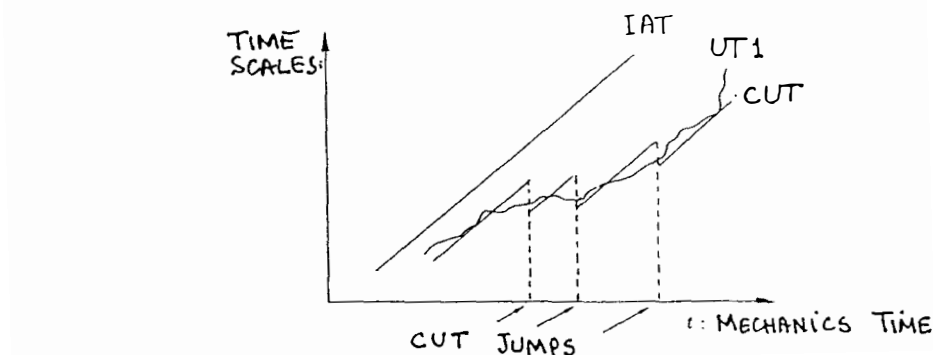


Fig. 3 - The three time scales (from Zarrouati [3])

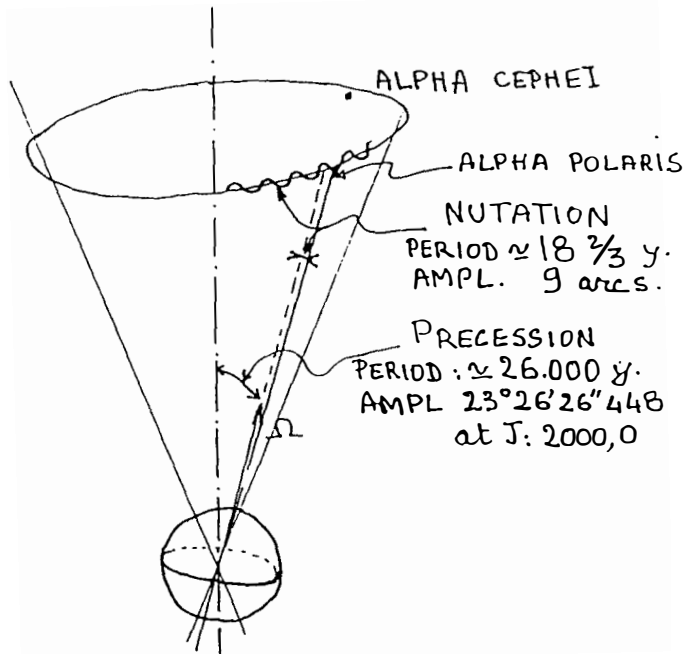


Fig. 4 - Precession and nutation

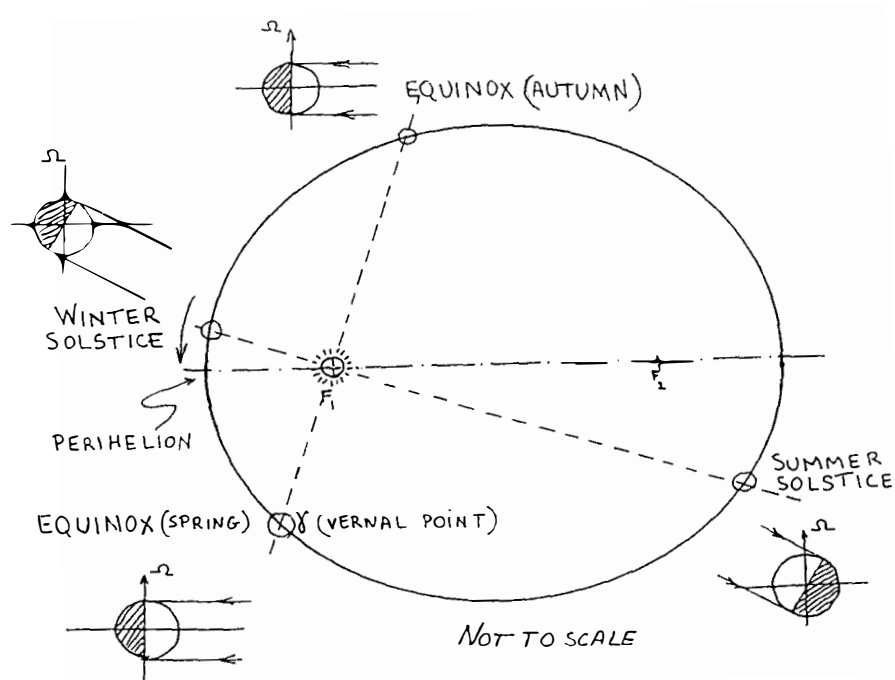


Fig. 5 - Seasons and Perihelion

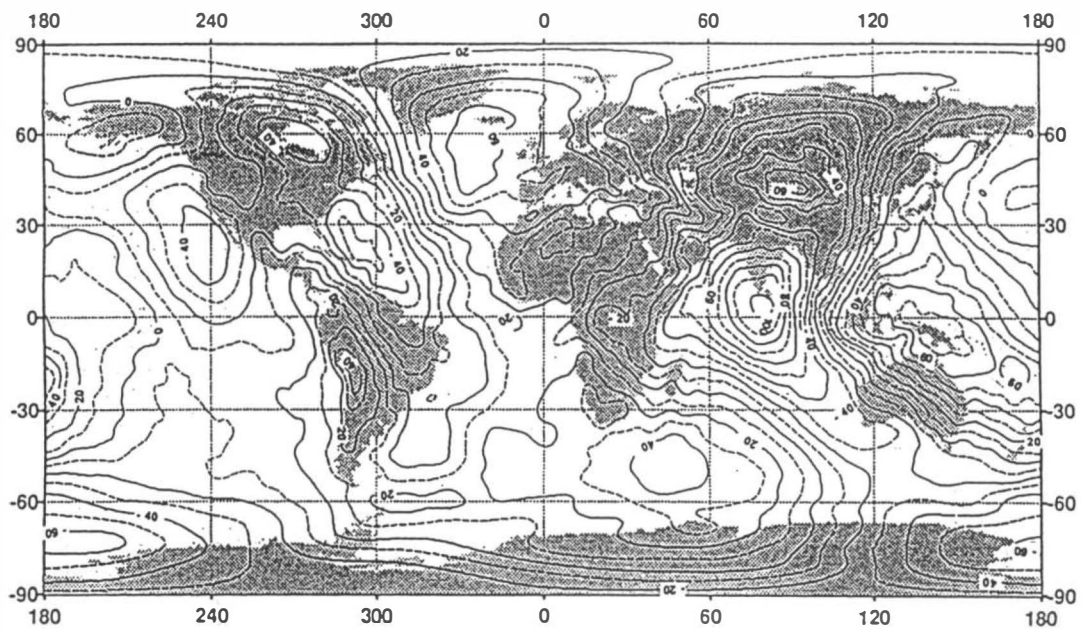


Fig. 6 - Ellipsoid and Geoid

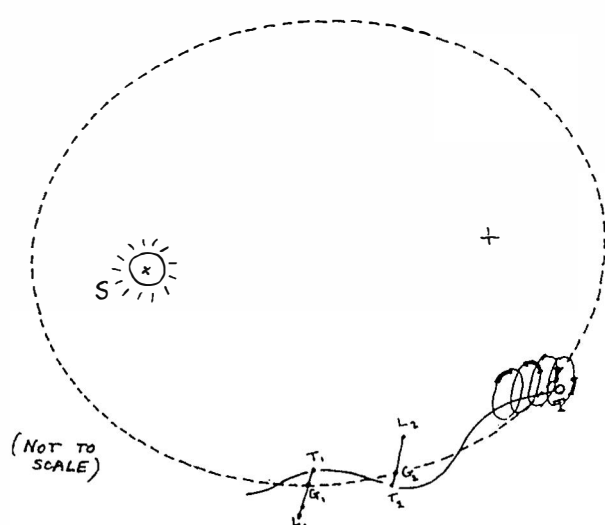


Fig. 7 - Satellite trajectory approximation

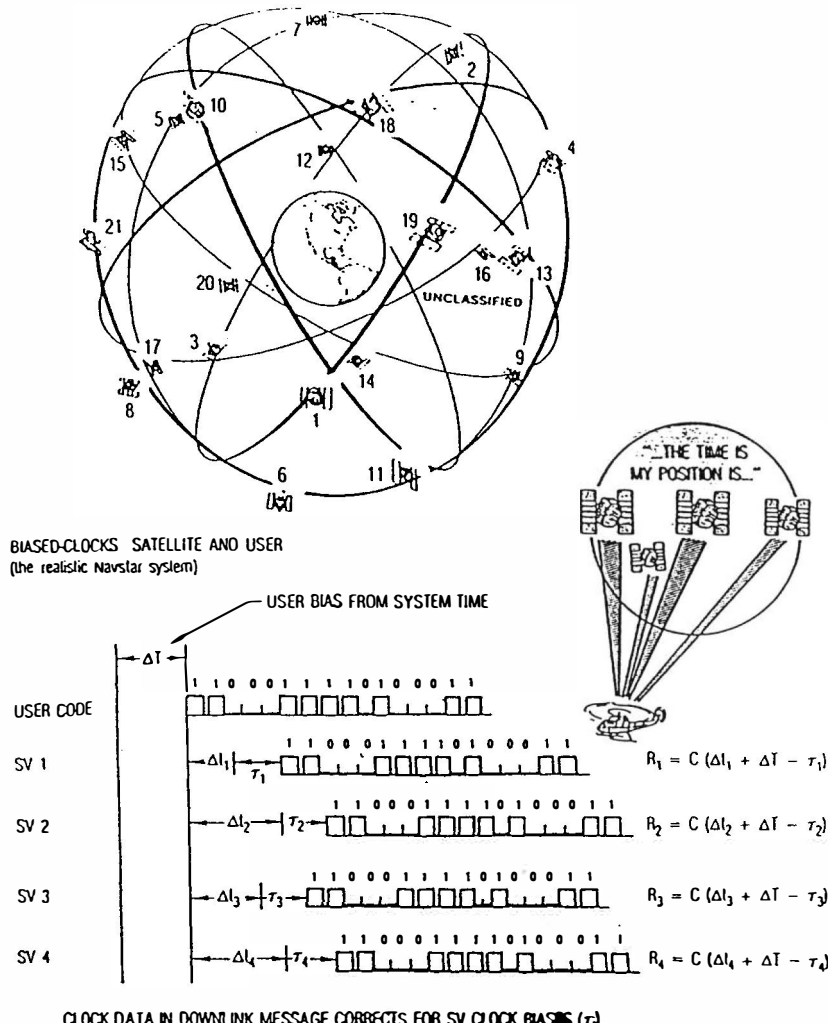


Fig. 8 - GPS System (from AGARD [5])

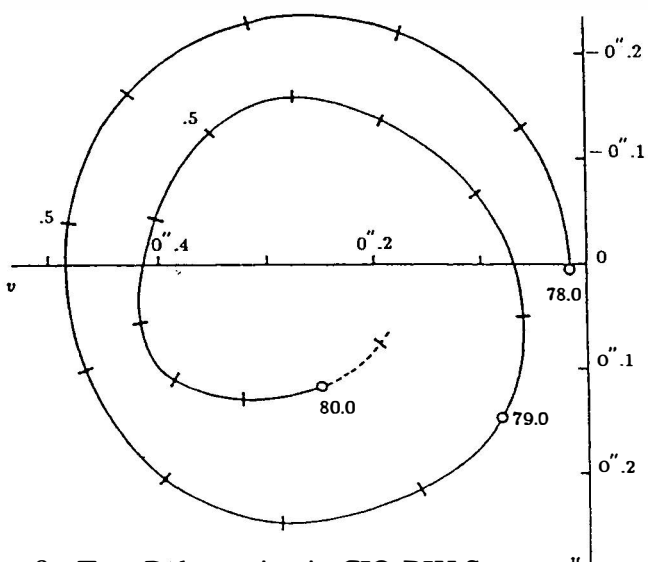


Fig. 9 - True Pole motion in CIO-BIH System  $^u$   
(from Zarrouati)

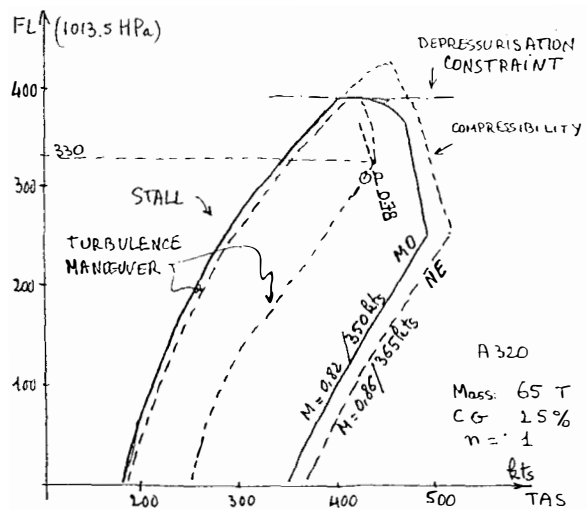


FIG 10 a

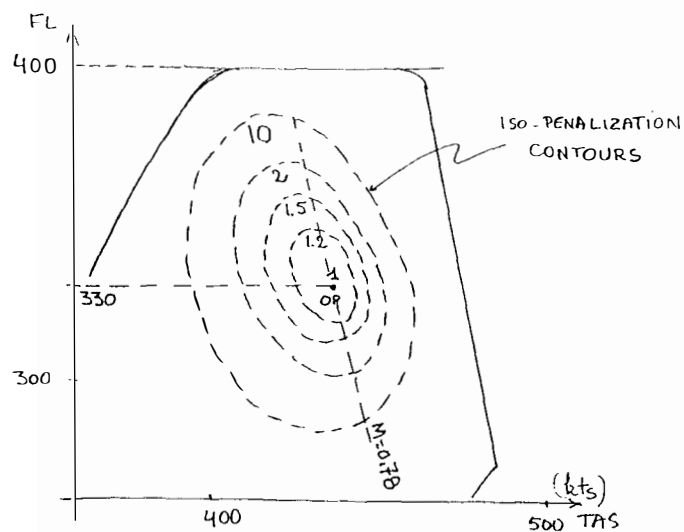


FIG 10 b

FIG 10 PENALIZATION CONTOURS

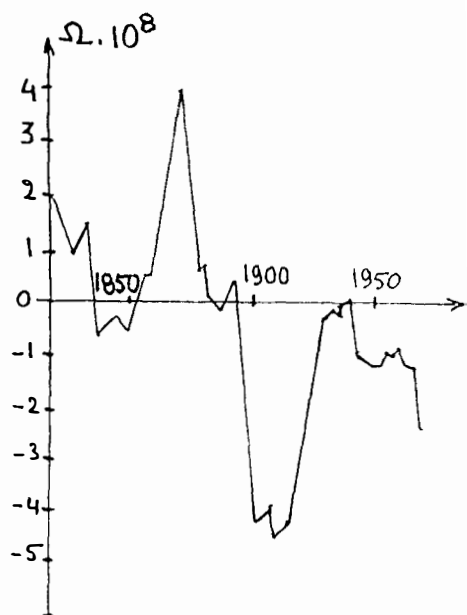


FIG 11 VARIATION OF THE DAY ( $10^{-8} \text{ rad/s}$ )

## AUTHOR INDEX

- Adolphs, P. 319  
Alazard, D. 293  
Albert, J.C. 121  
Ambrosino, G. 429  
Anderson, W.W. 387  
Aslam-Mir, S. 109  
Aubrun, J.-N. 307, 409
- Bangara, S. 203  
Barat, D. 435  
Bély, P.Y. 457  
Benoit, A. 11  
Bittner, H. 159  
Boehnhardt, H. 245  
Böinghoff, A. 145  
Boyd, I.D. 519  
Boykin, W.H. 401  
Broquet, J. 11  
Brüderle, E. 145  
Bulirsch, R. 483
- Carrier, A. 409  
Cavallo, A. 221  
Celentano, G. 429  
Champetier, C. 339  
Chang, B. 203  
Charmeau, M.C. 439  
Cher-Hiang Goh, 375  
Chrétien, J.P. 293  
Chu, C. 463  
Chudej, K. 483  
Claudinon, B. 11  
Colavita, M.M. 471
- d'Andrimont, E. 11  
de Lafontaine, J. 339  
De Maria, G. 221  
De Nicola, V. 221  
DeBra, D. 241, 525  
DeBra, D.B. 519
- Ebert, K. 77  
Elfving, A. 363  
Elstner, Ch. 507  
Eriksson, K. 203  
Ersü, E. 301  
Everitt, F. 241
- Fehse, W. 331  
Ferrara, F. 221  
Fichter, W. 159  
Fischer, H.D. 159  
Fraser, R.J.C. 43  
Frazier, W.G. 381  
Frey, A. 435  
Froeliger, J.-L. 203
- Gardiner, P.T. 127  
Garofalo, F. 429  
Gay, C. 151  
Getzschmann, A. 331  
Glinkin, Yu. 137  
Glover, K. 97  
Glumineau, A. 121  
Gorter, R.J. 325  
Granier, J.P. 435  
Grinün, W. 495  
Grübel, G. 375  
Grünwald, F. 301  
Guglielmi, M. 121
- Habbak, A. 203  
Harris, C.J. 43  
Heyland, D. 275  
Hoshstrasser, B. 269  
Hyde, R.A. 97
- Ihara, H. 251  
Irwin, R.D. 381
- Jafry, Y. 241, 525  
Jafry, Y.R. 519  
Jaisimha, B.S. 235  
Jouhaud, F. 501
- Kaffer, L. 145  
Kanai, K. 103  
Kasdin, J. 241  
Kasdin, N.J. 183  
Kitching, I.D. 257  
Kline-Schoder, R. 307  
Kline-Schoder, R.J. 417  
Klotz, H. 227  
Koenemann, H. 275  
Kokaji, S. 197  
Küke, R. 275  
Kurokawa, H. 197
- Le Carpentier, E. 121  
Lecohier, G. 477  
Lepanto, J.A. 445  
Lu Zhendou 189
- Matthiesen, J. 301, 319  
May, B.S. 457  
McGuire, T. 203  
McLean, D. 109  
Mease, K.D. 489  
Mehlem, K. 477  
Melcher, J. 115  
Meldrum, D.R. 287  
Mitchell, J.R. 57, 381  
Moog, C.H. 121
- Nakasuka, S. 313  
Newsom, J.R. 387

- O'Brien, J. 463  
 Ochi, Y. 103  
 Ohlendorf, G. 275  
 Onken, R. 23
- Pairot, J.M. 331  
 Pallaschke, S. 257  
 Pélegrin, M.J. 531  
 Pelipenko, P. 439  
 Peterhaensel, W. 245  
 Pipe, H.J. 263  
 Putz, P. 363
- Rahman, Z. 463  
 Ratzsch, D. 507  
 Redding, D.C. 67  
 Regnier, P. 339  
 Reinel, Dr. 275  
 Roth, H. 355
- Sasiadek, J.Z. 33  
 Schilling, K. 355  
 Schmidt, D.K. 89  
 Schrempp, W. 145
- Seetharama Bhat, M. 235  
 Seltzer, S.M. 57, 423  
 Serrano, J.B. 339  
 Shao, M. 471  
 Shepard, G.D. 445  
 Shirley, P.S. 423  
 Sielaff, C. 275  
 Skarus, W. 507  
 Soop, E.M. 245  
 Spanos, J. 463  
 Steinberg, R. 203  
 Stieber, M.E. 279  
 Surauer, M. 159  
 Suzuki, A. 197
- Tanabe, T. 313  
 Taylor, D. 257  
 Theobold, B. 355  
 Thompson, H.A. 1  
 Timm, R. 275  
 Trudel, C.P. 279
- Udomkesmalee, S. 451  
 Uliashin, A. 137
- Van Allen, R.L. 423  
 van Bezoijen, R.W.H. 513  
 van den Bosch, P.P.J. 325  
 van Swieten, A. 325  
 Van't Veld, R. 257  
 Vanden Beukel, J. 519  
 Veltman, A. 325  
 Verde, L. 429  
 Vijayamohana Kumar, S.R. 235  
 Vinokurov, A. 137
- Welch, R.V. 151  
 Well, K.H. 77  
 Wienand, St. 301  
 Wiktor, P. 241, 525  
 Wöhlke, W. 369  
 Wright, M. 307  
 Wullstein, P. 145
- Yang Jiachi 189  
 Zhou Guangrui 189

## KEYWORD INDEX

- Acceleration control, 435  
Acceptance tests, 137  
Active damping, 463  
Active optics, 457  
Actuators, 67, 241, 525  
Adaptive control, 103, 121, 127, 287, 355  
Adaptive optics, 471  
Adaptive systems, 115, 269  
Advanced automation, 263  
Aeronomy, 519  
Aerospace control, 33, 109, 221, 251, 381, 429, 501  
Aerospace plane, 489  
Aerospace trajectories, 77  
AI-applications for space, 275  
Alignment, 401  
Angular measurement, 241, 507  
Anomaly diagnosis, 257  
AOCS, 11, 159  
Artificial intelligence, 251, 263, 269  
Ascent trajectory, 477  
Attitude and orbit control, 221  
Attitude control system, 137  
Attitude control, 151, 197, 293, 507  
Attitude determination, 513  
Automatic control, 33, 417  
Automation, 33, 257  
Autonomous systems architectures, 43  
Autonomous systems, 313, 355, 513  
  
Bang-bang controls, 483  
Boresight, 401  
Brushless DC, 325  
  
C++, 43  
Characteristic of Chinese spacecraft control system, 189  
Clocks stability, 531  
CMG, 197  
Cognitive systems, 269  
Collision avoidance, 319, 369  
Combat aircraft, 263  
Command and control, 43  
Complex payload, 293  
  
Computer aided design, 381  
Computer control, 471  
Computer-aided system design, 439  
Contour curvature, 451  
Control applications, 241, 251, 417, 463, 471  
Control architectures, 363  
Control design and flexibility, 325  
Control system design, 387, 439  
Control system requirements analysis, 363  
Control system synthesis, 67, 363  
Control systems design, 57, 109  
Control technology, 463  
Control, 121  
Controllers, 381  
Cooperative control, 287  
Cooperative Rendez-vous, 531  
Cranes, 251  
  
Damping, 435  
Decoupling, 435  
Diagnosis, 275  
Digital autopilot, 235  
Digital control, 103, 183, 417, 435  
Digital signal processing, 115  
Direct collocation, 477  
Direct digital control, 183  
Direct multiple shooting, 477  
Distributed architectures, 1  
Disturbance rejection, 183  
DMC, 159  
Drag-free control, 241  
DSMC simulations, 519  
Dynamic control, 293  
Dynamic output feedback control, 235  
Dynamic response, 57  
  
Earth motion, 531  
Earth rigidity, 531  
Environment modelling, 301  
Estimation, 525  
Existence of contact points, 483  
Experiments, 115, 293  
Expert systems, 257, 269  
Extensibility, 43

- Fault recovery, 513
- Fault tolerance, 1
- Feature extraction, 451
- Feedback control, 241, 495
- Feedback linearization, 103, 489
- Feedforward control, 235
- Finite element method, 429
- Flexible aerospace structures, 57
- Flexible members, 293
- Flexible structures, 409, 463
- Flexure, 401
- Flight control, 97, 103
- Flight Management Systems (FMS), 531
- Force control, 279, 307, 525
- Fourier transform, 451
- Free flyer, 369
- Frequency response, 381
- Fuzzy control, 251
- Fuzzy system, 251
  
- Geostationary satellites, 245
- Ground support systems, 151
- Ground tests, 137
- Guidance systems, 495
- Guidance, 121, 221
- Gyroscopes, 241
  
- H-infinity, 97
- Harmonic drive, 325
- Health monitoring, 445
- Helicopters, 401
- Helium thruster plumes, 519
- Helium thrusters, 241
- Hierarchical systems, 423
- Hierarchically intelligent control, 363
- Hypersonic vehicles, 495
  
- ICDS, 159
- Identification, 507
- Image processing, 507
- Impingement, 519
- In-flight management, 263
- In-orbit experience, 11
- Inertial measurement unit, 137
- Inertial navigation, 513
- Inertial, 401
- Inference processes, 269
- Initial orbit determination, 257
- Integration with operational environment, 275
- Intelligent sensors, 513
- Interior point conditions, 483
- Interoperability, 43
- Inverse Jacobian, 287
- Iterative methods, 307
  
- Knowledge based control, 301
- Laboratory techniques, 417, 463
- Large space structures, 375
- Laser beam control, 423
- Laser metrology, 471
- Launch vehicle, 235
- Launcher, 477
- Learning systems, 313
- Least-squares estimation, 451
- Life cycle, 11
- Linear optimal control, 375
- Linear quadratic regulator theory, 235
- Linearization techniques, 197
- Localization, 445
- Loop-shaping, 97
  
- Macro planning, 313
- Man-machine interface, 263
- Man-machine systems, 269
- Manipulators, 33
- Mission analysis, 355
- Modal characterization, 409
- Modal control, 417
- Model reduction, 57
- Modeling, 57, 67, 221, 429
- Multiobjective optimization, 251
- Multiple shooting method, 483
- Multipoint boundary-value problem, 483
- Multivariable control systems, 183
- Multivariable systems, 57
- MX filter, 115
  
- Nonlinear control systems, 103, 121, 501
- Nonlinear programming, 77
- Numerical methods, 77, 381
- Nutation, 531
  
- Object Oriented Systems, 43
- OLYMPUS, 245
- On-board computer complex, 137
- Optical interferometers, 463
- Optical navigation, 513
- Optical sensor, 137
- Optical variables control, 67
- Optimal control, 77, 109, 183, 483, 495
- Optimization, 77, 387, 477
- Orbit control, 245
- Overall safety, 531
  
- Parallel processing, 1
- Parameter identification, 287
- Parameter tuning, 313
- Pattern recognition, 451, 513
- Performance verification, 57

- Perturbations by attitude control, 245  
 Plume measurements, 519  
 Pointing control systems, 457  
 Poles, 445  
 Position control, 307  
 Position determination, 513  
 Positive real synthesis, 375  
 Precession, 531  
 Precision pointing, 423  
 Propulsion, 525  
  
 Rarified nozzle flows, 519  
 Recoverable satellite control, 189  
 Recursive least squares, 103, 525  
 Reduced models, 495  
 Reference models, 363  
 Rendezvous scenario, 369  
 Reusability, 43  
 Robot command languages, 43  
 Robot control, 307  
 Robotics, 33  
 Robots, 279, 301, 319, 363  
 Robust control, 97, 197, 417, 439  
 Robust multivariable control, 375  
 Robustness, 121, 435  
  
 Safe trajectory, 369  
 Sampled data systems, 183  
 Satellite attitude control, 439  
 Satellite control, 221, 241, 257, 387, 423, 525  
 Satellites, 151  
 Scheduling, 97, 275  
 Segmented optics, 409  
 Sensor data fusion, 301  
 Sensors, 67, 127, 507  
 Shape memory alloys, 115  
 Simulation, 11, 57, 263, 325, 439, 477  
 Singular controls, 483  
 Singular perturbations, 489  
 Singularity avoidance, 197  
 SIP, 159  
 Smart technology, 1  
 Software tools, 363, 439  
 Software, 77  
 Space astronomical observatories, 457  
 Space manipulators, 293  
 Space optics, 471  
 Space robotics, 287, 355  
 Space robots, 33, 313  
 Space station, 279  
 Space vehicles, 151, 387, 483, 501, 513  
  
 Spacecraft control, 519  
 Spacecraft operations, 355  
 Spacecraft testing, 151  
 Spacecraft, 121  
 SSR Mode S, 531  
 Star pattern recognition, 507  
 Star sensor, 507  
 Star trackers, 513  
 State inequality constraints, 483  
 Station keeping, 245  
 Steering law, 197  
 Stellar interferometry, 471  
 Stochastic systems, 471  
 Structural control, 387  
 Structural controllability, 127  
 Structural flaws, 445  
 Sun-synchronous satellite control, 189  
 System failure and recovery, 103  
 System identification, 57, 115, 409, 525  
 System integrity, 151, 445  
  
 Target tracking, 423  
 Task-level programming, 319  
 Temporal knowledge based systems, 43  
 Temporal planning, 43  
 Test, 11  
 Thrusters, 525  
 Tides (maritime and crust), 531  
 Tracking systems, 429  
 Train control, 251  
 Trajectory guidance, 489  
 Transfer functions, 445  
  
 Uncooled optics, 423  
 Universal times, 531  
  
 Validation, 11  
 Variable structure control, 489  
 Vibration control, 57, 375, 423, 429  
 Vibration isolation, 463  
 Vigilance, 531  
 Vision systems, 279  
 VSTOL, 97  
  
 Wavefront sensing, 457  
  
 Zeros, 445  
  
 3-body problem, 531  
 3D vision, 301  
  
 4D Trajectory, 531

**SYMPOSIA VOLUMES**

ADALI & TUNALI: Microcomputer Application in Process Control  
 AKASHI: Control Science and Technology for the Progress of Society, World Congress 1981, 7 volumes  
 ALBERTOS & DELA PUENTE: Components, Instruments and Techniques for Low Cost Automation and Applications  
 ALONSO CONCHEIRO: Real Time Digital Control Applications \*  
 AMOUROUX & EL JAI: Control of Distributed Parameter Systems (1989)  
 ATHERTON: Multivariable Technological Systems  
 BABARY & LE LETTY: Control of Distributed Parameter Systems (1982)  
 BALCHEN: Automation and Data Processing in Aquaculture  
 BALCHEN *et al*: Dynamics and Control of Chemical Reactors (DYCORD+ '92)  
 BANKS & PRITCHARD: Control of Distributed Parameter Systems (1977)  
 BANYASZ & KEVICZKY: Identification and System Parameter Estimation (1991)  
 BAOSHENG HU: Analysis, Design and Evaluation of Man-Machine Systems (1989)  
 BARKER: Computer Aided Design in Control Systems (1991)  
 BARKER & YOUNG: Identification and System Parameter Estimation (1985)  
 BASANEZ, FERRATE & SARIDIS: Robot Control "SYROCO '85"  
 BASAR & PAU: Dynamic Modelling and Control of National Economies (1983)\*  
 BAYLIS: Safety of Computer Control Systems (1983)\*  
 BEKEY & SARIDIS Identification and System Parameter Estimation (1982)  
 BINDER & PERRET: Components and Instruments for Distributed Computer Control Systems\*  
 CALVAER: Power Systems, Modelling and Control Applications  
 Van CAUWENBERGHE: Instrumentation and Automation in the Paper, Rubber, Plastics and Polymerisation Industries (1980)\* (1983)  
 CHEN HAN-FU: Identification and System Parameter Estimation (1988)  
 CHEN ZHEN-YU: Computer Aided Design in Control Systems (1988)  
 CHRETIEN: Automatic Control in Space (1985)  
 CHRISTODULAKIS: Dynamic Modelling and Control of National Economies (1989)  
 COBELLINI & MARIANI: Modelling and Control in Biomedical Systems  
 CUENOD: Computer Aided Design of Control Systems\*  
 DA CUNHA: Planning and Operation of Electric Energy Systems  
 DeBRA & GOTTCZEIN: Automatic Control in Aerospace (1992)  
 DE CARLI: Low Cost Automation  
 De GIORGIO & ROVEDA: Criteria for Selecting Appropriate Technologies under Different Cultural, Technical and Social Conditions\*  
 DEVANATHAN: Intelligent Tuning and Adaptive Control  
 DHURJATI & STEPHANOPOULOS: On-line Fault Detection and Supervision in the Chemical Process Industries  
 DUBUSSON: Information and Systems  
 DUGARD *et al*: Adaptive Systems in Control and Signal Processing 1992  
 EHRENBERGER: Safety of Computer Control Systems (SAFECOMP'88)  
 ELLIS: Control Problems and Devices in Manufacturing Technology (1980)\*  
 FERRATE & PUENTE: Software for Computer Control (1982)  
 FLEISS: Nonlinear Control Systems Design (1992)  
 FLEISSNER: Systems Approach to Appropriate Technology Transfer  
 FLORIAN & HAASE: Software for Computer Control (1986)  
 FRANKE & KRAUS: Design Methods of Control Systems  
 GEERING & MANSOUR: Large Scale Systems: Theory and Applications (1986)  
 GENSER *et al*: Control in Transportation Systems (1986)  
 GERTLER & KEVICZKY: A Bridge Between Control Science and Technology, World Congress 1984, 6 volumes\*  
 GHONAIMY: Systems Approach for Development (1977)  
 GU YAN & CHEN ZHEN-YU: Automation in Mining, Mineral and Metal Processing 1992  
 HAIMES & KINDLER: Water and Related Land Resource Systems  
 HARDT: Information Control Problems in Manufacturing Technology (1982)

HARVEY & EMSPAK: Automated Systems Based on Human Skill  
 HERBST: Automatic Control in Power Generation Distribution and Protection  
 HRUZ & CICEL: Automatic Measurement and Control in Woodworking Industry-Lignoautomatica'86  
 HUSSON: Advanced Information Processing in Automatic Control  
 ISERMANN: Automatic Control, World Congress 1987, 10 volumes  
 ISERMANN: Identification and System Parameter Estimation (1979)  
 ISERMANN & FREYERMUTH: Fault Detection, Supervision and Safety for Technical Processes  
 ISERMANN & KALTENECKER: Digital Computer Applications to Process Control\*  
 ISIDORI: Nonlinear Control Systems Design  
 JAAKSOO & UTKIN: Automatic Control, World Congress 1990, 6 volumes  
 JANSEN, PAU & STRASZAK: Dynamic Modelling and Control of National Economies (1980)  
 JELLALI: Systems Analysis Applied to Management of Water Resources  
 JOHANSEN & RIJNSDORP: Analysis, Design, and Evaluation of Man-Machine Systems\*  
 JOHNSON: Adaptive Systems in Control and Signal Processing  
 JOHNSON: Modelling and Control of Biotechnological Processes  
 KARIM & STEPHANOPOULOS: Modeling and Control of Biotechnical Processes  
 KAYA & WILLIAMS: Instrumentation and Automation in the Paper, Rubber, Plastics and Polymerization Industries (1986)  
 KHEIR *et al*: Advances in Control Education  
 KLAMT & LAUBER: Control in Transportation Systems (1984)\*  
 KOPACEK & GENSER: Skill Based Automated Production  
 KOPACEK, TROCH & DESOYER: Theory of Robots  
 KOPPEL: Automation in Mining, Mineral and Metal Processing (1989)  
 KUMMEL: Adaptive Control of Chemical Processes (ADCHEM'88)  
 LARSEN & HANSEN: Computer Aided Design in Control and Engineering Systems  
 LEININGER: Computer Aided Design of Multivariable Technological Systems\*  
 LEONHARD: Control in Power Electronics and Electrical Drives (1977)\*  
 LESKIEWICZ & ZAREMBA: Pneumatic and Hydraulic Components and Instruments in Automatic Control\*  
 LEVIS & STEPHANOU: Distributed Intelligence Systems (1991)  
 LINKENS & ATHERTON: Trends in Control and Measurement Education  
 MACLEOD & HEHER: Software for Computer Control (SOCOCO'88)  
 MAHALANABIS: Theory and Application of Digital Control  
 MANCINI, JOHANSEN & MARTENSSON: Analysis, Design and Evaluation of Man-Machine Systems (1985)  
 MARTOS, PAU & ZIERMANN: Dynamic Modelling and Control of National Economies (1986)  
 McGREGORY: Dynamics and Control of Chemical Reactors and Distillation Columns  
 MLADENOV: Distributed Intelligence Systems: Methods and Applications  
 MUNDAY: Automatic Control in Space (1979)  
 NAJIM & ABDEL FATTAH: System Approach for Development (1980)\*  
 NAJIM & DUFOUR: Advanced Control of Chemical Processes  
 NIEMI: A Link Between Science and Applications of Automatic Control, World Congress 1978, 4 volumes\*  
 NISHIKAWA & KAYA: Energy Systems, Management and Economics  
 NISHIMURA: Automatic Control in Aerospace  
 NORRIE & TURNER: Automation for Mineral Resource Development  
 NOVAK: Software for Computer Control (1979)  
 OLLERO & CAMACHO: Intelligent Components and Instruments for Control Applications  
 OSHEA & POLIS: Automation in Mining, Mineral and Metal Processing (1980)  
 OSHIMA: Information Control Problems in Manufacturing Technology (1977)  
 PAUL: Digital Computer Applications to Process Control (1985)  
 PERRIN: Control, Computers, Communications in Transportation  
 PONOMARYOV: Artificial Intelligence  
 PUENTE & NEMES: Information Control Problems in Manufacturing Technology (1989)

RAMAMOORTY: Automation and Instrumentation for Power Plants  
 RANTA: Analysis, Design and Evaluation of Man-Machine Systems (1988)  
 RAUCH: Applications of Nonlinear Programming to Optimization and Control\*  
 RAUCH: Control of Distributed Parameter Systems (1986)\*  
 REINISCH & THOMA: Large Scale Systems: Theory and Applications (1989)  
 REMBOLD: Robot Control (SYROCO'88)  
 RIJNSDORP: Case Studies in Automation Related to Humanization of Work  
 RIJNSDORP *et al*: Dynamics and Control of Chemical Reactors (DYCORD'89)  
 RIJNSDORP, PLOMP & MÖLLER: Training for Tomorrow-Educational Aspects of Computerized Automation  
 ROOS: Economics and Artificial Intelligence  
 SANCHEZ: Fuzzy Information, Knowledge Representation and Decision Analysis\*  
 SAWARAGI & AKASHI: Environmental Systems Planning, Design and Control  
 SINHA & TELKSNYS: Stochastic Control  
 SMEDEMA: Real Time Programming (1977)\*  
 STASSEN: Analysis, Design and Evaluation of Man-Machine Systems (1992)

#### WORKSHOP VOLUMES

ASTROM & WITTENMARK: Adaptive Systems in Control and Signal Processing  
 BOULLART *et al*: Industrial Process Control Systems  
 BRODNER: Skill Based Automated Manufacturing  
 BULL: Real Time Programming (1983)\*  
 BULL & WILLIAMS: Real Time Programming (1985)  
 CAMPBELL: Control Aspects of Prosthetics and Orthotics\*  
 CHESTNUT: Contributions of Technology to International Conflict Resolution (SWISS)  
 CHESTNUT *et al*: International Conflict Resolution using Systems Engineering (SWISS)  
 CHESTNUT *et al*: Supplemental Ways for Improving International Stability\*  
 CICHOCKI & STRASZAK: Systems Analysis Applications to Complex Programs  
 CRESPO & DE LA PUENTE: Real Time Programming (1988)  
 CRONHJORT: Real Time Programming (1978)\*  
 DI PILLO: Control Applications of Nonlinear Programming and Optimization  
 ELZER: Experience with the Management of Software Projects  
 FLEMING & JONES: Algorithms and Architectures for Real-Time Control  
 GELLIE & TAVAST: Distributed Computer Control Systems (1982)\*  
 GENSER *et al*: Safety of Computer Control Systems (SAFECOMP'89)  
 GOODWIN: Robust Adaptive Control  
 HAASE: Real Time Programming (1980)  
 HALANG & RAMAMRITHAM: Real Time Programming (1991)  
 HALME: Modelling and Control of Biotechnical Processes\*  
 HARRISON: Distributed Computer Control Systems (1979)  
 HASEGAWA: Real Time Programming (1981)\*  
 HASEGAWA & INOUE: Urban, Regional and National Planning - Environmental Aspects  
 JAMSA-JOUNELA & NIEMI: Expert Systems in Mineral and Metal Processing  
 JANSEN & BOULLART: Reliability of Instrumentation Systems for Safeguarding and Control  
 KOPETZ & RODD: Distributed Computer Control Systems (1991)  
 KOTOB: Automatic Control in Petroleum, Petrochemical and Desalination Industries  
 LANDAU, TOMIZUKA & AUSLANDER: Adaptive Systems in Control and Signal Processing  
 LAUBER: Safety of Computer Control Systems (1979)

STRASZAK: Large Scale Systems: Theory and Applications (1983)  
 SUBRAMANYAM: Computer Applications in Large Scale Power Systems  
 TAL: Information Control Problems in Manufacturing Technology (1986)  
 TITLI & SINGH: Large Scale Systems: Theory and Applications (1980)\*  
 TROCH, DESOYER & KOPACEK: Robot Control (1991)  
 TROCH, KOPACEK & BREITENECKER: Simulation of Control Systems  
 UHI AHN: Power Systems and Power Plant Control (1989)  
 VALADARES TAVARES & EVARISTO DA SILVA: Systems Analysis Applied to Water and Related Land Resources  
 VAN WOERKOM: Automatic Control in Space (1982)  
 WANG PINGYANG: Power Systems and Power Plant Control  
 WELFONDER *et al*: Control of Power Plants and Power Systems  
 WESTERLUND: Automation in Mining, Mineral and Metal Processing (1983)  
 YANG JIACHI: Control Science and Technology for Development  
 YOSHITANI: Automation in Mining, Mineral and Metal Processing (1986)  
 ZAREMBA: Information Control Problems in Manufacturing Technology (1992)  
 ZWICKY: Control in Power Electronics and Electrical Drives (1983)

LOTOTSKY: Evaluation of Adaptive Control Strategies in Industrial Applications  
 MAFFEZZONI: Modelling and Control of Electric Power Plants (1984)\*  
 MARTIN: Design of Work in Automated Manufacturing Systems\*  
 McAVOY: Model Based Process Control  
 MEYER: Real Time Programming (1989)\*  
 MILLER: Distributed Computer Control Systems (1981)  
 MILOVANOVIC & ELZER: Experience with the Management of Software Projects (1988)  
 MOWLE & ELZER: Experience with the Management of Software Projects (1989)  
 NARITA & MOTUS: Distributed Computer Control Systems (1989)  
 OLLUS: Digital Image Processing in Industrial Applications - Vision Control  
 QUIRK: Safety of Computer Control Systems (1985)(1986)  
 RAUCH: Control Applications of Nonlinear Programming\*  
 REMBOLD: Information Control Problems in Manufacturing Technology (1979)  
 RODD: Artificial Intelligence in Real Time Control (1989)  
 RODD: Distributed Computer Control Systems (1983)  
 RODD: Distributed Databases in Real Time Control  
 RODD & LALIVE D'EPINAY: Distributed Computer Control Systems (1988)  
 RODD & MULLER: Distributed Computer Control Systems (1986)  
 RODD & SUSKI: Artificial Intelligence in Real Time Control  
 RODD & SUSKI: Artificial Intelligence in Real-Time Control (1991)  
 SIGUERDIDJANE & BERNHARD: Control Applications of Nonlinear Programming and Optimization  
 SINGH & TITLI: Control and Management of Integrated Industrial Complexes\*  
 SKELTON & OWENS: Model Error Concepts and Compensation  
 SOMMER: Applied Measurements in Mineral and Metallurgical Processing  
 SUSKI: Distributed Computer Control Systems (1985)  
 SZLANKO: Real Time Programming (1986)  
 TAKAMATSU & O'SHIMA: Production Control in Process Industry  
 UNBEHA UEN: Adaptive Control of Chemical Processes  
 VILLA & MURARI: Decisional Structures in Automated Manufacturing

\*Out of stock • High quality repro print available. Details of prices sent on request from the IFAC Publisher.

#### IFAC related titles

BROADBENT & MASUBUCHI: Multilingual Glossary of Automatic Control Technology  
 EYKHOFF: Trends and Progress in System Identification  
 NALECZ: Control Aspects of Biomedical Engineering